

中草藥研究中心

2018 年 9 月 1 日~2019 年 8 月 31 日

論文集(下)



CHANG GUNG UNIVERSITY OF SCIENCE AND TECHNOLOGY

長庚科技大學
中草藥研究中心
2018年9月1日~2019年8月31日
論文集
目 錄

(下冊)

序號	期刊論文	學校主要 負責教師	頁碼
76.	Yang, H. C.; Yu, H.; Liu, Y. C.; Chen, T. L.; Stern, A.; Lo, S. J.; Chiu, D. T. IDH-1 deficiency induces growth defects and metabolic alterations in GSPD-1-deficient <i>Caenorhabditis elegans</i> . <i>J Mol Med (Berl)</i> 97:385-396; 2019. DOI: 10.1007/s00109-018-01740-2.	趙崇義	977
77.	Chi, H. C.; Tsai, C. Y.; Tsai, M. M.; Yeh, C. T.; Lin, K. H. Molecular functions and clinical impact of thyroid hormone-triggered autophagy in liver-related diseases. <i>J Biomed Sci</i> 26:24; 2019. DOI: 10.1186/s12929-019-0517-x.	蔡明明、 林光輝	989
78.	Jayasree, A.; Kottappally Thankappan, S.; Ramachandran, R.; Sundaram, M.N.; Chen, C. H.; Mony, U.; Chen, J. P.; Jayakumar, R. Bioengineered Braided Micro-Nano (Multiscale) Fibrous Scaffolds for Tendon Reconstruction. <i>ACS Biomaterials Science and Engineering</i> 5:1476-1486; 2019. DOI: 10.1021/acsbiomaterials.8b01328.	陳志平	1004
79.	Sethy, B.; Hsieh, C. F.; Lin, T. J.; Hu, P. Y.; Chen, Y. L.; Lin, C. Y.; Tseng, S. N.; Horng, J. T.; Hsieh, P. W. Design, Synthesis, and Biological Evaluation of Itaconic Acid Derivatives as Potential Anti-Influenza Agents. <i>J Med Chem</i> 62:2390-2403; 2019. DOI: 10.1021/acs.jmedchem.8b01683.	謝佩文、 洪錦堂	1015
80.	Yao, J. W.; Chi, W. C.; Xu, J. H.; Lee, G. H.; Chiang, M. Y.; Peng, B. R.; Lin, N. C.; Hu, C. C.; Fang, L. S.; Li, G. Q.; Chang, Y. C.; Hwang, T. L.; Sung, P. J. New hydroperoxybriarane diterpenoids from the octocoral <i>Briareum violaceum</i> . <i>Tetrahedron</i> 75:1510-1516; 2019. DOI: 10.1016/j.tet.2019.01.069.	張祐嘉、 黃聰龍	1029
81.	Jose, G.; Lu, Y. J.; Chen, H. A.; Hsu, H. L.; Hung, J. T.; Anilkumar, T.S.; Chen, J. P. Hyaluronic acid modified bubble-generating magnetic liposomes for targeted delivery of doxorubicin. <i>Journal of Magnetism and Magnetic Materials</i> 474:355-364; 2019. DOI: 10.1016/j.jmmm.2018.11.019.	陳志平	1036
82.	Chen, Y. T.; Huang, H. C.; Hsieh, Y. J.; Fu, S. H.; Li, L.; Chen, C. L.; Chu, L. J.; Yu, J. S. Targeting amine- and phenol-containing metabolites in urine by dansylation isotope labeling and liquid chromatography mass spectrometry for evaluation of bladder cancer biomarkers. <i>J Food Drug Anal</i> 27:460-474; 2019. DOI: 10.1016/j.jfda.2018.11.008.	余兆松	1046

83. Cheng, S. C.; Wu, Y. H.; Huang, W. C.; Pang, J. S.; Huang, T. H.; Cheng, C. Y. Anti-inflammatory property of quercetin through downregulation of ICAM-1 and MMP-9 in TNF- α -activated retinal pigment epithelial cells. *Cytokine* 116:48-60; 2019. DOI: 10.1016/j.cyto.2019.01.001. 黃文忠、鄭靜宜 1061
84. Yu, J. S. From discovery of tyrosine phosphorylation to targeted cancer therapies: The 2018 Tang Prize in Biopharmaceutical Science. *Biomed J* 42:80-83; 2019. DOI: 10.1016/j.bj.2019.03.004. 余兆松 1074
85. Hsieh, T. Y.; Chang, Y.; Wang, S. J. Piperine-mediated suppression of voltage-dependent Ca(2+) influx and glutamate release in rat hippocampal nerve terminals involves 5HT1A receptors and G protein betagamma activation. *Food Funct* 10:2720-2728; 2019. DOI: 10.1039/c8fo02189a. 王素珍 1078
86. Lin, C. Y.; Hsu, C. Y.; Elzoghby, A. O.; Alalaiwe, A.; Hwang, T. L.; Fang, J. Y. Oleic acid as the active agent and lipid matrix in cilomilast-loaded nanocarriers to assist PDE4 inhibition of activated neutrophils for mitigating psoriasis-like lesions. *Acta Biomater* 90:350-361; 2019. DOI: 10.1016/j.actbio.2019.04.002. 黃聰龍、方嘉佑 1087
87. Li, C. Y.; Lo, I. W.; Hsueh, Y. P.; Chung, Y. M.; Wang, S. W.; Korinek, M.; Tsai, Y. H.; Cheng, Y. B.; Hwang, T. L.; Wang, C.C.C.; Chang, F. R.; Wu, Y.-C. Epigenetic Manipulation Induces the Production of Coumarin-Type Secondary Metabolite from *Arthrobotrys foliicola*. *Israel Journal of Chemistry* 59:432-438; 2019. DOI: 10.1002/ijch.201800162. 黃聰龍 1099
88. Gong, Y. N.; Tsao, K. C.; Chen, G. W.; Wu, C. J.; Chen, Y. H.; Liu, Y. C.; Yang, S. L.; Huang, Y. C.; Shih, S. R. Population dynamics at neuraminidase position 151 of influenza A (H1N1)pdm09 virus in clinical specimens. *J Gen Virol* 100:752-759; 2019. DOI: 10.1099/jgv.0.001258. 施信如 1107
89. Huang, W. C.; Peng, H. L.; Hu, S.; Wu, S. J. Spilanthol from Traditionally Used *Spilanthes acmella* Enhances AMPK and Ameliorates Obesity in Mice Fed High-Fat Diet. *Nutrients* 11, pii: E991; 2019. DOI: 10.3390/nu11050991. 黃文忠、吳淑如 1115
90. Huang, T. H.; Lin, C. F.; Alalaiwe, A.; Yang, S. C.; Fang, J. Y. Apoptotic or Antiproliferative Activity of Natural Products against Keratinocytes for the Treatment of Psoriasis. *Int J Mol Sci* 20, pii: E2558; 2019. DOI: 10.3390/ijms20102558. 林傳福、方嘉佑 1130
91. Huang, W. C.; Huang, C. H.; Hu, S.; Peng, H. L.; Wu, S. J. Topical Spilanthol Inhibits MAPK Signaling and Ameliorates Allergic Inflammation in DNCB-Induced Atopic Dermatitis in Mice. *Int J Mol Sci* 20, pii: E2490; 2019. DOI: 10.3390/ijms20102490. 黃文忠、吳淑如 1154
92. Sun, N. K.; Kohli, A.; Huang, S. L.; Chang, T. C.; Chao, C. C. Androgen receptor transcriptional activity and chromatin modifications on the ABCB1/MDR gene are critical for taxol resistance in ovarian cancer cells. *J Cell Physiol* 234:8760-8775; 2019. DOI: 10.1002/jcp.27535. 孫念康 1167

93. Lee, W. R.; Hsiao, C. Y.; Huang, T. H.; Wang, C. L.; Alalaiwe, A.; Chen, E. L.; Fang, J. Y. Post-irradiation recovery time strongly influences fractional laser-facilitated skin absorption. *Int J Pharm* 564:48-58; 2019. DOI: 10.1016/j.ijpharm.2019.04.043. 蕭千祐、方嘉佑 1183
94. Cheng, S. C.; Huang, W. C.; JH, S. P.; Wu, Y. H.; Cheng, C. Y. Quercetin Inhibits the Production of IL-1 β -Induced Inflammatory Cytokines and Chemokines in ARPE-19 Cells via the MAPK and NF- κ B Signaling Pathways. *Int J Mol Sci* 20, pii: E2957; 2019. DOI: 10.3390/ijms20122957. 黃文忠、鄭靜宜 1194
95. Lin, C. C.; Hsiao, L. D.; Cho, R. L.; Yang, C. M. Carbon Monoxide Releasing Molecule-2-Upregulated ROS-Dependent Heme Oxygenase-1 Axis Suppresses Lipopolysaccharide-Induced Airway Inflammation. *Int J Mol Sci* 20, pii: E3157; 2019. DOI: 10.3390/ijms20133157. 楊春茂 1218
96. Chang, C. J.; Lin, T. L.; Tsai, Y. L.; Wu, T. R.; Lai, W. F.; Lu, C. C.; Lai, H. C. Next generation probiotics in disease amelioration. *J Food Drug Anal* 27:615-622; 2019. DOI: 10.1016/j.jfda.2018.12.011. 賴信志 1241
97. Lu, C. W.; Hung, C. F.; Lin, T. Y.; Hsieh, T. Y.; Wang, S. J. Allicin Inhibits Glutamate Release from Rat Cerebral Cortex Nerve Terminals Through Suppressing Ca(2+) Influx and Protein Kinase C Activity. *J Med Food* 22:696-702; 2019. DOI: 10.1089/jmf.2018.4337. 王素珍 1249
98. Huang, Y. C.; Hsu, C. C.; Wang, J. S. High-Intensity Interval Training Improves Erythrocyte Osmotic Deformability. *Med Sci Sports Exerc* 51:1404-1412; 2019. DOI: 10.1249/MSS.0000000000001923. 王鐘賢 1256
99. Yao, J. W.; Chi, W. C.; Lee, G. H.; Su, J. H.; Hwang, T. L.; Wu, Y. J.; Su, T. R.; Sheu, J. H.; Sung, P.-J. 2-Acetoxybriaranes from *Briareum violaceum*. *Tetrahedron* 75:3751-3757; 2019. DOI: 10.1016/j.tet.2019.05.053. 黃聰龍 1265
100. Shu, C. C.; Wu, L. S.; Wu, M. F.; Lai, H. C.; Wang, P. H.; Cheng, S. L.; Wang, J. Y.; Yu, C. J. Mono- and poly-functional T cells in nontuberculous mycobacteria lung disease patients: Implications in analyzing risk of disease progression. *Cytokine* 120:176-185; 2019. DOI: 10.1016/j.cyto.2019.05.001. 賴信志 1272
101. Liu, C. H.; Hsu, H. L.; Chen, J. P.; Wu, T.; Ma, Y. H. Thrombolysis induced by intravenous administration of plasminogen activator in magnetoliposomes: dual targeting by magnetic and thermal manipulation. *Nanomedicine* 20:101992; 2019. DOI: 10.1016/j.nano.2019.03.014. 陳志平 1282
102. Lee, C. W.; Chi, M. C.; Chang, T. M.; Liu, J. F. Artocarpin induces cell apoptosis in human osteosarcoma cells through endoplasmic reticulum stress and reactive oxygen species. *J Cell Physiol* 234:13157-13168; 2019. DOI: 10.1002/jcp.27986. 李江文 1294

103. Lee, C. W.; Chi, M. C.; Hsu, L. F.; Yang, C. M.; Hsu, T. H.; Chuang, C. C.; Lin, W. N.; Chu, P. M.; Lee, I. T. Carbon monoxide releasing molecule-2 protects against particulate matter-induced lung inflammation by inhibiting TLR2 and 4/ROS/NLRP3 inflammasome activation. *Mol Immunol* 112:163-174; 2019. DOI: 10.1016/j.molimm.2019.05.005. 李江文、楊春茂 1306
104. Huang, W. C.; Gu, P. Y.; Fang, L. W.; Huang, Y. L.; Lin, C. F.; Liou, C. J. Sophoraflavanone G from *Sophora flavescens* induces apoptosis in triple-negative breast cancer cells. *Phytomedicine* 61:152852; 2019. DOI: 10.1016/j.phymed.2019.152852. 黃文忠、林傳福、劉倩君 1318
105. Chen, Y. F.; Chen, W. F.; Wen, Z. H.; Hwang, T. L.; Zhang, Z. J.; Sung, P. J. New bioactive $\Delta^{11}(17)$ -furanoeunicellins from an octocoral *Cladiella* sp. *Phytochem Lett* 33:31-5; 2019. DOI: 10.1016/j.phytol.2019.07.002. 黃聰龍 1328
106. Sheu, J. H.; Peng, B. R.; Fang, L. S.; Hwang, T. L.; Su, J. H.; Wu, Y. C.; Sung, P. J. Hydroperoxyditerpenoids from Octocorals. *Isr J Chem* 59:1-12; 2019. DOI: 10.1002/ijch.201900011. 黃聰龍 1333
107. 林昱文(Yu-Wen Lin);李明怡(Ming-Yi Lee); 魏莉雯(Li-Wen Wei);鍾成沛(Cheng-Pei Chung)。複頻超音波對於臺灣金線連水草物化學組成之影響。中華科技大學學報 76 期 (2019/05), 119-134。 李明怡 1345
108. 吳麗娟(Li-Chuan Wu);陳振智(Cheng-Chih Chen);林志鴻(Chih-Hung Lin)。含雙苯乙炔基之側鏈液晶聚環氧丙烷之合成與鑑定。長庚科技學刊 30 期 (2019/06), 77-85。DOI: 10.6192/CGUST.201906_(30).7. 林志鴻 1361
109. 王如邦(Reuben Wang); 邱群惠(Chun-Hui Chiu)。功能性靜電紡絲纖維薄膜應用於羅漢果皂苷甜味劑之轉化。長庚科技學刊 30 期 (2019/06), 7-16。DOI: 10.6192/CGUST.201906_(30).2. 邱群惠 1370
110. 林琬蓉(Wan-Jung Lin); 李依潔(Yi-Chieh Lee); 謝明發(Ming-Fa Hsieh); 鄭靜宜(Ching-Yi Cheng)。葛根素微脂體製備並評估其對紫外線照射皮膚損傷的影響。長庚科技學刊 30 期 (2019/06), 37-47。DOI: 10.6192/CGUST.201906_(30).4. 鄭靜宜 1380
111. 黃雋(Jyun Huang); 林可欣(Ke-Shin Lin); 劉珍芳(Jen-Fang Liu)。慢性腎臟病合併糖尿病患者之血磷狀況與營養衛教成效。臺灣營養學會雜誌 42 卷 4 期 (2018/12), 121-130。DOI: 10.6691/NSJ.201812_42(4).0002. 劉珍芳 1391
112. 錢桂玉(Kuei-Yu Chien); 張凱馨(Kai-Hsin Chang); 劉珍芳(Jen-Fang Liu); 簡麗瑜(Li-Yu Chien)。健身指導教練對於提供運動營養資訊之學習需求。體育學報 52 卷 S 期 (2019/03), 47-59。DOI: 10.3966/10247297201903520S004. 劉珍芳 1401

113. 張家臻(Chia-Chen Chang); 邱麗玲(Li-Ling Chiu); 薛如婷(Ju-Ting Hsueh)。分析供膳場所人員工作聲音環境之感受與相關因素探討。弘光學報 82 期 (2018/09), 75-86。DOI: 10.6615/HAR.201809_(82).0008 邱麗玲 1414
114. 張家臻(Chia-Chen Chang); 陳惠櫻(Huei-Ying Chen); 李蕙蓉(Huei-Rong Lee); 林宗豪(Tsung-Hao Lin); 謝佩君(Pei-Chun Hsieh); 張雁雲(Yen-Yun Chang); 邱麗玲(Li-Ling Chiu)。國際吞嚥困難飲食標準中文繁體版本。亞東學報 38 (2018/12), 1-18。 邱麗玲 1426



IDH-1 deficiency induces growth defects and metabolic alterations in GSPD-1-deficient *Caenorhabditis elegans*

Hung-Chi Yang¹ · Hsiang Yu² · You-Cheng Liu³ · Tzu-Ling Chen³ · Arnold Stern⁴ · Szecheng J. Lo⁵ · Daniel Tsun-Yee Chiu^{2,3,6,7,8}

Received: 14 August 2018 / Revised: 10 December 2018 / Accepted: 21 December 2018
© The Author(s) 2018

Abstract

NADPH is a reducing equivalent that maintains redox homeostasis and supports reductive biosynthesis. Lack of major NADPH-producing enzymes predisposes cells to growth retardation and demise. It was hypothesized that double deficiency of the NADPH-generating enzymes, GSPD-1 (Glucose-6-phosphate 1-dehydrogenase), a functional homolog of human glucose-6-phosphate dehydrogenase (G6PD), the rate-limiting enzyme of the pentose phosphate pathway, and IDH-1 (isocitrate dehydrogenase-1) affect growth and development in the nematode, *Caenorhabditis elegans* (*C. elegans*). The *idh-1:gspd-1(RNAi)* double-deficient *C. elegans* model displayed shrinkage of body size, growth retardation, slowed locomotion, and impaired molting. Global metabolomic analysis was employed to address whether or not metabolic pathways were altered by severe NADPH insufficiency by the *idh-1:gspd-1(RNAi)* double-deficiency. The principal component analysis (PCA) points to a distinct metabolomic profile of *idh-1:gspd-1(RNAi)* double-deficiency. Further metabolomic analysis revealed that NADPH-dependent and glutamate-dependent amino acid biosynthesis were significantly affected. The reduced pool of amino acids may affect protein synthesis, as indicated by the absence of NAS-37 expression during the molting process. In short, double deficiency of GSPD-1 and IDH-1 causes growth retardation and molting defects, which are, in part, attributed to defective protein synthesis, possibly mediated by altered amino acid biosynthesis and metabolism in *C. elegans*.

Keywords *C. elegans* · GSPD-1 · IDH-1 · Development · Molting · Metabolomic · Amino acid

Introduction

Glucose-6-phosphate dehydrogenase (G6PD) is the first and rate-limiting enzyme in the hexose monophosphate shunt

(HMS), also known as the pentose phosphate pathway (PPP). The classical biochemical role of G6PD is to catalyze the oxidation of glucose-6-phosphate to 6-phosphogluconolactone and concomitantly produce the reduced form of nicotinamide

Hung-Chi Yang and Hsiang Yu contributed equally to this work.

Electronic supplementary material The online version of this article (<https://doi.org/10.1007/s00109-018-01740-2>) contains supplementary material, which is available to authorized users.

✉ Daniel Tsun-Yee Chiu
dtychiu@mail.cgu.edu.tw

¹ Department of Medical Laboratory Science and Biotechnology, Yuanpei University of Medical Technology, Hsinchu, Taiwan

² Department of Medical Biotechnology and Laboratory Sciences, College of Medicine, Chang Gung University, Taoyuan, Taiwan

³ Graduate Institute of Biomedical Sciences, College of Medicine, Chang Gung University, Taoyuan, Taiwan

⁴ New York University School of Medicine, New York, NY, USA

⁵ Department of Biomedical Sciences, College of Medicine, Chang Gung University, Taoyuan, Taiwan

⁶ Research Center for Chinese Herbal Medicine, College of Human Ecology, Chang Gung University of Science and Technology, Taoyuan, Taiwan

⁷ Department of Pediatric Hematology/Oncology, Linkou Chang Gung Memorial Hospital, Taoyuan, Taiwan

⁸ Healthy Aging Research Center, Chang Gung University, Taoyuan, Taiwan

adenine dinucleotide phosphate (NADPH) for antioxidant defense and reductive biosynthesis [1, 2]. G6PD deficiency is the most common enzymopathy affecting 400 million people in the world. Most G6PD mutations are point mutations causing amino acid substitution and reduced enzyme activity. Classically, G6PD deficiency has been linked to red blood cell disorders as the clinical manifestations. Novel functions of G6PD in cellular physiology have been discovered over recent years [3]. G6PD is required for life as severe deficiency of G6PD in mammals and nematodes is lethal for survival and reproduction [4, 5] and plays an important role in embryogenesis [6, 7].

The biological importance of G6PD is largely attributed to the production of NADPH. The reducing equivalent NADPH serves pivotal roles in cellular biology. It maintains cellular redox homeostasis by regenerating reduced glutathione, which is needed for detoxifying elevated oxidants. NADPH is also required for reductive biosynthesis of building blocks. Intracellular NADPH is supported by parallel pathways that are localized in different cellular compartments [8]. In the cytoplasm, the main source of NADPH is the oxidative branch of the PPP. Alternative NADPH-producing pathways include cytosolic malic enzyme (ME1), cytosolic and mitochondrial isocitrate dehydrogenase (IDH1 and IDH2), transhydrogenase (NNT), and cytosolic and mitochondrial methylene tetrahydrofolate dehydrogenase (MTHFD1 and MTHFD2) [9]. Understanding how compartmentalization of NADPH homeostasis affecting cell development in health and diseases presents a major investigative challenge.

The biochemical role of IDHs is the oxidation of isocitrate to oxalosuccinate followed by the decarboxylation and ultimately the production of α -ketoglutarate, which is coupled with the reduction of NADP^+ to NADPH. In humans, IDH1 and IDH2 are NADP^+ -dependent enzymes, while IDH3 is a NAD^+ -dependent multi-subunit mitochondrial enzyme. Human IDH1 localizes in the cytoplasm and peroxisome and is highly expressed in the liver. Human IDH2, which has the mitochondrial signal peptide at the amino terminus, localizes in mitochondria and is highly expressed in mammalian muscle, heart, and lymphocyte [10]. IDH1 is associated with lipid metabolism and glucose sensing [11, 12], whereas IDH2 regulates oxidative respiration [13]. In *Caenorhabditis elegans* (*C. elegans*), IDH-1 is predicted as a cytosolic enzyme, whereas IDH-2 is predicted as a mitochondrial enzyme [14]. Although the enzymatic activity of IDH1 has been discovered decades ago, the biological function of wild type (WT) IDH1 is still controversial. Compared to WT IDH1, oncogenic IDH1/2 mutants are well studied and received considerable attention. IDH1/2 mutations have been found in glioma, glioblastoma, acute myelogenous leukemia, chondrosarcoma, and enchondroma [15, 16]. Animal study shows that IDH null mice are healthy and fertile at steady state, while the liver displays altered amino acid utilization [17, 18].

How severe NADPH insufficiency, as a consequence of impairment of different NADPH-producing systems, affects metabolic networks and links to pathophysiology of an organism has not been defined. The notion that NADPH is indispensable for life is supported by the fact that knockdown of NADPH-producing enzymes leads to growth arrest and cell demise. G6PD-deficient human foreskin fibroblasts display slow growth and early onset of senescence [19]. A yeast model with co-disruption of major NADPH sources (G6PD and cytosolic IDH) undergoes growth inhibition and loses viability [20]. Whereas loss of G6PD or IDH alone fails to induce a growth defect, a NADPH compensatory mechanism at the cellular level may maintain NADPH homeostasis and warrant normal development. However, the contribution from each NADPH-producing system at the organismal level remains unclear.

Further study of NADPH-producing systems by applying metabolomic technology to *gspd-1* (G6PD homolog) and *idh-1* double-deficient *C. elegans* model will help in clarifying the role of redox homeostasis and regulation in growth and development. Metabolomics is a novel platform of systems biology that aims to characterize all small molecule metabolites (metabolome) in various forms of biological samples. It is a powerful tool to most closely reflect phenotypic expression and it acutely pinpoints the perturbations within metabolic networks. Such metabolic disturbances can be attributed to downstream alterations of genomic and proteomic outcomes. Current advances place metabolomics in the armamentarium of cutting-edge strategies to dissect the metabolic networks of human and animal models in health and diseases. The intermediary metabolic network is conserved among eukaryotic organisms. The nematode *C. elegans* has orthologs for most human metabolic enzymes, including G6PD and IDH1 [21]. *C. elegans* is a simple and ideal biological system to model human metabolic disturbances. A number of *C. elegans* studies have taken advantage of different metabolomic approaches, including nuclear magnetic resonance (NMR) spectroscopy, gas/liquid chromatography-coupled mass spectrometry (GC/LC-MS) for analyzing the metabolic pathways in a whole worm [22–28]. Lipidomics has been employed in characterizing the molecular pathway in *gspd-1(RNAi)* *C. elegans*. Embryonic lethality occurs through the induction of lipid oxidative damage and activation of lipid-modifying enzymes as identified by lipidomics [6].

In the current study, a global metabolomic platform has been employed for analyzing the metabolome of *idh-1:gspd-1(RNAi)* double-deficient *C. elegans*. Phenotypic characterization has shown that several developmental impairments are found in this double mutant, including defective molting and reduced growth (small body size, delayed growth, and slowed locomotion). The global metabolomic study has also shown that several amino acid metabolic pathways are altered, most notably in those amino acids requiring NADPH for their

synthesis and metabolism, such as the biosynthesis of valine, leucine, isoleucine; phenylalanine, tyrosine, and tryptophan biosynthesis as well as the metabolism of glutamine and glutamate. These findings enhance our understanding of the causal relationship between insufficient NADPH supply, altered amino acid metabolism, and the resulting developmental defects.

Results

Growth retardation and molting defect of *idh-1;gspd-1(RNAi)* double-deficient *C. elegans*

Mutants of isocitrate dehydrogenases were used to investigate the complementary roles of cytoplasmic NADPH-producing pathways during growth and development. In brief, *gspd-1* RNAi was used in *idh-1* and *idh-2* deletion mutants to generate *idh-1;gspd-1(RNAi)* and *idh-2;gspd-1(RNAi)* double-deficient *C. elegans*, respectively (Supplementary Fig. S1). After 72 h, *idh-1;gspd-1(RNAi)* double-deficient *C. elegans*, compare to controls including Mock, *gspd-1(RNAi)*, *idh-1* and *idh-2* mutant as well as *idh-1(RNAi)*; *idh-2* and *idh-1; idh-2(RNAi)* double-deficient *C. elegans*, displayed shrinkage of body size (Fig. 1a). The *idh-1;gspd-1(RNAi)* double-deficient *C. elegans* also showed growth retardation (Supplementary Fig. S2) and slowed locomotion (Supplementary Fig. S3). The body size of *idh-1;gspd-1(RNAi)* double-deficient *C. elegans* was significantly decreased ($P < 0.05$) as determined by the perimeter and area measurements (Fig. 1b, c). Growth defect was not observed in *gspd-1(RNAi)* *C. elegans*. Neither the *idh-1* nor the *idh-2* mutation affected *C. elegans* growth. Likewise, *idh-2;gspd-1(RNAi)* double-deficient *C. elegans* had no reduction in body size.

The *idh-1;gspd-1(RNAi)* double-deficient *C. elegans* displayed an abnormal molting process, which was not observed in Mock, *gspd-1(RNAi)*, and *idh-1* mutant *C. elegans*. Such an abnormal molting process is demonstrated in Fig. 2a showing the molting defects at the head and Fig. 2b showing the molting defects at the tail. *Gspd-1* and *idh-1* suppression results in a disruption of normal molting indicating that *gspd-1* and *idh-1* are complementary to each other.

Reduced NAS-37 protease expression in *idh-1;gspd-1(RNAi)* double-deficient *C. elegans*

Molting is critical for transition between larval stages in nematodes. In *C. elegans*, three key steps, including apolysis (breaking the connection between old cuticle to the hypoderm), cuticle synthesis, and ecdysis (shedding the old cuticle when new cuticle is formed), must be precisely executed in order to grow and survive. Isolation of the mutations responsible for defective ecdysis identifies that *nas-37* is responsible for such a phenotype [29]. The *idh-1;gspd-1(RNAi)*

double-deficient *C. elegans* (Fig. 2a) phenocopied the ecdysis mutants in which the cuticle cannot be shed. The *nas-37::gfp* fusion reporter strain of NAS-37 protease was used to determine whether or not the protein expression was affected during the molting process [29]. The expression level of NAS-37::GFP in all tested *C. elegans* was unaffected at late L3 (Fig. 3a). At late L4, the NAS-37::GFP signal of *idh-1;gspd-1(RNAi)* double-deficient *C. elegans* was reduced, compared with Mock, *gspd-1(RNAi)*, and *idh-1* mutant *C. elegans* (70% lower than that of Mock *C. elegans*, $P < 0.05$) (Fig. 3b). Consistently, reduced NAS-37::GFP expression level of *idh-1;gspd-1(RNAi)* double-deficient *C. elegans* at late L4 was found both at 25 °C (Fig. 3) and 20 °C (Supplementary Fig. S5). This indicates that sufficient NADPH derived from either GSPD-1 or IDH-1 or both is essential for NAS-37 protein expression to maintain normal molting at late L4 in *C. elegans*.

Metabolomic amino acid analysis in *idh-1;gspd-1(RNAi)* double-deficient *C. elegans*

Since decreased protein expression could be, in part, attributed to impaired amino acid metabolism, the metabolomics technique was employed to profile metabolomes of *idh-1;gspd-1(RNAi)* double-deficient *C. elegans* compared to controls. *Idh-1;gspd-1(RNAi)* double-deficient *C. elegans* exhibited distinct metabolic abnormalities as indicated by metabolomics analyses. The principal component analysis (PCA) model showed that while Mock control, *gspd-1(RNAi)*, and *idh-1*-deficient *C. elegans* were clustered together, *idh-1;gspd-1(RNAi)* double-deficient *C. elegans* was separated from the rest of the groups regardless of ESI positive or negative modes (Fig. 4a). The altered metabolites found in *idh-1;gspd-1(RNAi)* double-deficient *C. elegans* were selected in the ESI positive mode (90 metabolites out of 621 candidates) and in the ESI negative mode (34 metabolites out of 223 candidates). Fourteen metabolites of the ESI positive mode and ten metabolites of the ESI negative mode were identified by searching these selected metabolites against our metabolite database [30, 31]. Based on the pathway analysis, the metabolic pathways of several amino acids were found to be greatly affected. These amino acids included valine, leucine, isoleucine, phenylalanine, tyrosine and tryptophan biosynthesis, glutamine, glutamate, phenylalanine, arginine, and proline metabolism (Fig. 4b).

Quantitative analysis indicated that several amino acids from *idh-1;gspd-1(RNAi)* double-deficient *C. elegans* were significantly reduced compared with Mock (Fig. 5a–c). The glutamate level of *idh-1;gspd-1(RNAi)* double-deficient *C. elegans* decreased significantly to 22% of mock ($P < 0.001$) (Fig. 5a). The level of tryptophan was reduced to 63% in the *idh-1;gspd-1(RNAi)* double-deficient *C. elegans* compared with that of Mock ($P < 0.05$) (Fig. 5b), whereas the level of tryptophan of

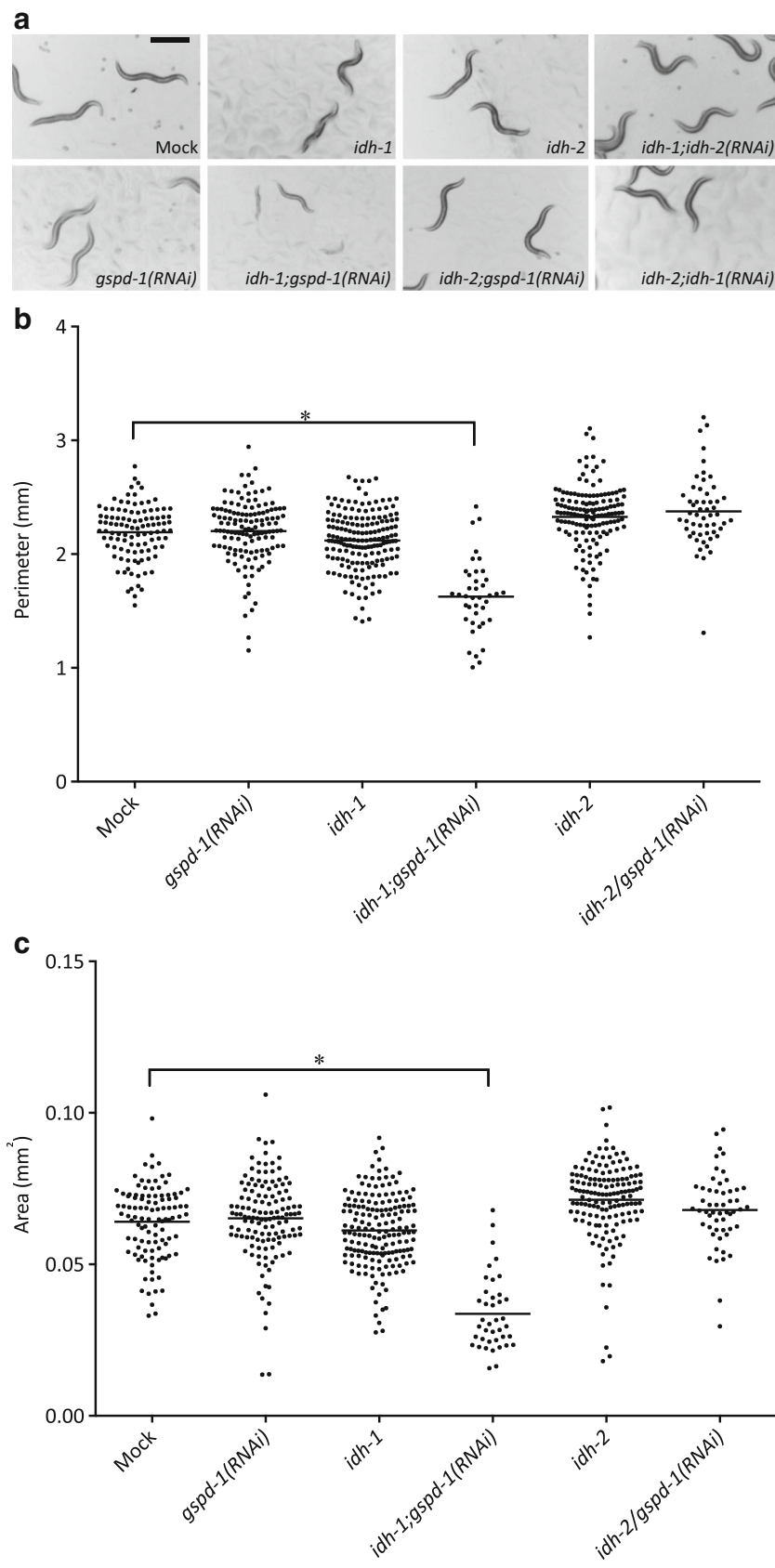


Fig. 1 Decreased body size of *idh-1:gspd-1(RNAi)* double-deficient *C. elegans* compared to mock and other controls. **(a)** The size of *idh-1:gspd-1(RNAi)* double-deficient *C. elegans* was decreased compared to other *C. elegans* strains at 72 h. Adult *C. elegans* were examined by image analysis software under dissecting microscope. *Idh-1:gspd-1(RNAi)* double-deficient *C. elegans* showed decreased perimeter **(b)** and area **(c)** compared to other *C. elegans* strains at 72 h. Each dot represented one adult worm. Horizontal line represented the mean of each *C. elegans* strain. The black scale bar represented 0.5 mm ($n \geq 40$, $*P < 0.05$)

gspd-1(RNAi) or *idh-1* mutant *C. elegans* showed no difference compared with Mock. Phenylalanine and tyrosine levels were reduced in *idh-1:gspd-1(RNAi)* double-deficient *C. elegans* compared with Mock (41% and 34% of mock, respectively, $P < 0.001$), while they were unchanged in *idh-1* mutant *C. elegans*, and *gspd-1(RNAi)* *C. elegans* (Fig. 5b). The biosynthesis of valine, leucine, and isoleucine was reduced in *idh-1:gspd-1(RNAi)* double-deficient *C. elegans* compared with Mock (34% of mock, $P < 0.005$; 22% of mock, $P < 0.001$; 26% of mock, $P < 0.001$, respectively) (Fig. 5c). The level of arginine and proline metabolism was decreased in *idh-1:gspd-1(RNAi)* double-deficient mutant compared with Mock (39% of mock, $P < 0.005$ and 37% of mock, $P < 0.001$, respectively) (Fig. 5d).

Discussion

Embryos derived from *C. elegans* fed with *Escherichia coli* expressing RNA-mediated interference (RNAi)-targeting *gspd-1* gene display developmental defects in their embryos, including hatching, membrane function, and eggshell structure [5, 6]. No defect in larval development is observed in the first generation of *gspd-1(RNAi)* *C. elegans* compared to control *C. elegans*. Perhaps, residual GSPD-1 activity and another NADPH-producing system can generate sufficient NADPH, in *gspd-1(RNAi)* *C. elegans*, to meet the basic requirement for larval growth until the reproduction period. It is not clear how IDH-1, another NADPH-producing system, can affect growth and development in GSPD-1 deficiency.

In the current study, the small body size of *idh-1:gspd-1(RNAi)* double-deficient *C. elegans* is consistent with a previous report [32]. Similar findings are seen in yeast and nematode models lacking both G6PD and IDH [20, 32]. The distinct metabolomic profile of *idh-1:gspd-1(RNAi)* double-deficient *C. elegans* suggests that severe NADPH insufficiency causes a major disturbance in metabolism and is linked to its defective phenotypes, including reduced body size and impaired molting in *C. elegans*. It is speculated that the compensation of the complementary NADPH-producing systems supports reductive biosynthesis and provides sufficient reducing power to meet the need of cells (Fig. 6a).

Essential amino acids, including arginine, histidine, isoleucine, leucine, lysine, methionine, phenylalanine, threonine, tryptophan, and valine, are required to support the growth of *C. elegans* [21, 33]. The global metabolomic analysis revealed that amino acid biosynthesis and metabolism were significantly affected by the diminution of both GSPD-1 and IDH-1 in *C. elegans*. Since glutamate dehydrogenase requires NADPH to synthesize glutamate from α -ketoglutarate and NH_4^+ , the level of glutamate was decreased in *idh-1:gspd-1(RNAi)* double-deficient *C. elegans*. Glutamate is a precursor of the non-essential amino acids, namely proline and arginine [21], which were reduced in *idh-1:gspd-1(RNAi)* deficient *C. elegans*. The essential branched chain amino acids, such as valine, leucine, and isoleucine, were decreased in *idh-1:gspd-1(RNAi)* double-deficient *C. elegans* due to the requirement of NADPH for the biosynthesis of these amino acids. In addition, the levels of tryptophan and phenylalanine were decreased in *idh-1:gspd-1(RNAi)* double-deficient *C. elegans*. The fact that decreased amino acid pool found in *idh-1:gspd-1(RNAi)* double-deficient *C. elegans* raises a question whether supplementation with amino acids rescues the growth defect. Preliminary study to address this issue is already being undertaken by our group; however, more detailed works are needed (Supplementary text). Taken together, decreased amino acids found in *idh-1:gspd-1(RNAi)* double-deficient *C. elegans* reiterate the importance of the NADPH supply in reductive biosynthesis during organismal development (Fig. 6a).

Fig. 2 Molting defect of *idh-1:gspd-1(RNAi)* double-deficient *C. elegans* compared to mock and other controls. *Idh-1:gspd-1(RNAi)* double-deficient *C. elegans* showed a molting defect at the L4/Adult stage. Head **(a)** and tail **(b)** cuticle of *C. elegans* cultured at 20 °C for 54 h was photographed using a DIC microscope

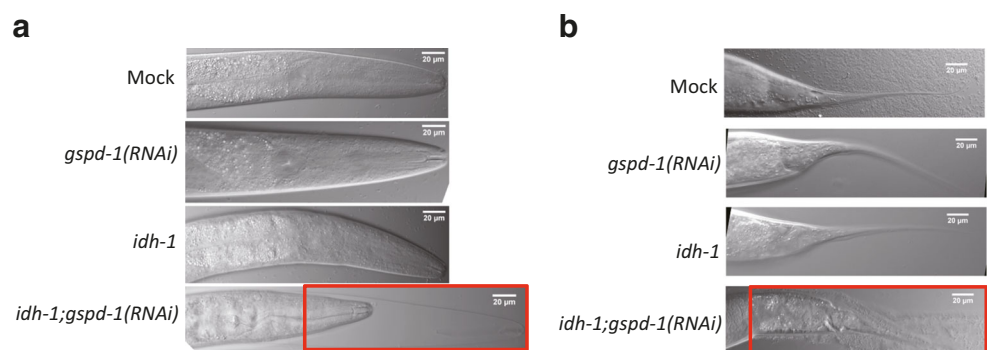
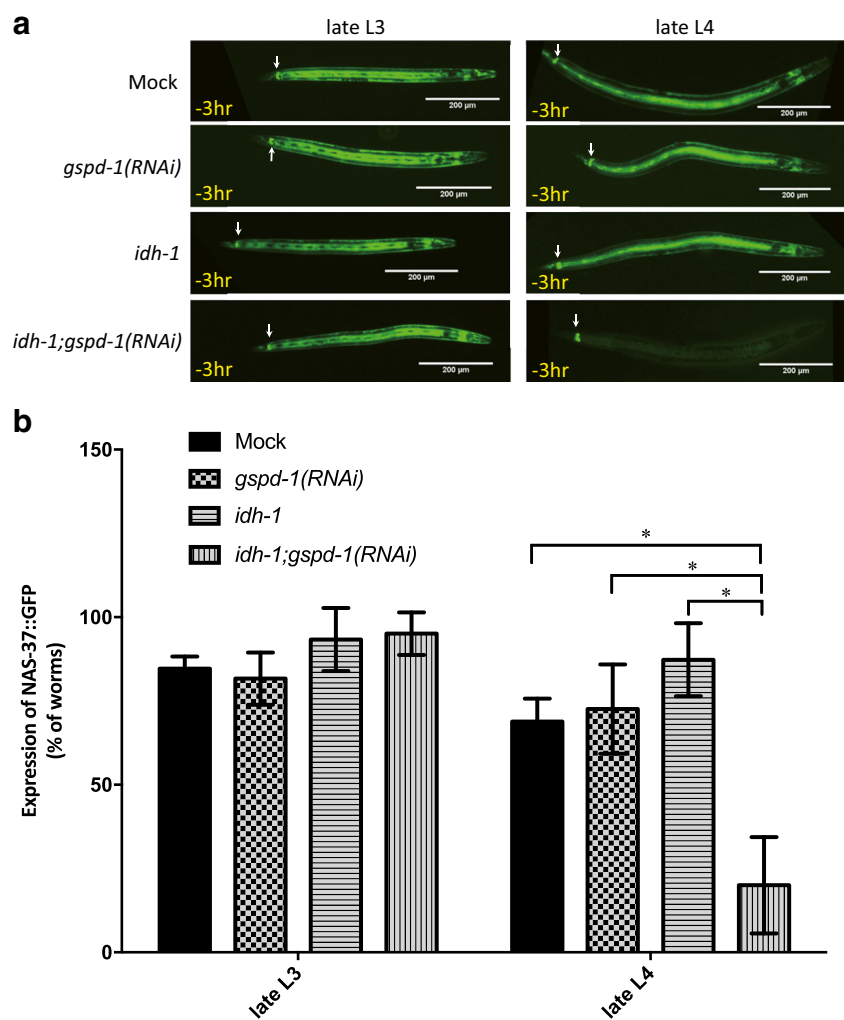


Fig. 3 Decreased molting protein expression of *idh-1:gspd-1(RNAi)* double-deficient *C. elegans* compared to controls. *Idh-1:gspd-1(RNAi)* double-deficient *C. elegans* showed decreased molting protein NAS-37::GFP expression 3 h before the L4/adult molting. **a** NAS-37::GFP expression of *C. elegans* cultured at 25 °C for 28 h (3 h before L3/L4 molting) and 34 h (3 h before L4/adult molting) was photographed using a fluorescence microscope. The arrow points to the position of the rectal epithelial (REP) cells. **b** The ratio of NAS-37::GFP expression of L3 and L4 *C. elegans* was analyzed. ($n > 60$, $*P < 0.05$)



The decrease in amino acids which requires NADPH in their biosynthetic pathways suggests that severe insufficiency of NADPH may affect protein synthesis as illustrated by the impaired molting process in *idh-1:gspd-1(RNAi)* double-deficient *C. elegans* model. *C. elegans* molting is a tissue remodeling process, which requires the activity of proteases to degrade old cuticle proteins. The status of proteases can lead to molting defects. A decrease in the level of NAS-37 expression in *idh-1:gspd-1(RNAi)* double-deficient *C. elegans* during the larval stage suggests that the protease is affected by NADPH insufficiency. *Nas-37* is expressed in the hypodermis prior to ecdysis at each larval stage in *C. elegans* [29]. The gene product of *nas-37*, an Astacin-class metalloprotease, accumulates in the anterior cuticle and is secreted to degrade the old cuticle after ecdysis. A scheme is outlined that describe the effects of *idh-1:gspd-1(RNAi)* double deficiency in *C. elegans* (Fig. 6b). NADPH is an important fuel to drive the development machinery. Decreased amino acid synthesis is a main metabolic alteration leading to growth retardation in *idh-1:gspd-1(RNAi)* double-deficient *C. elegans*. In addition, decreased NAS-37 expression and the molting defect are

likely to cause growth retardation through the unshed cuticle restricting the growth of *idh-1:gspd-1(RNAi)* double-deficient *C. elegans*. Solid evidence to prove a causal relationship between NAS-37 expression and impaired amino acid synthesis awaits further investigation.

Currently, there is little information of the relationship between NADPH and NAS-37 or molting in *C. elegans*. A few studies indicate that a collagen-modifying enzyme, known as NADPH dual oxidase or Bli-3, catalyzes the crosslinking of cuticular collagens [34, 35]. In the current study, however, the blister phenotype of *bli-3* mutant has not been observed in *idh-*

Fig. 4 Distinct metabolic alterations of *idh-1:gspd-1(RNAi)* double-deficient *C. elegans*. **a** Data were subject to principal component analysis, and the score plots (left panel: ESI positive, right panel: ESI negative; Mock: cyan, *gspd-1* deficiency: red, *idh-1*: blue, *idh-1:gspd-1(RNAi)* double deficiency: green) were shown. Colored areas represented 95% confidence regions. **b** Pathway analysis of datasets indicated potential pathways that were significantly changed in *idh-1:gspd-1(RNAi)* double-deficient *C. elegans*. The global metabolomic view displays all anabolic and catabolic pathways that are ranked based on scores from pathway topology analysis (X-axis: pathway impact) and from pathway enrichment analysis (Y-axis: log(p))

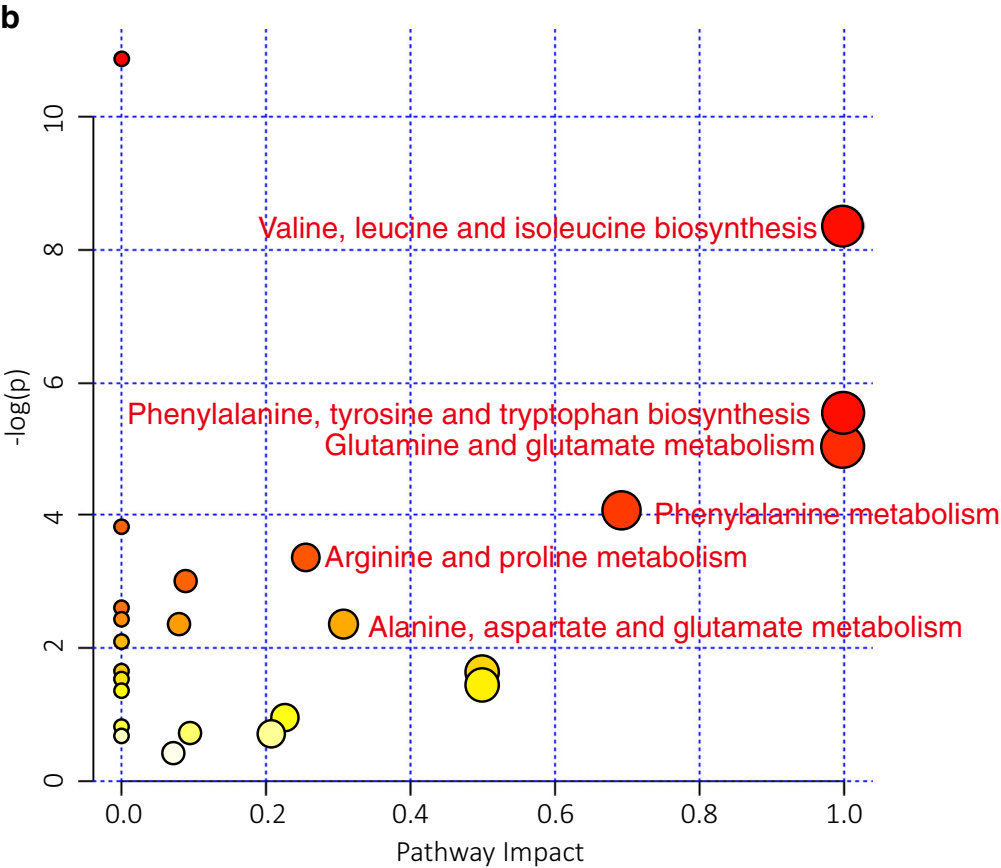
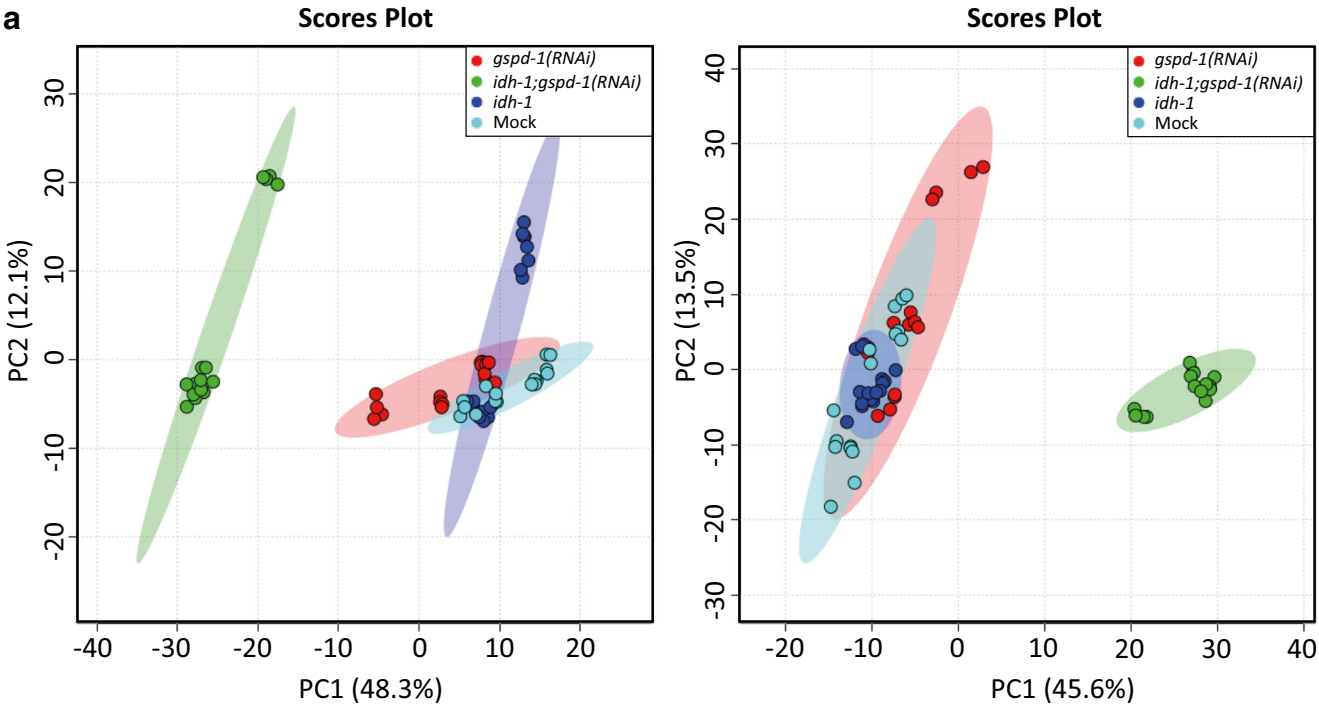
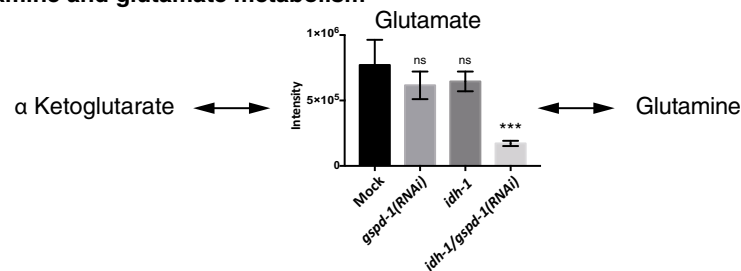
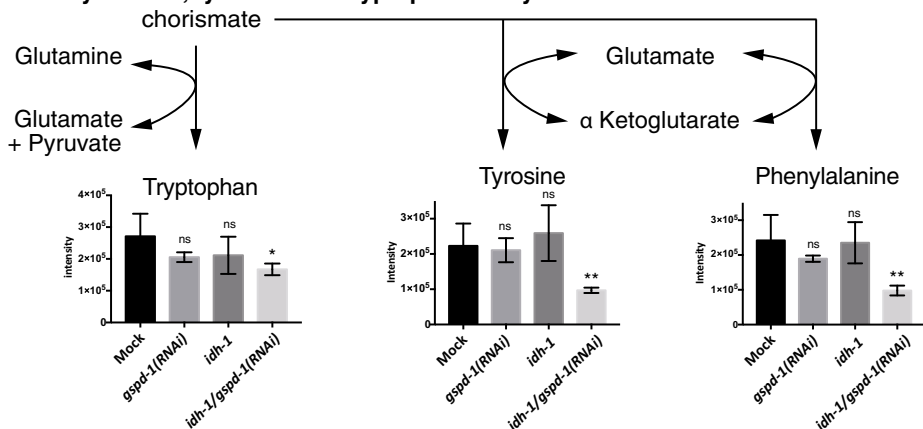


Fig. 5 Altered amino acid metabolism in *idh-1;gspd-1(RNAi)* double-deficient *C. elegans*. **a** Glutamine and glutamate metabolism. **b** Phenylalanine metabolism. **c** Valine, leucine, and isoleucine biosynthesis. **d** Arginine and proline metabolism. All data were presented as the mean \pm S.D., and the statistical difference was analyzed by the two-tailed *t* test. (* $P < 0.05$; ** $P < 0.005$; *** $P < 0.001$)

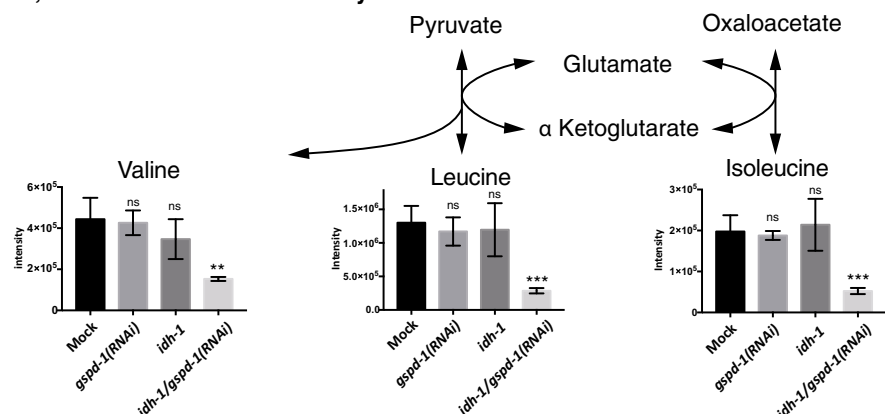
a Glutamine and glutamate metabolism



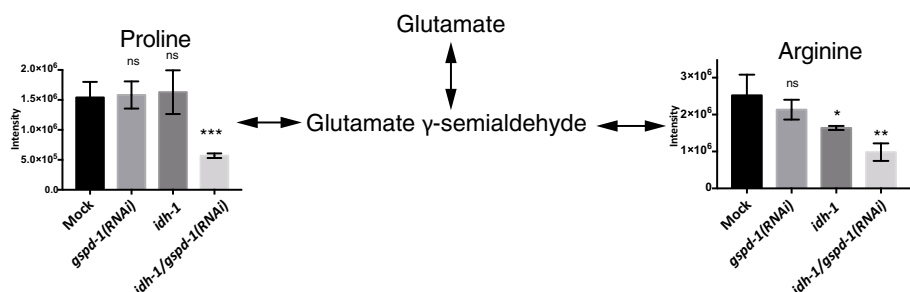
b Phenylalanine, tyrosine and tryptophan biosynthesis



c Valine, leucine and isoleucine biosynthesis



d Arginine and proline metabolism



Idh-1;gspd-1(RNAi) double-deficient *C. elegans*. Hence, another yet to be identified target(s) may be modulated by NADPH depletion leading to growth defects in *C. elegans*. Abnormal molting in *idh-1;gspd-1(RNAi)* double-deficient *C. elegans*

could be, in part, attributed to abnormal fatty acid synthesis because genes of fatty acid synthesis participate in the molting process in *C. elegans* [36]. Knockdown of *fasn-1* and *pod-2* by RNAi downregulates the protein expression of NAS-37.

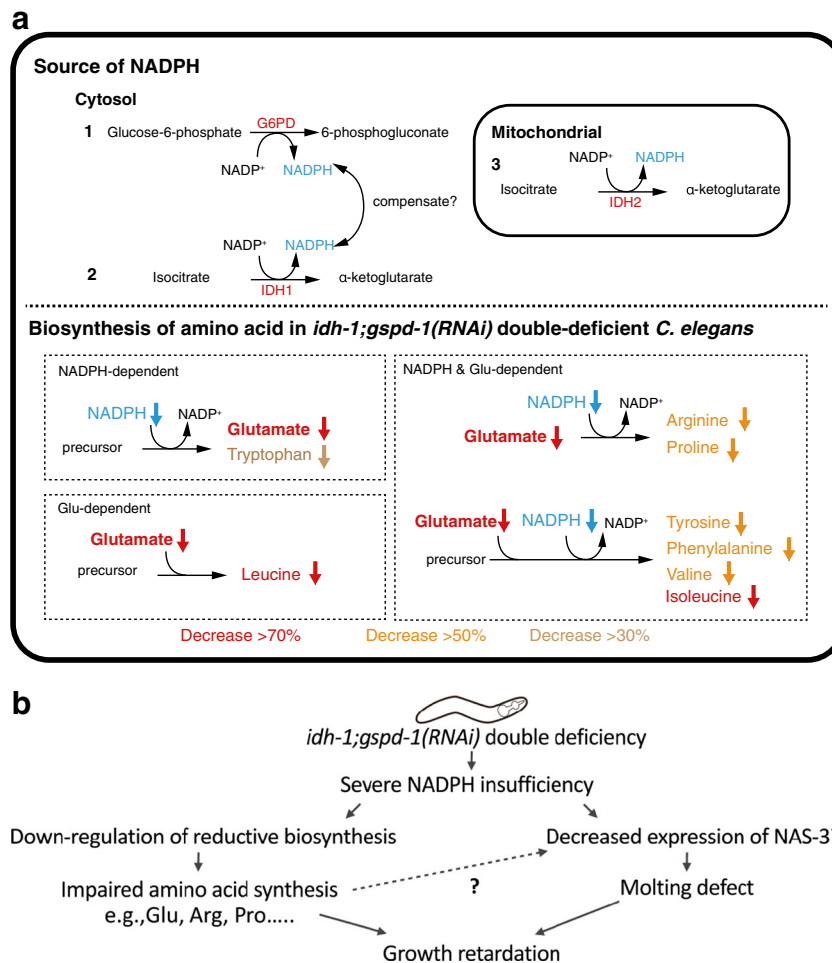


Fig. 6 Proposed schemes for amino acid metabolism as well as for growth and development in *idh-1;gspd-1(RNAi)* double-deficient *C. elegans*. **a** Upper panel depicts three NADPH producing systems in *C. elegans*. Both GSPD-1 and IDH-1 are cytosolic enzymes that produce NADPH, whereas IDH-2 is the source of NADPH in mitochondria. Lower panel shows altered amino acid pathways in *idh-1;gspd-1(RNAi)* double-deficient *C. elegans*. These pathways are classified into three categories based on the requirement of NADPH or glutamate in amino

acid synthesis. The decreased levels of amino acids are highlighted in red (> 70%), orange (> 50%), and beige (> 30%). **b** Hypothetical scheme of the physiological response in *idh-1;gspd-1(RNAi)* double-deficient *C. elegans*. The impaired amino acid synthesis may be due to the lack of NADPH for reductive biosynthesis. As a result, defective protein expression fails to support the growth of *C. elegans*. In addition, decreased expression of NAS-37 is linked to the molting defect, ultimately leading to retarded growth

Since NADPH is required for de novo fatty acid synthesis, it is possible that GSPD-1 and IDH-1 double-deficiency-derived NADPH insufficiency disrupts fatty acid biosynthesis leading to NAS-37 inactivation and the molting defect.

G6PD status is associated with many human diseases, including hemolytic disorders, cardiovascular diseases, and diabetes [2]. Although the relationship between G6PD and cancer is unclear, G6PD is involved in transformation and angiogenesis [37]. Overexpression and modification of G6PD promotes tumor growth and leads to a poor clinical outcome [38–43], while suppression of G6PD inhibits cancer development [42, 44–46]. The notion that G6PD favors rapid cell proliferation is consistent with the finding that inactivation of G6PD causes embryonic lethality [5, 6]. In short, the current study provides evidence for the involvement of G6PD and IDH1 in cellular as well as organismal growth and

development. Similar to G6PD, IDHs play a diverse role in pathophysiology [47–49].

G6PD-derived NADPH is implicated in maintaining redox homeostasis and reductive biosynthesis [3]. Metabolomic studies have demonstrated that G6PD participates in the rapid response of metabolic rerouting to counteract oxidative stress [30, 50]. Lipidomic analysis of embryos derived from GSPD-1-deficient *C. elegans* exhibit higher levels of lipid peroxidation [6]. Increased expression of G6PD in the transgenic mice model shows the enhanced NADPH production and reduces oxidative damage [51]. G6PD transgenic mice exhibit improved protection against an age-related functional decline and an extended health span in females. The metabolomic approach employed in the current study provides additional information concerning the complementary role of GSPD-1 and IDH-1 in maintaining cellular redox homeostasis and “redox-regulated biosynthesis.”

Materials and methods

Nematode culture and RNAi silencing

N2 (wild type), *idh-1(ok2832)*, and *idh-2(ok3184)* mutants were acquired from *Caenorhabditis* Genetics Center (University of Minnesota, Minneapolis, USA). The NAS-37 reporter strain EG3198 was a gift from Prof. Erik Jorgensen (University of Utah, Salt Lake City, USA). The strains were maintained at 20 °C on Nematode Growth Medium (NGM) agar plate seeded with live *E. coli* OP50 bacterial lawn based on standard protocols [52]. The *gspd-1*-RNAi silencing experiment was performed as described previously [5, 6]. The *idh-1* and *gspd-1* double-deficient strain was created by using *gspd-1* RNAi in *idh-1(ok2832)* background. The *idh-2* and *gspd-1* double-deficient strain was created by using *gspd-1* RNAi in *idh-2(ok3184)* background. The RNAi strains, using live *E. coli* HT115(DE3) as a food source, were maintained at 20 °C on NGM agar plate supplemented with 1 mM IPTG.

Phenotype assays

For the molting assay, synchronized L1 grown at 20 °C for 48 h was picked and mounted on a 2% agarose pad on a glass slide followed by anesthetizing with 0.2% levamisole, and a cover slide was placed on the agarose pad. DIC and fluorescent images were taken by using an epifluorescence microscope (Leica, Wetzlar, Germany). For the body size and locomotion assays, synchronized L1 was cultivated on NGM plates at 20 °C for 72 h. Images and video clips were taken by using a dissecting microscope (Nikon, Japan) with a MoticCam X CMOS camera (Motic, Xiamen, China) followed by image analysis (Metamorph 6.1r0; Molecular Device, CA, USA).

Metabolomic analysis

The synchronized L1 worms were cultured at 20 °C until adulthood. Four biological replicates of adult worms were washed off NGM plates by ultra-water. The samples were washed twice by M9 buffer and were centrifuged at 2500 rpm for 1 min. The samples were suspended with 80% methanol and transferred to a homogenization tube pre-filled with 1.0-mm diameter Zirconia beads (Biospec, Bartlesville, OK, USA) and were homogenized in a Precellys24 homogenizer coupled with a Cryolys Cooling System (Bertin Instrument, Rockville, MD, USA). The homogenization was set at two cycles of 6500 rpm for 30 s with an interval of 5 s. Subsequently, the samples were centrifuged at 12000 rpm for 15 min at 4 °C. The supernatant of each sample was transferred to a separate glass tube. The homogenization tube was refilled with 1 ml of 80% methanol followed by additional homogenization and centrifugation to recover residual

samples. The supernatant was transferred to the previous glass tube and air dried under nitrogen flow in a nitrogen evaporator (Taitec, Koshigaya-shi, Saitama-ken, Japan) and stored at –80 °C. The pellet was dissolved in 1 ml of 0.1 N NaOH at 65 °C for 30 min to determine the protein concentration (Bradford assay).

Prior to metabolomic analysis, the sample was dissolved in 300 µl LC-MS Chromasolv water (Fluka) containing 0.1% formic acid. The tube was vortexed for 30 s and repeated four times. The mixture was transferred to an eppendorf tube and centrifuged at 12000 rpm for 30 min at 4 °C. The supernatant was then transferred to an HPLC vial for liquid chromatography and mass spectrometry analysis. For LC-MS analysis, mass spectrometry analysis was carried out using an Agilent 1200 rapid resolution liquid chromatography system coupled with an Agilent 6510 Q-TOF MS system (Agilent Technologies, CA, USA), which is equipped with an electrospray ionization source. Chromatographic separation was performed on an Acquity UPLC HSST3 reversed phase C18 column (particle size of 1.8 µm, 2.1 mm × 150 mm) (Waters, Milford, USA). Column temperature was maintained at 40 °C and the flow rate was 0.25 ml/min. For metabolite profiling, the mobile phase consisted of 0.1% formic acid (solvent A) and 0.1% formic acid/acetonitrile (solvent B). The mobile phase condition was listed below: solvent A, 2 min; gradient from 0 to 40% solvent B, 4 min; 40% solvent B, 2 min; gradient from 40 to 98% solvent B, 2 min; 98% solvent B, 6 min; gradient from 98 to 0% solvent B, 2 min.

The samples were subjected to RRLC-ESI-TOF-MS. Mass spectrometric analysis was performed in the ESI positive and ESI negative modes. The pressure of the nitrogen nebulizer was set at 30 psi and the nitrogen drying gas was set at 350 °C with a flow rate of 10 l/min. The skimmer and capillary voltages were set at 65 V and 4000 V, respectively. Data were obtained over the range from *m/z* 50 to *m/z* 1000 at a rate of 1 scan per second. Data were collected in the profile mode using Agilent MassHunter Workstation Data acquisition software. For processing data, individual components, or called molecular features, in the sample were identified using the Molecular Feature Extraction (MFE) algorithm of MassHunter software. Upon processing, the raw data generated time-aligned ion features (isotopes, adducts, and dimers), the monoisotopic neutral mass, retention time, and ion abundance for each molecular feature. An Agilent GeneSpring-MS (Agilent Technologies, CA, USA) was used to visualize datasets in numerical data matrices (metabolite concentrations). MetaboAnalyst 3.0 was used for analysis and visualization of MS data sets in data matrices and principal components analysis (PCA) diagrams as well as multivariate data analysis and data representation, such as a volcano plot. PCA was employed for clustering and correlation analyses. Relative concentrations of metabolites were compared by ANOVA with a Tukey HSD correction. Accurate masses of

features showing significant differences between control and test groups were searched against our in-house and public metabolite databases, including HMDB (<http://www.hmdb.ca>), METLIN (<http://metlin.scripps.edu/index.php>), and KEGG (<http://www.genome.jp/kegg/>).

Statistical analysis

Where applicable, all data were shown as the mean \pm S.D. The statistical difference was analyzed by the two-tailed *t* test. All statistical tests were conducted using the GraphPad Prism 6.0 (San Diego, CA, USA). Values of $P < 0.05$ were considered statistically significant.

Acknowledgements The reporter strain EG3198 was kindly provided by Prof. Erik Jorgensen (University of Utah, Salt Lake City, USA).

Funding information This article is made possible by grants from the Ministry of Science and Technology of Taiwan (MOST105-2320-B-182-031-MY2, MOST107-2320-B-182-013 to DTYC, and MOST107-2320-B-264-001-MY2 to HCY) and from Chang Gung Memorial Hospital (BMRP098, CMRPD1F0462, CMRPD1F0622 to DTYC).

Open Access This article is distributed under the terms of the Creative Commons Attribution 4.0 International License (<http://creativecommons.org/licenses/by/4.0/>), which permits unrestricted use, distribution, and reproduction in any medium, provided you give appropriate credit to the original author(s) and the source, provide a link to the Creative Commons license, and indicate if changes were made.

Publisher's Note Springer Nature remains neutral with regard to jurisdictional claims in published maps and institutional affiliations.

References

- Beutler E (1994) G6PD deficiency. *Blood* 84:3613–3636
- Ho HY, Cheng ML, Chiu DT (2014) Glucose-6-phosphate dehydrogenase—beyond the realm of red cell biology. *Free Radic Res* 48:1028–1048
- Yang HC, Wu YH, Liu HY, Stern A, Chiu DT (2016) What has passed is prolog: new cellular and physiological roles of G6PD. *Free Radic Res* 50:1047–1064
- Longo L, Vanegas OC, Patel M, Rosti V, Li H, Waka J, Merghoub T, Pandolfi PP, Notaro R, Manova K, Luzzatto L (2002) Maternally transmitted severe glucose 6-phosphate dehydrogenase deficiency is an embryonic lethal. *EMBO J* 21:4229–4239
- Yang HC, Chen TL, Wu YH, Cheng KP, Lin YH, Cheng ML, Ho HY, Lo SJ, Chiu DT (2013) Glucose 6-phosphate dehydrogenase deficiency enhances germ cell apoptosis and causes defective embryogenesis in *Caenorhabditis elegans*. *Cell Death Dis* 4:e616
- Chen TL, Yang HC, Hung CY, Ou MH, Pan YY, Cheng ML, Stern A, Lo SJ, Chiu DT (2017) Impaired embryonic development in glucose-6-phosphate dehydrogenase-deficient *Caenorhabditis elegans* due to abnormal redox homeostasis induced activation of calcium-independent phospholipase and alteration of glycerophospholipid metabolism. *Cell Death Dis* 8:e2545
- Patrinostro X, Carter ML, Kramer AC, Lund TC (2013) A model of glucose-6-phosphate dehydrogenase deficiency in the zebrafish. *Exp Hematol* 41:697–710.e692
- Lewis CA, Parker SJ, Fiske BP, McCloskey D, Gui DY, Green CR, Vokes NI, Feist AM, Vander Heiden MG, Metallo CM (2014) Tracing compartmentalized NADPH metabolism in the cytosol and mitochondria of mammalian cells. *Mol Cell* 55:253–263
- Fan J, Ye J, Kamphorst JJ, Shlomi T, Thompson CB, Rabinowitz JD (2014) Quantitative flux analysis reveals folate-dependent NADPH production. *Nature* 510:298–302
- Reitman ZJ, Yan H (2010) Isocitrate dehydrogenase 1 and 2 mutations in cancer: alterations at a crossroads of cellular metabolism. *J Natl Cancer Inst* 102:932–941
- Ronnebaum SM, Ilkayeva O, Burgess SC, Joseph JW, Lu D, Stevens RD, Becker TC, Sherry AD, Newgard CB, Jensen MV (2006) A pyruvate cycling pathway involving cytosolic NADP-dependent isocitrate dehydrogenase regulates glucose-stimulated insulin secretion. *J Biol Chem* 281:30593–30602
- Koh HJ, Lee SM, Son BG, Lee SH, Ryoo ZY, Chang KT, Park JW, Park DC, Song BJ, Veech RL, Song H, Huh TL (2004) Cytosolic NADP+—dependent isocitrate dehydrogenase plays a key role in lipid metabolism. *J Biol Chem* 279:39968–39974
- Comte B, Vincent G, Bouchard B, Benderdour M, Des Rosiers C (2002) Reverse flux through cardiac NADP(+)-isocitrate dehydrogenase under normoxia and ischemia. *Am J Physiol Heart Circ Physiol* 283:H1505–H1514
- Nekrutenko A, Hillis DM, Patton JC, Bradley RD, Baker RJ (1998) Cytosolic isocitrate dehydrogenase in humans, mice, and voles and phylogenetic analysis of the enzyme family. *Mol Biol Evol* 15:1674–1684
- Cairns RA, Mak TW (2013) Oncogenic isocitrate dehydrogenase mutations: mechanisms, models, and clinical opportunities. *Cell Biosci* 3:730–741
- Ward PS, Patel J, Wise DR, Abdel-Wahab O, Bennett BD, Collier HA, Cross JR, Fantin VR, Hedvat CV, Perl AE, Rabinowitz JD, Carroll M, Su SM, Sharp KA, Levine RL, Thompson CB (2010) The common feature of leukemia-associated IDH1 and IDH2 mutations is a neomorphic enzyme activity converting alpha-ketoglutarate to 2-hydroxyglutarate. *Cancer Cell* 17:225–234
- Itsumi M, Inoue S, Elia AJ, Murakami K, Sasaki M, Lind EF, Brenner D, Harris IS, Chio II, Afzal S et al (2015) Idh1 protects murine hepatocytes from endotoxin-induced oxidative stress by regulating the intracellular NADP(+)/NADPH ratio. *Cell Death Differ* 22:1837–1845
- Ye J, Gu Y, Zhang F, Zhao Y, Yuan Y, Hao Z, Sheng Y, Li WY, Wakeham A, Cairns RA, Mak TW (2017) IDH1 deficiency attenuates gluconeogenesis in mouse liver by impairing amino acid utilization. *Proc Natl Acad Sci U S A* 114:292–297
- Ho HY, Cheng ML, Lu FJ, Chou YH, Stern A, Liang CM, Chiu DT (2000) Enhanced oxidative stress and accelerated cellular senescence in glucose-6-phosphate dehydrogenase (G6PD)-deficient human fibroblasts. *Free Radic Biol Med* 29:156–169
- Minard KI, Carroll CA, Weintraub ST, McAlister-Henn L (2007) Changes in disulfide bond content of proteins in a yeast strain lacking major sources of NADPH. *Free Radic Biol Med* 42:106–117
- Braeckman BP, Houthoofd K, Vanfleteren JR (2009) Intermediary metabolism. *WormBook*: 1–24. DOI <https://doi.org/10.1895/wormbook.1.146.1>
- Atherton HJ, Jones OA, Malik S, Miska EA, Griffin JL (2008) A comparative metabolomic study of NHR-49 in *Caenorhabditis elegans* and PPAR-alpha in the mouse. *FEBS Lett* 582:1661–1666
- Hughes SL, Bundy JG, Want EJ, Kille P, Sturzenbaum SR (2009) The metabolomic responses of *Caenorhabditis elegans* to cadmium are largely independent of metallothionein status, but dominated by changes in cystathionine and phytochelatin. *J Proteome Res* 8:3512–3519

24. Castro C, Sar F, Shaw WR, Mishima M, Miska EA, Griffin JL (2012) A metabolomic strategy defines the regulation of lipid content and global metabolism by Delta9 desaturases in *Caenorhabditis elegans*. *BMC Genomics* 13:36
25. Patti GJ, Tautenhahn R, Johannsen D, Kalisiak E, Ravussin E, Bruning JC, Dillin A, Siuzdak G (2014) Meta-analysis of global metabolomic data identifies metabolites associated with life-span extension. *Metabolomics* 10:737–743
26. Morgan PG, Higdon R, Kolker N, Bauman AT, Ilkayeva O, Newgard CB, Kolker E, Steele LM, Sedensky MM (2015) Comparison of proteomic and metabolomic profiles of mutants of the mitochondrial respiratory chain in *Caenorhabditis elegans*. *Mitochondrion* 20:95–102
27. Wang W, McReynolds MR, Goncalves JF, Shu M, Dhondt I, Braeckman BP, Lange SE, Kho K, Detwiler AC, Pacella MJ et al (2015) Comparative metabolomic profiling reveals that dysregulated glycolysis stemming from lack of salvage NAD⁺ biosynthesis impairs reproductive development in *Caenorhabditis elegans*. *J Biol Chem* 290:26163–26179
28. Wan QL, Shi X, Liu J, Ding AJ, Pu YZ, Li Z, Wu GS, Luo HR (2017) Metabolomic signature associated with reproduction-regulated aging in *Caenorhabditis elegans*. *Aging (Albany NY)* 9:447–474
29. Davis MW, Birnie AJ, Chan AC, Page AP, Jorgensen EM (2004) A conserved metalloprotease mediates ecdysis in *Caenorhabditis elegans*. *Development* 131:6001–6008
30. Tang HY, Ho HY, Wu PR, Chen SH, Kuypers FA, Cheng ML, Chiu DT (2015) Inability to maintain GSH pool in G6PD-deficient red cells causes futile AMPK activation and irreversible metabolic disturbance. *Antioxid Redox Signal* 22:744–759
31. Cheng ML, Shiao MS, Chiu DT, Weng SF, Tang HY, Ho HY (2011) Biochemical disorders associated with antiproliferative effect of dehydroepiandrosterone in hepatoma cells as revealed by LC-based metabolomics. *Biochem Pharmacol* 82:1549–1561
32. Penkov S, Kaptan D, Erkut C, Sarov M, Mende F, Kurzhachia TV (2015) Integration of carbohydrate metabolism and redox state controls dauer larva formation in *Caenorhabditis elegans*. *Nat Commun* 6:8060
33. Szewczyk NJ, Kozak E, Conley CA (2003) Chemically defined medium and *Caenorhabditis elegans*. *Bmc Biotechnol* 3. DOI Artn 19. Doi <https://doi.org/10.1186/1472-6750-3-19>
34. Thein MC, Winter AD, Stepek G, McCormack G, Stapleton G, Johnstone IL, Page AP (2009) Combined extracellular matrix cross-linking activity of the peroxidase MLT-7 and the dual oxidase BLI-3 is critical for post-embryonic viability in *Caenorhabditis elegans*. *J Biol Chem* 284:17549–17563
35. Moribe H, Konakawa R, Koga D, Ushiki T, Nakamura K, Mekada E (2012) Tetraspanin is required for generation of reactive oxygen species by the dual oxidase system in *Caenorhabditis elegans*. *PLoS Genet* 8:e1002957
36. Li Y, Paik YK (2011) A potential role for fatty acid biosynthesis genes during molting and cuticle formation in *Caenorhabditis elegans*. *BMB Rep* 44:285–290
37. Leopold JA, Walker J, Scribner AW, Voetsch B, Zhang YY, Loscalzo AJ, Stanton RC, Loscalzo J (2003) Glucose-6-phosphate dehydrogenase modulates vascular endothelial growth factor-mediated angiogenesis. *J Biol Chem* 278:32100–32106
38. Pu H, Zhang Q, Zhao C, Shi L, Wang Y, Wang J, Zhang M (2015) Overexpression of G6PD is associated with high risks of recurrent metastasis and poor progression-free survival in primary breast carcinoma. *World J Surg Oncol* 13:323
39. Wang J, Yuan W, Chen Z, Wu S, Chen J, Ge J, Hou F, Chen Z (2012) Overexpression of G6PD is associated with poor clinical outcome in gastric cancer. *Tumour Biol* 33:95–101
40. Rao X, Duan X, Mao W, Li X, Li Z, Li Q, Zheng Z, Xu H, Chen M, Wang PG, Wang Y, Shen B, Yi W (2015) O-GlcNAcylation of G6PD promotes the pentose phosphate pathway and tumor growth. *Nat Commun* 6:8468
41. Kowalik MA, Guzzo G, Morandi A, Perra A, Menegon S, Masgras I, Trevisan E, Angioni MM, Fornari F, Quagliata L, Ledda-Columbano GM, Gramantieri L, Terracciano L, Giordano S, Chiarugi P, Rasola A, Columbano A (2016) Metabolic reprogramming identifies the most aggressive lesions at early phases of hepatic carcinogenesis. *Oncotarget* 7:32375–32393
42. Xu SN, Wang TS, Li X, Wang YP (2016) SIRT2 activates G6PD to enhance NADPH production and promote leukaemia cell proliferation. *Sci Rep* 6:32734
43. Dore MP, Davoli A, Longo N, Marras G, Pes GM (2016) Glucose-6-phosphate dehydrogenase deficiency and risk of colorectal cancer in Northern Sardinia: a retrospective observational study. *Medicine (Baltimore)* 95:e5254
44. Chen Y, Xu Q, Ji D, Wei Y, Chen H, Li T, Wan B, Yuan L, Huang R, Chen G (2016) Inhibition of pentose phosphate pathway suppresses acute myelogenous leukemia. *Tumour Biol* 37:6027–6034
45. Gregory MA, D'Alessandro A, Alvarez-Calderon F, Kim J, Nemkov T, Adane B, Rozhok AI, Kumar A, Kumar V, Pollyea DA et al (2016) ATM/G6PD-driven redox metabolism promotes FLT3 inhibitor resistance in acute myeloid leukemia. *Proc Natl Acad Sci U S A* 113:E6669–E6678
46. Ju HQ, Lu YX, Wu QN, Liu J, Zeng ZL, Mo HY, Chen Y, Tian T, Wang Y, Kang TB, Xie D, Zeng MS, Huang P, Xu RH (2017) Disrupting G6PD-mediated redox homeostasis enhances chemosensitivity in colorectal cancer. *Oncogene* 36:6282–6292
47. Waitkus MS, DiPlas BH, Yan H (2016) Isocitrate dehydrogenase mutations in gliomas. *Neuro-Oncology* 18:16–26
48. Medeiros BC, Fathi AT, DiNardo CD, Pollyea DA, Chan SM, Swords R (2017) Isocitrate dehydrogenase mutations in myeloid malignancies. *Leukemia* 31:272–281
49. Al-Khallaif H (2017) Isocitrate dehydrogenases in physiology and cancer: biochemical and molecular insight. *Cancer Discov* 7:37
50. Kuehne A, Emmert H, Soehle J, Winnefeld M, Fischer F, Wenck H, Gallinat S, Terstegen L, Lucius R, Hildebrand J, Zamboni N (2015) Acute activation of oxidative pentose phosphate pathway as first-line response to oxidative stress in human skin cells. *Mol Cell* 59:359–371
51. Nobrega-Pereira S, Fernandez-Marcos PJ, Brioché T, Gomez-Cabrera MC, Salvador-Pascual A, Flores JM, Vina J, Serrano M (2016) G6PD protects from oxidative damage and improves healthspan in mice. *Nat Commun* 7:10894
52. Girard LR, Fiedler TJ, Harris TW, Carvalho F, Antoshechkin I, Han M, Sternberg PW, Stein LD, Chalfie M (2007) WormBook: the online review of *Caenorhabditis elegans* biology. *Nucleic Acids Res* 35:D472–D475

REVIEW

Open Access



Molecular functions and clinical impact of thyroid hormone-triggered autophagy in liver-related diseases

Hsiang-Cheng Chi^{1†}, Chung-Ying Tsai^{2†}, Ming-Ming Tsai^{3,4,7}, Chau-Ting Yeh⁵ and Kwang-Huei Lin^{5,6,7*} 

Abstract

The liver is controlled by several metabolic hormones, including thyroid hormone, and characteristically displays high lysosomal activity as well as metabolic stress-triggered autophagy, which is stringently regulated by the levels of hormones and metabolites. Hepatic autophagy provides energy through catabolism of glucose, amino acids and free fatty acids for starved cells, facilitating the generation of new macromolecules and maintenance of the quantity and quality of cellular organelles, such as mitochondria. Dysregulation of autophagy and defective mitochondrial homeostasis contribute to hepatocyte injury and liver-related diseases, such as non-alcoholic fatty liver disease (NAFLD) and liver cancer.

Thyroid hormones (TH) mediate several critical physiological processes including organ development, cell differentiation, metabolism and cell growth and maintenance. Accumulating evidence has revealed dysregulation of cellular TH activity as the underlying cause of several liver-related diseases, including alcoholic or non-alcoholic fatty liver disease and liver cancer. Data from epidemiologic, animal and clinical studies collectively support preventive functions of THs in liver-related diseases, highlighting the therapeutic potential of TH analogs. Elucidation of the molecular mechanisms and downstream targets of TH should thus facilitate the development of therapeutic strategies for a number of major public health issues.

Here, we have reviewed recent studies focusing on the involvement of THs in hepatic homeostasis through induction of autophagy and their implications in liver-related diseases. Additionally, the potential underlying molecular pathways and therapeutic applications of THs in NAFLD and HCC are discussed.

Keywords: Thyroid hormone, Thyroid hormone receptor, Autophagy, non-alcoholic fatty liver disease, hepatocellular carcinoma

Background

Thyroid hormones (TH) serve as potent regulators of cellular development, growth and metabolism in mammals [1] and control several metabolic activities related to anabolism or catabolism of macromolecules, including carbohydrates, proteins, lipids and damaged organelles within cells to maintain homeostasis under different physiological conditions [2]. In addition to their critical regulatory roles in cellular homeostasis, imbalance of TH levels in the

body is associated with multiple chronic diseases, including diabetes mellitus [3, 4], cardiovascular disease [5, 6] and liver-related disorders [7]. Liver is one of the most important target organs whereby THs regulate components involved in cellular metabolism, such as fatty acids, supporting the possibility that disruption of TH action in liver contributes to development of non-alcoholic fatty liver disease (NAFLD). Indeed, recent studies have reported associations between alterations in cellular TH signaling and several liver-related diseases, including NAFLD and hepatocellular carcinoma (HCC). Earlier epidemiological findings suggest that long-term

* Correspondence: khlin@mail.cgu.edu.tw

[†]Hsiang-Cheng Chi and Chung-Ying Tsai contributed equally to this work.

⁵Liver Research Center, Chang Gung Memorial Hospital, Linkou, Taoyuan, Taiwan 333

⁶Department of Biochemistry, College of Medicine, Chang-Gung University, 259 Wen-Hwa 1 Road, Taoyuan 333, Taiwan, Republic of China

Full list of author information is available at the end of the article



hypothyroidism is positively associated with high risk of NAFLD and HCC incidence, independent of other risk factors [8, 9]. Moreover, treatment with T_3 or its analogs has been shown to prevent a spectrum of liver-related diseases ranging from hepatic steatosis to HCC in rodents subjected to high-fat diet (HFD) or carcinogens [10–17]. These collective findings support the potential utility of TH analogs as therapeutic drugs to prevent liver disease progression. Analysis of the downstream signals of TH in liver may further shed light on the underlying TH pathways that induce therapeutic effects against liver-related diseases.

Autophagy is a self-digestion process primarily involving recycling of cellular fuel stores in lysosomes to generate amino acids, glucose and fatty acids [18]. Catabolism of lipids through autophagy is termed lipophagy [19]. In addition to metabolic functions, autophagy presents a cellular surveillance mechanism to suppress accumulation of toxic protein aggregates and impairment of organelles, thus facilitating maintenance of organelle integrity and cellular homeostasis [20]. The specific regulatory functions of autophagy in hepatic homeostasis have been increasingly explored in recent years. Dysregulation of the autophagic process is reported to cause an imbalance in energy metabolism in the liver and consequently affect hepatic physiology and trigger disease [21–24]. Several research groups, including ours, have shown that hepatic lipid turnover is stimulated by THs through lipophagy, preventing hepatosteatosis, both *in vitro* and *in vivo* [25, 26]. Additionally, TH stimulates the metabolic rate accompanied by increased mitochondrial turnover through mitophagy, leading to elimination of mitochondrial dysfunction induced by hepatic carcinogens or hepatitis B virus HBx protein [16, 17, 27]. The finding that THs and Thyroid hormone receptors (THRs) prevent hepatic damage, hepatosteatosis and hepatocarcinogenesis via autophagy stimulation supports their therapeutic potential in clinical applications. In the current report, we have reviewed studies published by our research group and other investigators on the involvement of TH-induced autophagy in liver-related diseases, particularly NAFLD and HCC. Elucidation of the network of molecular mechanisms underlying the effects of TH/THR on hepatic metabolism may aid in the design of effective therapeutic strategies for a range of liver-related diseases.

Molecular actions of thyroid hormones and receptors

Genomic actions of TH

T_3 (triiodothyronine) and T_4 (L-thyroxine) are the two major thyroid hormones affecting almost every organ system. Under physiological conditions, T_4 is the main hormone secreted into the bloodstream by the thyroid gland. However, the thyroid hormone receptor (THR)

binding affinity of T_4 is considerably lower (10-fold less) than that for T_3 . The conversion of T_4 to T_3 is regulated via iodothyronine deiodinases (DIO1, DIO2, and DIO3) in extrathyroidal tissue. Type I and type II iodothyronine deiodinases (DIO1, DIO2) deiodinate circulating T_4 to produce biologically active T_3 . Conversely, type III deiodinase (DIO3) suppresses intracellular thyroid activity by converting T_4 and T_3 to the comparatively inactive forms, reverse T_3 (rT_3) and T_2 . Recently, T_2 was shown to possess thyromimetic activity and mimic some of the effects of T_3 on liver metabolism [28, 29], implying that T_2 or rT_3 may not just be inert metabolites as originally suggested. Expression levels and activities of DIO1, DIO2 and DIO3 vary among different tissues, causing a tissue-specific increase or decrease in circulating TH levels or availability of active hormones for THR binding [7, 30]. To exert genomic effects, cytoplasmic T_3 enters the nucleus, most likely through passive diffusion, and binds THRs associated with thyroid hormone response elements (TRE) within the promoter regions of downstream genes of TH/THR [31–33]. Typical TREs within promoter regions of downstream genes contain two half-site sequences (A/G)GGT(C/A/G)A in a palindromic, direct repeat or inverted repeat arrangement that are recognized by THR [1].

THRs are T_3 -inducible transcription factors belonging to the nuclear receptor superfamily that are encoded by two tissue-specific genes, *THRA* ($TR\alpha$) and *THRB* ($TR\beta$). The *THRA* gene encodes one active T_3 -binding receptor, $TR\alpha 1$, and two dominant-negative spliced variants, $TR\Delta\alpha 1$ and $TR\Delta\alpha 2$ [34], that lack T_3 binding ability [35]. $TR\alpha 1$ is the predominant subtype highly expressed in brain, cardiac and skeletal muscle [36]. *THRB* encodes two functional T_3 -binding $TR\beta$ isoforms ($TR\beta 1$ and $TR\beta 2$) and another dominant-negative isoform, $TR\beta 4$ [34]. $TR\beta 1$ is predominately expressed in brain, liver and kidney whereas $TR\beta 2$ is limited to the hypothalamus, retina and pituitary. THRs exert transcriptional effects via formation of homodimers or heterodimers with other nuclear receptors, such as retinoid X receptor (RXR), Vitamin D receptors (VDR) and other retinoic acid receptor subtypes. RXR generally functions as a partner of several nuclear receptors to regulate target genes [47]. THRs form heterodimers with RXR on TREs within the promoter regions of target genes. In addition, recent ChIP-Seq studies have shown that THRs bind to specific response element motifs with non-conserved sequences and in non-promoter regions [37–39], implying that interactions with other transcription factors are required to regulate chromatin remodeling and gene expression.

In the absence of TH, THRs still bind to TREs but are associated with co-repressors displaying histone deacetylase (HDAC) activity, leading to modifications in

chromatin structure and repression of transcription. For instance, nuclear receptor corepressor 1 (NCoR1) and silencing mediator for retinoid or thyroid-hormone receptors (SMRT), well-characterized co-repressors with histone deacetylase activity, serve as platforms for repressor complex-mediated chromatin remodeling [40]. Binding of T_3 induces conformational changes of THR and recruitment of transcriptional coactivators with histone acetyl transferase (HAT) activity to increase histone acetylation at specific promoter regions, facilitating generation of a permissive chromatin state and further recruitment of general transcriptional machinery (Fig. 1). For instance, steroid hormone receptor coactivator (SRC), PCAF (p300/CBP-associated factor) and p160 family members facilitate ligand-bound THRs to activate T_3 target genes through histone acetyltransferase activity [41]. Moreover, transcriptional activities of THRs are stimulated by TR-associated protein (TRAP) family independently of HAT activity [42]. Alterations in THR-associated co-regulator complexes may induce differential responses for appropriate target gene expression (Table 1).

In addition to positively regulating downstream targets, TH binding to THR can lead to negative regulatory effects. Notably, these negatively regulated target genes are upregulated in the absence but downregulated in the presence of THs [30, 43] although the precise details remain to be established. In a typical case, high levels of THs exert a negative feedback effect on thyrotropin-releasing hormone (TRH) and thyroid stimulating hormone (TSH), and low levels of THs stimulate secretion of TSH from the anterior pituitary. This critical negative feedback loop regulates the hypothalamic-pituitary-thyroid axis [44–46]. TREs of genes negatively regulated by TH are frequently located near proximal promoter regions. However, binding of THRs to these putative regions is generally weak, suggesting that interactions between THRs and other co-factors may contribute significantly to negative regulatory effects of THs. Alterations in chromatin remodeling through histone modification via recruitment of HDACs and HATs may be involved in negative transcriptional regulation by THs. Recently, a novel THR co-repressor, LCOR, was identified as an inhibitor of TR β -dependent lipogenic gene activity. LCOR serves as a competitor for binding of coactivators SRC-1/3 to TR β leading to reduced recruitment of SRCs to TREs within the promoter regions of downstream target genes of TR, potentially representing a novel mechanism by which LCOR regulates gene transcription [47].

THRs are additionally reported to interact with transcription factors to negatively regulate expression of several genes, including Sp1 [48], p53 [49], Oct-1 [50], GHF-1 [51, 52] and CTCF [53, 54], although the underlying mechanisms remain largely unknown at present.

Nongenomic actions of TH

In addition to transmission of signals through interactions with nuclear THRs, activities of THs in the plasma membrane or cytoplasm are termed nongenomic effects (Fig. 1, Table 1). THs bind to integrin $\alpha\beta3$ membrane receptor protein independently of nuclear THRs [55–57], which has been further characterized as a membrane-bound THR. Integrin $\alpha\beta3$ was originally shown to contain the Arg-Gly-Asp (RGD) recognition region that interacts with extracellular matrix ligands [55]. Unexpectedly, TH could bind integrin $\alpha\beta3$ near its RGD recognition site [58]. Integrin $\alpha\beta3$ contains two TH-binding domains with no homology to nuclear THRs. The S1 domain mainly recognizes T_3 , consequently activating the phosphatidylinositol 3-kinase (PI3K)/Akt/protein kinase B (PKB) pathway through Src kinase [59]. Both T_4 and T_3 bind to the S2 domain and activate the mitogen-activated protein kinase/extracellular signal-regulated kinase (MAPK/ ERK1/2) pathway. Moreover, S1 and S2 domains mediate the specific effects of TH. For instance, S1 directs Src and PI3K-mediated TR α translocation from the cytoplasm to the nucleus and promotes expression of target genes, such as hypoxia-inducible factor-1 α (HIF-1 α) while S2 activates MAPK1 and MAPK2, leading to nuclear trafficking of TR β 1 from the cytoplasm and tumor cell proliferation [58, 60].

THs also cause serial phosphorylation and nuclear localization of other critical genes responsible for several cellular functions (Table 1). For instance, TH-activated ERK1/2 has been shown to promote estrogen receptor- α (ER α), signal transducer and activator of transcription-3 (STAT3), and several THR-associated proteins [61–67]. TR α 1 interacts with the p85 α subunit of PI3K in a T_3 -dependent manner, leading to activation of Akt and endothelial nitric oxide synthase (eNOS) [7, 68]. In addition, liganded TR β 1 associates with p85 α in the cytoplasm to activate Akt via phosphorylation. Activated Akt subsequently triggers the nuclear mammalian target of rapamycin (mTOR)-p70S6K cascade and sequential induction of several HIF-1 α target genes, including glucose transporter 1 (GLUT1), platelet-type phosphofructokinase (PFKP) and monocarboxylate transporter 4 (MCT 4) [69–71]. TR β 1 is additionally reported to modulate Na⁺/K⁺-ATPase activity by PI3K or ERK1/2. For instance, PI3K signaling slows potassium voltage-gated channel, subfamily H, member 2 (KCNH2) channel deactivation in the plasma membrane of pituitary cells [72–74]. Moreover, THRB-PV, a THRB mutant that shows loss of T_3 binding ability but interacts more significantly with the PI3K regulatory subunit, p85, triggers a greater increase in PI3K kinase activity and activation of the PI3K-AKT- mTOR-p70S6K pathway in cytoplasmic and nuclear compartments, with predisposition to tumor

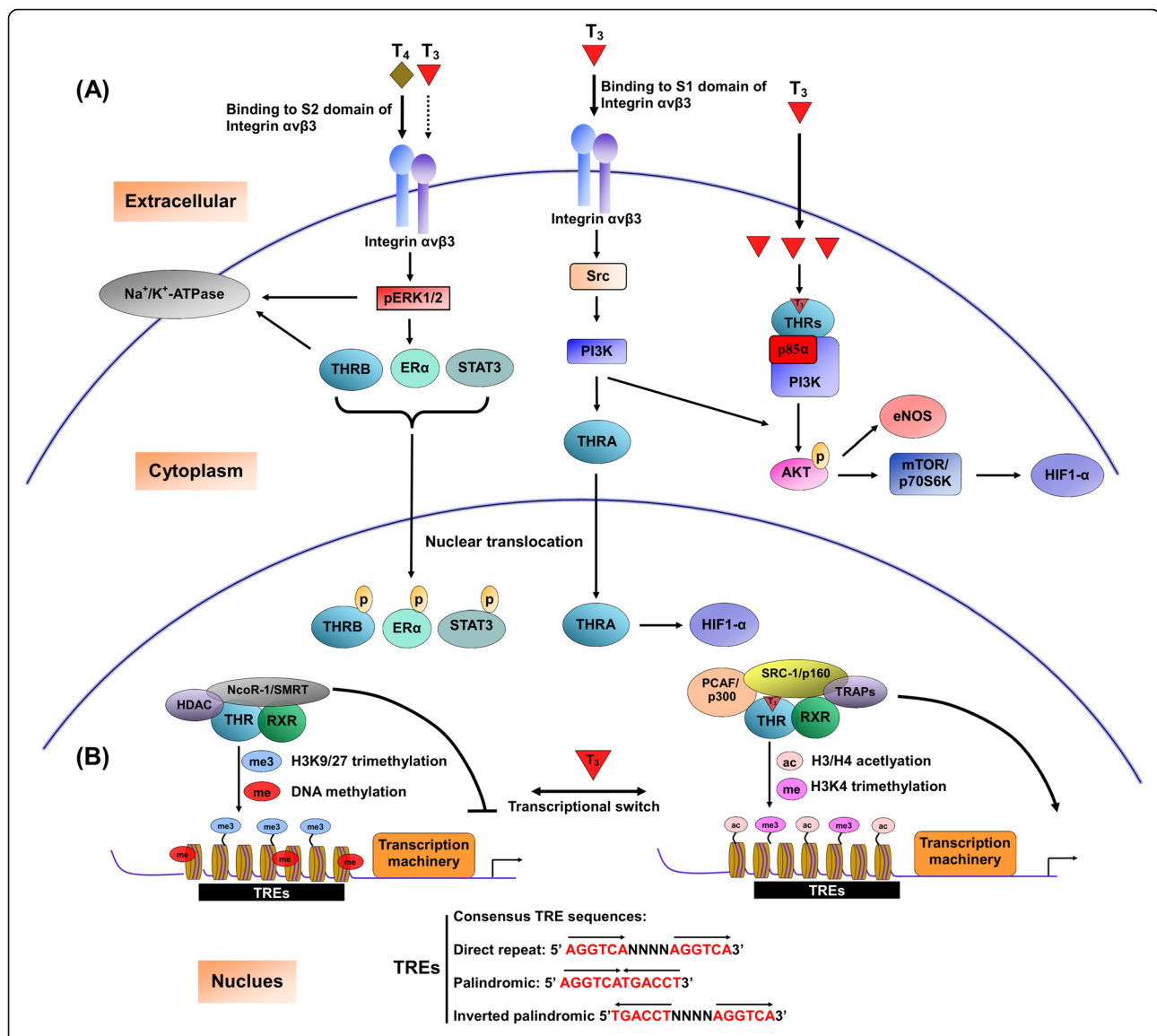


Fig. 1 Nongenomic and Genomic actions of Thyroid hormone and thyroid hormone receptor. The diagram of nongenomic and transcriptional actions of thyroid hormone (TH) and thyroid hormone receptor (THR). **a** Nongenomic effects of THs are initiated from Integrin αvβ3 localized on the plasma membrane or occurs at cytoplasm. T₃ interacts with S1 domain of Integrin αvβ3 to activate the PI3K signal pathway via Src kinase, leading to trafficking of THRA from the cytoplasm to nucleus and increases HIF-1α expression. THs, mainly T₄, also interact with S2 domain of Integrin αvβ3 to activate ERK 1/2 signal, causing phosphorylation and nuclear localization of THRβ, estrogen receptor α (ERα) and STAT3. Activated ERK1/2 and cytosolic THRβ increase the activity of the sodium pump (Na, K-ATPase). T₃-liganded THRs in the cytoplasm interact with the PI3K regulatory subunit, p85α, to activate Akt, subsequently triggering mTOR/p70S6K and eNOS signals. **b** In the nucleus, THRs form heterodimers with the retinoid X receptor (RXR) at thyroid hormone response elements (TREs), within the regulatory regions of downstream genes. In the absence of T₃, the co-repressor complex involving histone deacetylase (HDACs), NCoR1 and SMRT deacetylate histones in the regulatory regions. Consequently, trimethylation of histone H3 at lysine 9 and 27 along with DNA methylation causes a more closed conformation in chromatin and blocks the transcriptional machinery access to the DNA, causing suppression of downstream targets transcription. Binding of T₃ induces conformational changes of THRs and recruitment of transcriptional coactivators (such as PCAF/P300 and SRC-1/p160) with histone acetyltransferase (HAT) activity to increase histone acetylation at specific promoter regions, facilitating generation of a permissive chromatin state and further recruitment of general transcriptional machinery. Typical TREs within promoter regions of downstream genes contain two half-site sequences (A/G)GGT(C/A/G)A in a palindromic, direct repeat or inverted repeat arrangement that are recognized by THR

Table 1 Summary of the genes/signals regulated by genomic or nongenomic action of TH/THR signal axis

Molecular function	Gene/signal name	Reference
Nongenomic regulation by TH/THR		
Membrane receptor of TH	Integrin $\alpha\beta 3$	[55, 56]
Signal transducer	Src kinase	[59]
	PI3K/Akt	[7, 59, 68]
	p-ERK1/2	[58, 61–66, 60, 67]
	mTOR/p70S6K	[69]
	eNOS	[7, 68]
Transcriptional factor	Estrogen receptor	[62, 67]
	STAT3	[64]
	HIF1- α	[58, 60, 70, 69, 71]
	β -catenin	[77]
Metabolic regulator	GLUT1	[71]
	PFKP	[71]
	MCT 4	[71]
Na-K-ATPase	KCNH2	[72]
Apoptosis regulator	FOXO1	[136, 137, 176]
	BCL2L11	[176]
Genomic regulation by TH/THR		
Transcriptional coregulator of THR	SP1	[48]
	p53	[49]
	Oct-1	[50]
	GHF-1	[51, 52]
	CTCF	[53, 54]
	LCOR	[47]
Autophagy regulator	DAPK2	[16]
	Betatrophin	[26]
Cell cycle regulator	UHRF1	[171]
	STMN1	[172]
	Mir-214	[173]
	BC200	[174]
Apoptosis regulator	TRAIL	[175]
Metastatic regulator	BSSP4	[178]
	LCN2	[180]
	mir-130b	[177]
	mir-21	[179]

development in several cancer types, including thyroid and mammary tumors [75, 76]. The THRB-PV mutant additionally associates with β -catenin to regulate cell proliferation in thyroid tumors of THRB^{PV}/PV mice [77]. This interaction favors the unliganded state of TR β , and T₃-independent interactions between β -catenin and TR β promote activation of β -catenin-related downstream targets.

The TH/THR axis in regulation of hepatic autophagy

The autophagic process

Autophagy was originally characterized as a catabolic process targeting cellular constituents, including unfolded proteins, damaged organelles and intracellular pathogens, to lysosomes for degradation [19, 78]. Autophagy is categorized into three main types: macroautophagy, chaperone-mediated autophagy and microautophagy [79]. Macroautophagy, hereafter known as autophagy, is generally considered the major route for directing cytoplasmic components into lysosomes for degradation. The autophagic process involves membrane biogenesis and formation of a double-membrane phagophore (termed autophagosome), which sequesters partial cytoplasmic components or entire organelles and subsequently fuses with lysosomes for degradation. Amino acids and other metabolic compounds generated by this process are consequently released for energy production or recycling. Chaperone-mediated autophagy involves sequestration of proteins or polypeptides harboring the KFERQ-like motif by chaperone proteins. This process promotes translocation of target proteins into lysosomes for degradation through interactions with lysosome-associated membrane protein type 2A (LAMP2A). Microautophagy is implicated in invagination of cellular constituents within endosomes or lysosomes but small fractions of cytoplasmic constituents in the close vicinity of lysosomes are sequestered.

Under basal conditions, autophagy is implicated in the degradation of long-lived proteins while another catabolic system, the ubiquitin-proteasome process, is responsible for the turnover of short-lived proteins [80, 81]. However, under specific conditions, such as nutrient deprivation, the autophagy pathway leads to selective degradation of cytosolic materials (termed selective autophagy). Selective autophagy directs degraded products into highly spatiotemporally controlled metabolic pathways. When specific autophagic cargo, such as misfolded proteins or damaged cellular organelles, appear within the cytoplasm, they are tagged with molecular markers, such as ubiquitin [82, 83], resulting in assembly of autophagic adapter proteins, such as SQSTM1, that bind to both molecular marker-harboring cargo and LC3-II. A number of core autophagy proteins, such as the ULK-FIP200 complex, also recognize these tagged targets [84, 85], initiating autophagosome formation. Selective autophagy is predominantly regulated by cargo labeling as well as recruitment of adaptor proteins to cargo.

Significant links between the regulation of selective autophagy and liver complications associated with NAFLD and HCC have been reported, supporting the manipulation of this process as a potential therapeutic strategy for liver-related diseases.

Autophagy in liver-related diseases

In addition to the fundamental function of starvation-induced autophagy, basal and selective autophagy contribute to maintaining the quality and quantity of cellular organelles and cytosolic proteins efficiently in the liver. Consequently, dysregulation or malfunction of the autophagic process is associated with the pathogenesis of multiple disorders and liver-related diseases, such as age-related hepatic disorders, NAFLD and HCC [86].

Aging in liver Aging is positively associated with severity and poor prognosis of several liver-related diseases, including alcoholic liver disease, NAFLD and HCC [87]. Furthermore, the age-dependent frequent decrease in autophagic activity underlies the pathogenesis of hepatic diseases. The initial finding of age-dependent decrease in hepatic autophagy was based on a marked increase in oxidative damage-triggered protein carbonyl derivatives in liver of 27-month-old rats, compared to 2-month-old rats [88]. Further studies indicated that the efficiency of autophagic degradation and capacity of autophagic proteolysis of exogenous amino acids of primary hepatocytes from older rats is dramatically decreased relative to that in young rats [89, 90]. Moreover, decreased expression of LC3-II and number of autophagosomes in mice were age-dependent [91]. These results suggest that the age-dependent decrease in efficiency of autophagy leads to substantially diminished clearance of inactive organelles, including mitochondria, generating increased oxidative stress and consequent accumulation of oxidized protein aggregates.

NAFLD Fatty liver is attributed to continuous intake of excess dietary fat without consumption of excessive alcohol [92]. Nonalcoholic fatty liver disease (NAFLD) incorporates a spectrum of liver-related diseases ranging from steatosis to steatohepatitis, fibrosis and cirrhosis. Non-alcoholic steatohepatitis (NASH) presents as a hepatic disease histologically similar to alcoholic hepatitis but occurs without consumption of excessive alcohol, representing a stage within NAFLD [93, 94]. Recent metabolic studies on animals and humans demonstrated that NAFLD represents one feature of metabolic syndrome closely associated with several metabolic diseases, such as diabetes and insulin resistance. Moreover, diabetes or insulin resistance conditions accelerate the entire pathological spectrum of NAFLD [94]. Chronic hepatic steatosis can trigger inflammatory responses [95]. In some cases, NAFLD progresses to NASH, which frequently advances into fibrosis and cirrhosis, and 4–27% NASH cases develop HCC [96].

In response to accelerated lipid availability or nutrient starvation, hepatic autophagy degrades lipid droplets to produce free fatty acids (FFA) for ATP generation. This

autophagy-induced degradation of hepatic lipid droplets is termed lipophagy [97]. Since lipophagy involves the selective degradation of hepatic lipid droplets, autophagy in liver could serve as a preventive mechanism against NAFLD. In contrast, several studies indicate that lipotoxic effects, including oxidative stress or insulin resistance, elicited by excess triglycerides and free fatty acids in NAFLD, inhibit activation of autophagy [19, 98, 99]. Hepatic autophagy regulates lipid metabolism through elimination of triglyceride accumulation in liver and prevents the development of steatosis [97]. Enhancement of autophagic activity using pharmaceutical agents, such as rapamycin or carbamazepine, has been shown to retard liver steatosis [99–102]. Moreover, pharmacological inhibition of autophagy via 3-methyladenine or knock-down of the essential autophagy gene, *atg5*, in hepatocytes challenged with a lipid load induced a dramatic increase in the cellular triglyceride level. Excessive triglyceride and cholesterol ester accumulation in hepatic lipid droplets was observed owing to decreased lipolysis and fatty acid β -oxidation in cells with low autophagy activity.

Compared to hepatocytes, autophagy in stellate cells exerts opposite effects on NAFLD progression. In NAFLD, quiescent hepatic stellate cells are activated and transdifferentiate into myofibroblasts, which express a large number of inflammatory cytokines and collagen, thereby promoting hepatic fibrosis [103]. In stellate cells from livers of autophagy-deficient mice, CCl₄-induced hepatic fibrosis was dramatically inhibited [104].

Abnormal structural and functional alterations of hepatic mitochondria in NAFLD are frequently observed [105]. Mitochondria are the powerhouse of cells and decreased mitochondrial function concomitant with alterations in structural and molecular pathways may elicit a metabolic imbalance, contributing to NAFLD progression. Mitochondrial biogenesis and mitophagy, a highly selective form of autophagy that functions in removal of damaged mitochondria, are the major pathways that regulate mitochondrial mass [86, 105]. The balance of mitochondrial biogenesis and mitophagy is a precisely regulated process that influences cellular homeostasis. Activation of hepatic mitophagy is reported to eliminate the lipid content and oxidative stress, and dysregulation of mitophagy implicated in the progression of NAFLD [19, 86, 97].

Under oxidative stress conditions, SQSTM1 is phosphorylated and subsequently binds to KEAP1 with high affinity. KEAP1 is an adaptor of the ubiquitin ligase complex for nuclear factor-erythroid 2-related factor-2 (NRF2). Downstream target proteins of NRF2, such as NAD(P)H, dehydrogenase quinone 1 (NQO1) and glutathione *S*-transferase (GST), ameliorate ROS production by damaged mitochondria [106, 107]. Selective

autophagic degradation of the SQSTM1-KEAP1 complex inhibits KEAP1-driven ubiquitylation and degradation of NRF2. In NAFLD, the turnover of hepatic cytoplasm fractions is substantially impaired due to dysfunctional autophagy/mitophagy, leading to accumulation of damaged mitochondria and elevated oxidative stress, which activates the SQSTM1-KEAP1-NRF2 pathway to protect hepatocytes against oxidative stress. However, under conditions where ROS levels exceed the antioxidant capacity of NRF2-related signals, various harmful effects, including lipid peroxidation, protein oxidation, and DNA damage, trigger liver injury [106, 107].

HCC As autophagy plays important roles in maintenance of the quality of organelles and supply of energy to cancer cells, autophagy-related pathways are considered important for cancer cell survival [108]. Previous studies indicate that loss of autophagy inhibits KRAS-triggered tumorigenesis of non small-cell lung cancer [109, 110]. Indeed, several clinical trials using a combination of existing anticancer drugs and autophagy inhibitors, such as chloroquine and hydroxychloroquine, are currently underway for several cancer types [111, 112]. However, the specific functions of autophagy in different tumors are complex and context-dependent. Pancreas-specific activated KRAS in mice leads to the development of pancreatic ductal adenocarcinoma (PDAC), which is suppressed by inhibition of autophagy [113]. In contrast, in mice lacking *Tp53*, loss of autophagy facilitates tumor progression [113].

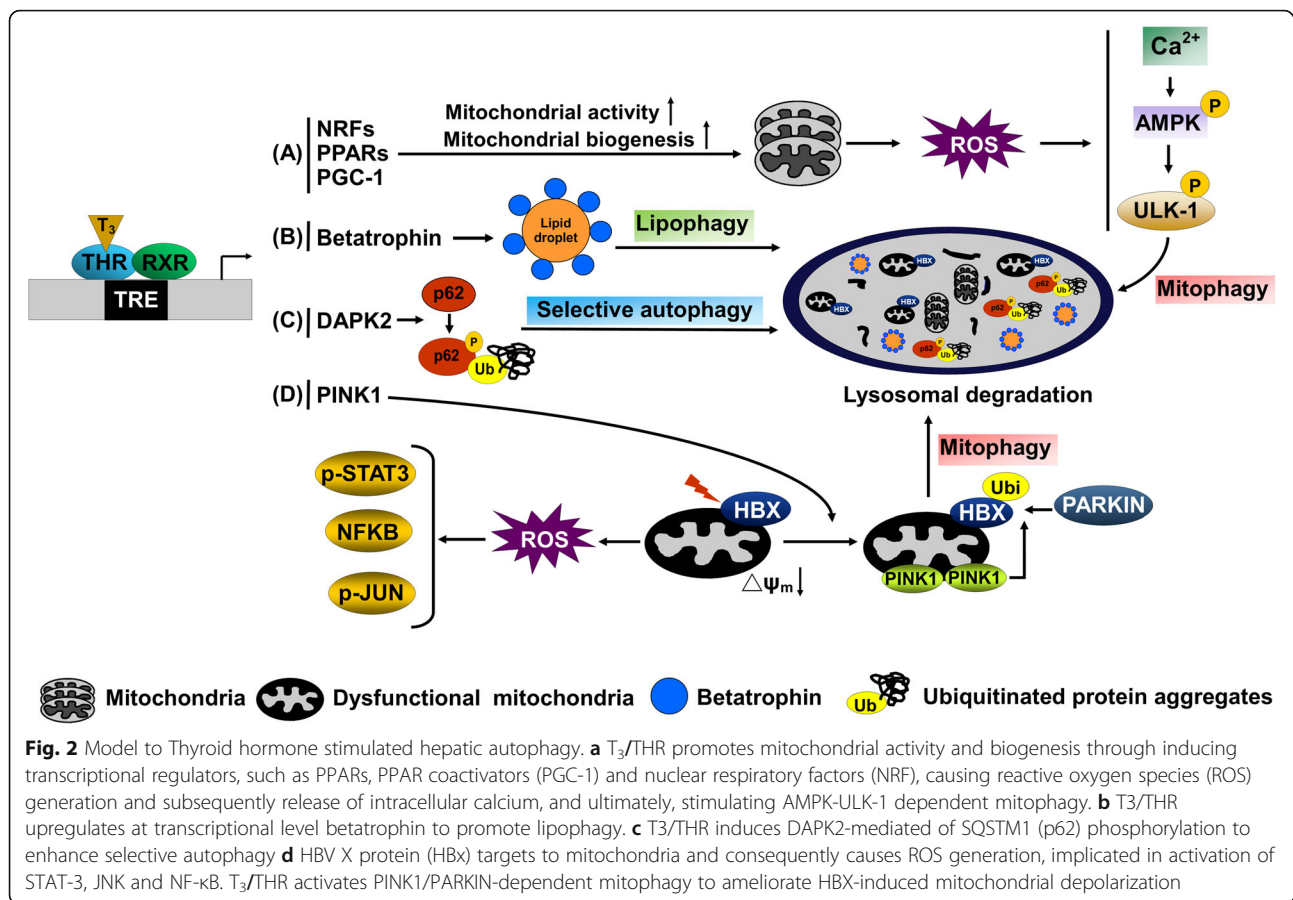
In the liver, autophagy appears to function as a tumor suppressor. For instance, mosaic depletion of *Atg5*, liver-specific *Atg7*, or *Beclin-1* in mice causes accumulation of degenerated protein aggregates, lipid droplets and damaged cellular organelles, including mitochondria and peroxisomes, as well as persistent activation of NRF2 owing to sequestration of KEAP1 by SQSTM1-positive cytoplasmic aggregates, leading to spontaneous hepatic carcinogenesis [114–116]. Simultaneous loss of *nrf-2* or *sqstm1* in mice with *Atg5* or *Atg7*-deficient liver suppresses tumor development [117]. Additionally, the cargo receptor degraded by autophagy, SQSTM1, accumulates in the hepatic tumor region [118], implying that the SQSTM1-KEAP1-NRF2 axis contributes to tumor growth. Further studies have revealed that heterozygous deletion of a major regulator of autophagy, *Beclin1*, increases the frequency of development of spontaneous tumors and HBV-induced hepatic premalignant lesions in mice [116, 119]. Additionally, ATG5 and BECLIN-1 levels are downregulated in hepatic tumor, compared to adjacent non-tumor regions [120]. HCC patients with low BECLIN-1 accompanied by high Bcl-xL (a crucial anti-apoptotic protein) expression display poorer disease-free and overall survival rates [120], indicating that

normal autophagic flux is important for HCC prevention in this apoptosis compromised background.

In view of the protective function of autophagy against hepatocarcinogenesis, researchers have focused on the mechanisms underlying autophagy-dependent tumor cell death identified in several cancer types [121–123]. The PI3K/Akt/mTOR axis is a known crucial signaling pathway for cell growth, survival and metabolism in tumor cells [124]. The mTOR pathway is activated in HCCs and manipulation of mTOR inhibitors shown to effectively exert anti-tumor effects in HCC [125, 126]. Rapamycin and its derivatives are mTOR inhibitors reported to serve as autophagy inducers with anti-tumor activity in a phase II study on 25 advanced HCC patients [127]. Liver transplantation is an important therapeutic option for the selected patients with unresectable HCC. In another study, rapamycin-directed immunosuppression was associated with improved survival after liver transplantation in HCC patients, but showed a trend toward lower survival in non-HCC patients, further showing the clinical evidence of its anti-cancer impact [128]. However, the utility of rapamycin and its derivatives in HCC therapy is controversial due to insufficient and conflicting clinical results. For example, everolimus (RAD001) exerted an anti-tumor effect in xenografts of human HCC models [129] whereas a recent clinical phase III trial disclosed no benefits on advanced HCC prognosis [130]. Co-targeting of mTOR via everolimus along with a PI3K/mTOR dual inhibitor, BEZ235, displayed greater efficacy through activating autophagy, specifically mitophagy, in tumors and led to decreased tumor sizes in a mouse model of HCC [131]. Interestingly, recent findings suggest that combination of mTOR inhibitors with SBI-0206965, a highly selective ULK1 inhibitor acting as a specific blocker of autophagy, has a promising effect on HCC [132]. Further investigations are required to validate the clinical utility of rapamycin. Sorafenib, a multi-kinase inhibitor used as first-line systemic therapy for advanced HCC, promotes autophagy-dependent cell death through Mcl-1 signaling [127]. A combination of sorafenib and autophagy inhibitors was also shown to induce an enhanced therapeutic effect. Sorafenib-induced autophagy-dependent cell death is reported to cause drug resistance in HCC [133]. Further research is therefore warranted to determine the utility of autophagy inducers in improving the current limits of HCC therapy and treatment outcomes. The involvement of autophagy as a function of tumor type, pathological stage and genetic context remains to be established.

TH/THR regulation of hepatic autophagy

The effects of TH on hepatic lysosomal activity and proteolysis were first described in 1978 [134], although the



underlying mechanisms were yet to be elucidated. Recently, T₃ was shown to enhance hepatic lysosomal activity accompanied by formation of autophagosomes in hepatic cells or livers of mice [25, 26]. The effects of T₃ on autophagy were THR-dependent and binding of NCoR-HDAC3, the corepressor of THR, abolished T₃-induced hepatic autophagy [25].

The T₃/THR axis is known to promote fatty acid β -oxidation in liver via activation of autophagy (Fig. 2A). Additionally, THs upregulate several critical genes involved in the autophagic process, including ULK1, PINK1, Beclin-1, DAPK2, betatrophin and LC3 (Fig. 2B-D) [16, 17, 25–27, 135]. These autophagy-related genes could be regulated directly by T₃/THR at the transcriptional level or indirectly through FOXO1 activation by dephosphorylation and deacetylation via TH-activated SIRT1 [136, 137]. SIRT1 is a NAD⁺-dependent deacetylase activated by increases in cellular NAD⁺ levels that serves as an energy sensor of cells to control transcriptional activity by T₃ and FOXO1. Furthermore, SIRT1 mediates T₃-induced autophagy through stimulation of expression as well as deacetylation of autophagy-related genes [136]. The master transcription factor, transcription factor EB (TFEB), regulates autophagy and lysosome-related genes may additionally be modulated by TH [44].

Other than transcriptional regulation, TH/THR complexes also regulate autophagy through post-transcriptional mechanisms. For instance, TH/THR is reported to activate the autophagy process through AMPK signaling. T₃ induces mitochondrial activity and biogenesis through inducing transcriptional regulators, such as PPARs, PPAR γ coactivator-1 (PGC-1) and nuclear respiratory factors [138], which causes the generation of reactive oxygen species (ROS) and subsequently release of intracellular calcium, and ultimately, CAMKK2 activation. Activated CAMKK2 phosphorylates AMPK, in turn, inhibiting mTOR signaling and stimulating autophagy via ULK1 phosphorylation [27]. SQSTM1 is a key adapter protein of autophagy, and accumulating evidence has demonstrated that phosphorylation of this protein facilitates clearance of ubiquitinated protein aggregates through the autophagic process [139, 140]. We previously showed that T₃/THR interactions induce transcription of DAPK2, which, in turn, phosphorylates SQSTM1 to promote clearance of protein aggregates through autophagy. Our results collectively indicate that the TH/THR signaling axis coordinates both transcriptional and post-translational regulation of hepatic autophagy [16].

TH regulation of selective autophagy Lipophagy is implicated in the digestion of neutral lipid droplets to release free fatty acids for mitochondrial lipid oxidation [97] and considered a major lipolytic pathway in hepatic cells [141]. Recently, we and other groups showed that T_3 induces lipophagy in both human and mouse hepatic cells that is essential for T_3 -mediated lipid catabolism [25, 26]. Although the specific receptors for recognition of lipid droplets by autophagosomes have not been identified, our results indicate that T_3 upregulates hepatic betatrophin transcription, which localizes to lipid droplets and possibly targets lipids for autophagic degradation [26].

TH is considered an inducer of mitochondrial activity and oxidative stress in the liver [142]. However, TH also induces mitophagy to prevent accumulation of damaged mitochondria and prevents hepatic injury by excessive ROS production [27]. TH is reported to stimulate the AMPK-ULK1 axis to initiate mitophagy. This process is dependent on translocation of ULK1 to mitochondria and subsequent recruitment of autophagic proteins, such as SQSTM1 and LC3-II, to damaged mitochondria for eventual degradation in autolysosomes. PINK1/PARKIN-mediated mitophagy is another pathway that contributes to protecting mitochondria against cellular ROS [143, 144]. PINK1 accumulates at the outer mitochondrial membrane upon membrane depolarization and subsequently recruits PARKIN to ubiquitinate damaged mitochondria, facilitating autophagic degradation. Experiments by our group showed that T_3 activates PINK1/PARKIN-dependent mitophagy to ameliorate HBX-induced mitochondrial depolarization [17]. Selective removal of damaged mitochondria by TH is crucial for preventing oxidative damage in the liver.

Recently, we demonstrated that transcriptional regulation of DAPK2 by TH promotes phosphorylation of SQSTM1 to facilitate clearance of diethylnitrosamine (DEN)-induced protein aggregates through autophagy, which may protect hepatocytes from DEN-induced hepatocarcinogenesis [16].

Potential application of TH and analogs in NAFLD and HCC

Thyroid hormones affect energy metabolism, glucose homeostasis and lipid utilization. Hypothyroidism is positively associated with high risk of NAFLD and HCC incidence, independent of other risk factors [8, 9]. THs may thus be useful in a therapeutic capacity in hyperlipidemia and NAFLD. However, excessive production or administration of exogenous THs triggers several side-effects, such as muscle wasting, increased heart rate with possible atrial arrhythmia, and heart failure [145]. Over the past few decades, biologists have focused on the possibility that TH derivatives have the beneficial actions of the thyroid hormone but without associated deleterious effects [145–149]. Recently, several analogs of TH

specific for THRB have been generated, which have therapeutic activity in liver-related diseases with limited side-effects in organs, such as heart or bone, with abundant THRA expression.

GC-1 was the first synthetic THRB agonist that could be used as a scaffold compound for developing other TH derivatives, which are easily modified and synthesized more efficiently than native TH [168]. GC-1 binds all major isoforms of THRB with similar affinity to T_3 . The binding affinity of GC-1 to THRB is 10-fold higher than that to THRA. GC-1 accumulates predominantly in the liver but its uptake is low in other organs, including skeletal muscle and heart. Due to the specific binding of GC-1 to THRB in liver, it may exhibit gene-specific actions relative to the native form of the thyroid hormone [145].

In the CMD diet-triggered NAFLD rat model, administration of either T_3 or GC-1 could prevent steatohepatitis. Notably, GC-1 treatment not only caused a more significant reduction in hepatic TG levels but also did not elicit significant side-effects, such as increased heart rate and muscle wasting [150, 151]. These findings support the potential therapeutic application of THs on NAFLD prevention. Furthermore, T_3 and GC-1 exert therapeutic effects on HCC [16, 29, 152, 153]. Upon treatment of rats with DEN combined with a choline-deficient (CD) diet for weeks, development of preneoplastic lesions was observed. Administration of T_3 or GC-1 dramatically reduced the preneoplastic lesions caused by DEN.

Recently, a liver-selective prodrug, MB07811, was developed. Following hepatic enzymatic cleavage, the active form, MB07344, is generated that has been characterized as a liver-selective THRB agonist [154]. In HFD-exposed or diabetic fatty animals, two weeks of MB07811 treatment significantly reduced both hepatic and plasma triglyceride levels with no other side-effects of TH [154]. Clearance of hepatic lipid droplets by MB07344 may be attributable to acceleration of mitochondrial activity and fatty acid catabolism [12].

KB2115 has been identified as another THRB-selective agonist preferentially taken up in the liver. In both animal and clinical studies, administration of KB2115 significantly lowered serum total and LDL cholesterol and prevented the development of hepatic steatosis [155–157]. Furthermore, treatment with KB2115 as well as GC-1 in rats induced hepatomitogenic activity with no evidence of hepatic toxicity [158], supporting its potential for regenerative therapy, including liver transplantation and other surgical modalities.

Despite encouraging results from human clinical studies showing that GC-1, MB07811 and KB2115 exert therapeutic effects via lowering the levels of serum LDL

cholesterol and triglycerides, these compounds have not reached human clinical trials or been developed into therapeutic agents. Phase II trials on GC-1 and MB07344 are yet to be performed. Clinical studies on KB2115 were discontinued due to cartilage damage and hepatic toxicity observed following long-term dosing in dogs [29, 159].

More recently, two liver-directed THRB selective agonists, MGL-3196 and VK2809, have been developed [160, 161]. Results from phase II trials showed preventive effects on NAFLD accompanied by a decrease in serum levels of LDL cholesterol and triglycerides as well as hepatic lipids with none of the side-effects of the thyroid hormone axis. Thus, therapeutic application of THs in liver-related diseases in the clinic is feasible.

Recent studies by our group revealed a mechanistic link between TH and HCC prevention [16, 17]. DEN-treated liver cells have been shown to cause ROS accumulation accompanied by increased DNA damage and hepatic injury [162]. Increased oxidative stress may occur due to the accumulation of SQSTM1-associated protein aggregates and damaged organelles. SQSTM1 is the major component of inclusion bodies in hepatocytes (termed Mallory bodies), which have been identified in the livers of patients diagnosed with alcoholic hepatitis and NAFLD [163, 164]. T_3 -treated mice exhibit higher DAPK2 expression, and consequently, T_3 -driven autophagy alleviates DEN triggered hepatic injury and hepatocellular carcinogenesis [16].

Chronic infection of hepatitis B virus in liver is one of the major risk factors for HCC development, and the HBV X protein (HBx) exerts powerful disruptive effects on mitochondrial dysfunction and ROS production, leading to progression of HCC [165]. Our group further showed that mitophagy triggered by the TH-PINK1-Parin axis is a putative pathway implicated in protection of HBx-induced hepatocellular carcinogenesis. Additionally, TH-triggered autophagy was shown to reduce hepatic lipid droplets and mitochondrial fatty acid oxidation [25, 27]. These results collectively support the involvement of TH-triggered autophagy in regulating mitochondrial metabolism in the development of NAFLD and HCC and provide insights into the physiological significance of THs in prevention of liver-related diseases [17]. However, the role of autophagy in the preventive and therapeutic potential of TH analogs (GC-1, MB07344, KB2115, MGL-3196 and VK2809) have not yet been determined.

Conclusions

Over the past decade, molecular mechanisms and physiological effects of THs in liver have gradually been elucidated. Disruption of TH signals is known to cause multiple organ dysfunction that is closely associated with several diseases [5, 6]. Liver is one of the major target

tissues of TH, and people with low thyroid function are closely associated with multiple liver-related diseases. The cross-sectional and systemic view studies indicated that subclinical hypothyroidism, and even in the upper normal limit of TSH levels were significantly associated with the risk of NAFLD and advanced fibrosis [166–169]. Interestingly, high level of TSH itself may be an important risk factor points to the pathogenesis of NAFLD, independent of thyroid hormones [168, 169], and the supplementation of levothyroxine shows clear benefits on NAFLD in subclinical- and mild subclinical- hypothyroidism patients with dyslipidemia [170]. Moreover, both *in vitro* and *in vivo* experiments demonstrated THs and THs analogs exhibit the potential therapeutic and preventive application in NAFLD and HCC [7, 16, 17, 142, 145–149], highlighting the urgent need to understand the complex mechanisms underlying the effects of thyroid hormone. The TH/THR axis is a strong inducer of hepatic autophagy, which promotes lipid droplet degradation as well as mitochondrial biogenesis and turnover. This process has been implicated in the removal of damaged mitochondria and ROS that cause hepatic injury [7, 16, 17, 26, 27, 28]. In the present review, we have discussed the growing complexity of TH-regulated autophagy, highlighted advantages associated with the TH/autophagy axis-based therapeutic strategy for liver-related diseases, and discussed recent findings that may be exploited for improving the therapeutic outcomes of NAFLD and HCC [11, 12, 148, 150, 151, 154].

However, several challenges in TH-based therapies for hepatic diseases, HCC in particular, remain to be overcome, since the actions of individual TH derivatives within the same tissue may be different. Alterations in TH deiodinases, transporters, co-activators or co-repressors may influence the cellular level and molecular actions of THs, in turn, causing metabolic changes [44]. Moreover, the processes of cancer progression are complex. Individual THR isoforms exert different effects in a cancer type- and stage-specific manner. The TH/THR signals and interacting partners may facilitate the switch from tumor suppression in the premalignant stages to promotion in the later stages of HCC [7]. For instance, administration of TH not only reduces the size of preneoplastic lesions in the livers of rats suffering with HCC, but suppresses the aberrant cellular growth via control the expression of cell cycle regulators, such as CDK2, Cyclin E, UHRF1, STMN1 mir-214 and BC200 lncRNA [7, 171–174]. Our recent studies further support the preventive effect of TH on hepatocarcinogenesis via activating autophagy [16, 17], whereas TH/THR is reported to promote metastasis and chemoresistance through control the expressions of BSSP4, TRAIL, BCL2L11, LCN2, mir-21, and mir-130b [7, 173, 175–180]. This characteristic of THs

supports the double-edged sword effect of autophagy in cancer progression. Autophagy mitigates stress-caused damage by removing damaged cellular organelles and protein aggregates and impaired autophagy causes accumulation of excess oxidative stress and DNA damage, leading to initiating hepatocarcinogenesis. Mosaic depletion of *Atg5*, liver-specific *Atg7* or *Beclin-1* in mice causes accumulation of degenerated protein aggregates, lipid droplets and damaged cellular organelles, leading to spontaneous hepatic carcinogenesis [114, 116]. By contrast, after the initiation of tumorigenesis, autophagy can also facilitate tumor cell survival under metabolic stress, becoming dormant and regenerating with anti-stress capacity that promotes tumor progression [181]. For instance, malfunction of autophagy inhibits KRAS-triggered tumorigenesis of non small-cell lung cancer and DEN-induced HCC. [109, 110, 182]. Moreover, inhibition of autophagy increases the sensitivity of chemotherapy and triggers cellular apoptosis and necrosis of HCC by activating several tumor suppressor genes, including p53, PTEN, CDKN1, CDKN2 and Rb1 [182–184]. Therefore, further animal and clinical studies are warranted to establish the specific functions of THs-induced autophagy in the different processes that lead to HCC development.

Abbreviations

CD: Choline-deficient; DEN: Diethylnitrosamine; eNOS: Nitric oxide synthase; ERK: Extracellular signal-regulated kinase; ERα: Estrogen receptor-α; GLUT1: Glucose transporter 1; GST: Glutathione S-transferase; DIO: Iodothyronine deiodinase; HAT: Histone acetyl transferase; HCC: Hepatocellular carcinoma; HDAC: Histone deacetylase; HFD: High-fat diet; HIF-1α: Hypoxia-inducible factor-1α; KCNH2: Potassium voltage-gated channel, subfamily H, member 2; LAMP2A: Lysosome-associated membrane protein type 2A; MAPK: Mitogen-activated protein kinase; MCT 4: Monocarboxylate transporter 4; mTOR: Mammalian target of rapamycin; NAFLD: Non-alcoholic fatty liver disease; NCoR1: Nuclear receptor corepressor 1; NQO1: NAD(P)H, dehydrogenase quinone 1; NRF2: Nuclear factor-erythroid 2-related factor-2; PCAF: p300/CBP-associated factor; PDAC: Pancreatic ductal adenocarcinoma; PFKF: Platelet-type phosphofructokinase; PGC-1: PPARγ coactivator-1; ROS: Reactive oxygen species; RGD: Arg-Gly-Asp; RXR: Retinoid X receptor; SMRT: Silencing mediator for retinoid or thyroid hormone receptors; SRC: Steroid hormone receptor coactivator; STAT3: Signal transducer and activator of transcription-3; TFEb: Transcription factor EB; TH: Thyroid hormone; THR: Thyroid hormone receptor; TRAP: TR-associated protein; TRE: Thyroid hormone response elements; TRH: Thyrotropin-releasing hormone; TSH: Thyroid stimulating hormone; VDR: Vitamin D receptors

Acknowledgments

Not applicable.

Ethics approval and consent participate

Not applicable.

Funding

This work was supported by grants from Chang Gung Memorial Hospital, Taoyuan, Taiwan (CMRPD1G0421, CMRPD1G0422, CRRPD1F0011, CRRPD1F0012, CRRPD1F0013, NMRPD1G0942, NMRPD1G0951 and CMRPD1H0631 to KHL) and the Ministry of Science and Technology of the Republic of China (MOST 106-2320-B-182-031-MY3 and 106-2320-B-182-032-MY3 to KHL, and MOST 105-2321-B-182-002-MY3 and 107-2320-B-182-025 to HCC).

Availability of data and materials

Not applicable.

Authors' contributions

HCC and CYT composed the idea and wrote the manuscript. CYT and MMT were involved in preparing the Figure content. CTY and KHL supervised the process. All authors read and approved the final manuscript.

Consent for publication

Not applicable.

Competing interests

The authors declare that they have no competing interests

Publisher's Note

Springer Nature remains neutral with regard to jurisdictional claims in published maps and institutional affiliations.

Author details

¹Radiation Biology Research Center, Institute for Radiological Research, Chang Gung University/Chang Gung Memorial Hospital, Linkou, Taoyuan, Taiwan. ²Kidney Research Center and Department of Nephrology, Chang Gung Immunology Consortium, Chang Gung Memorial Hospital, Taoyuan 333, Taiwan. ³Department of Nursing, Chang-Gung University of Science and Technology, Taoyuan, Taiwan 333. ⁴Department of General Surgery, Chang Gung Memorial Hospital, Chiayi, Taiwan 613. ⁵Liver Research Center, Chang Gung Memorial Hospital, Linkou, Taoyuan, Taiwan 333. ⁶Department of Biochemistry, College of Medicine, Chang-Gung University, 259 Wen-Hwa 1 Road, Taoyuan 333, Taiwan, Republic of China. ⁷Research Center for Chinese Herbal Medicine, College of Human Ecology, Chang Gung University of Science and Technology, Taoyuan, Taiwan.

Received: 19 February 2019 Accepted: 26 February 2019

Published online: 08 March 2019

References

1. Yen PM. Physiological and molecular basis of thyroid hormone action. *Physiol Rev*. 2001;81(3):1097–142.
2. Sinha RA, Singh BK, Yen PM. Direct effects of thyroid hormones on hepatic lipid metabolism. *Nat Rev Endocrinol*. 2018;14(5):259–69.
3. Feely J, Isles TE. Screening for thyroid dysfunction in diabetics. *Br Med J*. 1979;1(6179):1678.
4. Gray RS, Irvine WJ, Clarke BF. Screening for thyroid dysfunction in diabetics. *Br Med J*. 1979;2(6202):1439.
5. Tatar E, Kircelli F, Asci G, Carrero JJ, Gungor O, Demirci MS, et al. Associations of triiodothyronine levels with carotid atherosclerosis and arterial stiffness in hemodialysis patients. *Clin J Am Soc Nephrol*. 2011;6(9):2240–6.
6. Tatar E, Seziz Demirci M, Kircelli F, Gungor O, Yaprak M, Asci G, et al. The association between thyroid hormones and arterial stiffness in peritoneal dialysis patients. *Int Urol Nephrol*. 2012;44(2):601–6.
7. Chi HC, Chen CY, Tsai MM, Tsai CY, Lin KH. Molecular functions of thyroid hormones and their clinical significance in liver-related diseases. *Biomed Res Int*. 2013;2013:601361.
8. Hassan MM, Kaseb A, Li D, Patt YZ, Vauthey JN, Thomas MB, et al. Association between hypothyroidism and hepatocellular carcinoma: a case-control study in the United States. *Hepatology*. 2009;49(5):1563–70.
9. Lee J, Ha J, Jo K, Lim DJ, Lee JM, Chang SA, et al. Male-specific association between subclinical hypothyroidism and the risk of non-alcoholic fatty liver disease estimated by hepatic steatosis index: Korea National Health and Nutrition Examination Survey 2013 to 2015. *Sci Rep*. 2018;8(1):15145.
10. Liangpunsakul S, Chalasani N. Is hypothyroidism a risk factor for non-alcoholic steatohepatitis? *J Clin Gastroenterol*. 2003;37(4):340–3.
11. Perra A, Simbula G, Simbula M, Pibiri M, Kowalik MA, Sulas P, et al. Thyroid hormone (T3) and TRbeta agonist GC-1 inhibit/reverse nonalcoholic fatty liver in rats. *FASEB J*. 2008;22(8):2981–9.
12. Cable EE, Finn PD, Stebbins JW, Hou J, Ito BR, van Poelje PD, et al. Reduction of hepatic steatosis in rats and mice after treatment with a liver-targeted thyroid hormone receptor agonist. *Hepatology*. 2009;49(2):407–17.

13. Akino K, Akita S, Mizuguchi T, Takumi I, Yu R, Wang XY, et al. A novel molecular marker of pituitary tumor transforming gene involves in a rat liver regeneration. *J Surg Res*. 2005;129(1):142–6.
14. Mollica MP, Lionetti L, Moreno M, Lombardi A, De Lange P, Antonelli A, et al. 3,5-diiodo-L-thyronine, by modulating mitochondrial functions, reverses hepatic fat accumulation in rats fed a high-fat diet. *J Hepatol*. 2009;51(2):363–70.
15. Naehrlich L, Dorr HG, Bagheri-Behrouzi A, Rauh M. Iodine deficiency and subclinical hypothyroidism are common in cystic fibrosis patients. *J Trace Elem Med Biol*. 2012.
16. Chi HC, Chen SL, Tsai CY, Chuang WY, Huang YH, Tsai MM, et al. Thyroid hormone suppresses hepatocarcinogenesis via DAPK2 and SQSTM1-dependent selective autophagy. *Autophagy*. 2016;12(12):2271–85.
17. Chi HC, Chen SL, Lin SL, Tsai CY, Chuang WY, Lin YH, et al. Thyroid hormone protects hepatocytes from HBx-induced carcinogenesis by enhancing mitochondrial turnover. *Oncogene*. 2017;36(37):5274–84.
18. Klionsky DJ, Abdelmohsen K, Abe A, Abedin MJ, Abeliovich H, Acevedo Arozena A, et al. Guidelines for the use and interpretation of assays for monitoring autophagy (3rd edition). *Autophagy*. 2016;12(1):1–222.
19. Yang L, Li P, Fu S, Calay ES, Hotamisligil GS. Defective hepatic autophagy in obesity promotes ER stress and causes insulin resistance. *Cell Metab*. 2010;11(6):467–78.
20. Stolz A, Ernst A, Dikic I. Cargo recognition and trafficking in selective autophagy. *Nat Cell Biol*. 2014;16(6):495–501.
21. Feng GS. Conflicting roles of molecules in hepatocarcinogenesis: paradigm or paradox. *Cancer Cell*. 2012;21(2):150–4.
22. Ding WX. Role of autophagy in liver physiology and pathophysiology. *World J Biol Chem*. 2010;1(1):3–12.
23. Komatsu M. Liver autophagy: physiology and pathology. *J Biochem*. 2012;152(1):5–15.
24. Cui J, Gong Z, Shen HM. The role of autophagy in liver cancer: molecular mechanisms and potential therapeutic targets. *Biochim Biophys Acta*. 2013;1836(1):15–26.
25. Sinha RA, You SH, Zhou J, Siddique MM, Bay BH, Zhu X, et al. Thyroid hormone stimulates hepatic lipid catabolism via activation of autophagy. *J Clin Invest*. 2012;122(7):2428–38.
26. Tseng YH, Ke PY, Liao CJ, Wu SM, Chi HC, Tsai CY, et al. Chromosome 19 open reading frame 80 is upregulated by thyroid hormone and modulates autophagy and lipid metabolism. *Autophagy*. 2014;10(1):20–31.
27. Sinha RA, Singh BK, Zhou J, Wu Y, Farah BL, Ohba K, et al. Thyroid hormone induction of mitochondrial activity is coupled to mitophagy via ROS-AMPK-ULK1 signaling. *Autophagy*. 2015;11(8):1341–57.
28. Senese R, Cioffi F, de Lange P, Goglia F, Lanni A. Thyroid: biological actions of 'nonclassical' thyroid hormones. *J Endocrinol*. 2014;221(2):R1–12.
29. Kowalik MA, Columbano A, Perra A. Thyroid Hormones, Thyromimetics and Their Metabolites in the Treatment of Liver Disease. *Front Endocrinol*. 2018;9:382.
30. Brent GA. Mechanisms of thyroid hormone action. *J Clin Invest*. 2012;122(9):3035–43.
31. Weinberger C, Thompson CC, Ong ES, Lebo R, Gruol DJ, Evans RM. The c-erb-A gene encodes a thyroid hormone receptor. *Nature*. 1986;324(6098):641–6.
32. Sap J, Munoz A, Damm K, Goldberger Y, Ghysdael J, Leutz A, et al. The c-erb-A protein is a high-affinity receptor for thyroid hormone. *Nature*. 1986;324(6098):635–40.
33. Cheng SY, Leonard JL, Davis PJ. Molecular aspects of thyroid hormone actions. *Endocr Rev*. 2010;31(2):139–70.
34. Williams GR. Cloning and characterization of two novel thyroid hormone receptor beta isoforms. *Mol Cell Biol*. 2000;20(22):8329–42.
35. Mitsuhashi T, Tennyson GE, Nikodem VM. Alternative splicing generates messages encoding rat c-erbA proteins that do not bind thyroid hormone. *Proc Natl Acad Sci U S A*. 1988;85(16):5804–8.
36. Sakurai A, Nakai A, DeGroot LJ. Expression of three forms of thyroid hormone receptor in human tissues. *Mol Endocrinol*. 1989;3(2):392–9.
37. Ayers S, Switnicki MP, Angajala A, Lammel J, Arumanayagam AS, Webb P. Genome-wide binding patterns of thyroid hormone receptor beta. *PLoS One*. 2014;9(2):e81186.
38. Grontved L, Waterfall JJ, Kim DW, Baek S, Sung MH, Zhao L, et al. Transcriptional activation by the thyroid hormone receptor through ligand-dependent receptor recruitment and chromatin remodelling. *Nat Commun*. 2015;6:7048.
39. Ramadoss P, Abraham BJ, Tsai L, Zhou Y, Costa-e-Sousa RH, Ye F, et al. Novel mechanism of positive versus negative regulation by thyroid hormone receptor beta1 (TRbeta1) identified by genome-wide profiling of binding sites in mouse liver. *J Biol Chem*. 2014;289(3):1313–28.
40. Cheng SY. Multiple mechanisms for regulation of the transcriptional activity of thyroid hormone receptors. *Rev Endocr Metab Disord*. 2000;1(1-2):9–18.
41. McKenna NJ, O'Malley BW. Combinatorial control of gene expression by nuclear receptors and coregulators. *Cell*. 2002;108(4):465–74.
42. Fondell JD, Ge H, Roeder RG. Ligand induction of a transcriptionally active thyroid hormone receptor coactivator complex. *Proc Natl Acad Sci U S A*. 1996;93(16):8329–33.
43. Singh BK, Sinha RA, Ohba K, Yen PM. Role of thyroid hormone in hepatic gene regulation, chromatin remodeling, and autophagy. *Mol Cell Endocrinol*. 2017;458:160–8.
44. Chatterjee VK, Lee JK, Rentoumis A, Jameson JL. Negative regulation of the thyroid-stimulating hormone alpha gene by thyroid hormone: receptor interaction adjacent to the TATA box. *Proc Natl Acad Sci U S A*. 1989;86(23):9114–8.
45. Tagami T, Madison LD, Nagaya T, Jameson JL. Nuclear receptor corepressors activate rather than suppress basal transcription of genes that are negatively regulated by thyroid hormone. *Mol Cell Biol*. 1997;17(5):2642–8.
46. Wang D, Xia X, Liu Y, Oetting A, Walker RL, Zhu Y, et al. Negative regulation of TSHalpha target gene by thyroid hormone involves histone acetylation and corepressor complex dissociation. *Mol Endocrinol*. 2009;23(5):600–9.
47. Song Y, Shan S, Zhang Y, Liu W, Ding W, Ren W, et al. Ligand-dependent corepressor acts as a novel corepressor of thyroid hormone receptor and represses hepatic lipogenesis in mice. *J Hepatol*. 2012;56(1):248–54.
48. Tansey WP, Catanzaro DF. Sp1 and thyroid hormone receptor differentially activate expression of human growth hormone and chorionic somatomammotropin genes. *J Biol Chem*. 1991;266(15):9805–13.
49. Shih A, Lin HY, Davis FB, Davis PJ. Thyroid hormone promotes serine phosphorylation of p53 by mitogen-activated protein kinase. *Biochemistry*. 2001;40(9):2870–8.
50. Kakizawa T, Miyamoto T, Ichikawa K, Takeda T, Suzuki S, Mori J, et al. Silencing mediator for retinoid and thyroid hormone receptors interacts with octamer transcription factor-1 and acts as a transcriptional repressor. *J Biol Chem*. 2001;276(13):9720–5.
51. Palomino T, Sanchez-Pacheco A, Pena P, Aranda A. A direct protein-protein interaction is involved in the cooperation between thyroid hormone and retinoic acid receptors and the transcription factor GHF-1. *FASEB J*. 1998;12(12):1201–9.
52. Sanchez-Pacheco A, Pena P, Palomino T, Guell A, Castrillo JL, Aranda A. The transcription factor GHF-1, but not the splice variant GHF-2, cooperates with thyroid hormone and retinoic acid receptors to stimulate rat growth hormone gene expression. *FEBS Lett*. 1998;422(1):103–7.
53. Lutz M, Burke LJ, LeFevre P, Myers FA, Thorne AW, Crane-Robinson C, et al. Thyroid hormone-regulated enhancer blocking: cooperation of CTCF and thyroid hormone receptor. *EMBO J*. 2003;22(7):1579–87.
54. Weth O, Weth C, Bartkuhn M, Leers J, Uhle F, Renkawitz R. Modular insulators: genome wide search for composite CTCF/thyroid hormone receptor binding sites. *PLoS One*. 2010;5(4):e10119.
55. Davis FB, Tang HY, Shih A, Keating T, Lansing L, Hercbergs A, et al. Acting via a cell surface receptor, thyroid hormone is a growth factor for glioma cells. *Cancer Res*. 2006;66(14):7270–5.
56. Bergh JJ, Lin HY, Lansing L, Mohamed SN, Davis FB, Mousa S, et al. Integrin alpha5beta3 contains a cell surface receptor site for thyroid hormone that is linked to activation of mitogen-activated protein kinase and induction of angiogenesis. *Endocrinology*. 2005;146(7):2864–71.
57. Cody V, Davis PJ, Davis FB. Molecular modeling of the thyroid hormone interactions with alpha v beta 3 integrin. *Steroids*. 2007;72(2):165–70.
58. Davis PJ, Goglia F, Leonard JL. Nongenomic actions of thyroid hormone. *Nat Rev Endocrinol*. 2016;12(2):111–21.
59. Cao X, Kambe F, Yamauchi M, Seo H. Thyroid-hormone-dependent activation of the phosphoinositide 3-kinase/Akt cascade requires Src and enhances neuronal survival. *Biochem J*. 2009;424(2):201–9.
60. Davis PJ, Davis FB. Nongenomic actions of thyroid hormone. *Thyroid*. 1996;6(5):497–504.
61. Cao HJ, Lin HY, Luidens MK, Davis FB, Davis PJ. Cytoplasm-to-nucleus shuttling of thyroid hormone receptor-beta1 (Trbeta1) is directed from a plasma membrane integrin receptor by thyroid hormone. *Endocr Res*. 2009;34(1-2):31–42.
62. Tang HY, Lin HY, Zhang S, Davis FB, Davis PJ. Thyroid hormone causes mitogen-activated protein kinase-dependent phosphorylation of the nuclear estrogen receptor. *Endocrinology*. 2004;145(7):3265–72.

63. Baumann CT, Maruvada P, Hager GL, Yen PM. Nuclear cytoplasmic shuttling by thyroid hormone receptors: multiple protein interactions are required for nuclear retention. *J Biol Chem*. 2001;276(14):11237–45.
64. Lin HY, Shih A, Davis FB, Davis PJ. Thyroid hormone promotes the phosphorylation of STAT3 and potentiates the action of epidermal growth factor in cultured cells. *Biochem J*. 1999;338(Pt 2):427–32.
65. Chen Y, Chen PL, Chen CF, Sharp ZD, Lee WH. Thyroid hormone, T3-dependent phosphorylation and translocation of Trip230 from the Golgi complex to the nucleus. *Proc Natl Acad Sci U S A*. 1999;96(8):4443–8.
66. Vasudevan N, Ogawa S, Pfaff D. Estrogen and thyroid hormone receptor interactions: physiological flexibility by molecular specificity. *Physiol Rev*. 2002;82(4):923–44.
67. Meng R, Tang HY, Westfall J, London D, Cao JH, Mousa SA, et al. Crosstalk between integrin α v β 3 and estrogen receptor- α is involved in thyroid hormone-induced proliferation in human lung carcinoma cells. *PLoS One*. 2011;6(11):e27547.
68. Hiroi Y, Kim HH, Ying H, Furuya F, Huang Z, Simoncini T, et al. Rapid nongenomic actions of thyroid hormone. *Proc Natl Acad Sci U S A*. 2006;103(38):14104–9.
69. Moeller LC, Cao X, Dumitrescu AM, Seo H, Refetoff S. Thyroid hormone mediated changes in gene expression can be initiated by cytosolic action of the thyroid hormone receptor beta through the phosphatidylinositol 3-kinase pathway. *Nucl Recept Signal*. 2006;4:e020.
70. Cao X, Kambe F, Moeller LC, Refetoff S, Seo H. Thyroid hormone induces rapid activation of Akt/protein kinase B-mammalian target of rapamycin-p70S6K cascade through phosphatidylinositol 3-kinase in human fibroblasts. *Mol Endocrinol*. 2005;19(1):102–12.
71. Moeller LC, Dumitrescu AM, Refetoff S. Cytosolic action of thyroid hormone leads to induction of hypoxia-inducible factor-1 α and glycolytic genes. *Mol Endocrinol*. 2005;19(12):2955–63.
72. Storey NM, Gentile S, Ullah H, Russo A, Muessel M, Erxleben C, et al. Rapid signaling at the plasma membrane by a nuclear receptor for thyroid hormone. *Proc Natl Acad Sci U S A*. 2006;103(13):5197–201.
73. Lei J, Nowbar S, Mariash CN, Ingbar DH. Thyroid hormone stimulates Na-K-ATPase activity and its plasma membrane insertion in rat alveolar epithelial cells. *Am J Physiol Lung Cell Mol Physiol*. 2003;285(3):L762–72.
74. Lei J, Mariash CN, Bhargava M, Wattenberg EV, Ingbar DH. T3 increases Na-K-ATPase activity via a MAPK/ERK1/2-dependent pathway in rat adult alveolar epithelial cells. *Am J Physiol Lung Cell Mol Physiol*. 2008;294(4):L749–54.
75. Guigon CJ, Kim DW, Willingham MC, Cheng SY. Mutation of thyroid hormone receptor-beta in mice predisposes to the development of mammary tumors. *Oncogene*. 2011;30(30):3381–90.
76. Guigon CJ, Cheng SY. Novel oncogenic actions of TRbeta mutants in tumorigenesis. *IUBMB Life*. 2009;61(5):528–36.
77. Guigon CJ, Zhao L, Lu C, Willingham MC, Cheng SY. Regulation of beta-catenin by a novel nongenomic action of thyroid hormone beta receptor. *Mol Cell Biol*. 2008;28(14):4598–608.
78. Yoritatsu T, Klionsky DJ. Autophagy: molecular machinery for self-eating. *Cell Death Differ*. 2005;12(Suppl 2):1542–52.
79. Mizushima N, Levine B, Cuervo AM, Klionsky DJ. Autophagy fights disease through cellular self-digestion. *Nature*. 2008;451(7182):1069–75.
80. Ciechanover A, Orian A, Schwartz AL. Ubiquitin-mediated proteolysis: biological regulation via destruction. *Bioessays*. 2000;22(5):442–51.
81. Nedelsky NB, Todd PK, Taylor JP. Autophagy and the ubiquitin-proteasome system: collaborators in neuroprotection. *Biochim Biophys Acta*. 2008;1782(12):691–9.
82. Khaminets A, Behl C, Dikic I. Ubiquitin-Dependent And Independent Signals In Selective Autophagy. *Trends Cell Biol*. 2016;26(1):6–16.
83. Rogov V, Dotsch V, Johansen T, Kirkin V. Interactions between autophagy receptors and ubiquitin-like proteins form the molecular basis for selective autophagy. *Mol Cell*. 2014;53(2):167–78.
84. Fujita N, Morita E, Itoh T, Tanaka A, Nakaoka M, Osada Y, et al. Recruitment of the autophagic machinery to endosomes during infection is mediated by ubiquitin. *J Cell Biol*. 2013;203(1):115–28.
85. Lazarou M, Sliter DA, Kane LA, Sarraf SA, Wang C, Burman JL, et al. The ubiquitin kinase PINK1 recruits autophagy receptors to induce mitophagy. *Nature*. 2015;524(7565):309–14.
86. Ueno T, Komatsu M. Autophagy in the liver: functions in health and disease. *Nat Rev Gastroenterol Hepatol*. 2017;14(3):170–84.
87. Kim IH, Kisseleva T, Brenner DA. Aging and liver disease. *Curr Opin Gastroenterol*. 2015;31(3):184–91.
88. Vittorini S, Paradiso C, Donati A, Cavallini G, Masini M, Gori Z, et al. The age-related accumulation of protein carbonyl in rat liver correlates with the age-related decline in liver proteolytic activities. *J Gerontol A Biol Sci Med Sci*. 1999;54(8):B318–23.
89. Cavallini G, Donati A, Gori Z, Pollera M, Bergamini E. The protection of rat liver autophagic proteolysis from the age-related decline co-varies with the duration of anti-ageing food restriction. *Exp Gerontol*. 2001;36(3):497–506.
90. Donati A, Cavallini G, Paradiso C, Vittorini S, Pollera M, Gori Z, et al. Age-related changes in the regulation of autophagic proteolysis in rat isolated hepatocytes. *J Gerontol A Biol Sci Med Sci*. 2001;56(7):B288–93.
91. Uddin MN, Nishio N, Ito S, Suzuki H, Isobe K. Autophagic activity in thymus and liver during aging. *Age (Dordr)*. 2012;34(1):75–85.
92. Farrell GC, Larter CZ. Nonalcoholic fatty liver disease: from steatosis to cirrhosis. *Hepatology*. 2006;43(2 Suppl 1):S99–S112.
93. Das K, Kar P. Non-alcoholic steatohepatitis. *J Assoc Physicians India*. 2005;53:195–9.
94. Ota T, Takamura T, Kurita S, Matsuzawa N, Kita Y, Uno M, et al. Insulin resistance accelerates a dietary rat model of nonalcoholic steatohepatitis. *Gastroenterology*. 2007;132(1):282–93.
95. Brenner C, Galluzzi L, Kepp O, Kroemer G. Decoding cell death signals in liver inflammation. *J Hepatol*. 2013;59(3):583–94.
96. Yoon HJ, Cha BS. Pathogenesis and therapeutic approaches for non-alcoholic fatty liver disease. *World J Hepatol*. 2014;6(11):800–11.
97. Singh R, Kaushik S, Wang Y, Xiang Y, Novak I, Komatsu M, et al. Autophagy regulates lipid metabolism. *Nature*. 2009;458(7242):1131–5.
98. Fukuo Y, Yamashina S, Sonoue H, Arakawa A, Nakadera E, Aoyama T, et al. Abnormality of autophagic function and cathepsin expression in the liver from patients with non-alcoholic fatty liver disease. *Hepatol Res*. 2014;44(9):1026–36.
99. Park HW, Park H, Semple IA, Jang I, Ro SH, Kim M, et al. Pharmacological correction of obesity-induced autophagy arrest using calcium channel blockers. *Nat Commun*. 2014;5:4834.
100. Lin CW, Zhang H, Li M, Xiong X, Chen X, Dong XC, et al. Pharmacological promotion of autophagy alleviates steatosis and injury in alcoholic and non-alcoholic fatty liver conditions in mice. *J Hepatol*. 2013;58(5):993–9.
101. Sinha RA, Farah BL, Singh BK, Siddique MM, Li Y, Wu Y, et al. Caffeine stimulates hepatic lipid metabolism by the autophagy-lysosomal pathway in mice. *Hepatology*. 2014;59(4):1366–80.
102. Sun L, Zhang S, Yu C, Pan Z, Liu Y, Zhao J, et al. Hydrogen sulfide reduces serum triglyceride by activating liver autophagy via the AMPK-mTOR pathway. *Am J Physiol Endocrinol Metab*. 2015;309(11):E925–35.
103. Friedman SL. Mechanisms of hepatic fibrogenesis. *Gastroenterology*. 2008;134(6):1655–69.
104. Hernandez-Gea V, Ghiassi-Nejad Z, Rozenfeld R, Gordon R, Fiel MI, Yue Z, et al. Autophagy releases lipid that promotes fibrogenesis by activated hepatic stellate cells in mice and in human tissues. *Gastroenterology*. 2012;142(4):938–46.
105. Lavallard VJ, Gual P. Autophagy and non-alcoholic fatty liver disease. *Biomed Res Int*. 2014;2014:120179.
106. Hayes JD, McMahon M. NRF2 and KEAP1 mutations: permanent activation of an adaptive response in cancer. *Trends Biochem Sci*. 2009;34(4):176–88.
107. Taguchi K, Motohashi H, Yamamoto M. Molecular mechanisms of the Keap1-Nrf2 pathway in stress response and cancer evolution. *Genes Cells*. 2011;16(2):123–40.
108. White E. The role for autophagy in cancer. *J Clin Invest*. 2015;125(1):42–6.
109. Rao S, Tortola L, Perlot T, Wirnsberger G, Novatchkova M, Nitsch R, et al. A dual role for autophagy in a murine model of lung cancer. *Nat Commun*. 2014;5:3056.
110. Guo JY, Karsli-Uzunbas G, Mathew R, Aisner SC, Kamphorst JJ, Strohecker AM, et al. Autophagy suppresses progression of K-ras-induced lung tumors to oncocytomas and maintains lipid homeostasis. *Genes Dev*. 2013;27(13):1447–61.
111. Jiang P, Mizushima N. Autophagy and human diseases. *Cell Res*. 2014;24(1):69–79.
112. Zhi X, Zhong Q. Autophagy in cancer. *F1000Prime Rep*. 2015;7:18.
113. Rosenfeldt MT, O'Prey J, Morton JP, Nixon C, MacKay G, Mrowinska A, et al. p53 status determines the role of autophagy in pancreatic tumour development. *Nature*. 2013;504(7479):296–300.

114. Takamura A, Komatsu M, Hara T, Sakamoto A, Kishi C, Waguri S, et al. Autophagy-deficient mice develop multiple liver tumors. *Genes Dev.* 2011;25(8):795–800.
115. Inami Y, Waguri S, Sakamoto A, Kouno T, Nakada K, Hino O, et al. Persistent activation of Nrf2 through p62 in hepatocellular carcinoma cells. *J Cell Biol.* 2011;193(2):275–84.
116. Qu X, Yu J, Bhagat G, Furuya N, Hibshoosh H, Troxel A, et al. Promotion of tumorigenesis by heterozygous disruption of the beclin 1 autophagy gene. *J Clin Invest.* 2003;112(12):1809–20.
117. Ni HM, Woolbright BL, Williams J, Copple B, Cui W, Luyendyk JP, et al. Nrf2 promotes the development of fibrosis and tumorigenesis in mice with defective hepatic autophagy. *J Hepatol.* 2014;61(3):617–25.
118. Lozy F, Karantz V. Autophagy and cancer cell metabolism. *Semin Cell Dev Biol.* 2012;23(4):395–401.
119. Yue Z, Jin S, Yang C, Levine AJ, Heintz N. Beclin 1, an autophagy gene essential for early embryonic development, is a haploinsufficient tumor suppressor. *Proc Natl Acad Sci U S A.* 2003;100(25):15077–82.
120. Ding ZB, Shi YH, Zhou J, Qiu SJ, Xu Y, Dai Z, et al. Association of autophagy defect with a malignant phenotype and poor prognosis of hepatocellular carcinoma. *Cancer Res.* 2008;68(22):9167–75.
121. Kanzawa T, Kondo Y, Ito H, Kondo S, Germano I. Induction of autophagic cell death in malignant glioma cells by arsenic trioxide. *Cancer Res.* 2003;63(9):2103–8.
122. Kim EH, Sohn S, Kwon HJ, Kim SU, Kim MJ, Lee SJ, et al. Sodium selenite induces superoxide-mediated mitochondrial damage and subsequent autophagic cell death in malignant glioma cells. *Cancer Res.* 2007;67(13):6314–24.
123. Dupere-Richer D, Kinal M, Menasche V, Nielsen TH, Del Rincon S, Pettersson F, et al. Vorinostat-induced autophagy switches from a death-promoting to a cytoprotective signal to drive acquired resistance. *Cell Death Dis.* 2013;4:e486.
124. Yap TA, Garrett MD, Walton MI, Raynaud F, de Bono JS, Workman P. Targeting the PI3K-AKT-mTOR pathway: progress, pitfalls, and promises. *Curr Opin Pharmacol.* 2008;8(4):393–412.
125. Sieghart W, Fuereder T, Schmid K, Cejka D, Wertzowa J, Wrba F, et al. Mammalian target of rapamycin pathway activity in hepatocellular carcinomas of patients undergoing liver transplantation. *Transplantation.* 2007;83(4):425–32.
126. Villanueva A, Chiang DY, Newell P, Peix J, Thung S, Alsinet C, et al. Pivotal role of mTOR signaling in hepatocellular carcinoma. *Gastroenterology.* 2008;135(6):1972–83 e1–11.
127. Decaens T, Luciani A, Itti E, Hulin A, Roudot-Thoraval F, Laurent A, et al. Phase II study of sirolimus in treatment-naïve patients with advanced hepatocellular carcinoma. *Dig Liver Dis.* 2012;44(7):610–6.
128. Toso C, Merani S, Bigam DL, Shapiro AM, Kneteman NM. Sirolimus-based immunosuppression is associated with increased survival after liver transplantation for hepatocellular carcinoma. *Hepatology.* 2010;51(4):1237–43.
129. Huynh H, Chow KH, Soo KC, Toh HC, Choo SP, Foo KF, et al. RAD001 (everolimus) inhibits tumour growth in xenograft models of human hepatocellular carcinoma. *J Cell Mol Med.* 2009;13(7):1371–80.
130. Zhu AX, Kudo M, Assenat E, Cattani S, Kang YK, Lim HY, et al. Effect of everolimus on survival in advanced hepatocellular carcinoma after failure of sorafenib: the EVOLVE-1 randomized clinical trial. *Jama.* 2014;312(1):57–67.
131. Thomas HE, Mercer CA, Carnevali LS, Park J, Andersen JB, Conner EA, et al. mTOR inhibitors synergize on regression, reversal of gene expression, and autophagy in hepatocellular carcinoma. *Sci Transl Med.* 2012;4(139):139ra84.
132. Egan DF, Chun MG, Vamos M, Zou H, Rong J, Miller CJ, et al. Small Molecule Inhibition of the Autophagy Kinase ULK1 and Identification of ULK1 Substrates. *Mol Cell.* 2015;59(2):285–97.
133. Gauthier A, Ho M. Role of sorafenib in the treatment of advanced hepatocellular carcinoma: An update. *Hepatol Res.* 2013;43(2):147–54.
134. DeMartino GN, Goldberg AL. Thyroid hormones control lysosomal enzyme activities in liver and skeletal muscle. *Proc Natl Acad Sci U S A.* 1978;75(3):1369–73.
135. Webb AE, Brunet A. FOXO transcription factors: key regulators of cellular quality control. *Trends in biochemical sciences.* 2014;39(4):159–69.
136. Singh BK, Sinha RA, Zhou J, Tripathi M, Ohba K, Wang ME, et al. Hepatic FOXO1 Target Genes Are Co-regulated by Thyroid Hormone via RICTOR Protein Deacetylation and MTORC2-AKT Protein Inhibition. *J Biol Chem.* 2016;291(1):198–214.
137. Singh BK, Sinha RA, Zhou J, Xie SY, You SH, Gauthier K, et al. FoxO1 deacetylation regulates thyroid hormone-induced transcription of key hepatic gluconeogenic genes. *J Biol Chem.* 2013;288(42):30365–72.
138. Weitzel JM, Iwen KA. Coordination of mitochondrial biogenesis by thyroid hormone. *Mol Cell Endocrinol.* 2011;342(1–2):1–7.
139. Matsumoto G, Wada K, Okuno M, Kurosawa M, Nukina N. Serine 403 phosphorylation of p62/SQSTM1 regulates selective autophagic clearance of ubiquitinated proteins. *Mol Cell.* 2011;44(2):279–89.
140. Lim J, Lachenmayer ML, Wu S, Liu W, Kundu M, Wang R, et al. Proteotoxic stress induces phosphorylation of p62/SQSTM1 by ULK1 to regulate selective autophagic clearance of protein aggregates. *PLoS Genet.* 2015;11(2):e1004987.
141. Cingolani F, Czaja MJ. Regulation and Functions of Autophagic Lipolysis. *Trends Endocrinol Metab.* 2016;27(10):696–705.
142. Cioffi F, Senese R, Lanni A, Goglia F. Thyroid hormones and mitochondria: with a brief look at derivatives and analogues. *Mol Cell Endocrinol.* 2013;379(1–2):51–61.
143. Koyano F, Okatsu K, Kosako H, Tamura Y, Go E, Kimura M, et al. Ubiquitin is phosphorylated by PINK1 to activate parkin. *Nature.* 2014;510(7503):162–6.
144. Kane LA, Lazarou M, Fogel AI, Li Y, Yamano K, Sarraf SA, et al. PINK1 phosphorylates ubiquitin to activate Parkin E3 ubiquitin ligase activity. *J Cell Biol.* 2014;205(2):143–53.
145. Baxter JD, Webb P. Thyroid hormone mimetics: potential applications in atherosclerosis, obesity and type 2 diabetes. *Nat Rev Drug Discov.* 2009;8(4):308–20.
146. Baxter JD, Dillmann WH, West BL, Huber R, Furlow JD, Fletterick RJ, et al. Selective modulation of thyroid hormone receptor action. *J Steroid Biochem Mol Biol.* 2001;76(1–5):31–42.
147. Webb P. Selective activators of thyroid hormone receptors. *Expert Opin Investig Drugs.* 2004;13(5):489–500.
148. Moreno M, de Lange P, Lombardi A, Silvestri E, Lanni A, Goglia F. Metabolic effects of thyroid hormone derivatives. *Thyroid.* 2008;18(2):239–53.
149. Brenta G, Danzi S, Klein I. Potential therapeutic applications of thyroid hormone analogs. *Nat Clin Pract Endocrinol Metab.* 2007;3(9):632–40.
150. Grover GJ, Egan DM, Sleph PG, Beehler BC, Chiellini G, Nguyen NH, et al. Effects of the thyroid hormone receptor agonist GC-1 on metabolic rate and cholesterol in rats and primates: selective actions relative to 3,5,3'-triiodo-L-thyronine. *Endocrinology.* 2004;145(4):1656–61.
151. Trost SU, Swanson E, Gloss B, Wang-Iverson DB, Zhang H, Volodarsky T, et al. The thyroid hormone receptor-beta-selective agonist GC-1 differentially affects plasma lipids and cardiac activity. *Endocrinology.* 2000;141(9):3057–64.
152. Ledda-Columbano GM, Perra A, Piga R, Pibiri M, Loi R, Shinozuka H, et al. Cell proliferation induced by 3,3',5-triiodo-L-thyronine is associated with a reduction in the number of preneoplastic hepatic lesions. *Carcinogenesis.* 1999;20(12):2299–304.
153. Puliga E, Min Q, Tao J, Zhang R, Pradhan-Sundt T, Poddar M, et al. Thyroid Hormone Receptor-beta Agonist GC-1 Inhibits Met-beta-Catenin-Driven Hepatocellular Cancer. *Am J Pathol.* 2017;187(11):2473–85.
154. Erion MD, Cable EE, Ito BR, Jiang H, Fujitaki JM, Finn PD, et al. Targeting thyroid hormone receptor-beta agonists to the liver reduces cholesterol and triglycerides and improves the therapeutic index. *Proc Natl Acad Sci U S A.* 2007;104(39):15490–5.
155. Berkenstam A, Kristensen J, Mellstrom K, Carlsson B, Malm J, Rehnmark S, et al. The thyroid hormone mimetic compound KB2115 lowers plasma LDL cholesterol and stimulates bile acid synthesis without cardiac effects in humans. *Proc Natl Acad Sci U S A.* 2008;105(2):663–7.
156. Martagon AJ, Lin JZ, Cimini SL, Webb P, Phillips KJ. The amelioration of hepatic steatosis by thyroid hormone receptor agonists is insufficient to restore insulin sensitivity in ob/ob mice. *PLoS One.* 2015;10(4):e0122987.
157. Ladenson PW, Kristensen JD, Ridgway EC, Olsson AG, Carlsson B, Klein I, et al. Use of the thyroid hormone analogue eprotirome in statin-treated dyslipidemia. *N Engl J Med.* 2010;362(10):906–16.
158. Szydlowska M, Pibiri M, Perra A, Puliga E, Mattu S, Ledda-Columbano GM, et al. The Thyromimetic KB2115 (Eprotirome) Induces Rat Hepatocyte Proliferation. *Gene Expr.* 2017;17(3):207–18.

159. Sjouke B, Langslet G, Ceska R, Nicholls SJ, Nissen SE, Ohlander M, et al. Eprotirome in patients with familial hypercholesterolaemia (the AKKA trial): a randomised, double-blind, placebo-controlled phase 3 study. *Lancet Diabetes Endocrinol*. 2014;2(6):455–63.
160. Kelly MJ, Pietranico-Cole S, Larigan JD, Haynes NE, Reynolds CH, Scott N, et al. Discovery of 2-[3,5-dichloro-4-(5-isopropyl-6-oxo-1,6-dihydropyridazin-3-yloxy)phenyl]-3,5-dioxo-2,3,4,5-tetrahydro[1,2,4]triazine-6-carbonitrile (MGL-3196), a Highly Selective Thyroid Hormone Receptor beta agonist in clinical trials for the treatment of dyslipidemia. *J Med Chem*. 2014;57(10):3912–23.
161. Taub R, Chiang E, Chabot-Blanchet M, Kelly MJ, Reeves RA, Guertin MC, et al. Lipid lowering in healthy volunteers treated with multiple doses of MGL-3196, a liver-targeted thyroid hormone receptor-beta agonist. *Atherosclerosis*. 2013;230(2):373–80.
162. Scherz-Shouval R, Elazar Z. Regulation of autophagy by ROS: physiology and pathology. *Trends Biochem Sci*. 2011;36(1):30–8.
163. Zatloukal K, Stumptner C, Fuchsichler A, Heid H, Schnoelzer M, Kenner L, et al. p62 Is a common component of cytoplasmic inclusions in protein aggregation diseases. *Am J Pathol*. 2002;160(1):255–63.
164. Zatloukal K, French SW, Stumptner C, Strnad P, Harada M, Toivola DM, et al. From Mallory to Mallory-Denk bodies: what, how and why? *Exp Cell Res*. 2007;313(10):2033–49.
165. Kremsdorf D, Soussan P, Paterlini-Brechot P, Brechot C. Hepatitis B virus-related hepatocellular carcinoma: paradigms for viral-related human carcinogenesis. *Oncogene*. 2006;25(27):3823–33.
166. Xu L, Ma H, Miao M, Li Y. Impact of subclinical hypothyroidism on the development of non-alcoholic fatty liver disease: a prospective case-control study. *J Hepatol*. 2012;57(5):1153–4.
167. Liu Y, Wang W, Yu X, Qi X. Thyroid Function and Risk of Non-Alcoholic Fatty Liver Disease in Euthyroid Subjects. *Ann Hepatol*. 2018;17(5):779–88.
168. Guo Z, Li M, Han B, Qi X. Association of non-alcoholic fatty liver disease with thyroid function: A systematic review and meta-analysis. *Dig Liver Dis*. 2018;50(11):1153–62.
169. Mandato C, D'Acunzo I, Vajro P. Thyroid dysfunction and its role as a risk factor for non-alcoholic fatty liver disease: What's new. *Dig Liver Dis*. 2018;50(11):1163–5.
170. Liu L, Yu Y, Zhao M, Zheng D, Zhang X, Guan Q, et al. Benefits of Levothyroxine Replacement Therapy on Nonalcoholic Fatty Liver Disease in Subclinical Hypothyroidism Patients. *Int J Endocrinol*. 2017; 2017:5753039.
171. Wu SM, Cheng WL, Liao CJ, Chi HC, Lin YH, Tseng YH, et al. Negative modulation of the epigenetic regulator, UHRF1, by thyroid hormone receptors suppresses liver cancer cell growth. *Int J Cancer*. 2015;137(1):37–49.
172. Tseng YH, Huang YH, Lin TK, Wu SM, Chi HC, Tsai CY, et al. Thyroid hormone suppresses expression of stathmin and associated tumor growth in hepatocellular carcinoma. *Sci Rep*. 2016;6:38756.
173. Huang PS, Lin YH, Chi HC, Chen PY, Huang YH, Yeh CT, et al. Thyroid hormone inhibits growth of hepatoma cells through induction of miR-214. *Sci Rep*. 2017;7(1):14868.
174. Lin YH, Wu MH, Huang YH, Yeh CT, Chi HC, Tsai CY, et al. Thyroid hormone negatively regulates tumorigenesis through suppression of BC200. *Endocr Relat Cancer*. 2018;25(12):967–79.
175. Chi HC, Chen SL, Liao CJ, Liao CH, Tsai MM, Lin YH, et al. Thyroid hormone receptors promote metastasis of human hepatoma cells via regulation of TRAIL. *Cell Death Differ*. 2012;19(11):1802–14.
176. Chi HC, Chen SL, Cheng YH, Lin TK, Tsai CY, Tsai MM, et al. Chemotherapy resistance and metastasis-promoting effects of thyroid hormone in hepatocarcinoma cells are mediated by suppression of FoxO1 and Bim pathway. *Cell Death Dis*. 2016;7(8):e2324.
177. Lin YH, Wu MH, Liao CJ, Huang YH, Chi HC, Wu SM, et al. Repression of microRNA-130b by thyroid hormone enhances cell motility. *J Hepatol*. 2015;62(6):1328–40.
178. Chen CY, Chung IH, Tsai MM, Tseng YH, Chi HC, Tsai CY, et al. Thyroid hormone enhanced human hepatoma cell motility involves brain-specific serine protease 4 activation via ERK signaling. *Mol Cancer*. 2014;13:162.
179. Huang YH, Lin YH, Chi HC, Liao CH, Liao CJ, Wu SM, et al. Thyroid hormone regulation of miR-21 enhances migration and invasion of hepatoma. *Cancer Res*. 2013;73(8):2505–17.
180. Chung IH, Chen CY, Lin YH, Chi HC, Huang YH, Tai PJ, et al. Thyroid hormone-mediated regulation of lipocalin 2 through the Met/FAK pathway in liver cancer. *Oncotarget*. 2015;6(17):15050–64.
181. White E, DiPaola RS. The double-edged sword of autophagy modulation in cancer. *Clin Cancer Res*. 2009;15(17):5308–16.
182. Tian Y, Kuo CF, Sir D, Wang L, Govindarajan S, Petrovic LM, et al. Autophagy inhibits oxidative stress and tumor suppressors to exert its dual effect on hepatocarcinogenesis. *Cell Death Differ*. 2015;22(6):1025–34.
183. Sui X, Chen R, Wang Z, Huang Z, Kong N, Zhang M, et al. Autophagy and chemotherapy resistance: a promising therapeutic target for cancer treatment. *Cell Death Dis*. 2013;4:e838.
184. Sheng J, Qin H, Zhang K, Li B, Zhang X. Targeting autophagy in chemotherapy-resistant of hepatocellular carcinoma. *Am J Cancer Res*. 2018;8(3):354–65.

Ready to submit your research? Choose BMC and benefit from:

- fast, convenient online submission
- thorough peer review by experienced researchers in your field
- rapid publication on acceptance
- support for research data, including large and complex data types
- gold Open Access which fosters wider collaboration and increased citations
- maximum visibility for your research: over 100M website views per year

At BMC, research is always in progress.

Learn more biomedcentral.com/submissions



Bioengineered Braided Micro–Nano (Multiscale) Fibrous Scaffolds for Tendon Reconstruction

Anjana Jayasree,[†] Shalumon Kottappally Thankappan,[‡] Rethesh Ramachandran,[‡] M. Nivedhitha Sundaram,[†] Chih-Hao Chen,[§] Ullas Mony,[†] Jyh-Ping Chen,^{*,‡,§,||,⊥} and Rangasamy Jayakumar^{*,†,||}

[†]Amrita Centre for Nanosciences and Molecular Medicine, Amrita Institute of Medical Sciences and Research Centre, Amrita Vishwa Vidyapeetham, Kochi 682 041, India

[‡]Department of Chemical and Materials Engineering, Chang Gung University, Kwei-San, Taoyuan 33302, Taiwan

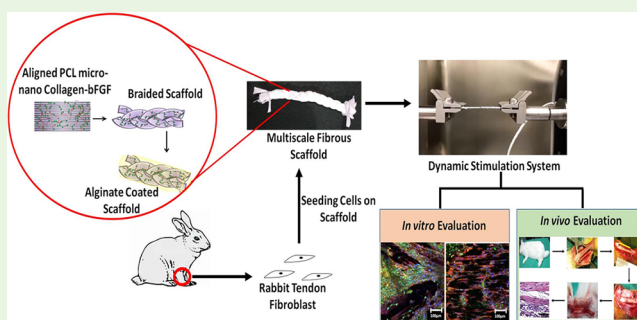
[§]Department of Plastic and Reconstructive Surgery and Craniofacial Research Center, Chang Gung Memorial Hospital, Linkou, Chang Gung University School of Medicine, Kwei-San, Taoyuan 33305, Taiwan

^{||}Research Center for Food and Cosmetic Safety, Research Center for Chinese Herbal Medicine, College of Human Ecology, Chang Gung University of Science and Technology, Taoyuan 33302, Taiwan

[⊥]Department of Materials Engineering, Ming Chi University of Technology, Tai-Shan, New Taipei City 24301, Taiwan

ABSTRACT: A braided multiscale fibrous scaffold consisting of aligned PCL micro/collagen-bFGF nano fibers was fabricated (mPCL-nCol-bFGF) to mimic native tendon tissue architecture which was further coated with alginate to aid in prevention of peritendinous adhesion. The bFGF release kinetics showed a sustained release of growth factors for a period of 20 days. Further, *in vitro* cell viability, attachment, and proliferation were performed using rabbit tenocytes under static and dynamic conditions. mPCL-nCol-bFGF showed a higher cell proliferation and enhanced expression of tenogenic markers compared to mPCL-nCol (braided scaffold without bFGF). When subjected to dynamic stimulation in a bioreactor, mPCL-nCol-bFGF-DS (braided scaffold with bFGF after dynamic stimulation) showed enhanced cellular proliferation and tenogenic marker expression, compared to mPCL-nCol-bFGF. The *in vivo* studies of the cell seeded scaffold after dynamic stimulation in Achilles tendon defect model showed tendon tissue regeneration with aligned collagen morphology within 12 weeks of implantation.

KEYWORDS: tendon regeneration, multiscale fibers, braided scaffold, bFGF, poly(*ε*-caprolactone)



BACKGROUND

Tendons are an integral part of the musculoskeletal system which enable joint movements and maintain structural stability.^{1,2} These fibrous connective tissues not only act as the connectors between the muscular system and the skeletal system but also facilitate the transmission of load between them.¹ Due to its load bearing functions, these tissues are generally prone to injuries due to repetitive high tension exposure and atrophy.³ Severe trauma also contributes to tendon injuries. Tendons possess a complex structure of collagen fibrils arranged hierarchically into primary bundles, fascicles, tertiary bundles, and finally the whole tendon.⁴ The complexity in their structure and their distinctive mechanical properties lead to poor tendon healing as the scar tissue formed may possess neither the mechanical strength nor the structural hierarchy that native tendon has. The hypocellular and hypovascular nature of the tendon also contributes to the delay in tissue healing and regeneration.^{5,6} Minor injuries can be easily rectified by proper immobilization and rest, whereas

major injuries require surgical intervention. The most common approach in any tendon damage is autograft. However, these lead to donor site morbidity and further weakness. Many synthetic and biological grafts like Gore-Tex, Leed-Keio, Artelon, Graftjacket, and Restore are available commercially for tendon applications.⁷ However, they show many drawbacks like unsuitable inflammatory response, high rate of rerupture, low cellular infiltration, and irregular arrangement of newly formed tissue.^{7,8}

An ideal scaffold for tendon regeneration should possess mechanical properties comparable to native tendon, and it must be biocompatible and biodegradable; its structure should mimic the extracellular matrix of the native tendon and facilitate cellular infiltration and formation of neotissue. Natural polymers like collagen⁹ and silk^{10,11} and degradable

Received: November 1, 2018

Accepted: February 14, 2019

Published: February 14, 2019

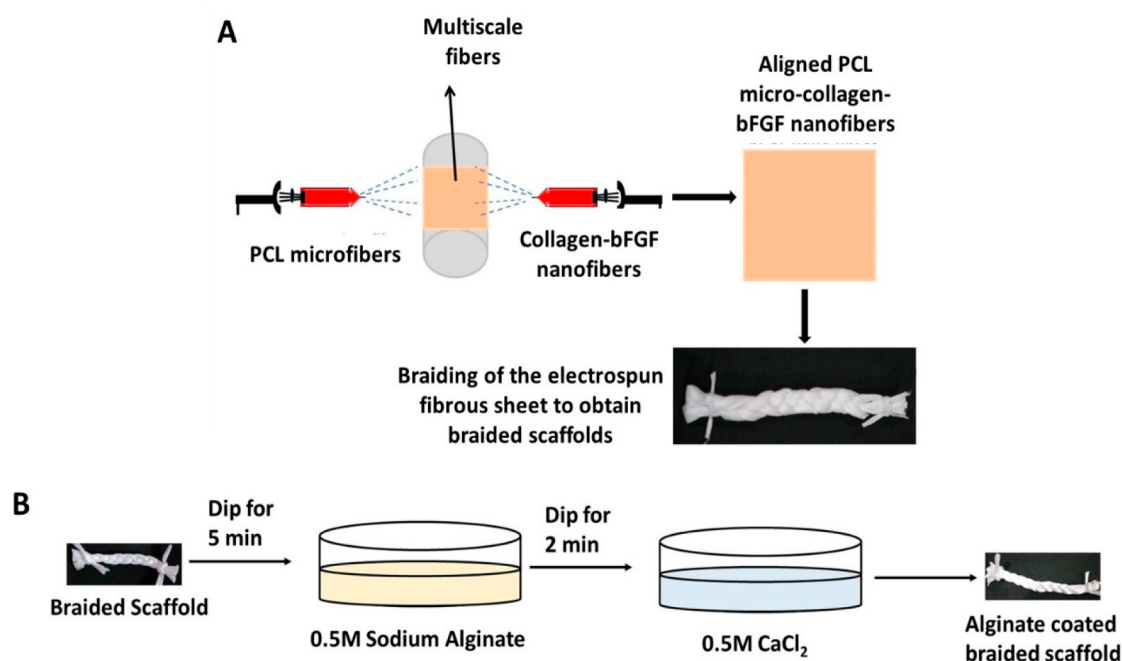


Figure 1. (A) Schematic representation is showing the simultaneous electrospinning to produce multiscale fibrous scaffolds. (B) Schematic representation of alginate coating on the braided scaffold.

synthetic polymers like poly(glycolic acid)¹² and poly(lactic acid)¹³ have been investigated previously and showed promising results. However, they lacked sufficient porosity to facilitate cellular infiltration, and their morphology was different from that of the native tendon ECM (extracellular matrix). Fibrous scaffolds with topography comparable to native tendon ECM, with tunable fiber diameter and with suitable porosity, can be fabricated by the process of electrospinning.¹⁴ The advantage of using natural polymer based fibers is that they are comparable to native ECM, whereas synthetic fibers have the advantage that their size can be easily tuned to the requirements.¹⁵ However, natural fibers when employed alone showed lower mechanical strength but when used in combination with synthetic fibers can help aid regeneration.

Poly(ϵ -caprolactone) (PCL), a biodegradable aliphatic polyester, is gaining great attention for biomedical applications due to its biodegradable and biocompatible nature; it can be easily fabricated to meet specific structural requirements, approved by the Food and Drug Administration (FDA) for biomedical applications in humans.¹⁶ By the process of electrospinning, PCL can be tailored to microfibers to mimic the native tendon ECM. Collagen is a major component of the tendon ECM, and the aligned structure of these collagen fibers provides the structural and functional properties of tendon.

Here we are utilizing PCL and collagen to develop a multiscale fibrous scaffold system suitable for tendon tissue engineering. The aligned PCL microfiber is expected to impart the desired mechanical and structural environment that is similar to that of the native tendon, whereas the random collagen in the form of nanofibers further helps mimic the chemical composition of native tendon. Earlier reports indicate that, compared to nanofibers and microfibers, a combination of nano- and microfibers (multiscale) showed enhanced cellular migration.¹⁷ Thus, here we are developing a micro–nano multiscale fiber system to obtain a scaffold with suitable

mechanical properties and good cell attachment and migration. With tendon being a hypocellular tissue, an agent that can initiate or aid in cellular migration and infiltration into the scaffold will help accelerate the healing of wounded tissue.¹⁸ Basic fibroblast growth factor (bFGF) has shown promising results in enabling fibroblast proliferation.¹⁹ Thus, to ensure a sustained release of the growth factor from the scaffold system, we have incorporated bFGF within the collagen nanofiber system. Textile technologies like braiding, knitting, and weaving are being incorporated nowadays into biomedical applications to obtain scaffolds with the required mechanical properties. In this work, we have braided the multiscale fibrous scaffolds to improve the mechanical properties of the fibers.

Peritendinous adhesion is referred to as adhesion of surrounding tissues onto the injured area which hinders smooth gliding of tendon during flexion.²⁰ Several approaches have been developed for the prevention of these adhesions.^{21–23} Alginate solution has previously been reported to prevent adhesion.²⁴ In this study we have developed a braided multiscale fibrous scaffold loaded with bFGF, which can mimic the native ECM and impart sufficient mechanical properties, and further coated it with alginate so as to prevent the peritendinous adhesion.

MATERIALS AND METHODS

Materials. PCL (MW 45 000 Da) was purchased from Polysciences (USA); collagen (Col), acetic acid, and sodium alginate were from Sigma-Aldrich (India). Calcium chloride (CaCl₂) was purchased from Merck (India) and chloroform from Spectrochem (India). Dubelcco's Modified Eagle's Medium-high glucose (DMEM) was from Sigma-Aldrich (USA), and penicillin streptomycin (Pen Strep) was from Gibco (USA). Rhodamine-phalloidin, fetal bovine serum (FBS), trypsin–EDTA, 6-diamidino-2-phenylindole dihydrochloride (DAPI), and the live–dead viability/cytotoxicity kit were acquired from Life Technologies (USA). The BCA assay kit was from ThermoFisher Scientific (USA), and the bFGF ELISA kit was from Raybiotech (USA). Antibodies specific for collagen I were obtained from Novus Biologicals (USA), and those for tenascin C were from

Abcam (USA). The dual RNA isolation kit was purchased from Genedirect (Taiwan), and SuperScript III reverse transcriptase was from Invitrogen (USA). SYBR Green Supermix was from Bio-Rad Laboratories Inc. (USA), and primers were from Tri-I Biotech, Inc. (Taiwan).

Methods. Preparation of Braided Multiscale Fibrous Scaffolds. PCL (35% w/v) was dissolved in chloroform and electrospun at a voltage of 7 kV, at a flow rate of 1.5 mL/h, with a tip to target distance of 15 cm to obtain aligned microfibers. Collagen nanofibers were obtained by spinning 8% PVA solution with collagen (1.5 mg/mL) and electrospun at 15 kV voltage, with a flow rate of 0.2 mL/h and a tip target distance of 20 cm. Multiscale fibers were obtained by spinning PCL microfibers and collagen nanofibers simultaneously at room temperature as shown in Figure 1A.

For the fabrication of bFGF loaded scaffolds, bFGF at a concentration of 7 μ g/mL was loaded into the collagen-PVA solution and electrospun as per the conditions mentioned above. The electrospun sheets were collected from the rotating mandrel and cut into strips of 0.5 mm width. Two strips were stacked one on top of the other. Three of the double stacked strips were braided together, and knots were tied on either side manually to obtain the braided scaffold.

Coating of Alginate on the Braided Scaffold. The braided scaffold was immersed in 0.5% alginate solution followed by immersion in 0.5 M CaCl_2 .²⁵ The process of alginate coating is depicted in Figure 1B.

Scanning Electron Microscopy (SEM) Analysis of the Braided Scaffold. The morphology of the braided fibrous scaffold was analyzed using a scanning electron microscope (JEOL JSM 6490LA, Japan). Prior to SEM, the scaffolds were coated with gold using a JEOL auto fine coater (JFC-1600, Japan) at 10 mA for 120 min. SEM was also performed for the alginate coated scaffold to ensure uniform coating of the gel on the scaffold.

Fourier Transform Infrared Spectroscopy (FT-IR) Analysis. The braided scaffold was further analyzed to confirm the presence of both PCL and collagen by evaluating the presence of major functional groups using FT-IR (Shimadzu IRAffinity IS, Japan).²⁴

Evaluation of Mechanical Properties of the Braided Scaffold. The mechanical properties of the scaffold were evaluated using a Tinius Olsen mechanical testing system (HSKL, USA) with load cell capacity of 250 N. Scaffolds of 5 cm length were strongly attached to the grips and were elongated at an extension speed of 10 mm/min.

Protein Adsorption Study. Protein adsorption on the uncoated and alginate coated scaffolds was evaluated by a previously reported procedure.²⁵ The scaffolds were incubated at 37 °C in DMEM with 10% FBS for specific time intervals. The scaffolds were later washed, and total protein was estimated using bicinchoninic acid (BCA) assay. The blank used in the experiment was scaffold incubated in basal medium.

In Vitro bFGF Release Study. The *in vitro* growth factor release was conducted in PBS of pH 7.4. Scaffolds were immersed in 5 mL of PBS and incubated at 37 °C under gentle shaking. A known volume of release was drawn out at defined time points. The released growth factor was quantified using bFGF ELISA kit.

Isolation and Culturing of Tenocytes. Tenocytes were isolated from the flexor tendons excised from New Zealand White rabbit after euthanasia following the guidelines of the Institutional Animal Care and Use Committee of Chang Gung University, ROC, Taiwan. The excised tendons were washed thoroughly and minced to pieces. The minced tendons were placed in a petriplate, and DMEM with 20% FBS was added. The cells that grow out of the explants were further cultured in culture flasks. For all experiments, cells belonging to passage 5 were taken, and cells were seeded at a density of 1×10^6 cells on each side of the scaffold. All the scaffolds were UV sterilized before seeding of cells. For preparation of coated scaffolds, the scaffolds are UV sterilized, and cells were seeded on either side of the scaffold, allowed to attach, and further coated with alginate gel under sterile conditions.

Dynamic Stimulation of Scaffolds. ElectroForce 5100 (TA Instruments, USA) was employed to perform a comparative analysis

between the static condition and cyclic loading. There were 1×10^6 cells loaded on either side of the scaffold and allowed to attach properly onto the scaffold for a period of 24 h at 37 °C and 5% CO_2 . The scaffolds are properly anchored onto the clamps within the bioreactor system and placed in an incubator maintained at 37 °C and 5% CO_2 . The samples were cyclically loaded at 0.5 Hz for 3 h/day at 5% elongation. Samples were extracted after 24 h and 7 days of cyclic loading for evaluation. From now on we will be referring to the different experimental groups in the following manner: PCL-collagen multiscale braided scaffold as mPCL-nCol, PCL-collagen multiscale braided scaffold with bFGF as mPCL-nCol-bFGF, and PCL-collagen multiscale braided scaffold subjected to dynamic stimulation as mPCL-nCol-bFGF-DS.

Cell Viability Assay. Viability of cells seeded on the scaffold was determined by live–dead staining. The cells were seeded on either sides of scaffold and cultured at 37 °C in an incubator maintained at 5% CO_2 . The samples for dynamic stimulation were subjected to cyclic strain as discussed earlier. At the specific time points (1 and 7 days), the scaffolds were taken out and washed well with PBS. The scaffolds were then incubated in Calcein AM (live stain) and ethidium bromide (EtBr, dead stain) for 15 min. The samples were washed and imaged using a confocal microscope (Leica TCSSP2, Germany).

Cell Proliferation Study. A Hoechst 33258 DNA assay was used to determine the amount of DNA on the cell seeded scaffolds at first and seventh day time points. For the static condition, the cell seeded scaffolds were placed in an incubator at 37 °C and 5% CO_2 , whereas the samples for dynamic stimulation are placed in the bioreactor system as described above. The samples were taken out at specific time intervals, washed well, and lysed with lysis buffer. Fluorescence was measured at 520 nm.

Cell Attachment Study. SEM and confocal microscopy were employed to evaluate the attachment of cells on the scaffold. For SEM analysis, the samples were taken out at the desired time points (first and seventh day) and fixed in 10% formaldehyde. They were then dehydrated by consequently immersing in 50%, 70%, 80%, 90%, and 95% each for 10 min and finally in 99.5% for 20 min. The samples were then air-dried, sputter coated, and imaged using SEM (Hitachi S3000N, Japan). Actin–DAPI staining was performed to observe the attachment and alignment of cells on the scaffolds. The cell seeded scaffolds were retrieved at specific time points (first and seventh day) and fixed using 10% formaldehyde at 37 °C for 1 h. The samples were then washed well and permeabilized using 1% Triton in PBS for 1 min. Finally, the samples were stained with tetramethyl rhodamine (TRITC) tagged phalloidin to stain the cytoskeleton and 4,6-diamino-2-phenylindole (DAPI) to stain the nucleus. The images were captured using a confocal microscope (Leica TCSSP8, Germany).

Immunofluorescence Assay. The expression of tendon specific markers like collagen I and tenascin C was evaluated by immunofluorescence. The samples were taken out at specific time points (first day and seventh day) and fixed in 10% formaldehyde for 60 min at 37 °C. The samples were washed properly and treated with blocking buffer for 1 min. The samples were treated with the primary antibody specific to collagen I and tenascin C and incubated overnight with gentle shaking at 4 °C. Secondary antibody that is tagged with fluorescein isothiocyanate (FITC) was added to the scaffold and further incubated for 2 h. The scaffolds were washed well and imaged using confocal microscope (Leica TCSSP8).

mRNA Isolation and Reverse Transcription. The cell seeded scaffolds were retrieved at specific time points (first and seventh day) and homogenized in TRIzol. The total RNA was extracted and purified using Genedirect Dual RNA isolation Kit, following the manufacturer's protocol. Nanodrop was employed to evaluate the quality of mRNA. 50 ng/ μ L of mRNA was reverse transcribed using SuperScript III reverse transcriptase.

Quantitative Polymerase Chain Reaction (qPCR). qPCR was carried out with A CFD-3120 mini Option detection system (Bio-Rad, USA) along with SYBR Green Supermix. PCR primers were designed for evaluating the expression levels of collagen I, collagen III, tenascin C, biglycan, and fibronectin using glyceraldehyde 3-

Table 1. Sequence of Primers Used for qPCR Reaction

gene		sequence (5'–3')	size (mer)	temp (°C)
collagen type I	F	GCATGTCTGGTTAGGAGAAACC	22	59.4
	R	ATGTATGCAATGCTGTTCTTGC	21	
collagen type III	F	AAGCCCCAGCAGAAAATTC	19	59.4
	R	TGGTGGAACAGCAAAAATCA	20	
biglycan	F	AGATCTGCCAGAGACCCCTGA	20	59.4
	R	ACCCTGGACAGCTTGTGTGT	20	
fibronectin	F	CTCACCCGAGGCGCCACCTA	20	62.1
	R	TCGCTCCCCTCTCTCCAACG	22	
tenascin C	F	TCTCTGCACATAGTAAAAACAATACC	27	51.4
	R	TCAAGGCAGTGGTGTCTGTGA	21	
GAPDH	F	GACATCAAGAAGGTGGTGAAGC	22	63.9
	R	CTTCACAAAGTGGTCATTGAGG	22	



Figure 2. Steps involved in creation of Achilles tendon defect model.

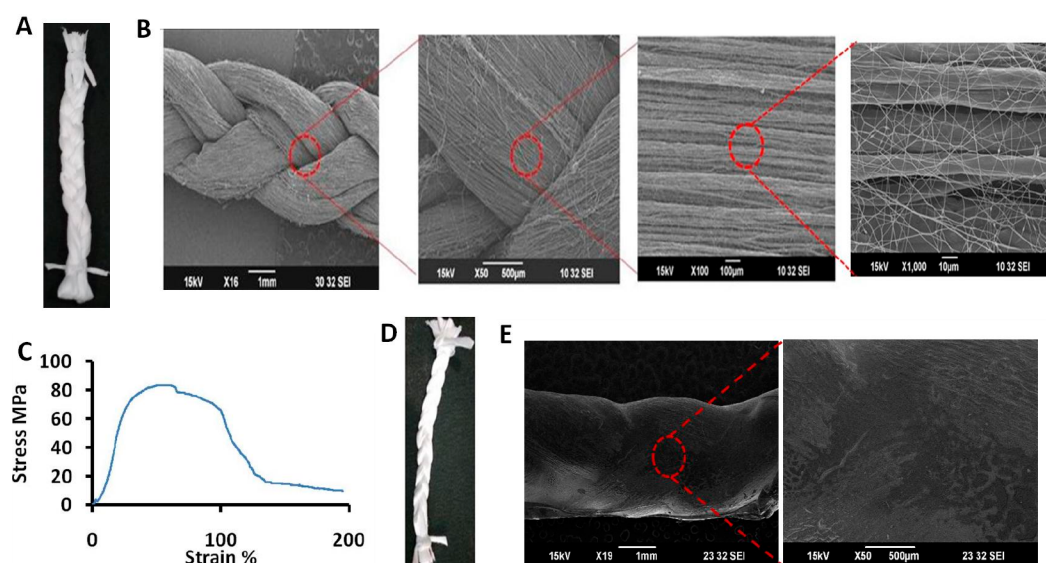


Figure 3. (A) Photograph of the braided multiscale fibrous scaffold. (B) SEM images showing the morphology of braided scaffold (aligned microfibers and random nanofibers can be observed). (C) Characteristic stress–strain curve of the braided scaffold. (D) Photograph of the alginate coated braided multiscale fibrous scaffold. (E) SEM images showing uniform coating of alginate on the braided scaffold.

phosphate dehydrogenase (GAPDH) as a control (Table 1). The expression levels were normalized with respect to GAPDH and calculated employing the delta–delta C_T method.

Evaluation of *in Vivo* Tendon Regeneration Potential of Braided Scaffold. New Zealand white rabbits (3 months old) obtained from National Laboratory Animal Breeding and Research Center, Taipei,

Taiwan, ROC, were used for the surgical procedures. The *in vivo* studies and procedures followed were in accordance with the guidelines of the Institutional Animal Care and Use Committee of Chang Gung University (IACUC Approval CGU14-139). An Achilles tendon defect model was created and implanted with the developed scaffold (Figure 2). Implantation was carried out only for the bFGF

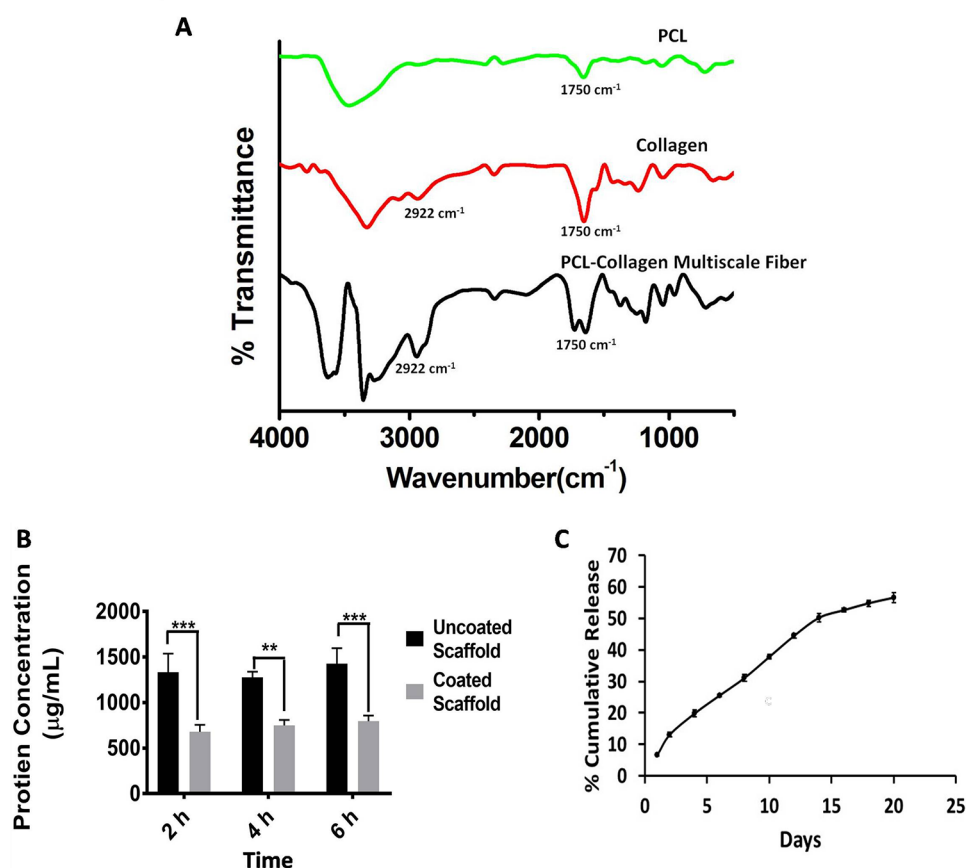


Figure 4. (A) FT-IR analysis of the braided PCL microcollagen nanofibers. (B) Protein adsorption on coated and uncoated scaffolds evaluated by BCA assay. (C) bFGF release profile from braided scaffold evaluated by ELISA.

loaded-braided multiscale fibrous scaffold seeded with tenocytes and subjected to dynamic stimulation in a bioreactor for 7 days in 9 animals. The animals were prepped for surgery as reported earlier.²⁶ A 15 mm defect was created in the Achilles tendon, and the scaffolds were carefully sutured on both ends of the cut tendon.

At 6 and 12 weeks, the rabbits were euthanized, and their Achilles tendon was harvested and placed in 10% formaldehyde. The samples were sectioned,²⁶ evaluated by performing hematoxylin and eosin (H&E) staining and immunohistological (IHC) analyses with tendon specific markers like collagen I and tenascin C and Masson's trichrome (MT) staining, and examined using a light microscope (Leica DM4000B).

Statistical Analysis. All the experiments were performed with sample size $n = 3$. The data are expressed as mean \pm standard deviation. One-way Anova was used to evaluate statistical significance and, with $p < 0.05$ (*), $p < 0.01$ (**), and $p < 0.001$ (***), was found to be statistically significant.

RESULTS

Preparation and Characterization of Multiscale Fibrous Scaffold. Multiscale fibers composed of aligned PCL microfibers of diameter 8–10 μm and collagen nanofibers of diameter 300–400 nm were obtained by electrospinning. The electrospun sheets were cut into strips, double stacked, and finally braided to obtain the three-dimensional scaffold (Figure 3A). The SEM images of the scaffold show the multiscale fiber morphology clearly (Figure 3B). SEM clearly depicts the aligned morphology of PCL microfibers and also the highly random nature of the collagen nanofibers. The tensile strength of the double stacked braided scaffold was found to be 89.4 ± 5.3 MPa, and the maximum force that it

could endure was 46.75 ± 3.2 N. Characteristic stress–strain curve of the braided scaffold is shown in Figure 3C. Alginate gel was coated on the scaffold by dipping the scaffold in alginate followed by dipping in CaCl_2 (Figure 3D). SEM images show that the coating was uniform throughout the scaffold (Figure 3E).

FT-IR characterization of the braided scaffold was evaluated, and it was observed that the peak of PCL at 1750 cm^{-1} ($\text{C}=\text{O}$ vibration) and peaks of collagen at 2922 cm^{-1} (CH_2 stretching vibration) and 1750 cm^{-1} ($\text{C}=\text{O}$ vibration) were observed in the final multiscale fibrous scaffold indicating its presence (Figure 4A).

Protein Adsorption Study. The protein adsorption on the coated and uncoated scaffolds was evaluated using a BCA assay. It was observed that the adsorption of proteins on the uncoated scaffold was significantly higher than the coated scaffolds as shown in Figure 4B.

In Vitro bFGF Release Study. The *in vitro* growth factor release was determined by ELISA for a period of 20 days. It was observed that a sustained release of bFGF was obtained from the scaffold with almost 55% growth factor being released by the 20th day (Figure 4C). Upon alginate coating it was observed that initially the release pattern was similar, but gradually, a lower release was observed. Upon alginate coating about 51% of growth factor was released by the 20th day.

Cell Viability. Viability of the cells on the scaffold was evaluated by live–dead staining. Dynamic stimulation was performed by attaching the scaffolds to the clamps and subjected to cyclic strain within the bioreactor (Figure 5A). As

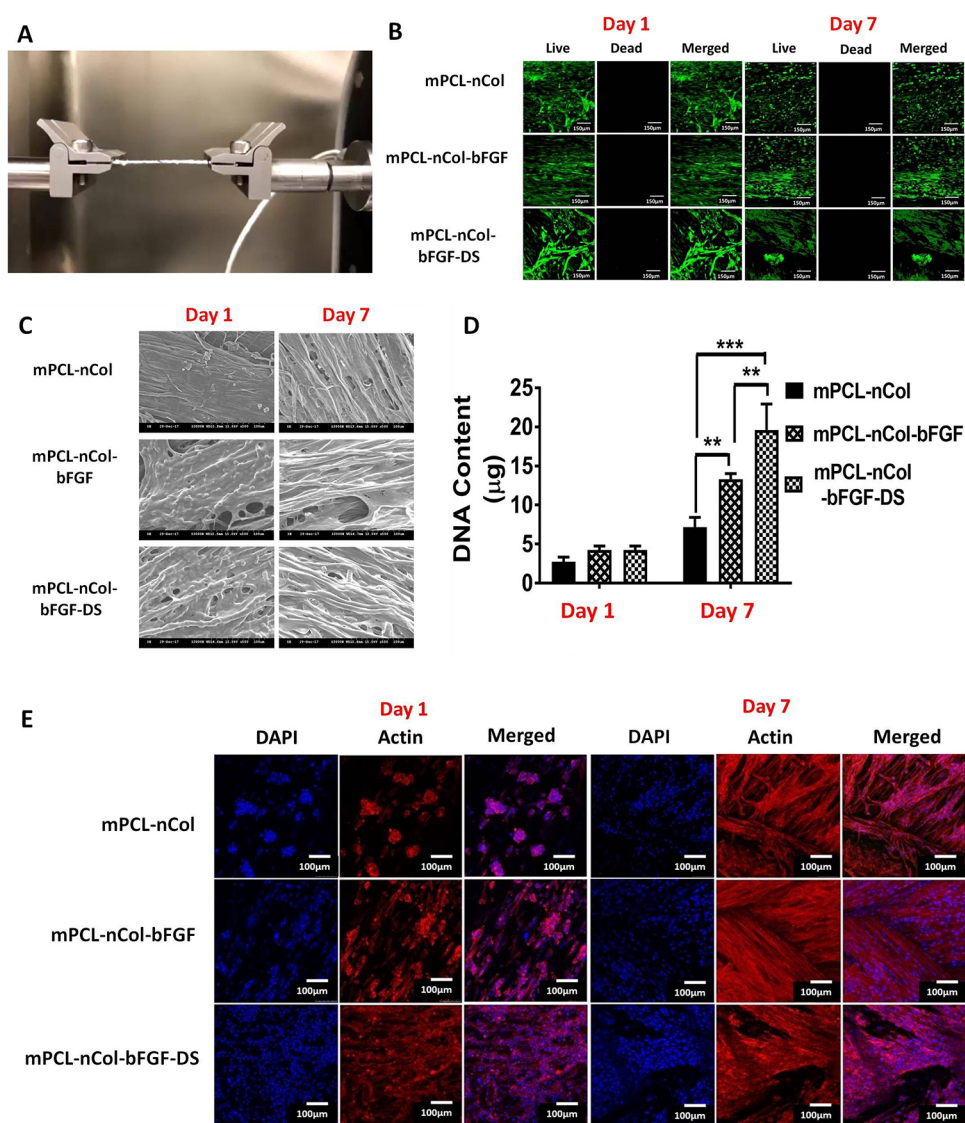


Figure 5. (A) Photograph of the braided multiscale scaffold mounted in the bioreactor. (B) Cell viability of tenocytes on braided multiscale scaffold evaluated by live (green)–dead (red) staining. (C) SEM showing the attachment of tenocytes on the braided scaffold. (D) Cell proliferation of cells on braided scaffold by evaluating the DNA content. (E) Cell attachment and spreading of tenocytes on the braided scaffold evaluated by Actin (red)–DAPI (blue) staining.

observed in Figure 5B the cells were viable in all the three groups indicating that the scaffolds did not show any cellular toxicity.

Cell Attachment. SEM images showed that the tenocytes had attached well to the fibrous scaffolds. The cells were attached along the alignment of the microfibers. By the seventh day the cells were well-spread and aligned along the fibers in all three groups (Figure 5C).

Further, the alignments of tenocytes on the scaffolds were observed using cytoskeleton-nucleus staining (Figure 5E). On day 1 the cells showed minimal spreading and alignment on all the groups. However, mPCL-nCol-bFGF showed better alignment compared to mPCL-nCol. On day 7, it was observed that the cells were well-spread and aligned along the fibers. Upon dynamic stimulation the alignment of the cells were further improved.

Cell Proliferation Study. Cell proliferation was determined by quantifying the amount of DNA on days 1 and 7 (Figure 5D). The DNA content on day 7 was comparatively

higher than day 1 on all scaffolds indicating cell proliferation. The proliferation of cells seeded on mPCL-nCol-bFGF and mPCL-nCol-bFGF-DS was significantly higher than that on mPCL-nCol indicating that bFGF facilitates cell proliferation. Further, it was observed that mPCL-nCol-bFGF-DS, which underwent cyclic dynamic strain treatment, showed significantly higher DNA content compared to mPCL-nCol-bFGF. This led to a conclusion that dynamic stimulation may enhance cell proliferation.

Immunofluorescence Assay. Expression of tenogenic markers like collagen I (Figure 6A) and tenascin C (Figure 6B) on the cell seeded scaffolds was evaluated by immunofluorescent staining. The expression of both collagen I and tenascin C was found to be higher on day 7 compared to day 1 in all the scaffolds. However, it was observed that the levels of collagen I and tenascin C in mPCL-nCol-bFGF and mPCL-nCol-bFGF-DS were higher in comparison to those in mPCL-nCol. Dynamic stimulation was found to enhance the expression of tenogenic markers. The expression of both tenascin C and

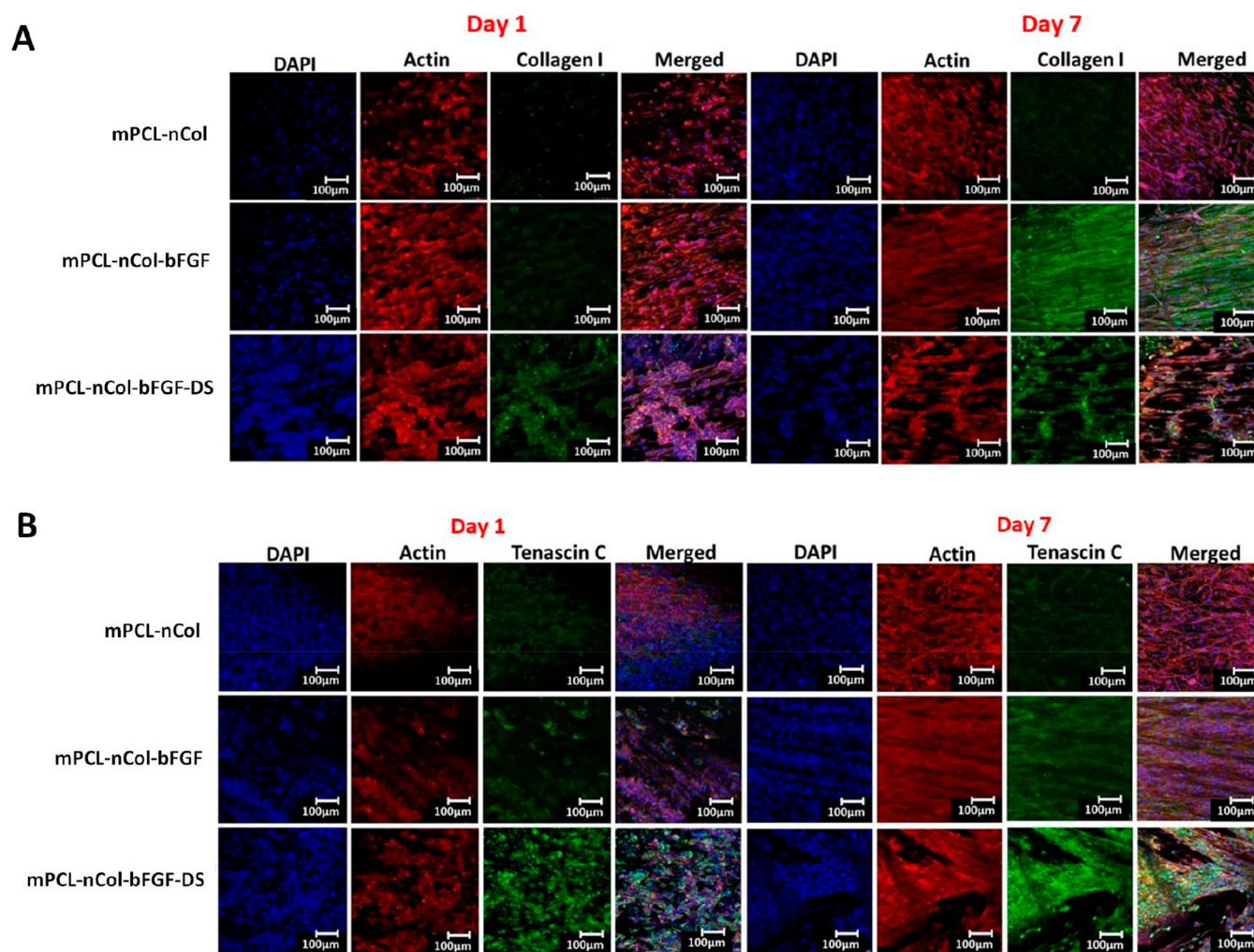


Figure 6. Expression of tendon specific markers evaluated by immunofluorescence: (A) collagen I expression of tenocytes on the braided scaffold and (B) tenascin C expression of tenocytes on the braided scaffold.

collagen I on mPCL-nCol-bFGF-DS was higher than mPCL-nCol-bFGF.

Gene Expression Analysis by qPCR. The expressions of collagen I, collagen III, tenascin C, fibronectin, and biglycan were evaluated and normalized with respect to GAPDH as housekeeping gene. The gene expression levels of cells seeded on scaffolds under static and dynamic conditions are depicted in Figure 7. It was observed that all the groups showed an increased expression of tenogenic markers on day 7 compared to day 1. mPCL-nCol-bFGF showed increased expressions of tenascin C, collagen I, and fibronectin compared to mPCL-nCol on day 7, indicating that the presence of bFGF increases the expression of tenogenic markers. Upon dynamic stimulation, mPCL-nCol-bFGF-DS scaffolds showed significantly higher expression of tenascin C, collagen I, biglycan, and fibronectin compared to mPCL-nCol-bFGF. Upon comparison, it was observed that upon dynamic stimulation the expression of tenogenic markers increases. mPCL-nCol-bFGF-DS showed a significantly higher expression of tenascin C, collagen I, biglycan, and fibronectin in comparison to mPCL-nCol, indicating that the presence of both bFGF and dynamic stimulation simultaneously can enhance tenogenic expression.

Evaluation of *in Vivo* Tendon Regeneration Potential of Braided Scaffold. To evaluate the tendon regeneration

potential of cell seeded mPCL-nCol-bFGF-DS, histological analysis was performed. H&E, IHC analyses with tendon specific markers like collagen I and tenascin C, and MT staining to evaluate the collagen content were performed and shown in Figure 8A,B. In a comparison with native tendon, H&E staining shows that, after 6 weeks of implantation, highly unorganized tissue morphology was observed. The empty spaces in the images indicate the region of scaffold that has not undergone degradation. However, by 12 weeks aligned tissue morphology was clearly observed. The expression of tendon specific markers like collagen I and tenascin C was also evaluated. The samples stained positive for collagen I and tenascin C. The alignment of collagen was highly unorganized in comparison to native tendon which showed perfectly aligned fiber morphology, whereas, by 12 weeks, the implants showed more aligned nature of collagen fibers which was further confirmed by MT staining.

DISCUSSION

ECM of a native tissue not only provides support to the cells but also facilitates their functions, sequesters the growth factors secreted by the cells, and enables cell differentiation. During development of a scaffold for tissue regeneration, special importance is to be given for scaffold design, so as to ensure

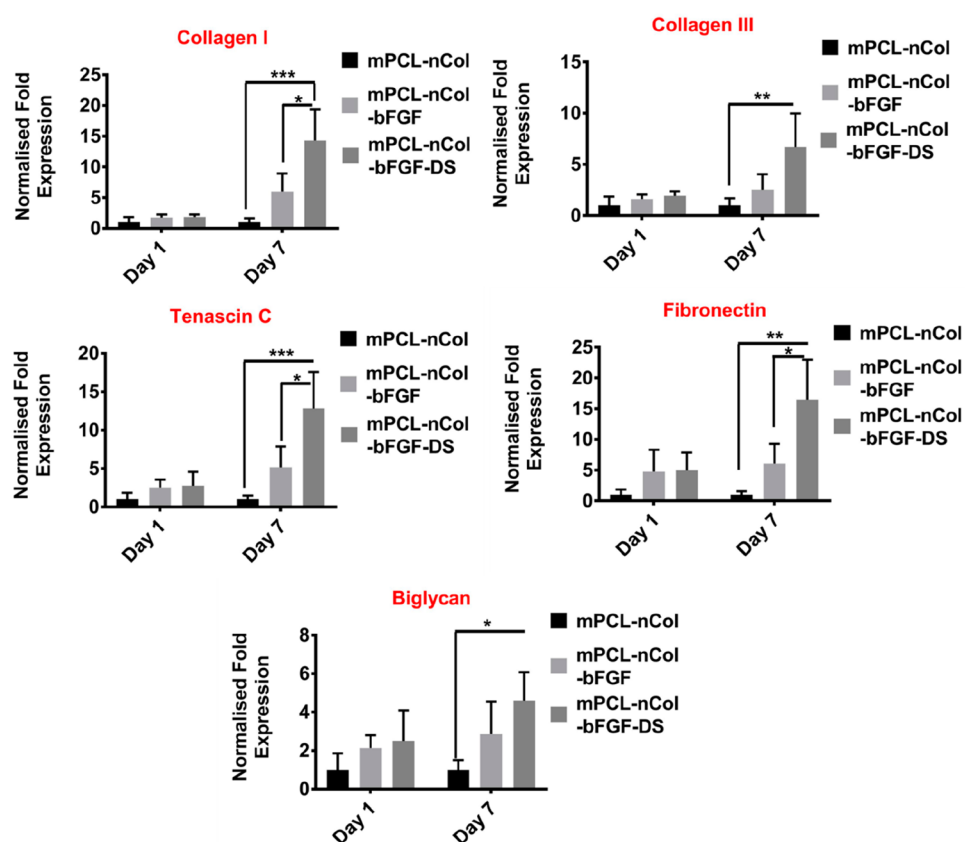


Figure 7. Gene expression analysis of tenogenic markers performed by qPCR.

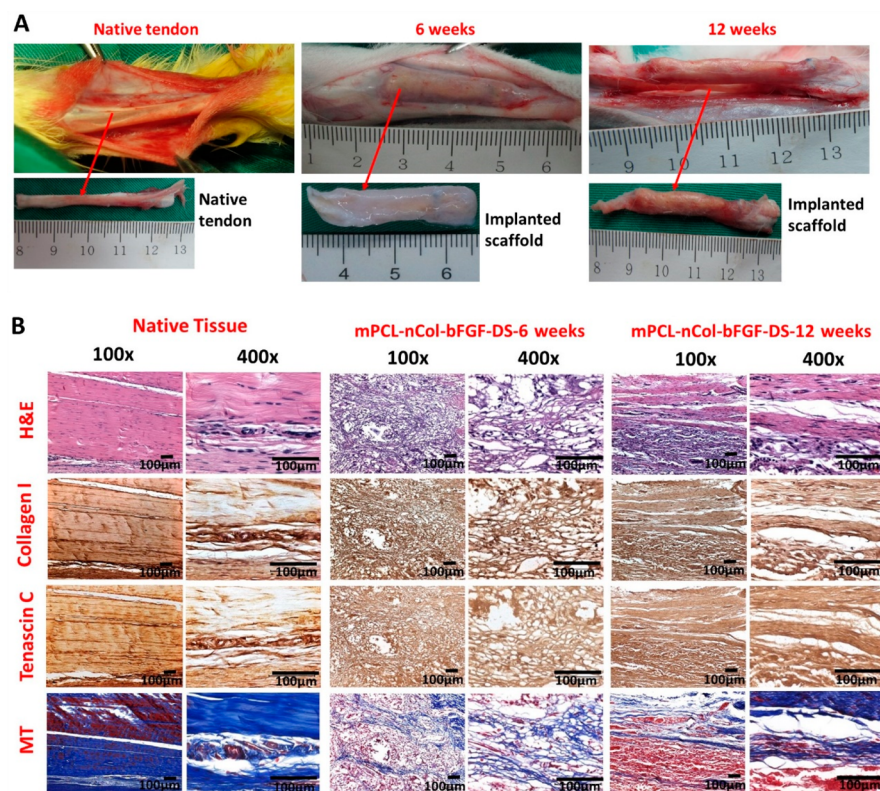


Figure 8. (A) Gross view of native tendon and implanted scaffold after 6 weeks and 12 weeks of implantation. (B) Morphology of the native tissue and implanted scaffolds analyzed by H&E. Tenogenic marker expression was analyzed by immunofluorescence, and collagen deposition was evaluated by MT staining.

that the developed scaffold has a morphology comparable to that of its native tissue.^{27,28} The developed multiscale fibrous scaffold is composed of aligned PCL microfibers of diameter in the range 8–10 μm and is comparable to the aligned collagen fiber structure and diameter in native tendon. The random collagen-bFGF nanofibers provide a niche comparable to native tendon as their ECM is composed of collagen fibers and bFGF plays a major role in tenocyte proliferation and migration. Previous literature reports support that the alignment of the fibers improves tenogenic differentiation of cells.^{29,30} Thereby, the bFGF loaded multiscale fibrous scaffolds provide both physical and biochemical cues to facilitate tenocyte proliferation and differentiation. The application of textile technologies like braiding, weaving, and knitting has shown great promise in increasing the mechanical properties of electrospun fibers.^{31,32,10,33} The double stacked braided scaffold showed a tensile strength of 89.4 ± 5.3 MPa which is comparable to that of human Achilles tendon.³⁴

The braided multiscale fibrous scaffolds were then uniformly coated with alginate to aid in prevention of peritendinous adhesion. When compared to uncoated scaffolds, the protein adsorptions on coated scaffolds were much lower, which may lead to a lower cellular and fibrous tissue attachment.^{35,25} However, the efficacy of alginate coating can be effectively evaluated *in vivo* using a flexor tendon defect model rather than an Achilles tendon defect, which needs to be further investigated. Earlier reports indicated that a sustained release of bFGF for a period of 7 days induces proliferation and tenogenic differentiation in bone marrow derived stem cells.³⁶ We observed a sustained release of bFGF for about 20 days, and its effect on tenocyte proliferation and expression of tenogenic markers could be clearly observed. When compared to the control scaffolds, scaffolds with bFGF showed significantly higher cell proliferation.

During the early stages of tendon repair, collagen I is an important component in ECM and disorganized collagen III is usually highly produced.^{37,15} Scaffolds with bFGF (mPCL-nCol-bFGF) showed a comparatively higher expression of both collagen I and collagen III on the seventh day. Other noncollagenous ECM components like tenascin C and fibronectin which aid in cell signaling, attachment, and survival during the early stages of healing were also upregulated significantly in scaffolds loaded with bFGF. bFGF acts on the receptors present on the cell surface leading to their phosphorylation which can lead to the activation of several intracellular secondary messenger molecules which leads to expression of tenogenic markers. Upon phosphorylation of receptors, the NIK/IKK pathway gets activated, leading to activation of the NF- κB pathway and an increase in the tenocyte proliferation.³⁸

As a tissue that is constantly being exposed to mechanical forces, the effects of mechanical tension on cellular activity, and on its ability to regulate cellular proliferation and differentiation, are studied extensively.³⁹ Here we have compared the effects of dynamic stimulation on tenocyte activity on the braided scaffold with scaffolds under static conditions. The dynamic stimulation of scaffolds was carried out at 5% strain rate and 0.5 Hz amounting to 5400 cycles per day to mimic the *in vivo* cyclic strain conditions.⁴⁰ Cells that underwent dynamic stimulation (mPCL-nCol-bFGF-DS) showed a better alignment on the fibrous scaffold compared to static cultures (mPCL-nCol, mPCL-nCol-bFGF), indicating that mechanotransduction plays a major role in cellular

alignment. The combination of bFGF along with dynamic stimulation (mPCL-nCol-bFGF-DS) showed significantly enhanced cell proliferation and expression of collagen I and tenascin C compared to static bFGF loaded scaffolds (mPCL-nCol-bFGF). This enhanced expression of ECM components in the simulated samples indicates that mechanical stimulation and bFGF may act synergistically and accelerate tendon healing potential. Wu et al. showed that, upon dynamic stimulation, knitted scaffolds showed enhanced tenogenic potential as these mechanical cues trigger intracellular signaling pathway via the adhesion receptor stimulation leading to synthesis of components of ECM.⁴¹ However, in comparison to our work, Wu et al. performed studies using a triculture of HADMSC/HT/HUVEC where it was observed that a coculture condition can improve tenogenesis. However, the efficacy of the triculture system was not evaluated in *in vivo* conditions.

The combination of bFGF and mechanical stimulation showed good tenogenic potential in the *in vitro* studies. Thereby, we moved forward to evaluate the *in vivo* tendon regeneration potential of multiscale bFGF loaded-braided scaffold seeded with cells and subjected to mechanical stimulation within a bioreactor for 7 days (mPCL-nCol-bFGF-DS). Previous literature reports have compared the regeneration potential of scaffolds with and without cell seeding. They observed that scaffolds seeded with cells showed better integration with host tissue and enhanced production of ECM components.⁴² Histological analysis shows that cells have infiltrated well into the fibrous matrix. The IHC analysis showed an increased positive staining for collagen I compared to that of tenascin C. This pattern is comparable to the native tendon as collagen I is the most abundant ECM component in tendon. The change in morphology of the tissues from a random structure (6 weeks) to an aligned structure (12 weeks) indicates that the tissue regeneration and remodeling process is ongoing. MT staining showed aligned collagen fibrous structure. H&E staining also indicated the presence of cells within the implanted scaffold. However, one of the drawbacks is that we cannot determine if the cells were the ones initially seeded or ones which migrated into the scaffold from the surrounding tissue. Seeding of a GFP tagged cells on the scaffold may help us better understand the fate of the seeded cells and distinguish them from the migrated cells. We cannot draw conclusions regarding the effect of dynamic stimulation or the presence of bFGF on cells in an *in vivo* environment with the current study. Further evaluation and comparison with groups like scaffolds without cells, without bFGF, and without dynamic stimulation need to be performed and will be performed as part of future work

CONCLUSION

A multiscale braided scaffold loaded with bFGF was developed. Where the microfibers impart suitable mechanical properties, the nanofibers facilitate cellular attachment and bFGF aids in cell proliferation and ECM production. These scaffolds showed enhanced tendon regeneration potential when subjected to dynamic stimulation in both *in vitro* and *in vivo* conditions.

AUTHOR INFORMATION

Corresponding Authors

*E-mail: jpchen@mail.cgu.edu.tw. Phone: +88-6-3-211880. (J.-P.C.)

*E-mail: rjayakumar@aims.amrita.edu and jayakumar77@yahoo.com. Phone: 0484-2801234 ext 8762. (R.J.)

ORCID

Jyh-Ping Chen: 0000-0001-6527-4801

Rangasamy Jayakumar: 0000-0002-0066-4208

Notes

The authors declare no competing financial interest.

ACKNOWLEDGMENTS

The authors wish to thank the Global Innovation & Technology Alliance (GITA), India, Department of Science and Technology (DST), India, and the Ministry of Science and Technology (MOST), Taiwan, for providing funds under the India-Taiwan Joint Program in Science and Technology (nos. GITA/DST/TWN/P-71/2015, MOST104-2923-E-182-001-MY3). A.J. acknowledges the Council of Scientific and Industrial Research (CSIR) for the financial support through the Senior Research Fellowship (SRF-09/963(0041)2K18-EMR-1). The authors thank the Microscope Core Laboratory in Chang Gung Memorial Hospital Linkou Medical Center for technical assistance.

REFERENCES

- (1) Andarawis-Puri, N.; Flatow, E. L.; Soslowsky, L. J. Tendon basic science: Development, repair, regeneration, and healing. *J. Orthop. Res.* **2015**, *33*, 780–784.
- (2) Voleti, P. B.; Buckley, M. R.; Soslowsky, L. J. Tendon healing: repair and regeneration. *Annu. Rev. Biomed. Eng.* **2012**, *14*, 47–71.
- (3) Sharma, P.; Maffulli, N. Basic biology of tendon injury and healing. *Surgeon* **2005**, *3*, 309–316.
- (4) Weinreb, J. H.; Sheth, C.; Apostolakis, J.; McCarthy, M.-B.; Barden, B.; Cote, M. P.; Mazzocca, A. D. Tendon structure, disease, and imaging. *Muscles Ligaments Tendons J.* **2014**, *4*, 66–73.
- (5) Lin, T. W.; Cardenas, L.; Soslowsky, L. J. Biomechanics of tendon injury and repair. *J. Biomech.* **2004**, *37*, 865–877.
- (6) Docheva, D.; Müller, S. A.; Majewski, M.; Evans, C. H. Biologics for tendon repair. *Adv. Drug Delivery Rev.* **2015**, *84*, 222–239.
- (7) Chen, J.; Xu, J.; Wang, A.; Zheng, M. Scaffolds for tendon and ligament repair: Review of the efficacy of commercial products. *Expert Rev. Med. Devices* **2009**, *6*, 61–73.
- (8) Longo, U. G.; Lamberti, A.; Petrillo, S.; Maffulli, N.; Denaro, V. Scaffolds in tendon tissue engineering. *Stem Cells Int.* **2012**, *2012*, 517165 DOI: [10.1155/2012/517165](https://doi.org/10.1155/2012/517165).
- (9) Caliar, S. R.; Harley, B. A. C. The effect of anisotropic collagen-GAG scaffolds and growth factor supplementation on tendon cell recruitment, alignment, and metabolic activity. *Biomaterials* **2011**, *32*, 5330–5340.
- (10) Sharifi-Aghdam, M.; Faridi-Majidi, R.; Derakhshan, M. A.; Chegeni, A.; Azami, M. Preparation of collagen/polyurethane/knitted silk as a composite scaffold for tendon tissue engineering. *Proc. Inst. Mech. Eng., Part H* **2017**, *231*, 652–662.
- (11) Shen, W.; Chen, X.; Hu, Y.; Yin, Z.; Zhu, T.; Hu, J.; et al. Long-term effects of knitted silk-collagen sponge scaffold on anterior cruciate ligament reconstruction and osteoarthritis prevention. *Biomaterials* **2014**, *35*, 8154–8163.
- (12) Deng, D.; Wang, W.; Wang, B.; Zhang, P.; Zhou, G.; Zhang, W. J.; et al. Repair of Achilles tendon defect with autologous ASCs engineered tendon in a rabbit model. *Biomaterials* **2014**, *35*, 8801–8809.
- (13) Lopes, M. S.; Jardini, A. L.; Filho, R. M. Poly (lactic acid) production for tissue engineering applications. *Procedia Eng.* **2012**, *42*, 1402–1413.
- (14) Dahlin, R. L.; Kasper, F. K.; Mikos, A. G. Polymeric Nanofibers in Tissue Engineering. *Tissue Eng., Part B* **2011**, *17*, 349–364.
- (15) Ramos, D.; Peach, M. S.; Mazzocca, A. D.; Yu, X.; Kumbar, S. G. Tendon Tissue Engineering. In *Regenerative Engineering of Musculoskeletal Tissues and Interfaces*, 1st ed.; Nukavarapu, S., Freeman, J., Laurencin, C., Eds.; Woodhead Publishing, 2015; pp 195–217.
- (16) Shalumon, K. T.; Anulekha, K. H.; Chennazhi, K. P.; Tamura, H.; Nair, S. V.; Jayakumar, R. Fabrication of chitosan/poly-(caprolactone) nanofibrous scaffold for bone and skin tissue engineering. *Int. J. Biol. Macromol.* **2011**, *48*, 571–576.
- (17) Srinivasan, S.; Jayakumar, R.; Chennazhi, K. P.; Levorson, E. J.; Mikos, A. G.; Nair, S. V. Multiscale fibrous scaffolds in regenerative medicine. *Adv. Polym. Sci.* **2011**, *246*, 1–20.
- (18) Longo, U. G.; Lamberti, A.; Maffulli, N.; Denaro, V. Tissue engineered biological augmentation for tendon healing: A systematic review. *Br. Med. Bull.* **2011**, *98*, 31–59.
- (19) Sahoo, S.; Toh, S. L.; Goh, J. C. H. A bFGF-releasing silk/PLGA-based biohybrid scaffold for ligament/tendon tissue engineering using mesenchymal progenitor cells. *Biomaterials* **2010**, *31*, 2990–2998.
- (20) Liu, S.; Hu, C.; Li, F.; Li, X.; Cui, W.; Fan, C. Prevention of peritendinous adhesions with electrospun ibuprofen-loaded poly(L-lactic acid)-polyethylene glycol fibrous membranes. *Tissue Eng., Part A* **2013**, *19*, 529–537.
- (21) Chen, S. H.; Chen, C. H.; Shalumon, K. T.; Chen, J. P. Preparation and characterization of antiadhesion barrier film from hyaluronic acid-grafted electrospun poly(caprolactone) nanofibrous membranes for prevention of flexor tendon postoperative peritendinous adhesion. *Int. J. Nanomed.* **2014**, *9*, 4079–4092.
- (22) Chen, C. H.; Chen, S. H.; Shalumon, K. T.; Chen, J. P. Prevention of peritendinous adhesions with electrospun polyethylene glycol/polycaprolactone nanofibrous membranes. *Colloids Surf., B* **2015**, *133*, 221–230.
- (23) Hu, C.; Liu, S.; Zhang, Y.; Li, B.; Yang, H.; Fan, C.; et al. Long-term drug release from electrospun fibers for in vivo inflammation prevention in the prevention of peritendinous adhesions. *Acta Biomater.* **2013**, *9*, 7381–7388.
- (24) Namba, J.; Shimada, K.; Saito, M.; Murase, T.; Yamada, H.; Yoshikawa, H. Modulation of peritendinous adhesion formation by alginate solution in a rabbit flexor tendon model. *J. Biomed. Mater. Res., Part B* **2007**, *80*, 273–279.
- (25) Deepthi, S.; Nivedhitha Sundaram, M.; Deepthi Kadavan, J.; Jayakumar, R. Layered chitosan-collagen hydrogel/aligned PLLA nanofiber construct for flexor tendon regeneration. *Carbohydr. Polym.* **2016**, *153*, 492–500.
- (26) Shalumon, K. T.; Sheu, C.; Chen, C. H.; Chen, S. H.; Jose, G.; Kuo, C. Y.; et al. Multi-functional electrospun antibacterial core-shell nanofibrous membranes for prolonged prevention of post-surgical tendon adhesion and inflammation. *Acta Biomater.* **2018**, *72*, 121–36.
- (27) Rodrigues, M. T.; Reis, R. L.; Gomes, M. E. Engineering tendon and ligament tissues: Present developments towards successful clinical products. *J. Tissue Eng. Regen. Med.* **2013**, *7*, 673–686.
- (28) Liu, C.; Xia, Z.; Czernuszka, J. T. Design and development of three-dimensional scaffolds for tissue engineering. *Chem. Eng. Res. Des.* **2007**, *85*, 1051–1064.
- (29) Orr, S. B.; Chainani, A.; Hippensteel, K. J.; Kishan, A.; Gilchrist, C.; Garrigues, N. W.; et al. Aligned multilayered electrospun scaffolds for rotator cuff tendon tissue engineering. *Acta Biomater.* **2015**, *24*, 117–126.
- (30) Chen, C.-H.; Chen, S.-H.; Kuo, C.-Y.; Li, M.-L.; Chen, J.-P. Response of dermal fibroblasts to biochemical and physical cues in aligned polycaprolactone/silk fibroin nanofiber scaffolds for application in tendon tissue engineering. *Nanomaterials* **2017**, *7*, 219–239.
- (31) Cooper, J. A.; Lu, H. H.; Ko, F. K.; Freeman, J. W.; Laurencin, C. T. Fiber-based tissue-engineered scaffold for ligament replacement: Design considerations and in vitro evaluation. *Biomaterials* **2005**, *26*, 1523–1532.
- (32) Barber, J. G.; Handorf, A. M.; Allee, T. J.; Li, W.-J. Braided Nanofibrous Scaffold for Tendon and Ligament Tissue Engineering. *Tissue Eng., Part A* **2013**, *19*, 1265–1274.
- (33) Laranjeira, M.; Domingues, R. M. A.; Costa-Almeida, R.; Reis, R. L.; Gomes, M. E. 3D Mimicry of native-tissue-fiber architecture

guides tendon-derived cells and adipose stem cells into artificial tendon constructs. *Small* **2017**, *13*, 1700689.

(34) Wren, T. A. L.; Yerby, S. A.; Beaupré, G. S.; Carter, D. R. Mechanical properties of the human achilles tendon. *Clin Biomech* **2001**, *16*, 245–251.

(35) Schneider, A.; Francius, G.; Obeid, R.; Schwinté, P.; Hemmerlé, J.; Frisch, B.; et al. Polyelectrolyte multilayers with a tunable young's modulus: Influence of film stiffness on cell adhesion. *Langmuir* **2006**, *22*, 1193–1200.

(36) Sahoo, S.; Ang, L. T.; Goh, J. C.; Toh, S. L. Growth factor delivery through electrospun nanofibers in scaffolds for tissue engineering applications. *J. Biomed. Mater. Res., Part A* **2009**, *93*, 1539–1550.

(37) Kjaer, M. Role of extracellular matrix in adaptation of tendon and skeletal muscle to mechanical loading. *Physiol. Rev.* **2004**, *84*, 649–698.

(38) Tang, J. B.; Xu, Y.; Wang, X. T. Tendon healing in vitro: activation of NIK, IKKalpha, IKKbeta, and NF- kappaB genes in signal pathway and proliferation of tenocytes. *Plast Reconstr Surg* **2004**, *113*, 1703–1711.

(39) Subramony, S. D.; Dargis, B. R.; Castillo, M.; Azeloglu, E. U.; Tracey, M. S.; Su, A.; et al. The guidance of stem cell differentiation by substrate alignment and mechanical stimulation. *Biomaterials* **2013**, *34*, 1942–1953.

(40) Teh, T. K.; Toh, S. L.; Goh, J. C. Aligned fibrous scaffolds for enhanced mechanoreponse and tenogenesis of mesenchymal stem cells. *Tissue Eng., Part A* **2013**, *19*, 1360–1372.

(41) Wu, S.; Wang, Y.; Streubel, P. N.; Duan, B. Living nanofiber yarn-based woven biotextiles for tendon tissue engineering using cell tri-culture and mechanical stimulation. *Acta Biomater.* **2017**, *62*, 102–115.

(42) Fan, H.; Liu, H.; Wong, E. J. W.; Toh, S. L.; Goh, J. C. H. In vivo study of anterior cruciate ligament regeneration using mesenchymal stem cells and silk scaffold. *Biomaterials* **2008**, *29*, 3324–3337.

Design, Synthesis, and Biological Evaluation of Itaconic Acid Derivatives as Potential Anti-Influenza Agents

Bidyadhar Sethy,[†] Chung-Fan Hsieh,[‡] Ta-Jen Lin,[‡] Po-Yuan Hu,[‡] Yu-Li Chen,[‡] Chia-Yi Lin,[‡] Sung-Nain Tseng,[§] Jim-Tong Horng,^{*,‡,§,||,#} and Pei-Wen Hsieh^{*,‡,||,#,¶}

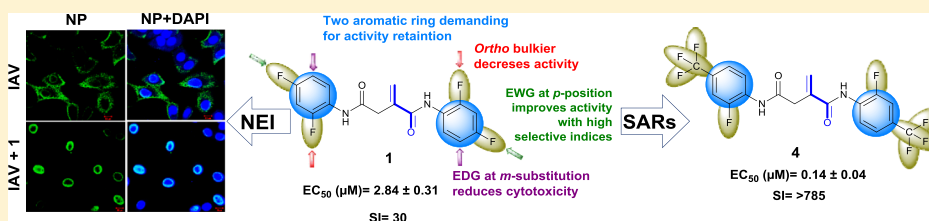
[†]Graduate Institute of Biomedical Sciences, Division of Natural Products, College of Medicine, [‡]Department of Biochemistry and Molecular Biology, [§]Research Center for Emerging Viral Infections, and [¶]Graduate Institute of Natural Products, School of Traditional Chinese Medicine, College of Medicine, Chang Gung University, Taoyuan 33302, Taiwan

^{||}Molecular Infectious Disease Research Center, Chang Gung Memorial Hospital, College of Medicine, Chang Gung University, Linkou 333, Taiwan

[#]Research Center for Chinese Herbal Medicine, Chang Gung University of Science and Technology, Taoyuan 33303, Taiwan

[¶]Department of Anesthesiology, Chang Gung Memorial Hospital, Linkou 333, Taiwan

Supporting Information



ABSTRACT: Influenza A viruses (IAVs) have caused worldwide epidemics and pandemics by reassortment and generation of drug-resistant mutants, which render antivirals and current vaccinations no longer usable. In this study, an itaconic acid derivative **1** was identified from a chemical library of 20 000 compounds, by performing a cell-based screening assay, as a lead agent exhibiting anti-influenza A activity. Accordingly, a series of itaconic acid derivatives were designed and synthesized by adopting a rational design strategy to obtain more potent anti-influenza agents. The results of an in vitro pharmacological study showed that compounds **4** and **8** exhibited the most potent anti-IAV effect with half-maximal effective concentration values of 0.14 and 0.11 μM, respectively, in Madin–Darby canine kidney cells. The mechanism of action studies showed that lead agents **1** and **4** reduced virus replication by directly targeting IAV nucleoproteins and disrupting virus ribonucleoprotein export from the nucleus to the cytosol. On the basis of its high potential as an anti-IAV agent and its selectivity index >785, compound **4** was found to be a promising candidate for further development against IAVs.

INTRODUCTION

Influenza A virus (IAV) is a negative-sense single-stranded RNA virus that belongs to the family of *Orthomyxoviridae*. IAV is the most virulent human pathogen and causes severe diseases in infants, elderly people, pregnant women, and people with weakened immune systems.¹ The symptoms of influenza virus infections include fever, muscle aches, headaches, vomiting, and diarrhea, and influenza may cause pneumonia, myocarditis, encephalitis, myositis, and sometimes even death.² In the past century, five notorious influenza pandemics occurred, which not only caused >45 million human deaths but also resulted in stupendous economic losses because of their high rates of morbidity and mortality.^{3–6} Currently, H1N1, H3N2, H5N1, and H7N9 subtypes of influenza A are highly aggressive seasonal flu strains that circulate in human populations and are a significant threat to human health.^{7,8} To overcome these pathogens and other emerging mutants, development of unique therapeutic strategies or drugs is urgently needed.^{7–11}

To prevent or reduce IAV infections, vaccination is generally recommended.^{12–14} For influenza therapy, two classes of antiviral drugs have been clinically used: virion ion-channel (M2 protein) inhibitors (amantadine and rimantadine) and neuraminidase inhibitors (oseltamivir and zanamivir). However, IAVs have developed resistance to these anti-influenza agents.^{6,15–18} Consequently, there is an urgent need to develop agents with different mechanisms of action on viral life cycles.

Because influenza viruses replicate, transcript, and generate viral proteins, such as virus ribonucleoproteins (vRNPs), in the nuclei of infected cells and then transport them to the cytoplasm, transfer of nuclear viral materials is a critical step in the influenza virus life cycle.^{19,20} In this step, the well-known host chromosomal region maintenance 1 (CRM1; also referred to as exportin 1 or XPO1) can interact with nuclear export signal-containing viral nuclear export proteins, which are then

Received: October 30, 2018

Published: February 12, 2019

exported to the cytoplasm.^{21–24} CRM1 is an important protein involved in the nuclear export process that regulates cell proliferation, cell-cycle progression, and apoptosis and is related to many diseases, such as cancer and viral infection.^{20,21,25,26} Accordingly, development of nuclear export inhibitors (NEIs) to block this pathway could be useful to provide a new therapeutic strategy against influenza.^{19,20}

In an effort to explore new lead compounds for anti-influenza A agents, large-scale screening of a chemical library containing >20 000 compounds against IAV was performed by using a cell-based anti-cytopathic effect (CPE) assay. Our first hit was *N,N'*-bis(2,4-difluorophenyl)-2-methylenesuccinamide (**1**, Figure 1), an itaconic acid derivative that exhibited anti-

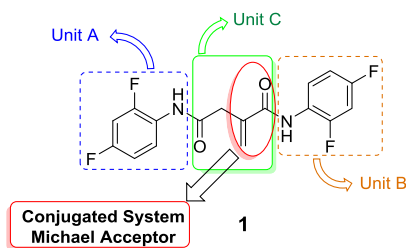


Figure 1. Lead compound **1** with its structural units.

influenza activity with a half-maximal effective concentration (EC_{50}) of 2.84 μ M. This compound is the first itaconic acid derivative to show anti-influenza activity. We then synthesized 25 itaconic acid derivatives, and their effects against IAV were evaluated. Subsequently, structure–activity relationships (SARs) were established. Furthermore, since the chemical structure of **1** bears a Michael-acceptor moiety, which is a privileged structure for NEIs,²¹ the mechanism of action of **1** against IAV was examined.

RESULTS AND DISCUSSION

The chemical structure of **1** consists of two 2,4-di-fluorophenyl moieties (units A and B, Figure 1) and an itaconic acid moiety (unit C, Figure 1), which are linked together by two amide bonds. Previous literature reports concluded that unit C of **1** has a conjugated system that is able to react with the cysteine residue of the active site through Michael addition.²¹ Therefore, to discuss the correlation between the reactivity of the conjugated system in **1** toward the active site and its bioactivities, units A and B were modified by varying their aromatic substituents. Using an addition/elimination reaction mechanism, a one-step synthetic route was developed (Scheme 1), which led to 25 itaconic acid derivatives. The purities of all compounds (>96%) were evaluated by high-performance liquid chromatography (HPLC) (Tables S1 and S2). Furthermore, the anti-IAV effects and cytotoxicities of these compounds were determined in an influenza A (A/WSN/33)

virus-infected Madin–Darby canine kidney (MDCK) epithelial cell model.

SARs Based on Anti-IAV (H1N1) Activity. To evaluate the antiviral activity and cytotoxicity of the itaconic acid derivatives, a CPE assay and an 3-(4,5-dimethylthiazol-2-yl)-2,5-diphenyltetrazolium bromide (MTT) assay were performed in parallel (Tables 1 and 2). Two NEIs, leptomycin B (LMB) and verdinexor, were used as positive controls. The cytotoxic results (50% cytotoxic concentration, CC_{50}) indicated that, except for compounds **1** and **6–8**, most of the derivatives were noncytotoxic at 110 μ M. Compounds **4**, **7**, **8**, and **9** exhibited the most potent effects on anti-IAV, with EC_{50} values of 0.14, 0.18, 0.11, and 0.48 μ M, respectively. The selectivity indices (SIs) of **4** and **9** were better than that of verdinexor, indicating that **4** and **9** could be good candidates against IAV. The SARs of the synthetics are discussed below on the basis of their antiviral activities.

Initially, we modified the para (p) position of the two aromatic rings (units A and B) of the lead agent **1** by introducing different electron-withdrawing groups (EWGs), such as Cl, Br, or trifluoromethyl ($-CF_3$), or an electron-donating group (EDG). The results showed that when *p*-F (**1**) was replaced with *p*-Cl (**2**), *p*-Br (**3**), or *p*- CF_3 (**4**), the antiviral activities were significantly improved by the presence of lipophilic (halo) groups, with the electron-withdrawing property at the para position. Subsequently, to gain a better understanding of the electronic property at the p-position, we introduced a methoxy group ($-OCH_3$), which resulted in reduced activity. From these results, we concluded that the presence of a highly EWG ($-CF_3$) at the p-position (units A and B) improved the activity while decreasing the cytotoxicity. These effects were most likely caused by the presence of the strong EWG at the p-position facilitating a Michael-type addition and favoring the lipophilic interaction with the active core, which would increase the inhibitory property with high SIs. Accordingly, we concluded that EWG substitution, compared with EDG substitution, at the p-position improved antiviral activity.

We observed that moving the fluoro-group of units A and B from the para to the meta position (**6**) slightly enhanced the antiviral activity but led to increased cytotoxicity. Similarly, replacing *m*-F (**6**) with *m*-Cl (**7**) or *m*- CF_3 (**8**) not only improved potency but also triggered cytotoxicity (Table 1). We also found that the compounds containing a *p*- or *m*-trifluoromethyl group (**4** and **8**) exhibited 20–25-fold higher anti-IAV activity (Table 1). Because the Cys-539 residue is a prime target located within the hydrophobic nuclear export sequences-binding region of CRM1, the hydrophobic trifluoromethyl group may occupy the hydrophobic groove, being buried deeply into the active site, thereby promoting antiviral activity.²⁷ To test our hypothesis, we performed molecular docking of compounds **4** and **8** in the active sites of LMB in CRM1 (PDB ID: 4HAT). The results showed that the

Scheme 1. Reaction Conditions and Reagents (A) Dry Dichloromethane, MS, -4 to 0 $^{\circ}$ C for 1 h, rt for 4 h to 1 d (TLC Confirmation Necessary)

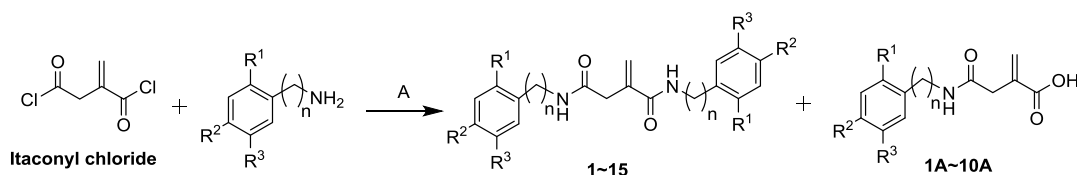
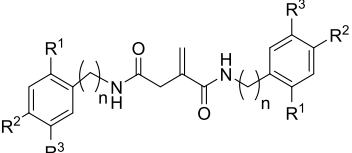
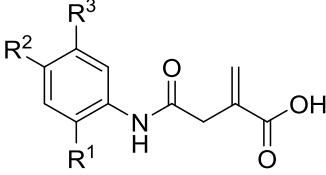


Table 1. In Vitro Anti-Influenza A Virus Activities of the Itaconic Acid Derivatives (1–15)^a


compounds	R ¹	R ²	R ³	n	NH signals	EC ₅₀ (μM)	CC ₅₀ (μM)	SI
1	F	F	H	0	8.73, 8.21	2.84 ± 0.31	84.72 ± 4.41	29.83
2	F	Cl	H	0	8.75, 8.18	0.67 ± 0.04	>110	>164
3	F	Br	H	0	8.77, 8.18	0.99 ± 0.11	>110	>111
4	F	CF ₃	H	0	8.92, 8.32	0.14 ± 0.04	>110	>785
5	F	OCH ₃	H	0	8.60, 8.12	31.04 ± 0.66	>110	>3
6	F	H	F	0	8.82, 8.24	1.26 ± 0.03	32.77 ± 2.46	26.01
7	F	H	Cl	0	8.73, 8.21	0.18 ± 0.12	19.91 ± 0.30	110.61
8	F	H	CF ₃	0	8.82, 8.30	0.11 ± 0.03	14.97 ± 1.97	136.09
9	F	H	OCH ₃	0	8.72, 8.23	0.48 ± 0.02	>110	>229
10	Br	F	H	0	8.51, 8.27	2.59 ± 0.20	>110	>42
11	CF ₃	F	H	0	8.50, 8.10	>50	>110	ND
12	CF ₃	H	H	0	8.55, 8.20	>50	>110	ND
13	Br	Br	H	0	8.56, 8.34	41.56 ± 2.15	>110	>2
14	F	F	H	1	7.00, 7.00	>50	>110	ND
15	F	H	F	1	6.98, 6.85	>50	>110	ND
LMB						0.18 ± 0.02	>0.88	>4
Verdinexor						3.28 ± 0.21	31.77 ± 2.40	9.69

^aEffective concentration for 50% inhibition (EC₅₀) in μM; cytotoxicity concentration for 50% cell death (CC₅₀) in μM; SI calculated as the ratio of CC₅₀ to EC₅₀; data represent the mean ± SD (n ≥ 3), ND: not determined; LMB and verdinexor used as positive controls.

Table 2. In Vitro Anti-Influenza A Virus Activity of the Itaconic Acid Derivatives (1A–10A)^a


compounds	R ¹	R ²	R ³	EC ₅₀ (μM)	CC ₅₀ (μM)	SI
1A	F	F	H	>50	>110	ND
2A	F	Cl	H	>50	>110	ND
3A	F	CF ₃	H	>50	>110	ND
4A	F	H	F	>50	>110	ND
5A	F	H	CF ₃	>50	>110	ND
6A	F	F	Cl	>50	>110	ND
7A	CF ₃	F	H	>50	>110	ND
8A	CF ₃	H	F	>50	>110	ND
9A	CF ₃	H	H	>50	>110	ND
10A	H	H	CF ₃	>50	>110	ND

^aEffective concentration for 50% inhibition (EC₅₀) in μM; cytotoxicity concentration for 50% cell death (CC₅₀) in μM; SI calculated as the ratio of CC₅₀ to EC₅₀; data represent the mean ± SD (n ≥ 3); ND: not determined.

Michael-acceptor moiety (unit C) of 4 and 8 (Figure 2A and B) and the LMB lactone (Figure 2C) were closely fit at the active residue (Cys-539). Moreover, a comparison of the docking poses of 4 (purple) and 8 (green) with the binding site of LMB (blue) showed that an aromatic ring, conjugated with the hydrophobic trifluoromethyl group of compounds 4 and 8, was located in the hydrophobic groove of the LMB binding sites of CRM1 (Figure 2D). Notably, 4 bound to the active site by hydrogen bonding with the Lys-579 residue and 8 interacted

with Lys-548 through hydrogen bonding, and the presence of Cys-539 helped preserve their activities. Conversely, introducing an EDG, such as the methoxy (–OCH₃) group (9), promoted antiviral activity with lower cytotoxicity (Table 1). Comparison of the data of 9 and 5 showed that the strong effect of a donating group at the meta position on the electron density of the aromatic ring may concomitantly improve efficiency against IAV.

Next, to examine the effect of substitution at the ortho position, the F group in 1 was replaced with Br (10), which led to relatively similar activity and slightly reduced cytotoxicity (Table 1). However, the antiviral activities completely vanished after introducing a CF₃ group in the o-position (11 and 12) (Table 1). These results indicated that the presence of a strong EWG at the o-position had a negative effect on activity. Moreover, two analogues (1 and 6) containing both *m*- and *p*-F substitutions along with *o*-F on each aromatic ring exerted an inhibitory effect against IAV, most likely because of the hydrophobic property of the F group promoting the formation of π -alkyl hydrophobic interactions with the active site (Figure S51A,B), which would lead to activity retention.

Extending the carbon chain between the amides and aromatic rings inhibited the effect against IAV (Table 1), which suggested that 14 and 15 are unable to fit the active site. Furthermore, the presence of a lone electron pair on the amide nitrogen atom may disturb the conjugate system present on 14 (Figure 3A) or 15 by direct conjugation with the carbonyl carbon. This contrasts with the case of 1 (Figure 3B) in which direct conjugation with the Michael-acceptor moiety was hindered by the withdrawal property of the EWG, which resulted in a resonance effect on the nitrogen lone pair that is drawn toward the benzene ring.

It was previously reported that the high electronegativity of fluorine substitution can enhance potency and affect target

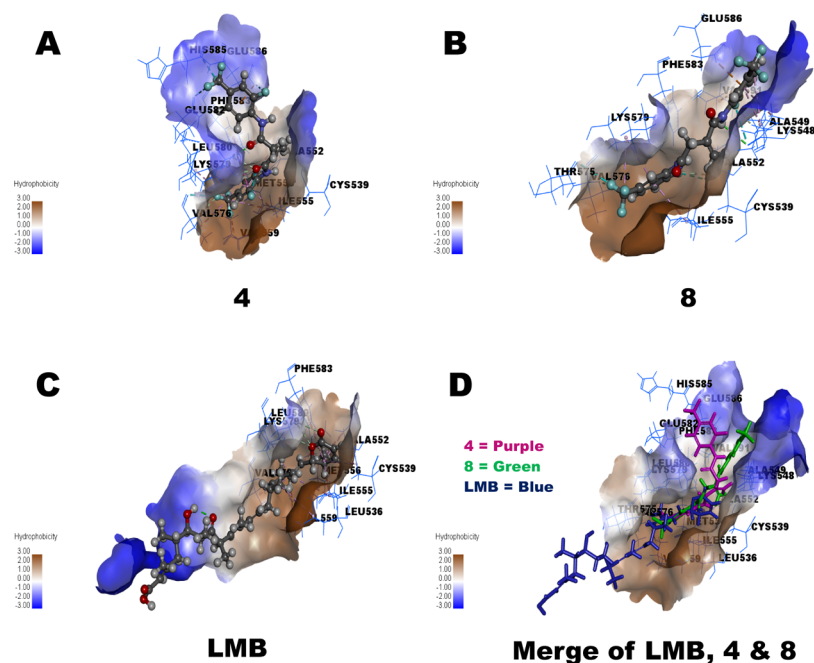


Figure 2. Molecular docking of interaction between inhibitors 4 and 8 and CRM1 in the binding sites of LMB. (A) 4-CRM1 complex; (B) 8-CRM1 complex; (C) LMB-CRM1 complex; and (D) merge of 4 (purple) and 8 (green) with LMB (blue) in the binding groove of LMB in CRM1 (PDB ID: 4HAT).

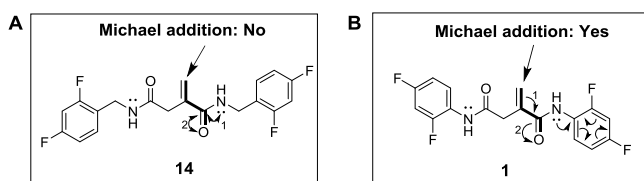


Figure 3. Compounds 14 and 1 with its Michael addition characteristics.

selectivity by affecting pK_a , lipophilicity, hydrophobic interactions, and drug metabolism. In addition, a fluoro atom at the *o*-position interacts with the amide proton (N–H), thereby leading to improved permeability.²⁸ In synthetics possessing an F group at the *o*-position, the interaction with N–H by intramolecular hydrogen bonding could have an effect on the antiviral activity. Accordingly, ¹H nuclear magnetic resonance (NMR) data showed that the NH signals were downfield shifted when an *o*-F group was present on the aromatic ring (units A and B).²⁹ The presence of different substituents (EWG or EDG) on the aromatic ring counterbalanced the electron-withdrawing effect of the *o*-F group by a resonance effect, which preserved the intramolecular hydrogen bonding and anti-IAV activity. However, in systems containing CF₃ where π -resonance is not possible, the inductive electron-withdrawing effect of fluorine could exert a powerful influence on *o*-substituents and increase the chemical shift of the NH signals. On the other hand, extending the carbon chain between the amide proton and the aromatic ring could disrupt the conjugating system and the N–H–F interaction, which might contribute to the reduced activity in 14 and 15 (Table 1). This idea suggests that intermolecular hydrogen bonding might also enhance the anti-IAV activities of these analogues.

To further investigate the activity of unit A, we synthesized 10 derivatives (1A–10A) of itaconic acid by conjugating the aromatic ring only at the unit A side and evaluated their anti-

influenza A activity. Additionally, the chemical structures of this series were confirmed by 2D nuclear Overhauser enhancement spectroscopy. According to the results summarized in Table 2, all of these products were nonactive, which indicated that the presence of two aromatic rings (units A and B) is necessary for anti-influenza activity.

Since the two aromatic rings containing derivatives have similar structures, we initially selected lead agent 1 to examine its effectiveness against different strains of influenza virus and other viruses as well as to study the stage of action on IAV.

Antiviral Activity of Compounds 1 and 4 on Various Strains of Viruses. To evaluate the effectiveness of the itaconic acid analogues (1 and 4) against various strains of viruses, we chose some strains, especially those which are clinically resistant to the drug oseltamivir (A/TW/7855/09 and A/TW/6663/09) and the swine origin influenza virus (SOIV) strain caused pandemic (A/TW/90206/09 and A/TW/2235/09) in the last decade and also others those which have been endemic in Taiwan in recent years. Cytotoxicity tests using 1 and 4 were conducted in different cell lines, and the results are expressed as the median CC₅₀. EC₅₀ was used to express the inhibitory effects of 1 and 4 on different virus strains. Both of these compounds can effectively inhibit the replication of influenza virus in MDCK cells with high CC₅₀ values. The inhibitory effect of 1 was satisfactory on many IAV strains, such as A/WSN/33 (H1N1), A/TW/90206/09 (H1N1pdm), A/TW/2235/09 (H1N1pdm), A/TW/7855/09 (H1N1), A/TW/6663/09 (H1N1), and A/TW/3446/02 (H3N2), with EC₅₀ values of approximately 2–5 μ M (Table 3). It is worth noting that the A/TW/7855/09 (H1N1) and A/TW/6663/09 (H1N1) strains are resistant to the drug oseltamivir, which suggests that 1 could exert a therapeutic effect on virus strains that show resistance to oseltamivir. In addition, 1 exhibited a good inhibitory effect on the influenza B virus strains popular in recent years, including B/TW/00482/13, B/TW/03384/13, B/TW/00642/14, and B/TW/01061/

Table 3. Inhibition Spectrum of **1** and **4** Against Different Virus Strains

cells	^a CC ₅₀ (μM)			
	1		4	
RD	74.60 ± 6.47		9.31 ± 0.42	
MDCK	84.72 ± 4.41		>110	
viruses	^b EC ₅₀ (μM)		^c SI	
	1	4	1	4
influenza virus				
A/WSN/33 (H1N1)	2.84 ± 0.31	0.33 ± 0.02	30	>333
A/TW/90206/09 (H1N1pdm) ^d	2.98 ± 0.83	ND	28	ND
A/TW/2235/09 (H1N1pdm) ^d	2.36 ± 0.11	1.62 ± 0.07	36	>67
A/TW/7855/09 (H1N1) ^e	2.60 ± 0.12	ND	33	ND
A/TW/6663/09 (H1N1) ^e	4.83 ± 1.89	ND	18	ND
A/TW/3446/02 (H3N2)	4.60 ± 0.16	0.96 ± 0.04	18	>114
B/TW/00482/13	3.77 ± 0.03	ND	22	ND
B/TW/03384/13	3.75 ± 0.04	ND	23	ND
B/TW/00642/14	3.44 ± 0.21	ND	25	ND
B/TW/01061/14	3.97 ± 0.03	ND	21	ND
viruses	^b EC ₅₀ (μM)		^c SI	
	1	4	1	4
enterovirus (EV)				
EV A71 TW/2231/1998	4.50 ± 0.91	ND	16	ND
EV A71 TW/4643/1998	ND	6.69 ± 0.27	ND	1
EV D68 TW/2795/2014 (clade B3)	>50	>50	ND	ND
viruses	^b EC ₅₀ (μM)		^c SI	
	1	4	1	4
rhinovirus				
rhinovirus/71803	>50	>50	ND	ND
rhinovirus/71903	>50	>50	ND	ND

^aCC₅₀ was determined by the MTT assay. ^bEC₅₀ was determined by the neutralization assay using crystal violet staining, MDCK cells were used for influenza viruses, and RD cells were used for enterovirus and rhinovirus. ^cSI calculated as the ratio of CC₅₀ to EC₅₀. ^dPandemic H1N1 (SOIV) strains. ^eStrains clinically resistant to oseltamivir. Data are presented as the mean ± SDs of the results from three independent experiments. ND: not determined.

14, with EC₅₀ values between 3 and 4 μM (Table 3) and greater SIs (>18). Further, the anti-influenza effect of **4** gave a 5–8-fold higher activity for A/WSN/33 (H1N1) and A/TW/3446/02 (H3N2) strains and slightly improved activity for A/TW/2235/09 (H1N1pdm) than those of compound **1** with higher SI values. Compounds **1** and **4** also had inhibitory effects on enterovirus A71, with an EC₅₀ value of approximately 4–7 μM, whereas it had no inhibitory effect on either enterovirus D68 or rhinovirus, which were evaluated by using rhabdomyosarcoma (RD) cells. Although the influenza virus has high variability, this does not affect the inhibitory effect of **1** on different strains of influenza A and B types along with **4** on IAVs. Thus, **1** and **4** show an extensive spectrum of inhibition against influenza viruses, drug-resistant strains, and enterovirus A71.

Microscopic Observation of IAV-Induced CPE Inhibition by 1. Virus-induced cytopathic changes were examined in MDCK cells, which were infected with influenza virus A/WSN/33 with a multiplicity of infection (MOI) of 0.5 for 1 h, washed with phosphate-buffered saline (PBS), treated with **1** (10 μM), and observed under a microscope post infection (pi) (12 or 36 h) (Figure 4). We found that the influenza virus caused some cytopathic changes after 12 h and serious CPEs

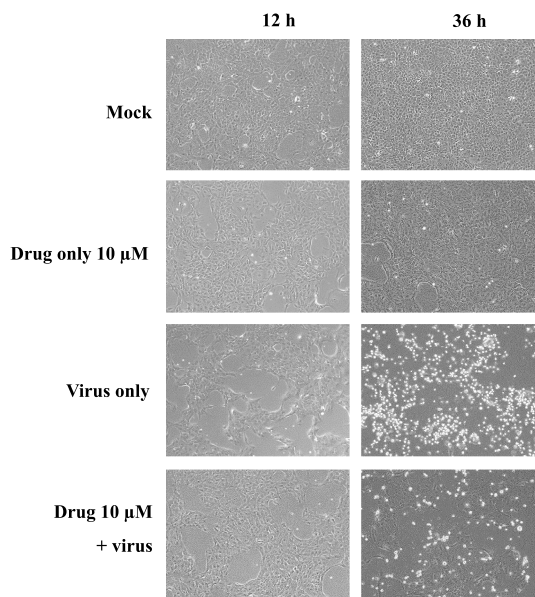


Figure 4. Compound **1** alleviates cytopathic changes induced by influenza A/WSN/33. MDCK cells were infected with the A/WSN/33 influenza virus strain with an MOI = 0.5 for 1 h, washed with PBS, and then incubated with 10 μM of **1** in E0 medium. At pi of 12 and 36 h, the cytopathic phenomenon was recorded by observation using a microscope (Zeiss Axiovert 200M, 20× objective). The experiment was performed in three repetitions.

with more round-up cells after 36 h in the virus-only group. When cotreating drugs and viruses, we found that **1** could avoid cytopathic phenomena caused by viral infection after 36 h, and the infection did not spread through the surrounding cells (Figure 4). With regard to toxicity, no cytotoxic effect caused by **1** was observed after 36 h. It seems reasonable to conclude that **1** has very low or no toxicity to MDCK cells.

Mechanism of Action Study: Estimation of the Inhibition Period of 1 in A/WSN/33 by Using Time-Course Test. The influenza virus life replication/cycle occurs in multiple steps, which requires approximately 8–10 h to complete.³⁰ For the time-of-addition (TOA) assay, the following main steps are to be considered: virus attachment, entry, uncoating, translation, replication, and release. In this study, we performed a TOA experiment by using MDCK cells infected with A/WSN/33 (MOI = 0.1) and treated with 10 μM of **1**. We designed this experiment according to the indicated time points for drug treatments, and the virus was allowed to absorb at −1 to 0 h pi. The supernatant was collected after 9 h for a plaque assay (Figure 5A). To examine whether compound **1** targets the host cell factor, the drug was treated 2 h prior to virus infection (−3 to 9 h pi; complete cycle). The periods indicate virus attachment, virus entry or uncoating (−1 to 9 h and 0 to 9 h pi, respectively), the middle stage of virus cycle endocytosis, translation, replication (3–9 h pi), and finally the assembly and release of progeny virus (6–9 h pi). From the TOA experiment, we found that **1** mainly inhibited the virus during the early and middle stages of replication, whereas it was less effective at the late stage relative to that in the virus-only lane (Figure 5B). To verify the actual stage of inhibition, the following experiments, that is, hemagglutination inhibition (HAI) assay, viral RNA synthesis, and viral protein distribution test by immunofluorescence (IF) staining, were performed.

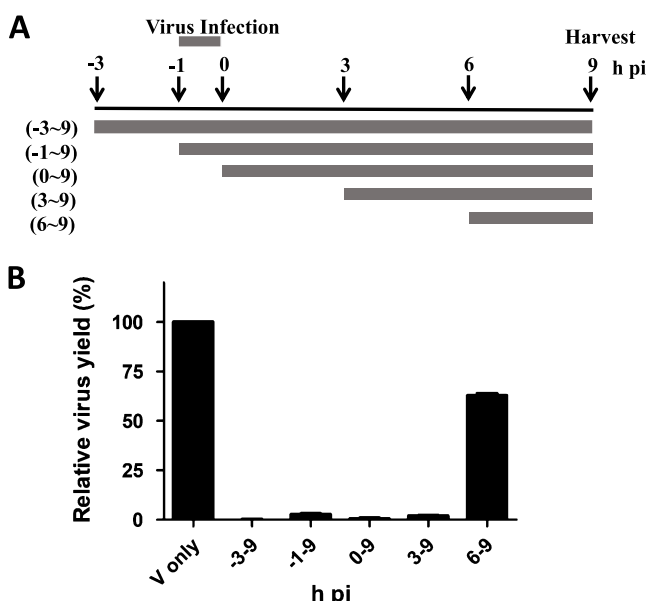


Figure 5. TOA assay to identify the step of viral life cycle targeted by **1** on influenza A/WSN/33 in MDCK cells. (A) Infection of MDCK cells with an MOI = 0.1 A/WSN/33 virus strain, and the virus adsorption time is -1 to 0 h. Compound **1** (10 μ M) was added at the following periods: -3 to 9 h pi, -1 to 9 h pi, 0 to 9 h pi, 3 to 9 h pi, and 6 to 9 h pi. The supernatant was collected after 9 h pi, and the remaining viral titers were determined by the plaque test. (B) The quantification of the results was normalized with virus only (arbitrarily set as 100%), and the experimental results are the averages from three independent experiments.

Effect of Hemagglutinin Activity on A/WSN/33 Virus upon Treatment with 1. In the early stage of viral replication, the virus attaches to the host cells by their surface glycoprotein hemagglutinin (HA). From the TOA experiment, we found that **1** inhibited the early steps of virus replication. Therefore, we used the HAI assay to verify whether **1** blocked the early virus attachment by inhibiting the hemagglutination of red blood cells (RBCs) caused by the viral HA protein. When the viral protein HA was used to contact the receptor on the surface of RBCs, hemagglutination was generated to detect whether the drug inhibited HA activity. RBCs were treated with various concentrations of **1** (2-fold serial dilution from 50 μ M) and incubated with influenza A/WSN/33 at 4 \times HA on ice for 1 h. The results showed that **1** alone (upper row, Figure 6) was not able to form agglutination similar to that of RBCs only (mock, lane 12), and virus treated with **1** could not inhibit the hemagglutination caused by viral HA (lower row, Figure

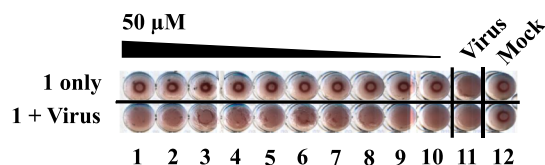


Figure 6. Effect of **1** on HA by HAI. The guinea pig RBCs were incubated with influenza A/WSN/33 at 4 \times HA on ice for 1 h with various concentrations of **1** (two-fold serial dilution from 50 μ M). The RBCs precipitate at the bottom in the control group when RBCs are mixed with DMSO (lane 12), whereas the RBCs appear foggy in the virus-only group (lane 11). This result is from one of three independent experiments.

6). Therefore, this result indicated that **1** did not inhibit the activity of HA, and there was no significant correlation between **1** and influenza virus attachment and entry into cells.

Compound 1 did Not Interrupt Viral RNA and Protein Synthesis. According to time-course experiments, **1** also inhibited the middle stages of viral replication; therefore, it was necessary to investigate whether **1** inhibits viral RNA and protein synthesis. After infecting MDCK cells with the influenza virus (MOI = 0.1) for 1 h, **1** was added, and cell lysates were collected at pi = 3, 6, and 9 h for RNA and protein determination by reverse transcription-quantitative polymerase chain reaction (RT-qPCR) and immunoblotting assay (Figure 7A). From the RT-qPCR results depicted in Figure 7B, it can be seen that no significant increase in viral RNA synthesis occurred at 0–3 h pi, whereas they showed an exponential rise at 3–9 h pi. The matrix protein 1 (M1) RNA levels indicated that **1** did not inhibit viral RNA synthesis. Additionally, the effect of **1** on viral protein synthesis was examined by western blotting as indicated by the level of various viral proteins (Figure 7C). The results implied that **1** did not inhibit the biosynthesis of viral proteins [nucleoprotein (NP), M1, HA, polymerase acidic protein (PA), nonstructural protein 2 (NS2), and NS1]. Thus, we confirmed that **1** did not inhibit viral RNA and protein expression.

Effect of 1 on the Subcellular Distribution of Viral Proteins. We used IF staining to detect the location of viral proteins in the cells to examine whether **1** affected their distribution. Thus, the effect of **1** was evaluated by using MDCK cells, which were infected with the influenza virus A/WSN/33 (MOI = 0.1), and the infected cells were treated with dimethyl sulfoxide (DMSO; mock; 0.05%) or **1** (10 μ M), or LMB (10 nM) as the control group. Then, the cells were fixed after 9 h pi and stained using the specific antibodies. From the results of IF staining, it can be seen that NP (Figure 8A,B) was transported into the cytoplasm in the case of influenza virus infection, but after **1** or LMB treatment, the NP of the influenza virus was confined to the nucleus. In contrast, the viral proteins NS2 (Figure S52A), PA (Figure S52B), and M1 (Figure S52C) did not exhibit significant differences in their nucleus/cytosol distribution after treatment with **1** or LMB compared with the virus-only control (Figure S52D). Notably, LMB is an NEI that acts as an antiviral and anticancer agent, and its main function is to block the cargo/exportin transport from the nucleus to cytoplasm by targeting the host cellular CRM1 protein. During the viral infection, the CRM1 protein helps to localize viral proteins in appropriate positions and interrupts the cellular cargoes. LMB efficiently binds the receptor sites of CRM1, resulting in inhibition of nuclear export of viral NP by disturbing the nuclear export signal 3-dependent CRM1 binding. In addition, as can be extracted from the literature, LMB has been shown to inhibit vRNP export while not affecting the subcellular localization of other viral proteins, such as M1 and NS2.³¹ As we hypothesized, **1** gave rise to a similar phenomenon (such as NEI). The IF staining result indicated that **1** specifically inhibited the nuclear export of viral NP, and PA also exhibited a different pattern in the presence of **1** because it surrounds the nucleus, thereby preventing its release into the cytoplasm, but the subcellular distribution of M1 and NS2 proteins is not affected.

In addition, the mechanism of action for compound **4**, which has the highest SI among all itaconic acid derivatives presented here, was also investigated by performing the TOA assay, HAI assay, and indirect IF assay. TOA data indicated that **4** (1 μ M)

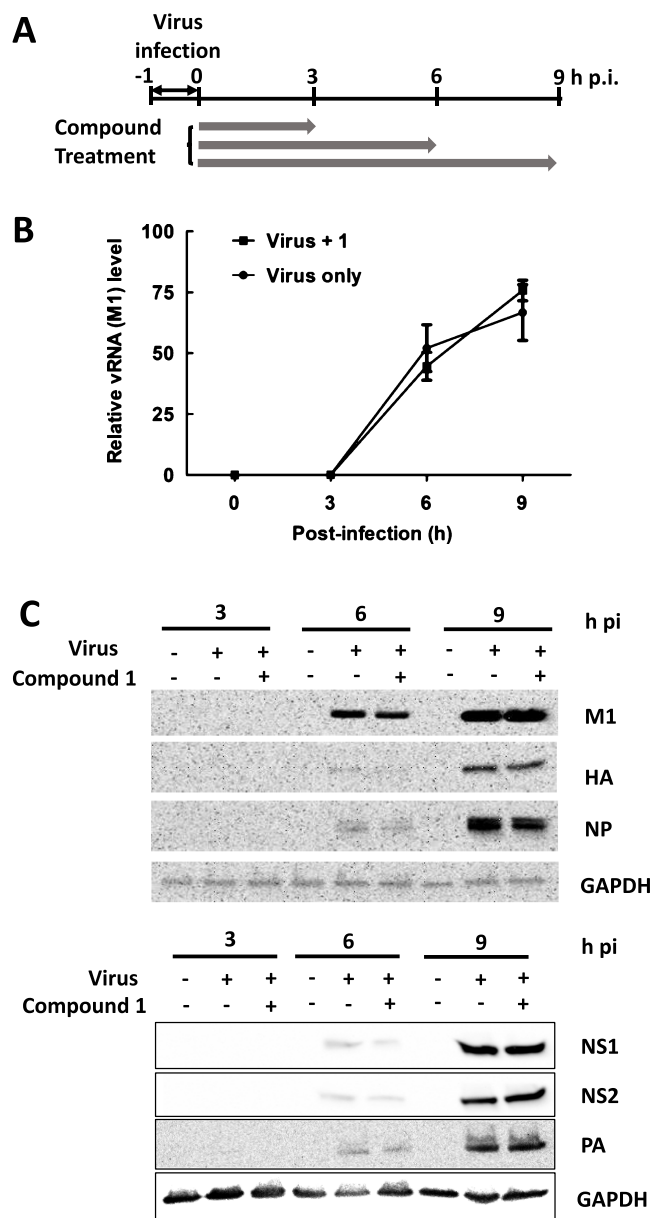


Figure 7. Exploration of the postadsorption test by vRNA inhibition assay using compound 1 treatment. (A) Design of compound 1 treatment profile. 1 (10 μ M) was added to MDCK cells during or after infection at an MOI = 0.1 by A/WSN/33 strain. (B) Total RNA was extracted at the indicated time (h p.i. = 0, 3, 6, and 9) by using TRIzol (Invitrogen, Carlsbad, CA). An M1-specific primer was used to measure the vRNA level by RT-qPCR. GAPDH was used to prepare the quantitative standards. This experiment is from one of three independent experiments. (C) Time-course protein synthesis using western blot immunoblotting analysis with antibodies against different viral proteins at 9 h p.i. of cell lysates.

efficiently inhibited the virus in the early and middle stages of replication, similar to 1 (10 μ M) (Figure S53). Furthermore, 4 also did not inhibit the hemagglutination caused by viral HA, which suggested that 4 does not inhibit the virus attachment (Figure S54). Finally, the IF data revealed that the 4-treated group showed inhibition of the middle stage of virus replication by specifically blocking subcellular distribution of viral NP to cytosol (Figure 9), without affecting other viral proteins, such as M1 (Figure S55). As these phenomena are similar to those of treatment with LMB and 1, it appears that

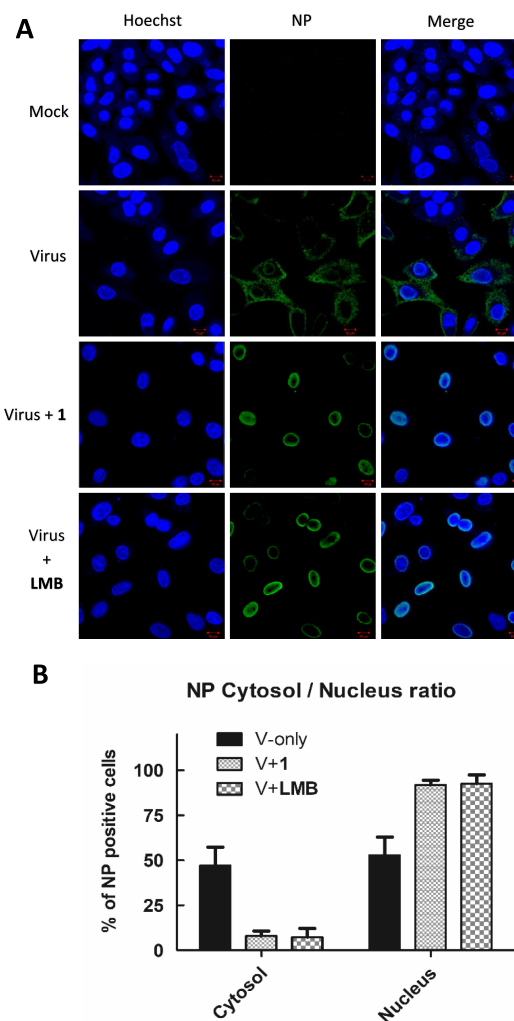


Figure 8. Detection by IF staining of the distribution of influenza virus proteins NP by treatment with compound 1. (A) One hour after infection of MDCK cells with an MOI = 0.1 A/WSN/33 strain, 10 μ M of 1 was added, and after 9 h of infection, it was fixed with 4% paraformaldehyde and immunostained with respective primary antibodies against NP (1:50). The secondary antibody used was Alexa Fluor 488, and the nuclei were stained with Hoechst. The influenza virus protein distribution was observed under a confocal microscope LSM 510 with a 63 \times objective. (B) ImageJ Plugins was used to quantify the intensity of the ratio of nuclear/cytoplasm distribution of NP viral protein. This experiment was verified by three independent experiments.

the mechanism underlying the activity of 4 is similar to that underlying 1.

CONCLUSIONS

With the aim of developing a new class of anti-influenza agents, we designed and synthesized 25 itaconic acid derivatives based on the chemical structure of lead agent 1, and their activities against IAV were evaluated in MDCK cells. The corresponding SARs of the derivatives were also proposed according to the bioactivity results. Activity and cytotoxicity improved after substitution with a highly EWG with larger size at the p-position of the aromatic rings. In contrast, the presence of an EDG at the m-position lowered the cytotoxicity. Bulky groups at the o-position also caused a decrease in activity. Additionally, the presence of two aromatic rings bonded to itaconic acid

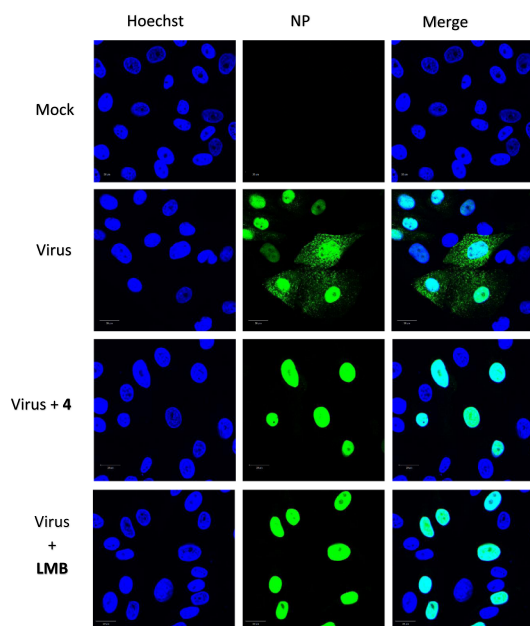


Figure 9. Detection by IF staining of the distribution of influenza virus proteins NP by treatment with compound 4. One hour after infection of MDCK cells with an MOI = 0.1 of A/WSN/33 strain, 1 μ M of 4 was added, and after 9 h of infection, it was fixed with 4% paraformaldehyde and immunostained with respective primary antibodies against NP (1:50). The secondary antibody used was Alexa Fluor 488, and the nuclei were stained with Hoechst. Influenza virus protein distribution was observed under a confocal microscope LSM 510 with a 63 \times objective. LMB was used as a positive control. Two independent experiments were performed for verification.

was crucial for activity retention. Among all compounds tested, 4 showed excellent activity (EC_{50} = 0.14 μ M) with a high SI (>785). Further, the initial hit agent 1 and its derivative 4 showed a broad spectrum of inhibition on different influenza strains along with enterovirus A71 viruses. A preliminary mechanism study using the lead agents 1 and 4 was conducted, which showed that the reduction of virus replication was caused by disruption of viral NP export from the nucleus to the cytoplasm. This finding suggests that the viral NP may be a possible molecular target for these agents as NEIs, which presents a new opportunity for antiviral drug development. Therefore, 4 and its active derivatives are promising anti-influenza agents that should be further investigated in more detail.

EXPERIMENTAL SECTION

Chemistry: Materials and Methods. All of the chemical reagents and solvents were purchased from commercial suppliers and used without further purification unless stated otherwise. Thin-layer chromatography (TLC; silica gel 60 F254 HX244089, Merck KGaA, Darmstadt, Germany) was used to monitor the chemical reactions, and the TLC plates were read under ultraviolet (UV) light (Entela UVGL-25 254/365 nm; CA, USA). Compounds were purified by flash column chromatography on silica gel (SiliaFlash G60, 70–230 mesh and SiliaFlash P60, 230–400 mesh, SiliCycle, QC, Canada). A Bruker AVANCE-400 MHz FT-NMR (Karlsruhe, Germany) instrument was used to measure ^1H and ^{13}C NMR spectra at 400 and 100 MHz, respectively. Deuterated solvents (CDCl_3 and acetone- d_6) were used to calibrate the peaks, and trimethylsilane was used as the internal standard for CDCl_3 . Mass spectra were measured on a TSQ Quantum triple quadrupole mass spectrometer, Thermo Finnigan, CA, USA. A Hitachi U-2010 spectrophotometer (Tokyo,

Japan) was used to record the UV spectra, and a JASCO FT/IR-4100 spectrophotometer (Tokyo, Japan) was used to measure the infrared spectra of all title compounds. Melting points were measured by using a MEL-TEMP (Laboratory Devices, Inc., MA, USA) apparatus. A rotary vacuum evaporator (N-1100; EYELA, Tokyo, Japan) was used for the removal of solvents. HPLC purity analyses were conducted by using a JASCO system: UV–visible detector (UV-1575), autosampler (AS-1555-10), and pump (PU-1580), with UV detection at 230 nm, two different solvent systems ($\text{MeOH}/\text{H}_2\text{O}$ and $\text{MeCN}/\text{H}_2\text{O}$), and a reversed-phase column (Nucleodur C18 HTec EC250/4.65 μm , Macherey-Nagel, Duren, Germany). All target compounds had purities >96% tested by HPLC.

PAINS Analysis. We examined all of the itaconic acid derivatives (1–15 and 1A–10A) for known classes of assay-interference compounds. First, according to the “free ADME/Tox Filtering Tool 4 (FAF-Drugs4)” program (<http://fafdrugs4.mti.univ-paris-diderot.fr/>), compounds 1–15 and 1A–10A were not perceived as pan assay interference compounds (PAINS). The database “Aggregator Advisor” (<http://advisor.bkslab.org/>) showed that all of the synthetics were not aggregators. Further, all of the synthetics, either as aggregators and/or PAINS, were verified by using the Bulk Pattern Checker tool (<http://zinc15.docking.org/patterns/home/>). Thus, the activities provided herein are highly likely not to have been caused by pan assay interference.

General Synthetic Protocol for all Title Compounds (1–15) and (1A–10A). To a solution of itaconyl chloride (1 equiv) in anhydrous CH_2Cl_2 with a molecular sieve (MS) at -4 to 0°C , halo-substituted aromatic aniline (2 equiv) was added slowly by using a micropipette. The reaction mixture was stirred at -4 to 0°C for 1 h and then allowed to warm to room temperature for 4 h to 1 d. After confirming the completion of the reaction by TLC, the whole reaction mixture was filtered, and the filtrate was washed with CH_2Cl_2 . The organic layer was quenched with a small volume of H_2O , the two layers were separated by using a separation funnel, and the organic layer was dried over MgSO_4 . Evaporation of the solvent afforded a mixture of expected products, along with some impurities, according to TLC. The mixture was purified by using silica gel column chromatography (hexane/ethyl acetate = 10/4) to obtain the desired products.

N,N'-Bis(2,4-difluorophenyl)-2-methylenesuccinamide (1). Yield of 17.1% as a white solid; mp ($^\circ\text{C}$): 132–133; IR ν_{max} (KBr) cm^{-1} : 3385, 3247, 3232, 3090, 3028, 1665, 1616, 1518, 1430, 1263, 1223, 1143, 1098, 961, 853, 813, 628, 553, 490. UV $\lambda_{\text{max}}^{\text{MeOH}}$ nm (log ϵ): 202.5 (4.5), 235.5 (4.1), 274.5 (3.8, sh); ^1H NMR (CDCl_3 , 400 MHz): δ_{H} 8.73 (1H, s, NH), 8.26–8.14 (3H, m, NH, H6', and H6''), 6.93–6.82 (4H, m, H3', H3'', H5' and H5''), 5.99 (1H, s, H_b), 5.83 (1H, s, H_a), 3.49 (2H, s, H3); ^{13}C NMR (CDCl_3 , 100 MHz): δ_{C} 168.4 (s, C4), 166.7 (s, C1), 159.3 (dd, J = 245.6, 11.5 Hz, C4'), 158.9 (dd, J = 244.7, 11.4 Hz, C4''), 153.3 (dd, J = 245.7, 11.7 Hz, C2'), 153.0 (dd, J = 246.1, 11.7 Hz, C2''), 138.6 (s, C2), 123.5 (t, C5), 123.4 (d, J = 9.1, Hz, C1'), 123.2 (d, J = 9.1 Hz, C1''), 122.8 (dd, J = 10.8, 10.8 Hz, C6'), 122.3 (dd, J = 10.2, 10.2 Hz, C6''), 111.5 (dd, J = 21.6, 3.7 Hz, C5'), 111.2 (dd, J = 21.5, 3.7 Hz, C5''), 103.9 (dd, J = 23.0, 23.1 Hz, C3'), 103.7 (dd, J = 23.1, 23.2 Hz, C3''), 41.5 (t, C3). ESI-MS (m/z): 375.2 [$\text{M} + \text{Na}$] $^+$.

4-((2,4-Difluorophenyl)amino)-2-methylene-4-oxobutanoic Acid (1A). Yield of 13.3% as a white solid; mp ($^\circ\text{C}$): 170–171; IR ν_{max} (KBr) cm^{-1} : 3212, 3151, 3018, 2968, 2900, 1708, 1649, 1550, 1512, 1432, 1361, 1305, 1263, 1226, 1169, 1144, 1099, 968, 910, 859, 580, 485, 437; UV $\lambda_{\text{max}}^{\text{MeOH}}$ nm (log ϵ): 203.0 (4.4), 232.0 (4.1), 274.0 (3.3); ^1H NMR (acetone- d_6 , 400 MHz): δ_{H} 8.99 (1H, s, NH), 8.19–8.12 (1H, m, H6'), 7.06 (1H, ddd, J = 8.8, 8.4, 2.8 Hz, H5'), 6.96 (1H, dd, J = 8.8, 8.4 Hz, H3'), 6.32 (1H, s, H_b), 5.86 (1H, s, H_a), 3.51 (2H, s, H3); ^{13}C NMR (acetone- d_6 , 100 MHz): δ_{C} 169.4 (s, C1), 168.2 (s, C4), 159.5 (dd, J = 242.2, 11.3 Hz, C2'), 154.4 (dd, J = 245.4, 11.9 Hz, C4'), 136.3 (s, C2), 128.8 (t, C5), 124.4 (dd, J = 10.9, 3.4 Hz, C1'), 124.9 (d, J = 8.6 Hz, C6'), 111.7 (dd, J = 21.6, 3.6 Hz, C5'), 104.4 (dd, J = 23.7, 23.7 Hz, C3'), 40.8 (t, C3); ESI-MS (m/z): 239.9 [$\text{M} - \text{H}$] $^-$; HRMS: calcd for $\text{C}_{11}\text{H}_8\text{F}_2\text{NO}_3$ [$\text{M} - \text{H}$] $^-$, 240.0467; found, 240.0476.

N,N'-Bis(4-chloro-2-fluorophenyl)-2-methylenesuccinamide (2). Yield of 11.8% as a white solid; mp (°C): 164–165; IR ν_{\max} (KBr) cm^{-1} : 3273, 3193, 3111, 3033, 3009, 1657, 1611, 1537, 1492, 1413, 1343, 1199, 1077, 948, 901, 851, 813, 758, 575, 547, 473; UV $\lambda_{\max}^{\text{MeOH}}$ nm (log ϵ): 203.5 (4.7), 246.0 (4.4), 280.0 (4.0, sh); ^1H NMR (CDCl_3 , 400 MHz): δ_{H} 8.75 (1H, s, NH), 8.29 (1H, dd, $J = 8.8, 8.4$ Hz, H6'), 8.24 (1H, dd, $J = 9.2, 8.4$ Hz, H6''), 8.18 (1H, s, NH), 7.18–7.09 (4H, m, H3', H3'', H5', and H5''), 5.99 (1H, s, H_b), 5.86 (1H, s, H_a), 3.50 (2H, s, H3); ^{13}C NMR (CDCl_3 , 100 MHz): δ_{C} 168.2 (s, C4), 166.6 (s, C1), 152.6 (d, $J = 246.0$ Hz, C2' and C2''), 138.6 (s, C2), 129.9 (s, $J = 9.9$ Hz, C4'), 129.2 (s, $J = 9.9$ Hz, C4''), 125.4 (d, $J = 10.3$ Hz, C6''), 124.9 (d, $J = 9.9$ Hz, C6'), 123.6 (t, C5), 122.7 (d, $J = 15.5$ Hz, C1'), 116.0 (d, $J = 22.6$ Hz, C3'), 115.8 (d, $J = 22.5$ Hz, C3''), 42.3 (t, C3); ESI-MS (m/z): 407.3 [$\text{M} + \text{Na}$]⁺, 409.2 [($\text{M} + 2$) + Na]⁺; HRMS: calcd for $\text{C}_{17}\text{H}_{12}\text{Cl}_2\text{F}_2\text{N}_2\text{O}_2\text{Na}$ [$\text{M} + \text{Na}$]⁺, 407.0136; found, 407.0150.

4-((4-Chloro-2-fluorophenyl)amino)-2-methylene-4-oxobutanoic Acid (2A). Yield of 4.4% as a white solid; mp (°C): 184–185; IR ν_{\max} (KBr) cm^{-1} : 3255, 3194, 3113, 3015, 2889, 1668, 1523, 1410, 1359, 1297, 1224, 1165, 1077, 973, 907, 834, 583, 496, 466; UV $\lambda_{\max}^{\text{MeOH}}$ nm (log ϵ): 204.0 (4.5), 244.0 (4.2), 280.0 (3.5); ^1H NMR (acetone- d_6 , 400 MHz): δ_{H} 9.10 (1H, s, NH), 8.24 (1H, dd, $J = 8.8, 8.4$ Hz, H6'), 7.27 (1H, dd, $J = 11.2, 2.4$ Hz, H3'), 7.19 (1H, ddd, $J = 8.8, 2.8, 1.6$ Hz, H5'), 6.32 (1H, d, $J = 0.8$ Hz, H_b), 5.86 (1H, s, H_a), 3.52 (2H, s, H3); ^{13}C NMR (acetone- d_6 , 100 MHz): δ_{C} 169.5 (s, C1), 168.3 (s, C4), 153.7 (d, $J = 253.8$ Hz, C2'), 136.3 (s, C2), 128.8 (t, C5), 127.1 (d, $J = 10.6$ Hz, C4'), 125.4 (d, $J = 3.2$ Hz, C5'), 124.3 (d, $J = 11.9$ Hz, C6'), 116.6 (d, $J = 23.1$ Hz, C1'), and C3'), 41.0 (t, C3); ESI-MS (m/z): 256.1 [$\text{M} - \text{H}$][−], 258.0 [($\text{M} + 2$) − H][−]; HRMS calcd for $\text{C}_{11}\text{H}_8\text{ClFNO}_3$ [$\text{M} - \text{H}$][−], 256.0171; found, 256.0181.

N,N'-Bis(4-bromo-2-fluorophenyl)-2-methylenesuccinamide (3). Yield of 8.6% as a white solid; mp (°C): 169–170; IR ν_{\max} (KBr) cm^{-1} : 3276, 3190, 3093, 3030, 2997, 1677, 1657, 1608, 1534, 1487, 1408, 1340, 1271, 1194, 879, 809, 519, 476; UV $\lambda_{\max}^{\text{MeOH}}$ nm (log ϵ): 203.0 (4.7), 248.0 (4.5), 279.5 (4.1, sh); ^1H NMR (CDCl_3 , 400 MHz): δ_{H} 8.77 (1H, s, NH), 8.25 (1H, dd, $J = 8.4, 8.4$ Hz, H6''), 8.20 (1H, dd, $J = 8.8, 8.4$ Hz, H6'), 8.18 (1H, s, NH), 7.32–7.23 (4H, m, H3', H3'', H5' and H5''), 5.99 (1H, s, H_b), 5.86 (1H, s, H_a), 3.49 (2H, s, H3); ^{13}C NMR (CDCl_3 , 100 MHz): δ_{C} 168.2 (s, C4), 166.6 (s, C1), 152.6 (d, $J = 246.9$ Hz, C2'), 152.4 (d, $J = 247.3$ Hz, C2''), 138.5 (s, C2), 128.1 (d, $J = 3.7$ Hz, C6'), 127.8 (d, $J = 3.6$ Hz, C6''), 125.9 (d, $J = 10.1$ Hz, C1'), 125.4 (d, $J = 10.0$ Hz, C1''), 123.7 (t, C5), 123.0 (d, C5'), 122.9 (d, C5''), 118.8 (d, $J = 22.2$ Hz, C3'), 118.6 (d, $J = 22.1$ Hz, C3''), 116.8 (d, $J = 9.5$ Hz, C4'), 116.0 (d, $J = 9.2$ Hz, C4''), 42.3 (t, C3); ESI-MS (m/z): 497.1 [$\text{M} + \text{Na}$]⁺, 499.1 [($\text{M} + 2$) + Na]⁺; HRMS calcd for $\text{C}_{17}\text{H}_{12}\text{Br}_2\text{F}_2\text{N}_2\text{O}_2\text{Na}$ [$\text{M} + \text{Na}$]⁺, 494.9126; found, 494.9141.

4-((2-Fluoro-4-(trifluoromethyl)phenyl)amino)-2-methylene-4-oxobutanoic Acid (3A). Yield of 8.2% as a white solid; mp (°C): 170–171; IR ν_{\max} (KBr) cm^{-1} : 3276, 3196, 3110, 3066, 3025, 2916, 2887, 1677, 1631, 1526, 1429, 1334, 1224, 1174, 1131, 979, 914, 570, 456, 432; UV $\lambda_{\max}^{\text{MeOH}}$ nm (log ϵ): 203.0 (4.5), 246.0 (4.3), 280.0 (3.5); ^1H NMR (acetone- d_6 , 400 MHz): δ_{H} 9.33 (1H, s, NH), 8.53 (1H, dd, $J = 8.4, 8.0$ Hz, H6'), 7.54–7.51 (4H, m, H3', and H5'), 6.34 (1H, d, $J = 0.8$ Hz, H_b), 5.88 (1H, s, H_a), 3.58 (2H, s, H3); ^{13}C NMR (acetone- d_6 , 100 MHz): δ_{C} 170.0 (s, C1), 168.2 (s, C4), 152.9 (d, $J = 244.4$ Hz, C2'), 136.1 (s, C2), 131.8 (d, $J = 10.3$ Hz, C1'), 129.1 (t, C5), 124.8 (qd, $J = 269.2, 2.7$ Hz, C7'), 126.5–125.5 (m, C4'), 122.7–122.6 (m, C5'), 123.0 (d, C6'), 113.3 (dq, $J = 22.8, 3.7$ Hz, C3'), 41.1 (t, C3); ESI-MS (m/z): 289.7 [$\text{M} - \text{H}$][−]; HRMS calcd for $\text{C}_{12}\text{H}_8\text{F}_4\text{NO}_3$ [$\text{M} - \text{H}$][−], 290.0435; found, 290.0445.

N,N'-Bis(2-fluoro-4-(trifluoromethyl)phenyl)-2-methylenesuccinamide (4). Yield of 8.8% as a white solid; mp (°C): 160–161; IR ν_{\max} (KBr) cm^{-1} : 3305, 3261, 3116, 3025, 2943, 1669, 1627, 1529, 1504, 1428, 1336, 1175, 1127, 1066, 910, 884, 831, 662, 492, 447; UV $\lambda_{\max}^{\text{MeOH}}$ nm (log ϵ): 203.5 (4.8), 248.5 (4.5); ^1H NMR (CDCl_3 , 400 MHz): δ_{H} 8.92 (1H, s, NH), 8.54 (1H, dd, $J = 8.4, 8.0$ Hz, H6'), 8.49 (1H, dd, $J = 8.4, 8.0$ Hz, H6''), 8.32 (1H, s, NH), 7.48–7.34 (4H, m, H3', H3'', H5', and H5''), 6.04 (1H, s, H_b), 5.92 (1H, s, H_a), 3.55

(2H, s, H3); ^{13}C NMR (CDCl_3 , 100 MHz): δ_{C} 168.4 (s, C4), 166.8 (s, C1), 152.0 (d, $J = 244.3$ Hz, C2'), 151.8 (d, $J = 244.6$ Hz, C2''), 138.3 (s, C2), 129.8 (d, $J = 10.3$ Hz, C1'), 129.3 (d, $J = 9.8$ Hz, C1''), 127.3–126.2 (m, C4' and C4''), 123.4 (qd, $J = 269.2, 2.7$ Hz, C7' and C7''), 124.2 (t, C5), 122.3–122.0 (m, C5' and C5''), 121.9 (d, C6'), 121.6 (d, C6''), 112.6 (dq, $J = 22.4, 3.7$ Hz, C3'), 112.4 (dq, $J = 22.3, 3.7$ Hz, C3''), 42.2 (t, C3); ESI-MS (m/z): 451.0 [$\text{M} - \text{H}$][−]; HRMS calcd for $\text{C}_{19}\text{H}_{11}\text{F}_8\text{N}_2\text{O}_2$ [$\text{M} - \text{H}$][−], 451.0687; found, 451.0693.

4-((2,5-Difluorophenyl)amino)-2-methylene-4-oxobutanoic Acid (4A). Yield of 12.4% as a white solid; mp (°C): 153–154; IR ν_{\max} (KBr) cm^{-1} : 3294, 3078, 3015, 2952, 2903, 2871, 1695, 1626, 1551, 1488, 1439, 1282, 1154, 977, 888, 808, 721, 524; UV $\lambda_{\max}^{\text{MeOH}}$ nm (log ϵ): 203.0 (4.5), 237.0 (4.2), 275.0 (3.8); ^1H NMR (acetone- d_6 , 400 MHz): δ_{H} 9.17 (1H, s, NH), 8.14 (1H, ddd, $J = 9.6, 6.4, 3.2$ Hz, H6'), 7.18 (1H, ddd, $J = 9.2, 8.8, 5.2$ Hz, H3'), 6.86–6.80 (1H, m, H4'), 6.33 (1H, d, $J = 1.2$ Hz, H_b), 5.87 (1H, d, $J = 1.2$ Hz, H_a), 3.55 (2H, s, H3); ^{13}C NMR (acetone- d_6 , 100 MHz): δ_{C} 169.8 (s, C1), 168.2 (s, C4), 159.5 (d, $J = 237.1$ Hz, C2'), 149.7 (d, $J = 239.7$ Hz, C5'), 136.1 (s, C2), 129.2 (dd, $J = 12.4, 3.6$ Hz, C1'), 129.0 (t, C5), 116.6 (dd, $J = 22.0, 9.9$ Hz, C3'), 110.6 (dd, $J = 24.6, 7.7$ Hz, C4'), 109.6 (dd, $J = 29.3, 7.8$ Hz, C6'), 41.1 (t, C3); ESI-MS (m/z): 240.2 [$\text{M} - \text{H}$][−]; HRMS calcd for $\text{C}_{11}\text{H}_8\text{F}_2\text{NO}_3$ [$\text{M} - \text{H}$][−], 240.0467; found, 240.0475.

N,N'-Bis(2-fluoro-4-methoxyphenyl)-2-methylenesuccinamide (5). Yield of 8.1% as a white solid; mp (°C): 144–145; IR ν_{\max} (KBr) cm^{-1} : 3275, 3238, 3028, 2946, 2844, 1664, 1627, 1521, 1429, 1273, 1233, 1155, 1113, 1026, 941, 837, 808, 718, 595, 508, 476; UV $\lambda_{\max}^{\text{MeOH}}$ nm (log ϵ): 202.0 (4.7), 242.0 (4.3, sh), 278.0 (4.1, sh); ^1H NMR (CDCl_3 , 400 MHz): δ_{H} 8.60 (1H, s, NH), 8.12 (1H, s, NH), 8.09 (1H, dd, $J = 9.6, 8.8$ Hz, H6''), 8.02 (1H, dd, $J = 8.8, 8.8$ Hz, H6'), 6.72–6.63 (4H, m, H3', H3'', H5', and H5''), 5.96 (1H, s, H_b), 5.80 (1H, s, H_a), 3.79 (3H, s, H7''), 3.76 (3H, s, H7'), 3.47 (2H, s, H3); ^{13}C NMR (CDCl_3 , 100 MHz): δ_{C} 168.3 (s, C4), 166.6 (s, C1), 157.4 (s, $J = 10.5$ Hz, C5'), 157.0 (s, $J = 10.1$ Hz, C5''), 154.1 (d, $J = 243.0$ Hz, C2'), 154.0 (d, $J = 243.5$ Hz, C2''), 139.0 (s, C2), 123.6 (d, $J = 10.5$ Hz, C6' and C6''), 122.9 (t, C5), 119.5 (d, $J = 11.1$ Hz, C1'), 118.9 (d, $J = 10.9$ Hz, C1''), 109.7 (d, $J = 3.0$ Hz, C5'), 109.4 (d, $J = 3.0$ Hz, C5''), 102.0 (d, $J = 22.8$ Hz, C3'), 101.9 (d, $J = 22.7$ Hz, C3''), 55.9 (q, C7' and C7''), 42.1 (t, C3); ESI-MS (m/z): 375.3 [$\text{M} - \text{H}$][−]; HRMS calcd for $\text{C}_{19}\text{H}_{17}\text{F}_2\text{N}_2\text{O}_4$ [$\text{M} - \text{H}$][−], 375.1151; found, 375.1159.

4-((2-Fluoro-5-(trifluoromethyl)phenyl)amino)-2-methylene-4-oxobutanoic Acid (5A). Yield of 9.0% as a brown solid; mp (°C): 144–145; IR ν_{\max} (KBr) cm^{-1} : 3264, 3151, 3106, 3064, 3018, 2908, 2853, 1687, 1627, 1542, 1489, 1437, 1335, 1263, 1228, 1169, 1124, 1064, 977, 918, 825, 689, 512, 487; UV $\lambda_{\max}^{\text{MeOH}}$ nm (log ϵ): 203.0 (4.4), 241.0 (4.0); ^1H NMR (acetone- d_6 , 400 MHz): δ_{H} 9.34 (1H, s, NH), 8.71 (1H, dd, $J = 7.2, 2.0$ Hz, H6'), 7.48–7.44 (1H, m, H4'), 7.40 (1H, dd, $J = 10.4, 8.8$ Hz, H3'), 6.34 (1H, d, $J = 1.2$ Hz, H_b), 5.88 (1H, d, $J = 1.2$ Hz, H_a), 3.57 (2H, s, H3); ^{13}C NMR (acetone- d_6 , 100 MHz): δ_{C} 170.1 (s, C1), 168.2 (s, C4), 155.4 (d, $J = 248.6$ Hz, C2'), 136.1 (s, C2), 129.0 (t, C5), 128.9 (d, $J = 15.5$ Hz, C1'), 127.6–126.8 (m, C5'), 125.1 (q, $J = 269.6$ Hz, C7'), 122.2 (d, C4'), 119.9 (d, C6'), 116.9 (d, $J = 21.0$ Hz, C3'), 41.0 (t, C3); ESI-MS (m/z): 289.9 [$\text{M} - \text{H}$][−]; HRMS calcd for $\text{C}_{12}\text{H}_8\text{F}_4\text{NO}_3$ [$\text{M} - \text{H}$][−], 290.0435; found, 290.0442.

N,N'-Bis(2,5-difluorophenyl)-2-methylenesuccinamide (6). Yield of 21.2% as a white solid; mp (°C): 140–141; IR ν_{\max} (KBr) cm^{-1} : 3393, 3301, 3285, 3255, 3222, 3141, 3089, 3024, 2962, 1682, 1628, 1548, 1487, 1438, 1197, 967, 866, 805, 526, 462; UV $\lambda_{\max}^{\text{MeOH}}$ nm (log ϵ): 202.5 (4.5), 239.0 (4.2), 277.5 (4.0); ^1H NMR (CDCl_3 , 400 MHz): δ_{H} 8.82 (1H, s, NH), 8.24 (1H, s, NH), 8.19 (1H, ddd, $J = 10.4, 6.4, 3.2$ Hz, H6'), 8.13 (1H, ddd, $J = 10.4, 6.4, 3.2$ Hz, H6''), 7.10–6.99 (2H, m, H3' and H3''), 6.81–6.69 (2H, m, H4' and H4''), 6.00 (1H, s, H_b), 5.88 (1H, s, H_a), 3.51 (2H, s, H3); ^{13}C NMR (CDCl_3 , 100 MHz): δ_{C} 168.2 (s, C4), 166.6 (s, C1), 158.7 (d, $J = 243.0$ Hz, C5' and C5''), 148.8 (d, $J = 235.3$ Hz, C2') 148.6 (d, $J = 235.3$ Hz, C2''), 138.5 (s, C2), 127.4 (dd, $J = 12.2, 12.0$ Hz, C1'), 126.9 (dd, $J = 12.1, 11.7$ Hz, C1''), 123.7 (t, C5), 115.7–115.2 (m, C6' and C6''), 111.0 (dd, $J = 24.4, 7.7$ Hz, C3'), 110.3 (dd, $J = 24.4,$

7.7 Hz, C3''), 109.1 (dd, $J = 30.1, 16.5$ Hz, C4' and C4''), 42.2 (t, C3); ESI-MS (m/z): 353.1 $[M + H]^+$, 375.2 $[M + Na]^+$; HRMS calcd for $C_{17}H_{13}F_4N_2O_2$ $[M + H]^+$, 353.0908; found, 353.0912.

4-((5-Chloro-2-fluorophenyl)amino)-2-methylene-4-oxobutanoic Acid (6A). Yield of 9.9% as a white solid; mp ($^{\circ}C$): 171–172; IR ν_{max} (KBr) cm^{-1} : 3266, 3123, 3092, 3048, 3018, 2919, 2886, 1700, 1667, 1609, 1536, 1488, 1414, 1238, 1196, 963, 907, 803, 704, 523, 503; UV λ_{max}^{MeOH} nm (log ϵ): 206.0 (4.6), 241.0 (4.2), 280.0 (3.6); 1H NMR (acetone- d_6 , 400 MHz): δ_H 9.17 (1H, s, NH), 8.38 (1H, ddd, $J = 6.8, 6.4, 2.4$ Hz, H6'), 7.20 (1H, dd, $J = 10.8, 8.8$ Hz, H3'), 7.12–7.08 (1H, m, H4'), 6.33 (1H, d, $J = 1.2$ Hz, H_b), 5.87 (1H, d, $J = 1.2$ Hz, H_a), 3.55 (2H, s, H3); ^{13}C NMR (acetone- d_6 , 100 MHz): δ_C 169.8 (s, C1), 168.1 (s, C4), 152.2 (d, $J = 242.2$ Hz, C2'), 136.2 (s, C2), 129.8 (d, $J = 3.3$ Hz, C5'), 129.2 (d, $J = 12.2$ Hz, C1'), 129.0 (t, C5), 124.5 (d, $J = 7.7$ Hz, C4'), 122.5 (d, C6'), 117.3 (d, $J = 21.1$ Hz, C3'), 41.0 (t, C3); ESI-MS (m/z): 256.3 $[M - H]^-$, 258.2 $[(M + 2) - H]^-$; HRMS calcd for $C_{11}H_8ClFNO_3$ $[M - H]^-$, 256.0171; found, 256.0181.

***N,N'*-Bis(5-chloro-2-fluorophenyl)-2-methylenesuccinamide (7).** Yield of 11.7% as a white solid; mp ($^{\circ}C$): 140–141; IR ν_{max} (KBr) cm^{-1} : 3333, 3265, 3247, 3114, 3091, 3019, 1678, 1631, 1611, 1538, 1519, 1489, 1416, 1393, 1324, 1257, 1222, 1186, 1148, 1111, 937, 875, 812, 708, 647, 462; UV λ_{max}^{MeOH} nm (log ϵ): 205.0 (4.7), 242.0 (4.3), 279.0 (3.9); 1H NMR ($CDCl_3$, 400 MHz): δ_H 8.73 (1H, s, NH), 8.40 (1H, dd, $J = 7.6, 5.6$ Hz, H6'), 8.35 (1H, dd, $J = 7.6, 5.6$ Hz, H6''), 8.21 (1H, s, NH), 7.07–6.99 (4H, m, H3', H3'', H4', and H4''), 5.99 (1H, s, H_b), 5.87 (1H, s, H_a), 3.50 (2H, s, H3); ^{13}C NMR ($CDCl_3$, 100 MHz): δ_C 168.2 (s, C4), 166.6 (s, C1), 151.3 (d, $J = 242.3$ Hz, C2'), 151.2 (d, $J = 242.5$ Hz, C2''), 138.5 (s, C2), 130.1 (d, $J = 3.3$ Hz, C5'), 129.8 (s, $J = 3.2$ Hz, C5''), 127.4 (d, $J = 11.6$ Hz, C4'), 127.0 (d, $J = 11.4$ Hz, C4''), 124.8 (d, $J = 7.7$ Hz, C6'), 124.2 (d, $J = 7.4$ Hz, C6''), 123.7 (t, C5), 121.8 (d, $J = 12.3$ Hz, C1', and C1''), 115.9 (d, $J = 20.8$ Hz, C3'), 115.8 (d, $J = 20.8$ Hz, C3''), 42.1 (t, C3); ESI-MS (m/z): 407.3 $[M + Na]^+$, 409.2 $[(M + 2) + Na]^+$; HRMS calcd for $C_{17}H_{12}Cl_2F_2N_2O_2Na$ $[M + Na]^+$, 407.0136; found, 407.0151.

4-((4-Fluoro-2-(trifluoromethyl)phenyl)amino)-2-methylene-4-oxobutanoic Acid (7A). Yield of 6.2% as a white solid; mp ($^{\circ}C$): 146–148; IR ν_{max} (KBr) cm^{-1} : 3274, 3150, 3087, 3015, 2979, 2925, 2885, 1700, 1665, 1533, 1433, 1323, 1279, 1246, 1171, 1131, 1048, 964, 915, 876, 836, 668, 576, 497, 422; UV λ_{max}^{MeOH} nm (log ϵ): 203.0 (4.4), 231.0 (3.9), 272.0 (3.4); 1H NMR (acetone- d_6 , 400 MHz): δ_H 8.72 (1H, s, NH), 7.91–7.86 (1H, m, H6'), 7.50–7.42 (1H, m, H3', H5'), 6.34 (1H, s, H_b), 5.89 (1H, s, H_a), 3.48 (2H, s, H3); ^{13}C NMR (acetone- d_6 , 100 MHz): δ_C 169.9 (s, C1), 168.3 (s, C4), 160.3 (d, $J = 243.7$ Hz, C4'), 136.3 (s, C2), 133.1 (brs, C1'), 131.2 (brd, C6'), 129.0 (t, C5), 128.2–120.0 (m, C2' and C7'), 120.5 (d, $J = 22.0$ Hz, C5'), 114.2 (dq, $J = 26.3, 5.5$ Hz, C3'), 40.8 (t, C3); ESI-MS (m/z): 290.2 $[M - H]^-$; HRMS calcd for $C_{12}H_8F_4NO_3$ $[M - H]^-$, 290.0435; found, 290.0439.

***N,N'*-Bis(2-fluoro-5-(trifluoromethyl)phenyl)-2-methylenesuccinamide (8).** Yield of 12.3% as a white solid; mp ($^{\circ}C$): 90–92; IR ν_{max} (KBr) cm^{-1} : 3268, 3163, 3094, 3027, 1670, 1622, 1550, 1491, 1438, 1338, 1267, 1174, 1128, 1070, 942, 898, 823, 606, 556, 524, 457; UV λ_{max}^{MeOH} nm (log ϵ): 203.0 (4.8), 243.5 (4.4); 1H NMR ($CDCl_3$, 400 MHz): δ_H 8.82 (1H, s, NH), 8.71 (1H, dd, $J = 7.2, 2.0$ Hz, H6'), 8.65 (1H, d, $J = 7.2$ Hz, H6''), 8.30 (1H, s, NH), 7.41–7.38 (1H, m, H4'), 7.34–7.31 (1H, m, H4''), 7.24 (1H, dd, $J = 9.2, 9.2$ Hz, H3'), 7.18 (1H, dd, $J = 10.0, 9.2$ Hz, H3''), 6.03 (1H, s, H_b), 5.90 (1H, s, H_a), 3.55 (2H, s, H3); ^{13}C NMR ($CDCl_3$, 100 MHz): δ_C 168.5 (s, C4), 166.8 (s, C1), 154.4 (d, $J = 247.5$ Hz, C2'), 154.2 (d, $J = 248.0$ Hz, C2''), 138.3 (s, C2), 128.0–127.1 (m, C5' and C5''), 127.1 (d, $J = 11.2$ Hz, C1'), 126.7 (d, $J = 10.8$ Hz, C1'), 123.7 (qd, $J = 269.9, 6.8$ Hz, C7' and C7''), 124.1 (t, C5), 122.4–121.7 (m, C4' and C4''), 119.7–119.3 (m, C6' and C6''), 115.6 (d, $J = 20.6$ Hz, C3'), 115.5 (d, $J = 20.6$ Hz, C3''), 42.0 (t, C3); ESI-MS (m/z): 451.1 $[M - H]^-$; HRMS calcd for $C_{19}H_{11}F_8N_2O_2$ $[M - H]^-$, 451.0687; found, 451.0693.

4-((5-Fluoro-2-(trifluoromethyl)phenyl)amino)-2-methylene-4-oxobutanoic Acid (8A). Yield of 9.2% as a white solid; mp ($^{\circ}C$):

147–148; IR ν_{max} (KBr) cm^{-1} : 3283, 3099, 3048, 3016, 2926, 2865, 1703, 1676, 1605, 1537, 1496, 1438, 1395, 1316, 1235, 1159, 1117, 1048, 968, 944, 872, 827, 657, 585, 492, 455, 414; UV λ_{max}^{MeOH} nm (log ϵ): 204.0 (4.5), 239.0 (4.1); 1H NMR (acetone- d_6 , 400 MHz): δ_H 8.74 (1H, s, NH), 7.98–7.93 (1H, m, H6'), 7.76 (1H, dd, $J = 8.8, 8.8$ Hz, H3'), 7.14–7.09 (1H, m, H4'), 6.37 (1H, d, $J = 0.8$ Hz, H_b), 5.94 (1H, s, H_a), 3.52 (2H, s, H3); ^{13}C NMR (acetone- d_6 , 100 MHz): δ_C 169.7 (s, C1), 168.2 (s, C4), 165.7 (d, $J = 247.7$ Hz, C5'), 139.3–139.1 (m, C1'), 135.9 (s, C2), 129.6–129.4 (m, C5, C6'), 124.8 (q, $J = 270.3$ Hz, C7'), 118.1–117.8 (m, C2'), 113.5–113.1 (m, C3'), 112.6–112.3 (m, C4'), 41.4 (t, C3); ESI-MS (m/z): 290.2 $[M - H]^-$; HRMS calcd for $C_{12}H_8F_4NO_3$ $[M - H]^-$, 290.0435; found, 290.0440.

***N,N'*-Bis(2-fluoro-5-methoxyphenyl)-2-methylenesuccinamide (9).** Yield of 7.2% as a white solid; mp ($^{\circ}C$): 121–122; IR ν_{max} (KBr) cm^{-1} : 3301, 3154, 3066, 3006, 2946, 2835, 1672, 1618, 1541, 1482, 1428, 1353, 1316, 1252, 1211, 1038, 957, 867, 807, 716, 547, 468; UV λ_{max}^{MeOH} nm (log ϵ): 204.0 (4.7), 239.0 (4.3), 289.0 (4.1); 1H NMR ($CDCl_3$, 400 MHz): δ_H 8.72 (1H, s, NH), 8.23 (1H, s, NH), 8.00 (1H, dd, $J = 6.4, 3.2$ Hz, H6'), 7.95 (1H, dd, $J = 6.4, 3.2$ Hz, H6''), 7.01 (1H, dd, $J = 9.2, 8.8$ Hz, H3'), 6.96 (1H, dd, $J = 9.2, 8.8$ Hz, H3''), 6.60 (1H, ddd, $J = 8.8, 7.2, 3.6$ Hz, H4'), 6.54 (1H, ddd, $J = 8.8, 7.2, 3.6$ Hz, H4''), 5.98 (1H, s, H_b), 5.84 (1H, s, H_a), 3.80 (3H, s, H7'), 3.77 (3H, s, H7''), 3.51 (2H, s, H3); ^{13}C NMR ($CDCl_3$, 100 MHz): δ_C 168.3 (s, C4), 166.5 (s, C1), 156.1 (s, C5'), 156.0 (s, C5''), 147.3 (d, $J = 234.8$ Hz, C2'), 147.2 (d, $J = 235.0$ Hz, C2''), 138.9 (s, C2), 127.0 (d, $J = 11.6$ Hz, C4'), 126.5 (d, $J = 11.5$ Hz, C4'), 123.2 (t, C5), 115.2 (d, $J = 20.7$ Hz, C3'), 115.1 (d, $J = 20.6$ Hz, C3''), 110.4 (d, $J = 7.2$ Hz, C6'), 109.8 (d, $J = 7.2$ Hz, C6''), 106.9 (d, $J = 11.2$ Hz, C1' and C1''), 55.9 (q, C7' and C7''), 42.3 (t, C3); ESI-MS (m/z): 375.1 $[M - H]^-$; HRMS calcd for $C_{19}H_{17}F_2N_2O_4$ $[M - H]^-$, 375.1151; found, 375.1158.

2-Methylene-4-oxo-4-((2-(trifluoromethyl)phenyl)amino)-butanoic Acid (9A). Yield of 11.2% as a white solid; mp ($^{\circ}C$): 153–154; IR ν_{max} (KBr) cm^{-1} : 3298, 3214, 3130, 3059, 3013, 2910, 2864, 1703, 1676, 1637, 1593, 1537, 1451, 1393, 1320, 1290, 1235, 1163, 1122, 1051, 948, 902, 764, 653, 512, 454; UV λ_{max}^{MeOH} nm (log ϵ): 203.0 (4.4), 233.0 (3.9), 269.0 (3.3); 1H NMR (acetone- d_6 , 400 MHz): δ_H 8.68 (1H, s, NH), 7.98–7.94 (1H, m, H3'), 7.69 (1H, d, $J = 7.6$ Hz, H6'), 7.64 (1H, dd, $J = 8.0, 7.6$ Hz, H5'), 7.36 (1H, dd, $J = 7.6, 7.6$ Hz, H4'), 6.35 (1H, d, $J = 1.6$ Hz, H_b), 5.91 (1H, d, $J = 1.2$ Hz, H_a), 3.50 (2H, s, H3); ^{13}C NMR (acetone- d_6 , 100 MHz): δ_C 169.6 (s, C1), 168.3 (s, C4), 136.8 (brs, C1'), 136.3 (s, C2), 133.7 (d, C5'), 129.0 (t, C5), 127.8 (brd, C3'), 126.9 (q, $J = 5.3$ Hz, C6'), 126.2 (d, C4'), 125.0 (q, $J = 270.9$ Hz, C7'), 123.1–122.5 (m, C2'), 41.0 (t, C3); ESI-MS (m/z): 271.8 $[M - H]^-$.

***N,N'*-Bis(2-bromo-4-fluorophenyl)-2-methylenesuccinamide (10).** Yield of 6.6% as a white solid; mp ($^{\circ}C$): 165–166; IR ν_{max} (KBr) cm^{-1} : 3263, 3193, 3110, 3033, 3006, 1655, 1629, 1599, 1527, 1484, 1390, 1315, 1261, 1189, 1141, 817, 657, 513, 482, 443; UV λ_{max}^{MeOH} nm (log ϵ): 205.0 (4.7), 243.0 (4.1, sh), 277.0 (3.7, sh); 1H NMR ($CDCl_3$, 400 MHz): δ_H 8.51 (1H, s, NH), 8.34 (1H, dd, $J = 9.2, 5.6$ Hz, H6'), 8.27 (1H, s, NH), 8.22 (1H, dd, $J = 9.2, 5.6$ Hz, H6''), 7.33 (1H, dd, $J = 7.6, 2.8$ Hz, H3'), 7.28 (1H, dd, $J = 8.0, 2.8$ Hz, H3''), 7.08 (1H, ddd, $J = 8.0, 8.0, 2.8$ Hz, H5'), 7.03 (1H, ddd, $J = 8.4, 8.0, 2.8$ Hz, H5''), 6.05 (1H, s, H_b), 5.90 (1H, s, H_a), 3.55 (2H, s, H3); ^{13}C NMR ($CDCl_3$, 100 MHz): δ_C 168.1 (s, C4), 166.1 (s, C1), 159.0 (d, $J = 247.6$ Hz, C4' and C4''), 139.8 (s, C2), 132.5 (s, $J = 3.2$ Hz, C1'), 131.9 (s, $J = 3.2$ Hz, C1''), 123.8 (d, $J = 7.7$ Hz, C6'), 123.3 (d, $J = 8.2$ Hz, C6'), 123.1 (t, C5), 119.7 (d, $J = 25.7$ Hz, C3'), 119.6 (d, $J = 25.3$ Hz, C3''), 115.5 (d, $J = 21.8$ Hz, C5'), 115.2 (d, $J = 21.4$ Hz, C5''), 114.4 (s, C2'), 114.3 (s, C2''), 42.0 (t, C3); ESI-MS (m/z): 472.7 $[M - H]^-$, 474.7 $[(M + 2) - H]^-$; HRMS calcd for $C_{17}H_{11}Br_2F_2N_2O_2$ $[M - H]^-$, 470.9150; found, 470.9167.

2-Methylene-4-oxo-4-((3-(trifluoromethyl)phenyl)amino)-butanoic Acid (10A). Yield of 12.2% as a white solid; mp ($^{\circ}C$): 132–133; IR ν_{max} (KBr) cm^{-1} : 3286, 3195, 3143, 3112, 3078, 3006, 2907, 1690, 1656, 1599, 1532, 1445, 1334, 1246, 1170, 1136, 1066, 978, 902, 701, 535, 493; UV λ_{max}^{MeOH} nm (log ϵ): 203.5 (4.6), 244.0 (4.3); 1H NMR (acetone- d_6 , 400 MHz): δ_H 9.54 (1H, s, NH), 8.16 (1H, s,

H2'), 7.81 (1H, d, J = 8.0 Hz, H6'), 7.52 (1H, t, J = 8.0 Hz, H5'), 7.37 (1H, d, J = 7.6 Hz, H4'), 6.32 (1H, d, J = 1.2 Hz, H_b), 5.84 (1H, d, J = 1.2 Hz, H_a), 3.46 (2H, s, H3); ¹³C NMR (acetone-*d*₆, 100 MHz): δ_c 169.6 (s, C1), 167.9 (s, C4), 141.1 (s, C1'), 136.1 (s, C2), 131.3 (q, J = 31.7 Hz, C3'), 130.6 (d, C5'), 129.3 (t, C5), 125.2 (q, J = 269.9 Hz, C7'), 123.3 (d, C6'), 120.5–120.4 (m, C4'), 116.4–116.3 (m, C2'), 40.9 (t, C3); ESI-MS (m/z): 272.1 [M – H][–]; HRMS calcd for C₁₂H₆F₃N₂O₃ [M – H][–], 272.0529; found, 272.0535.

***N,N'*-Bis(4-fluoro-2-(trifluoromethyl)phenyl)-2-methylenesuccinamide (11).** Yield of 5.6% as a white solid; mp (°C): 130–131; IR ν_{\max} (KBr) cm^{–1}: 3278, 3084, 3017, 2927, 2846, 1671, 1628, 1531, 1505, 1433, 1319, 1277, 1251, 1204, 1167, 1129, 1049, 912, 882, 831, 741, 672, 637, 525; UV $\lambda_{\max}^{\text{MeOH}}$ nm (log ϵ): 204.0 (4.2), 232.0 (4.1), 272.0 (3.7); ¹H NMR (CDCl₃, 400 MHz): δ_H 8.50 (1H, s, NH), 8.15 (1H, dd, J = 9.2, 8.8 Hz, H6'), 8.10 (1H, s, NH), 8.00 (1H, dd, J = 8.8, 8.8 Hz, H6''), 7.38–7.22 (4H, m, H3', H3'', H5', and H5''), 5.98 (1H, s, H_b), 5.89 (1H, s, H_a), 3.51 (2H, s, H3); ¹³C NMR (CDCl₃, 100 MHz): δ_c 168.6 (s, C4), 166.6 (s, C1), 159.4 (d, J = 246.3 Hz, C4'), 159.2 (d, J = 246.0 Hz, C4''), 138.5 (s, C2), 131.3 (s, C1'), 130.9 (s, C1''), 128.2 (d, J = 7.6 Hz, C6'), 127.5 (d, J = 7.8 Hz, C6''), 123.4 (t, C5), 124.6–121.7 (m, C2', C2'', C7', and C7''), 119.9 (d, J = 21.8 Hz, C5'), 119.6 (d, J = 21.7 Hz, C5''), 114.0–113.5 (m, C3' and C3''), 41.8 (t, C3); ESI-MS (m/z): 451.1 [M – H][–]; HRMS calcd for C₁₉H₁₁F₈N₂O₂ [M – H][–], 451.0687; found, 451.0692.

2-Methylene-*N,N'*-bis(2-(trifluoromethyl)phenyl)succinamide (12). Yield of 6.6% as a white solid; mp (°C): 131–132; IR ν_{\max} (KBr) cm^{–1}: 3278, 3120, 3047, 3008, 2926, 2846, 1670, 1631, 1588, 1525, 1456, 1322, 1280, 1161, 1113, 1060, 1038, 943, 761, 654, 497, 430; UV $\lambda_{\max}^{\text{MeOH}}$ nm (log ϵ): 204.0 (4.6), 233.0 (4.2), 272.0 (3.7, sh); ¹H NMR (CDCl₃, 400 MHz): δ_H 8.55 (1H, s, NH), 8.26 (1H, d, J = 8.4 Hz, H6'), 8.20 (1H, s, NH), 8.09 (1H, d, J = 8.0 Hz, H6''), 7.65–7.52 (4H, m, H3', H3'', H5', and H5''), 7.29–7.21 (2H, m, H4', and H4''), 5.98 (1H, s, H_b), 5.89 (1H, s, H_a), 3.53 (2H, s, H3); ¹³C NMR (CDCl₃, 100 MHz): δ_c 168.5 (s, C4), 166.4 (s, C1), 138.9 (s, C2), 135.3 (s, C1'), 135.0 (s, C1''), 133.2 (d, C5'), 132.8 (d, C5''), 126.4–126.1 (m, C3' and C3''), 125.5 (d, C4'), 125.1 (d, C6'), 124.9 (d, C4'), 124.6 (d, C6'), 124.3 (q, J = 271.4 Hz, C7'), 124.0 (q, J = 271.4 Hz, C7''), 123.0 (t, C5), 121.2–120.3 (q, C2', and C2''), 119.9 (d, J = 21.8 Hz, C5'), 119.6 (d, J = 21.7 Hz, C5''), 41.8 (t, C3); ESI-MS (m/z): 415.2 [M – H][–]; HRMS calcd for C₁₉H₁₃F₆N₂O₂ [M – H][–], 415.0876; found, 415.0891.

***N,N'*-Bis(2,4-dibromophenyl)-2-methylenesuccinamide (13).** Yield of 7.8% as a white solid; mp (°C): 195–196; IR ν_{\max} (KBr) cm^{–1}: 3407, 3299, 3256, 3076, 3025, 2947, 1660, 1576, 1524, 1464, 1375, 1312, 1282, 1194, 861, 819, 543, 483, 445; UV $\lambda_{\max}^{\text{MeOH}}$ nm (log ϵ): 206.5 (4.8), 251.0 (4.3); ¹H NMR (CDCl₃, 400 MHz): δ_H 8.56 (1H, s, NH), 8.34 (1H, s, NH), 8.31 (1H, d, J = 8.8 Hz, H6'), 8.21 (1H, d, J = 8.8 Hz, H6''), 7.71 (1H, d, J = 2.0 Hz, H3'), 7.67 (1H, d, J = 2.0 Hz, H3''), 7.46 (1H, dd, J = 8.8, 2.0 Hz, H5'), 7.40 (1H, dd, J = 8.8, 2.0 Hz, H5''), 6.05 (1H, s, H_b), 5.91 (1H, s, H_a), 3.54 (2H, s, H3); ¹³C NMR (CDCl₃, 100 MHz): δ_c 168.1 (s, C4), 165.9 (s, C1), 138.9 (s, C2), 135.3 (s, C1'), 134.7 (d, C3', and C3''), 134.6 (s, C1''), 131.7 (d, C5'), 131.4 (d, C5''), 123.3 (t, C5), 122.9 (d, C6' and C6''), 117.5 (s, C2'), 117.5 (s, C2''), 114.4 (s, C4'), 114.3 (s, C4'') 42.1 (t, C3); ITMS + c ESI-MS (m/z): 618.9 [M + Na]⁺, 620.8 [(M + 2) + Na]⁺; HRMS calcd for C₁₇H₁₂Br₄N₂O₂Na [M + Na]⁺, 618.7484; found, 618.7498.

***N,N'*-Bis(2,4-difluorobenzyl)-2-methylenesuccinamide (14).** Yield of 11.4% as a white solid; mp (°C): 143–144; IR ν_{\max} (KBr) cm^{–1}: 3303, 3174, 3063, 2946, 2858, 1654, 1615, 1540, 1510, 1429, 1273, 1245, 1141, 1096, 1017, 962, 850, 731, 511, 469; UV $\lambda_{\max}^{\text{MeOH}}$ nm (log ϵ): 203.0 (4.4), 259.0 (3.3, sh), 268.0 (3.2, sh); ¹H NMR (CDCl₃, 400 MHz): δ_H 7.33–7.22 (2H, m, H6' and H6''), 7.00 (2H, s, NH), 6.84–6.75 (4H, m, H3', H3'', H5' and H5''), 5.78 (1H, s, H_b), 5.55 (1H, s, H_a), 4.47 (2H, d, J = 6.0 Hz, H7'), 4.38 (2H, d, J = 6.0 Hz, H7''), 3.23 (2H, s, H3); ¹³C NMR (CDCl₃, 100 MHz): δ_c 170.4 (s, C4), 168.5 (s, C1), 162.6 (dd, J = 245.9, 12.6 Hz, C2', and C2''), 161.1 (dd, J = 247.2, 12.3 Hz, C4', and C4''), 138.7 (s, C2), 131.2 (dd, J = 9.4, 9.7 Hz, C6'), 130.9 (dd, J = 9.7, 9.7 Hz, C6''), 122.5 (t, C5), 121.3 (dd, J = 14.7, 3.6 Hz, C1'), 121.0 (dd, J = 15.0, 3.6 Hz,

C1''), 111.6 (dd, J = 12.1, 3.7 Hz, C5'), 111.4 (dd, J = 12.1, 3.7 Hz, C5''), 104.2 (dd, J = 25.2, 25.2 Hz, C3'), 103.9 (dd, J = 25.2, 25.3 Hz, C3''), 41.2 (t, C3), 37.5 (t, J = 3.5 Hz, C7'), 37.2 (t, J = 3.8 Hz, C7''); ESI-MS (m/z): 381.2 [M + H]⁺, 403.2 [M + Na]⁺; HRMS calcd for C₁₉H₁₆F₄N₂O₂Na [M + Na]⁺, 403.1040; found, 403.1046.

***N,N'*-Bis(2,5-difluorobenzyl)-2-methylenesuccinamide (15).** Yield of 14.2% as a white solid; mp (°C): 153–154; IR ν_{\max} (KBr) cm^{–1}: 3336, 3060, 2925, 1658, 1618, 1538, 1494, 1433, 1263, 1186, 1022, 947, 881, 807, 714, 543, 493, 441; UV $\lambda_{\max}^{\text{MeOH}}$ nm (log ϵ): 203.0 (4.4), 267.0 (3.7, sh), 273.0 (3.6, sh); ¹H NMR (CDCl₃, 400 MHz): δ_H 7.06–6.88 (7H, m, NH, H3', H3'', H4', H4'', H6' and H6''), 6.85 (1H, s, NH), 5.81 (1H, s, H_b), 5.62 (1H, s, H_b), 4.52 (2H, d, J = 6.0 Hz, H7'), 4.43 (2H, d, J = 6.0 Hz, H7''), 3.28 (2H, s, H3); ¹³C NMR (CDCl₃, 100 MHz): δ_c 170.4 (s, C4), 168.6 (s, C1), 158.8 (d, J = 239.3 Hz, C5', C5'', C2', and C2''), 138.6 (s, C2), 127.2–126.9 (m, C1' and C1''), 122.6 (t, C5), 116.8–115.3 (m, C3', C3'', C4', C4'', C6' and C6''), 41.3 (t, C3), 37.8 (t, C7'), 37.5 (t, C7''); ESI-MS (m/z): 381.5 [M + H]⁺, 403.3 [M + Na]⁺; HRMS calcd for C₁₉H₁₆F₄N₂O₂Na [M + Na]⁺, 403.1040; found, 403.1053.

Biology: Cells, Viruses, and Chemicals. The information regarding all clinical enterovirus strains and influenza viruses listed in Table 1 is the same as that reported previously.³² MDCK cells used for IAV infection was cultured in E10 [Dulbecco's modified Eagle medium (DMEM) containing 10% fetal bovine serum (FBS), 100 U/mL penicillin (Gibco, USA), 100 μ g/mL streptomycin (Gibco, USA), 2 mM L-glutamine (L-glutamine) (Gibco, Brazil), and 0.1 mM nonessential amino acid mixture (Gibco, USA)]. The E0 medium is the same as E10, except for FBS. RD cells were used to infect enterovirus and rhinovirus and cultured in DMEM containing 10% FBS with 100 U/mL penicillin (Gibco, USA) and 100 μ g/mL streptomycin (Gibco, USA). All cells were maintained in a 37 °C incubator with 5% carbon dioxide.

Half-Maximal Effectiveness Assay (EC₅₀ Assay). The 96-well tissue culture plates were seeded with MDCK cells (2 × 10⁴ per well) or RD cells (2 × 10⁴ cells/well) in E10 medium and incubated under 5% CO₂ for 16–24 h at 37 °C. Then, the culture medium was withdrawn, and the wells were washed once with Dulbecco's PBS (DPBS). Then, the cells were infected with the influenza virus (A/WSN/33) or enteroviruses at a 9-fold median tissue culture infective dose, with or without the addition of distinct concentrations of the synthesized compounds. The treated cells were further incubated for 72 h at 37 °C in an incubator containing 5% CO₂. After 72 h, the medium was removed, and the cells were fixed with 4% paraformaldehyde for 1 h at room temperature. Then, 0.1% crystal violet was used to stain the cells for 20 min at room temperature. The cell density was measured by using a VICTOR3 multilabel plate reader (PerkinElmer). The EC₅₀ value was calculated by using the Reed–Muench method based on the concentration of the compound that could inhibit virus-CPE by 50%.³³

Cytotoxicity Test (CC₅₀ Assay). MDCK cells or RD cells were cultured in a 96-well plate (2 × 10⁴ cells per well) in E10 medium and incubated at 37 °C under 5% CO₂ overnight. Then, the wells were washed once with DPBS. Next, various concentrations of the synthetic compounds were added and further incubated under 5% CO₂ at 37 °C for 72 h. The cell wells were washed again with DPBS, and 50 μ L of MTT was loaded into each well and incubated for 3 h at 37 °C with 5% CO₂. The medium was removed, 200 μ L of dimethyl sulfoxide was added to each well to dissolve the formazan crystals, and the cell density of each well was measured at 570 nm on a VICTOR3 multilabel plate reader. Then, the median CC₅₀ was calculated by the Reed–Muench method based on the concentration of the compound responsible for 50% cell death.³³

CPE Detection. MDCK cells (2 × 10⁵ cell/well) were uniformly seeded into a six-well culture dish, placed in a 37 °C incubator with 5% CO₂ for 16–24 h, infected with 0.5 MOI of influenza strain A/WSN/33 for 1 h, and then rinsed twice with DPBS. E0 medium containing 10 μ M compound 1 was added and incubated at 37 °C for different time points. CPE production was observed by using a microscope (Zeiss Axiovert 200M; 20× objective lens) at 12 and 36 h pi.³⁴

HAI. In this experiment, guinea pig RBCs were used as material for detecting the activity of influenza virus HA. First, we determined the hemagglutination unit of blood agglutination by diluting the virus stock solution (50 $\mu\text{L}/\text{well}$) in a 2-fold sequence, and then we added 0.5% RBCs (50 $\mu\text{L}/\text{well}$) to the round-bottom 96-well plates. After 1 h, the amount of virus capable of agglutinating the RBCs at the maximum dilution was defined as 1HAU, and the amount of 4HAU virus was taken for HAI assay. In the HAI assay, the drug was diluted in a 2-fold sequence (25 $\mu\text{L}/\text{well}$), 4HAU virus was added (25 $\mu\text{L}/\text{well}$), and the wells were kept at room temperature for 30 min. Then, 0.5% RBCs were added (50 $\mu\text{L}/\text{well}$) to the well, and the phenomenon of RBC agglutination was observed after 1 h.³⁴

TOA Assay. MDCK cells (5×10^5 cells/well) were uniformly seeded into a six-well culture dish and placed in a 37 °C incubator with 5% CO₂. After the cells grew into a single layer, the culture solution was removed. The cells were washed once with DPBS, compound 1 (10 μM) was added at different time points at pi = -3 to 9, -1 to 9, 0 to 9, 3 to 9, and 6 to 9 h, and the virus adsorption was between -1 and 0 h pi with MOI = 0.1. One hour after influenza A/WSN/33 virus infection, the virus solution was aspirated and washed once with PBS, and the supernatant was collected after 9 h pi to test for plaque changes.³⁴

RNA Purification and RT-qPCR. MDCK cells (5×10^5 cell/well) were seeded into a six-well plate and placed in a 37 °C incubator with 5% CO₂ for 16–24 h. After the cells grew into a single layer every other day, the culture was removed. The solution was washed once with Hank's balanced salt solution and infected with the virus A/WSN/33 of MOI = 0.01 for 1 h in E0. Then, using the reagent TRIzol (Invitrogen, Carlsbad, CA), total RNA was extracted at different harvesting time points (0, 3, 6, and 9 h pi). The extracted RNA was subjected to reverse transcription reaction using Moloney murine leukemia virus reverse transcriptase to generate cDNA, followed by qPCR analysis using SYBR Green PCR Master (Protech Technology Enterprise) and StepOnePlus RT-qPCR (Applied Biosystem, Foster city, CA) instruments and their software for RNA content analysis comparisons. Primers used: (detecting whole RNA) M1-forward primer: 5'-GAC CAA TCC TGT CAC CTC-3'; M1-reverse primer: 5'-GAT CTC CGT TCC CAT TAA GAG-3'.³⁵

Western Immunoblotting Assay. MDCK cells (5×10^5 cells/well) were cultured into a six-well tissue culture plate for 16–24 h under 5% CO₂ and 37 °C incubation. The cells were washed with DPBS once and then infected with the A/WSN/33 virus (MOI = 0.1). After infection, the cells were washed with DPBS twice. Then, drug treatment (with or without 1) was performed in E0 medium, and the cells were harvested at the indicated times. The cells were washed again with DPBS buffer and an appropriate amount of lysis buffer [150 mM NaCl, 1% Triton X-100 (Plusone), 0.5% sodium deoxycholate (Sigma-Aldrich, New Zealand), 2 mM ethylene diamine tetraacetic acid (Amresco Inc), 50 mM Tris-HCl (pH 7.5), and 50 \times protease inhibitors (Roche, Germany)]. Then, the cells were scraped and collected into Eppendorf tubes and kept for 30 min on ice. The supernatant was collected by centrifugation at 14 000g at 4 °C for 10 min, and the protein concentration was quantified by using a Bio-Rad protein assay kit (Bio-Rad USA). An equal concentration of protein was mixed with 3 \times sodium dodecyl sulfate (SDS) sample buffer and heated with boiling water for 10 min, and the protein was separated by SDS polyacrylamide gel electrophoresis (SDS-PAGE). The protein on SDS-PAGE was transferred onto polyvinylidene difluoride membranes for western immunoblotting analysis. The antibodies used in the western blotting method were GAPDH (sc-25778; Santa Cruz Biotechnology, Inc, Santa Cruz, CA), M1 (Cat# 1321; ViroStat, Portland, ME), NP (Abcam, 20343), NS1 (Genetex, GTX125990), NS2 (Genetex, GTX125952), and PA (Genetex, GTX125932).³⁵

Indirect IF Assay. MDCK cells (2×10^5 cells/well) were cultivated on coverslips in a 12-well plate and placed in a 37 °C incubator with 5% CO₂ for 16 h. After the cells grew into a single layer, the culture solution was removed, washed once with DPBS, and infected with the influenza virus (MOI = 0.1) for 1 h. The virus solution was removed and washed with DPBS. Then, 1 (10 μM) or 4 (1 μM) or LMB (10 nM) was added in E0, and after pi = 9 h, the

supernatant was removed, washed with DPBS again, and 4% paraformaldehyde added for 1 h to fix the cells. The following primary antibodies were used for IF microscopy: M1 (1:50) (GTX-125928), NP (1:50) (Abcam-128193), NS2 (1:50) (GTX-125952), PA (1:50) (GTX-125932), and secondary antibodies (Alexa Fluor-488). The nuclei were stained with 4,6-diamidino-2-phenylindole. The staining was observed by using a LSM 510 microscope with a 63X oil-immersion objective lens. LMB (Sigma, MFCD-06795848) was used as the control group.³⁵

Molecular Docking Study. To investigate the interaction of itaconic acid derivatives into the LMB binding site of CRM1, we performed a docking study by using the LibDock program of Discovery Studio Visualizer 2016 (Biovia, Corp. CA, USA). The 3D chemical structures were drawn by using Chem3D Professional 15.0 software (PerkinElmer Informatics, Inc. CA, USA). Ligand energy minimization was performed by using a root-mean-square gradient tolerance of 0.01. The crystal structure of CRM1 inhibitor LMB in complex with CRM1-Ran-RanBP1 (PDB ID: 4HAT) was downloaded from the RCSB protein data bank and imported into the Discovery Studio Visualizer 2016 and then to the working environment of LibDock. The protein was processed by removing crystal water and other hetero atoms and adding hydrogen. The prepared protein was then used to define the binding site from the active site of LMB for the docking of all prepared ligands (1, 4, 6, and 8), including LMB, by using LibDock. On the basis of the highest LibDock score of the docking pose of LMB, all compounds and their interactions with CRM1 were analyzed.

■ ASSOCIATED CONTENT

§ Supporting Information

The Supporting Information is available free of charge on the ACS Publications website at DOI: 10.1021/acs.jmedchem.8b01683.

HPLC purity analysis data; ¹H and ¹³C NMR spectra of all target compounds; 2D interaction diagram of compounds 1 and 6 in the LMB binding site of CRM1; IF staining to assess the effect of compound 1 on NS2, PA, and M1 protein data; and mechanism of action of compound 4 determined by TOA assay, HAI assay, and IF staining of M1 (PDF)

Molecular formula strings with activity data (CSV)

Docking pose of compound 1 (PDB)

Docking pose of compound 4 (PDB)

Docking pose of compound 6 (PDB)

Docking pose of compound 8 (PDB)

Docking pose of compound LMB (PDB)

■ AUTHOR INFORMATION

Corresponding Authors

*E-mail: jimtong@mail.cgu.edu.tw. Phone: +886-3-2118800 ext.5156 (J.-T.H.).

*E-mail: pewehs@mail.cgu.edu.tw. Phone: +886-3-2118800, ext. 3105 (P.-W.H.).

ORCID

Pei-Wen Hsieh: 0000-0002-8882-4711

Author Contributions

B.S. performed the research, designed, synthesized, and analyzed the data, and wrote the manuscript. P.-Y.H., Y.-L.C., and C.-Y.L. performed the mechanistic experiments and analyzed the data. S.-N.T. measured the antiviral activity tests. C.-F.H. and T.-J.L. designed and analyzed the data. J.-T.H. and P.-W.H. designed the research, analyzed the data, and wrote the manuscript.

Notes

The authors declare no competing financial interest.

■ ACKNOWLEDGMENTS

We are very grateful for the support of this work by the grant from the Chang Gung Memorial Hospital and the Chang Gung University (CMRPD1F0561-2 and BMRPB23 to P.-W.H. and CMRPD1E0041-3, CMRPD1G0301-3, and BMRP416 to J.-T.H.) and from The Ministry of Science and Technology of Taiwan (106-2320-B-182-004-MY3 and 106-2632-B-182-001) and the Research Center for Emerging Viral Infections from The Featured Areas Research Center Program within the framework of the Higher Education Sprout Project by the Ministry of Education in Taiwan (MOST 107-3017-F-182-001) to J.-T.H. The founders had no role in the study design, data collection and analysis, decision to publish, or preparation of the manuscript.

■ ABBREVIATIONS

CPE, cytopathic effect; CRM1, chromosomal region maintenance 1; HA, hemagglutinin protein; IAV, influenza A virus; IF, immunofluorescence; LMB, leptomycin B; MDCK, Madin–Darby canine kidney cells; MOI, multiplicity of infection; NEI, nuclear export inhibitor; NP, nucleoprotein; NS1, non-structural protein 1; NS2, non-structural protein 2; PA, polymerase acidic protein; RBC, red blood cell; pi, post infection; RD, rhabdomyosarcoma cells; SAR, structure–activity relationship; SI, selective index; TOA, time-of-addition; vRNP, viral ribonucleoprotein complex

■ REFERENCES

- (1) Khanna, M.; Kumar, P.; Choudhary, K.; Kumar, B.; Vijayan, V. K. Emerging influenza virus: a global threat. *J. Biosci.* **2008**, *33*, 475–482.
- (2) Patel, K. K.; Patel, A. K.; Shah, S.; Ranjan, R.; Shah, S. V. Adult patient with novel H1N1 infection presented with encephalitis, rhabdomyolysis, pneumonia and polyneuropathy. *J. Global Infect. Dis.* **2012**, *4*, 178–181.
- (3) Kilbourne, E. D. Influenza pandemics of the 20th century. *Emerging Infect. Dis.* **2006**, *12*, 9–14.
- (4) Al Hajjar, S.; McIntosh, K. The first influenza pandemic of the 21st century. *Ann. Saudi Med.* **2010**, *30*, 1–10.
- (5) Iuliano, A. D.; Roguski, K. M.; Chang, H. H.; Muscatello, D. J.; Palekar, R.; Tempia, S.; Cohen, C.; Gran, J. M.; Schanzer, D.; Cowling, B. J.; Wu, P.; Kyncl, J.; Ang, L. W.; Park, M.; Redlberger-Fritz, M.; Yu, H.; Espenhain, L.; Krishnan, A.; Emukule, G.; van Asten, L.; da Silva, S. P.; Aungkulanon, S.; Buchholz, U.; Widdowson, M. A.; Bresee, J. S. Estimates of global seasonal influenza-associated respiratory mortality: a modelling study. *Lancet* **2018**, *391*, 1285–1300.
- (6) Leiva, R.; Barniol-Xicota, M.; Codony, S.; Ginex, T.; Vanderlinden, E.; Montes, M.; Caffrey, M.; Luque, F. J.; Naesens, L.; Vázquez, S. Aniline-based inhibitors of influenza H1N1 virus acting on hemagglutinin-mediated fusion. *J. Med. Chem.* **2018**, *61*, 98–118.
- (7) Wu, X.; Wu, X.; Sun, Q.; Zhang, C.; Yang, S.; Li, L.; Jia, Z. Progress of small molecular inhibitors in the development of anti-influenza virus agents. *Theranostics* **2017**, *7*, 826–845.
- (8) Massari, S.; Goracci, L.; Desantis, J.; Tabarrini, O. Polymerase acidic protein-basic protein 1 (PA-PB1) protein-protein interaction as a target for next-generation anti-influenza therapeutics. *J. Med. Chem.* **2016**, *59*, 7699–7718.
- (9) Hayden, F. Developing new antiviral agents for influenza treatment: what does the future hold? *Clin. Infect. Dis.* **2009**, *48*, S3–S13.
- (10) Shen, Z.; Lou, K.; Wang, W. New small-molecule drug design strategies for fighting resistant influenza A. *Acta Pharm. Sin. B* **2015**, *5*, 419–430.
- (11) Dilly, S.; Fotso, A. F.; Lejal, N.; Zedda, G.; Chebbo, M.; Rahman, F.; Companys, S.; Bertrand, H. C.; Vidic, J.; Noiray, M.; Alessi, M.; Tarus, B.; Quideau, S.; Riteau, B.; Slama-Schwok, A. From naproxen repurposing to naproxen analogues and their antiviral activity against influenza A virus. *J. Med. Chem.* **2018**, *61*, 7202–7217.
- (12) World Health Organization. *WHO Guidelines on the Use of Vaccines and Antivirals during Influenza Pandemics*; Geneva, 2004.
- (13) Allen, U. D.; Aoki, F. Y.; Stiver, H. G. The use of antiviral drugs for influenza: recommended guidelines for practitioners. *Can. J. Infect. Dis. Med. Microbiol.* **2006**, *17*, 273–284.
- (14) Govorkova, E. A.; Webster, R. G. Combination chemotherapy for influenza. *Viruses* **2010**, *2*, 1510–1529.
- (15) Hussain, M.; Galvin, H.; Haw, T. Y.; Nutsford, A.; Husain, M. Drug resistance in influenza A virus: the epidemiology and management. *Infect. Drug Resist.* **2017**, *10*, 121–134.
- (16) Shao, W.; Li, X.; Goraya, M.; Wang, S.; Chen, J.-L. Evolution of influenza A virus by mutation and re-assortment. *Int. J. Mol. Sci.* **2017**, *18*, 1650–1663.
- (17) Fiore, A. E.; Fry, A.; Shay, D.; Gubareva, L.; Bresee, J. S.; Uyeki, T. M.; Centers for Disease Control and Prevention (CDC). Antiviral agents for the treatment and chemoprophylaxis of influenza—recommendations of the Advisory Committee on Immunization Practices (ACIP). *MMWR Recomm. Rep.* **2011**, *60*, 1–24.
- (18) Hoang Vu, M.-P.; Nguyen Co, T.; Nguyen Le, K. H.; Nguyen Thi, K. P.; Le Quynh, M. Oseltamivir resistance among influenza viruses: surveillance in northern Viet Nam, 2009–2012. *Western Pac. Surveill. Response J.* **2013**, *4*, 25–29.
- (19) Pervitasari, O.; Johnson, S.; Yan, X.; Howerth, E.; Shacham, S.; Landesman, Y.; Baloglu, E.; McCauley, D.; Tamir, S.; Tompkins, S. M.; Tripp, R. A. Verdinexor, a novel selective inhibitor of nuclear export, reduces influenza A virus replication in vitro and in vivo. *J. Virol.* **2014**, *88*, 10228–10243.
- (20) Pickens, J.; Tripp, R. Verdinexor targeting of CRM1 is a promising therapeutic approach against RSV and influenza viruses. *Viruses* **2018**, *10*, 48.
- (21) Mathew, C.; Ghildyal, R. CRM1 inhibitors for antiviral therapy. *Front. Microbiol.* **2017**, *8*, 1171–1191.
- (22) Xu, D.; Grishin, N. V.; Chook, Y. M. NESdb: a database of NES-containing CRM1 cargoes. *Mol. Biol. Cell* **2012**, *23*, 3673–3676.
- (23) Nguyen, K. T.; Holloway, M. P.; Altura, R. A. The CRM1 nuclear export protein in normal development and disease. *Int. J. Biochem. Mol. Biol.* **2012**, *3*, 137–151.
- (24) Pemberton, L. F.; Blobel, G.; Rosenblum, J. S. Transport routes through the nuclear pore complex. *Curr. Opin. Cell Biol.* **1998**, *10*, 392–399.
- (25) Le Sage, V.; Moulard, A. Viral subversion of the nuclear pore complex. *Viruses* **2013**, *5*, 2019–2042.
- (26) Kudo, N.; Matsumori, N.; Taoka, H.; Fujiwara, D.; Schreiner, E. P.; Wolff, B.; Yoshida, M.; Horinouchi, S. Leptomycin B inactivates CRM1/exportin 1 by covalent modification at a cysteine residue in the central conserved region. *Proc. Natl. Acad. Sci. U.S.A.* **1999**, *96*, 9112–9117.
- (27) Sun, Q.; Carrasco, Y. P.; Hu, Y.; Guo, X.; Mirzaei, H.; MacMillan, J.; Chook, Y. M. Nuclear export inhibition through covalent conjugation and hydrolysis of Leptomycin B by CRM1. *Proc. Natl. Acad. Sci. U.S.A.* **2013**, *110*, 1303–1308.
- (28) Gillis, E. P.; Eastman, K. J.; Hill, M. D.; Donnelly, D. J.; Meanwell, N. A. Applications of fluorine in medicinal chemistry. *J. Med. Chem.* **2015**, *58*, 8315–8359.
- (29) Mishra, S.; Suryaprakash, N. Intramolecular hydrogen bonding involving organic fluorine: NMR investigations corroborated by DFT-based theoretical calculations. *Molecules* **2017**, *22*, 423–467.
- (30) Zhao, X.; Li, R.; Zhou, Y.; Xiao, M.; Ma, C.; Yang, Z.; Zeng, S.; Du, Q.; Yang, C.; Jiang, H.; Hu, Y.; Wang, K.; Mok, C. K. P.; Sun, P.; Dong, J.; Cui, W.; Wang, J.; Tu, Y.; Yang, Z.; Hu, W. Discovery of Highly Potent Pinanamine-Based Inhibitors against Amantadine- and

Oseltamivir-Resistant Influenza A Viruses. *J. Med. Chem.* **2018**, *61*, 5187–5198.

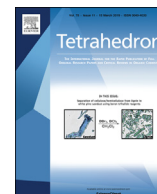
(31) Watanabe, K.; Takizawa, N.; Katoh, M.; Hoshida, K.; Kobayashi, N.; Nagata, K. Inhibition of nuclear export of ribonucleoprotein complexes of influenza virus by leptomycin B. *Virus Res.* **2001**, *77*, 31–42.

(32) Hsu, J. T.-A.; Yeh, J.-Y.; Lin, T.-J.; Li, M.-L.; Wu, M.-S.; Hsieh, C.-F.; Chou, Y. C.; Tang, W.-F.; Lau, K. S.; Hung, H.-C.; Fang, M.-Y.; Ko, S.; Hsieh, H.-P.; Horng, J.-T. Identification of BPR3P0128 as an inhibitor of cap-snatching activities of influenza virus. *Antimicrob. Agents Chemother.* **2012**, *56*, 647–657.

(33) Hsieh, C.-F.; Chen, Y.-L.; Lin, C.-F.; Ho, J.-Y.; Huang, C.-H.; Chiu, C.-H.; Hsieh, P.-W.; Horng, J.-T. An extract from *Taxodium distichum* targets hemagglutinin-and neuraminidase-related activities of influenza virus in vitro. *Sci. Rep.* **2016**, *6*, 36015–36028.

(34) Hsieh, C.-F.; Lo, C.-w.; Liu, C.-H.; Lin, S.; Yen, H.-R.; Lin, T.-Y.; Horng, J.-T. Mechanism by which ma-xing-shi-gan-tang inhibits the entry of influenza virus. *J. Ethnopharmacol.* **2012**, *143*, 57–67.

(35) Hsieh, C.-F.; Yen, H.-R.; Liu, C.-H.; Lin, S.; Horng, J. T. Ching-fang-pai-tu-san inhibits the release of influenza virus. *J. Ethnopharmacol.* **2012**, *144*, 533–544.



New hydroperoxybriarane diterpenoids from the octocoral *Briareum violaceum*

Jia-Wen Yao ^{a, b, 1}, Wei-Chiung Chi ^{c, 1}, Jing-Hao Xu ^{a, b}, Gene-Hsiang Lee ^d, Michael Y. Chiang ^{e, f}, Bo-Rong Peng ^{b, g, h}, Nai-Cheng Lin ^b, Chiung-Chin Hu ^b, Lee-Shing Fang ^{i, j}, Guo-Qiang Li ^{k, l}, Yu-Chia Chang ^m, Tsong-Long Hwang ^{m, n, o, p, **}, Ping-Jyun Sung ^{a, b, q, r, s, t, *}

^a Graduate Institute of Marine Biology, National Dong Hwa University, Pingtung 94450, Taiwan

^b National Museum of Marine Biology and Aquarium, Pingtung 94450, Taiwan

^c Department of Food Science, National Quemoy University, Kinmen 89250, Taiwan

^d Instrumentation Center, National Taiwan University, Taipei 10617, Taiwan

^e Department of Chemistry, National Sun Yat-sen University, Kaohsiung 80424, Taiwan

^f Department of Medicinal and Applied Chemistry, Kaohsiung Medical University, Kaohsiung 80708, Taiwan

^g Doctoral Degree Program in Marine Biotechnology, National Sun Yat-sen University, Kaohsiung 80424, Taiwan

^h Doctoral Degree Program in Marine Biotechnology, Academia Sinica, Taipei 11529, Taiwan

ⁱ Center for Environmental Toxin and Emerging-Contaminant Research, Cheng Shiu University, Kaohsiung 83347, Taiwan

^j Super Micro Mass Research and Technology Center, Cheng Shiu University, Kaohsiung 83347, Taiwan

^k Key Laboratory of Marine Drugs, Chinese Ministry of Education, School of Medicine and Pharmacy, Ocean University of China, Qingdao 266003, China

^l Laboratory of Marine Drugs and Biological Products, National Laboratory for Marine Science and Technology, Qingdao 266235, China

^m Research Center for Chinese Herbal Medicine, Research Center for Food and Cosmetic Safety, Graduate Institute of Healthy Industry Technology, College of Human Ecology, Chang Gung University of Science and Technology, Taoyuan 33303, Taiwan

ⁿ Graduate Institute of Natural Products, College of Medicine, Chang Gung University, Taoyuan 33302, Taiwan

^o Chinese Herbal Medicine Research Team, Healthy Aging Research Center, Chang Gung University, Taoyuan 33302, Taiwan

^p Department of Anaesthesiology, Chang Gung Memorial Hospital, Taoyuan 33305, Taiwan

^q Department of Marine Biotechnology and Resources, National Sun Yat-sen University, Kaohsiung 80424, Taiwan

^r Chinese Medicine Research and Development Center, China Medical University Hospital, Taichung 40447, Taiwan

^s Graduate Institute of Natural Products, Kaohsiung Medical University, Kaohsiung 80708, Taiwan

^t Research Center for Natural Products and Drug Development, Kaohsiung Medical University, Kaohsiung 80708, Taiwan

ARTICLE INFO

Article history:

Received 23 December 2018

Received in revised form

23 January 2019

Accepted 30 January 2019

Available online 2 February 2019

Keywords:

Briareum violaceum

Briaviolide

Brianthein W

Superoxide anion

ABSTRACT

A known briarane, brianthein W (**1**), along with four new hydroperoxybriaranes, briaviolides R–U (**2–5**), have been obtained from the octocoral *Briareum violaceum*. The absolute configuration of **1** was determined by X-ray analysis for the first time and the structures of briaranes **2–5** were established by spectroscopic methods. Bioactivity study showed that briarane **3** decreased the production of superoxide anions from human neutrophils.

© 2019 Elsevier Ltd. All rights reserved.

* Corresponding author. National Museum of Marine Biology and Aquarium, Pingtung 94450, Taiwan.

** Corresponding author. Research Center for Chinese Herbal Medicine, Research Center for Food and Cosmetic Safety, Graduate Institute of Healthy Industry Technology, College of Human Ecology, Chang Gung University of Science and Technology, Taoyuan 33303, Taiwan.

E-mail addresses: htl@mail.cgu.edu.tw (T.-L. Hwang), pjsung@nmmba.gov.tw (P.-J. Sung).

¹ These authors contributed equally to this work.

1. Introduction

The octocoral *Briareum violaceum* (Quoy & Gaimard, 1883) (family Briareidae) [1] is a rich source of diterpenoids of briarane carbon skeleton that often have complex structures and bioactivities [2–9]. Recently, in our ongoing study on the chemical constituents of *B. violaceum* has resulted in the isolation of a known briarane, brianthein W (**1**) [10], as well as four new

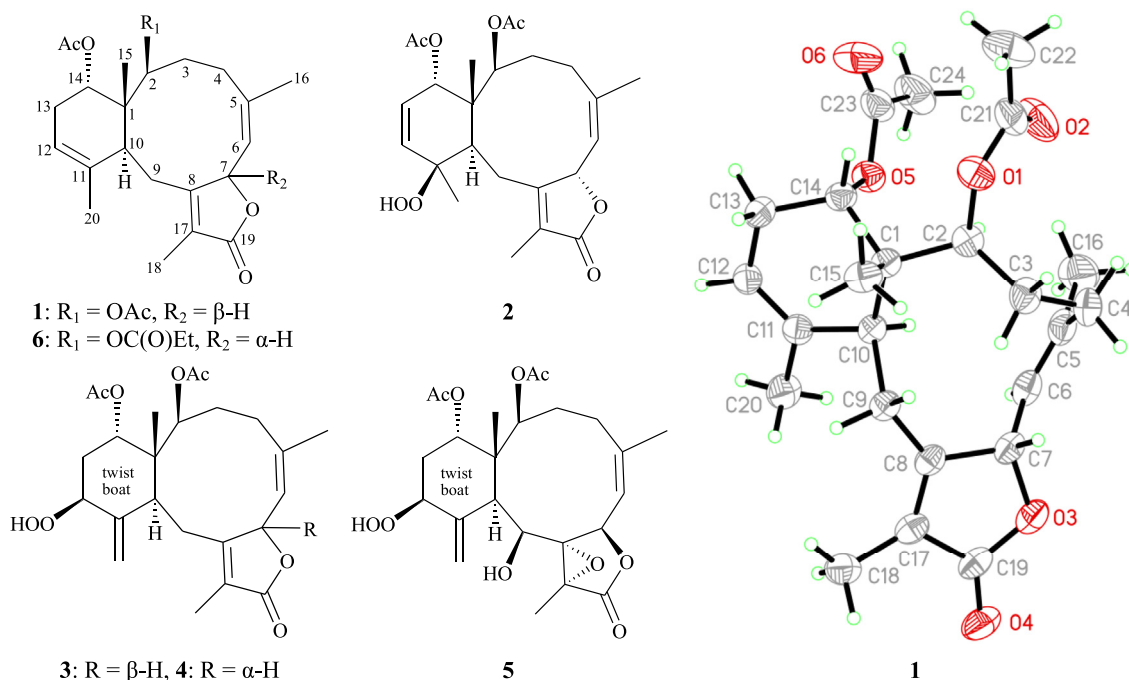


Fig. 1. Structures of briarthein W (1), briaviolides R–U (2–5), 7-*epi*-funicolide A (6), and the computer-generated ORTEP plot of 1.

hydroperoxybriaranes, briaviolides R–U (2–5) (Fig. 1). The isolated compounds were evaluated for anti-inflammatory activity using the inhibition of superoxide anions in an *in vitro* pro-inflammatory model.

2. Results and discussion

Briarthein W (1), was first isolated from a Caribbean octocoral *Briareum polyanthes*, and its structure, including relative configuration, was determined by X-ray analysis [10]. However, the absolute configuration for this metabolite was established in this study by a single-crystal X-ray diffraction analysis (Flack parameter $x = 0.06(5)$) and the orpex diagram (Fig. 1) showed that the configurations of C-1, C-2, C-7, C-10, and C-14 are 1*S*, 2*S*, 7*S*, 10*S*, and 14*S* [11–13].

Briaviolide R (2) was obtained as an amorphous powder. The HRESIMS of 2 showed a pseudomolecular peak at m/z 471.19892, which established the molecular formula $\text{C}_{24}\text{H}_{32}\text{O}_8$ (calcd for $\text{C}_{24}\text{H}_{32}\text{O}_8 + \text{Na}$, 471.19894), indicating nine degrees of unsaturation. Analysis of the ^1H , ^{13}C NMR, and DEPT spectra together with the molecular formula, suggested that there must be an exchangeable proton. The ^{13}C NMR spectrum (Table 1), in combination with DEPT and HSQC spectra, revealed the presence of two acetoxy groups (δ_{C} 21.4, 21.1, $2 \times \text{CH}_3$; δ_{C} 169.6, 169.6, $2 \times \text{C}$), a γ -lactone moiety (δ_{C} 175.1, C-19), a tetrasubstituted olefin (δ_{C} 160.6, C-8; 125.1, C-17), a trisubstituted olefin (δ_{C} 141.0, C-5; 123.4, CH-6), and a disubstituted carbon-carbon double bond (δ_{C} 136.0, CH-12; 126.1, CH-13). Based on the ^{13}C NMR data and numbers of unsaturation, 2 established as a tricyclic briarane-type diterpenoid. Moreover, a methyl singlet (δ_{H} 0.99, 3H, s, H₃-15), a singlet of the tertiary methyl bonded to an oxygenated carbon (δ_{H} 1.09, 3H, s, H₃-20), two vinyl methyls (δ_{H} 1.96, 3H, s, H₃-18; 1.85, 3H, s, H₃-16), three pairs of methylene protons (δ_{H} 2.34, 2H, m, H₂-3; 2.03, 1H, m, H-4 α ; 2.76, 1H, m, H-4 β ; 2.85, 1H, d, $J = 14.0$ Hz, H-9 α ; 3.18, 1H, d, $J = 14.0$, 11.6 Hz, H-9 β), an aliphatic methine proton (δ_{H} 3.06, 1H, d, $J = 11.6$ Hz, H-10), three oxymethine protons (δ_{H} 5.60, 1H, d, $J = 7.2$ Hz, H-7; 5.11, 1H, dd, $J = 4.8$, 3.2 Hz, H-2; 4.88, 1H, d, $J = 6.0$ Hz, H-14), three olefinic

protons (δ_{H} 6.07, 1H, dd, $J = 9.6$, 6.0 Hz, H-13; 5.92, 1H, d, $J = 9.6$ Hz, H-12; 5.19, 1H, d, $J = 7.2$ Hz, H-6), two acetyl methyls (δ_{H} 2.13 and 2.06, both 3H s), and a hydroperoxy proton (δ_{H} 7.68, 1H, br s, OOH-11) [5,14–16] were observed in the ^1H NMR spectrum of 2 (Table 1). Due to electronegativity effects, the chemical shift of a hydroperoxy-bearing oxygenated carbon is more shielded than that of a hydroxy-bearing oxygenated carbon in briarane-type natural products [5,17]; therefore, the ^{13}C and ^1H NMR signals at δ_{C} 81.0 (C-11) and δ_{H} 7.68 (1H, br s, OOH-11) indicated the presence of a hydroperoxy group at an oxygenated quaternary carbon in 2.

The ^1H NMR coupling information in the COSY spectrum analysis of 2 (Table 1) enabled the determination of the proton sequences between H-2/H₂-3/H₂-4, H-6/H-7, and H-9 β /H-10. These data, together with the HMBC from H-9 α to C-1, C-8, C-10; H-9 β to C-8 and H-10 to C-8, established the connectivity from C-1 to C-10 in a ten-membered ring connecting C-1 to C-10 (Table 1). HMBC from H₃-16 to C-4, C-5, and C-6 confirmed the presence of the methyl substituent on C-5. The COSY correlations from H-12/H-13/H-14 and the HMBC from H-13 to C-1, H-14 and H₃-20 to C-10 suggested that the methylcyclohexene ring was fused to the ten-membered ring at C-1 and C-10. That the methyl group (C-15) was on C-1 was substantiated by the HMBC from H₃-15 to C-1, C-2, C-10, C-14. Furthermore, the HMBC from the oxymethine proton at δ_{H} 4.88 (H-14) to the ester carbonyl at δ_{C} 169.6 placed the acetoxy group on C-14. Thus, the remaining acetoxy group was on C-2, as indicated by characteristic ^1H NMR signal analysis (δ_{H} 5.11, 1H, dd, $J = 4.8$, 3.2 Hz, H-2), even though no HMBC was observed between H-2 and acetate carbonyl; and the hydroperoxy group was positioned at C-11, an oxygenated quaternary carbon (δ_{C} 81.0). The aforementioned data, together with the HMBC from H₃-18 to C-8, C-17, C-19, allowed to establish the planar structure of 2.

Based on previous studies, all naturally occurring briarane-type diterpenes have the C-15 methyl group *trans* to H-10, and are assigned as β - and α -oriented, respectively, as shown in most briarane derivatives [18]. The stereochemistry of 2 was established by NOESY spectral analysis. The NOESY spectrum of 2 (Fig. 2) exhibited correlations from H-10 to H₃-20, and not to H₃-15,

Table 1
¹H and ¹³C NMR data, COSY correlation, and HMBC for **2**.

C/H	δ_H^a (J in Hz)	δ_C^b	COSY	HMBC
1		42.9 (C) ^c		
2	5.11 dd (4.8, 3.2)	80.0 (CH)	H ₂ -3	—
3	2.34 m	27.5 (CH ₂)	H-2, H ₂ -4	—
4 α/β	2.03 m; 2.76 m	26.0 (CH ₂)	H ₂ -3	—
5		141.0 (C)		
6	5.19 d (7.2)	123.4 (CH)	H-7	—
7	5.60 d (7.2)	81.3 (CH)	H-6	—
8		160.6 (C)		
9 α/β	2.85 d (14.0); 3.18 dd (14.0, 11.6)	24.3 (CH ₂)	H-10	C-1, C-8, C-10, C-17
10	3.06 d (11.6)	41.4 (CH)	H-9 β	C-8
11		81.0 (C)		
12	5.92 d (9.6)	136.0 (CH)	H-13	C-14
13	6.07 dd (9.6, 6.0)	126.1 (CH)	H-12, H-14	C-1, C-11, C-14
14	4.88 d (6.0)	75.0 (CH)	H-13	C-10, C-12, C-13, acetate carbonyl
15	0.99 s	17.6 (CH ₃)		C-1, C-2, C-10, C-14
16	1.85 s	22.8 (CH ₃)		C-4, C-5, C-6
17		125.1 (C)		
18	1.96 s	9.2 (CH ₃)		C-8, C-17, C-19
19		175.1 (C)		
20	1.09 s	27.0 (CH ₃)		C-10, C-11, C-12
OAc-2		169.6 (C)		
	2.13 s	21.1 (CH ₃)		Acetate carbonyl
OAc-14		169.6 (C)		
	2.06 s	21.4 (CH ₃)		Acetate carbonyl
OOH-11	7.68 br s			

^a Spectrum recorded at 400 MHz in CDCl₃.

^b Spectrum recorded at 100 MHz in CDCl₃.

^c Multiplicity deduced from DEPT and HSQC spectra and indicated by usual symbols.

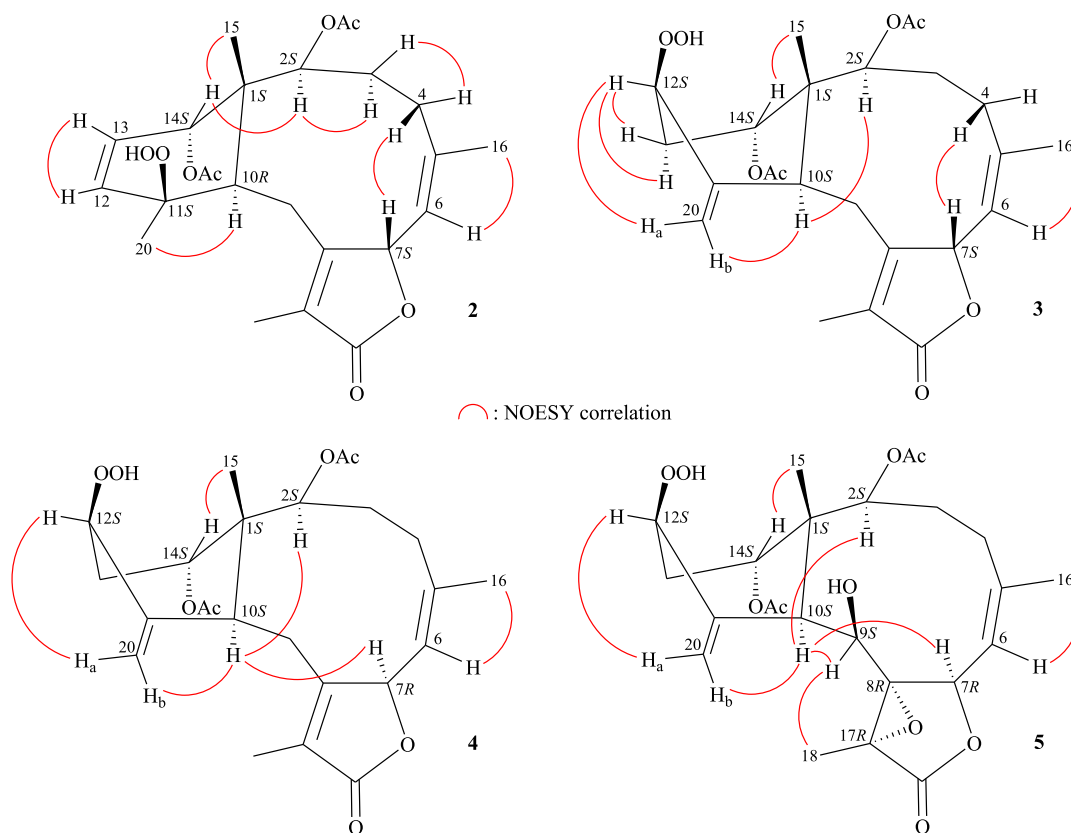


Fig. 2. Selected NOESY correlations of **2**–**5**.

indicating that H-10 and Me-20 are on the same face and were assigned to the α -position. Since H-14 exhibited a correlation to H₃-

15, and not with H-10, it was β -oriented. Moreover, H-2 also showed a correlation to H-14, and not with H₃-15. From modeling study, H-2 was close to H-14 when it was α -oriented. As one of the

C-4 methylene protons (δ_{H} 2.76) exhibited a correlation to H-7, and not to H-2-3 suggesting the β -orientations of this proton and H-7 by modeling study, and the other was assigned as H-4 α (δ_{H} 2.03). H-2-3 displayed correlations with H-4 α and H-2, and not with H-7, which further confirmed that H-7 was in the β -orientation. Moreover, the NOESY spectrum showed correlations from H-6 to H-16 and H-12 to H-13, revealing the *Z* geometry of C-5/6 and C-12/13 double bonds. As briaranes **2**–**5** were isolated along with briarthein W (**1**) from the same organism, it is reasonable on biogenetic grounds to assume that briaranes **2**–**5** have the same absolute configurations as **1**. Therefore, based on above findings, the configurations of the stereogenic centers of **2** were elucidated as 1*S*,2*S*,7*S*,10*R*,11*S*,14*S*. It is noted that the C-12/13 double bond in briarane diterpenoids are rarely found [17,19–22].

Briaviolide S (**3**) had the molecular formula of $\text{C}_{24}\text{H}_{32}\text{O}_8$ as determined by HRESIMS at m/z 471.19878 (calcd for $\text{C}_{24}\text{H}_{32}\text{O}_8+\text{Na}$, 471.19894). The ^1H and ^{13}C NMR spectra of **3** resembled those of **2**. The presence of a hydroperoxy group in **3** was also supported by a broad singlet at δ_{H} 7.99 observed in the ^1H NMR spectrum [5,14–16]. Additionally, the ^1H NMR spectrum (Table 2), also showed the presence of two methyl singlets at δ_{H} 1.99 and 1.89, respectively, probably belonging to the acetoxy groups while the ^{13}C NMR spectrum (Table 2) exhibited the signals of three carbonyls at δ_{C} 174.4, 170.6, and 170.3, suggesting the presence of a γ -lactone and two acetoxy groups. Comparison of the ^1H and ^{13}C NMR data of **3** and **2** (Tables 2 and 1), revealed that the C-12/C-13 double bond in **2** was shifted to C-11 and the methyl group on C-11, forming the methyldiene group in **3**. This exocyclic double bond at C-11 in **3** was confirmed by the HMBC from H-20 to C-10 and C-12, and H-10 to C-20. The oxymethine carbon at δ_{C} 83.1 showed a correlation to the methine proton at δ_{H} 4.50 (H-12) in the HSQC spectrum; this proton also showed 3J -correlations with H-13 (δ_{H} 2.24, 1*H*, *m* and 2.02, 1*H*, *m*) in the COSY spectrum, proving the attachment of a hydroperoxy group at C-12.

The stereochemistry of **3** was elucidated from the correlations observed in a NOESY experiment (Fig. 2). In the NOESY spectrum of

3, H-10 was correlated with H-2, while no correlation was seen with Me-15, which suggested that H-10 and H-2 were on the same face and assigned as α . As H-14 exhibited a correlation with H-15, it was assigned to be β . H-12 correlates with one of C-20 methylene protons (δ_{H} 5.02, H-20*a*) and H-13 α/β protons; but not with H-10 and H-15 while H-10 correlated to H-20*b* (δ_{H} 4.80), indicating that the C-12 hydroperoxy group was β -oriented and supported that the methyldienecyclohexane ring in **3** existed in a twist boat conformation. The *Z*-configuration of C-5/6 double bond was established by a correlation from H-6 (δ_{H} 5.19) and H-16 (δ_{H} 2.00). As one of the C-4 methylene protons (δ_{H} 2.58) exhibited a correlation to H-7, H-7 was β -oriented as was proposed in the modeling study. On the basis of above results, **3** was found to possess the configurations 1*S*,2*S*,7*S*,10*S*,12*S*,14*S*.

Briarane **4** (briaviolide T) was found to have a molecular formula of $\text{C}_{24}\text{H}_{32}\text{O}_8$ based on its HRESIMS peak at m/z 471.19881 (calcd. for $\text{C}_{24}\text{H}_{32}\text{O}_8+\text{Na}$, 471.19894). It was found that the spectroscopic data of **3** and **4** were similar; however, comparison of the ^1H and ^{13}C NMR chemical shifts of the oxymethine (δ_{H} 5.73, 1*H*, *d*, $J = 7.2$ Hz; δ_{C} 79.3, CH-7), sp^2 methine (δ_{H} 4.94, 1*H*, *dd*, $J = 7.2, 1.2$ Hz; δ_{C} 121.1, CH-6), and sp^2 quaternary (δ_{C} 160.7, C-8) carbons of **4** (Table 3) with those of **3** (δ_{H} 5.44, 1*H*, *d*, $J = 8.0$ Hz; δ_{C} 80.8, CH-7; δ_{H} 5.19, 1*H*, *d*, $J = 8.0$ Hz; δ_{C} 124.9, CH-6; δ_{C} 158.6, C-8) (Table 2) showed that the H-7 in **4** was α -oriented. The NOESY spectrum exhibited a strong correlation from H-7 to H-10, supporting that H-7 was α -oriented (Fig. 2). By comparing the chemical shift of H-7 (δ_{H} 5.73, 1*H*, *d*, $J = 7.2$ Hz) with that of a known metabolite, 7-*epi*-funicolide A (**6**) (δ_{H} 5.78, 1*H*, *br d*, $J = 7.0$ Hz) (Fig. 1) [23], H-7 in **4** was α -oriented and the stereogenic centers of **4** were assigned as 1*S*,2*S*,7*R*,10*S*,12*S*,14*S* by the correlations observed in a NOESY experiment (Fig. 2). To the best of our knowledge, only two briarane analogues, pachyclavariolide A [8] and 7-*epi*-funicolide A [23] were found to possess α -oriented C-7 proton.

The new diterpenoid, briaviolide U (**5**) had a molecular formula $\text{C}_{24}\text{H}_{32}\text{O}_{10}$ as determined by HRESIMS at m/z 503.18882 (calcd. for $\text{C}_{24}\text{H}_{32}\text{O}_{10}+\text{Na}$, 503.18877). The general feature of the ^1H and ^{13}C

Table 2
 ^1H and ^{13}C NMR data, COSY correlations, and HMBC for **3**.

C/H	$\delta_{\text{H}}^{\text{a}}$ (J in Hz)	$\delta_{\text{C}}^{\text{b}}$	COSY	HMBC
1		42.1 (C) ^c		
2	4.71 dd (4.8, 4.8)	74.9 (CH)	H-2-3	C-1, C-4, C-15, acetate carbonyl
3 α/β	1.88 m; 2.06 m	31.8 (CH ₂)	H-2, H-2-4	—
4 α/β	2.28 dd (14.4, 2.0); 2.58 ddd (14.4, 5.6, 5.6)	29.1 (CH ₂)	H-2-3	—
5		141.5 (C)		
6	5.19 d (8.0)	124.9 (CH)	H-7	C-4
7	5.44 d (8.0)	80.8 (CH)	H-6	—
8		158.6 (C)		
9 α/β	2.63 d (13.2); 3.03 dd (13.2, 12.0)	30.9 (CH ₂)	H-10	C-1, C-8, C-10, C-11, C-17
10	3.03 d (12.0)	37.9 (CH)	H-9 β	C-9, C-20
11		144.2 (C)		
12	4.50 dd (9.2, 2.0)	83.1 (CH)	H-13	—
13/13'	2.24 m; 2.02 m	30.6 (CH ₂)	H-12, H-14	C-1, C-14
14	4.87 br s	72.2 (CH)	H-2-13	—
15	1.18 s	14.1 (CH ₃)		C-1, C-2, C-10, C-14
16	2.00 s	25.9 (CH ₃)		C-4, C-5, C-6
17		126.1 (C)		
18	1.83 s	8.8 (CH ₃)		C-8, C-17, C-19
19		174.4 (C)		
20a/b	5.02 s; 4.80 s	117.0 (CH ₂)		C-10, C-12
OAc-2		170.3 (C)		
	1.89 s	21.0 (CH ₃)		Acetate carbonyl
OAc-14		170.6 (C)		
	1.99 s	21.0 (CH ₃)		Acetate carbonyl
OOH-12	7.99 br s			—

^a Spectrum recorded at 400 MHz in CDCl_3 .

^b Spectrum recorded at 100 MHz in CDCl_3 .

^c Multiplicity deduced from DEPT and HSQC spectra and indicated by usual symbols.

Table 3
¹H and ¹³C NMR data, COSY correlations, and HMBC for **4**.

C/H	$\delta_{\text{H}}^{\text{a}}$ (J in Hz)	$\delta_{\text{C}}^{\text{b}}$	COSY	HMBC
1		43.4 (C)		
2	4.83 d (7.2)	77.0 (CH)	H ₂ -3	C-3, C-15
3	2.43 m	30.6 (CH ₂)	H-2, H ₂ -4	—
4/4'	1.86 m; 1.92 m	30.5 (CH ₂)	H ₂ -3	—
5		142.1 (C)		
6	4.94 dd (7.2, 1.2)	121.1 (CH)	H-7, H ₃ -16	—
7	5.73 d (7.2)	79.3 (CH)	H-6	C-6
8		160.7 (C)		
9 α /10	2.50 br d (11.4); 2.76 dd (11.4, 10.8)	27.9 (CH ₂)	H-10	C-10
10	2.75 d (10.8)	40.4 (CH)	H-9 β	C-1, C-8
11		157.8 (C)		
12	4.51 dd (9.0, 3.0)	83.0 (CH)	H ₂ -13	—
13/13'	2.24 ddd (17.4, 9.0, 2.4); 2.11 ddd (17.4, 4.8, 3.0)	31.1 (CH ₂)	H-12, H-14	—
14	4.93 dd (4.8, 2.4)	71.9 (CH)	H ₂ -13	—
15	1.20 s	13.0 (CH ₃)		C-1, C-2, C-10, C-14
16	1.74 d (1.2)	22.6 (CH ₃)	H-6	C-4, C-5, C-6
17		125.4 (C)		
18	1.81 s	8.8 (CH ₃)		C-8, C-17, C-19
19		175.1 (C)		
20a/b	5.09 s; 4.74 s	117.3 (CH ₂)		C-10, C-11, C-12
OAc-2		170.3 (C)		
	2.01 s	21.0 (CH ₃)		Acetate carbonyl
OAc-14		170.3 (C)		
	1.98 s	21.0 (CH ₃)		Acetate carbonyl
OOH-12	7.92 s			—

^a Spectrum recorded at 600 MHz in CDCl₃.

^b Spectrum recorded at 150 MHz in CDCl₃. Due to the absence signals, the ¹³C chemical shifts were assigned by the assistances of HSQC and HMBC spectra.

NMR spectra of **5** resembled that of **4**. However, the ¹³C NMR data revealed that the signals corresponding to the C-8/17 tetrasubstituted carbon-carbon double bond (δ_{C} 160.7, C-8; 125.4, C-17) and C-9 methylene (δ_{C} 27.9) in **4** were replaced by an epoxy group (δ_{C} 71.3, C-8; 59.7, C-17) and an oxymethine carbon group (δ_{C} 71.5) in **5**. The position of the acetoxy group at C-2 was confirmed by the HMBC from the oxymethine proton at δ_{H} 4.77 (H-2) to the ester carbonyl at δ_{C} 170.5. Thus, another acetoxy and the hydroperoxy groups were at C-14 and C-12 as indicated by the COSY correlations. In the NOESY spectrum (Fig. 2), correlations were observed from H-10/H-9 and H-10/H-7, indicating that these three protons should be on the α face. H₃-18 was found to show a correlation with H-9 and from molecular modeling study, was found to be reasonably closed to H-9; therefore, H₃-18 should be placed on the β face in the γ -lactone ring. In addition, the correlations from H-10/H-20b and H-12/H-20a, indicated that the methylidene-cyclohexane ring of **5** also possesses a twist-boat conformation, similar to those of **3** and **4**, and the stereogenic centers of **5** were assigned as 1S,2S,7R,8R,9S,10S,12S,14S,17R.

In vitro anti-inflammatory activity assay was performed using human neutrophils, and the results demonstrated that briarane **3** had an inhibitory effect on the generation of superoxide anion, with an IC₅₀ value of 5.37 μ M (Table 5).

B. violaceum was reported to demonstrate a wide structural diversity of interesting diterpenoids with extensive pharmacological properties [24]. Our continuous search for more potent briaranes resulted in an acquisition of briarthein W (**1**), along with four new hydroperoxybriaranes **2–5**. In this study, the absolute configuration of **1** was determined by a single-crystal X-ray diffraction analysis to prove that most briarane-type natural products have the C-15 methyl group *trans* to H-10, and these two groups are β - and α -oriented. Besides, hydroperoxy groups in briaranes **2–5**; C-12/13 double bond in briarane **2**; and twist-boat methylidenecyclohexane rings in briaranes **3–5**, once again to prove the novelty on the chemistry for briarane-type natural products. The anti-inflammatory capabilities of briaranes **1–3** and **5** were further examined by targeting to superoxide anion. Among the tested

compounds, briaviolide S (**3**) exhibited the most potent effect in inhibiting the superoxide anion production.

3. Experimental

3.1. General experimental procedures

NMR spectra were recorded on a Jeol Resonance ECZ400S or a Jeol Resonance ECZ600R NMR spectrometers using the residual CHCl₃ signal (δ_{H} 7.26 ppm) as an international standard for ¹H NMR and CDCl₃ (δ_{C} 77.1 ppm) for ¹³C NMR, respectively. Coupling constants (*J*) are presented in Hz. ESIMS and HRESIMS were recorded using a Bruker Tesla Solarix FTMS system. Column chromatography, IR spectra and optical rotation values (with 2.0 or 0.3 mL cells) were performed as described in our previous study [2–4].

3.2. Animal material

Specimens of *B. violaceum* were collected from the waters off Taiwan, and relocated to a 270-ton cultivation tank located in the National Museum of Marine Biology and Aquarium (NMMBA), Taiwan, in 2011; the material used for this study was collected from the tank in December 2016. This organism was identified by comparison with previous descriptions [1]. A voucher specimen was deposited in the NMMBA, Taiwan (NMMBA-CSC-002).

3.3. Extraction and isolation

Sliced bodies of *B. violaceum* (wet and dry weights, 251 and 95.0 g, respectively) were extracted with a mixture of MeOH and CH₂Cl₂ (1:1; v/v). The resulting 9.79 g extract was partitioned between EtOAc and H₂O. The EtOAc layer (3.30 g) was applied on a silica gel column and eluted with a mixture of *n*-hexane/EtOAc (stepwise from 100:1–100% EtOAc; volume ratio) to yield 15 fractions A–O. Fraction J was applied on a silica gel column chromatography and then eluted with a mixture of *n*-hexane/EtOAc (stepwise 8:1 to 1:1; volume ratio) to afford 12 subfractions J1–J12.

Subfraction J7 was separated by reverse-phase open column chromatography and then eluted with MeOH/H₂O (65:35; volume ratio) to afford **1** and 18 subfractions J7A–J7R. Subfraction J7J was purified by RP-HPLC using a mixture of acetonitrile/H₂O (v:v = 1:1 of volume ratio at a flow rate of 5.0 mL/min) to yield **3**, **4**, and **2**, respectively. Fraction J8 was purified by RP-HPLC using a mixture of MeOH/H₂O (v:v = 7:3 of volume ratio at a flow rate of 5.0 mL/min) to yield **5**.

3.3.1. Brianthein W (**1**)

Colorless prisms (41.1 mg); $[\alpha]_D^{20} +47$ (c 1.59, CHCl₃) (ref. [9] $[\alpha]_D^{24} +62$ (c 0.45, CHCl₃)); IR (neat) ν_{\max} 1727 cm⁻¹; ¹H (400 MHz, CDCl₃) and ¹³C (100 MHz, CDCl₃) NMR data were found to be in complete agreement with previous reports [9,10]; ESIMS: *m/z* 439 (M + Na)⁺.

3.3.2. Briaviolide R (**2**)

Amorphous powder (1.0 mg); $[\alpha]_D^{20} +162$ (c 0.05, CHCl₃); IR (neat) ν_{\max} 1732 cm⁻¹; ¹H (CDCl₃, 400 MHz) and ¹³C (CDCl₃, 100 MHz) NMR data (see Table 1); ESIMS: *m/z* 471 (M + Na)⁺; HRESIMS: *m/z* 471.19892 (calcd for C₂₄H₃₂O₈+Na, 471.19894).

3.3.3. Briaviolide S (**3**)

Amorphous powder (1.5 mg); $[\alpha]_D^{20} -9$ (c 0.08, CHCl₃); IR (neat) ν_{\max} 1732 cm⁻¹; ¹H (CDCl₃, 400 MHz) and ¹³C (CDCl₃, 100 MHz) NMR data (see Table 2); ESIMS: *m/z* 471 (M + Na)⁺; HRESIMS: *m/z* 471.19878 (calcd for C₂₄H₃₂O₈+Na, 471.19894).

3.3.4. Briaviolide T (**4**)

Amorphous powder (0.2 mg); $[\alpha]_D^{20} +4$ (c 0.07, CHCl₃); IR (neat) ν_{\max} 1740 cm⁻¹; ¹H (CDCl₃, 600 MHz) and ¹³C (CDCl₃, 150 MHz) NMR data (see Table 3); ESIMS: *m/z* 471 (M + Na)⁺; HRESIMS: *m/z* 471.19881 (calcd for C₂₄H₃₂O₈+Na, 471.19894).

Table 4
¹H and ¹³C NMR data, COSY correlations, and HMBC for **5**.

C/H	δ_H^a (J in Hz)	δ_C^b	COSY	HMBC
1		45.6 (C) ^c		
2	4.77 dd (4.4, 4.0)	74.8 (CH)	H ₂ -3	C-1, C-3, C-5, C-10, C-15, acetate carbonyl
3 α /β	1.80 dq (16.0, 4.8); 2.59 m	30.8 (CH ₂)	H-2, H ₂ -4	C-2, C-4, C-5
4 α /β	2.16 m; 2.69 ddd (14.4, 4.8, 4.4)	29.4 (CH ₂)	H ₂ -3	C-2, C-3, C-5, C-6, C-16
5		144.7 (C)		
6	5.53 d (9.2)	120.9 (CH)	H-7	C-4
7	5.56 d (9.2)	73.8 (CH)	H-6	C-6
8		71.3 (C)		
9	4.36 dd (6.8, 5.6)	71.5 (CH)	H-10, OH-9	C-7, C-8, C-10, C-11, C-17
10	3.50 d (6.8)	42.1 (CH)	H-9	C-1, C-2, C-8, C-9, C-11, C-12, C-15, C-20
11		142.6 (C)		
12	4.48 dd (9.2, 4.0)	83.5 (CH)	H ₂ -13	C-10, C-14, C-20
13/13'	2.24 (16.4, 9.2, 2.8); 1.93 ddd (16.4, 4.0, 3.6)	30.3 (CH ₂)	H-12, H-14	C-1, C-14
14	4.70 dd (3.6, 2.8)	73.4 (CH)	H ₂ -13	—
15	1.39 s	16.2 (CH ₃)		C-1, C-2, C-10, C-14
16	2.04 s	26.3 (CH ₃)		C-4, C-5, C-6
17		59.7 (C)		
18	1.54 s	9.2 (CH ₃)		C-8, C-17, C-19
19		172.3 (C)		
20a/b	5.20 s; 5.23 s	119.8 (CH ₂)		C-10, C-11, C-12
OAc-2	1.98 s	170.5 (C)		Acetate carbonyl
OAc-14		21.0 (CH ₃)		
	1.89 s	170.3 (C)		Acetate carbonyl
OH-9	2.96 d (5.6)	21.0 (CH ₃)		—
OOH-12	8.38 br s		H-9	—

^a Spectrum recorded at 400 MHz in CDCl₃.

^b Spectrum recorded at 100 MHz in CDCl₃.

^c Multiplicity deduced from DEPT and HSQC spectra and indicated by usual symbols.

3.3.5. Briaviolide U (**5**)

Amorphous powder (3.7 mg); $[\alpha]_D^{20} -35$ (c 0.18, CHCl₃); IR (neat) ν_{\max} 3400, 1765, 1727 cm⁻¹; ¹H (CDCl₃, 400 MHz) and ¹³C (CDCl₃, 100 MHz) NMR data (see Table 4); ESIMS: *m/z* 503 (M + Na)⁺; HRESIMS: *m/z* 503.18882 (calcd for C₂₄H₃₂O₁₀+Na, 503.18877).

3.4. Single-crystal X-ray crystallography of brianthein W (**1**)

Suitable colorless prisms of **1** were obtained from a solution of MeOH. The crystal (0.343 × 0.168 × 0.137 mm³) belongs to the monoclinic system, space group *P*2₁2₁2₁ (#19), with *a* = 8.71640(10) Å, *b* = 9.40210(10) Å, *c* = 28.0565(4) Å, *V* = 2299.30(5) Å³, *Z* = 4, *D*_{calcd} = 1.203 Mg/m³, λ (Cu K α) = 1.54178 Å. Intensity data were measured on a Bruker D8 Venture diffractometer up to θ_{\max} of 75.0°. All 12911 reflections were collected. The structure was solved by direct methods and refined by a full-matrix least-squares procedure. The refined structural model converged to a final *R*1 = 0.0345; *wR*2 = 0.0923

Table 5

Inhibitory effects of briaranes **1–3** and **5** on superoxide anion generation by human neutrophils in response to fMet-Leu-Phe/Cytochalasin B.

Compound	Superoxide anion	
	IC ₅₀ (μM) ^a	Inh %
1		18.94 ± 7.77
2		16.32 ± 6.67 *
3	5.37 ± 1.10	76.93 ± 7.44 ***
5		47.07 ± 2.06 ***
LY294002 ^b	1.59 ± 0.11	98.27 ± 1.34 ***

Percentage of inhibition (Inh %) at 10 μM concentration. Results are presented as mean ± SEM (*n* = 3–4). **P* < 0.05, ***P* < 0.01, ****P* < 0.001 compared with the control (DMSO).

^a Concentration necessary for 50% inhibition (IC₅₀).

^b LY294002 (2-morpholin-4-yl-8-phenylchromen-4-one) was used as the reference compound.

for 4699 observed reflections [$I > 2\sigma(I)$] and 277 variable parameters. The absolute configuration was determined by Flack parameter $x = 0.06(5)$ [11–13].

3.5. Superoxide anion generation by human neutrophils

Human neutrophils were obtained by means of dextran sedimentation and Ficoll centrifugation. Measurement of superoxide anion generation was carried out according to previously described procedures [25,26]. Briefly, superoxide anion production was assayed by monitoring the superoxide dismutase-inhibitors were performed using MeO-Suc-Ala-Ala-Pro-Valp-nitroanilide as the elastase substrate.

Acknowledgments

This research was supported by grants from the National Museum of Marine Biology and Aquarium; the National Dong Hwa University; and the Ministry of Science and Technology, Taiwan (Grant Nos: MOST 104-2320-B-291-001-MY3 and 107-2320-B-291-001-MY3) awarded to P.-J.S.

Appendix A. Supplementary data

Supplementary data to this article can be found online at <https://doi.org/10.1016/j.tet.2019.01.069>.

References

- [1] K. Samimi-Namin, L.P. van Ofwegen, *ZooKeys* 557 (2016) 1.
- [2] T.C. Tsai, J.H. Xu, M.J. Li, J.J. Chen, J.H. Su, Y.C. Wu, Z.H. Wen, P.J. Sung, *Nat. Prod. Commun.* 13 (2018) 1235.
- [3] J.H. Xu, Y.C. Chang, G.Q. Li, Z.H. Wen, Y.C. Wu, P.J. Sung, *Phytochem. Lett.* 27 (2018) 129.
- [4] J.H. Xu, K.H. Lai, Y.D. Su, Y.C. Chang, B.R. Peng, A. Backlund, Z.H. Wen, P.J. Sung, *Mar. Drugs* 16 (2018) 75.
- [5] C.C. Liaw, Y.B. Cheng, Y.S. Lin, Y.H. Kuo, T.L. Hwang, Y.C. Shen, *Mar. Drugs* 12 (2014) 4677.
- [6] H. Ito, J. Iwasaki, Y. Sato, M. Aoyagi, K. Iguchi, T. Yamori, *Chem. Pharm. Bull.* 55 (2007) 1671.
- [7] J. Iwasaki, H. Ito, M. Aoyagi, Y. Sato, K. Iguchi, *J. Nat. Prod.* 69 (2006) 2.
- [8] L. Xu, B.O. Patrick, M. Roberge, T. Allen, L. van Ofwegen, R.J. Andersen, *Tetrahedron* 56 (2000) 9031.
- [9] J.H. Sheu, P.J. Sung, L.H. Huang, S.F. Lee, T. Wu, B.Y. Chang, C.Y. Duh, L.S. Fang, K. Soong, T.J. Lee, *J. Nat. Prod.* 59 (1996) 935.
- [10] J.H. Cardellina II, T.R. James Jr., M.H.M. Chen, J. Clardy, *J. Org. Chem.* 49 (1984) 3398.
- [11] H.D. Flack, *Acta Crystallogr. A* 39 (1983) 876.
- [12] H.D. Flack, G. Bernardinelli, *Acta Crystallogr. A* 55 (1999) 908.
- [13] Crystallographic data for the structure of brianthein W (1) have been deposited with the Cambridge Crystallographic Data Center as supplementary publication numbers CCDC 1876574. Copies of the data can be obtained, free of charge, on application to CCDC, 12 Union Road, Cambridge CB2 1EZ, UK [fax: +44(0)1223 336033 or e-mail: deposit@ccdc.cam.ac.uk].
- [14] P.J. Sung, M.R. Lin, M.Y. Chiang, I.C. Huang, S.M. Syu, L.S. Fang, W.H. Wang, J.H. Sheu, *Chem. Lett.* 39 (2010) 1030.
- [15] J.H. Su, P.J. Sung, Y.H. Kuo, C.H. Hsu, J.H. Sheu, *Tetrahedron* 63 (2007) 8282.
- [16] S. Aoki, M. Okano, K. Matsui, T. Itoh, R. Satari, S.I. Akiyama, M. Kobayashi, *Tetrahedron* 57 (2001) 8951.
- [17] A. Bahl, S.M. Jachak, K. Palaniveloo, T. Ramachandram, C.S. Vairappan, H.K. Chopra, *Nat. Prod. Commun.* 9 (2014) 1139.
- [18] Y.D. Su, J.H. Su, T.L. Hwang, Z.H. Wen, J.H. Sheu, Y.C. Wu, P.J. Sung, *Mar. Drugs* 15 (2017) 44 (and previous reports in this series).
- [19] A. Guerriero, M. D'Ambrosio, F. Pietra, *Helv. Chim. Acta* 71 (1988) 472.
- [20] A. Guerriero, M. D'Ambrosio, F. Pietra, *Helv. Chim. Acta* 73 (1990) 277.
- [21] S.J. Bloor, F.J. Schmitz, M.B. Hossain, D. van der Helm, *J. Org. Chem.* 57 (1992) 1205.
- [22] J. Rodríguez, R.M. Nieto, C. Jiménez, *J. Nat. Prod.* 61 (1998) 313.
- [23] A. Guerriero, M. D'Ambrosio, F. Pietra, *Helv. Chim. Acta* 78 (1995) 1465.
- [24] Y.C. Chang, J.H. Sheu, Y.C. Wu, P.J. Sung, *Mar. Drugs* 15 (2017) 382.
- [25] S.C. Yang, P.J. Chung, C.M. Ho, C.Y. Kuo, M.F. Hung, Y.T. Huang, W.Y. Chang, Y.W. Chang, K.H. Chan, T.L. Hwang, *J. Immunol.* 190 (2013) 6511.
- [26] H.P. Yu, P.W. Hsieh, Y.J. Chang, P.J. Chung, L.M. Kuo, T.L. Hwang, *Free Radic. Biol. Med.* 50 (2011) 1737.



Research articles

Hyaluronic acid modified bubble-generating magnetic liposomes for targeted delivery of doxorubicin



Gils Jose^a, Yu-Jen Lu^b, Huai-An Chen^a, Hao-Lung Hsu^a, Jung-Tung Hung^c, Anilkumar T.S.^a, Jyh-Ping Chen^{a,d,e,f,*}

^a Department of Chemical and Materials Engineering, Chang Gung University, Kwei-San, Taoyuan 33302, Taiwan, ROC

^b Department of Neurosurgery, Chang Gung Memorial Hospital, Linkou, Kwei-San, Taoyuan 33305, Taiwan, ROC

^c Institute of Stem Cell & Translational Cancer Research, Chang Gung Memorial Hospital, Linkou, Kwei-San, Taoyuan 33305, Taiwan, ROC

^d Department of Plastic and Reconstructive Surgery and Craniofacial Research Center, Chang Gung Memorial Hospital, Kwei-San, Taoyuan 33305, Taiwan, ROC

^e Research Center for Chinese Herbal Medicine and Research Center for Food and Cosmetic Safety, College of Human Ecology, Chang Gung University of Science and Technology, Kwei-San, Taoyuan 33302, Taiwan, ROC

^f Department of Materials Engineering, Ming Chi University of Technology, New Taipei City 24301, Taiwan, ROC

ARTICLE INFO

Keywords:

Bubble-generating
Hyaluronic acid
Magnetic liposomes
Doxorubicin
Targeted delivery
Cancer therapy

ABSTRACT

The combination of liposomes and magnetic nanoparticles (MNPs) is a promising approach for cancer therapy due to its capability for magnetic field-directed targeted drug delivery at the diseased area. Contemporaneously, bubble-generating liposomes are of great interest in the field of cancer therapy, due to its triggered drug release properties and its ability to rupture cancer cells through cavitation induction. Therefore, the objective of the current study is to develop a bubble-generating magnetic liposomal (BMLs) drug delivery system with triggered drug release properties for targeted delivery of doxorubicin (DOX) in cancer therapy. Citric acid-coated iron oxide MNPs was co-entrapped with ammonium bicarbonate to produce BMLs by lipid film hydration method. BMLs were further modified by coating hyaluronic acid-polyethylene glycol (HA-PEG) on liposome surface to produce HA-PEG-BMLs for ligand-mediated active targeting of tumor cells. The resultant liposomes were found to be spherical in shape with an average particle size ranging from 100 to 170 nm. The physico-chemical properties and bubble-generating properties of liposomes were studied. In vitro drug release studies showed enhanced drug release under hyperthermia condition (43 °C) from BMLs/DOX and HA-PEG-BMLs/DOX due to more intense CO₂ bubbles generation with faster decomposition rates of co-entrapped ammonium bicarbonate. In vitro cell culture studies using human glioblastoma cells (U87) were performed to evaluate the targeting efficiencies and anti-tumor efficacy of DOX-loaded liposomes. Magnetic targeted delivery of DOX was also demonstrated from LIVE/DEAD cell viability assays. The confocal microscopy and flow cytometry analysis confirmed enhanced intracellular uptake of HA-PEG-BMLs by U87 through binding of HA to overexpressed CD44 receptors on cell surface, which facilitated internalization of HA-PEG-BMLs/DOX through endocytosis and resulted in elevated DOX concentration in cancer cells. The combination of elevated intracellular DOX concentration and triggered DOX release at 43 °C led to enhanced cytotoxicity toward U87 cells in vitro. Thus, HA-PEG-BMLs will be useful for hyperthermia-induced targeted delivery of DOX for cancer therapy.

1. Introduction

Undoubtedly, cancer is one of the deadliest diseases in human history. In defiance of the role played by conventional chemotherapy in elevating the lifespan of many cancer sufferers, the vague distribution of therapeutics and limited bioavailability engendered to significant toxicity towards healthy tissues and to inefficacious therapy [1]. Within all nanometer-scale systems used to deliver chemical drugs, genes,

vaccines, and imaging agents, the liposomal system was found to be one of the most effective delivery systems, due to its capability to transport the therapeutics by overcoming physiological barriers, and to release the cargo at maximum concentration to the diseased area [2–4]. Contemporaneously, bubble-generating liposomes are of great interest in the field of cancer therapy, due to its triggered drug release properties [5]. Also, utilizing its tendency to cause cavitation during bubble formation, which involves either rapid growth followed by the collapse of

* Corresponding author at: 259 Wen-Hwa 1st Road, Kwei-San, Taoyuan 33302, Taiwan, ROC.

E-mail address: jpchen@mail.cgu.edu.tw (J.-P. Chen).

<https://doi.org/10.1016/j.jmmm.2018.11.019>

Received 24 June 2018; Received in revised form 26 October 2018; Accepted 4 November 2018

Available online 05 November 2018

0304-8853/ © 2018 Elsevier B.V. All rights reserved.

bubbles or sustained oscillatory motion of bubbles, bubble-generating liposomes also have the capability to rupture cancer cells [6]. This cavitation produces shock waves or high velocity micro jets that in turn damage the tissues physically, chemically and biologically, leaving other cells unscathed.

Liposomes are imperceptible particles composed of self-assembled lipid molecules having hydrophilic head group and hydrophobic tail, which exist either as unilamellar vesicle with one lipid bilayer enclosing a single aqueous compartment or as multilamellar vesicles with a number of concentric bilayers enclosing equal number of aqueous spaces [7,8]. Because of the amphipathic nature of lipids, these vesicles with one or more phospholipid bilayer membranes can carry both hydrophilic and hydrophobic drugs, depending on the nature of those drugs [4,9]. The application of magnetic nanoparticles (MNPs) in guiding drugs and nanoparticles to the tissue or organ with the help of an external magnetic field has been discussed before [10]. On the other hand, it is also possible to produce magnetic liposomes by encapsulated MNPs within aqueous cores of liposomes, which can offer multiple functions including *in vivo* guidance, contrast enhancement of MRI imaging and localized hyperthermia [11–13].

Although nanocarriers are considered to be efficient as carriers for chemotherapeutic drugs, a more efficient outcome of cancer therapy could be fulfilled by using targeted drug delivery, where most of the administered drug will be guided to the targeted site to eliminate or minimize the accumulation of the drug at any non-targeted sites [14]. This could be achieved through the modification of nanocarriers so that they can be directed by a magnetic field or by ligand-receptor interactions, which would result in active tumor targeting after extravasation [15]. Indeed, using the ligand-mediated internalization, which is attained through the binding of certain ligands to their receptors on cancer cell surface, internalization of drug-loaded nanocarriers into cancer cells could lead to higher intracellular drug concentrations and raise cancer cell killing efficacy [16]. Among ligands considered for tumor targeting, hyaluronic acid (HA) could be recognized by the CD44 receptor that is overexpressed on the surface of many types of cancer cells, including glioblastoma cells [17,18]. In this way, a more significant therapeutic outcome for brain tumor therapy could be expected through enhanced internalization of drug-loaded HA-modified magnetic liposomes through active targeting to glioblastoma cells.

In this study, we first prepared bubble-generating magnetic liposomes (BMLs) loaded with citric acid-coated magnetic nanoparticles (CMNPs) and further modified them with hyaluronic acid-polyethylene glycol (HA-PEG) to prepare a dual targeted nano-vehicle (HA-PEG-BMLs) for doxorubicin (DOX) delivery. We expect that after the liposomes were internalized by cancer cells, they can be thermally triggered at 43 °C to generate CO₂ bubbles, which can produce a disruptive force to disrupt the lipid bilayer membrane, followed by DOX release and death of cancer cells. Therefore, we tested the hypothesis that HA-PEG-BMLs/DOX could show chemotherapeutic accumulation and increased cytotoxicity to U87 human glioblastoma cells *in vitro*.

2. Materials and method

2.1. Materials

Fe(II) chloride tetrahydrate (99%) and Fe(III) chloride hexahydrate (97%) were acquired from Acros Organics. 1,2-Distearoyl-*sn*-glycero-3-phosphocholine (DSPC) was purchased from Avanti Polar Lipids. Cholesterol, dimethyldioctadecylammonium bromide (DDAB) and Triton X-100 were purchased from Sigma-Aldrich. Hyaluronic acid (HA) in the form of sodium hyaluronate (M.W. = 1.3×10^6 Da) was purchased from Shandong Freda Biochem. Co. Methoxy polyethylene glycol amine (MPEG-NH₂, M.W. = 5000 Da) was obtained from Alfa Aesar. CdS/Se/ZnS Quantum Dots with amine end groups (QDs-NH₂) was a product of Ocean NanoTech. Doxorubicin (hydrochloride salt) was acquired from LC Laboratories. Reagent grade chemicals were used

for all experiments without further purification.

2.2. Synthesis of citric acid-coated iron oxide magnetic nanoparticles (CMNPs)

The CMNPs were prepared by the co-precipitation method as described before [19,20]. For this, 0.875 g of FeCl₃·4H₂O and 2.375 g of FeCl₃·6H₂O were mixed in 40 mL of double-distilled water (DDI water) in a three-neck flask. The mixture was heated to 70 °C with constant stirring at 100 rpm under nitrogen atmosphere. Subsequently, the temperature and rotation speed were increased to 90 °C and 1150 rpm, and 5 mL of 25% NH₄OH solution was added to the mixture. Two milliliters of citric acid solution (0.5g/ml) was then added using a syringe, and the reaction was continued for another 90 min at 1150 rpm. The black-colored colloidal CMNPs obtained were magnetically separated after diluting with DDI water to 1:1 vol ratio. The CMNPs were then dialyzed against DDI water using a hollow fiber module (Spectrum Laboratories) to remove unbound citric acid and NH₄OH.

2.3. Synthesis of hyaluronic acid-polyethylene glycol (HA-PEG)

PEG-grafted hyaluronic acid was synthesized by following the procedure reported before with slight modifications [21]. In brief, 1.2 g of HA was dissolved in 50 mM 2-(N-morpholino)ethanesulfonic acid (MES) buffer. To this solution, equimolar amount of MPEG-NH₂ was added and stirred until complete dissolution. 1-Ethyl-3-(3-dimethylaminopropyl) carbodiimide (EDC, 1 mM) was then added and allowed to react for 2 h at room temperature. The viscous HA-PEG solution obtained was dialyzed against DDI water using a 10 kDa MWCO dialysis tubing for 48 h at room temperature to remove unreacted MPEG-NH₂.

2.4. Preparation of liposomes

The bubble-generating magnetic liposomes (BMLs) were prepared in the phosphate buffered saline (PBS) containing NH₄HCO₃ using the thin film hydration method [20]. DSPC, cholesterol and DDAB (molar ratio 6:4:1) were mixed in a 100 mL round-bottom flask and dissolved in 2:1(v/v) mixture of chloroform/methanol solution. 1.5 mL of this solution was then roto-evaporated (EYELA N-1200AVF, Japan) at 100 psi and 55 °C for 20 min, and kept in the vacuum oven overnight, to remove the organic solvent completely and to form the lipid film. The phospholipid film so obtained on the wall of the round-bottom flask was hydrated with 10 mL PBS solution containing 2 M NH₄HCO₃ and 0.2 mg/ml CMNPs for 20 min at 20 °C. The suspension obtained after the hydration process was sonicated using Q700 sonicator (Qsonica) for 20 min at 30% amplitude with 5 s pulse on/off cycles. This was followed with centrifugation at 1000g for 5 min to remove the un-encapsulated CMNPs. To remove the excess NH₄HCO₃, the liposomes were dialyzed against 10 wt% sucrose solution containing 5 mM NaCl for 24 h, and again centrifuged for 30 min at 60000g using a high speed centrifuge (Hermle Z36HK). Blank liposomes without NH₄HCO₃ and CMNPs were prepared using the same procedure but replacing the hydration solution with PBS. To prepare HA-PEG-BMLs, BMLs was modified with HA-PEG though the electrostatic interaction between cationic liposomal surface (due to the presence of DDAB) and negatively charged HA-PEG. Briefly, HA-PEG solution (1 mg/mL) was added drop-wisely to an equal volume of BMLs solution (1 mg/ml) under stirring at 4 °C for 30 min. The resulting solution was centrifuged at 60000g for 30 min to remove the free HA-PEG, and modified liposomes were re-suspended in DDI water.

2.5. DOX loading in liposomes

The remote loading technique using the *trans*-membrane gradients is applied to achieve an optimum intra-liposome concentrations of DOX

[22]. After the un-encapsulated NH_4HCO_3 is removed via dialysis, some of the encapsulated ammonium (NH_4^+) ions undergo dissociation to form protons (H^+) and ammonia (NH_3), and the resultant ammonia molecules rapidly cross the liposomal membrane, which leaves free protons trapped in the liposome because of their low membrane permeability. At this stage, DOX was added to the liposome suspension in different lipid/drug ratio (1: 0.01, 1: 0.05, 1: 0.1 and 1: 0.15) and allowed it to mix well at room temperature for 4 h. When the un-protonated DOX enters the proton-rich aqueous layer of the liposome by diffusion, it becomes protonated and reacts with bicarbonate ions to form DOX-bicarbonate salt. In this way, drug in the outer aqueous phase was encapsulated into the liposome and precipitated in the inner phase to achieve better penetration of drug into the liposome. Once the drug was encapsulated into the liposome, the suspension was centrifuged at 60000g for 30 min to remove un-encapsulated DOX from the liposome suspension. The DOX-loaded liposomes (BMLs/DOX and HA-PEG-BMLs/DOX) obtained after three-time centrifugation was re-suspended in DDI water. The encapsulation efficiency (EE) and loading efficiency (LE) of DOX in liposomes was calculated using the following equations.

$$\text{Encapsulation efficiency (\%)} = \frac{\text{Weight of encapsulated DOX}}{\text{Total weight of DOX}} \times 100 \quad (1)$$

$$\text{Loading efficiency (\%)} = \frac{\text{Weight of encapsulated DOX}}{\text{Weight of liposomes}} \times 100 \quad (2)$$

2.6. Physico-chemical characterization

The morphology of the prepared samples was analyzed using a transmission electron microscope (TEM, JEOL JEM2000 EX II) at an acceleration voltage of 100 kV. The particle size and zeta potential was detected by dynamic light scattering (DLS) using a Zetasizer (Nano ZS 90, Malvern, UK) by suspending the sample in distilled deionized water. Thermal behavior and the encapsulation of Fe_3O_4 MNPs into the liposomes were determined by thermogravimetric analysis (TGA) using Q50 TGA (TA instruments, New Castle, USA) with 10 mg freeze-dried samples in a platinum pan under nitrogen atmosphere from 50 to 700 °C. The nominal nitrogen flow rate and the heating rate were maintained at 60 mL/min and 10 °C/min, respectively. The Fe_3O_4 loading was further confirmed by inductively coupled plasma mass spectrometry (ICP, Varian 710-ES). A superconducting quantum interference device magnetometer (SQUID, Quantum Design MPMS-3) at 25 °C and $\pm 10,000\text{G}$ applied magnetic field was used to measure the magnetization of samples. Bubble generation in the liposomes, after decomposition of encapsulated NH_4HCO_3 , was visualized by a portable ultrasound imaging system (Terason t3200). For the characterization of chemical compounds using Fourier transform infrared spectroscopy (FTIR, Horiba FT-730 spectrometer), the samples were blended with KBr and then compressed to form a pellet.

2.7. DOX release from liposomes

The temperature-dependent drug release properties of the liposomes were analyzed by incubating BMLs/DOX or HA-PEG-BMLs/DOX in 1 mL PBS (pH 7.4) at 37 °C for 24 h [23]. Hyperthermia-induced drug release was studied by immersing the sample at 43 °C for 24 h. At specific times, all PBS was removed and replenished with equal volume of fresh PBS. The concentration of DOX in PBS was determined at 490 nm using a UV-visible spectrophotometer (UV-1700, Shimadzu, Kyoto, Japan). The accumulative drug release percentage was calculated from the total weight of encapsulated DOX after incubating drug-loaded liposomes in lysis buffer (0.1% Triton X-100 in PBS, pH 7.4) for 30 min at 37 °C.

2.8. Intracellular uptake

To evaluate the effect of HA-PEG coating on intracellular uptake qualitatively, U87 cells seeded in 24-well cell culture plate at 5×10^4 cells/well were treated with quantum dots (QDs)-labelled liposomes (final concentration of 100 $\mu\text{g/mL}$ liposome in culture medium) for 24 h. The labelling of liposomes was achieved through covalent binding after activating carboxylate groups in liposomes with EDC (5 μM), followed by reacting with QDs- NH_2 for 1 h room temperature. The product was centrifuged at 65000g for 30 min to remove unbound reagents from the liposomes. After incubation with QDs-labelled liposomes for 24 h, the cells were washed with PBS and the lysosomes were labeled with LysoTracker Red DND-99 (1 μM , Thermo Fisher Scientific) for 1 h at 37 °C. Labeled cells were fixed with 4% paraformaldehyde and further treated with Triton X-100 (0.1% in PBS). Subsequently, the cell nuclei were counterstained with blue fluorescence-producing Hoechst 33342 (1 $\mu\text{g/mL}$, Thermo Fisher Scientific) for 15 min. The identification of liposomes was made possible by the green fluorescence signals from QDs-labeled liposomes. To confirm whether the uptake of the HA-PEG-BMLs is specific to CD44 receptor, the uptake study was also performed with U87 cells pretreated with 1 mg/mL free HA to block the CD44 on cell surface before adding HA-PEG-BMLs. Cellular internalization of liposomes was assessed by confocal laser scanning microscopy (Zeiss LSM 510 Meta) at excitation wavelength 350 nm/492 nm/577 nm (blue/green/red) and emission wavelength 451 nm/517 nm/590 nm (blue/green/red). All three fluorescence were visualized individually at its corresponding wavelengths and were then merged together to visualize the cellular internalization of liposomes.

2.9. Flow cytometry analysis

The expression of CD44 surface marker on U87, mouse embryonic fibroblast (MEF) and Lewis lung carcinoma (LLC1) cells were analyzed using flow cytometry. The cells were seeded in T25 tissue culture flasks at 2.5×10^5 cells per flask. After 24 h incubation in a humidified incubator at 37 °C under 5% CO_2 atmosphere, the cells were stained with CD44 mouse monoclonal antibody (Cell Signaling Technology 3570) for 30 min at 4 °C, followed by washing the cells with 2 mL FACS buffer to remove unbound antibody from the cells. After centrifugation (300g for 5 min), cells were re-suspended in 0.5 mL FACS buffer and conjugated with goat polyclonal secondary antibody to mouse IgG-H&L(Cy3[®]), preadsorbed (Abcam ab97035) for 1 h. The cells were washed again twice and the final cell pellet was re-suspended in 500 μL of buffer. Analysis of fluorescence was carried out using the FACS instrument (Attune NxT flow cytometer, Life Technologies, USA) with a 488 nm air-cooled argon laser as the excitation source.

For the analysis of DOX accumulation, U87 cells were seeded in the T-25 tissue culture flasks at 2.5×10^5 cells per flask and incubated at 37 °C under 5% CO_2 atmosphere. After the incubation, cells were treated with free DOX, BMLs/DOX or HA-PEG-BMLs/DOX at the same DOX concentration (10 $\mu\text{g/mL}$ DOX prepared in cell culture medium) for 24 h. Subsequently, the medium was removed; cells were washed twice with PBS, detached from the flask using trypsin-EDTA solution and collected in a tube by centrifugation at 2000g for 5 min. The cells were washed again twice and the final cell pellet was re-suspended in 500 μL binding buffer. Analysis of DOX fluorescence was carried out using the FACS instrument (Attune NxT Flow cytometer, Life Technologies, USA) with a 488 nm air-cooled argon laser as the excitation source. Fluorescence from cell-associated DOX was detected using a 550 nm long pass emission filter.

The cell apoptosis studies of U87 cells were conducted with the apoptosis detection kit (Thermo Fischer Scientific) containing fluorescein isothiocyanate-labeled Annexin V (Annexin V-FITC) and propidium iodide (PI). U87 cells were seeded in a six-well plate with a cell density of 5×10^5 cells per well and cultured for 24 h. Followed by this, the cells were treated with blank liposome, BMLs, BMLs/DOX or HA-

PEG-BMLs/DOX, as well as with free DOX of the same DOX concentration (10 µg/mL DOX in medium) for 24 h at 37 °C and 43 °C. After the incubation, the cells were trypsinized, washed with PBS and incubated with Annexin V-FITC for 30 min at room temperature to label the live cells. Subsequently, the samples were incubated with PI for dead cell marking, and further analyzed quantitatively using Sony SA 3800 Spectral cell analyzer.

2.10. Magnetic targeting

To investigate the magnetic targeting effect, U87 cells were seeded in a 24-well cell culture plate at 5×10^4 cells/well. To create a permanent magnetic field, a disk-shaped magnet of 7.5 mm diameter was placed under each well of the culture plate. HA-PEG-BMLs/DOX was added to each well at 0.1 mg/mL and the plate was incubated in a humidified CO₂ incubator at 37 °C under 5% CO₂ atmosphere. After incubation for 24 h, the cells were washed with PBS and stained with LIVE/DEAD Cell Viability Assays kits for mammalian cells and observed under an inverted microscope (Olympus IX-71). A control was used for comparison following the same procedure but without magnetic targeting (without using a magnet). The areas of live (green) and dead (red cells) were analyzed using PAX-it software and the percentage of live and dead cells was calculated to compare cell viability.

2.11. In vitro cytotoxicity

The in vitro cytotoxicity of the prepared samples was determined from MTT assays using 3-(4,5-dimethylthiazol-2-yl)-2,5-diphenyltetrazolium bromide. U87 cells were seeded in 96-well culture plates at a density of 2.5×10^3 cells/well and cultured for 24 h in a humidified CO₂ incubator at 37 °C under 5% CO₂ atmosphere. The pre-incubated cells were then treated with BMLs/DOX or HA-PEG-BMLs/DOX, as well as with free DOX of the same DOX concentration (10 µg/mL DOX in medium) for 24 h at 37 °C and 43 °C. After the treatment, the samples were removed, and cells were incubated with 1 mg/mL MTT in cell culture medium for 4 h followed by adding 0.1 mL dimethyl sulfoxide. The optical density readings were recorded using an ELISA plate reader (BioTek Synergy HT) and normalized to readings of the control at each data point, which was taken as 100%. The biocompatibility of the prepared liposomes was also evaluated using MTT assays in the same way, after incubating the cells with DOX-free liposomes (100 µg/mL BMLs or HA-PEG-BMLs).

2.12. Statistical analysis

All data were reported as mean \pm standard deviation (SD) and subjected to one-way analysis of variance (ANOVA) analysis with Tukey's HSD Post Hoc Test by IBM SPSS Statistics Software with p value < 0.05 considered to be statistically significant.

3. Results and discussion

3.1. Preparation and characterization of bubble-generating liposomes

From the TEM micrograph, CMNPs agglomerated as shown in Fig. 1A. Nonetheless, the average size of discrete CMNPs could be estimated from the TEM image to be below 20 nm, which was within the size distribution of superparamagnetic particles [24]. The morphology of BMLs examined under TEM revealed successful encapsulation of spherical-shaped CMNPs in the liposomes (Fig. 1B). From DLS studies, the particle size distribution was in the order of HA-PEG-BMLs $>$ BMLs $>$ CMNPs (Fig. 1C), and zeta potential distribution changed from a negative value for CMNPs to a positive value for BMLs and changed back again to a negative value after HA-PEG coating (Fig. 1D). As shown in Table 1, the DLS measurements showed mean values of hydrodynamic diameters of CMNPs, BMLs and HA-PEG-BMLs to be

significantly different at 24 nm, 106 nm and 168 nm, respectively, with the polydispersity index (PDI) values below 0.3 for all samples. Coating with HA-PEG therefore led to increase of liposome size measured by DLS. Electrophoretic mobility measurements indicated the average zeta potential increased from -15.4 mV to 12.0 mV after encapsulating CMNPs in BMLs while the average zeta potential value is -18.5 mV for HA-PEG-BMLs (Table 1). Indeed, the change of zeta potential from a positive value to a negative value illustrates the successful coating of liposome with HA-PEG as BMLs are cationic liposomes with the positively charged lipid DDAB while HA is a negative charged polysaccharide (Fig. 1D).

From the FTIR spectra (Fig. 2A), CMNPs shows characteristic peaks of Fe₃O₄ MNPs at 3420 cm^{-1} ($-\text{OH}$), 1645 cm^{-1} ($-\text{NH}_2$) and 571 cm^{-1} (Fe-O) [25]. The presence of these characteristic peaks along with the characteristic peaks assigned to citric acid, i.e. 3442 cm^{-1} ($-\text{OH}$) and 1394 cm^{-1} (C=O asymmetric stretching on $-\text{COOH}$), confirms the successful synthesis of CMNPs [19]. Nonetheless, the characteristic peak at 1715 cm^{-1} due to C=O stretching of citric acid is not visible in the spectrum of CMNPs. This could indicate complex formation between the carboxylate group of citric acid and the Fe atoms on the magnetite surface, which will result in the shifting of the stretching frequency to a lower value as reported previously [26]. The FTIR spectrum of blank liposomes displays characteristic peaks of symmetric and asymmetric $-\text{PO}_2$ stretching vibrations at 1090 and 1220 cm^{-1} , $-\text{CH}_2$ bending vibrations at 1470 cm^{-1} and symmetric and asymmetric stretching vibrations of the $-\text{CH}_2$ in the acyl chain at around 2850 and 2920 cm^{-1} . All characteristics of blank liposomes are also visible in the spectrum of BMLs with additional peaks of CMNPs, which confirms the encapsulation of CMNPs in BMLs. The surface coating with HA-PEG can be identified from the spectrum of HA-PEG-BMLs, which contains additional peaks due to of HA, including the peaks at 611 cm^{-1} and 1043 cm^{-1} corresponding to the C-O-C stretching, 1411 cm^{-1} from C-O group with C=O combination, and 1616 cm^{-1} due to amide II group, in addition to the peaks associated with BMLs [27].

The XRD patterns of CMNPs shown in Fig. 2B shows characteristics peaks of Fe₃O₄ MNPs at $2\theta = 30.5^\circ, 35.8^\circ, 43.8^\circ, 53.4^\circ, 57.3^\circ$ and 62.9° , which is similar to the values in JCPDS file, No. 19-0629. For HA-PEG-BMLs, the XRD patterns show diffraction peaks of CMNPs and blank liposomes without distinguishable difference in 2θ values, indicating the successful encapsulation of CMNPs in HA-PEG-BMLs without making any significant changes of the crystalline structure. It should be noted that CMNPs peaks are not clearly visible for HA-PEG-BMLs, due to the presence of very high intensity peaks from the lipids.

The TGA curves of CMNPs, blank liposomes, BMLs and HA-PEG-BMLs were analyzed to evaluate the thermal behavior of liposomes as well as the loading percentage of CMNPs in liposomes (Fig. 2C). All samples show small mass loss initially below 200°C due to the loss of adsorbed CO₂ and water. For CMNPs, there is an additional $\sim 4\%$ weight loss at 700°C with no observable peak temperature from the DTA curve in the insert of Fig. 2C. From the TGA/DTA curve of blank liposomes, a substantial weight loss is observed when the temperature was increased to 240°C and peak decomposition temperatures are observed at $\sim 270^\circ\text{C}$ and $\sim 330^\circ\text{C}$ with a residual weight of $\sim 95\%$ at 700°C . For HA-PEG-BMLs, the TGA/DTA curve shows a similar trend as blank liposomes with an additional smaller decomposition peak temperature shown as a shoulder in the DTA curve at 230°C , which can be ascribed to the decomposition of HA in HA-PEG. From the difference between the residual weight of HA-PEG-BMLs and blank liposomes at 700°C , the weight percentage of CMNPs in HA-PEG-BMLs could be estimated to be $\sim 26\%$. The results obtained from the inductively coupled plasma mass spectrometry (ICP) analysis also showed 25% Fe₃O₄ MNPs were loaded into HA-PEG-BMLs.

From SQUID analysis at room temperature, the saturation magnetization value of HA-PEG-BMLs was 16 emu/g , which is lower than that of CMNPs (65 emu/g) (Fig. 2D). This downturn in magnetization value

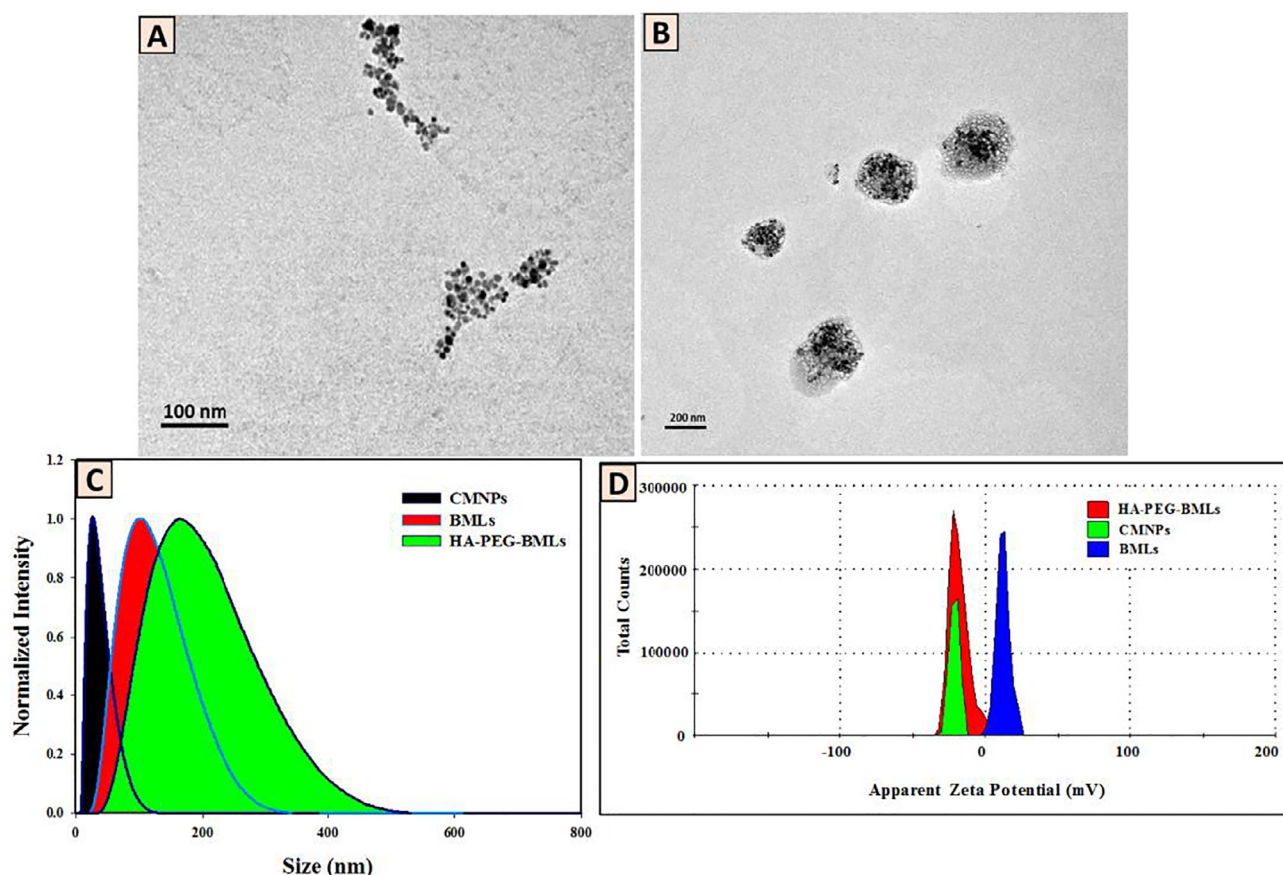


Fig. 1. TEM images of citric acid-coated magnetic nanoparticles (CMNPs) (A) and bubble-generating magnetic liposomes (BMLs) (B). Particle size (C) and zeta potential (D) distribution curves of CMNPs, BMLs and HA-PEG coated bubble-generating magnetic liposome (HA-PEG-BMLs).

Table 1

The average particle size and zeta potential of citric acid-coated magnetic nanoparticles (CMNPs), bubble-generating magnetic liposomes (BMLs) and HA-PEG coated bubble-generating magnetic liposomes (HA-PEG-BMLs). The data are expressed as means \pm standard deviations ($n = 4$).

Sample	Particle Size (nm)	Polydispersity index	Zeta Potential (mV)
CMNPs	24 ± 3	0.213 ± 0.029	-15.4 ± 1.3
BMLs	$106 \pm 7^*$	$0.278 \pm 0.019^*$	$12.0 \pm 0.9^*$
HA-PEG-BMLs	$168 \pm 6^{*,\#}$	$0.299 \pm 0.021^*$	$-18.5 \pm 1.4^{*,\#}$

* $p < 0.05$ compared with CMNPs, # $p < 0.05$ compared with BMLs.

is interrelated with the encapsulation of CMNPs inside the liposome. Generally, the saturation magnetization would decrease when the CMNPs surface was covered by lipids [28]. Nonetheless, reduced saturation magnetization is expected with reduced CMNPs weight percentages in HA-PEG-BMLs, as this value is based on unit weight of samples. It should be noted that the calculated saturation magnetization of HA-PEG-BMLs would be 16.3 emu/g , using Fe_3O_4 MNPs content determined by ICP. Thus, the diamagnetic contribution of the lipid bilayer surrounding the magnetite contributed less to the reduced saturation magnetization value than the weight effect. It should be noted even though the saturation magnetization value decreased after CMNPs were encapsulated in the liposomes, the saturation magnetization for HA-PEG-BMLs is still higher than that reported for magnetic liposomes prepared from soybean phosphatidylcholine [29]. The high magnetization value of HA-PEG-BMLs also suggested the possibility to use the nanocarrier for targeted drug delivery guided by a magnetic field. Fig. 2D also revealed the prepared CMNPs and HA-PEG-BMLs exhibited superparamagnetic property, which is characterized by the magnetization curve having no magnetic hysteresis. This endowed HA-

PEG-BMLs with the important property needed for nano-sized magnetic carriers for target delivery [30].

3.2. Bubble generation, drug loading and drug release

The temperature-sensitive bubble-generating capability of liposomes was compared in Fig. 3A. For blank liposomes, the presence of bubbles was not observed at both 37°C and 43°C . However, in the case of bubble-generating liposome containing NH_4HCO_3 , bubble formation around the liposomes could be detected by ultrasound at both temperatures with increased bubble intensity when temperature was increased from 37°C to 43°C . Indeed, this temperature-sensitive bubble generating capability could be related to different CO_2 bubble formation rates from decomposition of NH_4HCO_3 in the liposomes and could be explored for triggered drug release of encapsulated drug in the liposomes.

For better drug loading in the liposomes, the effect of lipid/drug ratio on DOX loading efficiency and encapsulation efficiency was studied. As shown in Fig. 3B, the encapsulation efficiency decreased with an increase in the amount of DOX used during liposome preparation, whereas the loading efficiency increased initially and then leveled off when more DOX was used. Considering both the loading efficiency and encapsulation efficiency, we optimized the preparation of HA-PEG-BMLs/DOX at a lipid/drug ratio of 1:0.05 for further studies.

Fig. 3C shows the temperature-sensitive drug release characteristics of different liposomal systems at 37°C and 43°C . The drug release for blank liposomes was similar at both temperatures as expected with no bubble formation. Nonetheless, in the case of bubble-generating liposomes, a distinctive temperature-dependent drug release profile could be observed. The elevation in drug release rate at 43°C could be explained as the result of cavitation found inside the liposomes [31].

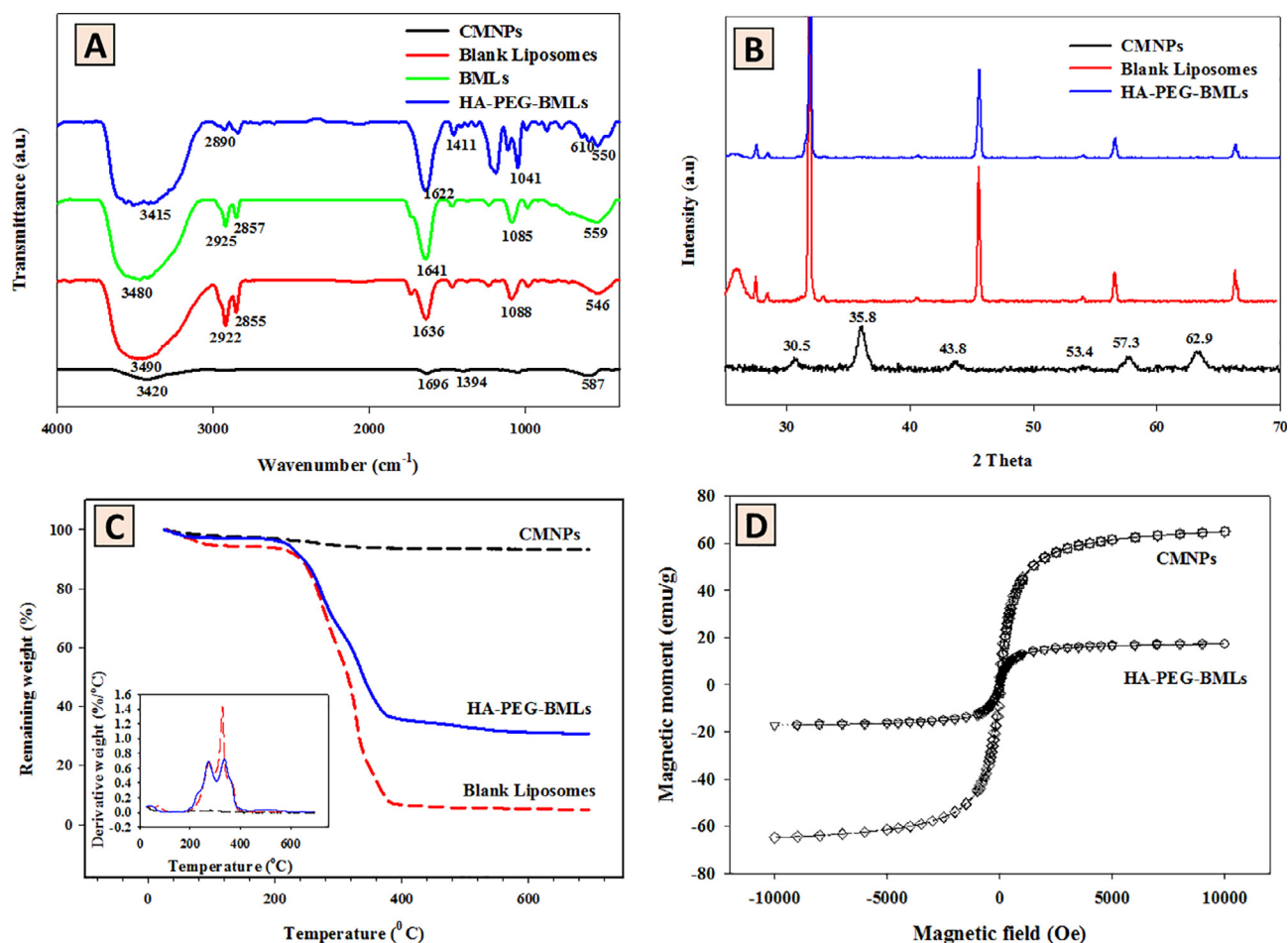


Fig. 2. Physico-chemical characterizations from Fourier transform infrared spectroscopy (FTIR) (A), X-ray diffraction (XRD) patterns (B), thermogravimetric analysis (TGA)/differential thermal analysis (DTA) (C) and superconducting quantum interference device (SQUID) magnetization curves (D).

While comparing the bubble-generating liposomes and blank liposomes at 43°C , a faster drug release could be observed for BMLs and HA-PEG-BMLs than blank liposomes. This characteristic property is attributed to the slower decomposition behavior of NH_4HCO_3 at 37°C , as evident from less bubble formation at this temperature than at 43°C (Fig. 3A). On the other hand, blank liposomes at two different temperatures shows similar release properties, due to higher thermal stability of DSPC lipid used for the preparation of liposomes [32,33]. Comparing BMLs and HA-PEG-BMLs, it is also noted that the drug release rate was diminished after HA-PEG modification; indicating coating HA-PEG on liposome surface may hinder the rupture of liposomes due to the action of CO_2 bubbles. Taken together, the drug release studies confirm the effect of bubble formation on drug release and the variation in bubble intensities at different temperatures, as shown from the ultrasound images in Fig. 3A, determines the drug release rate.

3.3. Intracellular uptake and flow cytometry analysis

Confocal images revealed intracellular green fluorescence corresponding to QDs-labeled liposomes when U87 cells were exposed to BMLs and HA-PEG-BMLs for 24 h (Fig. 4). This illustrates endocytosis and the subsequent accumulation of liposomes in cell cytoplasm after internalization. In addition, the green fluorescence intensity was higher for HA-PEG-BMLs. When CD44 receptors on U87 cell surface were blocked by HA before contacting with HA-PEG-BMLs, less ligand-mediated intracellular uptake was expected for HA-PEG-BMLs [34]. Indeed, we observed drastically diminished intracellular fluorescence signal when cells were pre-treated with excess HA before contacting

with HA-PEG-BMLs (Fig. 4). This difference is due to the efficient blockage of CD44 receptor on U87 cell surface with free HA in solution, which competitively inhibited the affinity of CD44 toward HA-PEG-BMLs [35]. Further confirmation of intracellular uptake through endocytosis was provided by the LysoTracker probes that could label lysosomes in living cells. As from the merged images in Fig. 4, only the HA-PEG-BMLs group shows high fluorescence intensity (yellow) corresponding to both liposomes (green) and LysoTracker (red), indicating active uptake of HA-coated liposomes by endocytosis.

The expression of CD44 on U87 cells was confirmed by flow cytometry using fluorescence-label anti-CD44 monoclonal antibody and compared with CD44 expression of normal fibroblastic cells and cancer cells. As shown in Fig. 5A, the intensity of U87 cells stained with anti-CD44 monoclonal antibody was much stronger than those of Lewis lung carcinoma (LLC1) and mouse embryonic fibroblast (MEF) cells (geometric mean intensity: 168855, 4316,1066, respectively), suggesting that U87 cells overexpress CD44 receptor on cell surface. Thus, the results of the flow cytometry support the enhanced intracellular uptake of HA-PEG-BMLs by U87 cells, as observed from the confocal images in Fig. 4. FACS analysis conducted to analyze accumulation of DOX in U87 cells also shows higher DOX accumulation when U87 cells were incubated with BMLs/DOX and HA-PEG-BMLs/DOX compared to cells treated with free DOX (Fig. 5B). The geometric mean intensities are 353, 442, 9053, 14,326 and 21,010 for control, BMLs, free DOX, BMLs/DOX and HA-PEG-BMLs/DOX, respectively. This shows that the DOX accumulation inside the cells increases when it is delivered through the liposomal nanocarrier. Most importantly, the DOX intensity was enhanced in cells treated with HA-PEG-BMLs/DOX than BMLs/DOX [36].

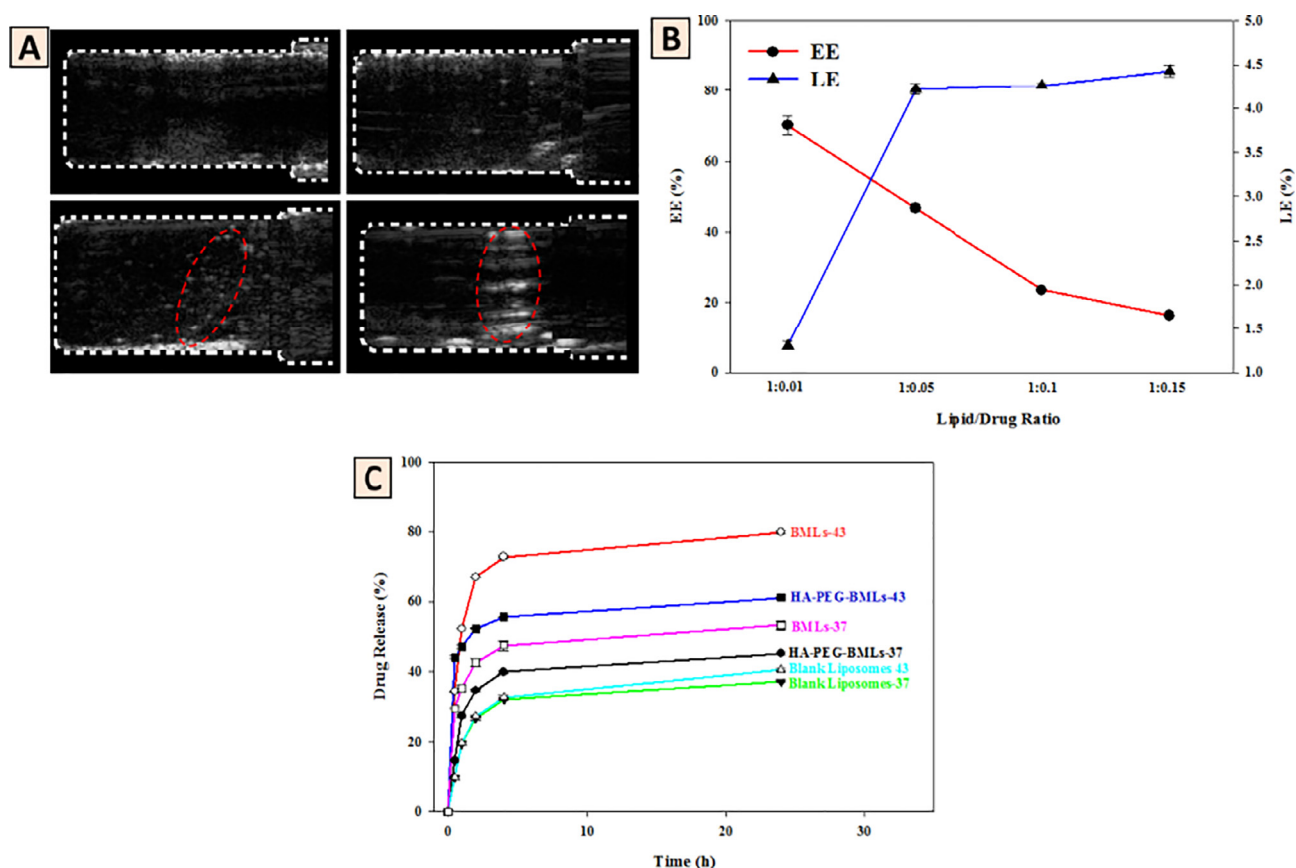


Fig. 3. (A) Ultrasound images of blank liposomes (top) and bubble-generating liposomes (BMLs) (bottom) at 37 °C (left) and 43 °C (right). CO₂ bubbles were marked with red circles. (B) The effect of lipid/drug ratio during the preparation of drug-loaded liposomes on loading efficiency (LE) and encapsulation efficiency (EE) of DOX (n = 4). (c) The drug release profiles of blank liposomes and bubble-generating liposomes (BMLs and HA-PEG-BMLs) at 37 °C and 43 °C (n = 4).

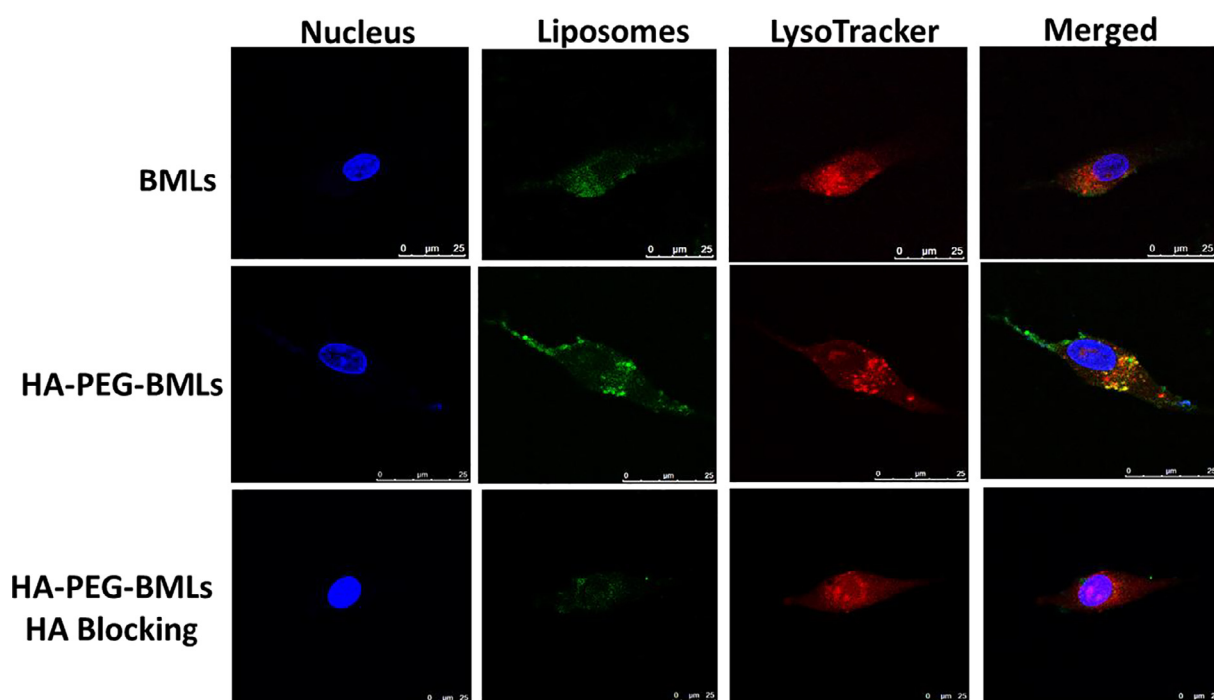


Fig. 4. Intracellular uptake studies of BMLs and HA-PEG-BMLs by U87 cells as examined by confocal microscopy after 24 h. Liposomes were labelled with QDs (green), nuclei were counter stained with Hoechst (blue) and LysoTracker probes was used to label lysosomes (red). Bar = 25 μm.

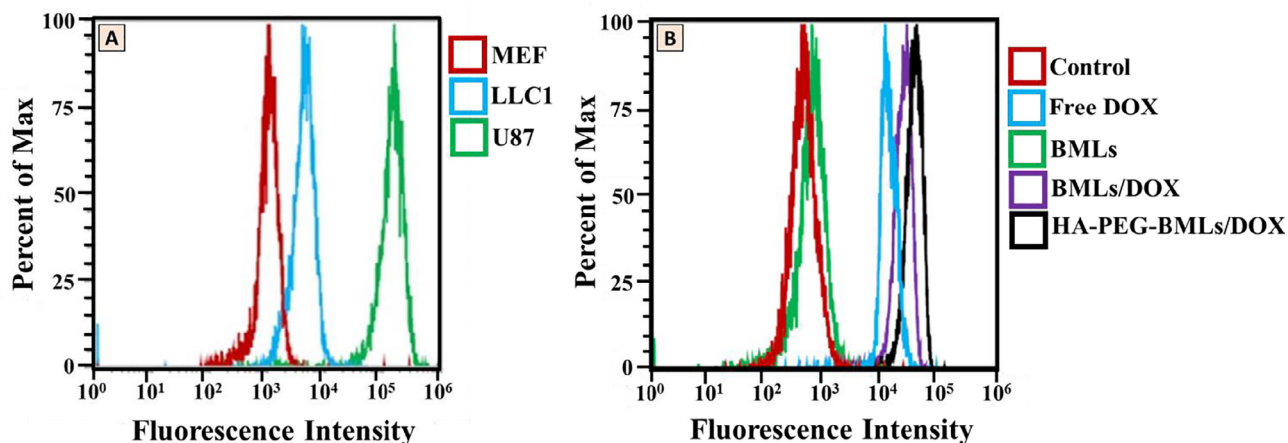


Fig. 5. (A) Flow cytometry analysis for identification of CD44 surface marker in mouse embryonic fibroblast (MEF), Lewis lung carcinoma (LLC1) and U87 cells and (B) flow cytometry analysis of DOX in U87 cells.

This result substantiates the presence and functioning of CD44 receptors on the surface of U87 cells, which could bind to HA-PEG on HA-PEG-BMLs to critically enhance the uptake of HA-PEG-BMLs/DOX for cancer therapy.

3.4. Magnetic targeting

For magnetic targeting effect, U87 cells were treated with HA-PEG-BMLs/DOX in a 24-well culture plate that has a small permanent magnet placed at the center of each well. The LIVE/DEAD staining images indicated few viable cells (green) could be identified in the magnetically targeted area (enclosed by the blue dotted line) while abundant dead cells (red) were found in the same area (Fig. 6A). The percentages of live and dead cells were calculated to be 12% and 88%, respectively. In contrast, most of the cells outside this area (outside of the blue dotted line) were viable with 92% live cells and 8% dead cells. Furthermore, it could be also confirmed that most live cells in the targeted area and most dead cells in the non-targeted area are found close to the boundary of the magnetically targeted area (i.e. blue dotted line). This indicates DOX-loaded magnetic liposomes could be magnetically guided by a permanent magnetic field for targeted DOX delivery [37]. On the contrary, in the absence of magnetic targeting, HA-PEG-

BMLs/DOX would distribute randomly in the well, which resulted in nonspecific cell death as revealed from Fig. 6B with almost equal percentage of live (55%) and dead (45%) cells. Therefore, HA-PEG-BMLs/DOX could therefore be magnetically guided to the tumor site with a magnetic field for specific killing of cells at the targeting site with minimum side effects toward surrounding healthy cells. Combining with HA ligand-directed targeting, HA-PEG-BMLs is a promising nanocarrier for dual targeted drug delivery of DOX.

3.5. In vitro cytotoxicity

In vitro cytotoxicity study was first conducted to evaluate the biocompatibility of the nanocarrier. The result shown in Fig. 7A indicates no appreciable toxicity for all liposomal formulation without DOX, demonstrating high biocompatibility of the prepared liposomes (Fig. 7A). Nonetheless, both BMLs and HA-PEG-BMLs show lower cell viability compared to blank liposomes, which could be ascribed to the formation, growth, and collapse of CO_2 bubbles, generated from the decomposition of NH_4HCO_3 inside the liposomes. Furthermore, BMLs and HA-PEG-BMLs, but not blank liposomes, showed significantly lower cytotoxicity at 37°C than at 43°C . This result is consistent with the observation of bubble formation in Fig. 3A, although bubble formation

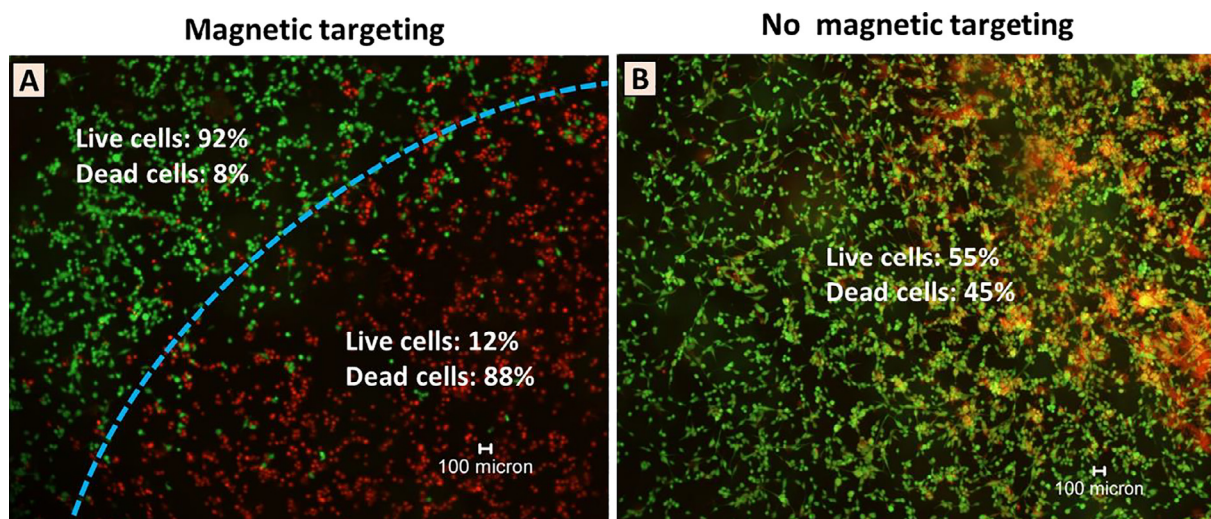


Fig. 6. The effect of magnetic guidance on distribution of live and dead cells after U87 cells were treated with HA-PEG-BMLs/DOX for 24 h with or without magnetic targeting. The cells were analyzed by LIVE/DEAD assays and examined under a fluorescence microscope where green and red fluorescence represent live and dead cells, respectively. The blue dotted line indicates the boundary of the magnetically targeted area using a permanent magnet. Bar = 100 μm .

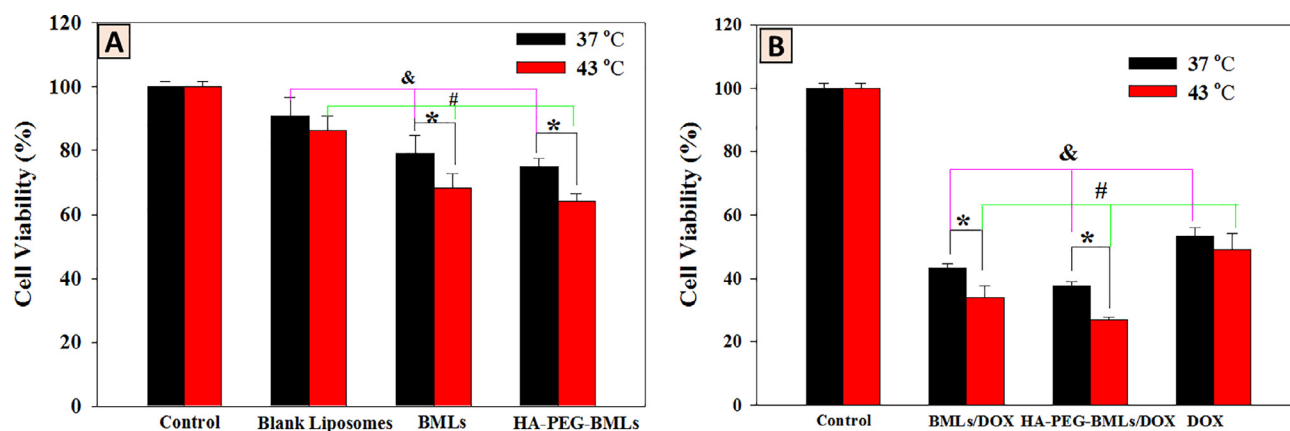


Fig. 7. Biocompatibility (A) and cytotoxicity (B) of various liposomal formulations at 37 °C and 43 °C (n = 6). The concentration of DOX was fixed at 10 µg/mL DOX. *p < 0.05 compared with 37 °C in each group, &p < 0.05 among groups at 37 °C, #p < 0.05 among groups at 43 °C.

started from 37 °C; increased bubble intensity was observed at 43 °C. This phenomenon is expected to induce more cavitation and influence cell viability. On the other hand, as modification of BMLs with HA-PEG plays a significant role in enhancing intracellular uptake, HA-PEG-BMLs showed significantly lower cell viability than BMLs at both temperatures. It is worth pointing out that most normal tissues remain undamaged following treatment for 1 h at temperatures up to 43 °C [6]. This feature makes the new liposomal system potentially safe for clinical use.

The cytotoxicity of the DOX-loaded liposomes was studied at 37 °C and 43 °C and compared with free DOX at the same drug concentration (Fig. 7B). Compared with DOX, BMLs/DOX and HA-PEG-BMLs/DOX were found to be significantly more cytotoxic to cancer cells at both temperatures, indicating their efficacy for cancer therapy. The enhanced cytotoxicity is also in line with the higher intracellular DOX concentration found from flow cytometry (Fig. 5B) when the drug is delivered through liposomes. For both BMLs/DOX and HA-PEG-BMLs/DOX, treatment at 43 °C shows predominantly higher cytotoxicity when compared to 37 °C due to the higher bubble intensity and elevated drug release at 43 °C (Fig. 3A and C). As expected, HA-PEG-BMLs/DOX showed the highest cytotoxicity against U87 among all DOX-treated groups due to ligand-mediated enhanced intracellular uptake, which gave the highest intracellular DOX concentration from flow cytometry analysis (Fig. 5B).

We further used flow cytometry to confirm the cytotoxicity of BMLs/DOX and HA-PEG-BMLs/DOX was induced by apoptosis. The cells were stained with Annexin V/PI to quantify live, early apoptotic, late apoptotic and necrotic cells by flow cytometry analysis according to differences in plasma membrane integrity and permeability. The percentage of necrotic (Q1), late apoptotic (Q2), early apoptotic (Q4) and live cells (Q3) are shown in Fig. 8. The flow cytometry data confirm cell death occurred mainly from early and late apoptosis associated with DOX [38]. Similar to the result obtained from the MTT assay (Fig. 7), blank liposomes show high biocompatibility with U87 cells. For BMLs, increase in temperature from 37 °C to 43 °C results in formation of more bubbles, which leads to more cavitation and higher cell apoptosis rate and live cells decrease from 79.0% to 71.0%. When this cavitation effect is combined with DOX release for BMLs/DOX, the live cells further decrease from 79.0% to 64.1% at 37 °C and from 71.0% to 62.1% at 43 °C, as the bubble can rupture liposome membrane for drug release along with cell rupture. This results in the release of more DOX intracellularly and enhances the cytotoxicity. BMLs/DOX treatment also results in less live cells than free DOX, which is 69.5% (37 °C) and 65.0% (43 °C). For HA-PEG-BMLs/DOX, enhanced cytotoxicity was expected due to ligand-mediated intracellular uptake of HA-PEG-BMLs through interaction of HA with CD44 receptor on U87 cell surface. Although the drug release profiles indicate the drug release percentage of HA-PEG-BMLs/DOX was less than that of BMLs/DOX at both

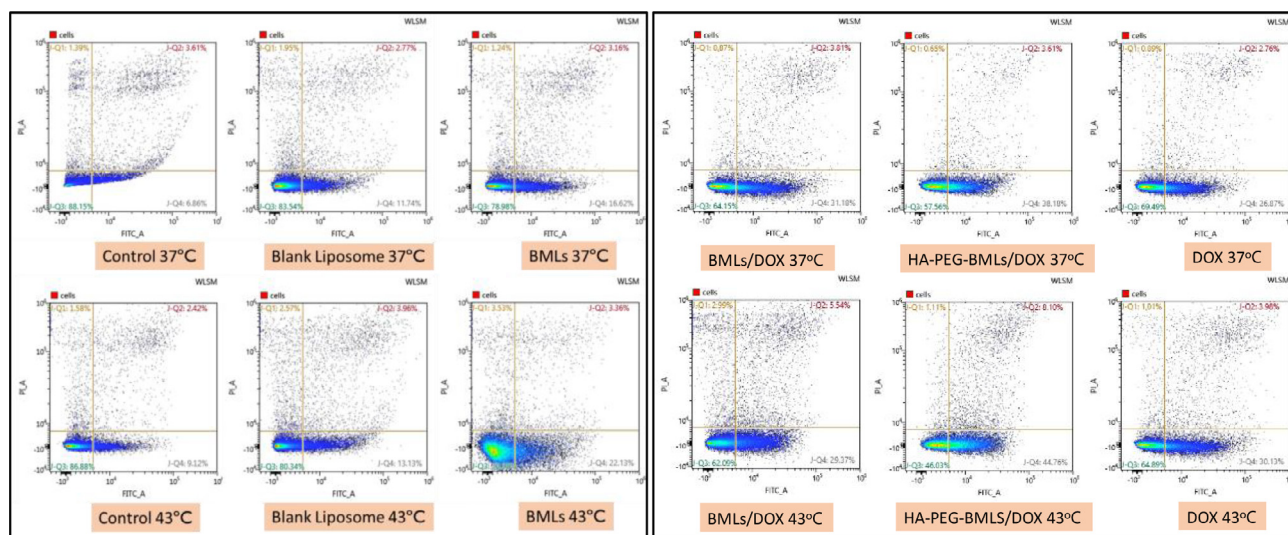


Fig. 8. The flow cytometry analysis of apoptotic and necrotic cells by Annexin V/PI staining (Q1: necrotic; Q2: late apoptotic; Q3: live; Q4: early apoptotic) after 24 h incubation with free DOX, liposomes or DOX-loaded liposomes at 37 °C and 43 °C. The concentration of DOX was fixed at 10 µg/mL.

temperatures (Fig. 3C), we could still find much less live cells for HA-PEG-BMLs/DOX than BMLs/DOX (57.6% vs 64.1% at 37 °C; 46.0% vs 62.1% at 43 °C) due to enhanced intracellular uptake of the former. Taken together, the results reveal the combinatory effect of bubble generation and DOX release for cell cytotoxicity, which could be further enhanced at higher temperature.

The results obtained from in vitro experiments suggest the effectiveness of HA-PEG-BMLs/DOX in cancer therapy. It should be noted that hyperthermia-based drug release could be conveniently accomplished under an applied alternating magnetic field (AMF), which works based on principles of Brownian relaxation and Neel effect [39]. The MNPs in the liposomes will therefore generate hyperthermia effect in the presence of AMF for drug release, which could be translated into a drug delivery system in vivo using bubble-generating magnetic liposomes. This will provide a remotely controlled drug delivery system using HA-PEG-BMLs/DOX for cancer therapy in vivo. The in vitro cytotoxicity study endorses intravenous administration of HA-PEG-BMLs/DOX, which exhibits the highest cytotoxicity under hyperthermia condition at 43 °C, for targeted delivery of DOX to cancer cells, followed by AMF treatment to induce hyperthermia for future translational study in vivo.

4. Conclusion

We successfully prepared and characterized bubble-generating magnetic liposomes in this study and demonstrated dual targeted DOX delivery was possible through magnetic targeting (with encapsulated CMNPs) and ligand-mediated intracellular uptake (by interaction of HA with CD44). We confirmed the modification of BMLs with HA-PEG is a promising strategy for the enhanced intracellular uptake of the liposomal nano-carrier by cancer cells, which elevated DOX concentration intracellularly in the cancer cells for enhanced cytotoxicity. The bubble-generating liposomes, BMLs and HA-PEG-BMLs, provide a powerful tool for temperature-sensitive bubble generation, and temperature-responsive DOX release for killing U87 cancer cells. Hyperthermia-based bubble generation followed by triggered drug release render HA-PEG-BMLs/DOX to be a promising nano-carrier for dual targeted cancer therapy.

Acknowledgements

The financial assistance was provided by grants from the Ministry of Science and Technology, Taiwan (106-2221-E-182-056-MY3) and Chang Gung Memorial Hospital (BMRP 249, CMRPD2G0081 and CMRPD2G0082). The Microscope Core Laboratory in Chang Gung Memorial Hospital, Linkou is acknowledged for the confocal microscopy study.

References

- [1] E.Y. Chuang, C.C. Lin, K.J. Chen, D.H. Wan, K.J. Lin, Y.C. Ho, P.Y. Lin, H.W. Sung, A FRET-guided, NIR-responsive bubble-generating liposomal system for in vivo targeted therapy with spatially and temporally precise controlled release, *Biomaterials* 93 (2016) 48–59.
- [2] S.-L. Huang, Liposomes in ultrasonic drug and gene delivery, *Adv. Drug Deliv. Rev.* 60 (2008) 1167–1176.
- [3] R. Mo, T. Jiang, R. DiSanto, W. Tai, Z. Gu, ATP-triggered anticancer drug delivery, *Nature Commun.* 5 (2014) 3364.
- [4] V.P. Torchilin, Recent advances with liposomes as pharmaceutical carriers, *Nat. Rev. Drug Discov.* 4 (2005) 145–160.
- [5] Z. Deng, M. Tang, L. Zhao, Y. Long, Z. Wen, Y. Cheng, H. Zheng, Targeted H(+)-triggered bubble-generating nanosystems for effective therapy in cancer cells, *Colloids Surf. B* 160 (2017) 207–214.
- [6] M.F. Chung, K.J. Chen, H.F. Liang, Z.X. Liao, W.T. Chia, Y. Xia, H.W. Sung, A liposomal system capable of generating CO₂ bubbles to induce transient cavitation, lysosomal rupturing, and cell necrosis, *Ang. Chem. Int. Ed.* 51 (2012) 10089–10093.
- [7] D.A. Balazs, W. Godbey, Liposomes for use in gene delivery, *J. Drug Deliv.* 2011 (2011) 326497.
- [8] M.B. Yatvin, J.N. Weinstein, W.H. Dennis, R. Blumenthal, Design of liposomes for enhanced local release of drugs by hyperthermia, *Science* 202 (1978) 1290–1293.
- [9] A. Akbarzadeh, R. Rezaei-Sadabady, S. Davaran, S.W. Joo, N. Zarghami, Y. Hanifepour, M. Samiei, M. Kouhi, K. Nejati-Koshki, Liposome: classification, preparation, and applications, *Nanoscale Res. Lett.* 8 (2013) 102.
- [10] R. Fernández-Pacheco, C. Marquina, J. Gabriel Valdivia, M. Gutiérrez, M. Soledad Romero, R. Cornudella, A. Laborda, A. Viloria, T. Higuera, A. García, J.A.G. de Jalón, M. Ricardo Ibarra, Magnetic nanoparticles for local drug delivery using magnetic implants, *J. Mag. Mag. Mater.* 311 (2007) 318–322.
- [11] M. De Cuyper, M. Joniau, Magnetoliposomes. Formation and structural characterization, *Eur. Biophys. J.* 15 (1988) 311–319.
- [12] H.-L. Hsu, J.-P. Chen, Preparation of thermosensitive magnetic liposome encapsulated recombinant tissue plasminogen activator for targeted thrombolysis, *J. Mag. Mag. Mater.* 427 (2017) 188–194.
- [13] J. Giri, S. Guha Thakurta, J. Bellare, A. Kumar Nigam, D. Bahadur, Preparation and characterization of phospholipid stabilized uniform sized magnetite nanoparticles, *J. Mag. Mag. Mater.* 293 (2005) 62–68.
- [14] I.K. Kwon, S.C. Lee, B. Han, K. Park, Analysis on the current status of targeted drug delivery to tumors, *J. Control. Release* 164 (2012) 108–114.
- [15] D. Peer, J.M. Karp, S. Hong, O.C. Farokhzad, R. Margalit, R. Langer, Nanocarriers as an emerging platform for cancer therapy, *Nature Nanotechnol.* 2 (2007) 751.
- [16] Y.-S. Huang, Y.-J. Lu, J.-P. Chen, Magnetic graphene oxide as a carrier for targeted delivery of chemotherapy drugs in cancer therapy, *J. Mag. Mag. Mater.* 427 (2017) 34–40.
- [17] L.Y. Bourguignon, M. Shiina, J.J. Li, Hyaluronan-CD44 interaction promotes oncogenic signaling, microRNA functions, chemoresistance, and radiation resistance in cancer stem cells leading to tumor progression, *Adv. Cancer Res.* 123 (2014) 255–275.
- [18] A. Persch, J. Lesley, N. English, I. Trowbridge, R. Hyman, Role of CD44 cytoplasmic domain in hyaluronan binding, *Eur. J. Immunol.* 25 (1995) 495–501.
- [19] M. Racuciu, D.E. Creanga, A. Airinei, Citric-acid-coated magnetite nanoparticles for biological applications, *Eur. Phys. J. E, Soft Matter.* 21 (2006) 117–121.
- [20] A. Hardiansyah, L.-Y. Huang, M.-C. Yang, T.-Y. Liu, S.-C. Tsai, C.-Y. Yang, C.-Y. Kuo, T.-Y. Chan, H.-M. Zou, W.-N. Lian, C.-H. Lin, Magnetic liposomes for colorectal cancer cells therapy by high-frequency magnetic field treatment, *Nanoscale Res. Lett.* 9 (2014) 497.
- [21] K. Moriyama, T. Ooya, N. Yui, Hyaluronic acid grafted with poly(ethylene glycol) as a novel peptide formulation, *J. Control. Release* 59 (1999) 77–86.
- [22] A. Cern, A. Golbraikh, A. Sedykh, A. Tropsha, Y. Barenholz, A. Goldblum, Quantitative structure – property relationship modeling of remote liposome loading of drugs, *J. Control. Release* 160 (2012) 147–157.
- [23] K.-J. Chen, E.-Y. Chaung, S.-P. Wey, K.-J. Lin, F. Cheng, C.-C. Lin, H.-L. Liu, H.-W. Tseng, C.-P. Liu, M.-C. Wei, C.-M. Liu, H.-W. Sung, Hyperthermia-mediated local drug delivery by a bubble-generating liposomal system for tumor-specific chemotherapy, *ACS Nano* 8 (2014) 5105–5115.
- [24] T. Neuberger, B. Schöpf, H. Hofmann, M. Hofmann, B. von Rechenberg, Superparamagnetic nanoparticles for biomedical applications: Possibilities and limitations of a new drug delivery system, *J. Mag. Mag. Mater.* 293 (2005) 483–496.
- [25] H. Salehizadeh, E. Hekmatian, M. Sadeghi, K. Kennedy, Synthesis and characterization of core-shell Fe₃O₄-gold-chitosan nanostructure, *J. Nanobiotechnol.* 10 (2012) 3.
- [26] A. Goodarzi, Y. Sahoo, M.T. Swihart, P.N. Prasad, Aqueous ferrofluid of citric acid coated magnetite particles, *MRS Proceedings* 789 (2011) N6.6.
- [27] J.A. Alkhrd, Y. Merstani, R.H. Neubert, New approaches for quantifying hyaluronic acid in pharmaceutical semisolid formulations using HPLC and CZE, *J. Pharm. Biomed. Anal.* 30 (2002) 913–919.
- [28] M. Mahmoudi, S. Sant, B. Wang, S. Laurent, T. Sen, Superparamagnetic iron oxide nanoparticles (SPIONs): development, surface modification and applications in chemotherapy, *Adv. Drug Deliv. Rev.* 63 (2011) 24–46.
- [29] S. Garcia-Jimeno, E. Escribano, J. Queral, J. Estelrich, Magnetoliposomes prepared by reverse-phase followed by sequential extrusion: characterization and possibilities in the treatment of inflammation, *Int. J. Pharm.* 405 (2011) 181–187.
- [30] A.K. Gupta, A.S.G. Curtis, Surface modified superparamagnetic nanoparticles for drug delivery: Interaction studies with human fibroblasts in culture, *J. Mater. Sci. Mater. Med.* 15 (2004) 493–496.
- [31] T. Ta, E. Bartolak-Suki, E.J. Park, K. Karroby, N.J. McDannold, T.M. Porter, Localized delivery of doxorubicin in vivo from polymer-modified thermosensitive liposomes with MR-guided focused ultrasound-mediated heating, *J. Control. Release* 194 (2014) 71–81.
- [32] C.M. González-Henríquez, V.A. Villegas-Opazo, D.H. Sagredo-Oyarce, M.A. Sarabia-Vallejos, C.A. Terraza, Thermal response analysis of phospholipid bilayers using ellipsometric techniques, *Biosensors* 7 (2017) 34.
- [33] N. Kucerka, M.P. Nieh, J. Katsaras, Fluid phase lipid areas and bilayer thicknesses of commonly used phosphatidylcholines as a function of temperature, *Biochim. Biophys. Acta* 1808 (2011) 2761–2771.
- [34] S.L. Hayward, C.L. Wilson, S. Kidambi, Hyaluronic acid-conjugated liposome nanoparticles for targeted delivery to CD44 overexpressing glioblastoma cells, *Oncotarget* 7 (2016) 34158–34171.
- [35] L. Mo, J.G. Song, H. Lee, M. Zhao, H.Y. Kim, Y.J. Lee, H.W. Ko, H.-K. Han, PEGylated hyaluronic acid-coated liposome for enhanced in vivo efficacy of sorafenib via active tumor cell targeting and prolonged systemic exposure, *Nanomed. Nanotechnol.* 14 (2018) 557–567.
- [36] Y.T. Fong, C.H. Chen, J.P. Chen, Intratumoral delivery of doxorubicin on folate-conjugated graphene oxide by in-situ forming thermo-sensitive hydrogel for breast cancer therapy, *Nanomaterials* 7 (2017) 388.
- [37] Y.J. Lu, K.C. Wei, C.C. Ma, S.Y. Yang, J.P. Chen, Dual targeted delivery of doxorubicin to cancer cells using folate-conjugated magnetic multi-walled carbon nanotubes, *Colloids Surf. B* 89 (2012) 1–9.
- [38] H. Mizutani, S. Tada-Oikawa, Y. Hiraku, M. Kojima, S. Kawanishi, Mechanism of apoptosis induced by doxorubicin through the generation of hydrogen peroxide, *Life Sci.* 76 (2005) 1439–1453.
- [39] C.S. Kumar, F. Mohammad, Magnetic nanomaterials for hyperthermia-based therapy and controlled drug delivery, *Adv. Drug Deliv. Rev.* 63 (2011) 789–808.

Available online at www.sciencedirect.com

ScienceDirect

journal homepage: www.jfda-online.com

Original Article

Targeting amine- and phenol-containing metabolites in urine by dansylation isotope labeling and liquid chromatography mass spectrometry for evaluation of bladder cancer biomarkers

Yi-Ting Chen ^{a,b,c,d,*}, Hsin-Chien Huang ^b, Ya-Ju Hsieh ^b, Shu-Hsuan Fu ^b,
Liang Li ^e, Chien-Lun Chen ^{f,g}, Lichieh Julie Chu ^{b,h}, Jau-Song Yu ^{b,h,i,j}

^a Graduate Institute of Biomedical Sciences, College of Medicine, Chang Gung University, Taoyuan, Taiwan

^b Molecular Medicine Research Center, College of Medicine, Chang Gung University, Taoyuan, Taiwan

^c Department of Biomedical Sciences, College of Medicine, Chang Gung University, Taoyuan, Taiwan

^d Department of Nephrology, Chang Gung Memorial Hospital, Linkou Medical Center, Taoyuan, Taiwan

^e Department of Chemistry, University of Alberta, Edmonton, AB, T6G2G2, Canada

^f Department of Urology, Chang Gung Memorial Hospital, Taoyuan, Taiwan

^g College of Medicine, Chang Gung University, Taoyuan, Taiwan

^h Liver Research Center, Chang Gung Memorial Hospital at Linkou, Gueishan, Taoyuan, 33305, Taiwan

ⁱ Department of Cell and Molecular Biology, Chang Gung University, Guishan, Taoyuan, 33302, Taiwan

^j Research Center for Food and Cosmetic Safety, Research Center for Chinese Herbal Medicine, College of Human Ecology, Chang Gung University of Science and Technology, Taoyuan, Taiwan

ARTICLE INFO

Article history:

Received 27 June 2018

Received in revised form

29 October 2018

Accepted 23 November 2018

Available online xxx

Keywords:

Bladder cancer

Biomarker

Phosphoethanolamine

Uridine

Metabolites

ABSTRACT

Metabolomics is considered an effective approach for understanding metabolic responses in complex biological systems. Accordingly, it has attracted increasing attention for biomarker discovery, especially in cancer. In this study, we used a non-invasive method to evaluate four urine metabolite biomarker candidates—o-phosphoethanolamine, 3-amio-2-piperidone, uridine and 5-hydroxyindoleacetic acid—for their potential as bladder cancer diagnostic biomarkers. To analyze these targeted amine- and phenol-containing metabolites, we used differential ¹²C₂-/¹³C₂-dansylation labeling coupled with liquid chromatography/tandem mass spectrometry, which has previously been demonstrated to exhibit high sensitivity and reproducibility. Specifically, we used ultra-performance liquid chromatography (UPLC) coupled with high-resolution Fourier transform ion-cyclotron resonance MS system (LC-FT/MS) and an ion trap MS with MRM function (LC-HCT/MS) for targeted quantification. The urinary metabolites of interest were well separated and quantified using this approach. To apply this approach to clinical urine specimens, we spiked samples with ¹³C₂-dansylated synthetic compounds, which served as standards for targeted quantification of ¹²C₂-dansylated urinary endogenous metabolites using LC-FT/MS

* Corresponding author. Department of Biomedical Sciences, College of Medicine, Chang Gung University, Taoyuan, Taiwan.

E-mail address: ytschen@mail.cgu.edu.tw (Y.-T. Chen).

<https://doi.org/10.1016/j.jfda.2018.11.008>

1021-9498/Copyright © 2019, Food and Drug Administration, Taiwan. Published by Elsevier Taiwan LLC. This is an open access article under the CC BY-NC-ND license (<http://creativecommons.org/licenses/by-nc-nd/4.0/>).

as well as LC-HCT/MS with MRM mode. These analyses revealed significant differences in two of the four metabolites of interest—o-phosphoethanolamine and uridine—between bladder cancer and non-cancer groups. O-phosphoethanolamine was the most promising single biomarker, with an area-under-the-curve (AUC) value of 0.709 for bladder cancer diagnosis. Diagnostic performance was improved by combining uridine and o-phosphoethanolamine in a marker panel, yielding an AUC value of 0.726. This study confirmed discovery-phase features of the urine metabolome of bladder cancer patients and verified their importance for further study.

Copyright © 2019, Food and Drug Administration, Taiwan. Published by Elsevier Taiwan LLC. This is an open access article under the CC BY-NC-ND license (<http://creativecommons.org/licenses/by-nc-nd/4.0/>).

1. Introduction

It has been estimated that bladder cancer will account for 81,990 new cases and 17,240 bladder cancer-estimated deaths worldwide during 2018 [1]. Bladder cancer progression and death rates are highly related to tumor stage and cancer grade; thus, these metrics are crucial indicators of clinic prognosis and optimal treatments [2]. The progression rate for bladder cancer patients with low-grade tumors is approximately 6%, whereas that for patients with high-grade lesions is approximately 17% [3]. Hence, early detection and precise prognosis of cancer severity are critical for clinical management and assessment of progression risk.

Among the current methods for diagnosing disease, predicting progression and monitoring recurrence are cystoscopy, biopsy, urine cytology, and imaging [4]. However, these prognostic tools are not without drawbacks. Both cystoscopies and biopsies are invasive processes, and cystoscopy is expensive, painful and less sensitive for detecting high-grade tumors [4]. Although urine cytology is a highly sensitive, specific, cost-effective and convenient screening technique, it lacks the ability to detect low-grade bladder cancer [2]. An ideal screening test would retain these desirable characteristics (inexpensiveness, high sensitivity, specificity and non-invasiveness), while minimizing drawbacks.

Metabolomics, one of the “omics” technologies, is a comprehensive technique for global metabolite screening and profiling. Metabolomics is capable of investigating relatively small molecules in biofluids (blood, urine, plasma) or tissue, and is therefore complementary to genomics, transcriptomics, and proteomics. Moreover, because metabolism-related proteins are subject to modification through a series of complex biological processes at transcriptional, translational and post-translational levels [5], metabolomics reflects the dynamic responses of living systems to path physiological stimuli or genetic influences [6]. Similarly, specific metabolites secreted into biofluids reflect the operation of molecular pathways involving cellular ontogenesis, providing information that cannot be obtained directly using other omics approaches [6].

The bladder is the organ responsible for the storage of urine. Therefore, screening for cancer-associated metabolites in urine is a potentially on-invasive approach for disease prognosis and examination of bladder cancer recurrence.

Accordingly, metabolomics is a promising approach for the discovery of bladder cancer biomarkers. Despite these potential advantages, current research on metabolic biomarker discovery faces certain limits. After applying metabolomics as a platform for biomarker discovery, candidate metabolic biomarker candidates must be confirmed and accurately quantified, a requirement made more difficult by the small, but significant, differences in levels of metabolites in biological specimens; even efforts to subsequently confirm metabolites identified in the discovery phase have met with limited success [7]. The lack of synthetic standards and limited availability of clinical specimens for novel metabolite identification are the main reasons for difficulties in verifying metabolite biomarker candidates.

One approach for addressing these issues is ultra-performance liquid chromatography (UPLC) coupled with mass spectrometry (LC-MS), which provides a good platform for metabolic biomarker discovery. Advantages of LC-MS include the ability to separate, ionize and detect a wide range of analytes and identify chemical features of molecules, such as retention time and mass-to-charge ratio (m/z). Multiple reaction monitoring (MRM)-MS provides additional information on fragments of targeted metabolites [7] and can be used for absolute quantification. Nevertheless, urinary metabolites are highly diverse [8] and some have properties that limit their retention on a reverse phase column, resulting in difficulties in analyzing the entire metabolome at once. Kuo et al. [8] demonstrated a solution to this challenging problem, showing that the chemical behaviors of amine- and phenol-containing metabolites could be altered by dansyl chloride labeling. This study [8] also demonstrated several important characteristics of differential isotope dansylation labeling, including high sensitivity, an expanded detection range for highly diverse molecules, and impressive reproducibility. Dansylated metabolites, even polar or ionic metabolites that are normally not retained on a reverse-phase (RP) column, can be separated by RPLC, increasing metabolite signal intensity and producing a better signal-to-noise ratio [8]. In addition, $^{12}\text{C}/^{13}\text{C}$ -isotope dansylation labeling offers the characteristic of signal pairs on a spectrum that facilitates the confidence in identification and quantification of endogenous metabolites. Because it uses isotope-labeled synthetic compounds as a quantitative reference standard, $^{12}\text{C}/^{13}\text{C}$ -isotope dansylation labeling coupled with LC-MS/MS is considered as a promising

technique for metabolic quantification and biomarker discovery [8–11].

Our previous work [12] identified numerous putative markers for bladder cancer using isotope dansylation labeling in conjunction with HPLC-MS (Supplemental Table 1). However, analytical methods for assessing these potential markers have not been established for metabolite identification and large-scale quantification for clinical applications. The identification of these previous potential metabolite biomarker candidates was based on matching their molecular weight with compounds from metabolome databases. An alternative identification and quantification strategy is to perform analyses after dansylation labeling utilizing highly purified commercial compounds. In this study, we sought to apply HPLC coupled with two types of mass spectrometry—Fourier transform ion-cyclotron resonance MS (FT/MS) and ion trap MS with MRM function (HCT/MS)—to verify the clinical utility of five potential urinary metabolite biomarkers discovered in our previous work [12] using the five commercially-available compounds as standards. The standard compounds were used to compare features (e.g., m/z , fragmentation masses, and method specific retention time) to confirm the identification of candidate metabolite. As indicated above, stage and grade of bladder cancer are crucial for clinical prognosis. Accordingly, three clinical subgroups of bladder cancer patients were recruited for the current study: patients with low-grade, early-stage (LgEs) cancer; patients with high-grade, early-stage (HgEs) cancer; and patients with high-grade, advanced-stage (HgAs) cancer. Age-matched hernia patients were selected as the control group for targeted quantification of these five metabolites and evaluation of their utility as bladder cancer biomarkers. Fig. 1 shows the workflow for targeting amine- and phenol-containing metabolites in bladder cancer urine using dansylation isotope labeling and LC-MS.

2. Material and methods

2.1. Reagents

Compounds used for dansylation, including sodium carbonate (NaHCO_3), sodium bicarbonate (Na_2CO_3), sodium hydroxide (NaOH), formic acid, and the authentic reference standards of the previously annotated putative urine biomarkers, 3-amino-2-piperidone, pyroglutamic acid, o-phosphoethanolamine, 5-hydroxyindoleacetic acid and uridine, and amino acid standards (#AAS 18) were purchased from Sigma–Aldrich (St. Louis, MO, USA). MS grade water, acetonitrile (ACN) containing 0.1% formic acid, and water containing 0.1% formic acid were also obtained from Sigma–Aldrich. Can and formic acid used as elution buffers for LC-UV were purchased from J.T. Baker-Avantor (Easton, PA, USA) and Sigma–Aldrich, respectively. Ultrapure water was obtained by purification using a Milli-Q system (Merck Millipore, Darmstadt, Germany). $^{12}\text{C}_2$ -Dansyl chloride ($^{12}\text{C}_2$ -DnsCl) was from Sigma–Aldrich, and $^{13}\text{C}_2$ -dansyl chloride ($^{13}\text{C}_2$ -DnsCl) was obtained from Wuxi Beita Pharmatech (Jiangsu, China).

2.2. Samples and preparation

2.2.1. Urine sample collection and preparation of quality control (QC) urine

All urine specimens were collected followed a previously established protocol [12]. In brief, the first morning urine was collected from each subject and kept on ice; thereafter, samples were filtered twice with 0.22 μm filters (Millipore) and stored at -80°C before dansylation labeling. All human urine samples were collected at Chang Gung Memorial Hospital in Taiwan with approval of the local Institutional Review Board.

In this study, metabolites discovered as bladder cancer biomarker candidates in our previous study were subjected to new quantitative analytical methods. Our original statistical analysis showed that these biomarkers exhibited differences in concentration between cancer and control specimens [12]. Clinical urine specimens included those from hernia patients (control group) and bladder cancer patients, the latter of which was further divided into three subgroups: LgEs, HgEs, and HgAs. An external quality control sample (QC urine) was prepared by pooling 150 human urine specimens followed by dansylation labeling for analysis by LC-MS. QC urine samples were analyzed daily to ensure the performance stability and reproducibility of the LC-MS system.

2.2.2. Dansylation labeling

The dansylation method used was based on a previous study by Peng and coworkers [12]. In brief, clinical urine samples were thawed at 4°C , and authentic reference standard compounds were dissolved in MS grade water (Fluka). Sample solutions were centrifuged at 10,000 rpm at 4°C for 10 min using an Eppendorf 5417R centrifuge to remove cells and debris before labeling.

Urine and standard compounds were labeled with $^{12}\text{C}_2$ -DnsCl and $^{13}\text{C}_2$ -DnsCl, respectively, by first adding 25 μl of 0.5 M $\text{NaHCO}_3/\text{Na}_2\text{CO}_3$ and 75 μl of dansyl chloride solution (1 mg in 80.5 μl of ACN) into 50 μl of each individual sample or 50 μl of the standard compounds (2 mM). Urine specimens were diluted with water if the concentrations of metabolites in original urines were high [13,14]. Dansylation reactions were performed by incubating sample mixtures at 40°C for 45 min on an orbital shaker at 200 rpm, and reactions were stopped by immediately transferring reaction mixtures to ice. The reaction was quenched by adding 10 μl of 250 mM NaOH, followed by shaking at 200 rpm at 40°C for 10 min. Samples on ice were prepped for LC-UV concentration determination by adding 50 μl of 425 mM formic acid in 50% ACN to each specimen.

2.2.3. Concentration normalization of dansylated metabolites by LC-UV

Since the efficiencies of dansylation of all metabolites from different urine samples may vary, a concentration normalization process is essential. To this end, we used an Acquity UPLC with ultra violet detection (Acquity TUV) system (Waters, Milford, MA, USA) to determinate the total concentration of dansylated metabolites after dansylation labeling.

A standard curve for quantification of dansylated metabolites was prepared by dansyl chloride labeling of a serially

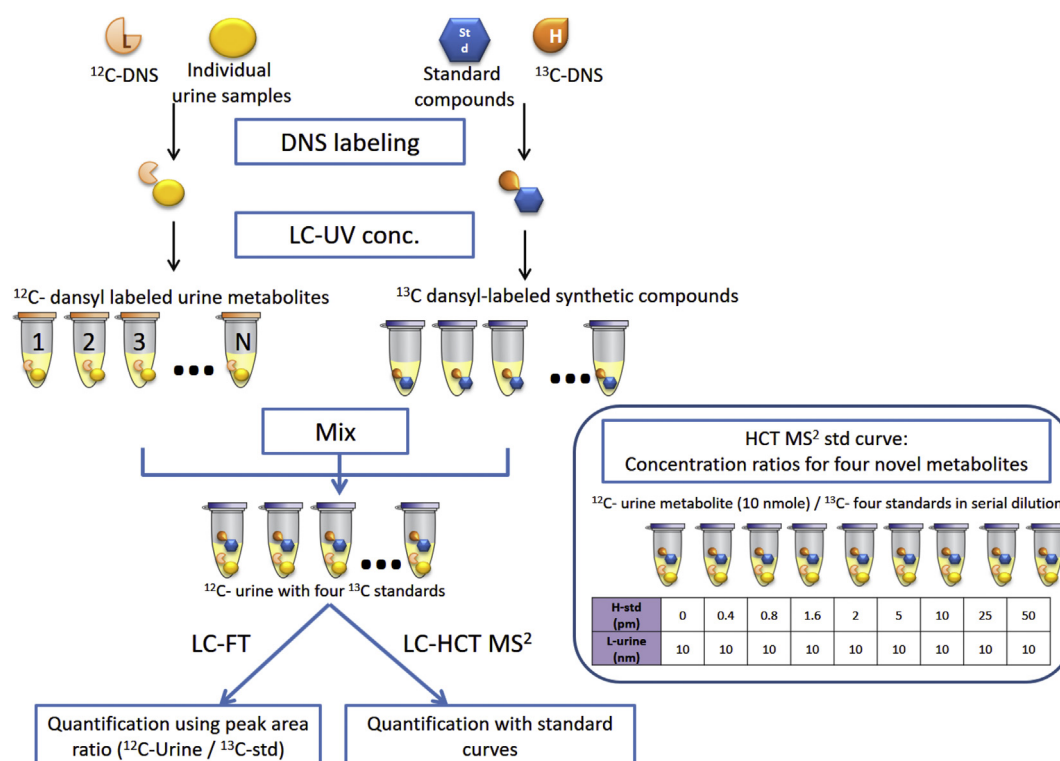


Fig. 1 – Workflow for targeting amine- and phenol-containing metabolites in bladder cancer urine using dansylation isotope labeling and LC-MS. Commercial standard compounds were labeled with ¹³C₂-DnsCl, spiked with ¹²C₂-DnsCl-labeled urinary metabolites, and then analyzed by LC-FT/MS and LC-HCT/MS. The blue block on the right represents serial dilutions used to prepare standard curves in LC-HCT/MS.

diluted (0.52, 1.3, 2.6, 5.2, and 7.8 mM) 18-amino-acid standard mixture, followed by LC with UV detection of absorption at 338 nm. LC-UV concentration normalization was performed by injecting 2 µl of labeled samples onto an ACQUITY LC-UV system (Waters) at a flow rate of 0.45 ml/min and eluting with the following gradient: 1% ACN (J.T. Baker) from 0 to 1 min, 95% ACN from 1 to 3 min; and 1% ACN from 3 to 6 min. A fixed amount (45 nmol) of each individual of ¹²C₂-Dns-labeled urine sample was spiked with the mixture of ¹³C₂-Dns-labeled standards (45 pmole for each compound). Samples were dried, re-dissolved in 30 µl 50% ACN containing 0.1% formic acid, and subsequently analyzed by LC/MS.

2.3. Sample analysis

2.3.1. MS analysis

Two mass specters, an ion trap MS (HCT/MS; Bruker Daltonics, Bremen, Germany), and a Fourier transform ion cyclotron resonance MS (FT/MS) system (Apex-Qe-SHEDS FTICR, 9.4 T; Bruker Daltonics, Bremen, Germany) were utilized for quantification of metabolites. Both MS systems were linked to an ACQUITY UPLC system (Waters), eluted with MS grade solvents (solvent A: 5% ACN in water containing 0.1% formic acid; solvent B: 99% ACN containing 0.1% formic acid) according to the following program: 0–2 min, 5% B; 2–3 min, 5% B to 15% B; 3–13 min, 15% B to 35% B; 13–25 min, 35% B to 70% B; 25–28 min, 70% B to 99% B; 28–30 min, 99% B; 30–30.1 min, 99% B to 5% B; 30.1–32.5 min, 5% B. All MS spectra were obtained in positive ion mode.

All samples for the two systems were prepared as described above. The optimized injection amount was 10 nmole (6.6 µl) of ¹²C₂-Dns-labeled endogenous urinary metabolites and 10 pmole of each ¹³C₂-Dns-labeled standard compound per LC-MS run. A QC sample was analyzed daily to ensure the stability of the system. Measurements of control group and study group samples were randomized to minimize instrument- and environment-related variations. Each metabolite sample was analyzed in triplicate in consecutive runs, with a wash run in between; an additional blank run (5% ACN containing 0.1% formic acid) was performed to prevent signal interference by carry-over between different clinical samples.

2.3.2. Confirmation of synthetic standards detection and relative quantification using LC-FT/MS system

An LC-FT/MS system with Waters binary management was configured by connecting an Acquity UPLC Waters system with an Acquity UPLC HSS T3 1.8 µm column (Waters) to an FT/MS system (Bruker). To investigate ionization abilities of these reference compounds without labeling, the compounds were dissolved at a concentration of 2 mM in LC-MS grade water (Fluka), then diluted to yield 10, 100, and 500 pmol/µl samples, which were injected separately by direct infusion at a flow rate of 180 µl/min apart from this, ionization and detectability of dansyl-labeled standard compounds (5, 10, and 50 pmol/run) were evaluated by injecting standards onto the LC-FT/MS system. The LC gradient used for LC-FT/MS analysis of individual specimen was the same as that used for LC-HCT/MS.

individual urine samples were labeled with $^{12}\text{C}_2$ -Dns. The endogenous concentration of targeted metabolites in urine samples was then quantified based on the signals of known concentrations of standard compounds using LC-FT/MS and LC-HCT/MS. The workflow for targeting amine- and phenol-containing metabolites in bladder cancer urine using dansylation isotope labeling and LC-MS is shown as Fig. 1.

To ensure the detectability of dansylated commercial standards, we injected 5, 10, and 50 pmole of dansylated standard compounds into the LC-FT/MS system. This analysis showed that four of the five labeled commercial standards (Supplementary Table 2)—O-phosphoethanolamine, 3-amino-2-piperidone, uridine, and 5-hydroxyindoleacetic acid—but not dansylated pyroglutamic acid, were detectable by UV and LC-MS. Therefore, only these four ^{13}C -standard compounds were targeted for the development of quantification methods based on optimization of MS^2 fragmentation using the LC-HCT/MS system.

Complex compounds in urine samples were analyzed by applying a LC system to separate metabolites of interest. The accuracy of quantitative results largely depends on establishing LC conditions under which the four targeting metabolites can be well separated. Accordingly, we investigated different LC conditions to determine optimal elution conditions for separation of commercial standards. Using these conditions (see Materials and methods), we found that, of the four dansylated standard compounds of interest, 3-amino-2-piperidone and uridine eluted with very similar retention times in LC-MS spectra, but the peaks of the remaining two metabolites were well separated.

3.1. Selection of MS^2 fragments using LC-HCT/MS and application for quantification

Using dansyl chloride-labeled standard compounds, we examined MRM fragments of the corresponding parent ions to evaluate suitable daughter ions that would not be susceptible to detect ion interference, ion suppression, or matrix effects contributed by the biological samples. As described above, the four detectable standard compounds were analyzed by HCT/MS by direct injection at a flow rate of 180 $\mu\text{L}/\text{min}$, followed by MS/MS fragmentation at the appropriate ion mass. The resulting MS^2 spectra from direct infusion in HCT MRM mode yielded the following daughter ions of the four labeled metabolites: 186.2, 188.2, 234.1 and 236.1 for dansylated 3-amino-2-piperidone; 252.1, 254.1277.1 and 279.1 for dansylated O-phosphoethanolamine; 366.1 and 368.2 for dansylated uridine; and 381.2 and 383.2 for dansylated 5-hydroxyindoleacetic acid.

Given the relatively short interval separating Dns-3-amino-2-piperidone (~11.7 min) and Dns-uridine (~12.6 min), we sought to collect specific daughter ions between these time frames for these particular metabolites. Hence, for MRM ionization on the LC-HCT system, we defined three time segments with appropriate ionized ions: (1) ionization of O-phosphoethanolamine (m/z 375.1 or m/z 377.1) from 5 to 9.5 min, (2) ionization of 3-amino-2-piperidone (m/z 348.2 or m/z 350.1) and uridine (m/z 478.1 or m/z 480.1) from 9.5 to 17.1 min, and (3) ionization of 5-hydroxyindoleacetic acid (m/z 425.1 or m/z 427.1) from 17.1 to 30 min. After comparison of the LC-MS experimental conditions of metabolomics profiling

[12] and targeted analyses by two LC-MS systems in this work, Eclipse plus C18 column (2.1 mm \times 100 mm, 1.8 μm), an Waters Acquity UPLC BEH C₁₈ (1.0 mm \times 100 mm, 1.7 μm) as well as Waters Acquity UPLC HSS T3 (1.0 mm \times 100 mm, 1.8 μm) were utilized for the metabolomic analysis [12], LC-HCT/MS and LC-FT/MS, respectively. To optimize each elution condition, LC gradient of elution solvents were different in these studies. The difference in elution order of 3-amino-2-piperidone and uridine in the previous work (Table 1A) could be caused by the different columns and gradient of LC systems.

3.2. Development of a method for measuring the urinary concentration of four targeted metabolites

Because we applied two mass systems in this study for analysis of biological samples, we needed to apply two different quantification methods. Although LC-FT is a high-resolution chromatographic technique, it may be susceptible to isobaric inference. Because peak area is based on parent ions under full-scan mode, there is a concern that other compounds with the same m/z value as the isobaric interference could contribute to peak areas. By contrast, the LC-HCT system is able to fragment parent ions into MS^2 or MS^3 , and thus is able to more reliably identify parent/daughter ion pairs as the correct compounds. However, the resolution of HCT/MS is lower than that of FT/MS. Accordingly, using both of these systems provides increased confidence in both the identification (LC-HCT/MS) and quantification (LC-HCT/MS) of the metabolites of interests.

Only five out of the ten putative metabolites were commercially available for the following work. Among the five metabolites, dimethylated-pyroglutamic acid standard could not be accurately quantified due to poor detectability by UV and MS. The identification of the metabolites was based on accurate mass of the MS result for searching metabolite databases to gain one or more putative identifications. The putative identification will need further validation experiment to confirm its true chemical identification. In this study, commercially available pyroglutamic acid standard after dimethylation was not detected on UV nor on MS. We speculated the reasons were possibly due to poor yield of dansylation during sample preparation, or low-ionization efficiency in MS analysis, or wrong putative identification in the database searching of the discovery phase of metabolite biomarker discovery. Metabolites were quantified based on the isotopic ratio of $^{12}\text{C}_2$ (endogenous metabolites) and known concentrations of $^{13}\text{C}_2$ -DnsCl-labeled metabolite standards. The first step in this process was identification of peaks of endogenous and standards of four of the five previously discovered metabolite biomarker candidates using isotopic pairs with accurate m/z and co-eluted retention times. For quantification by high-resolution FT/MS, EIC isotopic pairs for the four labeled analytes of interest were acquired according to the molecular weights listed in Supplementary Table 2. For quantification by HCT/MS, MS^2 signals in Table 1A were acquired in MRM mode, which has lower background interference. The defined peaks of the designated m/z values were extracted, and their areas were integrated and converted to measures of the concentrations of the corresponding

labeled metabolites by applying the arithmetic operation described below.

3.2.1. FT/MS – peak area ratio

The concentrations of metabolites of interest in individual urine specimens were calculated from the ratio of the corresponding $^{12}\text{C}_2$ -DnsCl-labeled metabolites to $^{13}\text{C}_2$ -DnsCl-labeled standards. To avoid possible interference from the matrix background, we first used high-resolution FT/MS to quantify these metabolite biomarker candidates. Since the amounts of $^{13}\text{C}_2$ -DnsCl-labeled standards are known (10 pmol), the quantities of labeled urinary metabolites in all individual urine specimens could be obtained by conversion of peak area ratios of $^{12}\text{C}_2$ -DnsCl-labeled metabolites to their corresponding $^{13}\text{C}_2$ -DnsCl-labeled standards. The relative quantification was obtained according to the formula below:

$$\text{Concentration of dansyl-labeled urinary metabolites} = 10 \text{ pmole} \times \frac{\text{Peak intensity of } ^{12}\text{C}_2\text{-Dansyl-labeled urinary metabolites}}{\text{Peak intensity of } ^{13}\text{C}_2\text{-Dansyl-labeled standards}}$$

3.2.2. HCT/MS – standard curve

To evaluate the dynamic range for quantification of the four endogenous metabolites, we established a response curve using HCT/MS in MRM scanning mode. A fixed amount of labeled, total endogenous urine metabolites was separately added into different concentrations of $^{13}\text{C}_2$ -DnsCl-labeled standards. Because the amount of the four metabolites in urine varied, the level of each $^{12}\text{C}_2$ -DnsCl-labeled metabolite in urine was calculated based on the peak areas of corresponding serially diluted $^{13}\text{C}_2$ -DnsCl-labeled standards

using the average peak areas ($n = 3$) of isotopically labeled metabolite pairs. The concentrations of the four detectable $^{12}\text{C}_2$ -DnsCl-labeled metabolites in urine samples were applied separately to the serially diluted $^{13}\text{C}_2$ -DnsCl-labeled standards (0, 0.4, 0.8, 1.6, 2, 5, 10, 25 and 50 pmol), yielding individual regression formulas for ratio-to-ratio plots for the different analytes. Each of the four response curves showed a linear response with good R^2 values, as shown in Fig. 2. Uridine (m/z 366.1) showed a remarkable drop in peak area for the 50 pmol $^{13}\text{C}_2$ -DnsCl-labeled standard; thus, this point was excluded from the standard curve. Using the resulting standard curves, we calculated the concentrations of the four urinary metabolites—o-phosphoethanolamine, 3-amino-2-piperidone, uridine and 5-hydroxyindoleacetic acid—in all individual clinical urine samples.

3.2.3. Correlation between HCT and FT quantification of metabolites

The performance of FT/MS and HCT/MS in terms of mass resolution and scan rates differs. Thus, taking into account signal interference, mass-to-charge accuracy and quantitative dynamic range, using a single system for quantification might be problematic. We thus next examined the correlation between metabolite quantification results obtained by HCT/MS and FT/MS. Concentration estimates for all four compounds were well correlated between the two methods,

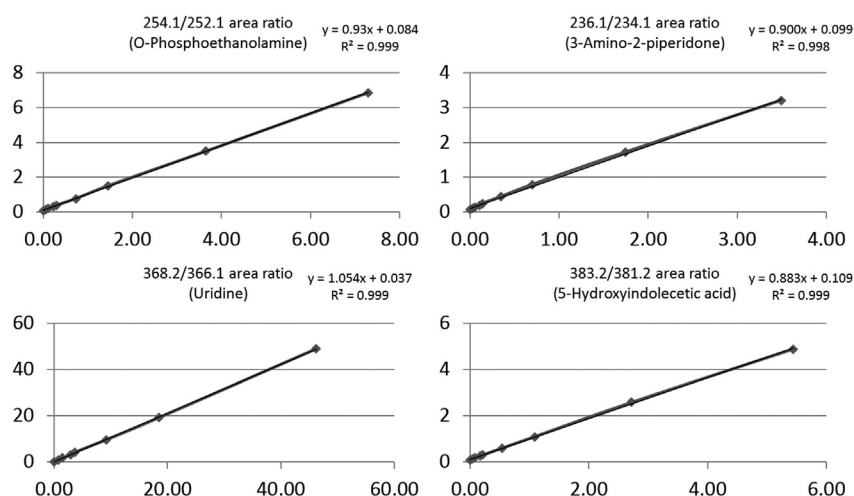


Fig. 2 – Response curves of dansylated standard compounds. Response curves are presented as the ratio of the dansylated standards to the corresponding dansylated endogenous urinary metabolites. Mass-to-charge (m/z) corresponds to MS^2 fragment ions obtained by LC-HCT/MS in MRM mode. Serial dilutions of $^{13}\text{C}_2$ -DnsCl-labeled standard concentrations (0, 0.4, 0.8, 1.6, 2, 5, 10, 25 and 50 pmole) were spiked with a fixed amount (10 nmole) of $^{12}\text{C}_2$ -DnsCl-labeled urinary metabolites. The x-axis is the concentration ratio and y-axis is the EIC peak area ratio ($^{13}\text{C}_2$ -DnsCl-labeled standards/ $^{12}\text{C}_2$ -DnsCl-labeled metabolites).

with Pearson *r*-values greater than 0.9; notably, the Pearson *r*-values for uridine and 5-hydroxyindoleacetic acid reached 0.99. Correlation plots of *o*-phosphoethanolamine and 3-amino-2-piperidone in urine exhibited some dispersion of points at higher levels of metabolites, resulting in a slight reduction in Pearson *r*-values (0.97). We then conducted an additional experiment to validate the precision and accuracy of the quantification methods used in the study. The standard curves of the four metabolites were established and quantification of a spiked sample based on the methods described in the method section (*n* = 3). A mixture of 10 pmol of each ¹³C₂-dansylated standard compounds (as internal standards for quantification) with ¹²C₂-dansylated endogenous urinary metabolites were measured first to quantify the endogenous concentration of four targeted metabolites based the peak area ratios of ¹²C₂- to ¹³C₂-dansylated signals. Then, comparison of quantitative results in triplicates of spiked ¹²C₂-dansylated standard compounds to their certified values (5 pmol) in the above mixture samples provided a measure of method accuracy and precision for the targeted metabolites. The results showed that the spike recoveries fell within the range of 80–120% for all the four compounds which is used for evaluation of accuracy. Among them, spike recoveries were within 90–110% for *o*-phosphoethanolamine and 5-hydroxyindoleacetic acid which showing good accuracy (Supplementary Table 4). The coefficient of variation (CV) values were all below 10% which were also satisfactory.

3.3. Comparison of concentrations of urinary metabolites between control and bladder cancer patients

To evaluate concentration differences between control and bladder cancer groups, we performed statistical analyses on urinary quantification data for the four metabolites in 119 clinical urine specimens. The clinical information of samples used in this study are listed as Table 1C. These analyses showed that urinary concentrations of two of the four urinary metabolites—*o*-phosphoethanolamine and uridine—were significant different between bladder cancer and control groups by both FT/MS (Fig. 3) and HCT/MS (Fig. 4). As shown in Tables 1B and C, the *o*-phosphoethanolamine concentration in urine samples from the bladder cancer group was ~1.6-times higher than that in the control group, based on HCT/MS. The urinary concentration of uridine was also higher significantly in bladder cancer patients than in the control group. Notably, *o*-phosphoethanolamine levels in bladder cancer patients, determined by HCT/MS, were correlated with cancer stage severity, exhibiting a 1.3-, 1.5-, and 1.9-fold increase compared with controls in LgEs, HgEs and HgAs subgroups, respectively. Results obtained using FT/MS were similar to those of HCT/MS (Table 1B, Fig. 5 and Supplementary Fig. 1). Furthermore, the small values of absolute differences between the two LC-MS systems indicated well correspondence in quantification of four target metabolites as shown in Supplementary Table 5. In contrast, there was no significant difference in the urinary concentration of 3-amino-2-piperidone or 5-hydroxyindoleacetic acid between hernia control and bladder cancer patients using either FT/MS or HCT/MS.

Table 1B – The amount average (pmole) of the four urinary metabolites in total amount of 10 nmol dansylated urine metabolites.

	FT/MS					HCT/MS				
	Mean (pmol) ± SEM					Mean (pmol) ± SEM				
	Hernia	BC	LgEs	HgEs	HgAs	Hernia	BC	LgEs	HgEs	HgAs
O-Phosphoethanolamine	3.86 ± 0.27	6.29 ± 0.5	5.19 ± 0.56	5.68 ± 0.62	8.01 ± 1.17	4.51 ± 0.29	7.08 ± 0.52	5.91 ± 0.61	6.76 ± 0.73	8.57 ± 1.21
3-Amino-2-piperidone	10.03 ± 0.54	11.53 ± 0.86	13.06 ± 1.78	11.97 ± 1.4	9.54 ± 1.17	10.07 ± 0.57	11.94 ± 0.91	13.44 ± 1.88	12.79 ± 1.64	9.59 ± 1.05
Uridine	0.72 ± 0.07	1.29 ± 0.24	1.23 ± 0.44	1.24 ± 0.27	1.40 ± 0.5	0.73 ± 0.07	1.32 ± 0.24	1.27 ± 0.47	12.79 ± 0.29	1.39 ± 0.47
5-Hydroxyindoleacetic acid	5.8 ± 0.4	6.43 ± 0.4	6.47 ± 0.88	6.75 ± 0.57	6.08 ± 0.64	5.95 ± 0.39	6.41 ± 0.38	6.46 ± 0.81	6.72 ± 0.54	6.05 ± 0.62

Table 1C – Clinical information of samples used in this study.

Classification	Diagnosis Status	Number of male Patients	Age
Hernia	Hernia	59	67.2 ± 7.6
Low grade/Early stage (LgEs) – BC	pTa	20	66.6 ± 12.1
High grade/Early stage (HgEs) – BC	Tis, pTa, pT1	20	67.3 ± 9.5
High grade/Advanced stage (HgAs) – BC	pT2, pT3, pT3b, pT4	20	65.8 ± 10.5

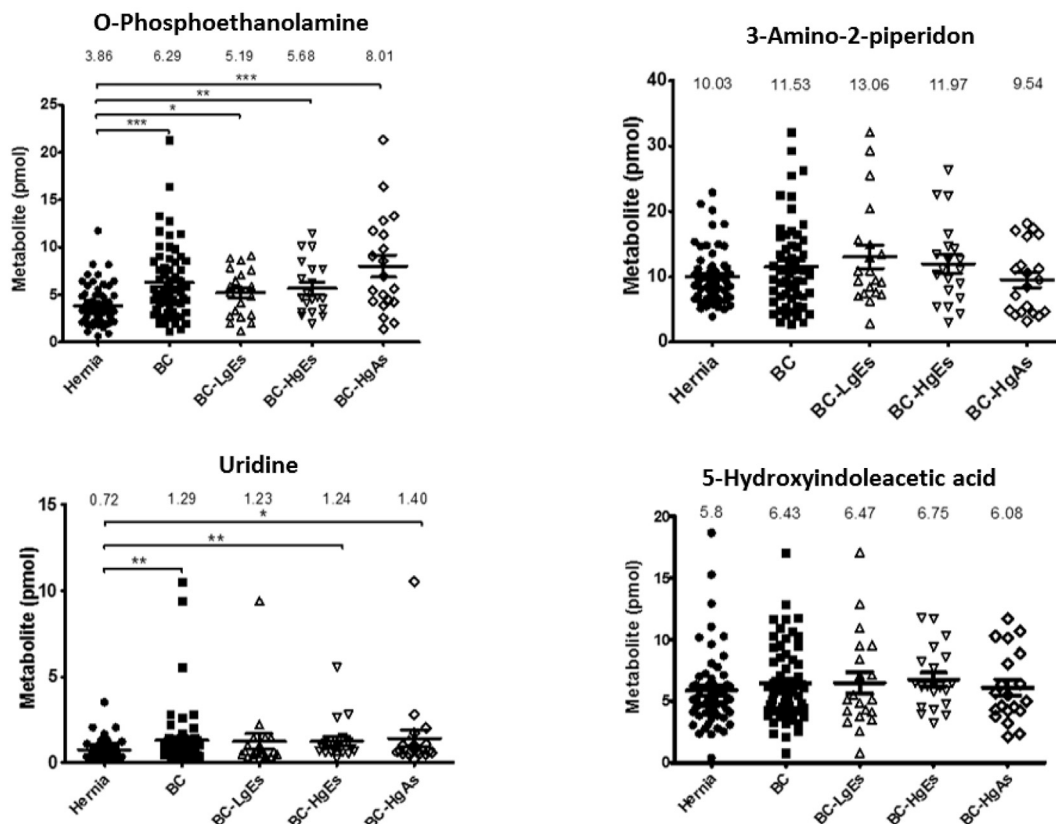
FT/MS scatter plots

Fig. 3 – Scatter plots of urinary metabolite concentrations (pmole) in different clinical groups obtained by LC-FT/MS. Each dot represents the concentration of a urinary metabolite from the analysis of LC-FT/MS data, expressed as means ± SEM (error bars). Labels: Hernia, control group (filled circles); BC, bladder cancer (total study group; filled squares); BC-LgEs, low-grade early-stage subgroup (open triangles); BC-HgEs, high-grade early-stage subgroup (open inverted triangles); BC-HgAs, high-grade advanced-stage subgroup (open diamonds). $P < 0.05$, $P < 0.01$, $***P < 0.001$; ns, not significant. Y-axis values are pmole of individual urinary metabolites in a total of 10 nmole.**

3.4. Diagnostic efficacies of four dansylated amine- and phenol-containing metabolites in detecting bladder cancer

It is conceivable that changes in the concentrations of urinary metabolites could result from factors other than diseases, such as age. Accordingly, we performed Chi square tests to investigate the relationship between age and metabolite levels in urines. Similar tests for effects of biological sex were not performed because all study subjects were male. For HCT/MS results on o-phosphoethanolamine, Pearson r-values for disease stage and age were 0.005 and 0.583, respectively (Supplementary Table 6), indicating that changes in o-phosphoethanolamine concentration were correlated with disease status rather than patients' age.

A previous study [12] reported 10 urinary metabolites as potential biomarkers for bladder cancer, five of which were examined in the current study. To test the performance of these metabolites as biomarkers, we carried out a receiver operating characteristic (ROC) curve analysis. In an analysis of single-marker performance (Fig. 6), we found that o-phosphoethanolamine (m/z 252.1) in the HCT/MS system was moderately predictive, with an AUC (area under the curve) of 0.709; the AUC for uridine was 0.654. Combining these two biomarkers improved the AUC to 0.726 (Fig. 7), indicating that this two-biomarker panel has better predictive value than either single biomarker alone. Odds-ratio analysis was also performed to estimate that the different degrees of bladder cancer response to o-phosphoethanolamine in this study

HCT/MS scatter plots

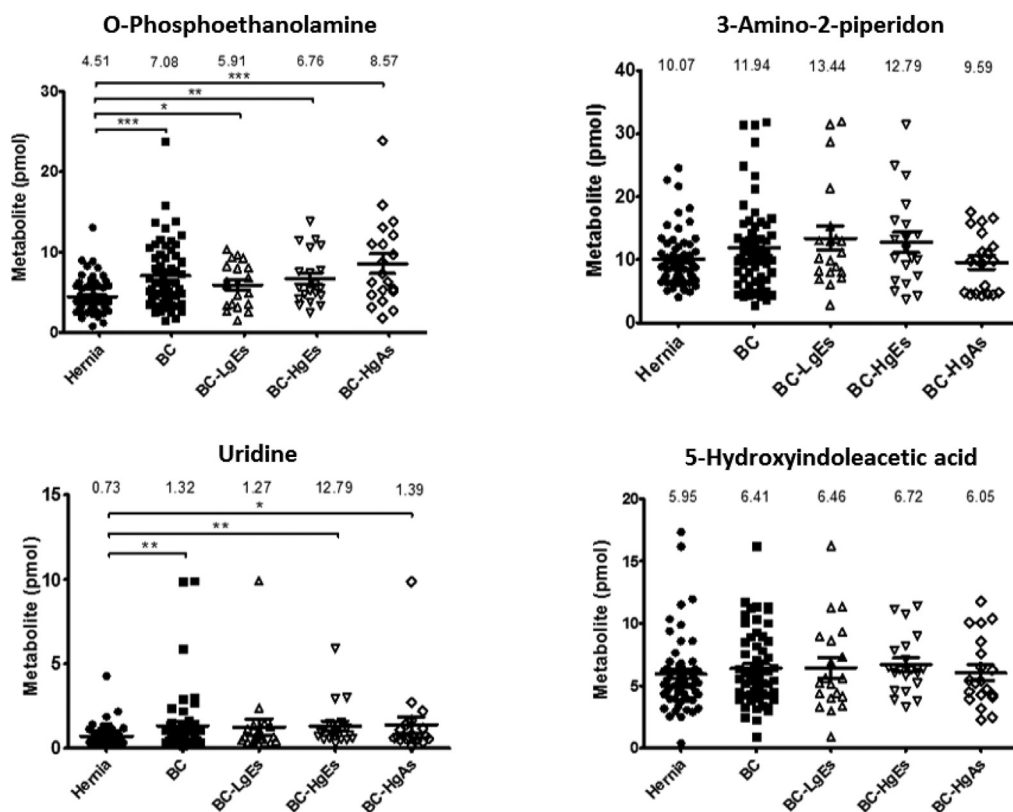


Fig. 4 – Scatter dot plots of urinary metabolic concentrations (pmole) of LC-HCT/MS results in different clinical groups. Each dot represents the concentration of a urinary metabolite from the analysis of LC-HCT/MS data, expressed as means \pm SEM (error bars). Labels: Hernia, control group (filled circles); BC, bladder cancer (total study group; filled squares); BC-LgEs, low-grade early-stage subgroup (open triangles); BC-HgEs, high-grade early-stage subgroup (open inverted triangles); BC-HgAs, high-grade advanced-stage subgroup (open diamonds). $P < 0.05$, $**P < 0.01$, $***P < 0.001$; ns, not significant. Y-axis values are pmole of individual urinary metabolites in a total of 10 nmole.

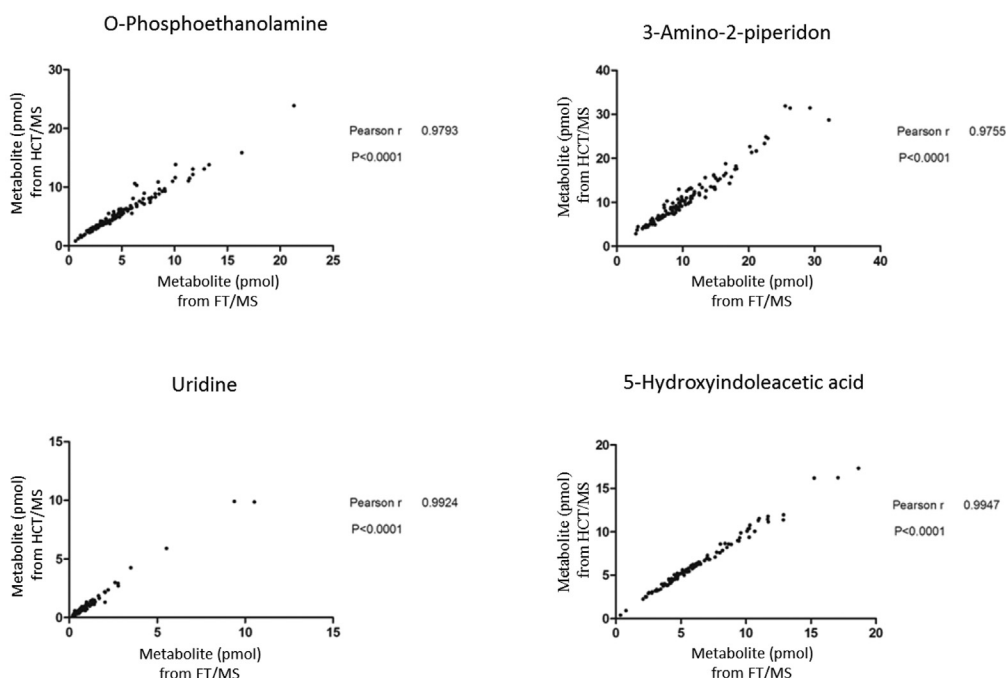
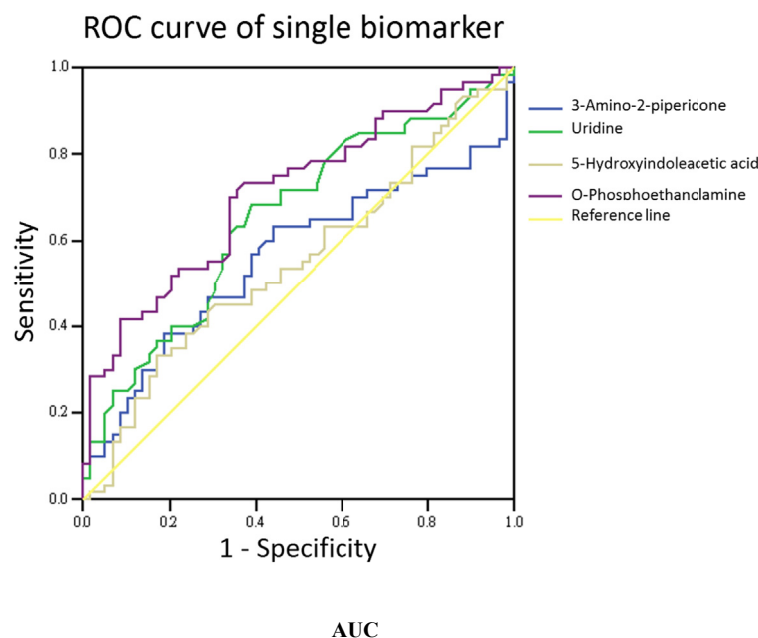


Fig. 5 – Correlation of quantitative results obtained by LC-HCT/MS and LC-FT/MS. Quantitative results obtained by LC-FT/MS are shown in the x-axis and results of LC-HCT/MS are shown in the y-axis.



Putative biomarkers	AUC	Std. Error(a)	Sig.(b)	95% Confidence interval for Difference	
				Lower bound	Upper bound
3-Amino-2-piperidone	.561	.054	.248	.456	.667
Uridine	.654	.050	.004	.555	.752
5-Hydroxyindoleacetic acid	.550	.053	.345	.446	.654
O-Phosphoethanolamine	.709	.047	.000	.616	.802

The test result variable(s): 3-Amino-2-piperidone, uridine, 5-hydroxyindoleacetic acid, O-phosphoethanolamine value has at least one tie between the positive actual stage group and the negative actual state group. Statistics may be biased.

(a) Under nonparametric assumption

(b) N hypothesis: true area = 0.5

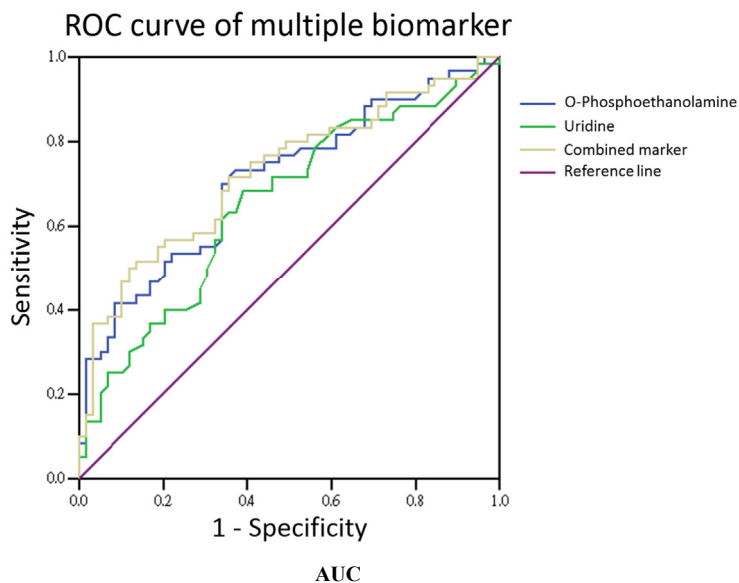
Fig. 6 – Single-biomarker performance. The performance of four urinary metabolites, quantified by LC-HCT/MS, as single markers of bladder cancer was evaluated using ROC curve analysis. The AUC for O-phosphoethanolamine was 0.709.

(Fig. 8). The cut off values of the analysis were determined by the sensitivity and specificity of ROC curve, which were equal to or greater than 0.6 with lower false-possibility. The odd-ratios with 95% confidence interval (CI) of hernia versus BC LgEs, HgEs and HgAs were 3.361 (1.162–9.721), 5.429 (1.729–17.039) and 7.8 (2.3–26.449), respectively. The odd ratios were greater than 1 and increased along the severity of bladder cancer in the study indicating a positive correlation between the metabolite and the severity of bladder cancer subgroups.

4. Discussion

The field of metabolomics has become increasingly important for exploring markers of changes in biological reactions that are associated with pathophysiology, environmental toxicity, changes in biological mechanisms, or disease [15,16]. This technology is considered as a complementary tool for genomics, transcriptomics, and proteomics approaches, given that the genome-scale changes detected by these latter

approaches occur at a higher, upstream level, and might not be reflected in subsequent changes in regulation or components [16]. Additionally, analyzing metabolites in urine is a non-invasive means for biomarker discovery—an advantage for clinical practice and diagnosis. Difficulties in analyzing metabolites in biological fluids include the high complexity of biological matrices, detection limits, and lower confidence in metabolite identification. Moreover, many hydrophilic metabolites are not likely to be retained on the reverse-phase columns commonly employed, resulting in difficulties in separating and analyzing complex mixtures. Dansylation labeling [8] represents a promising approach for increasing sensitivity and detection probability of compounds with specific functional groups, namely primary amines, secondary amines, or phenolic hydroxyl group(s) [8]. In the current study, clinical samples used for verification were collected, prepared, and analyzed according to the method described above. Using differential $^{12}\text{C}_2$ -/ $^{13}\text{C}_2$ -isotope dansylation labeling, we were able to explore analytes by identifying correct peak pairs of $^{12}\text{C}_2$ -labeled endogenous metabolites and corresponding $^{13}\text{C}_2$ -labeled commercial metabolite standards,



Putative markers	AUC	Std. Error(a)	Sig.(b)	95% Confidence interval for Difference	
				LowerBound	Upper Bound
O-phosphoethanolamine	.709	.047	.000	.616	.802
Uridine	.654	.050	.004	.555	.752
combined markers	.726	.047	.000	.634	.817

The test result variable(s): O-phosphoethanolamine, uridine value has at least one tie between the positive actual stage group and the negative actual state group. Statistics may be biased.

(a) Under nonparametric assumption

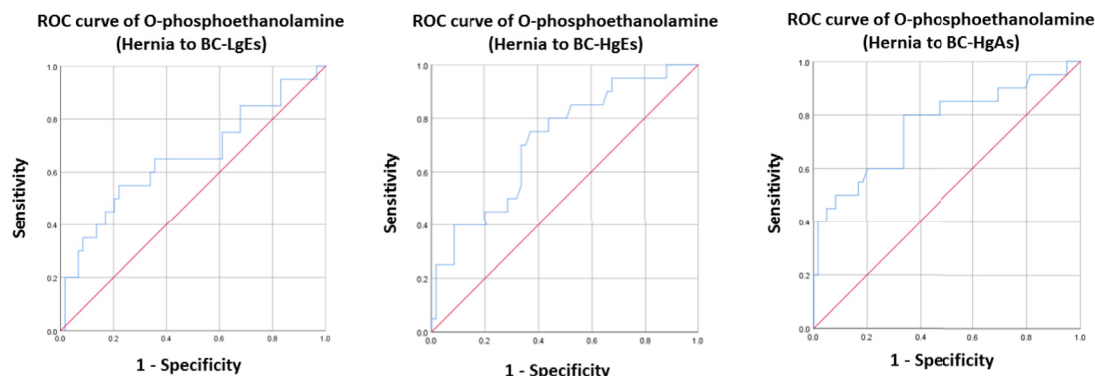
(b) N hypothesis: true area = 0.5

Fig. 7 – Two-biomarker panel performance. The four urinary metabolites, quantified by LC-HCT/MS, were combined by logistic regression, and the performance of multi-biomarker panels in detecting bladder cancer was assessed by ROC curve analysis. The performance of O-phosphoethanolamine and uridine as single markers is shown for comparison. The AUC for the performance of the o-phosphoethanolamine and uridine two-biomarker panel in detecting bladder cancer was increased to 0.726.

an approach that correctly and precisely targets metabolites with high confidence.

Because of clinical or biological variability, candidate biomarkers identified in the discovery stage need to be validated across a different set of individual samples. There are several reasons that part of the biomarker candidates that discovered in the previously work have not been verified successfully in this study. This could be the causes of different patient enrollment or LC systems between pervious work and this study. Besides, the identification of the metabolites in the previous work was potential biomarkers obtained from database according to accurate molecular weight, yet their true identification required further validation. The comparison of patient enrollment between discovery and verification phases is shown in [Supplementary Table 3](#). Only low percentage (5.5%) of patients were used in both metabolomics profiling and targeted quantification which was good for evaluation of biological variation. A biomarker candidate verification phase eliminates this bottleneck in biomarker development pipeline by ensuring that only the most promising putative biomarkers found in discovery go on to the validation stage.

The reason that we did not use the same LC methods in two LC-MS systems was due to the routine setting of two LC systems. In this work, the main purpose was targeted quantification of metabolite for verification the clinical performance of potential metabolite biomarkers. The metabolite identity could be confidently confirmed using the commercial standards although the LC methods of two MS systems were different. The first issue encountered in establishing a quantitative workflow for novel metabolite biomarkers is confirmation of the correctness of metabolite identification, determined by reference to a metabolite database based on accurate molecular masses. Therefore, a high-resolution MS system is required to confirm detected m/z signals and retention times in an LC-MS run. Fourier transform mass spectrometry (FT/MS) is known for its high accuracy and resolution, which are beneficial for metabolite identification. However, the ion capture mode in FT/MS has a limited ability to accurately quantify metabolites owing to its relative slow scan speed, which limits the number of data points during signal acquisition. Despite its accuracy, FT/MS is susceptible to effects of the complexity of analytes in urine sample, which



	Area under ROC	Sensitivity/ specificity	Odds	95% Confidence Interval
Hernia to BC-LgEs	0.654	0.60 / 0.644	3.361	1.162 ~ 9.721
Hernia to BC-HgEs	0.715	0.70 / 0.664	5.429	1.729 ~ 17.039
Hernia to BC-HgAs	0.758	0.75 / 0.661	7.800	2.3 ~ 26.449

Fig. 8 – The ROC curves of hernia group to BC-LgEs, BC-HgEs and BC-HgAs separately. The cut offs were defined as where the points on curves were close to the left top point (sensitivity = 1) and with lowest false-possibility.

may result in other molecules with the same mass-to-charge signal after ionization contributing to peak areas. In this case, signal interference caused by matrix complexity results in imprecise quantification. To overcome this issue, we implemented an additional MS system—HCT/MS—which has compensatory properties relative to FT/MS. Specifically, HCT/MS is capable of multiple-reaction monitoring (MRM), which gives information about chemical fragments, meaning that it is complementary to FT/MS for molecular quantification.

The second quantification method, LC-HCT/MS in MRM mode—an ion trap system that is robust and easy to use, and delivers a rapid MSⁿ function—was used to establish response curves for quantifying the four targeted amine- and phenol-metabolite in clinical urine specimens. The response curves also provided insight into ion suppression by matrix effects of the complex biological mixture. Moreover, based on scatter plots (Figs. 3 and 4) and response curves (Fig. 2), quantified urinary metabolites fell within reasonable measurement ranges, despite some outliers. In summary, the targeted metabolites could be quantified based on standard curves and provided accurate estimates of concentration using a simple ion-trap MS system. Notably, quantitative results obtained for the four amine- and phenol-metabolites using the two MS systems (Table 1B, Figs. 3 and 4) were highly correlated.

There was a slight, but significant, increase in the concentrations of the metabolites, uridine and o-phosphoethanolamine, in the bladder cancer group compared with the control group, whereas the other two metabolites showed no significant difference between groups. Of these two metabolites, o-phosphoethanolamine concentrations in urine

correlated with disease stage severity, increasing from low-grade early stage (LgEs), to high-grade early stage (HgEs) and high-grade advanced stage (HgAs). This suggests that o-phosphoethanolamine could be an indicator of bladder cancer generally as well as a marker of disease stage. However, the fold-changes in both uridine and o-phosphoethanolamine concentrations in urine samples from the bladder cancer group compared with those from the hernias group were not remarkable. Therefore, because changes in metabolite levels can be related to other factors (e.g., age, biological sex, hematuria), we performed Chi square tests on o-phosphoethanolamine levels to test the possible role of age in addition to disease stage (Supplementary Tables 2 and 3). These analyses demonstrated that o-phosphoethanolamine levels were related to bladder cancer, but did not likely reflect age effects.

Metabolites are the final products of a series of complex biological processes, and reflect the involvement of numerous gene-scale regulatory events, including transcription, as well as post-transcriptional and post-translational mechanisms. Moreover, various molecules are likely associated with complex interactions within a single pathway and the multiple regulatory cross-links among molecular and biological modifications involved in the development of cancer [17]. Given this, using a single metabolite as a disease biomarker may not provide a powerful, or even valid, clinical approach for diagnosing or predicting a disease. Accordingly, it is important to consider the use of multiple biomarkers in the form of a biomarker panel using ROC curve analysis together with logistic regression. To this end, we analyzed ROC curves to assess the performance of single and combined biomarkers

(Fig. 7). As a single biomarker (Fig. 6), o-phosphoethanolamine was confirmed to be capable of discriminating bladder cancer urine from control urine specimens. When combined with uridine, the resulting two-biomarker panel showed improved ability to discriminate between these two groups. Of these two urinary panel members, o-phosphoethanolamine is an important metabolite that is involved in phospholipid metabolism and is associated with several key cellular functions, including cell membrane turnover and lipid signaling pathways that regulate cell proliferation and survival; it may also exert therapeutic effects in animal melanoma models [18]. However, detailed mechanisms underlying the potential role of o-phosphoethanolamine in bladder cancer biology remain unclear and will require further study. In summary, we verified that urinary phosphoethanolamine is a potential non-invasive biomarker for use in bladder cancer screening that shows improved discriminating power when combined with uridine in a two-biomarker panel.

5. Conclusions

In this study, ^{12}C -/ ^{13}C -isotope dansylation labeling was utilized as a platform to quantify four targeted phenol- and amine-containing metabolites in urine samples and evaluate the performance of these metabolites as non-invasive biomarkers of bladder cancer. Using dansyl chloride-labeled synthetic standards, we verified the identity and quantify ability of four previously discovered novel urinary metabolites, and assessed their performance in differentiating bladder cancer specimens from control specimens. Two different MS systems—HCT/MS and FT/MS—were used for quantification, and the results obtained with the two systems were well correlated. This indicates that the platform is practical and accessible for use in precisely and accurately evaluating urinary metabolite levels. Although FT/MS offers high accuracy of m/z analysis, it has limitations including high cost and intense maintenance. On the other hand, HCT/MS is relative cost-effective and the MRM method established in the study is practical for clinical screening, such as newborn blood screening using tandem mass spectrometric platform. Therefore, as the consideration of accessibility and applicability, targeted analysis of patient specimens performed with an LC-HCT/MS or similar instrumentation is more practical for clinical screening. The results of quantification showed that o-phosphoethanolamine increased in the urine of bladder cancer patients, independent of the age of patients. Therefore, o-phosphoethanolamine is a potential biomarker for bladder cancer diagnosis. Diagnostic performance was further improved by combining uridine and o-phosphoethanolamine in a two-biomarker panel.

Conflicts of interest

The authors declare no conflict of interest.

Acknowledgement

This research was supported by grants from the Ministry of Science and Technology of Taiwan, Republic of China (106-2113-M-182-001-MY2), and Chang Gung Memorial Hospital (CMRPD1G0131, CMRPD1G0132, CMRPD3E0251, CMRPD3E0252, and BMRPD78). The instrumental and data analysis resources were supported by the proteomic core lab (CLRPD190017) at Chang Gung University, Taoyuan, Taiwan. This work was financially supported by the “Molecular Medicine Research Center, Chang Gung University” from The Featured Areas Research Center Program within the framework of the Higher Education Sprout Project by the Ministry of Education (MOE) in Taiwan.

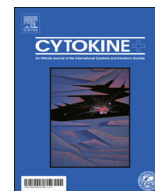
Appendix A. Supplementary data

Supplementary data to this article can be found online at <https://doi.org/10.1016/j.jfda.2018.11.008>.

REFERENCES

- [1] Society AC. Cancer facts & figures 2018. 2018.
- [2] Kirkali Z, Chan T, Manoharan M, Algaba F, Busch C, Cheng L, et al. Bladder cancer: epidemiology, staging and grading, and diagnosis. *Urology* 2005;66:4–34.
- [3] Chang SS, Boorjian SA, Chou R, Clark PE, Daneshmand S, Konety BR, et al. Diagnosis and treatment of non-muscle invasive bladder cancer: AUA/SUO guideline. *J Urol* 2016;196:1021–9.
- [4] Alberice JV, Amaral AF, Armitage EG, Lorente JA, Algaba F, Carrilho E, et al. Searching for urine biomarkers of bladder cancer recurrence using a liquid chromatography-mass spectrometry and capillary electrophoresis-mass spectrometry metabolomics approach. *J Chromatogr A* 2013;1318:163–70.
- [5] Ganti S, Weiss RH. Urine metabolomics for kidney cancer detection and biomarker discovery. *Urol Oncol* 2011;29:551–7.
- [6] Huang Z, Lin L, Gao Y, Chen Y, Yan X, Xing J, et al. Bladder cancer determination via two urinary metabolites: a biomarker pattern approach. *Mol Cell Proteomics* 2011;10. M111 007922.
- [7] Evans AM, DeHaven CD, Barrett T, Mitchell M, Milgram E. Integrated, nontargeted ultrahigh performance liquid chromatography/electrospray ionization tandem mass spectrometry platform for the identification and relative quantification of the small-molecule complement of biological systems. *Anal Chem* 2009;81:6656–67.
- [8] Guo K, Li L. Differential ^{12}C -/ ^{13}C -isotope dansylation labeling and fast liquid chromatography/mass spectrometry for absolute and relative quantification of the metabolome. *Anal Chem* 2009;81:3919–32.
- [9] Guo K, Bamforth F, Li L. Qualitative metabolome analysis of human cerebrospinal fluid by ^{13}C -/ ^{12}C -isotope dansylation labeling combined with liquid chromatography Fourier transform ion cyclotron resonance mass spectrometry. *J Am Soc Mass Spectrom* 2011;22:339–47.

- [10] Wu Y, Li L. Dansylation metabolite assay: a simple and rapid method for sample amount normalization in metabolomics. *Anal Chem* 2014;86:9428–33.
- [11] Zhou R, Li L. Quantitative metabolomic profiling using dansylation isotope labeling and liquid chromatography mass spectrometry. *Methods Mol Biol* 2014;1198:127–36.
- [12] Peng J, Chen YT, Chen CL, Li L. Development of a universal metabolome-standard method for long-term LC-MS metabolome profiling and its application for bladder cancer urine-metabolite-biomarker discovery. *Anal Chem* 2014;86:6540–7.
- [13] Han W, Li L. Matrix effect on chemical isotope labeling and its implication in metabolomic sample preparation for quantitative metabolomics. *Metabolomics* 2015;11:1733–42.
- [14] Panuwet P, Hunter Jr RE, D'Souza PE, Chen X, Radford SA, Cohen JR, et al. Biological matrix effects in quantitative tandem mass spectrometry-based analytical methods: advancing biomonitoring. *Crit Rev Anal Chem* 2016;46:93–105.
- [15] Timbrell JA. Biomarkers in toxicology. *Toxicology* 1998;129:1–12.
- [16] van Ravenzwaay B, Cunha GC, Leibold E, Looser R, Mellert W, Prokoudine A, et al. The use of metabolomics for the discovery of new biomarkers of effect. *Toxicol Lett* 2007;172:21–8.
- [17] Urquidi V, Rosser CJ, Goodison S. Molecular diagnostic trends in urological cancer: biomarkers for non-invasive diagnosis. *Curr Med Chem* 2012;19:3653–63.
- [18] Mambelli LI, Teixeira SF, Jorge SD, Kawamura B, Meneguelo R, Barbuto JAM, et al. Phosphoethanolamine induces caspase-independent cell death by reducing the expression of C-RAF and inhibits tumor growth in human melanoma model. *Biomed Pharmacother* 2018;103:18–28.



Anti-inflammatory property of quercetin through downregulation of ICAM-1 and MMP-9 in TNF- α -activated retinal pigment epithelial cells

Shu-Chen Cheng^{a,b,1}, Yi-Hong Wu^{c,d,1}, Wen-Chung Huang^{e,f}, Jong-Hwei S. Pang^{b,g},
Tse-Hung Huang^{d,h}, Ching-Yi Cheng^{e,h,i,*}

^a Department of Traditional Chinese Medicine, Chang Gung Memorial Hospital, Taoyuan, Taiwan

^b Graduate Institute of Clinical Medical Sciences, College of Medicine, Chang Gung University, Taoyuan, Taiwan

^c Division of Chinese Internal Medicine, Center for Traditional Chinese Medicine, Chang Gung Memorial Hospital, Taoyuan, Taiwan

^d School of Traditional Chinese Medicine, College of Medicine, Chang Gung University, Taoyuan, Taiwan

^e Graduate Institute of Health Industry Technology, Research Center for Chinese Herbal Medicine and Research Center for Food and Cosmetic Safety, College of Human Ecology, Chang Gung University of Science and Technology, Taoyuan, Taiwan

^f Division of Allergy, Asthma, and Rheumatology, Department of Pediatrics, Chang Gung Memorial Hospital, Taoyuan, Taiwan

^g Department of Physical Medicine and Rehabilitation, Chang Gung Memorial Hospital, Taoyuan, Taiwan

^h Department of Traditional Chinese Medicine, Chang Gung Memorial Hospital, Keelung, Taiwan

ⁱ Department of Ophthalmology, Chang Gung Memorial Hospital, Linkou, Taiwan

ARTICLE INFO

Keywords:

Retinal pigment epithelial cells

Inflammation

Quercetin

Cytokine

ABSTRACT

Quercetin is a flavonoid polyphenolic compound present in fruits and vegetables that has proven anti-inflammatory activity. The goal of the present investigation was to investigate the effects of quercetin on tumor necrosis factor- α (TNF- α)-induced inflammatory responses via the expression of ICAM-1 and MMP-9 in human retinal pigment epithelial cells (ARPE-19 cells). Real-time PCR, gelatin zymography, and Western blot analysis showed that TNF- α induced the expression of ICAM-1 and MMP-9 protein and mRNA in a time-dependent manner. These effects were attenuated by pretreatment of ARPE-19 cells with quercetin. Quercetin inhibited the TNF- α -induced phosphorylation of PKC δ , JNK1/2, ERK1/2. Quercetin, rottlerin, SP600125 and U0126 attenuated TNF- α -stimulated c-Jun phosphorylation and AP-1-Luc activity. Pretreatment with quercetin, rottlerin, SP600125, or Bay 11-7082 attenuated TNF- α -induced NF- κ B (p65) phosphorylation, translocation and RelA/p65-Luc activity. TNF- α significantly increased MMP-9 promoter activity and THP-1 cell adherence, and these effects were attenuated by pretreatment with quercetin, rottlerin, SP600125, U0126, tanshinone IIA or Bay 11-7082. These results suggest that quercetin attenuates TNF- α -induced ICAM-1 and MMP-9 expression in ARPE-19 cells via the MEK1/2-ERK1/2 and PKC δ -JNK1/2-c-Jun or NF- κ B pathways.

1. Introduction

Retinal pigment epithelial cells (RPEs) form the cell layer between photoreceptor outer segments and choriocapillaris [1]. RPEs have multiple functions including phagocytosis of shed photoreceptor outer segments, maintenance of the blood–retinal barrier, secretion of cytokine, chemokines, and growth and neurotrophic factors, and immune defense of the central retina [2–6]. Because of their strategic location and vital functions, RPEs play a central role in the pathogenesis of

various retinal inflammatory diseases, and their dysfunction and atrophy can lead to vision loss [2,7].

Retinal inflammation contributes to vision-threatening injury and is a pathogenic factor in most retinal diseases such as uveitis [8], diabetic retinopathy [9], and age-related macular degeneration (AMD) [4]. These retinal inflammatory diseases have certain similarities, including the presence of an inflammatory response throughout the course of disease and activation of inflammatory proteins such as intercellular adhesion molecule-1 (ICAM-1) [10–13] and matrix metalloproteinases

Abbreviations: ICAM-1, Intercellular adhesion molecule-1; MMP-9, matrix metalloproteinase-9; ARPE-19 cells, human retinal pigment epithelial cells; TNF- α , Tumor necrosis factor- α

* Corresponding author at: Graduate Institute of Health Industry Technology, Research Center for Chinese Herbal Medicine and Research Center for Food and Cosmetic Safety, College of Human Ecology, Chang Gung University of Science and Technology, 261 Wen-Hwa 1st Road, Guishan Dist., Taoyuan City, Taiwan.

E-mail address: jennycheng@mail.cgu.edu.tw (C.-Y. Cheng).

¹ Shu-Chen Cheng and Yi-Hong Wu made equal contributions to this paper.

<https://doi.org/10.1016/j.cyto.2019.01.001>

Received 27 April 2018; Received in revised form 29 December 2018; Accepted 2 January 2019

1043-4666/ © 2019 Elsevier Ltd. All rights reserved.

(MMPs). ICAM-1, a cell-surface glycoprotein, can facilitate recruitment of leukocytes to the site of tissue damage or infection [14] and thereby plays an important role in inflammatory processes. During retinal inflammation, ICAM-1 is strongly expressed in both retinal vascular endothelial cells and RPECs, where it contributes to severe retinal damage [15]. MMP levels are upregulated in many eye diseases including AMD, glaucoma, and diabetic retinopathy [16–18]. Among the MMPs, MMP-2 (gelatinase A) and MMP-9 (gelatinase B) expressions are increased in Bruch's membrane in association with AMD, especially in the choroidal new vessel area [19–21]. Increased MMP-2 and MMP-9 expressions have also been observed in the retina and vitreous in diabetic retinopathy [22]. Administration of inhibitors of ICAM-1 or MMPs is an attractive potential therapy and is being investigated in several experiments [23–25]. Understanding the roles of inflammatory mediators will provide a rationale for a therapeutic approach to treating retinal inflammatory diseases.

Quercetin is a natural flavonoid that is ubiquitously present in herbs, fruits, and vegetables such as berries, onions, tea, and apples, and has proven anti-inflammatory, antioxidant, antiangiogenic, anticancer, and antiapoptotic effects [26,27]. Recently, the use of quercetin to treat eye diseases has gained attention. It has been shown that quercetin downregulates the expression of monocyte chemoattractant protein-1 (MCP-1), interleukin 6 (IL-6), and IL-8 through the p38 and ERK1/2 pathways in human retinal pigment epithelial cells (ARPE-19 cells) [28]. Quercetin also inhibits Nuclear factor kappa B (NF- κ B) and caspase-3 expression, which protect against retinal neurodegeneration and oxidative stress in rats with streptozotocin-induced diabetes [29]. In addition, quercetin reduces MMP-2, MMP-9, ICAM-1, and VCAM-1 expression in a dry eye model [30]. Although the anti-inflammatory function of quercetin has been studied in several fields and the related multiple signaling molecules have received considerable attention, the mechanisms underlying the quercetin-mediated protection of RPECs against the effects of ICAM-1 and MMPs remain poorly understood.

In this study, we investigated whether quercetin can downregulate TNF- α -induced expression of ICAM-1 and MMP-9 in RPECs. We report for the first time that quercetin reduces the TNF- α -induced expression of ICAM-1 and MMP-9 through inhibition of the Protein kinase C δ (PKC δ)–JNK1/2, ERK1/2–c-Jun, or NF- κ B (p65) pathways in human RPECs. A better understanding of these underlying mechanisms may provide important insights for understanding the development of, and possibly preventing, retinal inflammation.

2. Materials and methods

2.1. Materials

Anti-phospho-c-Jun, anti-phospho-PKC δ , anti-phospho-NF- κ B (p65), anti-phospho-ERK1/2, and anti-phospho-JNK1/2 antibodies were from Cell Signaling Technology (Danvers, MA, USA). Anti-ICAM-1, anti-GAPDH, anti-NF- κ B (p65) and anti-lamin B antibodies were from Santa Cruz Biotechnology (Santa Cruz, CA, USA). Bay 11-7082, tanshinone IIA, rottlerin, SP600125, SB202190, and U0126 were from Enzo Life Sciences (Farmingdale, NY, USA). Human recombinant TNF- α was from R&D Systems (Minneapolis, MN, USA). All other reagents were obtained from Sigma-Aldrich (St. Louis, MO, USA). Quercetin was from Biotic Chemical Co., Ltd. (New Taipei City, Taiwan). Stock solution of quercetin was prepared in a 1:9 (v/v) mixture of dimethyl sulfoxide and 99% ethanol, and then diluted to the desired final concentration with culture medium.

2.2. Cell culture

ARPE-19 cells were purchased from Bioresource Collection and Research Center (Hsinchu City, Taiwan) and maintained in DMEM/F-12 (Gibco BRL, Grand Island, NY, USA), supplemented with 10% (v/v) FBS (HyClone, Logan, Utah, USA), sodium bicarbonate, and antibiotics

(50 ng/ml gentamycin, 100 U/ml penicillin G, 100 μ g/ml streptomycin; all from HyClone) at 37 °C in a humidified 5% CO₂ atmosphere.

2.3. Preparation of cell extracts and Western blot analysis

Growth-arrested ARPE-19 cells were incubated with TNF- α at 37 °C for the indicated times. When 100 μ M quercetin or inhibitors of JNK1/2 (SP600125), PKC δ (rottlerin), MEK1/2 (U0126), or NF- κ B (Bay 11-7082) were used, they were added 1 h before addition of TNF- α . The highest concentrations used of these inhibitors did not cause any toxic effects on ARPE-19 cells (data not shown). After treatment, ARPE-19 cells were rapidly rinsed with ice-cold PBS and solubilized in lysis buffer (25 mM Tris-HCl, pH 7.4, 25 mM NaCl, 25 mM NaF, 25 mM sodium pyrophosphate, 1 mM sodium vanadate, 2.5 mM EDTA, 2.5 mM EGTA, 0.05% (w/v) Triton X-100, 0.5% (w/v) SDS, 0.5% (w/v) deoxycholate, 0.5% (w/v) NP-40, 5 μ g/ml leupeptin, 5 μ g/ml aprotinin, and 1 mM PMSF) for 30 min on ice. The lysates were centrifuged at 15,000 rpm for 10 min at 4 °C. A Pierce BCA protein assay kit (Thermo Fisher Scientific, Rockford, IL, USA) was used to measure the protein concentration.

Samples (30 μ g protein) were denatured, subjected to SDS-PAGE using a 10% running gel, and then transferred to PVDF membranes. Membranes were blocked with blocking buffer (Visual Protein, Taipei, Taiwan) for 60 min and then incubated with specific primary antibodies, including anti-phospho-c-Jun, anti-phospho-PKC δ , anti-phospho-NF- κ B (p65), anti-phospho-ERK1/2, anti-phospho-JNK1/2, anti-ICAM-1, anti-GAPDH, and anti-lamin B at a dilution of 1:1000 in blocking buffer overnight at 4 °C. After incubation, membranes were washed extensively with Tween-Tris buffered saline and then incubated with a 1:10,000 dilution of anti-mouse or anti-rabbit horseradish peroxidase-conjugated secondary antibodies for 1 h at room temperature. Finally, the immunoreactive bands developed by ECL reagents were captured and analyzed using a ChemiDoc XRS+ system (Bio-Rad Laboratories, Inc., Hercules, CA, USA).

2.4. Total RNA extraction, RT-PCR, and real-time PCR

ARPE-19 cells were treated with or without drugs (quercetin or Bay 11-7082) for 1 h before exposure to TNF- α for the indicated times. Total RNA was extracted with TRIzol reagent (Sigma-Aldrich) according to the manufacturer's protocol. A microspectrophotometer (Nano-100; Allsheng Instruments, Hangzhou City, China) was used to measure the RNA concentration, and RNA was then reverse-transcribed into cDNA using an iScript cDNA Synthesis Kit (Bio-Rad). The synthesized cDNA was amplified using PCR, and the PCR products were assessed by agarose gel electrophoresis. The expression of β -actin was used as an internal control for the assay of a constitutively expressed gene. The primers used were as follows: 5'-CAGTGACCATCACAGCTTTCCGG-3' (sense) and 5'-GCTGCTACCACAGTGATGATGACAA-3' (anti-sense) for ICAM-1; 5'-CTAGAAGCATTTGCGGTGGACGATGGAGGG-3' (sense) and 5'-TGACGGGGTCACCCACACTGTGCCCATCTA-3' (anti-sense) for β -actin.

Using the cDNA templates, real-time PCR was performed using SYBR Green PCR reagents (Bio-Rad). The $\Delta\Delta$ Ct values were calculated, and the results are expressed as the ratio of the target gene mRNA copies to β -actin copies. All data are expressed as the fold change in mRNA expression relative to that in the control cells. The primers for real-time PCR spanning exon-exon boundaries were designed using a PrimerQuest® Tool software (Integrated DNA Technologies Pte. Ltd., Singapore, Republic of Singapore). The primers used were as follows: 5'-TGCATAAGGACGACGTGAAT-3' (sense) and 5'-GTGTGGTGGTGGTTGGAG-3' (anti-sense) for MMP-9; 5'-ACCATCTACAGCTTCCGGC-3' (sense) and 5'-CTGAGACCTCTGGCTTCGTC-3' (anti-sense) for ICAM-1.

2.5. Cell viability assay

Viability of ARPE-19 cells was determined using the 3-(4,5-dimethylthiazol-2-yl)-2,5-diphenyltetrazolium bromide (MTT) assay (Sigma-Aldrich). Cells were seeded into 96-well plates and then treated with quercetin (0.001–1000 μM) for 24 h, after which, the 0.5 mg/ml MTT solution was added to each well. The wells were incubated at 37 °C for 30 min, and the plates were analyzed using a SpectraMax i3x microplate reader (Molecular Devices, CA, USA) at 570 nm. Cell viability was calculated as $\text{OD (quercetin)}/\text{OD (control)} \times 100\%$. The assay was performed in triplicate at each concentration.

2.6. Immunofluorescence staining

ARPE-19 cells were plated into six-well culture plates with coverslips. When inhibitors were used, they were added 1 h before application of 15 ng/ml TNF- α . After treatment, cells were washed with warm PBS, fixed with 4% paraformaldehyde for 15 min, permeabilized with 0.3% Triton X-100, blocked with PBS containing 5% bovine serum albumin, and stained with an anti-p65 antibody. The coverslips were mounted with aqueous mounting medium with DAPI (Vector Laboratories, Burlingame, CA, USA). The images were observed using a fluorescence microscope (Leica Microsystems, Wetzlar, Germany).

2.7. Monocyte adhesion assay

ARPE-19 cells were seeded into six-well culture plates. When quercetin or inhibitors were used, they were added 1 h before application of TNF- α for 6 h at 37 °C in a humidified 5% CO₂ atmosphere. THP-1 cells (human acute monocytic leukemia cell line, obtained from ATCC) were labeled with a fluorescent dye (5 μM calcein AM) at 37 °C for 30 min in RPMI-1640 medium (Gibco) in the dark. The labeled THP-1 cells (5×10^5 cells/ml) were added to plates containing ARPE-19 cells, and the plates were incubated at 37 °C for 1 h and then washed gently with PBS three times to remove nonadherent THP-1 cells. The numbers of fluorescently labeled adherent THP-1 cells were counted in five random fields using a fluorescence microscope (Leica Microsystems).

2.8. Gelatin zymography

The conditioned medium was collected and mixed with 5 \times non-reducing sample buffer and electrophoresed on a 10% polyacrylamide gel containing 0.15% gelatin as the MMP substrate. After electrophoresis, the gel was washed in 2.5% Triton X-100 for 30 min to remove SDS and then incubated in developing buffer on a rotary shaker for 96 h at 37 °C. After incubation, the gel was stained with staining buffer (30% methanol, 10% acetic acid, and 0.5% (wt/vol) Coomassie brilliant blue) for 30 min and then destained. Gelatinolytic activity was manifested as horizontal white bands on a blue background.

2.9. Measurement of AP-1-, NF- κ B- and MMP-9-luciferase (Luc) activity

To prepare the AP-1-Luc, RelA/p65-Luc and MMP-9 plasmids, the human AP-1 promoter region (−861 to +146 bp), RelA/p65 promoter region (−620 to +323 bp) and MMP-9 promoter region (−720 to −11) were inserted between *Mlu*I and *Bgl*II sites of the pLightSwitch_Prom vector (SwitchGear Genomics, Inc, Carlsbad, CA, USA). All plasmids were prepared using an EasyPrep EndoFree Maxi Plasmid Extraction Kit (Biotools Co., Ltd, New Taipei City, Taiwan). Plasmid transient transfection of ARPE-19 cells was performed according to the protocol for Lipofectamine 3000 reagent (Thermo Fisher Scientific, Rockford, IL, USA). Briefly, ARPE-19 cells were plated in six-well culture plates. At 70–80% confluence, the cells were washed with PBS and cultured in 1 ml of Opti-MEN (Gibco BRL). The reporter DNA (2 μg) and β -galactosidase DNA (0.5 μg) were mixed with 5 μl of

Lipofectamine 3000 reagent in 250 μl of Opti-MEN for 10 min at room temperature. The mixture was gently added to plates containing ARPE-19 cells at 37 °C and, 4 h later, 1 ml of antibiotics-free DMEM/F-12 containing 10% FBS was added for 24 h. After transfection, the cells were shifted to DMEM/F-12 containing 1% FBS medium for 24 h. TNF- α was added to the medium for the indicated times. When quercetin or inhibitors were used, they were added 1 h before application of TNF- α . Cell extracts were prepared, and luciferase and β -galactosidase activities were measured. RelA/p65-Luc and MMP-9-Luc activity was determined using a luciferase assay system (Biotools) according to the manufacturer's instructions. The luciferase activities were standardized to β -galactosidase activity.

2.10. Statistical analysis

Data is combined from three independent experiments with three replicate samples per group in each experiment. The intensity of the bands on the Western blotting and gelatin zymography were assessed by Image Lab software (Bio-Rad). THP-1 monocyte adhesion assay was quantified using Image J software (W. Rasband, NIH, USA). Quantitative data were estimated using the GraphPad Prism program (GraphPad, San Diego, CA, USA) and are expressed as mean \pm SD. One-way ANOVA followed by Tukey's post hoc test was used to identify significant differences between multiple groups. A P-value of < 0.05 was considered significant.

3. Results

3.1. TNF- α induced the expression of ICAM-1 and MMP-9 in ARPE-19 cells

The expression of ICAM-1 and MMP-9 proteins is associated with eye diseases such as dry eye [30]. To explore the expression of TNF- α -induced ICAM-1 and MMP-9 in ARPE-19 cells, cells were treated with different concentrations of TNF- α for designated times (2, 4, 6, 18, and 24 h for ICAM-1 protein level; 1 and 4 h for ICAM-1 mRNA level; 48 and 72 h for MMP-9 mRNA and protein levels). TNF- α induced ICAM-1 protein expression and MMP-9 enzymatic activity in a positive time- and concentration-dependent manner, as shown in Fig. 1A, B, D and E. Real-time PCR was used to measure the levels of ICAM-1 and MMP-9 mRNA in TNF- α -stimulated ARPE-19 cells. After the TNF- α stimulation, the levels of ICAM-1 and MMP-9 mRNA were significantly upregulated in a time-dependent manner within 4 h and 72 h, respectively (Fig. 1C and F). These observations suggest that the ICAM-1 and MMP-9 expression was induced by TNF- α at both the translational and transcriptional levels in ARPE-19 cells.

3.2. Quercetin inhibited the expression of ICAM-1 and MMP-9 induced by TNF- α in ARPE-19 cells

Quercetin, a flavonoid polyphenolic compound, possesses antioxidant and anti-inflammatory properties in RPECs [28,31,32]. Before examining the effect of quercetin on TNF- α -induced ICAM-1 and MMP-9 expression, the viability of ARPE-19 cells was measured after quercetin treatment. As shown in Fig. 2A, quercetin at 0.001–100 μM had almost no influence on the cell viability of ARPE-19 cells, although quercetin at 1000 μM significantly reduced ARPE-19 cell viability. Therefore, quercetin was used at concentrations $\leq 100 \mu\text{M}$ in the following study to explore the pharmacological mechanisms of quercetin's effects on TNF- α -induced ICAM-1 or MMP-9 expression. Before incubation with TNF- α (15 ng/ml), ARPE-19 cells were treated with quercetin at different concentrations (10, 50, or 100 μM). Pretreatment with quercetin significantly inhibited ICAM-1 protein expression in a concentration-dependent manner (Fig. 2B) and reduced the mRNA level (Fig. 2C).

To investigate how quercetin affects TNF- α -induced MMP-9 expression, ARPE-19 cells were pretreated with quercetin at different

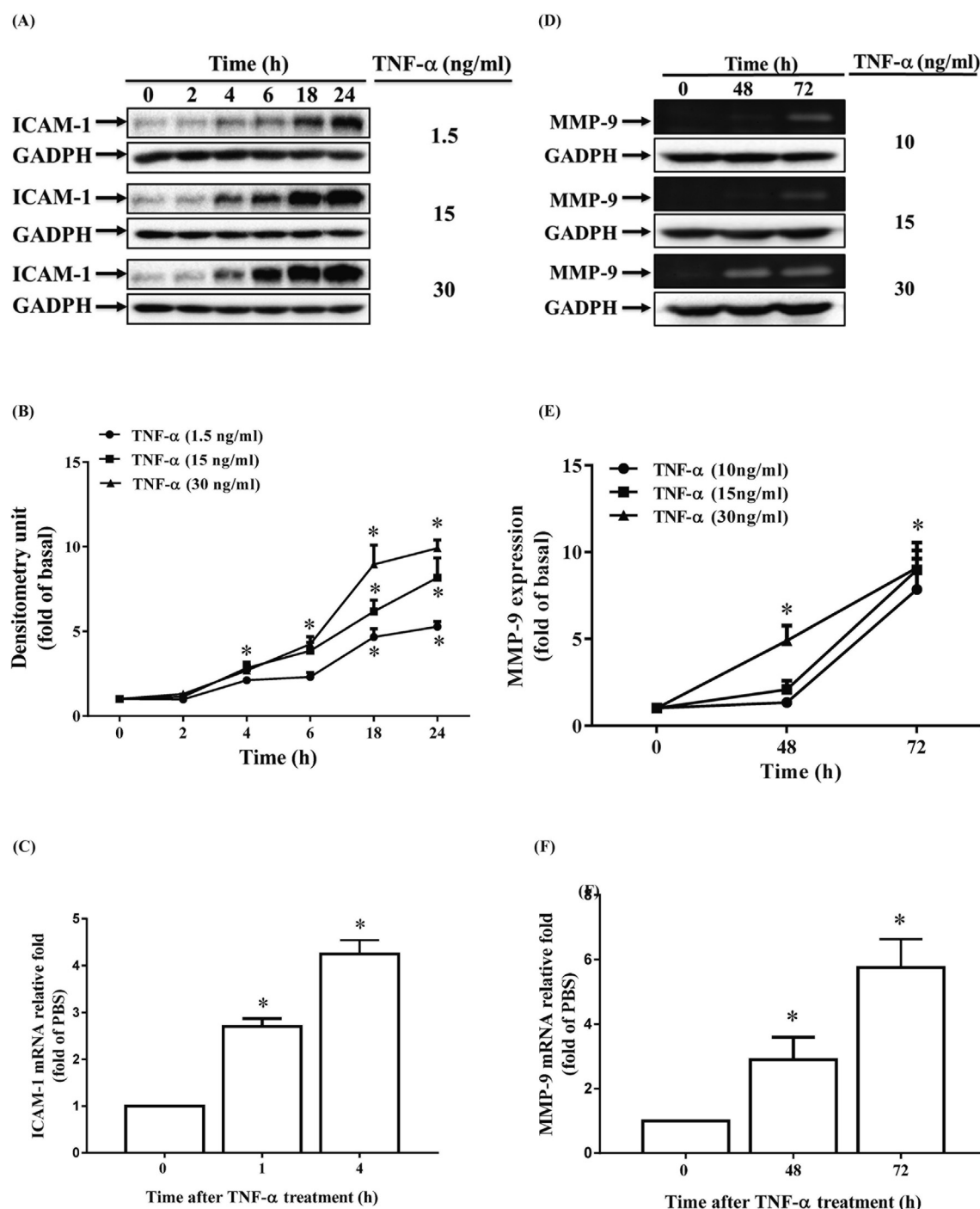


Fig. 1. TNF- α induces the expression of ICAM-1 and MMP-9 in ARPE-19 cells. TNF- α was used at different concentrations to stimulate ARPE-19 cells for designated times (2, 4, 6, 18 and 24 h for ICAM-1 protein level; 1 and 4 h for ICAM-1 mRNA level; 48 and 72 h for MMP-9 mRNA and protein levels) (A) ICAM-1 protein expression was detected by Western blotting. (B) ICAM-1 protein expression in cells used in the experiments shown in (A) was quantified by an image lab software. (C) ICAM-1 RNA transcripts were analyzed by real-time PCR (D) MMP-9 expression was analyzed by gelatin zymography. (E) MMP-9 expression in cells used in the experiments shown in (D) was quantified by an Image Lab software. (F) MMP-9 RNA transcripts were analyzed by real-time PCR. Data were obtained from at least three independent experiments and are expressed as mean \pm SD. *P < 0.05 compared with the basal level.

concentrations (5, 10, or 50 μ M) for 1 h and then incubated with TNF- α (30 ng/ml) for 48 h. Quercetin significantly attenuated both TNF- α -induced MMP-9 expression and mRNA level (Fig. 2D and E).

3.3. Quercetin attenuated ICAM-1 and MMP-9 expression induced by TNF- α in ARPE-19 cells via the PKC δ -JNK1/2-c-Jun pathway

Lee et al. reported that TNF- α -induced ICAM-1 expression was

mediated through the PKC δ -JNK1/2-c-Jun cascade in human RPECs [14]. To investigate whether quercetin inhibits TNF- α -induced ICAM-1 and MMP-9 expression through this pathway in ARPE-19 cells, the cells were pretreated with quercetin for 1 h and then incubated with TNF- α for 5, 10, 15, 30 and 60 min. As shown in Fig. 3A–C, PKC δ phosphorylation decreased, but this effect was not statistically significant. Quercetin also significantly attenuated TNF- α -induced JNK1/2 and c-Jun phosphorylation.

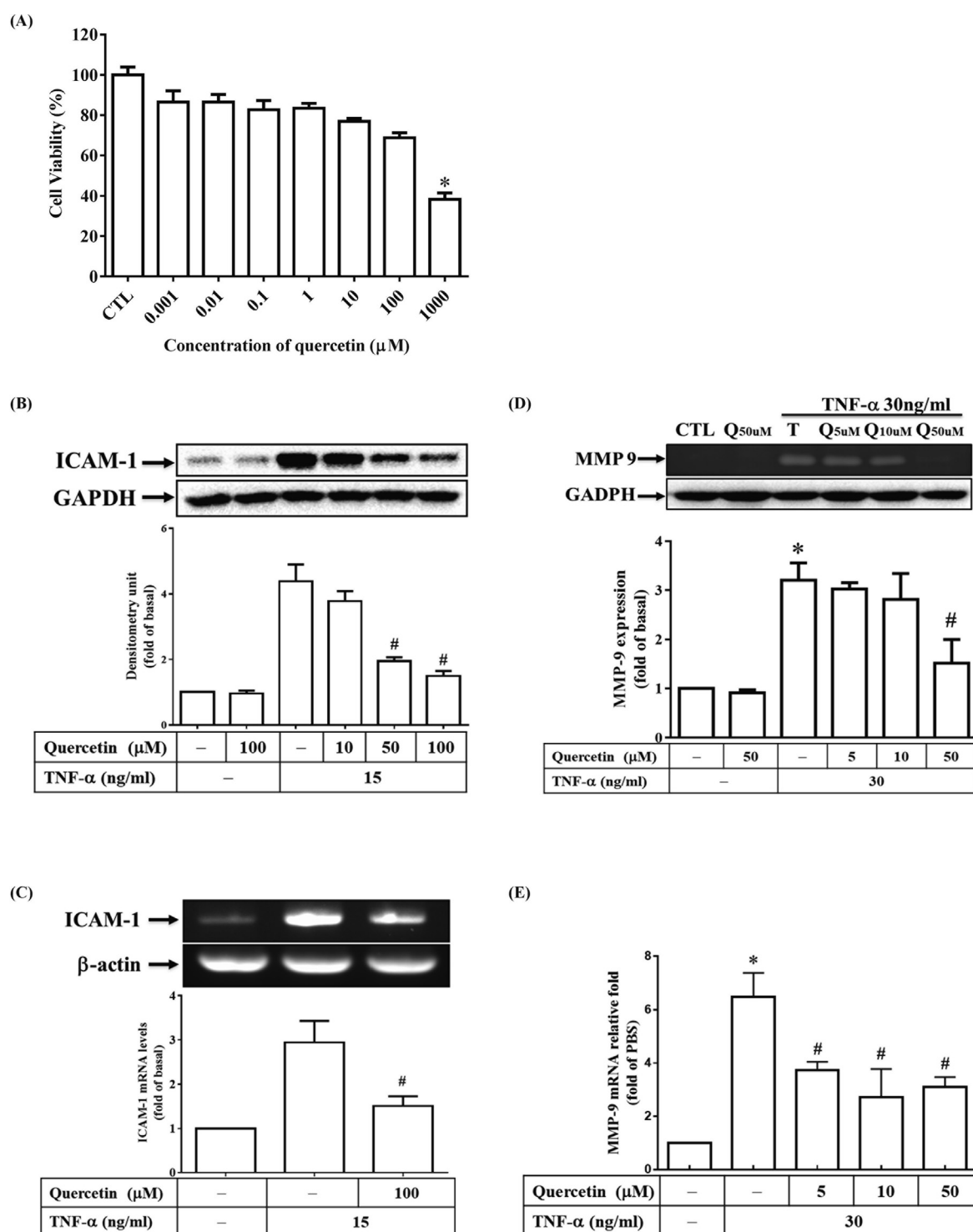


Fig. 2. Quercetin attenuates the expression of ICAM-1 and MMP-9 induced by TNF-α in ARPE-19 cells. (A) Effects of quercetin on the viability of ARPE-19 cells. ARPE-19 cells were treated with different concentrations of quercetin (0.001–1000 μM) for 24 h and the cell viability was analyzed using the MTT assay. ARPE-19 cells were incubated with TNF-α in the presence of quercetin for (B) 6 h, (C) 4 h, and (D, E) 48 h. (B, C) ICAM-1 protein expression and mRNA level were measured by (B) Western blotting and (C) RT-PCR and real-time PCR, respectively. (D, E) MMP-9 zymogen activity and mRNA level were analyzed by (D) gelatin zymography and (E) real-time PCR, respectively. (B) ICAM-1 protein expression was quantified using Image Lab software. (D) MMP-9 proteolytic activity was manifested as white bands on a blue background, and GADPH expression was used as an internal control. Data were obtained from at least three independent experiments and are expressed as mean ± SD. *P < 0.05 vs. control cells. #P < 0.05 vs. TNF-α-stimulated cells.

Next, SP600125 (a JNK1/2 inhibitor) and rottlerin (a PKCδ inhibitor) were used to investigate the relationship between PKCδ, JNK1/2, and c-Jun in the TNF-α-induced response. As shown in Fig. 3D and E, SP600125 and rottlerin downregulated JNK1/2 and c-Jun phosphorylation in TNF-α-stimulated ARPE-19 cells. These results suggest that

quercetin decreased TNF-α-induced ICAM-1 and MMP-9 expression via the PKCδ–JNK1/2–c-Jun pathway.

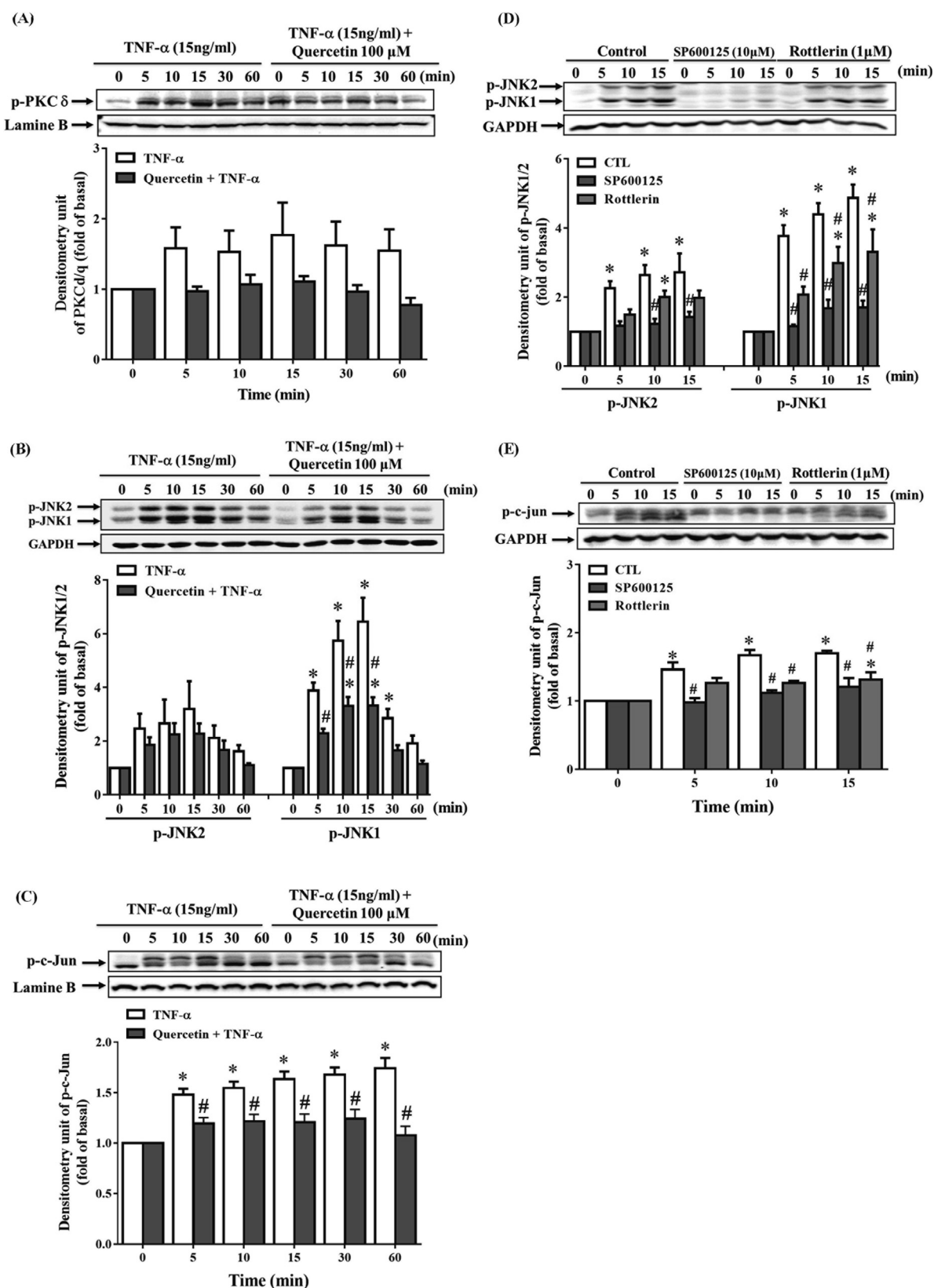


Fig. 3. Quercetin attenuates TNF- α -induced PKC δ -JNK1/2-c-Jun activation in ARPE-19 cells. ARPE-19 cells were pretreated with (A–C) quercetin, (D, E) SP600125 or rottlerin for 1 h, and the cells were then stimulated with 15 ng/ml TNF- α for designated times (5, 10, 15, 30 and 60 min for Quercetin; 5, 10 and 15 min for SP600125 and rottlerin). Phosphorylation of (A) PKC δ , (B, D) JNK1/2, or (C, E) c-Jun were analyzed by Western blotting. Data were obtained from at least three independent experiments and are expressed as mean \pm SD. *P < 0.05, vs. control cells. #P < 0.05 vs. TNF- α -stimulated cells.

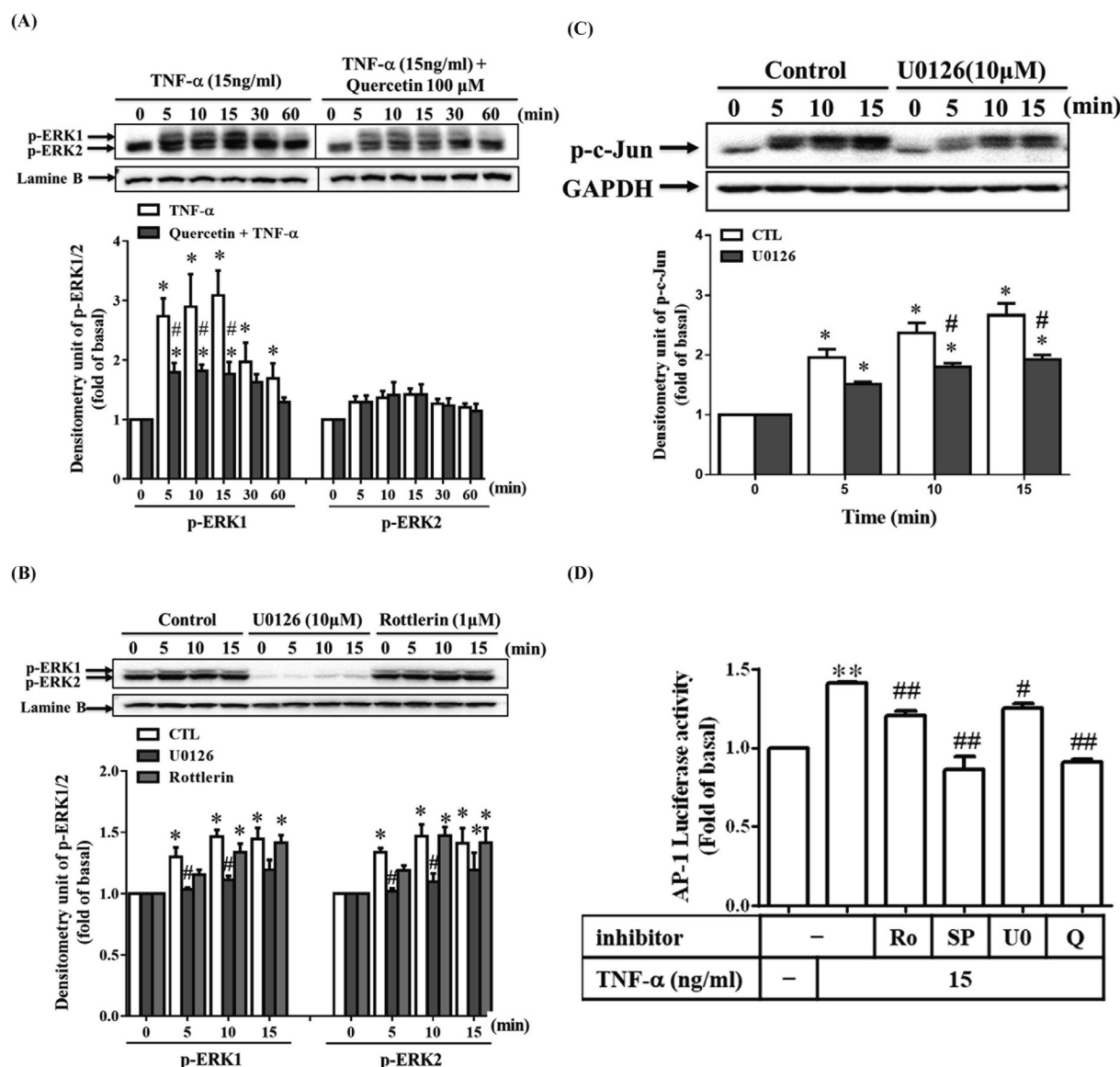


Fig. 4. Quercetin inhibits the TNF- α -activated MEK1/2-ERK1/2 pathway in ARPE-19 cells. ARPE-19 cells were pretreated with (A) quercetin, (B) rottlerin, or (B, C) U0126 for 1 h before stimulation with TNF- α for designated times. Phosphorylation of (A, B) ERK1/2 or (C) c-Jun was analyzed by Western blotting (D) To determine AP-1 promoter activity, ARPE-19 cells were transfected with AP-1-Luc and β -galactosidase plasmids. The cells were then pretreated with rottlerin (1 μ M), SP600125 (10 μ M), U0126 (10 μ M), or quercetin (100 μ M) for 1 h and then exposed to TNF- α for 1 h. Luciferase activity was determined. Data were obtained from at least three independent experiments and are expressed as mean \pm SD. *P < 0.05 vs. control cells. #P < 0.05 vs. TNF- α -stimulated cells.

3.4. Quercetin reduced ICAM-1 and MMP-9 expression induced by TNF- α in ARPE-19 cells via the MEK1/2-ERK1/2-c-Jun pathway

Previous studies have shown that TNF- α promoted ICAM-1 production through ERK1/2 phosphorylation in different cell types such as human lung epithelial alveolar and umbilical vein endothelial cells [33–35]. We first investigated the effects of quercetin on TNF- α -stimulated ERK1/2 phosphorylation. As shown in Fig. 4A, quercetin noticeably decreased TNF- α -induced ERK1/2 phosphorylation. We then examined the effect of a MEK1/2 inhibitor, U0126, on TNF- α -stimulated ERK1/2 phosphorylation. In ARPE-19 cells pretreated with U0126 (10 μ M) for 1 h, the TNF- α -induced ERK1/2 phosphorylation was almost completely inhibited (Fig. 4B).

To determine whether TNF- α -induced PKC δ phosphorylation is related to ERK1/2 activation, ARPE-19 cells were preincubated with rottlerin (1 μ M) before exposure to TNF- α . As shown in Fig. 4B, ARPE-19 cells pretreated with rottlerin was not decreased ERK1/2 phosphorylation. Fig. 4C shows the relationship between ERK1/2 and c-Jun

in the TNF- α -mediated responses. Pretreatment with U0126 inhibited TNF- α -induced c-Jun phosphorylation.

Next, a luciferase gene activity assay was used to confirm whether quercetin can attenuate AP-1 promoter activity and, if so, whether this occurs through the signaling pathways mentioned above. As shown in Fig. 4D, AP-1 promoter activity was significantly affected by TNF- α and reached its maximum at 1 h (Data not shown). Quercetin attenuated this AP-1 promoter activity, which might happen through the PKC δ -JNK1/2-ERK1/2 signaling pathway.

Taken together, these results suggest that quercetin reduced TNF- α -induced ICAM-1 and MMP-9 expression in ARPE-19 cells via the MEK1/2-ERK1/2-c-Jun pathway.

3.5. Quercetin attenuated ICAM-1 and MMP-9 expression induced by TNF- α via NF- κ B (p65) in ARPE-19 cells

Inflammation caused by stimulation of cytokines, such as TNF- α , depends on activation of NF- κ B. We next investigated the role of NF- κ B

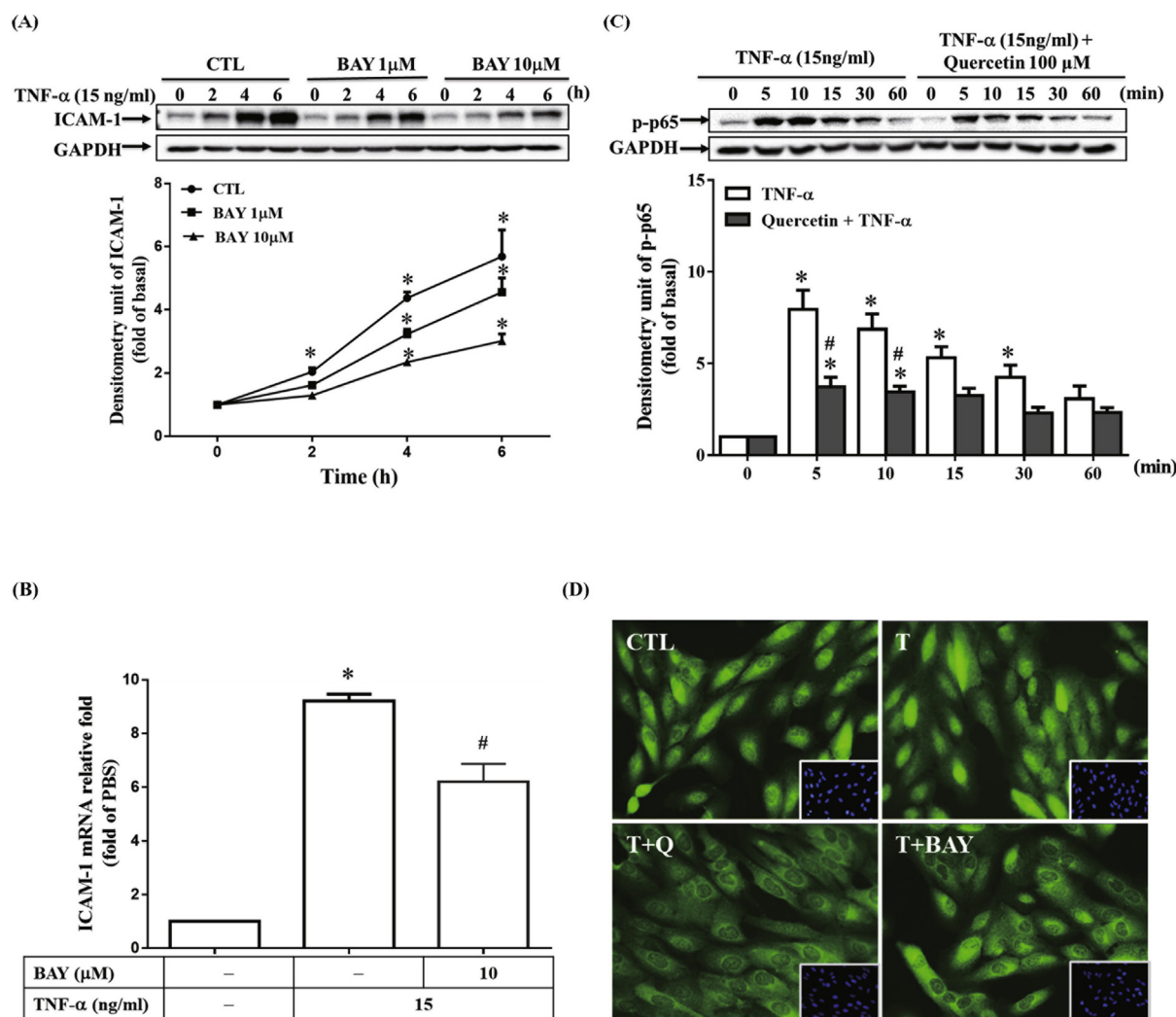


Fig. 5. Quercetin attenuates ICAM-1 expression induced by TNF- α via NF- κ B (p65) in ARPE-19 cells. ARPE-19 cells were pretreated with Bay 11-7082 or quercetin for 1 h before stimulation with 15 ng/ml TNF- α for (A, C) the designated time, (B) 4 h, or (D) 5 min. ICAM-1 protein expression and mRNA level were analyzed by (A) Western blotting and (B) real-time PCR, respectively. (C) NF- κ B (p65) phosphorylation was analyzed by Western blotting. Data were obtained from at least three independent experiments and are expressed as mean \pm SD. * P < 0.05 vs. control cells. # P < 0.05 vs. TNF- α -stimulated cells. (D) NF- κ B (p65) translocation was determined by immunofluorescence staining. The image is representative of the results of four independent experiments.

in ICAM-1 and MMP-9 expression induced by TNF- α in ARPE-19 cells. As shown in Fig. 5A, the TNF- α -induced ICAM-1 expression was reduced in a concentration- and time-dependent manner in cells pretreated with Bay 11-7082 (an NF- κ B inhibitor). ICAM-1 mRNA expression induced by TNF- α was also downregulated by pretreatment with Bay 11-7082 (Fig. 5B). Similar results were also obtained for TNF- α -induced MMP-9 expression (data not shown). These results suggest that NF- κ B played an important role in ICAM-1 and MMP-9 expression induced by TNF- α in ARPE-19 cells.

To elucidate whether quercetin attenuated ICAM-1 and MMP-9 expression induced by TNF- α in ARPE-19 cells through the inhibition of NF- κ B, the cells were pretreated with quercetin before TNF- α incubation. The results are displayed in Fig. 5C; NF- κ B (p65) phosphorylation was significantly reduced by quercetin in a time-dependent manner. Next, we used immunofluorescence staining to assess the effect of quercetin on NF- κ B translocation from the cytoplasm into the nucleus. Both quercetin and Bay 11-7082 reduced NF- κ B translocation induced by TNF- α (Fig. 5D). These results suggest that quercetin attenuated TNF- α -induced ICAM-1 and MMP-9 expression via NF- κ B (p65) in ARPE-19 cells.

3.6. Quercetin attenuated TNF- α -induced NF- κ B (p65) phosphorylation, translocation, and promoter activity via the PKC δ -JNK1/2 pathway in ARPE-19 cells

We next investigated whether MEK1/2-ERK1/2, PKC δ , and JNK1/2 are involved in NF- κ B (p65) phosphorylation induced by TNF- α in ARPE-19 cells. As shown in Fig. 6A and B, TNF- α -induced p65 phosphorylation was markedly reduced in cells pretreated with SP600125 and rottlerin, but not with U0126. Stimulation by TNF- α in ARPE-19 cells resulted in translocation of NF- κ B into the nucleus. Therefore, we examined further whether MAPK activation leads to NF- κ B translocation and then induces ICAM-1 and MMP-9 expression in ARPE-19 cells. First, cells were stimulated with TNF- α (15 ng/ml) for 5, 10 and 15 min. TNF- α induced NF- κ B translocation within 5 min and the maximal response was achieved within 15 min, as shown by immunofluorescence staining (Fig. 6C). These effects were attenuated by rottlerin or SP600125, as shown in Fig. 6D, but not by U0126 (data not shown).

Next, a luciferase gene activity assay was used to confirm whether quercetin can attenuate NF- κ B promoter activity and, if so, whether this occurs through the signaling pathways mentioned above. The RelA/p65-Luc reporter gene was transfected into ARPE-19 cells, which were then stimulated with TNF- α for 0.5, 1, 2, 4 and 6 h. As shown in Fig. 6E,

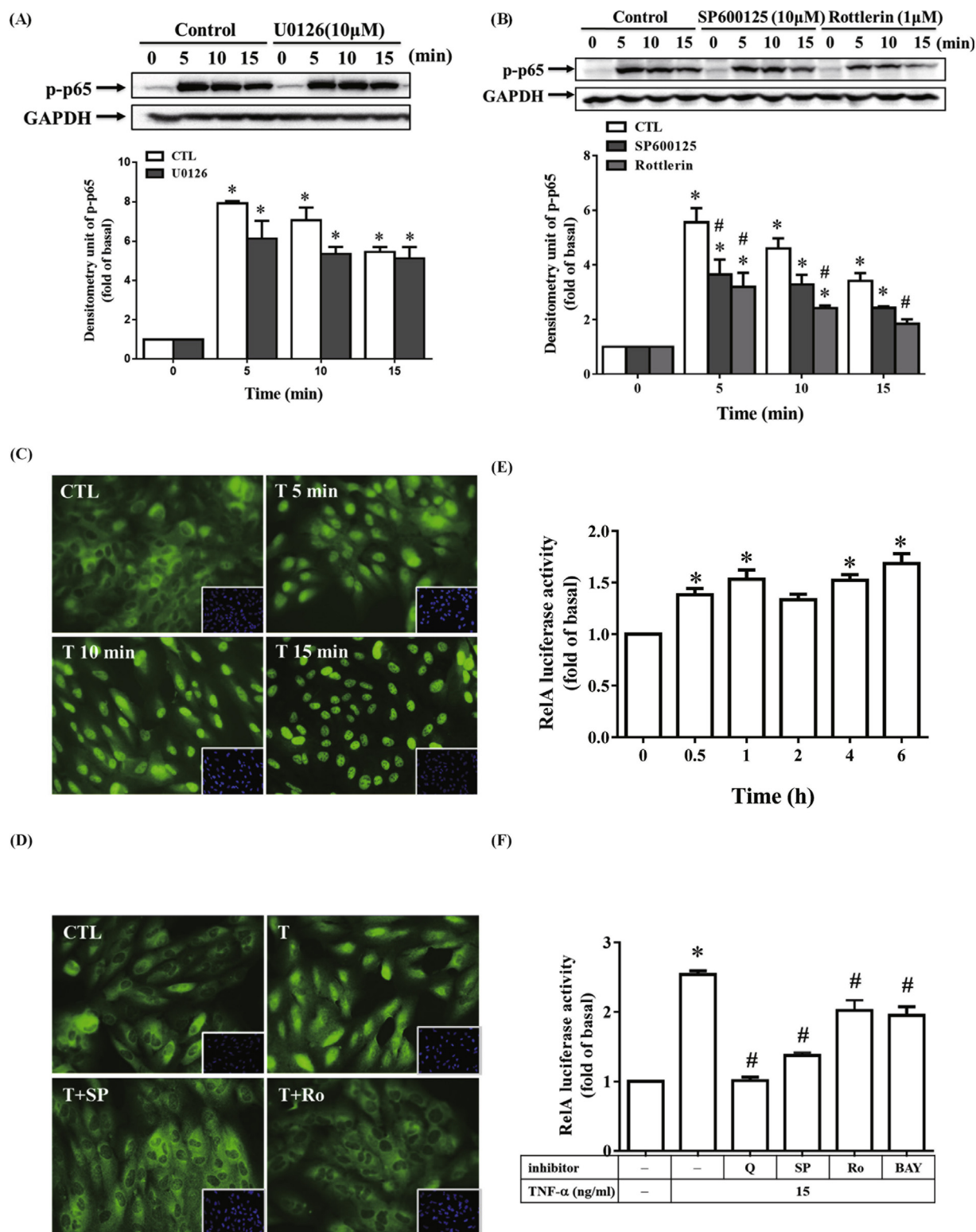


Fig. 6. Quercetin attenuates TNF- α -induced NF- κ B (p65) phosphorylation, translocation, and promoter activity via the PKC δ -JNK1/2 pathway in ARPE-19 cells. ARPE-19 cells were pretreated with (A) U0126, (B) SP600125, or rottlerin for 1 h before stimulation with 15 ng/ml TNF- α for 5, 10 and 15 min. NF- κ B (p65) phosphorylation was analyzed by Western blotting. (C, D) ARPE-19 cells were treated with 15 ng/ml TNF- α for 5, 10 and 15 min or with SP600125 (10 μ M) or rottlerin (1 μ M) for 1 h before stimulation with 15 ng/ml TNF- α for 5 min. NF- κ B (p65) translocation was determined by immunofluorescence staining. The image is representative of the results of four independent experiments. (E, F) To determine luciferase activity, ARPE-19 cells were first transiently transfected with RelA/p65-Luc and β -galactosidase plasmids. The cells were then treated with 15 ng/ml TNF- α for 0.5, 1, 2, 4 and 6 h. or pretreated with quercetin (100 μ M), SP600125 (10 μ M), rottlerin (1 μ M), or Bay 11-7082 (10 μ M) for 1 h and then exposed to TNF- α for 6 h. Data were obtained from at least three independent experiments and are expressed as mean \pm SD. *P < 0.05 vs. control cells. #P < 0.05 vs. TNF- α -stimulated cells.

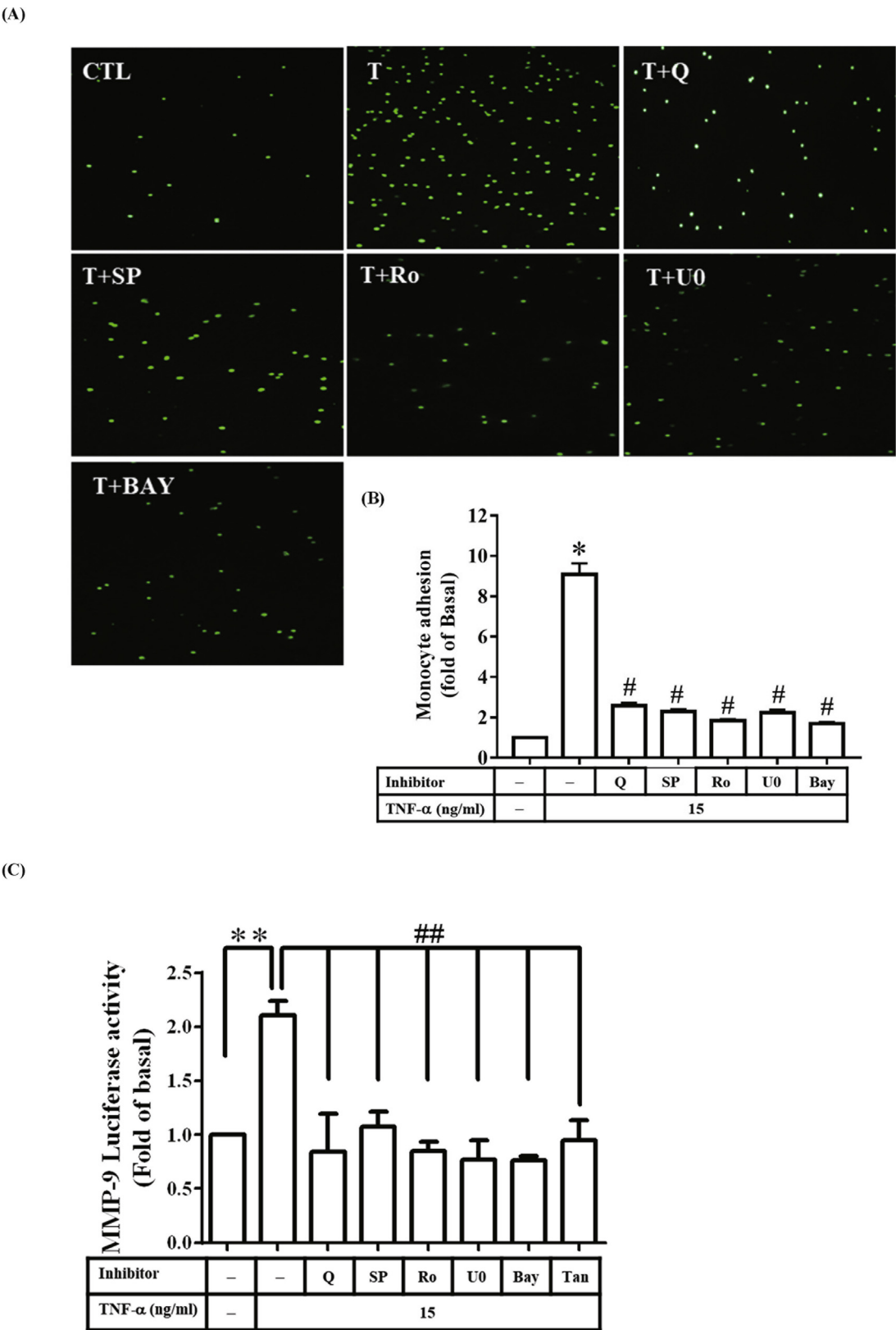


Fig. 7. Quercetin inhibition of TNF- α -induced monocyte adhesion and MMP-9 promoter activity involves PKC δ , ERK1/2, JNK1/2, c-Jun, and NF- κ B (p65) in ARPE-19 cells. ARPE-19 cells were preincubated with quercetin (100 μ M), SP600125 (10 μ M), rottlerin (1 μ M), U0126 (10 μ M), Bay 11-7082 (10 μ M), or tanshinone IIA (0.1 μ M) for 1 h and then stimulated with 15 ng/ml TNF- α for 6 h. (A, B) THP-1 monocyte adhesion assay was used to determine the physiological functional of ICAM-1, which was quantified using Image J software. (C) To determine MMP-9 promoter activity, cells were transfected with MMP-9-Luc and β -galactosidase plasmids. The cells were pretreated with quercetin or inhibitors for 1 h and then exposed to TNF- α for 1 h. The luciferase activity was determined. Data were obtained from at least three independent experiments and are expressed as mean \pm SD. *P < 0.05 vs. control cells. #P < 0.05 vs. TNF- α -stimulated cells.

RelA/p65–Luc activity was significantly stimulated by TNF- α at 0.5 h and this stimulation peaked at 6 h. This activity was attenuated by pretreatment with quercetin and the inhibitors rottlerin, SP600125, or Bay 11-7082 (Fig. 6F).

Taken together, these observations suggest that ICAM-1 and MMP-9 expression was regulated through the activation of a PKC δ –JNK1/2–NF- κ B-dependent pathway in ARPE-19 cells.

3.7. Quercetin attenuated TNF- α -induced THP-1 cell adherence and MMP-9 promoter activity via the PKC δ –JNK1/2–c-Jun or NF- κ B and MEK1/2–ERK1/2 pathways in ARPE-19 cells

Administration of inhibitors of ICAM-1 or MMPs is an attractive potential therapy for diabetic retinopathy and is being investigated in several experiments [23–25]. We investigated whether quercetin can attenuate ICAM-1-dependent monocyte adhesion to ARPE-19 cells stimulated by TNF- α . As shown in Fig. 7A, TNF- α significantly increased THP-1 cell adhesion to ARPE-19 cells, and this effect was attenuated by quercetin.

We next investigated whether PKC δ , JNK1/2, ERK1/2, and NF- κ B are involved in the inhibition by quercetin of THP-1 cell adhesion to ARPE-19 cells induced by TNF- α . The inhibitors of kinases, including rottlerin, SP600125, U0126 or Bay 11-7082 greatly attenuated TNF- α -induced THP-1 cell adhesion to ARPE-19 cells (Fig. 7B). This phenomenon was also observed for TNF- α -regulated MMP-9 promoter activity (Fig. 7C). These results suggest that ICAM-1 and MMP-9 expression induced by TNF- α was regulated through the PKC δ , JNK1/2, ERK1/2, c-Jun, and/or NF- κ B (p65) pathways, and that this effect contributed to retinal inflammatory responses.

4. Discussion

Quercetin, a polyphenolic flavonoid, was used in the present study because of its anti-inflammatory effects. Quercetin has been reported to significantly inhibit ICAM-1 expression in response to inflammatory stimuli in the A549 pulmonary epithelial cell line [36], human endothelial cells [37], and after acute lung injury in rats with sepsis [38]. A previous study has shown that quercetin downregulates MMP-9 expression and prevents ethanol-induced gastric inflammation [39]. Quercetin also has inhibitory effects on MMP-9 expression and the production of proinflammatory cytokines, which attenuates LPS-induced lung inflammation [40]. We observed that the expression of ICAM-1 and MMP-9, and THP-1 cell adherence were upregulated in TNF- α -stimulated ARPE-19 cells. We investigated further whether quercetin could inhibit the responses induced by TNF- α . The results indicated that quercetin significantly reduced the expression of ICAM-1 and MMP-9, and THP-1 cell adherence, which suggests that quercetin may be effective in preventing the progression of inflammation.

PKC is involved in various pathways that regulate cell functions and proliferation [41]. In this study, we found that quercetin decreased ICAM-1 and MMP-9 expression induced by TNF- α through the PKC δ –JNK1/2–c-Jun pathway. We also used the inhibitors SP600125 or rottlerin to investigate the relationships between PKC δ , JNK1/2, and c-Jun in TNF- α -stimulated ARPE-19 cells. Pretreatment with SP600125 or rottlerin significantly inhibited JNK1/2 and c-Jun phosphorylation, which indicated that TNF- α evoked ICAM-1 and MMP-9 expression through the PKC δ –JNK1/2–c-Jun pathway in ARPE-19 cells; this is consistent with the findings of a previous study [14].

Several researchers have provided evidence that the MAPK family participates in various pathophysiological processes in the retina and cornea [42–45]. Three prominent groups of MAPKs have been identified in mammals—ERK1/2, p38 MAPK, and JNK1/2—and play essential roles in cell proliferation and differentiation, and inflammation [46]. The expression of cytokines and ICAM-1 have been shown to be regulated through the MAPK and NF- κ B pathways [35]. IL-1 β has been reported to stimulate ICAM-1 expression via differential activation of

PI3K–Akt and MEK–ERK1/2 in the pulpal inflammatory processes [47]. Glucose or mannitol induce ICAM-1 expression through the ERK1/2, p38, and JNK1/2 cascades in glomerular endothelial cells [48]. TNF- α induces the expression of proinflammatory cytokines/chemokines and ICAM-1 via activation of NF- κ B, ERK1/2, and p38 MAPK in HaCaT cells [49].

In human RPECs, TNF- α induces ICAM-1 expression via ERK1/2 and JNK1/2 [14]. This evidence suggests that ICAM-1 expression induced by inflammatory stimuli is strongly associated with MAPKs in various cell types. Our findings suggest that quercetin inhibited TNF- α -induced ERK1/2 phosphorylation. The increase in TNF- α -induced ERK1/2 phosphorylation was markedly suppressed by pretreatment with U0126 but not with rottlerin. In addition, U0126 pretreatment suppressed the increase in c-Jun phosphorylation induced by TNF- α . Taken together, our findings suggest that TNF- α induced the expression of ICAM-1 and MMP-9 through both the PKC δ –JNK1/2–c-Jun and MEK1/2–ERK1/2–c-Jun signaling pathways in ARPE-19 cells.

NF- κ B plays an essential role in regulation of inflammatory responses. The stimulation of proinflammatory cytokines such as TNF- α can increase NF- κ B activity after phosphorylation and degradation of I κ B α . Active NF- κ B then translocates to the nucleus to regulate the expression of genes for proinflammatory factors including cytokines, chemokines, and adhesion molecules [50–52]. We observed that pretreatment with Bay 11-7082 attenuated ICAM-1 and MMP-9 expression induced by TNF- α in ARPE-19 cells. A previous study has reported that quercetin prevented esophageal mucosal injury caused by chronic mixed reflux esophagitis in rats via suppressing the NF- κ B signaling pathway [53].

Quercetin also downregulates the activation of NF- κ B and p38 MAPK, and inhibits the expression of inflammatory cytokines in the HMC-1 human mast cell line [54]. Our study found that quercetin reduced TNF- α -induced NF- κ B phosphorylation and translocation, and RelA/p65–Luc activity, which suggests that quercetin decreased TNF- α -induced ICAM-1 and MMP-9 expression by inhibiting NF- κ B activation. Given the previously reported implications that MAPKs are involved in regulating NF- κ B transcriptional activity [55,56], we investigated further whether ERK1/2, PKC δ , and JNK1/2 participate in TNF- α -induced NF- κ B transcriptional activity in ARPE-19 cells. We confirmed that TNF- α -induced NF- κ B (p65) phosphorylation and translocation, and RelA/p65–Luc activity were mediated via the PKC δ –JNK1/2 but not the ERK1/2 pathway. These findings suggest that quercetin attenuated ICAM-1 and MMP-9 expression induced by TNF- α partially by suppressing the PKC δ –JNK1/2–NF- κ B pathway.

5. Conclusion

Our results point to a possible mechanism for the effects of quercetin in the treatment of human retinal inflammatory diseases (Fig. 8). Quercetin seems to inhibit monocyte adherence ability, which then suppresses the expression of ICAM-1 and MMP-9. In our study, quercetin suppressed ICAM-1 and MMP-9 expression by inhibiting the phosphorylation of PKC δ , JNK1/2, ERK1/2, c-Jun, and NF- κ B. Our findings suggest that quercetin may provide a novel and effective therapeutic strategy for the prevention or treatment of retinal inflammatory diseases.

Conflict of interest

The authors declare that there is no conflict of interest.

Acknowledgements

This work was supported by the Ministry of Science and Technology, Taiwan, grant number MOST 101-2320-B-255-003-MY3; the Chang Gung Medical Research Foundation, grant number CMRPF3E0051, CMRPF3E0052, CMRPF3G0011, CMRPF3G0012 and

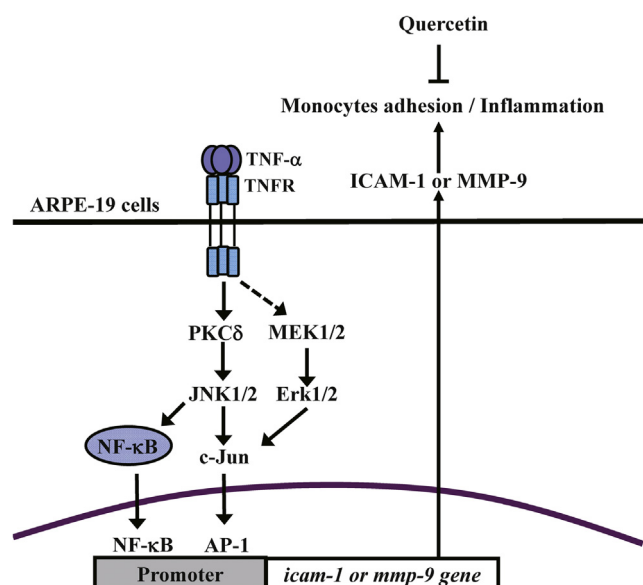


Fig. 8. Schematic diagram of the signaling pathways for attenuation by quercetin of TNF- α -induced inflammation via downregulation of ICAM-1 and MMP-9 expression in ARPE-19 cells. Quercetin attenuates TNF- α -induced ICAM-1 and MMP-9 expression in ARPE-19 cells via the MEK1/2–ERK1/2 and PKC δ –JNK1/2–c-Jun or NF- κ B pathways.

BMRPD16; Chang Gung University of Science and Technology, grant number EZRPF3E0601, EZRPF3E0161, EZRPF3E0201, EZRPF3E0191, EZRPF3E0181 and EZRPF3E0171, EZRPF3G0551.

References

- [1] L. da Cruz, F.K. Chen, A. Ahmado, J. Greenwood, P. Coffey, RPE transplantation and its role in retinal disease, *Prog. Retin. Eye Res.* 26 (6) (2007) 598–635.
- [2] B.P. Barnett, J.T. Handa, Retinal microenvironment imbalance in dry age-related macular degeneration: a mini-review, *Gerontology* 59 (4) (2013) 297–306.
- [3] E. Kucuksayan, E.K. Konuk, N. Demir, B. Mutus, M. Aslan, Neutral sphingomyelinase inhibition decreases ER stress-mediated apoptosis and inducible nitric oxide synthase in retinal pigment epithelial cells, *Free Radic. Biol. Med.* 72 (2014) 113–123.
- [4] A. Kauppinen, J.J. Paterno, J. Blasiak, A. Salminen, K. Kaarniranta, Inflammation and its role in age-related macular degeneration, *Cell Mol. Life Sci.* 73 (9) (2016) 1765–1786.
- [5] R. Simo, M. Villarreal, L. Corraliza, C. Hernandez, M. Garcia-Ramirez, The retinal pigment epithelium: something more than a constituent of the blood-retinal barrier—implications for the pathogenesis of diabetic retinopathy, *J. Biomed. Biotechnol.* 2010 (2010) 190724.
- [6] K. Kaarniranta, A. Salminen, E.L. Eskelinen, J. Kopitz, Heat shock proteins as gatekeepers of proteolytic pathways—Implications for age-related macular degeneration (AMD), *Ageing Res. Rev.* 8 (2) (2009) 128–139.
- [7] M.M. Al-Gayyari, N.M. Elsherbiny, Contribution of TNF- α to the development of retinal neurodegenerative disorders, *Eur. Cytokine Netw.* 24 (1) (2013) 27–36.
- [8] S. Merida, E. Palacios, A. Navea, F. Bosch-Morell, New immunosuppressive therapies in uveitis treatment, *Int. J. Mol. Sci.* 16 (8) (2015) 18778–18795.
- [9] A.P. Adamis, Is diabetic retinopathy an inflammatory disease? *Br. J. Ophthalmol.* 86 (4) (2002) 363–365.
- [10] R. Dewispelaere, D. Lipski, V. Foucart, C. Bruyns, A. Frere, L. Caspers, F. Willermain, ICAM-1 and VCAM-1 are differentially expressed on blood-retinal barrier cells during experimental autoimmune uveitis, *Exp. Eye Res.* 137 (2015) 94–102.
- [11] D.S. McLeod, D.J. Lefer, C. Merges, G.A. Lutty, Enhanced expression of intracellular adhesion molecule-1 and P-selectin in the diabetic human retina and choroid, *Am. J. Pathol.* 147 (3) (1995) 642–653.
- [12] T. Khalfaoi, G. Lizard, O. Beltaief, D. Colin, J. Ben Hamida, K. Errais, I. Ammous, W. Zbiba, L. Tounsi, R. Zhioua, R. Anane, A. Ouertani-Meddeb, Immunohistochemical analysis of cellular adhesion molecules (ICAM-1, VCAM-1) and VEGF in fibrovascular membranes of patients with proliferative diabetic retinopathy: preliminary study, *Pathol. Biol. (Paris)* 57 (7–8) (2009) 513–517.
- [13] K.R. Chirco, S.S. Whitmore, K. Wang, L.A. Potempa, J.A. Halder, E.M. Stone, B.A. Tucker, R.F. Mullins, Monomeric C-reactive protein and inflammation in age-related macular degeneration, *J. Pathol.* 240 (2) (2016) 173–183.
- [14] I.T. Lee, S.W. Liu, P.L. Chi, C.C. Lin, L.D. Hsiao, C.M. Yang, TNF- α mediates PKC δ /JNK1/2/c-Jun-dependent monocyte adhesion via ICAM-1 induction in human retinal pigment epithelial cells, *PLoS One* 10 (2) (2015) e0117911.
- [15] L. Devine, S.L. Lightman, J. Greenwood, Role of LFA-1, ICAM-1, VLA-4 and VCAM-1 in lymphocyte migration across retinal pigment epithelial monolayers in vitro, *Immunology* 88 (3) (1996) 456–462.
- [16] L. De Groef, I. Van Hove, E. Dekeyser, I. Stalmans, L. Moons, MMPs in the neuroretina and optic nerve: modulators of glaucoma pathogenesis and repair? *Invest. Ophthalmol. Vis. Sci.* 55 (3) (2014) 1953–1964.
- [17] J.M. Sivak, M.E. Fini, MMPs in the eye: emerging roles for matrix metalloproteinases in ocular physiology, *Prog. Retin. Eye Res.* 21 (1) (2002) 1–14.
- [18] M.A. Wride, J. Geatrell, J.A. Guggenheim, Proteases in eye development and disease, birth defects research, Part C Embryo Today Rev. 78 (1) (2006) 90–105.
- [19] L. Guo, A.A. Hussain, G.A. Limb, J. Marshall, Age-dependent variation in metalloproteinase activity of isolated human Bruch's membrane and choroid, *Invest. Ophthalmol. Vis. Sci.* 40 (11) (1999) 2676–2682.
- [20] M. Kamei, J.G. Hollyfield, TIMP-3 in Bruch's membrane: changes during aging and in age-related macular degeneration, *Invest. Ophthalmol. Vis. Sci.* 40 (10) (1999) 2367–2375.
- [21] V. Lambert, B. Wielockx, C. Munaut, C. Galopin, M. Jost, T. Itoh, Z. Werb, A. Baker, C. Libert, H.W. Krell, J.M. Foidart, A. Noel, J.M. Rakic, MMP-2 and MMP-9 synergize in promoting choroidal neovascularization, *Faseb J.* 17 (15) (2003) 2290–2292.
- [22] R.A. Kowluru, Q. Zhong, J.M. Santos, Matrix metalloproteinases in diabetic retinopathy: potential role of MMP-9, *Expert Opin. Invest. Drugs* 21 (6) (2012) 797–805.
- [23] S.H. Zhu, B.Q. Liu, M.J. Hao, Y.X. Fan, C. Qian, P. Teng, X.W. Zhou, L. Hu, W.T. Liu, Z.L. Yuan, Q.P. Li, Paoniflorin suppressed high glucose-induced retinal microglia MMP-9 expression and inflammatory response via inhibition of TLR4/NF- κ B pathway through upregulation of SOCS3 in diabetic retinopathy, *Inflammation* 40 (5) (2017) 1475–1486.
- [24] G. Mohammad, M. Mairaj Siddiquei, M. Imtiaz Nawaz, A.M. Abu, El-Asrar, the ERK1/2 Inhibitor U0126 attenuates diabetes-induced upregulation of MMP-9 and biomarkers of inflammation in the retina, *J. Diabetes Res.* (2013) 658548.
- [25] K. Masuzawa, K. Goto, S. Jesmin, S. Maeda, T. Miyauchi, Y. Kaji, T. Oshika, S. Hori, An endothelin type A receptor antagonist reverses upregulated VEGF and ICAM-1 levels in streptozotocin-induced diabetic rat retina, *Curr. Eye Res.* 31 (1) (2006) 79–89.
- [26] M. Russo, R. Palumbo, A. Mupo, M. Tosto, G. Iacomino, A. Scognamiglio, I. Tedesco, G. Galano, G.L. Russo, Flavonoid quercetin sensitizes a CD95-resistant cell line to apoptosis by activating protein kinase Calpha, *Oncogene* 22 (21) (2003) 3330–3342.
- [27] L. Gibellini, M. Pinti, M. Nasi, J.P. Montagna, S. De Biasi, E. Roat, L. Bertoncelli, E.L. Cooper, A. Cossarizza, Quercetin and cancer chemoprevention, *Evid. Based Complem. Alternat. Med.* 2011 (2011) 591356.
- [28] M. Hytti, N. Piiippo, A. Salminen, P. Honkakoski, K. Kaarniranta, A. Kauppinen, Quercetin alleviates 4-hydroxynonenal-induced cytotoxicity and inflammation in ARPE-19 cells, *Exp. Eye Res.* 132 (2015) 208–215.
- [29] B. Kumar, S.K. Gupta, T.C. Nag, S. Srivastava, R. Saxena, K.A. Jha, B.P. Srinivasan, Retinal neuroprotective effects of quercetin in streptozotocin-induced diabetic rats, *Exp. Eye Res.* 125 (2014) 193–202.
- [30] H.N. Oh, C.E. Kim, J.H. Lee, J.W. Yang, Effects of quercetin in a mouse model of experimental dry eye, *Cornea* 34 (9) (2015) 1130–1136.
- [31] D. Kook, A.H. Wolf, A.L. Yu, A.S. Neubauer, S.G. Priglinger, A. Kampik, U.C. Welge-Lüssen, The protective effect of quercetin against oxidative stress in the human RPE in vitro, *Invest. Ophthalmol. Vis. Sci.* 49 (4) (2008) 1712–1720.
- [32] X. Cao, M. Liu, J. Tuo, D. Shen, C.C. Chan, The effects of quercetin in cultured human RPE cells under oxidative stress and in Ccl2/Cx3cr1 double deficient mice, *Exp. Eye Res.* 91 (1) (2010) 15–25.
- [33] X. Zhong, X. Li, F. Liu, H. Tan, D. Shang, Omentin inhibits TNF- α -induced expression of adhesion molecules in endothelial cells via ERK/NF- κ B pathway, *Biochem. Biophys. Res. Commun.* 425 (2) (2012) 401–406.
- [34] L. Tang, W. Chai, F. Ye, Y. Yu, L. Cao, M. Yang, M. Xie, L. Yang, HMGB1 promotes differentiation syndrome by inducing hyperinflammation via MEK/ERK signaling in acute promyelocytic leukemia cells, *Oncotarget* 8 (16) (2017) 27314–27327.
- [35] H.C. Sung, C.J. Liang, C.W. Lee, F.L. Yen, C.Y. Hsiao, S.H. Wang, Y.F. Jiang-Shieh, J.S. Tsai, Y.L. Chen, The protective effect of eupafolin against TNF- α -induced lung inflammation via the reduction of intercellular cell adhesion molecule-1 expression, *J. Ethnopharmacol.* 170 (2015) 136–147.
- [36] B. Ying, T. Yang, X. Song, X. Hu, H. Fan, X. Lu, L. Chen, D. Cheng, T. Wang, D. Liu, D. Xu, Y. Wei, F. Wen, Quercetin inhibits IL-1 β -induced ICAM-1 expression in pulmonary epithelial cell line A549 through the MAPK pathways, *Mol. Biol. Rep.* 36 (7) (2009) 1825–1832.
- [37] H. Kobuchi, S. Roy, C.K. Sen, H.G. Nguyen, L. Packer, Quercetin inhibits inducible ICAM-1 expression in human endothelial cells through the JNK pathway, *Am. J. Physiol.* 277 (3 Pt 1) (1999) C403–C411.
- [38] L. Meng, Z. Lv, Z.Z. Yu, D. Xu, X. Yan, Protective effect of quercetin on acute lung injury in rats with sepsis and its influence on ICAM-1 and MIP-2 expression, *Genet. Mol. Res.* 15 (3) (2016).
- [39] S. Chakraborty, S. Stalin, N. Das, S.T. Choudhury, S. Ghosh, S. Swarnakar, The use of nano-quercetin to arrest mitochondrial damage and MMP-9 upregulation during prevention of gastric inflammation induced by ethanol in rat, *Biomaterials* 33 (10) (2012) 2991–3001.
- [40] K. Takashima, M. Matsushima, K. Hashimoto, H. Nose, M. Sato, N. Hashimoto, Y. Hasegawa, T. Kawabe, Protective effects of intratracheally administered quercetin on lipopolysaccharide-induced acute lung injury, *Respir. Res.* 15 (2014) 150.
- [41] Y. Nishizuka, The role of protein kinase C in cell surface signal transduction and tumour promotion, *Nature* 308 (5961) (1984) 693–698.
- [42] H.M. Jauhonen, A. Kauppinen, T. Paimela, J.K. Laihia, L. Leino, A. Salminen,

- K. Kaarniranta, Cis-urocanic acid inhibits SAPK/JNK signaling pathway in UV-B exposed human corneal epithelial cells in vitro, *Mol. Vis.* 17 (2011) 2311–2317.
- [43] T. Adachi, M. Teramachi, H. Yasuda, T. Kamiya, H. Hara, Contribution of p38 MAPK, NF-kappaB and glucocorticoid signaling pathways to ER stress-induced increase in retinal endothelial permeability, *Arch. Biochem. Biophys.* 520 (1) (2012) 30–35.
- [44] Y. Chen, A. Kijlstra, Y. Chen, P. Yang, IL-17A stimulates the production of inflammatory mediators via Erk1/2, p38 MAPK, PI3K/Akt, and NF-kappaB pathways in ARPE-19 cells, *Mol. Vis.* 17 (2011) 3072–3077.
- [45] L. Luo, D.Q. Li, A. Doshi, W. Farley, R.M. Corrales, S.C. Pflugfelder, Experimental dry eye stimulates production of inflammatory cytokines and MMP-9 and activates MAPK signaling pathways on the ocular surface, *Invest. Ophthalmol. Vis. Sci.* 45 (12) (2004) 4293–4301.
- [46] M.H. Cobb, MAP kinase pathways, *Prog. Biophys. Mol. Biol.* 71 (3–4) (1999) 479–500.
- [47] M.C. Chang, H.P. Hung, L.D. Lin, Y.C. Shyu, T.M. Wang, H.J. Lin, C.P. Chan, C.C. Huang, J.H. Jeng, Effect of interleukin-1beta on ICAM-1 expression of dental pulp cells: role of PI3K/Akt, MEK/ERK, and cyclooxygenase, *Clin. Oral Invest.* 19 (1) (2015) 117–126.
- [48] N. Watanabe, K. Shikata, Y. Shikata, K. Sarai, K. Omori, R. Kadera, C. Sato, J. Wada, H. Makino, Involvement of MAPKs in ICAM-1 expression in glomerular endothelial cells in diabetic nephropathy, *Acta Med. Okayama* 65 (4) (2011) 247–257.
- [49] D.J. Kwon, Y.S. Bae, S.M. Ju, A.R. Goh, S.Y. Choi, J. Park, Casuarinin suppresses TNF-alpha-induced ICAM-1 expression via blockade of NF-kappaB activation in HaCaT cells, *Biochem. Biophys. Res. Commun.* 409 (4) (2011) 780–785.
- [50] T. Lawrence, The nuclear factor NF-kappaB pathway in inflammation, *Cold Spring Harbor Perspect. Biol.* 1 (6) (2009) a001651.
- [51] S. Zhu, X. Xu, K. Liu, Q. Gu, F. Wei, H. Jin, Peptide GC31 inhibits chemokines and ICAM-1 expression in corneal fibroblasts exposed to LPS or poly(I:C) by blocking the NF-kappaB and MAPK pathways, *Exp. Eye Res.* 164 (2017) 109–117.
- [52] R. Gu, B. Lei, C. Jiang, G. Xu, Glucocorticoid-induced leucine zipper suppresses ICAM-1 and MCP-1 expression by dephosphorylation of NF-kappaB p65 in retinal endothelial cells, *Invest. Ophthalmol. Vis. Sci.* 58 (1) (2017) 631–641.
- [53] P. Wu, L. Zhou, Y.J. Li, B. Luo, L.S. Yi, S.F. Chen, H.H. Sun, Y. Chen, Z.J. Cao, S.C. Xu, Protective effects of quercetin against chronic mixed reflux esophagitis in rats by inhibiting the nuclear factor-kappaB p65 and interleukin-8 signaling pathways, *J. Digest. Dis.* 16 (6) (2015) 319–326.
- [54] L. Lei, R. Tzekov, H. Li, J.H. McDowell, G. Gao, W.C. Smith, S. Tang, S. Kaushal, Inhibition or stimulation of autophagy affects early formation of lipofuscin-like autofluorescence in the retinal pigment epithelium cell, *Int. J. Mol. Sci.* 18 (4) (2017).
- [55] X. Dolcet, D. Llobet, J. Pallares, X. Matias-Guiu, NF-kB in development and progression of human cancer, *Virchows Archiv. Int. J. Pathol.* 446 (5) (2005) 475–482.
- [56] M. Korus, G.M. Mahon, L. Cheng, I.P. Whitehead, p38 MAPK-mediated activation of NF-kappaB by the RhoGEF domain of Bcr, *Oncogene* 21 (30) (2002) 4601–4612.

Available online at www.sciencedirect.com

ScienceDirect

Biomedical Journal

journal homepage: www.elsevier.com/locate/bj

News and Perspectives

From discovery of tyrosine phosphorylation to targeted cancer therapies: The 2018 Tang Prize in Biopharmaceutical Science

Jau-Song Yu*

Department of Cell & Molecular Biology, Graduate Institute of Biomedical Sciences, and Molecular Medicine Research Center, College of Medicine, Chang Gung University, Taoyuan, Taiwan
 Liver Research Center, Chang Gung Memorial Hospital at Linkou, Taoyuan, Taiwan
 Research Center for Food and Cosmetic Safety, Research Center for Chinese Herbal Medicine, College of Human Ecology, Chang Gung University of Science and Technology, Taoyuan, Taiwan

ARTICLE INFO

Article history:

Received 11 February 2019

Accepted 11 March 2019

Available online 30 April 2019

Keywords:

Tyrosine phosphorylation

Oncogene

Tyrosine kinase inhibitor

Targeted cancer therapy

2018 Tang Prize

ABSTRACT

Protein tyrosine kinases (TKs) are a family of enzymes that catalyze the phosphorylation of proteins at tyrosine residues. TKs play key roles in controlling cell growth and many other functions by modulating the status of tyrosine phosphorylation of regulatory proteins critical for numerous cellular signaling pathways. Dysregulation of TKs caused by genetic abnormalities (mutation, amplification, fusion, etc.) results in uncontrolled cell growth, and ultimately leads to cancer. Thus, identification of dysregulated TK(s) in a specific cancer type and development of TK inhibitors (TKIs) that can potentially block activity of the dysregulated TK establish the foundation of modern targeted cancer therapies. The 2018 Tang Prize in Biopharmaceutical Science was awarded to Tony Hunter as well as Brian Druker and John Mendelsohn for their great contributions in discovering oncogene src as a TK and developing small molecule TKIs or therapeutic monoclonal antibodies against receptor TK, respectively.

Protein phosphorylation is a biological reaction that involves transfer of a phosphate group from ATP to specific amino acid residue(s) of a protein, which is catalyzed by a big family of enzymes called protein kinases. There are >500 protein kinases encoded in the human genome [1]. Serine, threonine and tyrosine are the three major amino acid residues in proteins that can be phosphorylated by protein kinases in eukaryotic cells, with an estimated ratio of 1000:100:1 [2]. Phosphorylation of proteins (or enzymes) at specific amino acid residue(s) can alter their 3D structures and thus modulate

their biological functions (or activities). The importance of protein phosphorylation as a biological regulatory mechanism to control a particular physiological function came from the pioneering studies by Edmond H. Fischer and Edwin G. Krebs on the hormone-dependent glucose metabolism in the early 1950s [3]. Soon after, numerous researchers confirmed the critical role of protein phosphorylation in modulating diverse biological processes other than glucose metabolism. However, only serine and/or threonine phosphorylation of proteins could be observed in all these prior studies. At that time,

* Corresponding author. Department of Cell and Molecular Biology, College of Medicine, Chang Gung University, 259, Wenhua 1st Rd., Gueishan, Taoyuan 333, Taiwan.

E-mail address: yusong@mail.cgu.edu.tw.

Peer review under responsibility of Chang Gung University.

<https://doi.org/10.1016/j.bj.2019.03.004>

2319-4170/© 2019 Chang Gung University. Publishing services by Elsevier B.V. This is an open access article under the CC BY-NC-ND license (<http://creativecommons.org/licenses/by-nc-nd/4.0/>).

nobody knows if a protein (or enzyme) can be phosphorylated on tyrosine residue(s), not to mention the biological meaning of protein tyrosine phosphorylation.

Discovery of protein tyrosine phosphorylation

The first discovery of protein tyrosine phosphorylation was made by Tony Hunter's lab in 1979, who found an activity phosphorylating tyrosine in the immunoprecipitates of the animal tumor virus transforming protein polyoma T antigen [4]. In the next few years (1980–1984), Hunter and other scientists quickly demonstrated that both v-Src (the Rous sarcoma virus transforming protein) and epidermal growth factor receptor (EGFR) possess intrinsic TK activity, and EGF can induce rapid tyrosine phosphorylation of proteins in A431 human tumor cells [5–9]. These seminal findings prompted other researchers to demonstrate the intrinsic TK activity of additional growth factor receptors, such as PDGF receptor and insulin receptor, in the 1980s. By this time, researchers began to realize that ligand-induced tyrosine phosphorylation can be a major and common mechanism for the transmission of signals across the plasma membrane.

The finding that v-Src had TK activity strongly indicated uncontrolled tyrosine phosphorylation as a potent transformation mechanism. Immediately, Hunter and his colleague's 1980 report showed the precise correlation between TK activity of v-Src from temperature-sensitive transforming mutants of Rous sarcoma virus and their transforming potential in mouse cells, providing direct evidence that the phosphorylation of tyrosine is essential for cellular transformation by Rous sarcoma virus [10]. Quickly, researchers investigating the BCR-ABL fusion protein, a human oncogene resulting from the fusion of the BCR gene with the c-ABL TK gene in chronic myelogenous leukemia (CML), found that BCR-ABL had increased TK activity (in 1984/1986) [11,12] and caused CML in mice (in 1990) [13–16]. Subsequent search for human tumor oncogenes identified many additional human TK mutants, and several of these are mutant forms of receptor TKs, such as KIT in gastrointestinal stromal tumors (in 1998) [17,18] and EGFR in lung cancer (in 2004) [19–21]. ERBB2, another transmembrane TK was observed to be frequently overexpressed in breast cancer (between 1987 and 1992) [22–24].

Development of tyrosine kinase inhibitors

Through the understanding of aberrant tyrosine phosphorylation caused by viral or cellular oncogenes as one of the major causes of cancer, the Hunter's pioneering work inspired other researchers to develop small molecule inhibitors of oncogenic TKs targeting the ATP binding site, with the hope that they might ultimately be useful in cancer therapy. The development of tyrphostins (tyrosine phosphorylation inhibitors) by Alex Levitzki in 1988 represents the first attempts at rational design of TKIs in academia, in which the most potent tyrphostins effectively blocked the EGF-dependent proliferation of A431 cells with little or no effect on the EGF-independent proliferation of these cells [25]. Their later studies further showed

that some tyrphostins were selective inhibitors of BCR-ABL, which induced the K562 CML cell line to terminally differentiate into nondividing erythroid cells [26,27]. In the pharmaceutical industry, CIBA-Geigy (now Novartis) initiated a TKI program in 1986 led by Nick Lydon, focusing first on the PDGF receptor to develop a series of 2-phenylaminopyrimidine derivative TKIs. Brian Druker, a physician scientist who had been working on CML and started treating CML patients since the early 1990s, made up his mind to find a better way for treating this disease. He collaborated and worked closely with the team of the TKI program at CIBA-Geigy, identifying CGP57148B (a 2-phenylaminopyrimidine derivative) as a potent and relatively selective inhibitor of v-Abl (the oncoprotein of the Abelson murine leukemia virus) [28] in 1996 and further demonstrating that CGP57148B could inhibit the growth of CML cells and BCR-ABL-transformed cells both in culture and in mice [29,30]. Based on these encouraging data, Druker and Charles Sawyers initiated in June 1998 a series of phase I/II clinical trials in CML patients, demonstrating the effectiveness of imatinib (the generic name of CGP57148B, also known as STI571 or Gleevec/Glivec) in treating chronic phase CML [31–33]. Due to these successful trial results, the United States Food and Drug Administration (FDA) approved imatinib for the treatment of CML on May 10, 2001. Moreover, as imatinib is also a potent inhibitor for the c-KIT receptor tyrosine kinases reported to be mutated/activated in gastrointestinal stromal tumor (GIST) [34], clinical trials have shown that imatinib was quite effective in GIST patients [35], leading to the FDA's approval of imatinib in treating GIST in February 2002.

Development of anti-EGFR monoclonal antibodies

In addition to targeting the TK's ATP binding site, blockage of the receptor TK's transmembrane signaling represents another approach to inhibit TK activity in cancer. Beginning from 1983, John Mendelsohn, Gordon H. Sato and their collaborators reported the production of murine monoclonal antibodies (mAbs) 528 and 225 against the extracellular domain of EGFR, which could inhibit human cancer cell proliferation by blocking the transduction of EGFR signaling in culture and in athymic mice [36,37]. Subsequent preclinical studies in the Mendelsohn's lab characterized the molecular events involved in mAb-mediated receptor internalization, mechanisms cause the cell growth inhibition, as well as additive effects of combining anti-EGFR mAb therapy of human tumor xenografts with chemotherapeutic agents [38]. In 1991, the initial phase I clinical trial was performed with indium-III-labeled murine mAb 225 in patients with advanced lung cancer [39]. After that, a chimeric human:mouse version of mAb 225 called C225 (chimeric 225, cetuximab) was created to obviate an immune response to repeated doses, which was licensed to ImClone Systems in 1994 for clinical trials. Subsequently, Bristol-Myers Squibb and Merck KGaA joined with ImClone for a series of trials in the United States and Europe, respectively, and cetuximab was approved by the U. S. FDA for treatment of colon cancer in 2004 and for head and neck cancer in 2006 [40,41].

Perspectives

Since the discovery of tyrosine phosphorylation and the first TK in 1979 by Hunter, it took more than 20 years for the first cancer drug (imatinib) that acts against a specific TK (BCR-ABL) to be approved for clinical use. Currently, more than 30 small molecule TKIs or therapeutic mAbs against protein kinases have been approved for cancer treatment [42], and dozens of protein kinase inhibitors are in cancer clinical trials, including several directed against serine/threonine kinases implicated in cancer. Apparently, the pioneering work from Hunter, Druker and Mendelsohn all together establish the foundation of modern targeted cancer therapies. In spite of the tremendous progress in targeted cancer treatment, significant challenges still remain. For example, development of resistance to TKI or anti-EGFR therapy is usually observed in patients, for which additional strategies are needed to overcome the resistance [38,43]. Moreover, due to the extremely complex nature of cancer, it is still hard to precisely select patients most likely receive benefit from TKI or anti-EGFR therapy. The use of modern multi-omics (genomics, transcriptomics, proteomics, and metabolomics, etc.) techniques in combination with bioinformatics and systems biology approaches has allowed the in-depth interrogation of clinical samples, which should greatly enable researchers to identify novel genes and signalling networks involved in determining the responsiveness of tumors to a specific drug treatment, as well as the molecular signatures and genotypes/proteotypes/metabolotypes that predict responses to certain drugs.

Conflicts of interest

The author declares that he has no competing interest.

Acknowledgements

This work was supported by grants from the Ministry of Science and Technology, Taiwan (MOST 106-2632-B-182-002 and MOST 106-2320-B-182-029-MY3) and the Chang Gung Memorial Hospital, Linkou, Taiwan (CMRPD1H0251, CRRPD1F0053, CIRPD3B0013 and CLRPD190019). This study was also supported by the “Molecular Medicine Research Center, Chang Gung University” from The Featured Areas Research Center Program within the framework of the Higher Education Sprout Project by the Ministry of Education in Taiwan.

REFERENCES

- [1] Manning G, Whyte DB, Martinez R, Hunter T, Sudarsanam S. The protein kinase complement of the human genome. *Science* 2002;298:1912–34.
- [2] Raggiaschi R, Gotta S, Terstappen GC. Phosphoproteome analysis. *Biosci Rep* 2005;25:33–44.

- [3] Krebs EG. The Albert Lasker Medical Awards. Role of the cyclic AMP-dependent protein kinase in signal transduction. *JAMA* 1989;262:1815–8.
- [4] Eckhart W, Hutchinson MA, Hunter T. An activity phosphorylating tyrosine in polyoma T antigen immunoprecipitates. *Cell* 1979;18:925–33.
- [5] Hunter T, Sefton BM. Transforming gene product of Rous sarcoma virus phosphorylates tyrosine. *Proc Natl Acad Sci USA* 1980;77:1311–5.
- [6] Hunter T, Cooper JA. Epidermal growth factor induces rapid tyrosine phosphorylation of proteins in A431 human tumor cells. *Cell* 1981;24:741–52.
- [7] Chinkers M, Cohen S. Purified EGF receptor-kinase interacts specifically with antibodies to Rous sarcoma virus transforming protein. *Nature* 1981;290:516–9.
- [8] Downward J, Yarden Y, Mayes E, Scrace G, Totty N, Stockwell P, et al. Close similarity of epidermal growth factor receptor and v-erb-B oncogene protein sequences. *Nature* 1984;307:521–7.
- [9] Lin CR, Chen WS, Kruiger W, Stolarsky LS, Weber W, Evans RM, et al. Expression cloning of human EGF receptor complementary DNA: gene amplification and three related messenger RNA products in A431 cells. *Science* 1984;224:843–8.
- [10] Sefton BM, Hunter T, Beemon K, Eckhart W. Evidence that the phosphorylation of tyrosine is essential for cellular transformation by Rous sarcoma virus. *Cell* 1980;20:807–16.
- [11] Konopka JB, Watanabe SM, Witte ON. An alteration of the human c-abl protein in K562 leukemia cells unmasks associated tyrosine kinase activity. *Cell* 1984;37:1035–42.
- [12] Ben-Neriah Y, Daley GQ, Mes-Masson AM, Witte ON, Baltimore D. The chronic myelogenous leukemia-specific P210 protein is the product of the bcr/abl hybrid gene. *Science* 1986;233:212–4.
- [13] Daley GQ, Van Etten RA, Baltimore D. Induction of chronic myelogenous leukemia in mice by the P210bcr/abl gene of the Philadelphia chromosome. *Science* 1990;247:824–30.
- [14] Elefanti AG, Hariharan IK, Cory S. Bcr-Abl, the hallmark of chronic myeloid leukaemia in man, induces multiple haemopoietic neoplasms in mice. *EMBO J* 1990;9:1069–78.
- [15] Kelliher MA, McLaughlin J, Witte ON, Rosenberg N. Induction of a chronic myelogenous leukemia-like syndrome in mice with v-abl and BCR/ABL. *Proc Natl Acad Sci USA* 1990;87:6649–53.
- [16] Heisterkamp N, Jenster G, ten Hoeve J, Zovich D, Pattengale PK, Groffen J. Acute leukaemia in bcr/abl transgenic mice. *Nature* 1990;344:251–3.
- [17] Hirota S, Isozaki K, Moriyama Y, Hashimoto K, Nishida T, Ishiguro S, et al. Gain-of-function mutations of c-kit in human gastrointestinal stromal tumors. *Science* 1998;279:577–80.
- [18] Nishida T, Hirota S, Taniguchi M, Hashimoto K, Isozaki K, Nakamura H, et al. Familial gastrointestinal stromal tumours with germline mutation of the KIT gene. *Nat Genet* 1998;19:323–4.
- [19] Lynch TJ, Bell DW, Sordella R, Gurubhagavatula S, Okimoto RA, Brannigan BW, et al. Activating mutations in the epidermal growth factor receptor underlying responsiveness of non-small-cell lung cancer to gefitinib. *N Engl J Med* 2004;350:2129–39.
- [20] Paez JG, Jänne PA, Lee JC, Tracy S, Greulich H, Gabriel S, et al. EGFR mutations in lung cancer: correlation with clinical response to gefitinib therapy. *Science* 2004;304:1497–500.
- [21] Pao W, Miller V, Zakowski M, Doherty J, Politi K, Sarkaria I, et al. EGF receptor gene mutations are common in lung cancers from “never smokers” and are associated with sensitivity of tumors to gefitinib and erlotinib. *Proc Natl Acad Sci USA* 2004;101:13306–11.

- [22] Slamon DJ, Clark GM, Wong SG, Levin WJ, Ullrich A, McGuire WL. Human breast cancer: correlation of relapse and survival with amplification of the HER-2/neu oncogene. *Science* 1987;235:177–82.
- [23] Slamon DJ, Godolphin W, Jones LA, Holt JA, Wong SG, Keith DE, et al. Studies of the HER-2/neu proto-oncogene in human breast and ovarian cancer. *Science* 1989;244:707–12.
- [24] Toikkanen S, Helin H, Isola J, Joensuu H. Prognostic significance of HER-2 oncoprotein expression in breast cancer: a 30-year follow-up. *J Clin Oncol* 1992;10:1044–8.
- [25] Yaish P, Gazit A, Gilon C, Levitzki A. Blocking of EGF-dependent cell proliferation by EGF receptor kinase inhibitors. *Science* 1988;242:933–5.
- [26] Anafi M, Gazit A, Gilon C, Ben-Neriah Y, Levitzki A. Selective interactions of transforming and normal abl proteins with ATP, tyrosine-copolymer substrates, and tyrphostins. *J Biol Chem* 1992;267:4518–23.
- [27] Anafi M, Gazit A, Zehavi A, Ben-Neriah Y, Levitzki A. Tyrphostin-induced inhibition of p210bcr-abl tyrosine kinase activity induces K562 to differentiate. *Blood* 1993;82:3524–9.
- [28] Buchdunger E, Zimmermann J, Mett H, Meyer T, Müller M, Druker BJ, et al. Inhibition of the Abl protein-tyrosine kinase in vitro and in vivo by a 2-phenylaminopyrimidine derivative. *Cancer Res* 1996;56:100–4.
- [29] Druker BJ, Tamura S, Buchdunger E, Ohno S, Segal GM, Fanning S, et al. Effects of a selective inhibitor of the Abl tyrosine kinase on the growth of Bcr-Abl positive cells. *Nat Med* 1996;2:561–6.
- [30] Carroll M, Ohno-Jones S, Tamura S, Buchdunger E, Zimmermann J, Lydon NB, et al. CGP 57148, a tyrosine kinase inhibitor, inhibits the growth of cells expressing BCR-ABL, TEL-ABL, and TEL-PDGFR fusion proteins. *Blood* 1997;90:4947–52.
- [31] Druker BJ, Talpaz M, Resta DJ, Peng B, Buchdunger E, Ford JM, et al. Efficacy and safety of a specific inhibitor of the BCR-ABL tyrosine kinase in chronic myeloid leukemia. *Engl J Med* 2001;344:1031–7.
- [32] Druker BJ, Sawyers CL, Kantarjian H, Resta DJ, Reese SF, Ford JM, et al. Activity of a specific inhibitor of the BCR-ABL tyrosine kinase in the blast crisis of chronic myeloid leukemia and acute lymphoblastic leukemia with the Philadelphia chromosome. *N Engl J Med* 2001;344:1038–42.
- [33] Sawyers CL, Hochhaus A, Feldman E, Goldman JM, Miller CB, Ottmann OG, et al. Imatinib induces hematologic and cytogenetic responses in patients with chronic myelogenous leukemia in myeloid blast crisis: results of a phase II study. *Blood* 2002;99:3530–9.
- [34] Buchdunger E, Cioffi CL, Law N, Stover D, Ohno-Jones S, Druker BJ, et al. Abl protein-tyrosine kinase inhibitor STI571 inhibits in vitro signal transduction mediated by c-kit and platelet-derived growth factor receptors. *J Pharmacol Exp Ther* 2000;295:139–45.
- [35] Demetri GD, von Mehren M, Blanke CD, Van den Abbeele AD, Eisenberg B, Roberts PJ, et al. Efficacy and safety of imatinib mesylate in advanced gastrointestinal stromal tumors. *N Engl J Med* 2002;347:472–80.
- [36] Kawamoto T, Sato JD, Le A, Polikoff J, Sato GH, Mendelsohn J. Growth stimulation of A431 cells by EGF: identification of high affinity receptors for epidermal growth factor by an anti-receptor monoclonal antibody. *Proc Natl Acad Sci USA* 1983;80:1337–41.
- [37] Masui H, Kawamoto T, Sato JD, Wolf B, Sato GH, Mendelsohn J. Growth inhibition of human tumor cells in athymic mice by anti-EGF receptor monoclonal antibodies. *Cancer Res* 1984;44:1002–7.
- [38] Mendelsohn J, Prewett M, Rockwell P, Goldstein NI. CCR 20th anniversary commentary: a chimeric antibody, C225, inhibits EGFR activation and tumor growth. *Clin Cancer Res* 2015;21:227–9.
- [39] Divgi CR, Welt S, Kris M, Real FX, Yeh SD, Gralla R, et al. Phase I imaging trial of indium 111-labeled anti-epidermal growth factor receptor monoclonal antibody 225 in patients with squamous cell lung carcinoma. *J Natl Cancer Inst* 1991;83:97–104.
- [40] Cunningham D, Humblet Y, Siena S, Khayat D, Bleiberg H, Santoro A, et al. Cetuximab monotherapy and cetuximab plus irinotecan in irinotecan-refractory metastatic colorectal cancer. *N Engl J Med* 2004;351:337–45.
- [41] Bonner JA, Harari PM, Giralt J, Azarnia N, Shin DM, Cohen RB, et al. Radiotherapy plus cetuximab for squamous-cell carcinoma of the head and neck. *N Engl J Med* 2006;354:567–78.
- [42] Di Martino S, Rainone A, Troise A, Di Paolo M, Pugliese S, Zappavigna S, et al. Overview of FDA-approved anti-cancer drugs used for targeted therapy. *WCRJ* 2015;2:e553.
- [43] Hunter T. Treatment for chronic myelogenous leukemia: the long road to imatinib. *J Clin Invest* 2007;117:2036–43.

Cite this: *Food Funct.*, 2019, **10**, 2720

Piperine-mediated suppression of voltage-dependent Ca^{2+} influx and glutamate release in rat hippocampal nerve terminals involves $5\text{HT}_{1\text{A}}$ receptors and G protein $\beta\gamma$ activation

Ting Yang Hsieh,^a Yi Chang^{b,c} and Su Jane Wang^{id} *^{c,d}

Piperine is the crucial alkaloid component of black pepper (*Piper nigrum* Linn.) and has neuroprotective effects. Because inhibition of glutamatergic excitatory neurotransmission is a possible mechanism involved in neuroprotection, we investigated the effect of piperine on the 4-aminopyridine (4-AP)-evoked release of glutamate from rat hippocampal synaptosomes. Piperine inhibited 4-AP-evoked glutamate release, and the inhibition was prevented by the chelation of extracellular Ca^{2+} ions and a vesicular transporter inhibitor. Piperine reduced the 4-AP-evoked elevation of intrasynaptosomal Ca^{2+} levels but did not affect the synaptosomal membrane potential. In the presence of ω -conotoxin MVIIC, an N- and P/Q-type channel blocker, the piperine-mediated inhibition of 4-AP-evoked glutamate release was markedly reduced; however, dantrolene and CGP37157, which are intracellular Ca^{2+} -release inhibitors, did not alter the piperine effect. In addition, immunocytochemical analysis confirmed the presence of presynaptic 5-hydroxytryptamine 1A ($5\text{-HT}_{1\text{A}}$) receptor proteins. The glutamate release-inhibiting effect of piperine was discovered to be prevented by the $5\text{-HT}_{1\text{A}}$ receptor antagonist WAY100635 and the G protein $\beta\gamma$ subunit inhibitor gallein; however, it was unaffected by the adenylate cyclase inhibitor SQ22536 or the protein kinase A inhibitor PKI622. These results suggest that piperine inhibits glutamate release from rat hippocampal nerve terminals by reducing Ca^{2+} influx through N- and P/Q-type Ca^{2+} channels and that the activation of presynaptic $5\text{-HT}_{1\text{A}}$ receptors and the G protein $\beta\gamma$ subunit is involved in this effect.

Received 7th November 2018,

Accepted 10th April 2019

DOI: 10.1039/c8fo02189a

rsc.li/food-function

Introduction

A growing body of evidence has established that natural products may be the single most productive source of leads for modern drug development.¹ Piperine (1-piperoylpiperidine) is the major alkaloid component of black pepper,² and it has received considerable attention for its possible role in the prevention of infection, cancer, diabetes, and some inflammatory diseases.^{3–5} Furthermore, piperine also exhibits a protective effect on the brain. For example, it can cross the blood–brain barrier,^{6,7} and it has been reported to ameliorate cognitive dysfunction and brain damage in various animal models with

neurological disorders including epilepsy, depression, Alzheimer's disease, and Parkinson's disease.^{8–12}

Glutamate is the primary excitatory neurotransmitter in the central nervous system, and it plays a crucial role in neurological processes including learning and memory.¹³ However, excessive glutamate release under pathophysiological conditions causes neuronal damage and death.¹⁴ This glutamate excitotoxicity has been implicated in the pathophysiology of numerous neurological diseases, including hypoxic–ischemic brain injury and epilepsy, and neurodegenerative diseases such as Alzheimer's disease and Parkinson's disease.^{15–17} Accordingly, inhibition of glutamate release is a crucial neuroprotective mechanism. Indeed, several neuroprotective drugs have been demonstrated to reduce glutamate release in human and rat brain tissues.^{18–20}

Piperine has been reported to offer a neuroprotective effect, and we hypothesized that piperine could influence the release of glutamate. Although an electrophysiological study showed that piperine can inhibit glutamate release in cultured hippocampal neurons,²¹ a direct effect of piperine on glutamate release in nerve terminal preparations has not yet been demonstrated. Therefore, the present study was designed to

^aP.H.D. Program in Nutrition & Food Science, Fu Jen Catholic University, New Taipei City, Taiwan

^bDepartment of Anesthesiology, Shin Kong Wu Ho-Su Memorial Hospital, Taipei, Taiwan

^cSchool of Medicine, Fu Jen Catholic University, New Taipei City, Taiwan.

E-mail: med0003@mail.fju.edu.tw; Fax: +886-2-29052096; Tel: +886-2-29053465

^dResearch Center for Chinese Herbal Medicine, College of Human Ecology, Chang Gung University of Science and Technology, Taoyuan City, Taiwan

determine the effects of piperine on glutamate release and to characterize the underlying molecular mechanisms by using rat hippocampal nerve terminals (synaptosomes), a system particularly suited to the evaluation of presynaptic effects on neurotransmitter release.^{22,23} Hippocampus was chosen because it is dependent on glutamate signaling to a greater extent than other brain tissues.²⁴ Moreover, hippocampus is one of the brain regions whose function is altered in neurodegenerative and psychiatric disorders, suggesting the potential relevance of glutamate transmission in this area to the pathophysiology of these diseases.^{25,26} Using hippocampal synaptosomes, the results of this study demonstrated that piperine inhibited glutamate release by suppressing presynaptic Ca^{2+} entry. Moreover, the inhibition was a consequence of an activated presynaptic 5-HT_{1A} receptor and G protein $\beta\gamma$ subunit ($\text{G}\beta\gamma$)-coupled cascade. The results of this investigation are crucial for understanding the role of piperine in the brain.

Materials and methods

Chemicals

Bafilomycin A1, DL-threo-beta-benzyloxyaspartate (DL-TBOA), dantrolene, 7-chloro-5-(2-chlorophenyl)-1,5-dihydro-4,1-benzothiazepin-2(3H)-one (CGP37157), WAY 100635, protein kinase A inhibitor fragment (6-22) amide [PKI (6-22) amide], 9-(tetrahydro-2-furanyl)-9H-purin-6-amine (SQ22536), propofol, pertussis toxin (PTX) and gallein were purchased from Tocris Cookson (Bristol, UK). Piperine, Percoll, ethylene glycol bis (β -aminoethyl ether)-N,N,N',N'-tetraacetic acid (EGTA) and 4-aminopyridine (4-AP) were purchased from Sigma-Aldrich (St Louis, MO, USA). 3,3'-Dipropylthiadicarbocyanine iodide [$\text{DiSC}_3(5)$] was purchased from Invitrogen (Carlsbad, CA, USA). ω -Conotoxin MVIIC (ω -CgTX MVIIC) was purchased from Alomone lab (Jerusalem, Israel). Fura-2-acetoxymethyl ester (Fura-2-AM) was purchased from Life Technologies (Bengaluru, India).

Experimental animals

Male Sprague-Dawley rats (BioLASCO, Taipei, Taiwan) weighing 150–200 g were used throughout the study. The animals were sacrificed by decapitation and the hippocampus rapidly removed at 4 °C. The experimental procedures were approved by the Institutional Animal Care and Use Committee at the Fu Jen Catholic University and carried out in accordance with the protocols issued, which followed National Institutes of Health Guide for the Care and Use of Laboratory (NAC 2011).

Synaptosome preparation

Percoll-purified synaptosomes were prepared according to previous studies.^{27,28} The final synaptosomal fraction was resuspended in approximately 2–3 ml HEPES buffer medium (HBM, mM: NaCl, 140; KCl, 5; NaHCO_3 , 5; $\text{MgCl}_2 \cdot 6\text{H}_2\text{O}$, 1; Na_2HPO_4 , 1.2; glucose, 10; HEPES, 10; pH 7.4) and the protein concentration (0.5 mg protein per ml) determined using the Bradford

assay. The synaptosomes were stored on ice as drained pellets and used within 4 h.

Glutamate release

The release of endogenous glutamate was measured using a continuous fluorometric assay, based on the reduction of nicotinamide adenine dinucleotide phosphate (NADP^+) to NADPH catalyzed by glutamate dehydrogenase (GDH) in the presence of glutamate. NADPH gives rise to a strong fluorometric signal at 460 nm when excited at 340 nm.²⁹ In brief, pelleted synaptosomes were resuspended in HBM containing bovine serum albumin (BSA) and transferred to a 1 cm² quartz cuvette in a PerkinElmer LS-55 spectrofluorometer equipped with a magnetic stirrer (PerkinElmer Life and Analytical Sciences, Waltham, MA, USA). NADP^+ (2 mM) and GDH (50 units per ml) were added in the presence of CaCl_2 (1.2 mM). After 10 min, the background fluorescence of NADPH was measured for 5 min. At that point, glutamate release was evoked by adding 4-AP (1 mM) to the preparation, and the fluorescence of NADPH was measured for 10 min. 4-AP is a potassium channel blocker that opens voltage-dependent Ca^{2+} channels and induced the release of glutamate.³⁰ Traces were calibrated by the addition of 5 nmol glutamate at the end of each assay. Data were collected at 2 s intervals.

Intraterminal Ca^{2+} concentration

Intraterminal Ca^{2+} concentration ($[\text{Ca}^{2+}]_i$) was measured with Fura-2 as described previously.³¹ Synaptosomes were resuspended in HBM with BSA in the presence of 5 μM Fura 2-AM and 1.2 mM CaCl_2 at 37 °C for 30 min. After Fura-2 loading, synaptosomes were pelleted and resuspended in fresh HBM with BSA. An aliquot (2 ml) was transferred to a stirred cuvette containing 1.2 mM CaCl_2 , and fluorescence was monitored at 340 and 510 nm. Data were collected at 5 s intervals. The value of $[\text{Ca}^{2+}]_i$ was calculated using the equations described previously by Grynkiewicz *et al.* (1985).³²

Plasma membrane potential

The synaptosomal membrane potential was estimated with $\text{DiSC}_3(5)$.³³ Synaptosomes in HBM containing BSA were preincubated at 37 °C for 30 min. After this time, an aliquot (2 ml) was transferred to a stirred cuvette containing 5 μM $\text{DiSC}_3(5)$ and 1.2 mM CaCl_2 . After allowing equilibration for 1 min, the fluorescence was determined at 646 and 674 nm. Data were collected at 2 s intervals.

Immunocytochemistry

Immunofluorescence analysis was performed on synaptosomes as described previously.²⁹ Synaptosomes were incubated with primary antibody solutions containing anti-synaptophysin (1:1000, Millipore, Billerica, MA, USA) and anti-5HT_{1A} receptor (1:200, Abcam, Cambridge, UK) for 90 min at 4 °C. Synaptosomes were then washed (three times for 5 min) in phosphate-buffered saline (PBS) and incubated in PBS with 1% BSA containing a mixture of fluorescently tagged markers as follows: goat anti-rabbit IgG-DyLight 488 (1:200,

Invitrogen, Carlsbad, CA, USA) and goat anti-mouse IgG-DyLight 594 (1:200, Invitrogen, Carlsbad, CA, USA). Immunoreactivity was visualized using a fluorescence microscope (Leica DM2000LED, Wetzlar, Germany).

Statistical analysis

Data are expressed as mean \pm SEM. Statistical significance was determined by unpaired Student's two-tailed *t*-tests and one-way ANOVA with Scheffe's *post hoc* test. A *p*-value < 0.05 was considered statistically significant.

Results

Piperine-mediated inhibition of 4-AP-evoked Ca^{2+} -dependent glutamate release

Fig. 1A shows that 4-AP evoked glutamate release at a rate of 7.6 ± 0.2 nmol per mg per 5 min from the hippocampal synaptosomes incubated in the presence of 1.2 mM CaCl_2 . Preincubation with 10 μM piperine before 4-AP addition reduced the rate of glutamate release to 4.4 ± 0.2 nmol per mg per 5 min [$t(14) = 9.4$, $P < 0.001$; 42.1% \pm 1.9% inhibition].

Piperine did not affect the basal prepolarization glutamate level [$t(14) = -1.8$, $P = 0.09$]. The effect of piperine was concentration dependent; the maximum inhibition ($74.7\% \pm 1.44\%$) was observed when the compound was applied at 30 μM piperine, and the half-maximal inhibitory concentration (IC_{50}) was 12 μM (Fig. 1B). Fig. 1C shows that the calcium-free medium containing 300 μM EGTA markedly inhibited 4-AP-evoked glutamate release [$t(13) = 27.6$, $P < 0.001$]. This Ca^{2+} -independent component of 4-AP-evoked glutamate release was unaltered by 10 μM piperine [$F(2, 17) = 374.7$, $P = 0.93$]. DL-TBOA (10 μM), an excitatory amino acid transporter blocker, increased 4-AP-evoked glutamate release [$t(13) = -3.9$, $P < 0.01$]. In the presence of DL-TBOA, piperine (10 μM) inhibited 4-AP-induced release of glutamate by $37\% \pm 5.2\%$ [$F(2, 17) = 24.1$, $P < 0.001$; Fig. 1C], which was not significantly different from the inhibition achieved using piperine alone [$42.1\% \pm 1.94\%$; $P > 0.05$]. By contrast, bafilomycin A1 (0.1 μM), a vesicular transporter inhibitor, inhibited 4-AP-evoked glutamate release [$t(13) = 24.9$, $P < 0.001$] and prevented the action of piperine [$F(2, 17) = 270.1$, $P < 0.001$; Fig. 1C]. On average, piperine produced a $2.8\% \pm 0.7\%$ inhibition of 4-AP-evoked glutamate release after treatment with bafilomycin A1, which was less

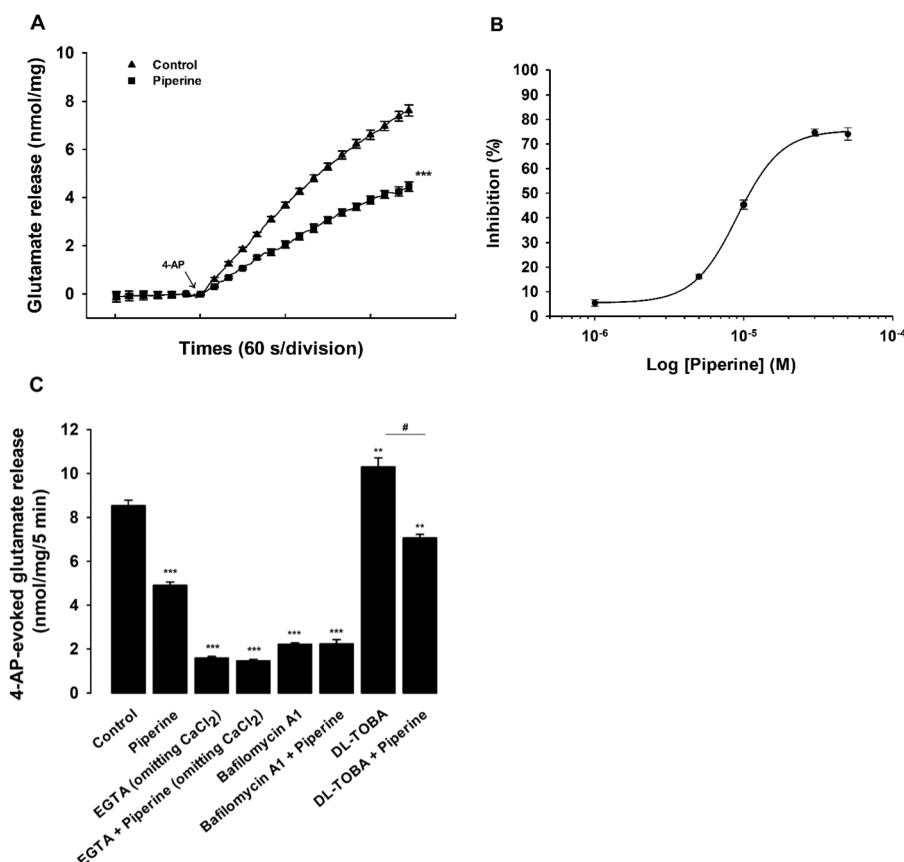


Fig. 1 Piperine inhibits 4-AP-evoked glutamate release from rat hippocampal synaptosomes: dependence on the extracellular calcium. (A) Glutamate release was evoked by the addition of 1 mM 4-AP (arrow) in the absence (control) and presence of 10 μM piperine added 10 min prior to depolarization. (B) Concentration–effect relationship of piperine (1–50 μM) on 4-AP-induced glutamate release. (C) The effect of piperine on glutamate release induced by 1 mM 4-AP in the absence (control) and presence of 300 μM EGTA (without CaCl_2), 10 μM DL-TBOA, or 0.1 μM bafilomycin A1. Data are mean \pm SEM ($n = 5$ –14). *** $P < 0.01$ compared with control; # $P < 0.05$ compared with DL-TBOA alone.

than the inhibition produced using piperine alone [$42.1\% \pm 1.9\%$, $P < 0.05$]. These results indicate that piperine only inhibits the Ca^{2+} -dependent, exocytotic component of 4-AP-evoked glutamate release.

Effects of piperine on intrasynaptosomal Ca^{2+} concentration and the synaptosomal membrane potential

Table 1 shows the effects of piperine on the intrasynaptosomal Ca^{2+} concentration $[\text{Ca}^{2+}]_i$ and synaptosomal membrane potential. The depolarization of synaptosomes due to 1 mM 4-AP elicited an increase in $[\text{Ca}^{2+}]_i$ to a plateau level. Preincubation with 10 μM piperine did not affect the basal $[\text{Ca}^{2+}]_i$, but it reduced the 4-AP-evoked increase in $[\text{Ca}^{2+}]_i$ [$t(9) = 4.8$, $P < 0.001$]. In addition, 4-AP caused an increase in DiSC₃(5) fluorescence. The presence of 10 μM piperine did not significantly affect the plasma membrane potential under either resting conditions or 4-AP stimulation [$t(8) = -0.87$, $P = 0.41$; Table 1]. The lack of effect of piperine was not due to an insufficient sensitivity of the DiSC₃(5) dye to alteration in synaptosomal membrane potential, because in parallel experiments, propofol (50 μM) was seen to effect a 75% inhibition of 4-AP-mediated increase in DiSC₃(5) fluorescence [$t(8) = 28.9$, $P < 0.001$; Table 1]. Propofol is an intravenous anesthetic that has been shown to inhibit evoked glutamate release from rat nerve terminals.^{34,35} These data indicate that the observed inhibition of the elevation of $[\text{Ca}^{2+}]_i$ by piperine was most likely due to a direct reduction in the entry of Ca^{2+} through voltage-dependent Ca^{2+} channels, which consequently reduced glutamate release.

Piperine-mediated inhibition of 4-AP-evoked glutamate release is abolished by N- and P/Q-type Ca^{2+} channel blockade

Fig. 2 depicts the role of N- and P/Q-type Ca^{2+} channels, which are known to directly participate in triggering glutamate release from synaptosomes.^{36,37} Glutamate release evoked by 1 mM 4-AP was significantly decreased in the presence of 4 μM ω -conotoxin MVIIC (ω -CgTX MVIIC), an N- and P/Q-type Ca^{2+} channel blocker [$t(16) = 22.1$, $P < 0.001$; Fig. 2A]. Notably, although the control release was significantly inhibited by 10 μM piperine [$t(19) = 9.6$, $P < 0.001$], this effect of piperine was abolished in the presence of ω -CgTX MVIIC [$F(2,20) = 317.4$, $P < 0.001$]. On average, piperine inhibited 4-AP-evoked glutamate release by $2.8\% \pm 2.2\%$ after treatment with ω -CgTX MVIIC, which was less than the inhibition produced using piperine alone [$41\% \pm 2.1\%$; $P < 0.05$; Fig. 2].

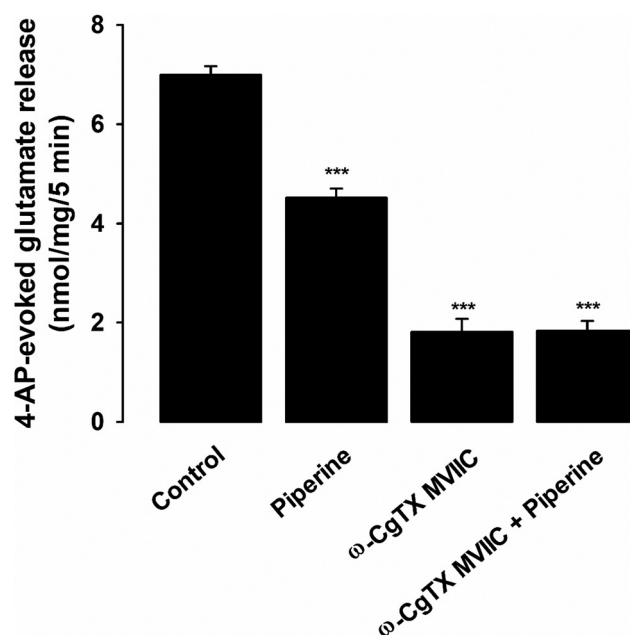


Fig. 2 Piperine-mediated inhibition of 4-AP-evoked glutamate release is prevented by N- and P/Q-type calcium channel blockade. The effect of piperine on glutamate release induced by 1 mM 4-AP in the absence (control) and presence of 4 μM ω -CgTX MVIIC. Data are mean \pm SEM ($n = 5-11$). *** $P < 0.01$ compared with control.

Involvement of presynaptic 5HT_{1A} receptors in piperine-mediated inhibition of 4-AP-evoked glutamate release

Because piperine-mediated effects have been reported to be associated with the modulation of γ -aminobutyric acid (GABA) type A (GABA_A) receptors and 5-hydroxytryptamine (5HT) 1A (5HT_{1A}) receptors,^{38,39} we examined the effects of piperine on 4-AP-evoked glutamate release in the presence of the GABA_A receptor antagonist SR95531 and the 5HT_{1A} receptor antagonist WAY10063. Table 2 shows that the two antagonists significantly affected the release of glutamate evoked by 4-AP at 1 mM [SR95531, $t(21) = 1.7$, $P = 0.11$; WAY100635, $t(21) = 4.5$, $P < 0.001$]. However, in the presence of 100 μM SR95531, 4-AP-evoked glutamate release was further inhibited by 10 μM piperine [$F(2,26) = 23.7$, $P < 0.001$]. The additive relationship between SR95531 and piperine indicated that GABA_A receptors apparently do not mediate piperine's observed inhibition of glutamate release. By contrast, the inhibitory effect of piperine on 4-AP-evoked glutamate release was obliterated by the

Table 1 Effect of piperine on intraterminal Ca^{2+} concentration ($[\text{Ca}^{2+}]_i$) and membrane potential in rat hippocampal synaptosomes

	Membrane potential (fluorescence units)			$[\text{Ca}^{2+}]_i$ (nM)		
	Basal	4-AP	<i>n</i>	Basal	4-AP	<i>n</i>
Control	1.7 ± 0.2	$40.6 \pm 0.6^{***}$	5	146.7 ± 2.6	$227.9 \pm 5.8^{***}$	5
Piperine	1.1 ± 0.8	$41.3 \pm 0.7^{***}$	5	144.3 ± 3.9	$185.4 \pm 5.4^{***}$	5
Propofol	2.2 ± 0.4	$10.1 \pm 0.9^{***}$	5			

*** $P < 0.001$ compared with the 4-AP group.

Table 2 Effects of GABA_A and 5HT_{1A} receptor antagonists on the inhibition of 4-AP-evoked glutamate release by piperine

	4-AP-evoked glutamate release (nmol per mg per 5 min)	<i>n</i>
Control	7.9 ± 0.3	18
Piperine	4.8 ± 0.2***	11
SR95531	6.8 ± 0.4**	5
SR95531 + piperine	3.9 ± 0.3***, #	6
WAY100635	5.0 ± 0.3***	5
WAY100635 + piperine	4.6 ± 0.4***	5
SR95531 + WAY100635	3.5 ± 0.5***	5
SR95531 + WAY100635 + piperine	2.8 ± 0.3***	5

****P* < 0.001, ***P* < 0.01 compared with control. #*P* < 0.05 compared with SR95531 alone.

addition of 10 μM WAY10063; the release measured in the presence of WAY10063 and piperine was similar to that obtained in the presence of WAY10063 alone [*F*(2,25) = 20.1, *P* = 0.91]. Furthermore, 100 μM SR95531 and 10 μM WAY10063 reduced 4-AP-evoked glutamate release [*t*(21) = 6.8, *P* < 0.001] and completely prevented the action of piperine [*F*(2,25) = 51.1; *P* < 0.001]. No statistical difference was observed between the release after the combined presence of SR95531 and WAY10063 and the release after the combined presence of SR95531, WAY10063, and piperine treatment (*P* = 0.62). Fig. 3 shows that hippocampal synaptosomes were double-labeled using antibodies against the synaptic vesicle marker synaptophysin (Fig. 3A) and 5HT_{1A} receptors (Fig. 3B). An analysis of six images revealed that approximately 74.4% ± 0.7% of synaptophysin-positive particles were positive for 5HT_{1A} receptors (Fig. 3C).

G protein βγ subunit-coupled cascades are involved in the piperine-mediated inhibition of 4-AP-evoked glutamate release

5HT_{1A} receptors are known to couple functionally to Gi/o proteins to inhibit adenylate cyclase (AC), thus leading to a reduced level of cyclic AMP and protein kinase A (PKA).⁴⁰ Fig. 4 shows that synaptosomes were incubated for 4 h in the presence of the Gi/o protein inhibitor pertussis toxin (PTX; 2 μg ml⁻¹), and 4-AP (1 mM)-evoked glutamate release was significantly decreased [*t*(13) = 14.3, *P* < 0.001]. In the PTX-treated synaptosomes, the inhibitory effect of piperine on 4-AP (1 mM)-evoked glutamate release was suppressed, there being no statistical difference between the release after PTX alone and after PTX + piperine treatment [*F*(2,17) = 179.1, *P* = 0.74]. In addition, 4-AP (1 mM)-evoked glutamate release was unaffected by the AC inhibitor SQ22536 (50 μM) [*t*(14) = 0.5, *P* = 0.586] and the PKA inhibitor PKI (6-22) amide (2 μM) [*t*(12) = 1.8, *P* = 0.12]. In the presence of SQ22536 or PKI (6-22) amide, 10 μM piperine produced 37.1% ± 4.3% and 40% ± 2.6% decreases in 4-AP-evoked glutamate release, respectively, which were not different from the inhibition produced by piperine alone [41.6 ± 1.1%, *P* > 0.05, Fig. 4]. Furthermore, the G protein βγ (Gβγ) subunit inhibitor gallein inhibited 4-AP-evoked glutamate release [*t*(12) = 15.7,

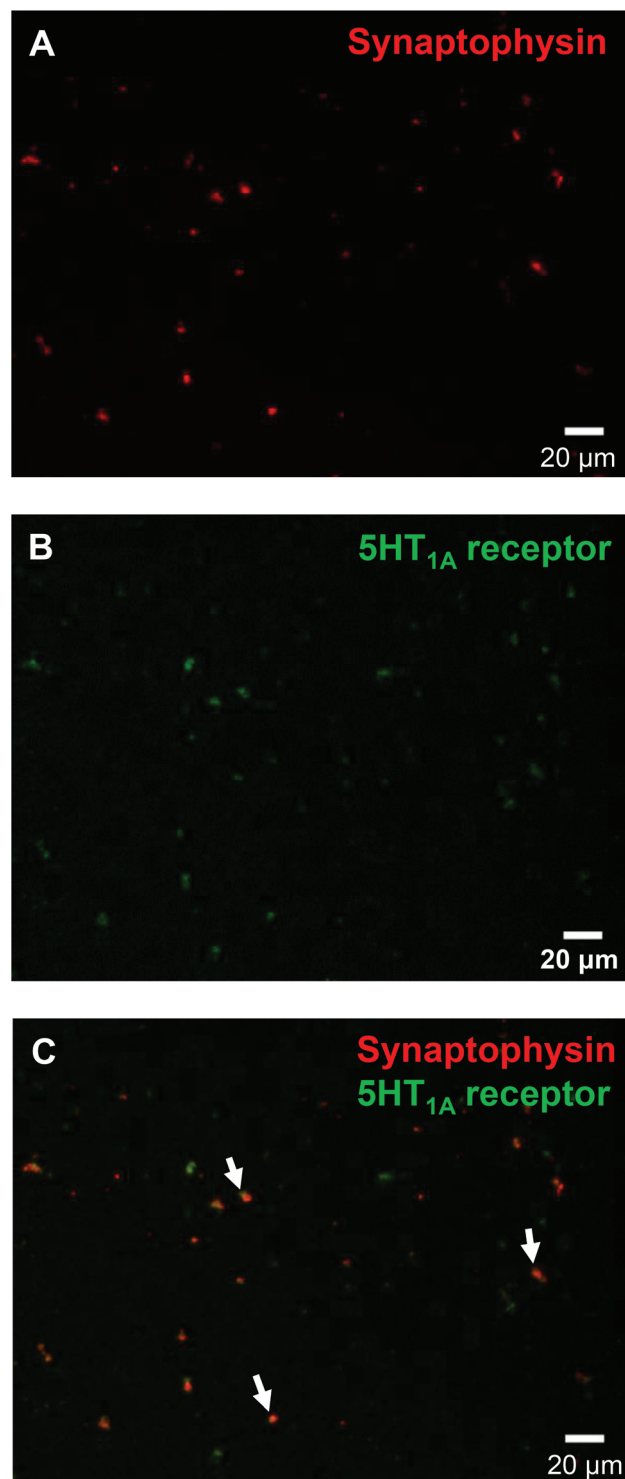


Fig. 3 5HT_{1A} receptors were co-expressed with the presynaptic marker synaptophysin in rat hippocampal synaptosomes. Synaptosomes were set onto coverslips and were double-stained for immunocytochemistry analysis with antibodies against synaptophysin (A), 5HT_{1A} receptors (B), and merge (C). Scale bar, 20 μm.

P < 0.001]. However, in the presence of gallein, 10 μM piperine continued to significantly reduce the release of glutamate evoked by 4-AP (20% ± 3.8%; *F*(2, 16) = 202.7, *P* < 0.05), but

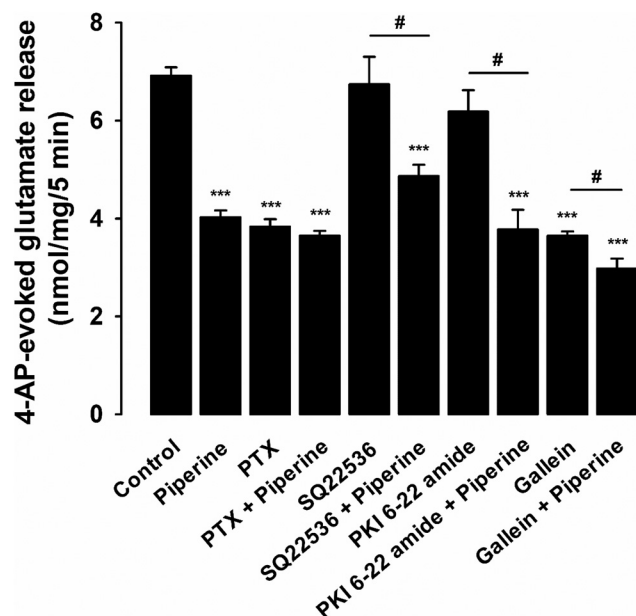


Fig. 4 Piperine-mediated inhibition of 4-AP-evoked glutamate release is partially blocked in the presence of the $G\beta\gamma$ inhibitor gallein. The effect of piperine on glutamate release induced by 1 mM 4-AP in the absence (control) and presence of $2\ \mu\text{g mL}^{-1}$ PTX, $50\ \mu\text{M}$ SQ22536, $2\ \mu\text{M}$ PKI (6-22) amide or $10\ \mu\text{M}$ gallein. Data are mean \pm SEM ($n = 5-9$). *** $P < 0.01$ compared with control; # $P < 0.05$ compared with SQ22536 alone or PKI (6-22) amide alone.

this inhibition was significantly different from the inhibition produced by piperine alone ($44.5\% \pm 1.6\%$, $P < 0.05$; Fig. 4). These results suggest that $G\beta\gamma$ signaling is involved in the observed effect of piperine on 4-AP-evoked glutamate release.

Discussion

The glutamate system is involved in the pathophysiology and treatment of numerous brain disorders, which are accompanied by an increased glutamate concentration in the brain.¹⁴ Several studies have also reported that reduced glutamate levels are necessary for the pharmacotherapeutic effects of neuroprotectants.^{41,42} Numerous *in vitro* and animal studies have shown that piperine has neuroprotective activity.^{43,44} An electrophysiological study using cultured hippocampal neurons discovered that piperine has neuroprotective activity through inhibiting presynaptic glutamate release.²¹ However, nothing is presently known about the effect of piperine on glutamate release from isolated nerve terminals (synaptosomes). Synaptosomes represent a well-established model for the specific study of presynaptic regulation without complications in interpretation produced by concomitant postsynaptic effects.²⁸ Using this model, we analyzed the characteristics and mechanisms of action of piperine in regulating glutamate release in the hippocampus. We demonstrated that piperine inhibits the depolarization-evoked Ca^{2+} -dependent exocytosis

release of glutamate in a concentration-dependent manner with a half-maximal effective concentration (EC_{50}) of $12\ \mu\text{M}$; this value lies within the range of EC_{50} values ($1-50\ \mu\text{M}$) that have been reported in other studies.^{45,46} The mechanism(s) contributing to the piperine-mediated inhibition of glutamate release from rat hippocampal synaptosomes are discussed subsequently.

In nerve terminals, Na^+ channel inhibition or K^+ channel activation can stabilize membrane excitability, resulting in a reduction in Ca^{2+} entry through the N- and P/Q-type Ca^{2+} channels and a consequent reduction in glutamate release.⁴⁷ The inhibitory effects of piperine on Na^+ channels have been reported from *in vitro* studies.⁴⁸ However, in the present study, piperine did not alter the synaptosomal plasma membrane potential. The effect of piperine on glutamate release in rat hippocampal synaptosomes was not caused by the attenuation of membrane depolarization, which reduced Ca^{2+} influx and glutamate release. In addition, we found that piperine significantly reduced the 4-AP-evoked increase in $[\text{Ca}^{2+}]_i$. This effect may be attributed to a decrease in extracellular Ca^{2+} influx through voltage-dependent calcium channels (VDCCs). This suggestion is based on the observation that the inhibition of glutamate release by piperine required an influx of Ca^{2+} from the extracellular milieu. Furthermore, the inhibitory effect of piperine on 4-AP-evoked glutamate release was decreased from 40.9% to 2.8% after exposure to $\omega\text{-CgTX MVIIC}$ (an N- and P/Q-type Ca^{2+} channel blocker). However, in the presence of $\omega\text{-CgTX MVIIC}$, total blockage was not observed, probably due to the participation of other presynaptic pathways. In summary, our data indicate the suppression of N- and P/Q-type Ca^{2+} channel activity as a potential mechanism underlying the inhibition of glutamate release by piperine in rat hippocampal nerve terminals. Our findings are consistent with those of Fu *et al.* (2010),²¹ which were that piperine inhibited Ca^{2+} channel activity in an *in vitro* study using rat hippocampal neurons.

In the present study, we also discovered that the piperine-mediated inhibition of 4-AP-evoked glutamate release was efficiently blocked by a 5-HT_{1A}-selective antagonist and not by a GABA_A-selective antagonist, thus indicating the involvement of 5-HT_{1A} receptors. This conclusion was further supported by our immunocytochemical data, which showed that 5HT_{1A} receptors were coexpressed with the synaptic vesicle marker synaptophysin. This finding confirmed that 5HT_{1A} receptors are present in hippocampal nerve terminals, which is consistent with the finding of a previous study.⁴⁹ Our finding, although discordant with those of other studies,^{50,51} is consistent with experimental evidence supporting the modulating activity of piperine on 5-HT_{1A} receptors.³⁹ Furthermore, piperine is reported to modulate transient receptor potential vanilloid 1 (TRPV1).^{52,53} Because TRPV1 is also expressed in hippocampal nerve terminals and its activation can inhibit glutamate release,²⁹ we cannot exclude the possibility of the involvement of TRPV1 in addition to 5-HT_{1A} receptors.

The mechanisms that underlie the inhibitory effect of piperine on glutamate release from the hippocampal nerve

terminals through presynaptic 5-HT_{1A} receptors remain to be elucidated. The 5-HT_{1A} receptors are coupled to Gi/o proteins, and their activation has been shown to inhibit presynaptic Ca²⁺ channels and glutamate release.^{49,54} This suppression of Ca²⁺ influx through 5-HT_{1A} receptor activation is thought to occur either directly through a membrane-delimited action of Gβγ subunits or indirectly through secondary messengers.^{55–57} In general, 5-HT_{1A} receptors are known to inhibit AC activity and cause a decrease in cyclic AMP levels, which, by lowering PKA activity, may indirectly lead to a reduction in voltage-dependent Ca²⁺ influx.^{55,58,59} In the present experiments, preincubation of the nerve terminals with PTX, a Gi/o protein inhibitor, prevented the inhibitory effect of piperine on glutamate release. However, the inhibitors of AC and PKA did not affect the piperine-mediated inhibition of glutamate release, thus suggesting that the contribution of AC/PKA to the piperine-mediated inhibition of glutamate release would be negligible. Furthermore, we found that the extent of piperine-mediated inhibition of glutamate release was significantly reduced by adding gallein, a Gβγ inhibitor. This result implies that the observed inhibitory effect of piperine on Ca²⁺ entry indicates the membrane-delimited Gβγ coupling of 5-HT_{1A} receptors with Ca²⁺ channels. In fact, Gβγ has been reported to attenuate presynaptic VDCCs, such as N- and P/Q-type Ca²⁺ channels.^{60,61} In addition to VDCCs, Gβγ can induce synaptic proteins to inhibit vesicular release.^{62,63} Additional studies are required to determine whether the inhibition of release machinery by Gβγ is also involved in the piperine-mediated inhibition of glutamate release.

In conclusion, the present study provides the first evidence that piperine inhibits glutamate release in rat hippocampal nerve terminals. This phenomenon occurs through the activation of presynaptic 5-HT_{1A} receptors by Gβγ coupled to N- and P/Q-type Ca²⁺ channels. Our finding is valuable because it provides new insight into the mechanisms underlying the action of piperine in the brain.

Abbreviations

4-AP	4-Aminopyridine
[Ca ²⁺] _i	Intraterminal Ca ²⁺ concentration
DiSC ₃ (5)	3',3',3'-Dipropylthiadicarbocyanine iodide
DL-TBOA	DL-threo-Beta-benzyl-oxy aspartate
Fura-2-AM	Fura-2-acetoxymethyl ester
GDH	Glutamate dehydrogenase
HBM	HEPES buffer medium
BSA	Bovine serum albumin
ω-CgTX	ω-Conotoxin MVIIC
MVIIC	
CGP37157	7-Chloro-5-(2-chlorophenyl)-1,5-dihydro-4,1-benzothiazepin-2(3H)-one
5-HT _{1A}	5-Hydroxytryptamine 1A
Gβγ	G protein βγ subunit
SQ22536	9-(Tetrahydro-2-furanyl)-9H-purin-6-amine

PKI (6-22)	Protein kinase A inhibitor fragment (6-22)
amide	amide
GABA _A	γ-Aminobutyric acid type A receptor
receptor	
AC	Adenylate cyclase
PKA	Protein kinase A
VDCC	Voltage-dependent Ca ²⁺ channel
CNS	Central nervous system.

Conflicts of interest

The authors declare there are no conflicts of interest.

Acknowledgements

This work was supported by the Shin Kong Wu Ho-Su Memorial Hospital (104-SKH-FJH-01).

References

- 1 S. Mathur and C. Hoskins, Drug development: Lessons from nature, *Biomed. Rep.*, 2017, **6**, 612–614.
- 2 M. Dutta, A. K. Ghosh, P. Mishra, G. Jain, V. Rangari, A. Chattopadhyay, T. Das, D. Bhowmick and D. Bandyopadhyay, Protective effects of piperine against copper-ascorbate induced toxic injury to goat cardiac mitochondria in vitro, *Food Funct.*, 2014, **5**, 2252–2267.
- 3 H. G. Kim, E. H. Han, W.-S. Jang, J. H. Choi, T. Khanal, B. H. Park, T. P. Tran, Y. C. Chung and H. G. Jeong, Piperine inhibits PMA-induced cyclooxygenase-2 expression through downregulating NF-κB, C/EBP and AP-1 signaling pathways in murine macrophages, *Food Chem. Toxicol.*, 2012, **50**, 2342–2348.
- 4 I. Bukhari, M. Alhumayyd, A. Mahesar and A. Gilani, The analgesic and anticonvulsant effects of piperine in mice, *J. Physiol. Pharmacol.*, 2013, **64**, 789–794.
- 5 M. Khalili-Fomeshi, M. G. Azizi, M. R. Esmaeili, M. Gol, S. Kazemi, M. Ashrafpour, A. A. Moghadamnia and S. Hosseinzadeh, Piperine restores streptozotocin-induced cognitive impairments: Insights into oxidative balance in cerebrospinal fluid and hippocampus, *Behav. Brain Res.*, 2018, **337**, 131–138.
- 6 D. E. Eigenmann, C. Dürig, E. A. Jähne, M. Smieško, M. Culot, F. Gosselet, R. Cecchelli, H. C. C. Helms, B. Brodin and L. Wimmer, In vitro blood–brain barrier permeability predictions for GABA A receptor modulating piperine analogs, *Eur. J. Pharm. Biopharm.*, 2016, **103**, 118–126.
- 7 P. Kundu, M. Das, K. Tripathy and S. K. Sahoo, Delivery of Dual Drug Loaded Lipid Based Nanoparticles across the Blood–Brain Barrier Impart Enhanced Neuroprotection in a Rotenone Induced Mouse Model of Parkinson's Disease, *ACS Chem. Neurosci.*, 2016, **7**, 1658–1670.

- 8 R. D'Hooge, Y. Pei, A. Raes, P. Lebrun, P. Van Bogaert and P. De Deyn, Anticonvulsant activity of piperine on seizures induced by excitatory amino acid receptor agonists, *Arzneim.-Forsch.*, 1996, **46**, 557–560.
- 9 J. Wattanathorn, P. Chonpathompikunlert, S. Muchimapura, A. Pripem and O. Tankamnerdthai, Piperine, the potential functional food for mood and cognitive disorders, *Food Chem. Toxicol.*, 2008, **46**, 3106–3110.
- 10 P. Chonpathompikunlert, J. Wattanathorn and S. Muchimapura, Piperine, the main alkaloid of Thai black pepper, protects against neurodegeneration and cognitive impairment in animal model of cognitive deficit like condition of Alzheimer's disease, *Food Chem. Toxicol.*, 2010, **48**, 798–802.
- 11 K. Mao, D. Lei, H. Zhang and C. You, Anticonvulsant effect of piperine ameliorates memory impairment, inflammation and oxidative stress in a rat model of pilocarpine-induced epilepsy, *Exp. Ther. Med.*, 2017, **13**, 695–700.
- 12 W. Yang, Y.-H. Chen, H. Liu and H.-D. Qu, Neuroprotective effects of piperine on the 1-methyl-4-phenyl-1, 2, 3, 6-tetrahydropyridine-induced Parkinson's disease mouse model, *Int. J. Mol. Med.*, 2015, **36**, 1369–1376.
- 13 M. P. Mattson, Glutamate and neurotrophic factors in neuronal plasticity and disease, *Ann. N. Y. Acad. Sci.*, 2008, **1144**, 97–112.
- 14 A. Lau and M. Tymianski, Glutamate receptors, neurotoxicity and neurodegeneration, *Pfluegers Arch.*, 2010, **460**, 525–542.
- 15 J. Lewerenz and P. Maher, Chronic glutamate toxicity in neurodegenerative diseases—what is the evidence?, *Front. Neurosci.*, 2015, **9**, 469.
- 16 T. Cassano, L. Pace, G. Bedse, A. Michele Lavecchia, F. De Marco, S. Gaetani and G. Serviddio, Glutamate and mitochondria: two prominent players in the oxidative stress-induced neurodegeneration, *Curr. Alzheimer Res.*, 2016, **13**, 185–197.
- 17 M. P. Parsons, M. P. Vanni, C. L. Woodard, R. Kang, T. H. Murphy and L. A. Raymond, Real-time imaging of glutamate clearance reveals normal striatal uptake in Huntington disease mouse models, *Nat. Commun.*, 2016, **7**, 11251.
- 18 C. W. Lu, T. Y. Lin, S. K. Huang and S. J. Wang, Inhibition of glutamate release by cilnidipine in rat cerebrocortical nerve terminals (synaptosomes), *NeuroReport*, 2017, **28**, 527–532.
- 19 M. Sitges, B. Sanchez-Tafolla, L. Chiu, B. Aldana and A. Guarneros, Vinpocetine inhibits glutamate release induced by the convulsive agent 4-aminopyridine more potently than several antiepileptic drugs, *Epilepsy Res.*, 2011, **96**, 257–266.
- 20 B. Cheah, S. Vucic, A. Krishnan and M. Kiernan, Riluzole, neuroprotection and amyotrophic lateral sclerosis, *Curr. Med. Chem.*, 2010, **17**, 1942–1959.
- 21 M. Fu, Z. H. Sun and H. C. Zuo, Neuroprotective effect of piperine on primarily cultured hippocampal neurons, *Biol. Pharm. Bull.*, 2010, **33**, 598–603.
- 22 L. Raiteri and M. Raiteri, Synaptosomes still viable after 25 years of superfusion, *Neurochem. Res.*, 2000, **25**, 1265–1274.
- 23 Y. Chang, T. Y. Lin, C. W. Lu, S. K. Huang, Y. C. Wang and S. J. Wang, Xanthohumol-induced presynaptic reduction of glutamate release in the rat hippocampus, *Food Funct.*, 2016, **7**, 212–226.
- 24 D. G. Amaral and M. P. Witter, The three-dimensional organization of the hippocampal formation: a review of anatomical data, *Neuroscience*, 1989, **31**, 571–591.
- 25 K. Moodley and D. Chan, The hippocampus in neurodegenerative disease, *Front. Neurol. Neurosci.*, 2014, **34**, 95–108.
- 26 C. A. Tamminga, A. D. Stan and A. D. Wagner, The hippocampal formation in schizophrenia, *Am. J. Psychiatry*, 2010, **167**, 1178–1193.
- 27 A. Rodríguez-Moreno and T. S. Sihra, Presynaptic kainate receptor facilitation of glutamate release involves protein kinase A in the rat hippocampus, *J. Physiol.*, 2004, **557**, 733–745.
- 28 D. G. Nicholls and T. S. Sihra, Synaptosomes possess an exocytotic pool of glutamate, *Nature*, 1986, **321**, 772–773.
- 29 C. W. Lu, T. Y. Lin, T. Y. Hsieh, S. K. Huang and S. J. Wang, Capsaicin presynaptically inhibits glutamate release through the activation of TRPV1 and calcineurin in the hippocampus of rats, *Food Funct.*, 2017, **8**, 1859–1868.
- 30 G. Tibbs, A. Barrie, F. Miegheem, H. A. McMahon and D. Nicholls, Repetitive action potentials in isolated nerve terminals in the presence of 4-aminopyridine: Effects on cytosolic free Ca^{2+} and glutamate release, *J. Neurochem.*, 1989, **53**, 1693–1699.
- 31 M. S. Perkinson and T. S. Sihra, Presynaptic GABAB receptor modulation of glutamate exocytosis from rat cerebrocortical nerve terminals: receptor decoupling by protein kinase C, *J. Neurochem.*, 1998, **70**, 1513–1522.
- 32 G. Grynkiewicz, M. Poenie and R. Y. Tsien, A new generation of Ca^{2+} indicators with greatly improved fluorescence properties, *J. Biol. Chem.*, 1985, **260**, 3440–3450.
- 33 K. E. Åkerman, I. G. Scott, J. E. Heikkilä and E. Heinonen, Ionic Dependence of Membrane Potential and Glutamate Receptor-Linked Responses in Synaptoneuroosomes as Measured with a Cyanine Dye, DiS-C2-(5), *J. Neurochem.*, 1987, **48**, 552–559.
- 34 R. Lingamaneni, M. L. Birch and H. C. Hemmings, Widespread inhibition of sodium channel-dependent glutamate release from isolated nerve terminals by isoflurane and propofol, *Anesthesiology*, 2001, **95**, 1460–1466.
- 35 L. Ratnakumari and H. C. Hemmings, Effects of propofol on sodium channel-dependent sodium influx and glutamate release in rat cerebrocortical synaptosomes, *Anesthesiology*, 1997, **86**, 428–439.
- 36 C. Millán and J. Sánchez-Prieto, Differential coupling of N- and P/Q-type calcium channels to glutamate exocytosis in the rat cerebral cortex, *Neurosci. Lett.*, 2002, **330**, 29–32.
- 37 E. Vázquez and J. Sánchez-Prieto, Presynaptic modulation of glutamate release targets different calcium channels in rat cerebrocortical nerve terminals, *Eur. J. Neurosci.*, 1997, **9**, 2009–2018.

- 38 G. M. P. da Cruz, C. F. B. Felipe, F. A. Scorza, M. A. C. da Costa, A. F. Tavares, M. L. F. Menezes, G. M. de Andrade, L. K. A. Leal, G. A. C. Brito and M. da Graça Naffah-Mazzacoratti, Piperine decreases pilocarpine-induced convulsions by GABAergic mechanisms, *Pharmacol., Biochem. Behav.*, 2013, **104**, 144–153.
- 39 Q. Q. Mao, Z. Huang, S. P. Ip, Y. F. Xian and C. T. Che, Role of 5-HT_{1A} and 5-HT_{1B} receptors in the antidepressant-like effect of piperine in the forced swim test, *Neurosci. Lett.*, 2011, **504**, 181–184.
- 40 S. J. Peroutka, 5-Hydroxytryptamine Receptors, *J. Neurochem.*, 1993, **60**, 408–416.
- 41 N. C. Danbolt, Glutamate uptake, *Prog. Neurobiol.*, 2001, **65**, 1–105.
- 42 M. Arundine and M. Tymianski, Molecular mechanisms of calcium-dependent neurodegeneration in excitotoxicity, *Cell Calcium*, 2003, **34**, 325–337.
- 43 Q. Q. Mao, Z. Huang, S. P. Ip, Y. F. Xian and C. T. Che, Protective effects of piperine against corticosterone-induced neurotoxicity in PC12 cells, *Cell. Mol. Neurobiol.*, 2012, **32**, 531–537.
- 44 Q.-Q. Mao, Y.-F. Xian, S.-P. Ip and C.-T. Che, Involvement of serotonergic system in the antidepressant-like effect of piperine, *Prog. Neuro-Psychopharmacol. Biol. Psychiatry*, 2011, **35**, 1144–1147.
- 45 J. Guo, Y. Cui, Q. Liu, Y. Yang, Y. Li, L. Weng, B. Tang, P. Jin, X.-J. Li and S. Yang, Piperine ameliorates SCA17 neuropathology by reducing ER stress, *Mol. Neurodegener.*, 2018, **13**, 4.
- 46 Y.-M. Wang, W. Lin, S. C. Chai, J. Wu, S. S. Ong, E. G. Schuetz and T. Chen, Piperine activates human pregnane X receptor to induce the expression of cytochrome P450 3A4 and multidrug resistance protein 1, *Toxicol. Appl. Pharmacol.*, 2013, **272**, 96–107.
- 47 L. G. Wu and P. Saggau, Presynaptic inhibition of elicited neurotransmitter release, *Trends Neurosci.*, 1997, **20**, 204–212.
- 48 A. Mishra, J. K. Punia, C. Bladen, G. W. Zamponi and R. K. Goel, Anticonvulsant mechanisms of piperine, a piperidine alkaloid, *Channels*, 2015, **9**, 317–323.
- 49 S. J. Wang, V. Coutinho and T. S. Sihra, Presynaptic cross-talk of β -adrenoreceptor and 5-hydroxytryptamine receptor signalling in the modulation of glutamate release from cerebrocortical nerve terminals, *Br. J. Pharmacol.*, 2002, **137**, 1371–1379.
- 50 V. Zabela, T. Hettich, G. Schlotterbeck, L. Wimmer, M. D. Mihovilovic, F. Guillet, B. Bouaita, B. Shevchenko, M. Hamburger and M. Oufir, GABA A receptor activity modulating piperine analogs: In vitro metabolic stability, metabolite identification, CYP450 reaction phenotyping, and protein binding, *J. Chromatogr. B: Anal. Technol. Biomed. Life Sci.*, 2018, **1072**, 379–389.
- 51 S. Khom, B. Strommer, A. Schöffmann, J. Hintersteiner, I. Baburin, T. Erker, T. Schwarz, C. Schwarzer, J. Zaugg and M. Hamburger, GABA A receptor modulation by piperine and a non-TRPV1 activating derivative, *Biochem. Pharmacol.*, 2013, **85**, 1827–1836.
- 52 C.-Y. Chen, W. Li, K.-P. Qu and C.-R. Chen, Piperine exerts anti-seizure effects via the TRPV1 receptor in mice, *Eur. J. Pharmacol.*, 2013, **714**, 288–294.
- 53 F. N. McNamara, A. Randall and M. J. Gunthorpe, Effects of piperine, the pungent component of black pepper, at the human vanilloid receptor (TRPV1), *Br. J. Pharmacol.*, 2005, **144**, 781–790.
- 54 I.-S. Choi, J.-H. Cho and I.-S. Jang, 5-Hydroxytryptamine 1A receptors inhibit glutamate release in rat medullary dorsal horn neurons, *NeuroReport*, 2013, **24**, 399–403.
- 55 P. S. Rojas and J. L. Fiedler, What do we really know about 5-HT_{1A} receptor signaling in neuronal cells?, *Front. Cell. Neurosci.*, 2016, **10**, 272.
- 56 F. DeBock, J. Kurz, S. Azad, C. Parsons, G. Hapfelmeier, W. Zieglgänsberger and G. Rammes, α 2-Adrenoreceptor activation inhibits LTP and LTD in the basolateral amygdala: involvement of Gi/o-protein-mediated modulation of Ca²⁺-channels and inwardly rectifying K⁺-channels in LTD, *Eur. J. Neurosci.*, 2003, **17**, 1411–1424.
- 57 L. L. Cheng, S. J. Wang and P. W. Gean, Serotonin depresses excitatory synaptic transmission and depolarization-evoked Ca²⁺ influx in rat basolateral amygdala via 5-HT_{1A} receptors, *Eur. J. Neurosci.*, 1998, **10**, 2163–2172.
- 58 A. M. Polter and X. Li, 5-HT_{1A} receptor-regulated signal transduction pathways in brain, *Cell. Signalling*, 2010, **22**, 1406–1412.
- 59 P. R. Albert and S. Lemonde, 5-HT_{1A} receptors, gene repression, and depression: guilt by association, *Neuroscientist*, 2004, **10**, 575–593.
- 60 T. Blackmer, E. C. Larsen, M. Takahashi, T. F. Martin, S. Alford and H. E. Hamm, G protein $\beta\gamma$ subunit-mediated presynaptic inhibition: regulation of exocytotic fusion downstream of Ca²⁺ entry, *Science*, 2001, **292**, 293–297.
- 61 Y. Kajikawa, N. Saitoh and T. Takahashi, GTP-binding protein $\beta\gamma$ subunits mediate presynaptic calcium current inhibition by GABAB receptor, *Proc. Natl. Acad. Sci. U. S. A.*, 2001, **98**, 8054–8058.
- 62 T. Gerachshenko, T. Blackmer, E.-J. Yoon, C. Bartleson, H. E. Hamm and S. Alford, G $\beta\gamma$ acts at the C terminus of SNAP-25 to mediate presynaptic inhibition, *Nat. Neurosci.*, 2005, **8**, 597–605.
- 63 T. Blackmer, E. C. Larsen, C. Bartleson, J. A. Kowalchuk, E.-J. Yoon, A. M. Preininger, S. Alford, H. E. Hamm and T. F. Martin, G protein $\beta\gamma$ directly regulates SNARE protein fusion machinery for secretory granule exocytosis, *Nat. Neurosci.*, 2005, **8**, 421–425.



Full length article

Oleic acid as the active agent and lipid matrix in cilomilast-loaded nanocarriers to assist PDE4 inhibition of activated neutrophils for mitigating psoriasis-like lesions

Cheng-Yu Lin^a, Ching-Yun Hsu^{b,c}, Ahmed O. Elzoghby^{d,e,f}, Ahmed Alalaiwe^g, Tsong-Long Hwang^{c,h,i,j,*}, Jia-You Fang^{c,h,i,j,*}

^a Graduate Institute of Biomedical Sciences, Chang Gung University, Kweishan, Taoyuan, Taiwan

^b Department of Nutrition and Health Sciences, Chang Gung University of Science and Technology, Kweishan, Taoyuan, Taiwan

^c Research Center for Food and Cosmetic Safety and Research Center for Chinese Herbal Medicine, Chang Gung University of Science and Technology, Kweishan, Taoyuan, Taiwan

^d Division of Engineering in Medicine, Department of Medicine, Brigham and Women's Hospital, Harvard Medical School, Boston, USA

^e Cancer Nanotechnology Research Laboratory (CNRL), Faculty of Pharmacy, Alexandria University, Alexandria, Egypt

^f Department of Industrial Pharmacy, Faculty of Pharmacy, Alexandria University, Alexandria, Egypt

^g Department of Pharmaceutics, College of Pharmacy, Prince Sattam Bin Abdulaziz University, Al Kharj, Saudi Arabia

^h Graduate Institute of Natural Products, Chang Gung University, Kweishan, Taoyuan, Taiwan

ⁱ Chinese Herbal Medicine Research Team, Healthy Aging Research Center, Chang Gung University, Kweishan, Taoyuan, Taiwan

^j Department of Anesthesiology, Chang Gung Memorial Hospital, Kweishan, Taoyuan, Taiwan

ARTICLE INFO

Article history:

Received 10 December 2018

Received in revised form 16 March 2019

Accepted 1 April 2019

Available online 3 April 2019

Keywords:

Psoriasis

Skin

Phosphodiesterase inhibitor

Oleic acid

Nanostructured lipid carriers

ABSTRACT

Both phosphodiesterase (PDE4) inhibitors and omega-9 fatty acids show anti-inflammatory activity for treating inflamed skin diseases, but their efficacy remains low. Combinatorial agents are anticipated to offer an advanced strategy for efficient therapy. We prepared cilomilast-loaded oleic acid (OA) nanocarriers to test the inhibitory capability against human neutrophil stimulation and a murine psoriasis model. OA played dual roles in the nanocarriers as both the active ingredient and lipid matrix in the nanoparticulate core. OA nanoparticles but not free OA could restrain calcium mobilization in activated neutrophils. The inhibition level of superoxide anion and elastase by cilomilast-loaded OA nanocarriers approximated that of free forms. In the mouse model, the intradermal nanosystems reduced imiquimod-induced epidermal thickening from 230.4 to 63.1 μm . Transepidermal water loss was decreased from 30.2 to 11.3 $\text{g/m}^2/\text{h}$ by integrated nanocarriers. The nanosystems mitigated neutrophil infiltration and hyperproliferation in the psoriasiform lesion via decreased expression of cytokines and chemokines.

Statement of Significance

The long-term therapy for psoriasis is unsatisfactory due to the possible adverse effects and inefficiency after prolonged use. Both phosphodiesterase (PDE4) inhibitors and omega-9 fatty acids such as oleic acid (OA) show anti-inflammatory activity for treating inflamed skin diseases. Combinatorial agents are anticipated to offer an advanced strategy for efficient therapy. OA is also ideal for incorporation into nanoparticles to enhance particulate emulsification, drug entrapment, and biocompatibility. We prepared cilomilast-loaded oleic acid (OA) nanocarriers to test the inhibitory capability against human neutrophil stimulation and a murine psoriasis lesion. OA nanocarriers are indigenous to prevent neutrophil activation and the deterioration of psoriatic lesion. Cilomilast incorporation in OA nanocarriers could further mitigate the clinical score and suppressing proinflammatory mediators.

© 2019 Acta Materialia Inc. Published by Elsevier Ltd. All rights reserved.

* Corresponding authors at: Pharmaceutics Laboratory, Graduate Institute of Natural Products, Chang Gung University, 259 Wen-Hwa 1st Road, Kweishan, Taoyuan, 333, Taiwan (Jia-You Fang), Cellular Pharmacology Laboratory, Graduate Institute of Natural Products, Chang Gung University, 259 Wen-Hwa 1st Road, Kweishan, Taoyuan 333, Taiwan (Tsong-Long Hwang).

E-mail addresses: htl@mail.cgu.edu.tw (T.-L. Hwang), fajy@mail.cgu.edu.tw (J.-Y. Fang).

1. Introduction

Psoriasis is an autoimmune skin disorder affecting 2%–5% of the world's population [1]. The immune response of psoriasis involves the inflammatory infiltration of dendritic cells, T cells, and polymorphonuclear neutrophils (PMNs). Among these immune cells,

PMNs are the first cells to be recruited to the psoriatic lesion [2]. The cluster of PMNs creates spongiform pustules in the stratum spinosum and microabscesses in the stratum corneum (SC). The reactive oxygen species (ROS) and proteases released by activated PMNs would damage the surrounding tissues. The inhibition of neutrophil stimulation can be a critical approach to alleviate psoriasis [3]. Phosphodiesterase (PDE)4 is an enzyme that hydrolyzes and degrades cyclic adenosine monophosphate (cAMP). PDE4 is expressed in the immune cells, including PMNs, and its regulation is essential for inflammation treatment [4]. Selective PDE4 inhibitors receive great attention owing to the anti-inflammatory activity in PMNs to treat chronic obstructive pulmonary disease, arthritis, atopic dermatitis, and psoriasis [5]. PDE4 inhibitors are reported to reduce PMN infiltration and hyperkeratosis in psoriasis [6]. Apremilast is a PDE4 inhibitor approved by the USFDA for oral administration to treat psoriasis. The side effects of emesis, nausea, and headache caused by oral PDE4 inhibitors have limited the clinical application [7].

The long-term therapy for psoriasis is unsatisfactory due to the possible adverse effects and inefficiency after prolonged use. Combinational therapy can improve the management efficacy by producing multiple therapeutic targets and decreasing the applied dose to reduce undesired off-target effects. The 18-carbon fatty acids can either inhibit or promote neutrophilic activation depending upon the experimental conditions and doses. Oleic acid (OA) is a monounsaturated omega-9 fatty acid found to show superoxide anion and elastase inhibition in PMNs superior to the other C18 fatty acids [8]. It is an important component in the cutaneous lipid bilayers. It could be beneficial to combine PDE4 inhibitor and omega-9 fatty acid in order to treat psoriasis. The incorporation of two agents in a single vehicle for combinational therapy achieves good patient compliance. Although OA demonstrates bioactivity on inflammation suppression, the poor aqueous solubility and chemical stability may result in ineffective application. The conventional drug carriers are unacceptable for the compounds with water solubility of $<1 \mu\text{g/ml}$ [9]. The use of nanoparticles as the carriers is a promising strategy to ameliorate the solubility and stability of highly lipophilic actives. Nanoparticles after suitable design can mediate the targeting to activated PMNs [10]. Previous studies [11–13] suggest that OA is ideal for incorporation into nanoparticles to enhance the particulate emulsification, drug entrapment, cellular uptake, and biocompatibility. Nanostructured lipid carriers (NLCs) consisting of both solid and liquid lipids are a colloidal drug delivery system offering the advantages of controlled drug delivery, increased drug stability, and high biocompatibility [14]. OA can exert both roles of an active ingredient and a lipid matrix in NLCs.

With the intention of improving psoriasis treatment by integrated therapy, the objective of this study was to estimate the potential of PDE4 inhibitor and OA co-loaded in NLCs for mitigating psoriatic lesion. Cilomilast was chosen as the model PDE4 inhibitor in this work because of its high selectivity for cAMP-specific PDE4 but specific side effects such as nausea and diarrhea [15]. A cellular model of isolated human PMNs was employed to explore the anti-inflammatory effect of NLCs. The *in vivo* antipsoriatic activity was evaluated using the imiquimod (IMQ)-induced murine model of psoriatic plaque.

2. Materials and methods

2.1. Fabrication of NLCs

The lipid and water phases of NLCs were prepared separately. The lipid phase consisted of 3% (w/v) OA, 3% hexadecyl palmitate, 2% soy phosphatidylcholine (SPC, Phospholipon 80H), and 0.1%

distearoyl-*sn*-glycero-3-phosphatidylethanolamine-polyethylene-glycol (DSPE-PEG, 5000 Da). The water phase consisted of 4% Pluronic F68 and double-distilled water. Cilomilast (6 mM) was included in the lipid phase if necessary. Both phases were heated to 85 °C for 15 min. The aqueous phase was added to the lipid phase with high-shear homogenization at 12,000 rpm for 20 min. Then the nanodispersion was cooled down at the room temperature for lipid recrystallization. A probe-type sonicator was utilized to further treat the mixture for 15 min at 35 W.

2.2. Average diameter and zeta potential of NLCs

The z-average, polydispersity index (PDI), and zeta potential of NLCs were estimated by a laser-scattering method (Nano ZS90, Malvern). The z-average was calculated as an intensity-based overall average size according to a specific fit to the correlation function data of laser scattering. The z-average is the mean of the particle distribution, and PDI is involved in the width of particle distribution. The colloidal dispersion was diluted by double-distilled water 100-fold before estimation.

2.3. Morphology of NLCs

The morphology of the nanoparticles was visualized by transmission electron microscopy (TEM). A drop of the nanodispersion was deposited onto a grid to form a thin-film sample without any staining. After the procedure of freeze drying, the sample was monitored by a TEM (Jeol JEM-1230).

2.4. Cilomilast encapsulation percentage in NLCs

The entrapment percentage of cilomilast was determined by utilizing the ultracentrifugation method to separate the incorporated drug from the free form. The NLCs were centrifuged at $48,000 \times g$ and 4 °C for 40 min. The free drug in the supernatant and the encapsulated drug in the precipitate were analyzed by UV/visible spectrometry at 230 nm to measure the entrapment efficiency.

2.5. Cilomilast release from NLCs

The release of cilomilast from the nanoparticles was examined by Franz diffusion cell. The dialysis membrane with a molecular weight cutoff of 6000–8000 Da was used as a semi-permeable membrane. The available release area was 0.785 cm^2 . The medium loaded in the receptor (5 ml) was 30% ethanol in pH 7.4 buffer for maintaining the sink condition. The donor compartment (0.5 ml) was loaded with cilomilast-containing NLCs or free cilomilast in DMSO (6 mM). At determined intervals, the medium was withdrawn from the receptor. Cilomilast concentration in the receptor was determined by UV/visible spectrometry at a wavelength of 230 nm.

2.6. Isolation of human PMNs

Human neutrophils were purified from healthy subjects between 20 and 30 years of age using a protocol approved by the institutional review board at Chang Gung Memorial Hospital. The volunteers provided written informed consent to participate. The PMNs were isolated with sedimentation prior to centrifugation and erythrocyte lysis according to the previous report [16].

2.7. PMN survival

The PMN viability was examined by lactate dehydrogenase (LDH) release using a CytoTox 96 assay kit. The PMNs (6×10^5

cells/ml) were treated by the nanoparticles at different concentrations for 17 min. The OA nanoparticle formulations included the nanosystems with and without cilomilast. The free controls (cilomilast or OA in DMSO) were also tested. The cytotoxicity was presented by LDH release in cell-free medium as a percentage of total LDH release. The total released LDH was measured by PMN lysis with 0.1% Triton X-100.

2.8. Superoxide anion generation

The ferricytochrome *c* reduction was used to evaluate the superoxide anion release. The PMNs (6×10^5 cells/ml) were incubated with ferricytochrome *c* (0.5 mg/ml) and CaCl_2 (1 mM) at 37 °C, and were subsequently treated with free or nanoparticulate cilomilast and OA for 10 min. The cells were activated by 0.1 μM formyl-methionyl-leucyl phenylalanine (fMLF) with 1 $\mu\text{g}/\text{ml}$ cytochalasin B. The reduction of ferricytochrome *c* was detected by UV/visible spectrometry at 550 nm.

2.9. Elastase release

The PMNs (6×10^5 cells/ml) were equilibrated by the substrate MeO-Suc-Ala-Ala-Pro-Val-*p*-nitroanilide at 37 °C for 2 min. The free or nanoparticulate cilomilast and OA were incorporated into the suspension for 10 min. The PMNs were stimulated by fMLF and cytochalasin B for 10 min. The elastase amount was determined by UV/visible spectrometry at 405 nm.

2.10. Intracellular calcium ($[\text{Ca}^{2+}]_i$)

The neutrophils (3×10^6 cells/ml) were incubated with 2 μM Fura-3/AM at 37 °C for 30 min, followed by centrifugation, and were resuspended in HBSS containing 1 mM CaCl_2 . The cells were exposed with free or nanoparticulate active agents for 5 min. The $[\text{Ca}^{2+}]_i$ in response to fMLF was recognized by fluorescence spectrometry with the wavelength of excitation and emission at 488 and 520 nm, respectively.

2.11. PMN migration assay

A chemotaxis assay was performed in 24-chamber Transwell plates with a pore size of 3 μm . The isolated cells (2.5×10^6 cells/well) were treated by free or nanoparticulate active agents. Then the PMNs were added into the upper wells and the conditioned medium containing fMLF was added to the lower wells at 37 °C for 1.5 h. A 100- μl EDTA (7 mM) was pipetted into each well at 4 °C for 10 min. The well insert was removed; then the cell suspension was collected for washing. The cells were counted using a Moxi® Z automated cell counter kit.

2.12. Nanoparticle uptake by PMNs

The NLCs were labeled with rhodamine 800 (0.1 mg/ml) as a fluorescence dye to monitor the uptake by neutrophils. The PMNs (1.8×10^7 cells/ml) were exposed to NLCs at 37 °C for 5 min. HBSS was added into the suspension to terminate the reaction at 4 °C. The fluorescence inside PMNs was visualized by confocal laser scanning microscopy.

2.13. In vivo psoriasis-like murine model

The means for inducing psoriasiform skin in the BALB/c mouse back was modified from the protocol by van der Fits et al [17]. The experiments involving mice (7 weeks old) were conducted in strict accordance with the recommendation in the Guidelines for the Care and Use of Laboratory Animals of Chang Gung University

(approval number: CGU16-020). The animals were divided into 6 groups each containing 6 mice: group 1, sham (healthy control); group 2, IMQ treatment without medical intervention; group 3, IMQ treatment with free cilomilast (10 mg/kg); group 4, IMQ treatment with free OA (300 mg/kg); group 5, IMQ treatment with OA nanocarriers; group 6, IMQ treatment with cilomilast-loaded OA nanocarriers. Free or nanoparticulate cilomilast and OA was intradermally injected into the IMQ-applied region before IMQ cream administration for 30 min. The IMQ cream (Aldara®, 3 M Health Care, UK) at a dose of 62.5 mg was topically applied on the shaved skin ($3 \times 2 \text{ cm}^2$) every day for 6 days. The appearance of the dorsal skin was monitored each day by a handheld digital microscope. Transepidermal water loss (TEWL) was examined by Tewameter (Courage and Khazaka). The objective scoring of the Psoriasis Area and Severity Index (PASI) was evaluated by recording scaling, erythema, and cutaneous thickness independently with a score from 0 to 4. The total scoring presented as the estimation of the cumulative score of the degree of severity.

2.14. Histological analysis

The animals were sacrificed at Day 5 after IMQ treatment. The skin specimen was immersed in a 10% buffered formaldehyde using ethanol, embedded in paraffin wax, and sliced at a thickness of 5 μm for hematoxylin and eosin (H&E) staining. The unstained slices were prepared for immunohistochemistry (IHC).

2.15. Determination of cytokines and chemokines

The treated mouse skin was subjected to ELISA for detecting cytokines and chemokines. These included TNF- α , IL-1 β , IL-6, CXCL1, and CXCL2. The biopsy was homogenized at 6500 rpm for 30 s and cooled down for 1 min. The cytokines and chemokines at the protein level were analyzed with Protein Assay Dye (Bio-Rad).

2.16. In vivo cutaneous tolerance

The formulations used in the psoriasis-like murine model were also employed to test the skin tolerance. The formulation was intradermally injected into the dorsal region of the mouse for 5 consecutive days. On Day 5, the treated skin area was examined by a handheld digital microscope and TEWL. The mouse was then sacrificed to obtain the excised skin for histological analysis.

2.17. Statistical measurement

The statistical examination was conducted by GraphPad Prism 5 software. Dual comparisons were made with unpaired Student's *t*-test. Groups of ≥ 3 were analyzed by analysis of variance (ANOVA) with Tukey or Dunnett post-tests. The significance was indicated as * for $p < 0.05$, ** for $p < 0.01$, and *** for $p < 0.001$ in the figures.

3. Results

3.1. Physicochemical properties and cytotoxicity of NLCs

The OA nanocarriers with or without cilomilast were prepared consisting of core lipids, emulsifiers, and PEG. Fig. 1A illustrates the inferred structure of cilomilast-loaded OA NLCs. We proposed that the nanocarriers showed a scheme with PEG moiety dangling outside the particles and offering the steric stabilization. As shown in Table 1, OA nanocarriers are found to have a hydrodynamic diameter of 116 nm. Entrapment of cilomilast resulted in a high encapsulation percentage in NLCs and the increase of size to

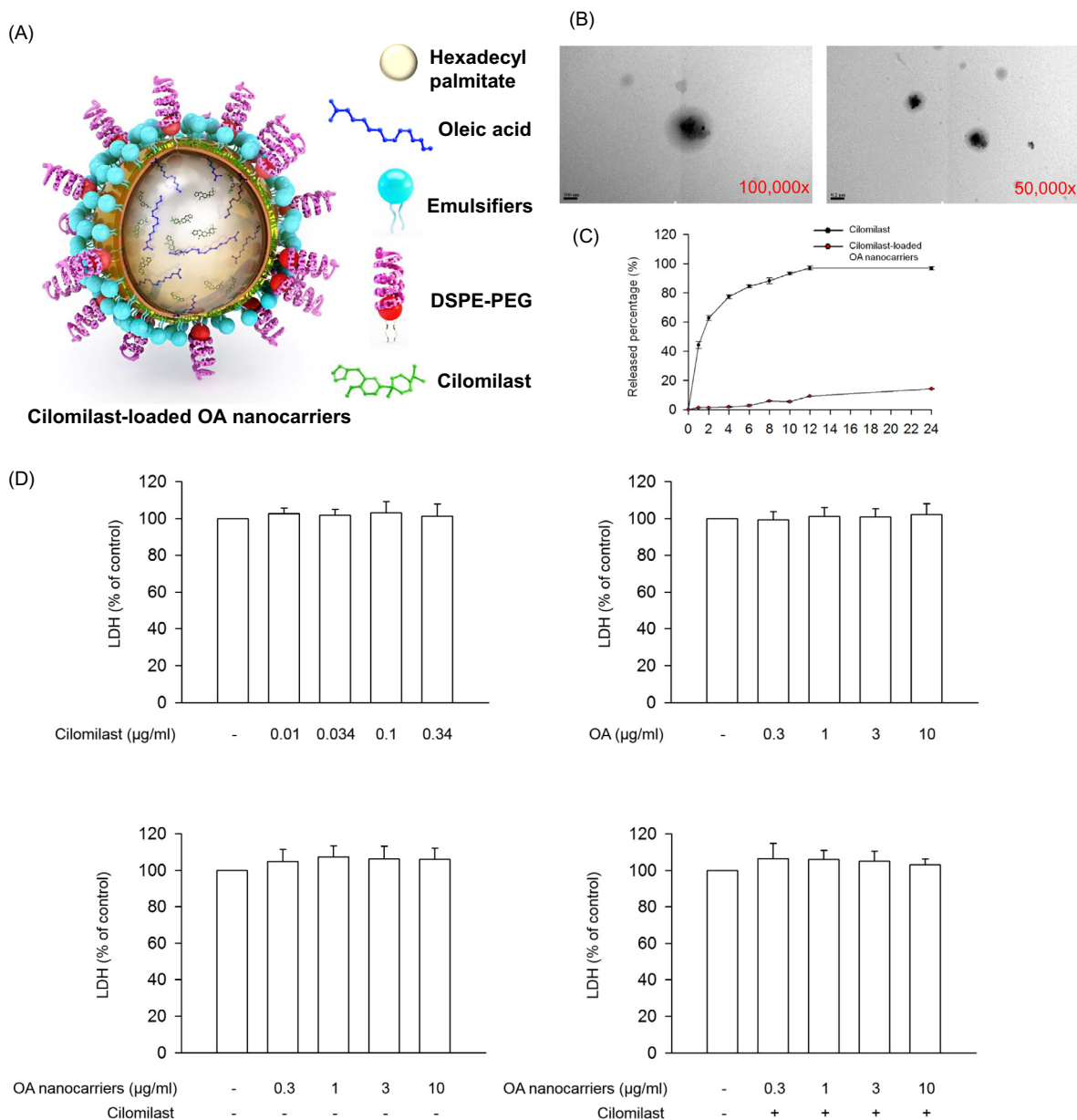


Fig. 1. Design of cilomilast-loaded OA nanocarriers and neutrophil cytotoxicity assay. (A) Schematic exhibition of cilomilast-loaded OA nanocarriers used in following experiments. (B) The morphology of nanoparticles visualized by TEM at the magnifications of 100,000 \times and 50,000 \times . (C) The cilomilast release profiles from free control and cilomilast-loaded OA nanocarriers. (D) The neutrophils (6×10^5 cells/ml) were treated with cilomilast, OA, OA nanocarriers and cilomilast-loaded OA nanocarriers for 15 min. The cytotoxicity was measured by LDH assay ($n = 6$). OA, oleic acid.

Table 1

The physicochemical properties of OA nanocarriers and cilomilast-loaded OA nanocarriers.

Formulation	Size (nm)	PDI	Zeta potential (mV)
OA nanocarriers	115.9 \pm 0.6	0.23 \pm 0.01	-35.7 \pm 1.6
Cilomilast-loaded OA nanocarriers	123.9 \pm 0.5	0.29 \pm 0.01	-27.1 \pm 0.4

Each value represents the mean \pm S.D. ($n = 3$).

PDI: polydispersity index.

124 nm, implying the enlargement of the lipid core space by this addition. Cilomilast incorporation increased the PDI from 0.23 to 0.29. OA nanocarriers were initially negatively charged due to

the inherently negative SPC and OA used. The negative charge was descended from -36 to -27 mV after cilomilast encapsulation. Fig. 1B shows the TEM images of the nanoparticles with the magnifications of 100,000 \times and 50,000 \times . The lipid matrix of NLCs revealed a darker color compared to the nanoparticulate surface. The faint area in the surface could be the evidence of PEGylation. The particulate size in TEM was greater than that detected by laser scattering. This was due to the artificial process of freeze drying before TEM imaging. The solid form after drying was quite different from the particles in aqueous medium.

The release behavior of cilomilast from solution and NLCs was investigated over 24 h as depicted in Fig. 1C. A complete release (100%) of cilomilast from solution was achieved within 12 h, whereas the cumulative cilomilast release from OA nanocarriers was 14% at 24 h. Greater affinity of lipophilic drug for a lipid-

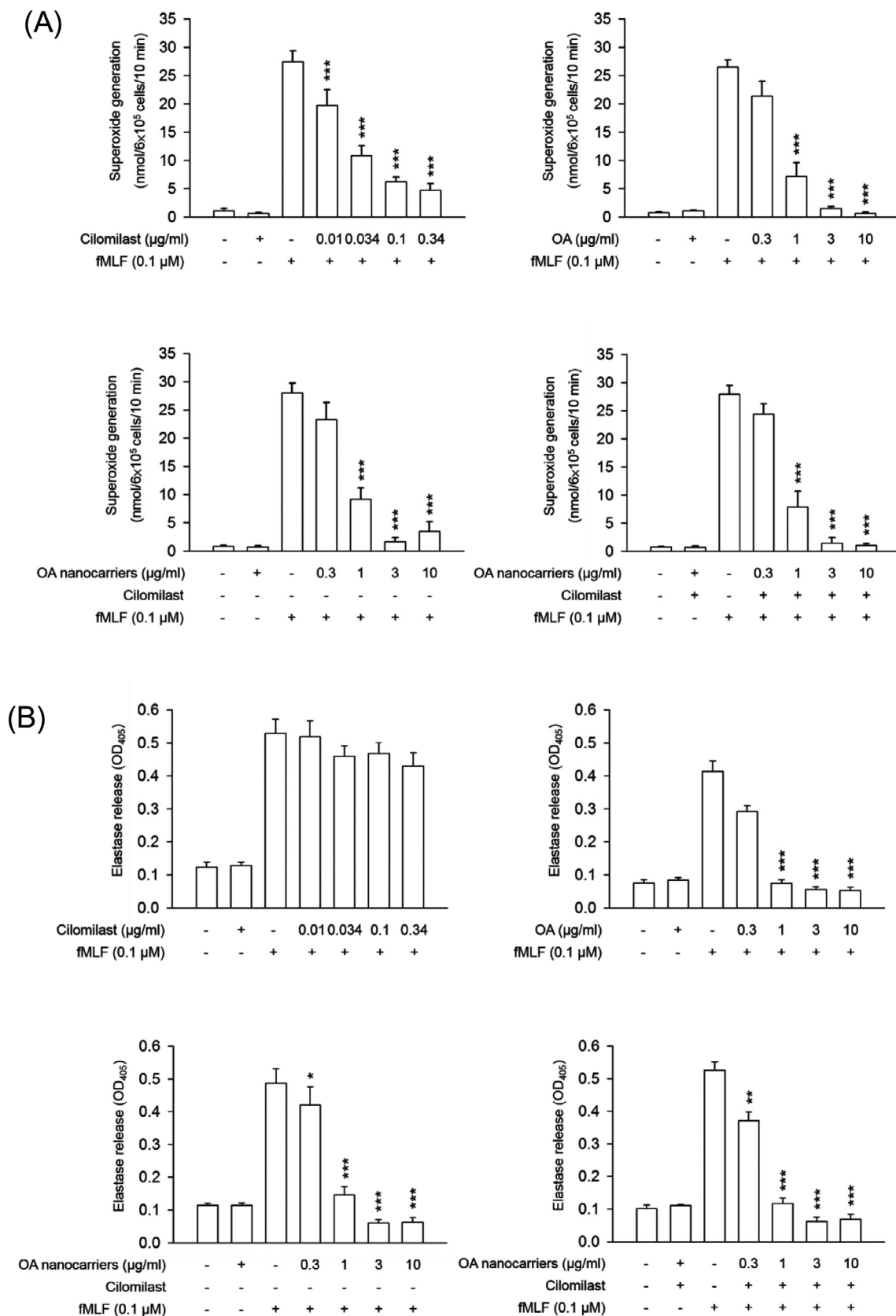


Fig. 2. Effects of cilomilast-loaded OA nanocarriers on superoxide anion release and elastase activity in fMLF-activated human neutrophils (6×10^5 cells/ml). Human PMNs were incubated with cilomilast (0.01–0.34 µg/ml), OA (0.3–10 µg/ml), OA nanocarriers, and cilomilast-loaded OA nanocarriers for 5 min before activation. (A) The measurement of extracellular superoxide production by fMLF/cytochalasin B (CB) for 10 min and SOD-inhibitable cytochrome *c* reduction. (B) Assay of absorbance at 405 nm for continuous measurement of human neutrophil elastase release. All data are expressed as the mean \pm S.E.M. ($n = 6$). * $p < 0.05$, ** $p < 0.01$, *** $p < 0.001$. OA, oleic acid; fMLF, formyl-methionyl-leucyl phenylalanine.

based nanosystem led to the slow release as compared to free form. The LDH assay is an indicator of PMN cytotoxicity. PMNs were treated by free cilomilast, free OA, OA nanocarriers, and nanoparticulate cilomilast in nanocarriers at different concentrations. The profiles in Fig. 1D demonstrate that all treatments did not affect PMN viability.

3.2. The inhibitory effect of NLCs on PMN activation

Superoxide anion and elastase are the important indicators of respiratory burst and degranulation of activated PMNs. Human neutrophils were treated with free cilomilast, free OA, nanoparticulate OA, and combined cilomilast and OA in nanoparticles for determining superoxide anion and elastase as shown in Fig. 2A and B, respectively. None of the treatments changed the basal superoxide anion and elastase under a non-stimulated condition (without fMLF). Superoxide anion inhibition was observed for all the treatment groups in a dose-dependent manner as compared to the fMLF group. The highest concentration of free OA (10 µg/ml) totally suppressed superoxide anion to the baseline control. OA nanocarriers with and without cilomilast could maintain this inhibitory effect. The free PDE4 inhibitor failed to restrain elastase release elicited by fMLF. On the other hand, free OA significantly and concentration dependently inhibited elastase toward fMLF. OA nanocarriers and cilomilast-containing NLCs revealed a similar trend of elastase inhibition with free OA. Table 2 summarizes the IC₅₀ values of OA in different forms. Free OA inhibited superoxide anion generation and elastase release in PMNs activated by fMLF with IC₅₀ of 0.72 and 0.42 µg/ml, respectively. OA NLCs with or without PDE4 inhibitor were as effective as free OA for reducing both biomarkers.

The [Ca²⁺]_i of PMNs rapidly and transiently increased via G protein-coupled receptor after fMLF activation. We next evaluated whether nanocarriers loaded with cilomilast and OA could reverse increased [Ca²⁺]_i and thus mitigate inflammation. Fig. 3A demonstrates the [Ca²⁺]_i of activated PMNs. The left panel of this figure is the profile of spectrofluorometry. Incubation of fMLF resulted in a rapid increase in [Ca²⁺]_i. Free cilomilast or OA failed to alter the peak concentration of Ca²⁺ in activated neutrophils. A significant reduction of peak [Ca²⁺]_i was found for both OA NLCs and cilomilast-loaded OA nanocarriers at higher concentrations, indicating the nanoparticulate form but not free form diminished substantial Ca²⁺ influx. Fig. 3B shows the calculation of the time required for [Ca²⁺]_i to return to half of the peak (t_{1/2}). Although cilomilast and OA in free form did not affect [Ca²⁺]_i, both agents could significantly shorten t_{1/2} in a concentration-dependent fashion. The OA nanocarriers with and without cilomilast could reduce t_{1/2}. This decrease was statistically significant as compared to free cilomilast.

fMLF can induce PMN migration, which is a sign of inflammatory infiltration in psoriasis. As shown in Fig. 3C, free cilomilast is statistically ineffective at hindering activated PMN migration although an inhibitory trend is detected following the increase of drug concentration. Either free or nanoparticulate OA was able to inhibit the migration through Transwell in a dose-dependent manner. OA nanoparticles were labeled with fluorescent dye to visual-

ize the uptake by PMNs under confocal microscopy as presented in Fig. 3D. As early as 5 min after treatment, high fluorescence could be obtained in the cells incubated with NLCs. The fluorescence intensity of the nanoparticle group was stronger than free dye. The nanoparticles were mainly distributed throughout the cytoplasm. The nuclei of PMNs stained by DAPI remained spherical and intact after the nanoparticle internalization.

3.3. The amelioration of psoriasis-like lesion by NLCs

The antipsoriatic activity of cilomilast-loaded OA NLCs was tested in comparison with free actives (cilomilast and OA) and OA nanocarriers in a murine model of psoriasis. IMQ was topically administered to the mouse to induce psoriasis features. Fig. 4A shows the phenotypic images of the mouse's back. Compared to the sham, the inflamed skin with white, scaly, and thickened characteristics was seen in the IMQ group. The groups with cilomilast and/or OA treatments displayed different levels of inflammation inhibition. In comparison, cilomilast-loaded OA nanocarriers showed a superior improvement in redness and scaling. The development progress by IMQ was monitored by the microscopic skin surface. As shown in Fig. 4B, the erythema and scaling started to appear from Day 3 and increased progressively until Day 5. The treatments of free actives and OA nanocarriers could partly ameliorate the symptoms. However, there were still some scales on the skin surface after treatments. The combination of cilomilast and OA in nanoparticles revealed maximum reduction with no scaly lesion compared to other groups. The semi-quantitative scoring of the psoriasiform skin was documented for 5 days to assess scaling, erythema, and skin thickness as depicted in Fig. 4C. A consistent progression in the intensity of the inflammation was observed during IMQ treatment. The animals treated with combined cilomilast and OA nanoparticles showed the scaling score which was near to the sham, whereas the scaling score was highly significant in the other groups. The reduction in skin thickening was found by cilomilast-loaded OA NLCs during a 5-day period. The cumulative score of total severity was calculated as shown in the right panel of Fig. 4C. On Day 5, cilomilast-loaded OA NLCs achieved a 53% reduction of PASI compared to the IMQ group. The PASI of the other groups approximated the value of IMQ treatment on Day 5.

The psoriasiform skin indicates a significantly greater degree of TEWL (30.22 g/m²/h) at Day 5 as compared to the sham (10.43 g/m²/h). As shown in Fig. 4D, OA nanocarriers with or without PDE4 inhibitor could decrease TEWL to ameliorate the barrier deficiency compared to the IMQ group. The level of TEWL was recovered to the baseline after a 5-day treatment of cilomilast-loaded OA nanocarriers. Analysis of H&E sections from the lesional skin demonstrated typical symptoms, including hyperkeratosis, epidermal hyperplasia, rete ridge elongation, and excess immune cell infiltration in the dermis as shown in Fig. 4E. The histological improvement was observed for all treatment groups, with cilomilast-loaded OA NLCs showing the greatest reduction of epidermal thickness and infiltration. The calculated epidermal thickness of the psoriasis-like lesions decreased from 230.4 to 139.0, 108.8, and 63.1 µm by free cilomilast, OA nanoparticles, and integrated nanocarriers, respectively (Fig. 4F). OA alone could not significantly lessen the thickening.

The effect of cilomilast-loaded OA NLCs on psoriasis amelioration was further examined by IHC and ELISA techniques. As revealed in Fig. 5A and B, the neutrophil recruitment in the dermis of the psoriasis-like skin is visualized by Ly6G and MPO staining. The cluster of PMNs in SC layer of the psoriasiform lesion confirmed the formation of Munro's microabscess. Free cilomilast cleared PMN infiltration in the SC but not in the viable skin. Treating the mice with OA-containing formulations significantly attenu-

Table 2

The IC₅₀ (µg/ml) of OA in free form, nanocarriers, or cilomilast-loaded nanocarriers against superoxide anion and elastase in the fMLF-activated human neutrophils.

Formulation	Superoxide anion	Elastase
Free OA	0.72 ± 0.15	0.42 ± 0.03
OA nanocarriers	0.66 ± 0.10	0.52 ± 0.05
Cilomilast-loaded OA nanocarriers	0.75 ± 0.19	0.42 ± 0.04

Each value represents the mean ± S.D. (n = 6).

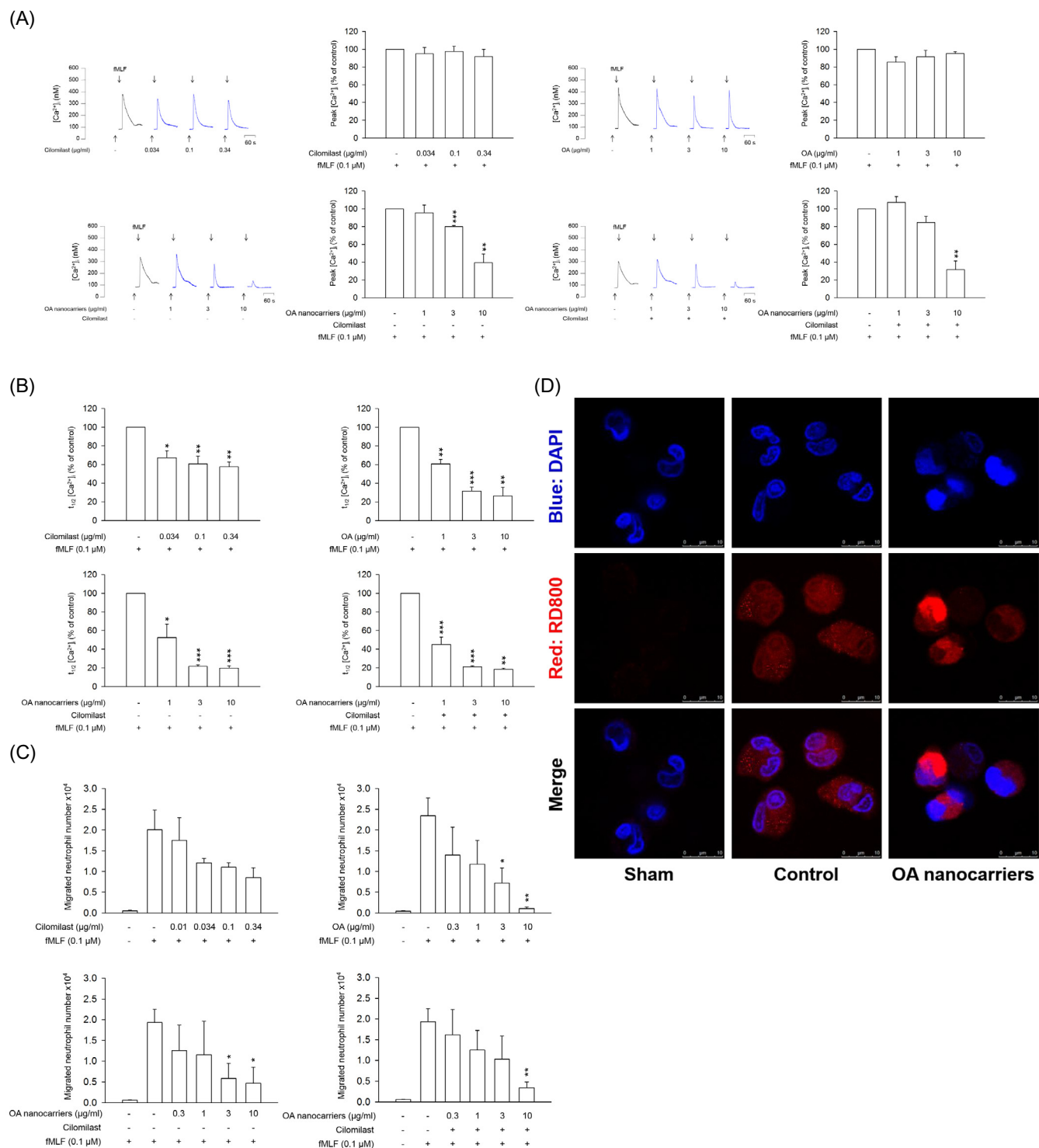


Fig. 3. The Ca^{2+} mobilization and functional change of fMLF-activated neutrophils. (A) Fluo-3/AM-labeled neutrophils were treated with cilomilast (0.034–0.34 $\mu\text{g/ml}$), OA (1–10 $\mu\text{g/ml}$), OA nanocarriers, and cilomilast-loaded OA nanocarriers for 5 min. Next, the cells were activated by fMLF (0.1 μM). Peak calcium concentration ($[\text{Ca}^{2+}]_i$) traces and (B) reduction of the time taken to decline to half of its peak values ($t_{1/2}$) are shown. (C) Transwell migration assay of human neutrophils pretreated with cilomilast, OA, OA nanocarriers, and cilomilast-loaded OA nanocarriers for 5 min and counting the number of neutrophil migration towards fMLF in the transwell. (D) The uptake of OA nanocarriers by human neutrophils. Confocal microscopy of neutrophils demonstrated that free rhodamine 800 (red) and rhodamine 800-loaded OA nanocarriers were internalized. Neutrophils nucleus stained (blue) were visualized by DAPI. Free rhodamine 800 as the control was dissolved in DMSO. All data represent mean \pm S.E.M. ($n = 3$). * $p < 0.05$, ** $p < 0.01$, *** $p < 0.001$. OA, oleic acid; fMLF, formyl-methionyl-leucyl phenylalanine. (For interpretation of the references to color in this figure legend, the reader is referred to the web version of this article.)

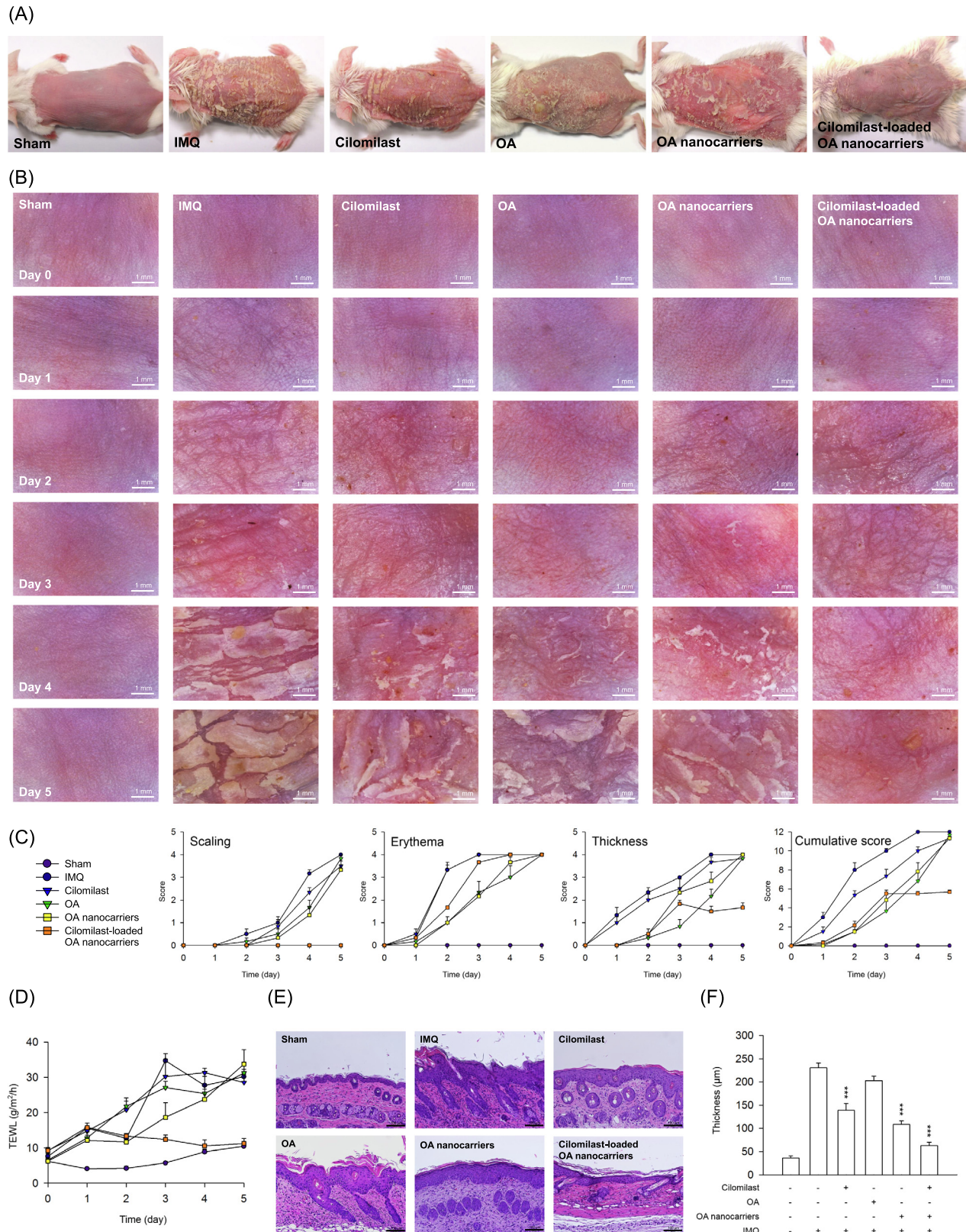


Fig. 4. The cilomilast-loaded OA nanocarriers prevent IMQ-induced psoriasis-like skin inflammation in mice. Psoriasis-like lesion was induced in BALB/c mice by IMQ, and mice were treated with cilomilast (10 mg/kg) and OA (300 mg/kg) at different formulations. (A) Gross imaging of the mice in the indicated treatment groups on Day 5. (B) Representative close-up pictures taken by handheld digital microscopy show 5 consecutive days of IMQ-induced psoriasis course. (C) Time course of the scores in mice intradermally administered with cilomilast, OA, and nanocarriers. PASI score was used to evaluate the severity. (D) Time course of skin barrier function in mice by TEWL measurement. (E) Skin sections represented by H&E staining, and (F) Epidermal thickness measured by H&E staining. All data are expressed as the mean \pm S.E.M. ($n = 6$). * $p < 0.05$, ** $p < 0.01$, *** $p < 0.001$. OA, oleic acid; IMQ, imiquimod; H&E, hematoxylin and eosin; PASI, Psoriasis Area and Severity Index; TEWL, transepidermal water loss.

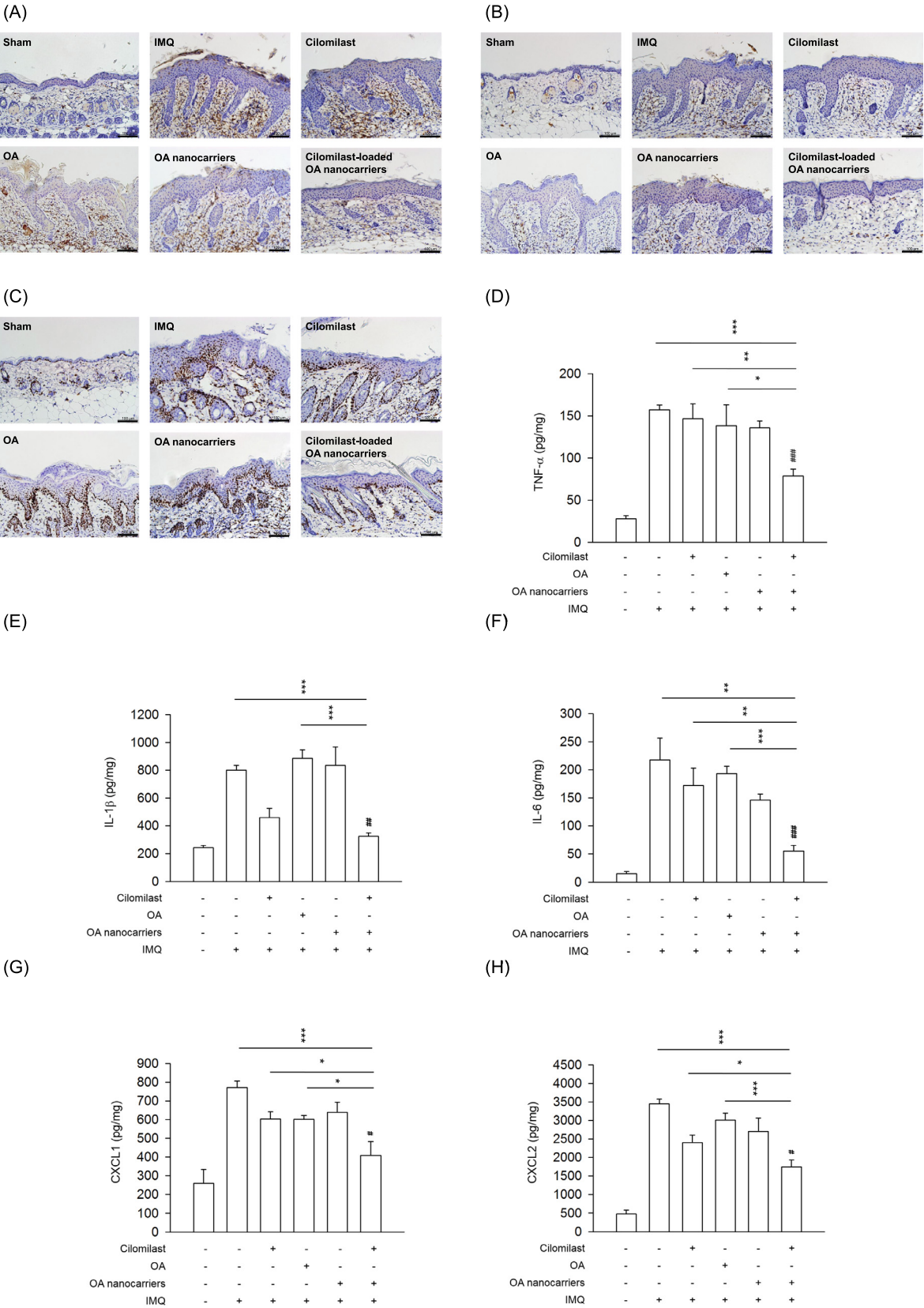


Fig. 5. The cilomilast-loaded OA nanocarriers inhibit IMQ-induced neutrophil-related cytokines and chemokines of psoriasis-like skin. (A) Ly6G, (B) MPO, (C) Ki-67, (D) TNF- α , (E) IL-1 β , (F) IL-6, (G) CXCL1, and (H) CXCL2 in psoriasis-like skin. * $p < 0.05$, ** $p < 0.01$, *** $p < 0.001$. # $p < 0.05$, ## $p < 0.01$, ### $p < 0.001$ as compared to IMQ treatment group. OA, oleic acid; IMQ, imiquimod; IHC, immunohistochemistry; Ly6G, lymphocyte antigen 6 complex locus G6D; MPO, myeloperoxidase.

ated the increase of PMN markers, especially the integrated nanosystems. Ki-67 is a protein associated with proliferation. Ki-67 largely appeared in the basal layer of IMQ-treated skin, suggesting epidermal hyperplasia. Incorporation of cilomilast in OA nanocarriers resulted in greater suppression of proliferation in comparison to the other treatment groups.

TNF- α , IL-1 β , and IL-6 are proinflammatory cytokines that play a role in psoriasis. Their expression in skin tissue homogenates is dramatically upregulated by IMQ (Fig. 5D–F). IMQ application increased the TNF- α level by 5.7-fold in comparison to the normal group. TNF- α did not reveal any significant change in all treatment groups, except that cilomilast-loaded OA NLCs showed a 2-fold inhibition compared to the IMQ group (Fig. 5D). The level of IL-1 β was increased by 3.3-fold in the IMQ group in comparison to the sham (Fig. 5E). IL-1 β was downregulated 43% and 59% by free and nanoparticulate cilomilast compared to the IMQ group. No effect was detected for free OA and OA nanoparticles on IL-1 β . Free actives and OA nanocarriers did not reduce IL-6 expression in psoriasisform skin (Fig. 5F). A significant IL-6 downregulation was found for the combined cilomilast and OA in nanosystems. The chemokines CXCL1 and CXCL2 were analyzed, as shown in Fig. 5G and 5H, respectively. Compared to the free actives and OA nanocarriers, decreased chemokines in the group treated with integrated nanosystems were found. Comparison of macroscopic appearance, histology, and proinflammatory mediators in the mouse model after administration of cilomilast or OA demonstrated that combined actives in NLCs were far more efficacious than the other groups for psoriasis mitigation.

3.4. In vivo cutaneous tolerance

Free actives, OA nanocarriers, and dual-active nanoparticles were intradermally applied on healthy mouse skin each day for 5 days. Fig. 6A and B illustrate the gross and close-up appearance of the skin surface, respectively. All formulations generally exhib-

ited no change in the appearance, indicating the compatibility with the skin. The mouse skin remains intact without obvious change in histopathological characteristics (Fig. 6C). Further, no TEWL increase is detected for the formulations compared to the sham control. The results suggested that the nanocarriers were safe for skin use. The additives used for nanoparticle formation seem to be acceptable for clinical application.

4. Discussion

We prepared lipid nanocarriers loading cilomilast and OA as active agents to inhibit neutrophil stimulation for psoriasis management. Our results showed that OA nanocarriers are indigenous to prevent PMN activation and the deterioration of psoriatic lesion. Cilomilast incorporation in OA nanocarriers could further mitigate the severity of the disease, reducing the clinical score and suppressing proinflammatory mediators. Both agents could be highly entrapped in the nanoparticles. Because of the emulsifier character of OA, some molecules might intercalate in the particulate shell contributing to negative zeta potential with SPC. The pH of the nanosystems was 4.34. Cilomilast is almost insoluble in acidic aqueous medium [18]. It is expected that most of the cilomilast molecules resided in the core and the surface of the nanoparticles. The reduction of negative surface charge by cilomilast incorporation is the evidence of a drug-enriched surface in our nanosystems since this drug exhibited a neutral form in the acidic environment. The release experiment confirmed that OA NLCs could significantly slow and sustain cilomilast delivery. The cytotoxicity study evaluated by LDH leakage demonstrated that nanoparticles did not decrease PMN viability. This suggests that the anti-inflammatory activity of NLCs on PMNs was not due to cytotoxicity. All the nanocarrier preparations were safe for human neutrophils. Calcium is an intracellular second messenger contributing to PMN activation [19]. OA has been reported to regulate Ca²⁺ homeostasis in different immune cells such as T cells and macrophages [20]. In

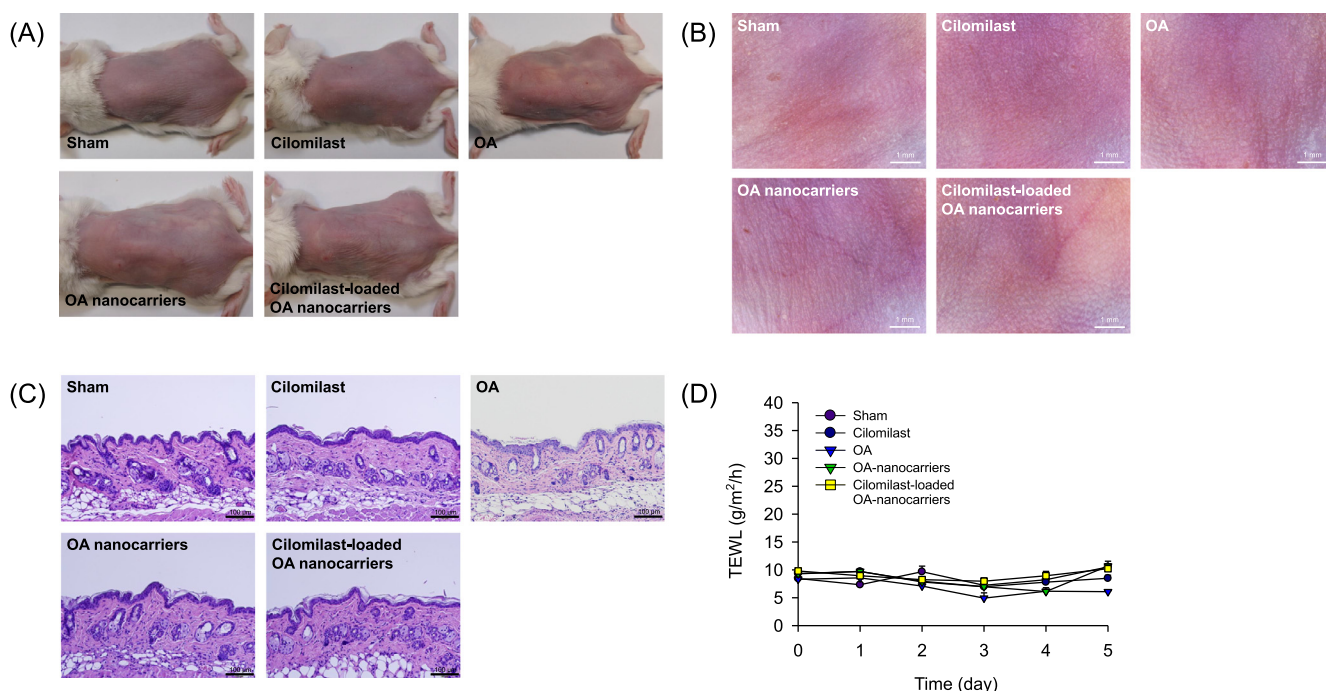


Fig. 6. A skin safety study. Intradermal injection of cilomilast, OA, OA nanocarriers, and cilomilast-loaded OA nanocarriers into mice for consecutive 5 days. (A) Gross imaging of the mice on Day 5. (B) Representative close-up pictures taken by handheld digital microscopy show 5 consecutive days of administration. (C) Skin sections represented by H&E staining. (D) Time course of skin barrier function in mice by TEWL measurement. All data are expressed as the mean \pm S.E.M. ($n = 6$). OA, oleic acid; H&E, hematoxylin; TEWL, transepidermal water loss.

the case of neutrophils, OA did not modulate fMLF-induced $[Ca^{2+}]_i$ but accelerated the speed of peak $[Ca^{2+}]_i$ decline. A similar result was found for free cilomilast. This suggests that free cilomilast and OA could not impede initial calcium influx into the cells but could eliminate $[Ca^{2+}]_i$ after its entry. Our result showed that OA nanocarriers reduced both $[Ca^{2+}]_i$ and $t_{1/2}$, indicating a stronger inhibition of calcium mobilization compared to the free form. A previous report [21] demonstrates that OA can promote the phagocytic capacity of PMNs. The increased surface-to-volume ratio of nanoparticles leads to the increased interaction with the cells for ingestion [22]. OA nanocarriers exhibited more facile internalization into neutrophils than free form. The cellular uptake is especially effortless for the nanoparticles with a phospholipid shell and negative surface charge [23]. Our nanocarriers fitted this criterion. The internalized OA nanoparticles may be engulfed as a phagosome and then fused with lysosomes for further degradation [24]. The high uptake by the nanoparticles was responsible for inhibiting $[Ca^{2+}]_i$ and $t_{1/2}$ of the inflamed neutrophils. Schütz et al. [11] also demonstrate that OA-stabilized nanoparticles displayed a better internalization into HT29 cancer cells than free OA.

The increase of calcium influx into PMNs is a potential mechanism behind superoxide generation and elastase release [25]. Oxidative stress and degranulation of neutrophils are linked to the tissue destruction in inflammatory diseases. With PDE4 inhibition in immune cells, the proinflammatory mediators can be decreased [7]. Our results exhibited that free cilomilast suppressed superoxide anion but not elastase. The ability of OA to diminish ROS production has been proved previously [26]. Both superoxide anion and elastase could be inhibited by free OA. However, unlike $[Ca^{2+}]_i$, OA participation in nanoparticles did not further enhance the inhibitory effect. A similar tendency was found in the PMN migration study.

As a convenient and promising model, IMQ-induced psoriasis-form skin has been extensively used for psoriasis investigation [27]. The macroscopic and microscopic observations in this study confirmed the formation of psoriasis plaque evidenced by desquamation, redness, thickening, and immune infiltration. The IMQ model also verifies the major contribution of neutrophils to psoriatic skin [28]. Our IHC showed the accumulation of PMNs in the SC to produce Munro's microabscess. The development of psoriasis leads to keratinocytes to activate cytokine generation. The hyperproliferation in the epidermis is a consequence of barrier deficiency [29]. The PMN chemoattractants CXCL1 and CXCL2 are upregulated in psoriasis-like lesions induced by IMQ [30]. These phenomena were observed in our study. The cytokine and chemokine mediators of psoriasis are regulated by PDE4 [6]. Cilomilast is proved to directly modulate keratinocyte function by suppressing cytokines and chemokines [31]. The PDE4 inhibitors including cilomilast were reported to decrease TNF- α , IL-1 β , IL-6, and chemostatic factors in neutrophils and other mammalian cells [32–34]. Previous investigations [8,35] have reported that OA was able to prohibit the activation and migration of PMNs. Nevertheless, our data suggested that free cilomilast and OA had a negligible or no effect on psoriasis-like lesions.

Cilomilast is highly bound to proteins (99.4%) in the body, especially albumin [18]. The metabolism of this drug is extensive with acyl glucuronidation, decyclopentylation, and 3-hydroxylation in vivo, leading to the prevention of clinical efficacy [36]. A previous report [37] also indicates that oral and intraperitoneal cilomilast administrations showed only weak inhibition on contact dermatitis. The anti-inflammatory activity of OA in the in vivo condition may be depressed since the inhibitory capacity of OA on activated PMNs was decreased in the presence of albumin that is abundant in plasma and interstitial fluid [8]. OA only moderately inhibits chemotaxis at very high doses [20]. The extremely high lipophilicity of OA molecules also keeps them from contact with

biosystems. The combination of cilomilast and OA in lipid nanocarriers significantly decreased the epidermal thickness and pathological features of psoriatic plaque. The reduced inflammatory response in the psoriasiform model was accompanied by the suppression of TNF- α , IL-1 β , and IL-6. These proinflammatory cytokines can be released by peripheral PMNs. All of them are important psoriasis mediators for developing the Th17 immune response. Cytokines are appreciated for the ability to magnify keratinocyte proliferation [38]. Ki-67 profiles showed an inhibition of hyperproliferation by cilomilast-loaded OA NLCs. fMLF is a chemotactic factor to evoke the migration of PMNs. Both human PMNs and the psoriasis-like animal model indicated the inhibition of neutrophil migration and chemokine expression by dual-active nanoparticles.

The improved efficacy of integrated nanocarriers may be due to the increased localization of actives in the nidus, enhanced bioavailability of the actives, and the sustained period of action. The drugs entrapped in the lipid matrix of NLCs would prevent the leaching, thus increasing the stability by blocking the enzymatic attack [39]. Another mechanism that could account for the better efficacy of combined actives in nanoparticles is the slow cilomilast release. Because of the comprehensive metabolism of cilomilast in vivo, the slow release process could protect the drug from rapid elimination. The in vitro PMN study showed that the treatment time for the nanoparticles to neutrophils did not exceed 20 min. Cilomilast might remain inside the nanoparticles in the in vitro assay. On the other hand, the treatment duration of the nanoparticles in the in vivo experiment was 24 h. There were 14% cilomilast molecules released from NLCs without a burst effect during this period. Besides the effect of nanoparticulate cilomilast on inflammation suppression, free cilomilast was also responsible for this inhibition in the in vivo situation. Sustained delivery is promised for chronic disorders to achieve better safety and patient compliance [40]. Of course it should be cautious that the in vivo condition demonstrates a more complex environment than the in vitro. The enzymes and proteins in the skin may accelerate the nanoparticle degradation and drug release. Further study is needed to explore cilomilast leakage from NLCs in the skin. With respect to the synergistic activity of combined cilomilast and OA, we may speculate that the nanoparticles were endocytosed into PMNs and led to the internalization inside endosomes or lysosomes. The subsequent degradation of nanoparticles contributed to the release of actives for inactivating the proinflammatory function, thereby offering a promising approach for relieving psoriasiform lesion. The keratinocyte proliferation, PMN infiltration, cytokine, and chemokine expression could be inhibited by the integrated nanocarriers based on in vivo psoriasis model. This may indicate a multitargeted capability of the nanosystems for mitigating inflammation because of the dual actives inside the nanoparticles.

The limitation of the present work was the use of invasive intradermal injection but not noninvasive topical delivery as the administration route. We aimed to employ an injection route to ensure the contact of intact nanoparticles with PMNs. The lipid nanoparticles may be destroyed when penetrating via the skin. Topical administration is more applicable for clinical psoriasis treatment. However, the antipsoriatic efficacy of PDE4 inhibitors is less by the topical pathway than by the systemic route [41]. Whether the topical nanocarrier application is advantageous for therapy remains to be elucidated.

5. Conclusions

We exploited a dual-active nanoparticle delivery system for improved psoriasis therapy, which not only revealed a sustained drug release but also enhanced cellular uptake by PMNs.

Cilomilast-loaded OA NLCs could maintain the superoxide anion and elastase release inhibition capability in activated PMNs as free cilomilast and OA. The in vivo animal model of psoriasis showed that combined cilomilast and OA were involved in the synergistic effect on inflammation suppression. The nanocarriers improved the psoriasis-like symptoms by inhibiting the neutrophil influx and cytokine/chemokine expression. The dual-agent efficiency was greater than that of the single active. Our study distinguishes the cilomilast-loaded OA nanocarriers as potential candidates for the treatment of psoriasiform lesions.

Acknowledgement

The authors are grateful to the financial support from Chang Gung Memorial Hospital (CMRPD1G0411-2 and EMRPD1H0381).

References

- [1] S.K. Raychaudhuri, E. Maverakis, S.P. Raychaudhuri, Diagnosis and classification of psoriasis, *Autoimmunity Rev.* 13 (2014) 490–495.
- [2] M.A. Lowes, M. Suárez-Fariñas, J.G. Krueger, Immunology of psoriasis, *Annu. Rev. Immunol.* 32 (2014) 227–255.
- [3] S. Ikeda, H. Takahashi, Y. Suga, H. Eto, T. Etoh, K. Okuma, K. Takahashi, T. Kanbara, M. Seishima, A. Morita, Y. Imai, T. Kanekura, Therapeutic depletion of myeloid lineage leukocytes in patients with generalized pustular psoriasis indicates a major role for neutrophils in the immunopathogenesis of psoriasis, *J. Am. Acad. Dermatol.* 68 (2013) 609–617.
- [4] E. Ogawa, Y. Sato, A. Minagawa, R. Okuyama, Pathogenesis of psoriasis and development of treatment, *J. Dermatol.* 45 (2018) 264–272.
- [5] R. Zebda, A.S. Paller, Phosphodiesterase 4 inhibitors, *J. Am. Acad. Dermatol.* 78 (Suppl. 1) (2018) S43–S52.
- [6] M. Wittmann, P.S. Helliwell, Phosphodiesterase 4 inhibition in the treatment of psoriasis, psoriatic arthritis and other chronic inflammatory diseases, *Dermatol. Ther.* 3 (2013) 1–15.
- [7] C.H. Lin, S.H. Chang, J.Y. Fang, Recent advances using phosphodiesterase 4 (PDE4) inhibitors to treat inflammatory disorders: animal and clinical studies, *Curr. Drug Ther.* 11 (2016) 21–40.
- [8] T.L. Hwang, Y.C. Su, H.L. Chang, Y.L. Leu, P.J. Chung, L.M. Kuo, Y.J. Chang, Suppression of superoxide anion and elastase release by C₁₈ unsaturated fatty acids in human neutrophils, *J. Lipid Res.* 50 (2009) 1395–1408.
- [9] K.O. Choi, J. Choe, S. Suh, S. Ko, Positively charged nanostructured lipid carriers and their effect on the dissolution of poorly soluble drugs, *Molecules* 21 (2016) 672.
- [10] Z. Wang, J. Li, J. Cho, A.B. Malik, Prevention of vascular inflammation by nanoparticle targeting of adherent neutrophils, *Nat. Nanotechnol.* 9 (2014) 204–210.
- [11] C.A. Schütz, D. Staedler, K. Crosbie-Staunton, D. Movia, C.C. Bernasconi, B.H. Kenzaoui, A. Prina-Mello, L. Juillerat-Jeanneret, Differential stress reaction of human colon cells to oleic-acid-stabilized and unstabilized ultrasmall iron oxide nanoparticles, *Int. J. Nanomed.* 9 (2014) 3481–3498.
- [12] H.R. Kelidari, M. Saeedi, J. Akbari, K. Morteza-Semnani, H. Valizadeh, M. Maniruzzaman, A. Farmoudeh, A. Nokhodchi, Development and optimisation of spirinolactone nanoparticles for enhanced dissolution rates and stability, *AAPS Pharm. Sci. Tech.* 18 (2017) 1469–1474.
- [13] J. Cai, Y.Q. Mao, B.Z. Yu, P. Ma, L. Li, H.M. Fan, Large-scale, facile transfer of oleic acid-stabilized iron oxide nanoparticles to the aqueous phase for biological applications, *Langmuir* 33 (2017) 1662–1669.
- [14] C.L. Fang, S.A. Al-Suwayeh, Fang, Nanostructured lipid carriers (NLCs) for drug delivery and targeting, *Recent Pat. Nanotechnol.* 7 (2013) 41–55.
- [15] C. Kroegel, M. Foerster, Phosphodiesterase-4 inhibitors as a novel approach for the treatment of respiratory disease: cilomilast, *Expert Opin. Invest. Drugs* 16 (2007) 109–124.
- [16] Y.F. Tsai, H.P. Yu, P.J. Chung, Y.L. Leu, L.M. Kuo, C.Y. Chen, T.L. Hwang, Osthol attenuates neutrophilic oxidative stress and hemorrhagic shock-induced lung injury in rats, *Biochem. Pharmacol.* 78 (2009) 983–992.
- [17] L. van der Fits, S. Mourits, J.S.A. Voerman, M. Kant, L. Boon, J.D. Laman, F. Cornelissen, A.M. Mus, E. Florencia, E.P. Prens, E. Lubberts, Imiquimod-induced psoriasis-like skin inflammation in mice is mediated via the IL-23/IL-17 axis, *J. Immunol.* 182 (2009) 5836–5845.
- [18] G. Down, S. Siederer, S. Lim, P.D. Yates, Clinical pharmacology of cilomilast, *Clin. Pharmacokinet.* 45 (2006) 217–233.
- [19] R.A. Clemens, C.A. Lowell, Store-operated calcium signaling in neutrophils, *J. Leukoc. Bio.* 98 (2015) 497–502.
- [20] C. Carrillo, del M. Cavia, S. Alonso-Torre, Role of oleic acid in immune system: mechanism of action; a review, *Nutr. Hosp.* 27 (2012) 978–990.
- [21] R. Padovese, R. Curi, Modulation of rat neutrophil function in vitro by cis- and trans-MUFA, *Br. J. Nutr.* 101 (2009) 1351–1359.
- [22] M.H. Lin, C.F. Lin, S.C. Yang, C.F. Hung, J.Y. Fang, The interplay between nanoparticles and neutrophils, *J. Biomed. Nanotechnol.* 14 (2018) 66–85.
- [23] M. Benfer, T. Kissel, Cellular uptake mechanism and knockdown activity of siRNA-loaded biodegradable DEAPA-PVA-g-PLGA nanoparticles, *Eur. J. Pharm. Biopharm.* 80 (2012) 247–256.
- [24] B. Fang, M. Zhang, H. Wu, X. Fan, F. Ren, Internalization properties of the anti-tumor α -lactalbumin-oleic acid complex, *Int. J. Biol. Macromol.* 96 (2017) 44–51.
- [25] Y.F. Tsai, H.P. Yu, W.Y. Chang, F.C. Liu, Z.C. Huang, T.L. Hwang, Sirtinol inhibits neutrophil elastase activity and attenuates lipopolysaccharide-mediated acute lung injury in mice, *Sci. Rep.* 5 (2015) 8347.
- [26] C.F. Gonçalves-de-Albuquerque, I.M. Medeiros-de-Moraes, F.M. de Jesus Oliveira, P. Burth, P.T. Bozza, M.V.C. Faria, A.R. Silva, H.C. de Castro-Faria-Neto, Omega-9 oleic acid induces fatty acid oxidation and decreases organ dysfunction and mortality in experimental sepsis, *PLoS One* 11 (2016) e0153607.
- [27] S.Y. Chuang, C.H. Lin, T.H. Huang, J.Y. Fang, Lipid-based nanoparticles as a potential delivery approach in the treatment of rheumatoid arthritis, *Nanomaterials* 8 (2018) 42.
- [28] H. Sumida, K. Yanagida, Y. Kita, J. Abe, K. Matsushima, M. Nakamura, S. Ishii, S. Sato, T. Shimizu, Interplay between CXCR2 and BLT1 facilitates neutrophil infiltration and resultant keratinocyte activation in a murine model of imiquimod-induced psoriasis, *J. Immunol.* 192 (2014) 4361–4369.
- [29] R. Wolf, E. Orion, E. Ruocco, V. Ruocco, Abnormal epidermal barrier in the pathogenesis of psoriasis, *Clin. Dermatol.* 30 (2012) 323–328.
- [30] B. Nedoszytko, M. Sokolowska-Wojdylo, K. Ruckemann-Dziurdzinska, J. Roszkiewicz, R.J. Nowicki, Chemokines and cytokines network in the pathogenesis of the inflammatory skin diseases: atopic dermatitis, psoriasis and skin mastocytosis, *Postepy Dermatol. Allergol.* 31 (2014) 84–91.
- [31] W. Bäumer, M. Kietzmann, Effects of cyclosporin A and cilomilast on activated canine, murine and human keratinocytes, *Vet. Dermatol.* 18 (2007) 107–114.
- [32] D.M. Murphy, C. Ward, I.A. Forrest, G. Pritchard, D. Jones, R. Stovold, A.J. Fisher, T.E. Cawston, J.L. Lordan, P.A. Corris, The phosphodiesterase Type IV inhibitor cilomilast decreases pro-inflammatory cytokine production from primary bronchial epithelial cells in lung transplantation patients, *J. Heart Lung Transplant.* 25 (2006) 1436–1440.
- [33] A.C. Palfreeman, K.E. McNamee, F.E. McCann, New developments in the management of psoriasis and psoriatic arthritis: a focus on apremilast, *Drug Des. Develop. Ther.* 7 (2013) 201–210.
- [34] N. Ishii, M. Shirato, H. Wakita, K. Miyazaki, Y. Takase, O. Asano, K. Kusano, E. Yamamoto, C. Inoue, I. Hishinuma, Antipruritic effect of the topical phosphodiesterase 4 inhibitor E6005 ameliorates skin lesions in a mouse atopic dermatitis model, *J. Pharmacol. Exp. Ther.* 346 (2013) 105–112.
- [35] A. Ferrante, D. Goh, D.P. Harvey, B.S. Robinson, C.S. Hii, E.J. Bates, S.J. Hardy, D. W. Johnson, A. Poulos, Neutrophil migration inhibitory properties of polyunsaturated fatty acids. The role of fatty acid structure, metabolism, and possible second messenger systems, *J. Clin. Invest.* 93 (1994) 1063–1070.
- [36] M.A. Gjembycz, An update and appraisal of the cilomilast phase III clinical development programme for chronic obstructive pulmonary disease, *Br. J. Clin. Pharmacol.* 62 (2006) 138–152.
- [37] W. Bäumer, U. Seegers, M. Braun, T. Tschernig, M. Kietzmann, TARC and RANTES but not CTACK, are induced in two models of allergic contact dermatitis. Effects of cilomilast and diflorasone diacetate on T-cell-attracting chemokines, *Br. J. Dermatol.* 151 (2004) 823–830.
- [38] J. Baliwag, D.H. Barnes, A. Johnston, Cytokines in psoriasis, *Cytokine* 73 (2015) 342–350.
- [39] Q. Li, T. Cai, Y. Huang, X. Xia, S.P.C. Cole, Y. Cai, A review of the structure, preparation, and application of NLCs PNP, and PLNs, *Nanomaterials* 7 (2017) 122.
- [40] J.V. Natarajan, C. Nugraha, X.W. Ng, S. Venkatraman, Sustained-release from nanocarriers: a review, *J. Control. Release* 193 (2014) 122–138.
- [41] P.H. Schafer, A. Parton, A.K. Gandhi, L. Capone, M. Adams, L. Wu, J.B. Bartlett, M. A. Loveland, A. Gilhar, Y.F. Cheung, G.S. Baillie, M.D. Houslay, H.W. Man, G.W. Muller, D.I. Stirling, Apremilast, a cAMP phosphodiesterase-4 inhibitor, demonstrates anti-inflammatory activity in vitro and in a model of psoriasis, *Br. J. Pharmacol.* 159 (2010) 842–855.

Epigenetic Manipulation Induces the Production of Coumarin-Type Secondary Metabolite from *Arthrotrrys foliicola*

Chi-Ying Li,^[a, b] I-Wen Lo,^[a] Yen-Ping Hsueh,^[c] Yu-Ming Chung,^[a] Shih-Wei Wang,^[a, d] Michal Korinek,^[a, e, f] Yi-Hong Tsai,^[a] Yuan-Bin Cheng,^[a, g] Tsong-Long Hwang,^[c, f, h] Clay C. C. Wang,^[b, i] Fang-Rong Chang,^{*,[a, j]} and Yang-Chang Wu^{*,[a, g, k]}

Abstract: Pursuing epigenetic manipulation approach in fungi led to the isolation of an unusual coumarin metabolite from fungi. An addition of the histone deacetylase inhibitor, suberohydroxamic acid (SBHA), to the culture medium of *Arthrotrrys foliicola* induced production of the coumarin-type secondary metabolite represented by a single intensive peak in the HPLC profile of the ethyl acetate extract. The compound which was identified as 4-ethyl-7-hydroxy-8-methyl-2H-chromen-2-one (**1**) was isolated from nature for the first time. Moreover, the investigation on the remaining

part of the HPLC profile led to the separation of 6-ethyl-2,4-dihydroxy-3-methylbenzaldehyde (**2**) and ten 2,5-diketopiperazine compounds (**3–12**). The structures of isolates were deduced by their mass and NMR spectroscopic data. The coumarin-type secondary metabolite (**1**) with peculiar smell induced by epigenetic stimulation is found for the first time in the *Arthrotrrys* species and the family Orbiliaceae. We evaluated **1** for the cytotoxic, anti-inflammatory, anti-allergic and nematocidal activities, however, it was found inactive.

Keywords: *Arthrotrrys foliicola* • epigenetic manipulation • secondary metabolites • coumarin • 2,5-diketopiperazine

1. Introduction

Fungi are important sources of natural products that are useful to humankind. Bioactive components generated by fungi have been used in pharmaceutical, food industries and agriculture.^[1,2,3] Natural products obtained from fungi are generally

cultivated under standardized laboratory growth conditions.^[4] Traditional methods to explore fungal natural products usually include species collection, optimization of strains cultivation conditions, extraction, bioassay-guided fractionation, purification, and structural elucidation. However, this approach often

[a] C.-Y. Li, I.-W. Lo, Y.-M. Chung, S.-W. Wang, M. Korinek, Y.-H. Tsai, Y.-B. Cheng, F.-R. Chang, Y.-C. Wu
Graduate Institute of Natural Products, College of Pharmacy
Kaohsiung Medical University, Kaohsiung, 807, Taiwan
phone: +886-7-312-1101 (ext. 2162)
phone: +886-7-312-1101(ext. 5437)
E-mail: aaronfrc@kmu.edu.tw
yachwu@kmu.edu.tw

[b] C.-Y. Li, C. C. C. Wang
Department of Pharmacology and Pharmaceutical Sciences
University of Southern California, School of Pharmacy
Los Angeles, CA 90089, USA

[c] Y.-P. Hsueh
Institute of Molecular Biology, Academia Sinica
Taipei, 11529, Taiwan

[d] S.-W. Wang
Department of Medicine, Mackay Medical College
New Taipei City, 252, Taiwan

[e] M. Korinek, T.-L. Hwang
Graduate Institute of Natural Products, College of Medicine, and
Chinese Herbal Medicine Research Team, Healthy Aging Research
Center, Chang Gung University, Taoyuan, 33302, Taiwan

[f] M. Korinek, T.-L. Hwang
Research Center for Chinese Herbal Medicine, Research Center for
Food and Cosmetic Safety, and Graduate Institute of Health In-
dustry Technology, College of Human Ecology, Chang Gung Uni-
versity of Science and Technology, Taoyuan, 33302, Taiwan


[g] Y.-B. Cheng, Y.-C. Wu
Department of Medical Research, Kaohsiung Medical University,
Kaohsiung, 807, Taiwan

[h] T.-L. Hwang
Department of Anesthesiology, Chang Gung Memorial Hospital,
Taoyuan 33305, Taiwan

[i] C. C. C. Wang
Department of Chemistry, University of Southern California
College of Letters, Arts, and Sciences,
Los Angeles, CA 90089, USA

[j] F.-R. Chang
National Research Institute of Chinese Medicine
Taipei, 112, Taiwan

[k] Y.-C. Wu
Research Center for Natural Products & Drug Development
Kaohsiung Medical University, Kaohsiung, 807, Taiwan

 Supporting information for this article is available on the WWW
under <https://doi.org/10.1002/ijch.201800162>

led to rediscover the same bioactive or major secondary metabolites.^[5]

Epigenetic manipulation is utilized in the development of fungal secondary metabolites produced from cryptic biosynthetic pathways. This strategy has been proved to be an effective technique for stimulating transcription of silent biosynthetic gene clusters.^[6] Histone deacetylase (HDAC) or DNA methyltransferase (DNMT) inhibitors were previously used for the fungal genomic manipulation, which may lead to the activation of silent gene clusters resulting in the production of variety of novel secondary metabolites.^[5] Previously, we triggered the filamentous fungi by applying this approach through the addition of suberohydroxamic acid (SBHA, HDAC inhibitor) or 5-azacytidine (5-AZ, DNMT inhibitor) to the fungal culture medium and several novel and functional secondary metabolites were discovered.^[5,7,8,9]

These results encouraged us to continue our efforts to develop fungal secondary metabolites using epigenetic manipulation approach. Screening filamentous fungi in the presence of these inhibitors demonstrated that the addition of 0.5 mM suberohydroxamic acid (SBHA, HDAC inhibitor) to the culture medium of *Arthrobotrys foliicola* induced a dramatic change, an intensive peak raised, in its HPLC secondary metabolite profile (Figure 1) of the ethyl acetate (EtOAc) extract.

The fungal genus *Arthrobotrys* was reported for its secondary metabolites that have the nematocidal activity.^[10,11,12,13] In past, secondary metabolites, oligosporon, oligosporol B, 4',5'-dihydrooligosporon, hydroxyoligosporon, 10',11'-epoxyoligosporon, 4',5'-dihydro-oligosporol B, arthrobotrisins A, B, C and arthrosporols A, B, C were reported from other species of this genus.^[10,11,14] However, to the best of our knowledge, there has been no chemical and biological investigation on the species of *Arthrobotrys foliicola* yet. In addition, this fungus was successfully modulated by epigenetic manipulation in our preliminary evaluation. Therefore, the fungal culture broth was scaled up, and the characteristic HPLC signal that appeared after epigenetic manipulation was further investigated, yielding a coumarin-type secondary

metabolite, which was isolated from nature for the first time. Moreover, it is the first time that coumarin skeleton compound was obtained from this genus of fungi. Eleven known compounds were also identified. The bioactivity of EtOAc crude extract and isolates was evaluated using cytotoxic, anti-inflammatory, anti-allergic, anti-angiogenesis assays.

2. Results and Discussion

The culture broth of *Arthrobotrys foliicola* was scaled up to produce 15 L (10 days cultivation) of culture broth, which was separated from mycelium by filtration. The broth was extracted with EtOAc to afford the crude extract (1.3 g). The crude extract was tested for cytotoxic, anti-inflammatory, anti-allergic and anti-angiogenesis activities, but was found inactive.

This crude extract was subjected to a series of column chromatography procedures, traced by the HPLC examination, and yielded the coumarin type of compound, 4-ethyl-7-hydroxy-8-methyl-2*H*-chromen-2-one (**1**),^[15] along with one benzaldehyde derivative, 6-ethyl-2,4-dihydroxy-3-methylbenzaldehyde (**2**)^[16] and ten 2,5-diketopiperazines, cyclo(L-Pro-Gly) (**3**),^[17] cyclo(L-Pro-L-Val) (**4**),^[18] cyclo(L-Pro-L-Leu) (**5**),^[19] cyclo(D-Pro-L-Ile) (**6**),^[20] cyclo(L-Pro-L-Phe) (**7**),^[18] cyclo(4*R*-hydroxy-L-Pro-L-Leu) (**8**),^[21] cyclo(4*S*-hydroxy-D-Pro-D-Ile) (**9**),^[22] cyclo(4*R*-hydroxy-L-Pro-L-Phe) (**10**),^[21] cyclo(L-Pro-L-Tyr) (**11**)^[23] and cyclo(L-Pro-L-Trp) (**12**).^[21]

All isolates were deduced according to their spectroscopic data and compared with the corresponding authentic samples or literature values (Figure 2). Moreover, the elution order of isolated compounds in the HPLC profile was illustrated individually in the Figure 1. Interestingly, these 12 compounds were all isolated from the *Arthrobotrys* genus for the first time.

Compound **1** was affording as colorless oil with peculiar smell. The HRESIMS for **1** showed a pseudomolecular ion peak at m/z 227.0680 $[M+Na]^+$, which corresponded to the molecular formula $C_{12}H_{12}O_3$, indicating seven degrees of

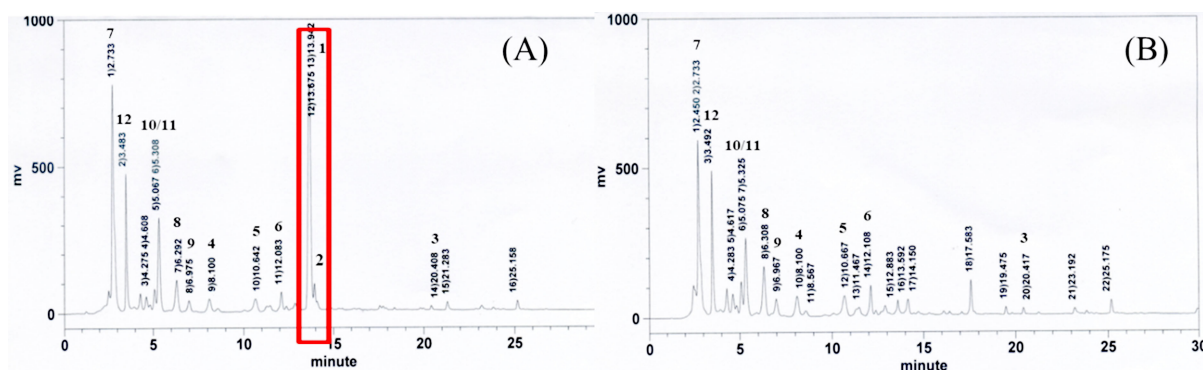


Figure 1. HPLC profile of *A. foliicola* EtOAc extract cultivated in YM medium containing 0.5 mM SBHA (A) and control (B) detected by UV absorption at 215 nm.

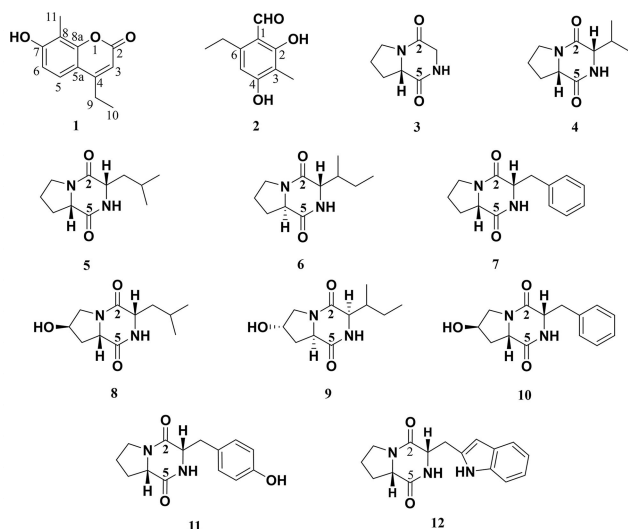


Figure 2. Structures of all isolates 1–12.

unsaturation. The ^1H NMR data (Table 1) revealed the presence of two methyl groups at δ_{H} 1.24 (t, $J=7.6$ Hz) and at δ_{H} 2.21 (s), two aliphatic protons at δ_{H} 2.81 (q, $J=7.6$) and three olefinic protons at δ_{H} 6.13 (d, $J=9.6$ Hz), 6.67 (s) and 8.07 (d, $J=9.6$). The ^{13}C NMR (Table 1) and DEPT spectra of **1** revealed that 12 carbons can be categorized into two methyls (δ_{C} 7.9 and δ_{C} 16.1), one methylenes (δ_{C} 25.8), three olefinic methines (δ_{C} 109.9, 113.9, 143.4) and six quaternary carbons (including four olefinic carbons, one oxygen-bearing carbon and, one ester carbonyl carbon at δ_{C} 110.6, 110.7, 142.1, 156.0, 162.8, 164.5).

Two fragment correlations of H-9 (δ_{H} 2.81)/H-10 (δ_{H} 1.24) and H-5 (δ_{H} 8.06)/H-6 (δ_{H} 6.13) were observed in COSY. The HMBC correlations of H-9 (δ_{H} 2.81)/C-4 (δ_{C} 142.1), C-5a (δ_{C} 110.6), C-3 (δ_{C} 113.9) and the COSY fragment of H-9/H10

suggested the connection of an ethyl side chain to C-4. Further, the HMBC correlations of H-3 (δ_{H} 6.67)/C-2 (δ_{C} 162.8), C-5a (δ_{C} 110.6) indicated a linkage of partial structure A (4-ethyl- σ -lactone). Moreover, the HMBC correlations of H-11 (δ_{H} 2.21)/C-7 (δ_{C} 164.5), C-8 (δ_{C} 110.7), C-8a (δ_{C} 156.0) and H-5 (δ_{H} 8.06)/C-4 (δ_{C} 142.1), C-5a (δ_{C} 110.5), C-7 (δ_{C} 164.5), C-8a (δ_{C} 156.0) and H-6 (δ_{H} 6.13)/C-5a (δ_{C} 110.6), C-7 (δ_{C} 164.5), C-8 (δ_{C} 110.7) could connect partial structure A with the remaining part of structure.

And according to the number of degrees of unsaturation, spectroscopic data and physical data, the structure of **1** was deduced as the coumarin and illustrated in Figure 3. Compound **1**, 4-ethyl-7-hydroxy-8-methyl-2*H*-1-benzopyran-2-one, turns out to be a new naturally occurring compound, which was previously identified as the precursor for advanced complex coumarin syntheses.^[15] Additionally, we proposed a plausible biosynthetic pathway of **1**. The biosynthetic route starts from glucose via phenylalanine to yield umbeliferone^[24] which undergoes alkylation^[25,26] to obtain **1** (Scheme 1).

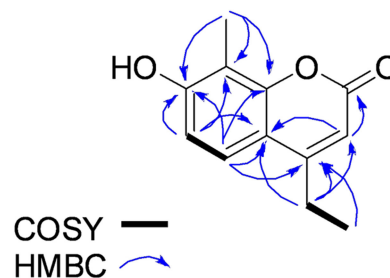
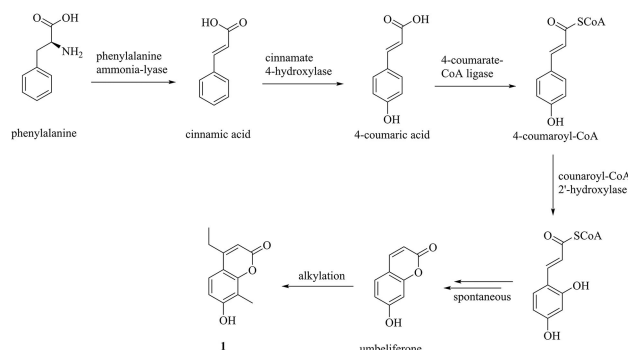


Figure 3. Selected COSY (bold bond) and HMBC (blue arrows) correlations of **1**.



Scheme 1. Plausible biosynthetic pathway of **1**.

Table 1. ^1H and ^{13}C NMR Data of **1** in CD_3OD .^a

No	δ_{H}	δ_{C}
1	—	—
2	—	162.8, C
3	6.67 (s)	113.9, CH
4	—	142.1, C
5	8.07 (d, 9.6)	143.4, CH
6	6.13 (d, 9.6)	109.9, CH
7	—	164.5, C
8	—	110.7, C
9	2.81 (q, 7.6) (2H)	25.8, CH_2
10	1.24 (t, 7.6)	7.9, CH_3
11	2.21 (s)	16.1, CH_3
5a	—	110.6, C
8a	—	156.0, C

^a ^1H and ^{13}C NMR data (δ) were measured at 400 and 100 MHz, respectively; Chemical shifts are in ppm; J values in Hz are in parentheses.

The secondary metabolites (SMs) produced by fungi previously demonstrated a wide range of bioactivities such as antibiotic,^[27,28] immunosuppressant,^[27,28] anti-fungal,^[29,30] anti-bacterial,^[30] cytotoxic and anticancer activities.^[3] Further, many studies reported that 2,5-diketopiperazines displayed bioactivities such as cytotoxic,^[31] anti-bacterial,^[31,32] anti-inflammatory,^[23] anti-fungal,^[31] anti-fouling,^[31] and inhibitory

effect on dengue virus replication.^[33] In current study, the isolated compounds were tested for several bioactivities, including cytotoxicity, anti-inflammation, anti-allergy, anti-angiogenesis and nematocidal activities. However, the results demonstrated that the isolates (**1–12**) had no significant activities in cytotoxic, anti-inflammatory, and anti-angiogenesis assays. And **1** was inactive in cytotoxic, anti-allergic and nematocidal assays.

Plant-parasitic nematodes have caused severe damage to agriculture and forestry worldwide over the past few decades. It has been considered that plant-parasitic nematodes cause more than \$100 billion worth of losses to the global agriculture and trees annually.^[34,35,36] Currently, the main strategy for controlling nematodes is based upon using the synthetic chemical agents combined with agriculture practice for the nematode management.^[36,37] However, the chemical products have generated several problems such as the resistance to chemical nematicides, high risks to human health, and the environment pollution.^[34,35,36,38,39] In order to discover more effective and environmental friendly nematode management, natural products or their derivatives have been investigated as the alternatives to synthetic chemical nematocidal agents.^[34,36,37,38,40]

Fungi of *Arthrobotrys* genus are well-known for their nematode-trapping ability and nematocidal activity. Previously, some of oligosporon group antibiotics isolated from *Arthrobotrys* species were reported to exert moderate nematocidal activity.^[14] Currently, there have been no nematocidal agent from this genus of fungi developed yet. Moreover, no coumarin-like secondary metabolite has been isolated either from *Arthrobotrys* genus or from Orbiliaceae family which implies the importance of epigenetic modulation in triggering the production of coumarins (compound **1** in our study). These compounds were previously reported for their nematocidal activity against phytonematode.^[34,37,40] Furthermore, several coumarin-related compounds displayed excellent nematocidal activity and were investigated for the further development of efficient nematocidal agents.^[37]

Therefore, we hypothesize that the isolated coumarin **1** might play a role in the nematocidal activity of *Arthrobotrys foliicola*. However, **1** displayed no activity in suppressing the growth of *Caenorhabditis elegans*.

3. Conclusion

Coumarins and their derivatives naturally occur in many organisms and up to date more than 1300 coumarins have been discovered from plants, bacteria and fungi.^[41,42,24] These secondary metabolites have many bioactivities such as anti-acetylcholinesterase, anti-bacterial, anti-cancer, anti-coagulant, anti-fungal, anthelmintic, anti-inflammatory, anti-HIV, anti-microbial, anti-oxidant and anti-viral activities.^[41,42,24,43] Coumarins are utilized in wide range of applications, not only as pharmaceuticals but also as cosmetics, fragrances, agrochemicals, insecticides, in food industry and in color technol-

ogy.^[24,44] Additionally, coumarins have been used in pharmaceutical industry as precursors in the synthesis of anticoagulant agents since 1868.^[24] In recent years, the production of chemicals by microbial conversion is becoming an important component of industrial biotechnology.^[24] By using the epigenetic manipulation method, we can modulate the fungus to produce the special coumarin-type secondary metabolite, 4-ethyl-7-hydroxy-8-methyl-2*H*-1-benzopyran-2-one (**1**) from *Arthrobotrys foliicola*.

We believe that this discovery could be utilized in the production of coumarins and as a source for advanced coumarin synthesis. However, so far, the studies on genomic sequences and biosynthetic pathways of the genus *Arthrobotrys* are scarce.^[45] The mechanism of the coumarin production, which corresponded to the epigenetic approach in our study, should be further explored.

4. Experimental Section

4.1 Experimental Procedures

TLC plates were performed on silica gel Kiesel 60 F254 (Merck, Darmstadt, Germany). Ultraviolet light absorbance at 254 and 365 nm were used for detecting compounds and sprayed 50 % H₂SO₄ for staining and heating on the hot plate. Column chromatography was carried out using Merck silica gel (70–230 and 230–400 mesh) and Sephadex LH-20 (Merck, Darmstadt, Germany). NMR measurements were carried out by JEOL JNM-ECS 400 NMR spectrometer (JEOL, Ltd., Tokyo, Japan). Optical rotation was estimated by JASCO P-1020 digital polarimeter (Tokyo, Japan). A Bruker APEX II spectrometer (Billerica, MA, USA) was utilized for HR-ESIMS data. IR spectrum measurement was accomplished by Perkin Elmer 2000 FT-IR spectrophotometer (Waltham, MA, USA). SBHA and 5-AZ were purchased from the Sigma Chemical Co. (St. Louis, MO, USA).

4.2 Fungal Material

The fungus *Arthrobotrys foliicola* Matsush, voucher number: 32937, collection number: CBS 242.90, was purchased from the Bioresource Collection and Research Center (Hsin-Chu, Taiwan). The YM agar media (1 % glucose, 0.5 % peptone, 0.3 % malt extract, and 0.3 % yeast extract) was used for maintaining the fungal strain at 25 °C for 7 days. One small piece of the mycelia agar was cut and inoculated into 250 mL Erlenmeyer flasks containing 75 mL of YM fermentation media, and treated with 0.5 mM SBHA or without 0.5 mM SBHA (control). The flasks were incubated on the shaker (150 rpm) at 25 °C for 10 days. The culture broth of these two conditions were extracted by EtOAc and condensed under reduced pressure to afford the EtOAc crude extracts. The EtOAc crude extracts of these two conditions were analyzed by reverse-phase (RP-HPLC) HPLC (C₁₈ column, 250 ×

4.6 mm, 5 μ m, 1.0 mL/min, Cosmosil, Nacalai Tesque, Kyoto, Japan) by using gradient elution with water and acetonitrile (0–5 min: 20% acetonitrile, 5–20 min: from 20% acetonitrile to 100% acetonitrile, 20–30 min: 100% acetonitrile). A voucher specimen (code no. MS-19) was stored in the Graduate Institute of Natural Products, College of Pharmacy, Kaohsiung Medical University, Kaohsiung, Taiwan.

4.3 Fermentation, Extraction and Isolation

The culture broth of *Arthrotrrys foliicola* was scaled up by using 100 Erlenmeyer flasks (500 mL), each flask containing 150 mL YM (1% glucose, 0.5% peptone, 0.3% malt extract, and 0.3% yeast extract) broth media and 0.5 mM SBHA. The flasks were incubated on the rotator shaker (150 rpm) at 25 °C. After 10 days, 15 L of culture broth was filtered under the pressure to separate the broth filtrate from the mycelium. Then, the filtrate was extracted by EtOAc and condensed under reduced pressure to yield the EtOAc extract (1.3 g). The EtOAc extract was subjected to Sephadex LH-20 column chromatography and eluted with MeOH:CH₂Cl₂ (1:2) to afford six fractions (F1–F6). Fraction F3 (382.5 mg) was separated by silica gel open column eluted with MeOH:CH₂Cl₂ (1:14) to yield five subfractions (F3-1–F3-5). Fraction F3-2 (23.9 mg) was further purified by RP-HPLC eluted with MeOH:H₂O (40:60) to give **7** (1.7 mg). Fraction F3-3 (100.4 mg) was isolated by RP-HPLC using MeOH:H₂O (40:60) as eluent to afford **4** (6.7 mg), **5** (27.9 mg), **6** (4.0 mg), **12** (3.9 mg). Fraction F3-4 (46.9 mg) was separated by RP-HPLC eluted with MeOH:H₂O (30:70) to obtain **8** (9.7 mg), **9** (1.9 mg), **10** (11.6 mg), **11** (7.4 mg).

Fraction F4 (310.7 mg) was chromatographed by silica gel column eluted with MeOH:CH₂Cl₂ (1:17) to furnish twelve subfractions (F4-1–F4-12). Fraction F4-3 (61.4 mg) was further purified by RP-HPLC eluted with MeOH:H₂O (60:40) to obtain **1** (2.4 mg) and **2** (4.5 mg). Fraction F4-11 (36.2 mg) was submitted to RP-HPLC using MeOH:H₂O (60:40) as the eluent to afford **3** (5.6 mg).

4-ethyl-7-hydroxy-8-methyl-2H-chromen-2-one (**1**): colorless oil; UV (MeOH) λ_{max} (log ϵ) 330 (3.67), 249 (3.54) nm; IR (ATR) ν_{max} : 3369, 2356, 2334, 1710, 1599, 1576 cm⁻¹; ¹H NMR (CD₃OD, 400 MHz) and ¹³C NMR (CD₃OD, 100 MHz) data shown in Table 1; HRESI-MS m/z 227.0680 [M + Na]⁺ (calcd for C₁₂H₁₂O₃Na, 227.0678).

4.4 Cytotoxic Assay on Cancer Cell Lines

MDA-MB-231 (breast), HepG2 (liver) and A549 (lung), human cancer cell lines, were inoculated onto 96-well plates and treated with the sample at 20 μ g/mL for 72 h. The medium was removed and 100 μ L of 0.5 mg/mL methylthiazol tetrazolium (MTT) solution was added into each well. After incubation at 37 °C for 1 h, the formation of formazan crystals (dissolved in 100 μ L DMSO) was detected by reading the

absorbance at 550 nm. Doxorubicin was used as positive control.^[46]

4.5 Anti-inflammatory Activity Assay

Human neutrophils were collected from healthy donors by venepuncture and were separated by Ficoll centrifugation. Dextran was used for sedimentation. After re-suspension in the calcium (Ca²⁺)-free HBSS buffer (pH 7.4), the purified neutrophils were maintained at 4 °C before use.^[47]

4.5.1 Measurement of Superoxide Generation

Neutrophils (6 \times 10⁵ cell/mL) were incubated with ferricytochrome *c* (0.5 mg/mL) and Ca²⁺ (1 mM) at 37 °C for 5 min and then with 0.1% of dimethyl sulfoxide (DMSO) or test samples for another 5 min. Cells were activated by using fMLF (0.1 μ M) for 10 min and primed with cytochalasin B (CB, 1 μ g/mL) for 3 min. The spectrophotometer (U-3010; Hitachi) was used for continuous monitoring of the change in absorbance at 550 nm.^[47,48]

4.5.2 Measurement of Elastase Release

Neutrophils (6 \times 10⁵ cell/mL) were incubated in MeO-Suc-Ala-Ala-Pro-Val-*p*-nitroanilide (100 μ M) and Ca²⁺ (1 mM) at 37 °C for 5 min and treated with 0.1% of dimethyl sulfoxide (DMSO) or test samples for another 5 min. Cells were activated with fMLF (0.1 μ M) for 10 min and primed with CB (0.5 μ g/mL) for 3 min. The spectrophotometer (U-3010; Hitachi) was used for continuous monitoring of the change in absorbance at 405 nm.^[47,48]

4.6 Anti-allergic Activity Assay

4.6.1 Cell Culture and Cell Viability Assay

The mucosal mast cell-derived rat basophilic leukemia cells (RBL-2H3, Bioresource Collection and Research Center) were cultured in DMEM medium (containing 10% FBS and 100 μ g/mL streptomycin with 100 U/mL penicillin). The potential cytotoxic effects of the samples on RBL-2H3 cells were determined by methylthiazol tetrazolium (MTT) assay as described previously.^[49] Tested samples were considered as nontoxic towards RBL-2H3 cells (viability over 80%, *n* = 3).

4.6.2 Degranulation Assay

The degree of A23187-induced degranulation in RBL-2H3 cells was evaluated by a β -hexosaminidase release assay as described previously.^[49] RBL-2H3 cells were seeded in 96-

well plate (2×10^4 cells/well) and treated with the samples for 20 h. The cells were stimulated by A23187 (1 μ M), a calcium ionophore, for 1 h. Dexamethasone (10 nM) was used as the positive control. The amount of β -hexosaminidase was detected by using the method that utilizes *p*-nitrophenyl-*N*-acetyl-d-glucosaminide (*p*-NAG) as a substrate for β -hexosaminidase according to the method described before.^[49] Tested samples showed insignificant inhibition of degranulation (below 20%, $n=3$). Dexamethasone (10 nM) inhibited $51.7 \pm 13.2\%$ of degranulation induced by A23187.

4.7 Anti-angiogenic Activity Assay

4.7.1 Isolation and Cultivation of EPCs

Peripheral blood (80 mL) from healthy donors was obtained with informed consent before the collection. The peripheral blood mononuclear cells (PBMCs) were fractionated from other blood components by centrifugation on Ficoll-Paque Plus (Amersham Biosciences, Uppsala, Sweden) on the basis of the manufacturer's protocol. CD34-positive progenitor cells were separated from the isolated PBMCs by using MACS Cell Separation System (Miltenyi Biotec, Bergisch Gladbach, Germany) and CD34 MicroBead kit. The maintenance and characterization of CD34-positive EPCs were done as described as previously.^[50,51,52] Shortly, the CD34-positive EPCs were inoculated on 1% gelatin-coated plastic-ware and cultured in MV2 medium (PromoCell, Heidelberg, Germany) containing 20% defined fetal bovine serum (FBS) (HyClone, Logan, UT) and deposited in humidified air with 5% CO₂ at 37 °C.^[50,51,52]

4.7.2 Tube Formation Assay

Matrigel (BD Biosciences, Bedford, MA) was made to facilitate the differentiation of EPCs into a capillary tube-like structure. Matrigel added into 96-well plates and incubated at 37 °C for 0.5 h for polymerization. After gel formation, EPCs (1.5×10^4 cells) were inoculated on the layer of polymerized Matrigel in MV2 medium (containing 2% FBS) with the presence of tested samples. After incubation at 37 °C for 24 h, photomicrographs of capillary tube formation were taken by microscope with the inverted phase contrast. Tube formation was quantified by estimating the long axis of each tube in 3 random fields each well using Image-J software.^[50,51,52]

4.7.3 Anti-cancer Assay

EPCs were incubated to 96-well plates at a density of 5×10^3 cells per well. Then, cells were processed with MV2 medium (containing 2% FBS) in the indicated concentration of samples for 24 h. The percentage of LDH release was

determined by the ratio of LDH activity in the medium to LDH activity in the cell lysate.^[50,51,52]

Author Contributions

Clay C.C. Wang, Fang-Rong Chang, and Yang-Chang Wu contributed to the manuscript revision and confirmation. Chi-Ying Li and I-Wen Lo contributed to the manuscript equally on designing the experiment, analyzing and discussing the data acquisition, and writing the manuscript. Yu-Ming Chung, Yi-Hong Tsai, and Yuan-Bin Cheng contributed to the data analyzing. Yen-Ping Hsueh contributed to the nematocidal activity assay. Shih-Wei Wang contributed to the anti-angiogenesis activity evaluation. Michal Korinek contributed to the anti-allergic activity test. Tsong-Long Hwang contributed to the anti-inflammation activity assay. Shu-Li Chen contributed to the cytotoxic assay on cancer cell lines.

Acknowledgements

This work was supported by grants from Ministry of Science and Technology, Taiwan (MOST 102-2628-B-037-003-MY3, MOST 103-2320-B-037-005-MY2, MOST 105-2628-B-037-001-MY3, MOST 106-2320-B-037-008-MY2 and MOST 107-2911-I-037-502, awarded to F.-R. Chang; MOST 106-2622-B-037-003-CC2, MOST 106-2320-B-037-007-MY3, awarded to Y.-C. Wu). We appreciated for the Center for Research Resources and Development providing 400 MHz NMR as well as ESI-MS instrumentation support at Kaohsiung Medical University and HRESI-MS was supported by National Sun Yat-sen University. Besides, this study also received support funding from Kaohsiung Medical University (106CM-KMU-02, KMU-DK107003). We are grateful to Dr. Mohamed El-Shazly for kind assistance with biosynthetic pathway.

References

- [1] N. P. Keller, G. Turner, J. W. Bennett, *Nat. Rev. Microbiol.* **2005**, 3, 937–947.
- [2] N. K. Singh, A. Blachowicz, A. Checinska, C. Wang, K. Venkateswaran, *Genome* **2016**, 4.
- [3] R. N. Kharwar, A. Mishra, S. K. Gond, A. Stierle, D. Stierle, *Nat. Prod. Rep.* **2011**, 28, 1208–1228.
- [4] K. Scherlach, C. Hertweck, *Org. Biomol. Chem.* **2009**, 7, 1753–1760.
- [5] Y.-M. Chung, M. El-Shazly, D.-W. Chuang, T.-L. Hwang, T. Asai, Y. Oshima, M. L. Ashour, Y.-C. Wu, F.-R. Chang, *J. Nat. Prod.* **2013**, 76, 1260–1266.
- [6] R. H. Cichewicz, *Nat. Prod. Rep.* **2010**, 27, 11–22.
- [7] T. Asai, Y.-M. Chung, H. Sakurai, T. Ozeki, F.-R. Chang, K. Yamashita, Y. Oshima, *Org. Lett.* **2012**, 14, 513–515.
- [8] T. Asai, Y.-M. Chung, H. Sakurai, T. Ozeki, F.-R. Chang, Y.-C. Wu, K. Yamashita, Y. Oshima, *Tetrahedron* **2012**, 68, 5817–5823.

- [9] T. Asai, T. Yamamoto, Y.-M. Chung, F.-R. Chang, Y.-C. Wu, K. Yamashita, Y. Oshima, *Tetrahedron Lett.* **2012**, 53, 277–280.
- [10] L.-X. Wei, H.-X. Zhang, J.-L. Tan, Y.-S. Chu, N. Li, H.-X. Xue, Y.-L. Wang, X.-M. Niu, Y. Zhang, K.-Q. Zhang, *J. Nat. Prod.* **2011**, 74, 1526–1530.
- [11] H.-X. Zhang, J.-L. Tan, L.-X. Wei, Y.-L. Wang, C.-P. Zhang, D.-K. Wu, C.-Y. Zhu, Y. Zhang, K.-Q. Zhang, X.-M. Niu, *J. Nat. Prod.* **2012**, 75, 1419–1423.
- [12] D.-K. Wu, C.-P. Zhang, C. Y. Zhu, Y. L. Wang, L. L. Guo, K. Q. Zhang, X. M. Niu, *J. Agric. Food Chem.* **2013**, 61, 4108–4113.
- [13] Z.-F. Xu, B.-L. Wang, H.-K. Sun, N. Yan, Z.-J. Zeng, K.-Q. Zhang, X.-M. Niu, *J. Agric. Food Chem.* **2015**, 63, 9076–9082.
- [14] M. G. Anderson, T. B. Jarman, R. W. Rickards, *J. Antibiot.* **1995**, 48, 391–398.
- [15] S. V. Shilin, M. M. Garazd, V. P. Khilya, *Chem. Nat. Compd.* **2008**, 44, 301–305.
- [16] C.-L. Shao, C.-Y. Wang, M.-Y. Wei, Z.-B. Jia, Z.-G. She, Y.-C. Lin, *Chem. Nat. Compd.* **2009**, 45, 779–781.
- [17] Z. Jiang, K. G. Boyd, A. Mearns-spragg, D. R. Adams, P. C. Wright, J. G. Burgess, *Nat. Prod. Lett.* **2006**, 14, 435–440.
- [18] E. Sansinenea, F. Salazar, J. Jiménez, Á. Mendoza, A. Ortiz, *Tetrahedron Lett.* **2016**, 57, 2604–2607.
- [19] L. Wen, Q. Wei, G. Chen, J. Cai, Z. She, *Chem. Nat. Compd.* **2013**, 49, 137–140.
- [20] S. D. Bull, S. G. Davies, R. M. Parkin, Francisco, Sánchez-Sancho, *J. Chem. Soc. Perkin Trans. 1* **1998**, 2313–2320.
- [21] J. M. Cronan, T. R. Davidson, F. L. Singleton, R. R. Colwell, J. H. Cardellina, *Nat. Prod. Lett.* **1998**, 11, 271–278.
- [22] S. P. Ovenden, J. L. Nielson, C. H. Liptrot, R. H. Willis, D. M. Tapiolas, A. D. Wright, C. A. Motti, *Mar. Drugs* **2011**, 9, 2469–2478.
- [23] H. Kang, S. K. Ku, H. Choi, J. S. Bae, *Bioorg. Med. Chem. Lett.* **2016**, 26, 1873–1876.
- [24] T. M. Costa, L. B. Tavares, D. de Oliveira, *Appl. Microbiol. Biotechnol.* **2016**, 100, 6571–6584.
- [25] E. Lederer, *Q. Rev. Chem. Soc.* **1969**, 4, 455–628.
- [26] U. Matern in *Phytochemicals in Human Health Protection, Nutrition, and Plant Defense*, Springer US, **1999**, pp. 161–183.
- [27] D. Hoffmeister, N. P. Keller, *Nat. Prod. Rep.* **2007**, 24, 393–416.
- [28] A. A. Brakhage, *Nat. Rev. Microbiol.* **2013**, 11, 21–32.
- [29] J. J. Coleman, S. Ghosh, I. Okoli, E. Mylonakis, *PLoS One* **2011**, 6, e25321.
- [30] L. Xu, W. Meng, C. Cao, J. Wang, W. Shan, Q. Wang, *Mar. Drugs* **2015**, 13, 3479–3513.
- [31] R.-M. Huang, X.-F. Zhou, T.-H. Xu, X.-W. Yang, Y.-H. Liu, *Chem. Biodiversity* **2010**, 7, 2809–2829.
- [32] R. He, B. Wang, T. Wakimoto, M. Wang, L. Zhu, I. Abe, *J. Braz. Chem. Soc.* **2013**, 24, 1926–1932.
- [33] C.-K. Lin, Y.-T. Wang, E.-M. Hung, Y.-L. Yang, J.-C. Lee, J.-H. Sheu, C.-C. Liaw, *Planta Med.* **2017**, 83, 158–163.
- [34] G. Liu, D. Lai, Q.-Z. Liu, L. Zhou, Z.-L. Liu, *Molecules* **2016**, 21, 1276.
- [35] X. B. Wang, G. H. Li, L. Li, L. J. Zheng, R. Huang, K. Q. Zhang, *Nat. Prod. Res.* **2008**, 22, 666–671.
- [36] H. Lu, S. Xu, W. Zhang, C. Xu, B. Li, D. Zhang, W. Mu, F. Liu, *J. Agric. Food Chem.* **2017**, 65, 544–550.
- [37] L. Pan, X.-Z. Li, D.-A. Sun, H. Jin, H.-R. Guo, B. Qin, *Chin. Chem. Lett.* **2016**, 27, 375–379.
- [38] F. Liu, Z. Yang, X. Zheng, S. Luo, K. Zhang, G. Li, *J. Asia Pac. Entomol.* **2011**, 14, 79–81.
- [39] O. Atolani, O. A. Fabiyi, G. A. Olatunji, *Acta agric. Slov.* **2014**, 25–31.
- [40] M. Stadler, H. Anke, *J. Antibiot.* **1995**, 48, 267–270.
- [41] B. G. Lake, *Food Chem. Toxicol.* **1999**, 37, 423–453.
- [42] K. N. Venugopala, V. Rashmi, B. Odhav, *BioMed Res. Int.* **2013**, 2013, 963248.
- [43] M. E. Riveiro, N. D. Kimpe, A. Moglioni, R. Vázquez, F. Monczor, C. Shayo, C. Davio, *Curr. Med. Chem.* **2010**, 17, 1325–1338.
- [44] X. He, Y. Shang, Y. Zhou, Z. Yu, G. Han, W. Jin, J. Chen, *Tetrahedron* **2015**, 71, 863–868.
- [45] J. Yang, L. Wang, X. Ji, Y. Feng, X. Li, C. Zou, J. Xu, Y. Ren, Q. Mi, J. Wu, S. Liu, Y. Liu, X. Huang, H. Wang, X. Niu, J. Li, L. Liang, Y. Luo, K. Ji, W. Zhou, Z. Yu, G. Li, Y. Liu, L. Li, M. Qiao, L. Feng, K.-Q. Zhang, *PLoS Pathog.* **2011**, 7, e1002179.
- [46] C.-Y. Li, I.-W. Lo, S.-W. Wang, T.-L. Hwang, Y.-M. Chung, Y.-B. Cheng, S.-P. Tseng, Y.-H. Liu, Y.-M. Hsu, S.-R. Chen, H.-C. Hu, F.-R. Chang, Y.-C. Wu, *Bioorg. Med. Chem. Lett.* **2017**, 27, 1978–1982.
- [47] H.-P. Yu, P.-W. Hsieh, Y.-J. Chang, P.-J. Chung, L.-M. Kuo, T.-L. Hwang, *Free Radical Biol. Med.* **2011**, 50, 1737–1748.
- [48] S.-C. Yang, P.-J. Chung, C.-M. Ho, C.-Y. Kuo, M.-F. Hung, Y.-T. Huang, W.-Y. Chang, Y.-W. Chang, K.-H. Chan, T.-L. Hwang, *J. Immunol.* **2013**, 190, 6511–6519.
- [49] M. Korinek, Y. H. Tsai, M. El-Shazly, K. H. Lai, A. Backlund, S. F. Wu, W. C. Lai, T. Y. Wu, S. L. Chen, Y. C. Wu, Y. B. Cheng, T. L. Hwang, B. H. Chen, F. R. Chang, *Front. Pharmacol.* **2017**, 8, 356.
- [50] C. A. Staton, M. W. Reed, N. J. Brown, *Int. J. Exp. Pathol.* **2009**, 90, 195–221.
- [51] C.-H. Chung, C.-H. Chang, S.-S. Chen, H.-H. Wang, J.-Y. Yen, C.-J. Hsiao, N.-L. Wu, Y.-L. Chen, T.-F. Huang, P.-C. Wang, H.-I. Yeh, S.-W. Wang, *Evid. Based. Complement. Alternat. Med.* **2013**, 2013, 943187.
- [52] C.-M. Su, C.-J. Hsu, C.-H. Tsai, C.-Y. Huang, S.-W. Wang, C.-H. Tang, *Stem Cells* **2015**, 33, 2243–2255.

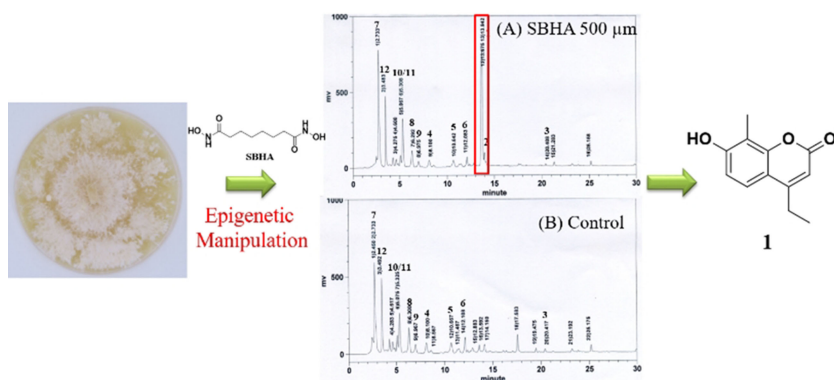
Manuscript received: November 14, 2018

Revised manuscript received: December 29, 2018

Accepted: December 31, 2018

Version of record online: ■■■, ■■■■

FULL PAPER



C.-Y. Li, I.-W. Lo, Y.-P. Hsueh, Y.-M. Chung, S.-W. Wang, M. Korinek, Y.-H. Tsai, Y.-B. Cheng, T.-L. Hwang, C. C. C. Wang, F.-R. Chang*, Y.-C. Wu*

1 – 8

Epigenetic Manipulation Induces the Production of Coumarin-Type Secondary Metabolite from *Arthrobotrys foliicola*



Population dynamics at neuraminidase position 151 of influenza A (H1N1)pdm09 virus in clinical specimens

Yu-Nong Gong,^{1,2†} Kuo-Chien Tsao,^{1,2,3†} Guang-Wu Chen,^{1,2,4} Chung-Jung Wu,¹ Yi-Hsiang Chen,¹ Yi-Chun Liu,² Shu-Li Yang,^{2,3} Yhu-Chering Huang^{5,6} and Shin-Ru Shih^{1,2,3,7,*}

Abstract

Influenza A virus mutates rapidly, allowing it to escape natural and vaccine-induced immunity. Neuraminidase (NA) is a surface protein capable of cleaving the glycosidic linkages of neuraminic acids to release newly formed virions from infected cells. Genetic variants within a viral population can influence the emergence of pandemic viruses as well as drug susceptibility and vaccine effectiveness. In the present study, 55 clinical specimens from patients infected with the 2009 pandemic influenza A/H1N1 virus, abbreviated as A(H1N1)pdm09, during the 2015–2016 outbreak season in Taiwan were collected. Whole genomes were obtained through next-generation sequencing. Based on the published sequences from A(H1N1)pdm09 strains worldwide, a mixed population of two distinct variants at NA position 151 was revealed. We initially reasoned that such a mixed population may have emerged during cell culture. However, additional investigations confirmed that these mixed variants were detectable in the specimens of patients. To further investigate the role of the two NA-151 variants in a dynamic population, a reverse genetics system was employed to generate recombinant A(H1N1)pdm09 viruses. It was observed that the mixture of the two distinct variants was characterized by a higher replication rate compared to the recombinant viruses harbouring a single variant. Moreover, an NA inhibition assay revealed that a high frequency of the minor NA-151 variant in A(H1N1)pdm09 was associated with a reduced susceptibility to NA inhibitors. We conclude that two distinct NA-151 variants can be identified in patient specimens and that such variants may increase viral replication and NA activity.

INTRODUCTION

Influenza A virus is a negative-sense segmented RNA virus that poses a significant public health burden in terms of morbidity and mortality. An influenza A virus that originated in swine appeared in April 2009 before the subsequent emergence of a pandemic influenza A/H1N1 virus strain termed A(H1N1)pdm09 [1]. Both the A(H1N1)pdm09 strain and H3N2 (another influenza A subtype that emerged in the 1960s) are seasonal human influenza A viruses that have caused epidemics in the past ten years and may cause the same potentially in the future.

Previous studies have shown that viral quasispecies that increase population fitness are associated with disease severity, virus growth and drug susceptibility. Neuraminidase (NA) is a surface protein of influenza A virus that is capable of cleaving the glycosidic linkages of neuraminic acid to release newly formed virions from infected cells. Xue *et al.* [2] demonstrated that mixed populations of H3N2 bearing Asp (D) and Gly (G) at amino acid 151 of NA (NA-151) are characterized by a higher growth rate than either variant alone in cell cultures, suggesting a cooperative interaction between the two variants. However, this mutation is frequently considered ambiguous in virus isolates and is

Received 18 January 2019; Accepted 15 March 2019; Published 17 April 2019

Author affiliations: ¹Research Center for Emerging Viral Infections, College of Medicine, Chang Gung University, Taoyuan, Taiwan, ROC; ²Department of Laboratory Medicine, Linkou Chang Gung Memorial Hospital, Taoyuan, Taiwan, ROC; ³Department of Medical Biotechnology and Laboratory Science, College of Medicine, Chang Gung University, Taoyuan, Taiwan, ROC; ⁴Department of Computer Science and Information Engineering, School of Electrical and Computer Engineering, College of Engineering, Chang Gung University, Taoyuan, Taiwan, ROC; ⁵Department of Pediatrics, Linkou Chang Gung Memorial Hospital, Taoyuan, Taiwan, ROC; ⁶College of Medicine, Chang Gung University, Taoyuan, Taiwan, ROC; ⁷Research Center for Chinese Herbal Medicine, Research Center for Food and Cosmetic Safety and Graduate Institute of Health Industry Technology, College of Human Ecology, Chang Gung University of Science and Technology, Taoyuan, Taiwan, ROC.

*Correspondence: Shin-Ru Shih, srshih@mail.cgu.edu.tw

Keywords: influenza; neuraminidase; A(H1N1)pdm09; viral replication; antiviral drug susceptibility.

Abbreviations: A(H1N1)pdm09, 2009 pandemic influenza A/H1N1 virus; FU, fluorescence units; HA, hemagglutinin; hpi, hours post-infection; IC₅₀, half maximal inhibitory concentration; MDCK, Madin-Darby canine kidney; MEM, minimum essential medium; NA, neuraminidase; NGS, next-generation sequencing; PBS, phosphate buffered saline; PFU, plaque-forming units; RBC, red blood cell; RG, reverse genetic.

†These authors contributed equally to this work.

One supplementary figure and one supplementary table are available with the online version of this article.

undetectable in primary clinical samples [3]. The NA D151G mutation, which arises after several passages in Madin–Darby canine kidney (MDCK) cells, confers resistance to NA inhibitors in H3N2 virus strains [4]. Isolates of A(H1N1)pdm09 having mixed variants at NA position 151 (according to both N1 and N2 numbering systems) have rarely been detected [5, 6]. Viruses containing mixed D151 and N151 variants at NA-151 exhibited reduced inhibition; however, such a mixture emerged in a cell culture system and not in patients [7]. Haemagglutinin (HA) is another surface protein of influenza A virus that is responsible for the virus binding to host cells. In A(H1N1)pdm09, a single substitution from Asp (D) to Gly (G) at amino acid 222 of HA has previously been associated with severe clinical symptoms [8, 9], especially in the lower respiratory tract [10]. The HA-D222/G222 quasispecies can cause serious influenza infections accompanied by lung inflammation and associated clinical symptoms [11].

In late 2015, severe A(H1N1)pdm09 outbreaks were reported in several Eastern European countries [12]. In Taiwan, the 2015–2016 epidemic led to significant morbidity and mortality, and several cases of severe complications in patients aged 50 to 64 years [13, 14]. The antigenicity of the 2015–2016 A(H1N1)pdm09 strains tested from human sera differed from that of the vaccine strain A/California/7/2009. Consequently, selection of A/Michigan/45/2015 as a recommended vaccine strain for the northern hemisphere by the World Health Organization began in the 2017–2018 season (https://www.who.int/influenza/vaccines/virus/recommendations/2017_18_north/en/).

Genetic variants within a viral population play a crucial role in the emergence of pandemic viruses and also influence drug susceptibility and vaccine effectiveness. The aims of the present study were as follows: (1) to investigate the prevalence of two distinct NA-151 variants within A(H1N1)pdm09 clinical specimens and assess their sequences; and (2) to examine the association between the NA-151 variants and viral replication, NA activity and susceptibility to NA inhibitor (i.e. oseltamivir carboxylate).

RESULTS

Prevalence of minor NA-151 variants in Taiwan and worldwide

We collected a total of 55 clinical specimens during the 2015–2016 outbreak season in Taiwan, including throat swabs ($n=36$), nasopharyngeal swabs ($n=11$), bronchoalveolar lavage fluid ($n=4$) and sputum ($n=4$) specimens. Pyrosequencing was performed to determine the composition and genetic diversity at NA-151, including the wild-type (residue D151) and mutant variant (N151). Four specimens either had low volume or their titre was below the PCR detection limit. Minor variants were detected at intermediate (3–13 %) and low (1–2 %) frequencies in eight and four specimens, respectively (Fig. 1a). The dominant mutant type (confirmed by Sanger sequencing) with 75 % frequency was identified in a single specimen. Interestingly, the

existence of mutant variants at NA-151 was directly confirmed in the clinical specimens. All the specimens were subsequently passaged to increase their viral titre before next-generation sequencing (NGS), which was performed to examine the dynamic frequency of the minor variant at NA-151. This variant was detected at high frequency (17–49 %), intermediate frequency (3–13 %) and low frequency (1–2 %) in 13, 8 and 4 isolates, respectively (Fig. 1a). Additionally, such minor variant frequencies were found to be dynamic after virus passage. Moreover, we examined 55 full-length sequences to detect other mutations at NA drug-resistant markers, including E119G/V, I223V/R, S247N, H275Y and N295S (in the N1 numbering system) [15]. Among the 2015–2016 strains, only two H275Y (N1 numbering) mutations were identified.

We also determined the presence of these variants among the published sequences. NA sequences ($n=25,365$) obtained during and after the 2009 pandemic were retrieved from the Global Initiative on Sharing All Influenza Data (Fig. 1b). Each season was defined as the time elapsed from 1 June to 31 May of the subsequent year. The 2015–2016 season displayed the dominant count ($n=6044$), followed by 2009–2010 (5847), 2017–2018 (4203) and other seasons (<1800). All coding sequences retrieved were translated into amino acids, with ambiguous nucleotides (e.g. G or A denoted by R, purine) in the codon presented as 'X' in the translation. The frequency of the X residue was calculated to estimate the prevalence of NA-151 variants. Among the retrieved sequences, NA-151 had a dominant population of D ($n=24,906$), followed by X ($n=434$), E ($n=22$) and N ($n=3$). Fig. 1c shows the seasonal percentage of the X residue at NA-151. For example, in the 2015–2016 season, 151 of 6044 (2.50 %) sequences had the X residue at NA-151. Notably, these results indicated that the seasonal percentage of X residue at NA-151 exceeded 2 % in the 2015–2016 season, with the variant still circulating worldwide in two subsequent seasons.

Comparison of plaque morphology and single-cycle growth kinetics of the RG and reference viruses

To investigate the phenotype of NA-151 variants, plaque assays were performed for reverse genetic (RG) and A(H1N1)pdm09 reference viruses (Fig. 2a). The wild-type RG virus with an aspartic acid (D; GAC) at NA-151 comprised one clinical isolate (A/Taiwan/03773/2015) from the 2015–2016 outbreak season. In contrast, for the A(H1N1)pdm09 reference virus, the wild-type virus produced clear plaques on MDCK cells (mean diameter 1.78 ± 0.75 mm) while the mutant RG virus with an asparagine acid (N; AAC) displayed smaller plaques (mean diameter 1.12 ± 0.48 mm). Notably, the mixture-type (D151+N151) RG virus produced plaques sized intermediately (mean diameter 1.54 ± 0.66 mm). The reference virus exhibited smaller and more opaque plaques compared with the RG viruses, with a mean plaque diameter of 1.01 ± 0.31 mm. To further clarify the growth phenotype, the single-cycle growth kinetics of the RG and reference viruses were examined. Significant

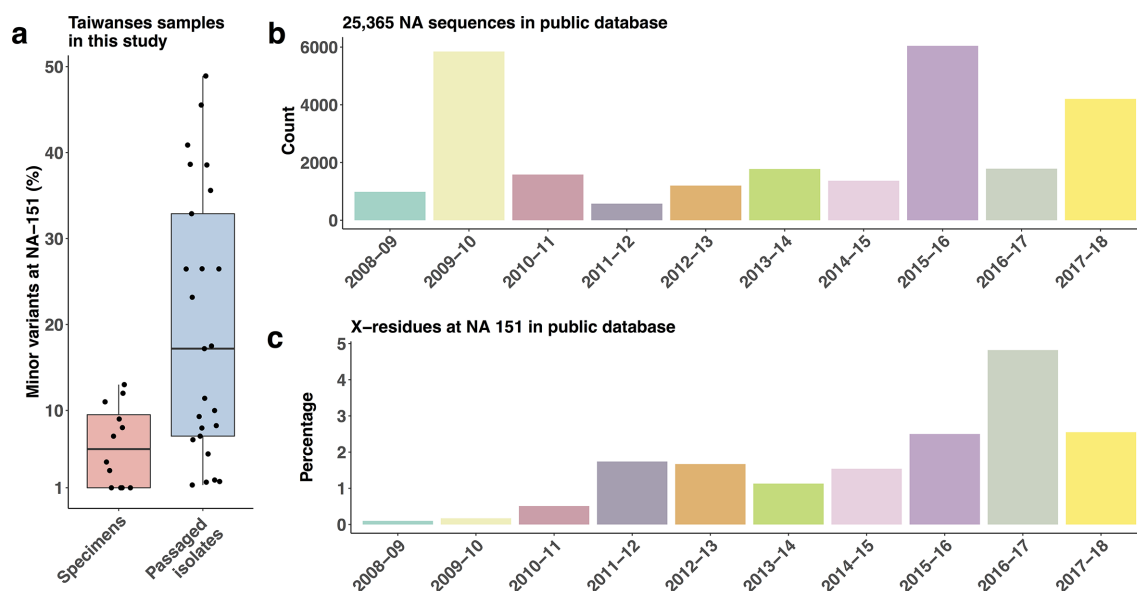


Fig. 1. Frequency of NA-151 variants in Taiwanese samples and published sequences. (a) Minor variants with frequency $\geq 1\%$ in a mixed population from 12 Taiwanese specimens and 25 isolates (first passage) are shown as box plots. (b) The distribution of the major NA-151 variant among 25,365 NA sequences from seasons 2008–2009 to 2017–2018 is represented in the bar graph. (c) Percentages of the X residue at NA-151 in published sequences are provided, suggesting a mixture of two genetic variants.

differences ($P < 0.001$ or 0.0001) were evident between the mixture and other types (Fig. 2b). The highest replication rate was observed for the mixture-type virus, with the lowest rate being evident for the mutant and reference viruses. The differences in replication rates between mixture and wild-type were twofold at 9 hours post-infection (hpi) and approximately 20 % at 12 hpi. In addition, the RG backbone and A(H1N1)pdm09 reference strain differed considerably in terms of growth kinetics and plaque morphology. Their genomes differed in 67 amino acids.

Comparison of NA activity of the wild-type and mutant viruses

NA enzyme activities were measured using a MUNANA-based NA assay as described in Methods. Cells transfected with the wild-type NA expression plasmid showed a dose-dependent increase in NA activity to approximately 1.4×10^5 fluorescence units (FU) with $4 \mu\text{g}$ of plasmid. In contrast, the mutant NA expression plasmid displayed a statistically significant difference ($P < 0.0001$) with the wild-type regardless of the amount transfected (Fig. 3a). We performed western blotting with anti-FLAG (to detect NA expression) and anti-glyceraldehyde 3-phosphate dehydrogenase (as control) antibodies. Whole-cell lysates were used to investigate the expression of the FLAG-NA protein (Fig. 3b). Although NA activity was barely detectable in cells transfected with the mutant NA expression plasmid, an expression similar to the wild-type at $4\text{--}6 \mu\text{g}$ of plasmid was evident on western blots. For example, the quantification data of a western blot of the wild-type and mutant showed a similar expression level at $4 \mu\text{g}$ (Fig. 3b). The mean NA

activity for the wild-type was 144,348 FU at $4 \mu\text{g}$, which was markedly higher than the value of 783 FU obtained for the mutant (Fig. 3a).

Additionally, we compared the NA activity of RG viruses. Fig. 3(c) shows that the wild-type virus had considerably higher NA activity compared with the mutant virus. The significant difference ($P < 0.0001$) between the wild-type and mutant viruses in NA activity also supported the results presented in Fig. 3(a and b).

Susceptibility of RG viruses and clinical isolates to oseltamivir carboxylate

Reverse genetics was employed to assess the impact of the NA-151 dynamic population on virus growth and NA activity. Furthermore, an inhibition assay was used to determine the susceptibility of RG viruses (except for the mutant virus with barely detectable activity) and clinical isolates (third passage) to the NA inhibitor, oseltamivir carboxylate (Fig. 4). We indicated the mixed population of NA-151 associated with the NA inhibition. For example, NA inhibition of the mixture-type RG virus was similar to the reference virus, and significantly higher ($P < 0.0001$) than the wild-type RG virus (Fig. 4a). Pyrosequencing results confirmed that minor variants in the mixture-type RG virus were present at 10 % frequency. Moreover, the half-maximal inhibitory concentration (IC_{50}) of the A/Taiwan/03773/2015 clinical isolate (which was the backbone of the RG viruses) for the NA inhibitor was similar to that of other clinical isolates, except for three isolates (Fig. 4b) of which one clinical isolate with the H275Y mutation displayed

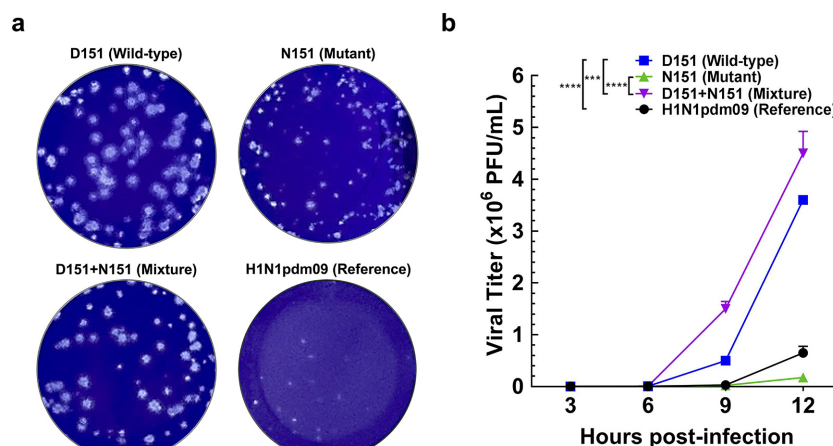


Fig. 2. Plaque morphology and single-cycle growth kinetics of reverse genetic (RG) viruses on MDCK cells. (a) Plaque assays for RG viruses were performed using MDCK cells. Representative wells are shown, and plaques were assessed for their morphology and size. (b) Two-way ANOVA was used to identify statistically significant differences in terms of viral replication. Growth curve of RG viruses; ***, $P < 0.001$; ****, $P < 0.0001$.

more than 100-fold (or two log-transformed) change, indicating highly reduced inhibition. The other two clinical isolates with a high minor variant frequency of >30% displayed higher IC_{50} values than the A/Taiwan/03773/2015 isolate. Collectively, these data indicate that a high frequency of the NA-151 minor variant in the A(H1N1)pdm09 virus is associated with the IC_{50} fold-change in the NA inhibitor, although IC_{50} fold-changes less than tenfold (or one log-transformed) were considered normal inhibition. In addition, the full NA sequence of those clinical samples with high minor variant frequencies did not reveal other drug-resistant markers, suggesting that this increased fold-change was related to the NA-151 variant.

DISCUSSION

In the present study, we sought to investigate the frequency of two distinct NA-151 variants in Taiwanese clinical specimens and isolates of A(H1N1)pdm09 (which have also been found circulating in recent seasons) and reported their sequences. In an effort to shed more light on the impact of this dynamic population of NA-151 variants, the virus isolated from the first non-severe A(H1N1)pdm09 case, occurring during the 2015–2016 outbreak season in Taiwan, was used to generate RG viruses. Notably, we found that this NA-151 mixture was associated with increased virus growth and NA activity, and also with an increasing inhibition to the NA inhibitor.

Our data indicate that the mixture-type (NA-D151+N151) H1N1pdm virus is characterized by higher viral replication, even though the mutant (NA-N151) virus can barely replicate alone. We also observed a similar trend for NA-151 variants in the sequences deposited in a public database. Specifically, D151 was dominant at NA-151 among the published sequences whereas N151 was rarely found. The

mixture-type D151+N151 (i.e. a quasispecies) appears to be increasing. It is possible that the frequency of ambiguous mutations at NA-151 may have been underestimated as a result of technical limitations in the sequencing methods (e.g. the detection limit for Sanger sequencing is 20%) [16]. Although mutations at NA-151 in H3N2 [4, 17] and A(H1N1)pdm09 [18] have previously been considered as laboratory adaptations, the pyrosequencing technique used in our study successfully detected mixed populations with an intermediate or low minor variant frequency in 12 clinical specimens and a mutant type case in a single specimen. Our findings indicate that a mixed NA-151 population of the A(H1N1)pdm09 virus exists in clinical samples. Moreover, it remains to be determined whether mixture-type viruses having both variants on their surface are generated from the co-infection of two variants in the same cell or whether a mixed population of D151 and N151 viruses is present in cells. Due to the dynamic changes occurring in the mutant population, a real-time approach is paramount to monitor the various populations, particularly in clinical specimens. This approach should ultimately shed more light on the association between viral quasispecies and disease severity. Viral quasispecies provide an opportunity for viruses to evolve and evade antiviral drugs [19].

Previous studies have shown that the growth of influenza A virus requires balanced receptor binding by HA and cleavage by NA [20, 21]. The cooperation of NA-151 variants in H3N2 promotes both binding and cleavage of the receptors [2]. However, the exact role of the NA-151 variants in mediating receptor binding in A(H1N1)pdm09 remains unclear. We observed that the expression level of the mutant type was not significantly different from that of the wild-type, even though NA activity was barely detectable. We compared intercellular and supernatant vRNA levels for the

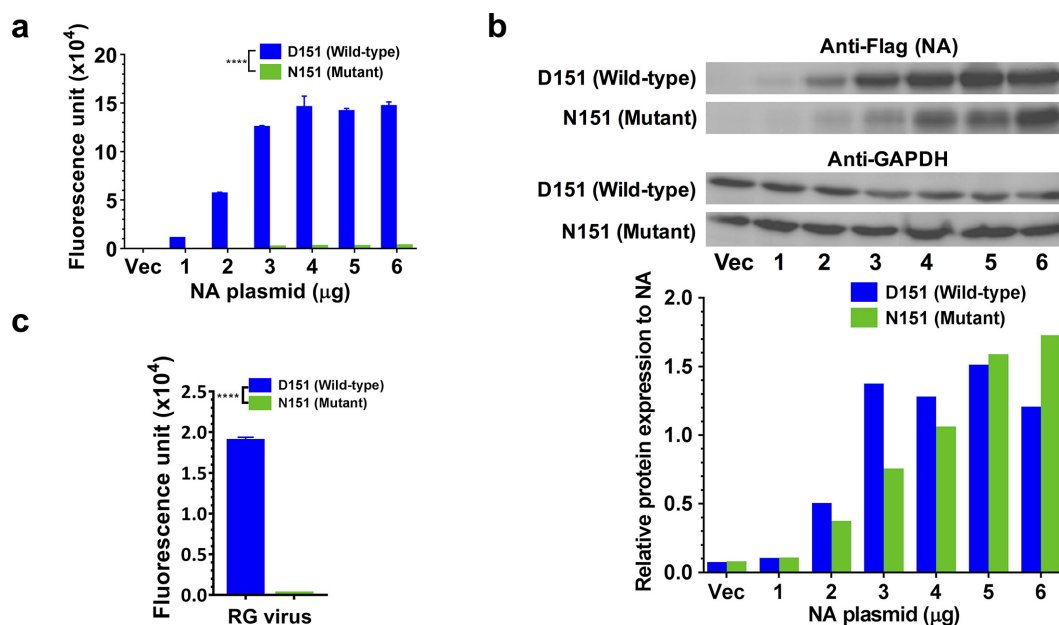


Fig. 3. Activity and expression of two NA-151 variants. (a) The activity of wild-type (D151) and mutant (N151) NA in transfected cells was measured by 4-MUNANA assay; ****, $P < 0.0001$. (b) The expression of FLAG-tagged wild-type and mutant NA proteins in transfected cells was examined by western blotting using anti-FLAG and anti-GAPDH (as internal control) antibodies. (c) The NA activity of wild-type and mutant reverse genetic viruses was measured; ****, $P < 0.0001$.

wild-type and mutant viruses (Fig. S1, available in the online version of this article). The supernatant vRNA/intracellular vRNA ratio of the wild-type was higher than that for the mutant, indicating that the latter may be impeded in the release step. Additionally, we compared HA titres of the wild-type and mutant viruses to gauge whether this NA-151 mutation would affect receptor binding. HA titres of these two RG viruses were the same in an eightfold dilution, and the fold-change of dilution was mainly dependent on the level of HA activity. Based on the results, we cannot draw the conclusion that NA-151 mutation has any effect on HA activity.

NA-151 is located within the 150-loop (amino acids 147–152 in the N2 numbering) that forms the 150-cavity designed as a drug target [22]. An increasing inhibition to oseltamivir carboxylate was observed in the present study in A(H1N1)pdm09 strains characterized by a high frequency of N151 variant (Fig. 4). Specifically, two clinical isolates with a high frequency of N151 displayed higher fold-changes of IC_{50} to oseltamivir carboxylate than isolates with the wild-type (D151). Although this increasing fold-change was <10 , which is considered normal inhibition, further *in vivo* studies are required in future to shed more light on the association between genetic population and drug susceptibility.

A mixture of two distinct variants at NA position 151 of A (H1N1)pdm09 has increasingly been observed in a public sequence database. In the present study, we have shown that

NA-151 promotes viral replication and is associated with NA activity and inhibition. A real-time approach for *in vitro* and *in vivo* studies will be essential to dynamically monitor virus populations during an outbreak, with the ultimate goal of elucidating the impact of genetic changes on virus growth and its response to drugs.

METHODS

Sequence retrieval from public database

In September 2018, all NA sequences ($n=28,749$) of A (H1N1)pdm09 from March 2009 to May 2018 were downloaded from the Global Initiative on Sharing All Influenza Data website (<https://www.gisaid.org/>). We removed partial-length entries that did not cover NA-151, sequences with redundant strain names and entries lacking clear year/month data. Sequences were aligned using the Clustal Omega software [23]. A total of 25,365 NA sequences were subjected to further analyses.

Detection of minor variants in clinical specimens by pyrosequencing

During the 2015–2016 season, a total of 55 clinical specimens were collected from Chang Gung Memorial Hospital with the goal of examining the prevalence of two distinct NA-151 variants. Viral RNA was extracted from clinical specimens according to the manufacturer's protocols (Qia-gen, Hilden, Germany). cDNA was synthesized with the Uni-12 primer (5'-AGCAAAAGCAGG-3') using the Super-Script III First-Strand Synthesis kit (Invitrogen, Carlsbad,

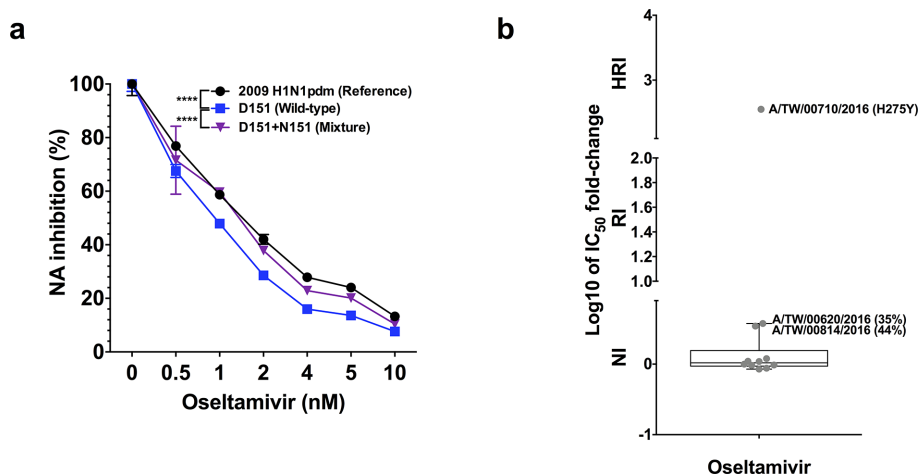


Fig. 4. Drug susceptibility of reverse genetic (RG) viruses and clinical isolates by neuraminidase inhibition assay (MUNANA). (a) NA inhibition of the mixture, wild-type and reference viruses to oseltamivir carboxylate was calculated. ****, $P < 0.0001$. (b) Fold-changes of IC_{50} for 11 clinical isolates (third passage) were calculated. Normal inhibition (NI) is reported when fold-changes of IC_{50} less than ten-fold (or one log-transformed) were detected, reduced inhibition (RI) with 10–100-fold-change, and highly reduced inhibition (HRI) with more than 100-fold-change (or two log-transformed). Except for one isolate (A/Taiwan/00710/2016) having the H275Y mutation and two isolates (A/Taiwan/00620/2016 and A/Taiwan/00814/2016) having high minor variant frequencies, strain names of other isolates are A/Taiwan/00988/2016, A/Taiwan/03773/2015, A/Taiwan/03467/2015, A/Taiwan/04153/2015, A/Taiwan/00643/2016, A/Taiwan/03791/2015, A/Taiwan/00226/2016 and A/Taiwan/01457/2016.

CA, USA). The biotinylated NA amplicon (length 142 bp) was amplified using High-Fidelity Platinum Taq DNA Polymerase (Invitrogen) with NA primers (forward: 5'-CTC TCCCTTGGAAATGCAGAAC-3'; reverse: 5'-biotin-GTTG TATGGAGAGGGAACCTTCACC-3'). The PCR conditions were as follows: 5 min at 95 °C, followed by 45 cycles each of 30 s at 95 °C, 30 s at 55 °C and 30 s at 68 °C, and a final extension of 10 min at 68 °C. The single-stranded biotinylated DNA PCR product was sequenced to determine the percentage of minor variants at NA-151. We used an NA sequencing primer (forward: 5'-TCCAATGGAACCA TTAA-3') on a PyroMark ID instrument (Qiagen). The Identifier software (Qiagen) was employed according to the manufacturer's protocol.

Virus nucleic acid enrichment and NGS

Viral nucleic acid was enriched by a multi-segment RT-PCR reaction performed with a SuperScript III high-fidelity RT-PCR kit (Invitrogen). The influenza-specific universal primers Opti1-F1 (5'-GTTACGCGCCAGCAAAGCAGG-3'), Opti1-F2 (5'-GTTACGCGCCAGCGAAAGCAGG-3') and Opti1-R1 (5'-GTTACGCGCCAGTAGAAACAAGG-3') were used for reverse transcription and amplification of all segments. NGS libraries were constructed from 0.4 ng of purified PCR products using the Nextera XT DNA Library Prep Kit and Nextera Index Kit (Illumina, San Diego, CA, USA) and sequenced with the Illumina MiSeq System. After subtraction of host sequences, virus genomes were assembled using an iterative mapping approach [24]. Finally, sequences were uploaded to NCBI GenBank. The accession numbers are listed in Table S1.

Reverse genetics system to generate recombinant A(H1N1)pdm09 viruses

A/Taiwan/03773/2015 strain was selected to generate the RG virus. The strain was isolated from the first patient with non-severe infection referred to the Chang Gung Memorial Hospital during the 2015–2016 outbreak season. Recombinant viruses, including wild-type (NA-D151), mutant (NA-N151) and mixture-type (NA-D151+N151) viruses (based on A/Taiwan/03773/2015), and the A (H1N1)pdm09 reference virus (A/Taiwan/126/2009) [25], were generated using a plasmid-based RG system [26]. Eight genome segments of the wild-type virus were cloned into the cloning vector pHW2000 [26]. A mutant plasmid was generated from the wild-type pHW2000-NA plasmid using the QuikChange Site-Directed Mutagenesis Kit (Stratagene, San Diego, CA, USA). The wild-type and mutant plasmids were subjected to Sanger sequencing. Plasmids for the eight virus genome segments, including the wild-type or mutant pHW2000-NA, were transfected into 293T cells using Lipofectamine 2000 (Invitrogen) to generate wild-type and mutant viruses, respectively. After 3–5 days, recombinant viruses in supernatants of transfected 293T cells were recovered by passaging in MDCK cells followed by plaque purification [25]. The resulting wild-type and mutant viruses were mixed to prepare the mixture-type virus. Plaque size and count were determined for each virus type using ImageJ software (<https://imagej.nih.gov/ij/>). The mean plaque diameter (mm) in a representative well was determined for RG viruses. Results are presented as means ± standard deviations.

Growth kinetics assay

MDCK cells (ATCC, Manassas, VA, USA) were maintained in minimum essential medium (MEM) (Gibco, Waltham, MA, USA) containing 10 % fetal bovine serum (Gibco) at 37 °C. Cells were infected with RG virus at a multiplicity of infection of 5 in serum-free MEM containing 2 µg/mL trypsin (Cat no. T9935; Sigma-Aldrich, St. Louis, MO, USA). Viruses were allowed to adsorb at 35 °C for 1 h, and the cells were subsequently washed with phosphate buffered saline (PBS) and incubated at 35 °C in serum-free MEM containing 2 µg/mL trypsin. Each experiment was performed in triplicate. At the indicated time points, supernatants containing RG virus were harvested and virus titres were determined in duplicate using a plaque assay.

Cell lysate preparation, NA activity (MUNANA) assay and western blot

293T cells were transfected with FLAG-tagged (Sigma-Aldrich) NA expression plasmid (wild-type or mutant). At 48 hpi, cells were lysed with CA630 lysis buffer [150 mM NaCl, 1 % CA630, 50 mM Tris-base (pH 8.0)]. Total protein concentrations were determined with the Bradford assay (Bio-Rad, Hercules, CA, USA).

The NA-Fluor Influenza Neuraminidase Assay Kit (Life Technologies, Carlsbad, CA, USA) was used to estimate NA activity. RG virus (1×10^4 plaque-forming units, PFU) or 100 µg of cell lysate from 293T cells transfected with FLAG-tagged NA were assayed in triplicate into wells. Subsequently, 50 µL of 200 µM 4-MUNANA substrate was added to each well and the assay plate was incubated at 37 °C. After 1 h, the reaction was stopped and the amount of released fluorescence unit, which is directly related to the amount of NA activity, was measured at an excitation wavelength of 355 nm and an emission wavelength of 450 nm. The FUs of each virus were normalized to control values.

Total lysates from 293T cells (100 µg) containing the NA protein were separated by SDS-PAGE and transferred to a polyvinylidene fluoride membrane. After blocking, the membrane was probed with anti-FLAG or anti-glyceraldehyde 3-phosphate dehydrogenase (as the cellular internal control) primary antibodies (Sigma-Aldrich). Horseradish peroxidase-conjugated anti-mouse IgG secondary antibody (GE Healthcare, Chicago, IL, USA) was used to detect bound antibodies.

NA inhibition assay

An NA inhibition assay was used to determine the concentration of the NA inhibitor required to reduce enzyme activity by 50 % (half-maximal inhibitory concentration, IC_{50}). FU data of the NA inhibition assay against drug concentration (nM) were expressed as relative FU and plotted with GraphPad Prism software, version 7.0 (GraphPad Software Inc., San Diego, CA, USA). Briefly, viruses from the RG system (1×10^4 PFU) or clinical isolates (1×10^3 PFU) were incubated at 37 °C for 30 min with various concentrations of oseltamivir carboxylate (MedChem Express, Monmouth

Junction, NJ, USA). After the addition of the 4-MUNANA substrate, the MUNANA assay procedure described above was applied. Inhibition rate was normalized by FU data obtained from control experiments. Relative NA activity was calculated as the percentage of FU measured in the drug-treated sample divided by that of the control. Clinical specimens were passaged three times owing to a virus titre below the experimental limit.

Haemagglutination assay

The HA assay was used to measure viral titre according to its ability to attach to the surface of red blood cells (RBCs). The wild-type and mutant viruses were normalized by real-time PCR. PBS was added to 96-well V-bottom plates at 100 µL/well. RG viruses (6.9×10^7 copies/mL) were dispensed into each well at 50 µL/well and serially twofold diluted across the plate. The excess 50 µL from all wells was discarded. Then, 1% of guinea pig serum was added to each well at 50 µL/well. The plates were incubated at room temperature for 60 min. Haemagglutinin on the surface of virus binds to the sialic acid receptors of RBCs and creates a lattice structure. Haemagglutinin titres of individual samples were determined as the final dilution where cells were agglutinated.

Statistical analysis

All calculations in Figs 2–4 were performed with GraphPad Prism software. Two-way ANOVA was used to estimate statistically significant differences in viral replication, NA activity and drug susceptibility. A *P*-value <0.05 was considered statistically significant.

Funding information

This work was financially supported by the Research Center for Emerging Viral Infections from The Featured Areas Research Center Program within the framework of the Higher Education Sprout Project by the Ministry of Education (MOE) in Taiwan, ROC, the Ministry of Science and Technology (MOST), Taiwan (Nos. MOST 107-3017-F-182-001, MOST 107-2221-E-182-064-MY2 and MOST 106-2320-B-182A-013-MY3) and Linkou Chang Gung Memorial Hospital, Taiwan (No. CLRP3B0047).

Conflicts of interest

The authors declare that there are no conflicts of interest.

Ethics statement

The study protocol was approved by the Institutional Review Board of the Chang Gung Medical Foundation, Linkou Medical Center, Taoyuan, Taiwan (approval Nos. 104-9663B and 201601853B0).

References

1. Dawood FS, Jain S, Finelli L, Shaw MW, Lindstrom S *et al.* Emergence of a novel swine-origin influenza A (H1N1) virus in humans. *N Engl J Med* 2009;360:2605–2615.
2. Xue KS, Hooper KA, Ollodart AR, Dingens AS, Bloom JD. Cooperation between distinct viral variants promotes growth of H3N2 influenza in cell culture. *Elife* 2016;5:e13974.
3. Xue KS, Greninger AL, Pérez-Osorio A, Bloom JD. Cooperating H3N2 Influenza Virus Variants Are Not Detectable in Primary Clinical Samples. *mSphere* 2018;3.
4. Mishin VP, Sleeman K, Levine M, Carney PJ, Stevens J *et al.* The effect of the MDCK cell selected neuraminidase D151G mutation on the drug susceptibility assessment of influenza A(H3N2) viruses. *Antiviral Res* 2014;101:93–96.

5. Meijer A, Rebelo-de-Andrade H, Correia V, Besselaar T, Drager-Dayal R *et al.* Global update on the susceptibility of human influenza viruses to neuraminidase inhibitors, 2012–2013. *Antiviral Res* 2014;110:31–41.
6. Gubareva LV, Besselaar TG, Daniels RS, Fry A, Gregory V *et al.* Global update on the susceptibility of human influenza viruses to neuraminidase inhibitors, 2015–2016. *Antiviral Res* 2017;146:12–20.
7. Okomo-Adhiambo M, Nguyen HT, Sleeman K, Sheu TG, Deyde VM *et al.* Host cell selection of influenza neuraminidase variants: implications for drug resistance monitoring in A(H1N1) viruses. *Antiviral Res* 2010;85:381–388.
8. Kilander A, Rykkvin R, Dudman SG, Hungnes O. Observed association between the HA1 mutation D222G in the 2009 pandemic influenza A(H1N1) virus and severe clinical outcome, Norway 2009–2010. *Euro Surveill* 2010;15.
9. Mak GC, Au KW, Tai LS, Chuang KC, Cheng KC *et al.* Association of D222G substitution in haemagglutinin of 2009 pandemic influenza A (H1N1) with severe disease. *Euro Surveill* 2010;15.
10. Chen H, Wen X, To KK, Wang P, Tse H *et al.* Quasispecies of the D225G substitution in the hemagglutinin of pandemic influenza A (H1N1) 2009 virus from patients with severe disease in Hong Kong, China. *J Infect Dis* 2010;201:1517–1521.
11. Manchanda H, Seidel N, Blaess MF, Claus RA, Linde J *et al.* Differential Biphasic Transcriptional Host Response Associated with Coevolution of Hemagglutinin Quasispecies of Influenza A Virus. *Front Microbiol* 2016;7:1167.
12. Newitt S, Mironenko A, Holubka O, Zaika O, Gubar O *et al.* Rapid risk assessment during the early weeks of the 2015–2016 influenza season in Ukraine. *Influenza Other Respir Viruses* 2018;12:241–249.
13. Gong YN, Kuo RL, Chen GW, Shih SR. Centennial review of influenza in Taiwan. *Biomed J* 2018;41:234–241.
14. Hsieh YC, Tsao KC, Huang CT, Chang KY, Huang YC *et al.* Clinical characteristics of patients with laboratory-confirmed influenza A (H1N1)pdm09 during the 2013/2014 and 2015/2016 clade 6B/6B.1/6B.2-predominant outbreaks. *Sci Rep* 2018;8:15636.
15. Samson M, Pizzorno A, Abed Y, Boivin G. Influenza virus resistance to neuraminidase inhibitors. *Antiviral Res* 2013;98:174–185.
16. Jonges M, Welkers MR, Jeeninga RE, Meijer A, Schneeberger P *et al.* Emergence of the virulence-associated PB2 E627K substitution in a fatal human case of highly pathogenic avian influenza virus A(H7N7) infection as determined by Illumina ultra-deep sequencing. *J Virol* 2014;88:1694–1702.
17. Mohr PG, Deng YM, McKimm-Breschkin JL. The neuraminidases of MDCK grown human influenza A(H3N2) viruses isolated since 1994 can demonstrate receptor binding. *Virol J* 2015;12:67.
18. Okomo-Adhiambo M, Sleeman K, Ballenger K, Nguyen HT, Mishin VP *et al.* Neuraminidase inhibitor susceptibility testing in human influenza viruses: a laboratory surveillance perspective. *Viruses* 2010;2:2269–2289.
19. Mori K, Murano K, Ohniwa RL, Kawaguchi A, Nagata K. Oseltamivir expands quasispecies of influenza virus through cell-to-cell transmission. *Sci Rep* 2015;5:9163.
20. Gulati U, Wu W, Gulati S, Kumari K, Waner JL *et al.* Mismatched hemagglutinin and neuraminidase specificities in recent human H3N2 influenza viruses. *Virology* 2005;339:12–20.
21. Neverov AD, Kryazhimskiy S, Plotkin JB, Bazykin GA. Coordinated Evolution of Influenza A Surface Proteins. *PLoS Genet* 2015;11:e1005404.
22. Mitrasinovic PM. On the structure-based design of novel inhibitors of H5N1 influenza A virus neuraminidase (NA). *Biophys Chem* 2009;140:35–38.
23. Sievers F, Wilm A, Dineen D, Gibson TJ, Karplus K *et al.* Fast, scalable generation of high-quality protein multiple sequence alignments using Clustal Omega. *Mol Syst Biol* 2011;7:539.
24. Gong YN, Chen GW, Yang SL, Lee CJ, Shih SR *et al.* A Next-Generation Sequencing Data Analysis Pipeline for Detecting Unknown Pathogens from Mixed Clinical Samples and Revealing Their Genetic Diversity. *PLoS One* 2016;11:e0151495.
25. Hsieh EF, Lin SJ, Mok CK, Chen GW, Huang CH *et al.* Altered pathogenicity for seasonal influenza virus by single reassortment of the RNP genes derived from the 2009 pandemic influenza virus. *J Infect Dis* 2011;204:864–872.
26. Hoffmann E, Neumann G, Kawaoka Y, Hobom G, Webster RG. A DNA transfection system for generation of influenza A virus from eight plasmids. *Proc Natl Acad Sci USA* 2000;97:6108–6113.

Five reasons to publish your next article with a Microbiology Society journal

1. The Microbiology Society is a not-for-profit organization.
2. We offer fast and rigorous peer review – average time to first decision is 4–6 weeks.
3. Our journals have a global readership with subscriptions held in research institutions around the world.
4. 80% of our authors rate our submission process as 'excellent' or 'very good'.
5. Your article will be published on an interactive journal platform with advanced metrics.

Find out more and submit your article at microbiologyresearch.org.

Article

Spilanthol from Traditionally Used *Spilanthes acmella* Enhances AMPK and Ameliorates Obesity in Mice Fed High-Fat Diet

Wen-Chung Huang ^{1,2,†}, Hui-Ling Peng ^{1,†}, Sindy Hu ^{3,4} and Shu-Ju Wu ^{4,5,*}

¹ Graduate Institute of Health Industry Technology, Research Center for Food and Cosmetic Safety, College of Human Ecology, Chang Gung University of Science and Technology, Taoyuan City 33303, Taiwan; wchuang@mail.cgust.edu.tw (W.-C.H.); hlpeng@mail.cgust.edu.tw (H.-L.P.)

² Division of Allergy, Asthma, and Rheumatology, Department of Pediatrics, Chang Gung Memorial Hospital, Linkou, Taoyuan City 33303, Taiwan

³ Department of Cosmetic Science, College of Human Ecology, Chang Gung University of Science and Technology, Guishan Dist., Taoyuan City 33303, Taiwan; sindyhu@hotmail.com

⁴ Department of Dermatology, Aesthetic Medical Center, Chang Gung Memorial Hospital, Linkou, Taoyuan City 33303, Taiwan

⁵ Department of Nutrition and Health Sciences, Research Center for Chinese Herbal Medicine, College of Human Ecology, Chang Gung University of Science and Technology, Taoyuan City 33303, Taiwan

* Correspondence: sjwu@mail.cgust.edu.tw; Tel.: +886-3-211-8999 (ext. 5493)

† These authors contributed equally to this work.

Received: 3 April 2019; Accepted: 29 April 2019; Published: 30 April 2019



Abstract: Spilanthol (SP) is a bioactive compound found in *Spilanthes acmella*, giving the flowers and leaves a spicy taste. Studies found that phyto-ingredients stored in spice plants act against obesity-related diseases. SP has antimicrobial, anti-inflammatory, and analgesic properties, but the effects on obesity are not yet known. We investigated the effects of SP in differentiated adipocytes (3T3-L1 cells) and mice fed a high-fat diet (HFD). SP significantly inhibited intracellular lipid accumulation and significantly reduced the expression of lipogenesis-related proteins, including acetyl-CoA carboxylase (ACC) and fatty-acid synthase (FAS). In contrast, SP increased the expression of carnitine palmitoyltransferase (CPT)1 and AMP-activated protein kinase (AMPK) in adipocytes. However, SP suppressed the levels of cyclooxygenase-2 (COX-2), phospho-p38 (pp38), and phospho-JNK (c-Jun N-terminal kinase) (pJNK) in LPS (lipopolysaccharide)-stimulated murine pre-adipocytes. SP administered to HFD-induced obese mice via intraperitoneal injections twice a week for 10 weeks decreased body weight gain, visceral adipose tissue weight, and adipocyte size. SP inhibited lipogenic proteins FAS and ACC, and suppressed adipogenic transcription factors, enhancing lipolysis and AMPK protein expression in the liver. SP has anti-obesity effects, upregulating AMPK to attenuate lipogenic and adipogenic transcription factors.

Keywords: spilanthol; 3T3-L1 cells; anti-obesity; AMPK; adipogenesis; lipogenesis

1. Introduction

Obesity is caused by excessive triglyceride (TG) accumulation, primarily due to imbalanced energy homeostasis. Obesity is one of the most prevalent diseases worldwide [1] and causes chronic inflammatory reactions, which activate T-cell and macrophage infiltration into adipose tissues, resulting in the release of inflammatory mediators, such as tumor necrosis factor (TNF)- α , interleukin (IL)-1 β , and monocyte chemoattractant protein (MCP)-1, from adipose tissue [2]. Importantly, insulin resistance is induced by obesity–leptin resistance, which activates the inflammatory mitogen-activated protein

kinase (MAPK) pathway [3]. In addition, obesity-induced cytokines, especially MCP-1, promote anti-inflammatory M2 macrophage transformation into inflammatory M1 macrophages with increasing obesity-induced inflammation and the expression of a variety of proteins, such as cyclooxygenase-2 (COX-2) [4]. Obesity-induced inflammation is associated with the development of insulin resistance, type 2 diabetes, hypertension, atherothrombosis, and chronic inflammatory diseases [5,6]. Obesity is a complex multifactorial disease, but novel therapeutic dietary interventions may have anti-inflammatory components that are beneficial.

Adipocytes are the depot for energy storage, but excessive numbers and size result in obesity. Pre-adipocyte differentiation into adipocytes is regulated by the transcription factors CCAAT/enhancer-binding protein (C/EBP), peroxisome proliferator-activated receptor (PPAR), and sterol regulatory element-binding protein (SREBP). Increasing C/EBP α expression can prompt 3T3-L1 adipocyte differentiation, and PPAR γ activates numerous genes in adipogenesis [7,8]. In addition, acetyl-CoA carboxylase (ACC) catalyzes acetyl-CoA to malonyl-CoA, and then malonyl-CoA is synthesized into fatty acid (FA) by fatty-acid synthase (FAS) during triglyceride production as lipogenesis [9]. In lipolysis, triglyceride lipase (ATGL) initiates TG hydrolysis in adipocytes [10]. Thus, blocking the expression of lipogenic and adipogenic transcription factors and promoting the activity of lipolysis proteins may reduce severe obesity. Studies found that sirtuin 1 (SIRT1)-mediated AMP-activated protein kinase (AMPK) activation regulates the cell energy metabolism involved in lipolysis [11]. Activation of SIRT1 and AMPK signaling decreases the expression of lipogenic enzymes and downregulates transcription factors involved in adipogenesis, respectively. Interestingly, SIRT1–AMPK increases the rate of FA oxidation [12–14]. Therefore, enhanced hepatic SIRT1–AMPK signaling may decrease obesity.

Spilanthol (*N*-isobutyl-2*E*, 6*Z*, 8*E*-decatrienamide) is found in the flowers, leaves, and roots of *Spilanthes acmella* as the major bioactive compound of this species. *S. acmella* has a wide range of medicinal effects, including hemostatic, analgesic, and diuretic properties, and is used to treat psoriasis and toothache in India [15]. In addition, *S. acmella* is used for the treatment of toothache in folk medicine in Taiwan and other areas of east Asia. Studies reported that *S. acmella* extract has anti-inflammatory, analgesic, anti-oxidant, antibacterial, immunomodulatory, and antifungal activity [16–20]. *S. acmella* has a pungent taste and causes a numbing and tingling sensation when people touch the flowers and leaves. When the plants are cooked, they lose the strong taste and flavor and can be edible as a green leafy vegetable. Fresh *S. acmella* leaves can also be used as a spice, similar to chili and garlic, to increase the flavor of salads, or cooked leaves can be used in stews and soups [21,22]. Interestingly, *S. acmella* used as a spice results in an estimated average daily intake of 24 μ g of spilanthol/person/day in the European Union [23,24]. Studies indicate that many spices (e.g., curcumin in turmeric, capsaicin in red chili, and piperine in black pepper extracts) have antioxidant and anti-inflammatory activities against obesity and attenuate type 2 diabetes, atherosclerosis, and other obesity-related metabolic diseases [25–28].

The anti-obesity effects of spilanthol are not known. In the present study, we investigated whether spilanthol modulates lipogenesis and adipogenesis in differentiated adipocytes and improves the metabolic profile of visceral adipose tissue in high-fat diet (HFD)-induced obese mice (Figure 1A). We also evaluated whether spilanthol reduces the inflammatory response in pre-adipocytes.

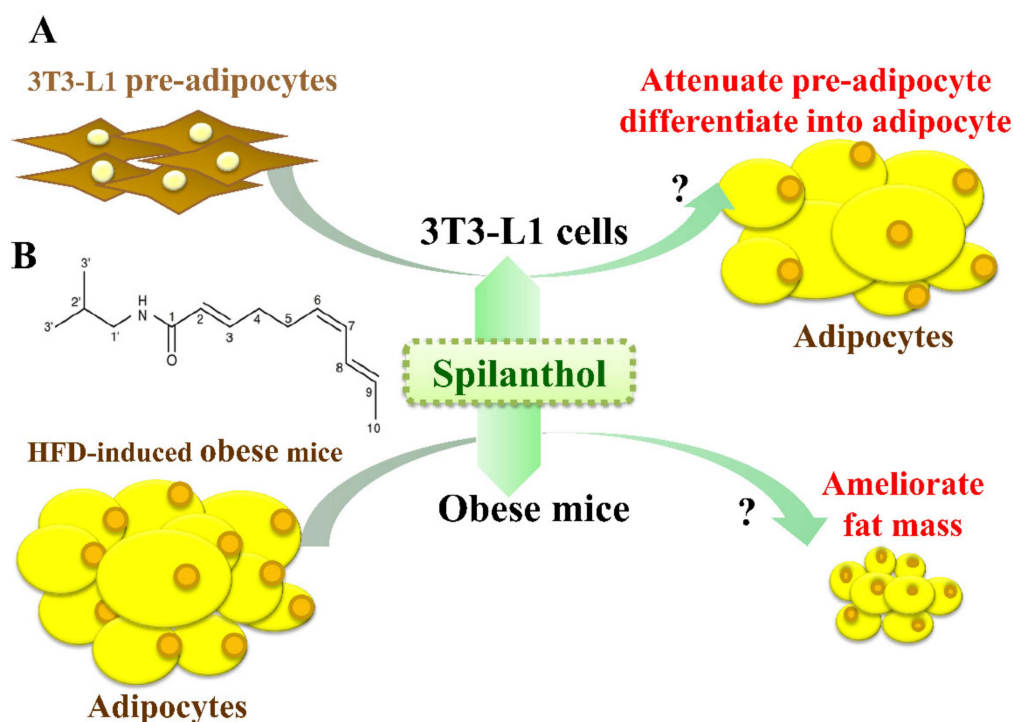


Figure 1. Experimental abstract. (A) Study the effects of spilanthol on 3T3-L1 adipocytes and high-fat diet-induced obese mice. (B) The structure of spilanthol.

2. Materials and Methods

2.1. Preparation of Spilanthol and Cell Culture

Spilanthol [29] (ChromaDex, Irvine, CA, USA; Figure 1B) was dissolved in dimethyl sulfoxide (DMSO) and prepared as a 100 mM stock solution that was stored at -20°C . In culture medium, the final DMSO concentration was $\leq 0.1\%$, as described previously [9]. Mouse 3T3-L1 pre-adipocytes were purchased from Bioresource Collection and Research Center (BCRC, Taiwan) and cultured in Dulbecco's modified Eagle medium (DMEM) (Invitrogen-Gibco, Paisley, Scotland) containing 10% heat-inactivated calf serum (Invitrogen-Gibco) at 37°C in a humidified atmosphere of 5% CO_2 . 3T3-L1 pre-adipocytes (5×10^4) were pretreated with or without various concentrations of spilanthol (3–100 μM) for 1 h, and then 1 $\mu\text{g}/\text{mL}$ LPS (Lipopolysaccharide) added for 24 h. Subsequently, 3T3-L1 pre-adipocytes were lysed for Western blot analysis.

2.2. Adipocyte Differentiation

3T3-L1 pre-adipocytes were cultured in DMEM containing 10% fetal bovine serum (FBS) and induced with 1 μM dexamethasone, 0.5 mM 1-isobutyl-3-methylxanthine, and 10 $\mu\text{g}/\text{mL}$ insulin for two days. The medium was then exchanged for DMEM medium containing 10 $\mu\text{g}/\text{mL}$ insulin for two days, and the DMEM medium was replaced every two days until day 8. The differentiated adipocytes were treated with or without various concentrations of spilanthol (3–100 μM) on day 8 for 24 h, and the 3T3-L1 adipocytes were lysed for Western blot analysis.

2.3. Animals and Spilanthol Administration

Four-week-old C57BL/6 male mice were purchased from the National Laboratory Animal Center in Taiwan and housed in polycarbonate cages under constant conditions (12-h dark/light cycles, room temperature $21 \pm 2^{\circ}\text{C}$, and humidity 45–65%). All animal experiments were approved by the ethical guidelines set out by the Laboratory Animal Care Committee of Chang Gung University of Science and Technology (IACUC Approval Number: 2016007). After acclimating the animals for seven

days, the mice were randomly divided into four groups and treated for 16 weeks: (1) normal diet (ND, $n = 8$), the mice were fed 11% fat normal diet and received DMSO via intraperitoneal injection (ip); (2) high-fat diet (60% energy from fat; HFD, $n = 8$), the mice were fed 60% fat normal diet and received ip DMSO; (3) HFD+SP5 ($n = 8$), the mice were fed a HFD and received ip 5 mg/kg spilanthol dissolved in DMSO; (4) HFD+SP10 ($n = 8$), the mice were fed a HFD and received ip 10 mg/kg spilanthol dissolved in DMSO. All of the ip injections were performed twice a week for 10 weeks. HFD (D12492) was purchased from Research Diets, Inc (Middlesex County, New Jersey, United States). At the end of the experimental period, all animals were fasted for 12 h and sacrificed. Blood samples were collected and the visceral adipocyte tissue and liver removed and weighed after rapidly rinsing with normal saline solution. The samples were stored at -80°C .

2.4. Oil Red O Staining

3T3-L1 cells were treated with or without SP (3–100 μM) for 24 h in six-well plates and fixed in 10% formalin for 30 min. The cellular lipid content was stained with Oil Red O dye solution (Sigma Chemical, St. Louis, MO, USA) at room temperature for 1 h. The plates were washed with phosphate-buffered saline (PBS) three times and 100% isopropanol was added. The intracellular lipid accumulation was photographed using an optical microscope (Olympus, Tokyo, Japan).

2.5. Fluorescence Staining

To analyze 3T3-L1 cells, oil droplets and lipid peroxidation were stained with BODIPY[®]493/503 and BODIPY[®]581/591 C1 (Invitrogen, Carlsbad, CA, USA), respectively. The 3T3-L1 cells were treated with or without SP (3–100 μM) for 24 h in six-well plates. After suctioning out the medium, the cells were washed with PBS and fixed in 10% formalin for 3 h. After washing with PBS, the fluorescent dyeing agent was added (BODIPY493/503 or BODIPY581/591). The dye was washed out with PBS and 4',6-diamidino-2-phenylindole (DAPI) was added to stain the nucleus. A fluorescence microscope (Olympus, Tokyo, Japan) was used to observe the intracellular lipid accumulation and lipid peroxidation.

2.6. Biochemical Analysis

Blood samples were centrifuged at 6000 rpm for 5 min at 4°C and the collected serum was used for analysis of the leptin and lipid concentrations, including triglycerides (TGs), total cholesterol (TC), and high-density lipoprotein cholesterol (HDL-C). Leptin levels were determined using a commercially available enzymatic reagent kit (R&D Systems, Minneapolis, MN, USA). The leptin levels were determined using a microplate reader (Multiskan FC, Thermo Fisher Scientific, Waltham, MA, USA) and measuring the absorbance at 450 nm. Serum TG, TC, and HDL-C levels were analyzed by commercially available TG-P III, TCHO-P III, and HDL-C-P III D FUJI slides in a FUJI DRI-CHEM analyzer according to the manufacturer's instructions (Fujifilm, Co., Tokyo, Japan).

2.7. Histopathological Examination

After the mice were sacrificed, the epididymal adipose, inguinal adipose, and liver tissues were collected and weighed. All of the tissues were fixed in 10% paraformaldehyde, embedded in paraffin wax, and sectioned into 5- μm sections. The epididymal and inguinal adipose and liver sections were stained with hematoxylin and eosin (H&E) and observed using an optical microscope (Olympus, Tokyo, Japan).

2.8. Western Blot Analysis

After treatment with spilanthol, the cells were lysed in protein lysis buffer (Sigma, St. Louis, MO, USA). Protein samples (10–30 μg) were separated on 10% SDS polyacrylamide gels and transferred to polyvinylidene fluoride membranes (PVDF; Millipore, Billerica, MA, USA). The PVDF membranes

were incubated with primary antibodies, including β -actin (Sigma, St. Louis, MO, USA); COX-2, heme oxygenase-1 (HO-1), AMPK (Santa Cruz, Delaware Avenue, Santa Cruz, CA, USA); JNK, phospho-JNK (pJNK), p38, phospho-p38 (pp38), CPT1, FAS, SREBP-1, SIRT1 (Cell Signaling Technology, Danvers, MA, USA); ATGL, ACC, phospho-ACC (pACC), PPAR α , PPAR γ , C/EBP α , or C/EBP β (Abcam, Cambridge, MA, USA), overnight at 4 °C. Tris-buffered saline with Tween-20 (TBST) buffer was used to wash the membranes three times, and the membranes were incubated with secondary antibodies at room temperature for 1 h. Luminol/enhancer solution (Millipore, Billerica, MA, USA) was used to detect the signals and the BioSpectrum 600 system (UVP, Upland, CA, USA) was used to quantitate protein bands.

2.9. Statistical Analysis

One-way analysis of variance (ANOVA) and Tukey's test were used to assess the values. The data were presented as the means \pm standard deviation (SD) with $p < 0.05$ considered significant.

3. Results

3.1. Spilanthol Inhibits Lipid Accumulation in 3T3-L1 Cells

Spilanthol reduced lipid droplet accumulation in 3T3-L1 adipocytes compared to control differentiated adipocytes in a dose-dependent manner (Figure 2A). The use of BODIPY[®]493/503 confirmed the significant decrease in lipid accumulation and lipid peroxidation with spilanthol (Figure 2B). The MTT (3-(4,5-Dimethylthiazol-2-yl)-2,5-diphenyltetrazoliumbromide) assay was used to evaluate the cytotoxicity of spilanthol in 3T3-L1 adipocytes. Spilanthol at concentrations ≥ 100 μ M showed no significant cytotoxicity in 3T3-L1 cells (data not shown).

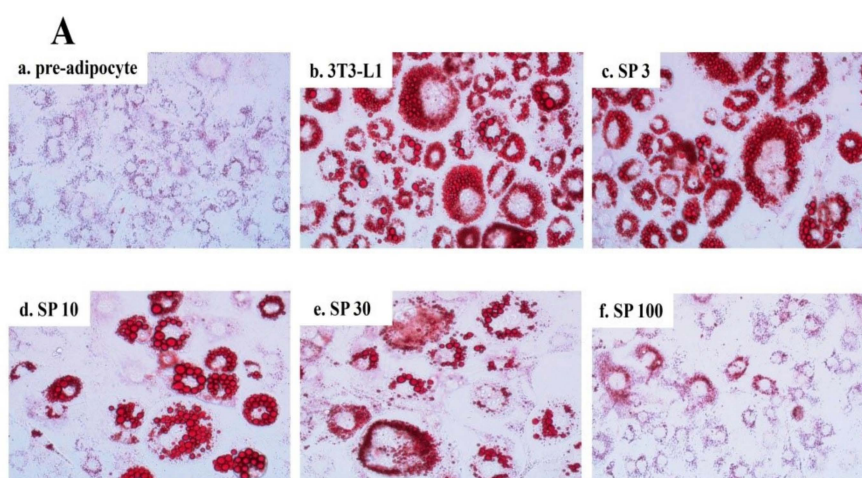


Figure 2. Cont.

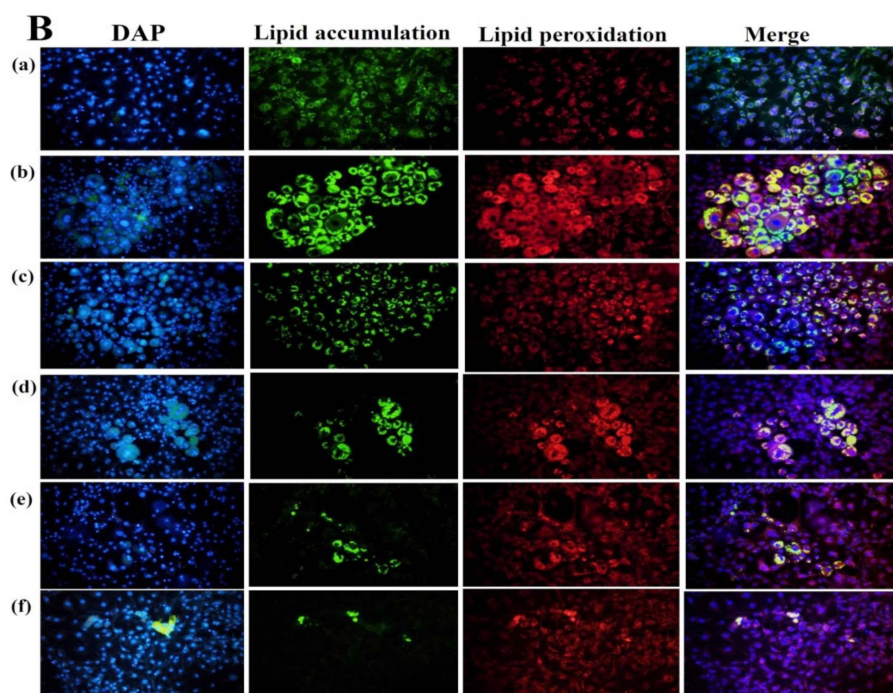


Figure 2. Effect of spilanthol (SP) lipid accumulation and droplets in 3T3-L1 cells. **(A)** 3T3-L1 pre-adipocytes were differentiated in medium containing various concentrations of SP and the differentiated adipocytes examined on day 8 by Oil Red staining: (a) 3T3-L1 pre-adipocytes; (b) 3T3-L1 adipocytes; (c) 3T3-L1 adipocytes + 3 μ M SP; (d) 3T3-L1 adipocytes + 10 μ M SP; (e) 3T3-L1 adipocytes + 30 μ M SP; (f) 3T3-L1 adipocytes + 100 μ M SP. **(B)** Intracellular triglyceride accumulation and lipid peroxidation measured using 4',6-diamidino-2-phenylindole (DAPI) staining.

3.2. Spilanthol Regulates Lipogenic Pathway Enzymes in 3T3-L1 Cells

To elucidate the mechanisms underlying the lipogenic effects of spilanthol, we analyzed the phosphorylation of ACC (pACC), as well as ACC and FAS protein expression. Spilanthol significantly increased the ratio of pACC and ACC protein expression, with lower FAS protein expression compared to control differentiated adipocytes (Figure 3A). Previous studies indicated that AMPK regulates energy metabolism via downregulation of the expression of lipogenic proteins (ACC and FAS) and activation of CPT1, with activated CPT1 transporting FAs into the mitochondria for β -oxidation [30]. We evaluated whether spilanthol enhances AMPK and CPT1 expression in 3T3-L1 cells and found that the protein expression of both was significantly increased in the presence of spilanthol compared to control differentiated adipocytes (Figure 3B,C). These data suggest that spilanthol is dependent on AMPK for inhibiting lipogenesis and involves controlling free FA β -oxidation during the differentiation of 3T3-L1 cells.

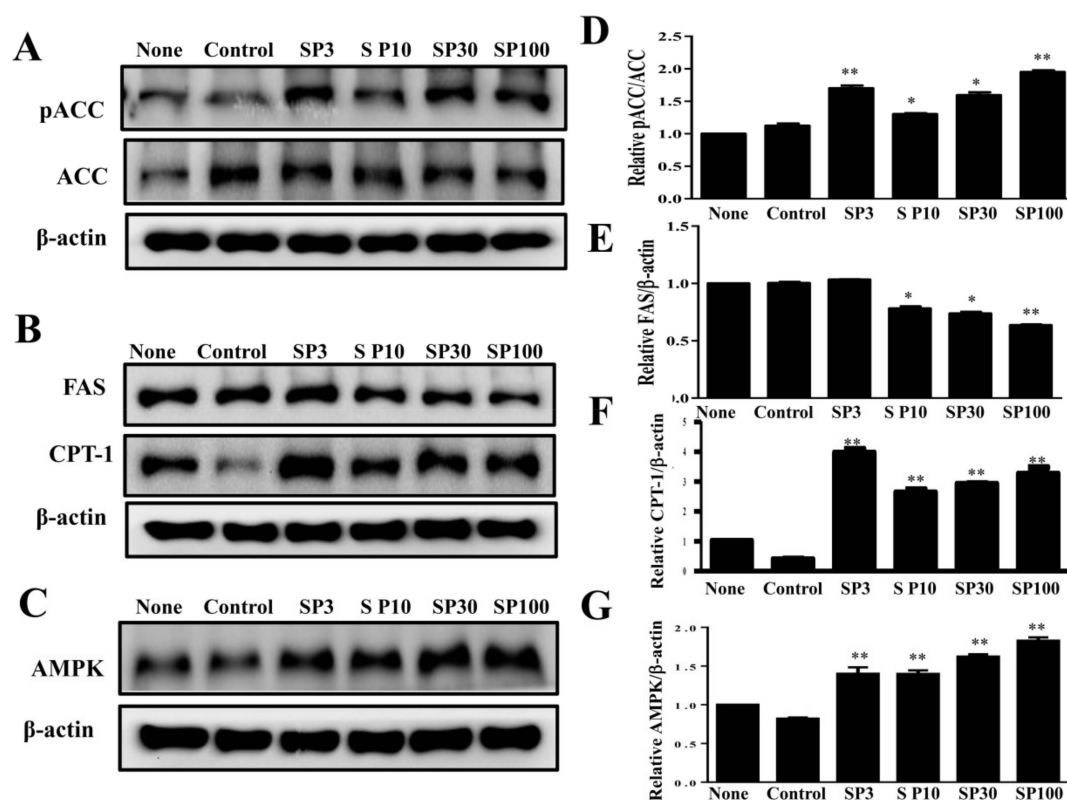


Figure 3. Effects of spilanthol (SP) on lipogenic and AMP-activated protein kinase (AMPK) protein expression in 3T3-L1 adipocytes. Differentiated 3T3-L1 adipocytes (10^4 cells/mL) were treated with 3–100 μ M SP for 24 h. (A) Western blots of phosphorylated acetyl-CoA carboxylase (pACC) and ACC, (B) fatty-acid synthase (FAS) and carnitine palmitoyltransferase 1 (CPT1), and (C) AMPK protein expression. β -Actin was used as an internal control. (D) The relative protein levels of pACC/ACC, (E) FAS, (F) CPT1, and (G) AMPK. Data are presented as means \pm SD ($n = 3$ per group); * $p < 0.05$, ** $p < 0.01$ compared to differentiated 3T3-L1 cells alone (control group). None: pre-adipocytes; control: differentiated adipocytes; SP3: differentiated adipocytes + 3 μ M SP; SP10: differentiated adipocytes + 10 μ M SP; SP30: differentiated adipocytes + 30 μ M SP; SP100: differentiated adipocytes + 100 μ M SP.

3.3. Spilanthol Reduces the Inflammatory Response by Downregulating MAPK Signaling Pathways in 3T3-L1 Pre-Adipocytes

Previous studies reported inflammatory responses in adipose tissue by pre-adipocytes, which share numerous phenotypic features with macrophages and have a greater inflammatory response than mature adipocytes mediated by MAPK signaling [31]. Obesity-induced chronic low-grade inflammation is associated with the development of a variety of metabolic diseases [28]. Therefore, we investigated whether spilanthol reduces the inflammatory response in 3T3-L1 pre-adipocytes. In the present study, spilanthol significantly suppressed inflammatory mediator COX-2 and promoted anti-inflammatory protein HO-1 expression (Figure 4A). In addition, spilanthol 3 μ M significantly suppressed the phosphorylation of JNK and p38 (Figure 4B,C) but did not inhibit the phosphorylation of ERK1/2 (Extracellular signal-regulated kinase 1/2) (data not shown). Taken together, our data indicate that spilanthol may be beneficial for preventing pre-adipocyte inflammatory responses to reduce obesity-related metabolic disease.

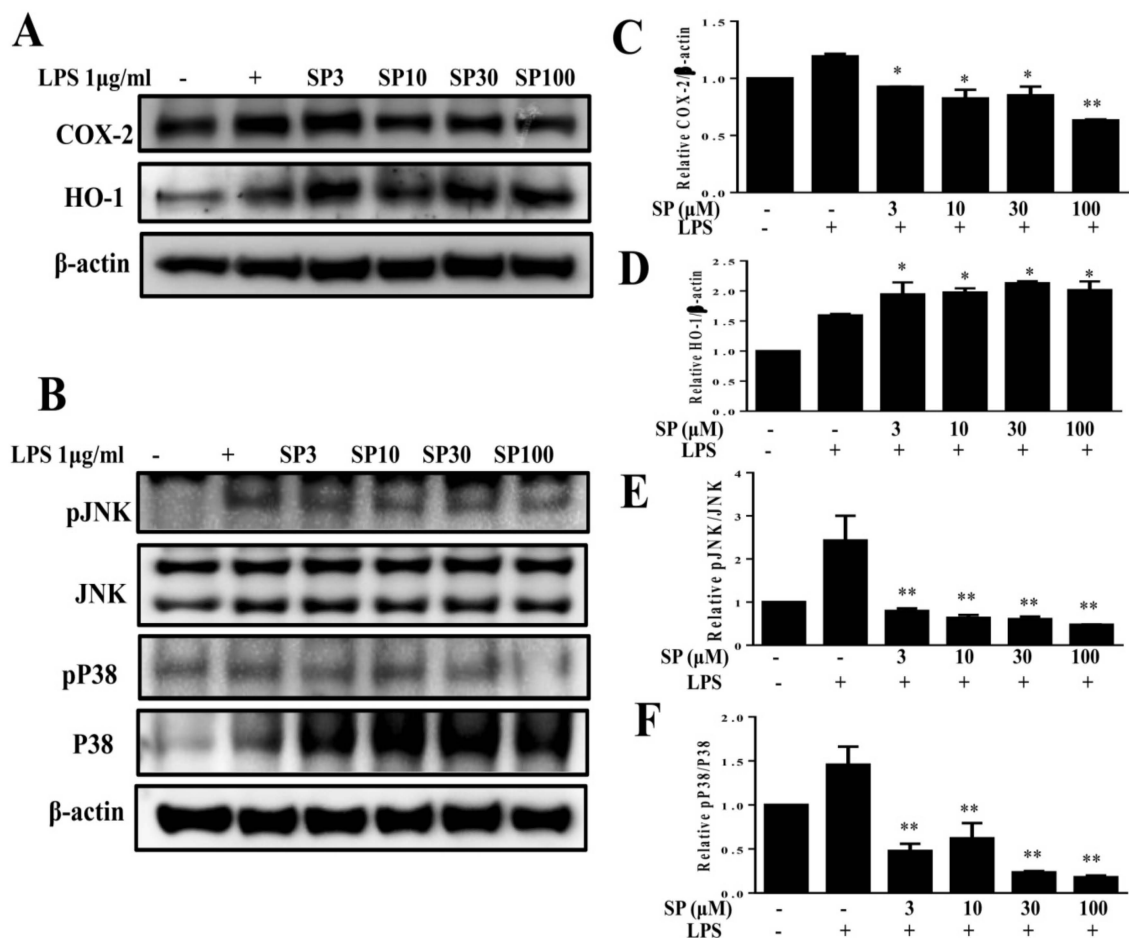


Figure 4. Spilanthol (SP) decreased cyclooxygenase-2 (COX-2), enhanced heme oxygenase-1 (HO-1) protein expression, and inhibited phosphorylation of mitogen-activated protein kinase (MAPK) in LPS-induced 3T3-L1 pre-adipocytes. Here, 10^4 cells/mL were pretreated with 3–100 μ M SP for 1 h and cultured with LPS (1 μ g/mL) for 24 h. (A) Western blots of COX-2 and HO-1, (B) pJNK, JNK, pP38, and P38 proteins ($n = 3$ per group). β -Actin was used as an internal control. (C) The relative protein levels of COX-2, (D) HO-1, (E) pJNK/JNK, and (F) pP38/P38. Data are presented as means \pm SD; * $p < 0.05$, ** $p < 0.01$ compared to differentiated 3T3-L1 cells alone (control group). None: pre-adipocytes; control: differentiated adipocytes; SP3: differentiated adipocytes + 3 μ M SP; SP10: differentiated adipocytes + 10 μ M SP; SP30: differentiated adipocytes + 30 μ M SP; SP100: differentiated adipocytes + 100 μ M SP.

3.4. Spilanthol Ameliorates Adiposity and Visceral Adipocyte Tissue in HFD-Induced Obese Mice

Spilanthol treatment significantly ameliorated HFD-induced obesity and weight gain compared to HFD-fed mice. We found no difference in total calorie intake (kcal) per day among all groups, suggesting that spilanthol did not reduce the calorie intake to reduce body weight gain (Figure 5). To clarify the suppression of visceral adipocyte tissue by spilanthol to ameliorate weight gain, we measured epididymal and inguinal adipose tissue depot masses. Epididymal adipose tissue and inguinal adipose tissue depot masses were lower in spilanthol-treated HFD-fed mice than in HFD-fed control mice. In addition, H&E staining showed that spilanthol-treated HFD-fed mice had significantly smaller adipocytes in the epididymal and inguinal adipose tissue compared to HFD-induced obese mice (Figure 6). The findings suggest that spilanthol decreased the visceral adipocyte tissue and ameliorated obesity in HFD-induced obese mice.

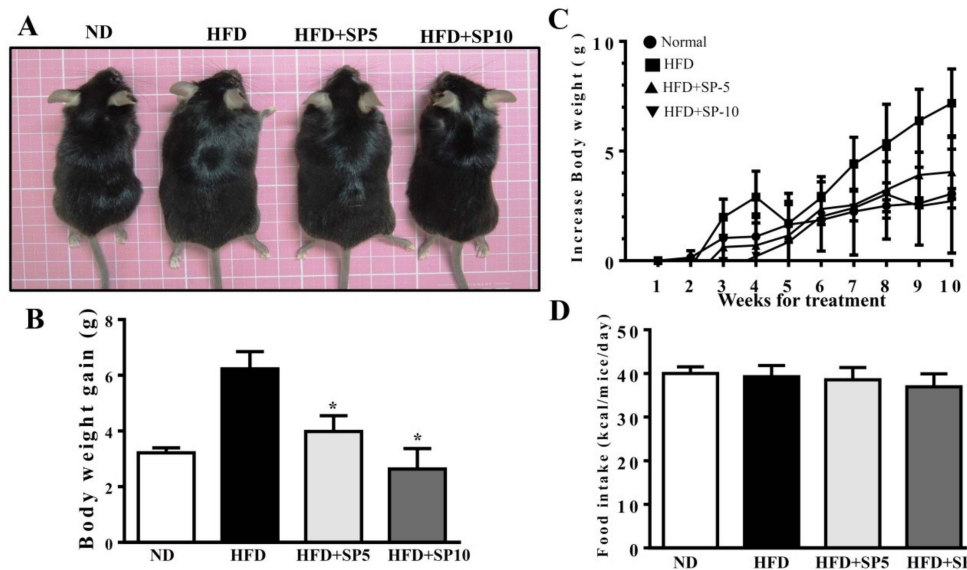


Figure 5. Spilanthol (SP) ameliorates adiposity and decreases body weight gain in high-fat diet (HFD)-induced obese mice. (A) Representative images of the whole body. (B) Body weight (BW) and (C) body weight gain. (D) Food intake (kcal/mice/day). C57BL/6 mice were fed a normal diet (ND) or high-fat diet (HFD) with or without a low dose of SP (5 mg spilanthol/kg BW; SP5) or high dose of SP (10 mg spilanthol/kg BW; SP10) for eight weeks. The data are presented as means \pm SD, $n = 8$; * $p < 0.05$ compared to HFD-fed mice alone.

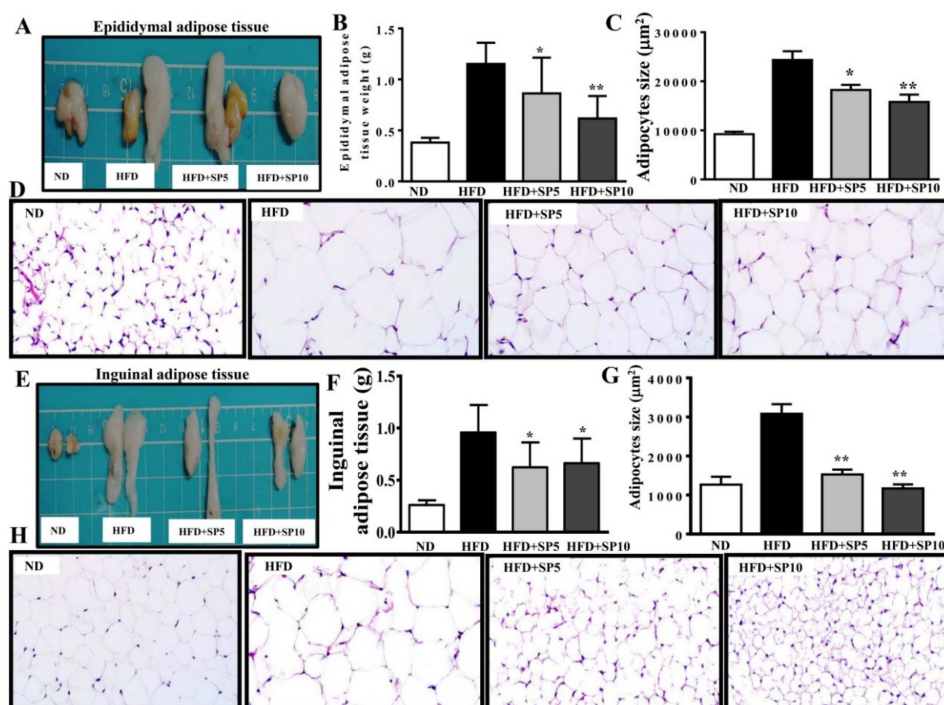


Figure 6. Spilanthol (SP) reduces HFD-induced visceral adipocyte tissue weight and adipocyte size. (A) Representative image of epididymal adipose tissue. (B) Epididymal adipose tissue weight. (C) Epididymal adipocyte size. (D) Histological sections of epididymal adipose tissues from mice (400 \times). (E) Representative image of inguinal adipose tissue. (F) Inguinal adipose tissue weight. (G) Inguinal adipocyte size. (H) Histological sections of inguinal adipose tissue (400 \times). C57BL/6 mice were fed a normal diet (ND) or high-fat diet (HFD) with or without a low dose of SP (5 mg spilanthol/kg BW; SP5) or high dose of SP (10 mg spilanthol/kg BW; SP10) for eight weeks. The data are presented as means \pm SD, $n = 8$; * $p < 0.05$, ** $p < 0.01$ compared to HFD-fed mice alone.

3.5. Spilanthol Ameliorates Hepatic Lipid Accumulation, Improves TC and HDL-c Levels, and Attenuates Serum Leptin in HFD-Induced Obese Mice

Studies demonstrated obesity-induced nonalcoholic fatty liver disease (NAFLD) in HFD-fed mice [32]. Therefore, we evaluated the effect of spilanthol on liver lipid accumulation in obese mice fed an HFD. We found no significant difference in liver weight among the groups (Figure 7A). However, H&E staining of the liver showed that spilanthol-treated HFD-fed mice had significantly fewer hepatic lipid droplets than HFD-induced obese mice (Figure 7B).

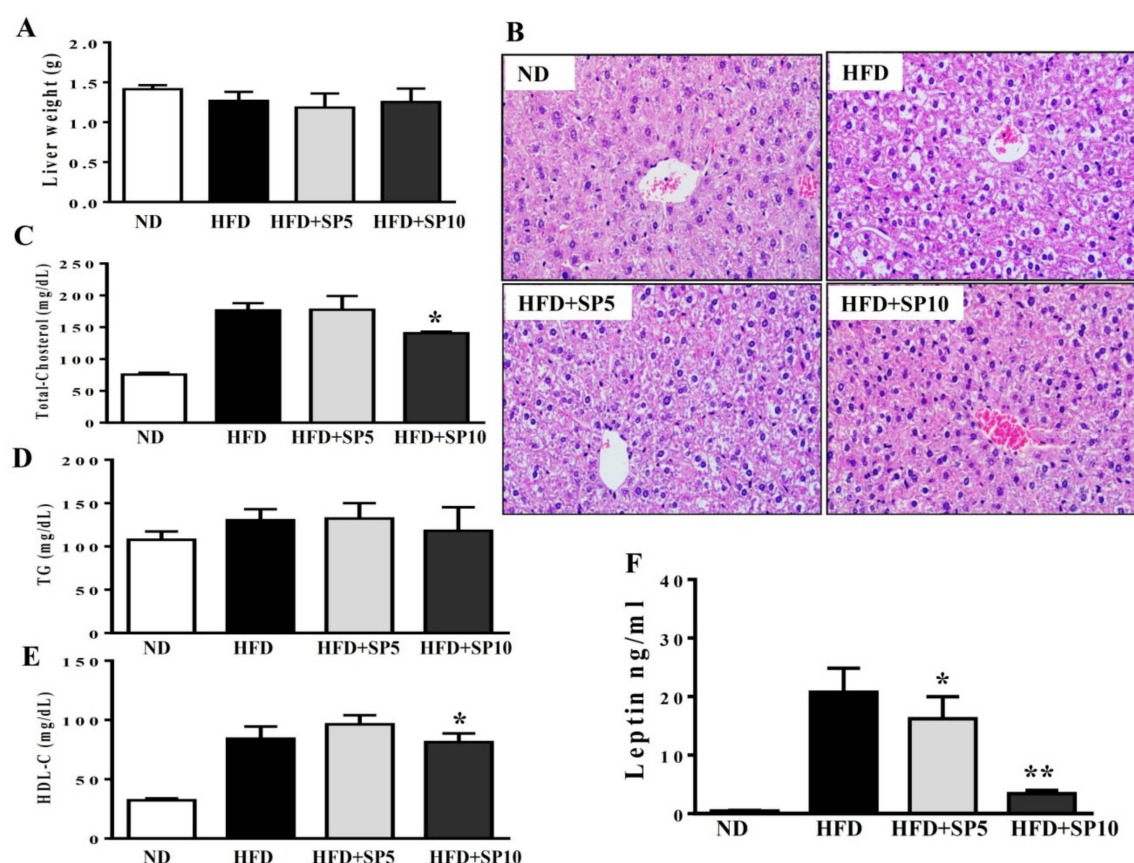


Figure 7. Spilanthol (SP) ameliorates hepatic steatosis, decreases serum leptin levels, and improves serum biochemical parameters in HFD-induced obese mice. (A) Final liver weight. (B) Hematoxylin and eosin (H&E)-stained liver tissue. (C) Serum total cholesterol level. (D) Serum triglyceride level. (E) Serum high-density lipoprotein cholesterol (HDL-C) level. (F) Serum leptin level. C57BL/6 mice were fed a normal diet (ND) or high-fat diet (HFD) with or without a low dose of SP (5 mg spilanthol/kg BW; SP5) or high dose of SP (10 mg spilanthol/kg BW; SP10) for eight weeks. The data are presented as means \pm SD, $n = 8$; * $p < 0.05$, ** $p < 0.01$ compared to HFD-fed mice alone.

Higher serum concentrations of metabolites are associated with lipid homeostasis in HFD-fed mice [33]. We found that the HFD group treated with 10 mg/kg spilanthol had lower serum TC levels and higher HDL-C levels than HFD-fed control mice. However, serum TG concentrations were not significantly different among the groups (Figure 7C–E).

Obesity is frequently associated with high serum levels of leptin. Leptin is secreted from adipocytes to maintain body weight and energy homeostasis [34]. Studies indicated that leptin in the hypothalamus mediates the anti-obesity actions and activation of the sympathetic nervous system (SNS) to induce lipolysis in white adipose tissue and thermogenesis in brown adipose tissue [35]. Serum leptin level is proportional to the adipocytes; hence, we analyzed whether spilanthol improves obesity and decreases leptin levels. In addition, studies showed that obesity-induced leptin and insulin resistance are associated with impaired hypothalamic regulation of energy homeostasis [35,36].

Serum leptin levels were significantly higher in HFD-fed control mice than ND-fed mice. Interestingly, serum leptin levels significantly decreased with spilanthal treatment (Figure 7F). These data suggest that spilanthal suppresses the obesity-induced accumulation of lipids in the liver to improve serum cholesterol content. Spilanthal possibly mediates changes in the hypothalamus to improve energy metabolism and, thus, reduce body weight and leptin levels.

3.6. Spilanthal Activates AMPK Signaling to Regulate Lipogenesis and Adipogenesis-Related Transcription Factors in HFD-Induced Obese Mice

To understand whether spilanthal regulates lipid metabolism, hepatic protein expression was measured by Western blot. FAS and pACC protein expression was significantly decreased in spilanthal-treated HFD-fed mice compared to HFD-induced obese mice (Figure 8A). In contrast, ATGL, SIRT1, and AMPK protein expression was significantly higher in spilanthal-treated HFD-fed mice than HFD-induced obese mice (Figure 8B). However, PPAR α , PPAR γ , C/EBP α , C/EBP β , and SREBP-1 protein expression was significantly inhibited in spilanthal-treated HFD-fed mice compared to HFD-induced obese mice (Figure 8C). These results suggest that spilanthal inhibited hepatic lipid accumulation via activation of the AMPK pathway, downregulating FAS and ACC expression and suppressing PPAR α , PPAR γ , C/EBP α , C/EBP β , and SREBP-1 expression. These results are consistent with previous studies in which activation of AMPK signaling decreased lipogenic and adipogenic transcription factors and promoted FA oxidation [12–14]. Therefore, spilanthal may attenuate obesity-induced hepatic lipid accumulation.

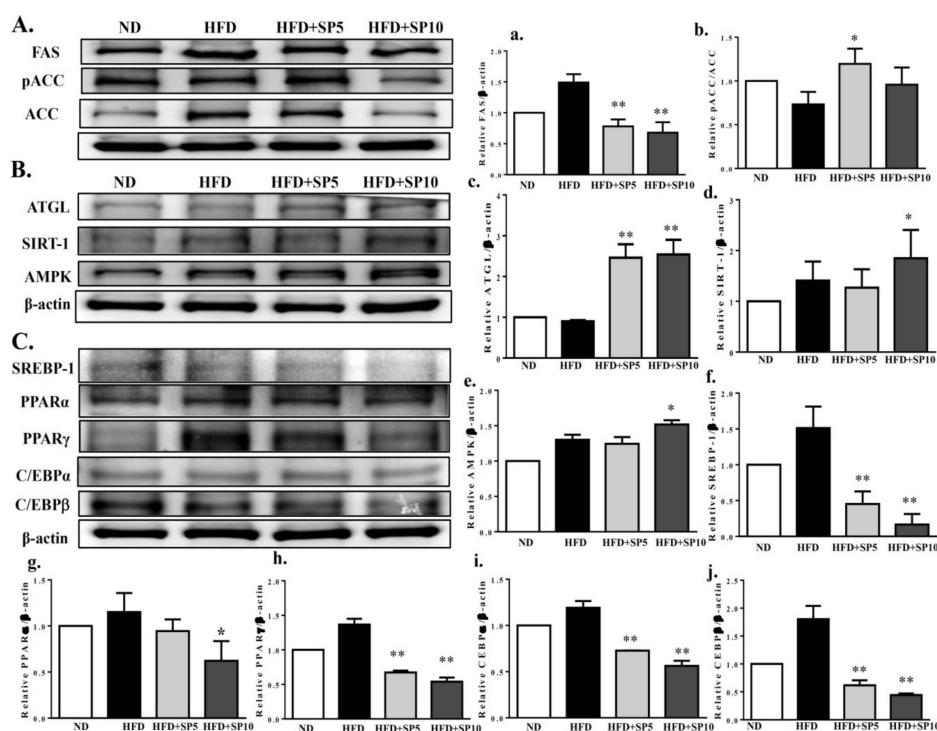


Figure 8. Treatment with spilanthal (SP) downregulates the lipogenesis and adipogenesis-related transcription factors, and upregulates lipolysis-related and AMPK pathway protein expression in the livers of HFD-fed mice. (A) Western blots of lipogenesis-related proteins FAS and pACC, (B) lipolysis protein triglyceride lipase (ATGL), sirtuin 1 (SIRT1), and AMPK, and (C) adipogenic transcription factors sterol regulatory element-binding protein (SREBP-1), peroxisome proliferator-activated receptor (PPAR) α , PPAR γ , CCAAT/enhancer-binding protein (C/EBP) α , and C/EBP β . β -Actin was used as an internal control. The relative protein levels of FAS (a), pACC (b), ATGL (c), SIRT1 (d), AMPK (e), SREBP-1 (f), PPAR α (g), PPAR γ (h), C/EBP α (i), and C/EBP β (j) in the liver are also given. Data are presented as means \pm SD ($n = 8$); * $p < 0.05$, ** $p < 0.01$ compared to HFD-induced obese mice.

4. Discussion

Obesity was identified as a chronic disease and can contribute to the development of many chronic diseases, including type 2 diabetes, hyperlipidemia, inflammatory diseases, and cancer. Improving obesity and preventing chronic diseases is the first step to maintaining a healthy lifestyle, and diet is the most important goal [5,6]. Many studies indicate that phyto-compounds from spice plants, including curcumin, capsaicin, and piperine, attenuate chronic metabolic diseases through anti-inflammatory and anti-obesity actions [25–28]. Compelling evidence supports positive benefits of dietary phyto-compounds for a healthy lifestyle to treat/prevent obesity and chronic metabolic diseases. Therefore, many studies focused on screening phyto-compounds and exploring the molecular mechanisms related to reducing obesity and obesity-related disease. In this study, we investigated the molecular mechanisms underlying the effects of spilanthol, finding that it has anti-obesity effects by mediating AMPK to reduce lipogenic and adipogenic transcriptional factors in 3T3-L1 adipocytes and HFD-induced obese mice.

In obesity, adipocyte hyperplasia and hypertrophy cause excessive accumulation of white adipose tissue (WAT) and increased body weight. Adipogenic transcription factors regulate 3T3-L1 pre-adipocyte differentiation into mature adipocytes [7,8]. Our results indicate that spilanthol significantly suppresses the expression of C/EBP, PPAR, and SREBP-1c expression in the livers of obese mice. In addition, lipogenesis involving FA synthesis and TG synthesis can promote WAT expansion. In the present study, spilanthol suppressed TG synthesis by reducing the expression of FAS and increasing pACC in 3T3-L1 cells and obese mice. The PPARRs also regulate lipogenesis and increase FA β -oxidation in adipose and liver tissue [36]. Here, we found that spilanthol attenuated lipogenesis and adipogenesis exist anti-obesity effect in obese mice mainly by blocking the expression of FAS, ACC, C/EBP, PPAR, and SREBP-1c proteins. SIRT1-mediated AMPK activation increases lipolysis and energy metabolism in obese mice and 3T3-L1 cells [11]. In addition, AMPK suppresses FA synthesis in adipocytes and hepatocytes [37]. Here, we found that spilanthol significantly increased the expression of AMPK, SIRT, ATGL, and pACC-1 proteins, but decreased FAS, in obese mice. We also found that spilanthol may induce AMPK activation to promote CPT1 expression and block lipogenesis in adipocytes. Thus, spilanthol treatment ameliorates obesity with consistent findings in vitro and in vivo.

HFD-induced hyperlipidemia, hyperleptinemia, and increased adipocyte tissue and body weight are major risk factors for metabolic disorders in mice [38]. Previous studies showed that leptin secreted from adipocyte tissue is related to the development of insulin resistance and diabetes [34,35]. Here, spilanthol significantly suppressed body weight gain, reduced the serum levels of leptin and TC, and increased HDL-C, but had no effect on TG levels. In addition, HFD-induced obesity correlated with hepatic TG accumulation [32]. Thus, spilanthol diminished HFD-induced hepatic lipid accumulation in obese mice. We showed that spilanthol significantly inhibits the adipogenic proteins C/EBP α , C/EBP β , PPAR α , PPAR γ , and SREBP-1 in the liver, and that spilanthol has notable effects against obesity and associated metabolic abnormalities, such as insulin resistance and hyperlipidemia. Therefore, spilanthol may be an effective agent in the diet for healthy lifestyle management.

It is worth mentioning that spilanthol has high permeation rate from the blood into the brain after intravenous injection in mice [39]. Spilanthol could regulate the central nervous system across the blood–brain barrier [39]. In hypothalamic neurons, increased malonyl-CoA would lead to food intake reduction [40]. In this study, we found that spilanthol inhibited ACC expression. We suggest that spilanthol, through a central action, stimulated energy expenditure but did not reduce appetite.

Furthermore, adipocyte tissue could release leptin to bind to leptin receptors of the hypothalamus to regulating appetite and energy expenditure [41]. In obese individuals, excessive leptin into hypothalamus would increase energy expenditure to decrease body weight [42]. We suggest that the reduced calorie intake (Figure 5D) and serum leptin levels (Figure 7F) with spilanthol produced the anti-obesity effects by promoting energy consumption by increasing the affinity of leptin for its receptor.

Obesity increases the circulation of inflammatory mediators and leptin resistance. Adipocytes release cytokines that induce M2 macrophages to transform into M1 macrophages, and inflammatory M1 macrophages infiltrate the adipose tissue, resulting in more serious chronic inflammatory mediators and insulin resistance in obesity [3,4]. In addition, pre-adipocytes share phenotypic features with macrophages and cause adipose tissue inflammation [31]. Here, we found that LPS-stimulated pre-adipocytes expressed significantly increased levels of COX-2, pJNK, and pp38 proteins. Spilanthol effectively inhibited the expression of COX-2, pJNK, and pp38 proteins but enhanced expression of anti-inflammatory protein HO-1 in LPS-stimulated pre-adipocytes. These findings provide evidence that spilanthol suppresses the levels of COX-2, pJNK, and pp38, which could attenuate or improve inflammatory-induced insulin resistance in adipocytes.

5. Conclusions

Our data demonstrate that spilanthol suppresses lipogenesis via activation of AMPK signaling, and inhibits inflammation by blocking JNK and P38 phosphorylation in differentiated 3T3-L1 cells. Moreover, spilanthol attenuates HFD-induced weight gain, fat deposition, and adipocyte size, and alleviates serum TC, HDL-C, and leptin levels. Importantly, spilanthol significantly attenuates obesity-induced hepatic lipid accumulation via activation of AMPK, downregulating lipogenesis and adipogenesis-related transcription factors in obese mice (Figure 9). We conclude that spilanthol is a natural anti-obesity agent that may improve obesity-related metabolic disorders.

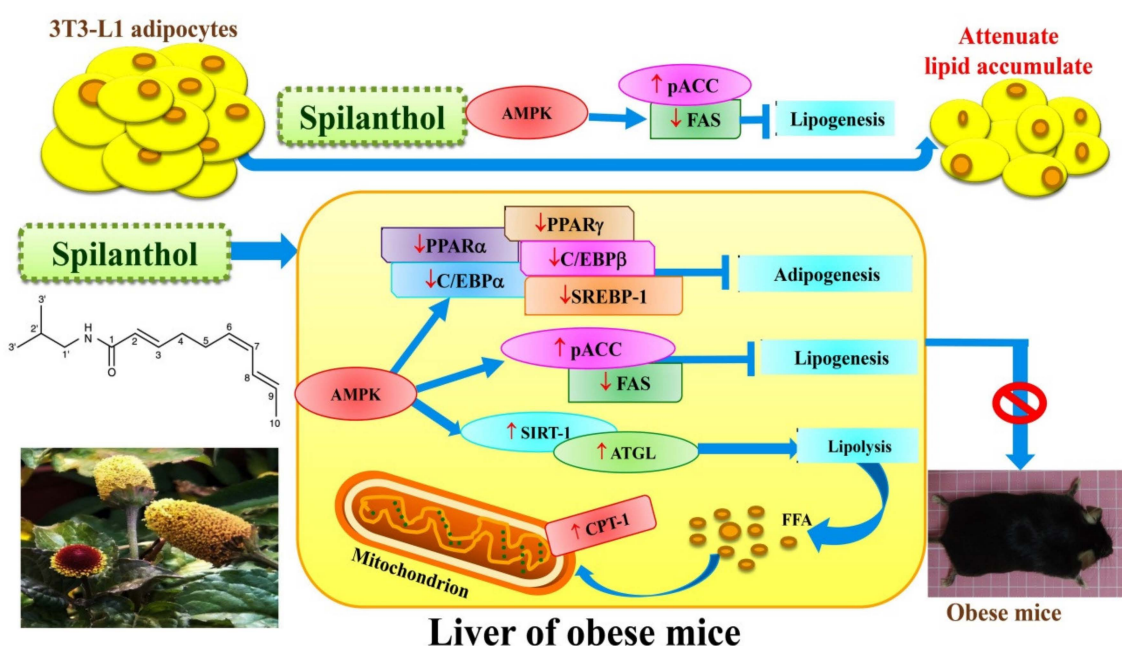


Figure 9. Model explaining the mechanism underlying the anti-obesity effects of spilanthol (SP). SP increases lipolysis-related proteins, suppresses the protein expression of adipogenesis-related transcript factors, and reduces lipogenic proteins via activation of AMPK in the liver of obese mice. SP also inhibits lipogenesis to reduce ACC and FAS expression in 3T3-L1 adipocytes. SP is a potential anti-obesity compound that could ameliorate liver lipid accumulation in obese mice.

Author Contributions: W.-C.H. and H.-L.P. designed the study and performed the experiments. S.H. searched the literature and performed the experiments. S.-J.W. interpreted the data and drafted the manuscript.

Funding: This study was supported in part by grants from Chang Gung Memorial Hospital (CMRPF1F0123, CMRPF1G0202) in Taiwan.

Conflicts of Interest: The authors declare no conflicts of interest.

References

- Seong, J.; Kang, J.Y.; Sun, J.S.; Kim, K.W. Hypothalamic inflammation and obesity: A mechanistic review. *Arch. Pharm. Res.* **2019**, *5*. [\[CrossRef\]](#)
- Ellulu, M.S.; Patimah, I.; Khaza'ai, H.; Rahmat, A.; Abed, Y. Obesity and inflammation: The linking mechanism and the complications. *Arch. Med. Sci.* **2017**, *13*, 851–863. [\[CrossRef\]](#)
- Hirabara, S.M.; Gorjão, R.; Vinolo, M.A.; Rodrigues, A.C.; Nachbar, R.T.; Curi, R. Molecular targets related to inflammation and insulin resistance and potential interventions. *J. Biomed. Biotechnol.* **2012**, 379024. [\[CrossRef\]](#)
- Tateya, S.; Kim, F.; Tamori, Y. Recent advances in obesity-induced inflammation and insulin resistance. *Front. Endocrinol.* **2013**, *4*, 93. [\[CrossRef\]](#) [\[PubMed\]](#)
- Seth, S.; Martin, B.S.; Qasim, A.; Muredach, P.; Reilly, M.B. Leptin resistance: A Possible interface of inflammation and metabolism in obesity-related cardiovascular disease. *J. Am. Coll. Cardiol.* **2008**, *7*, 1201–1210.
- Hsieh, P.S.; Jin, J.S.; Chiang, C.F. COX-2-mediated inflammation in fat is crucial for obesity-linked insulin resistance and fatty liver. *Obesity* **2009**, *17*, 1150–1157. [\[CrossRef\]](#) [\[PubMed\]](#)
- Koh, E.J.; Kim, K.J.; Choi, J.; Jeon, H.J.; Seo, M.J.; Lee, B.Y. Ginsenoside Rg1 suppresses early stage of adipocyte development via activation of C/EBP homologous protein-10 in 3T3-L1 and attenuates fat accumulation in high fat diet-induced obese zebrafish. *J. Ginseng. Res.* **2017**, *41*, 23–30. [\[CrossRef\]](#)
- Park, Y.K.; Obiang-Obounou, B.W.; Lee, J.; Lee, T.Y.; Bae, M.A.; Hwang, K.S.; Lee, K.B.; Choi, J.S.; Jang, B.C. Anti-adipogenic effects on 3T3-L1 cells and zebrafish by Tanshinone IIA. *Int. J. Mol. Sci.* **2017**, *18*, 2065. [\[CrossRef\]](#) [\[PubMed\]](#)
- Huang, W.C.; Chang, W.T.; Wu, S.J.; Xu, P.Y.; Ting, N.C.; Liou, C.J. Phloretin and phlorizin promote lipolysis and inhibit inflammation in mouse 3T3-L1 cells and in macrophage-adipocyte co-cultures. *Mol. Nutr. Food Res.* **2013**, *57*, 1803–1813. [\[CrossRef\]](#)
- Huang, W.C.; Chen, Y.L.; Liu, H.C.; Wu, S.J.; Liou, C.J. Ginkgolide C reduced oleic acid-induced lipid accumulation in HepG2 cells. *Saudi. Pharm. J.* **2018**, *26*, 1178–1184. [\[CrossRef\]](#) [\[PubMed\]](#)
- Trepiana, J.; Milton-Laskibar, I.; Gómez-Zorita, S.; Eseberri, I.; González, M.; Fernández-Quintela, A.; Portillo, M.P. Involvement of 50AMP-Activated Protein Kinase (AMPK) in the effects of resveratrol on liver steatosis. *Int. J. Mol. Sci.* **2018**, *19*, 3473. [\[CrossRef\]](#)
- Suchankova, G.; Nelson, L.E.; Gerhart-Hines, Z.; Kelly, M.; Gauthier, M.S.; Saha, A.K.; Ido, Y.; Puigserver, P.; Ruderman, N.B. Concurrent regulation of AMP-activated protein kinase and SIRT1 in mammalian cells. *Biochem. Biophys. Res. Commun.* **2009**, *378*, 836–841. [\[CrossRef\]](#)
- Cantó, C.; Auwerx, J. PGC-1α, SIRT1 and AMPK, an energy sensing network that controls energy expenditure. *Curr. Opin. Lipidol.* **2009**, *20*, 98–105. [\[CrossRef\]](#) [\[PubMed\]](#)
- Shen, Z.; Liang, X.; Rogers, C.Q.; Rideout, D.; You, M. Involvement of adiponectin-SIRT1-AMPK signaling in the protective action of rosiglitazone against alcoholic fatty liver in mice. *Am. J. Physiol. Gastrointest. Liver Physiol.* **2010**, *298*, G364–G374. [\[CrossRef\]](#)
- Joseph, B.; George, J.; Jeevitha, M.V. The role of *Acmella Oleracea* in Medicine—A review. *World J. Pharm. Res.* **2017**, *2*, 2781–2792.
- Tanwer, B.S.; Choudhary, R.K.; Vijayvergia, R. In vitro and in vivo comparative study of primary metabolites and antioxidant activity in *Spilanthes acmella* Murr. *Int. J. Biotechnol. Biochem.* **2010**, *6*, 819–825.
- Sahu, J.; Jain, K.; Jain, B.; Sahu, R.K. A review on phytopharmacology and micro propagation of *Spilanthes acmella*. *Pharmacologyonline* **2011**, *2*, 1105–1110.
- Yadav, R.; Kharya, M.D.; Yadav, N.; Savadi, R. Diuretic activity of *Spilanthes acmella* Murr. Leaves extract in rats. *Int. J. Pharm. Pharm. Sci.* **2011**, *1*, 57–61.
- Chakraborty, A.; Devi, B.R.K.; Sanjebam, R.; Khumbong, S.; Thokchom, I.S. Preliminary studies on local anesthetic and antipyretic activities of *Spilanthes acmella* Murr. in experimental animals models. *Indian. J. Pharmacol.* **2010**, *42*, 277–279. [\[CrossRef\]](#)
- Wu, L.C.; Fan, N.C.; Lin, M.H.; Chu, I.R.; Huang, S.J.; Hu, C.Y. Anti-inflammatory effect of spilanthol from *Spilanthes acmella* on murine macrophage by down-regulating LPS-induced inflammatory mediators. *J. Agric. Food. Chem.* **2008**, *56*, 2341–2349. [\[CrossRef\]](#)


21. Leng, T.C.; Ping, N.S.; Lim, B.P.; Keng, C.L. Detection of bioactive compounds from *Spilanthes acmella* (L.) plants and its various in vitro culture products. *J. Med. Plant. Res.* **2011**, *5*, 371–378.
22. Nabi, N.G.; Wani, T.A.; Abidwani, M.S.; Shah, S.N. *Spilanthes acmella* an endangered medicinal plant—Its traditional, phytochemical and therapeutic properties—An overview. *Int. J. Adv. Res.* **2016**, *4*, 627–639.
23. Paulraj, J.; Govindarajan, R.; Palpu, P. The genus *Spilanthes* ethnopharmacology, phytochemistry, and pharmacological properties: A review. *Adv. Pharmacol. Sci.* **2013**. [[CrossRef](#)]
24. Veryser, L.; Wynendaele, E.; Taevernier, L.; Verbeke, F.; Joshi, T.; Tatke, P.; DeSpiegeleer, B. N-alkylamides: From plant to brain. *Funct. Foods. Health. Dis.* **2014**, *4*, 264–275. [[CrossRef](#)]
25. Aggarwal, B.B. Targeting inflammation-induced obesity and metabolic diseases by curcumin and other nutraceuticals. *Annu. Rev. Nutr.* **2010**, *21*, 173–199. [[CrossRef](#)] [[PubMed](#)]
26. Pulido-Moran, M.; Moreno-Fernandez, J.; Ramirez-Tortosa, C.; Ramirez-Tortosa, M. Curcumin and Health. *Molecules* **2016**, *21*, 264. [[CrossRef](#)] [[PubMed](#)]
27. Zheng, J.; Zheng, S.; Feng, Q.; Zhang, Q.; Xiao, X. Dietary capsaicin and its anti-obesity potency: From mechanism to clinical implications. *Biosci. Rep.* **2017**, *37*. [[CrossRef](#)] [[PubMed](#)]
28. Chopra, B.; Dhingra, A.K.; Kapoor, R.P.; Prasad, D.N. Piperine and its various physicochemical and biological aspects: A review. *Open Chem. J.* **2016**, *3*, 75–96. [[CrossRef](#)]
29. Barbosaa, A.F.; de Carvalho, M.G.; Smithb, R.E.; Sabaa-Srura, A.U.O. *Spilanthes*: Occurrence, extraction, chemistry and biological activities. *Rev. Bra. Farmacogn.* **2016**, *26*, 128–133. [[CrossRef](#)]
30. Jeon, S.M. Regulation and function of AMPK in physiology and diseases. *Exp. Mol. Med.* **2016**, *15*, e245. [[CrossRef](#)]
31. Dordevic, A.L.; Konstantopoulos, N.; Cameron-Smith, D. 3T3-L1 Preadipocytes exhibit heightened monocyte-chemoattractant protein-1 response to acute fatty acid exposure. *PLoS ONE* **2014**, *9*, e99382. [[CrossRef](#)]
32. Na, H.Y.; Seol, M.H.; Kim, M.; Lee, B.C. Effect of soybean on obesity, insulin resistance, and nonalcoholic fatty liver disease of high-fat diet-fed C57BL/6 mice. *Evid. Based Complement. Altern. Med.* **2017**, *2017*, 4658543. [[CrossRef](#)] [[PubMed](#)]
33. Seyedan, A.; Mohamed, Z.; Alshagga, M.A.; Koosha, S.; Alshawsh, M.A. *Cynometra cauliflora* Linn. Attenuates metabolic abnormalities in high-fat diet-induced obese mice. *J. Ethnopharmacol.* **2019**, *23*, 173–182. [[CrossRef](#)]
34. Crujeiras, A.B.; Carreira, M.C.; Cabia, B.; Andrade, S.; Amil, M.; Casanueva, F.F. Leptin resistance in obesity: An epigenetic landscape. *Life. Sci.* **2015**, *140*, 57–63. [[CrossRef](#)]
35. Seoane-Collazo, P.; Ferno, J.; Gonzalez, F.; Dieguez, C.; Leis, R.; Nogueiras, R. Hypothalamic-autonomic control of energy homeostasis. *Endocrine* **2015**, *50*, 276–291. [[CrossRef](#)] [[PubMed](#)]
36. Vasilenko, M.A.; Kirienkova, E.V.; Skuratovskaia, D.A.; Zatolokin, P.A.; Mirnyuk, N.I.; Litvinova, L.S. The role of production of adiponectin and leptin in the development of insulin resistance in patients with abdominal obesity. *Dokl. Biochem. Biophys.* **2017**, *475*, 271–276. [[CrossRef](#)]
37. Lodhi, I.J.; Yin, L.; Jensen-Urstad, A.P.L.; Funai, K.; Coleman, T.; Baird, J.H. Inhibiting adipose tissue lipogenesis reprograms thermogenesis and PPAR γ activation to decrease diet-induced obesity. *Cell Metab.* **2012**, *8*, 189–201. [[CrossRef](#)]
38. Jung, U.J.; Choi, M.S. Obesity and its metabolic complications: The role of adipokines and the relationship between obesity, inflammation, insulin resistance, dyslipidemia and nonalcoholic fatty liver disease. *Int. J. Mol. Sci.* **2014**, *15*, 6184–6223. [[CrossRef](#)] [[PubMed](#)]
39. Veryser, L.; Taevernier, L.; Joshi, T.; Tatke, P.; Wynendaele, E. Mucosal and blood-brain barrier transport kinetics of the plant N-alkylamide *spilanthes* using in vitro and in vivo models. *BMC Complement. Altern. Med.* **2016**, *16*, 177. [[CrossRef](#)] [[PubMed](#)]
40. Hu, Z.; Cha, S.H.; Chohann, S.; Lane, M.D. Hypothalamic malonyl-CoA as a mediator of feeding behavior. *Proc. Natl. Acad. Sci.* **2003**, *100*, 12624–12629. [[CrossRef](#)] [[PubMed](#)]
41. Odle, A.K.; Haney, A.; Allensworth-James, M.; Akhter, N.; Childs, G.V. Adipocyte versus pituitary leptin in the regulation of pituitary hormones: Somatotropes develop normally in the absence of circulating leptin. *Endocrinology* **2014**, *155*, 4316–4328. [[CrossRef](#)] [[PubMed](#)]
42. Barateiro, A.; Mahú, I.; Domingos, A.I. Leptin resistance and the neuro-adipose connection. *Front. Endocrinol.* **2017**, *8*, 45. [[CrossRef](#)] [[PubMed](#)]





Review

Apoptotic or Antiproliferative Activity of Natural Products against Keratinocytes for the Treatment of Psoriasis

Tse-Hung Huang^{1,2,3,4,†}, Chwan-Fwu Lin^{5,6,7,†}, Ahmed Alalaiwe⁸, Shih-Chun Yang⁹ and Jia-You Fang^{6,7,10,11,*} 

- ¹ Department of Traditional Chinese Medicine, Chang Gung Memorial Hospital, Keelung 204, Taiwan; huangtsehung@gmail.com
- ² School of Traditional Chinese Medicine, Chang Gung University, Kweishan, Taoyuan 333, Taiwan
- ³ Graduate Institute of Health Industry Technology, Chang Gung University of Science and Technology, Kweishan, Taoyuan 333, Taiwan
- ⁴ School of Nursing, National Taipei University of Nursing and Health Sciences, Taipei 112, Taiwan
- ⁵ Department of Cosmetic Science, Chang Gung University of Science and Technology, Kweishan, Taoyuan 333, Taiwan; cflin@mail.cgust.edu.tw
- ⁶ Research Center for Food and Cosmetic Safety and Research Center for Chinese Herbal Medicine, Chang Gung University of Science and Technology, Kweishan, Taoyuan 333, Taiwan
- ⁷ Department of Anesthesiology, Chang Gung Memorial Hospital, Kweishan, Taoyuan 333, Taiwan
- ⁸ Department of Pharmaceutics, College of Pharmacy, Prince Sattam Bin Abdulaziz University, Al Kharj 11942, Saudi Arabia; alalaiwe@gmail.com
- ⁹ Department of Cosmetic Science, Providence University, Taichung 433, Taiwan; yangsc@pu.edu.tw
- ¹⁰ Pharmaceutics Laboratory, Graduate Institute of Natural Products, Chang Gung University, Kweishan, Taoyuan 333, Taiwan
- ¹¹ Chinese Herbal Medicine Research Team, Healthy Aging Research Center, Chang Gung University, Kweishan, Taoyuan 333, Taiwan
- * Correspondence: fajy@mail.cgu.edu.tw; Tel.: +886-3-211-8800; Fax: +886-3-211-8236
- † These authors contributed equally to this work.

Received: 1 May 2019; Accepted: 23 May 2019; Published: 24 May 2019



Abstract: Natural products or herbs can be used as an effective therapy for treating psoriasis, an autoimmune skin disease that involves keratinocyte overproliferation. It has been demonstrated that phytomedicine, which is used for psoriasis patients, provides some advantages, including natural sources, a lower risk of adverse effects, and the avoidance of dissatisfaction with conventional therapy. The herbal products' structural diversity and multiple mechanisms of action have enabled the synergistic activity to mitigate psoriasis. In recent years, the concept of using natural products as antiproliferative agents in psoriasis treatment has attracted increasing attention in basic and clinical investigations. This review highlights the development of an apoptotic or antiproliferative strategy for natural-product management in the treatment of psoriasis. We systematically introduce the concepts and molecular mechanisms of keratinocyte-proliferation inhibition by crude extracts or natural compounds that were isolated from natural resources, especially plants. Most of these studies focus on evaluation through an *in vitro* keratinocyte model and an *in vivo* psoriasis-like animal model. Topical delivery is the major route for the *in vivo* or clinical administration of these natural products. The potential use of antiproliferative phytomedicine on hyperproliferative keratinocytes suggests a way forward for generating advances in the field of psoriasis therapy.

Keywords: natural product; psoriasis; keratinocyte; apoptosis; proliferation; mechanism of action

1. Introduction

Psoriasis vulgaris is a genetic autoimmune disorder that manifests in the skin. Clinically, red plaques with silver or white multilayered scales characterize psoriasis, with a thickened acanthotic epidermis in patients who are markedly demarcated by adjacent nonlesional skin. Patients commonly report the symptoms of itching, pain sensation, and bleeding [1]. This disease has the features of high prevalence, chronicity, disfiguration, disability, and comorbidity [2]. Psoriasis can occur at any skin site, though it mostly features on the elbows and knees, back, trunk, and scalp. The fingernail and toenail regions are also often affected. The histopathological observation of psoriastic lesions reveals epidermal acanthosis, rete ridges, immune-cell infiltration in the dermis, and increased angiogenesis (Figure 1). The acanthosis is determined by keratinocyte proliferation that is associated with the altered differentiation procedure, as the maturation of keratinocytes occurs from the basal to the cornified layer [3]. Patients suffering from psoriasis are at risk of developing comorbid diseases. These include psoriatic arthritis, diabetes, cardiovascular disorders, Crohn's disease, lymphoma, anxiety, and depression [4]. In addition, psoriasis always reduces the quality of life, and patients are exposed to social stigma and discrimination [5]. Psoriasis affects 2% to 3% of the population worldwide [6]. The prevalence of psoriasis has a median percentage of 1.43%, according to the global regional data [7]. Michalek et al. [8], summarizing the data from 20 countries, estimate that the prevalence of psoriasis in adults ranges from 0.5% to 11.4%, and in children from 0.1% to 1.4%. Psoriasis is equally prevalent in males and females, though a recent study demonstrates a more severe form in men than in women [9].

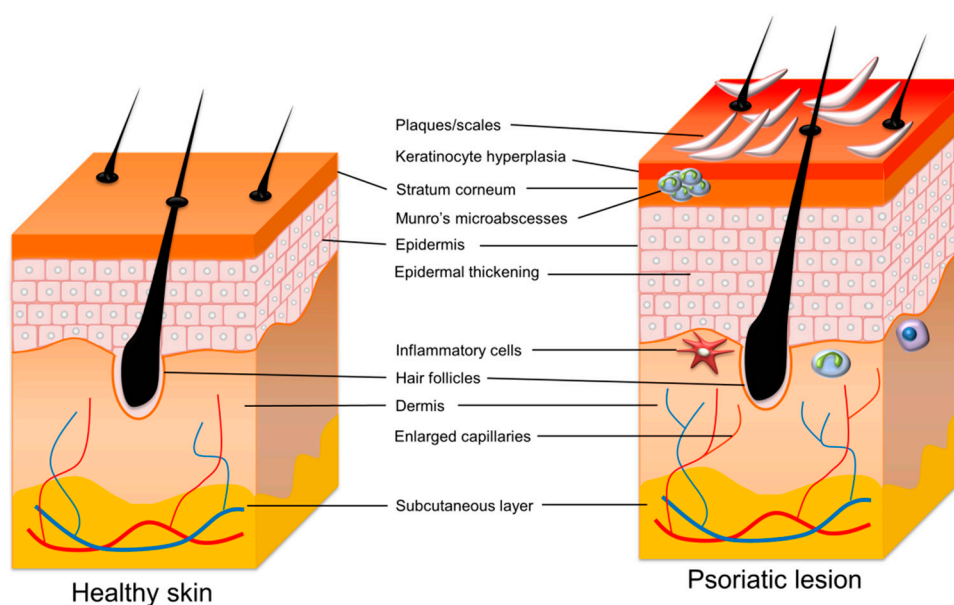


Figure 1. The comparison of healthy skin and psoriatic skin.

Psoriasis is an inflammatory skin disease that is derived from genetics, epigenetics, environments, and lifestyles. Different triggers, such as trauma, infection, drugs, and stress, can activate the immuno-inflammatory response in the skin, leading to excessive keratinocyte proliferation [10]. The initiation of psoriatic plaque starts with immune stimulation in susceptible subjects due to the exogenous triggers or the loss of immune tolerance via the recognition of autoantigens [11]. The antigens are presented to CD4⁺ and CD8⁺ T cells by dendritic cell (DC) subsets. Tumor necrosis factor (TNF)- α and interleukin (IL)-23 released by the activated DCs drive the polarization and clonal expansion of CD4⁺ and CD8⁺ IL-17- and IL-22-producing T lymphocytes, which results in the creation of a considerable amount of IL-17 and IL-22 in psoriatic lesions [12]. There are five types of psoriasis: plaque psoriasis, eruptive psoriasis, inverse psoriasis, pustular psoriasis, and erythrodermic psoriasis.

The most common form is plaque psoriasis, with more than 80% of patients presenting erythematous scaly plaque [10]. Clinical finding, but not biopsy often, makes the diagnosis of psoriasis. Psoriasis Area and Severity Index (PASI), based on the presence of erythema, thickness, infiltration, scaling, and the extent of the lesions, quantify the severity of the disease [13]. The easy-to-use scores, such as the Psoriasis Global Assessment (PGA) and Lattice System-Physicians Global Assessment (LS-PGA), are also employed in routine clinical practice [14]. Various psoriasis-screening methods, including the Psoriatic Arthritis Screening and Evaluation (PASE) questionnaire, the Toronto Psoriatic Arthritis Screening (ToPAS) questionnaire, and the Psoriasis Epidemiology Screening Tool (PEST), are helpful with the diagnosis. The sensitivity of the three tools is reportedly similar (74.5%~76.6%) [15].

Although psoriasis has long been considered to be an immune-cell-dependent disease, keratinocytes' critical role in inducing the early pathogenic events and sustaining the prolonged phase of the disorder cannot be ignored [16]. The hyperproliferation and abnormal differentiation as a secondary phenomenon elicited by the immune response is the pathogenic function of keratinocytes in psoriasis. Keratinocytes respond to the psoriatic lesions with an overactive wound-healing procedure. This process can produce epidermal thickening and expansion into the papillary dermis. Normally, the skin cells mature and shed from the cutaneous surface every 30 days. However, this maturation period shortens to three to six days, and it moves to the cutaneous surface as psoriasis develops [17]. The activated keratinocytes in psoriasis also play an important role in stimulating immune-cell infiltration. IL-1 α that is derived from keratinocytes represents an additional inducer of innate immunity, favoring the migration of monocytes and neutrophils in the early stage of papule formation. The chemokine chemerin that is released by the keratinocytes is responsible for the accumulation of BDCA-2⁺ plasmacytoid DCs into early psoriatic skin [18]. Hence, the inhibition of keratinocyte proliferation or the promotion of keratinocyte apoptosis is a feasible approach to mitigating psoriatic lesions. Many patients have not responded to conventional psoriasis therapy, or, until now, even to the best available therapy. The use of complementary and alternative medicine (CAM) can be an efficient way to provide patients with multiple choices for psoriasis treatment. CAM includes dietary supplements, herbal therapy, traditional Chinese medicine, and mind intervention [19]. A preference for natural sources, the lower risk of adverse effects, and dissatisfaction with conventional therapy can be the reasons for which patients select CAM to treat psoriasis. In the epidermis, more than 90% of cells are keratinocytes. They are stratified into five layers: the stratum basale, spinosum, granulosum, lucidum, and corneum. Keratinocytes are an essential target for psoriasis treatments while using natural products. This review aimed to summarize the therapeutic efficacy and delivery/targeting potency of natural products, including crude extracts and pure compounds, on psoriasis vulgaris.

2. Molecular Pathogenesis of Psoriasis

Some exogenous triggers can lead to the occurrence of psoriasis. These nonspecific triggers include trauma, scratching, sunburn, and chemical irritants. Some drugs, such as lithium, non-steroidal anti-inflammatory drugs, β blockers, and antimalarials, are reported to exacerbate this disorder [20]. Occupational risk that impairs the nature of the cutaneous barrier subsequently aggravates psoriasis. Human immunodeficiency virus (HIV) is also a trigger for psoriasis. The HIV-infected patients with pre-existing psoriasis usually show a flare-up of lesions, which is complicated to manage [21]. Skin is a very complex organ with different cell types and neuroendocrine property for maintaining homeostasis [22]. Several cells in the skin are involved in the pathogenesis of psoriasis, with keratinocytes and immune cells being the major cell types related to psoriasis. Both of these can form a vicious psoriasis-producing cycle. Some autoantigens that are derived from keratinocytes, such as the LL37 cathelicidin/nucleic acid complex and the newly generated lipid antigen, are identified as launching the initial T cell activation, especially the subset of T lymphocyte-expressing IL-17A (Th17 cells). Once stimulated, the Th17 cells release the mediators, such as IL-17A, IL-17F, and IL-22, to elicit keratinocyte proliferation and inflammatory-marker production. Subsequently, the activated keratinocytes generate antimicrobial peptides, cytokines, and chemokines as chemoattractants

for infiltrating the immune cells; this infiltration, in turn, amplifies the immune responses [23]. The chemoattractants that were derived from keratinocytes can activate the recruitment of plasmacytoid DCs, T cells, macrophages, and neutrophils to cause skin inflammation. The chronic inflammation within the skin also promotes skin aging [24,25].

DCs are the most potent antigen-presenting cells (APCs) of the immune system. There are significant increases of myeloid CD11c⁺ DCs in inflamed psoriatic skin. The plasmacytoid DCs are also largely present in psoriatic skin. The activated dermal DCs are important for initiating psoriatic plaque via the production of TNF, IL-12, and IL-23, and the excitation of the autoimmune CD4⁺ and CD8⁺ T cells [26]. Upon activation, the CD4⁺ and CD8⁺ T cells proliferate and migrate to the epidermis, where they recognize autoantigens and generate IL-17 and IL-22 [27]. Psoriatic lesions can be characterized by a marked accumulation of CD4⁺ T cells in the dermis and CD8⁺ T cells in the epidermis. Most of the epidermal CD8⁺ T cells express CD103, which is an integrin binding to E-cadherin to facilitate CD8⁺ T cell migration into the epidermis [28]. The naïve T cells also infiltrate the psoriatic lesions. Keratinocytes and APCs in the epidermis and dermis activate these cells, respectively. The cytokines contribute to expanding T cell infiltration by both modulating T cell proliferation and apoptosis and increasing the resistance of effector T cells to regulatory immunosuppression [29]. The plaque also comprises a large number of macrophages that secrete IL-6, IL-12, IL-23, and inducible nitric oxide synthase (iNOS). The macrophages have been proven to be the predominant source of TNF- α needed to initiate the inflammatory response for psoriasis-phenotype development [30]. Neutrophils are a characteristic component of lesional psoriatic skin. The activated neutrophils are recruited into the stratum corneum in the early stage and they create focal aggregates, called Munro's microabscesses [31]. The enhancement of TNF- α and IL-17 signaling in the psoriatic plaque drives the neutrophil accumulation into the inflamed skin area, activating keratinocytes to release chemokine (C-X-C motif) ligand (CXCL)1, CXCL2, CXCL3, CXCL5, and IL-8 [32]. In turn, neutrophils produce reactive oxygen species (ROS), IL-17, cathelicidin, and neutrophil extracellular traps (NETs) as proinflammatory signals to reduce the inflammation.

The TNF- α - and IL-23/Th17-dependent pathways are regarded as vital for psoriasis development. TNF- α is a pro-inflammatory cytokine that amplifies inflammation via several distinct pathways. This cytokine is produced through a number of cells, such as keratinocytes, lymphocytes, macrophages, and endothelial cells [33]. TNF- α increases the upregulation of adhesion molecules and secondary mediators, both of which are related to the development of psoriasis. Thus, the successful outcome of TNF- α 's blocking biologics in treating psoriasis is not surprising [34]. The exploration of the role of IL-17 and IL-23 in psoriasis pathogenesis has led to the understanding of immune events in this disease and a paradigm shift in the drug therapy. IL-23 largely acts on memory T lymphocytes, because the IL-23 receptor is absent in the naïve T cells. Other cytokines, such as IL-9, also support Th17-related inflammation. Under the regulation of IL-23, T lymphocytes that contain a high level of IL-17 form a self-amplifying and feed-forward inflammatory response in keratinocytes, which establishes a thickened epidermis with a cluster of immune-cell infiltration [35]. Figure 2 illustrates the mechanisms of psoriasis development at the cellular and molecular levels.

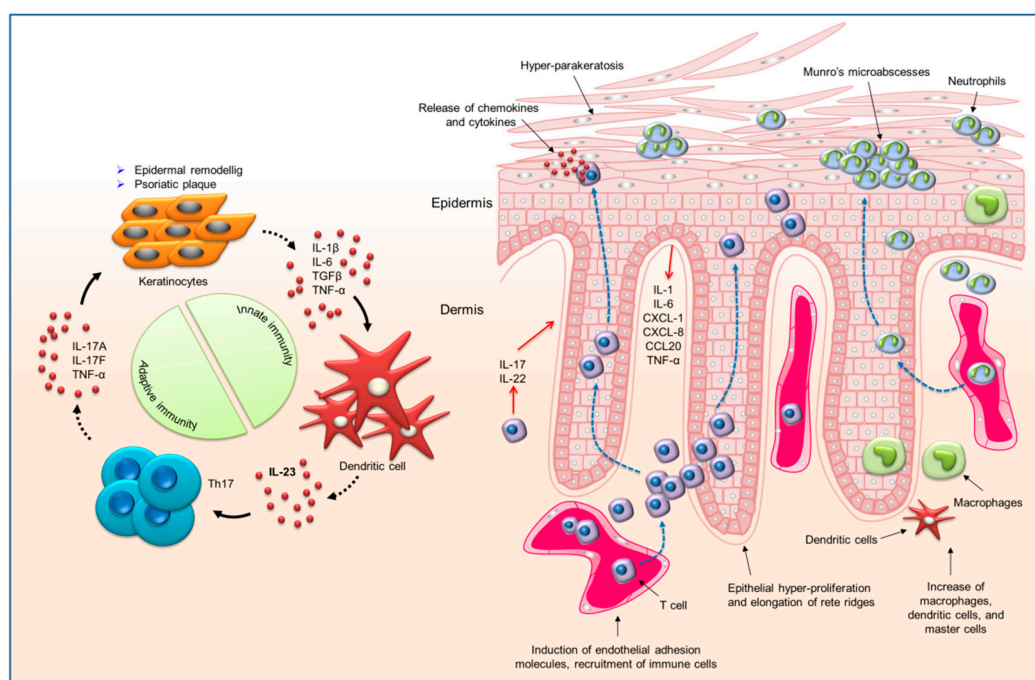


Figure 2. The cell types involved in psoriasis pathogenesis and the related pathways and interactions.

3. Therapeutic Drug Approaches for Psoriasis

Currently, the conventional therapies for psoriasis vulgaris can be divided into topical administration, systemic therapy, and biologics. The topical administration includes topical drugs and phototherapy. Some evidence-based guidelines are established for the management of psoriasis, including the North American guidelines, the International European guidelines, and the German S3 guidelines [2,36]. Approximately 70% of psoriasis patients present mild to moderate severity [37]. Topical treatment is recommended as the first-line therapy for the mild to moderate forms. The use of topical drugs in antipsoriatic therapy includes calcineurin inhibitors, steroids, vitamin D₃ derivatives, retinoids, keratolytic agents, dithranol, and coal tar. The selection of topical treatment depends on the patient's needs, the type of psoriasis, the lesional site, the cosmetic acceptability, and the duration that is available for application [38]. Topical calcineurin inhibitors, such as tacrolimus and pimecrolimus, are employed for the sites that are difficult to treat, e.g., the intertriginous region and the face. Potent corticosteroids are ideal for scalp treatment, which is also difficult. Vitamin D₃ analogs, such as calcipotriol, calcitriol, and tacalcitol, are effective in treating psoriasis via the normalization of keratinocyte proliferation and differentiation. In addition, the vitamin D₃ analogs inhibit the inflammatory response by modulating the immune events [39]. A combination of topical corticosteroids and vitamin D₃ analogs has reportedly shown a synergistically effective treatment of psoriasis [40]. The keratolytic agents include salicylic acid, lactic acid, and urea. They disrupt intra-keratinocyte adhesion in the uppermost layer of the epidermis to promote physiological shedding [41]. Phototherapy, such as ultraviolet B irradiation and psoralens plus ultraviolet A exposure (PUVA), can be classified as topical therapy for psoriasis. Photochemotherapy is one of the oldest therapies for psoriasis employing PUVA. It is useful for treating psoriasis due to the direct antiproliferative effect on keratinocytes [42]. The psoralens bind to the DNA, in which pyrimidine bases are the targets for photochemical apoptosis [43]. Table 1 summarizes the conventional therapeutic approaches for psoriasis treatment via topical application.

Table 1. Current topical drug therapy for psoriasis treatment.

Drug	Pharmacological Mechanisms	Side Effects on Skin
Calcineurin inhibitors	Inhibition of T cell activation and of pro-inflammatory cytokine synthesis	Itching and stinging
Glucocorticosteroids	Anti-inflammation, anti-mitosis, apoptosis, vasoconstriction, and immunomodulation	Skin atrophy after long term use
Vitamin D ₃ derivatives	Regulation of keratinocyte proliferation, differentiation and apoptosis	Stinging, burning, and peeling skin
Retinoids	Normalization of keratinocyte proliferation and differentiation	Redness, peeling, dryness, itching, and burning sensation
Keratolytics	Softening/hydration of the stratum corneum and desquamation of hyperkeratotic skin	Redness, swelling, tenderness, and pustules
Dithranol	Inhibition of keratinocyte proliferation and hyperproliferation, granulocyte function, and immune response	Redness and irritation
Coal tar	Inhibition of keratinocyte proliferation and correction of the defect of keratinocyte differentiation	Redness, burning, itching, and skin staining
Ultraviolet B irradiation (UVB)	Alteration of cytokine profile, induction of apoptosis, and promotion of immunosuppression	Burning and itching
Psoralens plus ultraviolet A exposure (PUVA)	Inhibition of DNA replication and production of cell cycle arrest, alteration in the expression of cytokines	A risk for skin cancer

The systemic drugs are another choice for achieving efficient psoriasis treatment. Patients with the moderate or severe form or associated psoriatic arthritis, and those who do not adequately respond to topical therapy, may be treated with systemic drugs, such as cyclosporin, methotrexate, retinoids, and fumarates [44]. Caution should be taken, because severe side effects can complicate systemic therapy. For example, methotrexate demonstrates the risk of hepatotoxicity. With appropriate monitoring, systemic therapy can be used for the maintenance treatment of psoriasis. Selective phosphodiesterase (PDE)4 inhibitors have gained great attention for their anti-inflammatory activity in neutrophils in the treatment of psoriasis [45]. PDE4 inhibitors are reported to reduce neutrophil infiltration and hyperkeratosis in psoriasis [46]. Apremilast is a new systemic agent of PDE4 inhibitor that is approved for oral administration to treat psoriasis.

Increasing knowledge regarding the molecular pathogenesis of psoriasis has hastened the development of targeted therapy for psoriasis with monoclonal antibodies. These biologics target cytokines or specific inflammatory pathways, such as TNF- α , IL-17, and IL-23, to achieve highly selective immune suppression [47]. The biologics reveal superior therapy efficiency when compared to the other classes of antipsoriatic agents for patients with severe psoriasis. The biologic therapy has proven to be highly effective in improving psoriasis in 80% to 90% of patients [12]. TNF- α inhibitors etanercept, adalimumab, and infliximab are approved for moderate-to-severe psoriasis management. Secukinumab, ixekizumab, and brodalumab are the antibodies targeting IL-17 for the treatment of psoriasis. The antibody guselkumab is directed against IL-23. Ustekinumab is an antibody targeting p40 subunit that IL-12 and IL-23 share. All of these antibodies are used for long-term psoriasis treatment with negligible evidence of cumulative toxicity and drug interaction [48]. The combination of biologics with other drug therapy allows for dosage reduction, side-effect minimization, maintenance of initial response of biologics, and acceleration of the response to biologics [49]. For example, the efficacy of methotrexate against psoriasis is increased with greater safety when used in combination with biologics [50]. A major concern that is associated with using biologics is the possible risk of developing nonmelanoma skin cancer [51]. Monoclonal antibodies should be avoided in patients with active malignancy.

4. The Trend in Using Natural Products as Antipsoriatic Agents

Although most of the conventional therapies can reduce the symptoms of psoriasis, this disease has no known cure. Moreover, many therapies cause side effects, such as atrophy, organ toxicity,

immunosuppression, infection, and carcinogenesis, which lead to the limitation of long-term use. It is necessary to develop alternative treatments for psoriasis to achieve the aims of superior effectiveness and fewer side effects. Natural medicine has gained much attention in the search for novel therapies. Natural products possess a richness of resources containing potentially bioactive compounds [52]. Herbal medicine is preferable for patients because it is safe. The herbal products' structural diversity and multiple mechanisms of action have led to the synergistic activity that mitigates psoriasis. The herbal drugs can also increase the bioavailability due to the possibility of the presence of permeation enhancers inside the phytomedicine. The two topicals that are most frequently used by psoriasis patients in North and South America are reportedly steroids (16% to 79%) and CAM (10% to 62%) [53]. The utilization of CAM in the psoriasis patient population ranges from 39% to 62% in Asia and the Middle East [54]. Damevska et al. [55] reported that 47% of patients in South Europe use CAM as an antipsoriatic remedy. All of these data encourage the investigators to find the antipsoriatic agents from the traditional phytomedicine. Some clinical trials have been conducted by employing natural products to examine the effect of psoriasis mitigation. The meta-analysis of the clinical trials demonstrates that aloe vera, indigo naturalis, kukui nut oil, *Mahonia aquifolium*, and capsaicin are the most efficacious topical phytomedicines for treating psoriasis [56,57]. These natural products can ameliorate psoriatic lesions via the molecular mechanisms that are related to apoptosis, angiogenesis inhibition, and inflammation suppression [58].

Aloe vera is a perennial succulent plant that belongs to the *Liliaceae* family. Anthraquinones, polysaccharides, vitamins, and salicylic acid are the active ingredients of aloe vera exhibiting anti-inflammatory and anti-pruritic activities [59]. Topical indigo naturalis ointment is effective in reducing the PASI of psoriasis patients due to the anti-inflammatory and antiproliferative activities of indirubin in this extract [60]. Kukui nut oil, which is rich in polyunsaturated fatty acids, especially oleic acid, linoleic acid, and linolenic acid, displays an anti-inflammatory effect [61]. *Mahonia aquifolium*, well known as Oregon grape, belongs to the *Berberidaceae* family. The extract of *Mahonia aquifolium* contains the primary active agent of berberine, which is an isoquinoline alkaloid that inhibits hyperproliferation and inflammation in psoriatic lesions [62]. Substance P is sensitive in the case of psoriatic lesions in stimulating inflammatory cells to induce keratinocyte proliferation, vasodilation, and angiogenesis. Capsaicin can activate substance P due to the affinity to vanilloid receptors, and it then depletes the cutaneous sensory neurons of substance P. This feature improves the redness and pruritus in psoriasis patients [63].

5. The Apoptotic or Antiproliferative Strategy to Ameliorate Psoriasis

It is supposed that the pathogenic pathways mainly involve keratinocytes in the beginning of psoriasis development. Upon activation by some triggers, such as mild trauma and pathogens, keratinocytes become a source of innate immune mediators [64]. In the chronic stage, the activation of DCs and effector T cells in the lesions establishes definite cytokines, which TNF- α , IL-17, IL-22, and interferon (IFN)- γ mainly represent. Keratinocytes contain cytokine receptors and potently respond by further releasing cytokines. The keratinocytes exhibit altered proliferation and differentiation under the impact of these cytokines [17]. The homeostasis between proliferation and differentiation is disrupted in psoriasis. The increased epidermal proliferation markers, such as Ki-67 and the proliferating cell nuclear antigen (PCNA), and the reduced differentiation markers, such as keratin 10, can describe the psoriatic plaque [65]. An increased resistance to apoptosis is also observed in the activated keratinocytes [66]. The keratinocyte proliferation that is induced by the cytokines contributes to thickened skin, a scaly surface appearance, epidermal hyperplasia, hyperkeratosis, and parakeratosis. The imbalance between proliferation and differentiation becomes a self-amplifying cycle, where the cytokines and altered homeostasis act on the immune cells to perpetuate the inflammatory response. An ideal agent for treating psoriasis should have the role in antiproliferation, anti-inflammation, and immunomodulation. Melatonin is an example, which is a natural hormone with the integration of

proliferation and inflammation suppression in the activated keratinocytes [67–69]. Figure 3 shows the apoptotic mechanisms of keratinocytes in the psoriatic lesion.

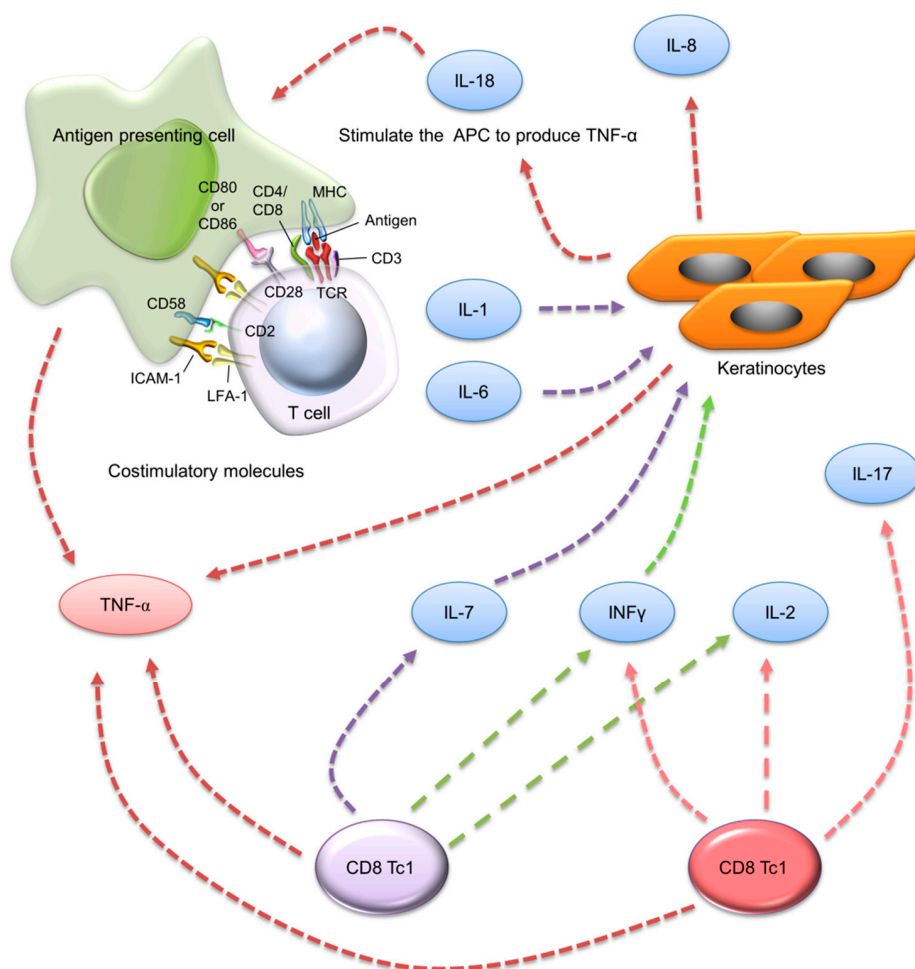


Figure 3. The apoptotic mechanisms of keratinocytes in psoriatic lesion.

The keratinocyte-proliferation inhibition, modulation of keratinocyte differentiation, and apoptosis are been considered to be the therapeutic targets of psoriasis inhibition for both approved drugs and unapproved phytomedicines [70]. The prescribed antipsoriatic drugs, such as dithranol, vitamin D₃ derivatives, and methotrexate, exhibit the therapeutic effect through restraining keratinocyte hyperproliferation or regulating keratinocyte differentiation. Among these agents, the vitamin D₃ analogs are the most commonly used clinically. The topically applied vitamin D₃ analogs can arrest the hyperproliferation of keratinocytes. Vitamin D₃ acts chiefly on the vitamin D receptor to regulate cell growth, differentiation, and immune function, as well as calcium and phosphorus metabolism [71]. The established phototherapies for psoriasis include narrowband UVB and PUVA. Phototherapy is one of the most efficient options for treating psoriasis. Apoptosis and immune suppression are the predominant mechanisms of action for diminishing psoriatic lesions by phototherapy [72]. PUVA induces apoptosis through the creation of ROS to impair the cellular, mitochondrial, and nuclear membranes. PUVA also directly causes linkage of psoralen to pyrimidine bases, leading to DNA-synthesis inhibition [73]. Besides inducing apoptosis in keratinocytes, phototherapy also induces apoptosis in T cells and Langerhans cells [74]. Although phototherapy is very effective for psoriasis treatment, its time-consuming nature and short-term control of the disease have limited its application. The possibility of carcinogenesis of PUVA also restricts its long-term use. The unpleasant side effects and practical difficulty for psoriasis patients limit the topical use of dithranol and vitamin

D₃ derivatives. The search for new antiproliferative agents with low toxicity and an effective outcome remains urgent. Natural products provide an abundant resource for achieving this goal.

6. Natural Products for Antiproliferation against Keratinocytes

The recent application of natural medicine derived from plants confirms the capability to exert an apoptotic or antiproliferative effect on keratinocytes. The use of natural products ameliorates the symptoms of psoriasis vulgaris. Some natural products have been approved for clinical use or they are under clinical trial for preventive or therapeutic use against psoriasis. In addition, some herbal formulations and natural compounds are approved for managing psoriasis in cell-based and animal studies. The following describes the different therapeutic approaches to using natural products against psoriasis through apoptosis and/or hyperproliferation inhibition. We divided the natural products into two classes: crude extracts and pure compounds.

6.1. Crude Extracts for Treating Hyperproliferation of Psoriasis

The crude extracts from the natural resources under discussion are the concentrates derived from plant or animal sources. There can be different compounds in the crude extracts showing bioactivity. The combination of these bioactive agents in the extracts may be beneficial for displaying the synergistic effect for treating diseases. The usefulness of crude extracts in treating hyperproliferation of psoriasis has been investigated. Most of these extracts have been used to treat inflammatory diseases in traditional or folk medicine. Traditional Chinese medicine is extensively employed with high effectiveness and safety in the treatment of psoriasis. Tse et al. [75] investigated the antiproliferative effect of 60 Chinese medicinal materials, which are prescribed in Chinese medicine practice for psoriasis management, on keratinocytes (HaCaT), in vitro. These medicinal materials were extracted with 80% ethanol/water for a 3-(4,5-cimethylthiazol-2-yl)-2,5-diphenyl tetrazolium bromide (MTT) assay. Three materials, *Rubia cordifolia*, realgar, and *Coptis chinensis*, were effective in showing antiproliferative potency with an IC₅₀ of 1.4, 6.6, and 23.4 µg/mL, respectively. Nevertheless, the realgar extract induced a modest inhibition of dermal fibroblast (Hs-68) growth with an IC₅₀ of 48.1 µg/mL, which demonstrated cytotoxicity against normal cells. Tse et al. [76] further explored the molecular mechanisms of antiproliferative activity against HaCaT by *R. cordifolia*. The IC₅₀ were >62.5, 18.3, 11.9, 5.8, 1.4, and 2.9 µg/mL for the treatment of *R. cordifolia* extract by 3, 6, 12, 24, 48, and 72 h, respectively. The percentage of keratinocytes in the sub-G1 phase increased from 0.3% to 15.2% following the increased concentration from 1 to 32 µg/mL. DNA fragmentation was found by gel electrophoresis and TUNEL. *R. cordifolia* could also activate caspase-3 expression. This evidence suggests that the induction of apoptosis was responsible for the antiproliferation that was stimulated by *R. cordifolia*.

Some polyphenols that are rich in the bark of forest trees are effective in the treatment of psoriasis [77]. García-Pérez et al. [78] examined the in vitro antiproliferative activity of Canadian wood species in the growth of primary normal and psoriatic human keratinocytes. The bark of yellow birch (*Betula alleghaniensis*), black spruce (*Picea mariana*), balsam fir (*Abies balsamea*), and jack pine (*Pinus banksiana*) trees was extracted while using 90% ethanol and hot water to obtain polyphenol-rich materials. The extracts of yellow birch and black spruce bark showed higher proliferation suppression than the others. The yellow birch extract at 90 µg/mL inhibited normal keratinocytes by 26%, but failed to affect psoriatic keratinocyte growth. The black spruce extract at 110 µg/mL inhibited the normal and psoriatic keratinocytes by 18% and 21%, respectively. The antiproliferative activity could be due to the presence of proanthocyanidins and hydroxycinnamic acids in the bark extracts. Huaier (*Trametes robiniophila*) is a fungus with potential as an antitumor agent through cell apoptosis [79]. Su et al. [80] evaluated the role of huaier in the treatment of psoriasis via the methodology of in vitro HaCaT growth inhibition. Huaier extract reduced HaCaT viability in a time- and concentration-dependent fashion. The extract concentration at 4, 8, and 16 mg/mL produced a cell viability percentage of about 60%, 40%, and 30%, respectively. The extract also blocked the cell cycle in the G1 phase, which indicated an apoptosis pathway. The oral huaier administration for four weeks efficiently reduced patients' PASI

score by 50%. Shraibom et al. [81] prepared a polyherbal formulation containing *Rheum palmatum*, *Lonicera japonica*, and *Rehmannia glutinosa* (1:1:3) to evaluate in vitro antipsoriatic activity. Chlorogenic acid, acteoside, and rhein were the major compounds in this formulation. The polyherbal formulation inhibited keratinocyte proliferation and elicited apoptosis. The formulation induced an increase in the early and late apoptotic cell percentage by 22- and 52-fold as compared to the control, respectively. DNA fragmentation increased by 1.8-fold when compared to the control cells. The downregulation of pro-inflammatory markers, such as IFN- γ , TNF- α , and IL-6, was also observed.

Malva sylvestris leaf is a medicinal herb that exerts the bioactivity of suppressing inflammation, gastric ulcers, and skin disorders [82]. It is proven to show anti-inflammatory activity in the acute skin inflammation animal model due to the main active compound of malvidin 3-glucoside [83]. Prudente et al. [84] further assessed the effect of the hydroalcoholic extract of *M. sylvestris* on hyperproliferation via in vitro HaCaT and in vivo 12-O-Tetradecanoylphorbol-13-acetate (TPA)-induced inflammation models. The cell viability was reduced by 36% and 91% at extract concentrations of 10 and 100 $\mu\text{g/mL}$, respectively. The cell-cycle profile confirmed the decreased proliferation by apoptosis. In vivo topical application of *M. sylvestris* caused an oedema reduction of 65%. The extract produced a decline of PCNA-positive cells by 66%, while the positive control (dexamethasone) showed a reduction of 92%. *Artemisia capillaris* is a phytomedicine that contains chlorogenic acids, coumarins, and flavonoids as the actives to exhibit therapeutic potential against cancers, hepatitis, malaria, obesity, and pathogen infection [85]. This herb has been proven to ameliorate atopic dermatitis-like lesions in Nc/Nga mice [86]. The therapeutic potential of the alcohol extract of *A. capillaris* was examined in HaCaT cells and in the imiquimod (IMQ)-induced psoriasis-like mouse model [87]. The IC_{50} of *A. capillaris* extract was 37.5 $\mu\text{g/mL}$ after 72-h incubation. The caspase-3 activity in HaCaT was 1.9-fold higher in the treatment group than in the nontreatment control. The epidermal thickness could be reduced by 55% when compared to the vehicle control after the topical application of *A. capillaris* (50 mg/mL) in the IMQ-treated mouse for four days. The expression of the hyperproliferative marker Ki-67 was also decreased by *A. capillaris*. A problematic alcoholic extract application on the skin is a toxicity-related concern. Lee et al. [88] developed a cream formulation of *A. capillaris* for convenient and safe use. The cream base containing *A. capillaris* lowered the erythema and scaling of the psoriasis-like lesion in the in vivo IMQ-induced model. The histology demonstrated a 49% reduction in the epidermal thickness by using the cream compared to the control group.

Some clinical trials were conducted to evaluate the possibility of the application of herbal materials for psoriasis therapy. The in vitro data verified the ability of the bark extract that was derived from *Mahonia aquifolium* to inhibit HaCaT growth with an IC_{50} of 35 μM based on the alkaloid content with respect to berberine [89]. A psoriatic patient clinical trial was performed to compare the antipsoriatic effect of *M. aquifolium* ointment and dithranol [90]. A half-body randomized controlled trial was used to assess the hyperproliferation markers (keratin 6, keratin 15, and Ki-67) and the adhesion molecules (intercellular adhesion molecule-1) in biopsy. Both of the treatments diminished epidermal and dermal T cell infiltration, with less inhibition by *M. aquifolium*. Lin et al. [91] estimated the efficacy and safety of topically applied indigo naturalis (*Baphicacanthus cusia*) ointment on psoriasis. Indigo naturalis has been utilized for treating various inflammatory conditions and dermatosis in traditional Chinese medicine. Indigo naturalis and its active ingredient indirubin reveal antitumor activity that is involved in the suppression of cancer cell proliferation [92]. In the eight-week trial, in which 14 patients were enrolled, a significant reduction in the clinical score was obtained after the topical administration of indigo naturalis. The biopsy assay showed a marked decrease of Ki-67 and inflammatory marker CD3. The efficacy of the indigo naturalis ointment could be mediated by proliferation and differentiation modulation of the epidermal keratinocytes. *Curcuma xanthorrhiza* is a traditional herbal medicine that belongs to the *Zingiberaceae* family. HaCaT treated with *C. xanthorrhiza* extract demonstrates the capability of inhibiting IL-6, IL-8, and keratinocyte proliferation [93]. A 1% *C. xanthorrhiza* ointment was topically applied on 17 psoriatic patients using a double-blinded randomized trial [94]. *C. xanthorrhiza*

significantly reduced the PASI score after topical application for four weeks. However, K6 expression showed no significant difference between the treatment and the placebo groups.

St. John's wort (*Hypericum perforatum*) is traditionally used for the treatment of burns and diarrhea, and as a diuretic. This extract is topically applied to treat wounds, sunburns, ulcers, keloid scars, and hemorrhoids [95]. Two clinical trials verified the efficacy of St. John's wort for psoriasis therapy. Ten patients with plaque-type psoriasis were enrolled for treatment with St. John's wort [96]. The St. John's wort ointment and the vehicle were topically applied on different sites of each patient twice daily. In estimating the PASI score, the St. John's wort ointment, as compared to the placebo, significantly lowered redness, scaling, and thickness. The PASI for the extract and placebo was 1.8–2.1 and 0.7–1.1, respectively. It was found that St. John's wort effectively mediated the TNF- α -induced apoptosis in keratinocytes in vitro [97]. Mansouri et al. [98] investigated the effect of topically applied St. John's wort on TNF- α expression through a double-blind placebo-controlled trial in 20 psoriatic patients. The histological observation revealed a marked reduction of acanthosis, parakeratosis, Munro's microabscesses, and spongiosis with the treatment using St. John's wort ointment. The TNF- α level in the epidermis, basal layer, and dendritic cells was lessened from 0.58, 1.58, and 0.66 pg/mL to 0.16, 0.92, and 0.25 pg/mL, respectively. Table 2 summarizes the profiles for the antipsoriatic activity of different crude extracts with the aim of inhibiting keratinocyte proliferation.

Table 2. Crude extracts derived from the plants for treating hyperproliferation of psoriasis.

Plant	Experimental Model	Cell or Animal	Method for Detecting Proliferation	Outcomes Offered by Extract	Reference
60 Chinese herbal medicines	In vitro	HaCaT	MTT assay	<i>Rubia cordifolia</i> , realgar, and <i>Coptis chinensis</i> showed high antiproliferative effect	Tse et al. [75]
<i>Rubia cordifolia</i>	In vitro	HaCaT	MTT and TUNEL	Apoptosis is the main mechanism for antiproliferation of HaCaT	Tse et al. [76]
Canadian wood species	In vitro	Normal and psoriatic human keratinocytes	MTT and trypan blue	Yellow birch and black spruce showed high antiproliferative effect	García-Pérez et al. [78]
Huaier	In vitro	HaCaT	CASY cell counting	A significant proliferation inhibition through apoptosis pathway	Su et al. [80]
<i>Rheum palmatum</i> , <i>Lonicera japonica</i> , and <i>Rehmannia glutinosa</i>	In vitro	HaCaT	Annexin-V staining and caspase-3	Antiproliferative and anti-inflammatory activities	Shraibom et al. [81]
<i>Malva sylvestris</i>	In vitro/in vivo	HaCaT/Swiss mouse	MTT assay/TPA-induced inflammation	Inhibition of HaCaT proliferation and oedema caused by TPA	Prudente et al. [83]
<i>Artemisia capillaris</i>	In vitro/in vivo	HaCaT/Balb/c mouse	Annexin-V staining/IMQ-induced lesion	Inhibition of HaCaT proliferation and epidermal thickness caused by IMQ	Lee et al. [87]
<i>Artemisia capillaris</i>	In vivo	Balb/c mouse	IMQ-induced lesion	Reduction of epidermal thickness caused by IMQ	Lee et al. [88]
<i>Mahonia aquifolium</i>	Clinical	Psoriatic patients	Biopsy	Reduction of epidermal and dermal T cell infiltration	Augustin et al. [90]
Indigo naturalis (<i>Baphicacanthus cusia</i>)	Clinical	Psoriatic patients	Clinical score and biopsy	Reduced Ki-67 and CD3	Lin et al. [91]
<i>Curcuma xanthorrhiza</i>	Clinical	Psoriatic patients	Clinical score and K6 expression	Reduced PASI score	Rahmayunita et al. [94]
St. John's wort (<i>Hypericum perforatum</i>)	Clinical	Psoriatic patients	Clinical score	Reduced PASI score	Najafizadeh et al. [96]
St. John's wort (<i>Hypericum perforatum</i>)	Clinical	Psoriatic patients	TNF- α expression	Reduced TNF- α in epidermis and dendritic cells	Mansouri et al. [98]
IMQ, imiquimod; MTT, 3-(4,5-cimethylthiazol-2-yl)-2,5-diphenyl tetrazolium bromide; TPA, 12-O-Tetradecanoylphorbol-13-acetate; TUNEL, terminal deoxynucleotidyl transferase dUTP nick end labeling.					

6.2. Pure Compounds for Treating Hyperproliferation of Psoriasis

The components in crude extracts are usually complex. The difficulty of quality control is a disadvantage of using herbal products for medicinal application. Moreover, some ingredients in the extracts show no or negligible bioactivity. The crude extracts can be further fractionated and separated to exclude the useless parts and acquire the pure compounds with higher bioactivity. This concept approximates the development of drugs. There are many compounds that are derived from the crude extracts for preventing hyperproliferation in psoriasis. Resveratrol is a stilbene

polyphenol from grapes and *Polygonum cuspidatum*. It is well known to present strong anti-inflammatory, anticancer, anti-diabetes, and antioxidant activities [99]. Holian and Walter [100] examined the antiproliferative activity of resveratrol against primary keratinocytes. Resveratrol produced a time- and concentration-dependent proliferation inhibition. The IC_{50} that was detected by hemocytometer cell count was 0.5 μ M. The modulation on the cellular redox state by resveratrol contributed to the antiproliferative effect. Wu et al. [101] further elucidated the role of aquaporin 3 on the antiproliferative mechanism of resveratrol. Aquaporin 3 is a water-transporting protein that is expressed in epidermal keratinocytes. The overexpression of aquaporin 3 leads to keratinocyte proliferation and epidermal thickening [102]. The nontoxic concentrations (<40 μ M) of resveratrol restrained the proliferation of the primary culture of neonatal human keratinocytes. Resveratrol at 40 μ M significantly decreased the aquaporin 3 mRNA level >5-fold. This compound also inhibited the phosphorylation of extracellular signal-regulated kinase (ERK).

Curcumin that is derived from *Curcuma longa* is another active demonstrating an antiproliferative effect on keratinocytes. Curcumin is reported to show anti-inflammation, anticancer, and antioxidant properties [103]. Sun et al. [104] investigated the impact of curcumin on apoptosis of TNF- α -activated HaCaT cells. The expression of anti-apoptotic proteins, including the inhibitor of apoptosis (IAP)1, IAP2, and B-cell lymphoma-extra large (Bcl-xL), was enhanced by TNF- α , but inhibited by 7.37 μ g/mL curcumin. Curcumin also inhibited TNF- α -activated NF- κ B, IL-6, and IL-8. The antiproliferative ability of resveratrol can be enhanced in combination with light irradiation. The HaCaT cells were pretreated with curcumin at 0.1~1 μ g/mL for 1 h and then irradiated with UVA or visible light [105]. The result revealed that the combination of curcumin (1 μ g/mL) and UVA (1 J/cm²) induced 40% of the cells with apoptotic nuclei. This was a much higher percentage than in the group without UVA (0.5%). Cytochrome c released from the mitochondria, caspases-8 and -9 activation, and NF- κ B inhibition represented the induction of apoptosis. Niu et al. [106] investigated the combination of curcumin, red light (630 nm), and blue light (405 nm) for attenuating the proliferation of TNF- α -activated HaCaT, a simulation of psoriasis lesions. The curcumin concentration at 0.16~2.5 μ M showed no proliferation inhibition on keratinocytes. A significant inhibition was observed in the presence of 0.16 and 0.62 μ M curcumin when it was combined with red light and blue light, respectively. The light alone showed no effect on proliferation. This indicated that the light exposure amplified the apoptosis of curcumin-treated keratinocytes. The combined treatment inhibited NF- κ B activity and stimulated caspases-8 and -9 with the preservation of cell-membrane integrity.

Rottlerin is a polyphenol that is purified from *Mallotus philippinensis*. This compound is reported to exert antihypertensive, antifertility, and antiallergic actions [107]. A previous study [108] demonstrated that rottlerin could block the cancer cell proliferation via the downregulation of cyclin D1 and the inhibition of NF- κ B activity. Rottlerin is also a potent suppressor of keratinocyte proliferation through the prevention of basal and hydrogen-peroxide-stimulated NF- κ B elevation [109]. Min et al. [110] investigated the inhibitory effect of rottlerin on primary keratinocyte proliferation. The apoptotic percentage of keratinocytes following treatment with rottlerin at 5 and 10 μ M was 27% and 56%, respectively. The levels of TNF- α , IL-6, and IL-23 were significantly reduced in the TPA-activated keratinocytes after rottlerin treatment. The oral rottlerin also relieved the IMQ-stimulated psoriasiform lesion by suppressing keratinocyte proliferation, immune-cell infiltration, and vascular proliferation. Acridone alkaloids are natural compounds that are purified from the *Rutaceae* family. Many synthetic analogs are developed to evaluate the antitumor effect, because they can inhibit cell growth [111]. The 10-substituted hydroxy-10H-acridin-9-ones are the synthetic derivatives of acridone and they can be regarded as aza-analogs of the antipsoriatic drug dithranol. Putic et al. [112] prepared a series of 10-substituted hydroxy-10H-acridin-9-ones to assess the antiproliferative potency against HaCaT. The compounds with benzyl substitution at the 10-position showed greater growth inhibition than the other substitutions. The most potent compound was the analog possessing N-methyl moiety and 1,3-dihydroxy arrangement at the acridone scaffold. The IC_{50} of this compound (0.6 μ M) was similar to that of dithranol (0.7 μ M). The extract of *R. cordifolia* was proven to induce the apoptosis

of psoriasis-relevant HaCaT cells [76]. 1,4-Dihydroxy-2-naphthoic acid (DHNA) is an anthraquinone precursor that is present in *R. cordifolia* extract. The possible application of DHNA in psoriasis was tested in an in vitro HaCaT model [113]. The IC₅₀ of DHNA (38.9 µg/mL) was higher than that of dithranol (9.4 µg/mL) after 72-h treatment. On the other hand, the cytotoxicity against skin fibroblasts was minor for DHNA when compared to dithranol. This may lead to the conclusion that the use of DHNA is safe. This compound elicited keratinocyte apoptosis via G0/G1 cell-cycle arrest.

Arsenic-containing minerals are considered as therapeutic materials for topical use in the treatment of scabies, carbuncles, herpes zoster, and psoriasis [114]. Three inorganic arsenics were tested to check whether they presented antiproliferative activity on HaCaT [115]. Arsenic trioxide (As₂O₃), arsenic pentoxide (As₂O₅), and arsenic iodide (AsI₃) displayed keratinocyte growth inhibition with IC₅₀ of 2.4, 16.0, and 6.8 µM, respectively. These molecules showed a moderate inhibition of fibroblast viability with the IC₅₀ of 43.4~223.0 µM. All of the arsenics produced DNA fragmentation and caspase-3 activation. Quercetin, a naturally occurring flavonoid, was reported to assist the keratinocyte-growth inhibition that is induced by arsenic trioxide [116]. Quercetin induced apoptosis through ROS generation in different cell systems, including MOLT-4 cells, leukemia cells, and MCF-7 cells [117]. The combined arsenic trioxide and quercetin led to keratinocyte apoptosis by ROS-related p53 protein ubiquitination. The apoptotic markers, such as caspase-3, DNA ladders, and poly (ADP-ribose) polymerase (PARP), were increased by the combination with a decrease of mitochondrial membrane potential. However, the application of arsenic for psoriasis therapy may be hindered due to the possibility of arsenic toxicity inducing skin carcinoma [118]. Baicalein is another flavonoid that regulates keratinocyte differentiation and proliferation [119]. The treatment of HaCaT with baicalein (10 µM) slightly inhibited the proliferation without affecting ROS production, cytochrome c, and apoptosis. Baicalein treatment increased the cell population in the G₀/G₁ phase from 60% to 70%. Baicalein also increased the expression of keratins 1 and 10, which are the indicators of cell differentiation.

Celastrol is a triterpene isolated from *Celastrus orbiculatus*. The extract of *C. orbiculatus* has long been used in Chinese medicine to treat bacterial infection, rheumatoid arthritis, and skin diseases. Zhou et al. [120] evaluated the antiproliferative effect of celastrol on HaCaT cells and primary human keratinocytes. Celastrol inhibited the growth of HaCaT and primary keratinocytes in a concentration-dependent manner, with an IC₅₀ of 1.1 and 2.9 µM, respectively. The IC₅₀ for fibroblasts was 6.8 µM. Celastrol significantly downregulated anti-apoptotic Bcl-2 expression and increased the pro-apoptotic Bcl-2-associated X protein (Bax), which suggests the involvement of both death-receptor and mitochondrial pathways in the apoptotic process. *Salvia miltiorrhiza* extract is employed in treating psoriasis, atopic dermatitis, and inflammation-related diseases [121]. Tanshinone IIA is the major constituent of *S. miltiorrhiza* extract. Li et al. [122] examined the possibility of using tanshinone IIA for keratinocyte apoptosis in connection with exploring the treatment mechanism of psoriasis. The IC₅₀ on the growth of mouse keratinocytes incubated for 24, 48, and 72 h was 4.3, 1.9, and 1.1 µg/mL, respectively. The apoptosis led to S phase arrest, accompanied by a decrease in cyclin A and phospho-cyclin-dependent kinase 2 (pCdk2). A caspase pathway was also involved in the keratinocyte apoptosis. Dehydrocostuslactone and costunolide are sesquiterpene lactones that were isolated from certain plants, such as *Magnolia sieboldii*. Both of the compounds are effective in mitigating inflammation and exerting pro-apoptotic activity [123,124]. Scarponi et al. [125] explored the effect of both naturally occurring lactones on the regulation of inflammation and proliferation of keratinocytes to cytokines. The lactones suppressed proliferation and cell-cycle progression-related gene expression, as the compounds enhanced cell-cycle arrest and apoptosis. Dehydrocostuslactone and costunolide decreased the inflammatory and regulatory genes in IL-22-activated keratinocytes, including C-C motif chemokine Ligand 2 (CCL2), C-X-C motif chemokine 10 (CXCL10), and intercellular adhesion molecule 1 (ICAM-1). These findings encourage the further application of psoriasis therapy.

Delphinidin is an anthocyanidin that provides the primary plant pigment and it serves as an antioxidant. Delphinidin has been determined as a possible treatment for psoriasis, because it can inhibit inflammation and regulate keratinocyte differentiation [126]. A three-dimensional (3D) reconstructed

human psoriasis skin equivalent was employed as a model to investigate the change in the proliferation and inflammation by delphinidin [127]. A prolonged treatment of delphinidin at 20 μ M on the skin equivalent for five days greatly inhibited the expression of the proliferation biomarkers Ki-67 and PCNA. Delphinidin also inhibited inflammatory biomarkers, including iNOS, S100A7-psoriasin, and S100A15-koebnerisin, which are usually found in psoriatic lesions. *Rhodomyrtus tomentosa* is a plant that belongs to the *Myrtaceae* family. The leaves of *R. tomentosa* have been traditionally used to treat a number of diseases, including diarrhea, infection, and open wounds. Rhodomyrtone is a major active of *R. tomentosa* extract, which demonstrates antibacterial, anti-inflammatory, and immunomodulatory properties [128]. Chorachoo et al. [129] investigated whether rhodomyrtone could affect the proliferation, growth arrest, and apoptosis of HaCaT. The antiproliferative percentage of HaCaT was 13.6%~61.6% after 24-h incubation with rhodomyrtone at 2~32 μ g/mL. In the scratching assay, rhodomyrtone at 2 μ g/mL delayed the wound closure by 61.8%. Chromatin condensation and nuclei fragmentation were detected after rhodomyrtone treatment. The flow cytometry demonstrated an elevation of the apoptotic percentage when compared to the control. An in vivo skin irritation test in a rabbit showed no redness or oedema after rhodomyrtone administration. The inhibitory effect of rhodomyrtone on TNF- α /IL-17A-driven inflammation was further rated [130]. Rhodomyrtone decreased the inflammatory gene expression in the human skin organ culture. This molecule also inhibited TNF- α -activated ERK, JNK, and p38 phosphorylation. The topical delivery of rhodomyrtone (0.18 and 0.64 mg/cm²) on an IMQ-induced psoriasiform lesion in a mouse effectively decreased the epidermal thickness and hyperplasia. Taken together, both antiproliferation and anti-inflammation are the therapeutic mechanisms for psoriasis inhibition by rhodomyrtone.

Phytosphingosine is found in plants, fungus, and the human epidermis. Phytosphingosine and its derivatives are known to prevent water loss from the skin, as well as to regulate epidermal cell growth, apoptosis, and differentiation [131]. Kim et al. [132] synthesized two phytosphingosine derivatives, (Z)-4-oxo-4-(((2S,3S,4R)-1,3,4-trihydroxyoctadecan-2-yl)amino)but-2-enoic acid (mYG-II-6) and (E)-4-oxo-4-(((2S,3S,4R)-1,3,4-trihydroxyoctadecan-2-yl)amino)but-2-enoic acid (fYG-II-6), to investigate the anti-inflammatory and antipsoriatic activity. Both of the derivatives enhanced the expression of the pro-apoptotic markers Bax and Bcl-2-associated death promoter (Bad), as well as caspase 3. TPA induced in vivo skin inflammation in mice. Both of the topically applied compounds effectively suppressed the inflammatory responses via the inhibition of mitogen-activated protein kinase (MAPK), NF- κ B, and Janus kinase/signal transducer of activation (JAK/STAT) signaling. Lower toxicity was observed for the derivatives than for phytosphingosine. Amentoflavone is a biflavonoid that possesses anti-inflammatory and antioxidant effects [133]. A possibility for the application of amentoflavone for psoriasis treatment was examined [134]. This biflavonoid inhibited proliferation and promoted apoptosis with the decreased cyclin D1, IL-17A, and IL-22 in cytokine-stimulated HaCaT. In the in vivo IMQ-induced psoriasis model, oral amentoflavone (50 mg/kg) decreased the epidermal thickness from about 300 to 180 μ m. This compound significantly downregulated a series of cytokines (IL-17A, IL-22, and IL-23) in the lesion. Zhang et al. [135] screened 250 Chinese medicine compounds for keratinocyte growth suppression and found that periplogenin exhibited the greatest ability to induce apoptosis. The IC₅₀ for periplogenin was 1.56 μ g/mL. Periplogenin is a cardenolide from *Aegle marmelos* leaves. The authors further performed the antiproliferative mechanism and the in vivo psoriasis-like hyperplasia model. The results indicated that this cardenolide elicited necroptotic cell death through oxidative stress. The ear thickness and the weight of the IMQ-treated mouse were decreased by periplogenin. The histological visualization showed a reduced hyperplasia and inflammatory cell infiltration by topically applied periplogenin.

Recently, Horinouchi et al. [136] investigated the anti-proliferative and anti-inflammatory effects of 3 β ,6 β ,16 β -trihydroxylup-20(29)-ene (TTHL) for the possible development on psoriasis treatment. This compound belongs to a triterpene structure that was purified from the *Combretum leprosum* flower, a folk medicine in Brazil for treating skin disorders. A previous study [137] suggests antiproliferative activity of TTHL against cancer cells through apoptosis and ROS generation. This mechanism was also shown in the case of keratinocytes. TTHL at 10 μ M reduced keratinocyte viability to 90%. Some 95% of keratinocytes entered the sub-G1 phase, which denoted apoptotic cells. TTHL with an ED₅₀ of 0.328 μ mol/ear inhibited the increase of the ear thickness by TPA. The neutrophil marker, myeloperoxidase, of the TPA-treated ear was reduced to the normal baseline by 1.3 μ mol/ear TTHL. This compound decreased PCNA-positive cells by 72%, which was comparable to the positive control dexamethasone. Rhododendrin is an arylbutanoid glycoside that was isolated from *Rhododendron brachycarpum*. It is an inhibitor of inflammation for use in treating inflammatory skin diseases [138,139]. Jeon et al. [140] elucidated the detailed action mechanism of this compound and its relevance as a therapy for psoriasis. The in vitro keratinocyte study demonstrated the inhibition of the toll-like receptor (TLR)-7/NF- κ B and MAPK pathways by rhododendrin. Caveolin-1 loss in keratinocytes contributes to psoriasis development. The caveolin-1 expression was preserved with TLR-7 upon treatment with rhododendrin, which indicated a critical role of this compound in maintaining skin homeostasis. Topical rhododendrin delivery significantly reduced IMQ-induced hyperplasia, immune-cell infiltration, and cytokines (TNF- α , IL-1, IL-6, IL-8, IL-17, and IL-23).

8-methoxypsoralen (8-MOP) is commonly used in PUVA therapy for treating psoriasis through keratinocyte-proliferation constraint. The chemical structure of 8-MOP, which is largely found in *Psoralea corylifolia*, is classified as furocoumarin. *P. corylifolia* extract for topical application is beneficial in mitigating psoriatic-lesion eczema and alopecia [141]. Some analogs of 8-MOP exist in *P. corylifolia*. Alalaiwe et al. [142] as compared the skin absorption and antipsoriatic activity of 8-MOP and its derivatives. 8-MOP, isopsoralen, and bakuchiol showed a comparable pig skin absorption of 0.47, 0.58, and 0.50 nmol/mg, which was greater than that of psoralen (0.25 nmol/mg) and psoralidin (0.14 nmol/mg). The combination of UVA with 8-MOP or isopsoralen led to greater proliferation inhibition than the other compounds. The concentration at 0.25 μ M could completely restrain keratinocyte growth. The topical application of PUVA on IMQ-treated mouse skin demonstrated a decrease in the epidermal thickness from 117 to 62 and 26 μ m by 8-MOP and isopsoralen, respectively. PUVA also depressed Ki-67-positive cells in the epidermis. However, PUVA, which is used in clinics, has a risk of causing squamous-cell cancer [143]. Epigallocatechin-3-gallate (EGCG) is a tea polyphenol that could reduce the risk of cancer associated with PUVA and promote the normal differentiation of keratinocytes [144]. Zhang et al. [144] investigated whether EGCG could inhibit IMQ-stimulated psoriasiform lesions. The topical delivery of EGCG for six consecutive days decreased the epidermal thickness from 70~150 to 30~80 μ m. This could be due to the capability of EGCG to reduce PCNA expression and enhance the caspase 14 level. The involvement of terminal differentiation and normal barrier formation is the predominant role of caspase 14 on keratinocytes. Table 3 summarizes the profiles for antipsoriatic activity of the natural compounds that aimed to suppress keratinocyte proliferation.

Table 3. Pure compounds derived from the plants for treating hyperproliferation of psoriasis.

Compound	Experimental Model	Cell or Animal	Method for Detecting Proliferation	Outcomes Offered by Extract	Reference
Resveratrol	In vitro	Primary culture of human keratinocytes	MTT assay and hemocytometer cell counting	Dose-dependent antiproliferative activity	Holian and Walter [100]
Resveratrol	In vitro	Primary culture of human keratinocytes	7-aminoactinomycin D assay	Reduced aquaporin 3 expression	Wu et al. [101]
Curcumin	In vitro	TNF- α -activated HaCaT	Annexin-V staining	Apoptosis is the main mechanism for antiproliferation of HaCaT	Sun et al. [104]
Curcumin	In vitro	HaCaT	Nuclei staining	Increased apoptosis by the combination with UVA or visible light	Dujic et al. [105]
Curcumin	In vitro	TNF- α -activated HaCaT	Cell counting kit-8 and LDH assay	Increased apoptosis by the combination with red and blue light	Niu et al. [106]
Rottlerin	In vitro	Primary culture of human keratinocytes	MTT assay	Increased apoptosis in an autophagy-dependent pathway	Min et al. [110]
Acridone analogs	In vitro	HaCaT	Cell counting and LDH assay	The compounds with benzyl substitution at the 10-position showed potent proliferation inhibition	Putic et al. [112]
1,4-Dihydroxy-2-naphthoic acid	In vitro	HaCaT	Sulphorhodamine B staining	Dose-dependent antiproliferative activity	Mok et al. [113]
Arsenics	In vitro	HaCaT	MTT assay	Significant inhibition on keratinocyte growth with moderate toxicity on fibroblasts	Tse et al. [115]
Arsenic trioxide	In vitro	HaCaT	MTT and LDH assay	Increased apoptosis via ROS-dependent p53 ubiquitination	Shen et al. [116]
Baicalein	In vitro	HaCaT	Cell counting	Minor inhibition of proliferation without affecting ROS production	Huang et al. [119]
Celastrrol	In vitro	HaCaT and primary human keratinocytes	MTT assay	Increased apoptosis via Bcl-2 attenuation and Bax upregulation	Zhou et al. [120]
Tanshinone IIA	In vitro	Primary mouse keratinocytes	MTT assay	Increased apoptosis via caspase pathway	Li et al. [122]
Dehydrocostuslactone and costunolide	In vitro	Primary human keratinocytes	Annexin-V staining	Inhibited proliferation and inflammation-related genes	Scarponi et al. [125]
Delphinidin	In vitro	reconstructed psoriatic skin equivalent	Ki-67 and PCNA	Inhibited proliferation and inflammation	Chamcheu et al. [126]
Rhodomyrton	In vitro/in vivo	HaCaT/rabbit	MTT assay	Elevated apoptosis with no skin irritation	Chorachoo et al. [129]
Rhodomyrton	In vitro/in vivo	Human skin organ culture/ICR mouse	Histology	Reduced epidermal thickness and hyperplasia	Chorachoo et al. [130]
Phytosphingosine derivatives	In vitro/in vivo	HaCaT/hairless mouse	Cell viability assay kit	Increased programmed keratinocyte death	Kim et al. [132]
Amentoflavone	In vitro/in vivo	HaCaT/Balb/c mouse	Cell counting kit	Inhibited proliferation and epidermal thickness	An et al. [134]
Periplogenin	In vitro/in vivo	HaCaT/Balb/c mouse	MTT assay	Inhibited proliferation via necroptotic cell death	Zhang et al. [135]
3 β ,6 β ,16 β -Trihydroxylup-20(29)-ene	In vitro/in vivo	HaCaT/Swiss mouse	MTT and neutral red assay	Reduced keratinocyte viability via apoptosis and ROS generation	Horinouchi et al. [136]
Rhododendrin	In vitro/in vivo	Normal human keratinocytes/C57BL/6 mouse	MTT assay	Inhibited proliferation and epidermal thickness	Jeon et al. [139]
8-Methoxypsoralen derivatives	In vitro/in vivo	HaCaT/Balb/c mouse	MTT assay	Inhibited proliferation and epidermal thickness	Alalaiwe et al. [142]
Epigallocatechin-3-gallate	In vivo	Balb/c mouse	PCNA	Inhibited epidermal thickness and differentiation regulation	Zhang et al. [144]

Bax, Bcl-2-associated X protein; LDH, lactate dehydrogenase; MTT, 3-(4,5-cimethylthiazol-2-yl)-2,5-diphenyl tetrazolium bromide; PCNA, proliferating cell nuclear antigen; ROS, reactive oxygen species.

7. Conclusions

The current therapeutic options for psoriasis patients have some disadvantages, which include frustration with medication efficacy, inconvenience, time constraints, and possible adverse effects. Until now, an effective and long-term regimen for psoriasis eradication has been lacking, especially for moderate to severe psoriasis. There is a great need for the continuous development of novel, safe, and effective treatment modalities for psoriasis. Among many active compounds that were investigated for psoriasis mitigation, phytochemicals derived from natural resources have become of great interest over the last decades. Several investigations assessing natural-sources-based psoriasis

therapy reveal potential activity, especially the antiproliferative effect. Until now, most of the reports concerning the antiproliferative efficacy of natural compounds for psoriasis treatment have been based on laboratory or animal-related work. Some of the investigations suggest the usefulness of natural products for psoriasis treatment, only for their ability to suppress keratinocyte proliferation. The evidence from in vitro cell study and in vivo animal tests offers limited information regarding the natural products' clinical success. Convincing results in human clinical studies are urgently needed to encourage future investigation on this topic. Scientists should pay attention, not only to the therapeutic benefits of natural products, but also to their adverse effects on human health. Caution should be used in optimizing the feasible conditions of phytomedicine to balance the effectiveness of psoriasis therapy and tissue damage or toxicity.

Funding: The authors are grateful to the financial support by Chang Gung Memorial Hospital (CMRPG2H0361-2 and CMRPF1F0051-3) and Ministry of Science and Technology of Taiwan (MOST-107-2320-B-182-016-MY3).

Conflicts of Interest: The authors declare no conflict of interest.

References

1. Pithadia, D.J.; Reynolds, K.A.; Lee, E.B.; Wu, J.J. Psoriasis-associated cutaneous pain: Etiology, assessment, impact, and management. *J. Dermatol. Treat.* **2018**, *19*, 1–6. [\[CrossRef\]](#)
2. Boehncke, W.H.; Schön, M.P. Psoriasis. *Lancet* **2015**, *386*, 983–994. [\[CrossRef\]](#)
3. Woo, Y.R.; Cho, D.H.; Park, H.J. Molecular mechanisms and management of a cutaneous inflammatory disorder: Psoriasis. *Int. J. Mol. Sci.* **2017**, *18*, 2684.
4. Takeshita, J.; Grewal, S.; Langan, S.M.; Mehta, N.N.; Ogdie, A.; Van Voorhees, A.S.; Gelfand, J.M. Psoriasis and comorbid diseases: Epidemiology. *J. Am. Acad. Dermatol.* **2017**, *76*, 377–390. [\[CrossRef\]](#)
5. Yang, E.J.; Beck, K.M.; Sanchez, I.M.; Koo, J.; Liao, W. The impact of genital psoriasis on quality of life: A systematic review. *Psoriasis* **2018**, *8*, 41–47. [\[CrossRef\]](#) [\[PubMed\]](#)
6. Lima, X.T.; Minnillo, R.; Spencer, J.M.; Kimball, A.B. Psoriasis prevalence among the 2009 AAD National Melanoma/Skin Cancer Screening Program participants. *J. Eur. Acad. Dermatol. Venereol.* **2013**, *27*, 680–685. [\[CrossRef\]](#) [\[PubMed\]](#)
7. Enamandram, M.; Kimball, A.B. Psoriasis epidemiology: The interplay of genes and the environment. *J. Invest. Dermatol.* **2013**, *133*, 287–289. [\[CrossRef\]](#)
8. Michalek, I.M.; Loring, B.; John, S.M. A systematic review of worldwide epidemiology of psoriasis. *J. Eur. Acad. Dermatol. Venereol.* **2017**, *31*, 205–212. [\[CrossRef\]](#)
9. Hägg, D.; Eriksson, M.; Sundström, A.; Schmitt-Egenolf, M. The higher proportion of men with psoriasis treated with biologics may be explained by more severe disease in men. *PLoS One* **2013**, *8*, e63619. [\[CrossRef\]](#) [\[PubMed\]](#)
10. Monteleone, G.; Pallone, F.; MacDonald, T.T.; Chimenti, S.; Costanzo, A. Psoriasis: From pathogenesis to novel therapeutic approaches. *Clin. Sci.* **2011**, *120*, 1–11. [\[CrossRef\]](#)
11. Arakawa, A.; Siewert, K.; Stöhr, J.; Besgen, P.; Kim, S.M.; Rühl, G.; Nickel, J.; Vollmer, S.; Thomas, P.; Krebs, S.; et al. Melanocyte antigen triggers autoimmunity in human psoriasis. *J. Exp. Med.* **2015**, *212*, 2203–2212. [\[CrossRef\]](#)
12. Hawkes, J.E.; Yan, B.Y.; Chan, T.C.; Krueger, J.G. Discovery of the IL-23/IL-17 signaling pathway and the treatment of psoriasis. *J. Immunol.* **2018**, *201*, 1605–1613. [\[CrossRef\]](#)
13. Schmitt, J.; Wozel, G. The psoriasis area and severity index is the adequate criterion to define severity in chronic plaque-type psoriasis. *Dermatology* **2005**, *210*, 194–199. [\[CrossRef\]](#) [\[PubMed\]](#)
14. Chow, C.; Simpson, M.J.; Luger, T.A.; Chubb, H.; Ellis, C.N. Comparison of three methods for measuring psoriasis severity in clinical studies (Part 1 of 2): Change during therapy in Psoriasis Area and Severity Index, Static Physician's Global Assessment and Lattice System Physician's Global Assessment. *J. Eur. Acad. Dermatol. Venereol.* **2015**, *29*, 1406–1414. [\[CrossRef\]](#)
15. Coates, L.C.; Aslam, T.; Al Balushi, F.; Burden, A.D.; Burden-The, E.; Caperon, A.R.; Cerio, R.; Chattopadhyay, C.; Chinoy, H.; Goodfield, M.J.; et al. Comparison of three screening tools to detect psoriatic arthritis in patients with psoriasis (CONTEST study). *Br. J. Dermatol.* **2013**, *168*, 802–807. [\[CrossRef\]](#) [\[PubMed\]](#)

16. Sabat, R.; Philipp, S.; Höflich, C.; Kreutzer, S.; Wallace, E.; Asadullah, K.; Volk, H.D.; Sterry, W.; Wolk, K. Immunopathogenesis of psoriasis. *Exp. Dermatol.* **2007**, *16*, 779–798. [[CrossRef](#)] [[PubMed](#)]
17. Albanesi, C.; Madonna, S.; Gisondi, P.; Girolomoni, G. The interplay between keratinocytes and immune cells in the pathogenesis of psoriasis. *Front. Immunol.* **2018**, *9*, 1549. [[CrossRef](#)] [[PubMed](#)]
18. Talbott, W.; Duffy, N. Complementary and alternative medicine for psoriasis: What the dermatologist needs to know. *Am. J. Clin. Dermatol.* **2015**, *16*, 147–165. [[CrossRef](#)]
19. Basavaraj, K.H.; Ashok, N.M.; Rashmi, R.; Praveen, T.K. The role of drugs in the induction and/or exacerbation of psoriasis. *Int. J. Dermatol.* **2010**, *49*, 1351–1361. [[CrossRef](#)]
20. Ceccarelli, M.; Venanzi Rullo, E.; Vaccaro, M.; Facciola, A.; d'Aleo, F.; Paolucci, I.A.; Cannavò, S.P.; Cacopardo, B.; Pinzone, M.R.; Pellicanò, G.F.; et al. HIV-associated psoriasis: Epidemiology, pathogenesis, and management. *Dermatol. Ther.* **2018**, *32*, e12806. [[CrossRef](#)]
21. Slominski, A. Neuroendocrine system of the skin. *Dermatology* **2005**, *211*, 199–208. [[CrossRef](#)] [[PubMed](#)]
22. Boehncke, W.H.; Brembilla, N.C. Unmet needs in the field of psoriasis: Pathogenesis and treatment. *Clin. Rev. Allergy Immunol.* **2018**, *55*, 295–311. [[CrossRef](#)] [[PubMed](#)]
23. Milani, M.; Sparavigna, A. Antiaging efficacy of melatonin-based day and night creams: A randomized, split-face, assessor-blinded proof-of-concept trial. *Clin. Cosmet. Invest. Dermatol.* **2018**, *11*, 51–57. [[CrossRef](#)] [[PubMed](#)]
24. Slominski, A.T.; Hardeland, R.; Zmijewski, M.A.; Slominski, R.M.; Reiter, R.J.; Paus, R. Melatonin: A cutaneous perspective on its production, metabolism, and functions. *J. Invest. Dermatol.* **2018**, *138*, 490–499. [[CrossRef](#)] [[PubMed](#)]
25. Hijnen, D.; Knol, E.F.; Gent, Y.Y.; Giovannone, B.; Beijin, S.J.; Kupper, T.S.; Bruijnzeel-Koomen, C.A.; Clark, R.A. CD8(+) T cells in the lesional skin of atopic dermatitis and psoriasis patients are an important source of IFN- γ , IL-13, IL-17, and IL-22. *J. Invest. Dermatol.* **2013**, *133*, 973–979. [[CrossRef](#)] [[PubMed](#)]
26. Cheuk, S.; Wikén, M.; Blomqvist, L.; Nylén, S.; Talme, T.; Stähle, M.; Eidsmo, L. Epidermal Th22 and Tc17 cells form a localized disease memory in clinically healed psoriasis. *J. Immunol.* **2014**, *192*, 3111–3120. [[CrossRef](#)]
27. Pauls, K.; Schön, M.; Kubitza, R.C.; Homey, B.; Wiesenborn, A.; Lehmann, P.; Ruzicka, T.; Parker, C.M.; Schön, M.P. Role of integrin α E(CD103) β 7 for tissue-specific epidermal localization of CD8⁺ T lymphocytes. *J. Invest. Dermatol.* **2001**, *117*, 569–575. [[CrossRef](#)]
28. Goodman, W.A.; Levine, A.D.; Massari, J.V.; Sugiyama, H.; McCormick, T.S.; Cooper, K.D. IL-6 signaling in psoriasis prevents immune suppression by regulatory T cells. *J. Immunol.* **2009**, *183*, 3170–3176. [[CrossRef](#)]
29. Parameswaran, N.; Patial, S. Tumor necrosis factor- α signaling in macrophages. *Crit. Rev. Eukaryot. Gene Expr.* **2010**, *20*, 87–103. [[CrossRef](#)]
30. Hoffmann, J.H.; Enk, A.H. Neutrophil extracellular traps in dermatology: Caught in the NET. *J. Dermatol. Sci.* **2016**, *84*, 3–10. [[CrossRef](#)]
31. Chiricozzi, A.; Guttman-Yassky, E.; Suárez-Fariñas, M.; Nogales, K.E.; Tian, S.; Cardinale, I.; Chimenti, S.; Krueger, J.G. Integrative responses to IL-17 and TNF- α in human keratinocytes account for key inflammatory pathogenic circuits in psoriasis. *J. Invest. Dermatol.* **2011**, *131*, 677–687. [[CrossRef](#)]
32. Mylonas, A.; Conrad, C. Psoriasis: Classical vs. paradoxical. The Yin-Yang of TNF and type I interferon. *Front. Immunol.* **2018**, *9*, 2746. [[CrossRef](#)]
33. Moots, R.J.; Curiale, C.; Petersel, D.; Rolland, C.; Jones, H.; Mysler, E. Efficacy and safety outcomes for originator TNF inhibitors and biosimilars in rheumatoid arthritis and psoriasis trials: A systematic literature review. *BioDrugs* **2018**, *32*, 193–199. [[CrossRef](#)]
34. Chuang, S.Y.; Lin, C.H.; Sung, C.T.; Fang, J.Y. Murine models of psoriasis and their usefulness for drug discovery. *Expert Opin. Drug Discov.* **2018**, *13*, 551–562. [[CrossRef](#)]
35. Nast, A.; Amelunxen, L.; Augustin, M.; Boehncke, W.H.; Dressler, C.; Gaskins, M.; Härle, P.; Hoffstadt, B.; Klaus, J.; Koza, J.; et al. S3 Guideline for the treatment of psoriasis vulgaris, update-Short version part 1-Systemic treatment. *J. Dtsch. Dermatol. Ges.* **2018**, *16*, 645–669. [[CrossRef](#)] [[PubMed](#)]
36. Chiricozzi, A.; Pitocco, R.; Saraceno, R.; Nistico, S.P.; Giunta, A.; Chimenti, S. New topical treatments for psoriasis. *Expert Opin. Pharmacother.* **2014**, *15*, 461–470. [[CrossRef](#)]
37. Samarasekera, E.J.; Sawyer, L.; Wonderling, D.; Tucker, R.; Smith, C.H. Topical therapies for the treatment of plaque psoriasis: Systematic review and network meta-analyses. *Br. J. Dermatol.* **2013**, *168*, 954–967. [[CrossRef](#)] [[PubMed](#)]

38. Van de Kerkhof, P.C. An update on topical therapies for mild-moderate psoriasis. *Dermatol. Clin.* **2015**, *33*, 73–77. [[CrossRef](#)]
39. Kim, E.S.; Frampton, J.E. Calcipotriol/betamethasone dipropionate foam: A review in plaque psoriasis. *Drugs* **2016**, *76*, 1485–1492. [[CrossRef](#)]
40. Jacobi, A.; Mayer, A.; Augustin, M. Keratolytics and emollients and their role in the therapy of psoriasis: A systematic review. *Dermatol. Ther.* **2015**, *5*, 1–18. [[CrossRef](#)]
41. Farahnik, B.; Nakamura, M.; Singh, R.K.; Abrouk, M.; Zhu, T.H.; Lee, K.M.; Jose, M.V.; DaLovichio, R.; Koo, J.; Bhutani, T.; et al. The patient's guide to psoriasis treatment. Part 2: PUVA phototherapy. *Dermatol. Ther.* **2016**, *6*, 315–324. [[CrossRef](#)]
42. Singh, T.P.; Schön, M.P.; Wallbrecht, K.; Michaelis, K.; Rinner, B.; Mayer, G.; Schmidbauer, U.; Strohmaier, H.; Wang, X.J.; Wolf, P. 8-Methoxypsoralen plus ultraviolet A therapy acts via inhibition of the IL-23/Th17 axis and induction of Foxp3⁺ regulatory T cells involving CTLA4 signaling in a psoriasis-like skin disorder. *J. Immunol.* **2010**, *184*, 7257–7267. [[CrossRef](#)]
43. Dubertret, L. Retinoids, methotrexate and cyclosporine. *Curr. Probl. Dermatol.* **2009**, *38*, 79–94. [[PubMed](#)]
44. Zebda, R.; Paller, A.S. Phosphodiesterase 4 inhibitors. *J. Am. Acad. Dermatol.* **2018**, *78* (Suppl. 1), S43–S52. [[CrossRef](#)]
45. Wittmann, M.; Helliwell, P.S. Phosphodiesterase 4 inhibition in the treatment of psoriasis, psoriatic arthritis and other chronic inflammatory diseases. *Dermatol. Ther.* **2013**, *3*, 1–15. [[CrossRef](#)]
46. Conrad, C.; Gilliet, M. Psoriasis: Pathogenesis to targeted therapies. *Clin. Rev. Allergy Immunol.* **2018**, *54*, 102–113. [[CrossRef](#)] [[PubMed](#)]
47. Kim, H.J.; Lebwohl, M.G. Biologics and psoriasis: The beat goes on. *Dermatol. Clin.* **2019**, *37*, 29–36. [[CrossRef](#)] [[PubMed](#)]
48. Jensen, J.D.; Delcambre, M.R.; Nguyen, G.; Sami, N. Biologic therapy with or without topical treatment in psoriasis: What does the current evidence say? *Am. J. Clin. Dermatol.* **2014**, *15*, 379–385. [[CrossRef](#)]
49. Nast, A.; Gisondi, P.; Ormerod, A.D.; Saiag, P.; Smith, C.; Spuls, P.I.; Arenberger, P.; Bachelez, H.; Barker, J.; Dauden, E.; et al. European S3-Guidelines on the systemic treatment of psoriasis vulgaris-Update 2015-Short version-EDF in cooperation with EADV and IPC. *J. Eur. Acad. Dermatol. Venereol.* **2015**, *29*, 2277–2294. [[CrossRef](#)]
50. Golbari, N.M.; Porter, M.L.; Kimball, A.B. Current guidelines for psoriasis treatment: A work in progress. *Cutis* **2018**, *101*, 10–12.
51. Bonesi, M.; Loizzo, M.R.; Provenzano, E.; Menichini, F.; Tundis, R. Anti-psoriasis agents from natural plant sources. *Curr. Med. Chem.* **2016**, *23*, 1250–1267. [[CrossRef](#)]
52. Svendsen, M.T.; Jeyabalan, J.; Andersen, K.E.; Andersen, F.; Johannessen, H. Worldwide utilization of topical remedies in treatment of psoriasis: A systematic review. *J. Dermatol. Treat.* **2017**, *28*, 374–383. [[CrossRef](#)]
53. Ben-Arye, E.; Ziv, M.; Frenkel, M.; Lavi, I.; Rosenman, D. Complementary medicine and psoriasis: Linking the patient's outlook with evidence-based medicine. *Dermatology* **2003**, *207*, 302–307. [[CrossRef](#)]
54. Damevska, K.; Neloska, L.; Nikolovska, S.; Gocev, G.; Duma, S. Complementary and alternative medicine use among patients with psoriasis. *Dermatol. Ther.* **2014**, *27*, 281–283. [[CrossRef](#)] [[PubMed](#)]
55. Deng, S.; May, B.H.; Zhang, A.L.; Lu, C.; Xue, C.C. Plant extracts for the topical management of psoriasis: A systematic review and meta-analysis. *Br. J. Dermatol.* **2013**, *169*, 769–782. [[CrossRef](#)] [[PubMed](#)]
56. Farahnik, B.; Sharma, D.; Alban, J.; Sivamani, R.K. Topical botanical agents for the treatment of psoriasis: A systematic review. *Am. J. Clin. Dermatol.* **2017**, *18*, 451–468. [[CrossRef](#)]
57. May, B.H.; Deng, S.; Zhang, A.L.; Lu, C.; Xue, C.C. In silico database screening of potential targets and pathways of compounds contained in plants used for psoriasis vulgaris. *Arch. Dermatol. Res.* **2015**, *307*, 645–657. [[CrossRef](#)]
58. Miroddi, M.; Navarra, M.; Calapai, F.; Mancari, F.; Giofrè, S.V.; Gangemi, S.; Calapai, G. Review of clinical pharmacology of *Aloe vera* L. in the treatment of psoriasis. *Phytother. Res.* **2015**, *29*, 648–655. [[CrossRef](#)]
59. Lin, Y.K.; See, L.C.; Huang, Y.H.; Chi, C.C.; Hui, R.C. Comparison of indirubin concentrations in indigo naturalis ointment for psoriasis treatment: A randomized, double-blind, dosage-controlled trial. *Br. J. Dermatol.* **2018**, *178*, 124–131. [[CrossRef](#)]
60. Brown, A.C.; Koett, J.; Johnson, D.W.; Semaskvich, N.M.; Holck, P.; Lally, D.; Cruz, L.; Young, R.; Higa, B.; Lo, S. Effectiveness of kukui nut oil as a topical treatment for psoriasis. *Int. J. Dermatol.* **2005**, *44*, 684–687. [[CrossRef](#)] [[PubMed](#)]

61. Bernstein, S.; Donsky, H.; Gulliver, W.; Hamilton, D.; Nobel, S.; Norman, R. Treatment of mild to moderate psoriasis with ReliÉva, a *Mahonia aquifolium* extract-A double-blind, placebo-controlled study. *Am. J. Ther.* **2006**, *13*, 121–126. [[CrossRef](#)]
62. Ellis, C.N.; Berberian, B.; Sulica, V.I.; Dodd, W.A.; Jarratt, M.T.; Katz, H.I.; Prawer, S.; Krueger, G.; Rex, I.H., Jr.; Wolf, J.E. A double-blind evaluation of topical capsaicin in pruritic psoriasis. *J. Am. Acad. Dermatol.* **1993**, *29*, 438–442. [[CrossRef](#)]
63. Šahmatova, L.; Sügis, E.; Šunina, M.; Hermann, H.; Prans, E.; Pihlap, M.; Abram, K.; Rebane, A.; Peterson, H.; Peterson, P.; et al. Signs of innate immune activation and premature immunosenescence in psoriasis patients. *Sci. Rep.* **2017**, *7*, 7553. [[CrossRef](#)] [[PubMed](#)]
64. Malakou, L.S.; Gargalionis, A.N.; Piperi, C.; Papadavid, E.; Papavassiliou, A.G.; Basdra, E.K. Molecular mechanisms of mechanotransduction in psoriasis. *Ann. Transl. Med.* **2018**, *6*, 245. [[CrossRef](#)] [[PubMed](#)]
65. Sestito, R.; Madonna, S.; Scarponi, C.; Cianfarani, F.; Failla, C.M.; Cavani, A.; Girolomoni, G.; Albanesi, C. STAT3-dependent effects of IL-22 in human keratinocytes are counterregulated by sirtuin 1 through a direct inhibition of STAT3 acetylation. *FASEB J.* **2011**, *25*, 916–927. [[CrossRef](#)]
66. Janjetovic, Z.; Nahmias, Z.P.; Hanna, S.; Jarrett, S.G.; Kim, T.K.; Reiter, R.J.; Slominski, A.T. Melatonin and its metabolites ameliorate ultraviolet B-induced damage in human epidermal keratinocytes. *J. Pineal Res.* **2014**, *57*, 90–102. [[CrossRef](#)]
67. Janjetovic, Z.; Jarrett, S.G.; Lee, E.F.; Duprey, C.; Reiter, R.J.; Slominski, A.T. Melatonin and its metabolites protect human melanocytes against UVB-induced damage: Involvement of NRF2-mediated pathways. *Sci. Rep.* **2017**, *7*, 1274. [[CrossRef](#)]
68. Skobowiat, C.; Brożyna, A.A.; Janjetovic, Z.; Jeayeng, S.; Oak, A.S.W.; Kim, T.K.; Panich, U.; Reiter, R.J.; Slominski, A.T. Melatonin and its derivatives counteract the ultraviolet B radiation-induced damage in human and porcine skin ex vivo. *J. Pineal Res.* **2018**, *65*, e12501. [[CrossRef](#)]
69. Herman, A.; Herman, A.P. Topically used herbal products for the treatment of psoriasis-Mechanism of action, drug delivery, clinical studies. *Planta Med.* **2016**, *82*, 1447–1455. [[CrossRef](#)] [[PubMed](#)]
70. Barrea, L.; Savanelli, M.C.; Di Somma, C.; Napolitano, M.; Megna, M.; Colao, A.; Savastano, S. Vitamin D and its role in psoriasis: An overview of the dermatologist and nutritionist. *Rev. Endocr. Metab. Disord.* **2017**, *18*, 195–205. [[CrossRef](#)]
71. Morita, A. Current developments in phototherapy for psoriasis. *J. Dermatol.* **2018**, *45*, 287–292. [[CrossRef](#)]
72. Stern, R.S. Psoralen and ultraviolet A light therapy for psoriasis. *N. Engl. J. Med.* **2007**, *357*, 682–690. [[CrossRef](#)] [[PubMed](#)]
73. Wong, T.; Hsu, L.; Liao, W. Phototherapy in psoriasis: A review of mechanisms of action. *J. Cutan. Med. Surg.* **2013**, *17*, 6–12. [[CrossRef](#)] [[PubMed](#)]
74. Tse, W.P.; Che, C.T.; Liu, K.; Lin, Z.X. Evaluation of the anti-proliferative properties of selected psoriasis-treating Chinese medicines on cultured HaCaT cells. *J. Ethnopharmacol.* **2006**, *108*, 133–141. [[CrossRef](#)] [[PubMed](#)]
75. Tse, W.P.; Cheng, C.H.K.; Che, C.T.; Zhao, M.; Lin, Z.X. Induction of apoptosis underlies the Radix Rubiae-mediated anti-proliferative action on human epidermal keratinocytes: Implications for psoriasis treatment. *Int. J. Mol. Med.* **2007**, *20*, 663–672. [[PubMed](#)]
76. Rihn, B.; Saliou, C.; Bottin, M.C.; Keith, G.; Packer, L. From ancient remedies to modern therapeutics: Pine bark uses in skin disorders revisited. *Phytother. Res.* **2001**, *15*, 76–78. [[CrossRef](#)]
77. García-Pérez, M.E.; Royer, M.; Duque-Fernandez, A.; Diouf, P.N.; Stevanovic, T.; Pouliot, R. Antioxidant, toxicological and antiproliferative properties of Canadian polyphenolic extracts on normal and psoriatic keratinocytes. *J. Ethnopharmacol.* **2010**, *132*, 251–258. [[CrossRef](#)]
78. Song, X.; Li, Y.; Zhang, H.; Yang, Q. The anticancer effect of huaier. *Oncol. Rep.* **2015**, *34*, 12–21. [[CrossRef](#)] [[PubMed](#)]
79. Su, D.; Zhang, X.; Zhang, L.; Zhou, J.; Zhang, F. A randomized, double-blind, controlled clinical study on the curative effect of huaier on mild-to-moderate psoriasis and an experimental study on the proliferation of Hacat cells. *Biomed. Res. Int.* **2018**, *2018*, 2372895. [[CrossRef](#)]
80. Shraibom, N.; Madaan, A.; Joshi, V.; Verma, R.; Chaudhary, A.; Mishra, G.; Awasthi, A.; Singh, A.T.; Jaggi, M. Evaluation of in vitro anti-psoriatic activity of a novel polyherbal formulation by multiparametric analysis. *Antiinflamm. Antiallergy Agents Med. Chem.* **2017**, *16*, 94–111. [[CrossRef](#)] [[PubMed](#)]

81. Gasparetto, J.C.; Martins, C.A.; Hayashi, S.S.; Otuky, M.F.; Pontarolo, R. Ethnobotanical and scientific aspects of *Malva sylvestris* L.: A millennial herbal medicine. *J. Pharm. Pharmacol.* **2012**, *64*, 172–189. [[CrossRef](#)] [[PubMed](#)]
82. Prudente, A.S.; Loddi, A.M.; Duarte, M.R.; Santos, A.R.; Pochapski, M.T.; Pizzolatti, M.G.; Hayashi, S.S.; Campos, F.R.; Pontarolo, R.; Santos, F.A.; et al. Pre-clinical anti-inflammatory aspects of a cuisine and medicinal millennial herb: *Malva sylvestris* L. *Food Chem. Toxicol.* **2013**, *58*, 324–331. [[CrossRef](#)] [[PubMed](#)]
83. Prudente, A.S.; Sponchiado, G.; Mendes, D.A.G.B.; Soley, B.S.; Cabrini, D.A.; Otuki, M.F. Pre-clinical efficacy assessment of *Malva sylvestris* on chronic skin inflammation. *Biomed. Pharmacother.* **2017**, *93*, 852–860. [[CrossRef](#)]
84. Koulu, M.; Örmä, S.; Liljeblad, A.; Niemelä, P. Artemisiae as medicinal and herbal medicinal plants from ancient times to the present day. *Duodecim* **2016**, *132*, 1763–1770. [[PubMed](#)]
85. Ha, H.; Lee, H.; Seo, C.S.; Lim, H.S.; Lee, J.K.; Lee, M.Y.; Shin, H. *Artemisia capillaris* inhibits atopic dermatitis-like skin lesions in Dermatophagoides farinae-sensitized Nc/Nga mice. *BMC Complement. Altern. Med.* **2014**, *14*, 100. [[CrossRef](#)] [[PubMed](#)]
86. Lee, S.Y.; Nam, S.; Hong, I.K.; Kim, H.; Yang, H.; Cho, H.J. Antiproliferation of keratinocytes and alleviation of psoriasis by the ethanol extract of *Artemisia capillaris*. *Phytother. Res.* **2018**, *32*, 923–932. [[CrossRef](#)]
87. Lee, S.Y.; Nam, S.; Kim, S.; Koo, J.S.; Hong, I.K.; Kim, H.; Han, S.; Kang, M.; Yang, H.; Cho, H.J. Therapeutic efficacies of *Artemisia capillaris* extract cream formulation in imiquimod-induced psoriasis models. *Evid. Based Complement. Alternat. Med.* **2018**, *2018*, 3610494. [[CrossRef](#)] [[PubMed](#)]
88. Müller, K.; Ziereis, K.; Gawlik, I. The antipsoriatic *Mahonia aquifolium* and its active constituents; II. Antiproliferative activity against cell growth of human keratinocytes. *Planta Med.* **1995**, *61*, 74–75. [[CrossRef](#)]
89. Augustin, M.; Andrees, U.; Grimme, H.; Schöpf, E.; Simon, J. Effects of *Mahonia aquifolium* ointment on the expression of adhesion, proliferation, and activation markers in the skin of patients with psoriasis. *Forsch. Komplementarmed.* **1999**, *6* (Suppl. 2), 19–21.
90. Lin, Y.K.; Wong, W.R.; Chang, Y.C.; Chang, C.J.; Tsay, P.K.; Chang, S.C.; Pang, J.H. The efficacy and safety of topically applied indigo naturalis ointment in patients with plaque-type psoriasis. *Dermatology* **2007**, *214*, 155–161. [[CrossRef](#)]
91. Li, Y.; Ligr, M.; McCarron, J.P.; Daniels, G.; Zhang, D.; Zhao, X.; Ye, F.; Wang, J.; Liu, X.; Osman, I.; et al. Natura-alpha targets forkhead box m1 and inhibits androgen-dependent and -independent prostate cancer growth and invasion. *Clin. Cancer Res.* **2011**, *17*, 4414–4424. [[CrossRef](#)] [[PubMed](#)]
92. Miquel, J.; Bernd, A.; Sempere, J.M.; Díaz-Alperi, J.; Ramírez, A. The curcuma antioxidants: Pharmacological effects and prospects for future clinical use. A review. *Arch. Gerontol. Geriatr.* **2002**, *34*, 37–46. [[CrossRef](#)]
93. Rahmayunita, G.; Jacob, T.N.A.; Novianto, E.; Indriatmi, W.; Rihatmadja, R.; Puspongoro, E.H.D. A double-blind randomized controlled trial of topical *Curcuma xanthorrhiza* Roxb. on mild psoriasis: Clinical manifestations, histopathological features, and K6 expressions. *Med. J. Indones.* **2018**, *27*, 178–184. [[CrossRef](#)]
94. Marrelli, M.; Statti, G.; Conforti, F.; Menichini, F. New potential pharmaceutical applications of *Hypericum* Species. *Mini Rev. Med. Chem.* **2016**, *16*, 710–720. [[CrossRef](#)]
95. Najafizadeh, P.; Hashemian, F.; Mansouri, P.; Farshi, S.; Surmaghi, M.S.; Chalangari, R. The evaluation of the clinical effect of topical St Johns wort (*Hypericum perforatum* L.) in plaque type psoriasis vulgaris: A pilot study. *Australas. J. Dermatol.* **2012**, *53*, 131–135. [[CrossRef](#)]
96. Wölfl, U.; Seelinger, G.; Schempp, C.M. Topical application of St. John's wort (*Hypericum perforatum*). *Planta Med.* **2014**, *80*, 109–120.
97. Mansouri, P.; Mirafzal, S.; Najafizadeh, P.; Safaei-Naraghi, Z.; Salehi-Surmaghi, M.H.; Hashemian, F. The impact of topical Saint John's Wort (*Hypericum perforatum*) treatment on tissue tumor necrosis factor-alpha levels in plaque-type psoriasis: A pilot study. *J. Postgrad. Med.* **2017**, *63*, 215–220. [[PubMed](#)]
98. Pangen, R.; Sahni, J.K.; Ali, J.; Sharma, S.; Baboota, S. Resveratrol: Review on therapeutic potential and recent advances in drug delivery. *Expert Opin. Drug Deliv.* **2014**, *11*, 1285–1298. [[CrossRef](#)]
99. Holian, O.; Walter, R.J. Resveratrol inhibits the proliferation of normal human keratinocytes in vitro. *J. Cell. Biochem.* **2001**, (Suppl. 36), 55–62. [[CrossRef](#)]
100. Wu, Z.; Uchi, H.; Morino-Koga, S.; Shi, W.; Furue, M. Resveratrol inhibition of human keratinocyte proliferation via SIRT1/ARNT/ERK dependent downregulation of aquaporin 3. *J. Dermatol. Sci.* **2014**, *75*, 16–23. [[CrossRef](#)] [[PubMed](#)]

101. Voss, K.E.; Bollag, R.J.; Fussell, N.; By, C.; Sheehan, D.J.; Bollag, W.B. Abnormal aquaporin-3 protein expression in hyperproliferative skin disorders. *Arch. Dermatol. Res.* **2011**, *303*, 591–600. [[CrossRef](#)]
102. Salehi, B.; Stojanović-Radić, Z.; Matejić, J.; Sharifi-Rad, M.; Anil Kumar, N.V.; Martins, N.; Sharifi-Rad, J. The therapeutic potential of curcumin: A review of clinical trials. *Eur. J. Med. Chem.* **2019**, *163*, 527–545. [[CrossRef](#)] [[PubMed](#)]
103. Sun, J.; Han, J.; Zhao, Y.; Zhu, Q.; Hu, J. Curcumin induces apoptosis in tumor necrosis factor- α -treated HaCaT cells. *Int. Immunopharmacol.* **2012**, *13*, 170–174. [[CrossRef](#)] [[PubMed](#)]
104. Dujic, J.; Kippenberger, S.; Hoffmann, S.; Ramirez-Bosca, A.; Miquel, J.; Diaz-Alperi, J.; Bereiter-Hahn, J.; Kaufmann, R.; Bernd, A. Low concentrations of curcumin induce growth arrest and apoptosis in skin keratinocytes only in combination with UVA or visible light. *J. Invest. Dermatol.* **2007**, *127*, 1992–2000. [[CrossRef](#)]
105. Niu, T.; Tian, Y.; Cai, Q.; Ren, Q.; Wei, L. Red light combined with blue light irradiation regulates proliferation and apoptosis in skin keratinocytes in combination with low concentrations of curcumin. *PLoS ONE* **2015**, *10*, e0138754. [[CrossRef](#)]
106. Maioli, E.; Valacchi, G. Rottlerin: Bases for a possible usage in psoriasis. *Curr. Drug Metab.* **2010**, *11*, 425–430. [[CrossRef](#)] [[PubMed](#)]
107. Torricelli, C.; Fortino, V.; Capurro, E.; Valacchi, G.; Pacini, A.; Muscettola, M.; Soucek, K.; Maioli, E. Rottlerin inhibits the nuclear factor κ B/cyclin-D1 cascade in MCF-7 breast cancer cells. *Life Sci.* **2008**, *82*, 638–643. [[CrossRef](#)] [[PubMed](#)]
108. Valacchi, G.; Pecorelli, A.; Mencarelli, M.; Carbotti, P.; Fortino, V.; Muscettola, M.; Maioli, E. Rottlerin: A multifaced regulator of keratinocyte cell cycle. *Exp. Dermatol.* **2009**, *18*, 516–521. [[CrossRef](#)] [[PubMed](#)]
109. Min, M.; Yan, B.X.; Wang, P.; Landeck, L.; Chen, J.Q.; Li, W.; Cai, S.Q.; Zheng, M.; Man, X.Y. Rottlerin as a therapeutic approach in psoriasis: Evidence from in vitro and in vivo studies. *PLoS One* **2017**, *12*, e0190051. [[CrossRef](#)]
110. Zhang, B.; Chen, K.; Wang, N.; Gao, C.; Sun, Q.; Li, L.; Chen, Y.; Tan, C.; Liu, H.; Jiang, Y. Molecular design, synthesis and biological research of novel pyridyl acridones as potent DNA-binding and apoptosis-inducing agents. *Eur. J. Med. Chem.* **2015**, *93*, 214–226. [[CrossRef](#)]
111. Putic, A.; Stecher, L.; Prinz, H.; Müller, K. Structure-activity relationship studies of acridones as potential antipsoriatic agents. 2. Synthesis and antiproliferative activity of 10-substituted hydroxy-10H-acridin-9-ones against human keratinocyte growth. *Eur. J. Med. Chem.* **2010**, *45*, 5345–5352. [[CrossRef](#)]
112. Mok, C.F.; Xie, C.M.; Sham, K.W.; Lin, Z.X.; Cheng, C.H. 1,4-Dihydroxy-2-naphthoic acid induces apoptosis in human keratinocyte: Potential application for psoriasis treatment. *Evid. Based Complement. Alternat. Med.* **2013**, *2013*, 792840. [[CrossRef](#)] [[PubMed](#)]
113. Hua, H.Q.; Wang, J.H.; Qin, S.Q. Discussion on use of arsenic trioxide in the past and present. *Chin. J. Chin. Mater. Med.* **2003**, *28*, 186–189.
114. Tse, W.P.; Cheng, C.H.; Che, C.T.; Lin, Z.X. Arsenic trioxide, arsenic pentoxide, and arsenic iodide inhibit human keratinocyte proliferation through the induction of apoptosis. *J. Pharmacol. Exp. Ther.* **2008**, *326*, 388–394. [[CrossRef](#)]
115. Shen, S.C.; Lee, W.R.; Yang, L.Y.; Tsai, H.H.; Yang, L.L.; Chen, Y.C. Quercetin enhancement of arsenic-induced apoptosis via stimulating ROS-dependent p53 protein ubiquitination in human HaCaT keratinocytes. *Exp. Dermatol.* **2012**, *21*, 370–375. [[CrossRef](#)]
116. Lee, Y.K.; Hwang, J.T.; Kwon, D.Y.; Surh, Y.J.; Park, O.J. Induction of apoptosis by quercetin is mediated through AMPK α 1/ASK1/p38 pathway. *Cancer Lett.* **2010**, *292*, 228–236. [[CrossRef](#)]
117. Siefring, M.L.; Lu, D.; States, J.C.; Van Hoang, M. Rapid onset of multiple concurrent squamous cell carcinomas associated with the use of an arsenic-containing traditional medicine for chronic plaque psoriasis. *BMJ Case Rep.* **2018**. [[CrossRef](#)]
118. Huang, K.F.; Ma, K.H.; Liu, P.S.; Chen, B.W.; Chueh, S.H. Baicalein increases keratin 1 and 10 expression in HaCaT keratinocytes via TRPV4 receptor activation. *Exp. Dermatol.* **2016**, *25*, 623–629. [[CrossRef](#)]
119. Zhou, L.L.; Lin, Z.X.; Fung, K.P.; Cheng, C.H.; Che, C.T.; Zhao, M.; Wu, S.H.; Zuo, Z. Celastrol-induced apoptosis in human HaCaT keratinocytes involves the inhibition of NF- κ B activity. *Eur. J. Pharmacol.* **2011**, *670*, 399–408. [[CrossRef](#)] [[PubMed](#)]

120. Zhang, C.S.; Yu, J.J.; Parker, S.; Zhang, A.L.; May, B.; Lu, C.; Xue, C.C. Oral Chinese herbal medicine combined with pharmacotherapy for psoriasis vulgaris: A systematic review. *Int. J. Dermatol.* **2014**, *53*, 1305–1318. [\[CrossRef\]](#)
121. Li, F.L.; Xu, R.; Zeng, Q.C.; Li, X.; Chen, J.; Wang, Y.F.; Fan, B.; Geng, L.; Li, B. Tanshinone IIA inhibits growth of keratinocytes through cell cycle arrest and apoptosis: Underlying treatment mechanism of psoriasis. *Evid. Based Complement. Alternat. Med.* **2012**, *2012*, 927658. [\[CrossRef\]](#)
122. Jin, M.; Lee, H.J.; Ryu, J.H.; Chung, K.S. Inhibition of LPS-induced NO production and NF- κ B activation by a sesquiterpene from *Saussurea lappa*. *Arch. Pharm. Res.* **2000**, *223*, 54–58. [\[CrossRef\]](#)
123. Oh, G.S.; Pae, H.O.; Chung, H.T.; Kwon, J.W.; Lee, J.H.; Kwon, T.O.; Kwon, S.Y.; Chon, B.H.; Yun, Y.G. Dehydrocostus lactone enhances tumor necrosis factor- α -induced apoptosis of human leukemia HL-60 cells. *Immunopharmacol. Immunotoxicol.* **2004**, *26*, 163–175. [\[CrossRef\]](#)
124. Scarponi, C.; Butturini, E.; Sestito, R.; Madonna, S.; Cavani, A.; Mariotto, S.; Albanesi, C. Inhibition of inflammatory and proliferative responses of human keratinocytes exposed to the sesquiterpene lactones dehydrocostuslactone and costunolide. *PLoS One* **2014**, *9*, e107904. [\[CrossRef\]](#)
125. Chamcheu, J.C.; Afaq, F.; Syed, D.N.; Siddiqui, I.A.; Adhami, V.M.; Khan, N.; Singh, S.; Boylan, B.T.; Wood, G.S.; Mukhtar, H. Delphinidin, a dietary antioxidant, induces human epidermal keratinocyte differentiation but not apoptosis: Studies in submerged and three-dimensional epidermal equivalent models. *Exp. Dermatol.* **2013**, *22*, 342–348. [\[CrossRef\]](#)
126. Chamcheu, J.C.; Pal, H.C.; Siddiqui, I.A.; Adhami, V.M.; Ayehunie, S.; Boylan, B.T.; Noubissi, F.K.; Khan, N.; Syed, D.N.; Elmets, C.A.; et al. Prodifferentiation, anti-inflammatory and antiproliferative effects of delphinidin, a dietary anthocyanidin, in a full-thickness three-dimensional reconstituted human skin model of psoriasis. *Skin Pharmacol. Physiol.* **2015**, *28*, 177–188. [\[CrossRef\]](#) [\[PubMed\]](#)
127. Srisuwan, S.; Tongtawe, P.; Srimanote, P.; Voravuthikunchai, S.P. Rhodomyrtone modulates innate immune responses of THP-1 monocytes to assist in clearing methicillin-resistant *Staphylococcus aureus*. *PLoS ONE* **2014**, *9*, e110321. [\[CrossRef\]](#)
128. Chorachoo, J.; Saeloh, D.; Srichana, T.; Amnuait, T.; Musthafa, K.S.; Sretrirutchai, S.; Voravuthikunchai, S.P. Rhodomyrtone as a potential anti-proliferative and apoptosis inducing agent in HaCaT keratinocyte cells. *Eur. J. Pharmacol.* **2016**, *772*, 144–151. [\[CrossRef\]](#)
129. Chorachoo, J.; Lambert, S.; Furnholm, T.; Roberts, L.; Reingold, L.; Auepemkiate, S.; Voravuthikunchai, S.P.; Johnston, A. The small molecule rhodomyrtone suppresses TNF- α and IL-17A-induced keratinocyte inflammatory responses: A potential new therapeutic for psoriasis. *PLoS One* **2018**, *13*, e0205340. [\[CrossRef\]](#)
130. Kim, H.J.; Kang, S.Y.; Kim, S.J.; Kim, S.H.; Kim, T.Y. Potentiation of UVB-induced apoptosis by novel phytosphingosine derivative, tetraacetyl phytosphingosine in HaCaT cell and mouse skin. *Apoptosis* **2004**, *9*, 449–456. [\[CrossRef\]](#) [\[PubMed\]](#)
131. Kim, B.H.; Lee, J.M.; Jung, Y.G.; Kim, S.; Kim, T.Y. Phytosphingosine derivatives ameliorate skin inflammation by inhibiting NF- κ B and JAK/STAT signaling in keratinocytes and mice. *J. Invest. Dermatol.* **2014**, *134*, 1023–1032. [\[CrossRef\]](#)
132. Yu, S.; Yan, H.; Zhang, L.; Shan, M.; Chen, P.; Ding, A.; Li, S.F. A review on the phytochemistry, pharmacology, and pharmacokinetics of amentoflavone, a naturally-occurring biflavonoid. *Molecules* **2017**, *22*, 299. [\[CrossRef\]](#)
133. An, J.; Li, Z.; Dong, Y.; Ren, J.; Huo, J. Amentoflavone protects against psoriasis-like skin lesion through suppression of NF- κ B-mediated inflammation and keratinocyte proliferation. *Mol. Cell. Biochem.* **2016**, *413*, 87–95. [\[CrossRef\]](#)
134. Zhang, W.J.; Song, Z.B.; Bao, Y.L.; Li, W.L.; Yang, X.G.; Wang, Q.; Yu, C.L.; Sun, L.G.; Huang, Y.X.; Li, Y.X. Periplogenin induces necroptotic cell death through oxidative stress in HaCaT cells and ameliorates skin lesions in the TPA- and IMQ-induced psoriasis-like mouse models. *Biochem. Pharmacol.* **2016**, *105*, 66–79. [\[CrossRef\]](#) [\[PubMed\]](#)
135. Horinouchi, C.D.; Mendes, D.A.; Nolte, S.; Brito, P.S.; Soley, B.D.; Favero, G.M.; Facundo, V.A.; Santos, A.R.; Cabrini, D.A.; Otuki, M.F. Anti-proliferative and anti-inflammatory effects of 3 β ,6 β ,16 β -Trihydroxylup-20(29)-ene on cutaneous inflammation. *J. Ethnopharmacol.* **2017**, *195*, 298–308. [\[CrossRef\]](#) [\[PubMed\]](#)
136. Viau, C.M.; Moura, D.J.; Facundo, V.A.; Saffi, J. The natural triterpene 3 β ,6 β ,16 β -trihydroxy-lup-20(29)-ene obtained from the flowers of *Combretum leprosum* induces apoptosis in MCF-7 breast cancer cells. *BMC Complement. Altern. Med.* **2014**, *14*, 280. [\[CrossRef\]](#)

137. Kim, M.H.; Nugroho, A.; Choi, J.; Park, J.H.; Park, H.J. Rhododendrin, an analgesic/anti-inflammatory arylbutanoid glycoside, from the leaves of *Rhododendron aureum*. *Arch. Pharm. Res.* **2011**, *34*, 971–978. [\[CrossRef\]](#)
138. Jeon, Y.J.; Kim, B.H.; Kim, S.; Oh, I.; Lee, S.; Shin, J.; Kim, T.Y. Rhododendrin ameliorates skin inflammation through inhibition of NF- κ B, MAPK, and PI3K/Akt signaling. *Eur. J. Pharmacol.* **2013**, *714*, 7–14. [\[CrossRef\]](#)
139. Jeon, Y.J.; Sah, S.K.; Yang, H.S.; Lee, J.H.; Shin, J.; Kim, T.Y. Rhododendrin inhibits toll-like receptor-7-mediated psoriasis-like skin inflammation in mice. *Exp. Mol. Med.* **2017**, *49*, e349. [\[CrossRef\]](#)
140. Alam, F.; Khan, G.N.; Bin Asad, M.H.H. *Psoralea corylifolia* L: Ethnobotanical, biological, and chemical aspects: A review. *Phytother. Res.* **2018**, *32*, 597–615. [\[CrossRef\]](#)
141. Alalaiwe, A.; Hung, C.F.; Leu, Y.L.; Tahara, K.; Chen, H.H.; Hu, K.Y.; Fang, J.Y. The active compounds derived from *Psoralea corylifolia* for photochemotherapy against psoriasis-like lesions: The relationship between structure and percutaneous absorption. *Eur. J. Pharm. Sci.* **2018**, *124*, 114–126. [\[CrossRef\]](#) [\[PubMed\]](#)
142. Hirose-Matsuda, H.; Okamoto, O.; Sakai, T.; Ito, A.; Kai, Y.; Hatano, Y.; Hanada, K.; Yamaoka, Y.; Fujiwara, S. Multiple malignant changes and recurrent infections in the skin associated with long-term exposure to ultraviolet light and topical psoralen plus ultraviolet A therapy. *J. Dermatol.* **2015**, *42*, 536–537. [\[CrossRef\]](#) [\[PubMed\]](#)
143. Balasubramanian, S.; Eckert, R.L. Keratinocyte proliferation, differentiation, and apoptosis—differential mechanisms of regulation by curcumin, EGCG and apigenin. *Toxicol. Appl. Pharmacol.* **2007**, *224*, 214–219. [\[CrossRef\]](#) [\[PubMed\]](#)
144. Zhang, S.; Liu, X.; Mei, L.; Wang, H.; Fang, F. Epigallocatechin-3-gallate (EGCG) inhibits imiquimod-induced psoriasis-like inflammation of BALB/c mice. *BMC Complement. Altern. Med.* **2016**, *16*, 334. [\[CrossRef\]](#) [\[PubMed\]](#)



© 2019 by the authors. Licensee MDPI, Basel, Switzerland. This article is an open access article distributed under the terms and conditions of the Creative Commons Attribution (CC BY) license (<http://creativecommons.org/licenses/by/4.0/>).



Article

Topical Spilanthol Inhibits MAPK Signaling and Ameliorates Allergic Inflammation in DNCB-Induced Atopic Dermatitis in Mice

Wen-Chung Huang ^{1,2,†} , Chun-Hsun Huang ^{3,4,†}, Sindy Hu ^{3,4}, Hui-Ling Peng ¹ and Shu-Ju Wu ^{4,5,*}

- ¹ Graduate Institute of Health Industry Technology, Research Center for Food and Cosmetic Safety, College of Human Ecology, Chang Gung University of Science and Technology, Taoyuan City 33303, Taiwan; wchuang@mail.cgust.edu.tw (W.-C.H.); hlpeng@mail.cgust.edu.tw (H.-L.P.)
 - ² Division of Allergy, Asthma, and Rheumatology, Department of Pediatrics, Chang Gung Memorial Hospital, Linkou, Taoyuan City 33303, Taiwan
 - ³ Department of Cosmetic Science, Research Center for Food and Cosmetic Safety, and Research Center for Chinese Herbal Medicine, College of Human Ecology, Chang Gung University of Science and Technology, Guishan Dist., Taoyuan City 33303, Taiwan; chuang@mail.cgust.edu.tw (C.-H.H.); sindyhu@hotmail.com (S.H.)
 - ⁴ Department of Dermatology, Aesthetic Medical Center, Chang Gung Memorial Hospital, Taoyuan City 33303, Taiwan
 - ⁵ Department of Nutrition and Health Sciences, Research Center for Chinese Herbal Medicine, College of Human Ecology, Chang Gung University of Science and Technology, Taoyuan City 33303, Taiwan
- * Correspondence: sjwu@mail.cgust.edu.tw; Tel.: +886-3-2118999 (ext. 5493)
- † These authors contributed equally to this work.

Received: 24 April 2019; Accepted: 18 May 2019; Published: 20 May 2019



Abstract: Atopic dermatitis (AD) is a recurrent allergic skin disease caused by genetic and environmental factors. Patients with AD may experience immune imbalance, increased levels of mast cells, immunoglobulin (Ig) E and pro-inflammatory factors (Cyclooxygenase, COX-2 and inducible NO synthase, iNOS). While spilanthol (SP) has anti-inflammatory and analgesic activities, its effect on AD remains to be explored. To develop a new means of SP, inflammation-related symptoms of AD were alleviated, and 2,4-dinitrochlorobenzene (DNCB) was used to induce AD-like skin lesions in BALB/c mice. Histopathological analysis was used to examine mast cells and eosinophils infiltration in AD-like skin lesions. The levels of IgE, IgG1 and IgG2a were measured by enzyme-linked immunosorbent assay (ELISA) kits. Western blot was used for analysis of the mitogen-activated protein kinase (MAPK) pathways and COX-2 and iNOS protein expression. Topical SP treatment reduced serum IgE and IgG2a levels and suppressed COX-2 and iNOS expression via blocked mitogen-activated protein kinase (MAPK) pathways in DNCB-induced AD-like lesions. Histopathological examination revealed that SP reduced epidermal thickness and collagen accumulation and inhibited mast cells and eosinophils infiltration into the AD-like lesions skin. These results indicate that SP may protect against AD skin lesions through inhibited MAPK signaling pathways and may diminish the infiltration of inflammatory cells to block allergic inflammation.

Keywords: spilanthol; IgE; allergic inflammation; MAPK; atopic dermatitis

1. Introduction

Common symptoms of atopic dermatitis (also known as atopic eczema) include itching, redness, and cracking skin. Pathological characteristics include dry, fragile skin as a result of epidermal defense

dysfunction. Due to abnormal immune function, a variety of allergens are able to penetrate the skin, making it more prone to allergic reaction or inflammation [1]. In addition, atopic dermatitis (AD) is the product of a series of complex interactions of innate and adaptive immune responses and IgE-mediated allergies to various exogenous antigens [2]. Serious inflammation is a hallmark of acute AD lesions, and chronic AD lesions are characterized by lichenified fibrosis and epidermal thickening [3].

Studies have found that allergic reactions activate T helper (Th) cells, and that an imbalance between Th1 and Th2 cells causes AD [4]. Activation of Th2 cells leads to an allergic response producing IgE and IgG1, which in turn strengthen the immune response [5,6]. IgE has a high affinity for the IgE receptor expressed on the surface of mast cells; if IgE adheres to the mast cells, they are called sensitized cells. Mast cells are Th2-activated regulatory cells that release a lot of inflammatory-related cytokines, which can cause inflammation and allergic reaction [7,8]. Th2-activated cells also enable the aggregation of eosinophils, causing localized severe inflammation. IgG2a production is dependent on Th1 cells, which can regulate the activity of Th2 cells. However, Th2 cells will inhibit the activity of Th1 cells, creating an imbalance in which Th2 cell activity is much higher than Th1 cell activity, which in turn can cause an allergic reaction. Th1 and Th2 immune response, AD, tend to Th2 and have allergic constitution [7,9,10]. Therefore, decreasing the activity of Th2 cells may improve skin symptoms of AD. In addition, MAPKs pathway, which include the extracellular signal-regulated kinase (ERK), c-jun N-terminal kinase (JNK), and p38 MAPK, have also been implicated in inflammatory signaling cascades. Phosphorylation of MAPKs causes the inflammatory mediators' production and promotes an allergic inflammatory response. MAPKs are important pathways in the inhibition of allergic inflammation. Therefore, inactivation of MAPKs subsequently decreases the allergic inflammatory response [11–13].

Spilanthes acmella Murr. is used as traditional folk medicine to treat toothache in the East Asia area. It has demonstrated a variety of biological effects, including anesthesia, analgesia, diuretic, and antibacterial effects [14–17]. Interestingly, research has supported the use of *Spilanthes* plant extract as a nutritional supplement and sweetener [18]. Alkamides are the most abundant phytochemicals present in *S. acmella*. Spilanthol (SP): ((2E,6Z,8E)-N-isobutylamide-2,6,8- deca trienamide) is a high-value bioactive compound and belongs to alkamides from *S. acmella* [19]. In addition, SP is also found in genus *Spilanthes*, including *Acmella brachyglossa*, *Acmella ciliate*, etc. [20,21]. SP reportedly has antibacterial, analgesic, and anti-wrinkle properties [22,23]. Previous studies showed that extract of *A. oleracea* is used in treatment of skin diseases including scabies and psoriasis, and used in anti-age applications (antiwrinkle cream) [20]. In a previous study, we found that SP exerts its anti-inflammatory activity by suppressing intercellular adhesion molecule 1 (ICAM-1) and COX-2 expression, and blocking the phosphorylated JNK signaling pathway [24]. However, it is not yet known about SP used in treatment of AD.

Therefore, in this study we evaluated the effects of SP on AD and sought to understand the mechanisms through which SP regulates allergic inflammation. Our findings indicate that SP reduces Th2-mediated infiltration by mast cells and eosinophils and decreases ear and dorsal skin thickness, and SP also inhibits COX-2 and iNOS expression by blocking MAPK pathways in mice with DNCB-induced AD.

2. Results

2.1. Spilanthol Attenuates Ear Swelling in BALB/c Mice with DNCB-Induced AD

To investigate the effect of SP on AD, we used DNCB-induced ear and dorsal skin inflammation of BALB/c mice (Figure 1A). DNCB-induced AD-like symptoms included ear swelling, scarring, and excoriation of the skin and ear compared with normal mice (Figure 1B). We measured ear thickness on day 30 of DNCB-induced experimental model ear swelling. Topical administration of SP significantly reduced ear swelling compared with DNCB-sensitized mice (Figure 1C) (SP-5: 0.461 ± 0.25 mm, $p < 0.05$; SP-10: 0.44 ± 0.18 mm, $p < 0.05$, vs. the DNCB group: 0.69 ± 0.24 mm).

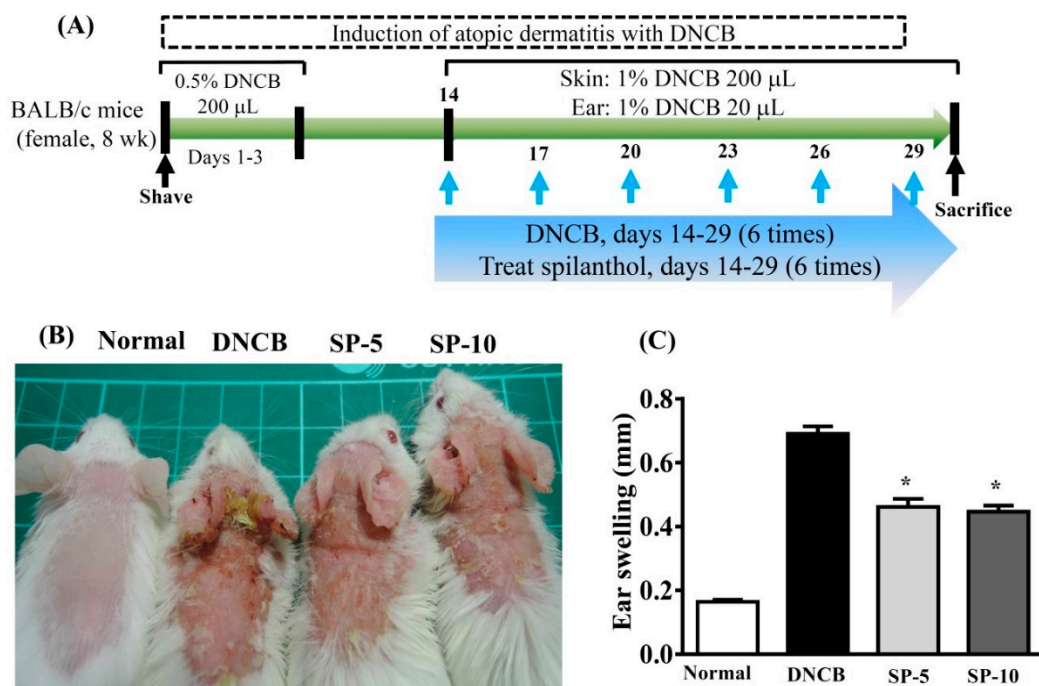


Figure 1. DNCB (2,4-dinitrochlorobenzene) induces atopic dermatitis (AD)-like lesions. **(A)** BALB/C mice were treated with 0.5% DNCB in acetone/olive oil (3:1) on days 1–3. Then, mice were challenged with 1% DNCB on days 14, 17, 20, 23, 26, and 29. AD-like lesions were treated with spilanthol (SP) (5 mg/kg or 10 mg/kg) or vehicle on days 14–27. Mice were sacrificed on day 30. **(B)** Clinical features of AD-like skin lesions treated topically with SP. **(C)** SP attenuates ear swelling by day 30 in DNCB-induced AD-like ear lesions. Data are presented as mean \pm SEM ($n = 8$ mice/group). * $p < 0.05$, versus DNCB mice.

2.2. Spilanthol Attenuates Collagen Deposition and Reduces Epidermal and Dermal Thickness in BALB/c Mice with DNCB-Induced AD

Masson's Trichrome staining was used to evaluate collagen deposition and tissue fibrosis in DNCB-induced AD-like lesions. The main object of Masson's Trichrome staining is collagen; collagen fibers were stained blue and the background was stained red. Hence, we used this staining to evaluate the improvement of collagen deposition after SP administration. Treatment with SP-5 or SP-10 significantly reduced ear thickness and hardening of the dorsal skin surface caused by inflammation; the remodeling on day 30 compared with the DNCB-sensitized group is shown in an image map (Figure 2A,C). Masson's Trichrome stain revealed that at day 30, collagen deposition in AD-like skin lesions was significantly lower in the ear (Figure 2B) and dorsal skin (Figure 2D) of the SP-5 and SP-10 groups than in the DNCB-sensitized group. Thicknesses of both the epidermis and dermis were also significantly reduced in the ear (Figure 2E) and dorsal skin (Figure 2F) of SP-treated groups compared with the DNCB-sensitized group at day 30. Collectively, these results support that SP administration modulates the recovery of AD-like lesions by reducing epidermal and dermal hyperplasia, down-regulating collagen over-build.

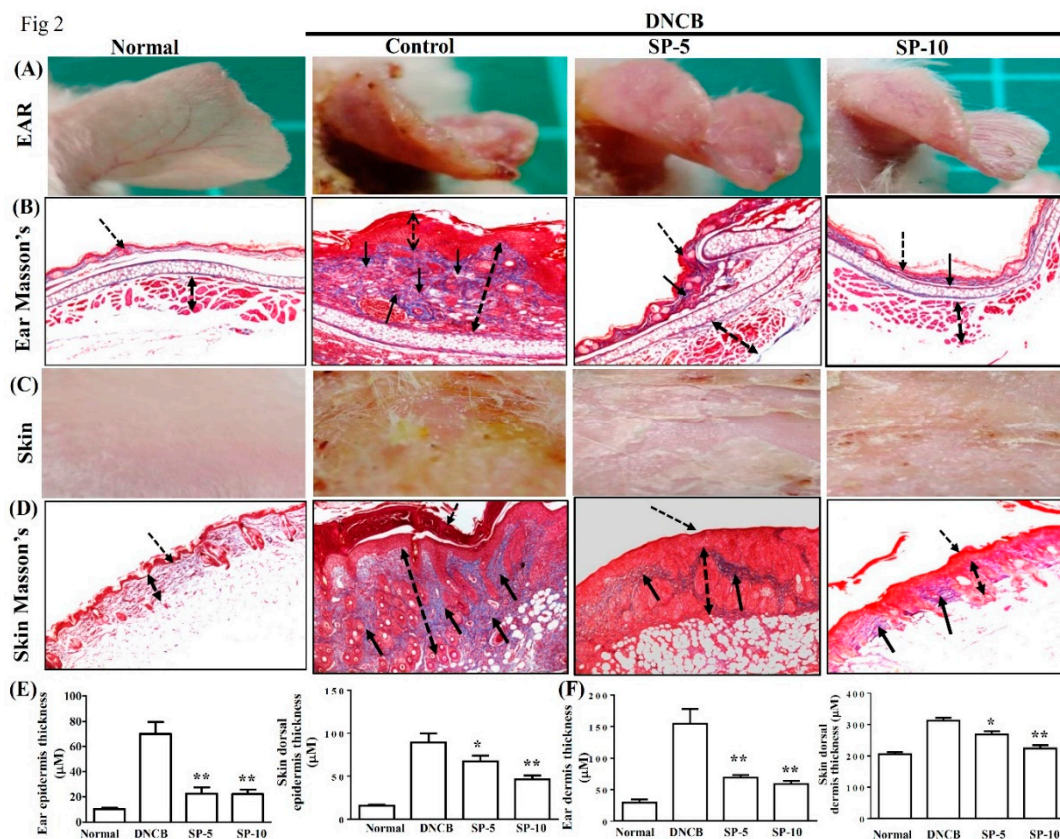


Figure 2. SP attenuated excessive dermal collagen and reduced epidermal thickness in DNCB-induced AD-like skin and ear lesions. (A) Ear lesions, (B) collagen deposition, (C) dorsal skin lesions, and (D) collagen deposition determined by Masson's Trichrome staining, day 30. Black arrows: Collagen deposition; dashed arrows: Dermal hyperplasia. (E) Epidermal and (F) dermal thickness of ear and skin. Data presented as mean \pm SEM ($n = 8$ mice/group). * $p < 0.05$, ** $p < 0.01$ versus DNCB mice.

2.3. Spilanthalol Inhibits Mast Cell Infiltration and Affects Serum Cytokines in BALB/c Mice with DNCB-Induced AD

Exposure to allergens stimulates IgE production in tissue and activates mast cells, then IgE and mast cells can induce complex immune responses and allergic symptoms [25]. Activated mast cells release inflammatory mediators, causing allergic inflammation in AD. To control activated mast cell release, inflammatory mediators can reduce allergic inflammation in AD [26,27]. Therefore, we focused on determining local infiltration by mast cells and assessing the inhibitory effect of SP on mast cell infiltration in mice with DNCB-induced AD. Toluidine blue staining of the ear and dorsal skin of DNCB-treated mice was performed to observe mast cell features. Topical administration of SP suppressed mast cell infiltration in the ears and dorsal skin compared with the DNCB-sensitized group (Figure 3A,B). The number of mast cells significantly decreased after SP administration compared with the DNCB-sensitized group (ear: SP-5: 61.5 ± 8.7 , $p < 0.01$, SP-10: 47.2 ± 7.2 , $p < 0.01$, vs. the DNCB-sensitized group: 137.4 ± 5.5 ; skin: SP-5: 54.6 ± 2.1 , $p < 0.01$, SP-10: 53.2 ± 2.4 , $p < 0.01$, vs. the DNCB-sensitized group: $87.8.0 \pm 3.1$) (Figure 3B,D). We also measured antibody levels to determine whether SP was able to modulate the allergic response in serum. Increasing serum IgE level is a major characteristic of AD, and we found that topical administration of SP significantly suppressed serum IgE and IgG1 levels in SP-10 mice, whereas serum IgG2a levels were significantly increased in SP-treated mice compared with the DNCB-sensitized group (Figure 3E). This suggests that SP can suppress the infiltration of mast cells and modulate the immune response.

Fig 3 toluidine blue

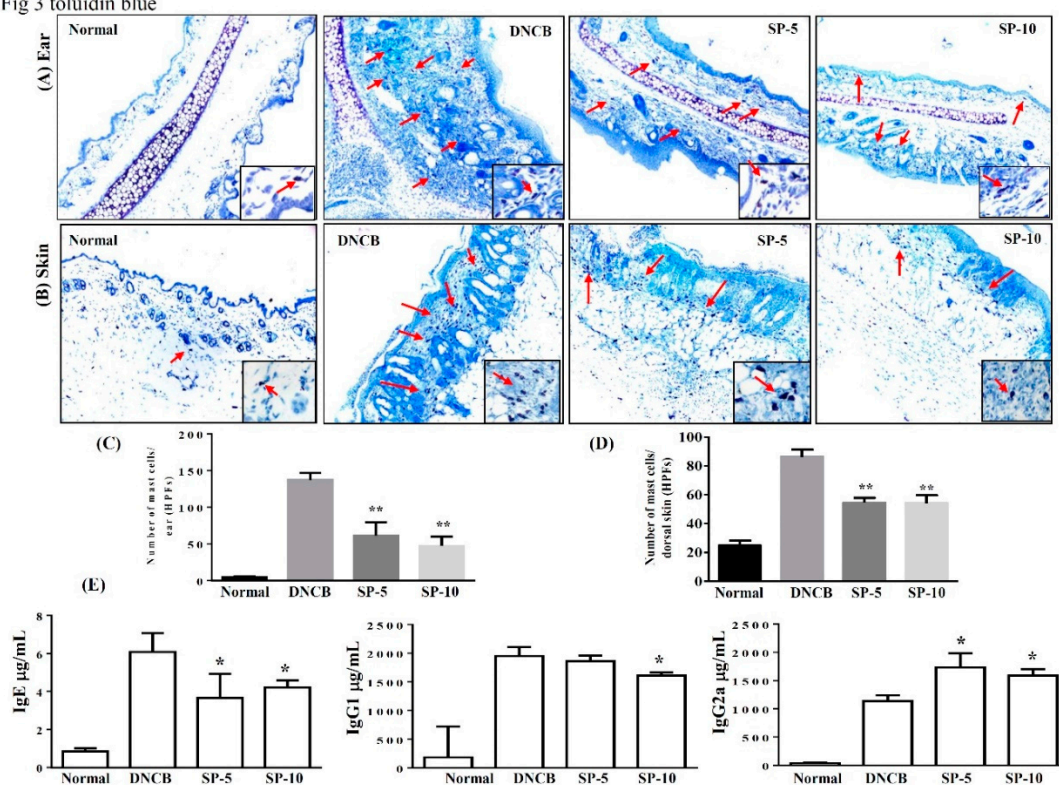


Figure 3. SP inhibits mast cell infiltration and modulates cytokine levels in DNCB-induced AD-like skin and ear lesions. Mast cell infiltration (red arrows) stained with toluidine blue in (A) ear and (B) dorsal skin sections. (C) Mast cells measured under 10–15 high-power fields (HPFs) in ear and (D) dorsal skin. (E) Serum levels of IgE, IgG1, and IgG2 measured using ELISA. Data presented as mean \pm SEM ($n = 8$ mice/group). * $p < 0.05$, ** $p < 0.01$ versus DNCB mice.

2.4. Spilanthal Suppresses Eosinophil Infiltration and Inhibits Protein Expression of MAPK Signaling Pathways in BALB/c Mice with DNCB-Induced AD

To investigate the effect of SP on ear and dorsal skin, sections were stained with hematoxylin and eosin (H&E) to examine eosinophil infiltration in AD-like skin lesions. DNCB-sensitized mice exhibited more eosinophil infiltration than non-sensitized control mice. Increasing the permeability of blood vessels allows eosinophils to infiltrate into tissue. Topical administration of SP significantly decreased eosinophil infiltration compared with DNCB-sensitized mice (Figure 4A,B). The number of eosinophils decreased significantly after administration of SP compared with DNCB-sensitized mice (ear: SP-5: 74.5 ± 8.1 , $p < 0.01$, SP-10: 40.7 ± 2.1 , $p < 0.01$, vs. the DNCB group: 196.8 ± 4.8 ; dorsal skin: SP-5: 90.8 ± 4.3 , $p < 0.01$, SP-10: 118.1 ± 2.6 , $p < 0.01$, vs. the DNCB group: 403.5 ± 8.3) (Figure 4C,D).

The production of inflammation mediators by activated MAPK signaling pathways is also related to allergic inflammation. Therefore, we also investigated the effect of SP on the expression of ERK1/2, p38, and JNK proteins (Figure 4E). Results showed that levels of phosphorylated MAPK proteins (p-p38, p-JNK, and p-ERK) were increased significantly more in DNCB mice than in non-sensitized control mice, and topical administration of SP significantly decreased phosphorylation of ERK1/2, p38, and JNK in SP-treated mice compared with DNCB-sensitized mice (Figure 4F). These results indicated that SP suppressed allergic inflammation by blocking MAPK signaling pathways.

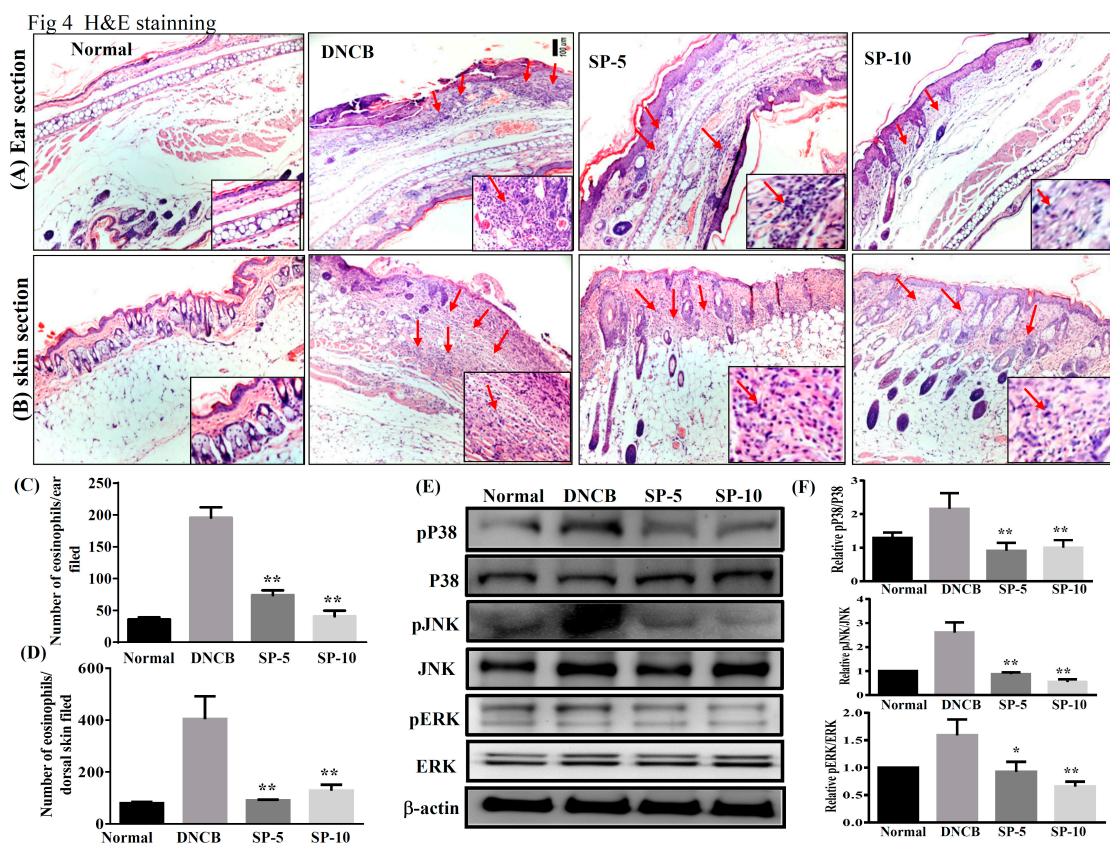


Figure 4. SP suppressed eosinophil infiltration and blocked mitogen-activated protein kinase (MAPK) signaling in DNCB-induced AD-like skin and ear lesions. Eosinophil infiltration (red arrows) in (A) ear and (B) dorsal skin lesions, determined by hematoxylin and eosin (H&E) stain. The number of eosinophils infiltrating the (C) ear and (D) dorsal skin measured under 10–15 high-power fields (HPFs). (E) Western blotting assays of p-extracellular signal-regulated kinase (p-ERK), p-p38, and p-c-jun N-terminal kinase (p-JNK) ($n = 6/\text{group}$), and (F) expression of p-ERK, p-p38, and p-JNK relative to ERK, p38, and JNK. The proteins were normalized to total JNK, ERK, and p38 protein levels, the total MAPK levels were used as internal controls. The relative intensity was calculated as the ratio of the intensities of the pP38, p-JNK, and p-ERK bands to the intensity of the total P38, JNK, and ERK bands, respectively. Data presented as mean \pm SEM; * $p < 0.05$, ** $p < 0.01$ versus DNCB mice. 100x magnification; amplified graph is 200x; $n = 8$ mice/group. Data presented as mean \pm SEM. * $p < 0.05$, ** $p < 0.01$ versus sensitized control mice.

2.5. Spilanthalol Inhibits the Expression of Pro-Inflammatory Factors COX-2 and iNOS in BALB/c Mice with DNCB-Induced AD

Studies have indicated that increases in pro-inflammatory factors COX-2 and iNOS are observed in patients with AD [28]. Next, we investigated the effect of SP on DNCB-induced COX-2 and iNOS expression in AD-like mice. Immunohistochemistry showed that expression of COX-2 was lower in paraffin sections of ear biopsies (Figure 5A). Immunoblot analysis revealed that the levels of COX-2 and iNOS were significantly lower in SP-treated groups than in DNCB-sensitized mice (Figure 5B,C). Immunoblot analysis of COX-2 expression was consistent with the results of the immunohistochemical analysis. These results demonstrate that SP can reduce the inflammatory response by down-regulating the expression of inflammatory mediators COX-2 and iNOS in AD-like mice. We also evaluated the effects of SP on liver and kidney toxicity, as demonstrated by the drastic elevation of serum glutamate-oxaloacetic transaminase (GOT), glutamate-pyruvate transaminase (GPT), creatinine, and blood urea nitrogen (BUN). We found that serum GOT and GPT in the four groups of mice were within the normal range, although SP significantly decreased serum GOT and GPT levels in

SP-treated mice compared with DNCB-sensitized mice (Figure 5D). In addition, serum creatinine and BUN levels were statistically similar among all experimental groups (Figure 5E). In brief, SP does not injure the liver or kidneys of AD-like mice.

Fig 5 IHC staining (A) Ear section

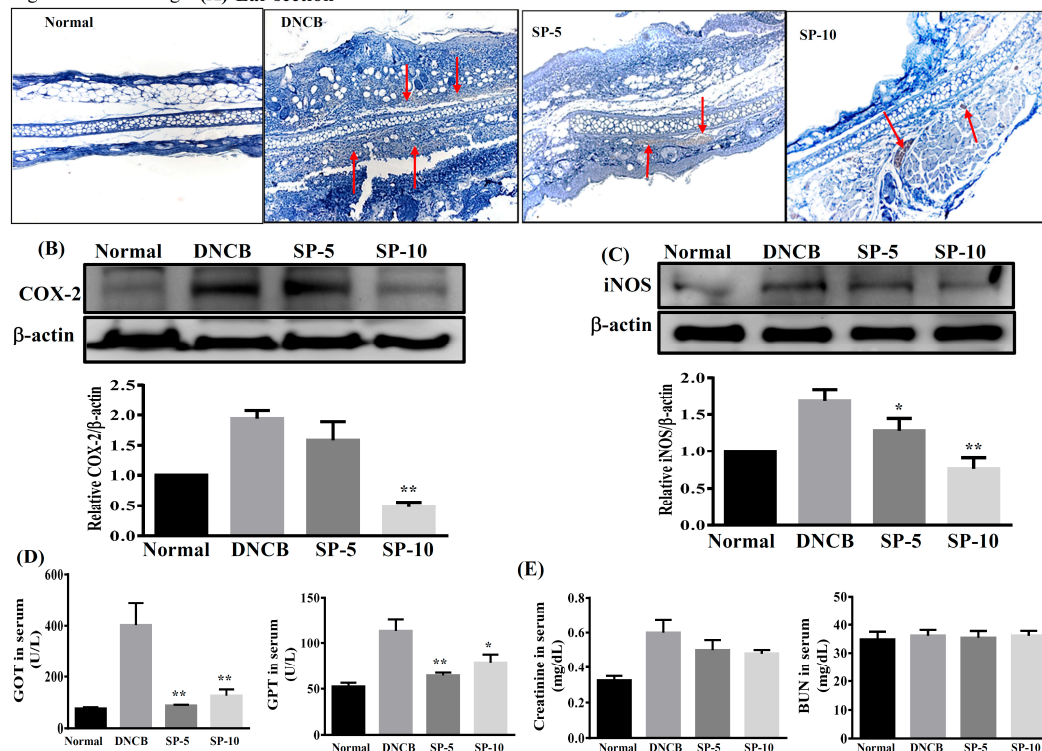


Figure 5. Effects of SP on cyclooxygenase-2 (COX-2) and inducible NO synthase (iNOS) in DNCB-induced AD-like skin lesions. (A) Immunohistochemical staining of COX-2 in ear (red arrows). (B) COX-2 level assayed by Western blot, and COX-2 protein expression relative to β -actin. (C) iNOS level assayed by Western blot, and iNOS protein expression relative to β -actin. Quantification of β -actin, iNOS, and COX-2 expression. β -actin expression was used as an internal control, the relative intensity was calculated as the ratio of the intensities of the COX-2 and iNOS bands to the intensity of the β -actin. Effects of spilanthol on (D) serum GOT and GPT, and (E) serum creatinine and BUN. Serum was centrifuged, collected, and evaluated by ELISA. Data presented as mean \pm SEM; * p < 0.05, ** p < 0.01 versus DNCB mice. 100x magnification; amplified graph is 200x; n = 8 mice/group. Data presented as mean \pm SEM. * p < 0.05, ** p < 0.01 versus sensitized control mice.

3. Discussion

In this study, we investigated the anti-AD activity of SP in BALB/c mice with DNCB-induced AD. DNCB is an allergenic chemical commonly used to induce AD in animal models [27,29]. Environmental or allergic AD is known as extrinsic type AD, and genetic or non-allergic AD is known as intrinsic type AD [30]. Extrinsic or environmental factors induce severe AD through stimulation, triggering IgE-mediated forms of skin inflammation and allergic reaction [31]. AD is one of the most common chronic inflammatory skin diseases, and is characterized by erythema, dry skin, pruritus, and abnormal immune responses [27]. Repeated triggering of the allergic-inflammatory response leads to remodeling and hardening of the skin surface, leading the epidermis to thicken and break, resulting in infiltration of eosinophils and mast cells in AD skin lesions [32]. We found that topical treatment with SP ameliorated DNCB-induced AD-like skin lesions and improved skin lesion severity, ear swelling, and epidermal thickness in DNCB-treated BALB/c mice (Figures 1 and 2). Moreover, SP reduced DNCB-induced collagen hyperplasia in AD-like skin lesions, as determined by Masson's stain

(Figure 2B,D). These results suggest that SP may be useful for the treatment of AD by reducing hyperkeratosis and fibrotic remodeling of the skin.

In the pathogenesis of AD, epidermal barrier function is impaired and the infiltration of environmental allergens into the skin increases, which in turn causes the allergic reactions and inflammation that are major characteristics of IgE-mediated hypersensitivity reactions [33]. Studies have shown that excessive IgE levels are closely related to imbalances of Th1 and Th2 cells in AD patients [30]. Th2-related cytokines, including of IL-4, are stimulators of IgE synthesis; excessive levels of IgE will activate mast cells and IL-5 induces eosinophil differentiation and infiltration into AD skin lesions, causing allergic inflammation. Excessive secretion of cytokines by activated Th2 cells will contribute to AD symptoms; therefore, down-regulation of Th2 cytokines may decrease production of IgE and improve AD [27,34]. Studies have indicated that increased secretion of Th1-related cytokines and decreased Th2-related cytokine levels may prevent excessive IgE production [35]. Reportedly, the IgG1 immune complex is responsible for class-switching to Th2 cytokines, and IgG2a is oriented toward Th1 cytokine immune deviation [36]. In addition, adjusting the balance of Th1/Th2 cytokines to inhibit mast cell activation, then decreasing the levels of IgG1 and increasing IgG2a has a significant anti-allergic inflammatory effect [37]. We found that topical treatment with SP reduced IgE levels and regulated IgG1 and IgG2a levels in DNCB-treated BALB/c mice (Figure 3E). In addition, SP also improved the infiltration of mast cells and eosinophils into AD skin lesions (Figure 3A,B and Figure 4A,B). These findings suggest that SP has a significant anti-allergic effect in AD. The SP may suppress eosinophil infiltration and down-regulate IgE expression to reduce mast cell infiltration into AD skin lesions.

Skin epidermal barrier dysfunction causing hardening and fragility of the skin surface is one of the main causes of AD, and inflammation can be modulated to reduce skin barrier function, thus aggravating lesions [29,30]. In addition, studies have indicated that constituents of MAPK pathways, including ERK, JNK, and p38, are involved in the pathogenesis of AD; in other words, AD is a chronic allergic inflammatory skin disease [38]. MAPK pathway activation promotes a number of inflammatory mediators, including COX-2 and iNOS [39]. COX-2 catalyzes arachidonic acid into prostaglandin, the levels of prostaglandin and COX-2 activity are related to promote inflammatory pain [40]. iNOS is produced by cytokines in inflammatory cells, which generate the free radical NO from L-arginine. iNOS and NO are related to cellular oxidative stress and the host cellular immune response [41]. Several reports have shown that SP exhibits anti-inflammatory efficacy *in vitro* and *in vivo* [18,20–22]. However, it has been unknown whether SP exhibits anti-inflammatory activity in AD skin lesions. DNCB is a potential allergen that can induce skin sensitivity and inflammation [42]. Therefore, we identified SP as a possible suppressor of MAPK signal pathways triggered by DNCB in mice with DNCB-induced AD. In this work, we found that the anti-allergic effects of SP seem to occur through the blocked phosphorylation of ERK1/2, JNK, and p38 MAPK signaling pathways, and suppress COX-2 and iNOS expression in DNCB-induced AD skin lesions (Figures 4 and 5). Based on these results, we suggest that SP may be useful as a treatment for allergic inflammation in AD.

We found that SP not only inhibited the levels of IgE and IgG2a, but also increased IgG1 level. SP may therefore be associated with mast cell-related allergic effects. Furthermore, SP significantly decreased eosinophil infiltration and reduced the expression of pro-inflammatory factors COX-2 and iNOS by suppressing MAPK pathways. SP may be associated with the improvement of eosinophil-related allergic inflammation in AD-like skin lesions. In addition, we found evidence that SP decreased collagen over-deposition in the dermis and reduced epidermal thickness in AD-like lesions. Collectively, we propose a model to explain the anti-allergic effects of SP in AD-like mice (Figure 6).

In summary, we present the first study demonstrating that SP has anti-AD potential. Results of this study demonstrate that SP can improve AD symptoms. SP-regulated Th1/Th2 balance, inhibited mast cell hyperplasia, and suppressed MAPK pathways ameliorated DNCB-induced AD-like skin inflammation in mice.

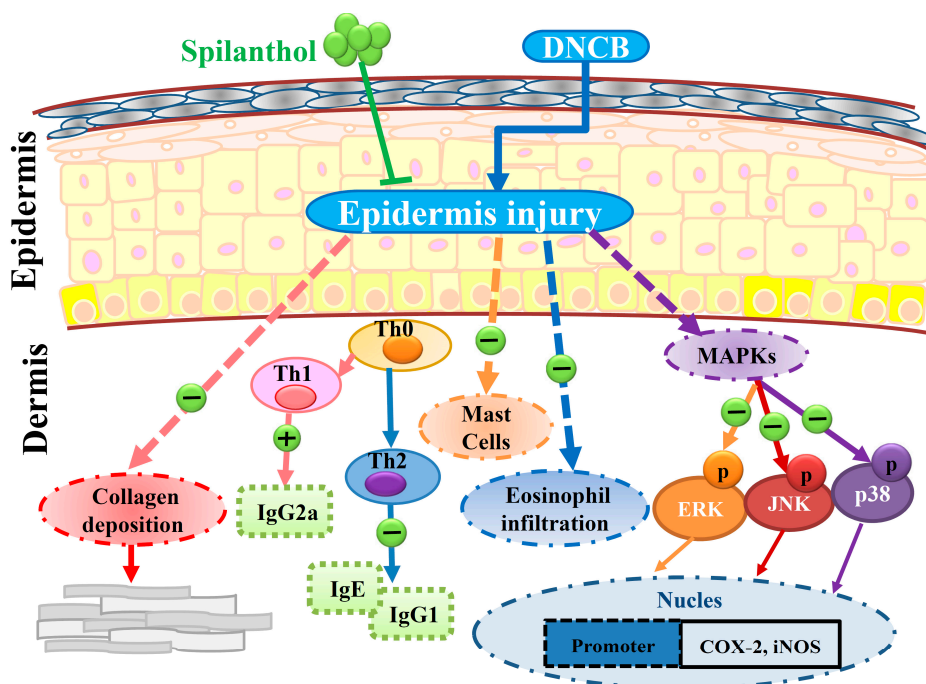


Figure 6. Topical spilanthol improves mast cell infiltration, modulates Th1/Th2 cytokine levels, and inhibits MAPK signaling, ameliorating allergic inflammation in DNCB-induced atopic.

4. Materials and Methods

4.1. Animals

Eight-week-old female BALB/c mice were purchased from the National Laboratory Animal Center (Taiwan) and housed at the Animal Center of Chang Gung University in an air-conditioned room at a consistent temperature ($23 \pm 2^\circ\text{C}$) and $55 \pm 15\%$ humidity, with a 12 h light–dark cycle. All procedures involving animals were approved in accordance with the guidelines and regulations of the Laboratory Animal Care Committee of Chang Gung University of Science and Technology and Chang Gung University (IACUC approval number: 2015-020; 29 December 2015).

4.2. DNCB Induction of AD-Like Skin Lesions and Spilanthol Treatment

Spilanthol was purchased from ChromaDex, Irvine, CA, USA. Mice were randomly divided into four groups ($n = 8$ per group): A mock-sensitized control group were sensitized and challenged with normal saline; a sensitized control group were treated with DNCB in a 3:1 ratio of acetone:olive oil; an SP-5 group were challenged with DNCB and treated topically with SP 5 g/kg; and an SP-10 group were challenged with DNCB and treated topically with SP 10 g/kg. The dorsal skin was shaved, and then sensitized using DNCB (Sigma-Aldrich, St. Louis, MO, USA) as described in a previous study [25]. To sensitize the skin, 200 μL 0.5% DNCB in acetone:olive oil (3:1) was applied to the shaved area on experimental days 1–3. Next, for the challenge process, 100 μL of 1% DNCB was applied to each ear and the dorsal skin on experimental days 14, 17, 20, 23, 26, and 29. All SP treatments were applied to the ears and backs of the mice daily on experimental days 14 to 29. The experimental design is described in Figure 1A.

4.3. Measurement of Ear and Epidermal Thickness

Images were captured weekly with a digital camera (Coolpix, Nikon Inc., Tokyo, Japan) to record clinical symptoms on the ear and dorsal skin. Ear thickness was measured using a dial gauge (Olympus, Tokyo, Japan) on day 30. Ear and skin epidermal thickness were measured using Masson's stain and the aid of a microscope with Image-Pro Plus software (version 6.0 for Windows).

4.4. Histopathological Analysis

The ear and dorsal skin of each mouse were obtained on day 30 and fixed in 10% formalin. These tissues were cut into 6- μ m thick sections and stained with Masson's, hematoxylin and eosin (H&E), toluidine blue, and immunohistochemical stain, as previously described [25,39]. The sections were under 10–15 high-power fields (HPFs) using a light microscope at 100–200 \times magnification to measure mast cells and eosinophils. Mast cells and eosinophils were stained with toluidine blue and H&E, respectively. Collagen accumulation was assessed by Masson's stain and using COX-2 antibody; immunohistochemical stain was used to observe positive COX-2 staining. Then, sections were examined using light microscopy to observe histological changes in all stained sections.

4.5. Measurement of Serum IgE and Cytokines

Blood samples were collected from BALB/c mice on day 30 and centrifuged at 3000 g for 10 min at 4 °C to obtain serum. The levels of serum IgE, IgG1, and IgG2a were measured using enzyme-linked immunosorbent assay (ELISA) kits (BD Biosciences, San Diego, CA, USA) according to the manufacturer's instructions. Optical density was measured using a microplate reader (Multiskan FC, Thermo, Waltham, MA, USA). In addition, liver function indices (GPT and GOT) and kidney function indices (BUN and creatinine) were analyzed enzymatically using commercially available assay kits (Wako Pure Chemical, Osaka, Japan).

4.6. Western Blot Analysis

Dorsal skin samples were harvested on day 30 and stored at –80 °C. To investigate protein expression, protein lysates were prepared using protein lysis buffer (Sigma, St. Louis, MO, USA). The protein amounts were quantitated using the BCA protein assay kit (Pierce). Then, equal amounts of protein were separated on 10% SDS-PAGE gels and electrotransferred to polyvinylidene fluoride membranes (PVDF; Millipore, Billerica, MA, United States). The PVDF membranes were probed with primary antibodies raised against COX-2 and iNOS (Santa Cruz, CA, USA); ERK1/2, p38, JNK, phospho-ERK 1/2, phospho-p38, and phospho-JNK (Millipore); and β -actin (Sigma) overnight at 4 °C. Next, membranes were washed 3 times in Tris-buffered saline with Tween 20 (TBST) buffer (150 mM NaCl, 10 mM Tris-HCl pH 8.0, 0.1% Tween 20), then incubated in secondary antibodies at room temperature for 1 h, followed by incubation with HRP-conjugated secondary antibodies at room temperature for 1 h. Finally, the membranes were washed using TBST and incubated with Luminol/Enhancer Solution (Millipore). Protein bands were quantitated using the BioSpectrum 600 system (UVP, Upland, CA, United States).

4.7. Statistical Analysis

Data are reported as the mean \pm standard error of the mean (SEM). All statistical significance was assessed using one-way analysis of variance (ANOVA) and Tukey's test. Differences were considered statistically significant at $p < 0.05$.

Author Contributions: W.-C.H. and H.-L.P. designed the study and performed the experiments. C.-H.H. and S.H. searched the literature and performed the experiments. S.-J.W. interpreted the data and drafted the manuscript.

Funding: This study was supported in part by grants from Chang Gung Memorial Hospital (CMRPF1G0202, CMRPF1H0111) and the Ministry of Science and Technology in Taiwan (MOST 105-2320-B-255-004).

Conflicts of Interest: The authors declare that they have no conflict of interest.

Abbreviations

AD	Atopic dermatitis
SP	Spilanthol
IgE	Immunoglobulin (Ig) E
IgG2a	Immunoglobulin (Ig) G2a
IgG1	Immunoglobulin (Ig) G1
COX-2	Cyclooxygenase-2
iNOS	Inducible NO synthase
DNCB	2,4-dinitrochlorobenzene
MAPK	Mitogen-activated protein kinase
ERK	Extracellular signal-regulated kinase
JNK	c-jun N-terminal kinase

References

1. Boguniewicz, M.; Leung, D.Y. Atopic dermatitis: A disease of altered skin barrier and immune dysregulation. *Immunol. Rev.* **2011**, *242*, 233–246. [\[CrossRef\]](#)
2. Kim, Y.J.; Choi, M.J.; Bak, D.H. Topical administration of EGF suppresses immune response and protects skin barrier in DNCB-induced atopic dermatitis in NC/Nga mice. *Sci. Rep.* **2018**, *8*, 11895. [\[CrossRef\]](#)
3. Lan, C.C.; Fang, A.H.; Wu, P.H.; Wu, C.S. Tacrolimus abrogates TGF- β 1-induced type I collagen production in normal human fibroblasts through suppressing p38MAPK signalling pathway: Implications on treatment of chronic atopic dermatitis lesions. *J. Eur. Acad. Dermatol.* **2014**, *28*, 204–215. [\[CrossRef\]](#)
4. Brandt, E.B.; Sivaprasad, U. Th2 cytokines and atopic dermatitis. *J. Clin. Cell. Immuno.* **2011**, *2*, 110. [\[CrossRef\]](#)
5. Turner, M.J.; Travers, J.B.; Kaplan, M.H. T helper cell subsets in the development of atopic dermatitis. *J. Drugs. Dermatol.* **2012**, *11*, 1174–1178.
6. Lefeber, D.J.; Benaissa-Trouw, B.; Vliegenthart, J.F. Th1-Directing Adjuvants Increase the Immunogenicity of Oligosaccharide-Protein Conjugate Vaccines Related to Streptococcus pneumoniae Type 3. *Infect. Immun.* **2003**, *12*, 6915–6920. [\[CrossRef\]](#) [\[PubMed\]](#)
7. Yosipovitch, G.; Papoiu, A.D.P. What causes itch in atopic dermatitis? *Curr. Allergy. Asthm. R.* **2008**, *8*, 306–311. [\[CrossRef\]](#)
8. Holgate, S.T. The role of mast cells and basophils in inflammation. *Clin. Exp. Allergy.* **2000**, *30*, 28–32. [\[CrossRef\]](#)
9. Rostamian, M.; Sohrabi, S.; Kavosifard, H. Lower levels of IgG1 in comparison with IgG2a are associated with protective immunity against Leishmania tropica infection in BALB/c mice. *J. Microbiol. Immunol. Infect.* **2017**, *50*, 160e166. [\[CrossRef\]](#) [\[PubMed\]](#)
10. Yoshihara, S.; Yamada, Y.; Abe, T. Association of epithelial damage and signs of neutrophil mobilization in the airways during acute exacerbations of paediatric asthma. *Clin. Exp. Immunol.* **2006**, *144*, 212–216. [\[CrossRef\]](#) [\[PubMed\]](#)
11. Hommes, D.W.; Peppelenbosc, M.P.; van Deventer, S.J. Mitogen activated protein (MAP) kinase signal transduction pathways and novel anti-inflammatory targets. *Gut* **2003**, *52*, 144–151. [\[CrossRef\]](#) [\[PubMed\]](#)
12. Arthur, J.S.; Ley, S.C. Mitogen-activated protein kinases in innate immunity. *Nat. Rev. Immunol.* **2013**, *13*, 679–692. [\[CrossRef\]](#) [\[PubMed\]](#)
13. Barnes, P.J. Pathophysiology of allergic inflammation. *Immunol. Rev.* **2011**, *242*, 31–50. [\[CrossRef\]](#) [\[PubMed\]](#)
14. Wu, L.C.; Fan, N.C.; Lin, M.H. Anti-inflammatory effect of spilanthol from Spilanthes acmella on murine macrophage by down-regulating LPS-induced inflammatory mediators. *J. Agr. Food. Chem.* **2008**, *9*, 2341–2349. [\[CrossRef\]](#) [\[PubMed\]](#)
15. Chakraborty, A.; Devi, B.R.; Sanjebam, R. Preliminary studies on local anesthetic and antipyretic activities of Spilanthes acmella Murr. in experimental animal models. *Indian. J. Pharmacol.* **2010**, *42*, 277–279. [\[CrossRef\]](#)
16. Gerbino, A.; Schena, G.; Milano, S. Spilanthol from Acemella Oleracea Lowers the Intracellular Levels of cAMP Impairing NKCC2 Phosphorylation and Water Channel AQP2 Membrane Expression in Mouse Kidney. *PLoS ONE* **2016**, *11*, e0156021. [\[CrossRef\]](#)

17. Cheng, Y.-B.; Liu, R.H.; Ho, M.-C.; Wu, T.-Y.; Chen, C.-Y.; Lo, I.-W.; Hou, M.-F.; Yuan, S.-S.; Wu, Y.-C.; Chang, F.-R. Alkylamides of *Acmella oleracea*. *Molecules* **2015**, *20*, 6970–6977. [\[CrossRef\]](#)
18. Singh, M.; Pradhan, S. In vitro production of spilanthol from *Spilanthes acmella* Murr.: State of the art and future prospect. *Int. J. Adv. Res.* **2015**, *3*, 1559–1567.
19. Joseph, B.; George, J.; Jeevitha, M.V. Tohle of *Acmella Oleracea* in Medicine—A review. *World J. Pharm. Res.* **2017**, *2*, 2781–2792.
20. Barbosaa, A.F.; de Carvalho, M.G.; Smithb, R.E. Spilanthol: Occurrence, extraction, chemistry and biological activities. *Rev. Bras. Farmacogn.* **2016**, *26*, 128–133. [\[CrossRef\]](#)
21. Prachayasittukul, V.; Prachayasittukul, S.; Ruchiwarat, S.; Prachayasittukul, V. High therapeutic potential of *Spilanthes acmella*: A review. *Excli. J.* **2013**, *12*, 291–312.
22. Dubey, S.; Maity, S.; Singh, M. Phytochemistry, pharmacology and toxicology of *Spilanthes acmella*: A review. *Adv. Pharmacol. Sci.* **2013**, *2013*, 423750. [\[PubMed\]](#)
23. Prachayasittikul, S.; Suphamong, S.; Worachartcheewan, A. Bioactive metabolites from *Spilanthes acmella* Murr. *Molecules* **2009**, *14*, 850–886. [\[CrossRef\]](#)
24. Huang, C.H.; Chang, L.C.; Hu, S. Spilanthol inhibits TNF α induced ICAM 1 expression and pro inflammatory responses by inducing heme oxygenase 1 expression and suppressing pJNK in HaCaT keratinocytes. *Mol. Med. Rep.* **2018**, *18*, 2987–2994. [\[CrossRef\]](#)
25. Leung, D.Y.; Soter, N.A. Cellular and immunologic mechanisms in atopic dermatitis. *J. Am. Acad. Dermatol.* **2001**, *44*, S1–S12. [\[CrossRef\]](#)
26. Galli, S.J.; Tsai, M. IgE and mast cells in allergic disease. *Nat. Med.* **2015**, *18*, 693–704. [\[CrossRef\]](#) [\[PubMed\]](#)
27. Fang, L.W.; Cheng, C.C.; Hwang, T.S. Danggui Buxue Tang Inhibits 2,4-Dinitrochlorobenzene: Induced Atopic Dermatitis in Mice. *Evid.-Based Complementary Altern. Med.* **2015**, *2015*, 672891.
28. Ahn, J.Y.; Choi, S.E.; Jeong, M.S.; Park, K.H.; Moon, N.J.; Joo, S.S.; Lee, C.S.; Choi, Y.W.; Li, K.; Lee, M.K.; et al. Effect of taxifolin glycoside on atopic dermatitis-like skin lesions in NC/Nga mice. *Phytother. Res.* **2010**, *24*, 1071–1077. [\[CrossRef\]](#) [\[PubMed\]](#)
29. Ku, J.M.; Hong, S.H.; Kim, S.R. The prevention of 2,4-dinitrochlorobenzene-induced inflammation in atopic dermatitis-like skin lesions in BALB/c mice by Jawoongo. *BMC. Complement. Altern. Med.* **2018**, *18*, 215. [\[CrossRef\]](#)
30. Jegal, J.; Park, N.J.; Bong, S.K. Dioscorea quinqueloba Ameliorates Oxazolone- and 2,4-Dinitrochlorobenzene-induced Atopic Dermatitis Symptoms in Murine Models. *Nutrients* **2017**, *9*, 1324. [\[CrossRef\]](#)
31. Darlenski, R.; Kazandjieva, J.; Hristakieva, E.; Fluhr, J.W. Atopic dermatitis as a systemic disease. *Clin. Dermatol.* **2014**, *32*, 409–413. [\[CrossRef\]](#) [\[PubMed\]](#)
32. Lee, K.S. A novel model for human atopic dermatitis: Application of repeated DNCB patch in BALB/c mice, in comparison with NC/Nga mice. *Lab. Anim. Res.* **2010**, *26*, 95–102. [\[CrossRef\]](#)
33. Danso, M.O. TNF- α and Th2 cytokines induce atopic dermatitis-like features on epidermal differentiation proteins and stratum corneum lipids in human skin equivalents. *J. Invest. Dermatol.* **2014**, *134*, 1941–1950. [\[CrossRef\]](#)
34. Deo, S.S.; Mistry, K.J.; Kakade, A.M. Role played by Th2 type cytokines in IgE mediated allergy and asthma. *Lung. India.* **2010**, *27*, 66–71. [\[CrossRef\]](#) [\[PubMed\]](#)
35. Baumann, U.; Chouchakova, N.; Gewecke, B. Distinct Tissue Site-Specific Requirements of Mast Cells and Complement Components C3/C5a Receptor in IgG Immune Complex-Induced Injury of Skin and Lung. *J. Immunol.* **2001**, *167*, 1022–1027. [\[CrossRef\]](#) [\[PubMed\]](#)
36. Govindaraj, D.; Sharma, S.; Singh, N.; Arora, N. T cell epitopes of Per a 10 modulate local-systemic immune responses and airway inflammation by augmenting Th1 and T regulatory cell functions in murine model. *Immunobiology* **2019**, *18*. [\[CrossRef\]](#)
37. Piaoa, C.H.; Kim, T.G.; Buic, T.T. Ethanol extract of *Dryopteris crassirhizoma* alleviates allergic inflammation via inhibition of Th2 response and mast cell activation in a murine model of allergic rhinitis. *J. Ethnopharmacol.* **2019**, *232*, 21–29. [\[CrossRef\]](#)
38. Johansen, C.; Kragballe, K.; Westergaard, M. The mitogen-activated protein kinases p38 and ERK1/2 are increased in lesional psoriatic skin. *Brit. J. Dermatol.* **2005**, *152*, 37–42. [\[CrossRef\]](#)
39. Senthil, K.J.; Hsieh, H.W.; Wang, S.Y. Anti-inflammatory effect of lucidone in mice via inhibition of NF- κ B/MAP kinase pathway. *Int. Immunopharmacol.* **2010**, *10*, 385–392. [\[CrossRef\]](#)

40. Giuliano, F.; Warner, T.D. Origins of prostaglandin E2: Involvements of cyclooxygenase (COX)-1 and COX-2 in human and rat systems. *J. Pharmacol. Exp. Ther.* **2002**, *303*, 1001. [[CrossRef](#)]
41. Shah, G.; Zhang, G.; Chen, F. iNOS expression and NO production contribute to the direct effects of BCG on urothelial carcinoma cell biology. *Urol. Oncol.* **2014**, *32*, 45e1–45e9. [[CrossRef](#)] [[PubMed](#)]
42. Chan, C.C.; Liou, C.J.; Xu, P.Y. Effect of dehydroepiandrosterone on atopic dermatitis-like skin lesions induced by 1-chloro-2,4-dinitrobenzene in mouse. *J. Dermatol. Sci.* **2013**, *72*, 149–157. [[CrossRef](#)] [[PubMed](#)]



© 2019 by the authors. Licensee MDPI, Basel, Switzerland. This article is an open access article distributed under the terms and conditions of the Creative Commons Attribution (CC BY) license (<http://creativecommons.org/licenses/by/4.0/>).



ORIGINAL RESEARCH ARTICLE

WILEY *Journal of Cellular Physiology*

Androgen receptor transcriptional activity and chromatin modifications on the *ABCB1/MDR* gene are critical for taxol resistance in ovarian cancer cells

Nian-Kang Sun^{1,2,3*} | Abhidha Kohli^{4*} | Shang-Lang Huang^{1,5} | Ting-Chang Chang³ | Chuck C.-K. Chao^{3,4,5,6}

¹Division of Biomedical Sciences, Chang Gung University of Science and Technology, Taoyuan, Taiwan

²Research Center for Chinese Herbal Medicine, Chang Gung University of Science and Technology, Taoyuan, Taiwan

³Department of Obstetrics and Gynaecology, Chang Gung Memorial Hospital Linkou Medical Centre, Taoyuan, Taiwan

⁴Graduate Institute of Biomedical Sciences, College of Medicine, Chang Gung University, Taoyuan, Taiwan

⁵Department of Biochemistry and Molecular Biology, College of Medicine, Chang Gung University, Taoyuan, Taiwan

⁶Liver Research Center, Chang Gung Memorial Hospital Linkou Medical Center, Taoyuan, Taiwan

Correspondence

Chuck C.-K. Chao, Department of Biochemistry and Molecular Biology, College of Medicine, Chang Gung University, No. 259, Wenhua 1st Rd., Guishan Dist., Taoyuan City 33302, Taiwan, China.
Email: cckchao@mail.cgu.edu.tw

Funding information

Chang Gung Memorial Hospital, Linkou, Grant/Award Numbers: BMRP071, CMRPD3E0093, CMRPD1G0101; Ministry of Science and Technology, Grant/Award Numbers: NSC100-2320-B-182-026-MY3, MOST103-2320-B-182-031, MOST106-2320-B-255-004

Abstract

We report here that the androgen receptor (AR) and *ABCB1* are upregulated in a model of acquired taxol resistance (txr) in ovarian carcinoma cells. AR silencing sensitizes txr cells to taxol threefold, whereas ectopic AR expression in AR-null HEK293 cells induces resistance to taxol by 1.7-fold. AR activation using the agonist dihydrotestosterone (DHT) or sublethal taxol treatment upregulates *ABCB1* expression in both txr cells and AR-expressing HEK293 cells. In contrast, AR inactivation using the antagonist bicalutamide downregulates *ABCB1* expression and enhances cytotoxicity to taxol. A functional *ABCB1* promoter containing five predicted androgen-response elements (AREs) is cloned. Deletion assays reveal a taxol-responsive promoter segment which harbors ARE4. Notably, DHT- or taxol-activated AR potentiates binding of the AR to ARE4 as revealed by the chromatin immunoprecipitation. On the other hand, txr cells display an increase in chromatin remodeling. AR/H3K9ac and AR/H3K14ac complexes bind specifically to ARE4 in response to taxol. Furthermore, acetyltransferase protein levels (p300 and GCN5) are upregulated in txr cells. Silencing of p300 or GCN5 reduces chromatin modification and enhances cytotoxicity in both parental and txr SKOV3 cells. While the phosphatidylinositol 3-kinase (PI3K)/serine/threonine protein kinase (AKT) pathway is significantly activated by taxol, taxol-induced *ABCB1* expression, histone posttranslational modifications, and p300 binding to ARE4 are suppressed following inhibition of the PI3K/AKT cellular pathway. These results demonstrate that the AKT/p300/AR axis can be activated to target *ABCB1* gene expression in response to taxol, thus revealing a new treatment target to counter taxol resistance.

KEYWORDS

ABCB1, AKT, androgen receptor (AR), ovarian carcinoma, taxol resistance

Abbreviations: AR, androgen receptor; DHT, dihydrotestosterone; DMSO, dimethyl sulfoxide; FBS, fetal bovine serum; GAPDH, glyceraldehyde-3-phosphate dehydrogenase; MDR, multiple drug resistance; MTT, 3-(4,5-dimethylthiazol-2-yl)-2,5-diphenyltetrazolium bromide; PBS, phosphate-buffered saline; PCR, polymerase chain reaction; PI3K, phosphatidylinositol 3-kinase; PVDF, polyvinylidene fluoride; q-PCR, quantitative real-time polymerase chain reaction; SDS-PAGE, sodium dodecyl sulfate-polyacrylamide gel electrophoresis; shRNA, short-hairpin RNA.

*Nian-Kang Sun and Abhidha Kohli have contributed equally to this study.

1 | INTRODUCTION

The taxanes paclitaxel (taxol) and docetaxel are chemotherapeutic drugs that function primarily by interfering with spindle microtubule dynamics, thereby causing cell cycle arrest and apoptosis in cancer cells. These drugs are widely used for the treatment of breast and ovarian cancers. However, their therapeutic efficiency is limited by acquired *de novo* resistance (McGrogan, Gilmartin, Carney, & McCann, 2008; Murray, Briasoulis, Linardou, Bafaloukos, & Papadimitriou, 2012). Drug resistance is mainly due to overexpression of membrane transporters from the ATP-binding cassette (ABC) and solute carrier (SLC) families. The *ABCB1* gene encodes an ABC protein called ABCB1 or glycoprotein P (multidrug resistance protein 1[MDR1]), which is often overexpressed in chemoresistant cells (Fletcher, Haber, Henderson, & Norris, 2010; Gottesman, Fojo, & Bates, 2002; Hille et al., 2006; Leonard, Fojo, & Bates, 2003). SLC transporters, which function mainly as an influx carrier (Hediger et al., 2004), represents another group of membrane transporters involved in drug resistance and are often downregulated in resistant cells (Huang, 2007; Huang & Sadee, 2006; Nakanishi, 2007). Given that taxol interrupts the cell cycle, cell resistance to this drug is characterized by the presence of specific checkpoint proteins, such as DNA repair protein BRCA1 and the spindle assembly checkpoint proteins MAD2, BUBR1, synuclein-gamma, and aurora A. Overexpression of ABCB1 and altered expression of microtubule-associated proteins, including tau, stathmin, and MAP4, may help identify patients at risk of recurrence and who are most likely to benefit from taxane treatment (McGrogan et al., 2008). Recently, a systematic meta-analysis showed that ABCB1 overexpression is significantly associated with chemoresistance and poor prognosis in patients with epithelial ovarian cancer (S. Sun et al., 2016). However, the mechanism underlying the upregulation of these proteins, especially ABCB1, remains elusive.

Activation of the androgen receptor (AR), a transcription factor, in response to androgen is required for prostate-specific antigen production and survival of prostate epithelial cells. While clinically advanced prostate cancers show enhanced AR activity, docetaxel is currently the only treatment providing survival benefits for patients with castration-resistant prostate cancer (Egan et al., 2014). However, studies on the role of androgen/AR in ovarian cancer are lacking. A study has found that steroid hormones are involved in the development and progression of epithelial ovarian cancer, suggesting a potential role for androgens in this context; accordingly, androgen production by cancer cells was reduced following chemotherapy (Wang & Chang, 2004). Notably, a number of studies show that the AR is overexpressed in ovarian cancer (Chadha, Rao, Slotman, van Vroonhoven, & van der Kwast, 1993; Ilekis et al., 1997; Lau, Mok, & Ho, 1999; Lee, Rosen, Zhu, Silva, & Liu, 2005; Kuhne, de Graaff, Rao, & Stolk, 1987). Laboratory data and epidemiological evidence strongly support a critical role for androgens in the origin and development of epithelial ovarian cancer and have led to clinical trials designed to target the AR (reviewed in Modugno et al., 2012). AR activation by dihydrotestosterone (DHT) in SKOV3 ovarian

cancer cells and ascites-derived OVCAS-16 cells prevented the growth inhibitory effect of transforming growth factor-beta, while DHT alone had no effect on cell growth (Evangelou, Jindal, Brown, & Letarte, 2000). However, it is unclear whether AR activity is an important target of taxol in the treatment of ovarian cancer.

The AR is composed of eight exons encoding five functional domains: A large amino-terminal transactivation domain (McEwan, 2004); a central DNA-binding domain, a carboxy-terminal, androgen-binding domain, and a hinge region (between the DNA-binding domain and androgen-binding domain) that contributes to nuclear localization and protein degradation (Cutress, Whitaker, Mills, Stewart, & Neal, 2008). Upon binding androgens or molecular analogs, the AR binds to cis-elements in the regulatory regions of target genes and regulates expression of androgen-dependent genes. This pathway can also be activated by treatment of cells with agonists such as DHT (Evangelou et al., 2000). Expression of active AR, overexpression of androgens, and increased drug efflux through ABCB1 are some of the many described mechanisms of drug resistance in prostate cancer cells (Armstrong, Allen, & Gao, 2015; Zhu et al., 2015). Posttranslational modifications such as histone acetylation can modify chromatin structure and modulate gene expression. Acetylation relaxes condensed chromatin structure by reducing the affinity of DNA for histones, thereby affecting the binding of various transcription factors and cofactors. Acetylation level represents a dynamic balance between the activities of histone acetyltransferase (HAT) and histone deacetylase (HDAC). P300 and GCN5 are two representative HATs which acetylate histone and nonhistone proteins involved in various cellular and metabolic processes (Dekker & Haisma, 2009). In addition, recent studies demonstrate that the HAT hMOF, a member of the MYST family, affects the prognosis of malignant ovarian tumors (Cai et al., 2015; Liu et al., 2013). HCP, also known as a target gene of hMOF, plays a role in tumor antigen-specific immune response and prognosis. Downregulation of hMOF reduces both H4K16 acetylation and HCP5 expression in ovarian cancer (Cai et al., 2015; Smith et al., 2000). Accumulating evidence suggests the involvement of epigenetic regulation of ABCB1 transactivation, including DNA methylation of the gene (Mishra et al., 2010), posttranslational modifications of the nuclear transcription factor Y (NF-Y), nuclear factor kappa light chain enhancer of activated B cells (NF- κ B/p65), and Sp1 by HATs or HDACs (Bourguignon, Xia, & Wong, 2009; Jin & Scotto, 1998). While a better understanding of these phenomena will enable the development of new treatment strategies to overcome drug resistance, less is known about chemoresistance in ovarian cancer.

Using a whole genome microarray to compare the transcriptome profile of parental and taxol-resistant ovarian cells, we have identified 2,677 genes that are differentially expressed at least twofold in these cell lines (N. K. Sun, Huang, Chang, Lu, & Chao, 2014). The "early onset" genes such as AR and those involved in the development of taxol resistance (txr), such as the widely recognized ABCB1 gene which is involved in the multidrug resistance phenotype, are thought to play a role in mediating cell response to mitotoxin-mediated chemotherapy (N. K. Sun, Huang, Lu, Chang, & Chao, 2015). In the present study, we

treated txr ovarian cancer cells with taxol to study the mechanism of ABCB1 upregulation. On the basis of the association between AR and ABCB1 and their involvement in taxol resistance via epigenetic regulation, we describe an important pathway involved in ABCB1 overexpression and propose that this pathway represents a potential target for the treatment of ovarian carcinoma.

2 | MATERIALS AND METHODS

2.1 | Cell lines and reagents

The txr SKOV3/Tx600 cell line had been developed from SKOV3 by stepwise selection, increasing the dose of paclitaxel (taxol) from 5 to 600 nM. These early txr cell lines displayed resistance to both taxol and vincristine but showed no resistance to cisplatin (N. K. Sun et al., 2014). SKOV3 cells and other ovarian cancer cell lines, including MDAH2774, TOV21G, and UWB1.289 cells (American Type Culture Collection, Rockville, MD) were grown as monolayers in a 1:1 mixture of DMEM/nutrient F-12 Ham (Life Technologies, Grand Island, NY) supplemented with 1% (w/v) penicillin/streptomycin and 10% (v/v) fetal bovine serum at 37°C in a humidified atmosphere containing 5% CO₂. An initial resistant cell line SKOV3/Tx600, which displayed a 50% inhibitory concentration (IC₅₀) of 2.9 µM to taxol, displayed unstable overexpression of ABCB1 among other txr genes without taxol stress (N. K. Sun et al., 2014). The SKOV3/Tx600 cells were maintained in the same medium containing 50 nM of taxol for this study. The chemotherapeutic drugs used include; vincristine, taxol (paclitaxel), and cisplatin (Bristol-Myers Squibb, New York, NY). Inhibitors of ERK (PD98059), p38 (SB203580), c-Jun N-terminal kinase (JNK) (SP600125), and serine/threonine protein kinase (AKT) (Wortmannin) kinases were purchased from Calbiochem (San Diego, CA). Antibodies include GCN5, MDR1, p300, Lamin, or glyceraldehyde-3-phosphate dehydrogenase (GAPDH; Santa Cruz Biotechnology, Santa Cruz, CA), α-tubulin (Sigma-Aldrich, St. Louis, MO); trichostatin A (TSA), H3, H3Ac, H3K9Ac, H3K14Ac, H3K56Ac, H4, H4K8Ac, and H4K12Ac (Cell Signaling Technology, MA). Restriction enzymes, including *KpnI* and *HindIII* were purchased from New England Biolabs, UK. Unless indicated otherwise, chemicals were purchased from Sigma-Aldrich. All reagents were used according to the instructions provided by the supplier.

2.2 | Plasmids and cell transfection

The pcDNA3 plasmid (Invitrogen, Carlsbad, CA) was used as a negative control in experiments using pSG5AR (kindly provided by Prof. Chawnshang Chang, Rochester University). A 2,075-bp (from -986 to +1,089) functional promoter segment of the ABCB1 gene cloned from SKOV3 cell genomic DNA and 5'-truncated promoter segments of ABCB1, inserted in the pGL3-basic reporter vector (Promega, Madison, WI), resulting in reporter plasmid pGL3-ABCB1 and deletion variants, were constructed as previously described (Fletcher et al., 2010). Plasmid construction and preparation was performed according to the standard protocols. Cells were transfected with plasmids using

Lipofectamine (Invitrogen) according to the instructions provided by the supplier. Transfected cells were incubated 48 hr, unless otherwise indicated, for overexpression of the plasmids.

2.3 | Cell viability assay and taxol resistance

Cell viability was determined using the in vitro 3-(4,5-dimethylthiazol-2-yl)-2,5-diphenyl-2H-tetrazolium bromide (MTT) colorimetric method as previously described (Chao, Lee, Cheng, & Lin-Chao, 1991). One hundred microliter of cells was seeded at a density of 3×10^4 cells/ml in 96-well microplates. Cells were exposed to taxol in culture medium at 37°C for 72 hr. Twenty microliter of MTT solution (5 mg/ml in phosphate-buffered saline [PBS]) was added to each well, before incubation for 4 hr. Optical density of the purple formazan product was measured at a wavelength of 540 nm using a spectrophotometer. Unless indicated otherwise, IC₅₀ values of cell proliferation or cell viability were defined as the levels that cause 50% reduction in cell viability versus the dimethyl sulfoxide (DMSO)-treated control. Taxol resistance was determined by the ratio of IC₅₀, drug concentration to inhibit 50% cell viability or otherwise indicated.

2.4 | Quantitative polymerase chain reaction analysis

Total RNA was extracted with the TRIzol reagent (Life Technologies) as previously described (Sun & Chao, 2005). RNA concentrations were assessed using a spectrophotometer, and only the samples with an A₂₆₀/A₂₈₀ ratio between 1.9 and 2.2 were used. Real-time quantitative polymerase chain reaction (qPCR) was performed on total RNA as before (Sun & Chao, 2005).

2.5 | Western blot analysis

Cells were washed twice with ice-cold PBS (pH 7.4) and lysed on ice for 30 min using standard cell lysis buffer. After centrifugation for 15 min at 4°C, the supernatant was removed and protein concentration was determined using the Bio-Rad protein assay (Bio-Rad, Hercules, CA). Fifty micrograms of proteins from each sample was separated on a 10% sodium dodecyl sulfate (SDS)-polyacrylamide gel and electroblotted onto polyvinylidene difluoride membranes (Millipore, Bedford, MA). After electroblotting, the membranes were blocked in 5% nonfat dry milk (dissolved in 0.1 M Trizma base; 0.15 M NaCl; 0.05% Tween 20; pH 7.4). Membranes were incubated with primary antibodies raised against either MDR1 or GAPDH (Santa Cruz Biotechnology) in the blocking solution containing 2% nonfat dry milk.

2.6 | Knockdown assay using short-hairpin RNA

Knockdown of the AR gene was performed using pLKO.1 plasmids expressing short-hairpin RNA (shRNA) purchased from the National RNAi Core Facility (Academia Sinica, Taipei, Taiwan) as described before (Wu, Lu, & Chao, 2010). Luciferase shRNA (TRCN0000072244)

was used as a negative control. Specific AR shRNA knockdown clones were selected for cell viability assay using puromycin. shRNA plasmids encoding genes highly overexpressed in taxol-resistant cells were selected as previously described (Wu et al., 2010) and used in the present study. Both shRNA clone ID and target sequence were included: AR (TRCN000003715, CCTGCTAATCAAGTCACACAT); p300 (TRCN0000231134, ATACTCAGCCGGAGGATATTT); and GCN5 (TRCN0000286981, GCTGAACCTTTGTGCAGTACAA).

2.7 | Chromatin immunoprecipitation assay

Formaldehyde cross-linking and chromatin immunoprecipitation (ChIP) assays of tissue culture cells were performed as described before (Shang, Hu, DiRenzo, Lazar, & Brown, 2000; Wu, Sun, Chien, & Chao, 2011). Briefly, chromatin was sonicated on ice to obtain an average length of 600 bp, ranging in size of 0.3–1.5 kb. Equal amounts of chromatin-crosslinked protein (500 µg) from each sample were incubated with 5 µg of antibodies at 4°C overnight and immunocomplexes were collected with 60 µl of salmon sperm DNA and protein-A/G agarose beads for 1 hr at 4°C with rotation. Beads with precipitated chromatin were washed successively with wash buffers 1, 2, 3, and 4 (buffer 1, low salt wash buffer: 0.1% SDS, 1% Triton X-100, 2 mM EDTA, 20 mM Tris, pH 8.1, 150 mM NaCl; buffer 2, high salt wash buffer: 0.1% SDS, 1% Triton X-100, 2 mM EDTA, 20 mM Tris, pH 8.1, 500 mM NaCl; buffer 3, LiCl wash buffer: 0.25 M LiCl, 1% NP-40, 1% deoxycholate, 1 mM EDTA, 10 mM Tris, pH 8.0; and buffer 4, wash twice with TE buffer). Extensively washed immunocomplexes were eluted using elution buffer (1% SDS; 0.1 M NaHCO₃). For verification of AR colocalization with both histone modifications and epigenetic factors, the re-ChIP assay was performed. The eluent from the immunocomplexes precipitated with the first antibody were re-ChIP with antibodies against specific epigenetic factors at 4°C overnight in ChIP buffer (diluted with fivefold ChIP dilution buffer: 0.01% SDS; 1% Triton X-100; 1.2 mM EDTA; 16.7 mM Tris; pH 8.1; 167 mM NaCl) containing protease inhibitors. Precipitates were completely washed and eluted. Chromatin DNA was decrosslinked in elution buffer containing both 0.3 M NaCl and 2 µg/µl RNase and incubated at 65°C for 4 hr, followed by recovery using QIAquick spin columns (Qiagen, Valencia, CA), and elution with 80 µl of 10 mM Tris (pH 8.0). Two microliters of the recovered DNA was subjected to 40 cycles of real-time qPCR. Five AR-binding sites on the endogenous *ABCB1* promoter on chromosome 7 (NC_000007.14) with a cutoff settings (80%) were determined by using JASPAR CORE database (Version: 5.0_ALPHA). The primers were designed using Primer 3.0. The primers used included: primer pair 1 for ARE1-binding site, forward, 5'-AACGGGGCTCTCTTTGT-3' and reverse, 5'-ACCCCTGCCCTCACTAAACT-3', which yielded a 167-bp product; ARE2-binding site, forward, 5'-AGCACAAATTGAAGGAAGGAG-3' and reverse, 5'-CTGGCCAGATCCCAATAC-3', which yielded a 195-bp product; ARE3-binding site, forward, 5'-TCTGGTTGCTTCCTGAAGTG-3' and reverse, 5'-CTCCTCTCTGGTACTGGGA-3', which yielded a 177-bp product; ARE4-binding site, forward, 5'-AGGAAATGCTTTCTGCCTTG-3' and reverse, 5'-GCCAAGCCATGTTTCTGTTT-3', which yielded a 145-bp product; ARE5-

binding site, forward, 5'-GTTTAAATGATTGGGTGGGG-3' and reverse, 5'-TTAAGAACAAGGCAGAAAGCA-3', which yielded a 99-bp product.

2.8 | Statistical analysis

Data were analyzed using a paired Student's *t* test to determine statistical significance and to compare the means of two different experimental groups. Data of experiments performed in triplicate were expressed as means ± standard deviation.

3 | RESULTS

3.1 | Co-upregulation of AR and *ABCB1* in taxol-resistant cells and sensitization to taxol following AR silencing

SKOV3/Tx600 cells which had acquired txr (as described in Section 2) displayed a resistance factor of 84.5-fold in response to taxol (N. K. Sun et al., 2014). Nearly, 150-fold and 2,500-fold overexpression of AR and *ABCB1* messenger RNA (mRNA), respectively, were observed in SKOV3/Tx600 cells compared with parental cells (Figure 1a). In addition to SKOV3 and SKOV3/Tx600 txr cells, we also examined the expression of AR and *ABCB1* in other ovarian cancer cell lines, including MDAH2774, TOV21G, and UWB1.289 cells (Figure 1b). Except for UWB1.289 cells, the ovarian cancer cells showed detectable AR protein levels. Taxol-resistant SKOV3/Tx600 cells showed a threefold overexpression of AR protein compared with parental SKOV3 cells. Basal *ABCB1* protein expression was not detectable in ovarian cancer cells, except for SKOV3/Tx600 cells in which the *ABCB1* protein was overexpressed ninefold. To evaluate the association between *ABCB1*/AR expression and taxol sensitivity, we determined the IC₅₀ values of SKOV3, SKOV3/Tx600, MDAH2774, TOV21G, and UWB1.289 cells to taxol (Figure 1b, bottom panel; values of 8.3, 476.5, 9.6, 10.2, and 4.1 nM were observed, respectively). While there was no significant correlation between AR protein level and taxol susceptibility in several ovarian cancer cell lines, a positive correlation between *ABCB1* expression and taxol resistance was observed in isogenic, parental, and txr SKOV3 cell lines (Figure 1b). To examine the possibility that *ABCB1* is modulated by the AR, we monitored *ABCB1* mRNA expression under a sublethal dose of taxol. Indeed, taxol-induced *ABCB1* expression was observed only in cells in which the AR was detected (Figure 1c; i.e., SKOV3, SKOV3/Tx600, MDAH2774, and TOV21G cells). Thus, our results support the possibility that AR level and activation may be required for *ABCB1* expression.

To assess the role of the AR in cell sensitivity to taxol, we silenced the AR gene using shRNA. Following AR silencing (Figure 1d, inset panel), txr cells displayed approximately threefold sensitization to taxol compared to control shLuc (Figure 1d). To further assess the possible regulation of *ABCB1* by the AR, txr cells were treated with the AR agonist DHT or the AR antagonist bicalutamide. While *ABCB1* mRNA was moderately induced by a cytotoxic concentration of taxol

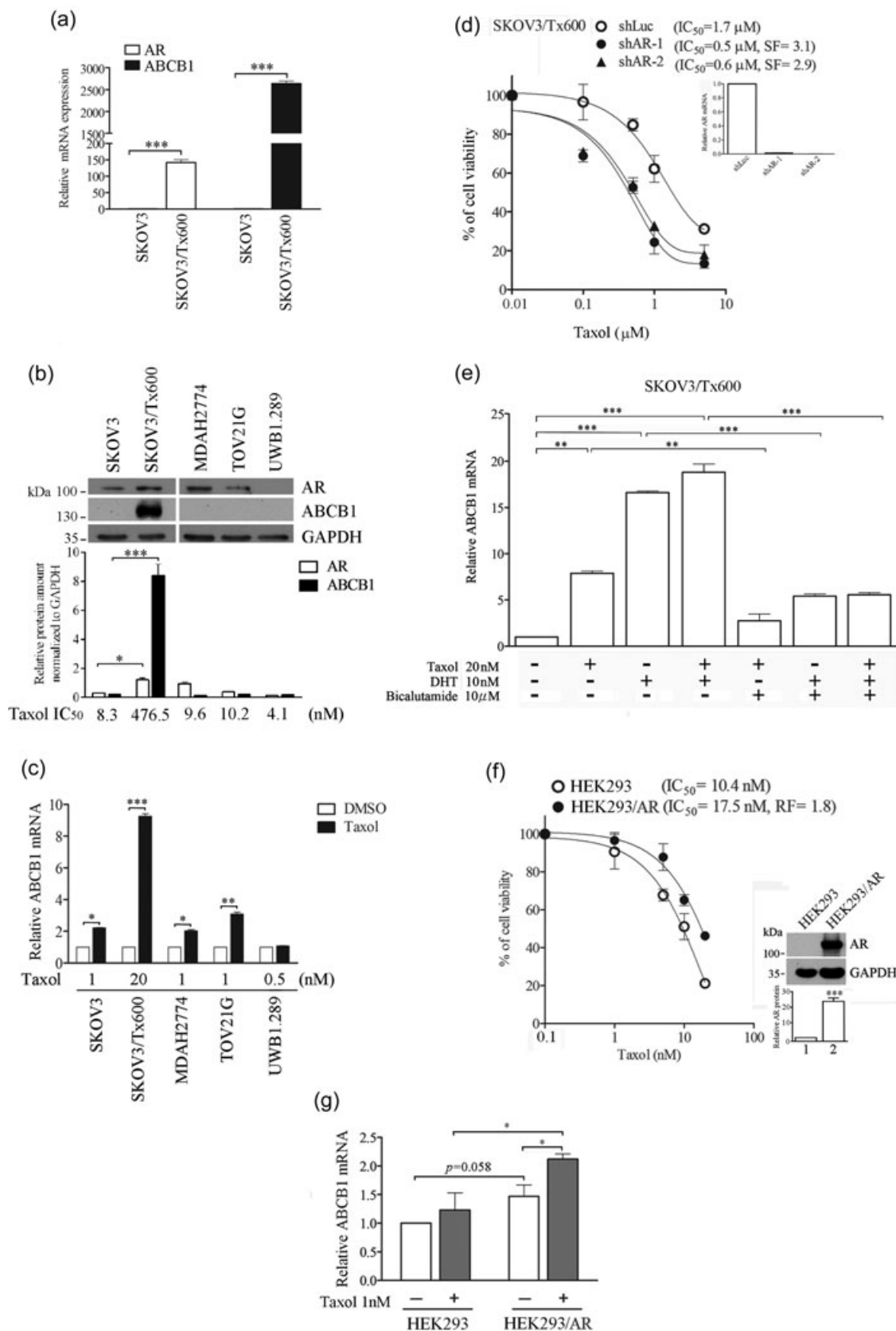


FIGURE 1 Continued.

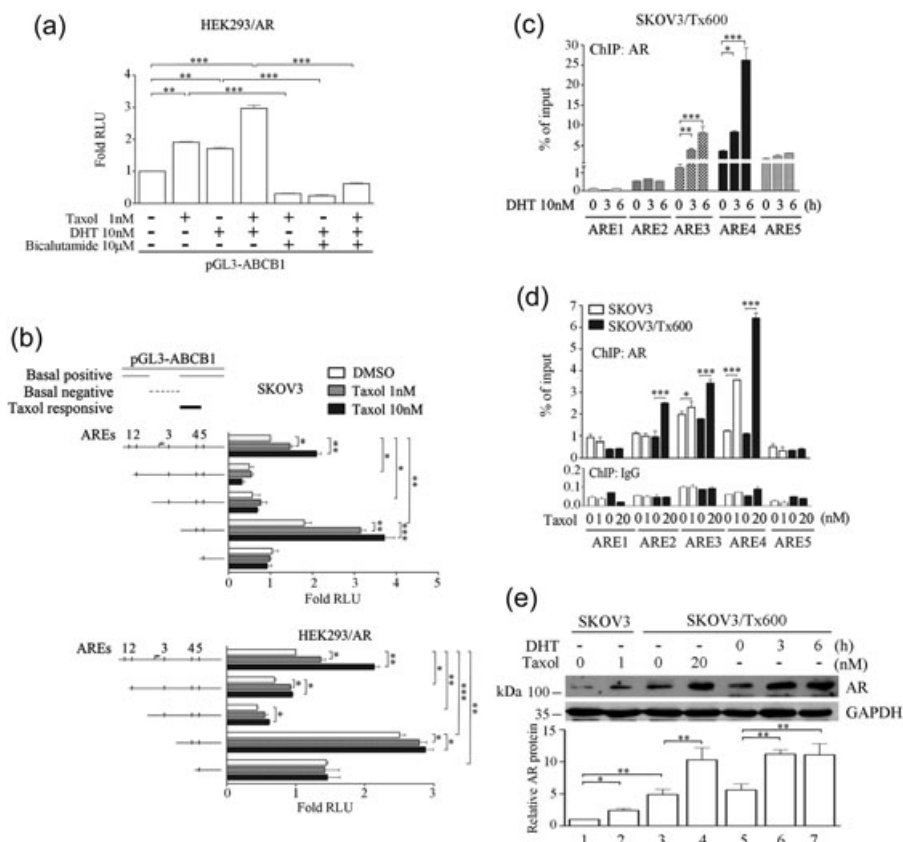


FIGURE 2 Identification of taxol-responsive AR element within the *ABCB1* promoter. (a) Activation of the *ABCB1* promoter by taxol and subsequent reduction by the AR antagonist bicalutamide in AR-expression HEK293 cells. A functional promoter of *ABCB1* gene (pGL3-*ABCB1*) with luciferase gene was used as expression vector. Luciferase activity signal in untreated cells was used as control. (b) Identification of a taxol-responsive segment of *ABCB1* gene by the promoter assay. Upper panel: luciferase activity of full-length and truncated promoters in SKOV3 cells in response to taxol was determined, and using the activity of untreated full-length promoter (DMSO) as control. Lower panel: Parallel study conducted in HEK293/AR cells. Taxol responsive region as well as basal positive and negative regions are annotated. Predicted AREs are indicated by numbers. (c) Identification of major ARE (ARE4) by the ChIP assay. Nuclear extracts from SKOV3 txr cells pretreated with the AR antagonist DHT were isolated following treatment time for ChIP assay. Cell extracts were IP with AR antibody followed by qPCR of co-immunoprecipitated chromatin DNA. The calculated amount of PCR products relative to each input was represented. (d) Enhanced ARE binding by taxol-activated AR in SKOV3 txr cells. The values of control IP with IgG are also indicated at bottom panel. (e) Western blot analysis of the nuclear AR protein level in SKOV3 and txr cells following treatment with DHT or taxol. Fifty micrograms protein extracts was loaded for assay. Quantitative analyses of AR protein levels were shown in the bottom panel. The experiments were performed in triplicate (* $p < 0.05$, ** $p < 0.01$, *** $p < 0.005$). AR: androgen receptor; ChIP assay: chromatin immunoprecipitation assay; DHT: dihydrotestosterone; DMSO: dimethyl sulfoxide; IgG: immunoglobulin G; IP: immunoprecipitation; qPCR: quantitative polymerase chain reaction

FIGURE 1 Upregulation of AR in taxol-resistant cells and sensitization to taxol by genetic silencing of AR. IC₅₀ and resistant factor (RF) are indicated. (a) Relative AR and *ABCB1* mRNA level in txr cells. The level of AR and *ABCB1* was first normalized to *GADPH* level of individual cell line. The RF of 57.4 was calculated as the ratio of IC₅₀ between SKOV3/Tx600 and parental cells (476.5/8.3). (b) Western blot analysis of the AR and *ABCB1* protein levels in various ovarian cancer cell lines. Fifty micrograms of protein extract was loaded. Quantified protein amounts were shown in the bottom panel. IC₅₀ values for each cell line is also indicated. (c) Induction of *ABCB1* mRNA level in ovarian cancer cell lines following taxol treatment. (d) Sensitization of SKOV3 txr cells to taxol by AR silencing using specific shRNA. Independent shRNA (shAR-1 and shAR-2) were used. Cell viability was conducted using the MTT assay. IC₅₀ and sensitization factor (SF) are indicated. SF, sensitization factor calculated as the ratio of IC₅₀ between control shLuc and shAR treatment. Relative AR mRNA level following RNA silencing is shown in the right panel. (e) Induction of *ABCB1* mRNA by taxol and subsequent reduction by the AR antagonist bicalutamide in txr cells. Relative *ABCB1* mRNA level in cells following treatment with the AR agonist DHT or antagonist bicalutamide is also indicated. *ABCB1* mRNA level was determined by qPCR and normalized to *GADPH* mRNA. (f) Protection of HEK293 cells against taxol by ectopic AR expression. AR protein levels are indicated in the right panel. Fifty micrograms of protein extracts was loaded. (g) Induction of *ABCB1* mRNA level in AR-expressing HEK293 cells following treatment with taxol. The experiments were performed in triplicate (* $p < 0.05$, ** $p < 0.01$, *** $p < 0.005$). AR: androgen receptor; DHT: dihydrotestosterone; *GADPH*: glyceraldehyde-3-phosphate dehydrogenase; IC₅₀: 50% inhibitory concentration; mRNA: messenger; MTT: 3-(4,5-dimethylthiazol-2-yl)-2,5-diphenyl-2H-tetrazolium bromide; qPCR: quantitative polymerase chain reaction; RF: resistance factor; shRNA: short-hairpin RNA

(20 nM), DHT induced a twofold *ABCB1* mRNA increase compared with taxol (Figure 1e). Taxol-induced *ABCB1* mRNA level was slightly potentiated by DHT, but reduced by approximately 60% by bicalutamide in SKOV3/Tx600 cells. Similarly, DHT-induced mRNA level was suppressed by 60% by this AR antagonist. Compared with this inhibition, both taxol- and DHT-induced mRNA level was also reduced by 60% by the same inhibitor (Figure 1e). Moreover, ectopic expression of AR by AR plasmid in AR-null HEK293 cells induced resistance to taxol by 1.8-fold (Figure 1f). This observation is consistent with previous findings showing that AR expression and nuclear location affect taxol sensitivity in early stage of acquired txr (N. K. Sun et al., 2015). Similarly, *ABCB1* mRNA level was also induced by taxol in HEK293 following transfection with AR complementary DNA (Figure 1g). Unlike SKOV3/Tx600 cells, nontumorigenic

HEK293 cells did not express the AR, and the *ABCB1* gene was not induced without ectopic AR expression. Together, these results suggest that AR activity is responsible for *ABCB1* upregulation in txr, and that upregulated and probably activated AR expression level may play a critical role in SKOV3/Tx600 cell resistance to taxol.

3.2 | Identification of taxol-responsive AR element of *ABCB1* promoter

To assess the mechanism underlying the positive regulation of *ABCB1* gene by AR, a 2,075-bp promoter of *ABCB1* gene (−986 to +1,089 bp) was cloned by PCR using predicted sequences. The promoter activity was confirmed by pGL3-*ABCB1*, a luciferase fusion construct. The AR reporter plasmid or its truncated plasmids were investigated for

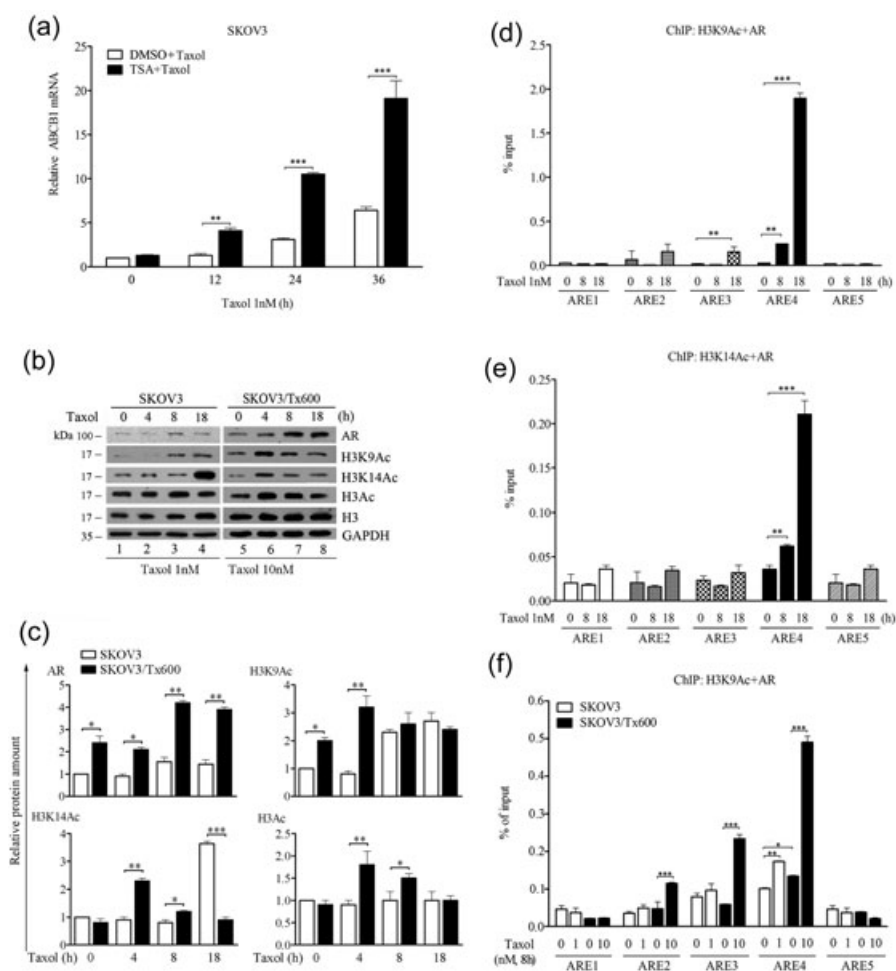


FIGURE 3 Chromatin modification and potentiated targeting of *ABCB1* ARE by taxol treatment. (a) Potentiation of taxol-induced *ABCB1* mRNA by TSA, an HDAC inhibitor, in SKOV3 cells. The level of mRNA was determined by qPCR as in Figure 1. (b) Western blot analysis of taxol-induced chromatin modification marks in SKOV3 and txr cells. Kinetic changes in the protein level of H3 and acetylated forms were detected in taxol treated cells. (c) Quantitative analysis of AR and acetylated H3 protein levels from the experiment shown in panel (b). (d) Kinetic increase in taxol-induced ARE binding by H3K9Ac and AR. Re-ChIP was conducted for H3K9Ac and AR complex binding to ARE (see Section 2 for details). (e) Kinetic increase in taxol-induced ARE binding by H3K14Ac and AR. (f) Comparison of kinetic increase in taxol-induced ARE binding by H3K9Ac and AR in SKOV3 and txr cells. Methods are same as for Figure 3d. The experiments were performed in triplicate (* $p < 0.05$, ** $p < 0.01$, *** $p < 0.005$). AR: androgen receptor; HDAC: histone deacetylase; mRNA: messenger RNA; qPCR: quantitative polymerase chain reaction; Re-ChIP: re-chromatin immunoprecipitation assay; TSA: trichostatin A

activation by taxol in SKOV3 cells or in HEK293 cells which had been engineered to ectopically express the AR expression plasmid (pSG5AR) (Figure 2a). While basal positive and negative regulated segments were identified, a taxol-responsive segment was identified in this expression system (Figure 2b). The predicted AR elements (AREs) of *ABCB1* gene have scores in the following order: ARE4 > ARE1 > ARE5 > ARE3 > ARE2 (see Supporting Information Table for the predicted ARE positions). Notably, the taxol-responsive segment covers ARE4 (indicated on top of the figure). Furthermore, DHT activated AR binding to ARE3 and ARE4 in a time-dependent manner as revealed by (ChIP) assays in SKOV3/Tx600 cells (Figure 2c). ChIP analysis indicated that taxol- or AR-agonist-induced AR binding to *ABCB1* gene occurred in the following order: ARE4 > ARE3 > ARE2 > ARE1 = ARE5. Notably, AR binding to these AREs was induced by equal toxic concentration of taxol in both SKOV3 and SKOV3/Tx600 cells, with stronger induction in resistant cells (Figure 2d). On the other hand, induced AR binding was also observed in txr cells, but not in parental cells. AR binding to these AREs remained the same in untreated cell lines, and only background levels were observed in parallel experiments using IgG precipitation as negative control. Nuclear protein loading in these experiments indicated that the AR was induced by either taxol or DHT in both cell lines (Figure 2e; quantified relative AR level is shown in the bottom panel, with untreated SKOV3 cells considered as a value of 1). These results strongly suggest that ARE4 is a preferential target of activated AR, consistent with ARE4 harboring a taxol-responsive segment as revealed by the promoter activity assay.

3.3 | Chromatin epigenetic modifications and potentiated targeting of *ABCB1* ARE by taxol treatment

Epigenetic regulation of AR-driven txr genes has been suggested to occur earlier (N. K. Sun et al., 2014). To assess this hypothesis, we treated SKOV3 cells with the HDAC inhibitor TSA. While *ABCB1* mRNA level was induced by taxol in a time-dependent manner, TSA significantly potentiated taxol-induced *ABCB1* mRNA level (Figure 3a), suggesting the involvement of epigenetic regulations. H3K9ac and H3K14ac were induced by equal toxic taxol treatment in both SKOV3 and SKOV3/Tx600 cells (Figure 3b,c). Histone epigenetic markers were induced transiently in txr cells and in a time-dependent manner in parental cells. The maximum level seems to be induced much faster in txr cells. However, the significance of this difference remains unclear. Furthermore, H3K9ac and AR complex binding to ARE4 was dramatically induced by taxol in SKOV3/Tx600 cells in a time-dependent manner (Figure 3d). However, minimal binding of this complex to ARE3 was also detected. Similarly, H3K14ac and AR complex binding to ARE4, but not ARE3, was also induced by taxol (Figure 3e), at approximately 10% that of H3K9ac and AR complex binding. As for AR binding, taxol-induced H3K9ac and AR complex interacted preferentially with ARE4 (Figure 3f). Unlike AR binding, however, a significant increase in the H3K9ac/AR complex binding to ARE4 was found in untreated txr cells compared with parental cells. Acetylation of H3 and targeting together with the AR to the *ABCB1* promoter was enhanced by taxol treatment (see Figure 3b), suggesting

that chromatin remodeling may be involved in *ABCB1* gene expression and possibly in the development of the txr phenotype as well.

3.4 | Silencing of p300 or GCN5 downregulates *ABCB1* expression and sensitizes cells to taxol

To assess the HATs involved in enhanced chromatin modification in txr cells, we examined p300 and GCN5 (GCN5L1), two major HATs known to modify H3K. Interestingly, both HAT protein levels were upregulated in SKOV3/Tx600 cells compared with parental cells (Figure 4a). p300 protein level was low in SKOV3 cells, whereas p300 mRNA was detected (Figure 4b). As shown in Figure 4b, mRNA overexpression of both HATs were observed in txr cells compared with parental SKOV3 cells. Silencing of each HAT resulted in more than 60% inhibition of *ABCB1* mRNA level in SKOV3/Tx600 cells (Figure 4c). Silencing efficiency of p300 and GCN5 was quantified by qPCR (see Figure 4d). Silencing p300 or GCN5 in SKOV3/Tx600 cells (Figure 4e) resulted in cell sensitization to taxol by 2.7-fold and 1.9-fold, respectively (Figure 4e, sensitization was calculated using the ratio of IC_{50} values). The sensitization effect of both HATs was even greater when IC_{20} values were compared (SF_{20} of 8.3 and 4.6). Notably, silencing of p300 or GCN5 in SKOV3/Tx600 cells produced SF_{50} values of 5.3 and 3.4, respectively, in response to a combination of bicalutamide (an AR antagonist) and taxol (Figure 4f), which represents a twofold sensitization compared with taxol alone. Even greater sensitization to taxol was observed for cells treated with shp300 and shGCN5 in the presence of bicalutamide when the ratio of SF_{20} values were calculated (25.7 and 21.2, respectively; cf. Figure 4f, e). These results suggest that silencing of both HATs exerts profound sensitization to taxol, especially at low concentrations. Together, these results suggest that upregulated p300 and GCN5 HATs in txr cells may play an important role in *ABCB1* overexpression and taxol resistance.

3.5 | Silencing of p300 or GCN5 ablates taxol-induced chromatin modification and H3K9ac/AR complex targeting to *ABCB1* ARE

To further confirm the role of HATs in chromatin modification, we used specific shRNA to silence their expression in txr cells. A cytotoxic concentration of taxol induced the accumulation of acetylated histone 3 (H3K9ac, H3K14ac, H3K56ac) and histone 4 (H4K12ac and H4K8ac) in SKOV3/Tx600 cells in the presence of verapamil, which was used to enrich drug accumulation (Figure 5a,c, and f; lanes 1 and 2; Figure 5b for statistical analysis). Notably, the protein level of p300 and GCN5 was induced by taxol by 1.3- and 2.2-fold, respectively. While the basal level of H3Kac chromatin modification marks was only slightly affected by shp300, the taxol-induced level of these marks were dramatically suppressed (Figure 5a,c, and f; lane 3 with lane 1, and lane 4 with lane 2; Figure 5b). While the basal level of H3Kac chromatin modification marks was severely affected by shGCN5, the taxol-induced level of these marks were even more severely suppressed (Figure 5a,c, and f; lane 5 with lane 1, and lane 6 with lane 2; Figure 5b). Furthermore, the extent of reduction of H4Kac chromatin modification marks by shp300

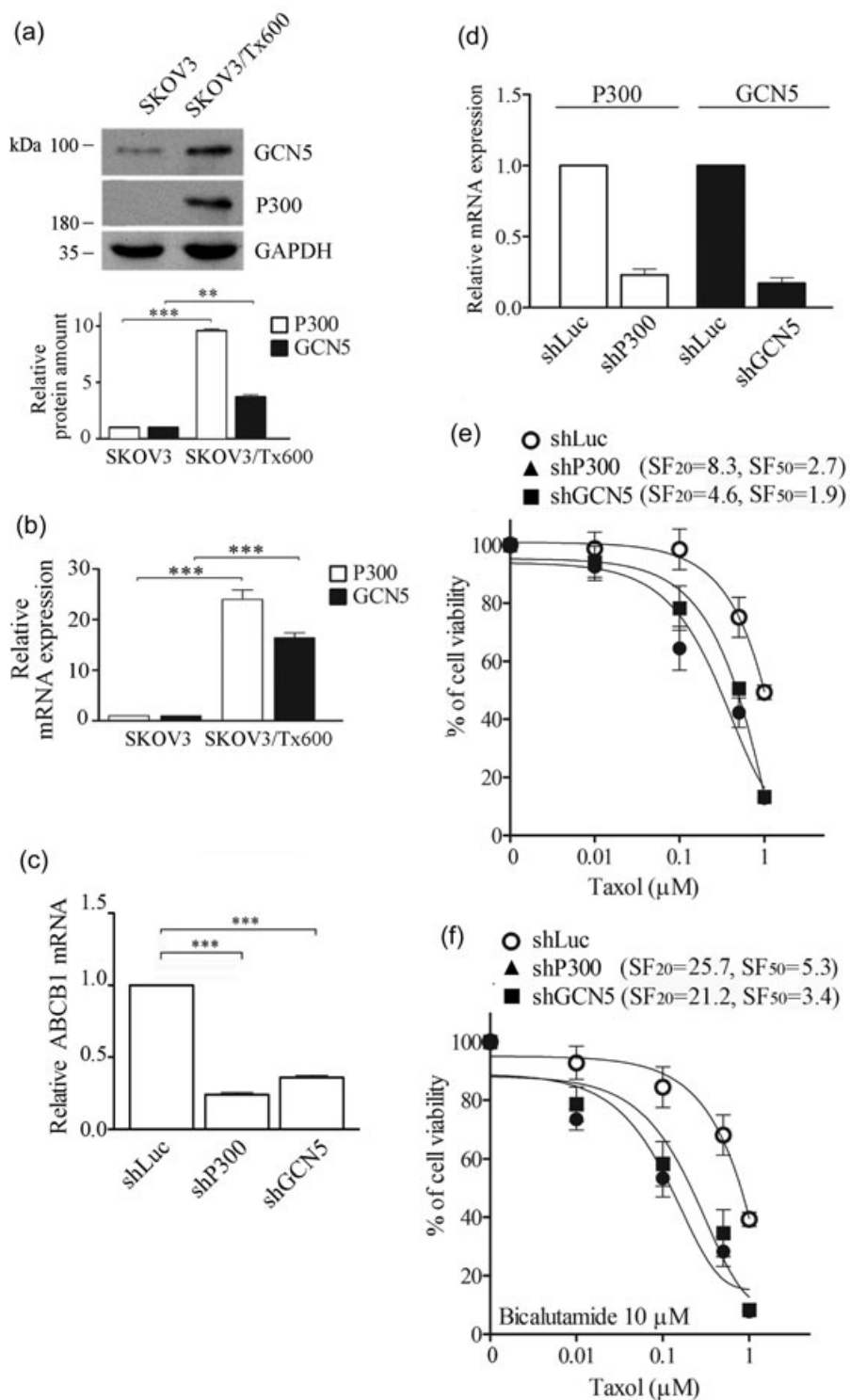


FIGURE 4 Silencing of p300 or GCN5 downregulates ABCB1 expression and sensitizes cells to taxol. (a) Western blot analysis of the acetyltransferases GCN5 and p300 in SKOV3 and txr cells. Fifty micrograms protein extracts was loaded. Lower panel, quantitative analysis of GCN5 and P300 protein levels of the experiment. (b) Differential mRNA expression levels of p300 and GCN5 in SKOV3 and txr cells. (c) Reduction of ABCB1 mRNA by silencing of p300 or GCN5. SKOV3 txr cells were treated with p300 or GCN5 shRNA (shp300, shGCN5) and ABCB1 mRNA level was determined by qPCR as described in Figure 1. mRNA level was compared using shLuc treated sample as control. (d) Silencing efficacy of shp300 and shGCN5. (e) Sensitization of SKOV3 txr cells to taxol by silencing of p300 or GCN5 using specific shRNA. SF_{20} and SF_{50} , calculated by ratio (shLuc vs. shp300 or shGCN5) of IC_{20} and IC_{50} , respectively, are indicated. (f) Sensitization of SKOV3 txr cells to taxol by silencing of p300 or GCN5 and AR inhibition. This experiment was done as in Figure 4e, except the presence of bicalutamide. The experiments were performed in triplicate (** $p < 0.01$, *** $p < 0.005$). AR: androgen receptor; IC_{50} : 50% inhibitory concentration; mRNA: messenger RNA; qPCR: quantitative polymerase chain reaction; shRNA: short-hairpin

was similar to that of H3Kac in taxol-treated samples. In contrast, the extent of reduction of H4Kac chromatin modification marks in response to shGCN5 in taxol-treated samples represented basal effects, suggesting that taxol-induced H4Kac is not affected by GCN5. These results suggest that taxol-induced chromatin modification may be controlled in a large part by p300 and/or GCN5 and marked by H3Kac. We also noted that AR level was downregulated following silencing of either p300 or GCN5 under these conditions.

To assess whether taxol-induced p300 is associated with AR-mediated ABCB1 expression, we used ChIP assays to investigate targeting of both p300/AR on the gene promoter. p300/AR was effectively targeted to the ABCB1 ARE4, a potent taxol-responsive element in our system, with binding peak observed four hrs following taxol treatment (Figure 5c). In addition, GCN5/AR were also induced to bind the ARE4 but reached high level (near 0.4% of input) 18 hr after taxol treatment (Figure 5d). Furthermore, H3K9ac/AR targeting to

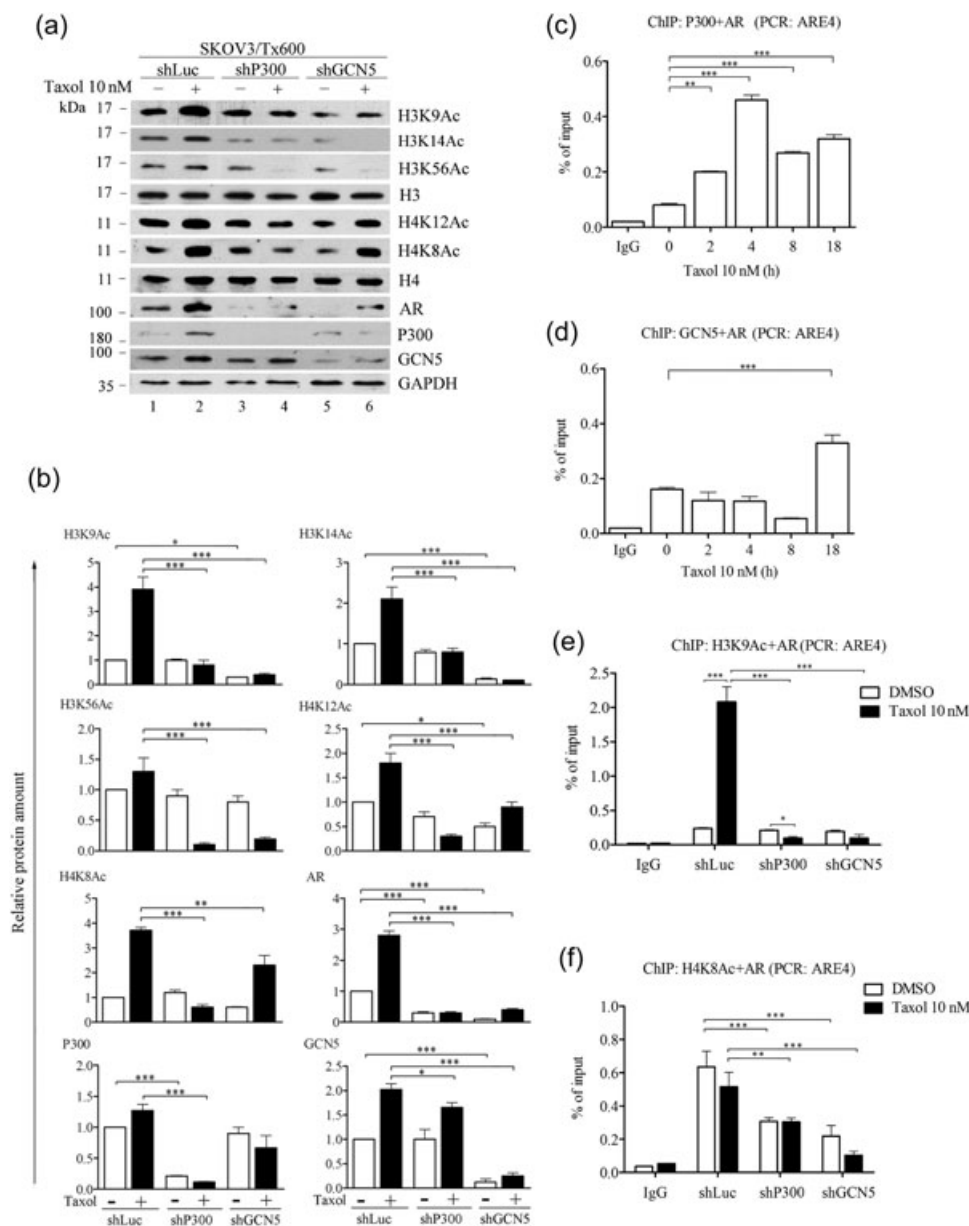


FIGURE 5 Silencing of p300 or GCN5 abrogates taxol-induced chromatin modification and H3K9ac/AR complex targeting to ABCB1 ARE. (a) Western blot analysis of the reduction of taxol-induced chromatin modification marks in SKOV3 txr cells by silencing of p300 or GCN5. Txr cells were treated with verapamil, an ABCB1 inhibitor, to enhance the level of taxol-induced histone marks. Protein levels of H3 and H4 and their acetylated forms were detected in taxol-treated cells. Protein levels of AR, p300, and GCN5 are indicated. (b) Quantitative analysis of protein levels of the experiment shown in panel (a). (c) Kinetic changes in taxol-induced ARE4 binding by p300 and AR. Re-ChIP was conducted for p300 and AR complex binding to ARE4 (see Section 2 for details). (d) Kinetic changes in taxol-induced ARE4 binding by GCN5 and AR. Re-ChIP was conducted for GCN5 and AR complex binding to ARE4. (e) Taxol induced ARE4 binding by H3K9Ac and AR was suppressed by silencing of p300 or GCN5. (f) ARE4 binding by H4K8Ac and AR in SKOV3 txr cells with silencing of p300 or GCN5. The experiments were performed in triplicate (* $p < 0.05$, ** $p < 0.01$, *** $p < 0.005$). AR: androgen receptor; Re-ChIP: re-chromatin immunoprecipitation

ARE4 was induced 10-fold following 4 hr of taxol treatment. On the other hand, this induced binding was completely eliminated by silencing of either p300 or GCN5 (Figure 5e). In contrast, H4K8ac/AR targeting to ARE4 was not regulated by the same concentration of taxol (Figure 5f). Basal level of H4K8ac/AR binding to ARE4 was lowered by both HATs. Together, these results demonstrate that p300- and/or GCN5-induced chromatin modification marks (predominantly H3Kac) and the AR target to ARE4 within the ABCB1 promoter.

3.6 | Phosphatidylinositol 3-kinase/AKT inhibitor impairs taxol-induced p300 expression, chromatin modification, and p300/AR interaction

To assess the signal pathway in taxol-induced ABCB1 expression, we examined the effects of specific inhibitors of major kinases. Inhibition of the phosphatidylinositol 3-kinase (PI3K) pathway with a PI3K inhibitor (PI3Ki) caused dramatic suppression of ABCB1 mRNA level

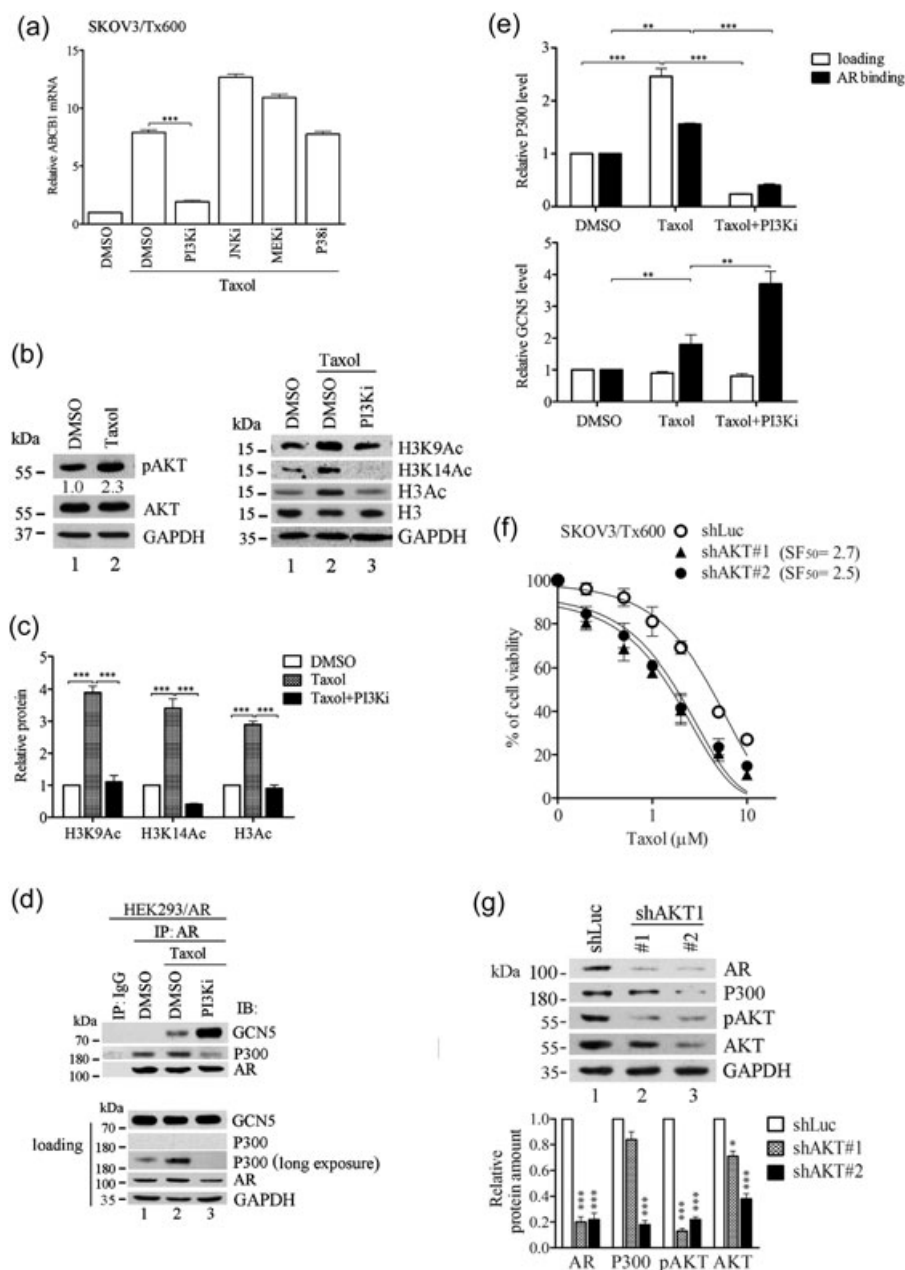


FIGURE 6 PI3K/AKT inhibitors impair taxol-induced p300 expression, chromatin modification, and p300/AR interaction. (a) Inhibition of taxol-induced ABCB1 mRNA by PI3K inhibitor. SKOV3 txr cells were pretreated with DMSO control or kinase inhibitor and then exposed to taxol stress. ABCB1 mRNA level was determined by qPCR. Following normalization to GAPDH, mRNA level was compared with DMSO control sample. (b) Inhibition of taxol induced chromatin modification marks by PI3K inhibitor. Left panel: Western blot analysis of the induction of pAKT by taxol in SKOV3 txr cells. Right panel: Taxol induced chromatin modification marks (acetylated H3) was reduced by PI3K inhibitor. (c) Quantification of Figure 6b. Image intensity of each Western blot was determined using Image scanner III (GE Healthcare, WI). (d) Interaction of AR with p300 and GCN5 in AR-expressing HEK293 cells following treatment with taxol or also pretreatment with PI3K inhibitor determined by the co-IP assay. Whole cell extracts (1000 μ g) of AR-expressing HEK293 cells were subjected to immunoprecipitation (IP) with AR antibody, followed by immunoblotting (IB) with indicated antibodies. Lower panel: Western blot analysis of the loading level of each protein. Twenty micrograms of protein extracts of each treatment were compared. (e) Quantification of interaction of AR with p300 and GCN5 in AR-expressing HEK293 cells following treatment with taxol or also pretreatment with PI3K inhibitor (Figure 6d). Upper panel: Relative level of p300. Lower panel: Relative level of GCN5 (lower panel). The protein level was indicated for loading and AR binding. (f) Sensitization of SKOV3 txr cells to taxol following AKT silencing using specific shRNAs. Two independent shRNAs (shAKT1#1 and shAKT1#2) were used. Calculated SF₅₀ are shown. (g) Relative AR and p300 protein level following AKT silencing. Calculated protein levels are shown in the bottom panel. The experiments were performed in triplicate (* p < 0.05, ** p < 0.01, *** p < 0.005). AKT: serine/threonine protein kinase; AR: androgen receptor; DMSO: dimethyl sulfoxide; GAPDH: glyceraldehyde-3-phosphate dehydrogenase; mRNA: messenger RNA; PI3K: phosphatidylinositol 3-kinase; qPCR: quantitative real-time polymerase chain reaction

in SKOV3/Tx600 cells, whereas other inhibitors produced no effects (Figure 6a). The PI3K pathway was activated by taxol, as shown by more than threefold increase in AKT phosphorylation (Figure 6b, left panel, pAKT). In addition, taxol-induced H3Kac level (H3K9ac and H3K14ac) was dramatically suppressed by PI3Ki (Figure 6b right panel, c, and f. lane 2 with lane 3). Inhibition of the levels of these chromatin modification marks by PI3Ki were quantified in Figure 6c. To further examine the interaction between the AR and HATs, we ectopically expressed the AR in HEK293 cells and, following taxol treatment with or without PI3Ki, we performed immunoprecipitation assays using an anti-AR antibody followed by immunoblotting for HATs. We found that the interaction between HATs and the AR was regulated by taxol treatment and inhibited by PI3Ki. While AR complexed with p300 or GCN5 could be induced by taxol (Figure 6c, d, and f; lane 2 with lane 1), PI3Ki ablated taxol-induced p300/AR level but not GCN5/AR complex level (Figure 6c,d, and f; lane 3 with 2). Notably, p300 protein level was considerably reduced by PI3Ki, whereas GCN5 level was not affected (see Figure 6d, bottom panel for protein loading). We noted that forced expression of AR in HEK293 cells was not regulated by taxol. The protein level of these HATs (p300 and GCN5) and their co-immunoprecipitation with AR was quantified. While the level of p300 protein induced by taxol was inhibited by PI3Ki, GCN5 protein level was not affected by either taxol or PI3Ki (Figure 6e). Taxol-induced p300/AR co-immunoprecipitation was prevented by PI3Ki at a level lower than that of the DMSO control (Figure 6e, top panel). In contrast, taxol-induced GCN5/AR complex level was not reduced by PI3Ki (Figure 6e, bottom panel). These observations suggest that PI3Ki attenuates p300/AR and eliminates the activity of epigenetic modification on H3 while GCN5 appears to play a minimal role in this context.

To confirm PI3K/AKT regulation on both P300 and AR, we knockdown AKT using shRNA. Silencing of AKT1 using two different shAKT1 clones sensitized SKOV3/Tx600 cells to taxol by 2.7- and 2.5-fold (Figure 6f). This result demonstrated that silencing of AKT not only plays an important role in cell survival but this treatment also enhances taxol toxicity. AKT silencing efficiency was quantified by Western blot and the two clones silenced AKT by 30% and 75% (Figure 6g). Interestingly, AR and P300 protein levels were also reduced by 80% after AKT knockdown (Figure 6c,f, and g; lanes 2 and 3 to lane 1; the bottom panel shows densitometry results). These results suggest that expression of p300 and AR is regulated by the PI3K/AKT pathway and that this pathway is activated by taxol.

To further assess how taxol upregulates p300 expression, we examined protein stability following cycloheximide treatment to prevent the production of new proteins. While p300 protein level was reduced in control DMSO-treated cells, the protein level of p300 increased following taxol treatment (20 nM), and this phenomenon was inhibited by PI3Ki (Figure 7a,b). Furthermore, p300 mRNA level was also slightly reduced by the same concentration of taxol in a PI3Ki-dependent manner (Figure 7c). We also detected a slight induction of p300 protein level in SKOV3/Tx600 cells treated with taxol (20–200 nM). In addition, AR protein level was induced in a dose-dependent manner by taxol (Figure 7d,e).

4 | DISCUSSION

In this study, we found that AR and ABCB1 levels are hyperexpressed in txr ovarian cancer cells. Notably, expression of both genes is effectively upregulated in sensitive ovarian cancer cells in response to sublethal concentration of taxol. Transcriptomic analysis of txr and sensitive parental cells suggested that the AR represents a driver of the ABCB1 gene, among others (N. K. Sun et al., 2015). Gain-of-function and loss-of-function studies further demonstrated that androgen/AR signaling is a potent pathway for upregulation of ABCB1 in response to sublethal concentration of taxol. In contrast, AR transactivity and ABCB1 expression are dramatically suppressed by lethal concentration of taxol in the same cell system (N. K. Sun et al., 2015), supporting the hypothesis that AR-driven txr gene overexpression (e.g., ABCB1) is responsible, at least in part, for taxol resistance. These findings may have clinical implications in that potentiated androgen/AR signaling is associated with poor therapy efficacy in prostate cancer (Egan et al., 2014). Accumulating laboratory and epidemiological evidence strongly support a critical role for androgen/AR signaling in the origin and promotion of epithelial ovarian cancer and have led to clinical trials designed to target the AR (reviewed in Modugno et al., 2012). However, the mechanism underlying AR signaling in targeting txr gene expression remains elusive. It was recently reported that antiandrogens diminish ABCB1 activity in both AR-positive and AR-negative prostate cancer cells (Zhu et al., 2015), suggesting the existence of an AR-independent pathway in this context. Here, we observed that potentiation of taxol-induced ABCB1 expression by the AR is controlled at the transcription level, but not by gene amplification, contrary to what is often observed in acquired MDR cells (Fletcher et al., 2010; Gottesman et al., 2002; Hille et al., 2006; Leonard et al., 2003). Consistent with observations that the AR/ABCB1 pathway is critical for ovarian carcinogenesis, our finding supports the possibility that the same pathway may be important for chemoresistance in ovarian cancers.

Using promoter reporter assay by deletion, we identified an AR responsive element (containing ARE4) within the promoter of the ABCB1 gene. ChIP assays further revealed that this element represents a major site for binding of AR in response to chemical agonists or sublethal concentrations of taxol. Other AREs such as ARE3 are also targeted by activated AR, but they do not participate in transactivation as revealed by the promoter assay. Moreover, taxol-induced chromatin modification, marked by H3K9ac and other proteins, is also required for efficient AR binding to ARE4 in response to taxol (see Figures 2 and 3). The HATs p300 and GCN5 are upregulated in txr ovarian cancer cells. Similar extent of silencing of either one of these HATs by shRNA sensitizes ovarian cancer cells to taxol. Notably, greater sensitization to the drug is detected in txr cells in the presence of AR antagonist than in control cells (see Figure 4), supporting the notion that p300 and/or GCN5 is important for the txr phenotype. Furthermore, targeting of p300 or GCN5 in complex with the AR to ARE4 within the ABCB1 gene is induced by taxol and is considerably reduced by silencing of either HAT. Chromatin modification is an appealing mechanism to explain the

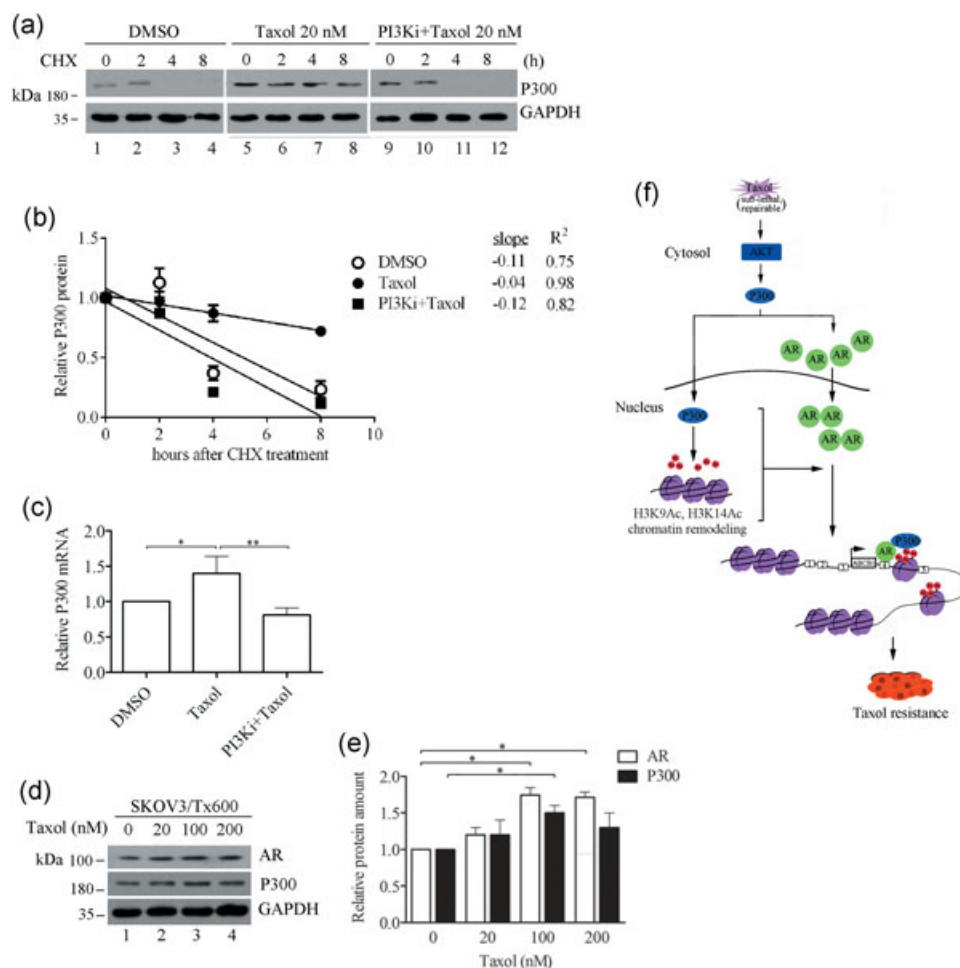


FIGURE 7 Taxol treatment stabilizes p300 protein but this effect is impaired by PI3K/AKT inhibitor. (a) Western blot of p300 protein levels following cycloheximide (CHX) treatment. The samples include treatment of SKOV3 trx cells with taxol (20 nM) or pretreatment with the PI3K inhibitor. (b) Quantification of relative p300 protein and linear regressions of the kinetic pattern of p300 protein level. (c) Inhibition of taxol-induced p300 mRNA level by PI3K inhibitor. The samples include treatment of SKOV3 trx cells with taxol or pre-treatment with PI3K inhibitor. These experiments were performed in triplicate (* $p < 0.05$, ** $p < 0.01$, *** $p < 0.005$). (d) Induction of AR and p300 protein level by taxol in a dose-dependent manner in SKOV3 trx cells. (e) Quantitative analysis of AR and P300 protein levels of the experiment shown in panel (d). (f) Working model of ABCB1 induction by sublethal concentration of taxol. PI3K/AKT regulated P300 expression is potentiated by taxol, and elicits chromatin modification (as reflected by acetylated H3 and H4 marks). Sublethal taxol treatment also stimulates nuclear translocation of AR (right panel). Together with epigenetic p300, AR targets at ARE4 of the ABCB1 promoter, and transactivates gene expression. This simplified model does not include details in modification of AR, such as acetylation by p300 and phosphorylation by AKT, or the role of the AR and p300 in targeting to the ARE site. In addition, possible involvement of FKBP5 which binds AR and is involved in taxol resistance (N. K. Sun et al., 2014) is not shown here. AKT: serine/threonine protein kinase; AR: androgen receptor; mRNA: messenger RNA; PI3K: phosphatidylinositol 3-kinase [Color figure can be viewed at wileyonlinelibrary.com]

trx phenotype as shown in the current study and in MDR cells by other authors (Toth, Boros, & Balint, 2012). This phenomenon may be explained by upregulated HATs in trx cells. Also, trx cells display larger amounts of nuclear AR in response to taxol compared with parental cells (N. K. Sun et al., 2015 and this study). However, our data could not distinguish the effects of epigenetic factors and transcription factors in recruiting these factors to the ABCB1 promoter site for gene transactivation in response to taxol. We believe that taxol at the concentration used in the current study may potentiate PI3K/AKT-regulated p300 expression which may cause chromatin modification via histone acetylation (i.e., H3K9ac) and interaction of the AR at ARE4 of the ABCB1 gene in close proximity to RNA polymerase and the

transcription start site (Figure 7e). While the AR is regulated by AKT and JNK which are downregulated by lethal concentration of taxol (N. K. Sun et al., 2015), AKT-regulated AR and subsequent ABCB1 is upregulated by sublethal concentration of taxol. Taken together, the AKT/p300/AR axis may play a critical role by acting in cis at a specific site (i.e., ARE4) to upregulate ABCB1 expression in response to sublethal concentration of taxol.

AR binding regions showed limited conservation across species, regardless of whether the metric for conservation was based on local sequence similarity or the presence of consensus AREs. The DNA-binding domain of the AR recognizes a palindromic response element that comprises an inverted repeat of the 5'-AGAACA-3' hexamer

with a 3-nucleotide spacer, usually termed the canonical androgen/glucocorticoid response element (Mangelsdorf et al., 1995). In our study, predicted AREs of the *ABCB1* gene scored in the following order: ARE4 > ARE1 > ARE5 > ARE3 > ARE2. On the other hand, ChIP analysis indicated that taxol- or AR-agonist-induced AR binding to *ABCB1* gene in ovarian cancer cells preferentially occurred in the following order: ARE4 > ARE3 > ARE2 > ARE1 = ARE5. While ARE4 shows the highest affinity for the activated AR as predicted, ARE1 and ARE5 which obtained high predicted score showed low binding to activated AR in our experiments. Factors other than the AR and their interactions with AREs may be important to explain this discrepancy. For example, ChIP-seq analysis showed that 94% of 19,377 AR-binding regions harbored consensus AREs enriched with multiple binding motifs that included nuclear factor 1 and activator protein 2 (AP-2) sites in mouse epididymis, suggesting a combinatorial regulation (Hu et al., 2010). Moreover, two collaborating factors for AR signaling in vivo were reported—Hnf4a (hepatocyte nuclear factor 4a) in mouse kidney and AP-2a in mouse epididymis—and these factors define tissue-specific AR recruitment (Pihlajamaa et al., 2014). Our results indicate that chromatin modification via p300-mediated histone acetylation (H3K9) also participates in AR recruitment on the target gene *ABCB1*, suggesting that the regulation conferred by sequence-specific binding transcription factors may be highly dependent on the three-dimensional structure of chromatin. In this context, ARE4 of *ABCB1* gene is preferential for recruitment of cis-acting H3K9ac and trans-acting AR factors. Comparison of AR-binding events in the epididymis and prostate of wild-type and mutant SPARK1 mice (whose AR-DNA-binding domain has the second zinc finger replaced by that of the glucocorticoid receptor) revealed that AR achieves selective chromatin binding through a less stringent sequence requirement for the 3'-hexamer (Sahu et al., 2014). Whether the 3'-hexamer of these AREs plays a role in modulation of the interaction with defined and yet undefined factors require further investigations. These results support the notion that the liganded AR and AREs are required but are not sufficient for establishment of tissue- or stress-specific transcription programs in vivo, and that AR-selective activities over other steroid receptors rely on relaxed chromatin rather than increased stringency of cis-elements on chromatin (Pihlajamaa, Sahu, & Jänne, 2015).

Changes in AR quality in SKOV3 cells in response to taxol were not investigated in this study. It is known that clinical outcome and cancer biology in ovarian epithelial cancer cells can be influenced by the AR, including short (CAG)_n or glutamine repeats in the AR, altered expression and activity of AR coactivators, and differential expression of androgen-mediated genes (Li & Karlan, 2008). In this study, AR expression level and its activity through interaction with other factors appears to be critical for ovarian oncogenesis as well as therapy efficacy. It has been demonstrated that AR activity is inhibited by phosphorylation at serine residues by activated AKT in a cell-type and cell stage-dependent manner (Lin et al., 2003; Lin, Wang, Hu, Altuwaijri, & Chang, 2002; Lin, Yeh, Kang, & Chang, 2001; Manin et al., 2002; Taneja et al., 2005). Phosphorylation of AR may lead to Mdm2-mediated protein degradation in prostate cancer cells

(Lin et al., 2002). In contrast, AR level was upregulated by the AKT pathway in ovarian cancer cells. Our results also indicated that AR protein level is upregulated by ectopic expression of p300 and GCN5 in ovarian cancer cells. While the AR protein level was apparently reduced by silencing of either p300 or GCN5 in ovarian cancer cells (Figure 5a), p300 level, but not GCN5 level, was dramatically reduced to a minimal level by AKT inhibition (Figure 6d). In this sense, AKT/p300 may regulate the AR or other transcription factors through acetylation, subsequently modulating *ABCB1* expression (Bourguignon et al., 2009; Fu et al., 2000). A combined analysis of genetic and epigenetic data as performed here suggests that important txr genes such as *ABCB1* may be overlooked by single assays. These results do not violate the notion that AR activity is regulated by AKT phosphorylation in a cell-type and cell stage-dependent manner (Lin et al., 2001; Lin et al., 2002; Lin et al., 2003; Manin et al., 2002; Taneja et al., 2005).

To identify the pathways mediating the effects of AR activation, we treated cells with taxol to induce activation of the major cellular kinases. Assuming that kinase activation is required for the effects of AR activation, inhibition of kinase activity should cause a reduction of AR expression level or activity. SKOV3/Tx600 cells were exposed to sublethal concentrations of taxol. Taxol-induced *ABCB1* expression and chromatin modification was dramatically suppressed by the AKT inhibitor, but not by the other kinase inhibitors tested (Figure 6a). AR expression is dependent on AKT and JNK pathways in these cells as only AKT and JNK inhibitors (Wortmannin and SP600125, respectively) downregulated AR expression (N. K. Sun et al., 2015). These results suggest that the AKT pathway likely represents a target of sub-lethal taxol treatment in upregulating *ABCB1* expression. While this processes is heavily dependent on chromatin modification, the level of AR remains unchanged. In contrast, lethal concentration of taxol downregulated AR expression and activity in these cells by inhibiting the AKT kinase pathway (N. K. Sun et al., 2015). Thus, activation or inactivation of this kinase pathway is differently regulated depending on the concentration of the drug or extent of damages in the cancer cells tested, and these effects dictate whether protective or apoptotic routes will be taken. Notably, we show that the AKT pathway is involved in potentiating p300-mediated chromatin modification and recruitment of the AR to ARE4 within the *ABCB1* gene, phenomena which appear to be critical for cell resistance to taxol in ovarian carcinoma cells. Identification of the AKT/p300/AR/*ABCB1* axis in the development of txr in ovarian cancer represents a new treatment target to limit chemoresistance during cancer therapy.

ACKNOWLEDGMENTS

We thank Dr. Chwangshan Chang (University of Rochester) for providing plasmids and Dr. Bertrand Tan (Chang Gung University) for helpful discussions. This study was supported by the Ministry of Science and Technology, Taiwan (Contract No. NSC100-2320-B-182-026-MY3, MOST103-2320-B-182-031, and MOST106-2320-B-

255-004), Chang Gung University and Chang Gung Memorial Hospital (Contract No. CMRPD3E0093, CMRPD1G0101, BMRP071).

CONFLICTS OF INTEREST

The authors declare no conflict of interest.

AUTHOR CONTRIBUTIONS

N.K.S., S.L.H., and C.K.C. designed and performed the experiments. All authors were involved in the study, interpreting the results, and writing the manuscript.

ORCID

Chuck C.-K. Chao  <http://orcid.org/0000-0001-5783-3159>

REFERENCES

- Armstrong, C. M., Allen, C., & Gao, A. C. (2015). Drug resistance in castration resistant prostate cancer: Resistance mechanisms and emerging treatment strategies. *American Journal of Clinical and Experimental Urology*, 3, 64–76.
- Bourguignon, L. Y., Xia, W., & Wong, G. (2009). Hyaluronan-mediated CD44 interaction with p300 and SIRT1 regulates β -catenin signaling and NF κ B-specific transcription activity leading to MDR1 and Bcl-xL gene expression and chemoresistance in breast tumor cells. *Journal of Biological Chemistry*, 284, 2657–2671.
- Cai, M., Hu, Z., Liu, J., Gao, J., Tan, M., Zhang, D., ... Lin, B. (2015). Expression of hMOF in different ovarian tissues and its effects on ovarian cancer prognosis. *Oncology Reports*, 33, 685–692.
- Chadha, S., Rao, B. R., Slotman, B. J., van Vroonhoven, C. C., & van der Kwast, T. H. (1993). An immunohistochemical evaluation of androgen and progesterone receptors in ovarian tumors. *Human Pathology*, 24, 90–95.
- Chao, C. C., Lee, Y. L., Cheng, P. W., & Lin-Chao, S. (1991). Enhanced host cell reactivation of damaged plasmid DNA in HeLa cells resistant to cis-diamminedichloroplatinum(II). *Cancer Research*, 51, 601–605.
- Cutress, M. L., Whitaker, H. C., Mills, I. G., Stewart, M., & Neal, D. E. (2008). Structural basis for the nuclear import of the human androgen receptor. *Journal of Cell Science*, 121, 957–968.
- Dekker, F. J., & Haisma, H. J. (2009). Histone acetyl transferases as emerging drug targets. *Drug Discovery Today*, 14, 942–948.
- Egan, A., Dong, Y., Zhang, H., Qi, Y., Balk, S. P., & Sartor, O. (2014). Castration-resistant prostate cancer: Adaptive responses in the androgen axis. *Cancer Treatment Reviews*, 40, 426–433.
- Evangelou, A., Jindal, S. K., Brown, T. J., & Letarte, M. (2000). Down-regulation of transforming growth factor beta receptors by androgen in ovarian cancer cells. *Cancer Research*, 60, 929–935.
- Fletcher, J. I., Haber, M., Henderson, M. J., & Norris, M. D. (2010). ABC transporters in cancer: More than just drug efflux pumps. *Nature Reviews Cancer*, 10, 147–156.
- Fu, M., Wang, C., Reutens, A. T., Wang, J., Angeletti, R. H., Siconolfi-Baez, L., ... Pestell, R. G. (2000). p300 and p300/cAMP-response element-binding protein-associated factor acetylate the androgen receptor at sites governing hormone-dependent transactivation. *Journal of Biological Chemistry*, 275, 20853–20860.
- Gottesman, M. M., Fojo, T., & Bates, S. E. (2002). Multidrug resistance in cancer: Role of ATP-dependent transporters. *Nature Reviews Cancer*, 2, 48–58.
- Hediger, M. A., Romero, M. F., Peng, J. B., Rolfs, A., Takanaga, H., & Bruford, E. A. (2004). The ABCs of solute carriers: Physiological, pathological, and therapeutic implications of human membrane transport proteins. *Introduction. Pflügers Archiv*, 447, 465–468.
- Hille, S., Rein, D. T., Riffelmann, M., Neumann, R., Sartorius, J., Pfutzner, A., ... Breidenbach, M. (2006). Anticancer drugs induce mdr1 gene expression in recurrent ovarian cancer. *Anti-cancer Drugs*, 17, 1041–1044.
- Hu, S., Yao, G., Guan, X., Ni, Z., Ma, W., Wilson, E. M., ... Zhang, Y. (2010). Research resource: Genome-wide mapping of in vivo androgen receptor binding sites in mouse epididymis. *Molecular Endocrinology*, 24, 2392–2405.
- Huang, Y. (2007). Pharmacogenetics/genomics of membrane transporters in cancer chemotherapy. *Cancer and Metastasis Reviews*, 26, 183–201.
- Huang, Y., & Sadee, W. (2006). Membrane transporters and channels in chemoresistance and -sensitivity of tumor cells. *Cancer Letters*, 239, 168–182.
- Ilekis, J. V., Connor, J. P., Prins, G. S., Ferrer, K., Niederberger, C., & Scoccia, B. (1997). Expression of epidermal growth factor and androgen receptors in ovarian cancer. *Gynecologic Oncology*, 66, 250–254.
- Jin, S., & Scotto, K. W. (1998). Transcriptional regulation of the MDR1 gene by histone acetyltransferase and deacetylase is mediated by NF- κ B. *Molecular and Cellular Biology*, 18, 4377–4384.
- Kuhne, I. R., de Graaff, J., Rao, B. R., & Stolk, J. G. (1987). Androgen receptor predominance in human ovarian carcinoma. *Journal of Steroid Biochemistry*, 26, 393–397.
- Lau, K. M., Mok, S. C., & Ho, S. M. (1999). Expression of human estrogen receptor- α and - β , progesterone receptor, and androgen receptor mRNA in normal and malignant ovarian epithelial cells. *Proceedings of the National Academy of Sciences of the United States of America*, 96, 5722–5727.
- Lee, P., Rosen, D. G., Zhu, C. C., Silva, E. G., & Liu, J. S. (2005). Expression of progesterone receptor is a favorable prognostic marker in ovarian cancer. *Gynecologic Oncology*, 96, 671–677.
- Leonard, G. D., Fojo, T., & Bates, S. E. (2003). The role of ABC transporters in clinical practice. *The Oncologist*, 8, 411–424.
- Li, A. J., & Karlan, B. Y. (2008). Androgens and epithelial ovarian cancer: What's the connection? *Cancer Biology Therapy*, 7, 1712–1716.
- Lin, H. K., Yeh, S. Y., Kang, H. Y., & Chang, C. S. (2001). Akt suppresses androgen-induced apoptosis by phosphorylating and inhibiting androgen receptor. *Proceedings of the National Academy of Sciences of the United States of America*, 98, 7200–7205.
- Lin, H. K., Wang, L., Hu, Y. C., Altuwaijri, S., & Chang, C. (2002). Phosphorylation-dependent ubiquitination and degradation of androgen receptor by Akt require Mdm2 E3 ligase. *EMBO Journal*, 21, 4037–4048.
- Lin, H. K., Hu, Y. C., Yang, L., Altuwaijri, S., Chen, Y. T., Kang, H. Y., & Chang, C. (2003). Suppression versus induction of androgen receptor functions by the phosphatidylinositol 3-kinase/Akt pathway in prostate cancer LNCaP cells with different passage numbers. *Journal of Biological Chemistry*, 278, 50902–50907.
- Liu, N., Zhang, R., Zhao, X., Su, J., Bian, X., Ni, J., ... Jin, J. (2013). A potential diagnostic marker for ovarian cancer: Involvement of the histone acetyltransferase, human males absent on the first. *Oncology Letters*, 6, 393–400.
- Mangelsdorf, D. J., Thummel, C., Beato, M., Herrlich, P., Schütz, G., Umesono, K., ... Evans, R. M. (1995). The nuclear receptor superfamily: The second decade. *Cell*, 83, 835–839.
- Manin, M., Baron, S., Goossens, K., Beaudoin, C., Jean, C., Veyssiere, G., ... Morel, L. (2002). Androgen receptor expression is regulated by the phosphoinositide 3-kinase/Akt pathway in normal and tumoral epithelial cells. *Biochemical Journal*, 366, 729–736.
- McEwan, I. (2004). Molecular mechanisms of androgen receptor-mediated gene regulation: Structure-function analysis of the AF-1 domain. *Endocrine-Related Cancer*, 11, 281–293.

- McGrogan, B. T., Gilmartin, B., Carney, D. N., & McCann, A. (2008). Taxanes, microtubules and chemoresistant breast cancer. *Biochimica et Biophysica Acta*, 1785, 96–132.
- Mishra, D. K., Chen, Z., Wu, Y., Sarkissyan, M., Koeffler, H. P., & Vadgama, J. V. (2010). Global methylation pattern of genes in androgen sensitive and androgen independent prostate cancer cells. *Molecular Cancer Therapeutics*, 9, 33–45.
- Modugno, F., Laskey, R., Smith, A. L., Andersen, C. L., Haluska, P., & Oesterreich, S. (2012). Hormone response in ovarian cancer: Time to reconsider as a clinical target? *Endocrine-Related Cancer*, 19, R255–R279.
- Murray, S., Briasoulis, E., Linardou, H., Bafaloukos, D., & Papadimitriou, C. (2012). Taxane resistance in breast cancer: Mechanisms, predictive biomarkers and circumvention strategies. *Cancer Treatment Reviews*, 38, 890–903.
- Nakanishi, T. (2007). Drug transporters as targets for cancer chemotherapy. *Cancer Genomics & Proteomics*, 4, 241–254.
- Pihlajamaa, P., Sahu, B., & Jänne, O. A. (2015). Determinants of receptor- and tissue-specific actions in androgen signaling. *Endocrine Reviews*, 36, 357–384.
- Pihlajamaa, P., Sahu, B., Lyly, L., Aittomäki, V., Hautaniemi, S., & Jänne, O. A. (2014). Tissue-specific pioneer factors associate with androgen receptor cisomes and transcription programs. *EMBO Journal*, 33, 312–326.
- Sahu, B., Pihlajamaa, P., Dubois, V., Kerkhofs, S., Claessens, F., & Jänne, O. A. (2014). Androgen receptor uses relaxed response element stringency for selective chromatin binding and transcriptional regulation in vivo. *Nucleic Acids Research*, 42, 4230–4240.
- Shang, Y., Hu, X., DiRenzo, J., Lazar, M. A., & Brown, M. (2000). Cofactor dynamics and sufficiency in estrogen receptor-regulated transcription. *Cell*, 103, 843–852.
- Smith, E. R., Pannuti, A., Gu, W., Steurnagel, A., Cook, R. G., Allis, C. D., & Lucchesi, J. C. (2000). The drosophila MSL complex acetylates histone H4 at lysine 16, a chromatin modification linked to dosage compensation. *Molecular and Cellular Biology*, 20, 312–318.
- Sun, C. L., & Chao, C. C. (2005). Cross-resistance to death ligand-induced apoptosis in cisplatin-selected HeLa cells associated with overexpression of DDB2 and subsequent induction of cFLIP. *Molecular Pharmacology*, 67, 1307–1314.
- Sun, N. K., Huang, S. L., Chang, P. Y., Lu, H. P., & Chao, C. C. K. (2014). Transcriptomic profiling of taxol-resistant ovarian cancer cells identifies FKBP5 and the androgen receptor as critical markers of chemotherapeutic response. *Oncotarget*, 5, 11939–11956.
- Sun, N. K., Huang, S. L., Lu, H. P., Chang, T. C., & Chao, C. C. K. (2015). Integrative transcriptomics-based identification of cryptic drivers of taxol- resistance genes in ovarian carcinoma cells: Analysis of the androgen receptor. *Oncotarget*, 6, 27065–27082.
- Sun, S., Cai, J., Yang, Q., Zhu, Y., Zhao, S., & Wang, Z. (2016). Prognostic value and implication for chemotherapy treatment of ABCB1 in epithelial ovarian cancer: A meta-analysis. *PLoS One*, 11, e0166058.
- Taneja, S. S., Ha, S., Swenson, N. K., Huang, H. Y., Lee, P., Melamed, J., ... Logan, S. K. (2005). Cell-specific regulation of androgen receptor phosphorylation in vivo. *Journal of Biological Chemistry*, 280, 40916–40924.
- Toth, M., Boros, I. M., & Balint, E. (2012). Elevated level of lysine 9-acetylated histone H3 at the MDR1 promoter in multidrug-resistant cells. *Cancer Prevention Research*, 103, 659–669.
- Wang, P. H., & Chang, C. (2004). Androgens and ovarian cancers. *European Journal of Gynaecological Oncology*, 25, 157–163.
- Wu, Z. Z., Lu, H. P., & Chao, C. C. K. (2010). Identification and functional analysis of genes which confer resistance to cisplatin in tumor cells. *Biochemical Pharmacology*, 80, 262–276.
- Wu, Z. Z., Sun, N. K., Chien, K. Y., & Chao, C. C. (2011). Silencing of the SNARE protein NAPA sensitizes cancer cells to cisplatin by inducing ERK1/2 signaling, synoviolin ubiquitination and p53 accumulation. *Biochemical Pharmacology*, 82, 1630–1640.
- Zhu, Y., Liu, C., Armstrong, C., Lou, W., Sandher, A., & Gao, A. C. (2015). Antiandrogens inhibit ABCB1 efflux and ATPase activity and reverse docetaxel resistance in advanced prostate cancer. *Clinical Cancer Research*, 21, 4133–4142.

SUPPORTING INFORMATION

Additional supporting information may be found online in the Supporting Information section at the end of the article.

How to cite this article: Sun N-K, Kohli A, Huang S-L, Chang T-C, Chao CC-K. Androgen receptor transcriptional activity and chromatin modifications on the ABCB1/MDR gene are critical for taxol resistance in ovarian cancer cells. *J Cell Physiol*. 2018;1–16. <https://doi.org/10.1002/jcp.27535>



Post-irradiation recovery time strongly influences fractional laser-facilitated skin absorption

Woan-Ruoh Lee^{a,b,1}, Chien-Yu Hsiao^{c,d,e,1}, Tse-Hung Huang^{f,g,h,i}, Chih-Liang Wang^j,
Ahmed Alalawi^k, En-Li Chen^l, Jia-You Fang^{d,l,m,*}

^a Graduate Institute of Medical Sciences, Taipei Medical University, Taipei, Taiwan

^b Department of Dermatology, Taipei Medical University Shuang Ho Hospital, New Taipei City, Taiwan

^c Department of Nutrition and Health Sciences, Chang Gung University of Science and Technology, Kweishan, Taoyuan, Taiwan

^d Research Center for Food and Cosmetic Safety and Research Center for Chinese Herbal Medicine, Chang Gung University of Science and Technology, Kweishan, Taoyuan, Taiwan

^e Aesthetic Medical Center, Department of Dermatology, Chang Gung Memorial Hospital, Kweishan, Taoyuan, Taiwan

^f Department of Traditional Chinese Medicine, Chang Gung Memorial Hospital, Keelung, Taiwan

^g School of Traditional Chinese Medicine, Chang Gung University, Kweishan, Taoyuan, Taiwan

^h Graduate Institute of Health Industry Technology, Chang Gung University of Science and Technology, Kweishan, Taoyuan, Taiwan

ⁱ School of Nursing, National Taipei University of Nursing and Health Sciences, Taipei, Taiwan

^j Division of Pulmonary Oncology and Interventional Bronchoscopy, Department of Thoracic Medicine, Chang Gung Memorial Hospital, Kweishan, Taoyuan, Taiwan

^k Department of Pharmaceutics, College of Pharmacy, Prince Sattam Bin Abdulaziz University, Al Kharj, Saudi Arabia

^l Pharmaceutics Laboratory, Graduate Institute of Natural Products, Chang Gung University, Kweishan, Taoyuan, Taiwan

^m Department of Anesthesiology, Chang Gung Memorial Hospital, Kweishan, Taoyuan, Taiwan

ARTICLE INFO

Keywords:

Fractional laser
Laser-facilitated drug delivery
Recovery time
Stratum corneum
Tight junction

ABSTRACT

Fractional CO₂ laser treatment has been used in some clinical trials to promote topical drug delivery. Currently, there is no standard for laser settings to achieve a feasible therapy. The cutaneous recovery following laser treatment and its influence on drug absorption have not been well explored. This study evaluated the kinetics of laser-treated skin-barrier restoration and drug permeation in nude mice. The skin recovery and observation of the process were characterized by transdermal water loss (TEWL), erythema measurement, gross appearance, optical microscopy, and scanning electron microscopy (SEM). The skin absorption of a lipophilic small permeant (tretinoin), a hydrophilic small permeant (acyclovir), and a large molecule (fluorescein isothiocyanate dextran 4 kDa, FD4) was examined in vitro using Franz cell. TEWL suggested that the laser-treated skin restored its barrier function at 16 h after irradiation. The fractional laser produced microchannels of about 150 μm in diameter and 25 μm in depth that were surrounded with thermal coagulation. The bright-field imaging indicated that the micropores were progressively closed during the recovery period but had not completely closed even after a 16-h recovery. The laser treatment led to a rapid tretinoin penetration across the skin immediately after irradiation, with a 5-fold enhancement compared to intact skin. This enhancement was gradually reduced following the increase of recovery time. Conversely, the acyclovir and FD4 permeation peaked at 1–2 h post-irradiation. The FD4 flux was even elevated as the recovery time increased. The reasons for this could have been the subsequent inflammation after laser exposure and the deficient tight junction (TJ) barrier. The confocal imaging demonstrated the perpendicular diffusion of rhodamine B and FD4 through microchannels immediately after laser exposure. The lateral diffusion from the microchannels was observed at 2 h post-irradiation. Our results revealed a time-dependent recovery of skin permeation. The time frame for applying the drugs after laser irradiation was dependent upon the permeants and their various physicochemical properties.

* Corresponding author at: Pharmaceutics Laboratory, Graduate Institute of Natural Products, Chang Gung University, 259 Wen-Hwa 1st Road, Kweishan, Taoyuan 333, Taiwan.

E-mail address: fajy@mail.cgu.edu.tw (J.-Y. Fang).

¹ Equal contribution.

<https://doi.org/10.1016/j.ijpharm.2019.04.043>

Received 12 November 2018; Received in revised form 16 March 2019; Accepted 14 April 2019

Available online 15 April 2019

0378-5173/ © 2019 Elsevier B.V. All rights reserved.

1. Introduction

Topical absorption is a route for therapeutic drug delivery into or across the skin. The stratum corneum (SC), the outermost layer of the skin, demonstrates great resistance to drug transport, especially in the case of the hydrophilic molecules and macromolecules. The SC's barrier characteristic can be modulated by chemical- and physical-enhancement strategies to ameliorate drug absorption.

Ablative laser resurfacing is traditionally employed to treat scarring, laxity, and photoaging. Ablative laser treatment at low fluences can be used to peel the superficial epidermis to remove the permeation barrier and enhance drug absorption (Lin et al., 2014). The low-fluence laser gives controllable, targeted, and precise topical drug delivery by adjustment of the laser energy, the ablation depth, and the irradiation zone. However, the resurfacing by conventional laser on the skin usually needs a prolonged recovery time of ≥ 1 week (Sarnoff, 2011).

Fractional laser has gained increasing attention in the last decade because the ablation area can be recovered within days (Haak et al., 2011). Fractional laser creates microscopic vertical channels on the skin surface with unaffected viable tissue surrounding these microchannels. Fractional CO₂ laser is a mature modality used in the treatment of scars, nigricans, melasma, and alopecia (Nilforoushzadeh et al., 2017; Zaki et al., 2018). This type of ablative laser has proved effective in assisting with topical drug absorption (Hsiao et al., 2012; Lee et al., 2013; Erlenndsson et al., 2016). Recently, clinical trials have been conducted to examine the usefulness of fractional CO₂ laser-assisted topical delivery. These include the medication of keloid scars, infantile hemangioma, macular amyloidosis, vitiligo, periocular scarring, basal cell carcinoma, and squamous cell carcinoma by CO₂ laser-facilitated absorption of triamcinolone, timolol, vitamin C, tacrolimus, and 5-fluorouracil, respectively (Waibel et al., 2013; Ma et al., 2014; Glenn et al., 2015; Chen et al., 2018; Lee et al., 2018; Sobhi et al., 2018).

Despite the successful result of fractional CO₂ laser-assisted drug delivery, there is still debate about the feasible application modes for maximizing permeability. To optimize the treatment recommendation for clinical use of laser-assisted absorption, it is important to establish a standard model for specific laser settings. A key factor can be the impact of post-irradiation recovery time on drug permeation. From a safety perspective, rapid recovery may be preferable. On the other hand, a slow recovery period is also beneficial by prolonging the time over which the drugs can be administered. The lifetime of the ablated microchannels is important to governing the drug transport. Until now, there has been no suggested standard for the post-treatment duration required to achieve efficient drug absorption. This may lead to the limitation of laser-assisted skin delivery used clinically. The present study aimed to explore the influence of recovery time after fractional CO₂ laser irradiation on the enhancement of drug penetration. The cutaneous absorption is variable with respect to the physicochemical nature and molecular size of the permeants (Nastiti et al., 2017). In this study, tretinoin, acyclovir, and fluorescein isothiocyanate dextran 4 kDa (FD4) were used as lipophilic small molecule, hydrophilic small molecule, and hydrophilic macromolecule, respectively. In vitro Franz cell was used to compare the absorption of these permeants. Nude mouse skin with different post-irradiation periods after in vivo laser intervention was utilized as the permeation barrier. The in vivo status assured the skin recovery through typical procedures mimicking clinical condition. The skin's permeant distribution was visualized by confocal microscopy. The microchannel dimension was monitored by optical microscopy and scanning electron microscopy (SEM). We also analyzed the transepidermal water loss (TEWL) and tight junction (TJ) proteins to assess the barrier-recovery progression of laser-treated skin.

2. Materials and methods

2.1. Animals

The eight-week-old female nude mice were purchased from the National Laboratory Animal Center (Taipei, Taiwan). All experiments were conducted in strict accordance with the recommendations in the Guidelines for Care and Use of Laboratory Animals of Chang Gung University. The protocol was approved by the Institutional Animal Care and Use Committee of Chang Gung University.

2.2. Laser assembly

The fractional CO₂ laser device (Mosaic eCO₂, San Jose, CA, USA) emitted a 10,600-nm wavelength irradiation with the scanning area of 12×12 mm. There were 400 spots/cm² in this area to create the microscopic thermal zone (MTZ). The diameter of each dot was 300 μ m. The fluence of 4 mJ with the pulse duration of 80 μ s was irradiated on the dorsal region of the nude mouse in vivo. The treated skin was excised at 0 (immediately after irradiation), 1, 2, 4, 8, 12, and 16 h post-treatment.

2.3. TEWL and erythema of the skin

The cutaneous physiology of the nude mouse skin after laser irradiation was detected by TEWL (TM300, Courage and Khazaka, Köln, Germany) and erythema (CD100, Yokogawa, Tokyo, Japan). The levels were measured at 0, 1, 2, 4, 8, 12, and 16 h post-irradiation.

2.4. In vitro Franz cell

Franz cell was employed to estimate the permeant delivery into and across the nude mouse skin. The skin was mounted between the donor and receptor with the SC facing toward the donor compartment. The donor was filled with 0.5 ml of tretinoin (10 mM) in 50% propylene glycol/pH 7.4 buffer, acyclovir (7.7 mM) in pH 7.4 buffer, or FD4 (150 μ M) in pH 7.4 buffer. The receptor medium (5 ml) was 40% ethanol/pH 7.4 buffer for tretinoin to maintain the sink condition. The receptor medium for acyclovir and FD4 permeation was pH 7.4 buffer. The effective area for penetration was 0.785 cm². The stirring rate and receptor temperature were kept at 600 rpm and 37 °C, respectively. A 300- μ l receptor aliquot was withdrawn from the receptor at the determined intervals. The fresh medium was added into the receptor for the maintenance of constant volume. At the end of the experiment (24 h), the skin was removed to detect permeant deposition within the skin. The permeant in the skin was extracted by methanol for tretinoin, and 0.1 N HCl for acyclovir and FD4. MagNA Lyser (Roche, Indianapolis, IN, USA) was used to homogenize the skin. The homogenates were centrifuged at $10,000 \times g$ for 10 min. The permeant amount in the supernatant and receptor medium was measured by HPLC for tretinoin and acyclovir (Stulzer et al., 2008; Hsieh et al., 2017). FD4 samples were quantified by fluorescence spectrophotometry.

2.5. Permeant distribution in the skin

Rhodamine B (0.03%) in 30% propylene glycol/water or FD4 (150 μ M) in pH 7.4 buffer was applied as the donor in the Franz cell. The receptor medium for rhodamine B and FD4 was 30% ethanol/pH 7.4 buffer and pH 7.4 buffer, respectively. The skin removed from Franz cell after a 24-h application was washed with double-distilled water five times (5 ml of each) for removing the permeant residual on skin surface, then directly positioned onto the stage plate of a confocal laser-scanning microscope (TCS SP2, Leica, Wetzlar, Germany). The skin thickness was scanned at 5 μ m increments via the z-axis from the skin surface. The images were taken by summing 15 fragments. The three-

dimensional images of the skin were processed by confocal microscopy software.

2.6. Macroscopic observation of the skin surface

The gross visualization of the skin surface after laser exposure at different periods was observed using a handheld digital magnifier (Mini Scope-V, M&T Optics, Taipei, Taiwan).

2.7. Microscopic observation of the skin surface

The skin surface was also observed by optical microscopy (DMI8, Leica). A magnification of $200\times$ was employed to capture the images.

2.8. Microscopic observation of the skin section

The excised skin was immersed in a 10% buffered formalin using ethanol, embedded in paraffin wax; it was sliced at a thickness of $3\mu\text{m}$ for hematoxylin and eosin (H&E) staining. The longitudinal section of the skin histology was observed by optical microscopy.

2.9. Ultrastructural observation of the skin surface

The skin surface with the MTZ was further examined by SEM (SU8220, Hitachi, Tokyo, Japan). The excised skin was fixed in 2% formalin and 2.5% glutaldehyde in pH 7.4 buffer at 4°C overnight. Postfixation was the 2% osmium tetroxide for 1 h, and then the samples were immersed in 0.5% aqueous uranyl acetate for 30 min. The specimens were dehydrated in graded concentrations of ethanol. The dried samples were affixed with Au-Pd in an ion coater before SEM examination.

2.10. Measurement of TJ-related proteins

The TJ-related proteins including filaggrin, involucrin, and integrin $\beta 1$ in the treated skin area were analyzed using ELISA technique. The 5-mm punch specimens were acquired from the dorsal region of the mouse and incubated in 1 ml PBS with complete protease inhibitors. The fragments of the skin samples were homogenized at 6500 rpm for 30 s and then cooled down for 1 min. The supernatant was obtained by a centrifugation at 13,000 rpm and 4°C for 10 min. The total protein was estimated by Protein Assay Dye (Bio-Rad, Hercules, CA, USA). The concentration of TJ-related proteins was quantified using the commercial kits (Wuhan Huamei Biotech, Hubei, China) based on the manufacturer's instructions.

2.11. Statistical analysis

The statistical difference in the data of the different treatment groups was analyzed using Kruskal-Wallis test. The post hoc test for checking individual differences was Dunn's test. A 0.05 level of probability was taken as statistical significance.

3. Results

3.1. TEWL and erythema of the skin

The barrier-function recovery of laser-treated skin was studied via TEWL determination. TEWL is recognized as a suitable measurement to monitor the degree of barrier damage. The baseline TEWL was about $7\text{ g/m}^2/\text{h}$. We calculated ΔTEWL (TEWL with laser treatment minus TEWL without laser treatment) as a function of post-irradiation time as shown in Fig. 1A. Immediately following laser treatment (0 h), ΔTEWL significantly increased from 0 to $27\text{ g/m}^2/\text{h}$. The ΔTEWL peaked at 0 h, followed by a gradual reduction until 16 h. The elevated TEWL was found in the laser-treated skin from 0 to 12 h after irradiation compared

to the intact skin in which elevated TEWL was not found. In the skin exposed to laser at 16 h after irradiation, TEWL was low and comparable to the control skin (non-laser). This demonstrated the healing of the laser-treated skin-barrier integrity after 16 h. Fig. 1B illustrates the time course of skin erythema (a^*) of the laser-treated skin. Fractional laser induced skin redness immediately after exposure. The Δa^* was most pronounced at 1 h after laser treatment. The erythema had disappeared within 2 h following laser treatment.

3.2. In vitro Franz cell

The absorption properties of the model permeants were investigated on nude mouse skin with an intact barrier and treated with laser to compromise the barrier integrity. Both permeant deposition in the skin and the flux across the skin were measured. The skin deposition identifies cutaneous uptake by topical delivery, whereas the flux predicts skin delivery to the deeper skin strata and/or systemic circulation. Fig. 2 summarizes the skin deposition and the flux of tretinoin, acyclovir, and FD4 with different post-irradiation periods. As shown in Fig. 2A, laser exposure did not alter tretinoin accumulation in the skin reservoir. Tretinoin deposition remained constant for 16-h post-treatment. Tretinoin flux across the skin without laser exposure was minimal (Fig. 2B). Fractional laser immediately increased the tretinoin flux from 1.4 to $6.4\text{ nmol/cm}^2/\text{h}$ at 0 h. The flux decreased as the recovery duration increased. At 8 h post-irradiation, the tretinoin flux equaled the flux of the non-laser. Comparison of acyclovir penetration via intact and laser-exposed skins exhibited a dramatic impact of ablation and its recovery. As shown in Fig. 2C, all laser-treated skin revealed less acyclovir deposition than intact skin. The laser ablation might drive a rapid acyclovir passage through the skin without the acyclovir residing in the cutaneous reservoir. The laser significantly enhanced the acyclovir flux (Fig. 2D). Different from the case of tretinoin, the peak flux of acyclovir was achieved at 2 h post-irradiation. We found an almost 6-fold increased flux at 2 h post-laser treatment compared to the control skin. Acyclovir flux later than 2 h after laser exposure resulted in a gradual decrease. Enhanced laser-assisted acyclovir flux compared to passive flux was sustained over a 16-h recovery time.

We next addressed whether the recovery time influenced the skin delivery of FD4 that is much greater in mass. CO_2 laser application could raise FD4 deposition in the skin as depicted in Fig. 2E. The trend of FD4 deposition at different time frames was similar to that of acyclovir flux. The skin deposition was increased by immediate irradiation (0 h) and then peaked after a 1-h recovery. The barrier function remained deficient for 2 h after laser exposure for facile FD4 deposition. There was a negligible amount detected in the receptor for FD4 penetration across the intact skin (Fig. 2F). FD4 became detectable in the receptor immediately after laser treatment (0 h). Surprisingly, FD4 flux progressively increased following the increase of the laser recovery time. This indicates different penetration patterns between small molecules and macromolecules in the laser-assisted drug absorption.

3.3. Permeant distribution in the skin

Skin distribution of model small molecule dye (rhodamine B) and macromolecule (FD4) was obtained by confocal microscopy in a horizontal scanning fashion. Fig. 3A shows the confocal images of the control skin and the laser-treated skin with rhodamine B absorption. The left panel is a planar image (x-y axis) summarizing 15 separate sections. The right panel is a three-dimensional image (x-y-z axis) of the skin. The blank skin without any treatment revealed a negligible autofluorescence. Rhodamine B fluorescence was homogeneously distributed in the intact skin with a weak signal. Compared to the control, increased rhodamine B absorption in the laser-treated skin was clearly visible. In the skin immediately after being treated with laser (0 h), the dye selectively attached to the micropores from where it was transported into the deeper layers. The diameter of the dye-stained circles

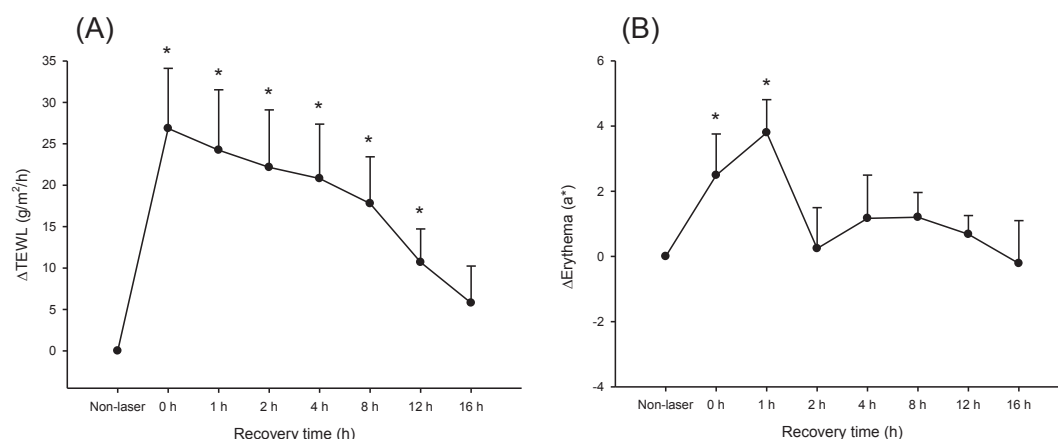


Fig. 1. The skin physiology of fractional CO₂ laser-treated skin as a function of different recovery times: (A) ΔTEWL and (B) Δa*. The data are presented as the mean of 6 experiments ± S.D.

was 200–300 μm, which approximated the diameter of the fractional dot. This indicates that the barrier nature was compromised by the formation of the MTZ to elevate rhodamine B delivery. The rest of the skin remained impermeable to rhodamine B. In the skin after a 2-h recovery from laser exposure, the rhodamine B distribution was not limited to the MTZ but diffused to the surrounding tissue. This suggests a radial leakage of rhodamine B from the MTZ. A further recovery after 8 and 16 h had lessened rhodamine B distribution in the skin. The dye absorption was restricted in the MTZ at 8 and 16 h post-irradiation.

As shown in Fig. 3B, a faint FD4 signal was observed in the intact skin. Immediately after laser exposure (0 h), the area of skin breached by the MTZ took up FD4 whereas the rest of the tissue remained impermeable. FD4 penetrated through the disrupted SC along the microchannels, and reached the lower skin layers. The FD4-stained area was much smaller than that of rhodamine B, indicating a laborious permeation of the macromolecule at the beginning of fractional laser treatment. FD4 radially diffused from the MTZ into the neighboring tissue after application on the skin with a 2-h recovery from laser treatment. The confocal image demonstrated deeper penetration of FD4 at 2 h post-irradiation than that at 0 h. The barrier retrieval at 8 and 16 h from laser exposure was sufficient to recover FD4 absorption to the basal level.

3.4. Macroscopic and microscopic observations of the skin surface

We next evaluated the effect of laser treatment on skin integrity and the kinetics of healing. The time taken to regain the barrier function and for micropore closure was first assessed by a handheld digital magnifier as observed in Fig. 4A. The en face view of the skin immediately treated by the laser (0 h) showed an array of dark-colored micropores on the skin surface (arrows). The laser-ablated holes appeared significantly until 4 h, then progressively closed from the time point of 8–16 h. The micropore appearance on the skin surface almost recovered at 16 h post-irradiation. A mild redness visualized after a 1-h laser treatment was resolved within 2 h. This time course of observed erythema was the same with that detected by a*. As shown in Fig. 4B, the mean diameter of the micropores on the skin surface was about 280 μm. This size mimicked the fractional laser dot size (300 μm). The pore size remained unchanged over a 4-h period, and decreased to 220 and 165 μm at 8 and 12 h, respectively. Sixteen hours after exposure, the micropores on the surface had fully closed without the observation of ablated spots.

The optical microscopy revealed more details about the formation and recovery of the MTZ. The bright field microscopy has the ability to observe the skin structure with some depth because of the light penetration into the skin. Fig. 4C displays the representative skin surface at

various recovery time points after laser treatment. The fractional laser efficiently penetrated the SC and epidermis, creating microdots on the skin. The MTZ was identified as a round and bright area with some black regions around the pores (arrows). The black region surrounding the MTZ could have been the coagulation zone. Different from the result shown in Fig. 4A, the microchannels could be clearly seen by optical microscopy during a 16-h period. This demonstrates that the open microchannels still existed inside the skin at 16 h after laser exposure although the pores on the skin surface were already repaired. As shown in Fig. 4D, the micropore diameter of about 150 μm was measured immediately after irradiation (0 h). This size was significantly smaller than that measured by the handheld digital magnifier. The micropore diameter showed a quick drop after a 1-h recovery, followed by a slow and incomplete regeneration. The average microchannel diameter still could be calculated to be 46 μm at 16 h, suggesting that the skin healing was incomplete at this time although TEWL had reversed to the baseline.

3.5. Histological and ultrastructural observations of the skin

The histological dimension of laser microchannels was observed by H&E staining. Fig. 5A reveals the skin sections at various time points after laser exposure. The untreated skin possessed all layers of the intact skin with no damage. The laser irradiation resulted in the creation of cylindrical ablation of both the SC and epidermis (arrows). The pore diameter was about 100 μm. The depth of the microchannels extended into the upper dermis. We estimated the pore depth to be about 25 μm for the skin immediately treated by the laser (0 h). The ablated holes were surrounded by the thermal coagulation zone. The laser-treated skin sample at 0 h revealed a symptom of inflammation as indicated by the immune-cell infiltration in the dermis. The MTZ was still apparent without any sign of healing after a 1-h recovery. Two hours after irradiation, the reepithelialization occurred as part of the wound-healing process (arrows). The immune-cell infiltration was still marked after 8 h of laser exposure. Twelve and sixteen hours after treatment, the epidermis appeared to have at least partially recovered as shown by the lesion closure by keratinocytes (arrows).

SEM was used to monitor ultrastructural details of the micropores in the superficial skin. As depicted in Fig. 5B, the untreated skin surface was found to be intact without evident damage. SEM imaging displayed spherical-shaped micropores enclosed by elevated edges immediately after irradiation (0 h). The microchannels produced were about 150 μm in diameter. This size was similar to that measured in optical microscopy. The diameter of the pores plus thermal coagulation (elevated edge) was calculated to be approximately 300 μm. The pore size showed minor change during an 8-h period. Nevertheless, it could be

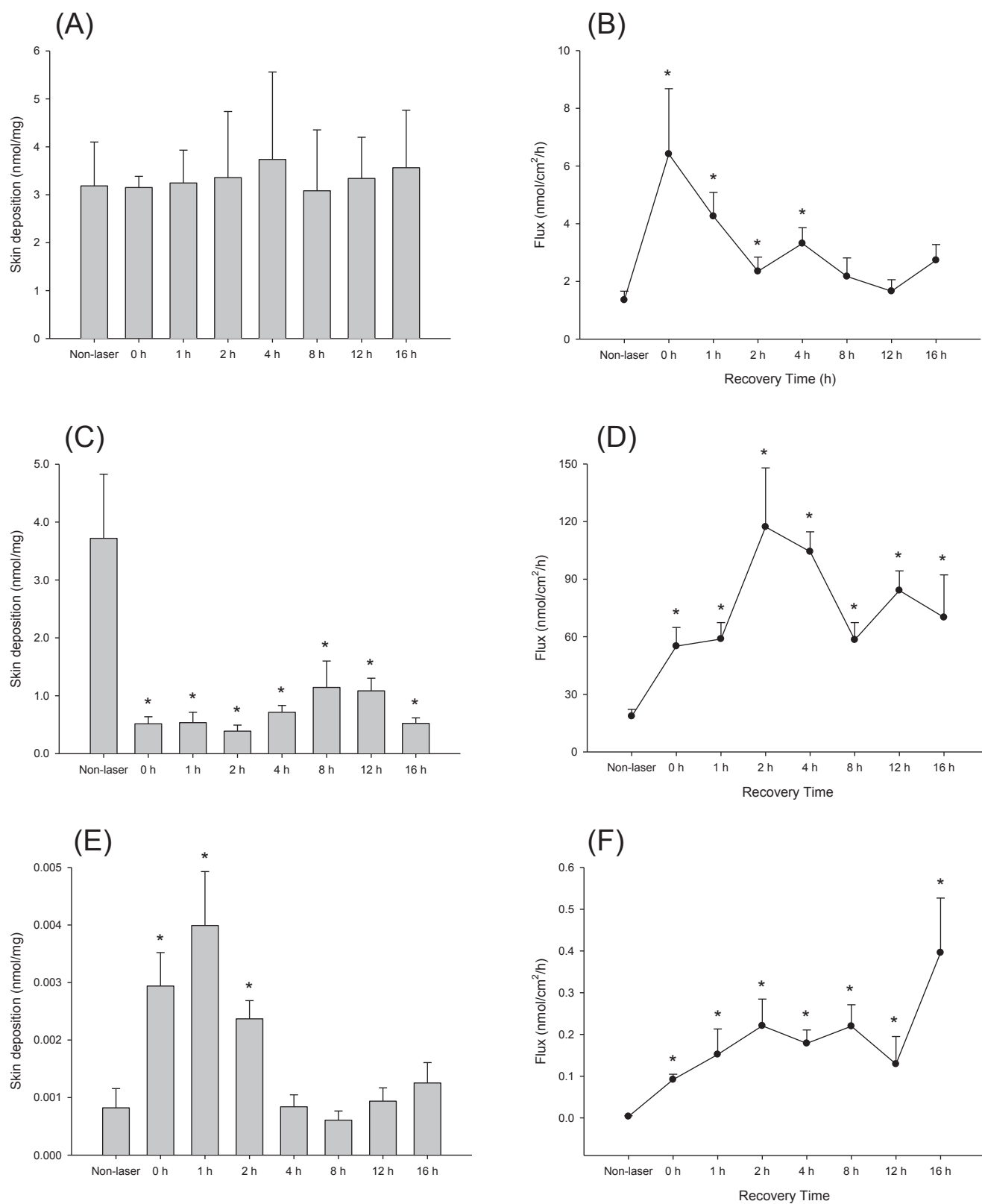


Fig. 2. The skin deposition (nmol/mg) and flux (nmol/cm²/h) of the permeants via fractional CO₂ laser-treated skin as a function of different recovery times: (A) skin deposition of tretinoin; (B) flux of tretinoin; (C) skin deposition of acyclovir; (D) flux of acyclovir; (E) skin deposition of FD4; and (F) flux of FD4. The data are presented as the mean of 4 experiments \pm S.D.

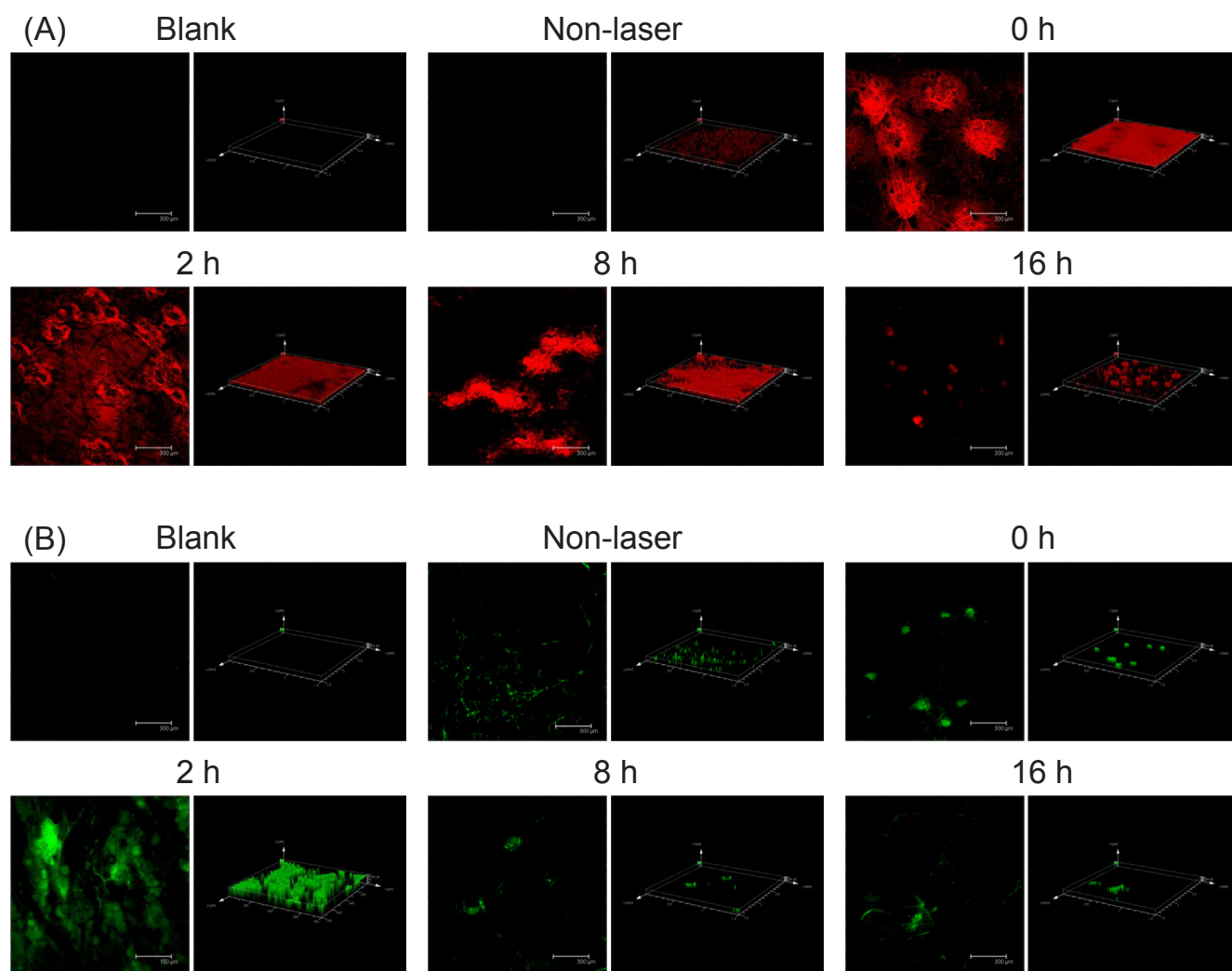


Fig. 3. The biodistribution of rhodamine B and FD4 in the fractional CO₂ laser-treated skin as a function of different recovery times by confocal microscopy: (A) topical application of rhodamine B and (B) topical application of FD4. The left panel is the 2-D (x-y axis) imaging of the skin structure. The right panel is the 3-D (x-y-z axis) imaging of the skin structure.

observed that the migrated or regenerated tissue gradually filled the micropores, leading to the shallower orifices. The openings were nearly closed at 12 and 16 h after irradiation.

3.6. Measurement of TJ-related proteins

Some proteins related to barrier function were analyzed by ELISA as shown in Fig. 6. Filaggrin and involucrin are major structural proteins in the SC and TJ essential to constituting the cellular envelope. The fractional laser ablation decreased the filaggrin amount in the skin immediately after irradiation (Fig. 6A). The filaggrin amount was not recovered to the level of the intact skin after 16 h. The filaggrin level in the laser-treated skin was 2-fold lower than in the control skin. Involucrin was significantly reduced by the laser. Unlike filaggrin, involucrin could be recovered to the normal level after a 16-h irradiation. Integrin $\beta 1$ is an adherens junction protein distributed in the dermal-epidermal junction. Laser treatment significantly reduced the expression of integrin $\beta 1$. This reduction continued to 16 h post-intervention without any sign of recovery. The inhibition level at 16 h was even greater as compared to the inhibition at 0 and 4 h.

4. Discussion

The improvement of drug diffusion into and across the skin can be

obtained by fractional CO₂ laser ablation. The creation of the MTZ in the skin treated by fractional laser can overcome the diffusion barrier for facile permeation. There appears to be a strong clinical potential for laser-facilitated drug delivery. However, the feasible laser settings for clinical application of laser-assisted drug absorption are not yet established. In this study, the laser-assisted penetration of tretinoin, acyclovir, and FD4 was investigated on nude mouse skin with different recovery times from laser exposure. A low fluence (4 mJ) of CO₂ laser was sufficient to show a superior skin permeation compared to the control skin for all permeants tested. We demonstrated for the first time that the recovery duration showed different impacts on different permeants. The immediate application of the drugs after laser exposure was not necessary to produce the greatest permeation enhancement, especially for the hydrophilic small molecule and macromolecule. An adequate recovery time was needed to fulfill the peak absorption.

A previous study (Andrews et al., 2011) demonstrated that hairy rodents' skin heals faster than human skin because of the higher density of hair follicles. The cells from the follicles migrate to the injury site for wound repair during the healing process. Thus, hairy rodents were unsuitable as model animals in this study. Nude mice show degenerated hair follicles as does human skin (Mecklenburg et al., 2001; Lee et al., 2014). We used nude mouse skin in the present work to simulate the healing process of human skin. The SC is a dynamic system with the skin's major barrier property. Nude mouse was irradiated with

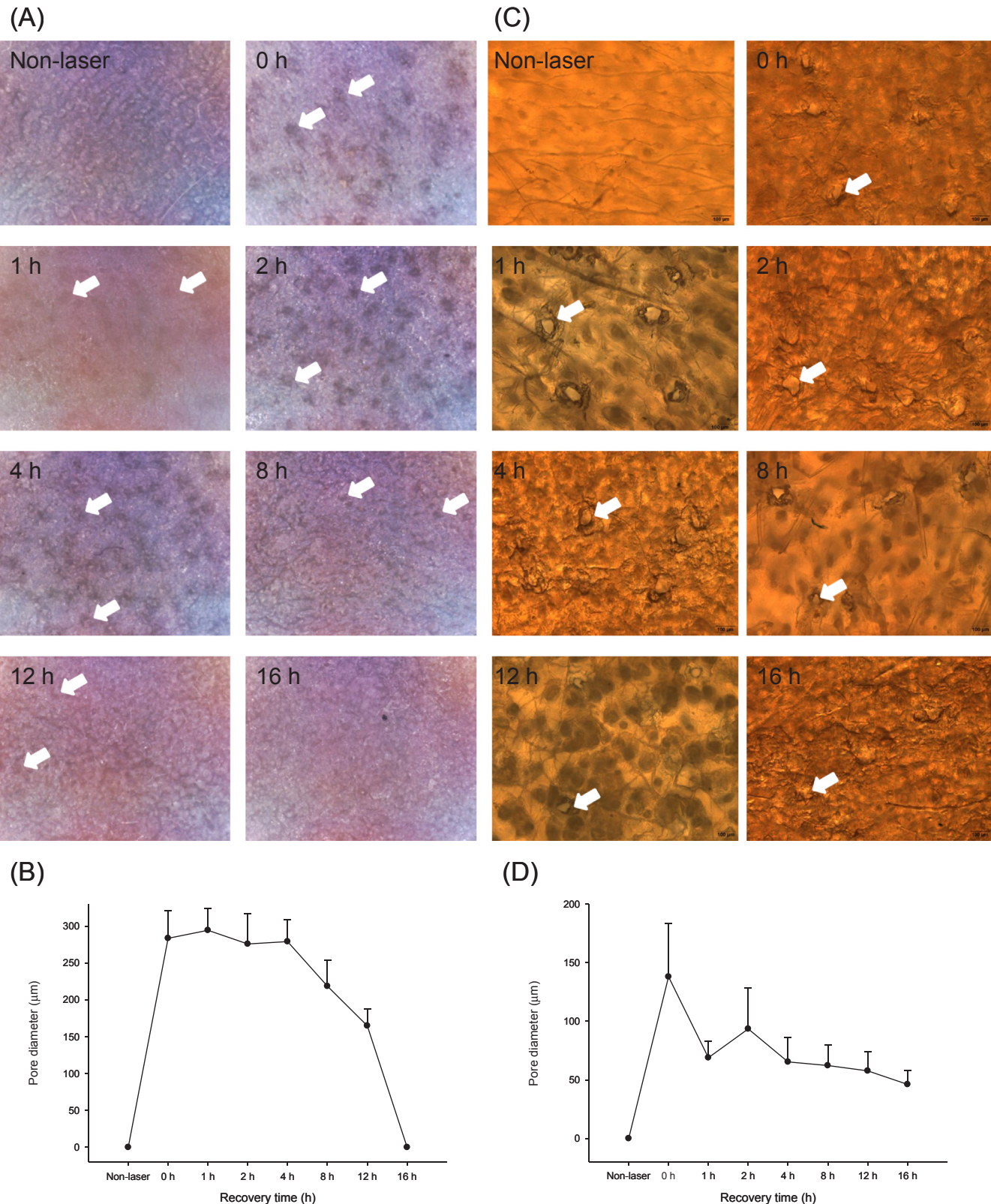


Fig. 4. The macroscopic and microscopic observations of the skin surface treated by fractional CO₂ laser-treated skin as a function of different recovery times: (A) the skin surface imaging captured by handheld digital magnifier; (B) the micropore diameter measured by handheld digital magnifier; (C) the skin surface imaging captured by optical microscopy; and (D) the micropore diameter measured by optical microscopy. The arrows in the images indicate the micropores.

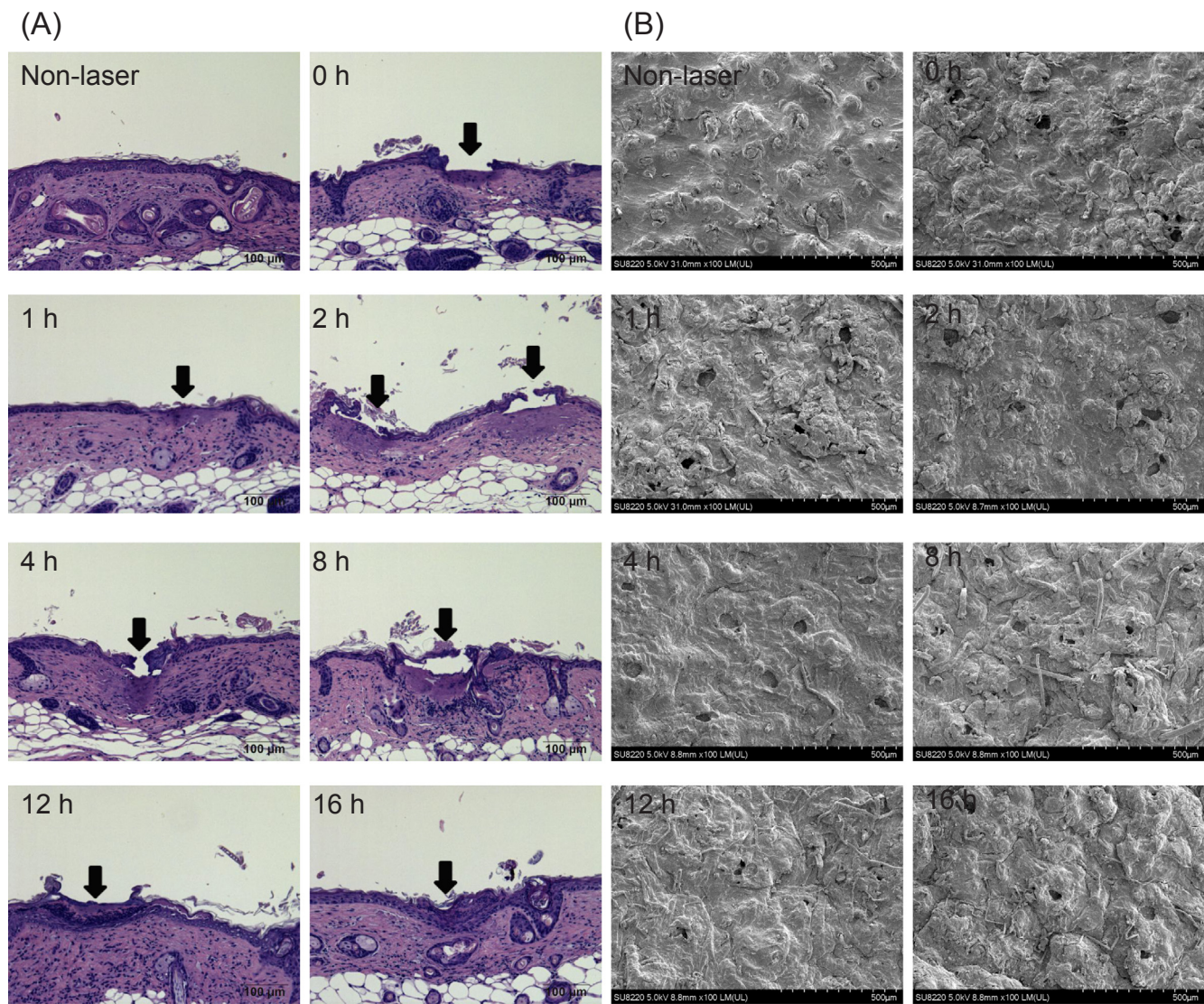


Fig. 5. The histological and ultrastructural observations of the skin treated by fractional CO₂ laser-treated skin as a function of different recovery times: (A) The H&E staining of the skin observed by optical microscopy and (B) ultrastructural imaging of the skin observed by SEM. The arrows in the images indicate the micropores.

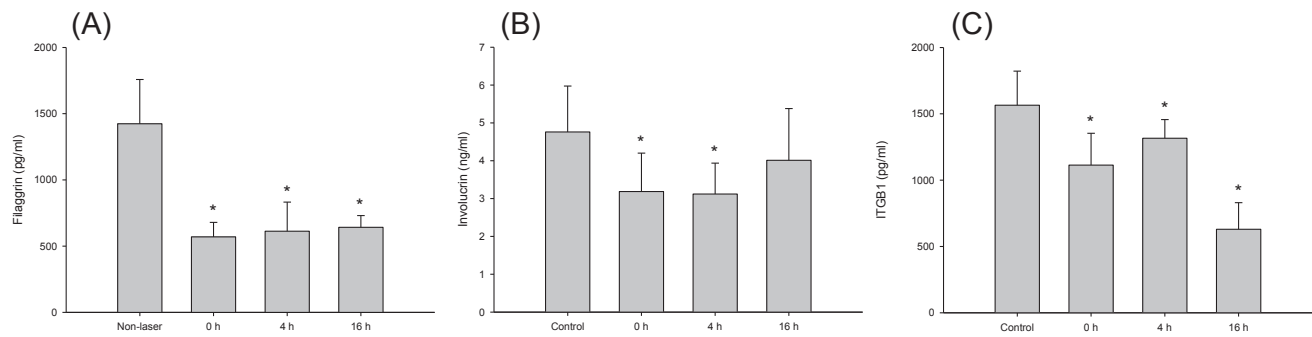


Fig. 6. The TJ-related protein expression in fractional CO₂ laser-treated skin as a function of different recovery times: (A) flaggrin; (B) involucrin; and (C) integrin β 1. The data are presented as the mean of 10–11 experiments \pm S.D.

fractional laser to assess the recovery of the SC barrier function by TEWL. Optimal wound care should enable fast re-epithelialization and reduce recovery time. The fractional modality largely preserves the skin's repairing capacity by the micropores surrounded by normal tissue aiding in recovery (Borges et al., 2016). A previous study (Kim et al., 2017) reported that TEWL could be recovered to the baseline level at

3 days post-irradiation by fractional CO₂ laser on human skin. Our data showed that a period of 16 h was needed for baseline recovery by CO₂ laser in nude mouse skin. This was due to the low fluence of laser energy used in our study to ablate only the superficial skin layer.

We employed a handheld magnifier, optical microscopy, H&E histology, and SEM to visualize the morphology of the skin after fractional

laser treatment and recovery. The laser caused vertical microchannels that were enclosed by a layer of coagulation, constituting the structure of the MTZ. This observation was the same as the clinical signs of fractional CO₂ laser-treated human skin (Paasch and Haedersdal, 2011). The diameter of each dot irradiated by the fractional laser was 300 μm . This diameter approximated the spot size on the skin surface monitored by a handheld magnifier. Conversely, the created microchannels showed a mean diameter of about 150 μm as measured by optical microscopy and SEM. The gross imaging of the laser-treated skin by a handheld magnifier provided the sum of micropores and thermal coagulation. The spot size shown in the magnifier could be an overestimation of the micropores. The coagulation occupied a large area of the irradiated spots. This is reasonable since the CO₂ laser generates a great degree of thermal disruption in the neighboring tissue (Haak et al., 2017). Another possibility explaining the limited space of the microchannels could be the rapid contraction of the laser-created pores soon after their formation because of the skin's elasticity (Gomaa et al., 2010).

Upon ablation of the skin, a set of biochemical events occurs in an orchestrated cascade to repair the wound. The fractional laser mainly affected the SC and viable epidermis. This wound can be classified as superficial. There is a similarity between the healing of human and mouse skin with respect to the overlapping stages of the complex molecular and cellular events (Zomer and Trentin, 2018). These include the phases of contraction, homeostasis, inflammation, proliferation, epithelialization, and remodeling (Sorg et al., 2017). The inflammation triggered by immune-cell infiltration was observed at 8 h post-laser treatment according to H&E imaging. The immune cells such as neutrophils and macrophages accumulated in the wound area not only to eradicate bacteria but also to generate growth factors for guiding re-epithelialization and remodeling (Takeo et al., 2015). Re-epithelialization starts some hours after a wound occurs by stimulating keratinocytes and fibroblasts to proliferate and migrate. We demonstrated a significant re-epithelialization from 2 h post-irradiation. This stage could continue to 16 h. The skin histology revealed a pseudo-ridge pattern, necrotic debris, and ongoing immune cell diffusion 12 h post-intervention. The water evaporation contributes to the skin imbalance, which induces the skin-healing procedure to restore the water. Our results suggested that TEWL could reach the base level 16 h after irradiation. This was an indication of barrier-property recovery. However, the restoration of barrier function did not necessarily signify the whole micropore closure and the retrieval to normal structure according to morphological observation. The drugs may have continuously been transported into the laser-treated skin even after restoration of TEWL. This phenomenon coincided with the microchannels created by microneedles (Kalluri et al., 2011). A previous clinical trial (Donnelly et al., 2014) suggested that a 24-h recovery of skin poration generated by microneedles was acceptable to the volunteers.

The most important barrier described for topical drug delivery originates in the SC. The SC ablation contributed to the enhancement effect of fractional CO₂ laser on the permeation of tretinoin, acyclovir, and FD4. The MTZ space could serve as a permeant reservoir to deliver into the deeper skin strata and ameliorate the availability in the full skin. Tretinoin is a topically applied drug for the therapy of psoriasis, actinic keratosis, and photoaging. The log *P* (partition coefficient) of 6.3 indicates an extremely lipophilic feature of this compound (Pan et al., 2015). It is difficult to achieve tretinoin partitioning into the hydrophilic resistance of the epidermis (Lee et al., 2016). The histology displayed an ablation of not only the SC but also the epidermis by fractional laser. This resulted in the prompt enhancement of tretinoin flux soon after laser treatment. The microchannels enabled vertical diffusion of tretinoin into the deeper skin strata, leading to the high flux extending into the receptor. In addition to vertical diffusion, the lateral transport into the neighboring tissue occurred once tretinoin entered into the MTZ. The profiles of confocal microscopy demonstrated the deep and radial diffusion of small molecule rhodamine B from the

microchannels for an extensive distribution within the skin. The laser-created MTZ greatly increased the surface for tretinoin delivery into the skin. The tretinoin flux was gradually decreased as the recovery time increased. The recovery of barrier function and re-epithelialization to diminish the passage surface could have caused the decreased flux. However, it should be cautious to correlate the rhodamine B distribution profiles with tretinoin permeation since they demonstrate different lipophilicities (log *P* 2.0 versus 6.3) although both compounds are categorized as small molecules. Nevertheless, rhodamine B as a model small molecule dye is ideal to examine the skin delivery pathways across laser-treated skin, which may be quite different from the pathways for macromolecules. It is noticeable that the laser treatment and the following recovery influenced the tretinoin flux but not the skin deposition. This result could be attributed to the saturation of the skin reservoir by tretinoin. Thus, tretinoin should pass across the cutaneous reservoir to accumulate in the receptor. Another possibility is that the SC could be a predominant reservoir for lipophilic tretinoin to reside in. The loss of the SC by laser treatment might restrict the space for tretinoin. The fractional laser creates microchannels generally classified as aqueous transport zone. The aqueous pathways may play no positive impact for tretinoin accumulation within the laser-irradiated skin but just influence the flux.

The kinetics of permeation of acyclovir and FD4 during a 16-h recovery were quite different from that of tretinoin. Acyclovir is an antiviral drug for treating herpes simplex. Both hydrophilic acyclovir and macromolecular FD4 do not readily pass across the lipophilic SC because of the unfavorable physicochemical natures. The CO₂ laser overcame the rate-limiting barrier of the SC to promote the flux of acyclovir and FD4. We found a great reduction of acyclovir deposition in the skin after laser exposure. CO₂ laser is known to generate a thermal effect on the skin, producing the coagulation zone. Our histology and SEM confirmed the coagulation formation after laser treatment. The constituents of coagulation are mainly the platelets and fibrin fibers. The matrix serves as a protective shield against pathogenic microbes (Minutti et al., 2017). This thermal denaturation in the rim of the MTZ is found to obstruct the passage of the drugs, especially the hydrophilic small molecules (Choi et al., 2017; Meesters et al., 2018; Nguyen and Banga, 2018). The lateral partitioning of acyclovir into the coagulation zone might be hampered. The loss of some hydrophilic epidermis due to the laser also limited the residing of acyclovir in the skin reservoir. However, the laser treatment could increase the acyclovir flux soon after irradiation. The acyclovir flux reached a maximum after a 2-h recovery. The laser ablation resulted in the exposure of viable epidermis for direct acyclovir penetration. This hydrophilic small drug might facilitate diffuse into the deeper skin strata for subsequent delivery into the receptor. The laser exposure caused a quick passage of acyclovir across the skin and then largely accumulated in the receptor. This is the reason why the cutaneous acyclovir deposition was significantly reduced after laser treatment.

The recovery of TEWL after laser irradiation indicated the restoration of barrier function. It is anticipated that the barrier restoration could result in the reduction of laser-assisted drug permeation, as was the case for tretinoin flux. However, this is not the case for acyclovir and FD4 since the permeation gradually reached the peak at 1–2 h and then decreased from 2 to 16 h after irradiation. Coagulation contributes to the subsequent inflammation via macrophage and neutrophil stimulation (Minutti et al., 2017). These immune cells release proinflammatory cytokines to affect the lipid metabolism of the epidermis, leading to the barrier dysfunction (Carniol et al., 2015; Chen et al., 2018). Besides their function in the SC, TJ play an important network role, acting as a primary barrier for drug absorption. Filaggrin and involucrin are structural proteins in the cornified envelope of the SC. Filaggrin, fundamental to corneocyte formation and intercellular lipid metabolism, contributes to the barrier function (van Smeden and Bouwstra, 2016). Integrin β 1 is the adherens junction protein confined to the basal layer for adhesion and stratification regulation (Hegde and

Raghavan, 2013). The downregulation of these proteins has been described in connection with the cytokine effect and skin inflammation (Bäsler and Brandner, 2017). TJ barrier deficiency raised by inflammation can facilitate the penetration of hydrophilic drugs and macromolecules (Fang et al., 2016; Rancan et al., 2017). Our data confirmed the decrease of these proteins during a 16-h period of post-irradiation, although TEWL could be recovered to normal status. The inflammation achieved the maximum at about 1 h after laser irradiation according to a^* measurement and the gross appearance of the skin surface. This is inferred to be the cause of the subsequent increase of acyclovir and FD4 permeation after 1 h of irradiation.

Haak et al. (2017) and Song et al. (2018) suggested that the thick coagulation zone induced by fractional CO₂ laser inhibited hydrophilic and large-molecule permeation, whereas a high uptake of the permeants was observed in a thin coagulation. The coagulation could be thick at the beginning of laser exposure and then become thinner because of the wound healing. This is another reason why the permeation of acyclovir and FD4 did not approach the maximum immediately after laser treatment. It can be suggested that the inflammation and coagulation become the factors of importance for laser-assisted delivery of hydrophilic and large permeants. A creation of thin coagulation zone is vital to increase laser-assisted permeation. Zorec et al. (2017) suggests that the modulation of pulse energy and pulse duration was useful to change the thermally damaged tissue. The optimization of the laser settings can change the laser-treated skin structure and the recovery condition, thus the subsequent drug permeation for maximizing the laser-assisted delivery. The micropores remained open up to 16 h after laser exposure. The continuous hydration of the skin by the donor fluid could be the mechanism of the lengthening period of pore existence. The continuous opening of the micropores was beneficial for the entrance of large molecules, leading to the greater FD4 flux across the laser-treated skin at the late stage of recovery. The skin penetration of hydrophilic macromolecules to the SC is lowered due to the dryness of the SC (Hung et al., 2015). The great TEWL elevation for water loss in the SC immediately after irradiation produced an unfavorable environment for FD4 transport. The subsequent SC recovery and the hydration by the donor medium could increase FD4 flux following the increase of recovery time.

The present investigation revealed some limitations. Although we used nude mice as an animal model for simulating the skin-repair process, the difference between murine and human skin still cannot be disregarded. Some instability and variation of laser-created microchannels and their recovery could be expected due to the difficulty in producing uniform vertical ablation in the skin. The skin-absorption profiles in the in vitro settings may be different from the in vivo condition. More studies of in vivo permeation for exploring the effect of recovery on laser-facilitated drug delivery would be needed to elucidate the details. A previous suggestion about the timing of drug application is the immediate medication treatment after laser exposure for maximal delivery (Waibel et al., 2017). Our results indicate a delayed permeation enhancement after laser irradiation, especially the hydrophilic and large molecules. The timing of topical drug application can be several hours post-irradiation. A moderate enhancement of drug absorption could be maintained during the recovery period of laser ablation. Of course the further study is needed to clarify the suitable timing for drug application on laser-treated skin since inflammation and remodeling were not the sole factors influencing drug permeation after irradiation. In addition, the experimental settings such as the types, fluences, and dot densities of fractional laser can largely impact the skin recovery and the subsequent drug delivery.

5. Conclusions

We had evaluated the impact of recovery time on the laser-facilitated absorption of tretinoin, acyclovir, and FD4. The fractional CO₂ laser microporation was a promising approach to enhance the skin

absorption of these permeants. We found that laser-treated skin recovery did not necessarily ensure less drug-permeation enhancement. There were different permeation patterns for different permeants in the recovery time after laser exposure. Laser-assisted tretinoin transport followed the trend of less penetration following the increase of recovery time due to the restoration of the barrier property. The subsequent inflammation after laser treatment might disrupt the TJ barrier to maximize acyclovir and FD4 absorption at 1–2 h post-irradiation. The thinning of the coagulation zone during the healing process also further increased the laser-assisted delivery of acyclovir and FD4. The laser-created micropores remained open during a 16-h post-irradiation period. The continuous hydration of SC led to the further enhancement of FD4 flux at the late stage of recovery. Our results indicated that molecular diffusion via microchannels strongly depended upon the recovery time. This study provided the information for the recommendation of suitable timing for topical drug application after laser treatment.

Declaration of interests

The authors declare that they have no known competing financial interests or personal relationships that could have appeared to influence the work reported in this paper.

Acknowledgement

The authors are grateful for the financial support from Chang Gung Memorial Hospital (CMRPG2B0281, CMRPG2D0093, and CMRPG3A0661).

Appendix A. Supplementary data

Supplementary data to this article can be found online at <https://doi.org/10.1016/j.ijpharm.2019.04.043>.

References

- Andrews, S., Lee, J.W., Prausnitz, M., 2011. Recovery of skin barrier after stratum corneum removal by microdermabrasion. *AAPS PharmSciTech* 12, 1393–1400.
- Bäsler, K., Brandner, J.M., 2017. Tight junctions in skin inflammation. *Pflügers Arch.* 469, 3–14.
- Borges, J., Manela-Azulay, M., Cuzzi, T., 2016. Photoaging and the clinical utility of fractional laser. *Clin. Cosmet. Invest. Dermatol.* 9, 107–114.
- Carniol, P.J., Hamilton, M.M., Carniol, E.T., 2015. Current status of fractional laser resurfacing. *JAMA Facial Plast. Surg.* 17, 360–366.
- Chen, W., Zhou, Y., Huang, F.R., Luo, D., Wang, D.G., 2018. Preliminary study on the treatment of vitiligo with carbon dioxide fractional laser together with tacrolimus. *Lasers Surg. Med.* 50, 829–836.
- Choi, J.H., Shin, E.J., Jeong, K.H., Shin, M.K., 2017. Comparative analysis of the effects of CO₂ fractional laser and sonophoresis on human skin penetration with 5-aminolevulinic acid. *Lasers Med. Sci.* 32, 1895–1900.
- Donnelly, R.F., Mooney, K., McCrudden, M.T.C., Vicente-Pérez, E.M., Belaid, L., González-Vázquez, P., McElroy, J.C., Woolfson, A.D., 2014. Hydrogel-forming microneedles increase in volume during swelling in skin, but skin barrier function recovery is unaffected. *J. Pharm. Sci.* 103, 1478–1486.
- Erlendsson, A., Doukas, A.G., Farinelli, W.A., Bhayana, B., Anderson, R.R., Haedersdal, M., 2016. Fractional laser-assisted drug delivery: active filling of laser channels with pressure and vacuum alteration. *Lasers Med. Sci.* 48, 116–124.
- Fang, Y.P., Yang, S.H., Lee, C.H., Aljuffali, I.A., Kao, H.C., Fang, J.Y., 2016. What is the discrepancy between drug permeation into/across intact and diseased skins? Atopic dermatitis as a model. *Int. J. Pharm.* 497, 277–286.
- Glenn, C.J., Parlette, E.C., Mitchell, C., 2015. Fractional CO₂ laser-assisted delivery of topical 5-fluorouracil as a useful modality for treating field cutaneous squamous cell carcinomas. *Dermatol. Surg.* 41, 1339–1342.
- Gomaa, Y.A., Morrow, D.I.J., Garland, M.J., Donnelly, R.F., El-Khordagui, L.K., Meidan, V.M., 2010. Effects of microneedle length, density, insertion time and multiple applications on human skin barrier function: assessments by transepidermal water loss. *Toxicol. In Vitro* 24, 1971–1978.
- Haak, C.S., Hannibal, J., Paasch, U., Anderson, R.R., Haedersdal, M., 2017. Laser-induced thermal coagulation enhances skin uptake of topically applied compounds. *Lasers Surg. Med.* 49, 582–591.
- Haak, C.S., Illes, M., Paasch, U., Haedersdal, M., 2011. Histological evaluation of vertical laser channels from ablative fractional resurfacing: an ex vivo pig skin model. *Lasers Med. Sci.* 26, 465–471.

- Hegde, S., Raghavan, S., 2013. A skin-depth analysis of integrins: role of the integrin network in health and disease. *Cell Commun. Adhes.* 20, 155–169.
- Hsiao, C.Y., Huang, C.H., Hu, S., Ko, Y.S., Sung, H.C., Chen, C.C., Huang, S.Y., 2012. Fractional carbon dioxide laser treatment to enhance skin permeation of ascorbic acid 2-glucoside with minimal skin disruption. *Dermatol. Surg.* 38, 1284–1293.
- Hsieh, P.W., Hung, C.F., Lin, C.H., Huang, C.W., Fang, J.Y., 2017. Anti-melasma codrug of retinoic acid assists cutaneous absorption with attenuated skin irritation. *Eur. J. Pharm. Biopharm.* 114, 154–163.
- Hung, C.F., Chen, W.Y., Aljuffali, I.A., Lin, Y.K., Shih, H.C., Fang, J.Y., 2015. Skin aging modulates percutaneous drug absorption: the impact of ultraviolet irradiation and ovariectomy. *Age* 37, 21.
- Kalluri, H., Kolli, C.S., Banga, A.K., 2011. Characterization of microchannels created by metal microneedles: formation and closure. *AAPS J.* 13, 473–481.
- Kim, J.M., Kim, W.I., Ko, H.C., Kim, M.B., Kim, B.S., 2017. Epidermal barrier function changes after ablative and non-ablative fractional laser administration. *J. Eur. Acad. Dermatol. Venereol.* 31, e83–e85.
- Lee, B.W., Levitt, A.E., Erickson, B.P., Ko, A.C., Nikpoor, N., Ezuddin, N., Lee, W.W., 2018. Ablative fractional laser resurfacing with laser-assisted delivery of 5-fluorouracil for the treatment of cicatricial ectropion and periorcular scarring. *Ophthalm. Plast. Reconstr. Surg.* 34, 274–279.
- Lee, W.R., Shen, S.C., Aljuffali, I.A., Lin, Y.K., Huang, C.W., Fang, J.Y., 2016. Non-ablative fractional laser assists cutaneous delivery of small- and macro-molecules with minimal bacterial infection risk. *Eur. J. Pharm. Sci.* 92, 1–10.
- Lee, W.R., Shen, S.C., Al-Suwayeh, S.A., Yang, H.H., Li, Y.C., Fang, J.Y., 2013. Skin permeation of small-molecule drugs, macromolecules, and nanoparticles mediated by a fractional carbon dioxide laser: the role of hair follicles. *Pharm. Res.* 30, 792–802.
- Lee, W.R., Shen, S.C., Chen, W.Y., Aljuffali, I.A., Suen, S.Y., Fang, J.Y., 2014. Noninvasive delivery of siRNA and plasmid DNA into skin by fractional ablation: erbium:YAG laser versus CO₂ laser. *Eur. J. Pharm. Biopharm.* 86, 315–323.
- Lin, C.H., Aljuffali, I.A., Fang, J.Y., 2014. Lasers as an approach for promoting drug delivery via skin. *Expert Opin. Drug Deliv.* 11, 599–614.
- Ma, G., Wu, P., Lin, X., Chen, H., Hu, X., Jin, Y., Qiu, Y., 2014. Fractional carbon dioxide laser-assisted drug delivery of topical timolol solution for the treatment of deep infantile hemangioma: a pilot study. *Pediatr. Dermatol.* 31, 286–291.
- Mecklenburg, L., Nakamura, M., Sundberg, J.P., Paus, R., 2001. The nude mouse skin phenotype: the role of *Foxn1* in hair follicle development and cycling. *Exp. Mol. Pathol.* 71, 171–178.
- Meesters, A.A., Nieboer, M.J., Kezic, S., de Rie, M.A., Wolkerstorfer, A., 2018. Parameters in fractional laser assisted delivery of topical anesthetics: role of laser type and laser settings. *Lasers Surg. Med.* 50, 813–818.
- Minutti, C.M., Knipper, J.A., Allen, J.E., Zaiss, D.M.W., 2017. Tissue-specific contribution of macrophages to wound healing. *Semin. Cell Dev. Biol.* 61, 3–11.
- Nastiti, C., Ponto, T., Abd, E., Grice, J.E., Benson, H.A.E., Roberts, M.S., 2017. Topical nano and microemulsions for skin delivery. *Pharmaceutics* 9, E37.
- Nguyen, H.X., Banga, A.K., 2018. Delivery of methotrexate and characterization of skin treated by fabricated PLGA microneedles and fractional ablative laser. *Pharm. Res.* 35, 68.
- Nilforoushadeh, M.A., Faghihi, G., Jaffary, F., Haftbaradaran, E., Hoseini, S.M., Mazaheri, N., 2017. Fractional carbon dioxide laser and its combination with subcision in improving atrophic acne scars. *Adv. Biomed. Res.* 6, 20.
- Paasch, U., Haedersdal, M., 2011. Laser systems for ablative fractional resurfacing. *Expert Rev. Med. Devices* 8, 67–83.
- Pan, T.L., Wang, P.W., Aljuffali, I.A., Huang, C.T., Lee, C.W., Fang, J.Y., 2015. The impact of urban particulate pollution on skin barrier function and the subsequent drug absorption. *J. Dermatol. Sci.* 78, 51–60.
- Rancan, F., Giulbudagian, M., Jurisch, J., Blume-Peytavi, U., Calderón, M., Vogt, A., 2017. Drug delivery across intact and disrupted skin barrier: identification of cell populations interacting with penetrated thermoresponsive nanogels. *Eur. J. Pharm. Biopharm.* 116, 4–11.
- Sarnoff, D.S., 2011. A comparison of wound healing between a skin protectant ointment and a medical device topical emulsion after laser resurfacing of the perioral area. *J. Am. Acad. Dermatol.* 64, S36–S43.
- Sobhi, R.M., Sharaoui, I., El Nabrawy, E.A., El Nemr Esmail, R.S., Hegazy, R.A., Aref, D.H.F., 2018. Comparative study of fractional CO₂ laser and fractional CO₂ laser-assisted drug delivery of topical steroid and topical vitamin C in macular amyloidosis. *Lasers Med. Sci.* 33, 909–916.
- Song, Y., Hemmady, K., Puri, A., Banga, A.K., 2018. Transdermal delivery of human growth hormone via laser-generated micropores. *Drug Deliv. Transl. Res.* 8, 450–460.
- Sorg, H., Tilkorn, D.J., Hager, S., Hauser, J., Mirastschijski, U., 2017. Skin wound healing: an update on the current knowledge and concepts. *Eur. Surg. Res.* 58, 81–94.
- Stulzer, H.K., Tagliari, M.P., Murakami, F.S., Silva, M.A., Laranjeira, M.C., 2008. Development and validation of an RP-HPLC method to quantitate acyclovir in cross-linked chitosan microspheres produced by spray drying. *J. Chromatogr. Sci.* 46, 496–500.
- Takeo, M., Lee, W., Ito, M., 2015. Wound healing and skin regeneration. *Cold Spring Harbor Perspect. Med.* 5, a023267.
- Van Smeden, J., Bouwstra, J.A., 2016. Stratum corneum lipids: their role for the skin barrier function in healthy subjects and atopic dermatitis patients. *Curr. Prob. Dermatol.* 49, 8–26.
- Waibel, J.S., Rudnick, A., Shagalov, D.R., Nicolazzo, M., 2017. Update of ablative fractionated lasers to enhance cutaneous topical drug delivery. *Adv. Ther.* 34, 1840–1849.
- Waibel, J.S., Wulkan, A.J., Shumaker, P.R., 2013. Treatment of hypertrophic scars using laser and laser assisted corticosteroid delivery. *Lasers Surg. Med.* 45, 135–140.
- Zaki, N.S., Hilal, R.F., Essam, R.M., 2018. Comparative study using fractional carbon dioxide laser versus glycolic acid peel in treatment of pseudo-acanthosis nigricans. *Lasers Med. Sci.* 33, 1485–1491.
- Zorec, B., Škrabelj, D., Marincek, M., Miklavčič, D., Pavšelj, N., 2017. The effect of pulse duration, power and energy of fractional Er:YAG laser for transdermal delivery of differently sized FITC dextran. *Int. J. Pharm.* 516, 204–213.



Article

Quercetin Inhibits the Production of IL-1 β -Induced Inflammatory Cytokines and Chemokines in ARPE-19 Cells via the MAPK and NF- κ B Signaling Pathways

Shu-Chen Cheng ^{1,2} , Wen-Chung Huang ^{3,4} , Jong-Hwei S. Pang ^{2,5}, Yi-Hong Wu ^{2,6,7,*} and Ching-Yi Cheng ^{3,8,9,*}

¹ Department of Traditional Chinese Medicine, Chang Gung Memorial Hospital, Taoyuan 33372, Taiwan; kkaren0330@yahoo.com.tw

² Graduate Institute of Clinical Medical Sciences, College of Medicine, Chang Gung University, Taoyuan 33302, Taiwan; jonghwei@mail.cgu.edu.tw

³ Graduate Institute of Health Industry Technology, Research Center for Chinese Herbal Medicine and Research Center for Food and Cosmetic Safety, College of Human Ecology, Chang Gung University of Science and Technology, Taoyuan 33303, Taiwan; wchuang@mail.cgust.edu.tw

⁴ Division of Allergy, Asthma, and Rheumatology, Department of Pediatrics, Chang Gung Memorial Hospital, Taoyuan 33305, Taiwan

⁵ Department of Physical Medicine and Rehabilitation, Chang Gung Memorial Hospital, Taoyuan 33305, Taiwan

⁶ Division of Chinese Internal Medicine, Center for Traditional Chinese Medicine, Chang Gung Memorial Hospital, Taoyuan 33372, Taiwan

⁷ School of Traditional Chinese Medicine, College of Medicine, Chang Gung University, Taoyuan 33302, Taiwan

⁸ Department of Thoracic Medicine, Chang Gung Memorial Hospital, Linkou 33305, Taiwan

⁹ Department of Ophthalmology, Chang Gung Memorial Hospital, Linkou 33305, Taiwan

* Correspondence: mzpjih@gmail.com (Y.-H.W.); jennycheng@mail.cgust.edu.tw (C.-Y.C.); Tel.: +886-3-3196200 (ext. 2611) (Y.-H.W.); +886-3-2118999 (ext. 5114) (C.-Y.C.)

Received: 13 May 2019; Accepted: 13 June 2019; Published: 17 June 2019



Abstract: Quercetin, a bioflavonoid derived from vegetables and fruits, exerts anti-inflammatory effects in various diseases. Our previous study revealed that quercetin could suppress the expression of matrix metalloproteinase-9 (MMP-9) and intercellular adhesion molecule-1 (ICAM-1) to achieve anti-inflammatory effects in tumor necrosis factor- α (TNF- α)-stimulated human retinal pigment epithelial (ARPE-19) cells. The present study explored whether quercetin can inhibit the interleukin-1 β (IL-1 β)-induced production of inflammatory cytokines and chemokines in ARPE-19 cells. Prior to stimulation by IL-1 β , ARPE-19 cells were pretreated with quercetin at various concentrations (2.5–20 μ M). The results showed that quercetin could dose-dependently decrease the mRNA and protein levels of ICAM-1, IL-6, IL-8 and monocyte chemoattractant protein-1 (MCP-1). It also attenuated the adherence of the human monocytic leukemia cell line THP-1 to IL-1 β -stimulated ARPE-19 cells. We also demonstrated that quercetin inhibited signaling pathways related to the inflammatory process, including phosphorylation of mitogen-activated protein kinases (MAPKs), inhibitor of nuclear factor κ -B kinase (IKK) α/β , c-Jun, cAMP response element-binding protein (CREB), activating transcription factor 2 (ATF2) and nuclear factor (NF)- κ B p65, and blocked the translocation of NF- κ B p65 into the nucleus. Furthermore, MAPK inhibitors including an extracellular signal-regulated kinase (ERK) 1/2 inhibitor (U0126), a p38 inhibitor (SB202190) and a c-Jun N-terminal kinase (JNK) inhibitor (SP600125) decreased the expression of soluble ICAM-1 (sICAM-1), but not ICAM-1. U0126 and SB202190 could inhibit the expression of IL-6, IL-8 and MCP-1, but SP600125 could not. An NF- κ B inhibitor (Bay 11-7082) also reduced the expression of ICAM-1, sICAM-1, IL-6, IL-8 and MCP-1. Taken together, these results provide evidence that quercetin protects ARPE-19 cells

from the IL-1 β -stimulated increase in ICAM-1, sICAM-1, IL-6, IL-8 and MCP-1 production by blocking the activation of MAPK and NF- κ B signaling pathways to ameliorate the inflammatory response.

Keywords: quercetin; retinal pigment epithelial cells; anti-inflammatory; cytokines; chemokines

1. Introduction

The retinal pigment epithelium (RPE), a single layer of cells located in the posterior part of the eye between the photoreceptors and vascularized choroid, is an indispensable part of the visual system and is responsible for several essential physiological functions. RPE cells can selectively transport nutrients and metabolic waste between the photoreceptors and choroid, maintain the ionic and fluid balance, absorb stray light, form the blood–retina barrier, phagocytose the photoreceptor outer segments, and secrete extracellular matrix components, hormones and growth factors for the photoreceptors, Bruch's membrane and choriocapillaris [1–3]. When RPE cells are stimulated with inflammatory mediators such as tumor necrosis factor (TNF)- α , interferon- γ and interleukin-1 β (IL-1 β), they will produce cytokines and chemokines and then trigger inflammatory responses. Therefore, RPE cells are crucial elements in the pathogenesis of inflammation-associated progressive eye diseases, of which age-related macular degeneration (AMD) is the most important [4].

It is estimated that 8.7% of the global population suffer from AMD, and this number will probably double in the next 20 years with the increase in life expectancy. Consequently, AMD has become a major public health issue and an increased social and economic burden [5]. AMD is currently considered to be an irreversible permanent disease in the older population that is characterized by distorted central vision, a dark or gray patch (scotoma) in the central vision, and then progressive loss of central vision, which causes difficulties in daily living activities such as reading fine print or recognizing faces and color [6]. AMD has been classified into two distinct subtypes: Dry AMD (geographic atrophy; nonexudative) and wet AMD (neovascular; exudative), and its pathological processes includes lipofuscin accumulation, drusen formation, RPE geographic atrophy, photoreceptor dysfunction and degeneration, plus choroidal neovascularization [6–8]. Because of the elevated levels of inflammatory cytokines and chemokines such as IL-6, IL-8, intercellular adhesion molecule-1 (ICAM-1) and monocyte chemoattractant protein-1 (MCP-1), either locally in the ocular fluids or tissue or systemically in the serum of AMD patients, chronic inflammation is thought to facilitate the progress of AMD [9–13].

Quercetin is a natural bioflavonoid widely distributed in various vegetables and fruits such as onions, cranberries and green tea [14,15]. Quercetin possesses anti-inflammatory, anticarcinogenic, antioxidative, free-radical scavenging, antifibrotic and antiproliferative capacities that can be expressed in different cell types and animal models [15–20]. Based on these properties, quercetin has been documented to have the potential to treat diabetes [21], cancer [22,23], and neurodegenerative [24], liver [25] and cardiovascular diseases [26,27]. In ophthalmology, quercetin has recently been used to treat dry eye, corneal inflammation and corneal neovascularization [28]. Quercetin has also been reported to protect human retinal pigment epithelial (ARPE-19) cells against H₂O₂-induced injury [29], inhibit the expression of vascular cell adhesion molecule-1, ICAM-1, matrix metalloproteinase-2 (MMP-2) and MMP-9 in vascular endothelial growth factor-stimulated 661W cells [30], decrease TNF- α and IL-1 β expression in rats with streptozotocin-induced diabetes [31], and reduce the production of IL-6, IL-8 and MCP-1 in 4-hydroxynonenal-stimulated ARPE-19 cells [15]. These studies provide a theoretical basis for the clinical application of quercetin in the prevention and treatment of retinal inflammatory diseases. However, the mechanisms by which quercetin mediates its anti-inflammatory effects are still debated.

In this study, we first investigated whether quercetin has anti-inflammatory properties in ARPE-19 cells stimulated by IL-1 β and then analyzed the potential underlying pathways of inflammation. Understanding the role and mechanisms of action of quercetin could contribute to the discovery of effective therapeutic targets for retinal inflammatory diseases.

2. Results

2.1. IL-1 β Induces the Expression of ICAM-1, sICAM-1, IL-6, IL-8 and MCP-1 in ARPE-19 Cells

The infiltration of macrophages or lymphocytes into the posterior chamber of the eye and the secretion of proinflammatory mediators such as IL-1 β are important processes in retinal inflammation. IL-1 β is an inducible proinflammatory cytokine that plays an early role in the production of inflammatory chemokines and cytokines. It triggers the inflammatory response and attracts more inflammatory cells to migrate into the retina, resulting in the functional impairment and degeneration of the retina. Therefore, ARPE-19 cells were treated for the specified time with or without various concentrations (0.1, 1, 2 ng/mL) of IL-1 β , to explore whether the production of ICAM-1, sICAM-1, IL-6, IL-8 and MCP increased after this stimulation. The concentrations of the IL-1 β (0.1, 1, 2 ng/mL) used alone had no toxic effects or changes in the cell viability on ARPE-19 cells, as tested for an LDH release test or a 3-(4,5-dimethylthiazol-2-yl)-2,5-diphenyltetrazolium bromide (MTT) assay (data not shown). As shown in Figure 1A–E, the increases in the levels of ICAM-1, sICAM-1, IL-6, IL-8 and MCP-1 detected by Enzyme-Linked Immunosorbent Assay (ELISA) or Western blotting were positively correlated with the concentration of IL-1 β and the stimulation time.

2.2. Quercetin Inhibits the Expression of ICAM-1, sICAM-1, IL-6, IL-8 and MCP-1 in IL-1 β -Stimulated ARPE-19 Cells

Numerous studies have reported the quercetin can inhibit the expression of IL-6, IL-8, ICAM-1 or MCP-1 induced by various stimuli such as LPS, TNF- α , high glucose and calcium ionophore A23187 in human mast cells, mesangial cells, neutrophils, airway epithelial cells and rat intestinal microvascular endothelial cells, respectively [32–36]. In these experiments, the efficacy and modes of action of quercetin appear to be affected by a diversity of cell types and inflammatory stimulants. Therefore, we evaluated whether quercetin has anti-inflammatory properties in IL-1 β -stimulated ARPE-19 cells. We first assessed the cytotoxicity of quercetin in ARPE-19 cells by an MTT assay. As shown in Figure 2A, the viability of ARPE-19 cells was significantly reduced at quercetin concentrations higher than 30 μ M. Accordingly, quercetin concentrations from 2.5 to 20 μ M were chosen for all subsequent experiments (ELISA, Western blotting, and Reverse Transcription-Quantitative Polymerase Chain Reaction (RT-qPCR) tests). Before being stimulated with 1 ng/mL IL-1 β for 24 h, ARPE-19 cells were pretreated with different concentrations of quercetin (2.5, 5, 10 or 20 μ M) for 1 h. As the quercetin concentration increased, the ICAM-1 level gradually decreased and the release of sICAM-1 into the culture medium was inhibited (Figure 2B,C). Twenty micromolar quercetin also significantly inhibited the expression of IL-6, IL-8 and MCP-1 (Figure 2D–F). To investigate whether quercetin affects the mRNA expression of ICAM-1, IL-6, IL-8 and MCP-1 in IL-1 β -stimulated ARPE-19 cells, cells were pretreated with 20 μ M quercetin for 1 h and then incubated with IL-1 β (1 ng/mL) for 4 h. Quercetin clearly reduced the IL-1 β -induced expression of mRNA for ICAM-1, IL-6, IL-8 and MCP-1 (Figure 3A–D).

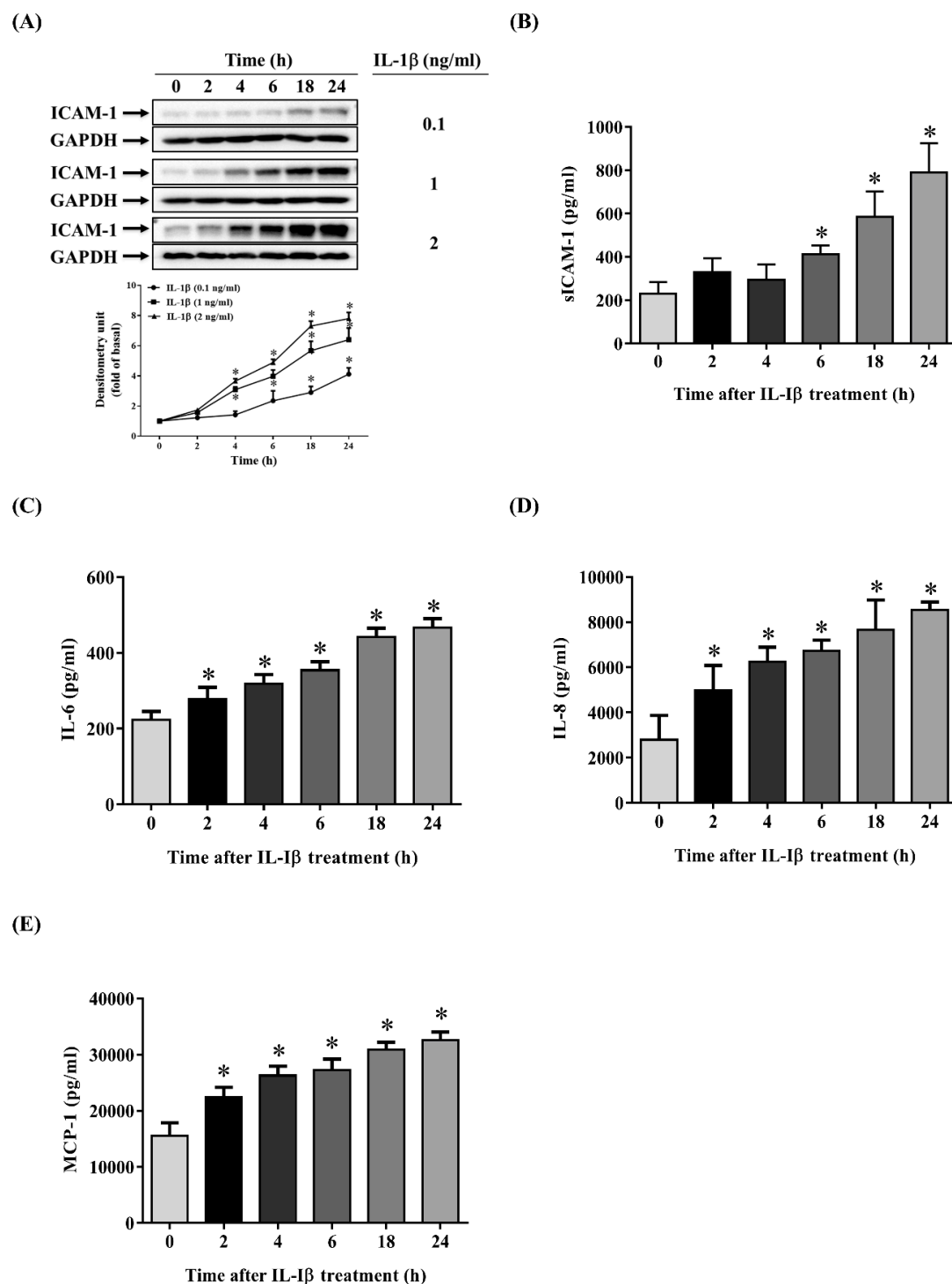


Figure 1. Interleukin-1 β (IL-1 β) induces the expression of intercellular adhesion molecule-1 (ICAM-1), soluble ICAM-1 (sICAM-1), IL-6, IL-8 and monocyte chemoattractant protein-1 (MCP-1) in human retinal pigment epithelial (ARPE-19) cells. (A) IL-1 β at concentrations of 0.1–2 ng/mL was used to stimulate ARPE-19 cells for the indicated times. The protein expression of ICAM-1 was analyzed by Western blotting (top panels) and quantified by Image Lab software (lower panels). (B) The levels of sICAM-1, (C) IL-6, (D) IL-8 and (E) MCP-1 in ARPE-19 cells were measured using Enzyme-Linked Immunosorbent Assay (ELISA) after stimulation with 1 ng/mL IL-1 β for the indicated times. The data are expressed as mean \pm SD of three independent experiments. * $p < 0.05$ compared with the basal level.

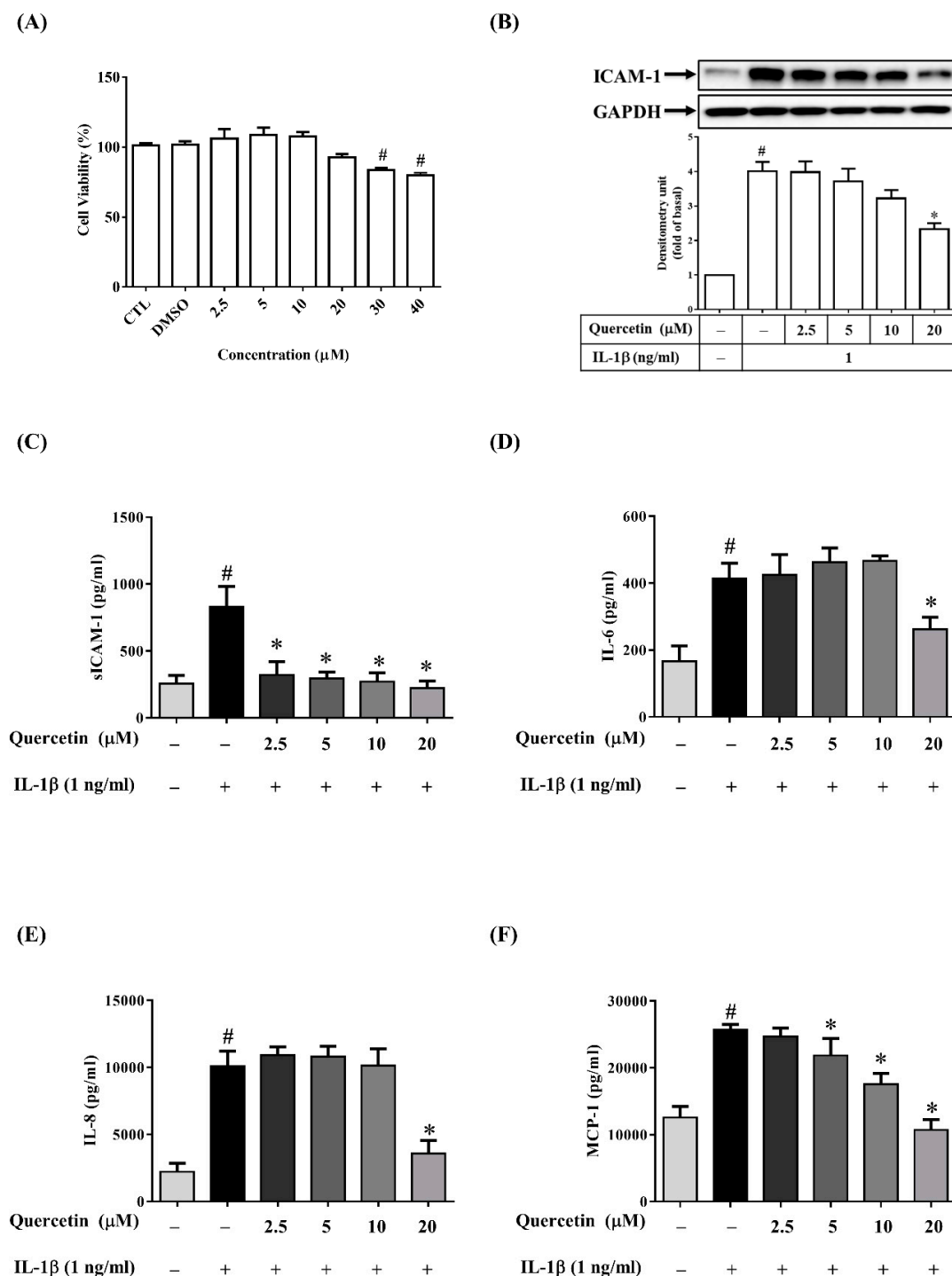


Figure 2. Quercetin attenuates the expression of ICAM-1, sICAM-1, IL-6, IL-8 and MCP-1 in IL-1β-stimulated ARPE-19 cells. (A) Effects of quercetin on ARPE-19 cell viability. ARPE-19 cells were treated for 24 h with 2.5–40 μM quercetin and a 3-(4,5-dimethylthiazol-2-yl)-2,5-diphenyltetrazolium bromide (MTT) assay was used to analyze the cell viability. (B) ICAM-1 protein level was evaluated by Western blotting and then quantified using Image Lab software. (C) The levels of sICAM-1, (D) IL-6, (E) IL-8 and (F) MCP-1 were assessed by ELISA after cells were incubated for 1 h with quercetin at the indicated doses and then activated with 1 ng/mL IL-1β for 24 h. The data are expressed as mean ± SD of three independent experiments. # $p < 0.05$ versus control cells. * $p < 0.05$ versus IL-1β-stimulated cells.

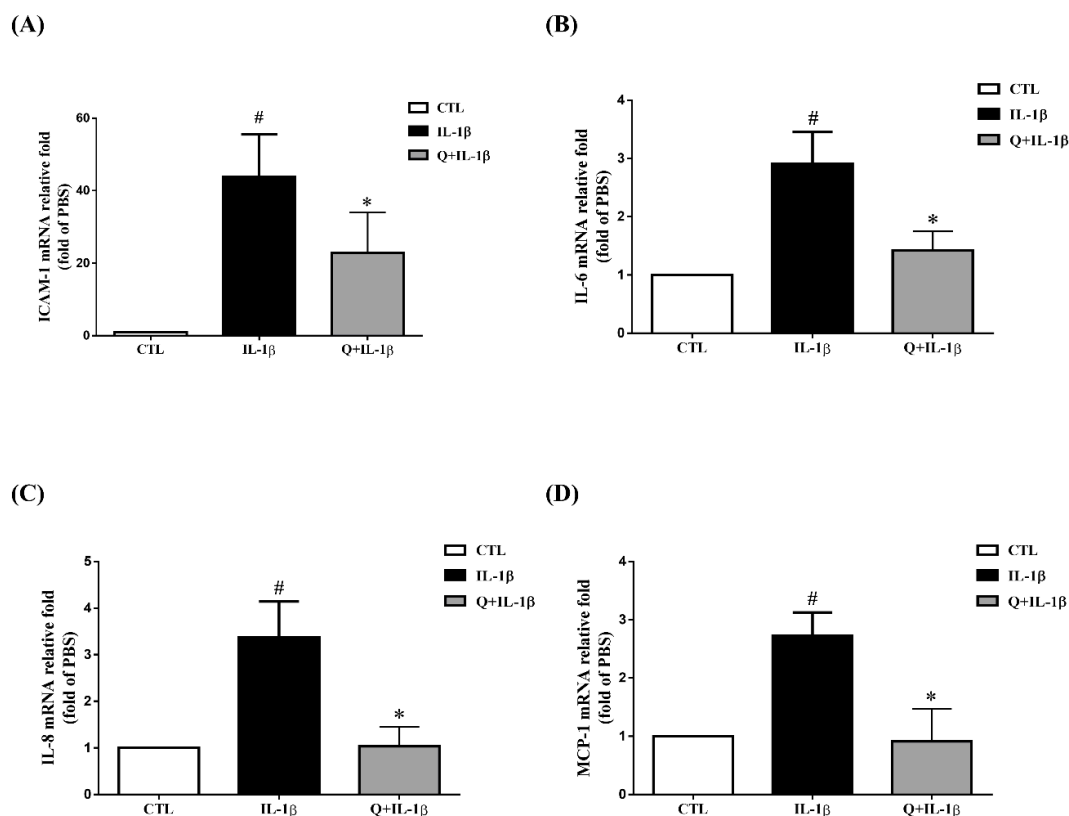


Figure 3. Quercetin attenuates the expression of ICAM-1, IL-6, IL-8 and MCP-1 mRNA in IL-1 β -stimulated ARPE-19 cells. ARPE-19 cells were pretreated with 20 μ M quercetin for 1 h before stimulation with 1 ng/mL IL-1 β for 4 h. Reverse Transcription-Quantitative Polymerase Chain Reaction (RT-qPCR) was used to determine the fold changes in (A) ICAM-1, (B) IL-6, (C) IL-8 and (D) MCP-1 gene expression with β -actin as an internal control. The data are expressed as mean \pm SD of three independent experiments. [#] $p < 0.05$ versus control cells. ^{*} $p < 0.05$ versus IL-1 β -stimulated cells.

2.3. Quercetin Suppresses Inflammatory Signaling Pathways in ARPE-19 Cells

Many studies have demonstrated that quercetin can combat inflammation through regulating mitogen-activated protein kinase (MAPK) pathways in different types of cells under different stimulants [14,32,36–38]. Because we observed that quercetin inhibited the expression of ICAM-1, sICAM-1, IL-6, IL-8 and MCP-1 in IL-1 β -stimulated ARPE-19 cells, we investigated whether quercetin could suppress the phosphorylation of signaling pathway proteins in these cells. The cells were incubated with 20 μ M quercetin for 1 h before stimulation with 1 ng/mL IL-1 β for the indicated times. The results demonstrated that quercetin significantly attenuated the phosphorylation of MAPKs (extracellular signal-regulated kinase (ERK) 1/2, p38, and c-Jun N-terminal kinase (JNK) 1/2), cAMP response element-binding protein (CREB), activating transcription factor 2 (ATF2) and c-Jun in IL-1 β -stimulated ARPE-19 cells, implying that these proteins may promote the production of ICAM-1, sICAM-1, IL-6, IL-8 and MCP-1 (Figure 4A–C and Figure 5A–C).

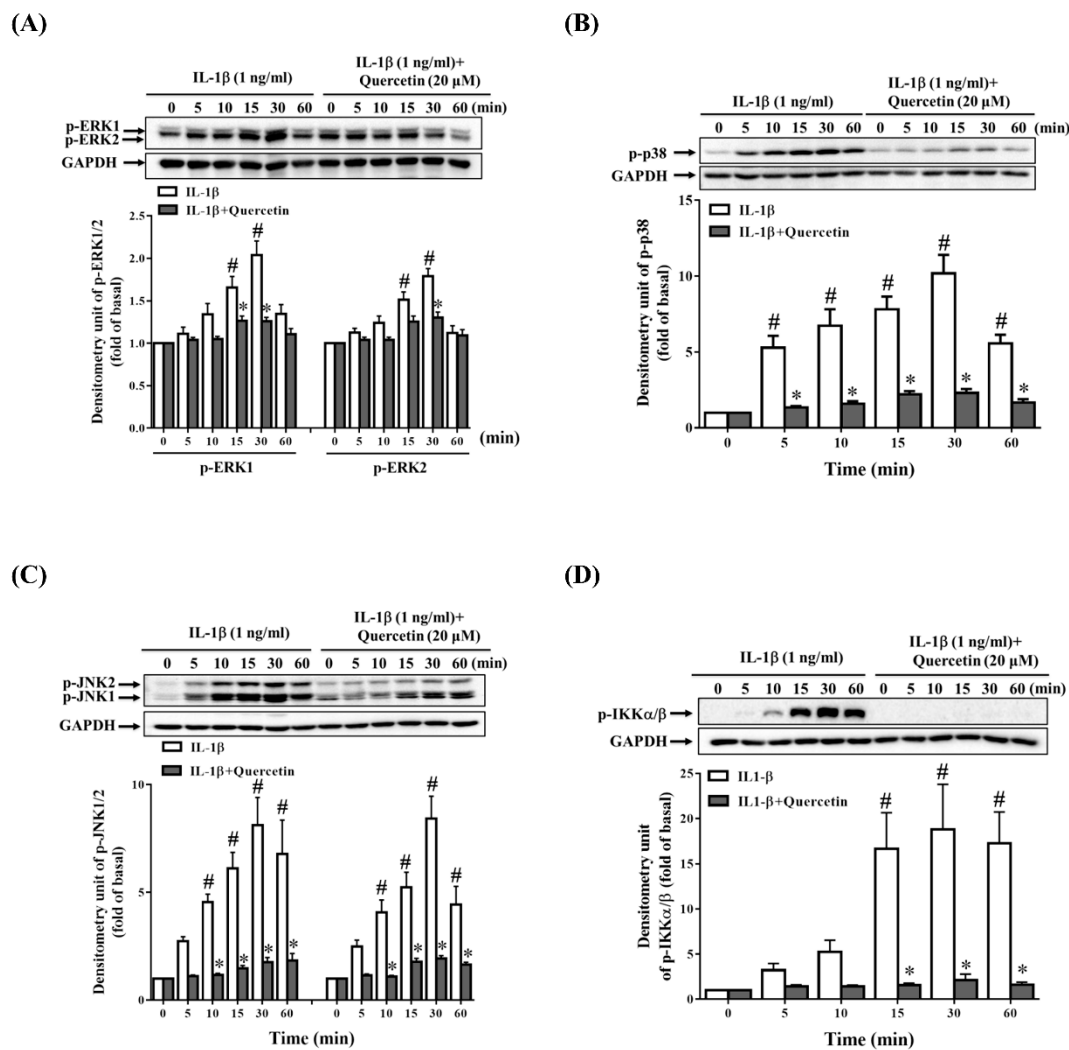


Figure 4. Quercetin inhibits the phosphorylation of mitogen-activated protein kinases (MAPKs) and inhibitor of nuclear factor κ -B kinase (IKK) α/β in IL-1 β -stimulated ARPE-19 cells. ARPE-19 cells were treated with 20 μ M quercetin for 1 h prior to the stimulation with 1 ng/mL IL-1 β for the indicated time. Western blotting and Image Lab software were used to analyze and quantify the phosphorylation of (A) extracellular signal-regulated kinase (ERK) 1/2, (B) p38, (C) c-Jun N-terminal kinase (JNK) 1/2 and (D) IKK α/β . The data are expressed as mean \pm SD of three independent experiments. # $p < 0.05$ versus control cells. * $p < 0.05$ versus IL-1 β -stimulated cells.

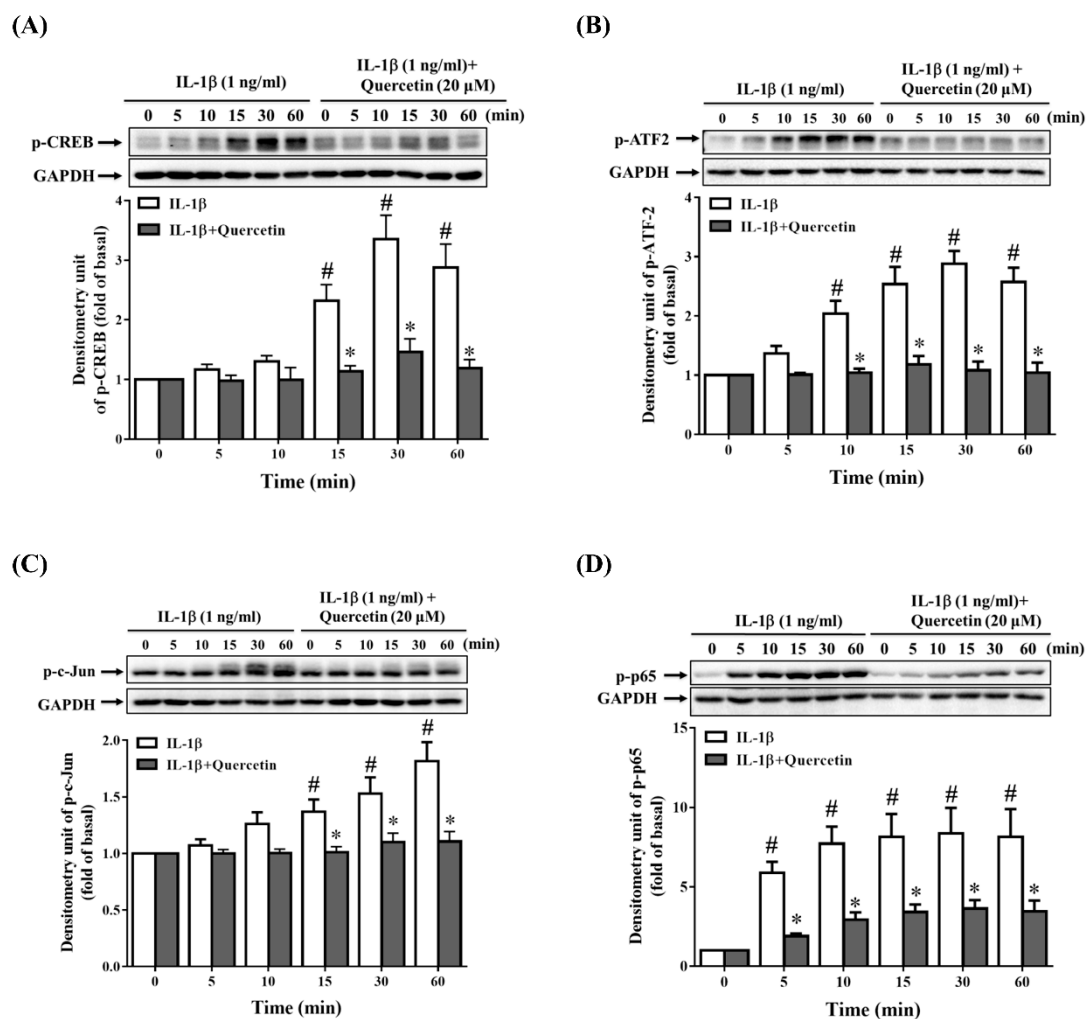


Figure 5. Quercetin attenuates the phosphorylation of cAMP response element-binding protein (CREB), activating transcription factor 2 (ATF2), c-Jun and nuclear factor (NF)-κB p65 in IL-1β-stimulated ARPE-19 cells. ARPE-19 cells were treated with 20 μM quercetin for 1 h prior to stimulation with 1 ng/mL IL-1β for the indicated time. Western blotting and Image Lab software were used to analyze and quantify the phosphorylation of (A) CREB, (B) ATF2, (C) c-Jun and (D) Nuclear factor (NF)-κB p65. The data are expressed as mean ± SD of three independent experiments. # $p < 0.05$ versus control cells. * $p < 0.05$ versus IL-1β-stimulated cells.

2.4. MAPK Inhibitors Decrease the IL-1β-Induced Expression of sICAM-1, IL-6, IL-8 and MCP-1 in ARPE-19 Cells

While previous studies have reported the potential roles of MAPKs in RPE cells treated with different stimulants and inhibitors, the results are inconsistent [39–42]. To explore the importance of three separate MAPKs in retinal inflammatory diseases, ARPE-19 cells were pretreated with MAPK inhibitors (10 μM p38 inhibitor SB202190, 10 μM ERK1/2 inhibitor U0126 or 10 μM JNK inhibitor SP600125) for 1 h prior to incubation with 1 ng/mL IL-1β for 24 h. Interestingly, the MAPK inhibitors reduced the IL-1β-induced expression of sICAM-1 but not that for ICAM-1 and ICAM-1 mRNA levels (Figure 6A,B and Figure 7A). Next, we investigated whether MAPK inhibitors could attenuate the IL-1β-stimulated production of inflammatory cytokines IL-6, IL-8 and MCP-1. As shown in Figure 6C–E, the release of IL-6, IL-8 and MCP-1 was reduced by U0126 and SB202190, but not by SP600125. Similar trends were observed for the expression of mRNA for IL-6, IL-8 and MCP-1 (Figure 7B–D). These results suggested that in IL-1β-stimulated ARPE-19 cells, quercetin reduces

sICAM-1 levels via the p38, ERK1/2 and JNK1/2 pathways and suppresses IL-6, IL-8 and MCP-1 levels via the p38 and ERK1/2 pathways.

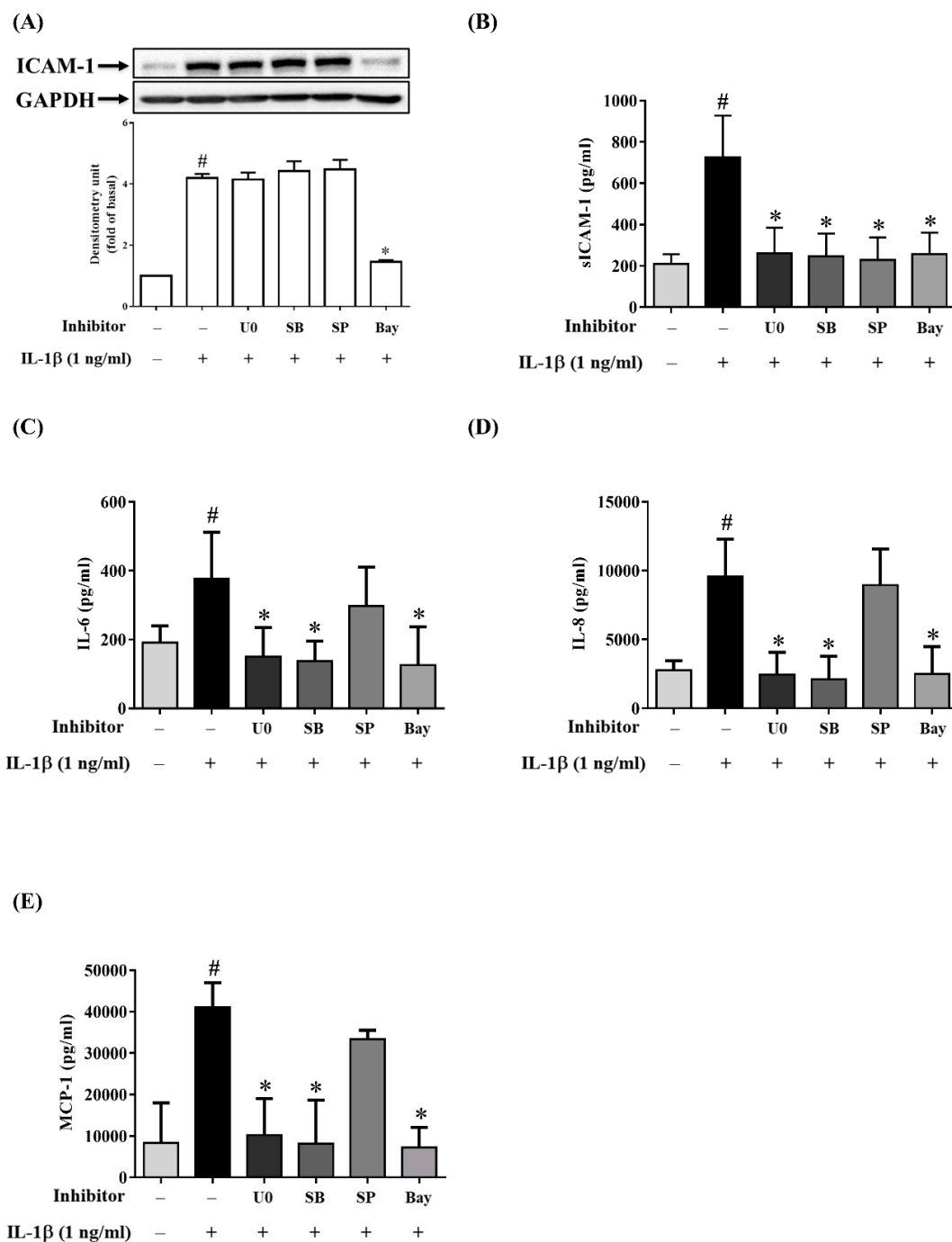


Figure 6. Inhibitory effects of MAPKs and NF-κB inhibitors on the protein expression of ICAM-1, sICAM-1, IL-6, IL-8 and MCP-1 in IL-1β-stimulated ARPE-19 cells. ARPE-19 cells were pretreated with 10 μM U0126 (U0), 10 μM SB202190 (SB), 10 μM SP600125 (SP) or 5 μM Bay11-7082 (Bay) for 1 h prior to stimulation with 1 ng/mL IL-1β for 24 h. (A) ICAM-1 protein expression was measured by Western blotting and quantified using Image Lab software. (B) The levels of sICAM-1, (C) IL-6, (D) IL-8 and (E) MCP-1 were detected by ELISA. The data are expressed as mean ± SD of three independent experiments. [#] $p < 0.05$ versus control cells. ^{*} $p < 0.05$ versus IL-1β-stimulated cells.

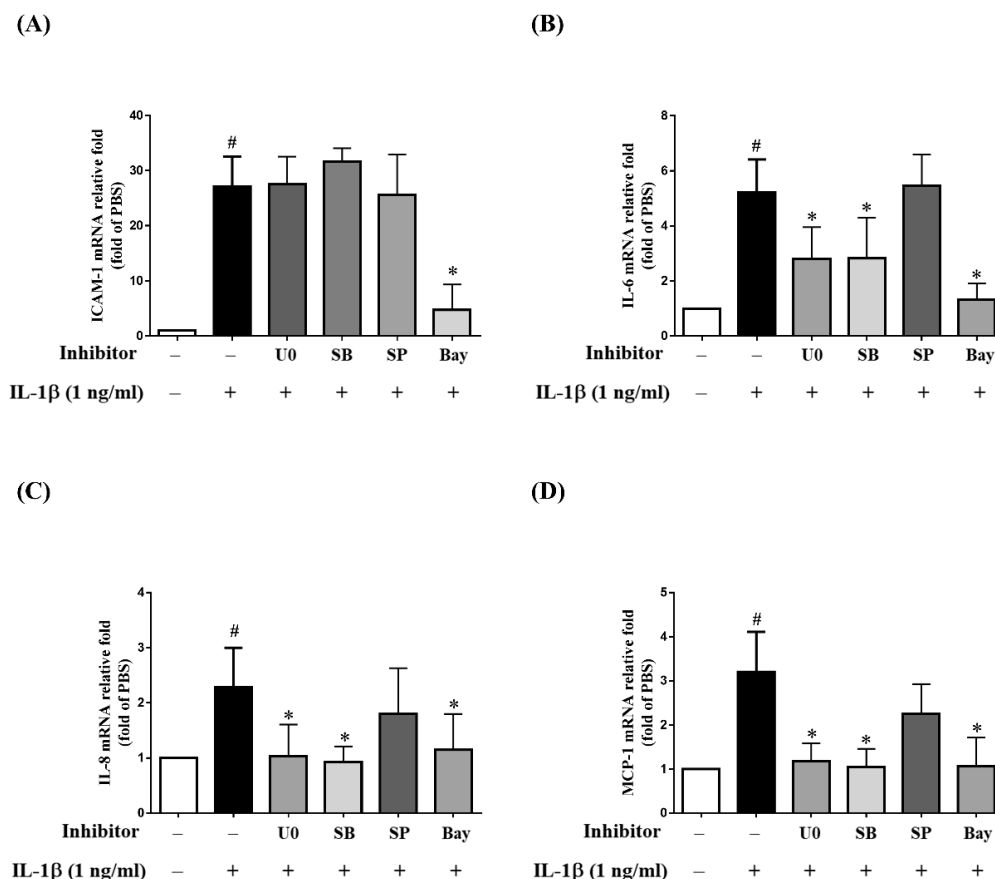


Figure 7. Inhibitory effects of MAPKs and NF- κ B inhibitors on the expression of mRNA for ICAM-1, IL-6, IL-8 and MCP-1 in IL-1 β -stimulated ARPE-19 cells. ARPE-19 cells were treated with 10 μ M U0126 (U0), 10 μ M SB202190 (SB), 10 μ M SP600125 (SP) or 5 μ M Bay11-7082 (Bay) for 1 h, followed by stimulation with 1 ng/mL IL-1 β for 4 h. The fold changes in (A) ICAM-1, (B) IL-6, (C) IL-8 and (D) MCP-1 gene expression were analyzed using RT-qPCR with β -actin as an internal control. The data are expressed as mean \pm SD of three independent experiments. [#] $p < 0.05$ versus control cells. ^{*} $p < 0.05$ versus IL-1 β -stimulated cells.

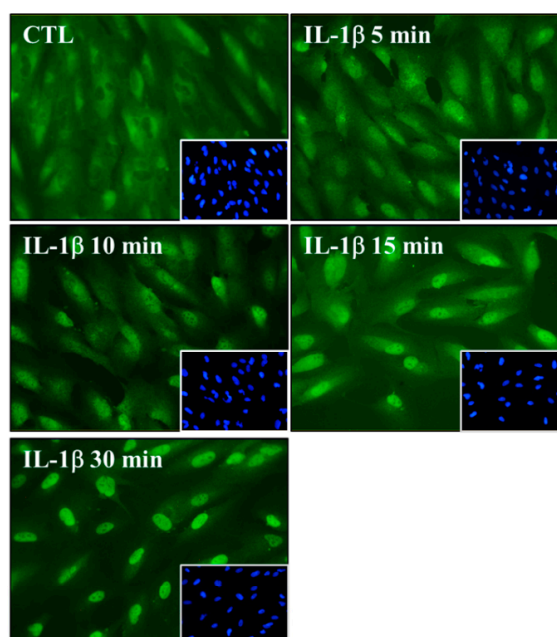
2.5. Quercetin Decreases Nuclear Factor (NF)- κ B Activation in IL-1 β -Stimulated ARPE-19 Cells

Previous studies have confirmed that NF- κ B plays an indispensable role in inflammation [43]. When RPE cells are stimulated by proinflammatory cytokines such as IL-1 β , phosphorylation of the inhibitor of NF- κ B (I κ B) is induced, leading to translocation of NF- κ B into the nucleus, which results in the transcription of cytokine and chemokine genes. Quercetin has been demonstrated to exert its anti-inflammatory effects through downregulating the NF- κ B signaling pathways in vitro [44–46] and in vivo [47,48]. In the present study, ARPE-19 cells were pretreated with 20 μ M quercetin for 1 h prior to the stimulation with IL-1 β (1 ng/mL) for the indicated times to investigate whether quercetin could reduce the phosphorylation of inhibitor of nuclear factor κ -B kinase (IKK) α/β and NF- κ B p65. As shown in Figures 4D and 5D, quercetin clearly suppressed the IL-1 β -induced phosphorylation of IKK α/β and NF- κ B p65 in ARPE-19 cells.

We next explored the role of NF- κ B in the expression of ICAM-1, sICAM-1, IL-6, IL-8 and MCP-1 in IL-1 β -stimulated ARPE-19 cells. As shown in Figure 6A,B, when cells were pretreated with 5 μ M Bay11-7082, the expression of both sICAM-1 and ICAM-1 was decreased. Pretreatment with Bay11-7082 also downregulated ICAM-1 mRNA expression (Figure 7A). Similar outcomes were also obtained for the expression of protein and mRNA for IL-6, IL-8 and MCP-1 (Figure 6C–E and Figure 7B–D). These results suggested that NF- κ B is the principal pathway mediating the reduction of ICAM-1, sICAM-1, IL-6, IL-8 and MCP-1 levels in IL-1 β -stimulated ARPE-19 cells.

Immunofluorescence staining was also used to elucidate whether quercetin attenuated IL-1 β -induced NF- κ B p65 translocation from the cytoplasm into the nucleus. First, we used 1 ng/mL IL-1 β to stimulate ARPE-19 cells for the indicated times. Although the NF- κ B p65 subunit was mainly present in the cytoplasm in the unstimulated ARPE-19 cells, the results indicated that IL-1 β induced NF- κ B p65 translocation within 5 min and achieved the maximal response within 30 min (Figure 8A). Pretreatment of cells with either quercetin or Bay 11-7082 before their stimulation with IL-1 β blocked NF- κ B p65 translocation into the nucleus so that the p65 subunit was retained in the cytoplasm (Figure 8B). These results suggested that quercetin attenuated the expression of ICAM-1, sICAM-1, IL-6, IL-8 and MCP-1 in IL-1 β -stimulated ARPE-19 cells by downregulating NF- κ B p65 translocation.

(A)



(B)

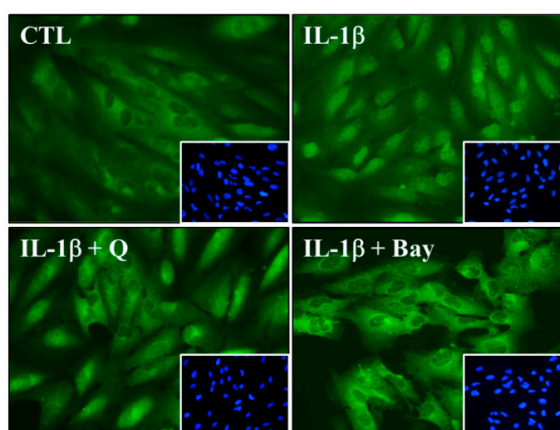
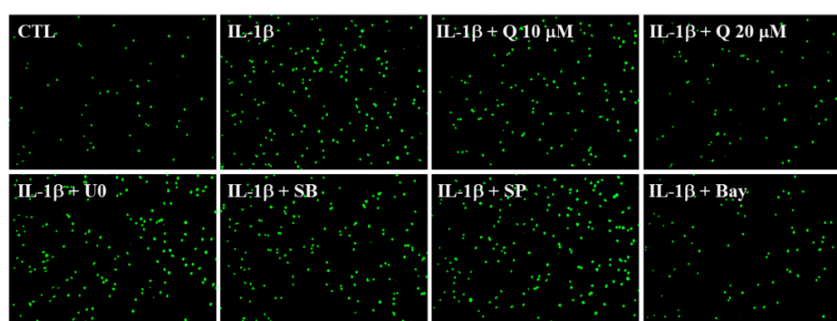


Figure 8. Quercetin attenuates NF- κ B p65 translocation in IL-1 β -stimulated ARPE-19 cells. Immunofluorescence staining was used to evaluate NF- κ B p65 translocation in (A) ARPE-19 cells stimulated with 1 ng/mL IL-1 β for the indicated time, and (B) ARPE-19 cells pretreated with 20 μ M quercetin or 5 μ M Bay 11-7082 for 1 h prior to activation with 1 ng/mL IL-1 β for 10 min. The image is representative of the results of four independent experiments. *Green*: the location of the p65 subunit; *Blue*: DAPI for nuclear staining.

2.6. Quercetin Attenuates THP-1 Cell Adherence to IL-1 β -Stimulated ARPE-19 Cells

It has been reported that decreased ICAM-1 expression results in the suppression of the adhesion of THP-1 cells [41,49]. Because we demonstrated that quercetin strongly inhibited ICAM-1 expression, we wanted to investigate whether quercetin could also attenuate THP-1 cell adhesion to IL-1 β -stimulated ARPE-19 cells. Indeed, pretreatment with 20 μ M quercetin seemed to significantly decrease THP-1 cell adherence to IL-1 β -activated ARPE-19 cells (Figure 9A,B). We next investigated whether the inhibitors of ERK1/2, p38, JNK1/2 and NF- κ B could modulate THP-1 cell adhesion and showed that NF- κ B inhibitor (5 μ M Bay 11-7082) significantly attenuated THP-1 cell adhesion to IL-1 β -stimulated ARPE-19 cells (Figure 9A,B). Combined with the fact that quercetin inhibited the phosphorylation of IKK α / β and NF- κ B p65 and blocked NF- κ B p65 translocation, these findings illustrate that quercetin decreased ICAM-1 expression via the NF- κ B pathway, which contributed to the enhancement of THP-1 cell adhesion to IL-1 β -stimulated ARPE-19 cells.

(A)



(B)

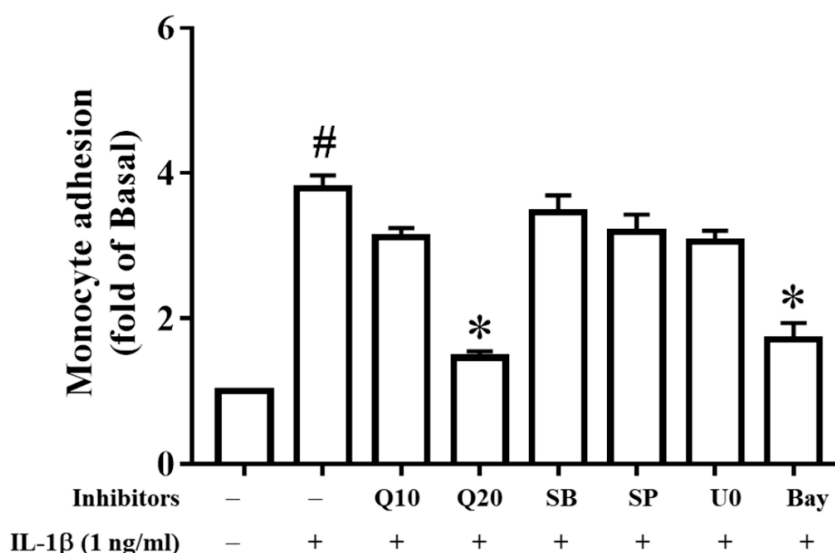


Figure 9. Quercetin significantly suppresses THP-1 cell adherence to IL-1 β -stimulated ARPE-19 cells. ARPE-19 cells were preincubated with quercetin (10, 20 μ M), 10 μ M U0126, 10 μ M SB202190, 10 μ M SP600125 or 5 μ M Bay 11-7082 for 1 h and then stimulated with 1 ng/mL IL-1 β for 24 h. (A,B) A THP-1 monocyte adhesion assay was used to evaluate the physiological function of ICAM-1. The fluorescence intensity represents THP-1 cell adhesion to IL-1 β -stimulated ARPE-19 cells, which was quantified using Image J software. The data are expressed as mean \pm SD of three independent experiments. [#] p < 0.05 versus control cells. ^{*} p < 0.05 versus IL-1 β -stimulated cells.

3. Discussion

Inflammation has been reported to be involved in the pathophysiology of various retinal diseases, including AMD, polypoidal choroidal vasculopathy, diabetic retinopathy and retinal vein occlusion [50–54]. RPE cells have been demonstrated to secrete cytokines in vitro after stimulation with IL-1 β [55]. IL-1 β is a proinflammatory cytokine that can trigger the inflammatory cascade and plays a major role in retinal inflammation [54,56]. Previous studies have also shown that IL-1 β upregulates the expression of IL-6 [55,57,58], IL-8 [55,59], ICAM-1 [60] and MCP-1 [39,61] in human RPE cells. In the present study, stimulation of ARPE-19 cells with IL-1 β induced increased production of ICAM-1, IL-6, IL-8 and MCP-1, which is consistent with these previous results.

ICAM-1, also known as CD54, is a transmembrane glycoprotein that plays a key role in recruitment, adhesion and infiltration of neutrophils and monocytes to the retina [62–64]. The excessive proinflammatory cytokines released by these neutrophils or monocytes initiate inflammation and aggravate damage. Previous studies have indicated that ICAM-1 expression is increased in posterior uveitis, proliferative vitreoretinopathy, proliferative diabetic retinopathy and AMD [12,60,64]. The sICAM-1 detected in culture supernatants and human body fluids such as serum, synovial fluid and urine has been documented to recruit lymphocytes and eosinophils to inflamed tissue [65,66]. Nevertheless, the mechanisms involved in sICAM-1 generation have not been fully elucidated. It is thought that sICAM-1 is either produced by proteolytic cleavage of membrane-bound ICAM-1 or is specifically encoded by distinct mRNA transcripts [67,68]. Previous studies have confirmed that sICAM-1 levels are elevated in patients with proliferative retinal disease [69], Graves' ophthalmopathy [70], idiopathic uveoretinitis [71] and various inflammatory diseases, and that sICAM-1 levels could be used to assess illness severity and prognosis [72–76]. IL-6, a multifunctional cytokine, contributes to activating T lymphocytes, stimulating immunoglobulin secretion, increasing vascular permeability and triggering acute-phase protein release [77–79]. MCP-1 (also called CCL2) belongs to the C–C chemokine family and stimulates and attracts monocytes and lymphocytes, resulting in monocyte/macrophage infiltration [80,81]. IL-8 belongs to the C–X–C chemokine family and is a chemoattractant for eosinophils and neutrophils [11]. Previous studies have demonstrated that IL-6, IL-8 and MCP-1 not only initiate inflammatory responses but also promote angiogenesis, thereby stimulating AMD progression [10,82–85]. Our results showed that the levels of ICAM-1, sICAM-1, IL-6, IL-8 and MCP-1 in IL-1 β -stimulated ARPE-19 cells were positively correlated with the IL-1 β concentration and the duration of stimulation, suggesting that these cytokines and chemokines play a crucial part in the process of RPE inflammation.

Previous ophthalmic studies suggested that quercetin reduced IL-6 and IL-8 mRNA expression in cultured tissue from Graves' orbitopathy [16], attenuated IL-6, IL-8 and ICAM-1 mRNA levels in IL-1 β -stimulated orbital fibroblasts from Graves' orbitopathy [86], and inhibited IL-6 and IL-8 secretion in TNF- α -stimulated human corneal epithelial (HCE) and conjunctival (IOBA-NHC) cell lines [87]. In addition, quercetin was shown to attenuate TNF- α -induced ICAM-1 and MMP-9 expression in ARPE-19 cells [88], and reduce both the RNA and protein levels of IL-6, IL-8 and MCP-1 in 4-hydroxynonenal-stimulated ARPE-19 cells [15]. Thus, there is increasing evidence that quercetin may protect RPE cells from damage in vitro [15,88–90]. The present study provides the first evidence that quercetin inhibits the mRNA and protein expression of IL-6, IL-8, MCP-1, ICAM-1 and sICAM-1 in IL-1 β -stimulated ARPE-19 cells. We also showed that quercetin suppressed THP-1 cell adherence to IL-1 β -stimulated ARPE-19 cells. These findings suggest that quercetin could have anti-inflammatory activity in IL-1 β -stimulated ARPE-19 cells.

Because inflammation may be a key factor in RPE degeneration, dysfunction and loss in retinal degenerative diseases, the intracellular signaling pathways involved in initiating the release of cytokines and chemokines in RPE cells are important. One of the most widely reported signaling pathways in many cell systems is the MAPK signaling pathway, in which inflammatory stimulants contribute to the activation of MAPKs, followed by increased release of cytokines and chemokines [91–93]. Quercetin has been reported to have anti-inflammatory effects via inhibiting the activation of MAPKs in a number of different cell lines treated with different inflammatory stimulants [14,34,36,37]. In this study, we illustrated that IL-1 β activated the phosphorylation of MAPKs (ERK1/2, p38 and JNK1/2), c-Jun and transcription factors (CREB and ATF2) in ARPE-19 cells, and that quercetin significantly suppressed this phosphorylation, which in turn led to a reduction in the expression of ICAM-1, sICAM-1, IL-6, IL-8 and MCP-1.

We also used MAPK-inhibitor treatment of IL-1 β -stimulated ARPE-19 cells to explore the significance of individual MAPKs. We discovered that MAPK inhibitors, including SB202190, SP600125 and U0126, did not reduce the expression of ICAM-1, but did reduce that of sICAM-1. These findings indicated that ICAM-1 and sICAM-1 were regulated by different signaling mechanisms in IL-1 β -stimulated ARPE-19 cells. We also showed that although ERK1/2 and p38 inhibitors suppressed the expression of IL-6, IL-8 and MCP-1, JNK inhibitor did not. Some of these observations are identical to the findings reported by Bian et al. who showed that only ERK1/2 or p38 inhibitors were able to reduce IL-8 and MCP-1 levels in IL-1 β -stimulated ARPE-19 cells [39].

There is increasing evidence that NF- κ B influences the inflammatory process by regulating the gene and protein expression of cytokines and chemokines [78]. The inflammatory signals generated by the stimulation of ARPE-19 cells by IL-1 β induce the production of phosphorylated IKK α / β and lead to the activation of NF- κ B. The activated NF- κ B then moves into the nucleus from the cytoplasm, resulting in inflammatory gene expression. Many studies have reported that quercetin exerts its anti-inflammatory effects mainly through downregulation of NF- κ B [15,30,32,94].

Our previous studies found that quercetin decreased ICAM-1 expression by downregulating NF- κ B in TNF- α -stimulated ARPE-19 cells [88]. In the present study, we demonstrated that quercetin significantly inhibited phosphorylation of IKK α / β and NF- κ B p65 and reduced NF- κ B p65 translocation into the nucleus. IL-1 β -stimulated ARPE-19 cells were treated with NF- κ B inhibitor (Bay 11-7082) to determine whether quercetin downregulated NF- κ B activation and thereby attenuated the mRNA and protein levels of ICAM, sICAM-1, IL-6, IL-8 and MCP-1. We observed that Bay11-7082 decreased the expression of ICAM, sICAM-1, IL-6, IL-8 and MCP-1 and that this inhibition was associated with the downregulation of the NF- κ B signaling pathway. Thus, we confirmed that NF- κ B has an effect on the regulation of cytokine and chemokine production in these cells.

Previous studies have shown that ICAM-1 is involved in the recruitment of monocytes, neutrophils and lymphocytes, and in the adhesive interactions of THP-1 cells [95–97]. In this study, we investigated whether quercetin reduced ICAM-1 levels and hence affected THP-1 cell adhesion to ARPE-19 cells. We found that 20 μ M quercetin reduced the expression of ICAM-1 in ARPE-19 cells and inhibited the adhesion of THP-1 cells to IL-1 β -stimulated ARPE-19 cells. We also observed that the ICAM-1 level was regulated only by the NF- κ B pathway, and not by the MAPK pathway: When inhibitors of MAPKs or NF- κ B were used to treat IL-1 β -stimulated ARPE-19 cells, only the NF- κ B inhibitor reduced THP-1 cell adhesion. Taken together, these observations indicated that quercetin downregulates the NF- κ B pathway to decrease the ICAM-1 level and thereby inhibits THP-1 cell adhesion to ARPE-19 cells.

4. Materials and Methods

4.1. Materials

Anti-phospho-ATF-2, anti-phospho-c-Jun, anti-phospho-CREB, anti-phospho-Erk1/2, anti-phospho-IKK α / β , anti-phospho-JNK1/2, anti-phospho-p38 and anti-phospho-NF- κ B p65 antibodies were obtained from Cell Signaling Technology (Danvers, MA, USA). Anti-ICAM-1,

anti-glyceraldehyde 3-phosphate dehydrogenase (GAPDH) and anti-NF- κ B p65 antibodies were obtained from Santa Cruz Biotechnology (Santa Cruz, CA, USA). Bay 11-7082, SB202190, SP600125 and U0126 were obtained from Enzo Life Sciences (Farmingdale, NY, USA). Human recombinant IL-1 β was obtained from R&D Systems (Minneapolis, MN, USA). Quercetin was obtained from HWI Analytik (Rheinzabern, Germany). Quercetin stock solution was dissolved in dimethyl sulfoxide (DMSO) and then diluted to the desired concentrations with culture medium. All other reagents used in the experiments were obtained from Sigma-Aldrich (St. Louis, MO, USA).

4.2. Cell Culture

The human retinal pigment epithelial cell line, ARPE-19 cells (Bioresource Collection and Research Center, Hsinchu City, Taiwan), was cultured in Dulbecco's modified Eagle's medium (DMEM)/F-12 medium (Gibco BRL, Grand Island, NY, USA) containing sodium bicarbonate, 10% (*v/v*) fetal bovine serum (FBS; HyClone, Logan, UT, USA) and antibiotics (50 ng/mL gentamycin, 100 U/mL penicillin G and 100 μ g/mL streptomycin (HyClone). Cells were subcultured every 3 to 4 days using 0.05% (*v/v*) trypsin-ethylenediaminetetraacetic acid (EDTA; Life Technologies, Carlsbad, CA, USA).

The human monocytic leukemia cell line (THP-1 cells) was obtained from the American Type Culture Collection (Manassas, VA, USA) and grown in RPMI 1640 medium (Gibco) containing antibiotics and 10% FBS in a humidified 5% CO₂ atmosphere at 37 °C. We changed the medium every 4 to 5 days.

4.3. Cell Viability Assay

The MTT (Sigma-Aldrich) assay was used to measure the inhibition of cell viability by quercetin. Cells were seeded into 96-well plates and treated with quercetin at different concentrations (2.5–40 μ M) for 24 h. Next, each well was incubated with 0.5 mg/mL MTT solution for 1 h at 37 °C. The plates were then washed and DMSO added to dissolve the formazan crystals followed by analysis using a SpectraMax i3x microplate reader (Molecular Devices, San Jose, CA, USA) at 570 nm. The MTT assay for each concentration was carried out in triplicate and the cell viability is presented as a percentage relative to the cells without quercetin treatment.

4.4. ELISA

ARPE-19 cells were pretreated with or without quercetin (2.5–20 μ M) for 1 h and then stimulated with IL-1 β (1 ng/mL) for the indicated times. The same experiments were also performed including specific inhibitors of JNK (10 μ M SP600125), p38 (10 μ M SB202190), MEK1/2 (10 μ M U0126) and NF- κ B (5 μ M Bay 11-7082). Cells in the negative control were treated with DMSO at the same concentrations as those present in quercetin or inhibitors. The levels of IL-6, IL-8, soluble ICAM-1 (sICAM-1) and MCP-1 were measured in samples of media using ELISA kits (R&D Systems, Minneapolis, MN, USA). The optical density of samples was measured spectrophotometrically with a microplate reader (Multiskan FC, Thermo) at 450 nm. All ELISAs were performed according to the manufacturers' instructions [98].

4.5. Preparation of Cell Extracts and Western Blot Analysis

First, ARPE-19 cells were incubated with or without IL-1 β at various concentrations (0.1, 1 or 2 ng/mL) for the indicated times. Second, cells were pretreated with quercetin (2.5 μ M–20 μ M) or inhibitors (10 μ M U0126, 10 μ M SP600125, 10 μ M SB202190 or 5 μ M Bay 11-7082) for 1 h before stimulation with 1 ng/mL IL-1 β for either 1 h to measure the phosphorylation of protein or for 24 h to evaluate the ICAM-1 protein level. The concentrations of the choice of inhibitors had no toxic effects or changes in the cell viability on ARPE-19 cells, as tested for an LDH release test or a MTT assay (data not shown). The negative control was prepared as described in the previous section.

Proteins were extracted from ARPE-19 cells after being washed rapidly with ice-cold phosphate-buffered saline (PBS) and subsequently added to lysis buffer (25 mM NaCl (pH 7.4), 25 mM NaF, 25 mM Tris-HCl, 1 mM sodium vanadate, 25 mM sodium pyrophosphate, 2.5 mM ethylenediaminetetraacetic acid (EDTA), 2.5 mM ethylene glycol-bis(β -aminoethyl ether)-N,N,N',N'-tetraacetic acid (EGTA), 0.05% (*v/v*) Triton X-100, 0.5% (*w/v*) sodium dodecyl sulfate (SDS), 0.5% (*w/v*) deoxycholate, 5 μ g/mL aprotinin, 0.5% (*w/v*) NP-40, 5 μ g/mL leupeptin and 1 mM phenylmethylsulfonyl fluoride (PMSF)). The resulting lysates were then centrifuged for 10 min at 15,000 rpm and 4 °C. A Pierce bicinchoninic acid (BCA) protein assay kit (Thermo Fisher Scientific, Rockford, IL, USA) was utilized to evaluate the protein concentration.

The same amount of protein (30 μ g) from each sample was denatured, separated on a 10% gel for SDS polyacrylamide gel electrophoresis and transferred onto Immobilon-P transfer membranes (Millipore, Billerica, MA, USA), which were then blocked with the blocking buffer (Visual Protein, Taipei, Taiwan) for 60 min and incubated with a 1:1000 dilution of primary antibodies (anti-phospho-c-Jun, anti-phospho-ATF-2, anti-phospho-CREB, anti-phospho-ERK1/2, anti-phospho-p38, anti-phospho-JNK1/2, anti-phospho-IKK α/β , anti-phospho-NF- κ B p65, anti-ICAM-1 and anti-GAPDH) at 4 °C overnight. Next, these membranes were washed with Tween-Tris-buffered saline (TTBS; 150 mM NaCl, 50 mM Tris-HCl, 0.05% (*v/v*) Tween 20, pH 7.4) and then incubated with anti-mouse or anti-rabbit horseradish peroxidase-conjugated secondary antibodies at a dilution of 1:10,000 for 1 h at room temperature. Finally, these membranes were washed four times for 15 min each with TTBS and incubated with enhanced chemiluminescence reagents to detect and quantify the specific protein using a ChemiDoc XRS+ system (Bio-Rad Laboratories, Inc., Hercules, CA, USA).

4.6. Total RNA Extraction and RT-qPCR

ARPE-19 cells were pretreated with or without 20 μ M quercetin or inhibitors (5 μ M Bay 11-7082, 10 μ M SB202190, 10 μ M U0126 or 10 μ M SP600125) for 1 h before being stimulated with 1 ng/mL IL-1 β for 4 h. The total RNA of ARPE-19 cells was extracted using TRIzol reagent (Sigma-Aldrich) as per the manufacturer's protocol. The RNA concentration was then measured with a microspectrophotometer (Nano-100; Allsheng Instruments, Hangzhou City, Zhejiang, China). The 260/280 ratios of all samples are between 1.8–2. An iScript cDNA Synthesis Kit (Bio-Rad) was used to reverse transcribe total RNA into cDNA. Gene expression was quantified using an iQTM SYBR Green Supermix kit (Bio-Rad Laboratories, Hercules, CA, USA) and a CFX connect Real-Time PCR Detection System (Bio-Rad).

A melting curve analysis was performed to verify the accuracy of the amplicon after the amplification program. The relative gene expression was estimated using the $\Delta\Delta$ Ct method: β -actin expression served as an internal control and the ratio of the number of copies of the target gene mRNA to the number of copies of β -actin was calculated. All data are expressed as the fold-change relative to the mRNA level in the control cells. Each sample was run in triplicate. Primer Express software (PrimerQuest Tool, IDT, Inc., Coralville, IA, USA) was used to design the primers for qPCR to span exon–exon boundaries. The primers used for the target genes are listed in Table 1.

Table 1. Primers used in RT-qPCR analyses of mRNA expression.

Gene	Primers	(5'-3' Sequence)	GenBank Accession Number	Product Size (bp)
IL-6	Forward Reverse	TCGGTCCAGTTGCCTTCTC GAGGTGAGTGGCTGTCTGT	NM_000600	121
IL-8	Forward Reverse	GCAGAGGGTTGTGGAGAAGT TGGCATCTTCACTGATTCTTGG	NM_000584	90
MCP-1	Forward Reverse	GAATCACCAGCAGCAAGTGT GAGTGTTCAGTCTTCGGAGTT	NM_002982	149
ICAM-1	Forward Reverse	ACCATCTACAGCTTCCCGC CTGAGACCTCTGGCTTCGTC	NM_000201.2	55

4.7. Immunofluorescence Staining

ARPE-19 cells were seeded into six-well culture plates with coverslips until they were 50–60% confluent and then pretreated with or without 1 ng/mL IL-1 β for the indicated times (0, 5, 10, 15, and 30 min). Quercetin (20 μ M) or an NF- κ B inhibitor (5 μ M Bay 11-7082) were added for 1 h before application of 1 ng/mL IL-1 β for 10 min. Next, cells were fixed with 4% (*w/v*) paraformaldehyde for 15 min, permeabilized with 0.3% Triton X-100 for 1 min, blocked with PBS containing 5% (*w/v*) bovine serum albumin for 15 min and stained with an anti-NF κ B p65 antibody overnight at 4 °C. The next day, the coverslips were treated with secondary antibody for 1 h at room temperature and mounted with aqueous mounting medium containing 4',6-diamidino-2-phenylindole (Vector Laboratories, Burlingame, CA, USA). Cells were washed 2–3 times with PBS between each of the above experimental steps. The images were examined using a fluorescence microscope (Leica Microsystems, Wetzlar, Germany).

4.8. Monocyte Adhesion Assay

Before being stimulated with 1 ng/mL IL-1 β for 24 h, ARPE-19 cells were pretreated with or without quercetin (10 or 20 μ M) or inhibitors (5 μ M Bay 11-7082, 10 μ M SB202190, 10 μ M SP600125 or 10 μ M U0126) for 1 h. THP-1 cells were labeled with 5 μ M calcein AM (a fluorescent dye) at 37 °C for 30 min in RPMI-1640 medium in the dark and then washed by centrifugation. Next, the labeled THP-1 cells (5×10^5 cells/mL) were cocultured with ARPE-19 cells in plates for 1 h and washed gently three times with PBS to remove nonadherent THP-1 cells. Finally, the numbers of fluorescently labeled adherent THP-1 cells in five random fields were counted under a fluorescence microscope (Leica Microsystems).

4.9. Statistical Analysis

The intensity of the bands on the Western blotting and the numbers of fluorescently labeled adherent THP-1 cells in the monocyte adhesion assay were quantified using Image Lab software (Bio-Rad) and Image J software (W. Rasband, NIH, USA), respectively. All quantitative data are presented as the mean \pm SD of at least three independent experiments. One-way analysis of variance followed by Tukey's post hoc test using GraphPad Prism version 7 (GraphPad Software Inc., San Diego, CA, USA) was performed to identify the differences among multiple groups. The results were considered significant if $p < 0.05$.

5. Conclusions

The results of this study clearly demonstrated that the proinflammatory cytokine IL-1 β significantly increased the protein and gene expression of ICAM-1, sICAM-1, IL-6, IL-8 and MCP-1 in ARPE-19 cells. We also provided evidence for the first time that quercetin markedly decreased the protein and gene expression of these cytokines and chemokines in IL-1 β -stimulated ARPE-19 cells. Quercetin also inhibited signaling pathways associated with the inflammatory process, including phosphorylation of MAPKs, NF- κ B p65, IKK α/β , c-Jun, CREB and ATF2, and blocked the translocation of NF- κ B p65 into the nucleus (Figure 10). In conclusion, quercetin has the potential to ameliorate inflammatory responses in RPE cells and may serve as a therapeutic intervention for retinal inflammatory diseases such as AMD.

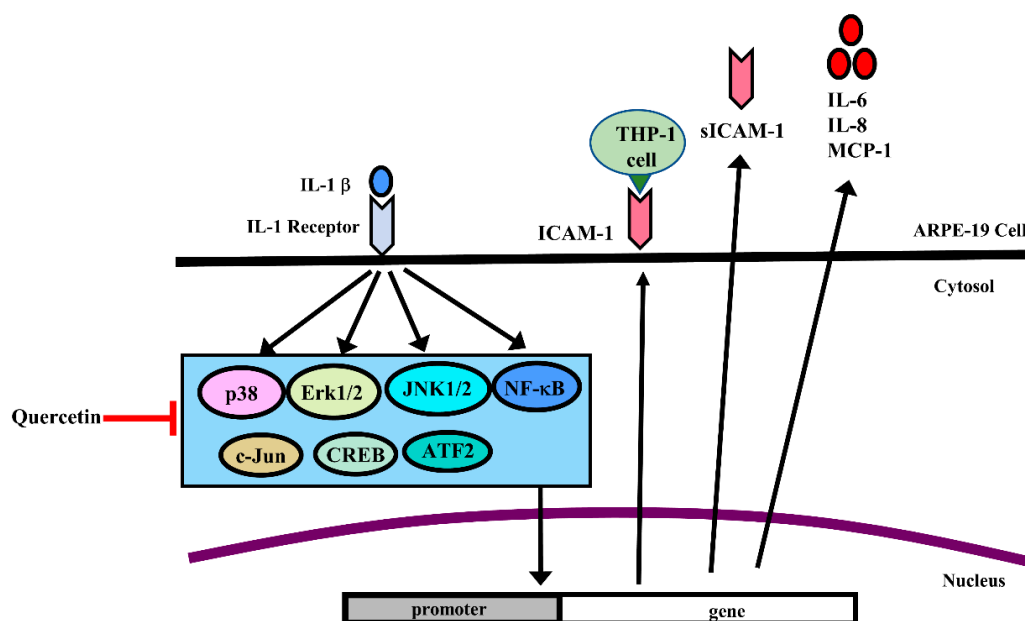


Figure 10. Schematic diagram of the signaling pathways involved in attenuation of IL-1 β -induced inflammation by quercetin via downregulation of ICAM-1, sICAM-1, IL-6, IL-8 and MCP-1 expression in ARPE-19 cells. Quercetin attenuated ICAM-1, sICAM-1, IL-6, IL-8 and MCP-1 expression via the MAPK or NF- κ B pathways in IL-1 β -stimulated ARPE-19 cells.

Author Contributions: Conceived and designed the experiments: C.-Y.C., Y.-H.W., W.-C.H. and J.-H.S.P.; analyzed and interpreted the data: C.-Y.C. and W.-C.H.; performed the experiments and wrote the original draft: S.-C.C.; and reviewed and edited: C.-Y.C.

Funding: This study was supported in part by grants from the Chang Gung Memorial Hospital, Linkou (CMRPF3E0051-52, CMRPF3G0011-13, CMRPG3C0901 and BMRPD16); the Ministry of Science and Technology, Taiwan (NSC 101-2320-B-255-003-MY3); Chang Gung University of Science and Technology (EZRP3E0161, EZRP3E0201).

Acknowledgments: The author acknowledges the technical assistance provided by Chia-Ming Pai and Wan-Jung Lin.

Conflicts of Interest: The authors declare that there are no conflicts of interest.

Abbreviations

AMD	age-related macular degeneration
ATF	activating transcription factor
ARPE-19 cells	human retinal pigment epithelial cells
CREB	cAMP response element-binding protein
DMSO	dimethyl sulfoxide
EDTA	ethylenediaminetetraacetic acid
ELISA	enzyme-linked immunosorbent assay
ERK	extracellular signal-regulated kinase
FBS	fetal bovine serum
GAPDH	glyceraldehyde 3-phosphate dehydrogenase
I κ B	inhibitor of NF- κ B
ICAM-1	intercellular adhesion molecule-1
IKK	inhibitor of nuclear factor κ -B kinase
IL-1 β	interleukin-1 β
IL-6	interleukin-6

IL-8	interleukin-8
JNK	c-Jun N-terminal kinase
MAPK	mitogen-activated protein kinase
MCP-1	monocyte chemoattractant protein-1
MMP	matrix metalloproteinase
MTT	3-(4,5-dimethylthiazol-2-yl)-2,5-diphenyltetrazolium bromide
NF- κ B	nuclear factor κ B
PBS	phosphate-buffered saline
SDS	sodium dodecyl sulfate
TNF- α	tumor necrosis factor- α

References

- Toops, K.A.; Tan, L.X.; Lakkaraju, A. A detailed three-step protocol for live imaging of intracellular traffic in polarized primary porcine RPE monolayers. *Exp. Eye Res.* **2014**, *124*, 74–85. [[CrossRef](#)] [[PubMed](#)]
- De Jong, P.T. Age-related macular degeneration. *N. Engl. J. Med.* **2006**, *355*, 1474–1485. [[CrossRef](#)] [[PubMed](#)]
- Holtkamp, G.M.; Van Rossem, M.; de Vos, A.F.; Willekens, B.; Peek, R.; Kijlstra, A. Polarized secretion of IL-6 and IL-8 by human retinal pigment epithelial cells. *Clin. Exp. Immunol.* **1998**, *112*, 34–43. [[CrossRef](#)] [[PubMed](#)]
- Kutty, R.K.; Nagineni, C.N.; Samuel, W.; Vijayasarathy, C.; Hooks, J.J.; Redmond, T.M. Inflammatory cytokines regulate microRNA-155 expression in human retinal pigment epithelial cells by activating JAK/STAT pathway. *Biochem. Biophys. Res. Commun.* **2010**, *402*, 390–395. [[CrossRef](#)] [[PubMed](#)]
- Wong, W.L.; Su, X.; Li, X.; Cheung, C.M.; Klein, R.; Cheng, C.Y.; Wong, T.Y. Global prevalence of age-related macular degeneration and disease burden projection for 2020 and 2040: A systematic review and meta-analysis. *Lancet Glob. Health* **2014**, *2*, e106–e116. [[CrossRef](#)]
- Mitchell, P.; Liew, G.; Gopinath, B.; Wong, T.Y. Age-related macular degeneration. *Lancet* **2018**, *392*, 1147–1159. [[CrossRef](#)]
- Nowak, J.Z. Age-related macular degeneration (AMD): Pathogenesis and therapy. *Pharmacol. Rep.* **2006**, *58*, 353–363.
- Zhang, K.; Zhang, L.; Weinreb, R.N. Ophthalmic drug discovery: Novel targets and mechanisms for retinal diseases and glaucoma. *Nat. Rev. Drug Discov.* **2012**, *11*, 541–559. [[CrossRef](#)] [[PubMed](#)]
- Knickelbein, J.E.; Chan, C.C.; Sen, H.N.; Ferris, F.L.; Nussenblatt, R.B. Inflammatory Mechanisms of Age-related Macular Degeneration. *Int. Ophthalmol. Clin.* **2015**, *55*, 63–78. [[CrossRef](#)]
- Lechner, J.; Chen, M.; Hogg, R.E.; Toth, L.; Silvestri, G.; Chakravarthy, U.; Xu, H. Peripheral blood mononuclear cells from neovascular age-related macular degeneration patients produce higher levels of chemokines CCL2 (MCP-1) and CXCL8 (IL-8). *J. Neuroinflamm.* **2017**, *14*, 42. [[CrossRef](#)]
- Motohashi, R.; Noma, H.; Yasuda, K.; Kotake, O.; Goto, H.; Shimura, M. Dynamics of Inflammatory Factors in Aqueous Humor during Ranibizumab or Aflibercept Treatment for Age-Related Macular Degeneration. *Ophthalmic Res.* **2017**, *58*, 209–216. [[CrossRef](#)] [[PubMed](#)]
- Mimura, T.; Funatsu, H.; Noma, H.; Shimura, M.; Kamei, Y.; Yoshida, M.; Kondo, A.; Watanabe, E.; Mizota, A. Aqueous Humor Levels of Cytokines in Patients with Age-Related Macular Degeneration. *Ophthalmologica* **2018**, *241*, 81–89. [[CrossRef](#)] [[PubMed](#)]
- Sato, T.; Takeuchi, M.; Karasawa, Y.; Enoki, T.; Ito, M. Intraocular inflammatory cytokines in patients with neovascular age-related macular degeneration before and after initiation of intravitreal injection of anti-VEGF inhibitor. *Sci. Rep.* **2018**, *8*, 1098. [[CrossRef](#)]
- Meng, L.Q.; Yang, F.Y.; Wang, M.S.; Shi, B.K.; Chen, D.X.; Chen, D.; Zhou, Q.; He, Q.B.; Ma, L.X.; Cheng, W.L.; et al. Quercetin protects against chronic prostatitis in rat model through NF-kappaB and MAPK signaling pathways. *Prostate* **2018**, *78*, 790–800. [[CrossRef](#)] [[PubMed](#)]
- Hytti, M.; Piippo, N.; Salminen, A.; Honkakoski, P.; Kaarniranta, K.; Kauppinen, A. Quercetin alleviates 4-hydroxynonenal-induced cytotoxicity and inflammation in ARPE-19 cells. *Exp. Eye Res.* **2015**, *132*, 208–215. [[CrossRef](#)] [[PubMed](#)]
- Yoon, J.S.; Chae, M.K.; Lee, S.Y.; Lee, E.J. Anti-inflammatory effect of quercetin in a whole orbital tissue culture of Graves' orbitopathy. *Br. J. Ophthalmol.* **2012**, *96*, 1117–1121. [[CrossRef](#)] [[PubMed](#)]

17. Russo, M.; Palumbo, R.; Mupo, A.; Tosto, M.; Iacomino, G.; Scognamiglio, A.; Tedesco, I.; Galano, G.; Russo, G.L. Flavonoid quercetin sensitizes a CD95-resistant cell line to apoptosis by activating protein kinase Calpha. *Oncogene* **2003**, *22*, 3330–3342. [[CrossRef](#)]
18. Cao, X.; Liu, M.; Tuo, J.; Shen, D.; Chan, C.C. The effects of quercetin in cultured human RPE cells under oxidative stress and in Ccl2/Cx3cr1 double deficient mice. *Exp. Eye Res.* **2010**, *91*, 15–25. [[CrossRef](#)]
19. Cao, Y.; Hu, J.; Sui, J.; Jiang, L.; Cong, Y.; Ren, G. Quercetin is able to alleviate TGF-beta-induced fibrosis in renal tubular epithelial cells by suppressing miR-21. *Exp. Ther. Med.* **2018**, *16*, 2442–2448.
20. Kumar, A.; Premoli, M.; Aria, F.; Bonini, S.A.; Maccarinelli, G.; Gianoncelli, A.; Memo, M.; Mastinu, A. Cannabimimetic plants: Are they new cannabinoidergic modulators? *Planta* **2019**, *249*, 1681–1694. [[CrossRef](#)]
21. Eid, H.M.; Haddad, P.S. The Antidiabetic Potential of Quercetin: Underlying Mechanisms. *Curr. Med. Chem.* **2017**, *24*, 355–364. [[PubMed](#)]
22. Nam, J.S.; Sharma, A.R.; Nguyen, L.T.; Chakraborty, C.; Sharma, G.; Lee, S.S. Application of Bioactive Quercetin in Oncotherapy: From Nutrition to Nanomedicine. *Molecules* **2016**, *21*, 108. [[CrossRef](#)] [[PubMed](#)]
23. Jana, N.; Bretislav, G.; Pavel, S.; Pavla, U. Potential of the Flavonoid Quercetin to Prevent and Treat Cancer—Current Status of Research. *Klin. Onkol.* **2018**, *31*, 184–190. [[PubMed](#)]
24. Suganthi, N.; Devi, K.P.; Nabavi, S.F.; Braidy, N.; Nabavi, S.M. Bioactive effects of quercetin in the central nervous system: Focusing on the mechanisms of actions. *Biomed. Pharmacother.* **2016**, *84*, 892–908. [[CrossRef](#)] [[PubMed](#)]
25. Miltonprabu, S.; Tomczyk, M.; Skalicka-Wozniak, K.; Rastrelli, L.; Daglia, M.; Nabavi, S.F.; Alavian, S.M.; Nabavi, S.M. Hepatoprotective effect of quercetin: From chemistry to medicine. *Food Chem. Toxicol.* **2017**, *108*, 365–374. [[CrossRef](#)] [[PubMed](#)]
26. Basu, A.; Das, A.S.; Majumder, M.; Mukhopadhyay, R. Antiatherogenic Roles of Dietary Flavonoids Chrysin, Quercetin, and Luteolin. *J. Cardiovasc. Pharmacol.* **2016**, *68*, 89–96. [[CrossRef](#)] [[PubMed](#)]
27. Gormaz, J.G.; Quintremil, S.; Rodrigo, R. Cardiovascular Disease: A Target for the Pharmacological Effects of Quercetin. *Curr. Top. Med. Chem.* **2015**, *15*, 1735–1742. [[CrossRef](#)] [[PubMed](#)]
28. McKay, T.B.; Karamichos, D. Quercetin and the ocular surface: What we know and where we are going. *Exp. Biol. Med. (Maywood)* **2017**, *242*, 565–572. [[CrossRef](#)] [[PubMed](#)]
29. Weng, S.; Mao, L.; Gong, Y.; Sun, T.; Gu, Q. Role of quercetin in protecting ARPE19 cells against H₂O₂ induced injury via nuclear factor erythroid 2 like 2 pathway activation and endoplasmic reticulum stress inhibition. *Mol. Med. Rep.* **2017**, *16*, 3461–3468. [[CrossRef](#)]
30. Lee, M.; Yun, S.; Lee, H.; Yang, J. Quercetin Mitigates Inflammatory Responses Induced by Vascular Endothelial Growth Factor in Mouse Retinal Photoreceptor Cells through Suppression of Nuclear Factor Kappa B. *Int. J. Mol. Sci.* **2017**, *18*, 2497. [[CrossRef](#)]
31. Kumar, B.; Gupta, S.K.; Nag, T.C.; Srivastava, S.; Saxena, R.; Jha, K.A.; Srinivasan, B.P. Retinal neuroprotective effects of quercetin in streptozotocin-induced diabetic rats. *Exp. Eye Res.* **2014**, *125*, 193–202. [[CrossRef](#)] [[PubMed](#)]
32. Min, Y.D.; Choi, C.H.; Bark, H.; Son, H.Y.; Park, H.H.; Lee, S.; Park, J.W.; Park, E.K.; Shin, H.I.; Kim, S.H. Quercetin inhibits expression of inflammatory cytokines through attenuation of NF-kappaB and p38 MAPK in HMC-1 human mast cell line. *Inflamm. Res.* **2007**, *56*, 210–215. [[CrossRef](#)] [[PubMed](#)]
33. Liu, J.; Li, X.; Yue, Y.; Li, J.; He, T.; He, Y. The inhibitory effect of quercetin on IL-6 production by LPS-stimulated neutrophils. *Cell. Mol. Immunol.* **2005**, *2*, 455–460. [[PubMed](#)]
34. Nanua, S.; Zick, S.M.; Andrade, J.E.; Sajjan, U.S.; Burgess, J.R.; Lukacs, N.W.; Hershenov, M.B. Quercetin blocks airway epithelial cell chemokine expression. *Am. J. Respir. Cell Mol. Biol.* **2006**, *35*, 602–610. [[CrossRef](#)] [[PubMed](#)]
35. Chen, P.; Shi, Q.; Xu, X.; Wang, Y.; Chen, W.; Wang, H. Quercetin suppresses NF-kappaB and MCP-1 expression in a high glucose-induced human mesangial cell proliferation model. *Int. J. Mol. Med.* **2012**, *30*, 119–125.
36. Bian, Y.; Liu, P.; Zhong, J.; Hu, Y.; Zhuang, S.; Fan, K.; Liu, Z. Quercetin Attenuates Adhesion Molecule Expression in Intestinal Microvascular Endothelial Cells by Modulating Multiple Pathways. *Dig. Dis. Sci.* **2018**, *63*, 3297–3304. [[CrossRef](#)] [[PubMed](#)]
37. Ying, B.; Yang, T.; Song, X.; Hu, X.; Fan, H.; Lu, X.; Chen, L.; Cheng, D.; Wang, T.; Liu, D.; et al. Quercetin inhibits IL-1 beta-induced ICAM-1 expression in pulmonary epithelial cell line A549 through the MAPK pathways. *Mol. Biol. Rep.* **2009**, *36*, 1825–1832. [[CrossRef](#)]

38. Li, C.; Zhang, W.J.; Frei, B. Quercetin inhibits LPS-induced adhesion molecule expression and oxidant production in human aortic endothelial cells by p38-mediated Nrf2 activation and antioxidant enzyme induction. *Redox Biol.* **2016**, *9*, 104–113. [[CrossRef](#)]
39. Bian, Z.M.; Elner, S.G.; Yoshida, A.; Kunkel, S.L.; Su, J.; Elner, V.M. Activation of p38, ERK1/2 and NIK pathways is required for IL-1beta and TNF-alpha-induced chemokine expression in human retinal pigment epithelial cells. *Exp. Eye Res.* **2001**, *73*, 111–121. [[CrossRef](#)]
40. Hytti, M.; Piippo, N.; Korhonen, E.; Honkakoski, P.; Kaarniranta, K.; Kauppinen, A. Fisetin and luteolin protect human retinal pigment epithelial cells from oxidative stress-induced cell death and regulate inflammation. *Sci. Rep.* **2015**, *5*, 17645. [[CrossRef](#)]
41. Lee, I.T.; Liu, S.W.; Chi, P.L.; Lin, C.C.; Hsiao, L.D.; Yang, C.M. TNF-alpha mediates PKCdelta/JNK1/2/c-Jun-dependent monocyte adhesion via ICAM-1 induction in human retinal pigment epithelial cells. *PLoS ONE* **2015**, *10*, e0117911.
42. Ozal, S.A.; Turkekul, K.; Gurlu, V.; Guclu, H.; Erdogan, S. Esculetin Protects Human Retinal Pigment Epithelial Cells from Lipopolysaccharide-induced Inflammation and Cell Death. *Curr. Eye Res.* **2018**, *43*, 1169–1176. [[CrossRef](#)] [[PubMed](#)]
43. Oeckinghaus, A.; Hayden, M.S.; Ghosh, S. Crosstalk in NF-κB signaling pathways. *Nat. Immunol.* **2011**, *12*, 695. [[CrossRef](#)] [[PubMed](#)]
44. Zhang, M.; Lin, J.M.; Li, X.S.; Li, J. Quercetin ameliorates LPS-induced inflammation in human peripheral blood mononuclear cells by inhibition of the TLR2-NF-kappaB pathway. *Genet. Mol. Res.* **2016**, *15*. [[CrossRef](#)]
45. Indra, M.R.; Karyono, S.; Ratnawati, R.; Malik, S.G. Quercetin suppresses inflammation by reducing ERK1/2 phosphorylation and NF kappa B activation in Leptin-induced Human Umbilical Vein Endothelial Cells (HUVECs). *BMC Res. Notes* **2013**, *6*, 275. [[CrossRef](#)] [[PubMed](#)]
46. Granado-Serrano, A.B.; Martin, M.A.; Bravo, L.; Goya, L.; Ramos, S. Quercetin attenuates TNF-induced inflammation in hepatic cells by inhibiting the NF-kappaB pathway. *Nutr. Cancer* **2012**, *64*, 588–598. [[CrossRef](#)] [[PubMed](#)]
47. Wei, X.; Meng, X.; Yuan, Y.; Shen, F.; Li, C.; Yang, J. Quercetin exerts cardiovascular protective effects in LPS-induced dysfunction in vivo by regulating inflammatory cytokine expression, NF-kappaB phosphorylation, and caspase activity. *Mol. Cell. Biochem.* **2018**, *446*, 43–52. [[CrossRef](#)]
48. Peng, Z.; Gong, X.; Yang, Y.; Huang, L.; Zhang, Q.; Zhang, P.; Wan, R.; Zhang, B. Hepatoprotective effect of quercetin against LPS/d-GalN induced acute liver injury in mice by inhibiting the IKK/NF-kappaB and MAPK signal pathways. *Int. Immunopharmacol.* **2017**, *52*, 281–289. [[CrossRef](#)]
49. Peng, H.L.; Huang, W.C.; Cheng, S.C.; Liou, C.J. Fisetin inhibits the generation of inflammatory mediators in interleukin-1beta-induced human lung epithelial cells by suppressing the NF-kappaB and ERK1/2 pathways. *Int. Immunopharmacol.* **2018**, *60*, 202–210. [[CrossRef](#)]
50. Ambati, J.; Atkinson, J.P.; Gelfand, B.D. Immunology of age-related macular degeneration. *Nat. Rev. Immunol.* **2013**, *13*, 438–451. [[CrossRef](#)]
51. Murugeswari, P.; Shukla, D.; Kim, R.; Namperumalsamy, P.; Stitt, A.W.; Muthukkaruppan, V. Angiogenic potential of vitreous from Proliferative Diabetic Retinopathy and Eales' Disease patients. *PLoS ONE* **2014**, *9*, e107551. [[CrossRef](#)] [[PubMed](#)]
52. Ehlers, J.P.; Fekrat, S. Retinal vein occlusion: Beyond the acute event. *Surv. Ophthalmol.* **2011**, *56*, 281–299. [[CrossRef](#)] [[PubMed](#)]
53. Whitcup, S.M.; Nussenblatt, R.B.; Lightman, S.L.; Hollander, D.A. Inflammation in retinal disease. *Int. J. Inflam.* **2013**, *2013*, 724648. [[CrossRef](#)] [[PubMed](#)]
54. Zhao, M.; Bai, Y.; Xie, W.; Shi, X.; Li, F.; Yang, F.; Sun, Y.; Huang, L.; Li, X. Interleukin-1beta Level Is Increased in Vitreous of Patients with Neovascular Age-Related Macular Degeneration (nAMD) and Polypoidal Choroidal Vasculopathy (PCV). *PLoS ONE* **2015**, *10*, e0125150.
55. Kuppner, M.C.; McKillop-Smith, S.; Forrester, J.V. TGF-beta and IL-1 beta act in synergy to enhance IL-6 and IL-8 mRNA levels and IL-6 production by human retinal pigment epithelial cells. *Immunology* **1995**, *84*, 265–271. [[PubMed](#)]
56. Lechner, J.; Chen, M.; Hogg, R.E.; Toth, L.; Silvestri, G.; Chakravarthy, U.; Xu, H. Alterations in Circulating Immune Cells in Neovascular Age-Related Macular Degeneration. *Sci. Rep.* **2015**, *5*, 16754. [[CrossRef](#)] [[PubMed](#)]

57. Elner, V.M.; Scales, W.; Elner, S.G.; Danforth, J.; Kunkel, S.L.; Strieter, R.M. Interleukin-6 (IL-6) gene expression and secretion by cytokine-stimulated human retinal pigment epithelial cells. *Exp. Eye Res.* **1992**, *54*, 361–368. [\[CrossRef\]](#)
58. Benson, M.T.; Shepherd, L.; Rees, R.C.; Rennie, I.G. Production of interleukin-6 by human retinal pigment epithelium in vitro and its regulation by other cytokines. *Curr. Eye Res.* **1992**, *11*, 173–179. [\[CrossRef\]](#)
59. Elner, V.M.; Strieter, R.M.; Elner, S.G.; Baggiolini, M.; Lindley, I.; Kunkel, S.L. Neutrophil chemotactic factor (IL-8) gene expression by cytokine-treated retinal pigment epithelial cells. *Am. J. Pathol.* **1990**, *136*, 745–750.
60. Chen, J.T.; Chen, P.L.; Chang, Y.H.; Chien, M.W.; Chen, Y.H.; Lu, D.W. Glucosamine sulfate inhibits leukocyte adhesion in response to cytokine stimulation of retinal pigment epithelial cells in vitro. *Exp. Eye Res.* **2006**, *83*, 1052–1062. [\[CrossRef\]](#)
61. Elner, S.G.; Strieter, R.M.; Elner, V.M.; Rollins, B.J.; Del Monte, M.A.; Kunkel, S.L. Monocyte chemotactic protein gene expression by cytokine-treated human retinal pigment epithelial cells. *Lab. Invest.* **1991**, *64*, 819–825. [\[PubMed\]](#)
62. Yang, L.; Froio, R.M.; Sciuto, T.E.; Dvorak, A.M.; Alon, R.; Luscinskas, F.W. ICAM-1 regulates neutrophil adhesion and transcellular migration of TNF-alpha-activated vascular endothelium under flow. *Blood* **2005**, *106*, 584–592. [\[CrossRef\]](#) [\[PubMed\]](#)
63. Whitcup, S.M.; Chan, C.C.; Li, Q.; Nussenblatt, R.B. Expression of cell adhesion molecules in posterior uveitis. *Arch. Ophthalmol.* **1992**, *110*, 662–666. [\[CrossRef\]](#) [\[PubMed\]](#)
64. Chen, J.T.; Liang, J.B.; Chou, C.L.; Chien, M.W.; Shyu, R.C.; Chou, P.I.; Lu, D.W. Glucosamine sulfate inhibits TNF-alpha and IFN-gamma-induced production of ICAM-1 in human retinal pigment epithelial cells in vitro. *Invest. Ophthalmol. Vis. Sci.* **2006**, *47*, 664–672. [\[CrossRef\]](#) [\[PubMed\]](#)
65. Rothlein, R.; Mainolfi, E.A.; Czajkowski, M.; Marlin, S.D. A form of circulating ICAM-1 in human serum. *J. Immunol.* **1991**, *147*, 3788–3793. [\[PubMed\]](#)
66. Witkowska, A.M.; Borawska, M.H. Soluble intercellular adhesion molecule-1 (sICAM-1): An overview. *Eur. Cytokine Netw.* **2004**, *15*, 91–98.
67. Whiteman, S.C.; Bianco, A.; Knight, R.A.; Spiteri, M.A. Human rhinovirus selectively modulates membranous and soluble forms of its intercellular adhesion molecule-1 (ICAM-1) receptor to promote epithelial cell infectivity. *J. Biol. Chem.* **2003**, *278*, 11954–11961. [\[CrossRef\]](#) [\[PubMed\]](#)
68. Wakatsuki, T.; Kimura, K.; Kimura, F.; Shinomiya, N.; Ohtsubo, M.; Ishizawa, M.; Yamamoto, M. A distinct mRNA encoding a soluble form of ICAM-1 molecule expressed in human tissues. *Cell Adhes. Commun.* **1995**, *3*, 283–292. [\[CrossRef\]](#)
69. Nowak, M.; Wielkoszynski, T.; Marek, B.; Kos-Kudla, B.; Swietochowska, E.; Sieminska, L.; Kajdaniuk, D.; Glogowska-Szelag, J.; Nowak, K. Blood serum levels of vascular cell adhesion molecule (sVCAM-1), intercellular adhesion molecule (sICAM-1) and endothelial leucocyte adhesion molecule-1 (ELAM-1) in diabetic retinopathy. *Clin. Exp. Med.* **2008**, *8*, 159–164. [\[CrossRef\]](#)
70. De Bellis, A.; Di Martino, S.; Fiordelisi, F.; Muccitelli, V.I.; Sinisi, A.A.; Abbate, G.F.; Gargano, D.; Bellastella, A.; Bizzarro, A. Soluble intercellular adhesion molecule-1 (sICAM-1) concentrations in Graves' disease patients followed up for development of ophthalmopathy. *J. Clin. Endocrinol. Metab.* **1998**, *83*, 1222–1225.
71. Zaman, A.G.; Edelsten, C.; Stanford, M.R.; Graham, E.M.; Ellis, B.A.; Direskeneli, H.; D'Cruz, D.P.; Hughes, G.R.; Dumonde, D.C.; Wallace, G.R. Soluble intercellular adhesion molecule-1 (sICAM-1) as a marker of disease relapse in idiopathic uveoretinitis. *Clin. Exp. Immunol.* **1994**, *95*, 60–65. [\[CrossRef\]](#) [\[PubMed\]](#)
72. Ozderya, A.; Aydin, K.; Temizkan, S.; Dogru Abbasoglu, S.; Vural, P.; Altuntas, Y. High circulating levels of sICAM-1 and sVCAM-1 in the patients with Hashimoto's thyroiditis. *Endocr. Res.* **2017**, *42*, 110–116. [\[CrossRef\]](#) [\[PubMed\]](#)
73. Fathollahi, A.; Massoud, A.; Amirzargar, A.A.; Aghili, B.; Nasli Esfahani, E.; Rezaei, N. sICAM-1, sVCAM-1 and sE-Selectin Levels in Type 1 Diabetes. *Fetal Pediatr. Pathol.* **2018**, *37*, 69–73. [\[CrossRef\]](#) [\[PubMed\]](#)
74. De Pablo, R.; Monserrat, J.; Reyes, E.; Diaz, D.; Rodriguez-Zapata, M.; de la Hera, A.; Prieto, A.; Alvarez-Mon, M. Circulating sICAM-1 and sE-Selectin as biomarker of infection and prognosis in patients with systemic inflammatory response syndrome. *Eur. J. Intern. Med.* **2013**, *24*, 132–138. [\[CrossRef\]](#) [\[PubMed\]](#)
75. Klimiuk, P.A.; Fiedorczyk, M.; Sierakowski, S.; Chwiecko, J. Soluble cell adhesion molecules (sICAM-1, sVCAM-1, and sE-selectin) in patients with early rheumatoid arthritis. *Scand. J. Rheumatol.* **2007**, *36*, 345–350. [\[CrossRef\]](#)

76. Kaufmann, P.; Demel, U.; Tilz, G.P.; Krejs, G.J. Time course of plasma soluble intercellular adhesion molecule-1 (sICAM-1) is related to severity of acute pancreatitis. *Hepatogastroenterology* **1999**, *46*, 2565–2571. [[PubMed](#)]
77. Planck, S.R.; Dang, T.T.; Graves, D.; Tara, D.; Ansel, J.C.; Rosenbaum, J.T. Retinal pigment epithelial cells secrete interleukin-6 in response to interleukin-1. *Invest. Ophthalmol. Vis. Sci.* **1992**, *33*, 78–82. [[PubMed](#)]
78. Sprague, A.H.; Khalil, R.A. Inflammatory cytokines in vascular dysfunction and vascular disease. *Biochem. Pharmacol.* **2009**, *78*, 539–552. [[CrossRef](#)] [[PubMed](#)]
79. Tanaka, T.; Narazaki, M.; Kishimoto, T. IL-6 in inflammation, immunity, and disease. *Cold Spring Harb. Perspect. Biol.* **2014**, *6*, a016295. [[CrossRef](#)]
80. Deshmane, S.L.; Kremlev, S.; Amini, S.; Sawaya, B.E. Monocyte chemoattractant protein-1 (MCP-1): An overview. *J. Interferon Cytokine Res.* **2009**, *29*, 313–326. [[CrossRef](#)]
81. Kramer, M.; Hasanreisoglu, M.; Feldman, A.; Axer-Siegel, R.; Sonis, P.; Maharshak, I.; Monselise, Y.; Gurevich, M.; Weinberger, D. Monocyte chemoattractant protein-1 in the aqueous humour of patients with age-related macular degeneration. *Clin. Exp. Ophthalmol.* **2012**, *40*, 617–625. [[CrossRef](#)] [[PubMed](#)]
82. Rodrigues, E.B. Inflammation in dry age-related macular degeneration. *Ophthalmologica* **2007**, *221*, 143–152. [[CrossRef](#)] [[PubMed](#)]
83. Du, Z.J.; Li, P.; Wang, L. Magnetic nanoparticles conjugated with “RPE cell -MCP-1 antibody -VEGF antibody” compounds for the targeted therapy of age-related macular degeneration: A hypothesis. *Int. J. Ophthalmol.* **2017**, *10*, 812–814. [[PubMed](#)]
84. Izumi-Nagai, K.; Nagai, N.; Ozawa, Y.; Mihara, M.; Ohsugi, Y.; Kurihara, T.; Koto, T.; Satofuka, S.; Inoue, M.; Tsubota, K.; et al. Interleukin-6 receptor-mediated activation of signal transducer and activator of transcription-3 (STAT3) promotes choroidal neovascularization. *Am. J. Pathol.* **2007**, *170*, 2149–2158. [[CrossRef](#)] [[PubMed](#)]
85. Du, Z.; Wu, X.; Song, M.; Li, P.; Wang, L. Oxidative damage induces MCP-1 secretion and macrophage aggregation in age-related macular degeneration (AMD). *Graefes Arch. Clin. Exp. Ophthalmol.* **2016**, *254*, 2469–2476. [[CrossRef](#)]
86. Yoon, J.S.; Lee, H.J.; Choi, S.H.; Chang, E.J.; Lee, S.Y.; Lee, E.J. Quercetin inhibits IL-1 β -induced inflammation, hyaluronan production and adipogenesis in orbital fibroblasts from Graves’ orbitopathy. *PLoS ONE* **2011**, *6*, e26261. [[CrossRef](#)] [[PubMed](#)]
87. Abengozar-Vela, A.; Calonge, M.; Stern, M.E.; Gonzalez-Garcia, M.J.; Enriquez-De-Salamanca, A. Quercetin and Resveratrol Decrease the Inflammatory and Oxidative Responses in Human Ocular Surface Epithelial Cells. *Invest. Ophthalmol. Vis. Sci.* **2015**, *56*, 2709–2719. [[CrossRef](#)] [[PubMed](#)]
88. Cheng, S.C.; Wu, Y.H.; Huang, W.C.; Pang, J.S.; Huang, T.H.; Cheng, C.Y. Anti-inflammatory property of quercetin through downregulation of ICAM-1 and MMP-9 in TNF- α -activated retinal pigment epithelial cells. *Cytokine* **2019**, *116*, 48–60. [[CrossRef](#)]
89. Chen, R.; Hollborn, M.; Grosche, A.; Reichenbach, A.; Wiedemann, P.; Bringmann, A.; Kohen, L. Effects of the vegetable polyphenols epigallocatechin-3-gallate, luteolin, apigenin, myricetin, quercetin, and cyanidin in primary cultures of human retinal pigment epithelial cells. *Mol. Vis.* **2014**, *20*, 242–258.
90. Wang, Y.; Kim, H.J.; Sparrow, J.R. Quercetin and cyanidin-3-glucoside protect against photooxidation and photodegradation of A2E in retinal pigment epithelial cells. *Exp. Eye Res.* **2017**, *160*, 45–55. [[CrossRef](#)]
91. O’Neil, J.D.; Ammit, A.J.; Clark, A.R. MAPK p38 regulates inflammatory gene expression via tristetraprolin: Doing good by stealth. *Int. J. Biochem. Cell Biol.* **2018**, *94*, 6–9. [[CrossRef](#)]
92. Krupkova, O.; Sadowska, A.; Kameda, T.; Hitzl, W.; Hausmann, O.N.; Klasen, J.; Wuertz-Kozak, K. p38 MAPK Facilitates Crosstalk Between Endoplasmic Reticulum Stress and IL-6 Release in the Intervertebral Disc. *Front. Immunol.* **2018**, *9*, 1706. [[CrossRef](#)] [[PubMed](#)]
93. Zhang, H.F.; Wang, Y.L.; Gao, C.; Gu, Y.T.; Huang, J.; Wang, J.H.; Wang, J.H.; Zhang, Z. Salvianolic acid A attenuates kidney injury and inflammation by inhibiting NF- κ B and p38 MAPK signaling pathways in 5/6 nephrectomized rats. *Acta Pharmacol. Sin.* **2018**, *39*, 1855–1864. [[CrossRef](#)] [[PubMed](#)]
94. Ruiz, P.A.; Braune, A.; Holzlwimmer, G.; Quintanilla-Fend, L.; Haller, D. Quercetin inhibits TNF-induced NF- κ B transcription factor recruitment to proinflammatory gene promoters in murine intestinal epithelial cells. *J. Nutr.* **2007**, *137*, 1208–1215. [[CrossRef](#)] [[PubMed](#)]
95. Gerszten, R.E.; Garcia-Zepeda, E.A.; Lim, Y.C.; Yoshida, M.; Ding, H.A.; Gimbrone, M.A., Jr.; Luster, A.D.; Luscinskas, F.W.; Rosenzweig, A. MCP-1 and IL-8 trigger firm adhesion of monocytes to vascular endothelium under flow conditions. *Nature* **1999**, *398*, 718–723. [[CrossRef](#)] [[PubMed](#)]

96. Hiraoka, M.; Nitta, N.; Nagai, M.; Shimokado, K.; Yoshida, M. MCP-1-induced enhancement of THP-1 adhesion to vascular endothelium was modulated by HMG-CoA reductase inhibitor through RhoA GTPase-, but not ERK1/2-dependent pathway. *Life Sci.* **2004**, *75*, 1333–1341. [[CrossRef](#)] [[PubMed](#)]
97. Yang, C.R.; Hsieh, S.L.; Ho, F.M.; Lin, W.W. Decoy receptor 3 increases monocyte adhesion to endothelial cells via NF-kappa B-dependent up-regulation of intercellular adhesion molecule-1, VCAM-1, and IL-8 expression. *J. Immunol.* **2005**, *174*, 1647–1656. [[CrossRef](#)]
98. Liou, C.J.; Lai, Y.R.; Chen, Y.L.; Chang, Y.H.; Li, Z.Y.; Huang, W.C. Matrine Attenuates COX-2 and ICAM-1 Expressions in Human Lung Epithelial Cells and Prevents Acute Lung Injury in LPS-Induced Mice. *Mediators Inflamm.* **2016**, *2016*, 3630485. [[CrossRef](#)]



© 2019 by the authors. Licensee MDPI, Basel, Switzerland. This article is an open access article distributed under the terms and conditions of the Creative Commons Attribution (CC BY) license (<http://creativecommons.org/licenses/by/4.0/>).



Article

Carbon Monoxide Releasing Molecule-2-Upregulated ROS-Dependent Heme Oxygenase-1 Axis Suppresses Lipopolysaccharide-Induced Airway Inflammation

Chih-Chung Lin ¹, Li-Der Hsiao ¹, Rou-Ling Cho ²  and Chuen-Mao Yang ^{1,2,3,*}

¹ Department of Anesthetics, Chang Gung Memorial Hospital at Linkuo, and College of Medicine, Chang Gung University, Kwei-San, Tao-Yuan 33302, Taiwan

² Department of Physiology and Pharmacology and Health Aging Research Center, College of Medicine, Chang Gung University, 259 Wen-Hwa 1 Road, Kwei-San, Tao-Yuan 33302, Taiwan

³ Research Center for Chinese Herbal Medicine and Research Center for Food and Cosmetic Safety, College of Human Ecology, Chang Gung University of Science and Technology, Tao-Yuan 33302, Taiwan

* Correspondence: chuenmao@mail.cgu.edu.tw or chuenmao@gmail.com; Tel.: +886-3-211-8800 (ext. 5123); Fax: +886-3-211-8365

Received: 3 June 2019; Accepted: 26 June 2019; Published: 28 June 2019



Abstract: The up-regulation of heme oxygenase-1 (HO-1) is mediated through nicotinamide adenine dinucleotide phosphate (NADPH) oxidases (Nox) and reactive oxygen species (ROS) generation, which could provide cytoprotection against inflammation. However, the molecular mechanisms of carbon monoxide-releasing molecule (CORM)-2-induced HO-1 expression in human tracheal smooth muscle cells (HTSMCs) remain unknown. Here, we found that pretreatment with CORM-2 attenuated the lipopolysaccharide (LPS)-induced intercellular adhesion molecule (ICAM-1) expression and leukocyte count through the up-regulation of HO-1 in mice, which was revealed by immunohistochemical staining, Western blot, real-time PCR, and cell count. The inhibitory effects of HO-1 by CORM-2 were reversed by transfection with HO-1 siRNA. Next, Western blot, real-time PCR, and promoter activity assay were performed to examine the HO-1 induction in HTSMCs. We found that CORM-2 induced HO-1 expression via the activation of protein kinase C (PKC) α and proline-rich tyrosine kinase (Pyk2), which was mediated through Nox-derived ROS generation using pharmacological inhibitors or small interfering ribonucleic acids (siRNAs). CORM-2-induced HO-1 expression was mediated through Nox-(1, 2, 4) or p47^{phox}, which was confirmed by transfection with their own siRNAs. The Nox-derived ROS signals promoted the activities of extracellular signal-regulated kinase 1/2 (ERK1/2). Subsequently, c-Fos and c-Jun—activator protein-1 (AP-1) subunits—were up-regulated by activated ERK1/2, which turned on transcription of the HO-1 gene by regulating the HO-1 promoter. These results suggested that in HTSMCs, CORM-2 activates PKC α /Pyk2-dependent Nox/ROS/ERK1/2/AP-1, leading to HO-1 up-regulation, which suppresses the lipopolysaccharide (LPS)-induced airway inflammation.

Keywords: CORM-2; NADPH oxidase; ROS; AP-1; HO-1

1. Introduction

Heme oxygenase (HO), a rate-limiting enzyme, metabolizes heme to biliverdin-IX α , ferrous iron, and carbon monoxide (CO). These secondary products are involved in the regulation of different physiological processes. HO-1, a member of the HO family [1,2], is inducible and directly protects various organs from oxidative damages [1,3]. Biliverdin-IX α is converted to the endogenous radical scavenger bilirubin-IX α and has anti-inflammatory properties [4,5]. The ferrous iron is rapidly sequestered with ferritin to function additional antioxidant and anti-apoptotic effects [5,6]. Moreover,

CO has been shown to exert anti-apoptotic and anti-inflammatory effects that are mediated via HO-1 up-regulation [4,7,8]. However, several pro-inflammatory cytokines and oxidative stresses can also trigger HO-1 expression [9–11]. For example, HO-1 is also induced by various factors in the airway cells of asthmatic patients [12]. Accumulating evidence concerning HO-1/CO-dependent cytoprotection elicits the mechanisms involved in the modulation of the inflammatory responses, including the down-regulation of pro-inflammatory mediators, atherosclerosis, ischemia-reperfusion systems, and airway disorders [8,13,14].

Nicotinamide adenine dinucleotide phosphate (NADPH) oxidase (Nox)-derived reactive oxygen species (ROS) generation has been approved to regulate either the expression of inflammatory or anti-inflammatory mediators in the airway and pulmonary diseases [15]. Excessive ROS production can regulate the expression of various inflammatory genes during airway disorders [15,16]. In contrast, low levels of ROS contribute to maintain cellular redox homeostasis under physiological conditions [15]. Several studies indicate that the exogenous application of CO and HO-1 can protect against oxidative stress and hyperoxic injury in the various organs [17,18]. It has also been reported that the up-regulation of HO-1 via the Nox/ROS formation is induced by lipopolysaccharide (LPS) or cytokines [8,19]. In addition, our previous reports have indicated that the Nox/ROS system is a key player for HO-1 expression induced by lipotechoic acid (LTA) and cigarette smoke particle extract (CSPE) in human tracheal smooth muscle cells (HTSMCs) [5,20]. Our previous studies and others have demonstrated that the carbon monoxide-releasing molecule (CORM)-2 mediates the Nox-dependent ROS generation in astrocytes [21,22] and human bronchial smooth muscle cells [23]. CORMs have been confirmed to provide the exogenous CO source and induce HO-1 expression in several cell types [8,9,24]. However, the roles of Nox/ROS involved in CORM-2-induced HO-1 expression were still unknown. HO-1 expression is regulated by various intracellular signaling pathways, such as ROS, growth factor receptors, non-receptor tyrosine kinases such as Pyk2, or mitogen-activated protein kinases (MAPKs) [25,26]. In our previous study, CORM-2 has been shown to induce HO-1 expression via c-Src/epidermal growth factor receptor (EGFR)/phosphoinositide 3-kinase (PI3K)/Akt/c-Jun N-terminal kinase 1/2 (JNK1/2) and p38 MAPK pathways in HTSMCs [27]. We also noticed that many stress-activated response elements on the upstream region of the HO-1 promoter, such as nuclear factor erythroid 2-related factor 2 (Nrf2) and activator protein 1 (AP-1), are involved in the expression of HO-1 in response to oxidative stresses [28,29]. Therefore, whether an alternative Nox/ROS-mediated pathway involved in HO-1 expression induced by CORM-2 has yet to be investigated in HTSMCs.

Besides, several reports have shown that administration with low concentrations of CO or pharmacological application of CORMs can also confer protective effects in the models of inflammatory responses and tissue injury [26,30,31]. Accumulating evidence has indicated that CORM-2-liberated CO reduces inflammatory responses in sepsis by interfering with nuclear factor (NF)- κ B activation [32]. Moreover, the overexpression of HO-1 by cobalt protoporphyrin (CoPP) can reduce tumor necrosis factor (TNF) α -induced oxidative stress and airway inflammation [7]. Therefore, CORM-2-induced HO-1 gene expression could prevent inflammatory responses. However, the detailed mechanisms by which CORM-2 induced HO-1 expression in HTSMCs are still unclear. Our results demonstrated that CORM-2-induced HO-1 expression is mediated via protein kinase C (PKC) α /proline-rich tyrosine kinase 2 (Pyk2)-dependent Nox/ROS generation linking to the ERK1/2-mediated activation of AP-1 in HTSMCs, which could protect against the lipopolysaccharide (LPS)-induced airway inflammatory diseases.

2. Results

2.1. CORM-2 Inhibits LPS-Induced Lung Inflammation in Mice

CORM-2 has been shown to protect against inflammatory responses induced by various insults [4,7,8]. First, we investigated the anti-inflammatory effects of CORM-2 on LPS-induced lung inflammation. We observed that LPS markedly induced intercellular adhesion molecule-1

(ICAM-1) expression, which was attenuated by CORM-2 via HO-1 expression, as determined by immunohistochemistry staining (Figure 1A). Bronchoalveolar lavage (BAL) fluid was collected to determine the number of leukocytes, and airway tissues were harvested to study the levels of protein and mRNA expression. As shown in Figure 1B,D, LPS significantly enhanced ICAM-1 protein expression and leukocytes count in BAL fluid. LPS also significantly induced ICAM-1 messenger ribonucleic acid (mRNA) expression (Figure 1C). In addition, pretreatment with CORM-2 also inhibited the LPS-induced ICAM-1 protein expression in HTSMCs (Figure 1E). Further, we confirmed the inhibitory effects of HO-1 induction by CORM-2 on the LPS-up-regulated ICAM-1 expression by transfection with HO-1 siRNA. We found that CORM-2 attenuated the LPS-induced ICAM-1 expression, which was partially reversed by transfection with HO-1 siRNA (Figure 1F). All of these LPS-mediated responses were attenuated by CORM-2 via the up-regulation of HO-1 in the airway tissues of mice (Figure 1). These results suggested that the up-regulation of HO-1 by CORM-2 protects airway tissues against the LPS-mediated inflammatory responses.

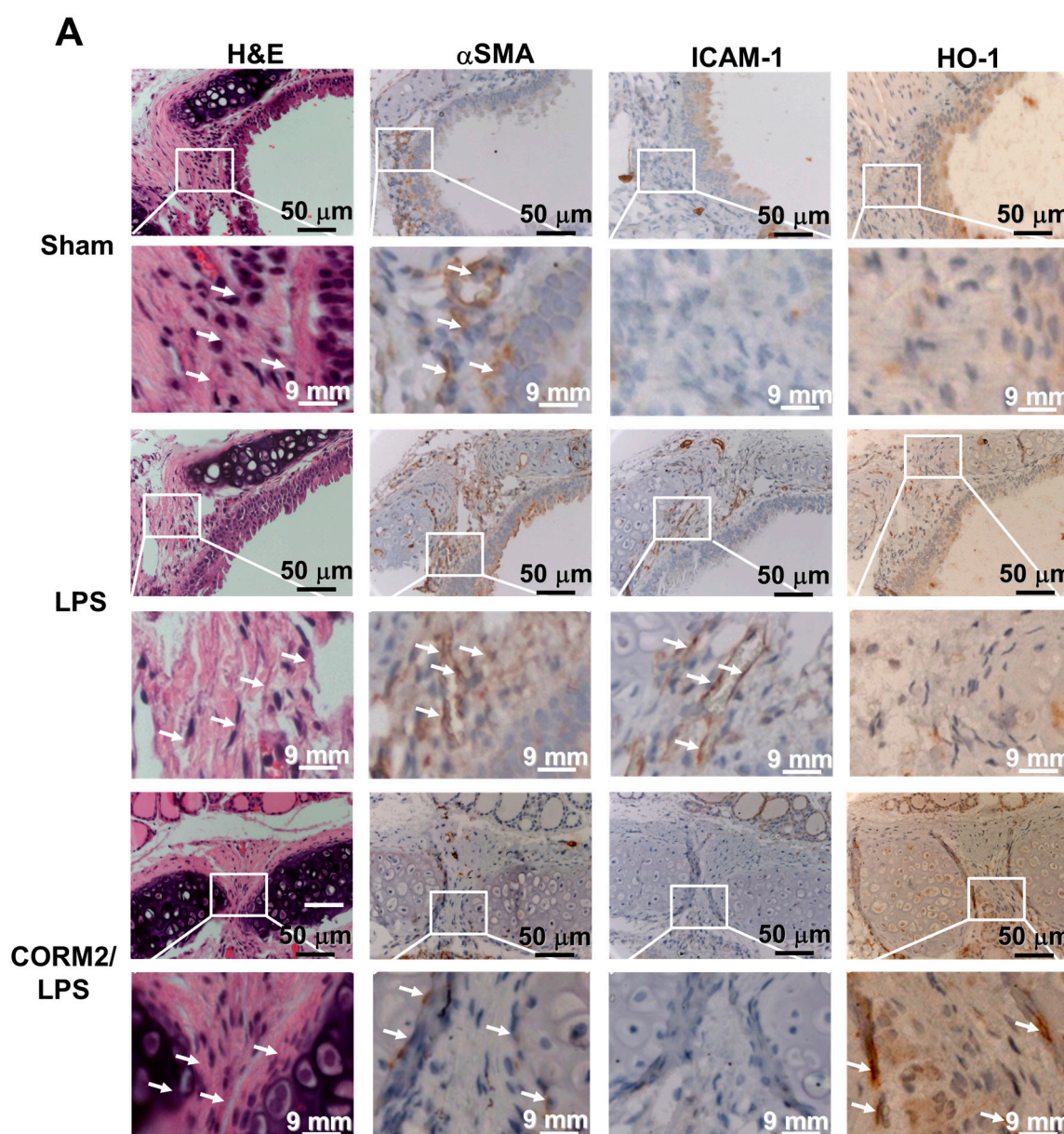


Figure 1. Cont.

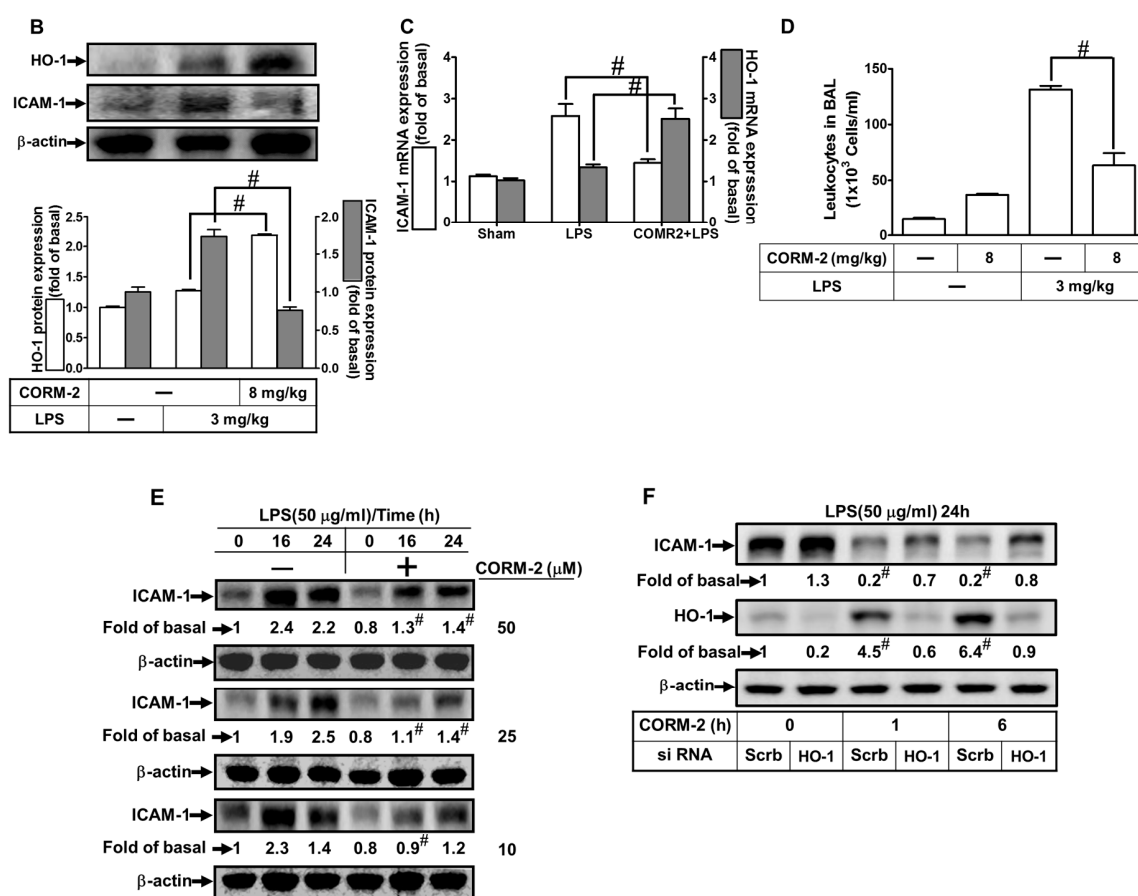


Figure 1. Induction of heme oxygenase (HO-1) by carbon monoxide-releasing molecule (CORM-2) suppresses intercellular adhesion molecule-1 (ICAM-1) expression and leukocyte infiltration in HTSMCs and mice. Institute of Cancer Research (ICR) mice were pretreated with CORM-2 (8 mg/kg of body weight) for 24 h, and then treated with lipopolysaccharide (LPS) (3 mg/kg of body weight). (A) H (hematoxylin) & E (Eosin) and immunohistochemical staining for α -smooth muscle actin (α -SMA), ICAM-1, and HO-1 in serial section of the airway tissues from sham [0.1 mL of DMSO–PBS (phosphate-buffered saline) (1:100) with 0.1% (*w/v*) BSA (bovine serum albumin) treated mice], LPS (LPS-injected mice) and CORM-2 + LPS mice. The arrows indicate tracheal smooth muscle cells displayed with ICAM-1 and HO-1 expression. (B,C) Airway tissues were homogenized to extract proteins and mRNAs (messenger ribonucleic acids), and analyzed by (B) Western blot and (C) real-time PCR to determine the levels of HO-1, ICAM-1, and β -actin (served as an internal control) protein and mRNA expression, respectively. (D) BAL fluid was collected to count the number of leukocytes infiltration. (E) Human tracheal smooth muscle cells (HTSMCs) were pretreated without or with various concentrations of CORM-2 for 1 h and then incubated with LPS (50 μ g/mL) for the indicated time periods. The levels of ICAM-1 and β -actin were determined by Western blot. (F) Cells were transfected with scrambled (Scrb) or HO-1 siRNA (small interfering ribonucleic acid), incubated with CORM-2 (50 μ M) for 1 or 6 h, and then stimulated with LPS (50 μ g/mL) for 16 h. The levels of ICAM-1, HO-1, and β -actin protein were determined by western blot. Data are expressed as mean \pm SEM of five independent experiments ($n = 5$). # $p < 0.05$, as compared with the mice exposed to the indicated reagents. Data analysis and processing are described in the section “Statistical Analysis of Data”.

2.2. ROS Participate in CORM-2-Induced HO-1 Expression

Low levels of ROS have been shown to contribute to maintain cellular redox homeostasis and protect cells against oxidative stress through the up-regulation of HO-1 [8,19]. To examine whether ROS participate in HO-1 induction in HTSMCs, a ROS scavenger N-acetyl cysteine (NAC) was used for this purpose. We found that pretreatment with NAC concentration-dependently attenuated the

CORM-2-induced both of HO-1 protein (Figure 2A) and mRNA expression (Figure 2B), suggesting the involvement of ROS in the CORM-2-induced HO-1 expression. Next, we evaluated whether CORM-2 stimulated ROS generation and the scavenging efficacy of NAC. Our results indicated that CORM-2 stimulated ROS generation in a time-dependent manner with a maximal response within 4 h (Figure 2C), which was markedly attenuated by pretreatment with 10 mM of NAC (Figure 2D), indicating that NAC can efficiently scavenge ROS in HTSMCs. These results were further supported by the data of 2',7'-chloromethyl 2',7'-dichloro fluorescein diacetate (CMH2DCF-DA; for H_2O_2) and dihydroethidium (DHE; for O_2^-) fluorescence images observed under a fluorescent microscope (Figure 2E). Pretreatment of HTSMCs with NAC (10 mM) significantly reduced CORM-2-stimulated H_2O_2 and O_2^- generation. In addition, treatment with an inactive form of CORM-2 [iCORM-2, ruthenium (III) chloride, $RuCl_3$] [33] failed to induce HO-1 expression (Figure 2F). These results concluded that ROS generation stimulated by CORM-2 contributes to up-regulation of HO-1 in HTSMCs.

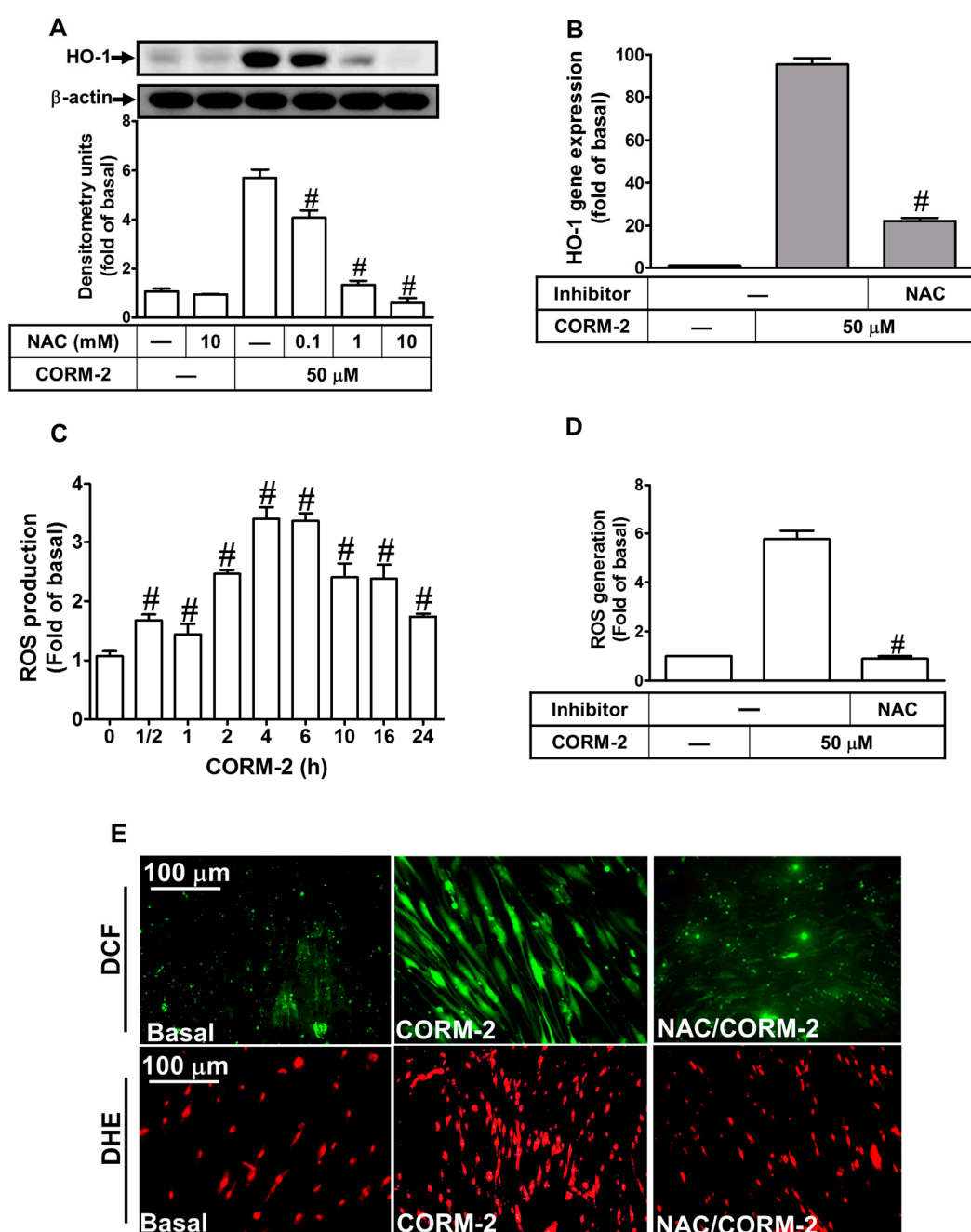


Figure 2. Cont.

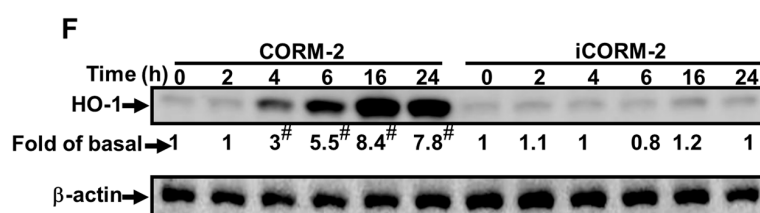


Figure 2. Reactive oxygen species (ROS) are required for CORM-2-induced HO-1 expression in HTSMCs. (A) Cells were pretreated with N-acetyl cysteine (NAC) for 1 h and then incubated with CORM-2 for 24 h. The protein levels of HO-1 and β-actin (served as an internal control) were determined by Western blot. (B) Cells were pretreated with NAC (10 mM) for 1 h, and then incubated with CORM-2 for 6 h. The mRNA expression of HO-1 was determined by real-time PCR. (C) Cells were incubated with the 2',7'-dichlorofluorescein diacetate (DCF-DA) (5 μM) for 45 min, followed by stimulation with 50 μM of CORM-2 for the indicated time intervals. (D) Cells were pretreated without or with NAC (10 mM) for 1 h before exposure to CORM-2 for 6 h. (C,D) The fluorescence intensity of cells was determined. (E) DCF-DA, and dihydroethidium (DHE) staining, cells were treated with CORM-2 for 6 h in the absence or presence of NAC (10 mM). The fluorescence images were observed by a fluorescence microscope. Image of fluorescence microscope, 400×. (F) Cells were treated with 50 μM of CORM-2 or iCORM-2 for the indicated time intervals. The protein levels of HO-1 were determined by Western blot. Data are expressed as mean ± SEM of five independent experiments ($n = 5$). [#] $p < 0.05$, as compared with the cells exposed to vehicle (C,F) or CORM-2 (A,B,D) alone. Data analysis and processing are described in the section “Statistical Analysis of Data”.

2.3. Nox-Derived ROS Generation Contributes to CORM-2-Induced HO-1 Expression

CORM-2 mediates the Nox-dependent ROS generation, leading to HO-1 expression [8,9,24]. Thus, the roles of Noxs in the ROS-dependent HO-1 expression were investigated. The inhibitors of Nox (diphenyleneiodonium, DPI) and p47^{phox} (apocynin, APO) were used to investigate whether Noxs mediated ROS-dependent HO-1 expression in CORM-2-treated HTSMCs. As shown in Figure 3A,B, pretreatment with either DPI or APO significantly attenuated CORM-2-induced both HO-1 protein and mRNA expression. To further investigate whether CORM-2 stimulates Nox activity, as shown in Figure 3C, CORM-2 time-dependently stimulated Nox activity, significantly increased within 30 min and sustained up to 24 h, which was blocked by pretreatment with either DPI (10 μM) or APO (100 μM) (Figure 3D, grey bars), accompanied with inhibiting the ROS generation induced by CORM-2 (Figure 3D, open bars). These results were further supported by the data of DCF (dichlorofluorescein) (for H₂O₂) and DHE (for O₂^{•−}) fluorescence images observed under a fluorescent microscope (Figure 3F), suggesting that CORM-2-stimulated Nox-derived ROS generation contributes to HO-1 expression. Moreover, we found that Nox/ROS generation stimulated by CORM-2 was mediated via Nox(1,2,4) or p47^{phox}, which was confirmed by using their own siRNAs in HTSMCs (Figure 3G).

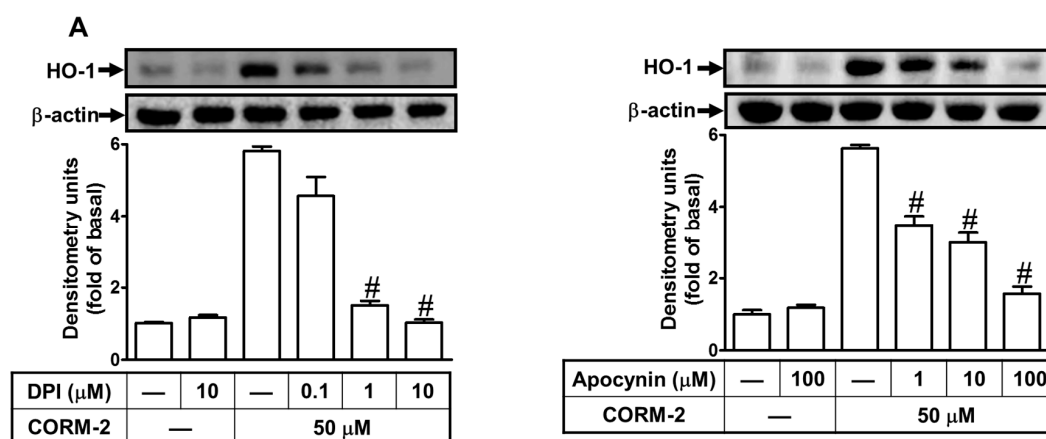


Figure 3. Cont.

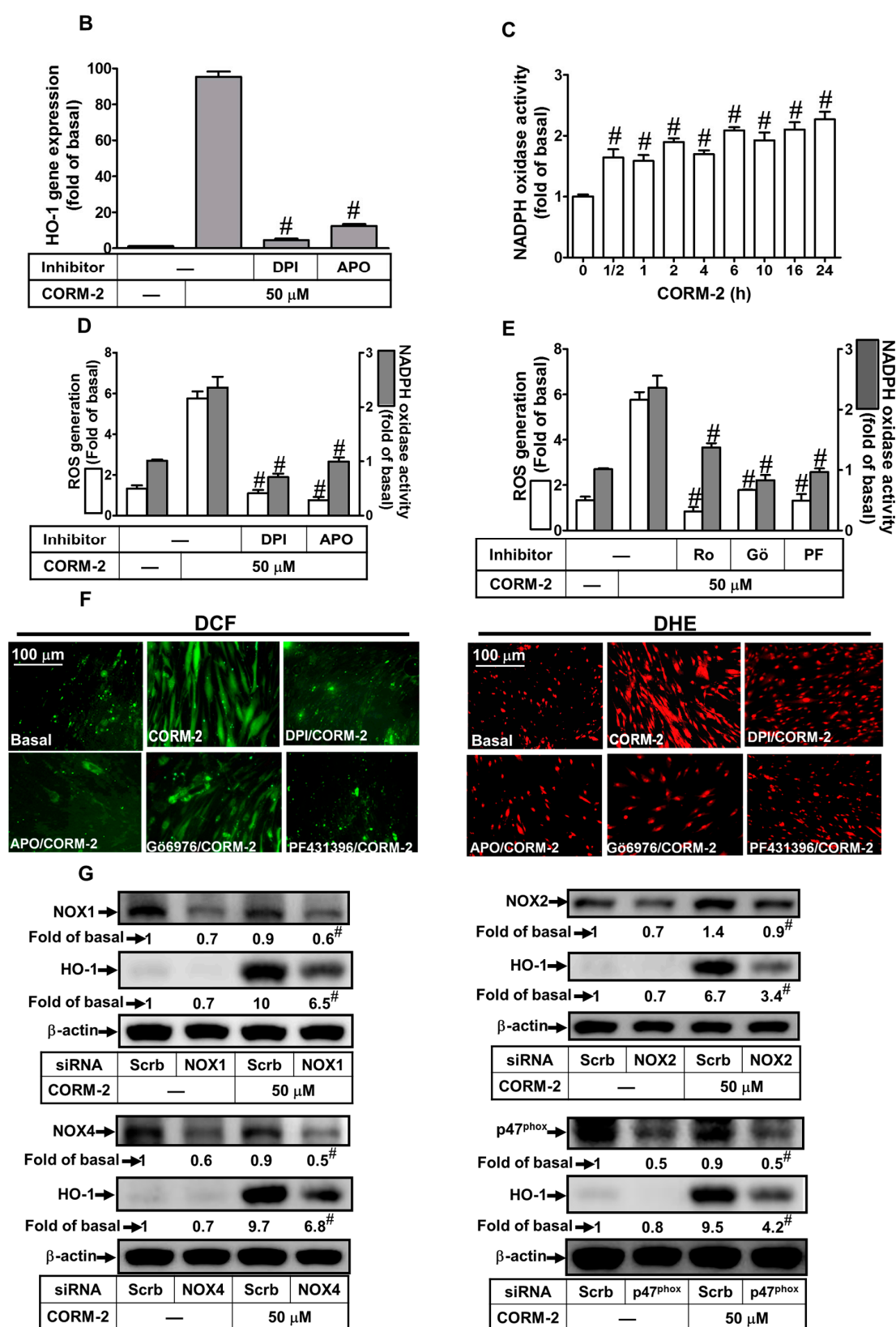


Figure 3. Nicotinamide adenine dinucleotide phosphate (NADPH) oxidase-dependent ROS generation contributes to CORM-2-induced HO-1 expression in HTSMCs. (A) Cells were pretreated without or with diphenyleneiodonium (DPI) or apocynin (APO) for 1 h before exposure to CORM-2 for 24 h.

The protein levels of HO-1 and β -actin (served as an internal control) were determined by Western blot. (B) Cells were pretreated with DPI (10 μ M) or APO (100 μ M) for 1 h, and then incubated with CORM-2 for 6 h. The mRNA expression of HO-1 was determined by real-time PCR. (C) Cells were incubated with CORM-2 (50 μ M) for the indicated time intervals. The Nox activity was analyzed. (D,E) Cells were pretreated without or with (D) DPI (10 μ M) or APO (100 μ M), and (E) Ro31-8220 (10 μ M), Gö6976 (10 μ M), or PF431396 (10 μ M) for 1 h, and then incubated with CORM-2 for 6 h. The Nox activity and ROS generation were analyzed. (F) CMH2, DCF-DA, and DHE staining, cells were treated with CORM-2 for 6 h in the absence or presence of DPI (10 μ M), APO (100 μ M), Gö6976 (10 μ M), or PF431396 (10 μ M). The fluorescence images were detected by a fluorescence microscope. Image of fluorescence microscope, 400 \times . (G) Cells were transfected with either scrambled (Scrb), Nox-(1,2,4), or p47^{phox} siRNA, and then incubated with CORM-2 for 24 h. The levels of Nox-(1,2,4), p47^{phox}, HO-1, and β -actin (served as an internal control) protein were determined by Western blot. Data are expressed as mean \pm SEM of five independent experiments ($n = 5$). # $p < 0.05$, as compared with the cells exposed to vehicle (C,G) or CORM-2 alone (A,B,D,E). Data analysis and processing are described in the section “Statistical Analysis of Data”.

2.4. CORM-2 Induces HO-1 Expression via PKC α

Our previous report and the others also indicate that PKCs are involved in HO-1 expression in brain astrocytes [25]. Thus, we investigated whether PKC members are involved in the CORM-2-induced HO-1 expression. We found that pretreatment of HTSMCs with Ro31-8220 (a pan-PKC inhibitor) concentration-dependently attenuated the HO-1 induction by CORM-2 (Figure 4A). Next, to determine which PKC isoforms, PKC α especially, mediate CORM-2-induced HO-1 expression, two selective PKC α inhibitors (Gö6976 and Gö6983) were used for these purposes. The usage of Gö6983, an ATP-competitive bisindolylmaleimide PKC inhibitor, blocks the PKC phosphorylation [34]. Our previous report also indicates that Gö6983 inhibits PKC α / β II phosphorylation stimulated by thrombin in SK-N-SH (human neuroblastoma) cells [35]. We found that pretreatment with either Gö6976 or Gö6983 concentration-dependently blocked CORM-2-induced HO-1 expression in HTSMCs (Figure 4A), indicating that PKC α was involved in CORM-2-induced HO-1 expression. Moreover, pretreatment with Ro31-8220 (10 μ M), Gö6976 (10 μ M), or Gö6983 (10 μ M) significantly inhibited CORM-2-induced HO-1 mRNA expression (Figure 4B). The role of PKC α in CORM-2-induced HO-1 expression was further confirmed by transfection with PKC α siRNA, which significantly knocked down PKC α protein and blocked the CORM-2-induced HO-1 expression (Figure 4C). In addition, the activation of PKC α / β II in CORM-2-induced responses was confirmed by determining their phosphorylation. As shown in Figure 4D, CORM-2 time-dependently stimulated PKC α / β II phosphorylation with a maximal response within 2–4 h, which was attenuated by pretreatment with Gö6983 (10 μ M), but not by pretreatment with APO, DPI, or NAC, indicating that PKC α / β II are the upstream components of Nox/ROS in HO-1 expression. This note was also supported by the results that pretreatment with either Ro31-8220 or Gö6976 inhibited the CORM-2-stimulated Nox activity and ROS generation (Figure 3E,F). These results suggested that HO-1 expression induced by CORM-2 is mediated via PKC α / β II-dependent Nox activation and ROS generation in HTSMCs.

2.5. Involvement of Pyk2 in CORM-2-Induced HO-1 Expression

Previous reports have indicated that PF431396 treatment attenuates proline-rich tyrosine kinase 2 (Pyk2) phosphorylation at Tyr (tyrosine)⁴⁰² in various types of cells [36,37]. To investigate the role of Pyk2 in HO-1 expression, PF431396 (a Pyk2 inhibitor) was used. In this study, we found that pretreatment with PF431396 concentration-dependently attenuated CORM-2-induced both of HO-1 protein (Figure 5A) and mRNA (Figure 5B) expression. To confirm the role of Pyk2 in CORM-2-induced HO-1 expression, Pyk2 siRNA transfection significantly knocked down the Pyk2 protein level and inhibited CORM-2-induced HO-1 expression (Figure 5C). We further determined whether CORM-2 stimulated activation of Pyk2; the phosphorylation of Pyk2 was detected by Western blot. As shown in Figure 5D, CORM-2 time-dependently stimulated Pyk2 phosphorylation, which was attenuated by

pretreatment of PF431396 (10 μ M), but not by APO, DPI, or NAC, indicating that Pyk2 is an upstream component of Nox/ROS in HO-1 expression. This note was also supported by the results that PF431396 attenuated the CORM-2-triggered Nox activity and ROS generation (Figure 3E,F). These findings indicated that HO-1 expression by CORM-2 is mediated via a Pyk2-dependent Nox/ROS activity in HTSMCs.

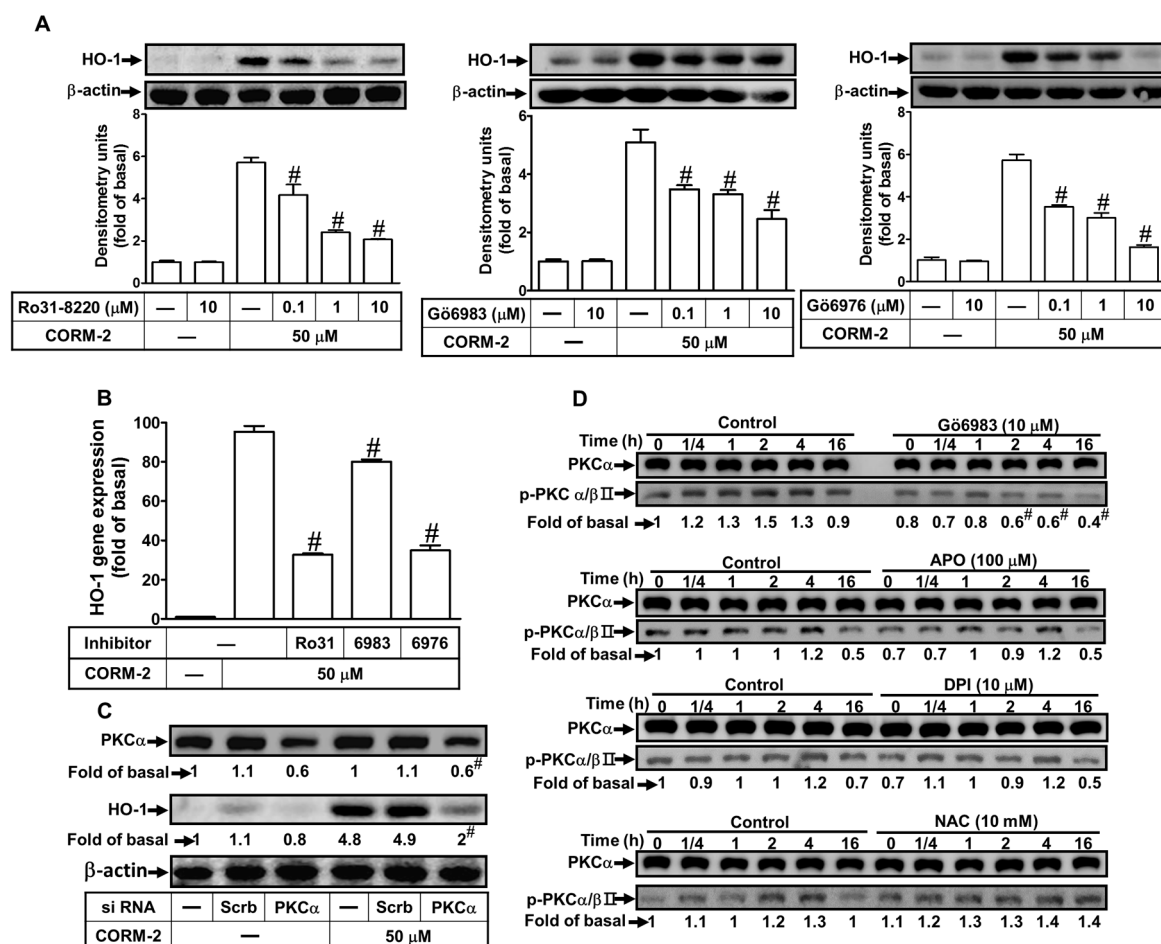


Figure 4. CORM-2 induces HO-1 expression via a PKC α -dependent pathway in HTSMCs. (A) Cells were pretreated with Ro31-8220, Gö6983, or Gö6976 for 1 h, and then incubated with CORM-2 (50 μ M) for 24 h. The protein levels of HO-1 and β -actin (served as an internal control) were determined by Western blot. (B) Cells were pretreated with Ro31-8220 (10 μ M), Gö6983 (10 μ M), or Gö6976 (10 μ M) for 1 h, and then incubated with CORM-2 for 6 h. The mRNA expression of HO-1 was determined by real-time PCR. (C) Cells were transfected with either scrambled (Scrb) or protein kinase C (PKC α) siRNA, and then incubated with CORM-2 for 24 h. The levels of PKC α , HO-1, and β -actin (served as an internal control) protein were determined by Western blot. (D) Cells were pretreated without or with Gö6983 (10 μ M), APO (100 μ M), DPI (10 μ M), or NAC (10 mM) for 1 h, and then incubated with CORM-2 for the indicated time intervals. The levels of phospho-PKC α and PKC α were determined by Western blot. Data are expressed as mean \pm SEM of five independent experiments ($n = 5$). [#] $p < 0.05$, as compared with the cells exposed to CORM-2 alone. Data analysis and processing are described in the section “Statistical Analysis of Data”.

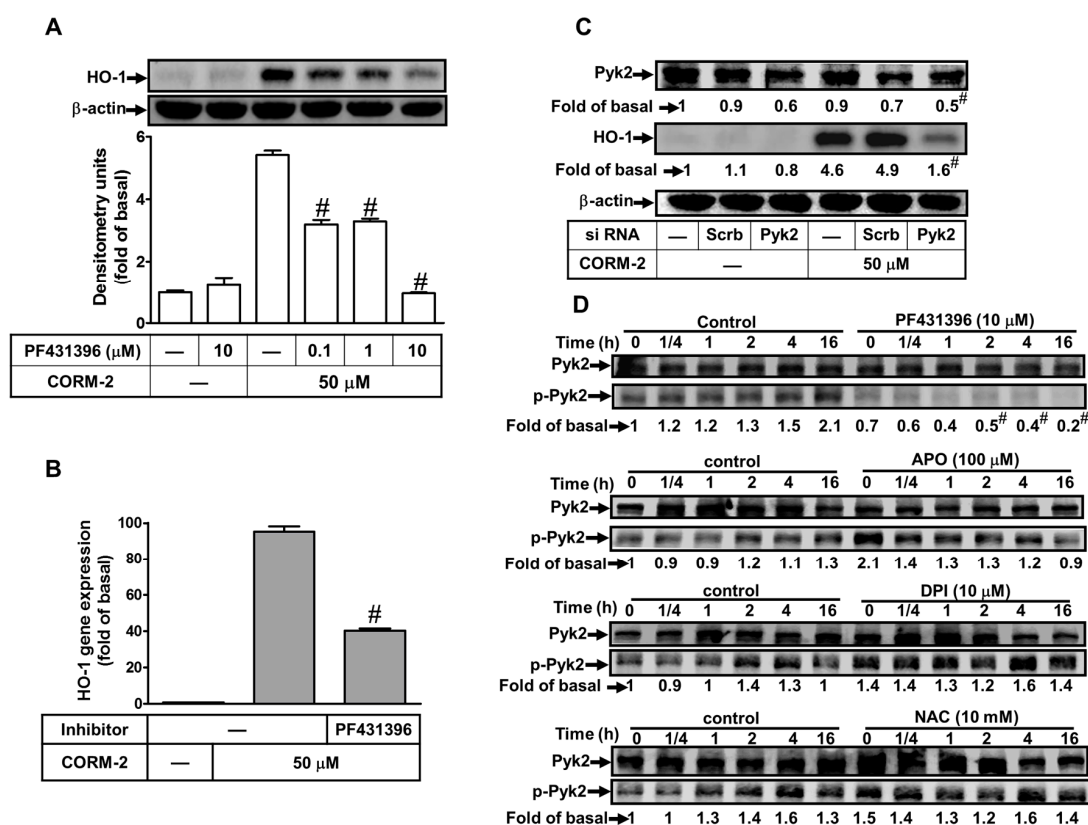


Figure 5. Proline-rich tyrosine kinase 2 (Pyk2) is involved in CORM-2-induced HO-1 expression in HTSMCs. (A) Cells were pretreated with PF431396 for 1 h, and then incubated with CORM-2 for 24 h. The protein levels of HO-1 and β -actin (served as an internal control) were determined by western blot. (B) Cells were pretreated with PF431396 (10 μ M) for 1 h, and then incubated with CORM-2 for 6 h. The mRNA expression of HO-1 was determined by real-time PCR. (C) Cells were transfected with either scrambled (Scrb) or Pyk2 siRNA, and then incubated with CORM-2 for 24 h. The levels of Pyk2, HO-1, and β -actin (served as an internal control) protein were determined by Western blot. (D) Cells were pretreated without or with PF431396 (10 μ M), APO (100 μ M), DPI (10 μ M), or NAC (10 mM) for 1 h, and then incubated with CORM-2 for the indicated time intervals. The levels of phospho-Pyk2 and Pyk2 (served as an internal control) were determined by Western blot. Data are expressed as mean \pm SEM of five independent experiments ($n = 5$). [#] $p < 0.05$, as compared with the cells exposed to CORM-2 alone. Data analysis and processing are described in the section “Statistical Analysis of Data”.

2.6. Involvement of ERK1/2 in CORM-2-Induced HO-1 Expression

We have previously demonstrated that MAPKs participate in the HO-1 induction by LTA and CSPE in HTSMCs [20]. Therefore, we further approached the roles of p42/p44 MAPK in CORM-2-induced HO-1 expression in these cells. We found that pretreatment with a MEK1/2 inhibitor (U0126) significantly blocked HO-1 protein and mRNA expressions (Figure 6A,B), which were both CORM-2-induced. To further ensure the role of p42/p44 MAPK in CORM-2-induced HO-1 expression, transfection with p44 siRNA markedly knocked down the p44 protein level and blocked the CORM-2-induced HO-1 expression (Figure 6C). To confirm whether p42/p44 MAPK phosphorylation is necessary for CORM-2-induced HO-1 expression, activation of the kinases was assayed by Western blot using an antibody specific for the phosphorylated form of p42/p44 MAPK. As shown in Figure 6D, CORM-2 stimulated a time-dependent phosphorylation of p42/p44 MAPK, which was inhibited by pretreatment with U0126 (10 μ M) during the period of observation. Further, pretreatment with Gö6983, PF431396, NAC, DPI, or APO significantly attenuated CORM-2-stimulated p42/p44 MAPK phosphorylation (Figure 5D), indicating that p42/p44 MAPK was a downstream component of PKC α , which is a

Pyk2-mediated Nox/ROS generation pathway. Our findings demonstrated that CORM-2-induced HO-1 expression is mediated through the activation of the PKC α , Pyk2/Nox/ROS/p42/p44 MAPK pathway in HTSMCs.

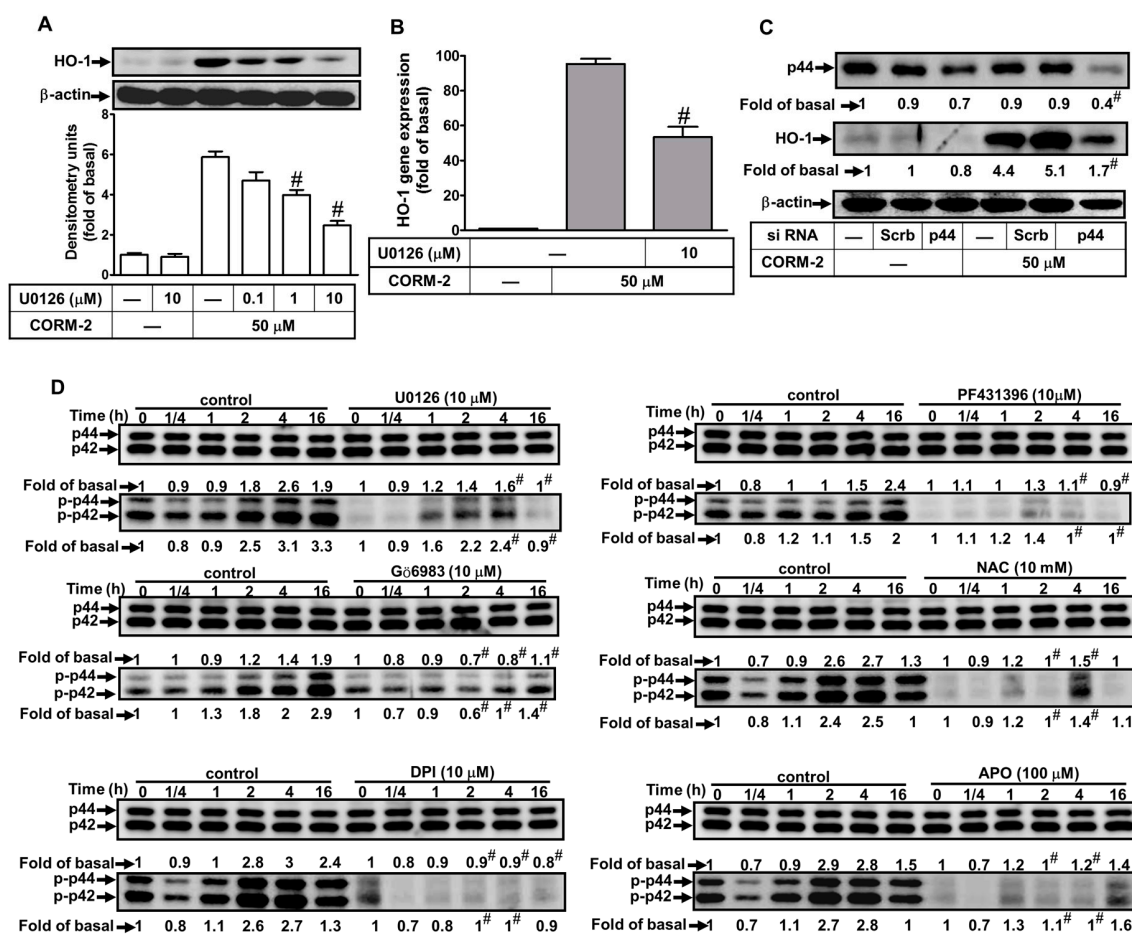


Figure 6. CORM-2-induced HO-1 expression is mediated through extracellular signal-regulated kinase 1/2 (ERK1/2) in HTSMCs. (A) Cells were pretreated with U0126 for 1 h, and then incubated with CORM-2 for 24 h. The protein levels of HO-1 and β -actin (served as an internal control) were determined by Western blot. (B) Cells were pretreated with U0126 (10 μ M) for 1 h, and then incubated with CORM-2 for 6 h. The mRNA expression of HO-1 was determined by real-time PCR. (C) Cells were transfected with either scrambled (Scrb) or p44 siRNA, and then incubated with CORM-2 for 24 h. The levels of p44 and HO-1 protein were determined by Western blot. (D) Cells were pretreated with or without U0126 (10 μ M), Gö6983 (10 μ M), PF431396 (10 μ M), NAC (10 mM), DPI (10 μ M), or APO (100 μ M), and then incubated with CORM-2 for the indicated time intervals. The levels of phospho-p42/p44 MAPK and p42/p44 MAPK (served as an internal control) were determined by Western blot. Data are expressed as mean \pm SEM of five independent experiments ($n = 5$). [#] $p < 0.05$, as compared with the cells exposed to CORM-2 alone. Data analysis and processing are described in the section “Statistical Analysis of Data”.

2.7. Induction of c-Fos and c-Jun/AP-1 is Required for CORM-2-Induced HO-1 Expression

Moreover, AP-1 has been shown to regulate HO-1 expression through binding to respective elements in the promoter region in response to oxidative stress [38,39]. Hence, we determined whether CORM-2-induced HO-1 expression was mediated via AP-1 using its inhibitor tanshinone IIA (TSIIA). As shown in Figure 7A,B, pretreatment with TSIIA attenuated CORM-2-induced HO-1 protein and mRNA expression, suggesting that in HTSMCs, activated AP-1 is an important event for CORM-2-induced HO-1 expression. To further approach the roles of c-Fos and c-Jun in CORM-2-induced HO-1 expression, transfection with either c-Fos or c-Jun siRNA significantly knocked down the c-Fos

or c-Jun protein expression, respectively, and attenuated HO-1 induction in CORM-2-treated HTSMCs (Figure 7C). To study whether CORM-2 accelerated AP-1 transcription activity, a reporter plasmid construct containing the AP-1 response element was used to evaluate AP-1 activity in HTSMCs. We found that CORM-2 stimulated a time-dependent AP-1 promoter activity (Figure 7D), which was inhibited by pretreatment with Gö6983, PF431396, NAC, DPI, APO, U0126, or TSIIA (Figure 7E). These results suggested that HO-1 induction is mediated via PKC α , Pyk2/Nox/ROS/p42/p44 MAPK-dependent activation of AP-1(c-Fos/c-Jun) in CORM-2-treated HTSMCs.

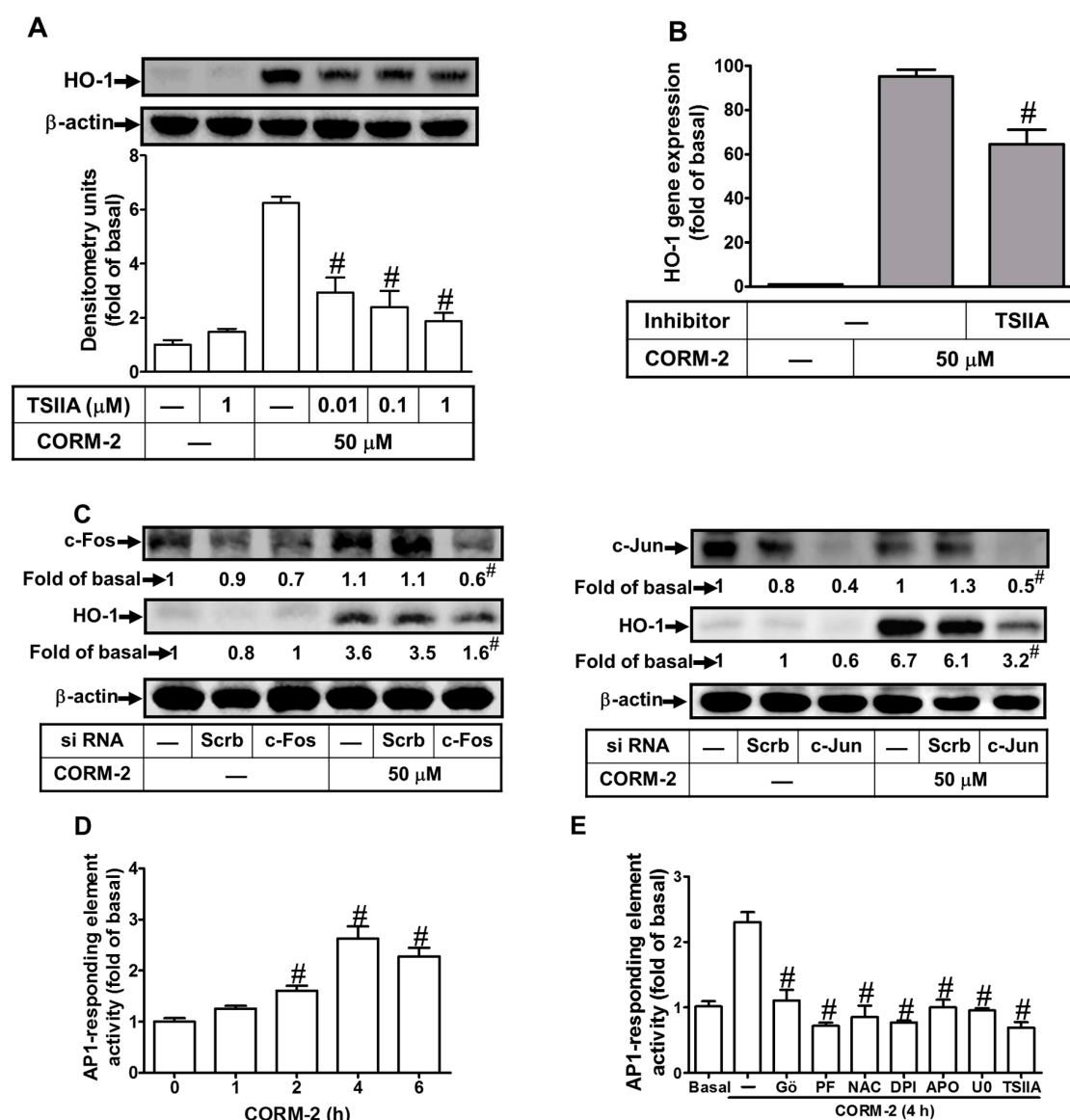


Figure 7. Involvement of c-Fos and c-Jun/activator protein 1 (AP-1) in CORM-2-mediated HO-1 expression. (A) Cells were pretreated with tanshinone IIA (TSIIA) for 1 h, and then incubated with CORM-2 for 24 h. The protein levels of HO-1 and β -actin (served as an internal control) were determined by Western blot. (B) Cells were pretreated with TSIIA (1 μ M) for 1 h, and then incubated with CORM-2 for 6 h. The mRNA expression of HO-1 was determined by real-time PCR. (C) Cells were transfected with either scrambled (Scrb), c-Fos, or c-Jun siRNA, and then incubated with CORM-2 for 24 h. The levels of c-Fos, c-Jun, HO-1, and β -actin (served as an internal control) protein were determined by Western blot. (D) Cells were transiently cotransfected with pAP1-Luc (activator protein-1 luciferase reporter plasmid) and pGal (plasmid contains the reporter gene β -galactosidase) for 24 h, and then incubated with CORM-2 for the indicated time intervals. (E) Cells were pretreated with Gö6983 (10 μ M),

PF431396 (10 μ M), N-acetyl-cysteine (NAC, 10 mM), DPI (10 μ M), APO (100 μ M), U0126 (10 μ M), or TSIIA (1 μ M) for 1 h and then incubated with CORM-2 for 4 h. The AP-1 promoter activity in the cell lysates was determined as described in the Methods section. Data are expressed as mean \pm SEM of five independent experiments ($n = 5$). $^{\#} p < 0.05$, as compared with the cells exposed to vehicle (D) or CORM-2 (A–C,E) alone. Data analysis and processing are described in the section “Statistical Analysis of Data”.

2.8. CORM-2 Induces HO-1 Expression via Its Promoter Transcriptional Activity

CORM-2 has been shown to induce HO-1 gene regulation and activate the AP-1 activity. Thus, human HO-1 promoter was constructed in a luciferase reporter plasmid to evaluate the CORM-2 induced HO-1 transcription in HTSMCs. The HO-1 promoter contains several putative recognition elements for a variety of transcriptional factors, including the AP-1 site. As expected, CORM-2 stimulated the HO-1 promoter activity in a time-dependent manner with a maximal response within 6 h (Figure 8A), which was inhibited by pretreatment with Gö6983, PF431396, NAC, DPI, APO, U0126, or TSIIA (Figure 8B). These results confirmed that CORM-2 stimulates HO-1 promoter activity via AP-1 activation, which was mediated through PKC α or Pyk2-regulated Nox/ROS/p42/p44 MAPK-dependent c-Fos-c-Jun/AP-1 pathway in HTSMCs.

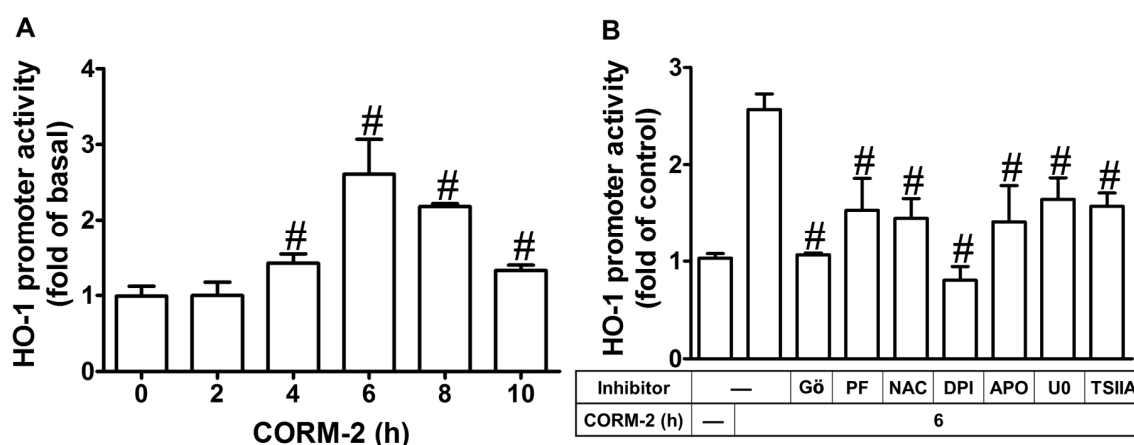


Figure 8. CORM-2 induces AP-1-dependent HO-1 expression via PKC α /Pyk2/Nox/ROS/ERK pathway in HTSMCs. (A) Cells were transiently cotransfected with pHO1-Luc and pGal for 24 h, and then incubated with CORM-2 (50 μ M) for the indicated time intervals. (B) Cells were pretreated with Gö6983 (10 μ M), PF431396 (10 μ M), NAC (10 mM), DPI (10 μ M), APO (100 μ M), U0126 (10 μ M), or TSIIA (10 μ M) for 1 h and then incubated with CORM-2 for 6 h. The HO-1 promoter activity in the cell lysates was determined. Data are expressed as mean \pm SEM of five independent experiments ($n = 5$). $^{\#} p < 0.05$, as compared with the cells exposed to vehicle (A) or CORM-2 alone. Data analysis and processing are described in the section “Statistical Analysis of Data”.

3. Discussion

CORMs exert anti-inflammatory effects through the up-regulation of anti-oxidant enzymes such as HO-1 [26]. However, the roles of Nox/ROS involved in CORM-2-induced HO-1 expression were still unknown. Here, we observed that pretreatment with CORM-2 inhibited the LPS-induced airway inflammation via HO-1 induction in mice. Further, our results demonstrated that the levels of HO-1 protein, mRNA, and promoter activity were increased in HTSMCs challenged with CORM-2. CORM-2-induced HO-1 expression was mediated through PKC α and Pyk2/Nox/ROS/ERK1/2 linking to the AP-1 pathway in HTSMCs (Figure 9). These results suggested that HO-1 expression induced by CORM-2 is mediated via a PKC α and Pyk2/Nox/ROS/p42/p44 MAPK-dependent AP-1 pathway in HTSMCs.

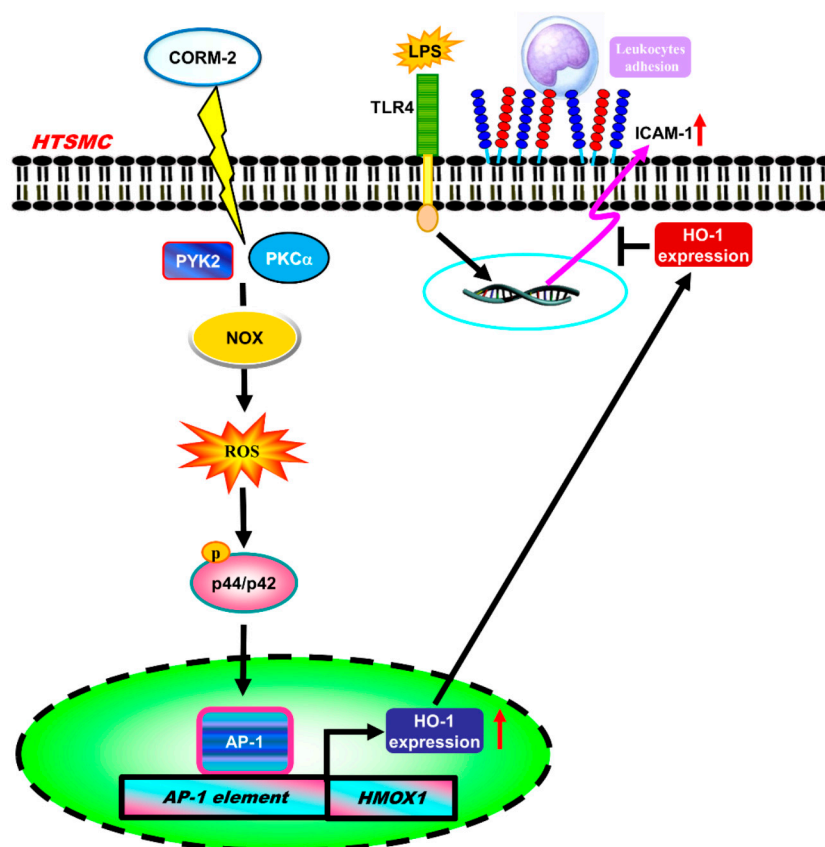


Figure 9. Schematic signaling pathways are involved in CORM-2-induced HO-1 expression in HTSMCs. CORM-2-induced HO-1 expression is mediated via a PKC α or Pyk2/Nox/ROS/ERK1/2 cascade linking to activation of c-Fos and c-Jun/AP-1. The up-regulation of HO-1 could protect against the LPS-induced airway inflammation.

ROS exert as a messenger in the normal physiological functions and the inflammatory responses dependent on their cellular concentrations [40]. The up-regulation of HO-1 due to Nox activity and ROS formation is induced by LPS and cytokines [8,19]. Others and our previous studies indicated that the CORMs mediate Nox-dependent ROS generation in astrocytes [21,22]. Therefore, Nox-dependent ROS generation is involved in HO-1 expression by CORM-2 in HTSMCs. We further clarified the role of ROS in HO-1 expression; a thiol-containing compound (NAC) was used to scavenge ROS. NAC has been shown to reduce the injurious effects of hydrogen peroxide in human alveolar and bronchial epithelial cells [41]. We also found that CORM-2-induced HO-1 expression was inhibited by NAC, and strongly supported the role of ROS in the CORM-2-induced HO-1 expression.

Moreover, two Nox-related inhibitors, DPI (a Nox inhibitor) and APO (a p47^{phox} inhibitor), have been shown to prevent p47^{phox} (a Nox subunit) translocation to the membrane and inhibit Nox activation [42]. Our results showed that pretreatment with either DPI or APO attenuated CORM-2-induced ROS generation and HO-1 expression. These data are consistent with previous reports showing that Nox-derived ROS generation is involved in HO-1 induction by LTA or CSPE in HTSMCs [5,20]. Indeed, low levels of ROS could regulate proliferation, gene expression, immunity, and wound healing [43]. Conversely, higher levels of ROS can exert antibacterial effect, and cause cell damage and death [23,44]. In addition, ROS generation could initiate HO-1 expression through the degradation of Keap1 and translocation of Nrf2 into the nucleus. In our previous study, CORM-2 has been shown to activate Nox and produce ROS in brain astrocytes [22]. Previous reports also indicate that CO release in mammal cells acts as a secondary messenger to mediate metabolism and gene expression, including HO-1 [45,46]. The members of Nox family such as Nox-(1,2,4) and p47^{phox} were shown to be involved in CORM-2-induced HO-1 expression, which were confirmed by using their own siRNAs. In this

study, we also demonstrated that PKC α and Pyk2 are the upstream components of ROS generation by their inhibitors. Our results showed that PKC α /Pyk2-mediated Nox/ROS signal contributes to CORM-2-induced HO-1 expression in HTSMCs. However, how CORM-2 activated PKC α /Pyk2 and led to Nox/ROS generation is an important issue preserved for further investigation.

Abnormal MAPK activations are implicated in a variety of inflammatory responses and tissue injury, and the induction of several inflammatory mediators in different cell types [25,47]. Here, we demonstrated that ERK1/2 was required for the CORM-2-induced HO-1 expression, which was attenuated by a selective MEK1/2 inhibitor U0126 or transfection with p44 siRNA. These kinases involved in CORM-2-stimulated pathways were further confirmed by CORM-2-mediated ERK1/2 phosphorylation. These results are consistent with the HO-1 expression mediated by ERK1/2 to activate the antioxidant response element (ARE) region, which is the Nrf2 binding site in HepG2 (liver hepatocellular carcinoma) Cells [48] and heme-mediated neuronal injury [49]. Moreover, pretreatment with the inhibitor of PKC α , Pyk2, Nox, or ROS scavenger significantly attenuated ERK1/2 phosphorylation, suggesting that PKC α /Pyk2-dependent Nox/ROS are required for ERK1/2 phosphorylation. These results are consistent with reports that ROS-dependent MAPK pathways are involved in the regulation of cellular functions [38,50,51]. Indeed, our previous study found that the inhibition of JNK1/2 or p38 MAPK attenuates CORM-2-induced HO-1 expression via a c-Src/EGFR/PI3K/Akt pathway [27]. In contrast, CORM-2-stimulated JNK1/2 and p38 MAPK phosphorylation was not mediated via the PKC α /Pyk2-mediated Nox/ROS signal, although these two kinases also regulate CORM-2-induced HO-1 expression in HTSMCs.

The activated transcription factors interact with response elements on the HO-1 promoter to regulate gene transcription [44]. Here, we focused on the role of transcription factor AP-1, which is modulated during oxidative stress associated with inflammatory diseases [52]. The involvement of AP-1 in these responses was further supported by the results that CORM-2 induced c-Fos and c-Jun, AP-1 subunits, and activation via PKC α /Pyk2-mediated Nox/ROS linking to the ERK1/2 pathway. Moreover, the roles of c-Fos-c-Jun/AP-1 in CORM-2-induced HO-1 expression were confirmed by transfection with c-Fos or c-Jun siRNA to attenuate CORM-2-induced HO-1 expression. Several reports have shown that many regulatory elements of transcription factors, including AP-1, were analyzed on the 5' region of the HO-1 promoter in several animal species [28,53]. Thus, we also demonstrated that CORM-2-stimulated HO-1 promoter activity was reduced by pretreatment with G66976, PF431396, NAC, DPI, APO, U0126, or TSIIA, indicating that CORM-2 induces HO-1 promoter activity via a PKC α /Pyk2-mediated Nox/ROS/ERK1/2/AP-1 pathway. These results are consistent with the reports that alpha-lipoic acid induced HO-1 expression in vascular smooth muscle cells [54], and BK induced HO-1 expression in brain astrocytes [38].

Previous reports indicated that the CORMs up-regulate the HO-1 activity and attenuate the LPS-induced inflammatory responses in macrophages [9] and animal study [8,31]. Moreover, the overexpression of HO-1 in ovalbumin (OVA)-sensitized guinea pigs effectively decreases inflammatory reaction, mucus secretion, and responsiveness to histamine in airways [55], suggesting that HO-1 exhibits protecting ability in the host during airway inflammation. In this study, the induction of HO-1 by CORM-2 protected against LPS-induced ICAM-1 expression and leukocytes infiltration in both in vitro and in vivo studies. Importantly, previous reports also indicated that CORM-2-derived CO release can attenuate the cell sequestration, NF- κ B activity, and ICAM-1 expression of leukocyte after lung injury [36,56] and regulate the expressions of adhesion molecules on human umbilical vein endothelial cells to affect leukocyte attachment [54]. Our previous report also indicated that the induction of HO-1 by CoPPiX inhibits the TNF- α -induced ICAM-1 and VCAM-1 expression which is reversed by zinc protoporphyrin IX (ZnPPiX, an inhibitor of HO-1 activity) in HTSMCs [14].

4. Materials and Methods

4.1. Reagents and Chemicals

DMEM/F-12 (Dbecco's Modified Eagle Medium/Nutrient Mixture F-12) medium, fetal bovine serum (FBS), TRIzol reagent, and PLUS-Lipofectamine were from Invitrogen (Carlsbad, CA, USA). Human siRNAs for PKC α (L-003523-00-0020) was from Dharmacon (Lafayette, CO, USA) and Pyk2 (SASI_Hs01_00032249), ERK1 (SASI_Hs01_00190617), HO-1 (SASI_Hs01_00035065), Nox-1 (SASI_Hs01_00342845), Nox-2 (SASI_Hs01_00086110), Nox-4 (SASI_Hs02_00349918), p47^{phox} (SASI_Hs02_00302212), and c-Fos (SASI_Hs01_00184572) were from Sigma (St. Louis, MO, USA). Hybond C membrane, enhanced chemiluminescence (ECL), and Western blotting detection system were from GE Healthcare Biosciences (Buckinghamshire, UK). PhosphoPlus PKC α (#9375), Pyk2 (#3291), and ERK1/2 (#9101) antibodies were from Cell Signaling (Danvers, MA, USA). The HO-1 (ADI-SPA-895) antibody was from Enzo (Farmingdale, NY, USA). PKC α (sc-208), Pyk2 (sc-9019), ERK1 (sc-94), c-Fos (sc-7202), and β -actin (sc-47778) antibodies were from Santa Cruz (Santa Cruz, CA, USA). Ro31-8220, Gö6983, Gö6976, PF431396, diphenyleneiodonium chloride (DPI), apocynin (APO), U0126, and tanshinone IIA (TSIIA) were from Biomol (Plymouth Meeting, PA, USA). The bicinchoninic acid (BCA) protein assay kit was from Pierce (Rockford, IL, USA). SDS-PAGE (sodium dodecyl sulfate polyacrylamide gel electrophoresis) reagents were from MDBio Inc (Taipei, Taiwan). Tricarbonyldichlororuthenium (II) dimer (CORM-2), ruthenium (III) chloride, RuCl₃ [inactive form of CORM-2, (iCORM-2)], N-acetyl-cysteine (NAC), lipopolysaccharide (LPS), enzymes, and other chemicals were from Sigma (St. Louis, MO, USA).

4.2. Animal Care and Experimental Procedures

Male ICR mice aged 6–8 weeks were purchased from the National Laboratory Animal Centre (Taipei, Taiwan) and handled according to the guidelines of Animal Care Committee of Chang Gung University (Approval Document No. Chang Gung University 16-046, 4 October 2016) and National Institute of Health (NIH) Guides for the Care and Use of Laboratory Animals. All the studies involving animals are reported in accordance with the ARRIVE guidelines [57,58]. Mice were assigned randomly into three groups: sham [0.1 mL of dimethyl sulfoxide (DMSO)-phosphate-buffered saline (PBS) (1:100) with 0.1% (*w/v*) bovine serum albumin (BSA) treated mice], LPS (LPS-treated mice), and CORM-2 + LPS; 5 mice in each group/cage and kept in standard individually ventilated cages in an animal facility under standardized conditions (12 h light/dark cycle, 21–24 °C, humidity of 50–60%) with food and water ad libitum. Mice were intraperitoneally (i.p.) injected with CORM-2 (8 mg/kg of body weight) for 24 h, and then anesthetized by i.p. injection of pentothal (50 mg/kg) placed individually on a board in a near-vertical position and the tongues withdrawn with a lined forceps. LPS (3 mg/kg) was placed posterior in the throat and aspirated into lungs for 16 h of development of a lung inflammation model [59]. At the end of the experimental period, mice were killed by a high dose of pentothal (100 mg/kg i.p.) for the collection of lung tissues extracted for protein (right superior lobe + post caval lobe) and mRNA (right middle lobe + right inferior lobe) expression of ICAM-1, HO-1, or β -actin analyses. BAL fluid was performed through a tracheal cannula using 1-mL aliquots of ice-cold PBS solution. BAL fluid was centrifuged at 500 \times g at 4 °C, and cell pellets were washed and re-suspended in PBS. Leukocyte count was determined by a hemocytometer, as previously described [7]. Data collection and evaluation of all the in vivo and in vitro experiments were performed blindly of the group identity.

4.3. Cell Culture and Treatment

HTSMCs were purchased from ScienCell Research Laboratories (San Diego, CA, USA). The cultured conditions and treatments were conducted as previously described [60]. Cells were plated onto 12-well culture plates and made quiescent at confluence by incubation in serum-free DMEM/F-12 for 24 h. Growth-arrested cells were incubated with or without CORM-2 at 37 °C for the indicated time

intervals. Our previous report indicates that CORM-2 induces HO-1 expression in time-dependent and concentration-dependent manners. The HO-1 expression is up-regulated to a maximal response within 16–24 h treatment with 50 μ M of CORM-2 [27]. Therefore, the concentration of CORM-2 at 50 μ M was used throughout this study. When the inhibitors were used, cells were pretreated with the inhibitor for 1 h before exposure to CORM-2. Experiments were performed using cells from passages four to seven.

4.4. Preparation of Cell Extracts and Western Blot Analysis

After treatment, the cells were washed with ice-cold PBS, scraped, and collected by centrifugation at $16,000\times g$ for 10 min at 4 °C to yield the whole cell extract, as previously described [7]. The supernatants were harvested and mixed with SDS-PAGE loading buffer (final concentration: 100 mM Tris-HCl pH 6.8, 1% SDS, 2.5% glycerol, 100 mM β -mercaptoethanol, 0.01% bromophenol blue). Samples were denatured, separated with 10% SDS-PAGE, and transferred to the nitrocellulose membrane. Membranes were probed overnight with an anti-phospho-PKC α , phospho-Pyk2, phospho-ERK1/2, HO-1, PKC α , Pyk2, ERK1, c-Fos, or β -actin antibody. Membranes were washed with Tween-Tris buffered solution (TTBS) four times for 5 min each, incubated with anti-rabbit or anti-mouse horseradish peroxidase antibody (1:2000) for 1 h. The immunoreactive bands were detected by ECL (enhanced chemiluminescence) reagents and captured by a UVP BioSpectrum 500 Imaging System (Upland, CA, USA). The image densitometry analysis was conducted using UN-SCAN-IT gel software (Orem, UT, USA).

4.5. Total RNA Extraction and Real Time-Quantitative PCR Analysis

Total RNA was isolated from HTSMCs treated with CORM-2 for the indicated time intervals in 10-cm culture dishes with TRIzol according to the protocol of the manufacturer. The mRNA was reverse-transcribed into cDNA and analyzed by real time-quantitative (q)PCR. Real time-qPCR was performed with the TaqMan gene expression assay system, using primers and probe mixes for HO-1, c-Fos, and endogenous GAPDH control genes. PCRs were performed using a 7500 Real Time-PCR System (Applied Biosystems, Foster City, CA, USA). Relative gene expression was determined by the $\Delta\Delta C_t$ method, where C_t meant threshold cycle. All the experiments were performed in triplicate.

4.6. Plasmid Construction, Transfection, and Luciferase Reporter Gene Assays

For construction of the HO-1 luciferase (Luc) plasmid, human HO-1 promoter, a region spanning –3106 to +186 bp provided by Dr. Y. C. Liang (Graduate Institute of Biomedical Technology, Taipei Medical University, Taipei, Taiwan) was inserted into a pGL3-basic vector (Promega, Madison, WI, USA). Plasmid pAP1-Luc, the fragment of the AP-1-responding element was inserted into the pGL3 (plasmid contains the reporter gene β -galactosidase) promoter. The plasmid DNA was extracted by using QIAGEN plasmid DNA preparation kits and transfected into HTSMCs with Lipofectamine reagent according to the standard protocol of the manufacturer. The plasmid pCMV- β -gal was cotransfected to be the internal control. The HO-1 promoter-driven-Luc activity was analyzed by a luciferase assay system (Promega, Madison, WI, USA). Firefly luciferase activities were standardized with β -galactosidase activity.

4.7. Transient Transfection with siRNAs

HTSMCs (3×10^5 cells) were plated in 12-well culture plates for 24 h to about 80% confluence. Cells were washed once with PBS, and 0.4 mL of serum-free DMEM/F-12 medium was added to each well. The transient transfection of siRNAs (scrambled, PKC α , Pyk2, ERK1, and c-Fos, 100 nM) was performed by using LipofectamineTM RNAiMAX reagent (from Sigma, St. Louis, MO, USA) according to the manufacturer's instructions.

4.8. Measurement of Intracellular ROS Generation

The peroxide-sensitive fluorescent probe CMH₂DCF-DA and DHE were used to assess the intracellular ROS generation [61] with minor modifications. Briefly, HTSMCs were incubated with 10 μ M of CMH₂DCF-DA (in warm PBS) for 45 min at 37 °C. The medium was removed and replaced with fresh DMEM/F-12 media for CORM-2 treatments. CMH₂ DCF-DA interacted with cells, and then generated a non-fluorescent product: H₂DCF. CORM-2 induced the generation of a ROS oxidized product: DCF. Relative fluorescence intensity was recorded (0.5 to 24 h) by a fluorescent plate reader (Thermo, Appliskan; Waltham, MA, USA) at an excitation wavelength of 485 nm, and emission was measured at a wavelength of 530 nm. For DHE staining, cells were treated with CORM-2 for the indicated time intervals and then incubated with 10 μ M of DHE (in DMEM/F12 medium) for 10 min. For immunofluorescence staining, the stained cells were washed three times with cold PBS, and then the fluorescence for DCF and DHE staining was detected at 495/529 and 518/605 nm, respectively, using a fluorescence microscope (Zeiss, Axiovert 200M; Oberkochen, Baden-Württemberg, Germany).

4.9. Determination of NADPH Oxidase Activity by Chemiluminescence Assay

The Nox activity in intact cells was assayed by lucigenin chemiluminescence [38]. After incubation, the cells were gently scraped and centrifuged at 400× *g* for 10 min at 4 °C. The cell pellet was re-suspended in a known volume (35 μ L/well) of ice-cold RPMI 1640 medium, and the cell suspension was kept on ice. To a final 200 μ L of pre-warmed (37 °C) PBS containing either NADPH (1 μ M) or lucigenin (20 μ M), 5 μ L of cell suspension (2×10^4 cells) was added to initiate the reaction followed by the immediate measurement of chemiluminescence using an Appliskan luminometer (Thermo®; Waltham, MA, USA) in an out-of-coincidence mode. Neither NADPH nor NADH enhanced the background chemiluminescence of lucigenin alone (30–40 counts/min). Chemiluminescence was continuously measured for 12 min, and the activity of Nox was expressed as counts per million cells. The calculated numbers of Nox activity were calibrated with protein concentration. The equal amount of warmed PBS medium (containing NADPH and lucigenin) was used as the blank, and the untreated cells were the basal group.

4.10. Statistical Analysis of Data

All the data were expressed as the mean \pm SEM in at least five individual experiments ($n = 5$). Statistical analysis was performed by using GraphPad Prism Program 6.0 software (GraphPad, San Diego, CA). We used one-way ANOVA followed by Dunnett's post hoc test when comparing more than two groups of data and a one-way ANOVA, non-parametric Kruskal–Wallis test, followed by Dunnett's post hoc test when comparing multiple independent groups. *p* values of 0.05 were considered to be statistically significant. Post tests were run only if *F* achieved $p < 0.05$ and there was no significant variance in homogeneity. Error bars were omitted when they fell within the dimensions of the symbols.

5. Conclusions

These results suggested that CORM-2-induced HO-1 expression is mediated through PKC α /Pyk2 and Nox/ROS-dependent activation of ERK1/2, linking to the up-regulation of AP-1 (c-Fos and c-Jun), which promotes HO-1 expression and enzymatic activity in HTSMCs. Based on the observations from literatures and our findings, we depict a model for the molecular mechanisms underlying CORM-2-induced HO-1 expression and activity in HTSMCs. The results obtained with cellular and animal experiments indicated that better understanding the mechanisms underlying CORM-2-induced HO-1 expression promotes the development of therapeutic strategies for airway inflammatory disorders.

Author Contributions: C.-C.L., L.-D.H., R.-L.C., and C.-M.Y. designed and conducted the study. C.-C.L., L.-D.H., and R.-L.C. performed and collected the data. C.-C.L., L.-D.H., R.-L.C., and C.-M.Y. analyzed and interpreted the data. C.-C.L. and C.-M.Y. prepared the manuscript. C.-C.L., L.-D.H., R.-L.C., and C.-M.Y. reviewed the manuscript. C.-C.L., L.-D.H., R.-L.C., and C.-M.Y. approved the final manuscript.

Funding: This work was supported by the Ministry of Education, Taiwan [grant number EMRPD1I0381]; the Ministry of Science and Technology, Taiwan [Grant numbers: MOST105-2320-B-182-005-MY3, MOST107-2320-B-182-020-MY2, and MOST107-2320-B-182A-011]; Chang Gung Medical Research Foundation, Taiwan [Grant numbers: CMRPD1F0023, CMRPD1F0552, CMRPD1F0553, CMRPD1I0051-3, CMRPG3F1533, CMRPG3H0062, CMRPG3H0063, and CMRPG5F0203, CMRPG5I0041].

Acknowledgments: We appreciated Chen-yu Wang for his suggestions and construction of plasmids applied in this study and YC Tai for her technical assistance.

Conflicts of Interest: The authors declare no conflict of interest.

Abbreviations

AP-1	activator protein 1
APO	apocynin
ARE	antioxidant response element
BAL	bronchoalveolar lavage
BCA	bicinchoninic acid
BSA	Bovine serum albumin
CO	carbon monoxide
CORM-2	carbon monoxide releasing molecule-2
CoPPiX	cobalt protoporphyrin
CSPE	cigarette smoke particle extract
DCF	dichlorofluorescein
DCF-DA	2',7'-dichlorofluorescein diacetate
DHE	dihydroethidium
DMEM/F-12	Dubecco's Modified Eagle Medium/Nutrient Mixture F-12
DMSO	dimethyl sulfoxide
DPI	diphenyleneiodonium
ECL	enhanced chemiluminescence
EGFR	epidermal growth factor receptor
ERK1/2	extracellular signal-regulated kinase 1/2
FBS	fetal bovine serum
MCH ₂ DCF-DA	chloromethyl 2',7'-dichloro fluorescein diacetate
H & E	hematoxylin & eosin
HO-1	heme oxygenase-1
HTSMCs	human tracheal smooth muscle cells
ICAM-1	intercellular adhesion molecule
ICR	Institute of Cancer Research
i.p.	intraperitoneally
LPS	lipopolysaccharide
LTA	lipotechoic acid
MAPKs	mitogen-activated protein kinases
mRNA	messenger ribonucleic acid
NAC	N-acetyl-cysteine
NADPH	nicotinamide adenine dinucleotide phosphate
NF-κB	nuclear factor-κB
Nox	NADPH oxidase
Nrf2	nuclear factor erythroid 2-related factor 2
PBS	phosphate-buffered saline
PI3K	phosphoinositide 3-kinase
PKC	protein kinase C
Pyk2	proline-rich tyrosine kinase 2
ROS	reactive oxygen species

SDS-PAGE	sodium dodecyl sulfate polyacrylamide gel electrophoresis
siRNA	small interfering ribonucleic acid
TNF	tumor necrosis factor
TSIIA	tanshinone IIA
TTBS	Tween-Tris buffered solution
VCAM-1	vascular cell adhesion molecule
XTT	2,3-bis-(2-methoxy-4-nitro-5-sulphophenyl)-2H-tetrazolium-5-carboxanilide
ZnPP IX	zinc protoporphyrin IX

References

1. Maines, M.D. The heme oxygenase system: A regulator of second messenger gases. *Annu. Rev. Pharmacol. Toxicol.* **1997**, *37*, 517–554. [[CrossRef](#)]
2. Ryter, S.W.; Alam, J.; Choi, A.M. Heme oxygenase-1/carbon monoxide: From basic science to therapeutic applications. *Physiol. Rev.* **2006**, *86*, 583–650. [[CrossRef](#)] [[PubMed](#)]
3. Tenhunen, R.; Marver, H.S.; Schmid, R. The enzymatic conversion of heme to bilirubin by microsomal heme oxygenase. *Proc. Natl. Acad. Sci. USA* **1968**, *61*, 748–755. [[CrossRef](#)] [[PubMed](#)]
4. Otterbein, L.E.; Soares, M.P.; Yamashita, K.; Bach, F.H. Heme oxygenase-1: Unleashing the protective properties of heme. *Trends Immunol.* **2003**, *24*, 449–455. [[CrossRef](#)]
5. Lee, I.T.; Wang, S.W.; Lee, C.W.; Chang, C.C.; Lin, C.C.; Luo, S.F.; Yang, C.M. Lipoteichoic acid induces HO-1 expression via the TLR2/MyD88/c-Src/NADPH oxidase pathway and Nrf2 in human tracheal smooth muscle cells. *J. Immunol.* **2008**, *181*, 5098–5110. [[CrossRef](#)] [[PubMed](#)]
6. Balla, G.; Jacob, H.S.; Balla, J.; Rosenberg, M.; Nath, K.; Apple, F.; Eaton, J.W.; Vercellotti, G.M. Ferritin: A cytoprotective antioxidant strategem of endothelium. *J. Biol. Chem.* **1992**, *267*, 18148–18153. [[PubMed](#)]
7. Matsumoto, H.; Ishikawa, K.; Itabe, H.; Maruyama, Y. Carbon monoxide and bilirubin from heme oxygenase-1 suppresses reactive oxygen species generation and plasminogen activator inhibitor-1 induction. *Mol. Cell. Biochem.* **2006**, *291*, 21–28. [[CrossRef](#)]
8. Jamal Uddin, M.; Joe, Y.; Kim, S.K.; Oh Jeong, S.; Ryter, S.W.; Pae, H.O.; Chung, H.T. IRG1 induced by heme oxygenase-1/carbon monoxide inhibits LPS-mediated sepsis and pro-inflammatory cytokine production. *Cell. Mol. Immunol.* **2016**, *13*, 170–179. [[CrossRef](#)]
9. Sawle, P.; Foresti, R.; Mann, B.E.; Johnson, T.R.; Green, C.J.; Motterlini, R. Carbon monoxide-releasing molecules (CO-RMs) attenuate the inflammatory response elicited by lipopolysaccharide in RAW264.7 murine macrophages. *Br. J. Pharmacol.* **2005**, *145*, 8008–8010. [[CrossRef](#)]
10. Rushworth, S.A.; Chen, X.L.; Mackman, N.; Ogborne, R.M.; O’Connell, M.A. Lipopolysaccharide-induced heme oxygenase-1 expression in human monocytic cells is mediated via Nrf2 and protein kinase C. *J. Immunol.* **2005**, *175*, 4408–4415. [[CrossRef](#)]
11. Aggeli, I.K.; Gaitanaki, C.; Beis, I. Involvement of JNKs and p38-MAPK/MSK1 pathways in H₂O₂-induced upregulation of heme oxygenase-1 mRNA in H9c2 cells. *Cell Signal.* **2006**, *18*, 1801–1812. [[CrossRef](#)] [[PubMed](#)]
12. Fredenburgh, L.E.; Perrella, M.A.; Mitsialis, S.A. The role of heme oxygenase-1 in pulmonary disease. *Am. J. Respir. Cell. Mol. Biol.* **2007**, *36*, 158–165. [[CrossRef](#)]
13. Ferrandiz, M.L.; Devesa, I. Inducers of heme oxygenase-1. *Curr. Pharm. Des.* **2008**, *14*, 473–486. [[CrossRef](#)] [[PubMed](#)]
14. Lee, I.T.; Luo, S.F.; Lee, C.W.; Wang, S.W.; Lin, C.C.; Chang, C.C.; Chen, Y.L.; Chau, L.Y.; Yang, C.M. Overexpression of HO-1 protects against TNF- α -mediated airway inflammation by down-regulation of TNFR1-dependent oxidative stress. *Am. J. Pathol.* **2009**, *175*, 519–532. [[CrossRef](#)] [[PubMed](#)]
15. Lee, I.T.; Yang, C.M. Role of NADPH oxidase/ROS in pro-inflammatory mediators-induced airway and pulmonary diseases. *Biochem. Pharmacol.* **2012**, *84*, 581–590. [[CrossRef](#)] [[PubMed](#)]
16. Zuo, L.; Otenbaker, N.P.; Rose, B.A.; Salisbury, K.S. Molecular mechanisms of reactive oxygen species-related pulmonary inflammation and asthma. *Mol. Immunol.* **2013**, *56*, 57–63. [[CrossRef](#)] [[PubMed](#)]
17. Otterbein, L.E.; Kolls, J.K.; Mantell, L.L.; Cook, J.L.; Alam, J.; Choi, A.M. Exogenous administration of heme oxygenase-1 by gene transfer provides protection against hyperoxia-induced lung injury. *J. Clin. Investig.* **1999**, *103*, 1047–1054. [[CrossRef](#)] [[PubMed](#)]

18. Li, F.J.; Duggal, R.N.; Oliva, O.M.; Karki, S.; Surolia, R.; Wang, Z.; Watson, R.D.; Thannickal, V.J.; Powell, M.; Watts, S.; et al. Heme oxygenase-1 protects corexit 9500A-induced respiratory epithelial injury across species. *PLoS ONE* **2015**, *10*, e0122275. [[CrossRef](#)] [[PubMed](#)]
19. Srisook, K.; Han, S.S.; Cho, H.S.; Li, M.H.; Ueda, H.; Kim, C.; Cha, Y.N. CO from enhanced HO activity or from CORM-2 inhibits both O₂- and NO production and downregulates HO-1 expression in LPS-stimulated macrophages. *Biochem. Pharmacol.* **2006**, *71*, 307–318. [[CrossRef](#)]
20. Cheng, S.E.; Lee, I.T.; Lin, C.C.; Kou, Y.R.; Yang, C.M. Cigarette smoke particle-phase extract induces HO-1 expression in human tracheal smooth muscle cells: Role of the c-Src/NADPH oxidase/MAPK/Nrf2 signaling pathway. *Free Radic. Biol. Med.* **2010**, *48*, 1410–1422. [[CrossRef](#)]
21. Choi, Y.K.; Por, E.D.; Kwon, Y.G.; Kim, Y.M. Regulation of ROS production and vascular function by carbon monoxide. *Oxid. Med. Cell. Longev.* **2012**, *2012*, 794237. [[CrossRef](#)] [[PubMed](#)]
22. Chi, P.L.; Lin, C.C.; Chen, Y.W.; Hsiao, L.D.; Yang, C.M. CO Induces Nrf2-Dependent Heme Oxygenase-1 Transcription by Cooperating with Sp1 and c-Jun in Rat Brain Astrocytes. *Mol. Neurobiol.* **2015**, *52*, 277–292. [[CrossRef](#)] [[PubMed](#)]
23. Taille, C.; El-Benna, J.; Lanone, S.; Boczkowski, J.; Motterlini, R. Mitochondrial respiratory chain and NAD(P)H oxidase are targets for the antiproliferative effect of carbon monoxide in human airway smooth muscle. *J. Biol. Chem.* **2005**, *280*, 25350–25360. [[CrossRef](#)] [[PubMed](#)]
24. Motterlini, R.; Green, C.J.; Foresti, R. Regulation of heme oxygenase-1 by redox signals involving nitric oxide. *Antioxid. Redox Signal.* **2002**, *4*, 615–624. [[CrossRef](#)] [[PubMed](#)]
25. Lee, I.T.; Yang, C.M. Inflammatory signalings involved in airway and pulmonary diseases. *Mediat. Inflamm.* **2013**, *2013*, 791231. [[CrossRef](#)] [[PubMed](#)]
26. Motterlini, R.; Otterbein, L.E. The therapeutic potential of carbon monoxide. *Nat. Rev. Drug Discov.* **2010**, *9*, 728–743. [[CrossRef](#)] [[PubMed](#)]
27. Yang, C.M.; Lin, C.C.; Lee, I.T.; Hsu, C.K.; Tai, Y.C.; Hsieh, H.L.; Chi, P.L.; Hsiao, L.D. c-Src-dependent transactivation of EGFR mediates CORM-2-induced HO-1 expression in human tracheal smooth muscle cells. *J. Cell. Physiol.* **2015**, *230*, 2351–2361. [[CrossRef](#)]
28. Alam, J.; Cook, J.L. How many transcription factors does it take to turn on the heme oxygenase-1 gene? *Am. J. Respir. Cell Mol. Biol.* **2007**, *36*, 166–174. [[CrossRef](#)]
29. Alam, J.; Stewart, D.; Touchard, C.; Boinapally, S.; Choi, A.M.; Cook, J.L. Nrf2, a Cap'n'Collar transcription factor, regulates induction of the heme oxygenase-1 gene. *J. Biol. Chem.* **1999**, *274*, 26071–26078. [[CrossRef](#)]
30. Constantin, M.; Choi, A.J.; Cloonan, S.M.; Ryter, S.W. Therapeutic potential of heme oxygenase-1/carbon monoxide in lung disease. *Int. J. Hypertens.* **2012**, *2012*, 859235. [[CrossRef](#)]
31. Xue, J.; Habtezion, A. Carbon monoxide-based therapy ameliorates acute pancreatitis via TLR4 inhibition. *J. Clin. Investig.* **2014**, *124*, 437–447. [[CrossRef](#)] [[PubMed](#)]
32. Qin, W.; Zhang, J.; Lv, W.; Wang, X.; Sun, B. Effect of carbon monoxide-releasing molecules II-liberated CO on suppressing inflammatory response in sepsis by interfering with nuclear factor kappa B activation. *PLoS ONE* **2013**, *8*, e75840. [[CrossRef](#)] [[PubMed](#)]
33. Takasuka, H.; Hayashi, S.; Koyama, M.; Yasuda, M.; Aihara, E.; Amagase, K.; Takeuchi, K. Carbon monoxide involved in modulating HCO₃⁻ secretion in rat duodenum. *J. Pharmacol. Exp. Ther.* **2011**, *337*, 293–300. [[CrossRef](#)] [[PubMed](#)]
34. Wu-Zhang, A.X.; Newton, A.C. Protein kinase C pharmacology: Refining the toolbox. *Biochem. J.* **2013**, *452*, 195–209. [[CrossRef](#)] [[PubMed](#)]
35. Yang, C.C.; Lin, C.C.; Chien, P.T.; Hsiao, L.D.; Yan, C.M. Thrombin/Matrix Metalloproteinase-9-Dependent SK-N-SH Cell Migration is Mediated Through a PLC/PKC/MAPKs/NF-kappaB Cascade. *Mol. Neurobiol.* **2016**, *53*, 5833–5846. [[CrossRef](#)] [[PubMed](#)]
36. Mills, R.D.; Mita, M.; Nakagawa, J.; Shoji, M.; Sutherland, C.; Walsh, M.P. A role for the tyrosine kinase Pyk2 in depolarization-induced contraction of vascular smooth muscle. *J. Biol. Chem.* **2015**, *290*, 8677–8692. [[CrossRef](#)] [[PubMed](#)]
37. Rhee, I.; Davidson, D.; Souza, C.M.; Vacher, J.; Veillette, A. Macrophage fusion is controlled by the cytoplasmic protein tyrosine phosphatase PTP-PEST/PTPN12. *Mol. Cell. Biol.* **2013**, *33*, 2458–2469. [[CrossRef](#)]
38. Hsieh, H.L.; Wang, H.H.; Wu, C.Y.; Yang, C.M. Reactive Oxygen Species-Dependent c-Fos/Activator Protein 1 Induction Upregulates Heme Oxygenase-1 Expression by Bradykinin in Brain Astrocytes. *Antioxid. Redox Signal.* **2010**, *13*, 1829–1844. [[CrossRef](#)]

39. Rochette, L.; Cottin, Y.; Zeller, M.; Vergely, C. Carbon monoxide: Mechanisms of action and potential clinical implications. *Pharmacol. Ther.* **2013**, *137*, 133–152. [[CrossRef](#)]
40. Kamata, H.; Hirata, H. Redox regulation of cellular signalling. *Cell Signal.* **1999**, *11*, 1–14. [[CrossRef](#)]
41. Mulier, B.; Rahman, I.; Watchorn, T.; Donaldson, K.; MacNe, W.; Jeffery, P.K. Hydrogen peroxide-induced epithelial injury: The protective role of intracellular nonprotein thiols (NPSH). *Eur. Respir. J.* **1998**, *11*, 384–391. [[CrossRef](#)] [[PubMed](#)]
42. Barbieri, S.S.; Cavalca, V.; Eligini, S.; Brambilla, M.; Caian, A.; Tremoli, E.; Colli, S. Apocynin prevents cyclooxygenase 2 expression in human monocytes through NADPH oxidase and glutathione redox-dependent mechanisms. *Free Radic. Biol. Med.* **2004**, *37*, 156–165. [[CrossRef](#)] [[PubMed](#)]
43. Stanley, A.; Hynes, A.; Brakebusch, C.; Quondamatteo, F. Rho GTPases and Nox dependent ROS production in skin. Is there a connection? *Histol. Histopathol.* **2012**, *27*, 1395–1406. [[PubMed](#)]
44. Tavares, A.F.; Teixeira, M.; Romao, C.C.; Seixas, J.D.; Nobre, L.S.; Saraiva, L.M. Reactive oxygen species mediate bactericidal killing elicited by carbon monoxide-releasing molecules. *J. Biol. Chem.* **2011**, *286*, 26708–26717. [[CrossRef](#)] [[PubMed](#)]
45. Prabhakar, N.R. NO and CO as second messengers in oxygen sensing in the carotid body. *Respir. Physiol.* **1999**, *115*, 161–168. [[CrossRef](#)]
46. Choi, Y.K.; Maki, T.; Mandeville, E.T.; Koh, S.H.; Hayakawa, K.; Arai, K.; Kim, Y.M.; Whalen, M.J.; Xing, C.; Wang, X.; et al. Dual effects of carbon monoxide on pericytes and neurogenesis in traumatic brain injury. *Nat. Med.* **2016**, *22*, 1335–1341. [[CrossRef](#)]
47. Alam, R.; Gorska, M.M. Mitogen-activated protein kinase signalling and ERK1/2 bistability in asthma. *Clin. Exp. Allergy* **2011**, *41*, 149–159. [[CrossRef](#)]
48. Yuan, X.; Xu, C.; Pan, Z.; Keum, Y.S.; Kim, J.H.; Shen, G.; Yu, S.; Oo, K.T.; Ma, J.; Kong, A.N. Butylated hydroxyanisole regulates ARE-mediated gene expression via Nrf2 coupled with ERK and JNK signaling pathway in HepG2 cells. *Mol. Carcinog.* **2006**, *45*, 841–850. [[CrossRef](#)]
49. Foresti, R.; Bani-Hani, M.G.; Motterlini, R. Use of carbon monoxide as a therapeutic agent: Promises and challenges. *Intensive Care Med.* **2008**, *34*, 649–658. [[CrossRef](#)]
50. Pawate, S.; Shen, Q.; Fan, F.; Bhat, N.R. Redox regulation of glial inflammatory response to lipopolysaccharide and interferon gamma. *J. Neurosci. Res.* **2004**, *77*, 540–551. [[CrossRef](#)]
51. Cheng, P.Y.; Lee, Y.M.; Shih, N.L.; Chen, Y.C.; Yen, M.H. Heme oxygenase-1 contributes to the cytoprotection of alpha-lipoic acid via activation of p44/42 mitogen-activated protein kinase in vascular smooth muscle cells. *Free Radic. Biol. Med.* **2006**, *40*, 1313–1322. [[CrossRef](#)] [[PubMed](#)]
52. Sen, C.K.; Packer, L. Antioxidant and redox regulation of gene transcription. *FASEB J.* **1996**, *10*, 709–720. [[CrossRef](#)] [[PubMed](#)]
53. Alam, J.; Igarashi, K.; Immenschuh, S.; Shibahara, S.; Tyrrell, R.M. Regulation of heme oxygenase-1 gene transcription: Recent advances and highlights from the International Conference (Uppsala, 2003) on Heme Oxygenase. *Antioxid. Redox Signal.* **2004**, *6*, 924–933. [[PubMed](#)]
54. Urquhart, P.; Rosignoli, G.; Cooper, D.; Motterlini, R.; Perretti, M. Carbon monoxide-releasing molecules modulate leukocyte-endothelial interactions under flow. *J. Pharmacol. Exp. Ther.* **2007**, *321*, 656–662. [[CrossRef](#)] [[PubMed](#)]
55. Almolki, A.; Taillé, C.; Martin, G.F.; Jose, P.J.; Zedda, C.; Conti, M.; Megret, J.; Henin, D.; Aubier, M.; Boczkowski, J. Heme oxygenase attenuates allergen-induced airway inflammation and hyperreactivity in guinea pigs. *Am. J. Physiol. Lung Cell. Mol. Physiol.* **2004**, *287*, L26–L34. [[CrossRef](#)] [[PubMed](#)]
56. Sun, B.; Sun, H.; Liu, C.; Shen, J.; Chen, Z.; Chen, X. Role of CO-releasing molecules liberated CO in attenuating leukocytes sequestration and inflammatory responses in the lung of thermally injured mice. *J. Surg. Res.* **2007**, *139*, 128–135. [[CrossRef](#)]
57. Kilkenny, C.; Browne, W.; Cuthill, I.C.; Emerson, M.; Altman, D.G.; Group NCRRGW. Animal research: Reporting in vivo experiments: The ARRIVE guidelines. *Br. J. Pharmacol.* **2010**, *160*, 1577–1579. [[CrossRef](#)] [[PubMed](#)]
58. McGrath, K.C.; Li, X.H.; McRobb, L.S.; Heather, A.K. Inhibitory Effect of a French Maritime Pine Bark Extract-Based Nutritional Supplement on TNF-alpha-Induced Inflammation and Oxidative Stress in Human Coronary Artery Endothelial Cells. *Evid. Based Complement. Altern. Med.* **2015**, *2015*, 260530. [[CrossRef](#)] [[PubMed](#)]

59. Hsu, C.K.; Lee, I.T.; Lin, C.C.; Hsiao, L.D.; Yang, C.M. Nox2/ROS-dependent human antigen R translocation contributes to TNF-alpha-induced SOCS-3 expression in human tracheal smooth muscle cells. *Am. J. Physiol. Lung Cell. Mol. Physiol.* **2014**, *306*, L521–L533. [[CrossRef](#)]
60. Lee, C.W.; Chien, C.S.; Yang, C.M. Lipoteichoic acid-stimulated p42/p44 MAPK activation via Toll-like receptor 2 in tracheal smooth muscle cells. *Am. J. Physiol. Lung Cell. Mol. Physiol.* **2004**, *286*, L921–L930. [[CrossRef](#)]
61. Hsieh, H.L.; Lin, C.C.; Hsiao, L.D.; Yang, C.M. High glucose induces reactive oxygen species-dependent matrix metalloproteinase-9 expression and cell migration in brain astrocytes. *Mol. Neurobiol.* **2013**, *48*, 601–614. [[CrossRef](#)] [[PubMed](#)]



© 2019 by the authors. Licensee MDPI, Basel, Switzerland. This article is an open access article distributed under the terms and conditions of the Creative Commons Attribution (CC BY) license (<http://creativecommons.org/licenses/by/4.0/>).

Available online at www.sciencedirect.com

ScienceDirect

journal homepage: www.jfda-online.com

Review Article

Next generation probiotics in disease amelioration



Chih-Jung Chang^{b,c,1}, Tzu-Lung Lin^{b,1}, Yu-Ling Tsai^{b,1}, Tsung-Ru Wuⁱ,
Wei-Fan Lai^g, Chia-Chen Lu^{h,*}, Hsin-Chih Lai^{a,b,c,d,e,f,**}

^a Department of Medical Biotechnology and Laboratory Science, College of Medicine, Chang Gung University, Gueishan, Taoyuan, 33302, Taiwan

^b Microbiota Research Center and Emerging Viral Infections Research Center, Chang Gung University, Gueishan, Taoyuan 33302, Taiwan

^c Chang Gung Immunology Consortium, Linkou Chang Gung Memorial Hospital, Gueishan, Taoyuan, 33305, Taiwan

^d Department of Laboratory Medicine, Linkou Chang Gung Memorial Hospital, Gueishan, Taoyuan, 33305, Taiwan

^e Research Center for Chinese Herbal Medicine, College of Human Ecology, Chang Gung University of Science and Technology, Gueishan, Taoyuan, 33303, Taiwan

^f Research Center for Food and Cosmetic Safety, College of Human Ecology, Chang Gung University of Science and Technology, Gueishan, Taoyuan 33303, Taiwan

^g Department of Medicine, College of Medicine, Chang Gung University, Gueishan, Taoyuan, 33302, Taiwan

^h Department of Respiratory Therapy, Fu Jen Catholic University, Xinzhuang, New Taipei City, 24205, Taiwan

ⁱ Institute of Biomedical Sciences, Academia Sinica, Taipei 115, Taiwan

ARTICLE INFO

Article history:

Received 28 September 2018

Received in revised form

20 December 2018

Accepted 27 December 2018

Available online 2 February 2019

Keywords:

Microbiota

Microbiome

Prebiotic

Probiotic

Metabolites

ABSTRACT

Studies on the role of gut commensal bacteria in health development have rapidly attracted much more attention beyond the classical pathogens over the last decade. Many important reports have highlighted the changes in the gut microbiota (dysbiosis) are closely related to development of intra- and extra-intestinal, chronic inflammation related diseases such as colitis, obesity/metabolic syndromes, diabetes mellitus, liver diseases, cardiovascular diseases and also cancer and neurodegenerative diseases. To circumvent these difficulties, the strategy of modulating the structure of the gut microbiota has been under intensive study and shed more light on amelioration of these inflammation related diseases. While traditional probiotics generally show marginal ameliorative effects, emerging next generation probiotics start to reveal as new preventive and therapeutic tools. Recent studies have unraveled many potential next generation probiotics (NGP). These include *Prevotella copri* and *Christensenella minuta* that control insulin resistance, *Parabacteroides goldsteinii*, *Akkermansia muciniphila* and *Bacteroides thetaiotaomicron* that reverse obesity and insulin resistance, *Faecalibacterium prausnitzii* that protects mice against intestinal diseases, and *Bacteroides fragilis* that reduces inflammation and shows anticancer effect. New agents will soon be revealed for targeted therapy on specific inflammation related diseases. The important roles of next generation probiotics and gut microbiota normobiosis on the maintenance of intestinal integrity and homeostasis are emphasized.

* Corresponding author. Department of Respiratory Therapy, College of Medicine, Fu Jen Catholic University Hospital and Fu Jen Catholic University, 510 Zhong-Zheng Road, Xinzhuang Dist., New Taipei City 24205, Taiwan.

** Corresponding author. Department of Medical Biotechnology and Laboratory Science, and Microbiota Research Center, Chang Gung University, 259 Wen-Hwa 1st Road, Guei-Shan, Tao-Yuan, 333, Taiwan.

E-mail addresses: 082385@mail.fju.edu.tw (C.-C. Lu), hclai@mail.cgu.edu.tw (H.-C. Lai).

¹ Authors contribute equally to this article.

<https://doi.org/10.1016/j.jfda.2018.12.011>

1021-9498/Copyright © 2019, Food and Drug Administration, Taiwan. Published by Elsevier Taiwan LLC. This is an open access article under the CC BY-NC-ND license (<http://creativecommons.org/licenses/by-nc-nd/4.0/>).

1. Introduction

Due to rapid development of advanced genetic sequencing tools and the bioinformatics platforms in the past 15 years, scientists are able to characterize the composition and function of microbiota and microbiomes from the intestine. Fast gathering of these big data strongly indicates that gut bacteria play important roles in maintaining the intestinal homeostasis and modulating host metabolism. During the process of microbiota study, some of the gut bacteria will soon be expected to emerge as potential sources of novel disease therapeutics [1]. The molecular mechanisms of interaction between the gut commensals and the host cells, and how commensals maintain optimal intestinal integrity and immunity are intensively studied [2]. Under the situation of gut microbiota dysbiosis, chronic inflammation related diseases such as metabolic syndromes, cardiovascular disorders, inflammatory bowel diseases, neuropsychiatric diseases, asthma and cancers etc. are developed [3]. As the microbiota studies proceed, single bacterial strains are screened and isolated, aiming to characterize their relationship with the amelioration of inflammation-related diseases. Among these, some of them are expected to emerge as next generation probiotics (NGP).

2. Interaction between microbiota and host intestinal immunity

Located along the border of the lumen in gastrointestinal tract, intestinal epithelial cells (IEC) play a most important role as a barrier bridging the key messages sent from gut microbiota to the immune and other cells residing in the lamina propria [2,3]. The host innate immunity system in IEC bears pattern recognition receptors (PRRs) such as toll-like receptors (TLRs) and NOD-like receptors (NLRs), essential elements recognizing the microbes' pathogen-associated molecular patterns (PAMPs) from microorganisms [4]. Important bacterial PAMP ligands comprise lipopolysaccharides (LPS), peptidoglycans, lipoteichoic acid, flagellin and muramyl dipeptide (MDP). On top, there are also danger-associated molecular patterns (DAMP) signals derived from destroyed host tissues that can be sensed by PRRs [5]. On the other hand, intestinal immune systems are required to continuously monitor the structure and abundance of the microbiota [6]. Thus dynamic interactions exist between the intestinal cells and the vast diversity of microbiota microbes [7]. Under normal situations (normobiosis), the barrier function from IEC is efficiently maintained due to multiple mechanisms including production of optimal amount of tight-junction proteins, optimal thickness and sugar composition of the mucus layer, production of antimicrobial proteins/peptides, and production of a certain amount of immunoglobulin A (IgA) [7].

Under the situation of microbiota dysbiosis, overgrowth of some microbiota bacteria such as those belonging to the phylum Proteobacteria may occur and results in overproduction of the PAMPs, leading to enhanced inflammations and loss of immune tolerance. This is followed by abrogation of intestinal integrity, leading to leaky gut phenomena and occurrence of chronic inflammations-related diseases [8]. Taking the LPS from the PAMP as an example, under high-fat-diet life style, due to the compromised intestinal integrity, LPS translocates across the IEC into the blood. Increased blood LPS concentration initiates systemic low-grade inflammation via its interaction with the surface receptors (i.e. TLR-4 and CD14) of systematic innate immune and cellular systems [9]. These results lead to development of metabolic endotoxemia, overweight and subsequently obesity-related syndromes including insulin resistance, glucose intolerance, dyslipidaemia, and hepatic steatosis [10]. Besides LPS, many other PAMPs such as peptidoglycans or flagellin also have been shown to show similarly causal effects [11].

3. Microbiota metabolites affect host metabolism

Besides classical interactions between bacterial PAMPs and the host immune systems, metabolites derived from gut microbiota also involve interactive activities affecting the systematic host cellular metabolism and physiology [12]. Many bacterial metabolites that include folate, indoles, secondary bile acids, trimethylamine-N-oxide (TMAO), serotonin, gamma amino butyric acid, and also short chain fatty acids (SCFA, acetate, propionate and butyrate) have been characterized [13]. Under different concentrations, these bacterial metabolites play important roles in regulating host physiological phenotypes. In contrast, disease development may occur under unbalanced situation [13]. The functional molecular mechanisms of these metabolites can be via binding to specific host membranes or nuclear receptors [14]. For example, SCFAs trigger the secretion of intestinal peptides [glucagon-like peptide-1 or peptide YY (PYY)] involved in glucose metabolism or food intake via G-protein-coupled receptors such as GPR-41 and GPR-43 [15]. Besides, the butyrate works as an essential energy source, allowing colonic cells to proliferate and maintain healthy gut barrier function [16]. On top of this, butyrate also activates β -oxidation and oxidative phosphorylation in the mitochondria in colonic cells to consume oxygen (maintain anaerobic condition) in the intestinal lumen and protect the host from the expansion of pathobionts such as those belonging to facultative anaerobic Enterobacteriaceae [17,18]. Therefore, gut microbes may work as an endocrine organ regulating the activities of different distal organs through close interactions with intestinal cells [19].

4. Why NGP are essential?

To achieve the goal of amelioration of diseases related to leaky gut syndromes, the administration of probiotics is one of the optimal approaches. Main aims of administration of probiotics may comprise enhancing the integrity of intestinal epithelial layer, increasing in optimal IgA production, modulation of homeostatic bile acids production and secretion, and increase in production of antimicrobial peptides [20]. In general, traditional widely used probiotics such as *Bifidobacterium spp.*, *Lactobacillus spp.* and many others were selected either randomly or through the gathering living experiences. While most of them show biological safety and some of them may show ameliorative effectiveness, however, the general effects and functions on amelioration of diseases are statistically marginal. On the other hand, the administration of traditional probiotics does not aim against specific diseases. Based on these situations, identification and characterization of novel and disease-specific NGP are urgently needed [21]. Besides safety concern, characteristics of the NGP will have to include comprehensive understanding of their targeted diseases, and the bacterial genetic features and physiological traits, including the growth dynamics, antibiotics sensitivity pattern. Moreover, the underlying molecular ameliorative mechanisms have to be clarified. To achieve this goal, screening and isolating the NGP through the cutting edge NGS (next generation sequencing) and bioinformatics technique platforms, followed by rigid functional validation of the new probiotics have to be performed. Strategically, these approaches are very different from those frequently used in isolation of traditional probiotics. Briefly, sectional (or even longitudinal) studies and more comprehensive bioinformatics analyses of the microbiota composition, metagenomics, and the host responses such as metabolites/metabolome produced (metabolomics) will have to be performed for selection of effective probiotics. Based on analyses results of the many multi-omics big data groups, potential probiotics or the consortium can then be highlighted and selected. These are followed by functional validation of the selected probiotics candidates, including assays of *in vitro* cell lines, *ex vivo* animal models, *in vivo* animals and even to human clinical trials. Furthermore, to get a more practical and applicable results, one may have to improve the quality of samples to be analysed, from the easily accessible faecal materials to those from local mucosa loci. Of note, standardized processing steps on samples harvesting, optimal storage conditions and detailed sequencing and bioinformatics analyses will have to be designed and performed strictly. Finally, the many big data results obtained from large scale analyses of blood/serum, tissues, urine, and fecal samples, under different environmental situations such as different nutrition and drug treatments ... etc. will have to be integrated together to form a whole-picture oriented biochemical outputs. These results can then show more practical interaction situation between the microbiota and the host [22].

4.1. How to isolate next generation probiotics?

In order to achieve the goals of identifying next generation probiotics, the first stage is to unravel whether there are

significant microbiota bacteria-host correlations between the study groups (such as the healthy, the disease and the experimental groups). Such associations can be derived either from animals or clinical studies. This is followed by isolation of potential probiotics and/or characterization of the related metabolites derived for subsequent functional validation studies. So far many microbiota bacteria still can not be cultured *in vitro*. However, as the technologies of culturomics are making rapid progress [23], targeted bacteria with significance can be specifically isolated and cultured by all means. Experimental design can subsequently be arranged in cell lines study to characterize whether there are any ameliorative effects originated from the bacterial isolate(s) at the cellular and molecular levels. The effects of selected probiotics on animal models of either SPF (specific pathogens free) or GF (germ free) mice will then be used for *in vivo* efficacy evaluation. These studies are basically performed for proof of concept. After completion of these studies, the functions, safety and molecular mechanisms of the probiotic(s) in animals will be addressed, followed by clinical human studies. Currently the United States FDA (food and drug administration) has started to initiate a program of LBP (live bio-therapeutic products) to specifically regulate the application, clinical trial and commercialization of emerging new probiotics [24]. It is expected that in near future the NGP will start to come to reality in health bio-industry.

5. Candidates for next generation probiotics

Through analyses using the next generation sequencing and bioinformatics platforms, many potential NGP are currently under intensive development (Table 1). Some of them are selectively described below.

5.1. *Bifidobacterium spp.*

Bifidobacterium spp. are Gram-positive, non-spore-forming, nonmotile, and polymorphic rod bacteria that belong to the family Bifidobacteriaceae of the Actinobacteria class and phylum [25]. They are generally reconed as traditional probiotics. *Bifidobacterium* comprises >1% of the total microbiota, and are numbered at peak by the age of 3–4 months in infancy, followed by decreasing over time in adults [26,27].

Besides the many traditional beneficial effects reported, the efficacy of *Bifidobacterium spp.* on the outcomes of anticancer therapies is the subject of extensive ongoing research. Substantially reduced tumor growth rates and improved responses to anti-PD-L1 therapy were observed in mice [28]. Significantly, a probiotic cocktail consisting of *B. breve* and *B. longum* potentiates the antitumour efficacy of anti-PD-L1 immunotherapy [28]. The increased efficacy was, at least in part, mediated by the activation of DCs, leading to enhanced CD8+ T cell priming and accumulation within the tumor microenvironment (TME) [28]. On top of these, *Bifidobacterium spp.* as probiotics also gained much attention on cancer development and therapy against colitis and CRC [29]. In a rat model of azoxymethane (AOM)/DSS-induced CRC, a synbiotic (prebiotic and probiotic) comprising resistant starch and *Bifidobacterium animalis subsp. lactis* (*B. lactis*) showed

Table 1 – The NGP under intensive development.

Next generation probiotics	Main characterizations	Functions and mechanisms	Potential weakness	references
<i>Bifidobacterium</i> spp.	Some Bifidobacterium species strains may enhance the efficacy of Immune Checkpoint Inhibitors cancer therapy. Ameliorate prediabetes syndromes.	Enhance DC and CD8 ⁺ T cells functions.	The anti-cancer effects may be strain specific.	[23, 26, 27]
<i>Prevotella copri</i>		Production of succinate, a TCA cycle intermediate.	Production of branch chain amino acids (BCAA) that may cause insulin resistance.	[33, 34]
<i>Akkermansia muciniphila</i>	Anti-obesogenicity and metabolic syndromes.	An outer membrane protein Amuc_1100 is reported to be responsible.	Positive association with Parkinson disease and multiple sclerosis.	[36–41]
<i>Bacteroides fragilis</i>	Anti-inflammations. Also may enhance efficacy of immune check point inhibitors cancer therapy.	A capsular polysaccharide PSA may enrich CD4 ⁺ FoxP3 T cells after plasmacytoid DC cells presentation.	Enterotoxin containing <i>B. fragilis</i> is closely related to colorectal cancer development.	[42, 45–47]
<i>Christensenella minuta</i>	Anti-obesogenicity.	Unknown.	Not applicable.	[48, 49]
<i>Faecalibacterium prausnitzii</i>	Highly heritable in a lean host phenotype.	Butyrate production.	Not applicable.	[53–55]
<i>Parabacteroides goldsteinii</i>	Anti-inflammation. May ameliorate IBD and CRC.	Enhanced production of Treg and IL-10.	Not applicable.	[10, 56]
	Anti-obesogenicity. Ameliorates prediabetes syndromes and liver inflammations.			

ameliorative effects on CRC development [30]. Furthermore, in patients with resected CRC, administration of a combination of inulin enriched with oligofructose, *B. lactis*, and *Lactobacillus rhamnosus* improved immune function [31]. In another study, CD8⁺ T cell memory responses against *B. longum* are positively associated with disease-free survival after tumor resection in patients with hepatocellular carcinoma [32].

Interestingly, *Bifidobacterium* spp. may also act as a vehicle for transporting anticancer genes to a target tumor [33]. *Bifidobacterium* spp. are shown to enter the bloodstream and can selectively accumulate in tumor mass due to the hypoxic condition in tumor. Take the *B. adolescentis* as an example, the underlying anti-tumor mechanism may lie in that *B. adolescentis* transformed with an antiangiogenic gene encoding endostatin can lead to bacterial proliferation within the tumor mass [34]. However, this does not occur in nonmalignant tissues. What's more, intratumoral expression of the endostatin can also inhibit tumor growth [34]. Further studies aiming at better understanding the mechanism of this association are warranted.

5.2. *Prevotella copri*

As a potential next generation probiotic, the *P. copri* belonging to the phylum Bacteroidetes was found to improve aberrant glucose tolerance syndromes and enhance hepatic glycogen storage in animals via the production of succinate, a tricarboxylic acid (TCA) cycle intermediate fermented from uptake of dietary fibers, that is responsible for glucose homeostasis through modulating intestinal gluconeogenesis [35].

Though *P. copri* shows beneficial effects on amelioration of prediabetic syndromes, however, recent study also showed that *P. copri* and *Bacteroides vulgatus* exacerbate glucose tolerance and enhance insulin resistance which occur before the development of ischaemic cardiovascular disease and type 2 diabetes. The underlying reason is related to synthesis of branch chain fatty acids (BCAA) [36]. In this study from 277 non-diabetic Danish individuals, the serum levels of BCAAs were observed to increase in insulin-resistant, prediabetes individuals. This phenomenon was further shown to be closely related to increased abundance of *P. copri* and *B. vulgatus* in a mouse study model [36]. Generally, whether *P. copri* works as a beneficial or deleterious bacterium requires further investigation. These phenomena strongly indicated that a careful analysis and demonstration of causality are essential before making functional conclusions of some microbes.

5.3. *Akkermansia muciniphila*

A. muciniphila belonging to the phylum Verrucomicrobia is another potential key probiotic candidate. This bacterium occupies up to 5% of the total microbiota bacteria and utilizes mucin as a nutrient for proliferation [37]. Numerous studies have shown that the composition of the gut microbiota differs between obese/T2D individuals and those of lean/non-diabetic ones. Currently it is widely accepted that administration of prebiotics such as the inulin-type fructans increases the abundance of *A. muciniphila*, leading to improvement of metabolic disorders and obesity [38]. The underlying mechanism by which *A. muciniphila* works is subsequently identified

to be through an immunomodulatory protein ‘Amuc_1100’ located in the bacterial outer membrane [39]. Other studies show *A. muciniphila* also modulates the endocannabinoid (eCB) system [40]. This is an important regulatory system in the aspect of targeting obesity, type 2 diabetes and inflammation. The eCB system is reported to involve the control of glucose and energy metabolism [40].

A. muciniphila may also involve anticancer immunotherapy such as anti-PD-1 treatment [41]. Besides clinical correlation, using the strategy of transferring of the faeces microbiota from responders or non-responders to germ free mice showed that *A. muciniphila* improved the compromised efficacy of anti-PD-1 blockade in contrast to the mice receiving the microbiota from non-responders [41]. How and why *A. muciniphila* shows such effects remain uncharacterized.

Even though *A. muciniphila* shows many beneficial effects, however, some other studies in animals reported a reverse situation on an increased abundance of *A. muciniphila* in the HFD mice [42] and the diseases multiple sclerosis (MS) and Parkinson's disease [43]. More studies on ameliorative effects of *A. muciniphila* are necessary.

5.4. *Bacteroides fragilis*

B. fragilis is another emerging probiotic [44]. As a prominent species of the genus *Bacteroides* in the phylum Bacteroidetes, *B. fragilis* is a Gram-negative absolute anaerobic commensal bacteria and occupies about 1% of the intestinal microbiota in humans [45]. Previous studies already showed that enterotoxin-containing *B. fragilis* strains (ETBF) significantly involve the abdominal infections and cause clinical abscesses arising from fecal spillage or bacteremia [46]. Although ETBF significantly contributes to intra-abdominal abscess formation, soft tissue infections, and bacteremia when present outside the gut, interestingly, *B. fragilis* strains that do not contain the enterotoxin gene show many beneficial effects [47].

After decades of studies using *B. fragilis* as a model organism, the research results from Dennis Kasper's group in Harvard University have highlighted the *B. fragilis* polysaccharide A (PSA) as an archetypical bacterial capsular polysaccharide example directing microbiota and host interactions [47]. PSA is rather unique due to its possessing zwitterionic motifs which enrich a specific subset of anti-inflammatory memory CD4⁺FoxP3 T cells after direct interactions of antigen presenting cells (APC) such as plasmacytoid dendritic Cells [48]. This can result in a systematic amelioration of inflammation related diseases such as abscess, neuro-inflammations and cancers [49].

5.5. *Christensenella minuta*

C. minuta also shows potential probiotic effects against obesity and associated metabolic disorders [50]. *C. minuta* is a Gram-positive, nonspore-forming, anaerobic probiotic candidate that shows the effects of reducing obesity and related syndromes [50]. Using the microbiota of more than 1000 fecal samples obtained from the UK twin pairs population, the family Christensenellaceae was found to form a co-occurrence network with other heritable bacteria [51]. The

abundance of Christensenellaceae was found to enrich in individuals of low body mass index (BMI) [51]. Further study indicated that an obesity-associated microbiome can be ameliorated by *C. minuta* which amends the body weight gain and alters the microbiome pattern of recipient mice [50].

5.6. *Faecalibacterium prausnitzii*

F. prausnitzii is a Gram-positive bacterium belonging to the family Ruminococcaceae (the Clostridia class and the Firmicutes phylum). It is the only known species of the *Faecalibacterium* genus, and occupies about 5% of the gut microbiota in healthy adult humans [52]. *F. prausnitzii* ferments glucose, and produces SCFAs such as butyrate, formic acid, and D-lactate [53]. Due to production of butyrate, the intestinal homeostasis and integrity, and thus health are maintained [54].

Increasing evidences indicate that bacteria of the *Faecalibacterium* genus can influence the efficacy of immune checkpoint blockade (ICB) therapy [55]. Furthermore, there is positively correlation between the abundance of *Faecalibacterium* spp. and longer progression-free survival (PFS) durations. Importantly, strong evidences showed positive correlation between the abundance of *Faecalibacterium* spp. in the gut and CD8⁺ T cell infiltration within the tumor environment (TME), in addition to the frequency of effector CD4⁺ and CD8⁺ T cells in the periphery [56]. Further confirmation of the ability of *F. prausnitzii* to modulate responses to ICB therapy is warranted [57].

On top, an enrichment of this bacterium in baseline stool samples from patients with metastatic melanoma who respond to anti-CTLA-4 antibody therapy in comparison to the nonresponders was observed [57]. At the same time, the responders also showed a higher incidence of immune-related colitis [57]. This enrichment was positively correlated with expression of inducible T cell costimulator (ICOS) on the surface of circulating effector CD4⁺ T cells and negatively correlated with the numbers of regulatory T cells and the levels of pro-inflammatory proteins, such as IL-6, IL-8, and soluble IL-2 receptor- α (IL-2R α), in the blood at baseline [57]. In brief, these findings highlight the tremendous potential of this bacterium as both a therapeutic target and a prognostic marker in patients with cancer.

5.7. *Parabacteroides goldsteinii*

Novel anti-obesity measures that are safe, effective and widely available are needed to combat the growing obesity epidemic. The bacterium *P. goldsteinii* also shows its potential as a novel probiotic for anti-obesity [10,58]. We recently reported that a water extract of the medicinal mushroom *Hirsutella sinensis* reduces obesity, inflammation and insulin resistance in high-fat diet (HFD)-fed mice. A high molecular weight polysaccharide fraction (>300 kDa) isolated from the water extract not only lowers body weight by 50% but it also reduces intestinal permeability, metabolic endotoxemia, inflammation and insulin resistance. Horizontal fecal transfer combined with antibiotic-induced depletion of specific gut bacteria shows that the effects of *H. sinensis* polysaccharides are dependent on neomycin-sensitive bacteria. Gut microbiota analysis reveals that the Gram-negative bacterium *P.*

goldsteinii is highly reduced in the microbiota of HFD-fed mice, while this bacterium is enriched in polysaccharide-treated mice. Notably, oral administration of live, but not heat-killed *P. goldsteinii* bacteria to HFD-fed mice considerably reduces weight gain and obesity-associated metabolic disorders. These results indicate that the anti-obesity, anti-inflammatory and insulin-sensitizing effects of mushroom polysaccharides are mediated by the gut microbiota and involve the newly identified probiotic *P. goldsteinii*. Mushroom polysaccharides and *P. goldsteinii* may thus be used respectively as prebiotics and probiotics for the treatment of obesity and related metabolic complications [10,56].

6. Immune checkpoints blockade (ICB) therapy and other potential candidates

A few other bacterial species also showed promising effects on promotion of the effectiveness of anticancer immunotherapies. These bacteria include *Eubacterium limosum*, *Enterococcus hirae*, *Enterococcus faecium*, *Collinsella aerofaciens*, and *Burkholderia cepacia*.

E. limosum belongs to the Class Clostridia, the order Clostridiales, and the phylum Firmicutes, and is an anaerobic, non-spore-forming, Gram-positive rod that is particularly prevalent in aged humans [59]. This bacterium shows effects on ameliorating DSS-induced colitis in mice, probably due to production of SCFAs to present anti-inflammation effects [59]. On top, the intestinal abundance of *E. limosum* was found to be related to a reduced risk of disease relapse and progression after allo-hematopoietic stem cell transplantation (HSCT) treatment in patients with haematological malignancies [60]. The underlying mechanisms of *E. limosum* to show the favorable outcome after allo-HSCT remains to be further characterized.

E. hirae belongs to Enterococcaceae and are grouped under the class of Bacilli and the phylum Firmicutes. It was found to be more abundant in faeces from responder patients with various carcinomas to PD-1–PD-L1 blockade than in samples from non-responders [61]. The potential ameliorated mechanism may be that *E. hirae* 13144 administration enhances the memory responses of T cells [62]. This was also closely related to progression-free survival (PFS) in patients with non-small cancer lung carcinoma (NSCLC) or ovarian cancer treated with immunogenic chemotherapy [61]. *E. hirae* was reported to translocate from the intestinal lumen to mesenteric lymph nodes, especially in the context of cyclophosphamide-based chemotherapy [62]. This may result in enhancement of T cells activity. However, *E. hirae* is also reported to cause clinical infections in humans [63]. Thus the roles of *E. hirae* in human health may be dual swords. One has to be careful in dealing with this bacterium.

In the aspect of clinical melanoma ICB study, the abundance of three bacterial species, *B. longum*, *C. aerofaciens*, and *E. faecium*, were found to increase in faeces from stool samples of responders to anti-PD-1 antibody therapy than those from non-responders [64]. Importantly, *E. faecium* was also found to be significantly increased in gut microbiota of responder patients with various carcinomas to PD-1 ICB therapy [65]. Even so, there is need of more independent cohort study to validate the

positive association of *C. aerofaciens* with the outcomes of ICB. What's more, *E. faecium* is also frequently reported to be associated with nosocomial outbreaks and infections [66]. Again, one has to be cautious in management of this bacterium.

B. cepacia belongs to the Family Burkholderiaceae, the class betaproteobacteria, and the phylum Proteobacteria. It is a ubiquitous Gram-negative opportunistic pathogens often associated with nosocomial infections in immunocompromised patients [67]. Even so, in the aspect of anticancer immunotherapy, *B. cepacia* alone or in combination with *B. fragilis* can potentiate the efficacy and tolerability of CTLA-4 blockade in antibiotic-treated mice via the stimulation of TH1 cell immune responses [68].

7. Conclusion and perspectives

Although there are many studies, more works are needed to go beyond the identified association between healthy and disease state gut microbiota. Multiomics and longitudinal studies are needed to finally clarify the functions of the emerging probiotics.

As mentioned in the text, several faecal bacteria particularly enriched in clinically healthy individuals, in contrast to the abundances in various diseases groups — are associated with clinical responses to ICB (*A. muciniphila*, *F. prausnitzii*, *Bifidobacterium spp.*, and *B. fragilis*). The underlying reason may lie in that the abundance of these health-associated bacteria might reflect the presence of a well-equilibrated intestinal microflora, leading to a homeostatic host–microbiota ecosystem associated with good health. The other possibility is that reduced number of these NGP candidates may be directly responsible for the aberrant ‘immune set point’. On the other hand, whether a single bacterial strain is enough to achieve such ameliorative effects, or a consortia are needed to achieve the effects of live bacterial biotherapeutics remain to be further addressed. On the other hand, is addition of prebiotics essential to significantly enhance probiotics effects? Future studies must discriminate between these possibilities using preclinical models and/or clinical trials.

Acknowledgements

We would like to express our thankfulness for funding provided from CORPD1F0013 and CMRPD1F0123 from Chang Gung Memorial Hospital, 107-2321-B-182-002 from Ministry of Science and Technology (MOST), Microbiota Research Center from Chang Gung University, and the Research Center for Emerging Viral Infections from The Featured Areas Research Center Program within the framework of the Higher Education Sprout Project by the Ministry of Education (MOE) in Taiwan and MOST, Taiwan (MOST 107-3017-F-182-001). We also are grateful to the National Center for High-performance Computing for computer time and facilities, the Microscope Core Laboratory, Chang Gung Memorial Hospital, Linkou, and the Taiwan Animal Consortium (MOST 107-2319-B-001-002)-Taiwan Mouse Clinic funded by MOST of Taiwan.

REFERENCES

- [1] Tlaskalova-Hogenova H, Stepankova R, Kozakova H, Hudcovic T, Vannucci L, Tuckova L, et al. The role of gut microbiota (commensal bacteria) and the mucosal barrier in the pathogenesis of inflammatory and autoimmune diseases and cancer: contribution of germ-free and gnotobiotic animal models of human diseases. *Cell Mol Immunol* 2011;8:110–20.
- [2] Ivanov II, Honda K. Intestinal commensal microbes as immune modulators. *Cell Host Microbe* 2012;12:496–508.
- [3] Lin CS, Chang CJ, Lu CC, Martel J, Ojcius DM, Ko YF, et al. Impact of the gut microbiota, prebiotics, and probiotics on human health and disease. *Biomed J* 2014;37:259–68.
- [4] Zhu G, Xu Y, Cen X, Nandakumar KS, Liu S, Cheng K. Targeting pattern-recognition receptors to discover new small molecule immune modulators. *Eur J Med Chem* 2018;144:82–92.
- [5] Mogensen TH. Pathogen recognition and inflammatory signaling in innate immune defenses. *Clin Microbiol Rev* 2009;22:240–73 [Table of Contents].
- [6] Willing BP, Gill N, Finlay BB. The role of the immune system in regulating the microbiota. *Gut Microb* 2010;1:213–23.
- [7] Belkaid Y, Hand TW. Role of the microbiota in immunity and inflammation. *Cell* 2014;157:121–41.
- [8] Kelly JR, Kennedy PJ, Cryan JF, Dinan TG, Clarke G, Hyland NP. Breaking down the barriers: the gut microbiome, intestinal permeability and stress-related psychiatric disorders. *Front Cell Neurosci* 2015;9:392.
- [9] Guo H, Diao N, Yuan R, Chen K, Geng S, Li M, et al. Subclinical-dose endotoxin sustains low-grade inflammation and exacerbates steatohepatitis in high-fat diet-fed mice. *J Immunol* 2016;196:2300–8.
- [10] Chang CJ, Lin CS, Lu CC, Martel J, Ko YF, Ojcius DM, et al. *Ganoderma lucidum* reduces obesity in mice by modulating the composition of the gut microbiota. *Nat Commun* 2015;6:7489.
- [11] Woting A, Blaut M. The intestinal microbiota in metabolic disease. *Nutrients* 2016;8:202.
- [12] Hooper LV, Littman DR, Macpherson AJ. Interactions between the microbiota and the immune system. *Science* 2012;336:1268–73.
- [13] Cani PD. Human gut microbiome: hopes, threats and promises. *Gut* 2018;67:1716–25.
- [14] Husted AS, Trauelsen M, Rudenko O, Hjorth SA, Schwartz TW. GPCR-mediated signaling of metabolites. *Cell Metabol* 2017;25:777–96.
- [15] Kimura I, Inoue D, Hirano K, Tsujimoto G. The SCFA receptor GPR43 and energy metabolism. *Front Endocrinol (Lausanne)* 2014;5:85.
- [16] Peng L, Li ZR, Green RS, Holzman IR, Lin J. Butyrate enhances the intestinal barrier by facilitating tight junction assembly via activation of AMP-activated protein kinase in Caco-2 cell monolayers. *J Nutr* 2009;139:1619–25.
- [17] Glover LE, Lee JS, Colgan SP. Oxygen metabolism and barrier regulation in the intestinal mucosa. *J Clin Invest* 2016;126:3680–8.
- [18] Byndloss MX, Olsan EE, Rivera-Chavez F, Tiffany CR, Cevallos SA, Lokken KL, et al. Microbiota-activated PPAR- γ signaling inhibits dysbiotic Enterobacteriaceae expansion. *Science* 2017;357:570–5.
- [19] Clarke G, Stilling RM, Kennedy PJ, Stanton C, Cryan JF, Dinan TG. Minireview: gut microbiota: the neglected endocrine organ. *Mol Endocrinol* 2014;28:1221–38.
- [20] Oliveira G, Gonzalez-Molero I. An update on probiotics, prebiotics and symbiotics in clinical nutrition. *Endocrinol Nutr* 2016;63:482–94.
- [21] Bottacini F, van Sinderen D, Ventura M. Omics of bifidobacteria: research and insights into their health-promoting activities. *Biochem J* 2017;474:4137–52.
- [22] Hiippala K, Jouhten H, Ronkainen A, Hartikainen A, Kainulainen V, Jalanka J, et al. The potential of gut commensals in reinforcing intestinal barrier function and alleviating inflammation. *Nutrients* 2018;10.
- [23] Bilen M, Dufour JC, Lagier JC, Cadoret F, Daoud Z, Dubourg G, et al. The contribution of culturomics to the repertoire of isolated human bacterial and archaeal species. *Microbiome* 2018;6:94.
- [24] Ross JJ, Boucher PE, Bhattacharyya SP, Kopecko DJ, Sutkowski EM, Rohan PJ, et al. Considerations in the development of live biotherapeutic products for clinical use. *Curr Issues Mol Biol* 2008;10:13–6.
- [25] Felis GE, Dellaglio F. Taxonomy of lactobacilli and bifidobacteria. *Curr Issues Intest Microbiol* 2007;8:44–61.
- [26] Russell DA, Ross RP, Fitzgerald GF, Stanton C. Metabolic activities and probiotic potential of bifidobacteria. *Int J Food Microbiol* 2011;149:88–105.
- [27] Delcenserie V, Gavini F, Beerens H, Tresse O, Franssen C, Daube G. Description of a new species, *Bifidobacterium crudilactis* sp. nov., isolated from raw milk and raw milk cheeses. *Syst Appl Microbiol* 2007;30:381–9.
- [28] Sivan A, Corrales L, Hubert N, Williams JB, Aquino-Michaels K, Earley ZM, et al. Commensal *Bifidobacterium* promotes antitumor immunity and facilitates anti-PD-L1 efficacy. *Science* 2015;350:1084–9.
- [29] Kahouli I, Tomaro-Duchesneau C, Prakash S. Probiotics in colorectal cancer (CRC) with emphasis on mechanisms of action and current perspectives. *J Med Microbiol* 2013;62:1107–23.
- [30] Le Leu RK, Hu Y, Brown IL, Woodman RJ, Young GP. Synbiotic intervention of *Bifidobacterium lactis* and resistant starch protects against colorectal cancer development in rats. *Carcinogenesis* 2010;31:246–51.
- [31] Roller M, Clune Y, Collins K, Rechkemmer G, Watzl B. Consumption of prebiotic inulin enriched with oligofructose in combination with the probiotics *Lactobacillus rhamnosus* and *Bifidobacterium lactis* has minor effects on selected immune parameters in polypectomised and colon cancer patients. *Br J Nutr* 2007;97:676–84.
- [32] Rong Y, Dong Z, Hong Z, Jin Y, Zhang W, Zhang B, et al. Reactivity toward *Bifidobacterium longum* and *Enterococcus hirae* demonstrate robust CD8(+) T cell response and better prognosis in HBV-related hepatocellular carcinoma. *Exp Cell Res* 2017;358:352–9.
- [33] Fu GF, Li X, Hou YY, Fan YR, Liu WH, Xu GX. *Bifidobacterium longum* as an oral delivery system of endostatin for gene therapy on solid liver cancer. *Cancer Gene Ther* 2005;12:133–40.
- [34] Li C, Chen X, Kou L, Hu B, Zhu LP, Fan YR, et al. Selenium-*Bifidobacterium longum* as a delivery system of endostatin for inhibition of pathogenic bacteria and selective regression of solid tumor. *Exp Ther Med* 2010;1:129–35.
- [35] De Vadder F, Kovatcheva-Datchary P, Zitoun C, Duchamp A, Backhed F, Mithieux G. Microbiota-produced succinate improves glucose homeostasis via intestinal gluconeogenesis. *Cell Metabol* 2016;24:151–7.
- [36] Pedersen HK, Gudmundsdottir V, Nielsen HB, Hyotylainen T, Nielsen T, Jensen BA, et al. Human gut microbes impact host serum metabolome and insulin sensitivity. *Nature* 2016;535:376–81.
- [37] Cani PD, de Vos WM. Next-generation beneficial microbes: the case of *Akkermansia muciniphila*. *Front Microbiol* 2017;8:1765.
- [38] Everard A, Belzer C, Geurts L, Ouwerkerk JP, Druart C, Bindels LB, et al. Cross-talk between *Akkermansia muciniphila* and intestinal epithelium controls diet-induced obesity. *Proc Natl Acad Sci U S A* 2013;110:9066–71.

- [39] Plovier H, Everard A, Druart C, Depommier C, Van Hul M, Geurts L, et al. A purified membrane protein from *Akkermansia muciniphila* or the pasteurized bacterium improves metabolism in obese and diabetic mice. *Nat Med* 2017;23:107–13.
- [40] Cani PD, Geurts L, Matamoros S, Plovier H, Duparc T. Glucose metabolism: focus on gut microbiota, the endocannabinoid system and beyond. *Diabetes Metab* 2014;40:246–57.
- [41] Wang Y, Ma R, Liu F, Lee SA, Zhang L. Modulation of gut microbiota: a novel paradigm of enhancing the efficacy of programmed death-1 and programmed death ligand-1 blockade therapy. *Front Immunol* 2018;9:374.
- [42] Schneeberger M, Everard A, Gomez-Valades AG, Matamoros S, Ramirez S, Delzenne NM, et al. *Akkermansia muciniphila* inversely correlates with the onset of inflammation, altered adipose tissue metabolism and metabolic disorders during obesity in mice. *Sci Rep* 2015;5:16643.
- [43] Heintz-Buschart A, Pandey U, Wicke T, Sixel-Doring F, Janzen A, Sittig-Wiegand E, et al. The nasal and gut microbiome in Parkinson's disease and idiopathic rapid eye movement sleep behavior disorder. *Mov Disord* 2018;33:88–98.
- [44] Erturk-Hasdemir D, Kasper DL. Finding a needle in a haystack: *Bacteroides fragilis* polysaccharide A as the archetypical symbiosis factor. *Ann N Y Acad Sci* 2018;1417:116–29.
- [45] Huang JY, Lee SM, Mazmanian SK. The human commensal *Bacteroides fragilis* binds intestinal mucin. *Anaerobe* 2011;17:137–41.
- [46] Sears CL, Islam S, Saha A, Arjumand M, Alam NH, Faruque AS, et al. Association of enterotoxigenic *Bacteroides fragilis* infection with inflammatory diarrhea. *Clin Infect Dis* 2008;47:797–803.
- [47] Round JL, Mazmanian SK. Inducible Foxp3+ regulatory T-cell development by a commensal bacterium of the intestinal microbiota. *Proc Natl Acad Sci U S A* 2010;107:12204–9.
- [48] Dasgupta S, Erturk-Hasdemir D, Ochoa-Reparaz J, Reinecker HC, Kasper DL. Plasmacytoid dendritic cells mediate anti-inflammatory responses to a gut commensal molecule via both innate and adaptive mechanisms. *Cell Host Microbe* 2014;15:413–23.
- [49] Lukiw WJ. *Bacteroides fragilis* lipopolysaccharide and inflammatory signaling in Alzheimer's disease. *Front Microbiol* 2016;7:1544.
- [50] Goodrich JK, Waters JL, Poole AC, Sutter JL, Koren O, Blekhman R, et al. Human genetics shape the gut microbiome. *Cell* 2014;159:789–99.
- [51] Goodrich JK, Davenport ER, Beaumont M, Jackson MA, Knight R, Ober C, et al. Genetic determinants of the gut microbiome in UK twins. *Cell Host Microbe* 2016;19:731–43.
- [52] Miquel S, Martin R, Rossi O, Bermudez-Humaran LG, Chatel JM, Sokol H, et al. *Faecalibacterium prausnitzii* and human intestinal health. *Curr Opin Microbiol* 2013;16:255–61.
- [53] Duncan SH, Hold GL, Harmsen HJ, Stewart CS, Flint HJ. Growth requirements and fermentation products of *Fusobacterium prausnitzii*, and a proposal to reclassify it as *Faecalibacterium prausnitzii* gen. nov., comb. nov. *Int J Syst Evol Microbiol* 2002;52:2141–6.
- [54] Wrzosek L, Miquel S, Noordine ML, Bouet S, Joncquel Chevalier-Curt M, Robert V, et al. *Bacteroides thetaiotaomicron* and *Faecalibacterium prausnitzii* influence the production of mucus glycans and the development of goblet cells in the colonic epithelium of a gnotobiotic model rodent. *BMC Biol* 2013;11:61.
- [55] Park YJ, Kuen DS, Chung Y. Future prospects of immune checkpoint blockade in cancer: from response prediction to overcoming resistance. *Exp Mol Med* 2018;50:109.
- [56] Gopalakrishnan V, Spencer CN, Nezi L, Reuben A, Andrews MC, Karpinets TV, et al. Gut microbiome modulates response to anti-PD-1 immunotherapy in melanoma patients. *Science* 2018;359:97–103.
- [57] Chaput N, Lepage P, Coutzac C, Soularue E, Le Roux K, Monot C, et al. Baseline gut microbiota predicts clinical response and colitis in metastatic melanoma patients treated with ipilimumab. *Ann Oncol* 2017;28:1368–79.
- [58] Wu TR, Lin CS, Chang CJ, Lin TL, Martel J, Ko YF, et al. Gut commensal *Parabacteroides goldsteinii* plays a predominant role in the anti-obesity effects of polysaccharides isolated from *Hirsutella sinensis*. *Gut* 2019 Feb;68(2):248–62.
- [59] Kanauchi O, Fukuda M, Matsumoto Y, Ishii S, Ozawa T, Shimizu M, et al. *Eubacterium limosum* ameliorates experimental colitis and metabolite of microbe attenuates colonic inflammatory action with increase of mucosal integrity. *World J Gastroenterol* 2006;12:1071–7.
- [60] Mulanovich VE, Desai PA, Popat UR. Allogeneic stem cell transplantation for HIV-positive patients with hematologic malignancies. *AIDS* 2016;30:2653–7.
- [61] Routy B, Le Chatelier E, Derosa L, Duong CPM, Alou MT, Daillere R, et al. Gut microbiome influences efficacy of PD-1-based immunotherapy against epithelial tumors. *Science* 2018;359:91–7.
- [62] Daillere R, Vetizou M, Waldschmitt N, Yamazaki T, Isnard C, Poirier-Colame V, et al. *Enterococcus hirae* and *barnesiella intestinihominis* facilitate cyclophosphamide-induced therapeutic immunomodulatory effects. *Immunity* 2016;45:931–43.
- [63] Bourafa N, Loucif L, Boutefnouchet N, Rolain JM. *Enterococcus hirae*, an unusual pathogen in humans causing urinary tract infection in a patient with benign prostatic hyperplasia: first case report in Algeria. *New Microbes New Infect* 2015;8:7–9.
- [64] Matson V, Fessler J, Bao R, Chongsuwat T, Zha Y, Alegre ML, et al. The commensal microbiome is associated with anti-PD-1 efficacy in metastatic melanoma patients. *Science* 2018;359:104–8.
- [65] Derosa L, Routy B, Kroemer G, Zitvogel L. The intestinal microbiota determines the clinical efficacy of immune checkpoint blockers targeting PD-1/PD-L1. *OncoImmunology* 2018;7:e1434468.
- [66] Ulrich N, Vonberg RP, Gastmeier P. Outbreaks caused by vancomycin-resistant *Enterococcus faecium* in hematology and oncology departments: a systematic review. *Heliyon* 2017;3:e00473.
- [67] Lipowski D, Rzadkiewicz E, Czekalska-Lachowicz E. [*Burkholderia cepacia*: a new pathogen causing nosocomial infections]. *Przegl Epidemiol* 2008;62:7–17.
- [68] Pitt JM, Vetizou M, Gomperts Boneca I, Lepage P, Chamaillard M, Zitvogel L. Enhancing the clinical coverage and anticancer efficacy of immune checkpoint blockade through manipulation of the gut microbiota. *OncoImmunology* 2017;6:e1132137.

Allicin Inhibits Glutamate Release from Rat Cerebral Cortex Nerve Terminals Through Suppressing Ca^{2+} Influx and Protein Kinase C Activity

Cheng-Wei Lu,^{1,2} Chi-Feng Hung,³ Tzu-Yu Lin,^{1,2} Ting Yang Hsieh,⁴ and Su Jane Wang^{3,5}

¹Department of Anesthesiology, Far-Eastern Memorial Hospital, New Taipei City, Taiwan.

²Department of Mechanical Engineering, Yuan Ze University, Taoyuan City, Taiwan.

³School of Medicine, Fu Jen Catholic University, New Taipei City, Taiwan.

⁴P.H.D. Program in Nutrition and Food Science, Fu Jen Catholic University, New Taipei City, Taiwan.

⁵Research Center for Chinese Herbal Medicine, College of Human Ecology, Chang Gung University of Science and Technology, Taoyuan City, Taiwan.

ABSTRACT Evidence indicates that indirect inhibitory regulation of glutamatergic transmission, via reducing glutamate release, may induce neuroprotection. The present work was designed to examine whether allicin, a major component of garlic with neuroprotective effects, affected the release of glutamate evoked by 4-aminopyridine in rat cerebrocortical nerve terminals (synaptosomes). Allicin caused a potent inhibition on the release of glutamate evoked by 4-aminopyridine, and this inhibitory effect was abolished in the presence of Ca^{2+} -free medium and vesicular transporter inhibitor. Allicin decreased the 4-aminopyridine-evoked elevation of intrasynaptosomal Ca^{2+} levels, but had no effect on the synaptosomal plasma membrane potential. The allicin-mediated inhibition of glutamate release was prevented by the N- and P/Q-type channel blocker and the protein kinase C (PKC) inhibitor, but was not affected by the intracellular Ca^{2+} -release inhibitors, mitogen-activated protein kinase inhibitor, and protein kinase A inhibitor. Western blotting data also showed that allicin significantly reduced the phosphorylation of PKC. Together, these data indicate that in rat cerebrocortical nerve terminals, allicin depresses glutamate release and appears to decrease N- and P/Q-type Ca^{2+} channel and PKC activity.

Keywords: • allicin • cerebrocortical synaptosomes • glutamate release • presynaptic Ca^{2+} channels • protein kinase C

INTRODUCTION

GLUTAMATE IS A PHYSIOLOGICALLY important excitatory neurotransmitter in the mammalian brain. Increased amounts of glutamate cause excessive stimulation of glutamate receptors and leads to neuronal death.¹ This phenomenon is well known as excitotoxicity, which has been implicated in several neuronal diseases, such as epilepsy, ischemia, stroke, trauma, or neurodegenerative diseases.² Animal studies have confirmed neuroprotective effects of the glutamate receptor antagonists in the central nervous system, however, these agents have been unsuccessful in clinical trials because of many adverse effects, such as ataxia, psychosis, and cognitive dysfunction.^{3,4} Therefore, a more promising neuroprotective strategy for treating brain disorders may be through indirect inhibitory modulation of glutamatergic transmission, such as reducing glutamate release.^{5–8}

Recently, there is an emerging trend to search for natural resources to combat against brain diseases. Many studies have reported the protective effects of various natural products against excitotoxicity models.^{9–11} Allicin is an active constituent of garlic and possesses antioxidative, anti-inflammatory, antimicrobial, anticancer, cardiovascular protective, and immunomodulatory properties.^{12,13} Allicin also presents neuroprotective properties and has been investigated in various animal models with neurological disorders, including stroke, traumatic brain injury, and Alzheimer's disorder.^{14–18} However, the mechanism involved in the neuroprotective effects of allicin in the brain is not adequately understood.

Given the involvement of excessive glutamate-mediated neurotoxicity in brain injury, this work aims to study the effect and possible mechanisms of allicin on glutamate release by using rat cerebral cortex nerve terminals (synaptosomes), a model particularly suited to the evaluation of presynaptic effects on neurotransmitter release.¹⁹ To our knowledge, a direct effect of allicin on glutamate release in synaptosome preparations has not yet been studied, and hence this will be the first report in this field.

Manuscript received 2 October 2018. Revision accepted 27 February 2019.

Address correspondence to: Su-Jane Wang, PhD, School of Medicine, Fu Jen Catholic University, No. 510, Chung-Cheng Road, Hsin-Chuang, New Taipei City 24205, Taiwan, E-mail: med0003@mail.fju.edu.tw

MATERIALS AND METHODS

Chemicals

DL-threo- β -benzyl-oxyaspartate (DL-TBOA), Bafilomycin A1, dantrolene, GP37157, bisindolylmaleimide I (GF109203X), 2-(2-amino-3-methoxyphenyl)-4H-1-benzopyran-4-one (PD98059), and N-[2-(*p*-bromocinnamylamino)ethyl]-5-isoquinolinesulfonamide (H89) were purchased from Tocris Cookson (Bristol, United Kingdom). 3,3'-dipropylthiadicarbocyanine iodide [DiSC₃(5)] was obtained from Invitrogen (Carlsbad, CA, USA). ω -Conotoxin MVIIC was purchased from Alomone Labs (Jerusalem, Israel). Fura-2-acetoxymethyl (Fura-2-AM) ester was obtained from Life Technologies (Bengaluru, India). Allicin, 4-aminopyridine, and all other reagents were obtained from Sigma-Aldrich (St. Louis, MO, USA).

Experimental animals

Male Sprague-Dawley rats (2-month-old; BioLASCO, Inc., Taiwan) were used throughout the study. Animals were sacrificed by rapid decapitation. All experiments with rats were conducted according to the guidelines established by the Institutional Animal Care and Utilization Committee at Fu Jen Catholic University.

Preparation of synaptosomes

Synaptosomes from rat cerebral cortex were isolated as described previously.^{20,21} In brief, the tissue was homogenized in 0.32 M sucrose; the homogenate was centrifuged for 2 min at 3000 g, and the supernatant (2 mL) was placed on a 3 mL Percoll discontinuous gradient (3%, 10%, and 23% in Tris-buffered sucrose). After centrifugation at 32,500 g for 7 min, the synaptosomes were collected from the 10% and 23% Percoll bands, and they were resuspended in hydroxyethyl piperazine ethanesulfonic acid (HEPES) buffer medium having the following composition (mM): NaCl, 140; KCl, 5; NaHCO₃, 5; MgCl₂·6H₂O, 1; Na₂HPO₄, 1.2; glucose, 10; HEPES, 10; and pH 7.4.

Glutamate release experiment

The release of glutamate was measured using a continuous fluorimetric assay, based on the reduction of NADP⁺ catalyzed by glutamate dehydrogenase in the presence of glutamate.^{22,23} In short, synaptosomes (0.5 mg) were incubated for 5 min at 37°C in HEPES buffer medium (HBM) containing bovine serum albumin (BSA; 16 μ M) in a PerkinElmer LS-55 spectrofluorimeter (PerkinElmer Life and Analytical Sciences, Waltham, MA, USA). After a further 5 min incubation, NADP⁺ (1 mM), glutamate dehydrogenase (50 units/mL) and CaCl₂ (1.2 mM) were added, and the fluorescence of nicotinamide adenine dinucleotide phosphate (NADPH) was measured, at excitation and emission wavelengths of 340 and 460 nm, respectively. Glutamate release was quantitated by the addition of 5 nmol glutamate at the end of each run, which acted as an internal standard. The data were obtained at 2-sec intervals.

Intraterminal Ca²⁺ concentration

Intraterminal Ca²⁺ concentration ([Ca²⁺]_i) was assayed with Fura-2 as described previously.²⁴ Synaptosomes were preincubated in HBM containing Fura-2-AM (5 μ M), CaCl₂ (0.1 mM), and BSA (16 μ M) for 30 min at 37°C. Then the synaptosomes were centrifuged for 1 min at 10,000 g and resuspended in HBM containing BSA (16 μ M) and CaCl₂ (1.2 mM) at 37°C. Fura-2-Ca fluorescence was assayed under continuous stirring, at the excitation wavelengths of 340 and 380 nm and emission wavelength of 505 nm and data accumulated at 5-sec intervals. The [Ca²⁺]_i was calculated with the equations described previously.²⁵

Membrane potential measurement using DiSC₃(5)

Synaptosomes in HBM containing BSA were preincubated for 30 min at 37°C. After this time, an aliquot (2 mL) was transferred to a stirred cuvette containing DiSC₃(5) (5 μ M) and CaCl₂ (1.2 mM). After 1 min incubation, DiSC₃(5) fluorescence was assayed at excitation and emission wavelengths of 646 and 674 nm, respectively, and data accumulated at 2-sec intervals.²⁶

Western blotting

Synaptosomes were lysed in ice-cold lysis buffer and quantified for protein content. Samples (20 μ g) were separated by 10% sodium dodecyl sulfate polyacrylamide gel electrophoresis and transferred onto polyvinylidene difluoride membrane. Membranes were incubated at room temperature for 1 h in Tris-buffered saline containing 5% skimmed milk and then probed with rabbit monoclonal anti-phospho-protein kinase C (PKC) (1:2000; Cell Signaling Technology, MA, USA) and anti- β -actin (1:5000; Cell Signaling Technology), overnight at 4°C. After extensive washes in Tris-buffered saline, membranes were incubated for 1 h at room temperature with appropriate peroxidase-conjugated goat anti-rabbit IgG secondary antibody (1:5000; Santa Cruz, CA, USA). Immunoblots were visualized with an enhanced chemiluminescence (Amersham, Buckinghamshire, United Kingdom) plus western blot detection system (Synoptics, Cambridge, United Kingdom).

Data analysis

Data are expressed as the mean \pm standard error of the mean (SEM). Statistical significance was determined by unpaired Student's two-tailed *t*-tests and two-way analysis of variance with Scheffe's *post hoc* test. A *P*-value < .05 was considered statistically significant.

RESULTS

Figure 1A shows that 4-aminopyridine triggered a glutamate release of 6.9 ± 0.2 nmol/mg/5 min in the cerebrocortical synaptosomes incubated in the presence of CaCl₂ (1.2 mM). Preincubation with 10 μ M allicin before 4-aminopyridine addition reduced glutamate release to 2.8 ± 0.1 nmol/mg/5 min [*t*(18) = 22.7, *P* < .001; $55.8\% \pm 1.5\%$].

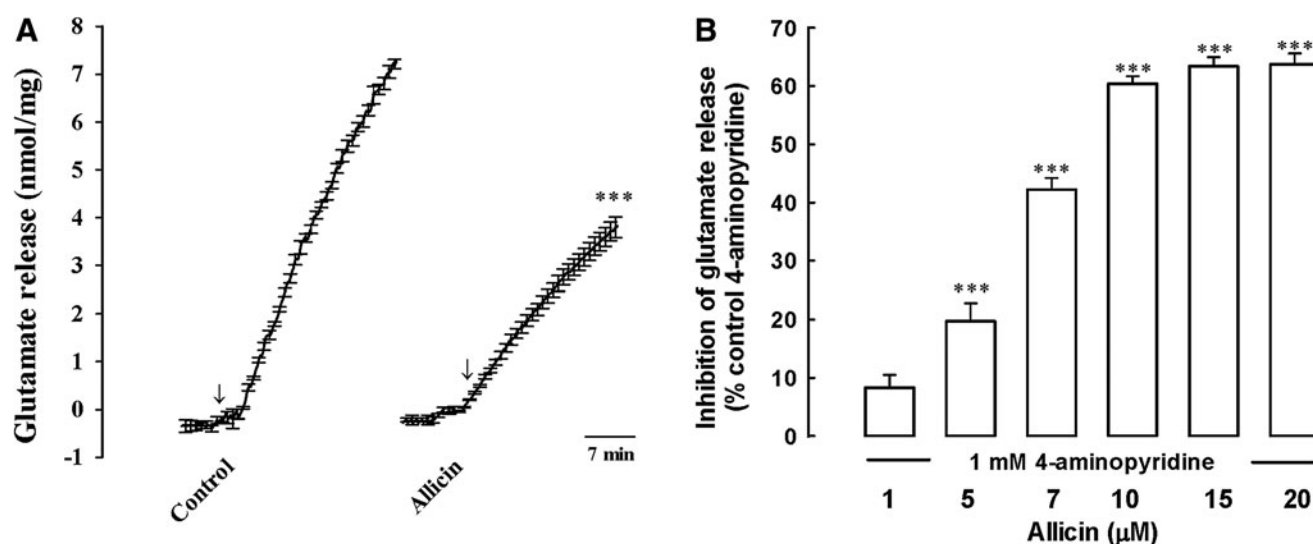


FIG. 1. Allacin inhibits 4-aminopyridine-evoked glutamate release from rat cerebrocortical synaptosomes. **(A)** Glutamate release was evoked by the addition of 1 mM 4-aminopyridine (arrow) in the absence (control) and presence of 10 μ M allacin added 10 min before depolarization. **(B)** Concentration-effect relationship of allacin (1–20 μ M) on 4-aminopyridine-induced glutamate release. Data are mean \pm SEM. ($n=5$). *** $P < .001$ compared with control. SEM, standard error of the mean.

inhibition; Fig. 1B]. Allacin had no effect on the basal release of glutamate ($P > .05$). The action of allacin was dose-dependent; the maximum inhibition was seen when allacin was applied at 10 μ M and the half-maximal inhibitory concentration (IC_{50}) was 6 μ M (Fig. 1B).

Figure 2A shows that the evoked glutamate release was decreased in the presence of calcium-free solution that contained 300 μ M ethylene glycol-bis(β -aminoethyl ether)-

N,N,N',N'-tetraacetic acid (EGTA) [$t(8) = 25.5$, $P < .001$]. In the absence of extracellular calcium, the allacin (10 μ M)-mediated inhibition of glutamate release was abolished [$F(1.17) = 233.2$, $P < .001$; Fig. 2A, B]. DL-TBOA (10 μ M), an excitatory amino acid transporter blocker, increased 4-aminopyridine-induced glutamate release [$t(9) = -8.9$, $P < .001$] and failed to affect the inhibitory effect of allacin on evoked glutamate release [$F(1.19) = 2.83$, $P = .11$; Fig. 2A].

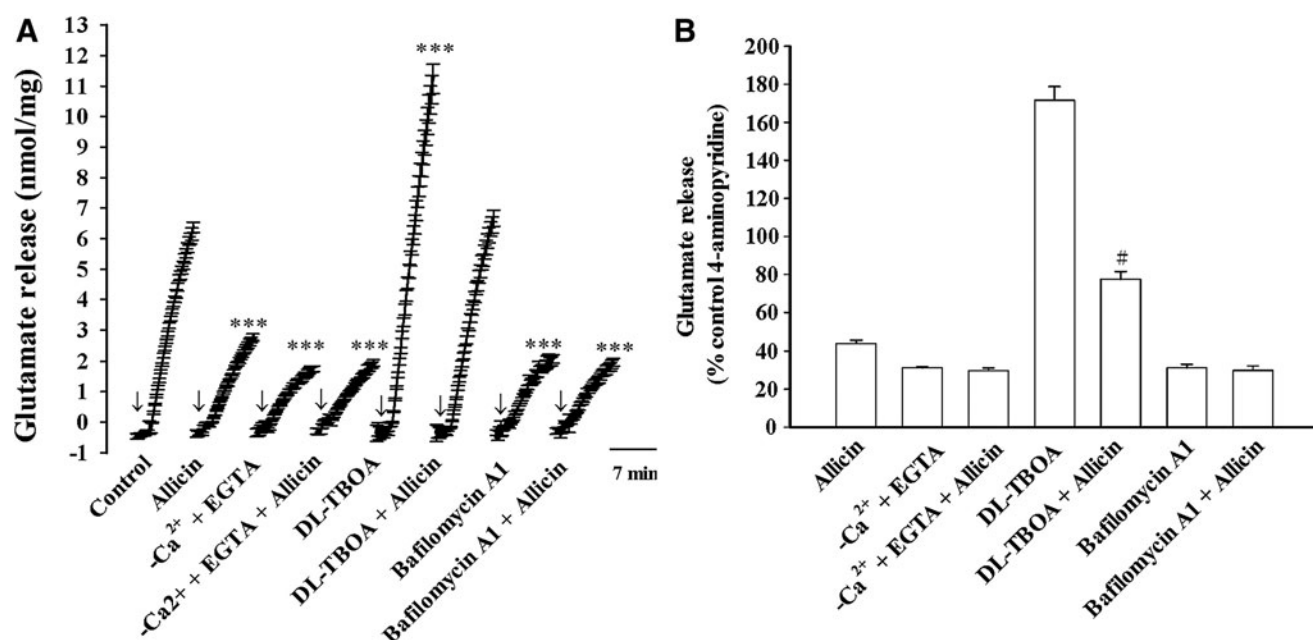


FIG. 2. Effect of external calcium omission, the glutamate transporter blocker DL-TBOA, and the vesicular transporter inhibitor bafilomycin A1 on the allacin-mediated inhibition of 4-aminopyridine-evoked glutamate release. **(A)** The effect of allacin on glutamate release induced by 1 mM 4-aminopyridine (arrow) in the absence (control) and presence of 300 μ M EGTA (without $CaCl_2$), 10 μ M DL-TBOA, or 0.1 μ M bafilomycin A1. **(B)** Quantitative comparison of the extent of glutamate release by 1 mM 4-aminopyridine with allacin alone and in the presence of EGTA (without $CaCl_2$), DL-TBOA or bafilomycin A1. Data are mean \pm SEM. ($n=5-6$). *** $P < .001$ compared with control; # $P < .05$ compared with DL-TBOA alone. DL-TBOA, DL-threo- β -benzyl-oxyaspartate; EGTA, ethylene glycol-bis(β -aminoethyl ether)-N,N,N',N'-tetraacetic acid.

TABLE 1. EFFECT OF ALLICIN ON INTRASYNAPTOSOMAL Ca^{2+} CONCENTRATION ($[\text{Ca}^{2+}]_i$) AND SYNAPTOSOMAL MEMBRANE POTENTIAL AND IN RAT CEREBROCORTICAL SYNAPTOSOMES

	$[\text{Ca}^{2+}]_i$ (nM)			Membrane potential (fluorescence units)		
	Basal	4-Aminopyridine	n	Basal	4-Aminopyridine	n
Control	1169.8 ± 8.4	216.7 ± 6.9***	5	0.7 ± 1.2	35.5 ± 2.7***	5
Allicin	1167.8 ± 5.1	194.6 ± 4.7 [#]	5	0.5 ± 0.1	33.5 ± 1.2	5

*** $P < .001$ versus the control group; [#] $P < .001$ versus the 4-aminopyridine group.

In the presence of DL-TBOA, allisin (10 μM) continued to significantly suppress 4-aminopyridine-induced release of glutamate ($P < .05$; Fig. 2B). In addition, the vesicular transporter inhibitor bafilomycin A1 (0.1 μM) reduced the glutamate release evoked by 4-aminopyridine [$t(8) = 21.4$, $P < .001$] and abolished the inhibitory effect of allisin [$F(1.19) = 167.1$, $P < .001$; Fig. 2A]. On average, in the presence of bafilomycin A1, allisin produced a $4.0\% \pm 7.4\%$ inhibition, which was significantly different from the inhibition produced by allisin alone [$55.8\% \pm 1.5\%$; $t(9) = 6.7$, $P < .05$; Fig. 2B]. These data indicate that allisin only inhibits the Ca^{2+} -dependent release of glutamate evoked by 4-aminopyridine.

Table 1 shows the effects of allisin on the $[\text{Ca}^{2+}]_i$ and synaptosomal membrane potential. The depolarization of synaptosomes due to 4-aminopyridine (1 mM) caused a rise in $[\text{Ca}^{2+}]_i$ to a plateau level. Preincubation with 10 μM allisin did not alter the basal $[\text{Ca}^{2+}]_i$, but it decreased the 4-aminopyridine-evoked rise in $[\text{Ca}^{2+}]_i$ [$t(8) = 8.1$, $P < .001$].

In addition, 4-aminopyridine caused an increase in DiSC₃(5) fluorescence. The presence of 10 μM allisin did not significantly affect the plasma membrane potential either under resting conditions or 4-aminopyridine stimulation [$t(8) = 0.67$, $P > .05$] (Table 1). These results suggest that the observed inhibition of the elevation of $[\text{Ca}^{2+}]_i$ by allisin was most likely due to a direct reduction of Ca^{2+} influx through voltage-dependent Ca^{2+} channels, which consequently reduced glutamate release.

Figure 3 assesses the role of N- and P/Q-type Ca^{2+} channels, which support glutamate release from synaptosomes.^{27,28} The glutamate release evoked by 4-aminopyridine (1 mM) was significantly decreased by 4 μM ω -conotoxin MVIIC, an N- and P/Q-type Ca^{2+} channel blocker [$t(8) = 21.7$, $P < .001$]. Notably, in the presence of ω -conotoxin MVIIC, the inhibitory effect of 10 μM allisin on the glutamate release evoked by 4-aminopyridine was abolished [$F(1.17) = 13.3$, $P < .001$; Fig. 3A, B]. We also examined the inhibitory effect of allisin in synaptosome

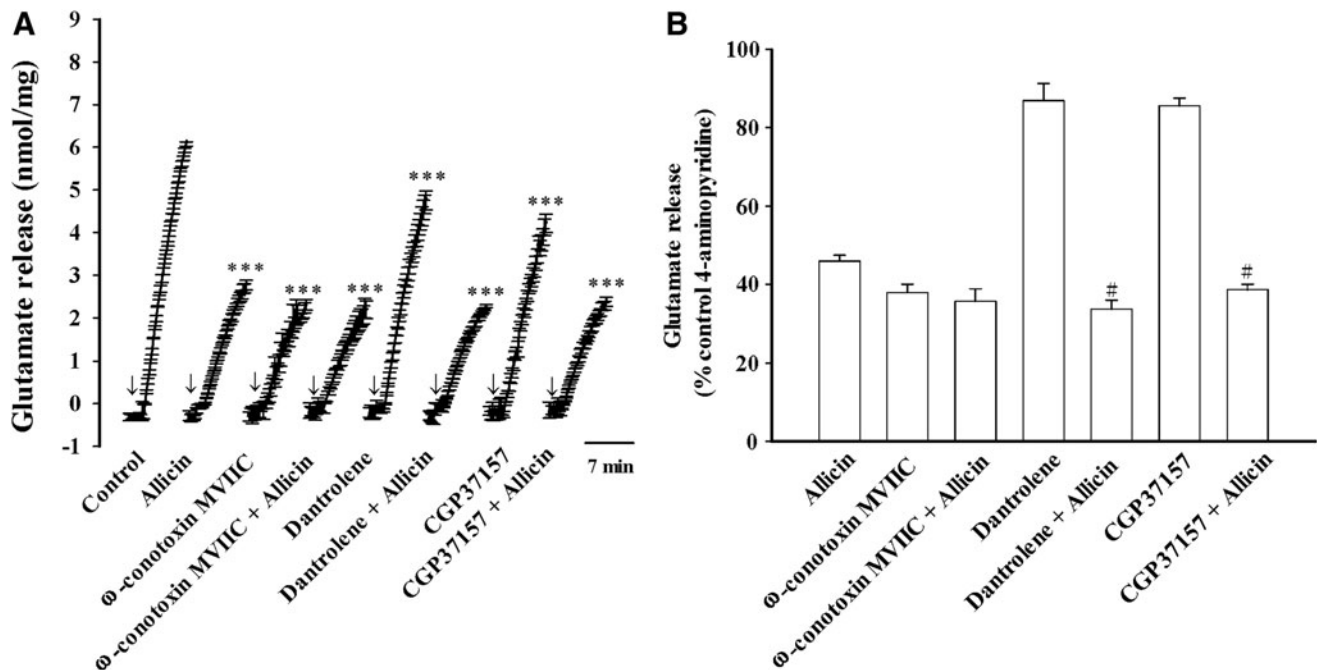


FIG. 3. Effects of N- and P/Q-type calcium channel blocker ω -conotoxin MVIIC or intracellular Ca^{2+} release inhibitors dantrolene and CGP37157 on the allisin-mediated inhibition of 4-aminopyridine-evoked glutamate release. (A) The effect of allisin on glutamate release induced by 1 mM 4-aminopyridine (arrow) in the absence (control) and presence of 4 μM ω -conotoxin MVIIC, 100 μM dantrolene, or 100 μM CGP37157. (B) Quantitative comparison of the extent of glutamate release by 1 mM 4-aminopyridine with allisin alone and in the presence of ω -conotoxin MVIIC, dantrolene, or CGP37157. Data are mean \pm SEM. ($n = 5$). *** $P < .01$ compared with control; [#] $P < .05$ compared with dantrolene or CGP37157 alone.

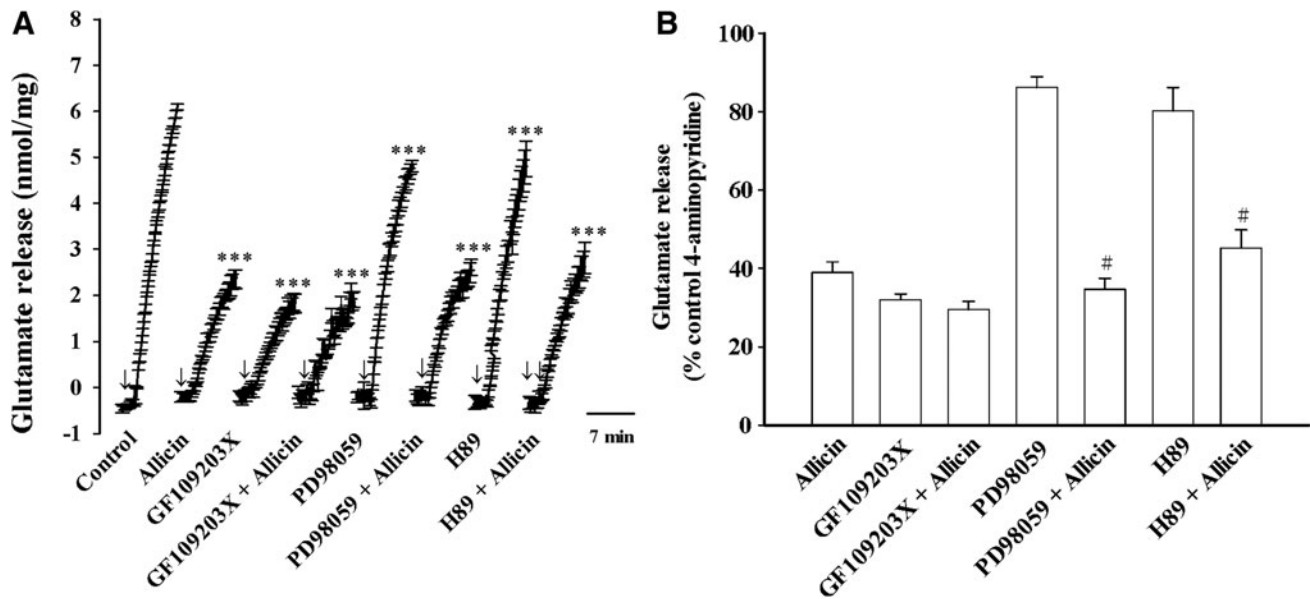


FIG. 4. Effects of the PKC inhibitor GF109203X, MAPK inhibitor PD98059 and PKA inhibitor H89 on the alliin-mediated inhibition of 4-aminopyridine-evoked glutamate release. (A) The effect of alliin on glutamate release induced by 1 mM 4-aminopyridine (arrow) in the absence (control) and presence of 10 μ M GF109203X, 10 μ M PD98059, or 100 μ M H89. (B) Quantitative comparison of the extent of glutamate release by 1 mM 4-aminopyridine with alliin alone and in the presence of GF109203X, PD98059, or H89. Data are mean \pm SEM. ($n=5$). *** $P < .001$ compared with control; # $P < .05$ compared with PD98059 or H89 alone. PKA, protein kinase A; MAPK, mitogen-activated protein kinase; PKC, protein kinase C.

pretreated with the intracellular Ca^{2+} -release inhibitors dantrolene (100 μ M) and CGP37157 (100 μ M). Figure 3A shows that the two inhibitors significantly affected the evoked glutamate release (dantrolene, $t(8)=2.6$, $P < .001$; CGP37157, $t(8)=8.7$, $P < .001$). However, dantrolene or CGP37157 was not able to influence the alliin-mediated inhibition of 4-aminopyridine (4-AP) evoked glutamate release [dantrolene, $F(1.17)=13.3$, $P > .05$; CGP37157, $F(1.17)=4.3$; $P > .05$; Fig. 3A]. In the presence of dantrolene or CGP37157, alliin induced a statistically significant inhibition ($P < .05$; Fig. 3B). Therefore, a reduction of Ca^{2+} entry through N- and P/Q-type Ca^{2+} channels is involved in the inhibitory action of alliin on evoked glutamate release.

Figure 4 shows that the evoked glutamate release was reduced by the PKC inhibitor GF109203X (10 μ M) [$t(8)=39.9$, $P < .001$], mitogen-activated protein kinase (MAPK) inhibitor PD98059 (10 μ M) [$t(8)=15.1$, $P < .001$], and protein kinase A (PKA) inhibitor H89 (100 μ M) [$t(8)=7.2$, $P < .001$]. PD98059 or H89 failed to affect the ability of alliin (10 μ M) to inhibit glutamate release [PD98059, $F(1.16)=3.9$, $P > .05$; H89, $F(1.16)=10.3$; $P > .05$; Fig. 4A]. In the presence of PD98059 or H89, alliin produced a statistically significant inhibition ($P < .05$; Fig. 4B). By contrast, alliin (10 μ M) only reduced glutamate release by an additional $8.2\% \pm 6.8\%$ in synaptosome pretreated with GF109203X [$F(1.16)=216.8$; $P < .001$], thus indicating a significantly higher reduction in release than that observed for the $59.5\% \pm 2.7\%$ inhibition produced by alliin alone ($P < .05$; Fig. 4A, B). In addition, the levels of

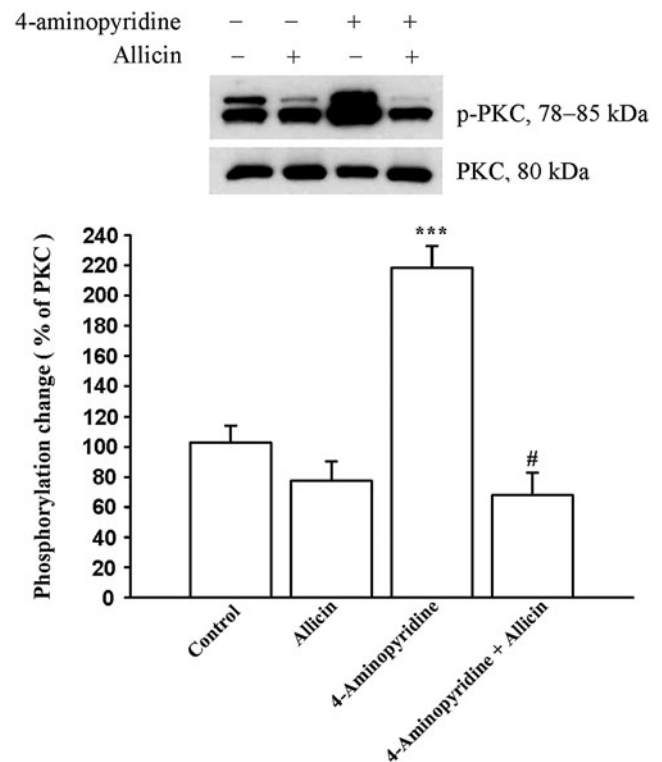


FIG. 5. Effect of alliin on the activation of PKC. The expression levels of p-PKC and PKC in synaptosomes were determined by western blotting. Data are mean \pm SEM. ($n=5$). *** $P < .001$ compared with control; # $P < .05$ compared with 4-aminopyridine alone.

phosphorylated PKC in synaptosomes were assessed with western blotting (Fig. 5). Increases in the phosphorylation of PKC was observed after 4-aminopyridine (1 mM) addition [control, $102.8\% \pm 11.4\%$; 4-aminopyridine, $218.6\% \pm 14.5\%$; $t(8) = -6.3$, $P < .001$]. This 4-aminopyridine-increased phosphorylation of PKC was also markedly reduced after exposure to $10 \mu\text{M}$ allicin ($67.9\% \pm 14.5\%$; $P < .05$; Fig. 5). Allicin did not significantly affect the phosphorylation of PKC in the control conditions [$77.5\% \pm 12.9\%$; $t(8) = 1.5$, $P > .05$].

DISCUSSION

It is well known that excitotoxicity caused by high concentrations of glutamate in the brain has been implicated in the pathophysiology of many brain diseases.¹ Moreover, several studies have reported that reduced brain glutamate level is an important strategy for neuroprotective actions.^{29,30} Allicin is a major component of garlic, which is a widespread dietary component without any toxic side effects.¹² Numerous studies have shown that allicin has a protective effect on the brain.^{14–17,31} However, a direct effect of allicin on glutamate release in isolated nerve terminals (synaptosomes) has not yet been demonstrated. Thus, in this study, the effect and probable mechanisms by which allicin affects glutamate release were evaluated using synaptosomes isolated from the rat cerebral cortex. We observed that allicin depressed the 4-aminopyridine-evoked Ca^{2+} -dependent glutamate release, and this effect was concentration-dependent, with an IC_{50} value derived from a dose–response curve of $\sim 6 \mu\text{M}$. Thus, we suggested that the neuroprotective effect of allicin in the brain is at least partially attributable to its glutamate release-inhibiting effect. Liu *et al.* reported that allicin attenuates glutamate-induced neurotoxicity in primary cultured spinal cord neurons,³² which supported our hypothesis.

The mechanism by which allicin inhibits the evoked glutamate release in rat cerebrocortical synaptosomes is not fully understood, but it probably involves a reduction of presynaptic Ca^{2+} entry without any effect on synaptosomal excitability. Indeed, we observed no effect of allicin on 4-aminopyridine-evoked membrane depolarization measured with a dye of DiSC₃(5). This suggests that the inhibition of glutamate release by allicin is not the result of an indirect effect via attenuation of membrane potential and thus synaptosomal excitability. Moreover, allicin failed to affect the evoked glutamate release in the absence of extracellular Ca^{2+} , suggesting that the inhibition of glutamate release by allicin required an influx of Ca^{2+} from the extracellular milieu. Using Fura-2, the present work has observed that allicin significantly inhibited the evoked rise in $[\text{Ca}^{2+}]_i$. The inhibitory action of allicin on the evoked glutamate release was decreased from 55% to 6% after exposure to the N- and P/Q-type Ca^{2+} channel inhibitor, but it was not affected by the intracellular Ca^{2+} release inhibitors. These data imply that the observed inhibitory effect of allicin on the evoked glutamate release is attributable to a decrease in extracellular Ca^{2+} entry via N- and P/Q-type Ca^{2+} channels that are supported for glutamate release from synaptosomes.^{27,28} Under

conditions in which the N- and P/Q-type Ca^{2+} channels have been inhibited, however, total blockage of allicin action was not observed, probably due to the participation of other presynaptic pathways. Although our data indicate that allicin depresses evoked glutamate release by decreasing Ca^{2+} entry through N- and P/Q-type Ca^{2+} channels in rat cerebrocortical synaptosomes, a central question that we have not addressed in this study is, how does allicin affect these presynaptic Ca^{2+} channel activity? In this respect, we hypothesize that allicin inhibits presynaptic voltage-dependent Ca^{2+} channels either via a direct effect on Ca^{2+} channel function or rather indirectly via the regulation of protein kinases and consequently affected the phosphorylation of Ca^{2+} channels.

In the present work, we also discovered that the inhibitory effect of allicin on the release of glutamate evoked by 4-aminopyridine was efficiently blocked by a PKC inhibitor, and not by a MAPK inhibitor and a PKA inhibitor, thus indicating the involvement of PKC suppression. This conclusion was further supported by our immunoblotting data, which showed that allicin reduced the 4-aminopyridine-evoked phosphorylation of PKC in rat cerebrocortical synaptosomes. PKC is known to be present in central nervous system glutamatergic nerve endings, where they enhance the release of glutamate through several different mechanisms, including inhibiting K^+ channels, increasing Ca^{2+} channels, and augmenting the release machinery.^{33–35} Thus, it seems that allicin elicits a reduction of Ca^{2+} entry through nerve terminal N- and P/Q-type Ca^{2+} channels, which subsequently suppresses the PKC activation to cause a decrease in evoked glutamate release. In addition to voltage-dependent Ca^{2+} channels, however, it has been shown that depolarization causes the reversal of the $\text{Na}^+/\text{Ca}^{2+}$ exchanger, leading to intracellular Ca^{2+} increase and glutamate release.³⁶ Whether allicin acts by decreasing the influx of Ca^{2+} through the reversal of the $\text{Na}^+/\text{Ca}^{2+}$ exchangers remains to be explored.

In conclusion, findings from our current study revealed that allicin, an active substance of garlic, inhibits evoked glutamate release in rat cerebrocortical nerve terminals. This phenomenon is dependent on suppression of Ca^{2+} influx and PKC activity. On the basis of our findings, we would suggest that allicin is a promising candidate for preventing and treating glutamate-induced neurological disorders.

ACKNOWLEDGMENT

This study was supported by the Far-Eastern Memorial Hospital (106-FEMH-FJU-03).

AUTHOR DISCLOSURE STATEMENT

No competing financial interests exist.

REFERENCES

1. Lau A, Tymianski M: Glutamate receptors, neurotoxicity and neurodegeneration. *Pflugers Arch* 2010;460:525–542.
2. Doble A: The role of excitotoxicity in neurodegenerative disease: Implications for therapy. *Pharmacol Ther* 1999;81:163–221.

3. Danysz W, Parsons CG: Glycine and N-methyl-D-aspartate receptors: Physiological significance and possible therapeutic applications. *Pharmacol Rev* 1998;50:597–664.
4. Ikonomidou C, Turski L: Why did NMDA receptor antagonists fail clinical trials for stroke and traumatic brain injury? *Lancet Neurol* 2002;1:383–386.
5. Mdzinarishvili A, Sambria RK, Lang D, Klein J: Ginkgo extract EGB761 confers neuroprotection by reduction of glutamate release in ischemic brain. *J Pharm Pharm Sci* 2012;15:94–102.
6. Nunez-Figueroa Y, Ramírez-Sánchez J, Hansel G, *et al.*: A novel multi-target ligand (JM-20) protects mitochondrial integrity, inhibits brain excitatory amino acid release and reduces cerebral ischemia injury in vitro and in vivo. *Neuropharmacology* 2014;85:517–527.
7. Chang CY, Lin TY, Lu CW, *et al.*: Hesperidin inhibits glutamate release and exerts neuroprotection against excitotoxicity induced by kainic acid in the hippocampus of rats. *Neurotoxicology* 2015; 50:157–169.
8. Santana-Gómez CE, Orozco-Suárez SA, Talevi A, *et al.*: Propylparaben applied after pilocarpine-induced status epilepticus modifies hippocampal excitability and glutamate release in rats. *Neurotoxicology* 2017;59:110–120.
9. Chang Y, Lu CW, Chen YJ, *et al.*: Astaxanthin protects against kainic acid-induced seizures and pathological consequences. *Neurochem Int* 2018;116:85–94.
10. Dar NJ, Bhat JA, Satti NK, *et al.*: Withanone, an active constituent from *Withania somnifera*, affords protection against NMDA-induced excitotoxicity in neuron-like cells. *Mol Neurobiol* 2017;54:5061–5073.
11. Lin TY, Lu CW, Wang SJ: Luteolin protects the hippocampus against neuron impairments induced by kainic acid in rats. *Neurotoxicology* 2016;55:48–57.
12. Borlinghaus J, Albrecht F, Gruhlke MC, Nwachukwu ID, Slusarenko AJ: Allicin: chemistry and biological properties. *Molecules* 2014;19:12591–12618.
13. Chung LY: The antioxidant properties of garlic compounds: Allyl cysteine, alliin, allicin, and allyl disulfide. *J Med Food* 2006;9: 205–213.
14. Zhang H, Wang P, Xue Y, *et al.*: Allicin ameliorates cognitive impairment in APP/PS1 mice via suppressing oxidative stress by blocking JNK signaling pathways. *Tissue Cell* 2018;50:89–95.
15. Kong X, Gong S, Su L, Li C, Kong Y: Neuroprotective effects of allicin on ischemia-reperfusion brain injury. *Oncotarget* 2017;8:104492.
16. Zhou YF, Li WT, Han HC, *et al.*: Allicin protects rat cortical neurons against mechanical trauma injury by regulating nitric oxide synthase pathways. *Brain Res Bull* 2014;100:14–21.
17. Chen W, Qi J, Feng F, *et al.*: Neuroprotective effect of allicin against traumatic brain injury via Akt/endothelial nitric oxide synthase pathway-mediated anti-inflammatory and anti-oxidative activities. *Neurochem Int* 2014;68:28–37.
18. Gonen A, Harats D, Rabinkov A, *et al.*: The antiatherogenic effect of allicin: Possible mode of action. *Pathobiology* 2005;72:325–334.
19. Raiteri L, Raiteri M: Synaptosomes still viable after 25 years of superfusion. *Neurochem Res* 2000;25:1265–1274.
20. Tibbs G, Barrie A, Van Mieghem F, McMahon Ha, Nicholls D: Repetitive action potentials in isolated nerve terminals in the presence of 4-aminopyridine: Effects on cytosolic free Ca^{2+} and glutamate release. *J Neurochem* 1989;53:1693–1699.
21. Nicholls DG, Sihra TS: Synaptosomes possess an exocytotic pool of glutamate. *Nature* 1986;321:772.
22. Chang Y, Chang CY, Wang SJ, Huang SK: Myricetin inhibits the release of glutamate in rat cerebrocortical nerve terminals. *J Med Food* 2015;18:516–523.
23. Lin TY, Lu CW, Huang SK, Wang SJ: Ferulic acid suppresses glutamate release through inhibition of voltage-dependent calcium entry in rat cerebrocortical nerve terminals. *J Med Food* 2013;16:112–119.
24. Perkinson MS, Sihra TS: Presynaptic GABAB receptor modulation of glutamate exocytosis from rat cerebrocortical nerve terminals: Receptor decoupling by protein kinase C. *J Neurochem* 1998;70: 1513–1522.
25. Grynkiewicz G, Poenie M, Tsien RY: A new generation of Ca^{2+} indicators with greatly improved fluorescence properties. *J Biol Chem* 1985;260:3440–3450.
26. Åkerman KE, Scott IG, Heikkilä JE, Heinonen E: Ionic dependence of membrane potential and glutamate receptor-linked responses in synaptoneuroosomes as measured with a cyanine dye, DiS-C2-(5). *J Neurochem* 1987;48:552–559.
27. Millán C, Sánchez-Prieto J: Differential coupling of N- and P/Q-type calcium channels to glutamate exocytosis in the rat cerebral cortex. *Neurosci Lett* 2002;330:29–32.
28. Vázquez E, Sánchez-Prieto J: Presynaptic modulation of glutamate release targets different calcium channels in rat cerebrocortical nerve terminals. *Eur J Neurosci* 1997;9:2009–2018.
29. Arundine M, Tymianski M: Molecular mechanisms of calcium-dependent neurodegeneration in excitotoxicity. *Cell Calcium* 2003;34:325–337.
30. Danbolt NC: Glutamate uptake. *Prog Neurobiol* 2001;65:1–105.
31. Liu H, Mao P, Wang J, Wang T, Xie CH: Allicin protects PC12 cells against 6-OHDA-induced oxidative stress and mitochondrial dysfunction via regulating mitochondrial dynamics. *Cell Physiol Biochem* 2015;36:966–979.
32. Liu SG, Ren PY, Wang GY, Yao SX, He XJ: Allicin protects spinal cord neurons from glutamate-induced oxidative stress through regulating Heat shock protein 70/inducible nitric oxide synthase pathway. *Food Funct* 2015;6:321–330.
33. Stevens CF, Sullivan JM: Regulation of the readily releasable vesicle pool by protein kinase C. *Neuron* 1998;21:885–893.
34. Coffey ET, Herrero I, Sihra TS, Sánchez-Prieto J, Nicholls DG: Glutamate exocytosis and MARCKS phosphorylation are enhanced by a metabotropic glutamate receptor coupled to a protein kinase C synergistically activated by diacylglycerol and arachidonic acid. *J Neurochem* 1994;63:1303–1310.
35. Millán C, Torres M, Sánchez-Prieto J: Co-activation of PKA and PKC in cerebrocortical nerve terminals synergistically facilitates glutamate release. *J Neurochem* 2003;87:1101–1111.
36. Blaustein MP, Lederer WJ: Sodium/calcium exchange: Its physiological implications. *Physiol Rev* 1999; 79:763–854.

High-Intensity Interval Training Improves Erythrocyte Osmotic Deformability

YU-CHIEH HUANG¹, CHIH-CHIN HSU², and JONG-SHYAN WANG^{1,2,3}

¹Healthy Aging Research Center, Graduate Institute of Rehabilitation Science, Medical College, Chang Gung University, Tao-Yuan, TAIWAN; ²Heart Failure Center, Department of Physical Medicine and Rehabilitation, Chang Gung Memorial Hospital, Keelung, TAIWAN; and ³Research Center for Chinese Herbal Medicine, College of Human Ecology, Chang Gung University of Science and Technology, Tao-Yuan, TAIWAN

ABSTRACT

HUANG, Y.-C., C.-C. HSU, and J.-S. WANG. High-Intensity Interval Training Improves Erythrocyte Osmotic Deformability. *Med. Sci. Sports Exerc.*, Vol. 51, No. 7, pp. 1404–1412, 2019. **Introduction:** Physical exercise or hypoxic exposure influences erythrocyte susceptibility to osmotic stress, and the aquaporin 1 (AQP1) facilitates the transport of water in erythrocytes. This study investigated whether high-intensity interval training (HIIT) and moderate-intensity continuous training (MICT) affect erythrocyte osmotic deformability by modulating AQP1 function under hypoxic stress. **Methods:** Forty-five healthy sedentary males were randomized to engage in either HIIT (3-min intervals at 40% and 80% $\dot{V}O_2$ reserve, $n = 15$) or MICT (sustained 60% $\dot{V}O_2$ reserve, $n = 15$) on a bicycle ergometer for 30 min·d⁻¹, 5 d·wk⁻¹ for 6 wk, or to a control group that did not perform any exercise ($n = 15$). All subjects were analyzed with osmotic gradient ektacytometry for assessing erythrocyte membrane stability and osmotic deformability after hypoxic exercise (HE) (100 W under 12%O₂ for 30 min). **Results:** Before the intervention, HE increased the shear stress at 50% of maximal elongation (SS_{1/2}) and the ratio of SS_{1/2} to maximal elongation index (SS_{1/2}/EI_{max}) on erythrocytes pretreated with 50 Pa of shear stress for 30 min and diminished HgCl₂-depressed osmolality at 50%EI_{max} (O_{hyper}). However, both HIIT and MICT for 6 wk diminished the elevations of erythrocyte SS_{1/2} and SS_{1/2}/EI_{max} caused by HE. Moreover, HIIT also increased contents of erythrocyte AQP1 proteins while enhancing HgCl₂-depressed O_{hyper} and area under elongation index–osmolality curve after HE. Additionally, changes in erythrocyte AQP1 contents were associated with changes in HgCl₂-depressed erythrocyte O_{hyper} and area under elongation index–osmolality curve. **Conclusions:** Acute HE reduces erythrocyte membrane stability, whereas either HIIT or MICT attenuates the depression of erythrocyte membrane stability by HE. Moreover, HIIT increases the AQP1 content and facilitates the HgCl₂-mediated osmotic deformability of erythrocytes after HE. **Key Words:** EXERCISE, HYPOXIA, ERYTHROCYTE, OSMOTIC DEFORMABILITY

It is well known that erythrocyte volume changes depending on the osmotic conditions and osmolality-mediated erythrocyte deformability plays a significant role in microhemorheology (1). Erythrocyte rheological properties affect blood viscoelasticity and consequently regulate vascular resistance to flow shear force (2), whereas rheological impairments of erythrocytes may result in circulatory disorders (3). Hypoxic stress leads to volume dysregulation in osmotically stressed erythrocytes and consequently suppresses the dynamic deformability of erythrocytes required for flow through capillaries, eventually limiting blood O₂ delivery to the tissues (4).

Aquaporin 1 (AQP1), a water transport channel, facilitates water transport across the erythrocyte membrane and is responsible for the rapid response of the cell volume to changes in plasma osmolality (5,6). Alternating aerobic and anaerobic metabolic responses caused by high-intensity interval training (HIIT) serve as preconditioning to hypoxic stress, which may increase resistance to hypoxia-induced hemorheological dysfunction (7). Our previous investigations demonstrated that HIIT effectively alleviated hypoxia-induced impairments of erythrocyte rheological characteristics in sedentary healthy males (7) and also improved hemorheological functions by depressing aggregability and enhancing deformability of erythrocytes in patients with heart failure (8,9). However, whether the HIIT regimen influences erythrocyte osmotic deformability by modulating AQP1 function under hypoxic stress remains unclear.

To address the above mentioned questions, this study evaluated the distinct effects of HIIT [3-min intervals at 40% and 80% $\dot{V}O_2$ reserve ($\dot{V}O_{2R}$)] and traditional moderate-intensity continuous training (MICT) (sustained 60% $\dot{V}O_{2R}$) for 6 wk on membrane stability and AQP1-mediated osmotic deformability of erythrocytes under hypoxic exercise (HE) (100 W under air 12%O₂ condition) in healthy sedentary men. The aim of this study was to establish an effective exercise strategy for improving individual aerobic capacity and for simultaneously

Address for correspondence: Jong-Shyan Wang, Ph.D., Graduate Institute of Rehabilitation Science, Chang Gung University, 259 Wen-Hwa 1st Rd, Kwei-Shan, Tao-Yuan, 333, Taiwan; E-mail: s5492@mail.cgu.edu.tw.

Submitted for publication October 2018.

Accepted for publication February 2019.

Supplemental digital content is available for this article. Direct URL citations appear in the printed text and are provided in the HTML and PDF versions of this article on the journal's Web site (www.acsm-msse.org).

0195-9131/19/5107-1404/0

MEDICINE & SCIENCE IN SPORTS & EXERCISE®

Copyright © 2019 by the American College of Sports Medicine

DOI: 10.1249/MSS.0000000000001923

ameliorating the risk of hemorheological dysfunction evoked by hypoxic stress.

METHODS

Subjects

Forty-five sedentary men who were nonsmokers, nonusers of medications/vitamins, and free of any cardiopulmonary/hematological risks were recruited from Chang Gung University (Tao-Yuan, Taiwan). According to our previous studies, the menstrual phases of women influence the activity of circulatory system (10,11). Hence, this study excluded female subjects to avoid the effects of gender and the menstrual phase on cardiovascular (10) and hematological (11) functions. None of subjects had regular exercise habits (i.e., exercise frequency of once per week, duration >20 min a time) or had been exposed to high altitudes (≥ 3000 m) for at least 1 yr before the experiment. All subjects provided informed consent after the experimental procedures had been explained. These subjects were randomly divided into three groups: HIIT ($n = 15$), MICT ($n = 15$), and control (CTL; $n = 15$). Anthropometric and cardiovascular characteristics of all individuals did not differ significantly before the interventions (Table 1). All subjects arrived at the testing center at 9:00 AM to eliminate any possible circadian effects. Participants were instructed to fast for at least 8 h and to refrain from strenuous physical exercise for at least 48 h before sampling. This investigation followed the Declaration of Helsinki and was approved by the Institutional Review Board of Chang Gung Memorial Hospital (Keelung, Taiwan).

Training Protocols

The HIIT subjects warmed up for 3 min at 30% of $\dot{V}O_2R$ [i.e., $30\% \times (\text{peak } O_2 \text{ consumption} - \text{resting } O_2 \text{ consumption}) + \text{resting } O_2 \text{ consumption}$] before performing five exercise cycles, each for 3 min at 80% of $\dot{V}O_2R$ interspersed

with 3 min of active recovery at 40% of $\dot{V}O_2R$. The exercise session was terminated by a 3-min cool-down at 30% of $\dot{V}O_2R$. The MICT group had the same warm-up and cool-down protocols as the HIIT group except that the training period was 30 min at 60% of $\dot{V}O_2R$. The two exercise protocols were isovolumic at the same exercise duration [i.e., HIIT exercise volume: $(3 \text{ min} \times 40\% \text{ of } \dot{V}O_2R + 3 \text{ min} \times 80\% \text{ of } \dot{V}O_2R) \times 5 \text{ cycles} = \text{MICT exercise volume: } (30 \text{ min} \times 60\% \text{ of } \dot{V}O_2R) \times 1 \text{ cycle}$]. CTL participants kept their original diets and physical activity habits for 6 wk (7). Each subject used a heart rate (HR) monitor (Tango, SunTech Medical, UK) to obtain the assigned intensity of exercise. The intensity of the exercise reaching the target HR was ensured by continuously adjusting the work rate of the bicycle ergometer throughout the training period.

The association between the percentages of $\dot{V}O_2R$ and HR reserve (HRR) was firstly demonstrated in 1997 with using of cycle ergometers in healthy populations (12) which was demonstrated that % HRR is more clearly aligned with % $\dot{V}O_2R$ than % $\dot{V}O_{2\text{max}}$. These findings have further been reported in healthy (13,14) and diseased populations (15). Accordingly, the target HR was determined due to the %HRR, which is well considered to be equivalent to the % $\dot{V}O_2R$ for exercise prescription purposes (13). The following equations were used to calculate the target HR of HIIT and MICT:

$$\text{peak HR} = 220 - \text{age}$$

$$\%HRR = \%(\text{peak HR} - \text{resting HR}) + \text{resting HR}$$

$$\text{target HR of HIIT} = 3\text{-min intervals at } 40\% \text{ HRR and } 80\% \text{ HRR}$$

$$\text{target HR of MICT} = \text{sustained } 60\% \text{ HRR}$$

The Borg 6- to 20-scale was used to assess the rate of perceived exertion during each 3-min test and after each exercise

TABLE 1. The effects of various exercise regimens on cardiopulmonary fitness.

	HIIT		MICT		CTL	
	Pre	Post	Pre	Post	Pre	Post
Anthropometric						
Age (yr)	21.8 \pm 0.7	—	22.1 \pm 0.7	—	21.2 \pm 0.8	—
Weight (kg)	67.5 \pm 1.6	66.7 \pm 2.2	67.1 \pm 1.8	66.7 \pm 1.8	66.5 \pm 2.0	66.7 \pm 1.8
Height (cm)	173.1 \pm 0.8	—	174.1 \pm 0.9	—	173.7 \pm 1.2	—
BMI ($\text{kg} \cdot \text{m}^{-2}$)	22.5 \pm 0.6	22.1 \pm 0.7	22.3 \pm 0.7	22.1 \pm 0.8	21.7 \pm 0.9	21.9 \pm 0.7
Heart rate (bpm)	73 \pm 2	68 \pm 2*	74 \pm 2	69 \pm 2*	74 \pm 3	73 \pm 4
Systolic BP (mm Hg)	116 \pm 5	112 \pm 3	117 \pm 3	113 \pm 4	116 \pm 3	118 \pm 2
Diastolic BP (mm Hg)	77 \pm 3	74 \pm 2	76 \pm 3	74 \pm 2	75 \pm 3	74 \pm 4
Ventilatory threshold						
Work-load (W)	118 \pm 7	150 \pm 8***	117 \pm 6	136 \pm 5*	117 \pm 6	118 \pm 9
Heart rate (bpm)	139 \pm 3	152 \pm 4***	141 \pm 4	149 \pm 4	137 \pm 6	138 \pm 8
\dot{V}_E ($\text{L} \cdot \text{min}^{-1}$)	38.4 \pm 3.2	47.5 \pm 4.1***	36.9 \pm 2.6	41.6 \pm 2.1*	36.7 \pm 2.1	37.2 \pm 3.4
$\dot{V}O_2$ ($\text{mL} \cdot \text{min}^{-1} \cdot \text{kg}^{-1}$)	20.2 \pm 1.6	26.1 \pm 1.5***	21.2 \pm 1.8	23.8 \pm 1.4*	20.1 \pm 1.7	21.6 \pm 2.2
$\dot{V}CO_2$ ($\text{mL} \cdot \text{min}^{-1} \cdot \text{kg}^{-1}$)	20.4 \pm 1.4	26.6 \pm 1.7***	21.4 \pm 1.6	23.9 \pm 1.6*	20.0 \pm 1.9	21.9 \pm 1.8
Peak exercise performance						
Work rate (W)	188 \pm 9	236 \pm 12***	190 \pm 8	221 \pm 9*	200 \pm 9	202 \pm 8
Heart rate (bpm)	196 \pm 3	195 \pm 2	196 \pm 3	196 \pm 5	196 \pm 4	197 \pm 3
\dot{V}_E ($\text{L} \cdot \text{min}^{-1}$)	106.7 \pm 4.1	129.9 \pm 5.0***	108.0 \pm 3.7	116.4 \pm 6.2*	109.2 \pm 5.1	106.7 \pm 4.7
$\dot{V}O_2$ ($\text{mL} \cdot \text{min}^{-1} \cdot \text{kg}^{-1}$)	34.9 \pm 1.8	45.6 \pm 2.7**	35.3 \pm 2.1	41.2 \pm 1.7*	34.0 \pm 1.6	33.9 \pm 1.5
$\dot{V}CO_2$ ($\text{mL} \cdot \text{min}^{-1} \cdot \text{kg}^{-1}$)	41.6 \pm 2.3	54.2 \pm 2.1***	42.7 \pm 2.0	50.4 \pm 2.1*	40.8 \pm 2.5	40.5 \pm 2.3

Values are means \pm SEM. Pre, before the intervention; Post, after the intervention; BMI, body mass index; BP, blood pressure; \dot{V}_E , ventilation.

* $P < 0.05$, Pre vs Post.

** $P < 0.05$, HIIT vs MICT.

session as well. Thus, a person's exertion rating may provide a fairly good estimate of the actual heart rate during physical activity though this parameter is subjective (16). The Borg 14 (somewhat hard) is about 60% HRR in MICT group, yet, the Borg 12 (fairly light) and 18 (very hard) are about 40% HRR and 80% HRR, respectively in HIIT group.

All subjects recorded their daily activities and nutrition intake by the International Physical Activity Questionnaire Short Form (17) and the Written Diet Record (18), respectively. These participants were instructed to maintain the same dietary habit as before, and there were no special restrictions, but try to avoid overeating. Also, they were asked to refrain from extra regular exercise until the end of this study. Compliance rates for the three interventions were 100%.

Graded exercise test. The graded exercise test (GXT) was performed with a cycle ergometer (Corival 400, Lode) 4 d before and after the 6-wk intervention. The GXT comprised of unloaded pedaling for 2 min followed by a continuous increase in work rate (20–30 W) every 3 min until exhaustion (i.e., $\dot{V}O_{2\max}$). Minute ventilation (\dot{V}_E), $\dot{V}O_2$, and $\dot{V}CO_2$ production ($\dot{V}CO_2$) were measured breath-by-breath using a computer-based system (MasterScreen CPX; Cardinal Health Germany). Mean arterial pressure was measured using an automatic blood pressure system (Tango), as described previously (19). $\dot{V}O_{2\max}$ was defined by the following criteria: (i) $\dot{V}O_2$ increased by less than $2 \text{ mL} \cdot \text{kg}^{-1} \cdot \text{min}^{-1}$ over at least 2 min; (ii) HR exceeded its predicted maximum; (iii) respiratory exchange ratio exceeded 1.2; and (iv) venous lactate concentration exceeded 8 mM, consistent with the American College of Sports Medicine guidelines for exercise testing (20).

HE test and blood collection. Each subject performed the HE test 2 d before and after the intervention in an air-conditioned normobaric hypoxia chamber (Colorado Mountain Room, Boulder, CO), as described in previous studies (21). The hypoxia chamber was maintained at a temperature of $22^\circ\text{C} \pm 0.5^\circ\text{C}$ with a relative humidity of $60\% \pm 5\%$; a CO_2 scrubber eliminated CO_2 in the air ($<3500 \text{ ppm}$). The HE test on the bicycle ergometer required 50 W of warm-up for 3 min, an increase of work rate to 100 W of continuous exercise for 30 min, and cool-down recovery to 50 W for 3 min (7). During the test, the O_2 concentration was set to 12%, which corresponds to an altitude of 4460 m. For safety reasons, the HE test was terminated immediately when the level of SaO_2 saturation dropped under 70% for any subject. In this study, all subjects maintained their SaO_2 above 70% throughout the HE test.

At rest and immediately after the HE test, 20 mL of blood sample was collected from the antecubital vein via clean venipuncture (20-gauge needle) under controlled venous stasis at 40 Torr. One blood sample (10 mL) was added to a tube with ethylenediaminetetraacetic acid (EDTA; final concentration, 4 mM) for measuring erythrocyte rheological characteristics, and another blood sample (10 mL) was added to a tube with

sodium citrate (1 volume of sodium citrate [$3.8 \text{ g} \cdot \text{dL}^{-1}$] for nine volumes of blood) for evaluating membrane stability and AQP1-mediated osmotic deformability of erythrocytes. Blood cells were counted using a Sysmax SF-3000 cell counter (GMI Inc., Ramsey, MN) (7). These tests were done immediately after blood draw.

Reticulocyte count. The erythrocytes were suspended ($1 \times 10^4 \text{ cells} \cdot \mu\text{L}^{-1}$) in a saturating concentration of monoclonal anti-human CD71 antibody conjugated with phycoerythrin (DB Pharmingen) and Vybrant DyeCycle Green (Invitrogen) for 30 min at 37°C in the dark and washed twice with Hank's balanced salt solution (HBSS). The count of CD71^+ reticulocytes obtained from 50,000 erythrocytes was measured using a two color FACScan flow cytometer (Becton Dickinson) (22).

Membrane stability test. Twenty-five μL of blood sample with EDTA was diluted in 5 mL of isotonic polyvinylpyrrolidone (PVP) solution (osmolality = $290\text{--}300 \text{ mOsm} \cdot \text{kg}^{-1}$; pH 7.3) (Sigma). Next, 1000 μL of the PVP-diluted blood sample was added into the sheared sample system in a laser assisted optical rotational red cell analyzer (LoRRca, RR Mechatronics, Hoom, The Netherlands) at 37°C for the elongation index (EI) measurements at various fluid shear stresses by laser diffraction analysis (23).

A laser beam directly passed through the sheared sample and the diffraction pattern produced by the deformed erythrocytes was analyzed by a computer. The EI was calculated based on the geometry of the elliptical diffraction pattern: $\text{EI} = (L - W)/(L + W)$, where L and W represent the length and width of the diffraction pattern, respectively. The shear stress at 50% of maximal elongation was defined as semi-maximal shear stress ($\text{SS}_{1/2}$). Hence, an increase in the $\text{SS}_{1/2}$ value or the ratio of $\text{SS}_{1/2}$ to EI_{\max} represents a decrease in erythrocyte deformability (23).

The erythrocyte membrane stability test included the initial deformability curve test at basal status and the secondary deformability curve test following the 50 Pa of shear stress for 30 min. These deformability curves present the shear stress–EI curves for 10 consecutive shear stresses: 0.3, 0.54, 0.96, 1.73, 3.1, 5.56, 9.97, 17.88, 32.07, and 57.50 Pa.

Osmotic deformability test. The osmotic gradient ektacytometric measurements were also obtained using the 'osmoscan function' of the device (24). For the experiments to evaluate the osmotic deformability modulated by AQP1, 250 μL of blood samples were pretreated with $10 \mu\text{M}$ HgCl_2 (i.e., the specific inhibitor of AQP1) for 30 min at 37°C . The device generated a constant shear stress of 30 Pa, while continuously aspirating the sample into the measurement site while changing the osmolality of the medium using gradual mixtures of PVP solutions of 0 and $700 \text{ mOsmol} \cdot \text{kg}^{-1}$, and therefore the EI was continuously registered (Fig. 1). The measured and calculated parameters by the device (all at shear stress of 30 Pa) were as follows: (i) O_{\max} [the osmolality at which the EI is maximum (EI_{\max})], (ii) O_{hyper} (the osmolality in the hypertonic region corresponding to 50% of EI_{\max}), (iii) EI_{\max} , (iv) EI_{hyper} (the EI in O_{hyper}), and (v) the area under the individual

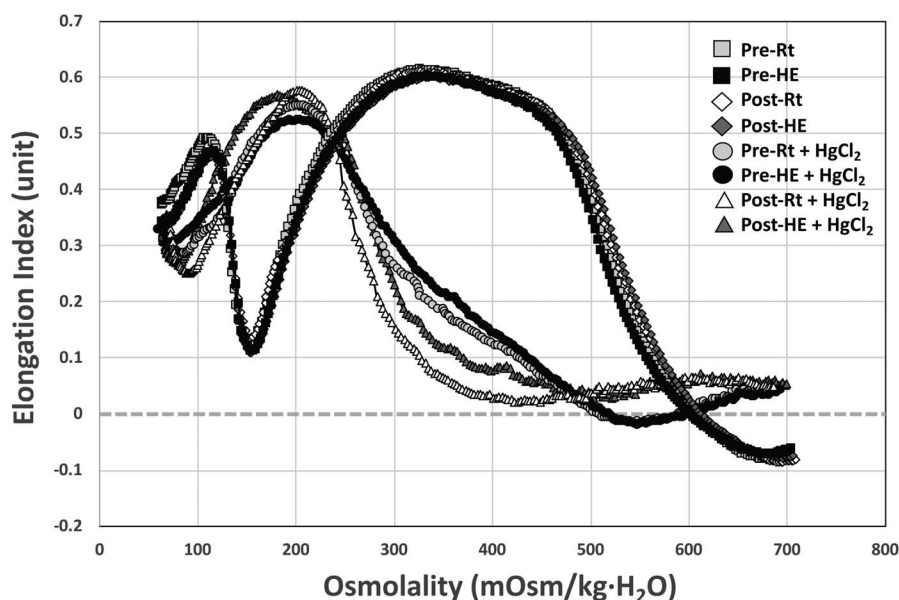


FIGURE 1—The analysis of erythrocyte osmotic deformability using the osmotic gradient ektacytometry. The device generated a constant shear stress of 30 Pa while continuously aspirating the sample into the measurement site while changing the osmolality of the medium using gradual mixtures of PVP solutions of 0 and 700 mOsmol·kg⁻¹, and therefore, the EI was continuously registered. For the experiments to evaluate the osmotic deformability modulated by AQP1, 250 μ L of blood samples were pretreated with 10 μ M HgCl₂ (i.e., the specific inhibitor of AQP1) for 30 min at 37°C. Pre-Rt, resting at normoxic condition before HIIT; Pre-HE, HE test before HIIT; Post-Rt, resting at normoxic condition after HIIT; Post-HE, HE test after HIIT.

EI–osmolality curve (AUC) (25). Additionally, the changes of erythrocyte osmotic deformability caused by HgCl₂ = [(HgCl₂-treated erythrocyte osmotic deformability/basal erythrocyte osmotic deformability) – 1] \times 100%.

Erythrocyte AQP1 content. For quantitating the erythrocyte AQP-1 by immunoblot analysis, the isolated erythrocytes were lysed in five volumes of hypotonic buffer containing a protease inhibitor mixture (s8830; Sigma-Aldrich), 3.3 mM NaF, 3.3 mM beta-glycerophosphate and 3.3 mM sodium orthovanadate on ice-cold double-distilled water, and then vortexed for 2 min. The sample was ultracentrifuged at 10,163g for 30 min at 4°C (Optima TL Ultracentrifuge; Beckman Instruments, CA), and the supernatant was then removed from the pellet. The pellet was washed with five volumes of the buffer. The level of AQP1 on erythrocytes was quantified by a commercially available ELISA kit (Cusabio), as described previously.

Statistical Analysis

Results are expressed as means \pm SEM. The statistical software package StatView was used for data analysis. Kolmogorov–Smirnov’s goodness-of-fit test was used and normal distribution was observed in the present study. Experimental results were analyzed by 3 (groups) \times 4 (time sample points) repeated-measures ANOVA and Bonferonni’s *post-hoc* test to compare reticulocyte and erythrocyte counts, as well as erythrocyte membrane stability, osmotic deformability, and AQP1 contents before and immediately after HE at the beginning of the present study and after 6 wk in various interventions. In addition, the comparison of cardiopulmonary fitness during GXT at the beginning of the present study and 6 wk later in various groups were analyzed

by 3 (groups) \times 2 (time sample points) repeated measures ANOVA and Bonferonni’s *post hoc* test. Pearson correlation analysis was used to elucidate the relationships between changes in AQP1 level and HgCl₂-treated osmotic deformability of erythrocytes after various interventions. The criterion for significance was $P < 0.05$.

RESULTS

Cardiopulmonary Fitness

Anthropometric variables did not significantly differ among the three groups at the beginning of the study (Table 1). Both HIIT and MICT for the 6 wk increased the work rate, \dot{V}_E , $\dot{V}O_2$, and VCO_2 at the ventilatory threshold and peak exercise performance (Table 1, $P < 0.05$). Moreover, the HIIT group exhibited greater enhancements of aerobic capacity than the MCT group (Table 1, $P < 0.05$). However, CTL for 6 wk did not influence these cardiopulmonary responses to GXT (Table 1).

Erythrocyte Characteristics

Acute HE significantly increased erythrocyte count and hematocrit ($P < 0.05$; see Table, Supplemental Digital Content 1, effects of various exercise regimens on erythrocyte characteristics in blood, <http://links.lww.com/MSS/B515>), but did not change the values of reticulocyte, mean corpuscular volume, mean corpuscular hemoglobin, and mean corpuscular hemoglobin concentration in the blood (Supplemental Digital Content 1, <http://links.lww.com/MSS/B515>). HIIT for 6 wk significantly increased blood reticulocyte counts at rest and after HE (Supplemental Digital Content 1, $P < 0.05$, <http://links.lww.com/MSS/B515>). However, all hematological parameters at rest and after

the HE test remained unchanged after the 6-wk intervention in the MICT or CTL group (Supplemental Digital Content 1, <http://links.lww.com/MSS/B515>).

Erythrocyte deformability and membrane stability.

Pretreatment of high shear stress (50 Pa) for 30 min increased the $SS_{1/2}$ and the ratio of $SS_{1/2}$ to EI_{max} (Table 2, $P < 0.001$), but did not affect the EI_{max} values of the erythrocytes. Acute HE further augmented the increases in the $SS_{1/2}$ and the ratio of $SS_{1/2}$ to EI_{max} of erythrocyte caused by high shear stress (Table 2, $P < 0.05$). However, either HIIT or MICT for 6 wk depressed the HE-enhanced $SS_{1/2}$ and the $SS_{1/2}/EI_{max}$ ratio on erythrocytes treated with high shear stress (Table 2, $P < 0.05$). No significant changes in basal erythrocyte deformability and HE-declined erythrocyte membrane stability occurred after 6 wk of CTL.

Erythrocyte osmotic deformability. Figure 1 shows the analysis of erythrocyte osmotic deformability using a the osmotic gradient ektacytometry. Pretreated erythrocytes with 10 μ M $HgCl_2$ (i.e., the specific inhibitor of AQP1) for 30 min meaningfully lowered O_{hyper} ($-40.3\% \pm 2.3\%$, $P < 0.01$), Q_{max} ($-33.1\% \pm 2.1\%$, $P < 0.01$), and AUC ($-30.1\% \pm 2.0\%$, $P < 0.01$), as well as, modestly depressed EI_{hyper} ($-7.2\% \pm 0.8\%$, $P < 0.05$) and EI_{max} ($-7.1\% \pm 0.9\%$, $P < 0.05$) (data not shown). Acute bout of exercise at 12% O_2 did not affect basal and $HgCl_2$ -treated EI_{max} , EI_{hyper} , O_{max} , and AUC levels (Fig. 2A–C; see Table; Supplemental Digital Content 2, effects of various exercise regimens on erythrocyte membrane stability, <http://links.lww.com/MSS/B516>), whereas this HE significantly diminished change of O_{hyper} depressed by $HgCl_2$ (Fig. 2D, $P < 0.05$). However, HIIT for 6 wk promoted the changes of O_{hyper} (Fig. 2D, $P < 0.05$) and AUC (Fig. 3A, $P < 0.05$) depressed by $HgCl_2$ at rest and after HE. Additionally, there were no changes in basal or $HgCl_2$ -depressed EI_{max} , EI_{hyper} , O_{max} , and Q_{hyper} (Figs. 2A–D and Supplemental Digital Content 2, <http://links.lww.com/>

MSS/B516) and AUC (Fig. 3A and Supplemental Digital Content 2, <http://links.lww.com/MSS/B516>) levels of erythrocytes after 6 wk of MICT and CTL.

Erythrocyte AQP1 content. Acute HE did not affect erythrocyte AQP1 levels before the intervention (Fig. 3B). However, HIIT for 6 wk increased erythrocyte AQP1 levels at rest and after HE (Fig. 3B, $P < 0.05$). However, no significant changes in basal and HE-mediated erythrocyte AQP1 levels were observed after 6 wk of MICT and CTL (Fig. 3B).

Relationships between changes in AQP1 levels and $HgCl_2$ -treated osmotic deformability of erythrocytes after various interventions. Pearson correlation coefficients of changes in AQP1 levels and $HgCl_2$ -treated osmotic deformability of erythrocytes after various intervention are presented in Table 3. The changes of erythrocyte AQP1 levels were negatively correlated with the changes of $HgCl_2$ -treated erythrocyte O_{hyper} ($r = -0.559$, $P = 0.0045$) and AUC ($r = -0.604$, $P = 0.0018$). However, no significant correlations were observed between changes in AQP1 levels and the $HgCl_2$ -treated EI_{max} ($r = -0.200$, $P = 0.3529$), O_{max} ($r = -0.164$, $P = 0.4436$), or EI_{hyper} ($r = -0.270$, $P = 0.2204$) of erythrocytes.

DISCUSSION

This study demonstrated, for the first time, that an acute bout of 12% O_2 exercise decreased erythrocyte membrane stability undergoing high shear stress, as well as, reduced the extent of osmotic deformability depressed by $HgCl_2$. However, both HIIT and MICT for 6 wk considerably alleviated the HE-declined erythrocyte membrane stability. Moreover, HIIT, rather than MICT, also increased erythrocyte AQP1 levels and were accompanied by the increases in $HgCl_2$ -depressed erythrocyte osmotic deformability at rest and after HE. Additionally, the changes in erythrocyte AQP1 levels were associated

TABLE 2. The effects of various exercise regimens on erythrocyte membrane stability.

	HIIT		MICT		CTL	
	Pre	Post	Pre	Post	Pre	Post
Basal status						
$SS_{1/2}$ (Pa)						
Rt	2.05 \pm 0.11	1.75 \pm 0.07*	2.04 \pm 0.09	1.76 \pm 0.07*	2.03 \pm 0.05	2.07 \pm 0.06
HE	2.07 \pm 0.12	1.88 \pm 0.08	2.05 \pm 0.14	1.90 \pm 0.09	2.09 \pm 0.06	2.05 \pm 0.07
EI_{max} (unit)						
Rt	0.655 \pm 0.004	0.665 \pm 0.003	0.654 \pm 0.004	0.663 \pm 0.005	0.654 \pm 0.004	0.656 \pm 0.005
HE	0.653 \pm 0.006	0.664 \pm 0.003	0.652 \pm 0.002	0.662 \pm 0.007	0.650 \pm 0.003	0.655 \pm 0.004
Ratio of $SS_{1/2}$ to EI_{max}						
Rt	3.12 \pm 0.05	2.63 \pm 0.04*	3.11 \pm 0.04	2.65 \pm 0.05*	3.10 \pm 0.03	3.15 \pm 0.04
HE	3.17 \pm 0.07	2.83 \pm 0.06	3.14 \pm 0.08	3.01 \pm 0.07	3.21 \pm 0.05	3.13 \pm 0.04
Pretreatment of high shear stress (50 Pa for 30 min)						
$SS_{1/2}$ (Pa)						
Rt	5.60 \pm 0.19	5.70 \pm 0.18	5.56 \pm 0.19	5.77 \pm 0.16	5.55 \pm 0.16	5.52 \pm 0.23
HE	6.05 \pm 0.22**	5.89 \pm 0.17	5.99 \pm 0.15**	5.90 \pm 0.23	6.00 \pm 0.17**	6.08 \pm 0.23**
EI_{max} (unit)						
Rt	0.616 \pm 0.009	0.626 \pm 0.007	0.611 \pm 0.011	0.616 \pm 0.006	0.608 \pm 0.015	0.611 \pm 0.005
HE	0.608 \pm 0.009	0.619 \pm 0.010	0.605 \pm 0.006	0.610 \pm 0.009	0.605 \pm 0.009	0.608 \pm 0.005
Ratio of $SS_{1/2}$ to EI_{max}						
Rt	9.09 \pm 0.26	9.11 \pm 0.31	9.10 \pm 0.32	9.36 \pm 0.26	9.13 \pm 0.22	9.04 \pm 0.28
HE	9.95 \pm 0.24**	9.51 \pm 0.29	9.90 \pm 0.25**	9.67 \pm 0.37	9.92 \pm 0.38**	9.96 \pm 0.35**

Values are means \pm SEM. Pre, before the intervention; Post, after the intervention; Rt, at rest.

* $P < 0.05$, Pre vs Post.

** $P < 0.05$, Rt vs HE.

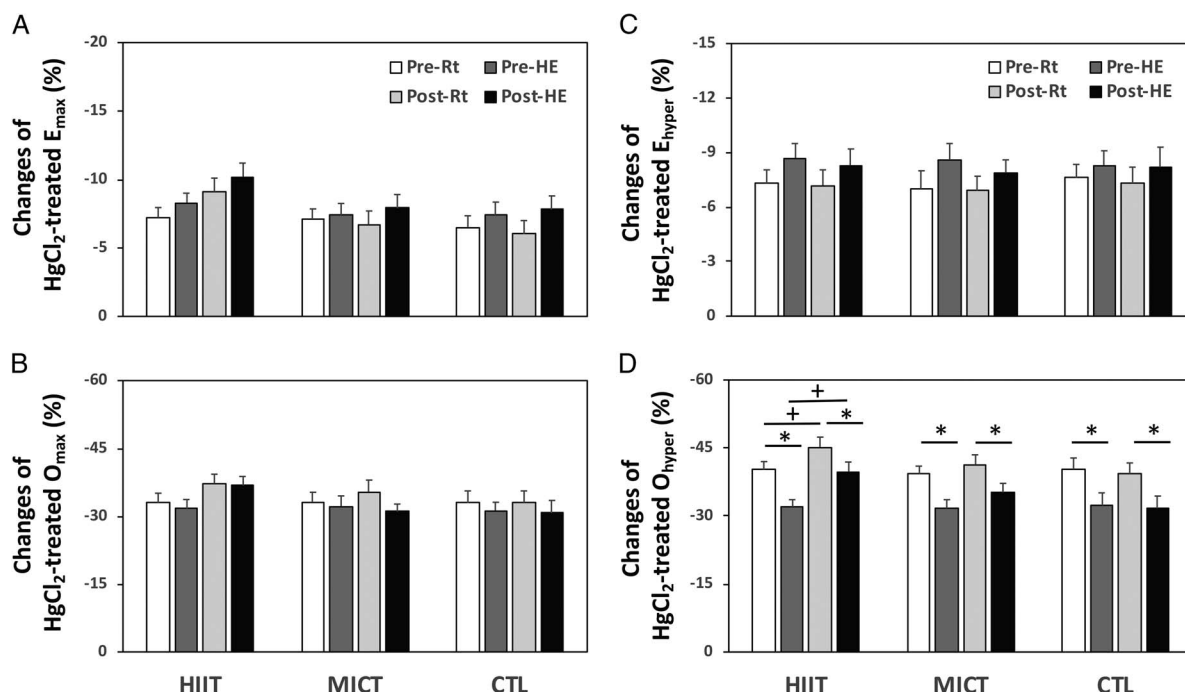


FIGURE 2—Comparisons of the effects of various exercise regimens on changes of HgCl₂-treated erythrocyte osmotic deformability at rest or after HE test. Changes of erythrocyte osmotic deformability caused by HgCl₂ = [(HgCl₂-treated erythrocyte osmotic deformability/basal erythrocyte osmotic deformability) - 1] × 100%. (A) EI_{max}, EI is maximum; (B) O_{max} (C) EI_{hyper}, (D) O_{hyper}. Values were mean ± SEM. **P* < 0.05, Pre-Rt or Post-Rt vs Pre-HE or Post-HE; +*P* < 0.05, Pre-Rt or Pre-HE vs Post-Rt or Post-HE.

with the changes in HgCl₂-depressed erythrocyte osmotic deformability after various interventions.

Erythrocyte Membrane Stability

The major function of the erythrocyte is to deliver O₂ to demand tissues by being highly deformable in order to pass

capillaries in the microcirculation (2,3). Erythrocyte deformability modulated by shear stress serves as a compensating mechanism for the maintenance of adequate microcirculatory perfusion (26). However, shears stress has a biphasic effect on the mechanical properties of erythrocytes, depending on the duration and magnitude of the applied shear stress (27,28). Prolonged shear stress exposure within the physiological range improved

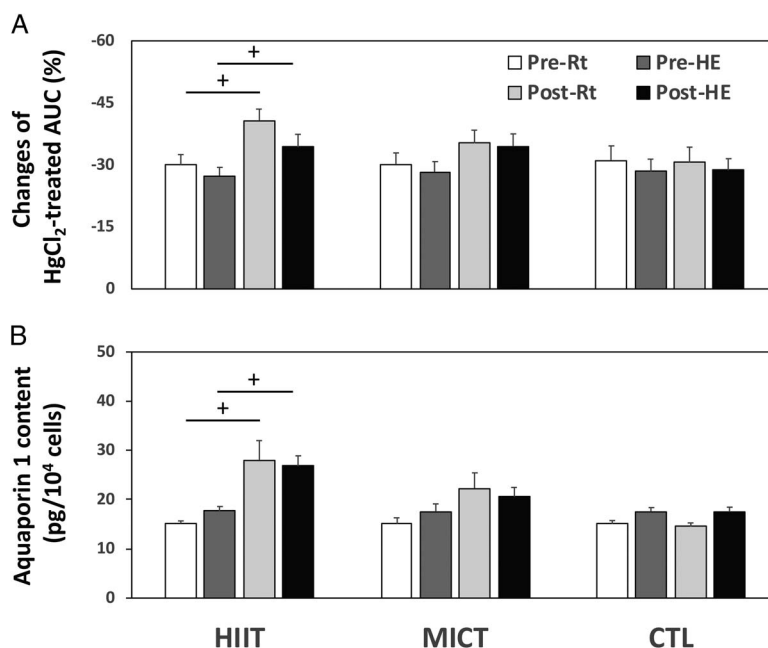


FIGURE 3—Comparisons of the effects of various exercise regimens on (A) changes of HgCl₂-treated erythrocyte AUC and (B) erythrocyte AQP1 contents at rest or after HE test. Changes of erythrocyte AUC caused by HgCl₂ = [(HgCl₂-treated erythrocyte AUC/basal erythrocyte AUC) - 1] × 100%. Values were mean ± SEM. +*P* < 0.05, Pre-Rt or Pre-HE vs Post-Rt or Post-HE.

TABLE 3. Relationships between changes in AQP1 levels and HgCl₂-induced osmotic deformability of erythrocytes after various interventions.

	Changes of Erythrocyte AQP1 Contents	
	<i>r</i>	<i>P</i>
Changes of HgCl ₂ -induced erythrocyte rheological functions		
El _{max}	-0.200	0.3529
O _{max}	-0.164	0.4436
El _{hyper}	-0.270	0.2204
O _{hyper}	-0.559	0.0045
AUC	-0.604	0.0018

erythrocyte deformability (27), whereas exposure to pathologically high shear stress resulted in mechanical damage of erythrocytes (28). In this investigation, pretreatment of high shear stress (50 Pa for 30 min) considerably increased the erythrocyte SS_{1/2}/El_{max} ratio, as reflected by the decreased erythrocyte deformability. Moreover, acute 12%O₂ exercise augmented the extent of erythrocyte rheological dysfunction caused by high shear stress.

An early study revealed that exposure to 12%O₂ in air decreased anti-oxidative capacity and increased lipid peroxidation in the circulation, leading to suppression of vascular endothelial function, which causes impairment of vascular hemodynamics (29). Additionally, elevated oxidative stress by hypoxic stress may also enhance Ca²⁺ influx by activated non-selective cation channels, further depressing the deformability of erythrocytes (4,30). Our previous study also demonstrated that the HE decreased Gardos channel-modulated erythrocyte deformability and promoted eryptotic responses to oxidative stress (13). Therefore, decreased erythrocyte deformability caused by HE may elevate resistance to blood flow and subsequently decrease O₂ delivery.

In this study, both HIIT and MICT enhanced basal erythrocyte deformability and diminished the HE-declined erythrocyte membrane stability (as a decrease in the shear-treated erythrocyte SS_{1/2}/El_{max} ratio). With respect to underlying mechanisms of the exercise training effects on erythrocyte rheological functions remain unclear, further investigations need to be undertaken. It has been reported that nitric oxide (NO) derived from erythrocytes regulated the deformability of erythrocyte membranes under shear flow (31). Moreover, the additional effects of S-nitrosylation of membrane proteins by NO are believed to be involved in the active regulation of RBC deformability (32). A previous human study has indicated that elevated shear stress by moderate-intensity exercise enhanced erythrocyte NO synthase (NOS) activity and NO production via activation of the PI3-kinase/Akt kinase pathway, thereby improving erythrocyte deformability (33). An early study using an animal model also demonstrated that exercise training suppressed platelet activation potentiated by oxidative stress through enhancing platelet-derived NO production (34). Hence, either HIIT or MICT for 6 wk may also enhance erythrocyte NOS activity and NO formation, thereby improving erythrocyte deformability under shear flow. Additionally, NO retards lipid peroxidation by acting as an antioxidant. Our early study also indicated that HE increased plasma myeloperoxidase (MPO) concentration, whereas HIIT exhibited a decrease in

plasma MPO level (35). Elevated MPO in plasma can react with the polyunsaturated fatty acids of lipid membranes, resulting in peroxidation of lipid (36). In the HIIT regimen, successive exercise phases at high intensity and interspersed with moderate-intensity exercise periods, as a form of intermittent ischemic preconditioning, may optimally have a beneficial effect on protecting individuals against oxidative damage (8,35). Therefore, it is reasonable that HIIT attenuates the HE-declined erythrocyte deformability by increasing production of NO or other antioxidants to scavenge HE-induced reactive oxygen species (ROS).

Erythrocyte osmotic deformability. Erythrocyte deformability is crucially affected by the changes of the cell shape and volume caused by osmotic stress (5,6). Erythrocyte AQP1 prevents osmotic loss of water under hypertonic condition, whereas HgCl₂ inhibits the erythrocyte osmotic water permeability from transit of water by depressing membrane AQP1 function (37). The EI–osmolality curves determined by osmotic gradient ektacytometry can effectually measure erythrocyte deformability by quantifying the cell elongation under high shear conditions in a continuum of osmolality (24). This present study demonstrated that pretreatment of HgCl₂ lowered erythrocyte O_{hyper}, which may reflect that the inhibition of AQP1 increases intracellular viscosity due to osmotic loss of water and consequently depresses erythrocyte deformability. Furthermore, acute HE attenuated HgCl₂-declined O_{hyper}, whereas 6 wk of HIIT augmented HgCl₂-declined O_{hyper} and was accompanied by an increase in AQP1 expression of the erythrocytes.

Acute exercise commonly causes hemoconcentration, whereas chronic exercise may lead to compensation of hemodilution (38). Additionally, alternating aerobic and anaerobic metabolic responses caused by HIIT rather than MICT (39) may create a concussion of osmotic stress, thus facilitating erythrocyte AQP1-mediated function. Recently, our study further demonstrated that HIIT effectively alleviated HE-evoked impairments of erythrocyte rheological characteristics through improving band 3 function on erythrocytes (7). This present investigation further demonstrated an increase in erythrocyte AQP1 expression after HIIT, which may provide a rapid pathway for promoting water inflow and limiting water outflow at hypertonicity, thereby contributing to improved osmotic deformability of the erythrocyte. Accordingly, the HIIT meaningfully enhances the AQP1-mediated erythrocyte susceptibility to osmotic stress.

Study Limitations

The small sample size (*n* = 15 in each group) was a major limitation of this study. However, the results for aerobic capacity and hemorheological properties obtained from this investigation have high statistical power (0.847 to 1.000). Although HgCl₂ can inhibit ~90% of the osmotic water permeability in erythrocytes by blocking AQP1 on the membrane, the mercury toxicity of erythrocytes must be considered in the study design. According to Tagliaferro et al. (40), erythrocytes treated with 20 μM Hg for 4 h had significantly reduced antioxidant glutathione concentration, while no ROS generation

was detected. In the present study, erythrocytes were only incubated in 10 μM HgCl_2 for 30 min. Hence, this experimental condition of HgCl_2 may be insufficient to damage the erythrocytes by inducing ROS production.

Clinical investigations have shown that reduced erythrocyte deformability has been closely correlated with various circulatory diseases, such as diabetes mellitus (41), sickle cell anemia (42), and heart failure (8,9). However, the subjects recruited in this study were young and healthy; thus, further clinical evidence is required to extrapolate the present results to patients with hemorheological or hemodynamic disorders.

CONCLUSIONS

An acute bout of exercise at air 12% O_2 condition reduced erythrocyte membrane stability and osmotic deformability in sedentary men. After 6 wk of the intervention, HIIT was superior to MICT for enhancing aerobic capacity and exercise performance. Moreover, both HIIT and MICT regimens effectively lessen the depression of erythrocyte membrane stability caused

by HE. Additionally, the HIIT regimen, but not MICT regimen, improved the AQP1-mediated osmotic deformability at rest and after HE. Therefore, HIIT can be considered an effective exercise strategy for improving individual aerobic fitness and simultaneously ameliorating the risk of hemorheological dysfunction evoked by hypoxic stress.

J.-S. W. was involved in conception and design of research. Y.-C. H. and J.-S. W. performed experiments. J.-S. W. and Y.-C. H. analyzed data, interpreted results of experiments, prepared the figures and drafted the article. J.-S. W., Y.-C. H., and C.-C. H. edited and revised the article. J.-S. W., Y.-C. H., and C.-C. H. approved the final version of article.

This work was supported by the National Science Council of Taiwan (grant NSC 106-2314-B-182-048-MY3), Chang Gung Medical Research Program (grant CMRPD1E0263 and CMRPD3G0032), and Healthy Aging Research Center, Chang Gung University (grant EMRPD1A0841).

The authors would like to thank the volunteers for their enthusiastic participation. The results of the present study do not constitute endorsement by ACSM. The results of the study are presented clearly, honestly, and without fabrication, falsification, or inappropriate data manipulation.

No conflicts of interest, financial or otherwise, are declared by the authors.

REFERENCES

- Baskurt OK, Meiselman HJ. Blood rheology and hemodynamics. *Semin Thromb Hemost.* 2003;29:435–50.
- Barshstein G, Ben-Ami R, Yedgar S. Role of red blood cell flow behaviour in hemodynamics and hemostasis. *Expert Rev Cardiovasc Ther.* 2007;5:743–52.
- Saldanha C, de Almeida JP. Erythrocyte as a link between basic and clinical research. *Clin Hemorheol Microcirc.* 2011;49:463–72.
- Mao TY, Fu LL, Wang JS. Hypoxic exercise training causes erythrocyte senescence and rheological dysfunction by depressed Gardos channel activity. *J Appl Physiol.* 2011;111:382–91.
- Sugie J, Intaglietta M, Sung LA. Water transport and homeostasis as a major function of erythrocytes. *Am J Physiol Heart Circ Physiol.* 2018;314:1098–107.
- Agre P, King LS, Yasui M, et al. Aquaporin water channels—from atomic structure to clinical medicine. *J Physiol.* 2002;542:3–16.
- Chou SL, Huang YC, Fu TC, Hsu CC, Wang JS. Cycling exercise training alleviates hypoxia-impaired erythrocyte rheology. *Med Sci Sports Exerc.* 2016;48:57–65.
- Wang JS, Fu TC, Lien HY, et al. Effect of aerobic interval training on erythrocyte rheological and hemodynamic functions in heart failure patients with anemia. *Int J Cardiol.* 2013;168:1243–50.
- Wang JS. Anemia, heart failure and exercise training. *Int J Cardiol.* 2013;168:1525–6.
- Huang SC, Wong AM, Ho CW, Weng TP, Cheng SC, Wang JS. Comparison of cardiac autonomic nervous system disturbed by sleep deprivation in sex and menstrual phase. *Chin J Phys.* 2015;58:114–23.
- Wang JS, Jen CJ, Lee H, Chen HI. Effects of short-term exercise on female platelet function during different phases of the menstrual cycle. *Arterioscler Thromb Vasc Biol.* 1997;17:1682–6.
- Swain DP, Leutholtz BC. Heart rate reserve is equivalent to % VO_2 reserve, not to % $\text{VO}_{2\text{max}}$. *Med Sci Sports Exerc.* 1997;29:410–4.
- Swain DP, Leutholtz BC, King ME, Haas LA, Branch JD. Relationship between % heart rate reserve and % VO_2 reserve in treadmill exercise. *Med Sci Sports Exerc.* 1998;30:318–21.
- Dalleck LC, Kravitz L. Relationship between % heart rate reserve and % VO_2 reserve during elliptical Crosstrainer exercise. *J Sports Sci Med.* 2006;5:662–71.
- Brawner C, Keteyian S, Ehrman J. The relationship of heart rate reserve to $\dot{\text{V}}\text{O}_2$ reserve in patients with heart disease. *Med Sci Sports Exerc.* 2002;34:418–22.
- Whaley MH, Brubaker PH, Kaminsky LA, Miller CR. Validity of rating of perceived exertion during graded exercise testing in apparently healthy adults and cardiac patients. *J Cardpulm Rehabil.* 1997;17:261–7.
- Lee PH, Macfarlane DJ, Lam TH, Stewart SM. Validity of the international physical activity questionnaire short form (IPAQ-SF): a systematic review. *Int J Behav Nutr Phys Act.* 2011;8:115.
- Ortega RM, Pérez-Rodrigo C, López-Sobaler AM. Dietary assessment methods: dietary records. *Nutr Hosp.* 2015;31:38–45.
- Tsai HH, Chang SC, Chou CH, Weng TP, Hsu CC, Wang JS. Exercise training alleviates hypoxia-induced mitochondrial dysfunction in the lymphocytes of sedentary males. *Sci Rep.* 2016;6:35170.
- Thompson WR, Gordon MF, Pescatello LS. Clinical exercise testing. In: American College of Sports Medicine, editors. *ACSM's Guidelines for Exercise Testing and Prescription*; 2009. pp. 105–32.
- Chen YC, Ho CW, Tsai HH, Wang JS. Interval and continuous exercise regimens suppress neutrophil-derived microparticle formation and neutrophil-promoted thrombin generation under hypoxic stress. *Clin Sci (Lond).* 2015;128:425–36.
- Dertinger SD, Bishop ME, McNamee JP, et al. Flow cytometric analysis of micronuclei in peripheral blood reticulocytes: I. Intra- and interlaboratory comparison with microscopic scoring. *Toxicol Sci.* 2006;94:83–91.
- Simmonds MJ, Atac N, Baskurt OK, Meiselman HJ, Yalcin O. Erythrocyte deformability responses to intermittent and continuous subhemolytic shear stress. *Biorheology.* 2014;51:171–85.
- Nemeth N, Kiss F, Miszti-Blasius K. Interpretation of osmotic gradient ektacytometry (osmoscan) data: a comparative study for methodological standards. *Scand J Clin Lab Invest.* 2015;75:213–22.
- Heo Y, Jung H, Shin S. Osmotic deformability of erythrocytes at various shear stresses. *Clin Hemorheol Microcirc.* 2015;59:211–8.
- Muraviov AV, Tikhomirova IA. Role molecular signaling pathways in changes of red blood cell deformability. *Clin Hemorheol Microcirc.* 2013;53:45–59.
- Meram E, Yilmaz BD, Bas C, Atac N, Yalcin O, Meiselman HJ. Shear stress-induced improvement of red blood cell deformability. *Biorheology.* 2013;50:165–76.

28. Nevaril CG, Lynch EC, Alfrey CP Jr, Hellums JD. Erythrocyte damage and destruction induced by shearing stress. *J Lab Clin Med.* 1968;7:784–90.
29. Wang JS, Chen LY, Fu LL, Cheng ML, Wong MK. Effects of moderate and severe intermittent hypoxia on vascular endothelial function and haemodynamic control in sedentary men. *Eur J Appl Physiol.* 2007;100:127–35.
30. Lisovskaya IL, Shcherbachenko IM, Volkova RI, Tikhonov VP. Modulation of RBC volume distributions by oxidants (phenazine methosulfate and tert-butyl hydroperoxide): role of Gardos channel activation. *Bioelectrochemistry.* 2008;73:49–54.
31. Bor-Kucukatay M, Wenby RB, Meiselman HJ, Baskurt OK. Effects of nitric oxide on red blood cell deformability. *Am J Physiol Heart Circ Physiol.* 2003;284:1577–84.
32. Grau M, Pauly S, Ali J, et al. RBC-NOS-dependent S-nitrosylation of cytoskeletal proteins improves RBC deformability. *PLoS One.* 2013;8: e56759.
33. Suhr F, Brenig J, Müller R, Behrens H, Bloch W, Grau M. Moderate exercise promotes human RBC-NOS activity, NO production and deformability through Akt kinase pathway. *PLoS One.* 2012; 7: e45982.
34. Wang JS, Lin CC, Chen JK, Wong MK. Role of chronic exercise in decreasing oxidized LDL-potentiated platelet activation by enhancing platelet-derived NO release and bioactivity in rats. *Life Sci.* 2000;66:1937–48.
35. Weng TP, Huang SC, Chuang YF, Wang JS. Effects of interval and continuous exercise training on CD4 lymphocyte apoptotic and autophagic responses to hypoxic stress in sedentary men. *PLoS One.* 2013;8: e80248.
36. Brennan ML, Hazen SL. Emerging role of myeloperoxidase and oxidant stress markers in cardiovascular risk assessment. *Curr Opin Lipidol.* 2003;4:353–9.
37. Esteva-Font C, Jin BJ, Lee S, Phuan PW, Anderson MO, Verkman AS. Experimental evaluation of proposed small-molecule inhibitors of water channel Aquaporin-1. *Mol Pharmacol.* 2016;89:686–93.
38. Connes P, Simmonds MJ, Brun JF, Baskurt OK. Exercise hemorheology: classical data, recent findings and unresolved issues. *Clin Hemorheol Microcirc.* 2013;53:187–99.
39. Fu TC, Wang CH, Lin PS, et al. Aerobic interval training improves oxygen uptake efficiency by enhancing cerebral and muscular hemodynamics in patients with heart failure. *Int J Cardiol.* 2013;167:41–50.
40. Tagliaferro L, Officioso A, Sorbo S, Basile A, Manna C. The protective role of olive oil hydroxytyrosol against oxidative alterations induced by mercury in human erythrocytes. *Food Chem Toxicol.* 2015;82:59–63.
41. Caimi G, Presti RL. Techniques to evaluate erythrocyte deformability in diabetes mellitus. *Acta Diabetol.* 2004;41:99–103.
42. Connes P, Alexy T, Detterich J, Romana M, Hardy-Dessources MD, Ballas SK. The role of blood rheology in sickle cell disease. *Blood Rev.* 2016;30:111–8.



2-Acetoxybriaranes from *Briareum violaceum*

Jia-Wen Yao ^{a, b, 1}, Wei-Chiung Chi ^{c, 1}, Gene-Hsiang Lee ^d, Jui-Hsin Su ^{a, b},
Tsong-Long Hwang ^{e, f, g, h}, Yu-Jen Wu ⁱ, Tzu-Rong Su ^{j, ***}, Jyh-Horng Sheu ^{k, **},
Ping-Jyun Sung ^{a, b, k, l, m, *}

^a Graduate Institute of Marine Biology, National Dong Hwa University, Pingtung 94450, Taiwan

^b National Museum of Marine Biology and Aquarium, Pingtung 94450, Taiwan

^c Department of Food Science, National Quemoy University, Kinmen 89250, Taiwan

^d Instrumentation Center, National Taiwan University, Taipei 10617, Taiwan

^e Research Center for Chinese Herbal Medicine, Research Center for Food and Cosmetic Safety, Graduate Institute of Healthy Industry Technology, College of Human Ecology, Chang Gung University of Science and Technology, Taoyuan 33303, Taiwan

^f Graduate Institute of Natural Products, College of Medicine, Chang Gung University, Taoyuan 33302, Taiwan

^g Chinese Herbal Medicine Research Team, Healthy Aging Research Center, Chang Gung University, Taoyuan 33302, Taiwan

^h Department of Anaesthesiology, Chang Gung Memorial Hospital, Taoyuan 33305, Taiwan

ⁱ Department of Biological Technology, Meiho University, Pingtung 91202, Taiwan

^j Antai Medical Care Cooperation Antai Tian-Sheng Memorial Hospital, Pingtung 92843, Taiwan

^k Department of Marine Biotechnology and Resources, National Sun Yat-sen University, Kaohsiung 80424, Taiwan

^l Chinese Medicine Research and Development Center, China Medical University Hospital, Taichung 40447, Taiwan

^m Graduate Institute of Natural Products, Kaohsiung Medical University, Kaohsiung 80708, Taiwan

ARTICLE INFO

Article history:

Received 10 April 2019

Received in revised form

21 May 2019

Accepted 24 May 2019

Available online 27 May 2019

Keywords:

Briareum violaceum

Briaviolide

Excavatulide

Elastase

ABSTRACT

Five 2-acetoxybriaranes, including two known analogues, excavatulides B (**1**), E (**2**), along with three new metabolites, briaviolides V–X (**3**–**5**), have been obtained from the octocoral *Briareum violaceum*. The absolute configurations of **1** and **2** were determined by X-ray analysis for the first time and the structures of **3**–**5** were established by spectroscopic methods. Bioactivity study showed that briarane **3** decreased the release of elastase from human neutrophils.

© 2019 Elsevier Ltd. All rights reserved.

1. Introduction

Briarane-type natural products are a family of marine-origin structurally unique 3,8-cyclized cembranoids distributed in octocorals, particularly isolated from the octocorals belonging to the genus *Briareum* (family Briareidae) [1] and *Juncella* (family Ellisellidae) [2]. Compounds of this type were suggested to be synthesized by host corals and not by its symbiotic zooxanthellae [3,4]

and have been shown to display extensive bioactivities [1,2]. However, due to complex structures, the total synthesis on briarane-type natural products has been facing challenging and therefore limited their further research on biomedical development [5]. Recently, in our ongoing study on the chemical constituents of a cultured *Briareum violaceum* has resulted in the isolation of two known analogues, excavatulide B (**1**) and excavatulide E (**2**) [6,7], as well as three new isolates, briaviolides V–X (**3**–**5**) (Fig. 1). The isolated compounds were evaluated for anti-inflammatory activity using the inhibition of elastase in an *in vitro* pro-inflammatory model.

2. Results and discussion

Excavatulides B (**1**) and E (**2**), were first isolated from a

* Corresponding author. National Museum of Marine Biology and Aquarium, Pingtung 94450, Taiwan.

** Corresponding author.

*** Corresponding author.

E-mail addresses: a081002@mail.tsmh.org.tw (T.-R. Su), sheu@mail.nsysu.edu.tw (J.-H. Sheu), pjsung@nmmba.gov.tw (P.-J. Sung).

¹ These authors contributed equally to this work.

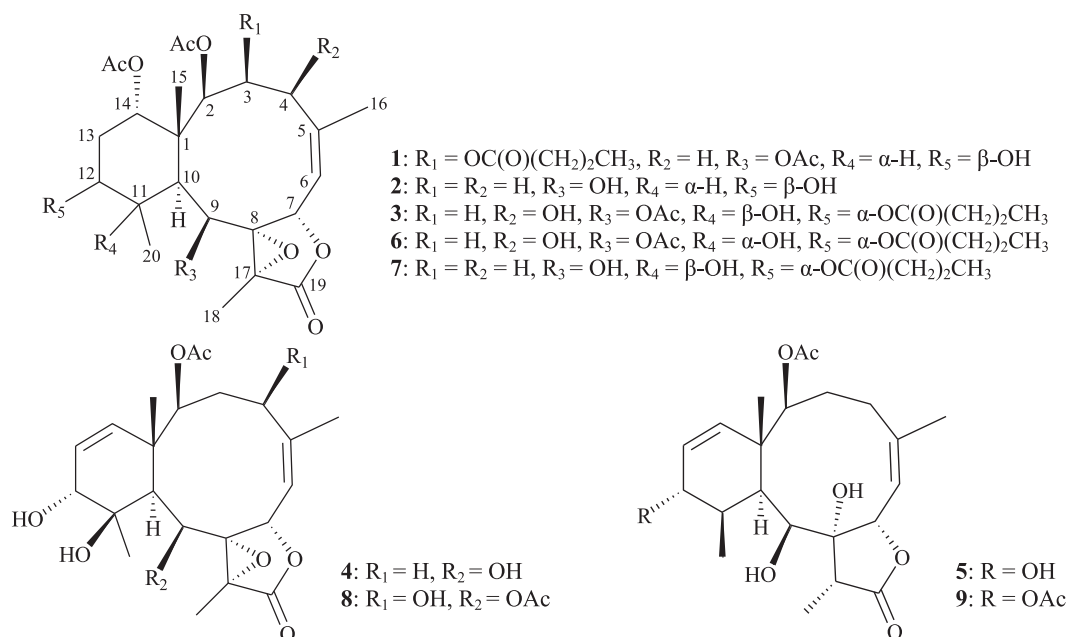


Fig. 1. Structures of excavatolide B (1), excavatolide E (2), briaviolides V–X (3–5), briacavatolide C (6), excavatolide Z (7), briacexcavatin K (8) and solenolide F (9).

Taiwanese octocoral *Briareum excavatum* [3]; and the structures of these two compounds, including the relative configurations, were elucidated by NMR spectral analysis and X-ray analysis [6,7]. The absolute configurations of these two compounds were determined in this study by single-crystal X-ray diffraction analyses (Flack parameter $x = 0.16(4)$ for **1**; and $x = 0.06(5)$ for **2**, respectively) and the ortep diagram (Fig. 2) showed that the configurations of stereogenic carbons of excavatolide B (**1**) are 1*R*,2*R*,3*S*,7*S*,8*R*,9*S*,10*S*,11*R*,12*S*,14*S*,17*R* and of **2** (excavatolide E) are 1*S*,2*S*,7*S*,8*R*,9*S*,10*S*,11*R*,12*S*,14*S*,17*R* [8–10].

Briaviolide V (**3**) was obtained as an amorphous powder and the molecular formula was determined to be $\text{C}_{30}\text{H}_{42}\text{O}_{13}$ (10° of unsaturation) by analysis of ^1H and ^{13}C NMR data (Table 1) in conjunction with DEPT results; this conclusion was further

confirmed by HRESIMS at m/z 633.25185 (calcd for $\text{C}_{30}\text{H}_{42}\text{O}_{13} + \text{Na}$, 633.25176). Analysis of the ^1H , ^{13}C NMR, and DEPT spectra together with the molecular formula, suggested that there must be two exchangeable protons, requiring the presence of two hydroxy groups, and this deduction was supported by a broad absorption in the IR spectrum at 3434 cm^{-1} . The IR spectrum also showed strong bands at 1779 and 1732 cm^{-1} , consistent with the γ -lactone and ester groups, respectively. The ^{13}C NMR spectrum (Table 1), in combination with DEPT and HSQC spectra, revealed the presence of an *n*-butyryloxy group (δ_{C} 13.7, CH_3 ; 18.3, 36.4 , $2 \times \text{CH}_2$; 172.5, C), three acetoxy groups (δ_{C} 21.5, 21.4, 21.2, $3 \times \text{CH}_3$; δ_{C} 169.4, 170.4, 170.6, $3 \times \text{C}$), a γ -lactone moiety (δ_{C} 171.2, C-19), a trisubstituted olefin (δ_{C} 147.4, C-5; 121.4, CH-6) and a tetrasubstituted epoxide group (δ_{C} 70.4, C-8; 64.3, C-17). Base on the ^{13}C NMR data and

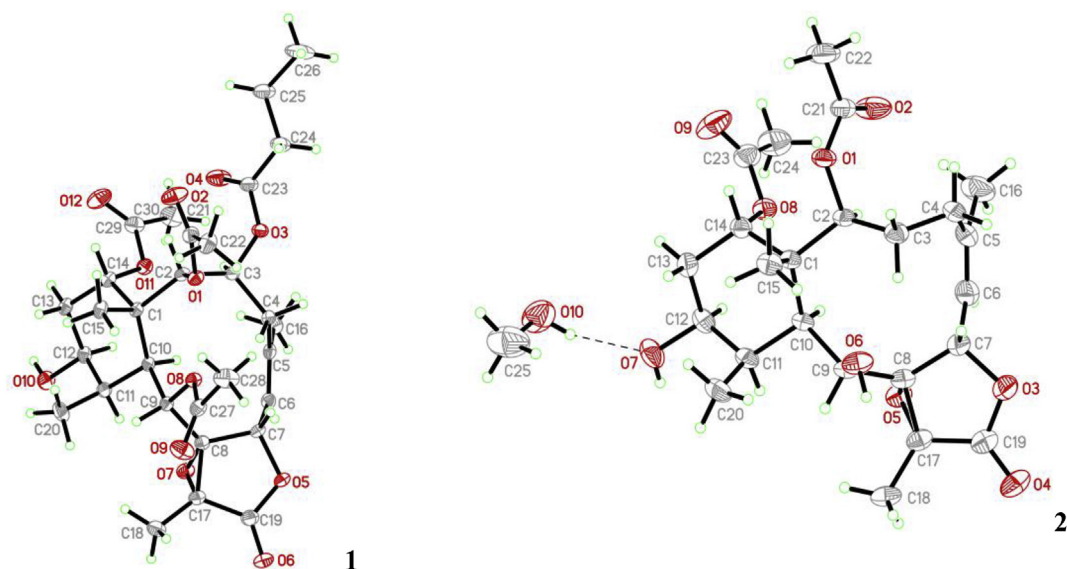


Fig. 2. The computer-generated ORTEP plots of **1** and **2**.

Table 1
¹H and ¹³C NMR data and COSY correlations and HMBC for briarane **3**.

C/H	δ_{H} (J in Hz) ^a	δ_{C} , Mult. ^b	COSY	HMBC
1		46.6, C		
2	5.01 d (7.5)	74.4, CH	H-3 α	C-1, -4, -15, acetate carbonyl
3 α	2.04 ddd (15.5, 7.5, 5.0)	40.7, CH ₂	H-2, H-3 β , H-4	C-4, -5
β	2.89 dd (15.5, 12.0)		H-3 α , H-4	C-4
4	4.22 dd (12.0, 5.0)	71.1, CH	H ₂ -3	—
5		147.4, C		
6	5.43 dd (9.5, 1.0)	121.4, CH	H-7, H ₃ -16	—
7	6.04 d (9.5)	73.9, CH	H-6	C-6
8		70.4, C		
9	5.77 s	67.6, CH	—	C-1, -7, -8, -10, -11, -17, acetate carbonyl
10	2.33 s	44.8, CH	—	C-1, -2, -8, -9, -11, -15
11		76.0, C		
12	4.85 br s	74.9, CH	H ₂ -13	—
13 α	1.99 m	24.3, CH ₂	H-12, H-13 β , H-14	C-12, -14
β	2.21 m		H-12, H-13 α , H-14	—
14	4.74 br s	74.8, CH	H ₂ -13	—
15	1.33 s	15.0, CH ₃		C-1, -2, -10, -14
16	2.15 d (1.0)	25.1, CH ₃	H-6	C-4, -5, -6
17		64.3, C ^c		
18	1.71 s	10.1, CH ₃		C-8, -17, -19
19		171.2, C		
20	1.29 s	30.0, CH ₃		C-10, -11, -12
OAc-2	1.96 s	170.4, C		Acetate carbonyl
OAc-9	2.25 s	21.4, CH ₃		Acetate carbonyl
OAc-14	2.00 s	169.4, C		Acetate carbonyl
n-OC(O)Pr-12		21.5, CH ₃		Acetate carbonyl
1'		170.6, C		
2'	2.33–2.12 m	21.2, CH ₃		
3'	1.65 sext (7.5)	172.5, C	H ₂ -3'	C-1', -3', -4'
4'	0.95 t (7.5)	36.4, CH ₂	H ₂ -2', H ₃ -4'	C-1', -2', -4'
		18.3, CH ₂	H ₂ -3'	C-2', -3'
		13.7, CH ₃		

^a Spectra recorded at 500 MHz in CDCl₃ at 25 °C.

^b Spectra recorded at 125 MHz in CDCl₃ at 25 °C.

^c Due to the absence of signal, the chemical shift for C-17 was assigned by the assistance of HMBC.

numbers of unsaturation, **3** was established as a tetracyclic briarane diterpenoid.

The ¹H NMR coupling information in the COSY spectrum analysis of **3** (Table 1) enabled the determination of the proton sequences between H-2/H₂-3/H-4 and H-6/H-7. These data, together with the HMBC from H-2/C-1, -4; H₂-3/C-4, -5; H-7/C-6; H-9/C-1, -7, -8, -10; and H-10/C-1, -2, -8, -9, established the connectivity from C-1 to C-10 in a ten-membered ring connecting C-1 to C-10 (Table 1). The vinyl methyl at C-5 was confirmed by the HMBC between H₃-16/C-4, -5, -6 and further supported by an allylic coupling between H₃-16/H-6 ($J = 1.0$ Hz). The COSY correlations from H-12/H₂-13/H-14 and HMBC from H-9/C-11; H-10/C-11; and H₃-20/C-10 suggested that the methylcyclohexane ring was fused to the ten-membered ring at C-1 and C-10. The methyl group (Me-15) on C-1 was substantiated by the HMBC from H₃-15/C-1, -2, -10, -14; H-2/C-15; and H-10/C-15. Based on the HMBC from the oxymethine protons at δ_{H} 5.77 (H-9) and 5.01 (H-2) to the ester carbonyls at δ_{C} 169.4 and 170.4, respectively, placed the acetoxy groups on C-9 and C-2. In addition, the carbon at δ_{C} 172.5 was correlated with the signals of the methylene protons at δ_{H} 2.33–2.12 and 1.65 in the HMBC spectrum and was assigned as the carbon atom of the *n*-butyrate carbonyl. Thus, the *n*-butyroxyl and remaining acetoxy groups were on C-12 or C-14, respectively, for their characteristic NMR signals (δ_{H} 4.85, 1H, br s; δ_{C} 74.9, CH-12; δ_{H} 4.74, 1H, br s; δ_{C} 74.8, CH-14), although no HMBC was observed from H-12 and H-14 to any ester carbonyl. The positions of *n*-butyroxyl and acetoxy groups at C-12 or C-14 were confirmed by comparison of the NMR chemical shifts of C-12 and C-14 oxymethines with those of known analogues briacavatulide C (**6**) (δ_{H} 4.80, 1H, m; δ_{C} 74.0, CH-12; δ_{H} 4.70,

1H, br s; δ_{C} 73.4, CH-14) [11] and excavatulide Z (**7**) (δ_{H} 4.87, 1H, br s; δ_{C} 75.1, CH-12; δ_{H} 4.68, 1H, br s; δ_{C} 74.9, CH-14) [12] (Fig. 1), which were isolated from octocoral *B. excavatum* and proved to possess *n*-butyroxyl and acetoxy groups at C-12 and C-14, respectively, in their structures [11,12]. The aforementioned data, together with the HMBC from H₃-18/C-8, -17, -19, allowed to establish the planar structure of **3**.

Based on previous studies, all naturally occurring briarane diterpenoids have the C-15 methyl group *trans* to H-10, and are assigned as β - and α -oriented, respectively, as shown in most briarane derivatives [1]. The relative stereochemistry of **3** was established by NOESY spectral analysis, which was further supported by MM2 force field analysis [13]. The NOESY spectrum (Fig. 3) exhibited correlations from H-10 to H-2 and H₃-20, and not to H-12 and H₃-15, indicating that H-2, H-10 and Me-20 are on the same face and were assigned to the α -position, since H-12 and Me-15 are β -substituents at C-12 and C-1, respectively. H-14 exhibited a correlation to H₃-15, and not with H-10, it was β -oriented. As one of the C-3 methylene protons (δ_{H} 2.89) exhibited a correlation to H-7, and not with H-2, suggesting the β -orientation of this proton. A correlation from H-7 to H-3 β , but not with H-6, as well as a large coupling constant between H-7 and H-6 ($J = 9.5$ Hz), suggested that the dihedral angle between H-7 and H-6 was nearly 180°, and H-7 was β -oriented and the 8,17-epoxy group was α -oriented according to modeling study. The *Z*-configuration of the C-5/6 double bond was confirmed based on the fact that the C-6 olefinic proton (δ_{H} 5.43) was correlated to C-16 vinyl methyl (δ_{H} 2.15). Correlation of H-4 to H-3 α (δ_{H} 2.04) and H₃-16; and H₃-16 correlated with H-2, indicated that the hydroxy group at C-4 was β -oriented. H-9 showed

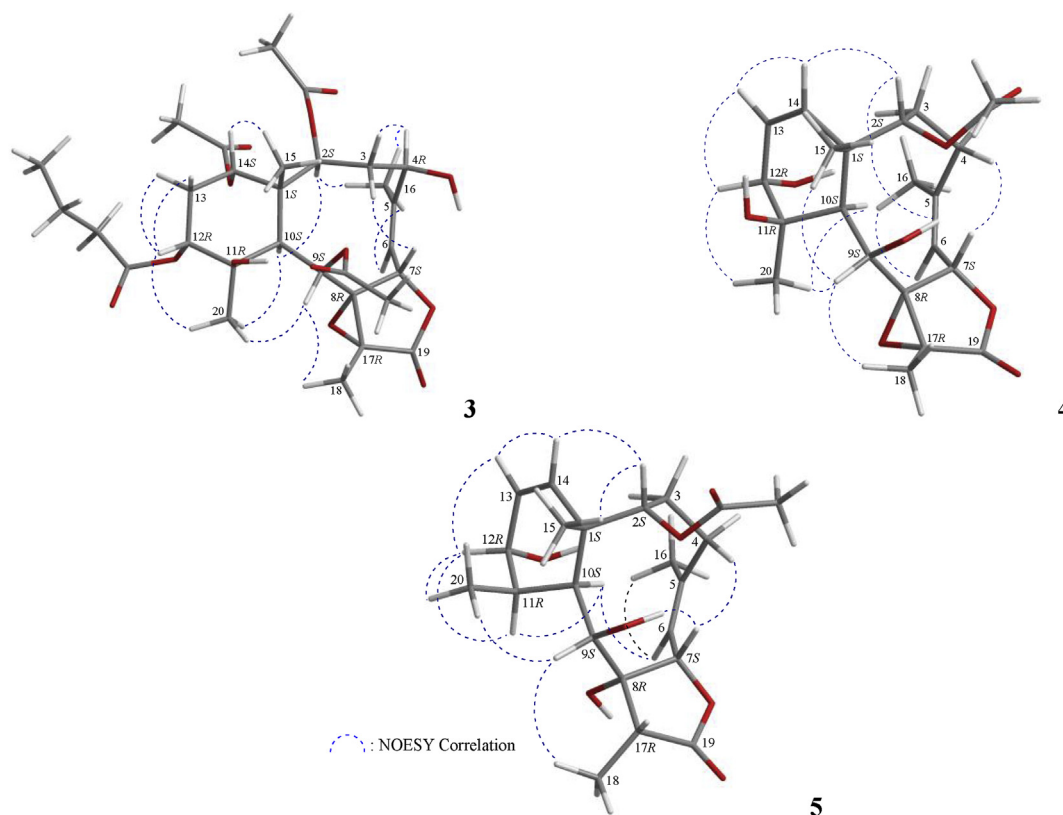


Fig. 3. Selected NOESY correlations of 3–5.

correlations to H₃-18 and H₃-20, and not with H-10 and H₃-15, as well as a lack of coupling constant was detected between H-9 and H-10, indicating that the dihedral angle between H-9 and H-10 is approximately 90° and 9-hydroxy group has a β-orientation. H-12 exhibited correlations to both H-13α/β and H₃-20, and not with H-10, revealing that the *n*-butyryloxy group at C-12 is on the α face. As briaranes 3–5 were isolated along with 1 and 2 from the same organism, it is reasonable on biogenetic grounds to assume that 3–5 have the same absolute configurations as 1 and 2. Therefore, based on above findings, the configurations of the stereogenic carbons of 3 were determined as 1*S*,2*S*,4*R*,7*S*,8*R*,9*S*,10*S*,11*R*,12*R*,14*S*,17*R*. By comparison of the related key NMR data of 3 with those of known briarane, briacavatolide C (6) (Table 2) [11], the structure of 3 was found to be the 11-*epi*-compound of 6.

Briarane 4 (briaviolide W) was found to have a molecular formula of C₂₂H₃₀O₈ based on its HRESIMS peak at *m/z* 445.18317 (calcd. for C₂₂H₃₀O₈ + Na, 445.18329). Its absorption peaks in the IR spectrum showed ester carbonyl, γ-lactone and broad OH stretching at 1765, 1785 and 3446 cm⁻¹, respectively. The ¹³C NMR spectrum indicated that an ester and a γ-lactone were present, as carbonyl resonances were observed at δ_C 168.2 and 172.8,

respectively (Table 3). The ¹H NMR spectrum also indicated the presence of an acetate methyl (δ_H 2.30, s, 3H) (Table 3). It was found that the ¹H and ¹³C NMR spectra of 4 resembled those of a known analogue, briacavatolide K (8) (Fig. 1) [7], except that the signals corresponding to the C-4 hydroxy and C-9 acetoxy groups in 8 were replaced by signals for a proton and a hydroxy group in 4, respectively. The locations of the functional groups were further confirmed by other HMBC and COSY correlations (Table 3), and hence briaviolide W was assigned the structure of 4, with the same stereochemistry as that of 8, and the configurations of the stereogenic carbons were elucidated as 1*S*,2*S*,7*S*,8*R*,9*S*,10*S*,11*R*,12*R*,17*R* (Fig. 3).

Briaviolide X (5) was found to have a molecular formula of C₂₂H₃₂O₇ based on its HRESIMS peak at *m/z* 431.20375 (calcd. for C₂₂H₃₂O₇ + Na, 431.20402). It was found that the spectroscopic data of 5 were similar to those of a known briarane, solenolide F (9), isolated from *Solenopodium* sp. (= *Briareum* sp.) [14], collected off the Western Caroline Islands of Palau [15]; however, by comparison of the ¹H and ¹³C NMR chemical shifts of the C-12 oxymethine (δ_H 3.88, 1H, br d, *J* = 6.0 Hz; δ_C 68.3) of 5 (Table 4) with those of 9 (δ_H 4.86, 1H, dd, *J* = 5.8, 1.4 Hz; δ_C 70.2 or 71.2) showed that the acetoxy group at C-12 in 9 was replaced by a hydroxy group in 5. The stereochemistry of the stereogenic centers C-1, C-2, C-7, C-8, C-9, and C-10 in the ten-membered ring was confirmed to be the same as that of 9 by comparison of the proton shifts, coupling constants and NOESY correlations (Fig. 3). The hydroxy group at C-12 was assigned as α-configuration, primarily due to NOESY correlations from H-12 to H-11 and H₃-20; but not with H-10. On the basis of above results, the stereogenic carbons were found to possess the configurations 1*S*,2*S*,7*S*,8*R*,9*S*, 10*S*,11*R*,12*R*,17*R*.

In *in vitro* anti-inflammatory activity assay, it was found that only briarane 3 (briaviolide V) showed a weakly inhibitory effect on

Table 2
Key ¹H and ¹³C NMR data differences between briaranes 3 and 6.

Position	3		6 ^a	
	δ _H (J in Hz)	δ _C , Mult.	δ _H (J in Hz) ^b	δ _C , Mult. ^c
11		76.0, C		73.8, C
20	1.29 s	30.0, CH ₃	1.25 s	23.2, CH ₃

^a Data were reported by Yeh et al. (see Ref. [11]).

^b Spectra recorded at 400 MHz in CDCl₃.

^c Spectra recorded at 100 MHz in CDCl₃.

Table 3
¹H and ¹³C NMR data and COSY correlations and HMBC for briarane **4**.

C/H	δ_{H} (J in Hz) ^a	δ_{C} , Mult. ^b	COSY	HMBC
1		45.9, C		
2	4.81 d (9.6)	82.2, CH	H-3 β	C-1, -3, -10, -14, -15, acetate carbonyl
3 α / β	1.79 m; 2.32 m	23.7, CH ₂	H-2, H ₂ -4	C-1, -2, -4, -5
4 α / β	1.89 dd (14.8, 11.2); 2.44 dd (14.8, 8.8)	25.3, CH ₂	H ₂ -3	C-2, -3, -5, -6, -16
5		144.4, C		
6	5.42 d (9.6)	120.6, CH	H-7	C-4
7	5.43 d (9.6)	73.2, CH	H-6	C-5, -6
8		71.6, C		
9	4.13 dd (9.6, 6.8)	68.5, CH	H-10, OH-9	C-7, -8, -10, -11
10	3.16 d (6.8)	39.7, CH	H-9	C-1, -8, -9, -15
11		74.0, C		
12	3.73 dd (5.6, 4.0)	72.5, CH	H-13, OH-12	C-10, -11, -13, -14, -20
13	5.88 dd (10.0, 5.6)	125.1, CH	H-12, H-14	C-1, -11, -12
14	5.42 d (10.0)	139.9, CH	H-13	C-1, -2, -10, -12, -15
15	1.42 s	22.4, CH ₃		C-1, -2, -10, -14
16	1.78 s	24.5, CH ₃		C-4, -5, -6
17		61.6, C		
18	1.66 s	9.7, CH ₃		C-8, -17, -19
19		172.8, C		
20	1.31 s	26.6, CH ₃		C-10, -11, -12
OAc-2		168.2, C		
	2.30 s	21.1, CH ₃		Acetate carbonyl
OH-9	4.59 br d (9.6)		H-9	—
OH-12	1.75 d (4.0)		H-12	C-11, -13

^a Spectra recorded at 400 MHz in CDCl₃ at 25 °C.^b Spectra recorded at 100 MHz in CDCl₃ at 25 °C.**Table 4**
¹H and ¹³C NMR data and COSY correlations and HMBC for briarane **5**.

C/H	δ_{H} (J in Hz) ^a	δ_{C} , Mult. ^b	COSY	HMBC
1		44.4, C		
2	4.74 d (9.6)	82.3, CH	H-3 β	C-1, -4, -10, -14, acetate carbonyl
3 α / β	1.73 ddd (15.6, 8.0, 1.2); 2.26 m	22.8, CH ₂	H-2, H ₂ -4	C-1, -5
4 α / β	1.84 m; 2.49 m	24.2, CH ₂	H ₂ -3	C-2, -5, -6, -16
5		144.7, C		
6	5.42 d (10.0)	120.2, CH	H-7	C-16
7	5.35 d (10.0)	76.8, CH	H-6	C-5, -6
8		84.9, C		
9	3.69 dd (8.4, 8.4)	70.0, CH	H-10, OH-9	C-7, -8, -11
10	2.95 dd (8.4, 3.2)	33.7, CH	H-9, H-11	—
11	2.45 m	38.7, CH	H-10, H-12, H ₃ -20	—
12	3.88 br d (6.0)	68.3, CH	H-11, H-13	—
13	5.85 ddd (10.0, 6.0, 0.8)	126.3, CH	H-12, H-14	C-1, -11
14	5.34 d (10.0)	139.2, CH	H-13	C-1, -2, -10, -12
15	1.24 s	20.1, CH ₃		C-1, -2, -10, -14
16	1.81 s	24.1, CH ₃		C-4, -5, -6
17	3.36 q (6.8)	41.8, CH	H ₃ -18	C-8, -18, -19
18	1.21 d (6.8)	6.5, CH ₃	H-17	C-8, -17, -19
19		178.0, C		
20	0.97 d (7.2)	12.8, CH ₃		C-10, -11, -12
OAc-2		168.0, C		
	2.25 s	20.8, CH ₃		Acetate carbonyl
OH-8	1.86 s			C-7, -8, -17
OH-9	4.46 d (8.4)		H-9	C-9, -10

^a Spectra recorded at 400 MHz in CDCl₃ at 25 °C.^b Spectra recorded at 100 MHz in CDCl₃ at 25 °C.

the release of elastase (inhibition rate = 13%) by human neutrophils at a concentration of 10 μ M and the rest compounds **1**, **2**, **4**, and **5** were inactive (inhibition rates < 10%). Due to the screening platforms are limited and lots of material were consumed in physical and spectral experiments, the other possible bioactivities for the new interesting natural substances will not be assayed at this stage. The possible bioactivity for these compounds will be studied if we can get enough material from the cultured *B. violaceum* in the future.

3. Experimental

3.1. General experimental procedures

Melting points of the natural products were determined using a Fargo apparatus, and the values were uncorrected. Optical rotation values were measured with a Jasco P-1010 digital polarimeter at 20 °C with 2.0 or 0.3 mL cells. IR spectra were obtained with a Thermo Scientific Nicolet iS5 FT-IR spectrophotometer. NMR spectra were recorded on a Jeol Resonance ECZ400S or a Varian

Inova 500 NMR spectrometers using the residual CHCl_3 signal (δ_{H} 7.26 ppm) as an international standard for ^1H NMR and CDCl_3 (δ_{C} 77.1 ppm) for ^{13}C NMR, respectively. Coupling constants (J) are presented in Hz. ESIMS and HRESIMS were recorded using a mass spectrometer (7 T Solarix FTMS system, Bruker). Column chromatography were performed as described in our previous study [16,17].

3.2. Animal material

Specimens of *B. violaceum* were collected from the waters off Taiwan, and relocated to a 270-ton cultivation tank located in the National Museum of Marine Biology and Aquarium (NMMBA), Taiwan, in 2011; the material used for this study was collected from the tank in December 2016. This organism was identified by comparison with previous descriptions [14]. A voucher specimen was deposited in the NMMBA, Taiwan (NMMBA-CSC-002).

3.3. Extraction and isolation

Sliced bodies of *B. violaceum* (wet and dry weights, 251 and 95.0 g, respectively) were extracted with a mixture of MeOH and CH_2Cl_2 (1:1; v/v). The resulting 9.79 g extract was partitioned between EtOAc and H_2O . The EtOAc layer (3.30 g) was applied on a silica gel column chromatography (C.C.) and eluted with a mixture of *n*-hexane/EtOAc (stepwise from 100:1–100% EtOAc; volume ratio) to yield 15 fractions A–O. Fraction M was chromatographed on silica gel C.C. and eluted with a mixture of *n*-hexane/EtOAc (stepwise 5:1 to 1:1) to afford 12 subfractions M1–M12. Fraction M8 was purified by RP-HPLC using a mixture of acetonitrile/ H_2O (v:v = 3:2 of volume ratio at a flow rate of 5.0 mL/min) to obtain **1** (6.0 mg). Fraction N was separated by silica gel C.C. and then eluted with a mixture of $\text{CH}_2\text{CH}_2/\text{acetone}$ (stepwise 100:1 to 1:1) afforded 21 subfractions N1–N21. Fraction N13 was purified by NP-HPLC using a mixture of *n*-hexane/acetone (3:1) to afford 9 subfractions N13A–N13I. Fraction N13D was purified by RP-HPLC using a mixture of acetonitrile/ H_2O (v:v = 1:1 of volume ratio at a flow rate of 4.0 mL/min) to obtain **5** (0.9 mg). Fraction N13E was repurified by RP-HPLC using a mixture of MeOH/ H_2O (65:35; volume ratio, flow rate = 4.0 mL/min) to afford **2** (21.8 mg) and **3** (0.6 mg). Fraction N13F was separated by RP-HPLC and then eluted with MeOH/ H_2O (1:1; volume ratio, flow rate = 4.0 mL/min) to afford **4** (3.2 mg).

3.3.1. Excavatulide B (**1**)

Colorless prisms; mp 223–226 °C (ref [6]. 224–225 °C); $[\alpha]_{\text{D}}^{20}$ –28 (c 0.3, CHCl_3) (ref [6]. $[\alpha]_{\text{D}}^{26}$ –23 (c 0.09, CHCl_3)); IR (neat) ν_{max} 3438, 1764, 1730 cm^{-1} ; ESIMS: m/z 617 $[\text{M} + \text{Na}]^+$.

3.3.2. Excavatulide E (**2**)

Colorless prisms; mp 190–191 °C (ref [6]. 190–191 °C); $[\alpha]_{\text{D}}^{20}$ +45 (c 0.4, CHCl_3) (ref [6]. $[\alpha]_{\text{D}}^{30}$ +53 (c 0.14, CHCl_3)); IR (neat) ν_{max} 3438, 1764, 1730 cm^{-1} ; ESIMS: m/z 489 $[\text{M} + \text{Na}]^+$.

3.3.3. Briaviolide V (**3**)

Amorphous powder; $[\alpha]_{\text{D}}^{20}$ –3 (c 0.1, CHCl_3); IR (neat) ν_{max} 3434, 1779, 1732 cm^{-1} ; ^1H (500 MHz, CDCl_3) and ^{13}C (125 MHz, CDCl_3) NMR data (see Table 1); ESIMS: m/z 633 $[\text{M} + \text{Na}]^+$; HRESIMS: m/z 633.25185 (calcd for $\text{C}_{30}\text{H}_{42}\text{O}_{13} + \text{Na}$, 633.25176).

3.3.4. Briaviolide W (**4**)

Amorphous powder; $[\alpha]_{\text{D}}^{20}$ –29 (c 0.2, CHCl_3); IR (neat) ν_{max} 3446, 1785, 1765 cm^{-1} ; ^1H (400 MHz, CDCl_3) and ^{13}C (100 MHz, CDCl_3) NMR data (see Table 2); ESIMS: m/z 445 $[\text{M} + \text{Na}]^+$; HRESIMS: m/z 445.18317 (calcd for $\text{C}_{22}\text{H}_{30}\text{O}_8 + \text{Na}$, 445.18329).

3.3.5. Briaviolide X (**5**)

Amorphous powder; $[\alpha]_{\text{D}}^{20}$ +1 (c 0.2, CHCl_3); IR (neat) ν_{max} 3484, 1771, 1753 cm^{-1} ; ^1H (400 MHz, CDCl_3) and ^{13}C (100 MHz, CDCl_3) NMR data (see Table 3); ESIMS: m/z 431 $[\text{M} + \text{Na}]^+$; HRESIMS: m/z 431.20375 (calcd for $\text{C}_{22}\text{H}_{32}\text{O}_7 + \text{Na}$, 431.20402).

3.4. Molecular mechanics calculations

Implementation of the MM2 force field [13] in CHEM3D PRO software from CambridgeSoft Corporation (Cambridge, MA, USA; ver. 9.0, 2005) was used to calculate molecular models.

3.5. Single-crystal X-ray crystallography of excavatulide B (**1**)

Suitable colorless prisms of **1** were obtained from a solution of EtOAc. The crystal (0.244 × 0.202 × 0.196 mm) belongs to the monoclinic system, space group $P2_1$ (#4), with $a = 10.2857(2)$ Å, $b = 9.7025(2)$ Å, $c = 15.2387(4)$ Å, $V = 1519.33(6)$ Å³, $Z = 2$, $D_{\text{calcd}} = 1.300 \text{ Mg/m}^3$, λ (Cu $K\alpha$) = 1.54178 Å. Intensity data were measured on a Bruker D8 Venture diffractometer up to θ_{max} of 75.0°. All 11236 reflections were collected. The structure was solved by direct methods and refined by a full-matrix least-squares procedure. The refined structural model converged to a final $R1 = 0.0367$; $wR2 = 0.0999$ for 6189 observed reflections [$I > 2\sigma(I)$] and 388 variable parameters. The absolute configuration was determined by Flack parameter $x = 0.16(4)$ [8–10].

3.6. Single-crystal X-ray crystallography of excavatulide E (**2**)

Suitable colorless prisms of **2** were obtained from a solution of MeOH. The crystal (0.321 × 0.277 × 0.173 mm) belongs to the orthorhombic system, space group $P2_12_12_1$ (#19), with $a = 9.5773(2)$ Å, $b = 14.4224(3)$ Å, $c = 18.8049(4)$ Å, $V = 2597.48(9)$ Å³, $Z = 4$, $D_{\text{calcd}} = 1.275 \text{ Mg/m}^3$, λ (Cu $K\alpha$) = 1.54178 Å. Intensity data were measured on a Bruker D8 Venture diffractometer up to θ_{max} of 75.0°. All 11419 reflections were collected. The structure was solved by direct methods and refined by a full-matrix least-squares procedure. The refined structural model converged to a final $R1 = 0.0425$; $wR2 = 0.1212$ for 5301 observed reflections [$I > 2\sigma(I)$] and 326 variable parameters. The absolute configuration was determined by Flack parameter $x = 0.06(5)$ [8–10].

3.7. Elastase generation by human neutrophils

Human neutrophils were obtained by means of dextran sedimentation and Ficoll centrifugation. Measurement of superoxide anion generation was carried out according to previously described procedures [18,19]. Briefly, superoxide anion production was assayed by monitoring the superoxide dismutase-inhibitable were performed using MeO-Suc-Ala-Ala-Pro-Valp-nitroanilide as the elastase substrate.

Acknowledgments

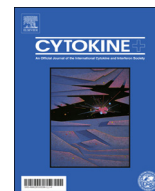
This research was supported by grants from the National Museum of Marine Biology and Aquarium; the National Dong Hwa University; and the Ministry of Science and Technology, Taiwan (Grant Nos: MOST 104-2320-B-291-001-MY3 and 107-2320-B-291-001-MY3) awarded to P.-J. Sung.

Appendix A. Supplementary data

Supplementary data to this article can be found online at <https://doi.org/10.1016/j.tet.2019.05.053>.

References

- [1] Y.D. Su, J.H. Su, T.L. Hwang, Z.H. Wen, J.H. Sheu, Y.C. Wu, P.J. Sung, *Mar. Drugs* 15 (2017) 44, and previous review article in this series.
- [2] H.M. Chung, Y.C. Wang, C.C. Tseng, N.F. Chen, Z.H. Wen, L.S. Fang, T.L. Hwang, Y.C. Wu, P.J. Sung, *Mar. Drugs* 16 (2018) 339, and previous review article in this series.
- [3] W.C.M.C. Kokke, S. Epstein, S.A. Look, G.H. Rau, W. Fenical, C. Djerassi, *J. Biol. Chem.* 259 (1984) 8168.
- [4] P.J. Sung, T.Y. Fan, M.C. Chen, L.S. Fang, M.R. Lin, P.C. Chang, *Biochem. Syst. Ecol.* 32 (2004) 111.
- [5] N.G. Moon, A.M. Harned, *Royal Soc. Open Sci.* 5 (2018) 172280.
- [6] J.H. Sheu, P.J. Sung, M.C. Cheng, H.Y. Liu, L.S. Fang, C.Y. Duh, M.Y. Chiang, *J. Nat. Prod.* 61 (1998) 602.
- [7] P.J. Sung, M.R. Lin, Y.D. Su, M.Y. Chiang, W.P. Hu, J.H. Su, M.C. Cheng, T.L. Hwang, J.H. Sheu, *Tetrahedron* 64 (2008) 2596.
- [8] H.D. Flack, *Acta Crystallogr.* A39 (1983) 876.
- [9] H.D. Flack, G. Bernardinelli, *Acta Crystallogr.* A55 (1999) 908.
- [10] Crystallographic Data for the Structures of Excavatolide B (**1**) and Excavatolide E (**2**) Have Been Deposited with the Cambridge Crystallographic Data Center as Supplementary Publication Numbers CCDC 1899811 and 1889879, Respectively. Copies of the Data Can Be Obtained, Free of Charge, on Application to CCDC, 12 Union Road, Cambridge CB2 1EZ, UK [fax: +44(0)1223 336033 or e-mail: deposit@ccdc.cam.ac.uk].
- [11] T.T. Yeh, S.K. Wang, C.F. Dai, C.Y. Duh, *Mar. Drugs* 10 (2012) 1019.
- [12] J.H. Sheu, P.J. Sung, J.H. Su, G.H. Wang, C.Y. Duh, Y.C. Shen, M.Y. Chiang, I.T. Chen, *J. Nat. Prod.* 62 (1999) 1415.
- [13] N.L. Allinger, *J. Am. Chem. Soc.* 99 (1977) 8127.
- [14] K. Samimi-Namin, L.P. van Ofwegen, *ZooKeys* 557 (2016) 1.
- [15] A. Groweiss, S.A. Look, W. Fenical, *J. Org. Chem.* 53 (1988) 2401.
- [16] J.H. Xu, Y.C. Chang, G.Q. Li, Z.H. Wen, Y.C. Wu, P.J. Sung, *Phytochem. Lett.* 27 (2018) 129.
- [17] J.H. Xu, K.H. Lai, Y.D. Su, Y.C. Chang, B.R. Peng, A. Backlund, Z.H. Wen, P.J. Sung, *Mar. Drugs* 16 (2018) 75.
- [18] S.C. Yang, P.J. Chung, C.M. Ho, C.Y. Kuo, M.F. Hung, Y.T. Huang, W.Y. Chang, Y.W. Chang, K.H. Chan, T.L. Hwang, *J. Immunol.* 190 (2013) 6511.
- [19] H.P. Yu, P.W. Hsieh, Y.J. Chang, P.J. Chung, L.M. Kuo, T.L. Hwang, *Free Radic. Biol. Med.* 50 (2011) 1737.



Mono- and poly-functional T cells in nontuberculous mycobacteria lung disease patients: Implications in analyzing risk of disease progression

Chin-Chung Shu^a, Lawrence Shih-Hsin Wu^b, Ming-Fang Wu^{c,d}, Hsin-Chih Lai^{e,f,g},
Ping-Huai Wang^{h,i,*}, Shih-Lung Cheng^{h,j}, Jann-Yuan Wang^a, Chong-Jen Yu^a

^a Department of Internal Medicine, National Taiwan University Hospital, Taiwan

^b Graduate Institute of Biomedical Sciences, China Medical University, Taiwan

^c Institute of Statistical Science, Academia Sinica, Taipei, Taiwan

^d Graduate Institute of Toxicology, College of Medicine, National Taiwan University, Taipei, Taiwan

^e Department of Medical Biotechnology and Laboratory Science, College of Medicine, Chang Gung University, Tao-Yuan, Taiwan

^f Research Center for Chinese Herbal Medicine and Research Center for Food and Cosmetic Safety, College of Human Ecology, Chang Gung University of Science and Technology, Tao-Yuan, Taiwan

^g Department of Laboratory Medicine, Xiamen Chang Gung Memorial Hospital, Xiamen, Fujian, China

^h Division of Chest Medicine, Department of Internal Medicine, Far Eastern Memorial Hospital, Taiwan

ⁱ Department of Nursing, Oriental Institute of Technology, Taiwan

^j Department of Chemical Engineering and Materials Science, Yuan-Ze University, Taiwan

ARTICLE INFO

Keywords:

Lung disease

Mycobacterium avium complex

Mycobacterium abscessus

Nontuberculous mycobacteria

Poly-functional T cells

ABSTRACT

Summary at a Glance: The diagnosis and progression of nontuberculous mycobacteria lung disease (NTN-LD) are important for clinical judgement but cannot easily be predicted. The immunological response of mono- and poly-functional T cells, a representative of host reactivity to NTM, could be a surrogate biomarker for disease and progression prediction.

Background: *Mycobacterium avium* complex (MAC) and *M. abscessus* (MAB) induced lung disease (LD) have become a clinical concern. Predicting clinical disease relevance and progression is important, but suitable biomarkers are lacking. The host immune response of mono- and poly-functional T cells might aid in clinical judgement.

Methods: We enrolled 140 participants, including 42 MAC-LD, 25 MAB-LD, 31 MAC airway colonization (MAC-Co), 15 MAB-Co patients, and 27 healthy controls. Their blood mono- and poly-functional T cells were measured and analyzed after in-vitro stimulation.

Results: Patients with MAC-LD generally had lower total IFN- γ +, total TNF- α + and triple-positive T cells but higher mono-IL-2 + expression than the controls and MAC-Co group. The MAB-LD group had lower total IL-2 and triple positive cells than the controls and colonization group. Multivariate analysis revealed that body mass index (BMI), mono-IL2 + CD4 + and triple positive-CD8 + cells (PMA stimulation) significantly predicted MAC-LD from the controls. By contrast, male gender and triple positive-CD4 + cells predicted MAC-LD from colonization. On the other hand, the triple positive-CD4 + cells (PMA stimulation) alone or together with the mock/MAB ratio of IL-2 + /TNF- α + CD4 cells could predict MAB-LD in the MAB-Co group or the controls. Among MAC/MAB-LD patients without anti-mycobacterial treatment, MAC-specific mono-IFN- γ + CD4 + cells and PMA-induced triple positive-CD4 + cells were correlated with progression, with an area under the ROC curve of 0.875.

Conclusions: The patients with MAC/MAB-LD had attenuated poly-functional T cells. The triple-positive CD4 + cells could be useful in diagnosing disease from colonization. MAC-specific mono-IFN- γ + CD4 + cells and triple positive-CD4 + might predict radiographic progression, which could be useful in making treatment decisions.

* Corresponding author at: Division of Chest Medicine, Department of Internal Medicine, Far Eastern Memorial Hospital, No. 21, Sec. 2, Nanya S. Rd., Banciao Dist., New Taipei City 220, Taiwan.

E-mail address: phwang@mail.femh.org.tw (P.-H. Wang).

<https://doi.org/10.1016/j.cyto.2019.05.001>

Received 5 January 2019; Received in revised form 29 April 2019; Accepted 1 May 2019

Available online 12 May 2019

1043-4666/ © 2019 Elsevier Ltd. All rights reserved.

1. Introduction

Nontuberculous mycobacteria induced lung infection (NTM-LD) has become a clinical concern [1,2] because the prevalence of NTM-LD has increased over the last two decades [3–5]. Among the NTM pulmonary infections, *Mycobacterium avium* complex (MAC) and *M. abscessus* (MAB) are the most frequently isolated pathogens responsible for lung disease in Southeast Asia and North America [3,6,7]. According to diagnosis guidelines established by the American Thoracic Society (ATS), NTM-LD is diagnosed according to clinical findings and radiographic findings as well as the microbiology of respiratory specimens [1]. Among the microbiology criteria, two or more sputum positive results for the same NTM within one year are required, but the culture is time-consuming, taking weeks [8]. In fact, NTM is ubiquitous in the environment, and the presences of MAC and MAB only have clinical relevance of around 35–42% [9,10] and 33%, respectively [10]. However, early diagnosis of NTM infection is important because NTM-LD can be a lethal infection in intensive care units or in patients without early proper treatment [11].

In addition to ATS guideline, immunological response might be helpful for diagnosis of NTM-LD. In previous studies, the detection of glycopeptidolipid antibody was MAC-specific for diagnosis of MAC-LD [12,13]. This finding indicates that a specific immune response, such as mycobacteria-induced T-cell response, may be a good candidate. Mycobacteria-induced Th1 type CD4+ cells and CD8+ cytotoxic T lymphocytes are essential for protective immunity in tuberculosis [14], and they are differentially impacted by disease stage and mycobacterial load [15,16], suggesting that certain subsets may serve as biomarkers of disease activity and pathogen burden [16]. However, the evidence of NTM-specific mono- and poly-functional T cells has rarely been studied in NTM-LD. Therefore, we conducted the present study to examine the roles of mono- and poly-functional T cells in the diagnosis and prognosis of NTM-LD.

2. Materials and methods

2.1. Patient enrollment

This prospective study was conducted at National Taiwan University Hospital and Far Eastern Memorial Hospital from January 2017 to August 2018 under the approval of the hospitals' Research Ethics Committees (IRB No.: 201703051RINC and 106134-F). Patients aged ≥ 20 years were recruited consecutively when they visited our chest or infection clinics if they were diagnosed as having MAC-LD or MAB-LD according to the diagnostic guidelines suggested by the American Thoracic Society (ATS) [1] (see [supplement file](#)). We classified patients as MAC or MAB airway colonization if they were sputum positive for MAC or MAB but did not fulfill the ATS diagnosis criteria. In addition, we recruited a healthy control group of individuals having negative chest radiographic images. All enrolled participants provided written informed consent. Patients with human immunodeficiency virus infection, chemotherapy treatment, active cancer or concomitant bacterial pulmonary infection were excluded.

2.2. Flow cytometry for peripheral blood mononuclear cells (PBMCs)

Peripheral blood mononuclear cells were isolated using Ficoll-Paque PLUS (GE Healthcare Life Sciences, Sweden) and were then suspended in medium containing RPMI-1640 (Life Technologies; USA), 10% fetal bovine serum (FBS), and 1% penicillin-streptomycin (Life Technologies, USA) in 48-well plates. Medium only (mock stimulation) or heat-killed *Mycobacterium avium* subspecies *avium* (MAC stimulation) (ATCC 25291) at multiplicity of infection (MOI) of 100 or heat-killed *Mycobacterium abscessus* (MAB stimulation) (ATCC 19977) at MOI of 100 were added for co-culturing for 48 h as bacilli stimulation. Because the response to the heat killed antigen alone was low ([Table S2 in](#)

[supplement file](#)), we used CD3 (5 μ g/ml, plate-coated, clone: OKT3) and CD28 (1 μ g/ml, soluble, clone: CD28.2) antibodies (eBioscience, San Diego, CA) in the mock, MAC and MAB stimulations to amplify the reaction in the last 16 h of the co-culture. One more condition, stimulation of Phorbol 12-myristate 13-acetate (50 ng/ml, TOCRIS, USA) plus ionomycin calcium salt (1 μ M/ml, Sigma-Aldrich, USA) (PMA stimulation) for 16 h, was also checked. Protein transport inhibitor (BD Bioscience, USA) was added to the co-culture 12 h before we retrieved the stimulation.

We measured the levels of mono- and poly-functional T cells by using flow cytometry (FACSVerse, BD Biosciences, USA). We gated the lymphocyte population by using forward scatter (FSC) and side scatter (SSC). CD4+ and CD8+ T cells were stained using anti-CD4-APC (clone: RPT-T4, Biolegend, USA) and anti-CD8-PE-cy7.0 (clone: RPA-T8, BD Biosciences, CA, USA). Different types of mono- and poly-functional T cells were further stained with anti-interferon-gamma (IFN- γ)-PerCP (clone: 4S.B3), anti-interleukin-2 (IL-2)-PE (clone: MQ1-17H12) and anti-tumor necrosis factor-alpha (TNF- α)-FITC antibodies (clone: MAb11) (Biolegend, USA). We also stained the post-stimulation T cells with anti-CD4-APC, anti-CD8-PE-cy7.0, anti-programmed death-1 (PD-1)-PE (clone: EH12.1) (BD Biosciences, CA, USA), anti-cytotoxic T Lymphocyte Antigen 4 (CTLA-4)-PE/cy7 (clone: L3DD10), and T-cell immunoglobulin and mucin-domain containing-3 (TIM-3)-PerCP/cy5.5 (clone: F38-2E2) (Biolegend, USA). The details of the gating protocol are provided in the [supplementary information \(Fig. S1\)](#). Data were analyzed using BD FACSuite V software (BD, Biosciences, USA).

2.3. Data collection and statistical analysis

Clinical data including age, sex, co-morbidities, radiographic findings and laboratory data at enrollment were recorded in a standardized case report form with default options. The radiographic patterns of the main pulmonary lesions were categorized as fibro-cavitary (FC), nodular-bronchiectasis (NB), and others. The extent of lung lesions was scored as in previous studies [17,18]. In brief, we divided each lung field into three zones according to two horizontal lines located at the distal end of the lobar pulmonary artery. We rated each zone from 0 to 3 points. If a lesion involved equal to or less than one-third of the area, we gave it one point. If a lesion involved more than one-third but less than two-thirds of the area, we gave it two points. The chest X-ray (CXR) score was the sum of scores in all lung fields. Inter-group differences were analyzed using the Mann-Whitney *U* test for numerical variables and the chi-square test for categorical variables. We performed multivariate logistic regressions to analyze the independent factors for NTM-LD and for radiographic progression. Then we generated the prediction probability with the formula of logits (probability) using all the factors in the corresponding multivariate analysis model. We then applied the probabilities from the multivariate model to receiver operating characteristic (ROC) curves. Statistical significance was set at $p < 0.05$. All analyses were performed in SPSS version 19.0 (Chicago, IL).

3. Results

3.1. Clinical characteristics of enrolled participants

During the study period, we enrolled 140 participants, including 42 MAC-LD, 25 MAB-LD, 31 MAC airway colonization (MAC-Co), and 15 MAB airway colonization (MAB-Co) patients, and 27 healthy controls. The average age, gender ratio and smoking status were similar between the disease group and the controls, and between the disease and colonization groups ([Table 1](#)). Patients with MAC-LD had lower BMI than those with colonization and controls, whereas the BMI of patients with MAB-LD was lower than that of controls. We did not include patients with active cancer or HIV or patients receiving chemotherapy. Diabetes mellitus was higher in the controls than in the MAC-LD group.

Table 1
Clinical characteristics according to the status of nontuberculous mycobacteria lung disease.

	MAC-LD n = 42	MAC-Co n = 31	MAB-LD n = 25	MAB-Co n = 15	Healthy subjects n = 27
Age (years)	61.8 [14.8]	63.7 [10.6]	60.6 [17.6]	66.9 [9.6]	56.0 [20.7]
Male sex	11 (26%)	14 (45%)	10 (40%)	8 (53%)	12 (48%)
Current smoker	3 (7%)	1 (7%)	2 (8%)	2 (13%)	4 (15%)
Body mass index, kg/m ²	21.4 [3.7] ^{*,#}	23.5 [4.1]	21.0 [3.9] ⁺	23.4 [4.1]	24.4 [3.7]
Diabetes mellitus	1 (2%)	1 (3%)	2 (8%)	0	5 (20%)
Autoimmune diseases	1 (2%)	2 (7%)	3 (12%)	4 (27%)	0
Prior TB history	3 (7%)	1 (3%)	1 (4%)	0	0
Hemoptysis	12 (29%) ⁺	7 (23%)	7 (28%) ^{*,#}	0	0
Sputum study within 1 year					
Max. positive AFS	1.4 [1.6] [#]	0	1.7 [1.6] [#]	0.1 [0.5]	–
Proportion of AFS (+)	22 (52%) [#]	0	15 (60%) [#]	1 (7%)	–
No. of positive cultures	3.5 [3.0]	–	3.0 [1.9]	–	–
Radiological finding					
CXR score [#]	5.1 [3.2]	–	6.5 [2.9]	–	–
FC pattern	9 (21%)	–	6 (24%)	–	–
NB pattern	27 (63%)	–	15 (60%)	–	–

Abbreviations: AFS, acid-fast smear; Co, colonization; CXR, chest X-ray; FC, fibro-cavitary; LD, lung disease; MAC, *Mycobacterium avium* complex; MAB, *Mycobacterium abscessus*; NB, nodular bronchiectasis; TB, tuberculosis.

Data are no. (%) or mean [standard deviation].

⁺ and [#] indicate $p < 0.05$ between the LD group and the controls or LD group and Co group, respectively, using the chi square test for categorical variables and the Mann-Whitney U test for numerical variables.

[#] CXR score was interpreted by a total score from six lung zones that contained three respective scores [17].

Hemoptysis was significantly higher in the MAC-LD and MAB-LD groups than in the controls. The maximal positive grades of acid fast smear of sputum were 1.4 and 1.7 in the MAC-LD and MAB-LD groups, respectively, and higher than in the colonization groups. The radiological patterns by chest image in the MAC-LD and MAB-LD groups were 21% and 24% of fibro-cavitary, respectively, and 63% and 60% of nodular-bronchiectasis.

3.2. Pattern of poly-functional T cells in enrolled participants

In the total expression of TNF α , IFN- γ or IL-2 on T lymphocytes (Fig. 1), patients with MAC-LD had lower CD4+ TNF- α expression after MAC stimulation, CD4+ IFN- γ and CD4+ TNF- α after MAB stimulation and CD4+ IFN- γ after PMA stimulation, whereas CD8+ TNF- α expression was lower in the patients after mock, MAC and MAB stimulation as compared with the controls. The MAC-Co group had higher CD4+ IFN- γ after all stimulations, CD4+ TNF- α after MAB stimulation, and CD8+ TNF- α after all than did the MAC-LD group. For MAB-LD, the patients had lower CD4+ IL-2+ after MAB stimulation and CD8+ IL-2+ after mock, MAC and MAB stimulations as compared with the controls. The comparison between MAC-LD and MAB-LD groups showed that MAC-LD had lower CD4+ IFN- γ after MAC or MAB stimulation, lower CD8+ TNF- α after all, and higher CD8+ IL-2+ after mock and MAC stimulation than those in the MAB-LD group.

In the isolated mono-cytokine expression (Fig. 2), TNF- α on CD8 lymphocytes was lower in MAC-LD patients than in controls after mock and MAB stimulation. Levels of mono-IL-2+ CD4+ and IL-2+ CD8+ cells during PMA stimulation were higher in MAC-LD patients than in controls. CD4+ IFN- γ upon MAB stimulation was lower but CD8+ IL-2+ by PMA stimulation was higher in MAC-LD patients than in the MAC-Co group. CD4+ IFN- γ was higher in MAB-LD patients than in the controls and in MAC-LD patients after mock and MAC stimulation.

Double and triple cytokine expressions were all weaker in the MAC-LD group than in controls for MAC stimulation. The MAC-Co group had higher CD4+ TNF- α IFN- γ cells after mock, MAB, and MAC stimulation and higher triple positive cells after MAB and PMA stimulation. In the MAB-LD group, almost all IL-2 expressed double or triple cytokine cells were lower than those in the controls. The MAB-Co group had higher triple positive cells in CD4 after PMA stimulation and in CD8

after mock, MAB and PMA stimulation.

We checked the data of PD-1/CTLA-4/Tim-3 on CD4+ or CD8+ T cells after different kinds of stimulation. However, the results for different kinds of stimulation (Table S1 in the supplemental file) were similar between MAC-LD, MAB-LD and controls.

We compared the mono-, double and triple cytokine producing T cells between mock stimulation (CD3/CD28) and MAC or MAB, respectively. The mono- and poly-functional T cells became attenuated significantly under MAC or MAB stimulation in comparison with mock stimulation with CD3/CD28 (Table S3 in the supplemental file), except that mono-IFN- γ on CD4+ cells increased significantly and was not influential on mono-IL-2+ (CD4+ or CD8+), total IL-2+ (CD8+ by MAB), mono-IFN- γ on CD8 T cells, and IL-2+/IFN- γ +, IL-2+/TNF- α & Triple positive CD4+ cells (by MAC stimulation). When we used the ratio of response to mock stimulation by dividing the mock stimulation by antigen stimulation, MAC-LD patients had significantly higher ratios of total IL-2+ (CD4+, mock/MAB stimulation), mono-IFN- γ (CD4+, mock/MAC stimulation), IL-2+/IFN- γ (CD8+, mock/MAC stimulation), and IL-2+/IFN- γ and IL-2+/TNF- α (CD4+, mock/MAB stimulation) but lower IFN- γ /TNF- α (CD8+, mock/MAC stimulation) as compared to controls. In addition, the ratios for MAB-LD patients were significantly higher for total IL-2+ (CD4+, mock/MAB stimulation), mono-IL-2+ (CD8+, mock/MAC stimulation) and IL-2+/TNF- α (CD4, mock/MAB stimulation) as compared to controls (Figs. 1 and 2).

3.3. Prediction for NTM-LD from the controls or the colonization group

To discriminate MAC-LD and controls, we used logistic regression with age, sex, BMI, and the data of poly-functional T cells. In multivariate analysis, BMI (OR 0.836 [0.714–0.977] per 1 kg/m² increment, $p = 0.024$), mono-IL2+ CD4+ cells (OR 1.095 [1.003–1.196] per 1% increment, $p = 0.044$) and triple positive cytokine CD8 cells for PMA stimulation (OR 0.623 [0.435–0.893] per 1% increment, $p = 0.010$) were significant factors correlated with MAC-LD. The probability using the three factors could predict or exclude MAC-LD well with AUC of 0.862 ($p < 0.001$) (Fig. 3A). For discriminating MAB-LD from the controls, IL-2+/TNF- α CD4 cell ratio (mock/MAB) (OR 1.455 [1.025–2.067], $p = 0.036$) and triple positive cytokine CD4 cells by PMA stimulation (OR 0.687 [0.502–0.939], $p = 0.019$) were

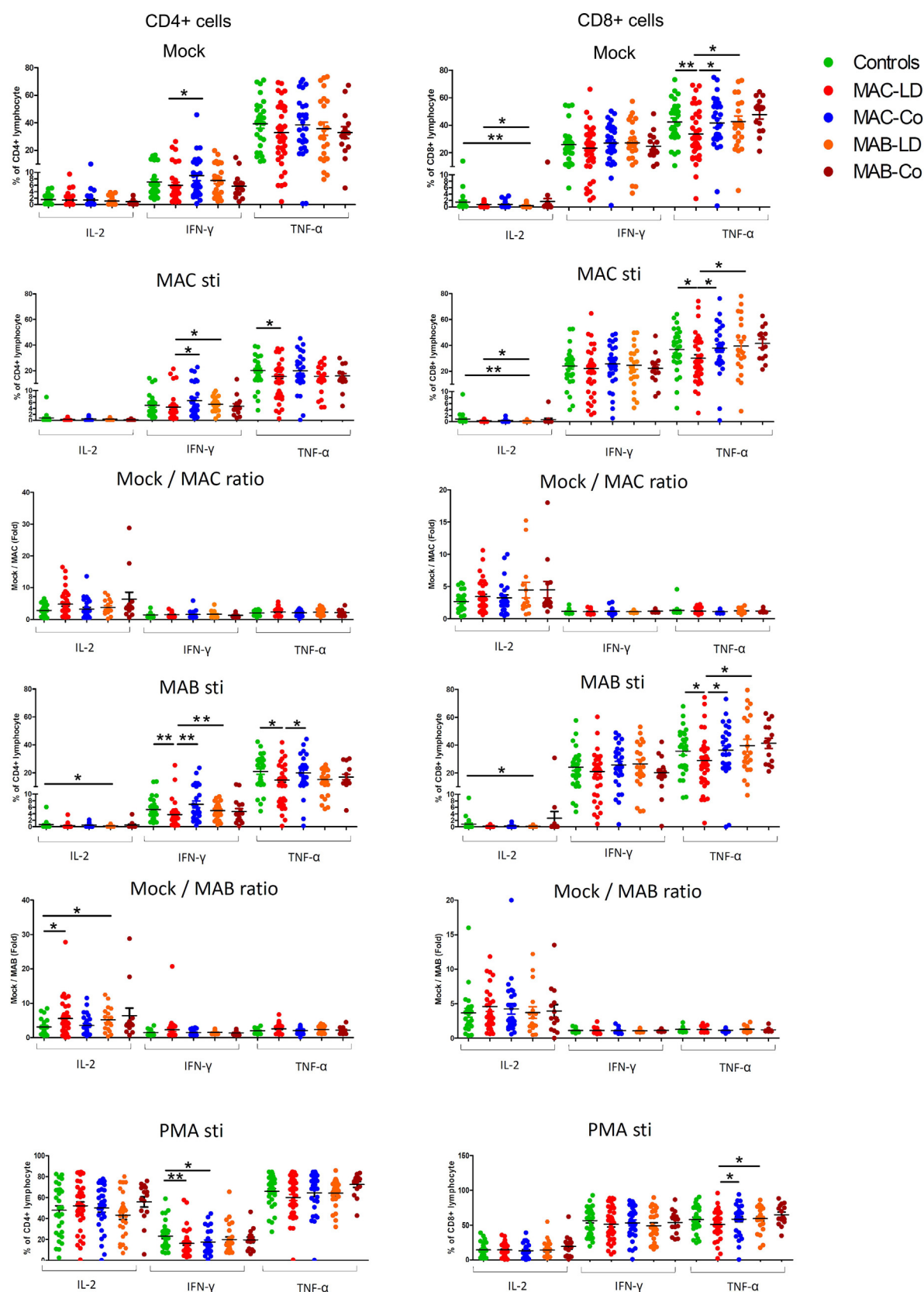
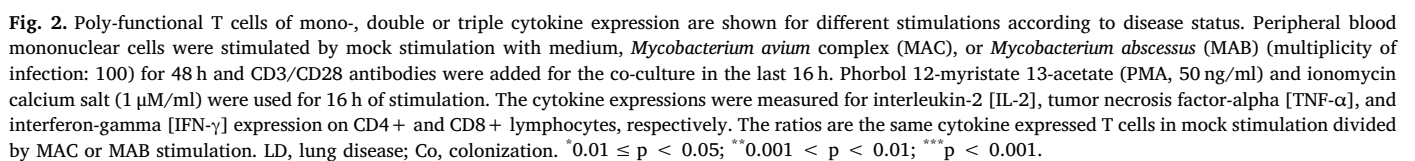


Fig. 1. Poly-functional T cells of total cytokine expression are shown for different stimulations according to disease status. Human peripheral blood mononuclear cells were co-cultured with mock stimulation of medium, *Mycobacterium avium* complex (MAC) (multiplicity of infection [MOI]: 100), or *Mycobacterium abscessus* (MAB) (MOI: 100) for 48 h and CD3 (5 μ g/ml)/CD28 (1 μ g/ml) antibodies were added for the co-culture in the last 16 h. Phorbol 12-myristate 13-acetate (PMA, 50 ng/ml) and ionomycin calcium salt (1 μ M/ml) were used for 16 hr of stimulation. The cytokine expressions were measured for total interleukin-2 [IL-2], tumor necrosis factor- α [TNF- α], and interferon- γ [IFN- γ] expression on CD4+ and CD8+ lymphocytes, respectively, by flow cytometry. The ratios are the same cytokine expressed T cells in mock stimulation divided by MAC or MAB stimulation. LD, lung disease; Co, colonization. *0.01 \leq p < 0.05; **0.001 < p < 0.01.



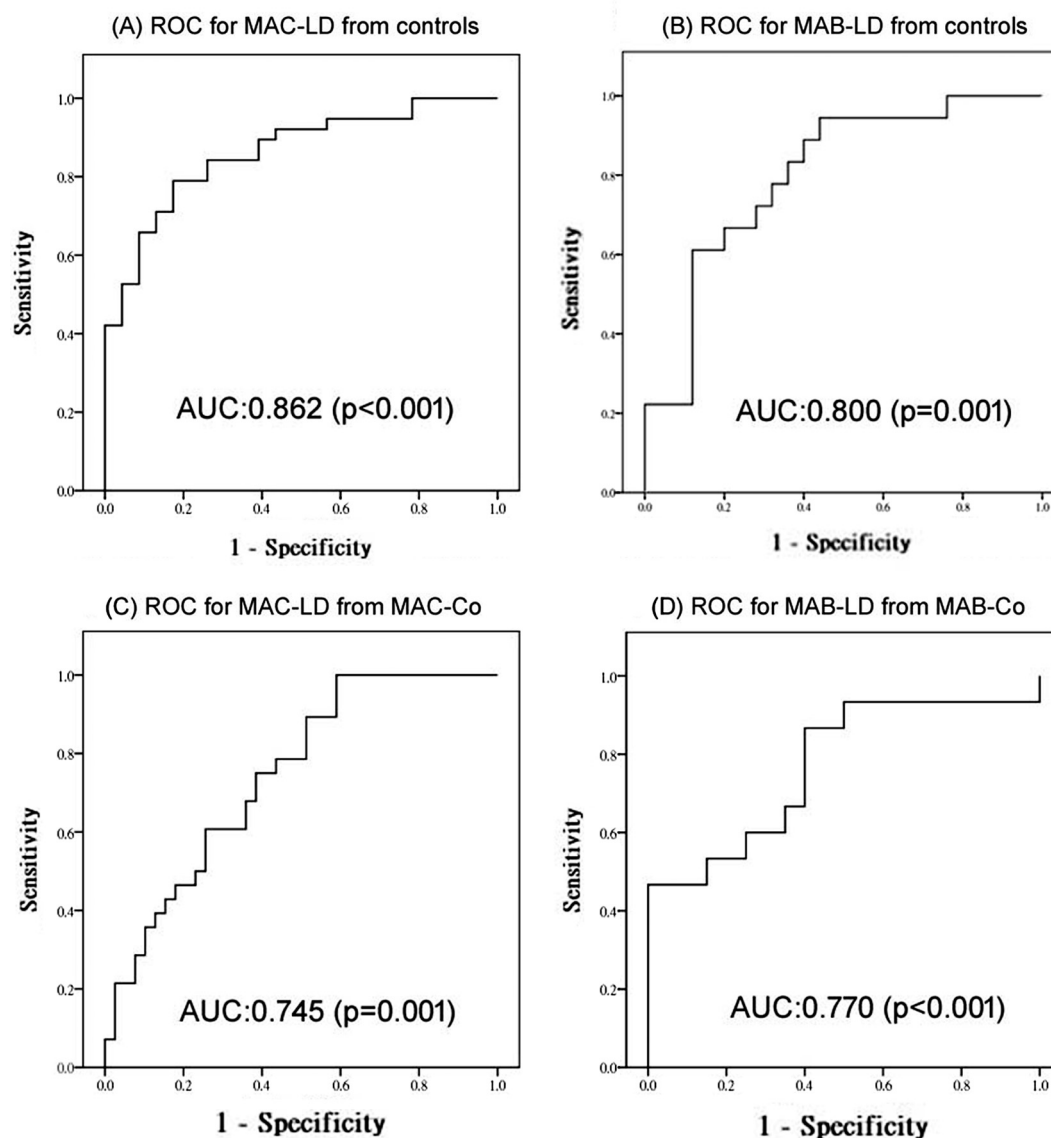


Fig. 3. Receiver operating characteristic (ROC) curves for discriminating (A) patients with *Mycobacterium avium* complex (MAC)-lung disease (LD) from the controls; (B) patients with *Mycobacterium abscessus* (MAB)-LD from the controls; (C) patients with MAC-LD from those with MAC airway colonization (MAC-Co); and (D) patients with MAB-LD from the MAB-Co group. The factors used in the ROC curves were those included in the final model by multivariate analyses.

independent factors. The probability using two-factor analysis had an AUC of 0.800 ($p = 0.001$) (Fig. 3B). The equations for generating the probabilities are listed in the [supplementary information](#).

For discriminating NTM-LD from NTM-Co, multivariate logistic regression revealed that gender (OR: 0.268 [0.084–0.858], if male, $p = 0.027$) and triple positive cytokine CD4 cells by PMA stimulation (OR: 0.813 [0.701–0.943] per 1% increment $p = 0.006$) were independent factors for MAC-LD. The triple positive cytokine CD4 cells for PMA stimulation were a significant predictor for MAB-LD (OR: 0.779 [0.629–0.966] per 1% increment, $p = 0.023$). The AUROCs by the probability generated by the multivariate model were 0.745 [$p = 0.001$] and 0.770 [$p < 0.001$] for MAC-LD and MAB-LD, respectively (Fig. 3C and D).

3.4. The radiographic pattern of NTM-LD vs. poly-functional T cells

Those with MAC-LD and MAB-LD were classified as the FC group ($n = 15$), NB group ($n = 42$) and others ($n = 10$). Those with FC had weaker CD4+ IFN- γ + (mock and PMA stimulation), CD8+ IFN- γ + (PMA), CD4+ TNF- α + and CD8+ TNF- α + after all stimulations (Fig. 4). The double positive and triple positive data had similar trends of lower IFN- γ + and TNF- α + expression, but single IL-2 expressions on CD4 (MAB stimulation) and on CD8 (mock and MAC stimulation) were higher in those with the FC pattern. The other details of single, double and triple cytokine expression are provided in the [supplementary information](#) (Fig. S1). The changes in ratio from mock to MAC or MAB stimulation were not significantly different between those with radiographic FC and NB pattern.

(PMA), CD4+ TNF- α + and CD8+ TNF- α + after all stimulations (Fig. 4). The double positive and triple positive data had similar trends of lower IFN- γ + and TNF- α + expression, but single IL-2 expressions on CD4 (MAB stimulation) and on CD8 (mock and MAC stimulation) were higher in those with the FC pattern. The other details of single, double and triple cytokine expression are provided in the [supplementary information](#) (Fig. S1). The changes in ratio from mock to MAC or MAB stimulation were not significantly different between those with radiographic FC and NB pattern.

3.5. Prediction for NTM-LD with radiographic progression

At 1-year follow-up, 62 (92.5%) received chest imaging, and 11 (17.7%) had radiographic progression. CD4+ IFN- γ + (MAC and PMA stimulation) and CD8+ IFN- γ + (all stimulation) were higher but the CD8+ TNF- α + ratio (mock/MAB) was lower in those with radiological progression than in those without progression (Fig. 4). After adjustment for age, sex, BMI, AFS grade, anti-NTM treatment and initial CXR score, multivariate logistic analysis showed CD4+ IFN- γ + on PMA

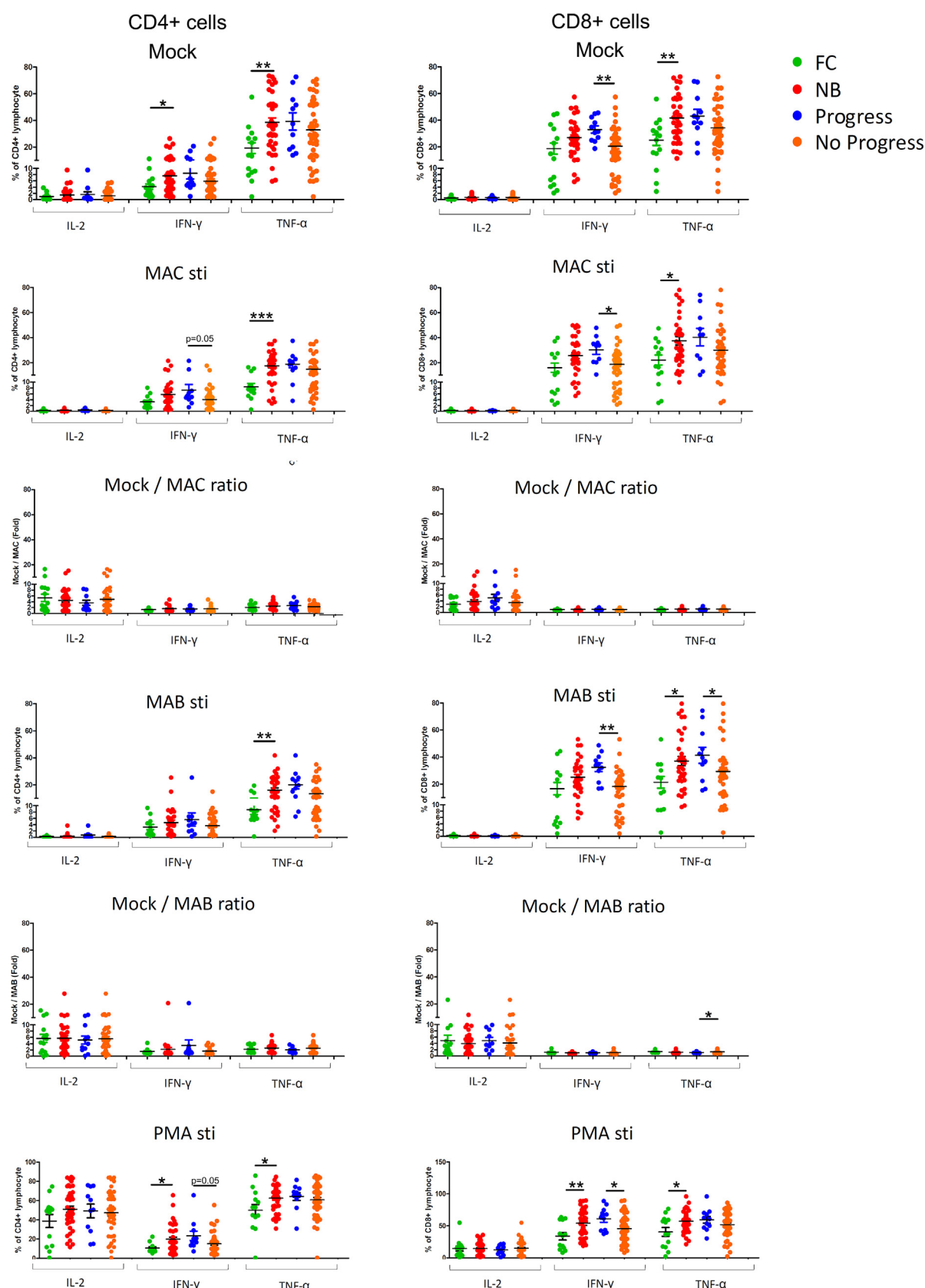


Fig. 4. Poly-functional T cells of total cytokine expression in patients with nontuberculous mycobacteria lung disease (NTM-LD) according to radiographic pattern and progression under different stimulation. Peripheral blood mononuclear cells were co-cultured with mock stimulation with medium, *Mycobacterium avium* complex (MAC), or *Mycobacterium abscessus* (MAB) (multiplicity of infection:100) for 48 h and added CD3/CD28 antibodies for the last 16 h. In comparison, phorbol 12-myristate 13-acetate (PMA, 50 ng/ml) and ionomycin calcium salt (1 μ M/ml) were used for 16 h of stimulation. The cytokine expressions were measured for total interleukin-2 [IL-2], tumor necrosis factor- α [TNF- α], and interferon- γ [IFN- γ] expression on CD4+ and CD8+ lymphocytes, respectively. The ratios are the same cytokine expressed T cells in mock stimulation divided by MAC or MAB stimulation. Co, colonization; FC, fibro-cavitary; LD, lung disease; NB, nodular-bronchiectasis; NP, non-progression; P, progression *0.01 \leq p < 0.05; **0.001 < p < 0.01; ***p < 0.001.

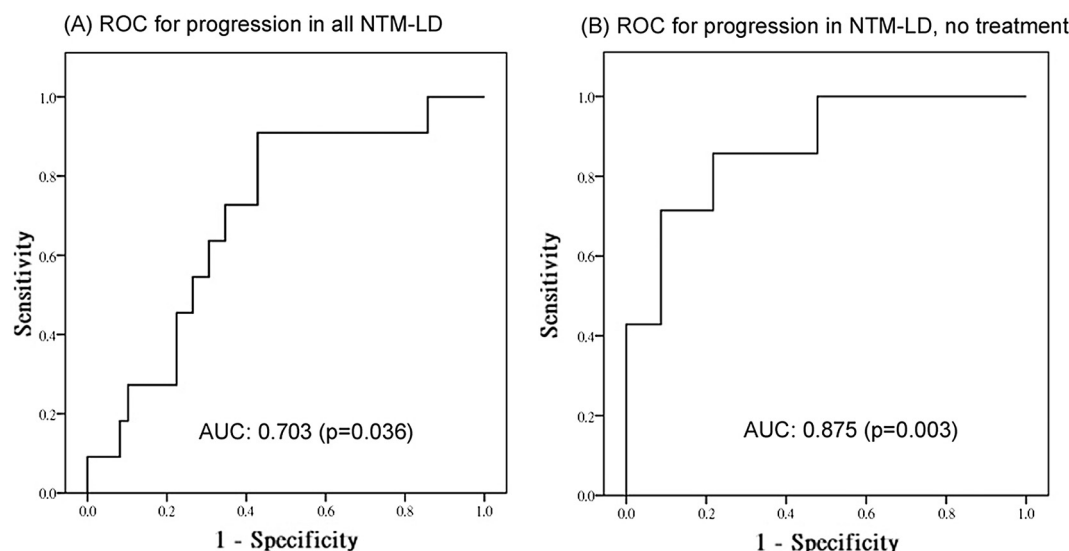


Fig. 5. Receiver operating characteristic (ROC) curves for radiographic progression. (A) To discriminate patients with all nontuberculous mycobacteria lung disease (NTM-LD) and radiographic progression from those without progression. (B) To discriminate NTM-LD patients without anti-NTM treatment but radiographic progression (+) from those without progression. The factors used in the ROC curves were those included in the final model by multivariate analyses.

stimulation was correlated with radiographic progression (OR: 1.132 [1.021–1.255], $p = 0.019$). The AUROC was 0.703 ($p = 0.036$) (Fig. 5A). In regard to those without anti-NTM therapy ($n = 38$), seven patients (18%) had radiographic progression, which was correlated with mono-IFN- γ + on CD4 cells on MAC stimulation (OR: 1.672 [0.993–2.814], $p = 0.053$) and triple cytokine (+) expressed CD4 on PMA stimulation (OR: 1.400 [0.998–1.963], $p = 0.051$) by multivariate logistic analysis. The equation for generating the probability of the two factors was as $\text{Logit (Probability)} = -4.832 + 0.514 \times \text{mono-IFN}\gamma + \text{CD4} + \text{during MAC stimulation (\%)} + 0.336 \times \text{Triple cytokine (+) on CD4 during PMA stimulation (\%)}$. Please see the details in the [supplementary file](#) for an explanation and example of the probability calculation. The AUROC by the probability generated from the two factors was 0.875 ($p = 0.003$) (Fig. 5B). According to the Youden index, when the probability was 0.297, the sensitivity was 86% and specificity was 78.3%.

4. Discussion

In the present study, we observed that the patients with MAC-LD generally had lower expression of triple-positive poly-functional T cells but higher single IL-2+ expression than the controls and MAC-Co group. On the other hand, the MAB-LD group had lower IL-2 expression, mostly on CD8+ cells, and lower triple positive cells than the controls and MAB-Co group. The triple positive CD4 cells (by PMA stimulation) could predict MAC-LD and MAB-LD from the corresponding colonization groups. For those with NTM-LD and not receiving anti-NTM treatment, mono-IFN- γ + on CD4 cells (MAC stimulation) and triple positive CD4+ (PMA) were correlated with progression, with a good AUROC of 0.875.

The status of mono- and poly-functional T cells in MAC-LD and MAB-LD patients might be impaired and thus responsible for the underlying immune problem leading to pulmonary infection. Functional CD4+ and CD8+ T-cell subsets have been defined based on the cytokine signatures of IFN- γ , IL-2, and TNF- α . For example, TNF- α -only and dual IFN- γ /TNF- α expression were greater in patients with active tuberculosis than in those with latent tuberculosis infection and controls [16]. In the present study, lower triple-positive CD8+ cells and higher mono-IL-2+ CD4+ cells (PMA stimulation) together with lower BMI favored MAC-LD. This finding is compatible with previous studies showing that PBMCs from MAC-LD patients had lower response of

cytokine production [19] and that anti-TNF biologic agents might be correlated with increased NTM infection [20,21]. The reason for the loss of polyfunctionality in the NTM-LD group of T cells as compared to healthy controls is very important, but it remains unclear and will require further investigation.

The higher response of mono-IL-2+ expression was the only positive predictor of MAC-LD from the controls and airway colonization. Traditionally, IL-2 is synthesized by T cells during the early stages of the immune response and has a pivotal role in cell expansion and effector functions after primary antigen challenge [22]. IL-2 is a marker of polyfunctional T-cells, which are crucial for protection against tuberculosis [23]. In this study, the increased IL-2-expressing lymphocytes might be compensating for reduced response and lower IFN- γ /TNF- α during MAC-LD. By contrast, for MAB-LD, weakened IL-2 expression was noted in MAB-specific poly-functional T cells, similar to a previous study in cystic fibrosis [24]. It may indicate differences in the immune deficiency of IL-2+ poly-functional T cells between MAB-LD and MAC-LD. But the attenuated triple positive poly-functional T cells were the same in the two NTM-LD.

On the other hand, CD4+ IFN- γ + was lower in the MAC-LD group than in the MAB-LD group. Although we reviewed the literature showing decreased Th1 response, such as IFN- γ level, in both the MAC-LD [19,25] and the MAB-LD groups [26], the literature directly comparing Th1 response between MAC-LD and MAB-LD is scarce. We speculated that the attenuation of CD4+ IFN- γ + in MAC-LD might be due to the disease-related T cell dysregulation because in a previous study, the IFN- γ response was improved after MAC treatment [19]. Although PD-1, Tim-3, and CTLA-4 on CD4 and CD8 T cells were not significantly increased in MAC-LD patients after stimulation in the present study, other immunomodulators might be responsible factors, like immunosuppressive macrophages and regulatory T cells [27]. By contrast, *M. abscessus*, a rapidly growing mycobacteria causing lung disease not as indolent as MAC, might lead to lower immune exhaustion than MAC-LD. However, this speculation needs to be studied in the future.

For differentiation of MAC-LD and MAB-LD from MAC-Co and MAB-Co, triple-positive CD4+ cells could provide a good diagnostic indicator if 1 or 2 sets of sputum yield MAC. Poly-functional triple-positive CD4+ T cells play a critical role in the control of chronic bacterial and viral infections [28], but only limited data on NTM-LD are available. Airway NTM colonization sometimes cannot be easily

differentiated by the clinical criteria recommended by the ATS [1]. The triple-positive CD4+ T cells could be a new diagnostic factor for clinical practice. Once poly-functional T-lymphocyte responses are attenuated, MAC or MAB bacilli could be considered.

In regard to the clinical characteristics of NTM-LD, the patients with radiographic FC patterns generally had higher bacilli loads [6], which might induce more immune suppression and low cytokine production [19,29]. The present study supported this point by finding lower cytokine expression of IFN- γ and TNF- α on poly-functional T cells in patients with FC patterns. For the clinical course, approximately 22% and 53% of MAC-LD patients reportedly present with radiographic deterioration at follow up after 5 and 10 years, respectively [30]. To predict radiographic progression that requires early anti-MAC treatment, we integrated clinical factors, AFS grade, radiographic pattern and poly-functional T cells into multivariate analysis. Notably, in the NTM-LD patients not receiving anti-NTM treatment, MAC-specific mono-IFN- γ + CD4 cells and triple-positive CD4+ cells by PMA could predict the radiographic progression with excellent effectiveness (sensitivity of 86% and specificity of 78.3%).

From interpretation of the study results, we found that the CD4+ IFN- γ + by MAC 24-hour stimulation was compatible between MAC-LD and the controls, which is similar to the results on Sensitin stimulation in a study by Lim et al. [31]. However, Lim et al. showed MAC-LD patients had higher CD4+ IFN- γ + T cell than the controls after 6-hour Sensitin stimulation, which was not performed in this study. In contrast, the attenuation of CD4+ IFN- γ + T cells in MAC-LD was detected after MAB and PMA 24-hour stimulation, which was not used by Lim et al. In addition to antigen and stimulation duration, the co-stimulatory antibodies were different (CD28/CD49d vs. CD3/CD28 antibodies respectively), as well as the participants' ethnicity. Therefore, the results should be carefully interpreted and generalized because differences may arise due to different study designs and subject ethnicities.

This study had several limitations. First, the case number was small, so some phenomenon observed in the present study will require validation. Second, a causal relationship could not be confirmed in this cross-sectional study. Third, the mechanism by which the heat-killed NTM antigen induced attenuation of mono- and poly-functional T cells is unclear and will require future investigation. Fourth, the participants were enrolled in Taiwan, so generalization to other areas or ethnicities may not be applicable.

In conclusion, patients with MAC-LD had lower BMI, higher mono-IL2+ CD4+ cells and lower triple positive poly-functional cells (PMA stimulation), whereas patients with MAB-LD had lower triple positive CD4 cells (PMA stimulation) and a higher mock/MAB ratio of IL-2+ / TNF- α + CD4 cells than the controls. The percentage of triple positive CD4 cells (PMA stimulation) could predict MAC-LD or MAB-LD from airway colonization. For those with NTM-LD but no treatment, MAC-specific mono-IFN- γ + CD4+ cells and triple positive CD4+ (PMA) might predict radiographic progression.

5. Declarations

5.1. Ethics approval and consent to participate

The Research Ethics Committee of National Taiwan University Hospital and Far Eastern Memorial Hospital approved this study (IRB No.: 201703051RINC and 106134-F).

5.2. Consent for publication

Not applicable. The present study did not contain any individual person's data in any form.

Funding

The study was supported in part by grants from the Far Eastern

Memorial Hospital National Taiwan University Hospital Joint Research Program (106-FTN07) and the Ministry of Science and Technology Taiwan (MOST 105-2628-B-002 -046 -MY3 and 107-2628-B-002-006). The funders had no role in study design, data collection and analysis, decision to publish, or preparation of the manuscript.

Data availability statement

Please contact author for data requests.

Declaration of Competing Interest

All authors declare no financial, professional or other personal interest of any nature or kind in a related product, service, and/or company.

Acknowledgments

The authors thank the staff of the Second, the Seventh and the Eighth Core Labs of the Department of Medical Research of National Taiwan University Hospital for their technical support.

Author contributions

Drs. Shu CC and Wang PH designed and conducted the study and performed the experiments. Drs. Shu CC, Cheng SL, and Wang PH performed the experiments, and data collection. Drs. Shu CC, Wang JY, Wang PH, Prof. Wu MF, Lai HC and Wu L. SH contributed for data analysis, manuscript writing and revision. Dr. Wang PH and Prof. Yu CJ were responsible for coordination.

Appendix A. Supplementary material

Supplementary data to this article can be found online at <https://doi.org/10.1016/j.cyto.2019.05.001>.

References

- [1] D.E. Griffith, T. Akshmit, B.A. Brown-Elliott, A. Catanzaro, C. Daley, F. Gordin, S.M. Holland, R. Horsburgh, G. Huit, M.F. Iademaro, M. Iseman, K. Olivier, S. Ruoss, C.F. von Reyn, R.J. Wallace Jr., K. Winthrop, An official ATS/IDSA statement: diagnosis, treatment, and prevention of nontuberculous mycobacterial diseases, *Am. J. Respir. Crit. Care Med.* 175 (4) (2007) 367–416.
- [2] D. Menzies, P. Nahid, Update in tuberculosis and nontuberculous mycobacterial disease 2012, *Am. J. Respir. Crit. Care Med.* 188 (8) (2013) 923–927.
- [3] C.C. Lai, C.K. Tan, C.H. Chou, H.L. Hsu, C.H. Liao, Y.T. Huang, P.C. Yang, K.T. Luh, P.R. Hsueh, Increasing incidence of nontuberculous mycobacteria, Taiwan, 2000–2008, *Emerg. Infect. Dis.* 16 (2) (2010) 294–296.
- [4] S.K. Field, R.L. Cowie, Lung disease due to the more common nontuberculous mycobacteria, *Chest* 129 (6) (2006) 1653–1672.
- [5] J. Adjemian, K.N. Olivier, A.E. Seitz, S.M. Holland, D.R. Prevots, Prevalence of nontuberculous mycobacterial lung disease in U.S. Medicare beneficiaries, *Am. J. Respir. Crit. Care Med.* 185 (8) (2012) 881–886.
- [6] C.C. Shu, C.H. Lee, C.L. Hsu, J.T. Wang, J.Y. Wang, C.J. Yu, L.N. Lee, Clinical characteristics and prognosis of nontuberculous mycobacterial lung disease with different radiographic patterns, *Lung* 189 (6) (2011) 467–474.
- [7] W. Hoefsloot, J. van Ingen, C. Andrejak, K. Angeby, R. Bauriaud, P. Bemer, N. Beylis, M.J. Boeree, J. Cacho, V. Chihota, E. Chimara, G. Churchyard, R. Cias, R. Daza, C.L. Daley, P.N. Dekhuijzen, D. Domingo, F. Drobniewski, J. Esteban, M. Fauville-Dufaux, D.B. Folkvardsen, N. Gibbons, E. Gomez-Mampaso, R. Gonzalez, H. Hoffmann, P.R. Hsueh, A. Indra, T. Jagielski, F. Jamieson, M. Jankovic, E. Jong, J. Keane, W.J. Koh, B. Lange, S. Leao, R. Macedo, T. Mannsaker, T.K. Marras, J. Maugein, H.J. Milburn, T. Mlinko, N. Morcillo, K. Morimoto, D. Papaventsis, E. Palenque, M. Paez-Pena, C. Piersimoni, M. Polanova, N. Rastogi, E. Richter, M.J. Ruiz-Serrano, A. Silva, M.P. da Silva, H. Simsek, D. van Soolingen, N. Szabo, R. Thomson, T. Tortola Fernandez, E. Tortoli, S.E. Totten, G. Tyrrell, T. Vasankari, M. Villar, R. Walkiewicz, K.L. Winthrop, D. Wagner, The geographic diversity of nontuberculous mycobacteria isolated from pulmonary samples: an NTM-NET collaborative study, *Eur. Respir. J.* 42 (6) (2013) 1604–1613.
- [8] D. Lu, B. Heeren, W.M. Dunne, Comparison of the Automated Mycobacteria Growth Indicator Tube System (BACTEC 960/MGIT) with Lowenstein-Jensen medium for recovery of mycobacteria from clinical specimens, *Am. J. Clin. Pathol.* 118 (4) (2002) 542–545.

- [9] W.J. Koh, O.J. Kwon, K. Jeon, T.S. Kim, K.S. Lee, Y.K. Park, G.H. Bai, Clinical significance of nontuberculous mycobacteria isolated from respiratory specimens in Korea, *Chest* 129 (2) (2006) 341–348.
- [10] J. van Ingen, S.A. Bendien, W.C. de Lange, W. Hoefsloot, P.N. Dekhuijzen, M.J. Boeree, D. van Soolingen, Clinical relevance of non-tuberculous mycobacteria isolated in the Nijmegen-Arnhem region, The Netherlands, *Thorax* 64 (6) (2009) 502–506.
- [11] C.C. Shu, C.H. Lee, J.Y. Wang, J.S. Jerng, C.J. Yu, P.R. Hsueh, L.N. Lee, P.C. Yang, Nontuberculous mycobacteria pulmonary infection in medical intensive care unit: the incidence, patient characteristics, and clinical significance, *Intensive Care Med.* 34 (12) (2008) 2194–2201.
- [12] S. Kitada, K. Kobayashi, S. Ichijima, S. Takakura, M. Sakatani, K. Suzuki, T. Takashima, T. Nagai, I. Sakurabayashi, M. Ito, R. Maekura, Serodiagnosis of Mycobacterium avium-complex pulmonary disease using an enzyme immunoassay kit, *Am. J. Respir. Crit. Care Med.* 177 (7) (2008) 793–797.
- [13] C.C. Shu, M. Ato, J.T. Wang, R. Jou, J.Y. Wang, K. Kobayashi, H.C. Lai, C.J. Yu, L.N. Lee, K.T. Luh, Sero-diagnosis of Mycobacterium avium complex lung disease using serum immunoglobulin A antibody against glycopeptidolipid antigen in Taiwan, *PLoS One* 8 (11) (2013) e80473.
- [14] C.H. Ladel, S. Dangelat, S.H. Kaufmann, Immune response to Mycobacterium bovis bacille Calmette Guérin infection in major histocompatibility complex class I- and II-deficient knock-out mice: contribution of CD4 and CD8 T cells to acquired resistance, *Eur. J. Immunol.* 25 (2) (1995) 377–384.
- [15] R. Casey, D. Blumenkrantz, K. Millington, D. Montamat-Sicotte, O.M. Kon, M. Wickremasinghe, S. Bremang, M. Magtoto, S. Sridhar, D. Connell, A. Lalvani, Enumeration of functional T-cell subsets by fluorescence-immunospot defines signatures of pathogen burden in tuberculosis, *PLoS One* 5 (12) (2010) e15619.
- [16] C.L. Day, D.A. Abrahams, L. Lerumo, E. Janse van Rensburg, L. Stone, T. O'Rie, B. Pienaar, M. de Kock, G. Kaplan, H. Mahomed, K. Dheda, W.A. Hanekom, Functional capacity of Mycobacterium tuberculosis-specific T cell responses in humans is associated with mycobacterial load, *J. Immunol.* 187 (5) (2011) 2222–2232.
- [17] G.L. Snider, L. Doctor, T.A. Demas, A.R. Shaw, Obstructive airway disease in patients with treated pulmonary tuberculosis, *Am. Rev. Respir. Dis.* 103 (5) (1971) 625–640.
- [18] C.C. Shu, C.H. Lee, M.C. Lee, J.Y. Wang, C.J. Yu, L.N. Lee, Hepatotoxicity due to first-line anti-tuberculosis drugs: a five-year experience in a Taiwan medical centre, *Int. J. Tuberc. Lung Dis.* 17 (7) (2013) 934–939.
- [19] C.C. Shu, J.Y. Wang, M.F. Wu, C.T. Wu, H.C. Lai, L.N. Lee, B.L. Chiang, C.J. Yu, Attenuation of lymphocyte immune responses during Mycobacterium avium complex-induced lung disease due to increasing expression of programmed death-1 on lymphocytes, *Sci. Rep.* 7 (2017) 42004.
- [20] S.K. Brode, F.B. Jamieson, R. Ng, M.A. Campitelli, J.C. Kwong, J.M. Paterson, P. Li, A. Marchand-Austin, C. Bombardier, T.K. Marras, Increased risk of mycobacterial infections associated with anti-rheumatic medications, *Thorax* 70 (7) (2015) 677–682.
- [21] J.W. Yoo, K.W. Jo, B.H. Kang, M.Y. Kim, B. Yoo, C.K. Lee, Y.G. Kim, S.K. Yang, J.S. Byeon, K.J. Kim, B.D. Ye, T.S. Shim, Mycobacterial diseases developed during anti-tumour necrosis factor- α therapy, *Eur. Respir. J.* 44 (5) (2014) 1289–1295.
- [22] J.H. Cho, H.O. Kim, K.S. Kim, D.H. Yang, C.D. Surh, J. Sprent, Unique features of naive CD8+ T cell activation by IL-2, *J. Immunol.* 191 (11) (2013) 5559–5573.
- [23] H. Kang, Q. Yuan, H. Ma, Z.D. Hu, D.P. Han, K. Wu, D.B. Lowrie, X.Y. Fan, Enhanced protective efficacy against Mycobacterium tuberculosis afforded by BCG prime-DNA boost regimen in an early challenge mouse model is associated with increased splenic interleukin-2-producing CD4 T-cell frequency post-vaccination, *Immunology* 143 (4) (2014) 661–669.
- [24] M. Steindor, V. Nkwouano, E. Mayatepek, C.R. Mackenzie, D. Schramm, M. Jacobsen, Rapid detection and immune characterization of Mycobacterium abscessus infection in cystic fibrosis patients, *PLoS One* 10 (3) (2015) e0119737.
- [25] M. Kartalija, A.R. Ovrutsky, C.L. Bryan, G.B. Pott, G. Fantuzzi, J. Thomas, M.J. Strand, X. Bai, P. Ramamoorthy, M.S. Rothman, V. Nagabhushanam, M. McDermott, A.R. Levin, A. Frazer-Abel, P.C. Giclas, J. Korner, M.D. Iseman, L. Shapiro, E.D. Chan, Patients with nontuberculous mycobacterial lung disease exhibit unique body and immune phenotypes, *Am. J. Respir. Crit. Care Med.* 187 (2) (2013) 197–205.
- [26] S.Y. Kim, W.J. Koh, Y.H. Kim, B.H. Jeong, H.Y. Park, K. Jeon, J.S. Kim, S.N. Cho, S.J. Shin, Importance of reciprocal balance of T cell immunity in Mycobacterium abscessus complex lung disease, *PLoS One* 9 (10) (2014) e109941.
- [27] K. Ogasawara, H. Tomioka, T. Shimizu, C. Sano, H. Kawauchi, K. Sato, Profiles of cell-to-cell interaction of Mycobacterium intracellulare-induced immunosuppressive macrophages with target T cells in terms of suppressor signal transmission, *Clin. Exp. Immunol.* 129 (2) (2002) 272–280.
- [28] S. Kannanganat, C. Ibegbu, L. Chennareddi, H.L. Robinson, R.R. Amara, Multiple-cytokine-producing antiviral CD4 T cells are functionally superior to single-cytokine-producing cells, *J. Virol.* 81 (16) (2007) 8468–8476.
- [29] A. Singh, A. Mohan, A.B. Dey, D.K. Mitra, Inhibiting the programmed death 1 pathway rescues Mycobacterium tuberculosis-specific interferon gamma-producing T cells from apoptosis in patients with pulmonary tuberculosis, *J. Infect. Dis.* 208 (4) (2013) 603–615.
- [30] S. Kitada, T. Uenani, K. Yoshimura, Y. Tateishi, K. Miki, M. Miki, H. Hashimoto, T. Fujikawa, M. Mori, K. Matsuura, M. Kuroyama, R. Maekura, Long-term radiographic outcome of nodular bronchiectatic Mycobacterium avium complex pulmonary disease, *Int. J. Tuberc. Lung Dis.* 16 (5) (2012) 660–664.
- [31] A. Lim, C. Allison, P. Price, G. Waterer, Susceptibility to pulmonary disease due to Mycobacterium avium-intracellulare complex may reflect low IL-17 and high IL-10 responses rather than Th1 deficiency, *Clin. Immunol.* 137 (2) (2010) 296–302.

Thrombolysis induced by intravenous administration of plasminogen activator in magnetoliposomes: dual targeting by magnetic and thermal manipulation

Chih-Hsin Liu, BS^{a,b,1}, Hao-Lung Hsu, PhD^{c,1}, Jyh-Ping Chen, PhD^{c,d,e,f,1},
Tony Wu, MD, PhD^g, Yunn-Hwa Ma, PhD^{b,g,*}

^aGraduate Institute of Biomedical Sciences, Chang Gung University, Taoyuan, Taiwan, ROC

^bDepartment of Physiology and Pharmacology, College of Medicine, Chang Gung University, Taoyuan, Taiwan, ROC

^cDepartment of Chemical and Materials Engineering, College of Engineering, Chang Gung University, Taoyuan, Taiwan, ROC

^dDepartment of Materials Engineering, Ming Chi University of Technology, New Taipei City, Taiwan, ROC

^eDepartment of Plastic and Reconstructive Surgery and Craniofacial Research Center, Chang Gung Memorial Hospital, Taoyuan, Taiwan, ROC

^fResearch Center for Chinese Herbal Medicine and Research Center for Food and Cosmetic Safety, College of Human Ecology, Chang Gung University of Science and Technology, Taoyuan, Taiwan, ROC

^gDepartment of Neurology, Chang Gung Memorial Hospital, Taoyuan, Taiwan, ROC

Revised 29 January 2019

Abstract

In previously published studies, intra-arterial (*i.a.*), but not intravenous (*i.v.*) delivery of recombinant tissue-type plasminogen activator (rtPA) immobilized on the surface of magnetic nanoparticles induces thrombolysis by magnetic targeting. We asked whether *i.v.* delivery of protected rtPA in a thermosensitive magnetoliposome (TML@rtPA) may achieve target thrombolysis. PEGylated TML@rtPA was optimized and characterized; controlled release of rtPA was achieved by thermodynamic and magnetic manipulation *in vitro*. The lysis index of TML@rtPA incubated with blood at 43 °C vs. 37 °C was 53 ± 11% vs. 81 ± 3% in thromboelastograms, suggesting thermosensitive thrombolysis of TML@rtPA. In a rat embolic model with superfusion of 43 °C saline on a focal spot on the iliac artery with clot lodging, release of rtPA equivalent to 20% regular dose from TML@rtPA administered *i.a.* vs. *i.v.* significantly restored iliac blood flow 15 vs. 55 min after clot lodging, respectively. TML@rtPA with magnetic guiding and focal hyperthermia may be potentially amendable to target thrombolysis.

© 2019 Elsevier Inc. All rights reserved.

Key words: Liposomes; Magnetic nanoparticles; Drug delivery; Recombinant tissue-type plasminogen activator; Thrombolysis

Ischemic stroke and acute myocardial infarction are often associated with high risk of mortality; recombinant tissue-type plasminogen activator (rtPA) is still the mainstream option for acute treatment of thrombosis in clinical practice.^{1,2} However, rtPA has extremely short half-life in mins,³ which requires a large dose of rtPA to achieve therapeutic efficacy and may thus

induce hemorrhagic adverse effects.^{1,4} Different strategies have been tested for reproducible thrombolysis using targeting ligands and/or carriers in animal models,^{5–15} including rtPA immobilized to^{5–8,11,13} or encapsulated in^{9,11–14,16} a carrier, indicating the feasibility of the approach. However, among these nanocomposites of rtPA designed for target thrombolysis, no

Conflicts of Interest: None.

Sources of Funding: The Ministry of Science and Technology, ROC (NSC 98-2120-M-182-001 and NSC102-2221-E182-046 to JPC), and Chang Gung Memorial Hospital (CMRPD1E0013; BMRP432; BMRP249 to JPC).

Acknowledgment: Sonya Y. Hsueh for assistance of the art work; Dr. Geng-Hao Liu for technical assistance of infrared thermal imaging.

*Corresponding author at: Department of Physiology and Pharmacology, College of Medicine, Chang Gung University, 33302 Taoyuan City, Taiwan, Republic of China.

E-mail address: yhma@mail.cgu.edu.tw. (Y.-H. Ma).

¹ Chih-Hsin Liu, Hao-Lung Hsu and Jyh-Ping Chen contributed equally to this work.

<https://doi.org/10.1016/j.nano.2019.03.014>

1549-9634/© 2019 Elsevier Inc. All rights reserved.

one allowed for a functional restoration of blood flow after intravenous (*i.v.*) administration.

Among all designs of the nanocomposites for targeted thrombolysis, magnetic nanoparticles (MNPs) with iron oxide core have been demonstrated with great potential.^{5–8,12,13,16} MNPs made by embedding magnetite (Fe₃O₄)/maghemite (γ-Fe₂O₃) in a polymer matrix exert superparamagnetism in magnetic field, allow aligning, movement of MNPs in the direction of the external field, and magnetic guidance to the target thrombus *in vivo*.^{5–8,12,13,16} Such strategy achieved targeting effects and thus induced effective thrombolysis using only 20% of regular dose of rtPA.^{5–7,12} Although application of a magnet may capture enough of magnetic nanocomposites at the target site following *i.v.* administration based on micro-computed tomography analysis,¹⁷ effective thrombolysis has not been demonstrated after *i.v.* administration of rtPA chemically immobilized to the surface of the carriers. The presence of endogenous inhibitors of rtPA, such as plasminogen activator inhibitor-1, in circulation may cause inactivation, and thus shortened half-life of rtPA.³ Therefore, encapsulated or protected rtPA from such inhibitors may be required for delivery from a remote site.

Previous studies comparing free plasminogen activators (PAs) with PAs encapsulated in long-circulating liposomes showed an equivalent thrombolytic activity for the liposomal formulations *in vitro*.¹⁸ The characteristics of cell membrane-like structure of liposomes, including fluidity and permeability, are similar to those of biomembrane, which are suitable for encapsulation of drugs with different sizes and characteristics.¹⁹ Several strategies have been used to achieve controlled release of drugs from liposomes, including enzyme digestion, pH, ultrasound, and temperature *etc.*¹⁹ Temperature-sensitive liposomes (TL) have been developed for hyperthermia-mediated drug release subsequent to passive accumulation of the nano-drug in the tumor site^{19–25}; in response to elevated temperature of 40–43 °C, drug released from TL has been used for cancer therapy in animal models.^{21–25} However, effective thrombolysis using PA-containing TL has only been demonstrated *in vitro*.^{26,27}

Liposomes are phospholipid-based vesicles with saturated hydrocarbon chains; the length of the fatty acid chains primarily determines the melting phase transition temperature (T_m).^{25,28} In response to an increase in temperature above its T_m value, liposomes become more permeable to water and solutes.²⁵ Different strategies have been tested to control hyperthermia and induce drug release from TL *in vivo*, such as using an external circular resistive heating coil²³ or a heating catheter with circulating water.^{20,21} Thermosensitive magnetoliposomes (TMLs) have been prepared by incorporation of MNPs and tested in a drug delivery system.²⁹ By localized heating in an alternating current magnetic fields, TMLs could be used for controlled release of chemotherapeutic drugs for cancer therapy.^{29,30} In addition, TMLs may be guided by a magnetic field, allowing its application in magnetic targeting in cancer therapy.^{29,31} However, such approach has not been tested in targeting thrombus.

Recently, TMLs containing rtPA (TML@rtPA) have been produced and optimized *in vitro*, allowing enhanced release of rtPA at 43 °C vs. 37 °C.²⁷ However, TMLs have not been demonstrated as carriers for target delivery of rtPA *in vivo*.

Considering the safety and the fast release of rtPA from TML@rtPA as the previously reported,²⁷ 43 °C was applied as the challenging temperature in this study. We further improved the preparation with higher rtPA release at 43 °C, and established a rat embolic model with a focal temperature gradient for testing whether magnetic guiding plus heat-induced release of rtPA from TML@rtPA may induce target thrombolysis *in vivo*. Our studies demonstrated, for the first time, that *i.v.* administration of magnetoliposomes with thermal controlled-release of rtPA induced effective thrombolysis.

Methods

Materials

FeCl₂•4H₂O (99%) and FeCl₃•6H₂O (97%) were purchased from Acros (Geel, Belgium). Citric acid monohydrate, cholesterol, Triton X-100 and Inactin® (thiobutabarbital sodium) were purchased from Sigma-Aldrich (St. Louis, MO). N-(carboxyl-methoxypolyethyleneglycol 2000)-1,2-distearoyl-*sn*-glycero-3-phosphoethanolamine (DSPE-PEG₂₀₀₀) was from NOF Co. (Tokyo, Japan); 1,2-ipalmitoyl-*sn*-glycero-3-phosphocholine (DPPC) was from Avanti Polar Lipid Inc. (Alabaster, AL); H-D-Ile-Pro-Arg-p-nitroanilide dihydrochloride (S-2288) was from Chromogenix (Bedford, MA). Isoflurane (FORANE) was obtained from Abbott Laboratories (Aesica, Queenborough, UK). Recombinant tissue-type plasminogen activator (rtPA; Actilyse®) was obtained from Boehringer Ingelheim (Ingelheim, Germany). Fetal bovine serum was from HyClone (Logan, UT).

Preparation of thermosensitive magnetoliposomes (TMLs)

Chemical co-precipitation for the synthesis of citric acid-coated iron oxide (Fe₃O₄) magnetic nanoparticles (CMNPs) was modified from a previously described method,²⁷ which was detailed in the Supplement. The biocompatibility of thermosensitive liposomes with similar composition has been demonstrated in previous studies.³² TMLs and rtPA-encapsulated TML (TML@rtPA) were prepared by solvent evaporation/sonication method and freeze–thaw method, respectively. Briefly, a mixture of DPPC, DSPE-PEG₂₀₀₀ and cholesterol (90:5:5) dissolved in 1 mL chloroform was subjected to a rotary evaporator to remove the solvent. The dry film was re-hydrated with 1 mL of CMNPs solution prepared in phosphate buffer (10 mM, pH 7.4) and the flask was rotated at 45 °C for 20 min to form a lipid solution, which was sonicated at a power of 150 W for 10 min (Q500 sonicator; Qsonica, Newton, CT) with a cup horn (5.5 inch cup) at 4 °C. The rtPA solution was added to the freshly prepared hydrated TMLs solution, vortexed for 10 s, and subjected to five freeze–thaw cycles, followed by sonication and extrusion five times through double-stacked polycarbonate membrane (0.2 μm, Whatman, NJ) at 45 °C. Un-encapsulated CMNPs and rtPA were removed by ultracentrifugation at 65,390×g, 4 °C for 30 min.

Determination of encapsulation efficiency (EE) and loading content (LC)

EE and LC of rtPA in TML@rtPA were assayed by an ELISA kit from Abcam (ab108914, Cambridge, UK). TML@rtPA was

mixed with 1% Triton X-100 solution at 37 °C for 30 min and the solution was centrifuged at 30,000 rpm for 30 min before measuring the rtPA concentration in the supernatant. EE and LC of rtPA were calculated as following:

$$EE (\%) = \frac{W_E}{W_T} \times 100 \quad (1)$$

$$LC \left(\frac{\mu g}{mg} \right) = \frac{W_E}{M_T} \quad (2)$$

W_E is the weight of rtPA encapsulated in TML@rtPA; W_T is the total weight of rtPA added; M_T is the total weight of TML@rtPA, which was obtained based on the dry weight per volume of the sample. EE value represents the percentage of rtPA encapsulated during the preparation; the LC value gives the weight ratio of rtPA in TML@rtPA. The final product was freshly prepared and stored in phosphate buffer at 4 °C prior to use.

Characterization of TML@rtPA

The size, polydispersity index (PDI), zeta potential of the liposomes were analyzed by dynamic light scattering (DLS) and transmission electron microscopy (TEM), as described previously.²⁷

In vitro release of rtPA from TML@rtPA

To optimize the temperature sensitivity of rtPA release from TML@rtPA, the kinetics of rtPA release from different TML@rtPA preparations was determined at 37 °C vs. 43 °C. TML@rtPA (1 mL; 10 mg/mL) prepared in phosphate buffered saline (PBS; pH 7.4) was placed in a microtube and shaken at 150 rpm. At predetermined time, the supernatant was removed by centrifugation at 65,000 ×g at 4 °C for 30 min and subjected to rtPA quantitation by ELISA; the pellet was re-suspended with fresh PBS and then incubated at 37 °C vs. 43 °C. The cumulative rtPA release was calculated using the following equation, where W_E is the weight (mg) of rtPA encapsulated and W_R is cumulative weight (mg) of rtPA released.

$$\text{Cumulative rtPA release } (\%) = \frac{W_R}{W_E} \times 100 \quad (4)$$

For the optimized TML@rtPA preparation (lipid molar ratio = 90:5:5, CMNPs = 0.1 mg/mL and rtPA = 0.1 mg/mL), rtPA release in serum was determined quantitatively in order to reveal temperature- and magnet-sensitivity. The cumulative release of rtPA from TML@rtPA (10% fetal bovine serum, pH 7.4 PBS; 150 rpm) at 37 °C vs. 43 °C was determined by ELISA using Eq. (4).

To determine the effects of magnetic field application on rtPA release, 1 mL of TML@rtPA (10 mg/mL) in 10% fetal bovine serum in pH 7.4 PBS was placed in a microtube and subjected to magnetic separation (DynaMag-2 Magnet, ThermoFisher Scientific, Waltham, MA), followed by agitation at 150 rpm in an incubator at 43 °C. Under the influence of the magnetic field, the supernatant was removed from the pellet of TML@rtPA for analysis, followed by suspension with 10% serum and

incubation at 43 °C without magnetic influence. The cumulative rtPA release in the supernatant was assayed using ELISA.

Chromogenic assay

The amidolytic activity of rtPA at 37 °C vs. 43 °C was measured spectrophotometrically using the protease substrate S-2288 (Chromogenix), a specific chromogenic substrate for rtPA, according to manufacturer's instructions. Enzymatic activity (U) = $OD_{405}/\text{reaction time} \times 0.313 \times \text{volume}$.

Thromboelastometry

Citrated whole blood from gas anesthetized male Sprague Dawley (SD) rats was obtained according to a protocol approved by the Institutional Animal Care and Use Committee (IACUC) of Chang Gung University, which is certified by American Association for Accreditation of Laboratory Animal Care. The blood was incubated with TML@rtPA (20 μL; with rtPA 0.34 μg) under 37 °C vs. 43 °C for 90 min prior to be tested by thromboelastometry at 37 °C.¹² The measurement of the coagulation time (CT), maximal clot firmness (MCF), and lysis index (LI) was determined from the thromboelastograms.

Rat embolic model with temperature controlled system

A rat embolic model was modified from a previous study.¹² The protocol was approved by IACUC of Chang Gung University. Briefly, male SD rats of 10–12-wk-old (357 ± 5 mg; $n = 32$) were anesthetized by intraperitoneal injection of Inactin® (100 mg/kg; 200 mg/mL), followed by cannulation of the right carotid artery, jugular vein, and the right iliac artery for blood pressure measurement, drug/serum administration, and emboli/drug introduction, respectively. Aortic blood flow (ABF) and iliac blood flow (IBF) were measured by placement of ultrasonic flow probes (T206; Transonic System Inc., Ithaca, NY) on the aorta downstream of the left renal artery and the left iliac artery. Tissue perfusion of left hind limb (HLP) was observed with a laser speckle imager (MoorFLPI; Moor Instruments Ltd., Wilmington, DE). A temperature-controlled system composed of a water bath and a peristaltic pump was arranged to maintain constant local temperature by superfusion of the target site with saline at 37 °C vs. 43 °C, which was achieved by maintaining a higher water bath temperature (Figure 5). Thermal resolution was further achieved by instantaneous removal of the heated saline using a draining tube driven by the same pump head. Temperature distribution was recorded by an infrared thermal imaging system (FLIR T420 system; FLIR Systems Inc., Täby, Sweden). After equilibration for 20 min, the embolus or 0.5 mL vehicle was introduced with gentle stretching of a piece of 3-odd suture placed around the left iliac artery downstream of the branch to the pudic epigastric artery. After clot lodging for 5 min, *i.a.* or *i.v.* administration of TML@rtPA at 37 °C or 43 °C with the external magnetic field (an NdFeB magnet; 0.5 T) applied on the bifurcation until all the nanocomposites were introduced in the system. The magnet was then moved back and forth between the bifurcation and downstream along the left iliac artery at every 2–5 sec for 60 min. At the end of the experiments, blood was collected from the

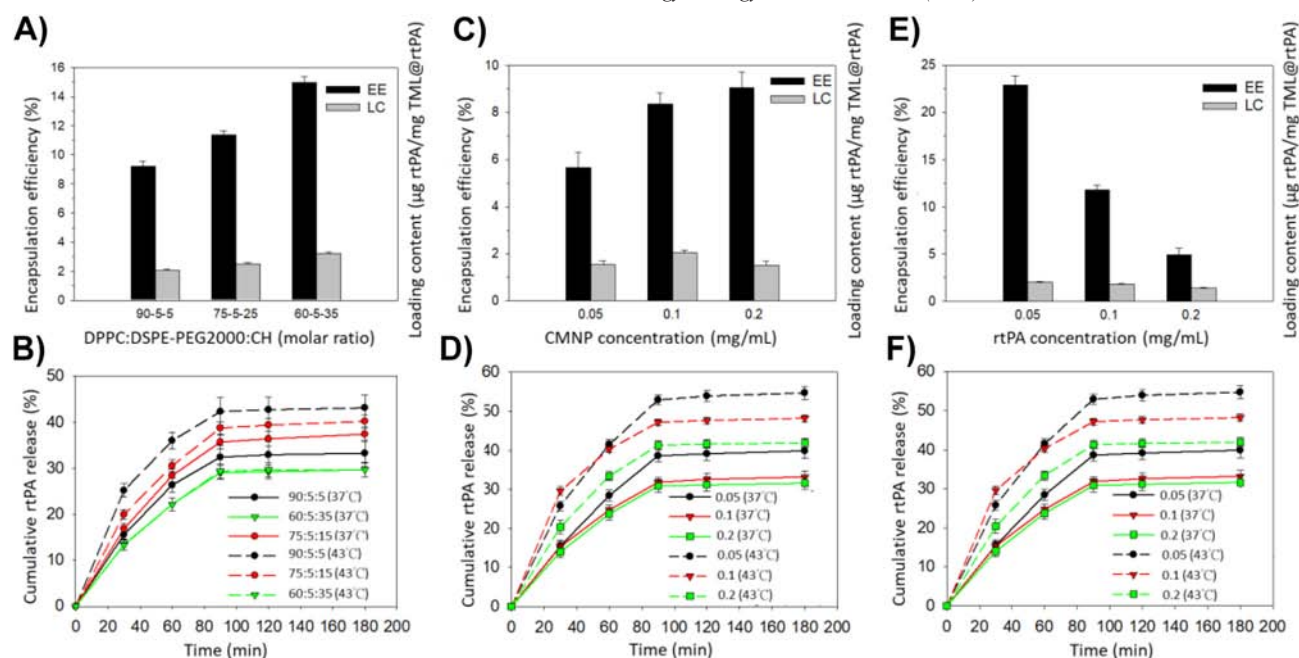


Figure 1. Effects of lipid molar ratio (A and B), citric acid-coated Fe_3O_4 magnetic nanoparticle (CMNP) concentration (C & D) and rtPA concentration (E & F) in mg/mL on the encapsulation efficiency (EE) and loading content (LC) of rtPA (A, C and E), and rtPA release at 37 °C and 43 °C (B, D and F) from rtPA-encapsulated thermosensitive magnetic liposome nanoparticles (TML@rtPA). The data are expressed as means \pm SD ($n = 6$).

left carotid artery cannula into a tube containing EDTA, and analyzed by the Sysmex XE-2100 (Sysmex Corp., Kobe, Japan).

Statistics

The results of material preparation and characterization were presented as means \pm standard deviation (SD). The thromboelastometric and pharmacological results of rats were presented as means \pm standard error of means (SEM), and analyzed by two-way ANOVA, followed by Duncan's post-hoc test. Repeated time measurement ANOVA was used when applicable. Statistical significance was defined as $P < 0.05$.

Results

Preparation and optimization of TML@rtPA

The effects of lipid component ratio, [CMNPs] and [rtPA] in preparation of TML@rtPA on EE and LC values and rtPA release at 37 °C or 43 °C are illustrated in Figure 1. As shown in Figure 1, A and B, increasing the molar ratio of DPPC in lipids decreased the EE and LC values but increased the temperature-sensitivity of rtPA release. At 60% DPPC, rtPA release from TML@rtPA was no longer temperature-sensitive. Increasing [CMNPs] led to increased EE value, whereas the LC value peaked at 0.1 mg/mL (Figure 1, C). Increasing [CMNPs] to higher than 0.1 mg/mL also resulted in less temperature-sensitive release of rtPA (Figure 1, D). Increasing [rtPA] drastically reduced EE value but showed moderate influence on LC value (Figure 1, E). The temperature-sensitivity of rtPA release also decreased with [rtPA] higher than 0.1 mg/mL (Figure 1, F). Taken together, TML@rtPA prepared with lipid molar ratio of

90:5:5 (DPPC:DSPE-PEG₂₀₀₀:CH), 0.1 mg/mL CMNPs and 0.1 mg/mL rtPA were used for the following studies, which gave a EE value of 10% and LC value of 2 μg/mg.

3.2 Characterization of TML@rtPA

As shown in Table 1, the hydrodynamic diameters of TML@rtPA were less than 200 nm, with the polydispersity index (PDI) value of 0.17. Electrophoretic mobility measurements indicated the zeta potential of TML@rtPA was close to zero after encapsulating CMNPs in liposomes formed by neutral lipids.

Differential scanning calorimetry (DSC) profiles of DPPC, TML and TML@rtPA are illustrated in Fig. S1. Fourier transform infrared (FTIR) spectra, X-ray diffraction (XRD) patterns and superconducting quantum interference device (SQUID) magnetization curves are illustrated in Fig. S2. Whereas thermogravimetric analysis (TGA) of MNP, CMNP, TML, TML@rtPA, and thermosensitive liposomes (TL) are illustrated in Fig. S3.

From the TEM micrographs of Figure 2, A insets, CMNPs showed a few agglomerates with size slightly lower than that from DLS measurements. Nonetheless, the average size of discrete CMNPs could be estimated from the TEM image to be 12 nm, which was within the size distribution of superparamagnetic particles. The structures of TML@rtPA characterized by cryo-TEM showed uniform morphology with CMNPs agglomerate in the aqueous core surrounded by a lipid bilayer and a particle size consistent with that from DLS measurements.

The stability of TML@rtPA under storage conditions (0.01 M phosphate buffer, pH 7.4, 4 °C) is shown in Figure 2, A, which was based on rtPA protein assay. Negligible rtPA release from TML@rtPA was observed up to 28 days. Further storage

Table 1

The mean diameter, polydispersity (PDI) and the zeta potential of citric acid-coated Fe_3O_4 magnetic nanoparticle (CMNP), thermosensitive magnetoliposomes (TMLs) and rtPA-encapsulated thermosensitive magnetoliposomes (TML@rtPA) were measured by dynamic light scattering technique. The data are expressed as means \pm standard deviations ($n = 6$).

Sample	Mean diameter (nm)	PDI*	Zeta potential (mV)
CMNP	54.1 ± 12.1	0.186 ± 0.013	-19.7 ± 0.8
TML	174.4 ± 9.6	0.166 ± 0.017	-6.1 ± 0.4
TML@rtPA	192.5 ± 11.4	0.171 ± 0.018	-6.7 ± 0.8

* polydispersity index

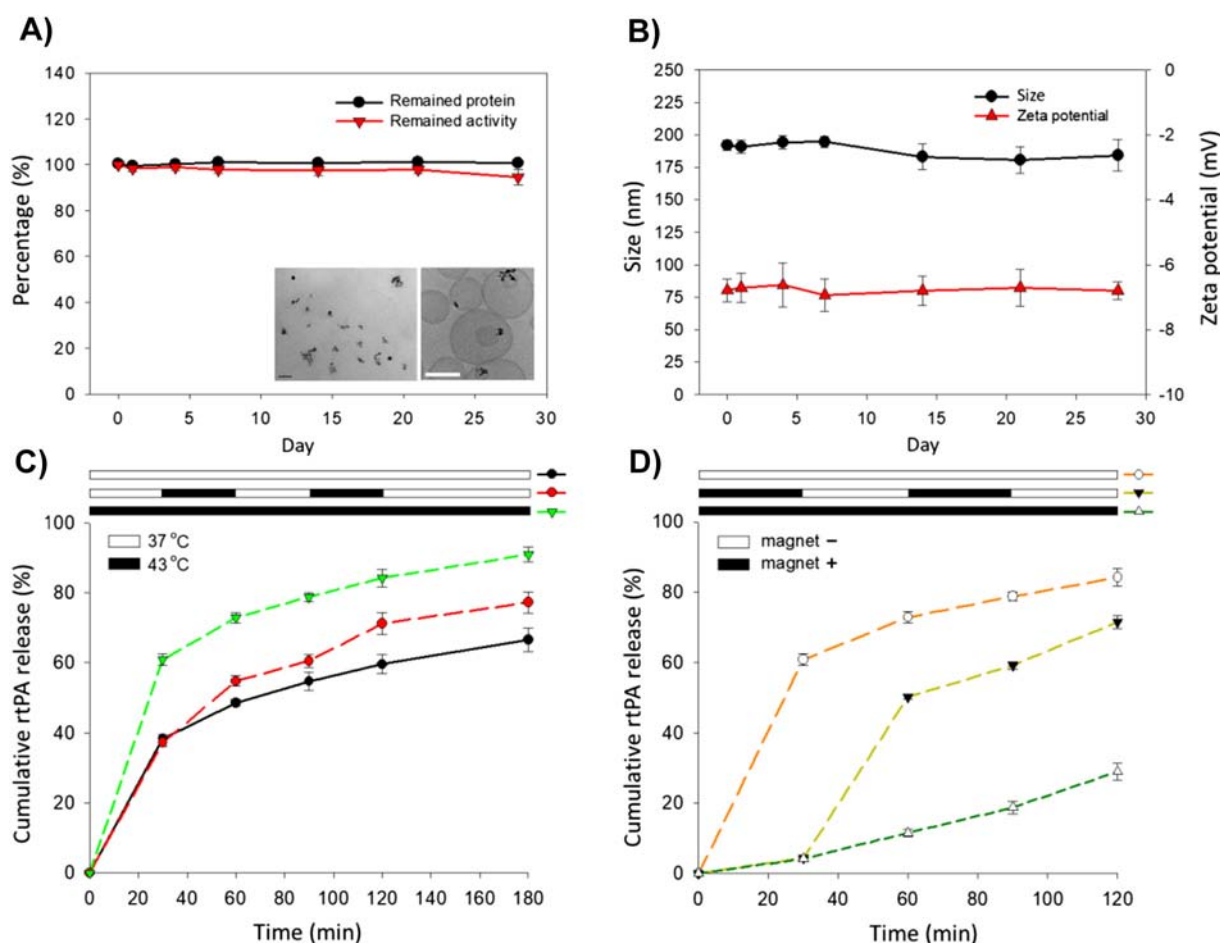


Figure 2. Characteristics of TML nanocomposites with and without rtPA. The storage stability of TML@rtPA in 0.01 M pH 7.4 phosphate buffer at 4 °C with time is presented as %protein and %activity (A). Representative images of citric acid-coated Fe_3O_4 magnetic nanoparticles (CMNP; left, bar = 50 nm) and TML@rtPA (right, bar = 100 nm) from TEM and cryo-TEM, respectively, are presented as insets (A). The size and zeta potential of TML@rtPA were determined by dynamic light scattering (B). Temperature-sensitive rtPA release at 37 °C, 43 °C and 37 °C/43 °C (C), and magnet-sensitive rtPA release at magnetic force off, magnetic force on and magnetic force on/off (D) from TML@rtPA are measured at 43 °C with time. The data are expressed as means \pm SD ($n = 5$).

stability was determined from the retained amidolytic activity of rtPA using the substrate S-2288. Slight decrease of rtPA activity was found after 21 days resulted in only 5% activity loss at day 28, which suggested the thrombolytic activity of TML@rtPA could be maintained in phosphate buffer at 4 °C. The particles size and zeta potential of TML@rtPA in 0.01 M phosphate buffer were very stable up to 28 days (Figure 2, B). To determine temperature-sensitive release of rtPA from TMLs, cumulative rtPA release in serum was measured at 37 °C and 43 °C using

ELISA. An initial burst release of rtPA at both 37 °C and 43 °C in serum was observed, followed by gradually reduced release rate (Figure 2, C). Comparing initial burst release at 30 min, higher temperature triggered more drug release and the cumulative release was 38% vs. 62% at 37 °C vs. 43 °C, respectively. During the observation period, the highest amount of rtPA released occurred at 180 min; the sustained release behavior followed and the cumulative release at 180 min reached 67% vs. 91% at 37 °C vs. 43 °C, respectively.

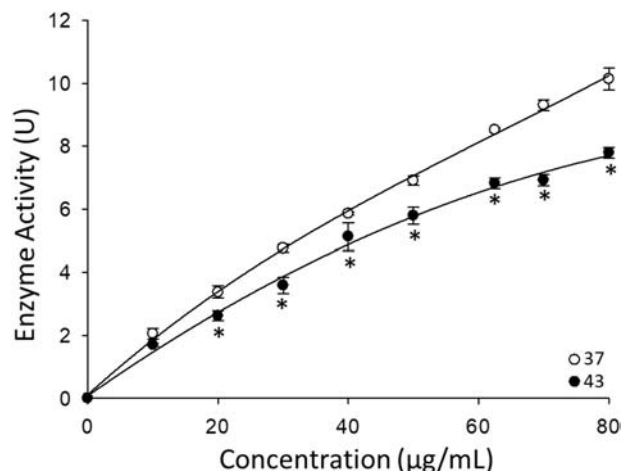


Figure 3. Temperature effects of rtPA activity at 37 °C vs. 43 °C. A chromogenic assay was conducted with various rtPA concentrations at 37 °C vs. 43 °C. The data are expressed as means \pm SEM ($n = 3$). *, $P < 0.05$ compared with corresponding group at 37 °C.

Figure 2, D depicts magnet-sensitive release of rtPA from TML@rtPA at 43 °C. In the presence of magnetic force, TML@rtPA formed a pellet and the release of rtPA was significantly retarded, *i.e.*, 29% vs. 84% rtPA release was observed with and without the magnet application in 2 hr. However, the enzyme activity of rtPA was slightly, but significantly jeopardized at 43 °C (Figure 3); the enzyme activity of rtPA reduced by 20% with 62.5 μ g/mL of rtPA at 43 °C.

3.3 Biocompatibility of TML@rtPA

To determine whether TML and TML@rtPA may induce hemolysis, the absorption spectra (Fig. S4A) of the supernatant of TML and TML@rtPA after incubation with RBCs in PBS at 37 °C or 43 °C for 2 hr. were analyzed (Fig. S4B). No visible hemolysis was observed after incubation with 5 mg/mL of TML or TML@rtPA, which was associated with no significant difference in OD₅₄₀ from PBS (negative control) at 37 °C or 43 °C. Further studies were conducted on blood samples from rats subjected to *i.v.* injection of TML. Fig. S4C indicated that TMLs did not significantly alter the levels of blood counts, HGB, HCT, MCV, MCH and MCHC. In addition, hepatic or renal function was not significantly altered in response to TML *i.v.* (Fig. S4D).

In vitro thrombolysis

Figure 4, A illustrates representative thromboelastograms in response to TML vs. TML@rtPA with 1 μ g/mL rtPA. After 37 °C vs. 43 °C incubation, lysis index at 60 min (LI₆₀) of TML@rtPA was 73% vs. 51%, respectively, suggesting a temperature-sensitive release of rtPA. The thrombolytic effects of TML@rtPA were associated with a coagulation time (CT) of 193 vs. 136 s after 37 °C vs. 43 °C incubation, respectively. Figure 4, B depicts summarized effects of temperature on TML@rtPA-induced changes of lysis index, CT and maximal clot formation (MCF). After incubation of TML@rtPA at 37 °C vs. 43 °C, released rtPA-induced LI₆₀ was 81% vs. 53%, respectively

($P < 0.05$). Although no significant difference of CT was observed in TML@rtPA at 37 °C, TML@rtPA at 43 °C significantly reduced CT to 64% of that in TML at 43 °C. Nevertheless, MCF was not different in vehicle vs. TML@rtPA or TML vs. TML@rtPA comparison, suggesting that platelet activation or fibrin polymerization may not be altered by the intervention.

In vivo thrombolysis: *i.a.* administration

Figure 5, A illustrates a focal hyperthermia system established with a rat embolic model for testing thrombolytic effects of TML@rtPA. The temperature resolution around the target site along the left iliac artery in response to saline of 37 °C vs. 43 °C is depicted in Figure 5, B. With placement of the outflow tubing, elevated temperature was confined within very limited area around the tip of the tubing.

Figure 6, A illustrates representative hind limb perfusion (HLP) at 37 °C vs. 43 °C in response to *i.a.* administration of TML@rtPA (0.2 rtPA mg/kg) 5 min after clot lodging. HLP in the defined area of the image of the basal level at 37 °C was acquired for quantitative analysis, which reduced to 63% of the basal level after clot lodging in both groups of rats with 37 °C and 43 °C superfusion. TML@rtPA restored HLP to 83% and 98% at 20 and 60 min after clot lodging in a rat at 43 °C, whereas HLP remained 59% and 55% in a rat at 37 °C, respectively. Quantitative analysis of mean arterial pressure (MAP), arterial blood flow (ABF), iliac blood flow (IBF) and HLP was summarized in Figure 6, B–E. Experimental intervention did not alter MAP in all groups studied (Figure 6, B). After clot lodging at 0 min, *i.a.* administration of TML@rtPA with magnetic guiding increased ABF, IBF and HLP in rats of 43 °C to a significantly higher level compared to that of 37 °C (Figure 6, C and D). At 15 min after clot lodging, TML@rtPA significantly restored IBF and ABF to 79% and 70% of basal level at 43 °C, respectively ($P < 0.05$); whereas no significant restoration of IBF or ABF was observed at 37 °C throughout the experiments. Nevertheless, even at 43 °C, both IBF and ABF gradually reduced to approximately 50% of the peak level at 120 min of the observed time. In addition, clot lodging reduced HLP to 70% vs. 67% of the basal level at 37 °C vs. 43 °C. TML@rtPA at 43 °C restored HLP to 92% after 70 min, respectively ($P < 0.05$; Figure 6, E). In contrast, no significant improvement of HLP was observed at 37 °C. The results suggest that the thrombolysis was induced by *i.a.* administration of TML@rtPA at 43 °C, but not 37 °C. No hemodynamic effect was observed with TML *i.a.* at 43 °C, as illustrated in Fig. S5. Representative values of the TML group at 120 min are included in the Figure 6, suggesting the restoration was not due to potentially released CMNPs *per se* at 43 °C. In another group of rats subjected to the sham procedure at 43 °C without introduction of the clot, all parameters measured were relatively stable throughout the observation period (Figure 6, B–E), suggesting elevated temperature at the local site did not cause a significant hemodynamic change in the system.

In vivo thrombolysis: *i.v.* administration

Figure 7, A illustrates the representative HLP pattern in response to rtPA vs. TML@rtPA (0.2 rtPA mg/kg, *i.v.*) in the rat embolic model at 43 °C. After introduction of the clot, HLP was

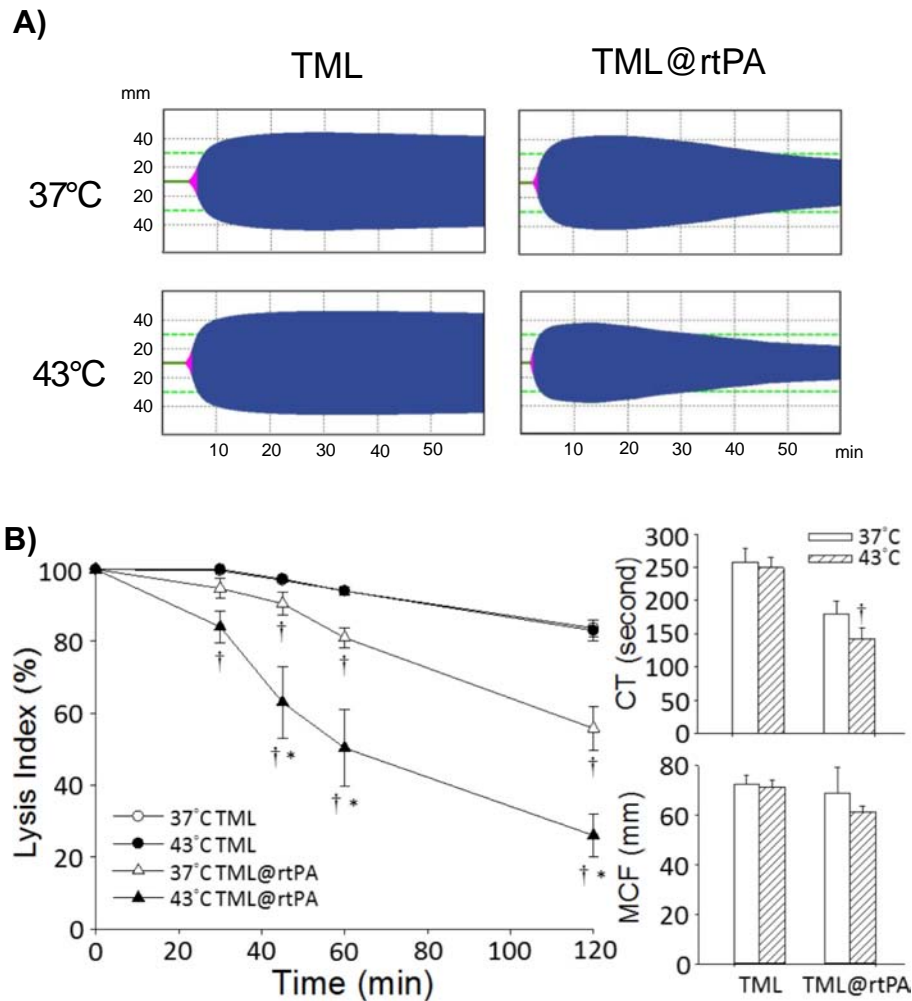


Figure 4. Thermal effects of thrombolysis induced by TML@rtPA *in vitro*. (A) Representative thromboelastograms of thrombolysis induced by TML@rtPA with rtPA 1 $\mu\text{g}/\text{mL}$, which was incubated with citrated blood at 37 °C or 43 °C for 90 min before initiation of coagulation. (B) The lysis index (LI), coagulation time (CT) and maximal clot firmness (MCF) of TML@rtPA were derived from thromboelastograms. Values are means \pm SEM ($n = 4$). *, $P < 0.05$ compared with TML@rtPA at 37 °C and TMLs, respectively.

reduced to 74% vs. 73% in rats subjected to rtPA vs. TML@rtPA. TML@rtPA at 43 °C increased HLP to 86% and 93% at 20 and 60 min, respectively, whereas rtPA at the same dose did not elicit significant restoration. Quantitative analysis of MAP, ABF, IBF and HLP was summarized in Figure 7, B–E. No significant difference on MAP was observed between the two groups at 43 °C (Figure 7, B). In response to *i.v.* administration of TML@rtPA at 43 °C, ABF, IBF and HLP were significantly restored at 40, 30 and 60 min after clot introduction, respectively, whereas the same dose of rtPA exerted no effect (Figure 7, C–E). Maximal restoration of ABF, IBF and HLP occurred 55–60 min after clot introduction, which were 67%, 62% and 99% of the basal levels, respectively. Although HLP remained stable after hemodynamic restoration (Figure 7, E), IBF peaked at 55 min after clot lodging, and gradually reduced to a significantly lower level at 100–120 min (Figure 7, D; $P < 0.05$). The hematologic analysis was conducted at the end of the experiments. No difference of RBC counts, platelet counts, HGB and HCT was observed between groups (Table S1).

Discussion

In this study, effective thrombolysis with improved hemodynamics was achieved with magnetic targeting and hyperthermia-induced rtPA release from TML@rtPA in a rat embolic model. Our results first demonstrated reproducible and targeted thrombolysis induced by *i.v.* administration of rtPA nanocomposites. In addition, effects of magnetic force-hyperthermia interplay on drug release were evident, providing a novel strategy to control release of therapeutic agents from a liposome-based nanocomposite for targeting therapy.

To prolong the half-life of rtPA and allow *i.v.* administration, protection of rtPA appears to be critical. The stability of a DPPC/DSPE-PEG/CH liposomal preparation in a sol–gel phase is dependent on whether the temperature of the lipid bilayer is below T_m .^{25,28} Thus, TML@rtPA remained stable with nearly 100% of enzyme activity at 4 °C during 28-day of storage time. The temperature-dependent rtPA release from TML@rtPA is due to temperature-induced phase change of lipid bilayers from the

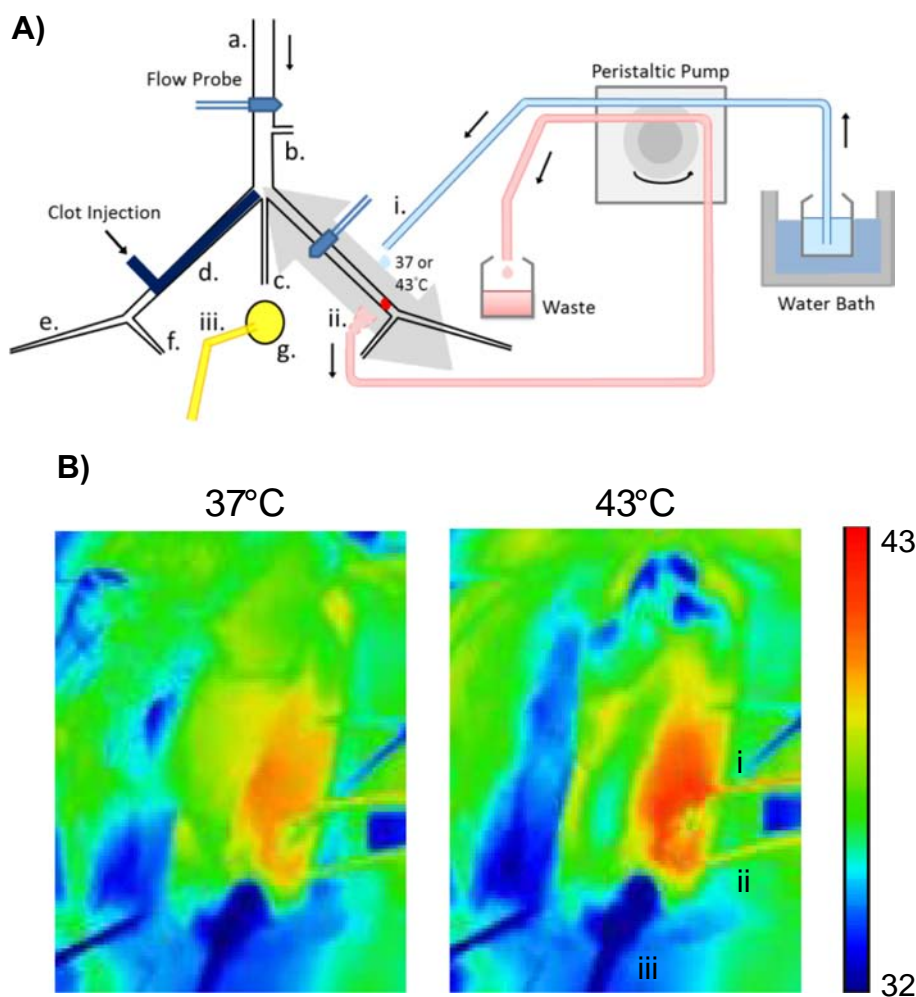


Figure 5. Establishment of a temperature-controlled release system in a rat embolic model. In the schematic diagram of the model (A), an embolus was introduced from the right iliac artery and lodged in the left iliac artery upstream of pudic epigastric branch. The temperature-controlled system was established surrounding the lodged clot in the left iliac artery to raise the local temperature with high resolution. Saline of 37 °C or 43 °C was superfused on the local area using a peristaltic pump with a draining tube close by to remove fluid at the same rate. The double arrow in gray indicates the magnet moving track; other arrows indicate the direction of flows in the vessels or tubings. Representative temperature profiles (B) in response to superfusion of 37 °C or 43 °C saline illustrates temperature distribution around superfusion tube (i.), draining tube (ii.) and urinary bladder cannula (iii.) areas. Abdominal artery (a.), genital artery (b.), tail artery (c.), iliac artery (d.), femoral artery (e.), pudic epigastric artery (f.) and urinary bladder (g.).

gel phase to liquid phase at 43 °C.²⁸ Therefore, more rtPA released from TML@rtPA at a temperature of 43 °C than that of 37 °C was observed, which may underlie temperature-sensitive thrombolysis observed *in vivo*.

Although the value of saturation magnetization decreased significantly after encapsulation of CMNPs in TMLs, application of the magnet still modulated TML@rtPA behavior and rtPA release (Figure 2, D). Similar results have been observed with rtPA encapsulated in chitosan-coated MNPs in previous studies.¹² Reduced rtPA release from aggregated TML@rtPA under magnetic influence was probably due to reduced surface area between serum and TML@rtPA interface. Slow-and-fast release rates of rtPA synchronized to on-and-off magnetic force and corresponded to aggregate-and-disperse states of TML@rtPA. The pattern of magnet-sensitive release may allow minimal loss of rtPA after magnetic capture at the target site, resulting in restoration of

hemodynamics with less amount of rtPA than the regular dose. In contrast, magnetic force may be used to trigger drug release from a gelatin/NPs composite film.³³ To our knowledge, TML@rtPA was the first nanocomposites with dual mechanisms for controlled rtPA release.

Since enzyme activity may be temperature-dependent, elevated temperature *per se* may have an effect on coagulation or thrombolysis. In spite of slightly reduced enzymatic activity of rtPA at 43 °C *in vitro*, effective thrombolysis was observed in response to both *i.a.* and *i.v.* administration of TML@rtPA. Furthermore, higher temperature of 41.8 °C has been shown to activate the coagulation cascade with shortened CT³⁴; however, it is unlikely that the elevated temperature during the pretreatment before thromboelastometric assay may exert a profound effect on coagulation, as the assay was conducted at 37 °C. Previous studies demonstrated that free or released rtPA

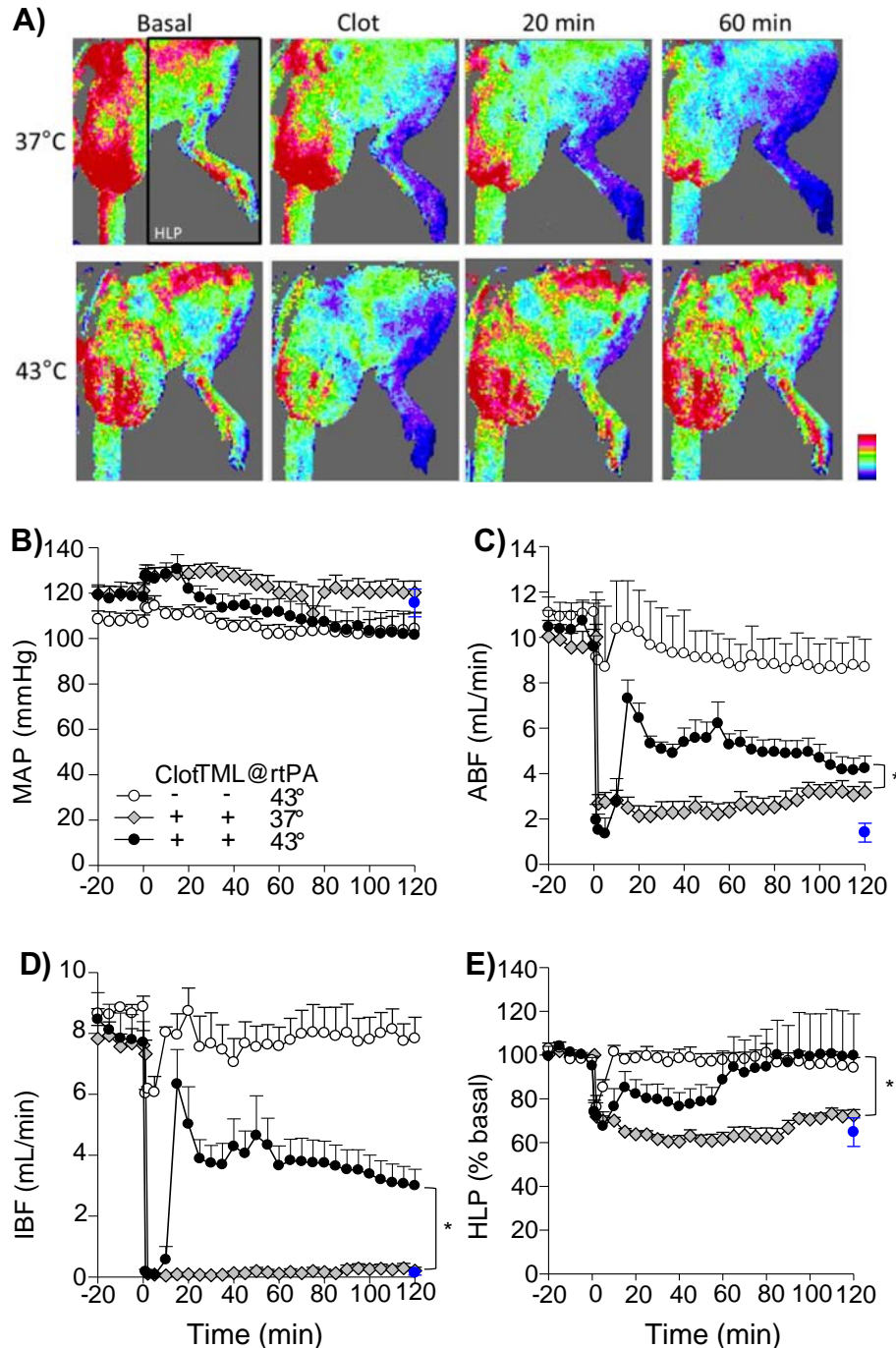


Figure 6. Intra-arterial TML@rtPA-induced target thrombolysis. (A) Representative restoration of hind-limb perfusion (HLP) in response to TML@rtPA under magnetic guiding at 43 °C. Quantitative HLP analysis was obtained from a defined area in each image, as illustrated in the basal image. Mean arterial perfusion (MAP; B), aortic blood flow (ABF; C), iliac blood flow (IBF; D), and HLP (E) were quantified with or without ($n = 5$) introduction of the clot at time 0. TML@rtPA (0.2 mg rtPA/kg) under 37 °C ($n = 10$) or 43 °C ($n = 7$) was administrated from the right iliac artery at 5 min. Blue circles denote the measurement of TML group at 120 min ($n = 5$). Values are means \pm SEM. *, $P < 0.05$ compared with the denoted group based on ANOVA.

from nanocomposites exerted no effect on CT¹²; however, TML@rtPA subjected to 43 °C exerted a shortened CT in the current study. Nevertheless, TML@rtPA subjected to 37 °C vs. 43 °C did not alter MCF, suggesting that FXIII-induced fibrin polymerization or platelet activation was not altered by TML@rtPA.³⁵

Immediate restoration of IBF and ABF was observed in response to TML@rtPA *i.a.*, but much slower restoration of the flow was observed in response to TML@rtPA *i.v.*, which is probably due to the distance between injection site and the location of the emboli. Since reticuloendothelial system may still capture nanocomposites even with PEG modification,³⁶ it is

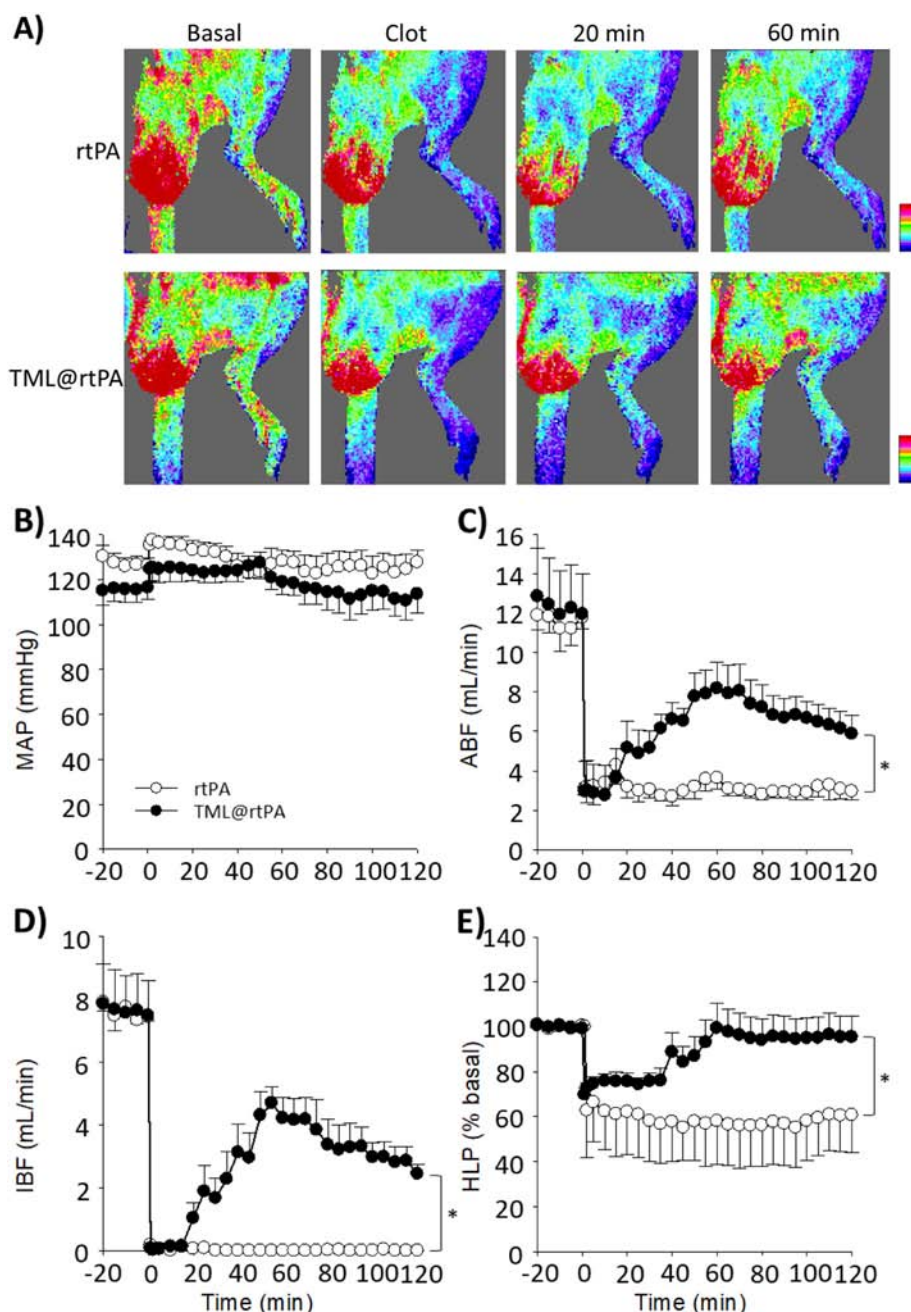


Figure 7. Intravenous TML@rtPA-induced target thrombolysis. (A) Representative restoration of hind-limb perfusion (HLP) in response to free rtPA ($n = 4$) vs. TML@rtPA ($n = 6$) with releasable rtPA of 0.2 mg/kg under magnetic guiding at 43 °C. MAP (B), ABF (C), IBF (D), and HLP (E) were quantified before and after the introduction of the clot. Values are as means \pm SEM. *, $P < 0.05$ compared with the denoted group based on ANOVA.

anticipated that less TML@rtPA may reach the emboli after *i.v.* administration. Nevertheless, non-PEGylated nanocomposites with rtPA adsorption and a targeting ligand of P-selectin have been demonstrated to achieve target thrombolysis after *i.v.* administration in a FeCl_3 -induced thrombosis model¹⁵; however, the dose of rtPA required was 12.5-fold of that used in the current study. PEGylation may be beneficial to reduce dose of nanocomposites for *i.v.* administration.

Application of a magnetic field at the time of *i.v.* or *i.a.* administration of TML@rtPA followed by a mobile magnetic

guiding may be critical to ensure maximized drug concentration at the target site with hyperthermia, which is consistent with previous finding that drug release from MNPs aggregated by magnet application was greatly attenuated.¹² However, we cannot rule out possible endothelial damage caused by magnetic guiding-induced movement of the nanocomposite aggregates along the left iliac artery, which may result in local vasoconstriction. In addition, focal hyperthermia-induced rtPA release from TML@rtPA appears to be a very efficient and precise strategy to induce target thrombolysis, compared to rtPA nanocomposite without a controlled release

design,¹² suggesting feasibility of hyperthermia-induced target thrombolysis in treatment of thromboembolic diseases.

After drug intervention, *i.a.* and *i.v.* TML@rtPA-induced restoration of blood flow peaked at 10 and ~55 min, respectively, suggesting possible re-occlusion occurred after lysis of the clot. The underlining mechanism is unknown, but may be due to reduced rtPA concentration around the residual clot with time, which triggered recurrent thrombosis. In contrast, preparations with immobilized rtPA consistently induced thrombolysis that was sustained in the rat embolic model,^{5,7} demonstrating advantages of immobilized rtPA preparation. In spite of a quick restoration of IBF and ABF, HLP restore was relatively slow, which may be due to incomplete digestion of clots that moved to and then lodged in the downstream vessels. After approximately one hour, HLP restored to near the basal levels in spite of reduced IBF and ABF. The phenomenon may be caused by the collateral networks that perfused ischemic hind limb of rat.³⁷ Although systemic hyperthermia of 43 °C may alter hemodynamics,³⁸ focal hyperthermia *per se* did not alter basal hemodynamic parameters measured in the current study.

The liposomal preparation appears to be with good compatibility, which is consistent with a previous study that DPPC and DSPC did not cause significant hemolysis after incubation with 5% human erythrocytes for up to 72 hr.³⁹ Although liposomal PAs have been developed to enhance the circulation half-life due to its protection from endogenous inhibitors more than 20 years ago,⁴⁰ the current study is the first time to demonstrate that TML@rtPA can be delivered *i.v.* to induce reproducible thrombolysis. Nevertheless, the invasiveness of the current technique to induce focal hyperthermia may limit further clinical application.

In conclusion, thermo-controlled release of rtPA from magnetoliposomes under magnetic guiding allows protected rtPA transport from distance to achieve target thrombolysis by *i.v.* administration of the nanocomposites. Encapsulation/rtPA protection, local retention and controlled release may all be paramount, which have been implemented with combination of magnetoliposomal preparation, magnetic targeting, and focal hyperthermia. Our studies suggested that *i.v.* administration of TML@rtPA with 20% of a regular dose of rtPA may induce effective target thrombolysis.

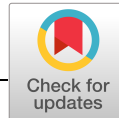
Appendix A. Supplementary data

Supplementary data to this article can be found online at <https://doi.org/10.1016/j.nano.2019.03.014>.

References

- Cheng NT, Kim AS. Intravenous thrombolysis for acute ischemic stroke within 3 hours versus between 3 and 4.5 hours of symptom onset. *Neurohospitalist* 2015;**5**:101-9.
- Powers WJ, Derdeyn CP, Biller J, Coffey CS, Hoh BL, Jauch EC, et al. 2015 AHA/ASA focused update of the 2013 guidelines for the early management of patients with acute ischemic stroke regarding endovascular treatment. *Stroke* 2015;**46**:3020-35.
- Colucci M, Paramo JA, Collen D. Inhibition of one-chain and two-chain forms of human tissue-type plasminogen activator by the fast-acting inhibitor of plasminogen activator *in vitro* and *in vivo*. *J Lab Clin Med* 1986;**108**:53-9.
- Prats Sánchez L, Camps Renom P, Sotoca Fernández J, Delgado Mederos R, Martínez Domeño A, Marín R, et al. Remote intracerebral hemorrhage after intravenous thrombolysis. *Stroke* 2016;**47**:2003-9.
- Ma YH, Wu SY, Wu T, Chang YJ, Hua MY, Chen JP. Magnetically targeted thrombolysis with recombinant tissue plasminogen activator bound to polyacrylic acid-coated nanoparticles. *Biomaterials* 2009;**30**:3343-51.
- Chen JP, Yang PC, Ma YH, Wu T. Characterization of chitosan magnetic nanoparticles for *in situ* delivery of tissue plasminogen activator. *Carbohydr Polym* 2011;**84**:364-72.
- Yang HW, Hua MY, Lin KJ, Wey SP, Tsai RY, Wu SY, et al. Bioconjugation of recombinant tissue plasminogen activator to magnetic nanocarriers for targeted thrombolysis. *Int J Nanomedicine* 2012;**7**:5159-73.
- M. K. H Chen, X Liu, PC Stepp, Y Xie, and AJ Rosengart, 2012. Non-invasive magnetically target tPA delivery for arterial thrombolysis, CRC press.
- Absar S, Nahar K, Kwon YM, Ahsan F. Thrombus-targeted nanocarrier attenuates bleeding complications associated with conventional thrombolytic therapy. *Pharm Res* 2013;**30**:1663-76.
- Absar S, Choi S, Ahsan F, Cobos E, Yang VC, Kwon YM. Preparation and characterization of anionic oligopeptide-modified tissue plasminogen activator for triggered delivery: an approach for localized thrombolysis. *Thromb Res* 2013;**131**:e91-9.
- Greineder CF, Howard MD, Carnemolla R, Cines DB, Muzykantor VR. Advanced drug delivery systems for antithrombotic agents. *Blood* 2013;**122**:1565-75.
- Chen JP, Liu CH, Hsu HL, Wu T, Lu YJ, Ma YH. Magnetically controlled release of recombinant tissue plasminogen activator from chitosan nanocomposites for targeted thrombolysis. *J Mater Chem B* 2016;**4**:2578-90.
- Klegerman ME. Translational initiatives in thrombolytic therapy. *Front Med* 2017;**11**:1-19.
- Pawlowski CL, Li W, Sun M, Ravichandran K, Hickman D, Kos C, et al. Platelet microparticle-inspired clot-responsive nanomedicine for targeted fibrinolysis. *Biomaterials* 2017;**128**:94-108.
- Juenet M, Aid-Launais R, Li B, Berger A, Aerts J, Ollivier V, et al. Thrombolytic therapy based on fucoidan-functionalized polymer nanoparticles targeting P-selectin. *Biomaterials* 2018;**156**:204-16.
- Vaidya B, Agrawal GP, Vyas SP. Functionalized carriers for the improved delivery of plasminogen activators. *Int J Pharm* 2012;**424**:1-11.
- Tu SJ, Wu SY, Wang FS, Ma YH. Retention assessment of magnetic nanoparticles in rat arteries with micro-computed tomography. *Phys Med Biol* 2014;**59**:1271-81.
- Kim JY, Kim JK, Park JS, Byun Y, Kim CK. The use of PEGylated liposomes to prolong circulation lifetimes of tissue plasminogen activator. *Biomaterials* 2009;**30**:5751-6.
- Allen TM, Cullis PR. Liposomal drug delivery systems: from concept to clinical applications. *Adv Drug Del Rev* 2013;**65**:36-48.
- Viglianti BL, Ponce AM, Michelich CR, Yu D, Abraham SA, Sanders L, et al. Chemodosimetry of *in vivo* tumor liposomal drug concentration using MRI. *Magn Reson Med* 2006;**56**:1011-8.
- Ponce AM, Viglianti BL, Yu D, Yarmolenko PS, Michelich CR, Woo J, et al. Magnetic resonance imaging of temperature-sensitive liposome release: drug dose painting and antitumor effects. *J Natl Cancer Inst* 2007;**99**:53-63.
- Li L, ten Hagen TL, Schipper D, Wijnberg TM, van Rhoon GC, Eggermont AM, et al. Triggered content release from optimized stealth thermosensitive liposomes using mild hyperthermia. *J Control Release* 2010;**143**:274-9.
- Li L, ten Hagen TL, Hossann M, Süß R, van Rhoon GC, Eggermont AM, et al. Mild hyperthermia triggered doxorubicin release from optimized stealth thermosensitive liposomes improves intratumoral drug delivery and efficacy. *J Control Release* 2013;**168**:142-50.

24. Lokse WJM, Bolkestein M, ten Hagen TLM, de Jong M, Eggermont AMM, Grull H, et al. Investigation of particle accumulation, chemosensitivity and thermosensitivity for effective solid tumor therapy using thermosensitive liposomes and hyperthermia. *Theranostics* 2016;**6**:1717-31.
25. Dou Y, Hynynen K, Allen C. To heat or not to heat: challenges with clinical translation of thermosensitive liposomes. *J Control Release* 2017;**249**:63-73.
26. Saxena V, Gacchina Johnson C, Negussie AH, Sharma KV, Dreher MR, Wood BJ. Temperature-sensitive liposome-mediated delivery of thrombolytic agents. *Int J Hyperthermia* 2015;**31**:67-73.
27. Hsu HL, Chen JP. Preparation of thermosensitive magnetic liposome encapsulated recombinant tissue plasminogen activator for targeted thrombolysis. *J Magn Magn Mater* 2017;**427**:188-94.
28. Kneidl B, Peller M, Winter G, Lindner LH, Hossann M. Thermosensitive liposomal drug delivery systems: state of the art review. *Int J Nanomedicine* 2014;**9**:4387.
29. Kralj S, Potrc T, Kocbek P, Marchesan S, Makovec D. Design and fabrication of magnetically responsive nanocarriers for drug delivery. *Curr Med Chem* 2017;**24**:454-69.
30. Lin Ai T, Pi Ju T, Chao W Yu, Jing W Yu, Leu Wei L, Chung Shi Y. Thermosensitive liposomes entrapping iron oxide nanoparticles for controllable drug release. *Nanotechnology* 2009;**20**:135101.
31. Zhu L, Huo Z, Wang L, Tong X, Xiao Y, Ni K. Targeted delivery of methotrexate to skeletal muscular tissue by thermosensitive magnetoliposomes. *Int J Pharm* 2009;**370**:136-43.
32. Yan F, Wu H, Liu H, Deng Z, Liu H, Duan W, et al. Molecular imaging-guided photothermal/photodynamic therapy against tumor by iRGD-modified indocyanine green nanoparticles. *J Control Release* 2016;**224**:217-28.
33. Marín T, Montoya P, Arnache O, Pinal R, Calderón J. Development of magnetite nanoparticles/gelatin composite films for triggering drug release by an external magnetic field. *Materials & Design* 2018;**152**:78-87.
34. Strother SV, Bull JM, Branham SA. Activation of coagulation during therapeutic whole body hyperthermia. *Thromb Res* 1986;**43**:353-60.
35. Görlinger K, Iqbal J, Dirkmann D, Tanaka KA. *Whole Blood Assay: Thromboelastometry*. Springer International Publishing; 2016.
36. Awasthi VD, Garcia D, Goins BA, Phillips WT. Circulation and biodistribution profiles of long-circulating PEG-liposomes of various sizes in rabbits. *Int J Pharm* 2003;**253**:121-32.
37. Schwarz JCV, van Lier MGJTB, Bakker ENTP, de Vos J, Spaan JAE, VanBavel E, et al. Optimization of vascular casting for three-dimensional fluorescence cryo-imaging of collateral vessels in the ischemic rat hindlimb. *Microsc Microanal* 2017;**23**:77-87.
38. Crandall C, Gonzalez-Alonso J. Cardiovascular function in the heat-stressed human. *Acta physiologica* 2010;**199**:407-23.
39. Momekova D, Momekov G, Rangelov S, Lambov N. *In vitro* biocompatibility study of free and liposomally-grafted copolymers bearing short blocks of aliphatic lipid-mimetic units cytotoxicity and hemolytic activity. *J Drug Deliv Sci Technol* 2007;**17**:393-7.
40. Kim IS, Choi HG, Choi HS, Kim BK, Kim CK. Prolonged systemic delivery of streptokinase using liposome. *Arch Pharm Res* 1998;**21**:248-52.



ORIGINAL RESEARCH ARTICLE

Artocarpin induces cell apoptosis in human osteosarcoma cells through endoplasmic reticulum stress and reactive oxygen species

Chiang-Wen Lee^{1,2,3*} | Miao-Ching Chi^{4,5,6*} | Tsung-Ming Chang⁷ | Ju-Fang Liu^{8,9}

¹Department of Nursing, Division of Basic Medical Sciences, and Chronic Diseases and Health Promotion Research Center, Chang Gung University of Science and Technology, Chia-Yi, Taiwan, Republic of China

²Research Center for Industry of Human Ecology and Research Center for Chinese Herbal Medicine, College of Human Ecology, Chang Gung University of Science and Technology, Taoyuan, Taiwan, Republic of China

³Department of Rehabilitation, Chang Gung Memorial Hospital, Chia-Yi, Taiwan, Republic of China

⁴Chronic Diseases and Health Promotion Research Center, Chang Gung University of Science and Technology, Chiayi County, Taiwan, Republic of China

⁵Department of Respiratory Care, Chang Gung University of Science and Technology, Chiayi County, Taiwan, Republic of China

⁶Division of Pulmonary and Critical Care Medicine, Chiayi Chang Gung Memorial Hospital, Taiwan, Republic of China

⁷Department of Physiology, School of Medicine, National Yang-Ming University, Taipei, Taiwan, Republic of China

⁸Central Laboratory, Shin-Kong Wu Ho-Su Memorial Hospital, Taipei, Taiwan, Republic of China

⁹Department of Medical Research, China Medical University Hospital, China Medical University, Taichung, Taiwan, Republic of China

Correspondence

Ju-Fang Liu, Central Laboratory, Shin-Kong Wu Ho-Su Memorial Hospital, No. 95, Wenchang road, Shilin, Taipei 11101, Taiwan. Email: T010615@ms.skh.org.tw

Funding information

Ministry of Science and Technology, Grant/Award Numbers: 106-2314-B-341-001-MY3, MOST-107-2314-B-341-003; Shin-Kong Wu Ho-Su Memorial hospital, Grant/Award Number: 2018SKHBND001; Chang Gung University of Science Foundation, Grant/Award Numbers: ZRRPF6H0011, ZRRPF6H0021

Abstract

Osteosarcoma is a malignant primary bone tumor that responds poorly to both chemotherapy and radiation therapy. However, because of side effects and drug resistance in chemotherapy and the insufficiency of an effective adjuvant therapy for osteosarcoma, it is necessary to research novel treatments. This study was the first to investigate the anticancer effects of the flavonoid derivative artocarpin in osteosarcoma. Artocarpin induced cell apoptosis in three human osteosarcoma cell lines—U2OS, MG63, and HOS. Artocarpin was also associated with increased intracellular reactive oxygen species (ROS). Mitochondrial dysfunction was followed by the release of cytochrome c from mitochondria and accompanied by decreased antiapoptotic Bcl-2 and Bcl-xL and increased proapoptotic protein Bak and Bax. Artocarpin triggered endoplasmic reticulum (ER) stress, as indicated by changes in cytosol calcium levels and increased glucose-regulated protein 78 and 94 expressions, and also increased calpains expression and activity. Animal studies revealed a dramatic 40% reduction in tumor volume after 18 days of treatment. This study demonstrated a novel anticancer activity of artocarpin against human osteosarcoma cells and in murine tumor models. In summary, artocarpin significantly induced cell apoptosis through ROS, ER stress, mitochondria, and the caspase pathway, and may thus be a novel anticancer treatment for osteosarcoma.

KEYWORDS

artocarpin, apoptosis, ER stress, osteosarcoma, ROS

*Lee and Chi have contributed equally to this work.

1 | INTRODUCTION

Osteosarcoma is high-grade primary malignant tumor characterized by the production of osteoid or immature bone through malignant cells (Yang & Zhang, 2013). The affected population consists predominantly of children, teenagers, and young adults (DelaGarza-Montano et al., 2015). The current management strategy for newly diagnosed osteosarcoma includes neoadjuvant chemotherapy followed by surgical removal of the primary tumor and all clinically evident metastatic disease, with additional adjuvant chemotherapy after surgery (Bacci & Lari, 2001). However, because chemotherapy carries the risk of side effects and induced drug resistance in osteosarcoma (Tsai, Huang, Su, & Tang, 2014) and because effective adjuvant therapy is insufficient, it is necessary to research novel treatment methods.

The endoplasmic reticulum (ER) is the central intracellular organelle for many cellular functions, including lipid synthesis, protein folding, and maturation (Chaudhari, Talwar, Parimisetty, Lefebvre d'Hellencourt, & Ravanan, 2014). Various physiological and pathological conditions such as viral infection, energy or nutrient deprivation, and alteration in the redox status can disturb ER functioning and result in stress-related events (He, 2006). Increasing evidence suggests that the ER also regulates apoptosis by both transferring Ca^{2+} to mitochondria and initiating its own cell death signals (Barateiro, Vaz, Silva, Fernandes, & Brites, 2012). Within the ER reside molecular chaperones that facilitate proper folding of proteins, maintain their folded state, and prevent protein-folding intermediates from aggregating. Among the most thoroughly characterized ER chaperones is glucose-regulated protein (GRP; Zhang, 2017). Several studies have established that induction of GRP78 is a marker for ER stress (Chen, Fu, Li, & Zhao, 2014; Kaira et al., 2016). GRP78 is a multifunctional chaperone involved in nascent chain translocation, polypeptide folding, resolving and removing misfolded proteins, and monitoring ER stress transducers. It is a central regulator for ER stress because of its role as a major ER chaperone with antiapoptotic properties and its ability to control activation of transmembrane ER stress sensors (IRE1, PERK, and ATF6) through a binding-release mechanism. Calpains are a family of Ca^{2+} -dependent intracellular cysteine proteases (Siman, Flood, Thinakaran, & Neumar, 2001). The ubiquitously expressed calpain I (μ -form) and calpain II (m-form) proteases are implicated in apoptosis development (Muruganandan & Cribb, 2006). They differ in their calcium requirements for activation (approximately 5–50 μM for calpain I and approximately 200–1,000 μM for calpain II; Salehin et al., 2010). Calpain activation can induce downstream apoptosis-related caspase cleavage and thus trigger apoptosis (Tan et al., 2006). Furthermore, activation of the mitochondrial-dependent cell death pathway is accompanied by reactive oxygen species (ROS) accumulation and further transformed sequentially into more toxic ROS, such as hydrogen peroxide ROS, consequently inducing cell death (Feig, Sowers, & Loeb, 1994; Roos & Kaina, 2006).

Artocarpus altilis (Moraceae) is found in the wild in tropical and subtropical parts of Asia (Tiraravesit et al., 2015), where it is prized for its extraordinary medicinal value, such as in treating inflammation, diabetes,

malarial fever, and diarrhea (Jagtap & Bapat, 2010). Artocarpin (6-(3-methyl-1-butenyl)-5,2',4'-trihydroxy-3-isoprenyl-7-methoxy flavone; Figure 1a) is an isoprenyl flavone compound with many antibacterial (Septama & Panichayupakaranant, 2015), anti-inflammatory (Lee et al., 2013), and antioxidation (Lan, Tzeng, Lin, Yen, & Ko, 2013) bioactivities in diverse cells. In addition, several studies have reported that the anticancer effect of artocarpin has been studied mainly in various cancers. For example, artocarpin induces p53-dependent or p53-independent apoptosis in non-small-cell lung cancer cells (Tsai et al., 2017). Lee et al. reported that artocarpin induced mitochondria-associated apoptosis in human glioblastoma cells (Lee et al., 2018). However, the molecular mechanisms underlying artocarpin's pharmacological properties and therapeutic effects for osteosarcoma remain unknown.

In this study, we demonstrated that artocarpin markedly increases cytotoxicity in osteosarcoma cell lines and observed, for the first time, that it activates ROS, mitochondria dysfunction, and ER stress, thereby activating caspase-dependent apoptotic pathways.

2 | MATERIALS AND METHODS

2.1 | Materials

Horseradish peroxidase-conjugated antimouse and antirabbit immunoglobulin G, and rabbit polyclonal antibodies specific for cytochrome c, VDAC, Bak, Bax, Bcl-2, Bcl-xL, GRP78, GRP94, calpain and II, PARP, caspase 3, caspase 9, and β -actin (1:1,000 dilution) were purchased from GeneTex (Irvine, CA). All other chemicals were obtained from Sigma-Aldrich Corp (St. Louis, MO).

2.2 | Cell culture

The human osteosarcoma cell lines (MG-63, U2OS, and HOS) and osteoblast cell line (hFOB 1.19) were purchased from American Type Culture Collection (ATCC; Manassas, VA). MG-63, U2OS, HOS, and hFOB 1.19 cells were maintained in Dulbecco's modified Eagle's medium (DMEM), McCoy's 5A, DMEM, and DMEM/Ham's F-12 medium respectively. MG-63, U2OS, and HOS cells were incubated at 37°C in an atmosphere of 5% CO_2 supplemented with 20 mM of hydroxyethyl piperazineethanesulfonic acid (HEPES), 10% heat-inactivated fetal calf serum (FBS), 2 mM of glutamine, 100 U/ml penicillin, and 100 $\mu\text{g}/\text{ml}$ of streptomycin (Invitrogen, Carlsbad, CA). The hFOB 1.19 cells were incubated at 34°C in an atmosphere of 5% CO_2 supplemented with 10% heat-FBS and 0.3% G418 (Sigma-Aldrich Corp., St. Louis, MO). The medium was changed every 48 hr.

2.3 | Cytotoxicity assay

The cytotoxicity of artocarpin was determined with the 3-(4,5-dimethylthiazol-2-yl)-2,5-diphenyl-2H-tetrazolium bromide (MTT) assay. The cells were seeded in 200 μl of the medium at a concentration of 5×10^3 in 96 well plate. After treating with

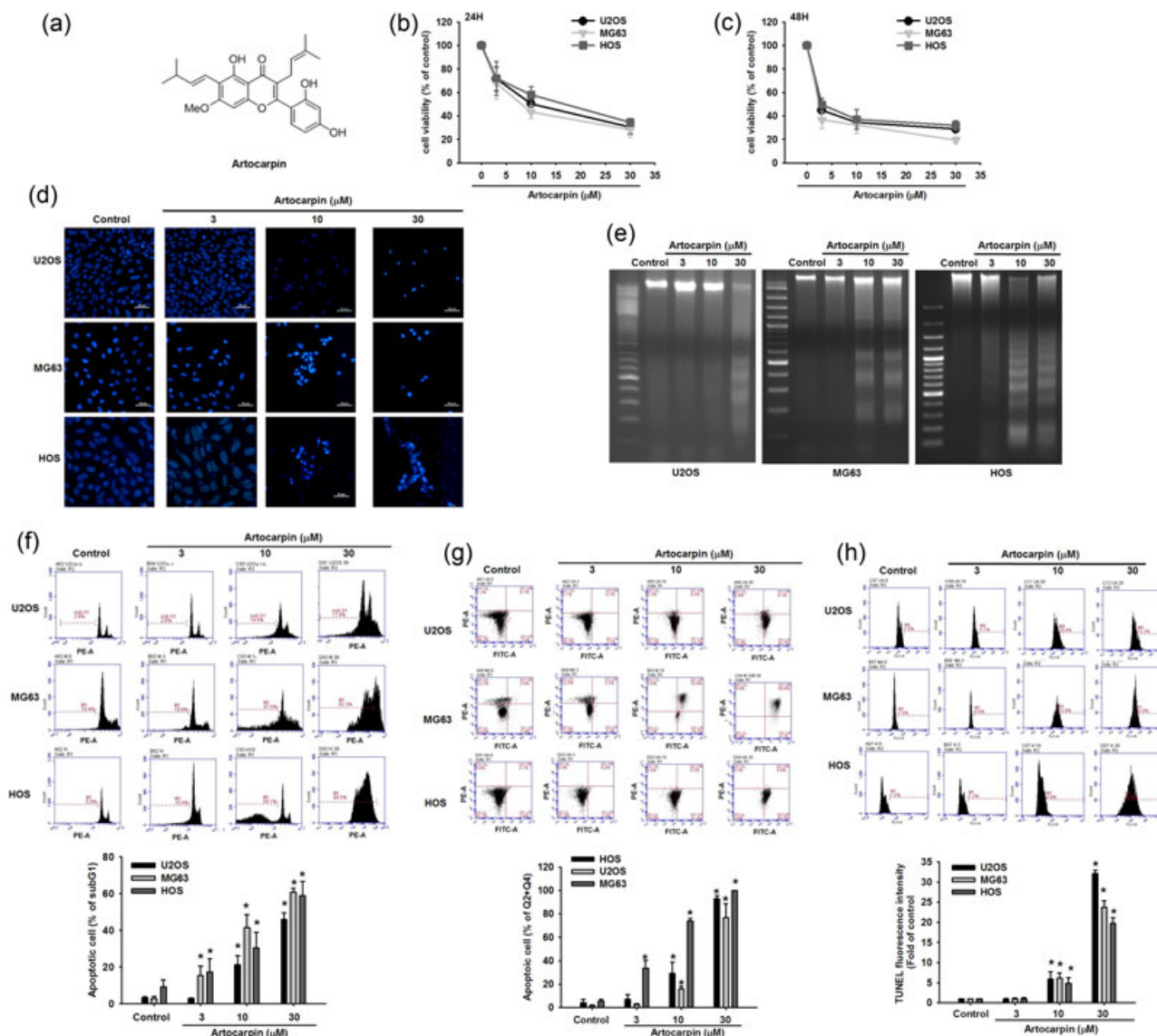


FIGURE 1 Artocarpin induced cell apoptosis in osteosarcoma cells. (a) Structure of artocarpin. (b,c) Cells were incubated with various concentrations of artocarpin for different periods of time (1 or 2 days), and cell viability was examined through MTT assay. (d) After cells were incubated with various concentrations of artocarpin for 24 hr, the nucleus morphology was determined by using DAPI staining and photographed. (e) After cell lysates were collected for DNA purification, DNA gel electrophoresis was performed as described in the materials and methods section. (f–h) After cells were incubated with various concentrations of artocarpin for 24 hr, the percentage of apoptotic cells was analyzed through flow cytometric analysis of PI-stained cells (g), Annexin V/PI double staining (f), and TUNEL staining (h). Results are expressed as mean \pm standard error of the mean. * $p < 0.05$ as compared with control group. DAPI, 4',6-diamidino-2-phenylindole; MTT, 3-(4,5-dimethylthiazol-2-yl)-2,5-diphenyl-2H-tetrazolium bromide; TUNEL, terminal deoxynucleotidyl transferase-mediated deoxyuridine triphosphate nick-end labeling [Color figure can be viewed at wileyonlinelibrary.com]

artocarpin (3–30 μ M) for 1 and 2 days, cultures were washed with PBS. Then MTT (0.5 mg/ml) was added to each well and the mixture was incubated at 37°C for 2 hr. To dissolve formazan crystals, the culture medium was then replaced with an equal volume of DMSO. After the mixture was shaken at room temperature for 10 min, the absorbance of each well was determined at 550 nm using a microplate reader (Bio-Tek, Winooski, VT; J.F. Liu, Fong, Chang, Kuo, Chang, & Tang, 2011b).

2.4 | DNA ladder assay

Cells (1×10^6 cells) were treated with artocarpin (3–30 μ M) for 24 hr, total DNA was extracted and used to agarose electrophoresis. Ethidium bromide staining was used to assess DNA fragmentation as detection for apoptosis. The DNA samples were performed to electrophoresis by 2% agarose gel, and the DNA was stained with ethidium bromide. Ultraviolet spectroscopy at 302 nm was used to report results.

2.5 | Analysis of cell cycle by flow cytometry

Quantitative assessment of apoptotic cells was assessed by examining the cell cycle. Cells were collected by centrifugation and adjusted to 2×10^6 cells/ml. Prechilled ethanol was added to 0.5 ml of cell suspensions and the mixture was incubated at 4°C for 30 min. Ethanol was then removed by centrifugation, and cellular DNA was stained with 500 μ l propidium iodide (PI) solution (0.1% Triton-X 100, 100 μ g/ml DNase-free RNase A, and 10 μ g/ml PI in phosphate-buffered saline [PBS]). After staining, cells were analyzed immediately with a FACScan and CellQuest program (Becton Dickinson, Mountain View, CA). The extent of apoptosis was determined by measuring the DNA content of cells below sub-G₁ peak (J. T. Chen et al, 2008).

2.6 | Quantification of apoptosis by flow cytometry

Apoptosis was assessed by using Annexin V, a protein that binds to phosphatidylserine residues exposed on the cell surface of apoptotic cells, as previously described (Dijkers et al., 2002). 1×10^6 cells were treated with artocarpin (3–30 μ M) for the indicated times, washed twice with cold PBS, and resuspended in staining buffer containing 1 μ g/ml propidium iodide (PI) and 0.025 μ g/ml Annexin V-fluorescein fluorescent dye (FITC). Double-labeling was performed at room temperature for 30 min in the dark, and cells were immediately analyzed by FACScan and the CellQuest program (Becton Dickinson, Mountain View, CA; Liu et al., 2011a).

Quantitative assessment of apoptotic cells was assessed by terminal deoxynucleotidyl transferase mediated deoxyuridine triphosphate nick-end labeling (TUNEL) assay, which examines DNA-strand breaks during apoptosis using BD Apo-Alert™ DNA Fragmentation Assay Kit. Briefly, cells were incubated with artocarpin for the indicated times. The cells were trypsinized and fixed with 4% paraformaldehyde for 15 min at 4°C. The fixed cells were incubated with digoxigenin-conjugated dUTP in a terminal deoxynucleotidyl transferase recombinant (rTdT)-catalyzed reaction and nucleotide mixture for 1 hr at 37°C in a humidified atmosphere, and then immersed in stop/wash buffer for 15 min at room temperature. The stained cells were then analyzed by flow cytometry (Liu, Huang, Yang, Chang, & Tang, 2012).

2.7 | 4',6-Diamidino-2-phenylindole (DAPI) staining

Cells (5,000 cells/ml) in 24-well plates were incubated with artocarpin (3–30 μ M) for the indicated times. Cells in each treatment were individually fixed with 3.7% (vol/vol) formaldehyde (Sigma-Aldrich Corp.) for 15 min and then stained by DAPI (0.5 μ g/ml) for determining cell chromatin condensation. All samples were examined and photographed using Nikon Eclipse TE300 inverted fluorescence microscope (Nikon Corp. Tokyo, Japan; Lin et al., 2013).

2.8 | Determination of the ROS, production, Ca²⁺ concentration, and mitochondrial membrane potential (MMP)

Cells (5×10^5) were plated in six-well plates, grown to confluence, and treated with artocarpin for the indicated times. After incubation, cells were stained with H₂DCFDA (10 μ M) for ROS determination, Fluo 3/AM (3 μ g/ml) for Ca²⁺ levels, and JC-1 (5 μ g/ml) for $\Delta\psi$ m. And cells were immediately analyzed by FACScan and the CellQuest program (Becton Dickinson, Mountain View, CA; Liu et al., 2011a).

2.9 | Western blot analysis

Cellular lysates were prepared as we described (Chen et al., 2008). Proteins were resolved on a 10–15% SDS-PAGE and transferred to Immobilon polyvinylidene difluoride membranes. The blots were blocked with 5% BSA for 1 hr at room temperature and then probed with rabbit anti-human antibodies against cytochrome c, VDAC, Bak, Bax, Bcl-2, Bcl-xL, GRP78, GRP94, calpain I, calpain II, PARP, caspase 3, caspase 9, and β -actin (1:1,000 dilution) for 1 hr at room temperature. After washed three times, the blots were incubated with a peroxidase-conjugated donkey anti-rabbit secondary antibody (1:1,000 dilution) for 1 hr at room temperature. Protein bands were visualized through enhanced chemiluminescence using an ultraviolet trans-illuminator with an UVP-Biochemi Imaging System (UVP-Bioimaging Systems, UVP, Inc., Upland, CA). Quantitative data were obtained using the ImageJ software (National Institute of Health).

2.10 | siRNA transfection

The siRNAs against human calpain I, calpain II, and control siRNA were purchased commercially from Santa Cruz Biotechnology (Dallas, TX). Calpain-I siRNA (catalog no. sc-29885), a pool of three target-specific 20–25 nt siRNAs; calpain-II siRNA (catalog no. sc-41459), a target-specific 20–25 nt siRNA. The control siRNA (catalog no. sc-37007) is a nontargeting 20–25 nt siRNA designed as a negative control. Cells were transfected with siRNAs (at a final concentration of 100 nM) using Lipofectamine 3,000 (Invitrogen, Carlsbad, CA) according to the manufacturer's instructions.

2.11 | Caspase activity assay

The assay is based on the ability of an active enzyme to cleave chromophore from enzyme substrate Ac-LEHD-pNA (for caspase 9) or Ac-DEVD-pNA (for caspase 3), appropriate substrates (200 μ M) were added for the respective caspases. Immunocomplexes were incubated with peptide substrate in assay buffer (100 mM NaCl, 50 mM HEPES, 10 mM dithiothreitol, 1 mM EDTA, 10% glycerol, 0.1% 3-[(3-cholamidopropyl)dimethylammonio]-1-propanesulfonate (pH 7.4) for 2 hr at 37°C. The release of *p*-nitroaniline was monitored at 405 nm. Results shown are the percent change in activity compared to untreated control.

In experiments with caspases inhibitors, recombinant enzymes were preincubated with specific inhibitors of caspases 3 (Z-DEVD-FMK; 100 μ M) and caspase 9 (Z-LEHD-FMK; 100 μ M) for 60 min before stimulation with artocarpin (10 μ M).

2.12 | In vivo tumor xenograft study

All animal experiments were performed in accordance with a protocol approved by the Institutional Animal Care and Use Committees of Shin-Kong Wu Ho-Su Memorial Hospital (Taipei, Taiwan). Male CB17-SCID mice 4-week old purchased from Lasco (BioLASCO Co., Ltd, Taipei, Taiwan) and maintained in pathogen-free conditions. MG63 cells were injected subcutaneously into the flanks of these SCID mice (2×10^6 cells in 200 μ l) and tumors were allowed to develop for 14 days until they reached a size of approximately 100 mm³, when treatment was initiated. Seven animals per group were used, and the experiment was repeated twice. The mice were treated with vehicle, artocarpin (1 mg/kg) every day for 18 days (10 mice/group). The volume of the implanted tumor in the dorsal side of mice was measured twice a week with a caliper, using the formula $V = (LW^2)/2$, where V is the volume (mm³), L is the biggest diameter (mm), W is the smallest diameter (mm). After 18 days, mice were killed by administering an overdose of anesthetic.

To investigate the cell apoptotic effect of artocarpin in tumor tissues in vivo, paraffin-embedded tumor sections were prepared, mounted on slides, deparaffinized in xylene, rehydrated, and washed in distilled water. Protein was removed by digesting the sections with 20 μ g/ml proteinase K for 15 min. After washing, labeling was performed by covering the sections with the TUNEL reaction mixture at 37°C for 60 min. The reaction was blocked in stop/wash buffer for 10 min. The TUNEL labeling was visualized using fluorescence microscopy. TUNEL staining was performed using the Apoptosis Detection Kit (Trevigen, Gaithersburg, MD).

2.13 | Statistical analysis

The values reported mean \pm standard error of the mean. Statistical analysis between two samples was performed using Student's t test. Statistical comparisons of more than two groups were performed using one-way analysis of variance with Bonferroni's post-hoc test. In all cases, $p < 0.05$ was considered significant.

3 | RESULTS

3.1 | Artocarpin induced apoptosis in human osteosarcoma cells

To investigate the artocarpin's effect on human osteosarcoma cells (U-2 OS, MG63, and HOS), we first examined its effect on cell survival using MTT assay. The osteosarcoma cells were incubated with artocarpin (0, 3, 10, and 30 μ M) for 24 or 48 hr, with the results indicating that artocarpin reduced cell viability (Figure 1b). The IC₅₀ values at 48 hr of artocarpin were 2.7, 2.1, and 3.14 μ M for U-2 OS,

MG63, and HOS, respectively (Figure 1c). To verify whether artocarpin induced cell death through an apoptotic mechanism, we performed DAPI staining and DNA ladder assay. The data indicated that artocarpin dramatically increased chromatin condensation and degradation in DAPI staining and DNA ladder assay, respectively (Figure 1d,e). In addition, artocarpin-induced apoptosis was also confirmed by an increased percentage of cells in the sub-G1 phase, annexin V/PI double-labeling, and TUNEL assay (Figure 1f–h). These results all indicated that artocarpin induced cell apoptosis in osteosarcoma cells.

3.2 | ROS and mitochondria dysfunction are involved in artocarpin-induced apoptosis in human osteosarcoma cells

Studies have indicated that ROS play a pivotal role in apoptosis and serve as anticancer agents (Kim et al., 2005; Zhang & Chen, 2004). Therefore, we investigated whether ROS accumulation was involved in artocarpin-induced cell death. As shown in Figure 2a, the results indicated that artocarpin treatment of osteosarcoma cells induced ROS accumulation. Pretreatment of cells with the ROS scavenger *N*-acetyl cysteine (NAC), the nicotinamide adenine dinucleotide phosphate oxidase inhibitor diphenyleneiodonium chloride (DPI), and catalase (H₂O₂ scavenging enzyme) reduced artocarpin-induced cell apoptosis (Figure 2b,c). One study reported that ROS production and accumulation in mitochondria led to decreased MMP, which elicits the mitochondrial apoptotic pathway (Kowaltowski, Castilho, & Vercesi, 2001). Tetraethylbenzimidazolylcarbocyanine iodide (JC-1), a cationic dye that accumulates in energized mitochondria. JC-1 accumulated as aggregates in the mitochondrial membranes, yielding a red to orange fluorescence in normal cells. In unhealthy cells showed a monomer that yields green fluorescence (FITC). Treatment of cells with artocarpin induced marked changes in mitochondrial membrane protein, as demonstrated by the disappearance of orange-red fluorescence or the increase of green fluorescence. Our data also indicated that artocarpin treatment of osteosarcoma cells induced MMP loss (Figure 2d), altered the expression of Bcl-2 family proteins, thereby resulting in an increased proapoptotic/antiapoptotic Bcl-2 ratio (Figure 2e,f). These results revealed that artocarpin induced apoptosis through ROS and the mitochondrial apoptotic pathway in osteosarcoma cells.

3.3 | Artocarpin induced Ca²⁺ release and GRP78, GRP94, and calpain expression

To determine whether artocarpin induced apoptosis by triggering ER stress, we first assessed its effect on the mobilization of Ca²⁺. When cells were treated with artocarpin, Ca²⁺ levels significantly increased compared with the sham-treated group. The results also demonstrated that artocarpin promoted Ca²⁺ release in a time-dependent manner (Figure 3a). However, pretreatment of cells with BAPTA-AM (Ca²⁺ chelator) reduced artocarpin-induced cell apoptosis in human osteosarcoma cells (Figure 3b,c). We next determined whether calpain expression in osteosarcoma cells would be induced by artocarpin. As

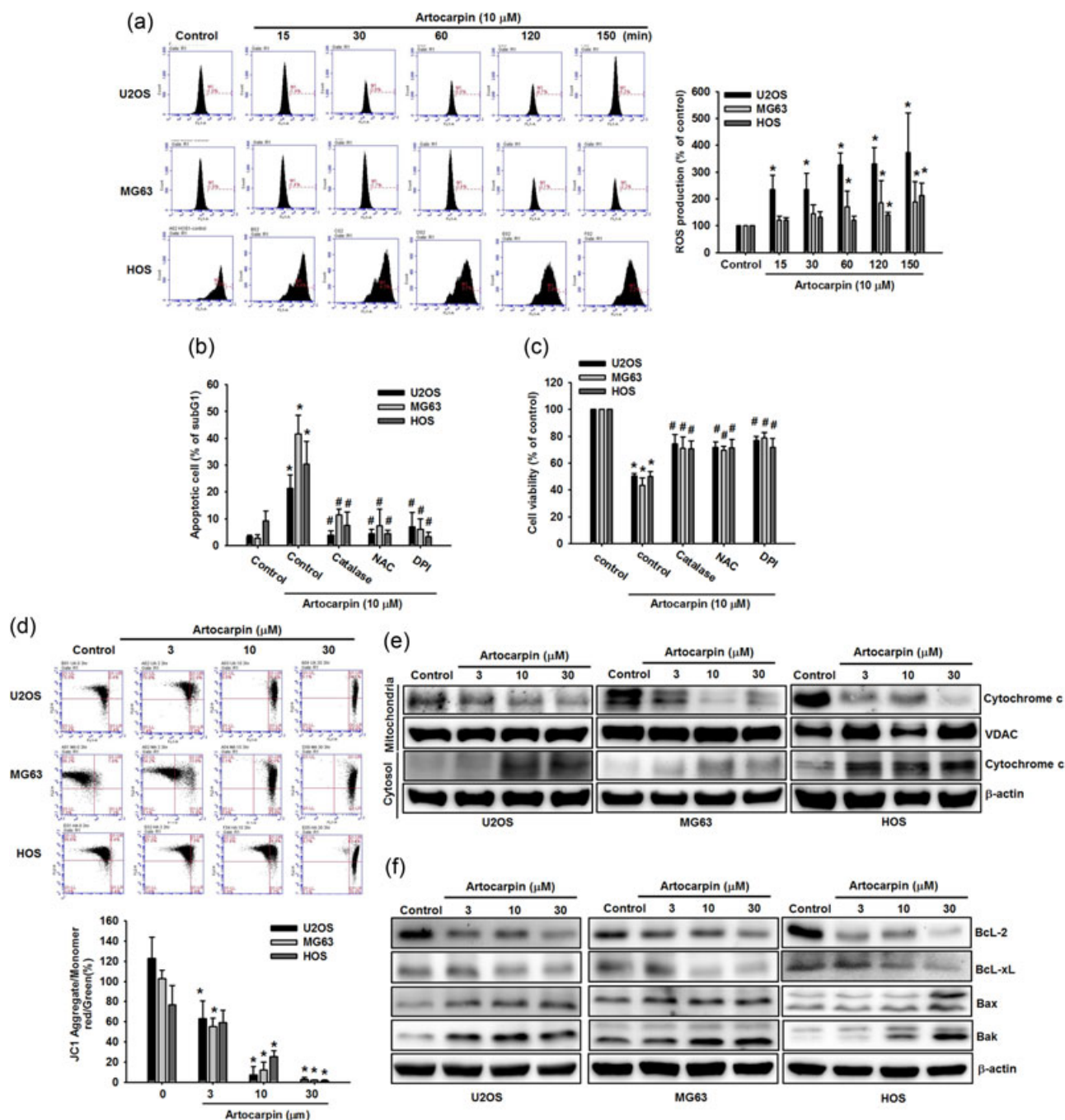


FIGURE 2 Artocarpin induced ROS generation and mitochondria dysfunction in human osteosarcoma cells. (a) Cells were treated with artocarpin (10 μ M) for different periods of time. ROS production (H₂O₂ concentration) was examined through flow cytometry. (b) After cells were pretreated for 30 min with NAC, DPI, and catalase, followed by stimulation with artocarpin (10 μ M) for 24 hr, cell viability was examined using MTT assay. (c) After cells were treated as described in (a), the percentage of apoptotic cells was analyzed through flow cytometric analysis of PI-stained cells. (d) After cells were incubated with various concentrations of artocarpin for 4 hr, their MMP was examined through flow cytometry using JC-1 staining. (e,f) After cells were treated with different concentrations of artocarpin for 8 hr, expression levels of Bcl-2, Bcl-xL, Bak, Bax, mitochondrial cytochrome c, and cytosolic cytochrome c were examined using western blot analysis, with β -actin and VDAC used as internal controls. Results are expressed as mean \pm standard error of the mean. * $p < 0.05$ compared with controls. # $p < 0.05$ compared with artocarpin-treated group. JC-1, tetraethylbenzimidazolylcarbocyanine iodide; MMP, mitochondrial membrane potential; MTT, 3-(4,5-dimethylthiazol-2-yl)-2,5-diphenyl-2H-tetrazolium bromide; ROS, reactive oxygen species [Color figure can be viewed at wileyonlinelibrary.com]

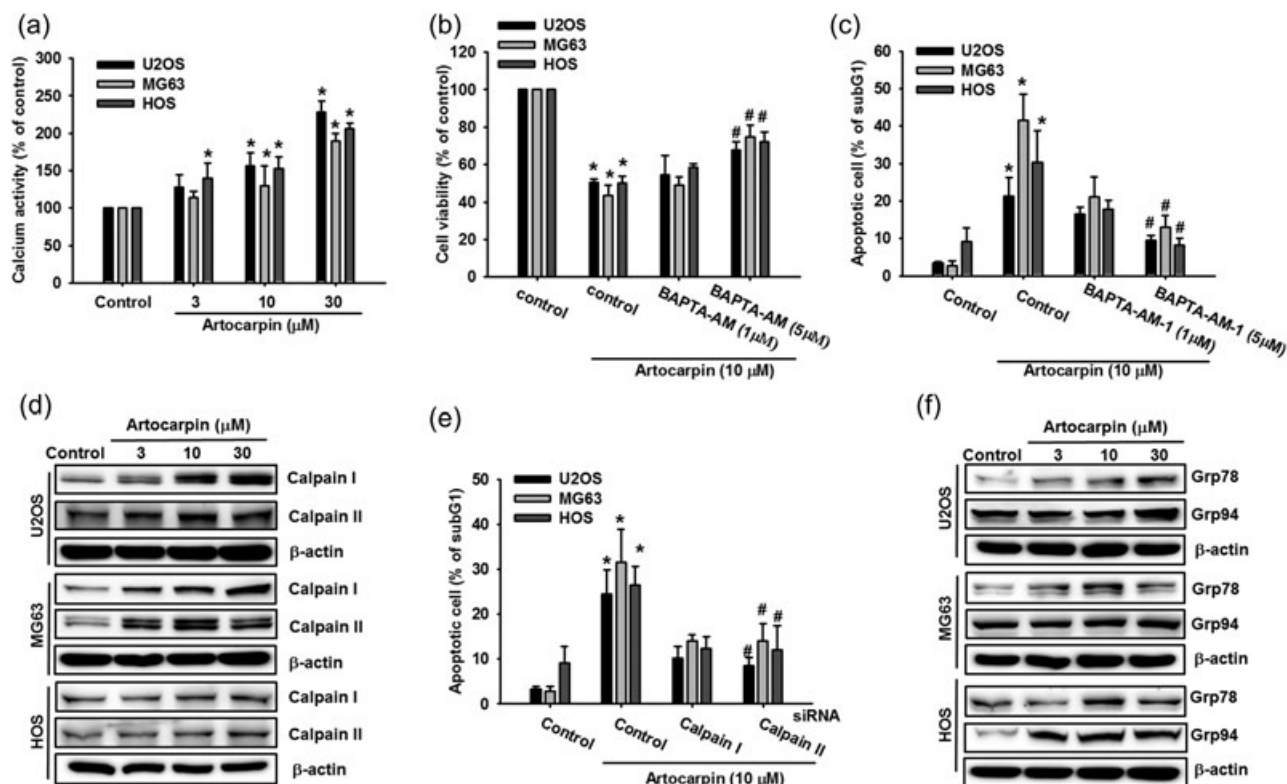


FIGURE 3 Artocarpin induced Ca^{2+} release and ER stress in osteosarcoma cells. (a) After cells were incubated with various concentrations of artocarpin, Ca^{2+} expression was examined through flow cytometry ($n = 4$). (b) After cells were pretreated for 1 hr with BAPTA-AM (1 or 5 μM), followed by stimulation with artocarpin (10 μM) for 24 hr, cell viability was examined through MTT assay. (c) After cells were treated as described in (b), the percentage of apoptotic cells was analyzed through flow cytometric analysis of PI-stained cells. (d) After cells were treated with different concentrations of artocarpin for 8 hr, expression levels of calpain I and II were examined using western blot analysis, with β -actin as an internal control. (e) After cells were transfected with calpain I, calpain II, or control siRNA for 24 hr, followed by incubation with artocarpin for 24 hr, the percentage of apoptotic cells was analyzed through flow cytometric analysis using cell cycle assay. (f) After cells were treated with different concentrations of artocarpin for 8 hr, GRP78 and GRP94 expression levels were examined using western blot analysis, with β -actin as an internal control. Results are expressed as means \pm standard error of the mean. * $p < 0.05$ compared with control. # $p < 0.05$ compared with artocarpin-treated group. ER, endoplasmic reticulum; MTT, 3-(4,5-dimethylthiazol-2-yl)-2,5-diphenyl-2H-tetrazolium bromide

shown in Figure 3d, artocarpin increased calpain I and II expression in a dose-dependent manner. Moreover, transfection of cells with calpain I or II siRNA markedly reduced artocarpin-mediated cell apoptosis (Figure 3d,e). Because GRP78 is a major ER chaperone and plays a vital role in regulating ER homeostasis, we examined the effects of artocarpin on GRP78 and GRP94 expression in human osteosarcoma cells. Artocarpin markedly increased GRP78 and GRP94 levels in a dose-dependent manner (Figure 3f). Our data thus indicated that Ca^{2+} release and GRP78, GRP94, and, calpain I and II activation were involved in artocarpin-mediated cell apoptosis.

3.4 | Artocarpin increased caspase 3 and caspase 9 expression in human osteosarcoma cells

ER stress-triggered apoptosis involves activation of the intrinsic apoptosis pathway, including caspase 3 and caspase 9 activity. Treatment with artocarpin reduced procaspase-3 expression, increased caspase-3 activity in osteosarcoma cells (Figure 4a,b), and reduced procaspase-9 expression (Figure 4a,c). Pretreatment of

cells with the caspase-3 inhibitor z-DEVD-FMK and the caspase-9 inhibitor z-LEDH-FMK reduced artocarpin-induced cell death (Figure 4d,e). These results indicated that artocarpin triggered caspases and induced apoptosis in osteosarcoma cells.

3.5 | Artocarpin inhibited tumor growth in mouse xenograft model

To determine whether artocarpin possesses antitumor activities in vivo, we established xenografts of MG63 cells in SCID mice. When the tumors reached 100 mm^3 in size, the mice were divided into two groups and treated with either vehicle or artocarpin (1 $\text{mg} \cdot \text{kg}^{-1} \cdot \text{day}^{-1}$). The average tumor volume in mice treated with artocarpin was significantly lower than that in vehicle-treated controls (Figure 5a,b). Treatment of mice with artocarpin significantly induced apoptosis (Figure 5d). Ex vivo analysis using western blot analysis of excised tumors demonstrated significantly increased Bcl-2, Bcl-xl, Bax, Bak, GRP78, GRP94, and calpain I and II expression in the artocarpin-treated group compared with the control group (Figure 5e,f). These

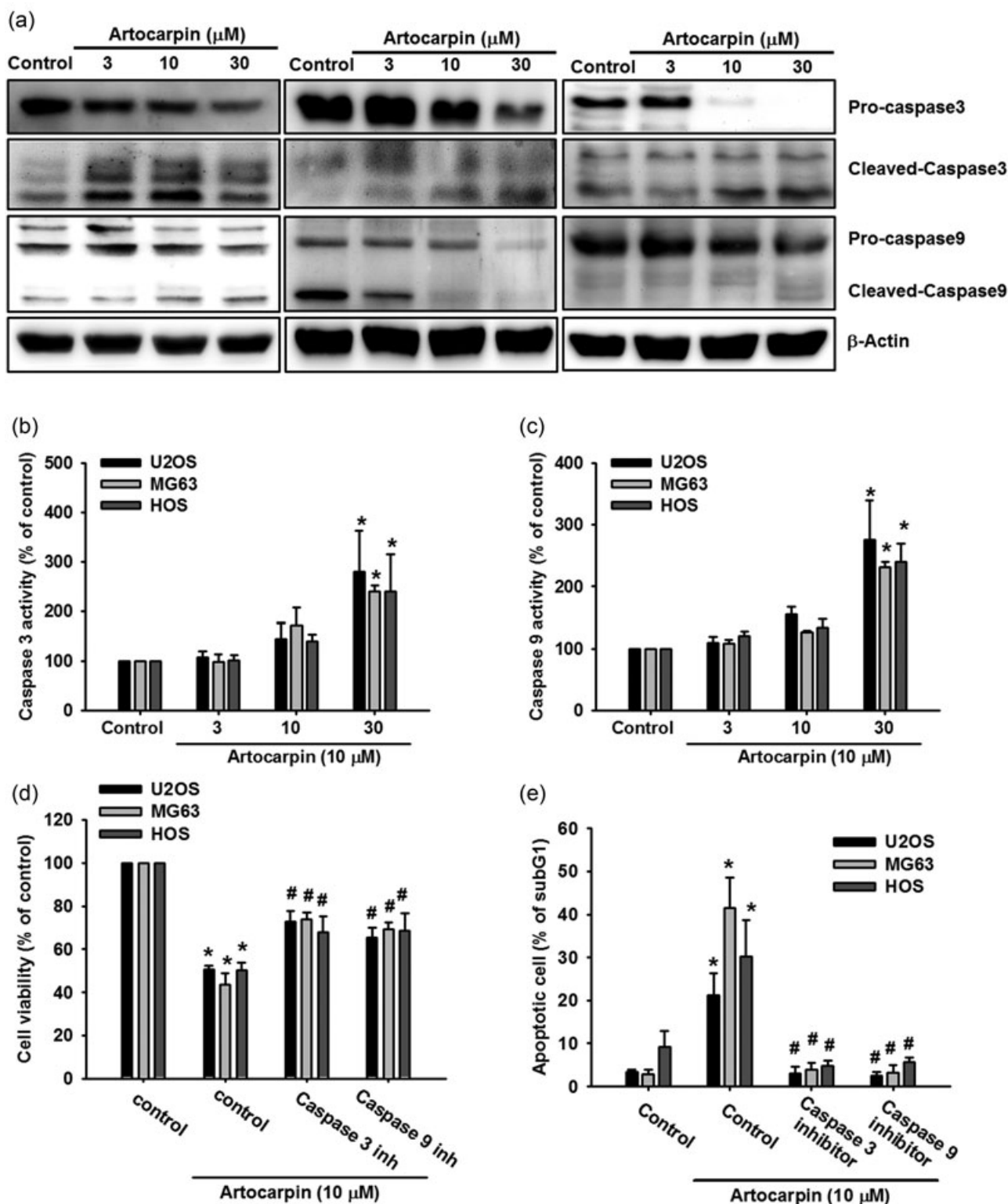


FIGURE 4 Artocarpin induced caspase activation in human osteosarcoma cells. (a) After cells were treated with different concentrations of artocarpin for 8 hr, caspase-3 and -9 expression levels were examined by using western blot analysis, with β -actin as an internal control. (b,c) After cells were incubated with artocarpin (10 μ M) for 8 hr, caspase 3 and caspase 9 activities were examined using the caspase ELISA kit. (d) After cells were pretreated for 1 hr with z-DEVD-FMK (caspase-3 inhibitor) or z-LEHD-FMK (caspase-9 inhibitor), followed by stimulation with artocarpin (10 μ M) for 24 hr, cell viability was examined through MTT assay. (e) After cells were treated as described in (d), the percentage of apoptotic cells was analyzed through flow cytometric analysis of PI-stained cells. Results are expressed as means \pm standard error of the mean. * p < 0.05 compared with control. # p < 0.05 compared with artocarpin-treated group. ELISA, enzyme-linked immunosorbent assay; MTT, 3-(4,5-dimethylthiazol-2-yl)-2,5-diphenyl-2H-tetrazolium bromide

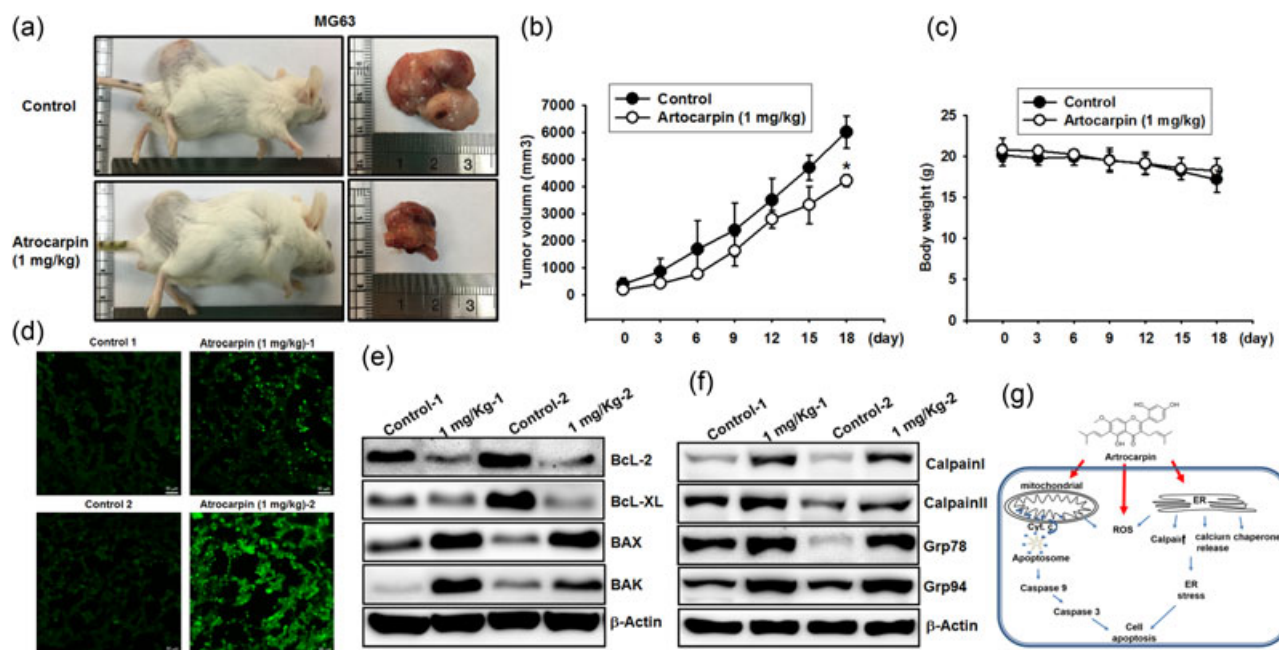


FIGURE 5 Artocarpin inhibited tumor growth in SCID mice. (a,b) Mice were injected subcutaneously with MG63 tumor cells. After the tumors reached 100 mm³ in size, artocarpin or vehicle (1 mg·kg⁻¹·day⁻¹) was administered for 18 days. The mean tumor volume was then measured at the indicated number of days after implantation ($n = 6-8$). (c) Mean body weight was measured at the indicated number of days after implantation. (d) Tumor sections were stained to identify apoptosis cells through TUNEL assay for DNA fragmentation. (e,f) Western blot analysis determined the levels of Bcl-2, Bcl-xl, Bax, Bak, GRP78, GRP94, calpain I, and calpain II expression in tumors with and without artocarpin treatment. (g) Schematic of artocarpin activity. Results are expressed as means \pm standard error of the mean. * $p < 0.05$ compared with control. TUNEL, terminal deoxynucleotidyl transferase-mediated deoxyuridine triphosphate nick-end labeling [Color figure can be viewed at wileyonlinelibrary.com]

results indicated that artocarpin inhibited tumor growth by inducing osteosarcoma cell apoptosis in vivo.

4 | DISCUSSION

Although osteosarcoma is a rare malignant cancer, it constitutes the most common primary bone malignancy. Its biology is most commonly characterized by an appendicular primary tumor with a high rate of lung metastasis (Ottaviani & Jaffe, 2009). Treatment of osteosarcoma requires the use of chemotherapy, surgery, and radiation therapy, with a 5-year survival rate of 60–70% (Fromiguet et al., 2011). Clinically, surgical resection remains the primary mode of therapy for osteosarcoma. Multiagent treatment of osteosarcoma is associated with acute long-term toxicities, including potential hearing loss and hypomagnesemia. Exploration and development of novel treatment methods for osteosarcoma are thus urgently required. In this study, we not only revealed a previously unknown effect of ER stress on apoptosis induction in cancer cells but also provided the first evidence that artocarpin induces apoptosis in osteosarcoma. We also demonstrated that artocarpin has anticancer effects in human osteosarcoma cells. Artocarpin inhibited cell proliferation and induced apoptosis of osteosarcoma cells, but not of normal bone cells. It also regulated the cell fate of osteosarcoma by activating mitochondrial proapoptotic proteins, ROS production, ER stress proteins, and caspases.

Evidence suggests that artocarpin, a prenylated flavonoid isolated from an agricultural *Artocarpus* plant, has multiple pharmacological properties (e.g., anti-inflammatory, antioxidant, antibacterial, and anticancer properties). For example, artocarpin demonstrated potent anti-inflammatory effects at different stages of phagocytosis and was able to suppress human phagocyte response (Septama, Jantan, & Panichayupakaranant, 2018). In addition, studies have indicated that artocarpin possesses anticancer effects through various mechanisms. Artocarpin induced apoptosis in human breast cancer, possibly via an extrinsic pathway (Arung et al., 2010). Other studies have reported that artocarpin induces apoptosis by increasing caspase-3 or caspase-7 activity through modulation of mitogen-activated protein kinase and Akt/mTOR pathways in human cutaneous squamous carcinoma cells (Hu et al., 2015). One related study reported that artocarpin induced p53-dependent or p53-independent apoptosis through ROS-mediated MAPKs and Akt activation in non-small-cell lung cancer cells (Tsai et al., 2017).

Oxidative stress results from increased exposure to ROS, the presence of decreased antioxidant defenses, mitochondrial dysfunction, or a combination of these factors (Packiriswamy, Coulson, Holcombe, & Sordillo, 2017). In oxidative stress, the oxidative and antioxidative systems of cells and tissues are imbalanced, resulting in increased ROS production. Some studies have reported that oxidative stress is associated with the apoptotic response induced by several anticancer agents (Ivanova, Zhelev, Aoki, Bakalova, & Higashi, 2016; Ray et al., 2000). ROS can cause redox-sensitive signaling pathways in many

cancer types, participating in cell growth and proliferation, differentiation, protein synthesis, glucose metabolism, cell survival, and inflammation. Therefore, targeting ROS represents an essential anticancer therapeutic strategy. In this study, we found that artocarpin triggered ROS generation and inhibited antioxidant agents, indicating that ROS act as a signal mediating artocarpin-induced apoptosis. This proved that artocarpin could cause oxidative damage of cytotoxic oxygen radicals and induce osteosarcoma cell apoptosis.

The ER is a major site of protein synthesis and modification, protein folding, lipid and steroid synthesis, carbohydrate metabolism, and calcium storage. ER stress is caused by the accumulation of unfolded or misfolded proteins within the ER lumen and can cause DNA damage and apoptosis (Han et al., 2013). Alteration of ER homeostasis may result in ER stress, which is significantly involved in metabolism, inflammation, and tumorigenesis. Under ER stress conditions, GRP78, ATF6, phosphor-PERK, and phosphor-IRE1 are upregulated, and therefore they are regarded as ER stress markers (Su & Li, 2016). Although increasing evidence indicates that ER stress contributes to cell death through apoptosis induction, its role in the occurrence of artocarpin remains unclear. We found that artocarpin induced a number of ER stress markers, including elevated cytosolic-calcium level and GRP 78 and GRP 94 activation. ER stress and cell death involve many Ca^{2+} -dependent processes, including calpains, calcineurin, FKBP38, fortilin, and Ca^{2+} -dependent pathways triggering apoptosis (Kim, Xu, & Reed, 2008). For instance, acute Ca^{2+} release from the ER can trigger a variety of signaling mechanisms promoting cell death mainly through Ca^{2+} -mediated mitochondrial cell death. We found that calcium chelator BAPTA-AM blocked artocarpin-induced cell apoptosis in human osteosarcoma cells. Taken altogether, these findings indicate that artocarpin triggered ER stress, as indicated by changes in cytosol calcium levels as a critical mediator in artocarpin-induced cell apoptosis.

Mitochondria play a central role in many essential cellular functions, including energy production, calcium homeostasis, and programmed cell death (Susin et al., 1997). Mitochondrial dysfunction can result in the release of proapoptotic factors involved in caspase activation and chromosome condensation and fragmentation (Martinou & Youle, 2011). Bcl-2 family proteins play a pivotal role in various cellular functions, such as cell apoptosis and resistance to conventional chemotherapy (Sturm et al., 2006). These proteins exist in the mitochondrial membrane and regulate mitochondria-dependent apoptosis through the ratio of Bax/Bcl-2 (Adams & Cory, 2001). In this study, we also found that artocarpin reduced mitochondria membrane potential and increased the release of cytochrome *c* from mitochondria into the cytosol. Furthermore, dysfunction caused by apoptotic stimuli can lead passively to cell death because of compromised energy production.

In conclusion, we found an antitumor effect of artocarpin by modulating multiple mechanisms in osteosarcoma. Artocarpin induced apoptosis in osteosarcoma cells by triggering of mitochondrial dysfunction, ROS accumulation, and caspases activation. Artocarpin also induced cell death mediated by increasing ER stress, GRP 78,

GRP 94 activation, and Ca^{2+} release which subsequently triggers calpains, caspase 3 and caspase 9 activity, resulting in apoptosis. We hope that our proposed working model for the molecular basis will provide valuable insights into the development of effective chemotherapy by targeting appropriate signal transducers.

ACKNOWLEDGMENTS

This study was supported by grants from the Ministry of Science and Technology, Taiwan (MOST106-2314-B-341-001-MY3 and MOST-107-2314-B-341-003) and Shin-Kong Wu Ho-Su Memorial hospital (2018SKHBND001).

CONFLICTS OF INTEREST

The authors declare that there are no conflicts of interest.

AUTHORS CONTRIBUTIONS

J. F. L. and C. W. L. conceived and designed the experiments. C. W. L., M. C. C., and T. M. C. performed the experiments. C. W. L., M. C. C. and T. M. C. analyzed the data. C. W. L., M. C. C. and T. M. C. contributed reagents/materials/analysis tools. J. F. L. wrote the paper. All authors read and approved the final manuscript.

ORCID

Ju-Fang Liu  <http://orcid.org/0000-0002-0887-6096>

REFERENCES

- Adams, J. M., & Cory, S. (2001). Life-or-death decisions by the Bcl-2 protein family. *Trends in Biochemical Sciences*, 26(1), 61–66.
- Arung, E. T., Wicaksono, B. D., Handoko, Y. A., Kusuma, I. W., Shimizu, K., Yulia, D., & Sandra, F. (2010). Cytotoxic effect of artocarpin on T47D cells. *Journal of Natural Medicines*, 64(4), 423–429.
- Bacci, G., & Lari, S. (2001). Adjuvant and neoadjuvant chemotherapy in osteosarcoma. *Chirurgia Degli Organi di Movimento*, 86(4), 253–268.
- Barateiro, A., Vaz, A. R., Silva, S. L., Fernandes, A., & Brites, D. (2012). ER stress, mitochondrial dysfunction, and calpain/JNK activation are involved in oligodendrocyte precursor cell death by unconjugated bilirubin. *NeuroMolecular Medicine*, 14(4), 285–302.
- Chen, J. T., Fong, Y. C., Li, T. M., Liu, J. F., Hsu, C. W., Chang, C. S., & Tang, C. H. (2008). DDTD, an isoflavone derivative, induces cell apoptosis through the reactive oxygen species/apoptosis signal-regulating kinase 1 pathway in human osteosarcoma cells. *European Journal of Pharmacology*, 597(1-3), 19–26.
- Chen, X., Fu, X. S., Li, C. P., & Zhao, H. X. (2014). ER stress and ER stress-induced apoptosis are activated in gastric SMCs in diabetic rats. *World Journal of Gastroenterology*, 20(25), 8260–8267.
- Chaudhari, N., Talwar, P., Parimisetty, A., Lefebvre D'Hellencourt, C., & Ravanian, P. (2014). A molecular web: Endoplasmic reticulum stress, inflammation, and oxidative stress. *Frontiers in Cellular Neuroscience*, 8, 213.
- Dijkers, P. F., Birkenkamp, K. U., Lam, E. W. F., Thomas, N. S. B., Lammers, J. W. J., Koenderman, L., & Coffey, P. J. (2002). FKHR-L1 can act as a critical effector of cell death induced by cytokine withdrawal: Protein

- kinase B-enhanced cell survival through maintenance of mitochondrial integrity. *Journal of Cell Biology*, 156(3), 531–542.
- DelaGarza-Montano, P., Estrada-Villasenor, E., Dominguez Rubio, R., Martinez-Lopez, V., Avila-Luna, A., Alfaro-Rodriguez, A., ... Bandala, C. (2015). Epidemiological aspects of osteosarcoma, giant cell tumor, and chondrosarcoma musculoskeletal tumors—experience of the national rehabilitation institute, Mexico City. *Asian Pacific Journal of Cancer Prevention*, 16(15), 6451–6455.
- Feig, D. I., Sowers, L. C., & Loeb, L. A. (1994). Reverse chemical mutagenesis: Identification of the mutagenic lesions resulting from reactive oxygen species-mediated damage to DNA. *Proceedings of the National Academy of Sciences of the United States of America*, 91(14), 6609–6613.
- Fromigue, O., Hamidouche, Z., Vaudin, P., Lecanda, F., Patino, A., Barbry, P., ... Marie, P. J. (2011). CYR61 downregulation reduces osteosarcoma cell invasion, migration, and metastasis. *Journal of Bone and Mineral Research*, 26(7), 1533–1542.
- Han, J., Back, S. H., Hur, J., Lin, Y. H., Gildersleeve, R., Shan, J., ... Kaufman, R. J. (2013). ER-stress-induced transcriptional regulation increases protein synthesis leading to cell death. *Nature Cell Biology*, 15(5), 481–490.
- He, B. (2006). Viruses, endoplasmic reticulum stress, and interferon responses. *Cell Death and Differentiation*, 13(3), 393–403.
- Hu, S. C., Lin, C. L., Cheng, H. M., Chen, G. S., Lee, C. W., & Yen, F. L. (2015). Artocarpin induces apoptosis in human cutaneous squamous cell carcinoma HSC-1 cells and its cytotoxic activity is dependent on protein-nutrient concentration. *Evidence-based complementary and alternative medicine*, 2015, 236159.
- Ivanova, D., Zhelev, Z., Aoki, I., Bakalova, R., & Higashi, T. (2016). Overproduction of reactive oxygen species-obligatory or not for induction of apoptosis by anticancer drugs. *Chinese Journal of Cancer Research*, 28(4), 383–396.
- Jagtap, U. B., & Bapat, V. A. (2010). Artocarpus: A review of its traditional uses, phytochemistry, and pharmacology. *Journal of Ethnopharmacology*, 129(2), 142–166.
- Kaira, K., Toyoda, M., Shimizu, A., Mori, K., Shino, M., Sakakura, K., ... Chikamatsu, K. (2016). Expression of ER stress markers (GRP78/BiP and PERK) in patients with tongue cancer. *Neoplasia*, 63(4), 588–594.
- Kim, B. C., Kim, H. G., Lee, S. A., Lim, S., Park, E. H., Kim, S. J., & Lim, C. J. (2005). Genipin-induced apoptosis in hepatoma cells is mediated by reactive oxygen species/c-Jun NH2-terminal kinase-dependent activation of mitochondrial pathway. *Biochemical Pharmacology*, 70(9), 1398–1407.
- Kim, I., Xu, W., & Reed, J. C. (2008). Cell death and endoplasmic reticulum stress: Disease relevance and therapeutic opportunities. *Nature Reviews. Drug Discovery*, 7(12), 1013–1030.
- Kowaltowski, A. J., Castilho, R. F., & Vercesi, A. E. (2001). Mitochondrial permeability transition and oxidative stress. *FEBS Letters*, 495(1–2), 12–15.
- Lan, W. C., Tzeng, C. W., Lin, C. C., Yen, F. L., & Ko, H. H. (2013). Prenylated flavonoids from *Artocarpus altilis*: Antioxidant activities and inhibitory effects on melanin production. *Phytochemistry*, 89, 78–88.
- Lee, C. W., Hsu, L. F., Lee, M. H., Lee, I. T., Liu, J. F., Chiang, Y. C., & Tsai, M. H. (2018). Extracts of *artocarpus communis* induce mitochondria-associated apoptosis via pro-oxidative activity in human glioblastoma cells. *Frontiers in Pharmacology*, 9, 411.
- Lee, C. W., Ko, H. H., Lin, C. C., Chai, C. Y., Chen, W. T., & Yen, F. L. (2013). Artocarpin attenuates ultraviolet B-induced skin damage in hairless mice by antioxidant and anti-inflammatory effect. *Food and Chemical Toxicology*, 60, 123–129.
- Lin, Y. T., Huang, A. C., Kuo, C. L., Yang, J. S., Lan, Y. H., Yu, C. C., ... Chung, J. G. (2013). Induction of cell cycle arrest and apoptosis in human osteosarcoma U-2 OS cells by *Solanum lyratum* extracts. *Nutrition and Cancer*, 65(3), 469–479.
- Liu, A., Chen, H., Wei, W., Ye, S., Liao, W., Gong, J., ... Lin, S. (2011a). Antiproliferative and antimetastatic effects of emodin on human pancreatic cancer. *Oncology Reports*, 26(1), 81–89.
- Liu, J. F., Fong, Y. C., Chang, K. W., Kuo, S. C., Chang, C. S., & Tang, C. H. (2011b). FPTB, a novel CA-4 derivative, induces cell apoptosis of human chondrosarcoma cells through mitochondrial dysfunction and endoplasmic reticulum stress pathways. *Journal of Cellular Biochemistry*, 112(2), 453–462.
- Liu, J. F., Huang, Y. L., Yang, W. H., Chang, C. S., & Tang, C. H. (2012). 1-Benzyl-2-phenylbenzimidazole (BPB), a benzimidazole derivative, induces cell apoptosis in human chondrosarcoma through intrinsic and extrinsic pathways. *International Journal of Molecular Sciences*, 13(12), 16472–16488.
- Martinou, J. C., & Youle, R. J. (2011). Mitochondria in apoptosis: Bcl-2 family members and mitochondrial dynamics. *Developmental Cell*, 21(1), 92–101.
- Muruganandan, S., & Cribb, A. E. (2006). Calpain-induced endoplasmic reticulum stress and cell death following cytotoxic damage to renal cells. *Toxicological Sciences*, 94(1), 118–128.
- Ottaviani, G., & Jaffe, N. (2009). The epidemiology of osteosarcoma. *Cancer Treatment and Research*, 152, 3–13.
- Packiriswamy, N., Coulson, K. F., Holcombe, S. J., & Sordillo, L. M. (2017). Oxidative stress-induced mitochondrial dysfunction in a normal colon epithelial cell line. *World Journal of Gastroenterology*, 23(19), 3427–3439.
- Ray, S. K., Fidan, M., Nowak, M. W., Wilford, G. G., Hogan, E. L., & Banik, N. L. (2000). Oxidative stress and Ca^{2+} influx upregulate calpain and induce apoptosis in PC12 cells. *Brain Research*, 852(2), 326–334.
- Roos, W. P., & Kaina, B. (2006). DNA damage-induced cell death by apoptosis. *Trends in Molecular Medicine*, 12(9), 440–450.
- Salehin, D., Fromberg, I., Haugk, C., Dohmen, B., Georg, T., Bohle, R. M., ... Friedrich, M. (2010). Immunohistochemical analysis for expression of calpain 1, calpain 2, and calpastatin in endometrial cancer. *Anticancer Research*, 30(7), 2837–2843.
- Septama, A. W., Jantan, I., & Panichayupakaranant, P. (2018). Flavonoids of *Artocarpus heterophyllus* lam. Heartwood inhibit the innate immune responses of human phagocytes. *Journal of Pharmacy and Pharmacology*, 70(9), 1242–1252.
- Septama, A. W., & Panichayupakaranant, P. (2015). Antibacterial assay-guided isolation of active compounds from *Artocarpus heterophyllus* heartwoods. *Pharmaceutical Biology*, 53(11), 1608–1613.
- Siman, R., Flood, D. G., Thinakaran, G., & Neumar, R. W. (2001). Endoplasmic reticulum stress-induced cysteine protease activation in cortical neurons: Effect of an Alzheimer's disease-linked presenilin-1 knock-in mutation. *The Journal of Biological Chemistry*, 276(48), 44736–44743.
- Sturm, I., Rau, B., Schlag, P. M., Wust, P., Hildebrandt, B., Riess, H., ... Daniel, P. T. (2006). Genetic dissection of apoptosis and cell cycle control in response of colorectal cancer treated with preoperative radiochemotherapy. *BMC Cancer*, 6, 124.
- Su, Y., & Li, F. (2016). Endoplasmic reticulum stress in brain ischemia. *International Journal of Neuroscience*, 126(8), 681–691.
- Susin, S. A., Zamzami, N., Castedo, M., Daugas, E., Wang, H. G., Geley, S., ... Kroemer, G. (1997). The central executioner of apoptosis: Multiple connections between protease activation and mitochondria in Fas/APO-1/CD95- and ceramide-induced apoptosis. *Journal of Experimental Medicine*, 186(1), 25–37.
- Tan, Y., Dourdin, N., Wu, C., De Veyra, T., Elce, J. S., & Greer, P. A. (2006). Ubiquitous calpains promote caspase-12 and JNK activation during endoplasmic reticulum stress-induced apoptosis. *Journal of Biological Chemistry*, 281(23), 16016–16024.
- Tiraravesit, N., Yakaew, S., Rukchay, R., Luangbudnark, W., Viennet, C., Humbert, P., & Viyoch, J. (2015). *Artocarpus altilis* heartwood extract protects skin against UVB in vitro and in vivo. *Journal of Ethnopharmacology*, 175, 153–162.

- Tsai, H. C., Huang, C. Y., Su, H. L., & Tang, C. H. (2014). CCN2 enhances resistance to cisplatin-mediated cell apoptosis in human osteosarcoma. *PLOS One*, 9(3), e90159.
- Tsai, M. H., Liu, J. F., Chiang, Y. C., Hu, S. C. S., Hsu, L. F., Lin, Y. C., ... Lee, C. W. (2017). Artocarpin, an isoprenyl flavonoid, induces p53-dependent or independent apoptosis via ROS-mediated MAPKs and Akt activation in non-small cell lung cancer cells. *Oncotarget*, 8(17), 28342–28358.
- Yang, J., & Zhang, W. (2013). New molecular insights into osteosarcoma targeted therapy. *Current Opinion in Oncology*, 25(4), 398–406.
- Zhang, C. (2017). Roles of Grp78 in Female Mammalian Reproduction. *Advances in Anatomy, Embryology and Cell Biology*, 222, 129–155.
- Zhang, Y., & Chen, F. (2004). Reactive oxygen species (ROS), troublemakers between nuclear factor-kappaB (NF-kappaB) and c-Jun NH(2)-terminal kinase (JNK). *Cancer Research*, 64(6), 1902–1905.

How to cite this article: Lee C-W, Chi M-C, Chang T-M, Liu J-F. Artocarpin induces cell apoptosis in human osteosarcoma cells through endoplasmic reticulum stress and reactive oxygen species. *J Cell Physiol*. 2018;1–12.
<https://doi.org/10.1002/jcp.27986>



Carbon monoxide releasing molecule-2 protects against particulate matter-induced lung inflammation by inhibiting TLR2 and 4/ROS/NLRP3 inflammasome activation

Chiang-Wen Lee^{a,b,c,1}, Miao-Ching Chi^{b,d,1}, Lee-Fen Hsu^{b,d}, Chuen-Mao Yang^{e,f,g}, Tsui-Hua Hsu^b, Chu-Chun Chuang^h, Wei-Ning Linⁱ, Pei-Ming Chu^j, I-Ta Lee^{k,*}

^a Department of Orthopaedic Surgery, Chang Gung Memorial Hospital, Puzi City, Chiayi County 61363, Taiwan

^b Department of Nursing, Division of Basic Medical Sciences, Chronic Diseases and Health Promotion Research Center, Chang Gung University of Science and Technology, Puzi City, Chiayi County 61363, Taiwan

^c Research Center for Industry of Human Ecology and Research Center for Chinese Herbal Medicine, Chang Gung University of Science and Technology, Guishan Dist., Taoyuan City 33303, Taiwan

^d Division of Pulmonary and Critical Care Medicine, Chiayi Chang Gung Memorial Hospital, Taiwan

^e Department of Anesthetics, Chang Gung Memorial Hospital at Linkuo and Chang Gung University, Kwei-San, Tao-Yuan, Taiwan

^f Department of Physiology and Pharmacology and Health Ageing Research Center, College of Medicine, Chang Gung University, Kwei-San, Tao-Yuan, Taiwan

^g Research Center for Chinese Herbal Medicine and Research Center for Food and Cosmetic Safety, College of Human Ecology, Chang Gung University of Science and Technology, Tao-Yuan, Taiwan

^h Department of Physical Therapy, China Medical University, Taichung, Taiwan

ⁱ Graduate Institute of Biomedical and Pharmaceutical Science, Fu Jen Catholic University, New Taipei City 242, Taiwan

^j School of Medicine, College of Medicine, China Medical University, Taichung, Taiwan

^k School of Dentistry, College of Oral Medicine, Taipei Medical University, Taipei, Taiwan

ARTICLE INFO

Keywords:

Carbon monoxide
Lung inflammation
Inflammasome
Particulate matter
Reactive oxygen species

ABSTRACT

Exposure to airborne particulate matter (PM) not only causes lung inflammation and chronic respiratory diseases, but also increases the incidence and mortality of cardiopulmonary diseases. The nucleotide-binding domain and leucine-rich repeat protein 3 (NLRP3) inflammasome activation has been shown to play a critical role in the formation of many chronic disorders. On the other hand, carbon monoxide (CO) has been shown to possess anti-inflammatory and antioxidant effects in many tissues and organs. Here, we investigated the effects and mechanisms of carbon monoxide releasing molecule-2 (CORM-2) on PM-induced inflammatory responses in human pulmonary alveolar epithelial cells (HPAECs). We found that PM induced C-reactive protein (CRP) expression, NLRP3 inflammasome activation, IL-1 β secretion, and caspase-1 activation, which were inhibited by pretreatment with CORM-2. In addition, transfection with siRNA of Toll-like receptor 2 (TLR2) or TLR4 and pretreatment with an antioxidant (N-acetyl-cysteine, NAC), the inhibitor of NADPH oxidase (diphenyleneiodonium, DPI), or a mitochondria-specific superoxide scavenger (MitoTEMPO) reduced PM-induced inflammatory responses. CORM-2 also inhibited PM-induced NADPH oxidase activity and NADPH oxidase- and mitochondria-derived ROS generation. However, pretreatment with inactivate CORM-2 (iCORM-2) had no effects on PM-induced inflammatory responses. Finally, we showed that CORM-2 inhibited PM-induced CRP, NLRP3 inflammasome, and ASC protein expression in the lung tissues of mice and IL-1 β levels in the serum of mice. PM-enhanced leukocyte count in bronchoalveolar lavage fluid in mice was reduced by CORM-2. The results of this study suggested a protective role of CORM-2 in PM-induced lung inflammation by inhibiting the TLR2 and TLR4/ROS-NLRP3 inflammasome-CRP axis.

1. Introduction

Air pollution can cause a lot of human health burden. The World

Health Organization (WHO) points out that approximately 3% and 5% of global cardiopulmonary diseases and lung cancer are attributable to particulate matter (PM) exposure each year, resulting in approximately

* Corresponding author at: School of Dentistry, College of Oral Medicine, Taipei Medical University, 250 Wuxing St., Taipei 11031, Taiwan.

E-mail address: itlee0128@tmu.edu.tw (I.-T. Lee).

¹ These authors contributed equally to this work.

3.1 million deaths worldwide each year. PM not only harms the respiratory tract, but also causes cancer and cardiovascular diseases (Li et al., 2018a). Due to the different composition of PM, its toxicity is very complicated. However, various diseases induced by particles are generally not attributable to a single pathogenic factor, but from a variety of different mechanisms. Many studies indicated that PM may cause respiratory disorders through various inflammatory signaling pathways activation, such as mitogen-activated protein kinase (MAPK), NF- κ B, reactive oxygen species (ROS), and interleukin (IL)-8 (Jeong et al., 2017; Liu et al., 2019).

The nucleotide-binding domain and leucine-rich repeat protein 3 (NLRP3) inflammasome has been shown to regulate pulmonary inflammation (Li et al., 2018b). When cells are stimulated by external stimuli, NLRP3 can recruit the adaptor protein ASC (Sun et al., 2013) and pro-caspase-1 to form NLRP3 inflammasome assembly, which can mediate caspase-1 activation and processes pro-IL-1 β to the bioactive IL-1 β (Mao et al., 2018). It is known that the initiation and persistence of inflammation can be regulated by IL-1 β (Mao et al., 2018). Previous study also indicated that IL-1 β can induce airway remodeling and emphysema through the up-regulation of CXCL2, MMP-12, and MMP-9 (Lappalainen et al., 2005). Recently, many studies have showed that some nanomaterials, including carbon nanotubes (Palomäki et al., 2011) and rare oxide nanomaterials (Li et al., 2014), can activate NLRP3 inflammasome that plays a key role in lung inflammation (Cassel et al., 2009). Previous studies proved that nanomaterials-promoted NLRP3 inflammasome activation involves oxidative stress and potassium (K⁺) efflux, which supply signals for the assembly of the NLRP3 inflammasome (Jin and Flavell, 2010). Thus, in this study, we investigated whether PM could cause NLRP3 inflammasome activation and induce lung inflammation. In addition, we also explored the signaling pathways involved in PM-induced NLRP3 inflammasome activation in human pulmonary alveolar epithelial cells (HPAEPiCs).

Carbon monoxide (CO) is considered a toxic gas due to its strong affinity for hemoglobin, which further causes tissue damage and cell death. However, a large number of studies have confirmed that CO has anti-inflammatory and antioxidative effects (Shao et al., 2018). The therapeutic potential of CO was also exploited in organ transplantation and inflammatory diseases. Caumartin et al. indicated that carbon monoxide releasing molecule-2 (CORM-2) protects renal transplants from ischemia-reperfusion injury by inhibiting inflammation (Caumartin et al., 2011). Uddin et al. also proved that CORM-2 mediates IL-10 levels and thus inhibits TNF- α -regulated inflammation in a septic mouse model (Uddin et al., 2015). ROS are involved in the development of chronic inflammatory diseases and cancers. However, CORM-2 has been shown to inhibit NADPH oxidase activity and ROS production induced by *Pseudomonas aeruginosa* (Lee et al., 2018). Here, we anticipate that CORM-2 may be effective as a therapeutic agent for PM-induced lung inflammation by inhibiting inflammatory responses and oxidative stress.

In this study, NLRP3 inflammasome assembly and IL-1 β release were studied in HPAEPiCs after exposure to PM, and the mechanisms of NLRP3 inflammasome activation were further explored. On the other hand, we also investigated whether the reduction of ROS production and NLRP3 inflammasome activation by CORM-2 may indeed inhibit PM-induced inflammation in HPAEPiCs and mice.

2. Materials and methods

2.1. Materials

We purchased anti-C-reactive protein (CRP), anti-NLRP3, anti-ASC, anti-GAPDH, anti-TLR2, and anti-TLR4 antibodies from Santa Cruz Biotechnology Inc (Santa Cruz, CA, USA). Diphenyleneiodonium (DPI) was purchased from Calbiochem (San Diego, CA, USA). MitoTEMPO, PM (SRM 1648a), N-acetyl-cysteine (NAC), CORM-2, and Thiazolyl Blue Tetrazolium Blue (MTT) were purchased from Sigma (St. Louis,

MO, USA). IL-1 β ELISA kit and caspase-1 (active) staining kit were purchased from Abcam (Cambridge, UK).

2.2. Cell culture

We obtained HPAEPiCs from the ScienCell Research Laboratory (San Diego, CA). HPAEPiCs were grown as previously described (Cho et al., 2016). In this study, we performed experiments with cells from passages 3 to 9.

2.3. Cell viability

HPAEPiCs were plated in 96-well plates at a density of 1×10^4 cells/well and incubated for one day. Cells were then incubated with medium containing different concentrations of PM or CORM-2 for 24 h. 20 μ l of MTT reagent (5 mg/ml) was then added to each well and the plates were incubated for 4 h at 37 °C. The supernatant was removed and 150 μ l dimethyl sulfoxide was added to each well to dissolve the formazan crystal with vigorous shaking for 10 min. The absorbance at 490 nm was detected with a microplate reader (SpectraMax 250, Molecular Device, Sunnyvale, CA, USA).

2.4. Western blot analysis

We cultured HPAEPiCs in 6-well culture plates. After reaching confluence, HPAEPiCs were treated with PM for the indicated times at 37 °C. Western blot analysis methods have been described (Cho et al., 2016). Finally, membranes were incubated with the anti-CRP, anti-NLRP3, anti-TLR2, anti-TLR4, or anti-ASC antibody for 24 h, and then incubated with the anti-mouse or anti-rabbit horseradish peroxidase antibody for 1 h. We used enhanced chemiluminescence reagents to detect immunoreactive bands.

2.5. Real-Time PCR

Total RNA was extracted by using TRIzol reagent. We then reverse-transcribed mRNA into cDNA and analyzed by real-time PCR using SYBR Green PCR reagents (Applied Biosystems, Branchburg, NJ, USA) and primers specific for human GAPDH, IL-1 β , CRP, ASC, NLRP3, caspase-1, TLR2, and TLR4 mRNAs. Finally, IL-1 β , CRP, NLRP3, caspase-1, TLR2, and TLR4 mRNA levels were determined by normalizing to that of GAPDH expression.

2.6. Transient transfection with human siRNAs

Human scrambled, NLRP3, caspase-1, TLR2, and TLR4 siRNAs were from Sigma (St. Louis, MO). Transient transfection of siRNAs was performed using a GeneMute reagent according to the manufacturer's instructions from SignaGen Lab (Rockville, MD).

2.7. Measurement of IL-1 β generation

Cells were cultured in 12-well culture plates. After reaching confluence, HPAEPiCs were incubated with PM for the indicated times. The media were gathered and IL-1 β levels were assayed by using an IL-1 β ELISA kit (Abcam, Cambridge, UK).

2.8. Measurement of caspase-1 (active) expression

Cells were cultured in 6-well culture plates. After reaching confluence, HPAEPiCs were treated with PM for the indicated times. The levels of caspase-1 (active) were assayed by using the caspase-1 (active) staining kit.

2.9. Measurement of intracellular ROS and mitochondrial ROS generation

CellROX Green Reagent and MitoSOX Red mitochondrial superoxide indicator (Molecular Probes, Eugene, OR) were used in these experiments. For the purpose of these experiments, HPAEpiCs were washed with warm Hank's Balanced Salt Solution (HBSS) and incubated in HBSS or cell medium containing 5 μ M CellROX Green Reagent or MitoSOX Red mitochondrial superoxide indicator at 37 °C for 30 min. Subsequently, HBSS or medium containing CellROX Green Reagent or MitoSOX Red mitochondrial superoxide indicator was removed and replaced with fresh medium. HPAEpiCs were then incubated with PM for the indicated times. Cells were washed twice with PBS and detached with trypsin/EDTA, and the fluorescence intensity of the cells was analyzed using a FACScan flow cytometer (BD Biosciences, San Jose, CA) at 485 nm excitation and 520 nm emission (CellROX Green Reagent) and 510 nm excitation and 580 nm emission (MitoSOX Red mitochondrial superoxide indicator), respectively.

2.10. Determination of NADPH oxidase activity

After incubation, cells were gently scraped and centrifuged at 400 \times g for 10 min at 4 °C. NADPH oxidase activity detection methods have been described (Cho et al., 2016).

2.11. Animal care and experimental procedures

Male BALB/c mice aged 6–8 weeks were from the National Laboratory Animal Centre (Taipei, Taiwan) and were handled according to NIH Guides for the Care and Use of Laboratory Animals. BALB/c mice were anesthetized with ethyl ether and placed individually on a board in a near vertical position, and the tongues were withdrawn with a lined forceps. 20 μ l PM suspension (8 mg/ml) was placed posterior in the throat and aspirated into lungs. Control mice were administered sterile 0.1% bovine serum albumin. Mice regained consciousness after 15 min. Mice were given i.v. one dose of CORM-2 (8 mg/kg) prior to PM treatment and were sacrificed after 72 h. IL-1 β levels in the serum of mice were measured.

2.12. Isolation of bronchoalveolar lavage (BAL) fluid

Male BALB/c mice were intra-tracheally administered with 20 μ l PM suspension (8 mg/ml) and sacrificed 72 h later. BAL fluid was administered through a tracheal cannula using 1-ml aliquots of ice-cold PBS medium. BAL fluid was centrifuged at 500 \times g at 4 °C, and cell pellets were washed and resuspended in PBS. Leukocyte count was determined by a hemocytometer.

2.13. Statistical software and analysis

We analyzed the data with the GraphPad Prism program (GraphPad, San Diego, CA, USA). Quantitative data were expressed as the mean \pm S.E.M. and analyzed with one-way ANOVA followed with Tukey's post-hoc test. We defined $P < 0.05$ as a significant difference.

3. Results

3.1. PM induces CRP, NLRP3 inflammasome, ASC, IL-1 β , and caspase-1 expression

PM has been shown to induce inflammation and tissue/organ damage (Zheng et al., 2018; Zhang et al., 2018a). We observed the effects of PM on the cell viability of HPAEpiCs. As shown in Fig. 1A, we proved that 25 or 50 μ g/cm² PM had no effects on the cell viability of HPAEpiCs. However, 100 or 200 μ g/cm² PM markedly reduced the cell viability of HPAEpiCs. CRP, a critical inflammatory factor, plays an important role in the pathogenesis of respiratory diseases. Here, we

showed that PM time-dependently induced CRP protein expression and mRNA levels (Fig. 1B). When cells are stimulated by external stimuli, NLRP3 can recruit the adaptor protein ASC (Sun et al., 2013) and procaspase-1 to form NLRP3 inflammasome assembly, which can mediate caspase-1 activation and processes pro-IL-1 β to the bioactive IL-1 β (Mao et al., 2018). As shown in Fig. 1C, we proved that PM induced NLRP3 inflammasome protein expression and mRNA levels in HPAEpiCs. In addition, the expression of ASC was also enhanced by 50 μ g/cm² PM (Fig. 1D). Level of IL-1 β is a key biomarker indicating activation of NLRP3 inflammasome. IL-1 β levels secreted by HPAEpiCs exposed to PM at the dose of 50 μ g/cm² for the indicated times was measured by ELISA. As shown in Fig. 1E, PM time-dependently induced IL-1 β release. On the other hand, IL-1 β mRNA levels were also enhanced by PM in these cells (Fig. 1E). Finally, we demonstrated that PM induced caspase-1 (active) expression and mRNA levels in a time-dependent manner in HPAEpiCs (Fig. 1F). These data indicate that up-regulated NLRP3 and ASC levels in HPAEpiCs in response to PM can consolidate the NLRP3 inflammasome assembly during the process of PM treatment.

3.2. Effects of NLRP3 inflammasome and caspase-1 on PM-enhanced IL-1 β release

Next, we investigated whether the NLRP3 inflammasome constitutively expressed in HPAEpiCs actually functioned to mediate IL-1 β release. To solve this problem, siRNAs of NLRP3 and caspase-1 were used in HPAEpiCs. As shown in Figs. 2A and B, siRNAs of NLRP3 and caspase-1 markedly reduced expression of their corresponding transcripts. Moreover, NLRP3 and caspase-1 siRNAs also inhibited IL-1 β release and caspase-1 activation induced by PM (Fig. 2D and E). However, both of them failed to decrease IL-1 β mRNA levels in response to PM (Fig. 2C). These data prove that PM induces IL-1 β release in HPAEpiCs in an NLRP3 inflammasome-dependent manner and that the NLRP3 inflammasome mediates IL-1 β generation at the level of caspase-1.

3.3. PM induces inflammatory responses via TLR2 and TLR4

There are a group of receptors on immune cells that are used to detect various foreign substances, called TLRs, which are mainly involved in "non-specific immune responses" (Shoenfelt et al., 2009). Previous studies have indicated that PM2.5 induces inflammation in the murine lung through TLR2 and TLR4 (Shoenfelt et al., 2009; Zhao et al., 2012). In this study, we also investigated whether PM could induce inflammatory responses via TLR2 and TLR4 in HPAEpiCs. As shown in Fig. 3A–D, transfection with TLR2 siRNA or TLR4 siRNA markedly reduced PM-induced NLRP3 mRNA and protein levels, IL-1 β secretion and mRNA levels, ASC protein expression, and caspase-1 (active) expression. In addition, PM-induced CRP mRNA levels and protein expression were also inhibited by transfection with NLRP3, TLR2, or TLR4 siRNA (Fig. 3E and F). Thus, these data suggest that PM induces inflammatory responses through TLR2 and 4/NLRP3 inflammasome in HPAEpiCs.

3.4. CORM-2 inhibits PM-induced inflammatory responses in HPAEpiCs

CORM-2 has been shown to possess anti-inflammatory and anti-oxidant effects in various cell types (Shao et al., 2018; Caumartin et al., 2011; Uddin et al., 2015; Lee et al., 2018). At first, we observed the effects of CORM-2 on the cell viability of HPAEpiCs. As shown in Fig. 4A, we proved that 10, 25, 50, or 100 μ M CORM-2 had no effects on the cell viability of HPAEpiCs. We further investigated whether CORM-2 could inhibit PM-induced inflammatory responses in these cells. As shown in Figs. 4B and C, we proved that pretreatment with CORM-2 inhibited PM-induced NLRP3 mRNA levels and protein expression. In addition, PM-induced IL-1 β secretion and caspase-1 (active) expression

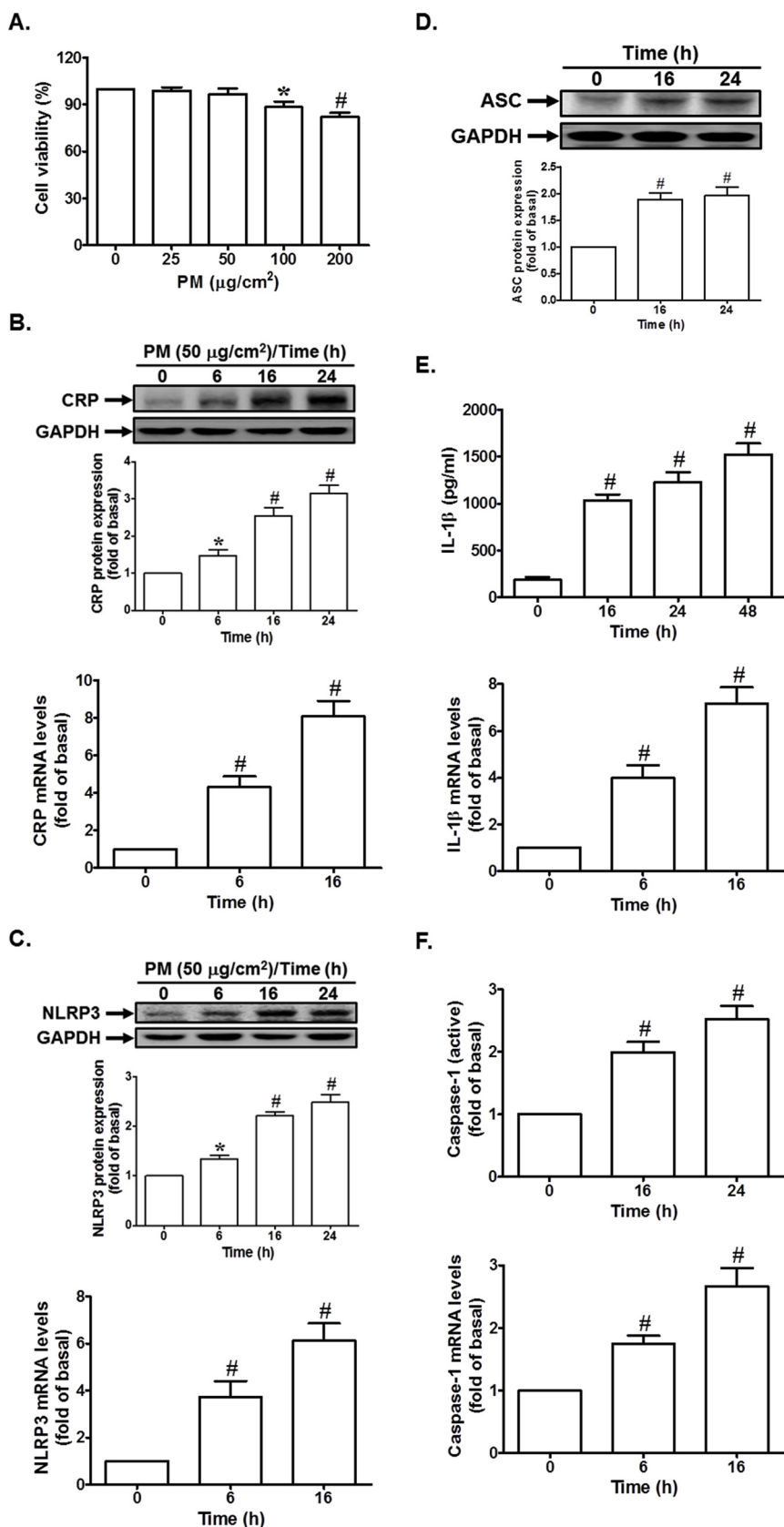


Fig. 1. PM induces CRP, NLRP3 inflammasome, ASC, IL-1 β , and caspase-1 expression in HPAEpiCs. (A) Cells were incubated with PM for the indicated times, and then the cell viability was determined. (B) Cells were incubated with PM for the indicated times, the protein expression and mRNA levels of CRP were determined by Western blot and real-time PCR, respectively. (C) Cells were incubated with PM for the indicated times, the protein expression and mRNA levels of NLRP3 were determined by Western blot and real-time PCR, respectively. (D) Cells were incubated with PM for the indicated times, the protein expression of ASC was determined by Western blot. (E) Cells were incubated with PM for the indicated times, the production and mRNA levels of IL-1 β were determined by ELISA and real-time PCR, respectively. (F) Cells were incubated with PM for the indicated times, the expression (active form) and mRNA levels of caspase-1 were determined by ELISA and real-time PCR, respectively. Data are expressed as mean \pm S.E.M. of three independent experiments. * $P < 0.05$; # $P < 0.01$, as compared with control.

were also reduced by preincubation with CORM-2 (Fig. 4D and E). As shown in Fig. 4F, we found that CORM-2, but not iCORM-2 could inhibit PM-induced CRP mRNA levels in these cells. Finally, we investigated whether CORM-2 could reduce PM-induced inflammatory

responses via the inhibition of TLR2 and TLR4 expression. As shown in Fig. 4G, we proved that CORM-2 could inhibit TLR2 and TLR4 mRNA levels induced by PM. Therefore, we suggest that CORM-2 can effectively inhibit PM-induced inflammatory responses.

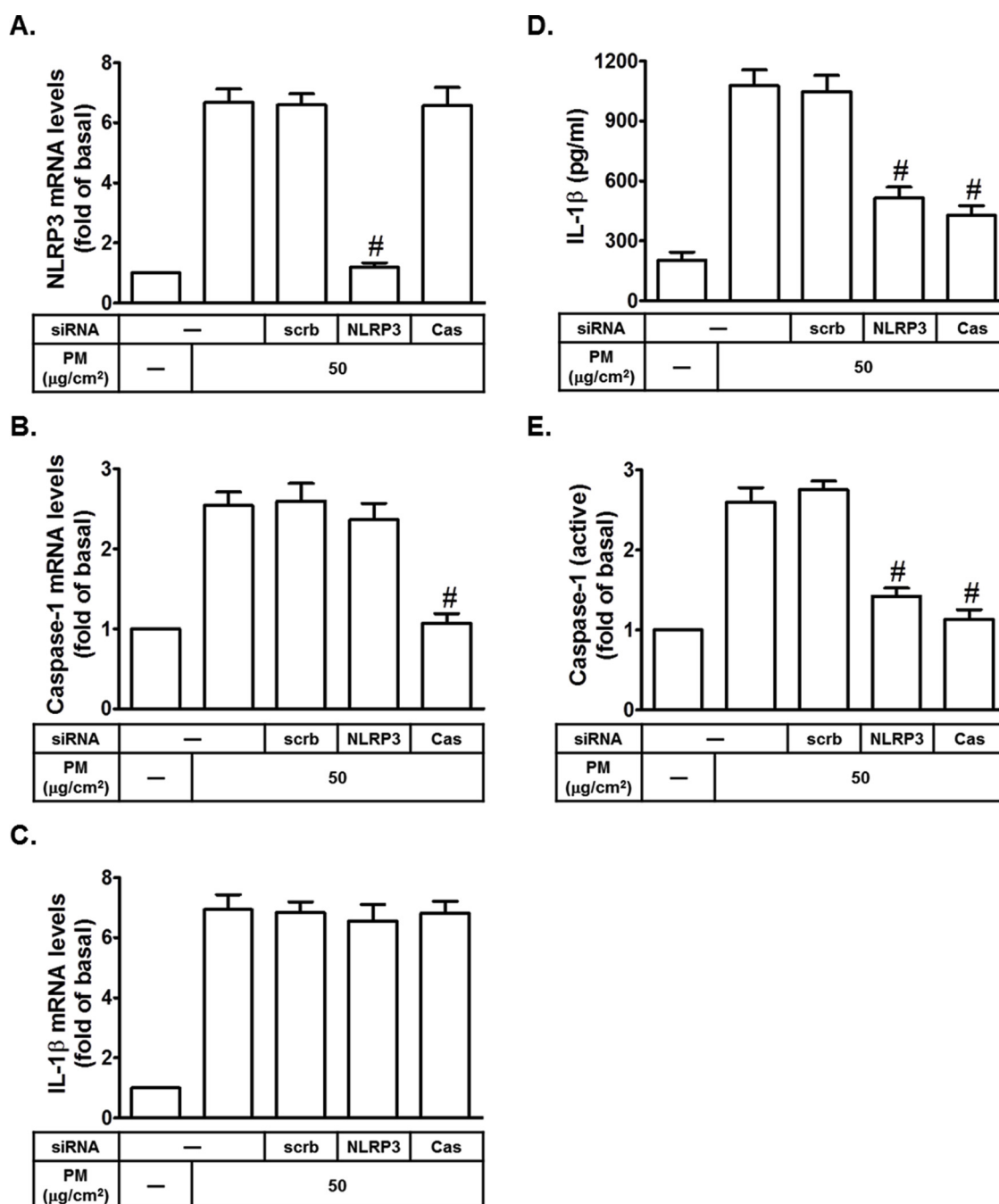


Fig. 2. Effects of NLRP3 inflammasome and caspase-1 on PM-induced IL-1 β release in HPAEpiCs. Cells were transfected with siRNA of scrambled (scrb), NLRP3, or caspase-1 (Cas), and then incubated with PM for (A–C) 16 h or (D, E) 24 h. The mRNA levels of NLRP3, caspase-1, and IL-1 β were determined by real-time PCR. The secretion of IL-1 β and expression (active form) of caspase-1 were measured by ELISA. Data are expressed as mean \pm S.E.M. of three independent experiments. # $P < 0.01$, as compared with the cells exposed to PM + scrambled siRNA.

3.5. PM induces NADPH oxidase- and mitochondria-derived ROS generation

Many studies have indicated that ROS are involved in PM-induced inflammation (Yang et al., 2018; Xu et al., 2018a). At first, we proved that pretreatment with an antioxidant (NAC), the inhibitor of NADPH oxidase (DPI), or a mitochondria-specific superoxide scavenger (Mito-TEMPO) reduced PM-induced CRP mRNAs (Fig. 5A). ROS have been shown to induce NLRP3 inflammasome activation (Li et al., 2018b; Zhang et al., 2018b). In this study, we proved that pretreatment with NAC, DPI, or MitoTEMPO did not inhibit PM-induced NLRP3, IL-1 β , and caspase-1 mRNA levels (Fig. 5B). However, as shown in Fig. 5C and

D, we showed that pretreatment with NAC, DPI, or MitoTEMPO markedly inhibited PM-induced ASC mRNA levels, IL-1 β secretion, and caspase-1 (active) expression in HPAEpiCs. Taken together, we suggest that NADPH oxidase- and mitochondria-derived ROS are involved in PM-induced NLRP3 inflammasome activation.

3.6. CORM-2 reduces NADPH oxidase- and mitochondria-derived ROS generation induced by PM

CO liberated from CORM-2 exerts an antioxidant effect (Lee et al., 2018). At first, we observed that PM induced intracellular ROS generation and mitochondrial ROS production in a time-dependent manner

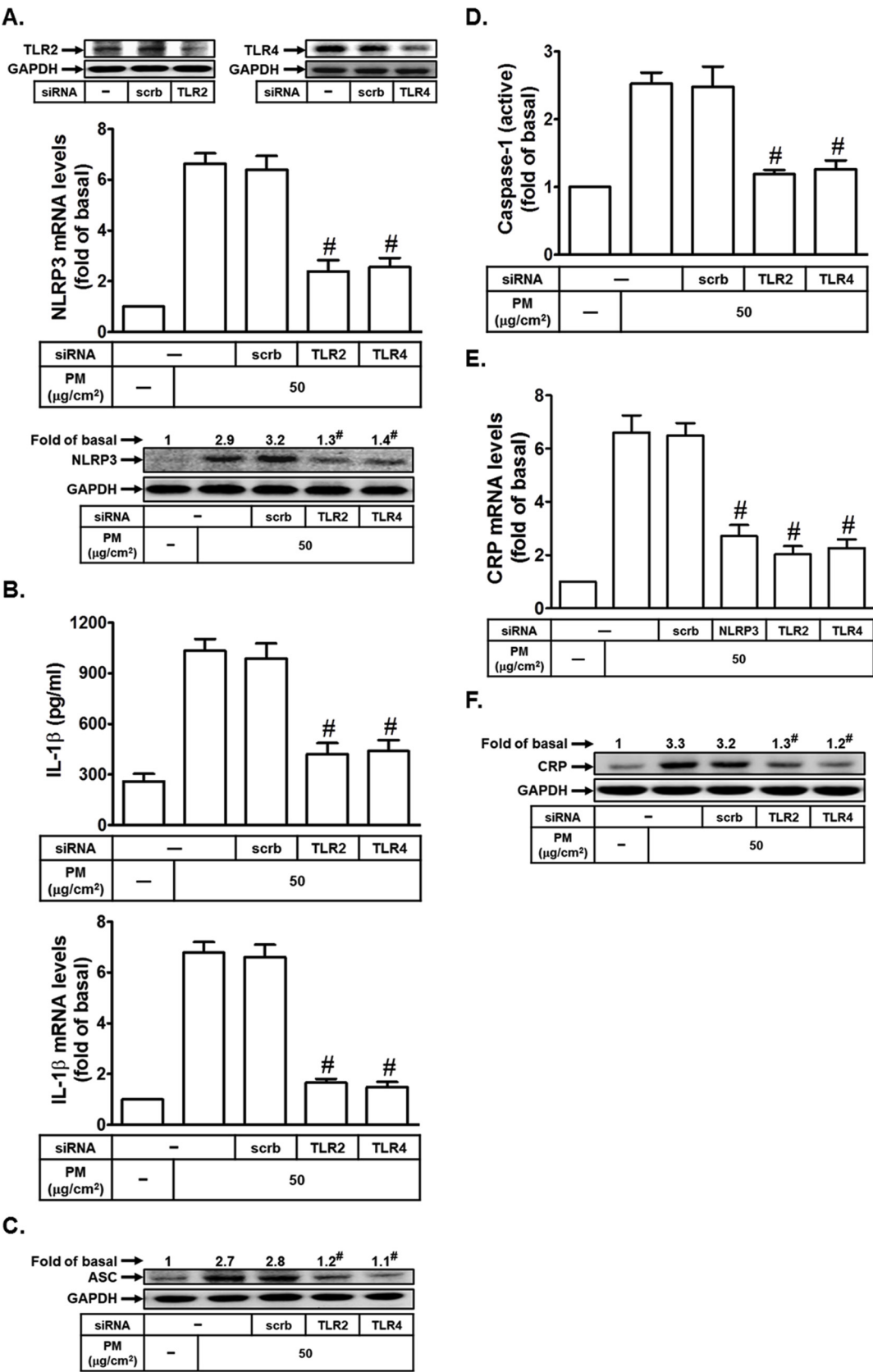
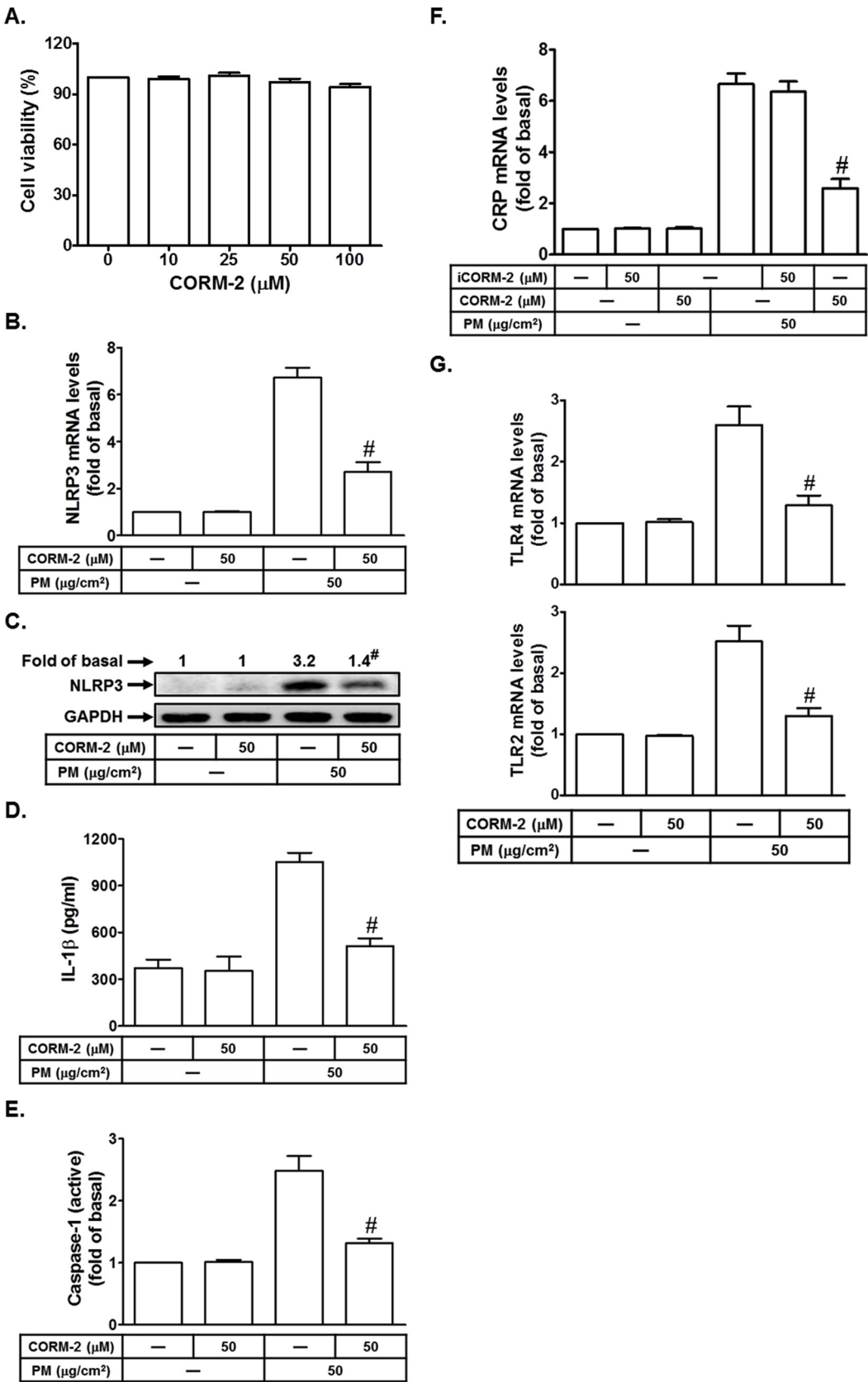


Fig. 3. PM induces inflammatory responses via TLR2 and TLR4. Cells were transfected with siRNA of scrambled (scrb), TLR2, TLR4, or NLRP3, and then incubated with PM for 16 h or 24 h. The mRNA levels of NLRP3, IL-1β, and CRP were determined by real-time PCR. The protein expression of TLR2, TLR4, NLRP3, ASC, and CRP was determined by Western blot. The secretion of IL-1β and expression (active form) of caspase-1 were measured by ELISA. Data are expressed as mean ± S.E.M. of three independent experiments. #*P* < 0.01, as compared with the cells exposed to PM + scrambled siRNA.



(caption on next page)

(Fig. 6A). We further investigated whether CORM-2 could inhibit PM-induced ROS generation. As shown in Fig. 6B, we proved that CORM-2, but not iCORM-2 markedly inhibited PM-induced intracellular ROS

generation and mitochondrial ROS production in HPAEpiCs. NADPH oxidases are one of the many sources of ROS in biologic systems. Moreover, we showed that PM time-dependently induced NADPH

Fig. 4. CORM-2 inhibits PM-induced inflammatory responses in HPAEpiCs. (A) Cells were incubated with CORM-2 for the indicated times, and then the cell viability was determined. (B) Cells were pretreated with CORM-2, and then incubated with PM for 16 h. The mRNA levels of NLRP3 were determined by real-time PCR. (C) Cells were pretreated with CORM-2, and then incubated with PM for 24 h. The protein expression of NLRP3 was determined by Western blot. (D) Cells were pretreated with CORM-2, and then incubated with PM for 24 h. The secretion of IL-1 β was measured by ELISA. (E) Cells were pretreated with CORM-2, and then incubated with PM for 24 h. The expression (active form) of caspase-1 was measured by ELISA. (F) Cells were pretreated with iCORM-2 or CORM-2, and then incubated with PM for 16 h. The mRNA levels of CRP were determined by real-time PCR. (G) Cells were pretreated with CORM-2, and then incubated with PM for 16 h. The mRNA levels of TLR2 and TLR4 were determined by real-time PCR. Data are expressed as mean \pm S.E.M. of three independent experiments. # P < 0.01, as compared with the cells exposed to PM alone.

oxidase activity (Fig. 6C). Finally, we showed that CORM-2, but not iCORM-2 also markedly inhibited PM-enhanced NADPH oxidase activity (Fig. 6D). Thus, we suggest that CORM-2 can reduce NADPH oxidase- and mitochondria-derived ROS generation induced by PM in HPAEpiCs.

3.7. PM induces lung inflammation in mice

In an *in vivo* study, mice were intra-tracheally administered with PM. As shown in Fig. 7A, PM induced CRP, NLRP3, and ASC protein expression in the lungs of mice, which was reduced by CORM-2. On the

other hand, we also showed that PM could enhance IL-1 β levels in the serum of mice, which was inhibited by pretreatment with CORM-2 (Fig. 7B). Finally, we proved that pretreatment with CORM-2 could inhibit PM-induced leukocyte count in BAL fluid in mice (Fig. 7C). Thus, we demonstrate that CORM-2 can inhibit lung inflammation via the inhibition of expression and activation of NLRP3 inflammasome.

4. Discussion

PM exposure is associated with mortality and morbidity and induced by pulmonary disorders and up-regulates the lung cancer risk.

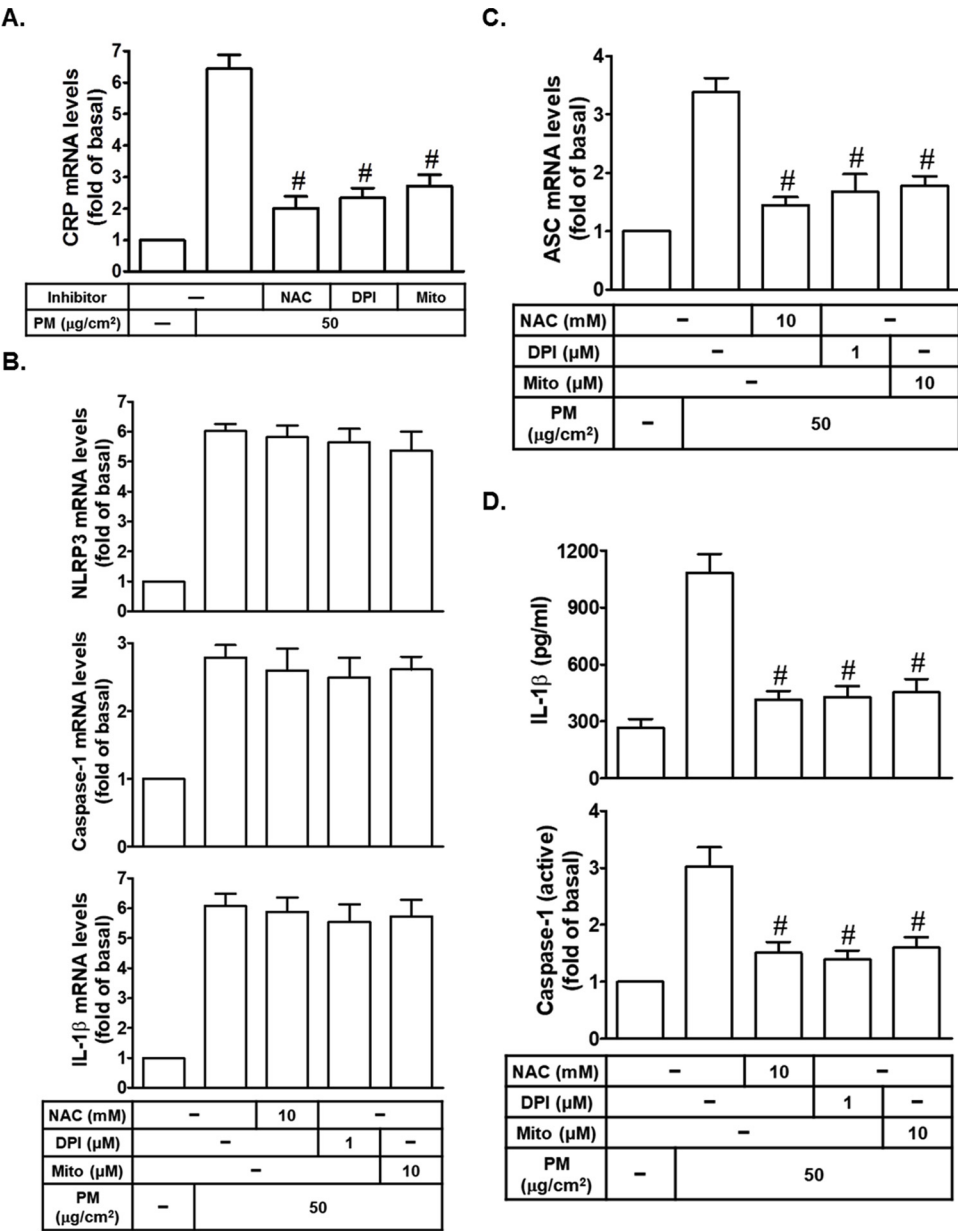


Fig. 5. PM induces NADPH oxidase- and mitochondria-derived ROS generation. (A) Cells were pretreated with NAC (10 mM), DPI (1 μM), or MitoTEMPO (10 μM) for 2 h, and then incubated with PM for 16 h. The mRNA levels of CRP were determined by real-time PCR. (B, C) Cells were pretreated with NAC (10 mM), DPI (1 μM), or MitoTEMPO (10 μM) for 2 h, and then incubated with PM for 16 h. The mRNA levels of NLRP3, IL-1 β , caspase-1, and ASC were determined by real-time PCR. (D) Cells were pretreated with NAC (10 mM), DPI (1 μM), or MitoTEMPO (10 μM), and then incubated with PM for 24 h. The secretion of IL-1 β and expression (active form) of caspase-1 were measured by ELISA. Data are expressed as mean \pm S.E.M. of three independent experiments. # P < 0.01, as compared with the cells exposed to PM alone.

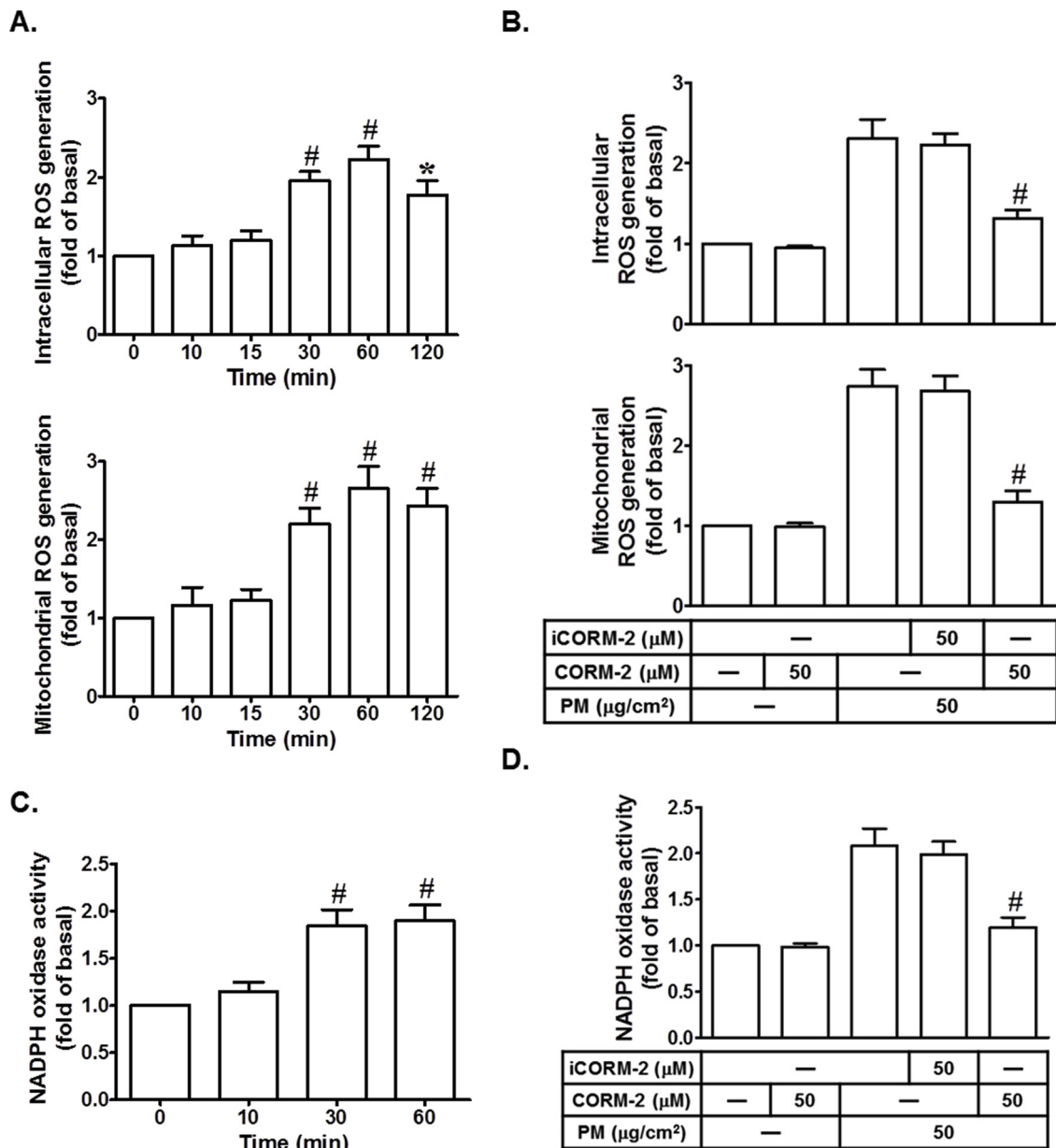


Fig. 6. CORM-2 reduces NADPH oxidase- and mitochondria-derived ROS generation induced by PM. (A) Cells were incubated with PM for the indicated times, and then the ROS generation was measured. (B) Cells were pretreated with iCORM-2 or CORM-2, and then incubated with PM for 1 h. The ROS generation was measured. (C) Cells were incubated with PM for the indicated times, and then the NADPH oxidase activity was measured. (D) Cells were pretreated with iCORM-2 or CORM-2, and then incubated with PM for 1 h. The NADPH oxidase activity was measured. Data are expressed as mean \pm S.E.M. of three independent experiments. * $P < 0.05$; # $P < 0.01$, as compared with control (A, C). # $P < 0.01$, as compared with the cells exposed to PM alone (B, D).

Recently, Zheng et al. indicated that airborne fine PM_{2.5} can cause NLRP3 inflammasome activation and lung fibrosis (Zheng et al., 2018). In addition, Xu et al. also proved that PM_{2.5} components can regulate IL-1 β signaling activation and pulmonary inflammation (Xu et al., 2018b). Moreover, CORM-2 has been proven to be effective in inhibiting lung inflammation and acute lung injury (Jiang et al., 2016). However, the mechanisms underlying CORM-2-inhibited PM-induced inflammatory responses in HPAEpiCs remain unclear. Here, in an *in vitro* study, we proved that PM induces NLRP3 inflammasome expression via the TLR2 and 4/NADPH oxidase- and mitochondria-derived ROS signaling pathway in HPAEpiCs. Assembly of the NLRP3 inflammasome triggers pro-caspase-1 into active-caspase-1, which converts pro-IL-1 β into IL-1 β . In an *in vivo* study, PM induced lung inflammation and enhanced leukocyte count in BAL fluid of mice. Moreover, CORM-2 can inhibit PM-induced inflammation via the

inhibition of activation of these inflammatory signaling pathways.

Air pollution often affects human health and causes various inflammatory diseases. Recently, more and more scholars paid attentions to the relationship between air pollution and chronic or acute inflammatory diseases. By improving air quality, countries can decrease the burden of chronic inflammatory disorders and cancers (Wu et al., 2018). PM is often a representative indicator of air pollution. It affects more people than any other pollutant. The main components of PM are complex, including ammonia, black carbon, nitrates, and sulfates, etc. Although PM₁₀ can penetrate deep into the lungs, PM_{2.5} can cause greater health damage (Lin et al., 2017). PM_{2.5} often penetrates the lung barrier and enters the blood system. Long-term exposure to particles can lead to cardiovascular and respiratory diseases and lung cancer (Wu et al., 2018; Lin et al., 2017). In this study, we found that PM could induce CRP (a marker of the inflammation) levels in

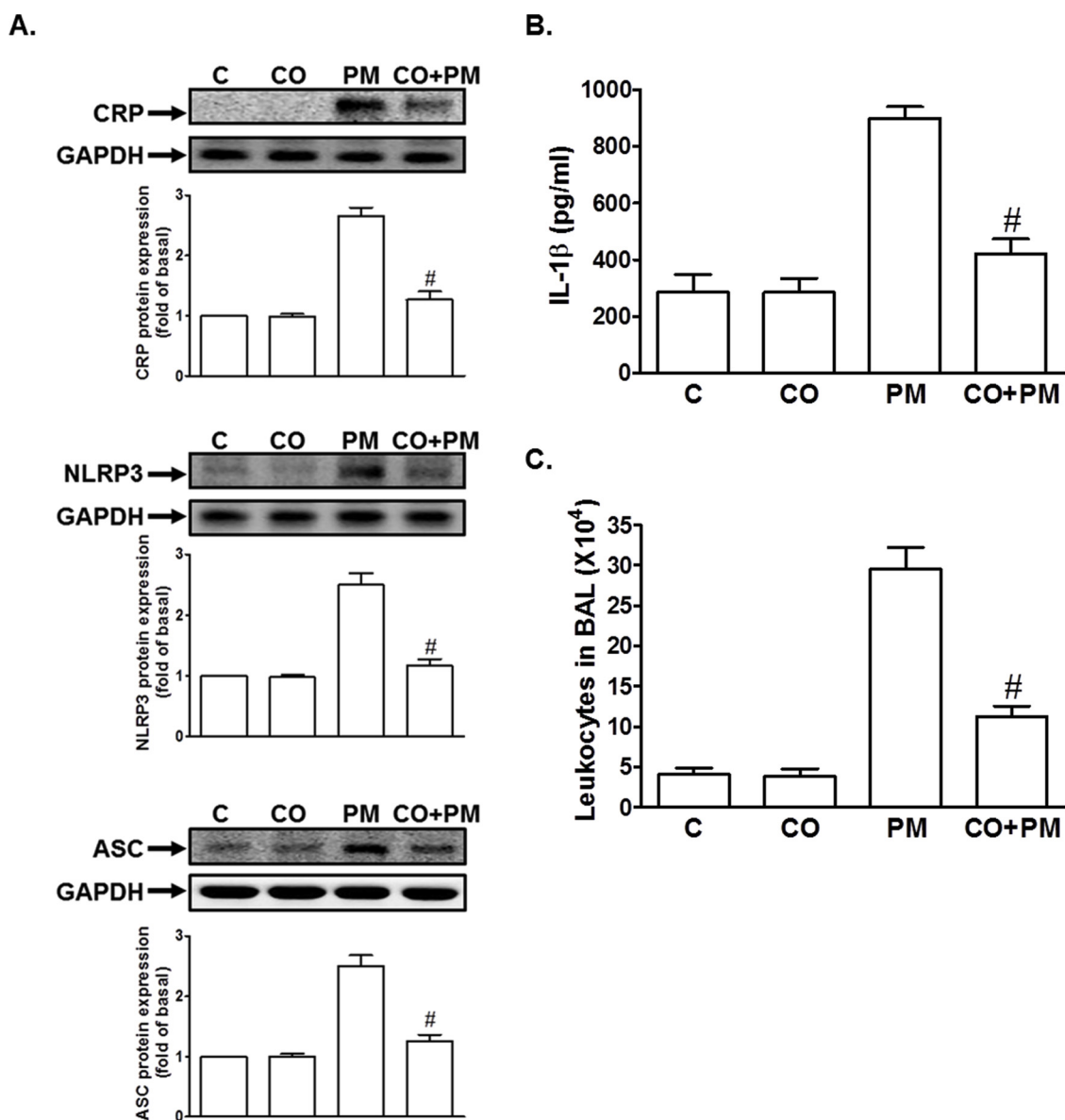


Fig. 7. PM induces lung inflammation in mice. (A) Mice were given i.v. one dose of CORM-2 (8 mg/kg), and then treated with PM for 72 h. Preparation of lung tissues was analyzed by Western blot to determine the expression of CRP, NLRP3, or ASC. (B) Mice were given i.v. one dose of CORM-2 (8 mg/kg), and then treated with PM for 72 h. The levels of IL-1 β were measured. (C) Mice were given i.v. one dose of CORM-2 (8 mg/kg), and then treated with PM for 72 h. BAL fluid was acquired and leukocyte count was determined by a hemocytometer. Data are expressed as mean \pm S.E.M. of three independent experiments. [#] $P < 0.01$, as compared with the mice exposed to PM alone.

HPAECs and in the serum of mice. The NLRP3 inflammasome plays a critical role in innate immunity by inducing IL-1 β and IL-18 secretion (Mao et al., 2018). These cytokines lead to various biological effects associated with inflammation, infection, and autoimmune processes (Moossavi et al., 2018). Here, in HPAECs and lung tissues of mice, we demonstrated that PM could induce NLRP3 expression and IL-1 β secretion. In addition, PM also induce caspase-1 activation via NLRP3 inflammasome activation. Moreover, these inflammatory responses induced by PM were reduced by CORM-2. These data indicated that CORM-2 has an anti-inflammatory effect. In the future, we will study whether CORM-2 will inhibit other inflammatory related factors.

There are a group of receptors on immune cells that are used to detect various foreign substances, called TLRs, which are mainly involved in "non-specific immune responses" (Shoenfelt et al., 2009; Vijay, 2018). Signaling of TLRs can regulate various cellular immune responses, such as the generation of pro-inflammatory cytokines, etc. So far, the scientists have identified 10 human and 12 murine TLRs (Vijay,

2018). TLR2 is critical for the recognition of bacterial lipoproteins, lipomannans, and lipoteichoic acids from Gram-positive bacteria (Roshan et al., 2016). TLR4 is predominantly activated by lipopolysaccharide (Roshan et al., 2016). However, many studies have proved that TLR2 and TLR4 are involved in PM-induced inflammation (Shoenfelt et al., 2009; Zhao et al., 2012). Indeed, in HPAECs, we also demonstrated that PM could induce inflammatory responses via TLR2 and TLR4 by using siRNAs of TLR2 and TLR4. On the other hand, we proved that CORM-2 had the inhibitory effects on TLR2 and TLR4 mRNA levels induced by PM. Thus, we suggest that CORM-2 can reduce lung inflammation induced by PM via the inhibition of TLR2 and TLR4 expression. In the future, we will investigate whether PM can induce inflammation via other TLRs in HPAECs.

Recently, many studies have proved that ROS can regulate gene expression, apoptosis, and cell signaling pathways activation (Lee and Yang, 2012). ROS can serve as both intra- and intercellular messengers. The main cellular sources of ROS include mitochondria and NADPH

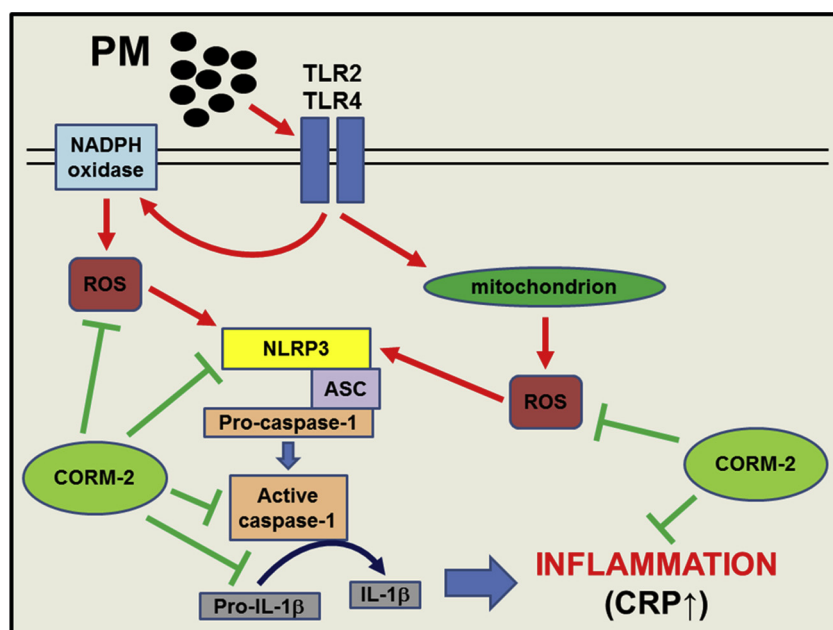


Fig. 8. Schematic diagram illustrating the proposed signaling pathway involved in the inhibitory effects of CORM-2 on PM-induced inflammatory responses. In HPAEpiCs, PM induces NLRP3 inflammasome activation via the TLR2 and 4/NADPH oxidase- and mitochondria-derived ROS signaling pathway. Assembly of the NLRP3 inflammasome triggers pro-caspase-1 into active-caspase-1, which converts pro-IL-1 β into IL-1 β . This response induced by PM further causes lung inflammation. Moreover, CORM-2 can inhibit PM-induced inflammation via the inhibition of activation of these inflammatory signaling pathways.

oxidases (Lee and Yang, 2012). However, overexpression of ROS leads to oxidative stress. Oxidative stress is a deleterious process that causes lung inflammation and damage (Rosanna and Salvatore, 2012). In addition, many studies have indicated that PM_{2.5} can induce tissue/organ damage and inflammation via ROS (Xu et al., 2018a; Li et al., 2018c; Zou et al., 2016). Indeed, in HPAEpiCs, we proved that PM could enhance NADPH oxidase activity and NADPH oxidase- and mitochondria-derived ROS generation. On the other hand, preincubation with an antioxidant, the inhibitor of NADPH oxidase, or a mitochondria-specific superoxide scavenger could inhibit PM-induced CRP expression. These results suggest that PM induces lung inflammation via NADPH oxidase- and mitochondria-derived ROS in HPAEpiCs. ROS have been shown to mediate NLRP3 inflammasome activation and IL-1 β secretion (Li et al., 2018b; Zhang et al., 2018b). This response is confirmed by our observation that PM-induced IL-1 β secretion and caspase-1 activation were reduced by pretreatment with an antioxidant. Interestingly, NAC (an antioxidant) had no effects on PM-induced NLRP3, IL-1 β , and caspase-1 mRNA levels. These results suggest that ROS cause lung inflammation through regulation of NLRP3 inflammasome activation, but not NLRP3 inflammasome expression. CO liberated from CORM-2 exerts an antioxidant effect (Lee et al., 2018). In HPAEpiCs, we proved that pretreatment with CORM-2, but not iCORM-2 significantly inhibited PM-induced NADPH oxidase activity and NADPH oxidase- and mitochondria-derived ROS production. In the future, we will investigate the detailed mechanisms involved in PM-induced ROS generation in HPAEpiCs.

In summary, as depicted in Fig. 8, our data demonstrate that in HPAEpiCs, PM induces NLRP3 inflammasome activation via the TLR2 and 4/NADPH oxidase- and mitochondria-derived ROS signaling pathway. Assembly of the NLRP3 inflammasome triggers pro-caspase-1 into active-caspase-1, which converts pro-IL-1 β into IL-1 β . This response induced by PM further causes lung inflammation. Moreover, CORM-2 can inhibit PM-induced inflammation via the inhibition of activation of these inflammatory signaling pathways.

Conflict of interest

The authors declare no conflict of interest.

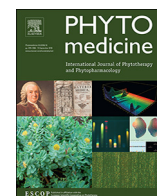
Acknowledgments

This work was supported by the Chang Gung Medical Research Program Foundation, grant number CMRPF6H0101; the China Medical University, grant number CMU106-S-14, CMU105-S-46, and CMU104-N-02.

References

- Li, R., Zhou, R., Zhang, J., 2018a. Function of PM_{2.5} in the pathogenesis of lung cancer and chronic airway inflammatory diseases. *Oncol. Lett.* 15, 7506–7514.
- Jeong, S.C., Cho, Y., Song, M.K., Lee, E., Ryu, J.C., 2017. Epidermal growth factor receptor (EGFR)-MAPK-nuclear factor(NF)- κ B-IL8: a possible mechanism of particulate matter(PM) 2.5-induced lung toxicity. *Environ. Toxicol.* 32, 1628–1636.
- Liu, B., Wu, S.D., Shen, L.J., Zhao, T.X., Wei, Y., Tang, X.L., Long, C.L., Zhou, Y., He, D.W., Lin, T., Wei, G.H., 2019. Spermatogenesis dysfunction induced by PM_{2.5} from automobile exhaust via the ROS-mediated MAPK signaling pathway. *Ecotoxicol. Environ. Saf.* 167, 161–168.
- Li, F., Xu, M., Wang, M., Wang, L., Wang, H., Zhang, H., Chen, Y., Gong, J., Zhang, J.J., Adcock, I.M., Chung, K.F., Zhou, X., 2018b. Roles of mitochondrial ROS and NLRP3 inflammasome in multiple ozone-induced lung inflammation and emphysema. *Respir. Res.* 19, 230.
- Sun, B., Wang, X., Ji, Z., Li, R., Xia, T., 2013. NLRP3 inflammasome activation induced by engineered nanomaterials. *Small* 9, 1595–1607.
- Mao, L., Kitani, A., Strober, W., Fuss, I.J., 2018. The role of NLRP3 and IL-1 β in the pathogenesis of inflammatory bowel disease. *Front. Immunol.* 9, 2566.
- Lappalainen, U., Whitsett, J.A., Wert, S.E., Tichelaar, J.W., Bry, K., 2005. Interleukin-1 β causes pulmonary inflammation, emphysema, and airway remodeling in the adult murine lung. *Am. J. Respir. Cell Mol. Biol.* 32, 311–318.
- Palomäki, J., Välimäki, E., Sund, J., Vippola, M., Clausen, P.A., Jensen, K.A., Savolainen, K., Matikainen, S., Alenius, H., 2011. Long, needle-like carbon nanotubes and asbestos activate the NLRP3 inflammasome through a similar mechanism. *ACS Nano* 5, 6861–6870.
- Li, R., Ji, Z., Chang, C.H., Dunphy, D.R., Cai, X., Meng, H., Zhang, H., Sun, B., Wang, X., Dong, J., Lin, S., Wang, M., Liao, Y.P., Brinker, C.J., Nel, A., Xia, T., 2014. Surface interactions with compartmentalized cellular phosphates explain rare earth oxide nanoparticle hazard and provide opportunities for safer design. *ACS Nano* 8, 1771.
- Cassel, S.L., Joly, S., Sutterwala, F.S., 2009. The NLRP3 inflammasome: a sensor of immune danger signals. *Semin. Immunol.* 21, 194–198.
- Jin, C., Flavell, R.A., 2010. Molecular mechanism of NLRP3 inflammasome activation. *J. Clin. Immunol.* 30, 628–631.
- Shao, L., Liu, C., Wang, S., Liu, J., Wang, L., Lv, L., Zou, Y., 2018. The impact of exogenous CO releasing molecule CORM-2 on inflammation and signaling of orthotopic lung cancer. *Oncol. Lett.* 16, 3223–3230.
- Caumartin, Y., Stephen, J., Deng, J.P., Lian, D., Lan, Z., Liu, W., Garcia, B., Jevnikar, A.M., Wang, H., Cepinskas, G., Luke, P.P., 2011. Carbon monoxide-releasing molecules protect against ischemia-reperfusion injury during kidney transplantation. *Kidney Int.* 79, 1080–1089.
- Uddin, M.J., Li, C.S., Joe, Y., Chen, Y., Zhang, Q., Ryter, S.W., Chung, H.T., 2015. Carbon monoxide inhibits tenascin-C mediated inflammation via IL-10 expression in a septic mouse model. *Mediators Inflamm.* 2015, 613249.

- Lee, C.W., Wu, C.H., Chiang, Y.C., Chen, Y.L., Chang, K.T., Chuang, C.C., Lee, I.T., 2018. Carbon monoxide releasing molecule-2 attenuates *Pseudomonas aeruginosa*-induced ROS-dependent ICAM-1 expression in human pulmonary alveolar epithelial cells. *Redox Biol.* 18, 93–103.
- Cho, R.L., Yang, C.C., Lee, I.T., Lin, C.C., Chi, P.L., Hsiao, L.D., Yang, C.M., 2016. Lipopolysaccharide induces ICAM-1 expression via a c-Src/NADPH oxidase/ROS-dependent NF- κ B pathway in human pulmonary alveolar epithelial cells. *Am. J. Physiol. Lung Cell Mol. Physiol.* 310, L639–L657.
- Zheng, R., Tao, L., Jian, H., Chang, Y., Cheng, Y., Feng, Y., Zhang, H., 2018. NLRP3 inflammasome activation and lung fibrosis caused by airborne fine particulate matter. *Ecotoxicol. Environ. Saf.* 163, 612–619.
- Zhang, J.B., Zhang, L., Li, S.Q., Hou, A.H., Liu, W.C., Dai, L.L., 2018a. Tubeimoside I attenuates inflammation and oxidative damage in a mice model of PM_{2.5}-induced pulmonary injury. *Exp. Ther. Med.* 15, 1602–1607.
- Shoenfelt, J., Mitkus, R.J., Zeisler, R., Spatz, R.O., Powell, J., Fenton, M.J., Squibb, K.A., Medvedev, A.E., 2009. Involvement of TLR2 and TLR4 in inflammatory immune responses induced by fine and coarse ambient air particulate matter. *J. Leukoc. Biol.* 86, 303–312.
- Zhao, C., Liao, J., Chu, W., Wang, S., Yang, T., Tao, Y., Wang, G., 2012. Involvement of TLR2 and TLR4 and Th1/Th2 shift in inflammatory responses induced by fine ambient particulate matter in mice. *Inhal. Toxicol.* 24, 918–927.
- Yang, X., Feng, L., Zhang, Y., Hu, H., Shi, Y., Liang, S., Zhao, T., Fu, Y., Duan, J., Sun, Z., 2018. Cytotoxicity induced by fine particulate matter (PM_{2.5}) via mitochondria-mediated apoptosis pathway in human cardiomyocytes. *Ecotoxicol. Environ. Saf.* 161, 198–207.
- Xu, C., Shi, Q., Zhang, L., Zhao, H., 2018a. High molecular weight hyaluronan attenuates fine particulate matter-induced acute lung injury through inhibition of ROS-ASK1-p38/JNK-mediated epithelial apoptosis. *Environ. Toxicol. Pharmacol.* 59, 190–198.
- Zhang, H., Chen, X., Zong, B., Yuan, H., Wang, Z., Wei, Y., Wang, X., Liu, G., Zhang, J., Li, S., Cheng, G., Wang, Y., Ma, Y., 2018b. Gypenosides improve diabetic cardiomyopathy by inhibiting ROS-mediated NLRP3 inflammasome activation. *J. Cell. Mol. Med.* 22, 4437–4448.
- Xu, F., Qiu, X., Hu, X., Shang, Y., Pardo, M., Fang, Y., Wang, J., Rudich, Y., Zhu, T., 2018b. Effects on IL-1 β signaling activation induced by water and organic extracts of fine particulate matter (PM_{2.5}) *in vitro*. *Environ. Pollut.* 237, 592–600.
- Jiang, L., Fei, D., Gong, R., Yang, W., Yu, W., Pan, S., Zhao, M., Zhao, M., 2016. CORM-2 inhibits TXNIP/NLRP3 inflammasome pathway in LPS-induced acute lung injury. *Inflamm. Res.* 65, 905–915.
- Wu, J.Z., Ge, D.D., Zhou, L.F., Hou, L.Y., Zhou, Y., Li, Q.Y., 2018. Effects of particulate matter on allergic respiratory diseases. *Chronic Dis. Transl. Med.* 4, 95–102.
- Lin, H., Wang, X., Liu, T., Li, X., Xiao, J., Zeng, W., Ma, W., 2017. Air Pollution and Mortality in China. *Adv. Exp. Med. Biol.* 1017, 103–121.
- Moossavi, M., Parsamanesh, N., Bahrani, A., Atkin, S.L., Sahebkar, A., 2018. Role of the NLRP3 inflammasome in cancer. *Mol. Cancer* 17, 158.
- Vijay, K., 2018. Toll-like receptors in immunity and inflammatory diseases: past, present, and future. *Int. Immunopharmacol.* 59, 391–412.
- Roshan, M.H., Tambo, A., Pace, N.P., 2016. The role of TLR2, TLR4, and TLR9 in the pathogenesis of atherosclerosis. *Int. J. Inflamm.* 2016, 1532832.
- Lee, I.T., Yang, C.M., 2012. Role of NADPH oxidase/ROS in pro-inflammatory mediators-induced airway and pulmonary diseases. *Biochem. Pharmacol.* 84, 581–590.
- Rosanna, D.P., Salvatore, C., 2012. Reactive oxygen species, inflammation, and lung diseases. *Curr. Pharm. Des.* 18, 3889–3900.
- Li, B., Guo, L., Ku, T., Chen, M., Li, G., Sang, N., 2018c. PM_{2.5} exposure stimulates COX-2-mediated excitatory synaptic transmission via ROS-NF- κ B pathway. *Chemosphere.* 190, 124–134.
- Zou, Y., Jin, C., Su, Y., Li, J., Zhu, B., 2016. Water soluble and insoluble components of urban PM_{2.5} and their cytotoxic effects on epithelial cells (A549) *in vitro*. *Environ. Pollut.* 212, 627–635.



Sophoraflavanone G from *Sophora flavescens* induces apoptosis in triple-negative breast cancer cells

Wen-Chung Huang^{a,b,1}, Pei-Yu Gu^{a,1}, Li-Wen Fang^c, Yu-Ling Huang^{d,e}, Chwan-Fwu Lin^{e,f,*}, Chian-Jiun Liou^{b,g,**}

^a Graduate Institute of Health Industry Technology, Research Center for Food and Cosmetic Safety, Research Center for Chinese Herbal Medicine, College of Human Ecology, Chang Gung University of Science and Technology, No.261, Wenhua 1st Rd., Guishan Dist., Taoyuan City 33303, Taiwan

^b Division of Allergy, Asthma, and Rheumatology, Department of Pediatrics, Chang Gung Memorial Hospital, Linkou, Guishan Dist., Taoyuan City 33303, Taiwan

^c Department of Nutrition, I-Shou University, No.8, Yida Rd. Yanchao Dist., Kaohsiung City, Taiwan

^d National Research Institute of Chinese Medicine, Ministry of Health and Welfare, No. 155-1, Sec. 2, Li-Nung St., Peitou, Taipei, Taiwan

^e Department of Cosmetic Science, Research Center for Food and Cosmetic Safety, Research Center for Chinese Herbal Medicine, College of Human Ecology, Chang Gung University of Science and Technology, No.261, Wenhua 1st Rd., Guishan Dist., Taoyuan City 33303, Taiwan

^f Department of Anesthesiology, Chang Gung Memorial Hospital, Linkou, Guishan Dist., Taoyuan City 33303, Taiwan

^g Department of Nursing, Division of Basic Medical Sciences, Research Center for Chinese Herbal Medicine, and Graduate Institute of Health Industry Technology, Chang Gung University of Science and Technology, No.261, Wenhua 1st Rd., Guishan Dist., Taoyuan City 33303, Taiwan

ARTICLE INFO

Keywords:

Apoptosis
Caspase-3
MDA-MB-231 cells
Sophoraflavanone G

ABSTRACT

Background: A compound isolated from *Sophora flavescens*—sophoraflavanone G (SG)—showed anti-tumor and anti-inflammatory properties. We previously demonstrated that SG promoted apoptosis in human leukemia HL-60 cells. In the present study, we investigated the effects of SG on apoptosis in human breast cancer MDA-MB-231 cells, and explored the underlying molecular mechanisms.

Methods: MDA-MB-231 cells were treated with various SG concentrations, and cell viability was evaluated by MTT assay. Apoptotic signal proteins were detected by western blotting, and cell apoptosis was assessed using flow cytometry.

Results: Our results demonstrated that SG induced nuclear condensation, DNA fragmentation, reactive oxygen species production, and increased cell apoptosis in MDA-MB-231 cells. SG also suppressed migration and invasion, likely via blockage of the MAPK pathway. In the apoptotic signaling pathway, SG increased cleaved caspase-8, caspase-3, and caspase-9. SG treatment also decreased Bcl-2 and Bcl-xL expression, increased Bax expression, and prompted release of more cytochrome c from mitochondria to the cytoplasm in MDA-MB-231 cells.

Conclusion: Overall, our findings suggest that SG might increase apoptosis, and decrease migration and invasion, in MDA-MB-231 cells through suppression of a MAPK-related pathway.

Introduction

Breast cancer is one of the most common cancers in the world, and shows a trend of increasing incidence (Shi et al., 2018). In 2011, about 508,000 people died of breast cancer worldwide (DeSantis et al., 2011). In 2017, about 250,000 new invasive breast cancer patients were diagnosed in American women (DeSantis et al., 2017). Breast cancer development is divided into four subtypes: luminal A (ER⁺, PR⁺,

HER2⁻), luminal B (ER⁺, PR⁻, HER2⁺), HER2 type (ER⁻, PR⁻, HER2⁺), and triple-negative breast cancer (ER⁻, PR⁻, HER2⁻). Of these types, triple-negative breast cancer is the most difficult to treat and has the highest mortality rate (Shi et al., 2018). Despite great progress in the early detection of breast cancer tumors, about 5–10% of women have confirmed cancer cell metastasis at the time of breast cancer diagnosis (DeSantis et al., 2011). Metastasis is the most common cause of death in breast cancer patients, and is associated with an

Abbreviations: DCFH-DA, 2',7'-dichlorofluorescein diacetate; MAPK, mitogen-activated protein kinase; PVDF, polyvinylidene fluoride; ROS, Reactive oxygen species; SG, sophoraflavanone G

* Corresponding author.

** Co-corresponding author.

E-mail addresses: cflin@mail.cgu.edu.tw (C.-F. Lin), ccliu@mail.cgu.edu.tw (C.-J. Liou).

¹ These authors contributed equally.

<https://doi.org/10.1016/j.phymed.2019.152852>

Received 19 October 2018; Received in revised form 23 January 2019; Accepted 27 January 2019

0944-7113/© 2019 Elsevier GmbH. All rights reserved.

average survival of 2 years, and a 5-year survival rate of only 5% (Dieci et al., 2018). Mastectomy is the main treatment for breast cancer. Chemotherapy or radiation therapy can also be administered to inhibit breast cancer cell growth. Breast cancer can use chemotherapy drugs, including adriamycin, docetaxel and paclitaxel, to reduce cancer cell metastasis (Bielopolski et al., 2017). However, patients who undergo chemotherapy or radiation therapy still have a 5-year recurrence rate of about 7–12% (DeSantis et al., 2011). Moreover, radiotherapy and chemotherapy can cause many side effects, including severe hair loss, vomiting, nausea, decreased appetite, and diarrhea (Celio and Fabbioni, 2018).

Induction of cancer cell apoptosis is a potential cancer treatment strategy (Burke, 2017). Apoptosis is characterized by morphological and structural changes, including plasma membrane blebbing, nucleus and chromatin condensation, attenuation of mitochondrial membrane potential, and DNA fragmentation for programmed cell death (Wong, 2011). Some cancer cells evade the apoptotic pathway, thus promoting cancer cell survival and increasing neoplastic metastasis (Philchenkov and Balcer-Kubiczek, 2016). Triple-negative breast cancer cells are highly metastatic, leading to rapid cancer progression and difficult treatment following breast cancer metastasis (Shi et al., 2018). There is great interest in developing novel drugs to induce apoptosis in cancer cells, particularly in triple-negative breast cancer cells, to suppress their growth and metastasis.

Previous studies show that natural products exert anti-cancer effects, and have great potential to induce apoptosis in breast cancer cells (Mitra and Dash, 2018). Alisol B and curcumin reportedly increase mitochondrial function dysregulation, and the generation of reactive oxygen species in MDA-MB-231 cells (Fan et al., 2016; Zhang et al., 2017). Astragaloside IV and kaempferol can suppress breast cancer cell invasion by inhibiting mitogen-activated protein kinase (MAPK) signaling (Jiang et al., 2017; Li et al., 2017b). In traditional Chinese medicine, root of *Sophora flavescens* is used to treat fevers and induce diuresis to reduce edema (Huang et al., 2017). A compound isolated from *S. flavescens* roots—sophoraflavanone G (SG; 5,7,8,2',4'-tetrahydroxy-8-lavandulylflavanone)—can reportedly suppress inflammatory response in lipopolysaccharide-stimulated macrophages (Guo et al., 2016; Shen et al., 2006; Wun et al., 2013). Moreover, we previously found that SG could enhance apoptosis in human leukemia HL-60 cells via involved MAPK activation (Li et al., 2016). A previous study also demonstrated that SG would be a promising target for induced apoptosis in Hodgkin's lymphoma L540 cell line through suppressing phosphorylation of STAT and JAK proteins (Kim et al., 2013). In the present study, we aimed to evaluate the effects of SG on apoptosis in MDA-MB-231 human breast cancer cells, and to explore the underlying molecular mechanism of these effects.

Materials and methods

Isolation of sophoraflavanone G

S. flavescens was identified by comparison with the voucher specimen (NRICM-03-011), which is deposited at the herbarium of the National Research Institute of Chinese Medicine, Taiwan (Shen et al., 2006). SG was isolated from *S. flavescens* as previously described (Li et al., 2016). Briefly, an extract was prepared from the roots of *S. flavescens* (1000 g) using 95% alcohol, and this extract was divided into fractions using ethyl acetate and H₂O. Next, the ethyl acetate fraction was separated by chromatography on a column containing silica gel, and the fraction was eluted by chromatography using a Sephadex LH-20 column. This process yielded 0.72 g SG of 98% purity. The structure of SG was determined using NMR, and the molecular weight (423.18) was measured by mass spectroscopic approaches.

Furthermore, curcumin ($\geq 98\%$ purity by HPLC) was purchased from Sigma-Aldrich (St. Louis, MO, USA). The stock solution was 30 mM in DMSO. The final DMSO concentration should not exceed

0.1% in culture medium.

Cell culture

MDA-MB-231 cells were purchased from the Bioresource Collection and Research Center in Taiwan. These cells were maintained in DMEM medium with 10% fetal bovine serum (Biological Industries, Haemek, Israel), 1% penicillin–streptomycin, and 2 mM L-glutamine. Cells were subcultured twice weekly, and incubated at 37 °C under 5% CO₂.

Cell viability assay

A stock solution was prepared by dissolving 100 mM SG in DMSO. The DMSO concentration was less than 0.1% in all cell experiments. Cell viability was determined by MTT assay as previously described (Peng et al., 2018). Briefly, cells (10^4 cells/well) were plated in 96-well culture plates and treated with various SG concentrations (1–40 μ M) for 24 h. Next, the cells were incubated with 0.5 mg/ml MTT solution for 4 h. Finally, isopropanol was added to dissolve the formazan crystals and the optical density at 570 nm was measured using a microplate reader (Multiskan FC, Thermo, Waltham, MA, USA).

Apoptotic cell assay

Apoptotic cells were assayed using the Annexin V & Dead Cell Assay Kit (Merck Ltd., Taiwan) following the manufacturer's instructions. Briefly, the cells were washed with cold PBS, and then incubated with 100 μ l Annexin V and Dead Cell Reagent for 20 min, in the dark, at room temperature. Next, apoptotic cells were detected and analyzed by flow cytometry (Muse® Cell Analyzer; Merck Ltd., Taiwan).

Caspase-3 activity assay

Caspase-3 activity was detected using the Caspase-3 Assay Kit (Sigma, St. Louis, MO, USA) according to the manufacturer's instructions, as previously described (Li et al., 2016). Briefly, MDA-MB-231 cells (5×10^5 cells/well) were seeded on 6 well culture plate and treated with SG for 24 h, and then lysed. The supernatant was collected and added to a 96-well plate. Next, Ac-DEVD-pNA (caspase-3 substrate) was added to each well, and the optical density at 450 nm was detected using a microplate reader (Multiskan FC, Thermo). In addition, Z-WEHD-FMK (caspase 8 inhibitor) (Santa Cruz Biotechnology, Dallas, USA) and Z-DEVD-FMK (caspase 3 inhibitor) (Santa Cruz Biotechnology) also treated with cells to detect the levels of caspase 3 activity.

DAPI staining of apoptotic cells

MDA-MB-231 cells (5×10^5 cells) were treated with various SG concentrations (0–30 μ M) for 24 h, and then stained with DAPI solution (Sigma). The apoptotic morphological changes were observed and photographed using fluorescence microscopy (Olympus, Tokyo, Japan).

DNA fragmentation analysis

Briefly, MDA-MB-231 cells (5×10^5 cells/well) were seeded on 6 well culture plate and treated with various SG concentrations (0–30 μ M) for 24 h. From these cells, fragmented DNA was extracted using the ApopLadder Ex™ Kit (TaKaRa, Kyoto Japan) following the manufacturer's instructions. DNA fragments were examined by gel electrophoresis on a 1.5% agarose gel.

Reactive oxygen species (ROS) assay

Briefly, MDA-MB-231 cells (5×10^5 cells/well) were seeded on 6 well culture plate and treated with various SG concentrations

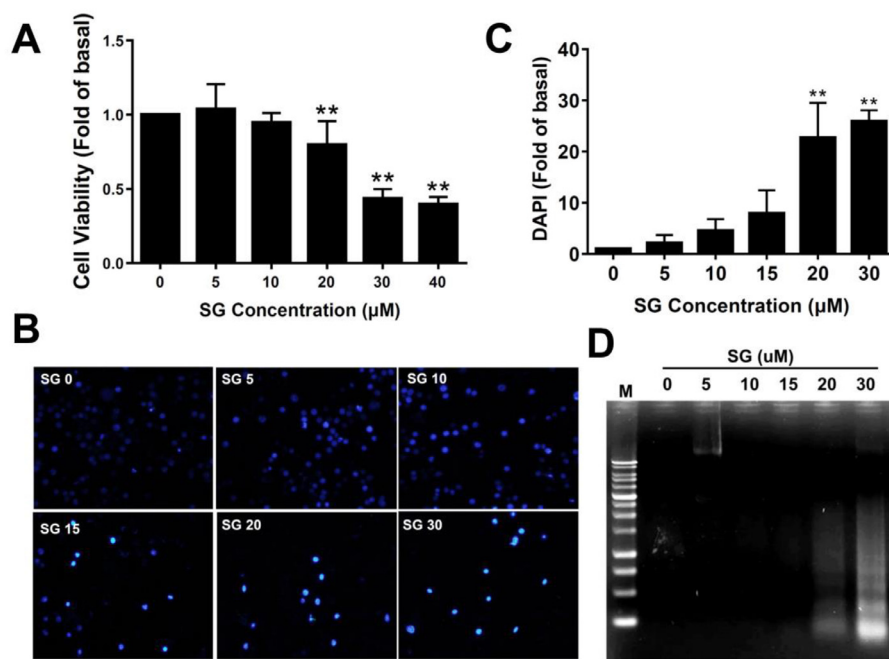


Fig. 1. (A) Cell viability of MDA-MB-231 cells treated with the indicated sophoraflavanone G (SG) concentrations (0–40 μM) for 24 h. (B) Morphological changes in MDA-MB-231 cells treated with SG for 24 h and stained with DAPI, and (C) the results of DAPI quantitative analysis. (D) Analysis of DNA fragmentation in MDA-MB-231 cells treated with the indicated SG concentrations (0–30 μM) for 24 h, using 1.5% agarose gel electrophoresis. M: DNA marker. Data are presented as mean ± SD. ** $p < 0.01$ compared to untreated cells (0 μM SG).

(0–30 μM) as previously described (Liou et al., 2018). These cells were then incubated with 20 μM 2',7'-dichlorofluorescein diacetate (DCFH-DA) for 30 min, and ROS levels were measured using a Multi-Mode microplate reader (BioTek synergy HT). Intracellular ROS were also observed using a fluorescence microscope (Olympus, Tokyo, Japan).

Transwell invasion assay

The upper chamber of transwell plate coated with Matrigel™ (BD Pharmingen, NJ, USA) for 1 h. DMEM medium (contained 15% FBS) added to the lower chamber. MDA-MB-231 cells (5×10^5 cells) treated with or without 30 μM SG for 24 h, and cells were seeded in the upper chamber of transwell plate. After 24 h, the upper chamber was washed with PBS, and treated with methanol. The invasive cells were then stained with 1% crystal violet, and observed using an inverted microscope (Olympus, Tokyo, Japan). Furthermore, MAPK inhibitors (p38 inhibitor SB203580, JNK inhibitor SP600125, and ERK inhibitor PD98059; Enzo Life Sciences, Inc., Farmingdale, NY, USA) and Akt1/2 kinase inhibitor (Sigma) treated with cells to detect invasion expression.

Wound healing assay

MDA-MB-231 cells (10^5 cells/well) were seeded in a 24-well plate containing culture inserts (Corning, Lowell, MA, USA). Then the culture inserts were removed, and we added 1 μM hydroxyurea (cell proliferation inhibitor) in the culture plate. One hour later, we added 30 μM SG, and observed the cell migration at 0, 24, and 48 h using an inverted microscope (Olympus, Tokyo, Japan).

Western blot analysis

MDA-MB-231 cells were lysed using RIPA buffer containing protease inhibitors (Sigma), and then mitochondrial proteins were extracted using a Mitochondria Isolation Kit (Sigma) following the manufacturer's instructions.

Equal amounts of protein were separated by 10–12% SDS polyacrylamide gel electrophoresis, and then transferred onto polyvinylidene fluoride (PVDF) membranes, which were incubated overnight with primary antibodies at 4 °C. Next, the PVDF membranes were

incubated with secondary antibodies, and specific proteins were detected using the BioSpectrum 600 system (UVP, Upland, CA, USA). Primary antibodies included, AKT, Atg5, Bax, Bal-xL, Bcl2, beclin 1, caspase-3, cleaved caspase-3, caspase-8, cleaved caspase-8, caspase-9, cleaved caspase-9, cleaved PARP1, cytochrome c, phosphorylated AKT (Ser473), phosphorylated ERK 1/2, phosphorylated p38, phosphorylated, JNK, ERK1/2, p38, JNK, LC3B, p62, PARP-1 (Cell Signaling Technology, MA, USA), and β-actin (Sigma). Moreover, cells also treated with N-acetylcysteine (NAC, as an antioxidant) (Sigma) for checked Bax expression. MAPK inhibitors (Enzo Life Sciences) and Akt1/2 kinase inhibitor (Sigma) treated with cells to detect Bax protein expression.

Statistical analysis

All statistical results were expressed as the mean ± standard deviation (SD). Data were analyzed using one-way analysis of variance (ANOVA) followed by the Tukey-Kramer post-hoc test. The p value of < 0.05 was considered to indicate significance.

Results

Effects of SG on viability of MDA-MB-231 cells

To evaluate SG cytotoxicity, MDA-MB-231 cells were treated with SG (0–40 μM) for 24 h, and cell viability was measured using the MTT assay. The results indicated that SG reduced MDA-MB-231 cell viability in a concentration-dependent manner, with an IC_{50} value of 29.7 ± 5.2 (Fig. 1A). DAPI staining revealed nuclear condensation, showing that SG increased nuclear condensation for the induction of apoptosis in MDA-MB-231 cells (Fig. 1B and C). We also found that 20–30 μM SG enhanced DNA fragmentation in MDA-MB-231 cells (Fig. 1D).

SG induced apoptosis in MDA-MB-231 cells

MDA-MB-231 cells were stained with annexin V/7-AAD to detect apoptosis by flow cytometry. The results indicated that SG significantly induced apoptosis in MDA-MB-231 cells in a concentration-dependent manner (Fig. 2).

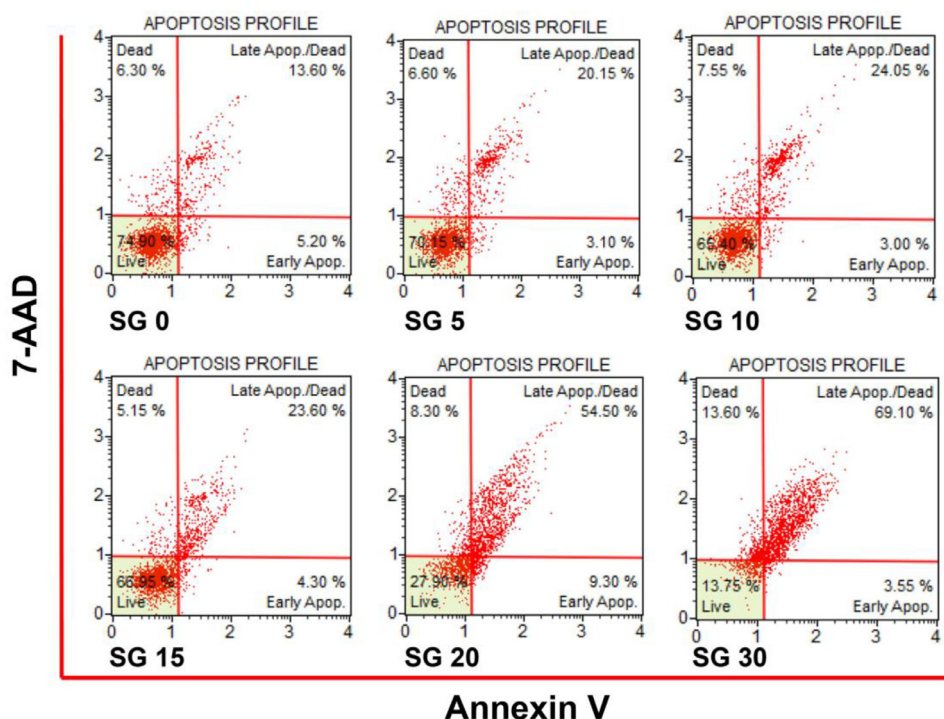


Fig. 2. Flow cytometry results showing that 24-h treatment with sophoraflavanone G (SG) induced apoptosis in MDA-MB-231 cells.

Effect of SG on ROS production

Fluorescence microscopy revealed that SG treatment increased intracellular ROS production compared to in untreated MDA-MB-231 cells (Fig. 3A). Measurement of ROS levels revealed that SG treatment dose-dependently elevated ROS production (Fig. 3B). MDA-MB-231 cells treated with 30 μM SG for different periods of time (0–120 min) showed that ROS levels increased in accordance with the duration of treatment (Fig. 3C).

SG inhibited breast cancer cell motility

We evaluated the effect of SG on MDA-MB-231 cell motility using migration and invasion assays. MDA-MB-231 cells treated with 30 μM SG exhibited significantly inhibited migration at the tested time-points (24 and 48 h) (Fig. 4A and B). Furthermore, treatment with 30 μM SG suppressed invasion compared to in the untreated group (Fig. 4C and D). These data imply that SG decreases the motility, and thus reduces metastasis, of MDA-MB-231 cells.

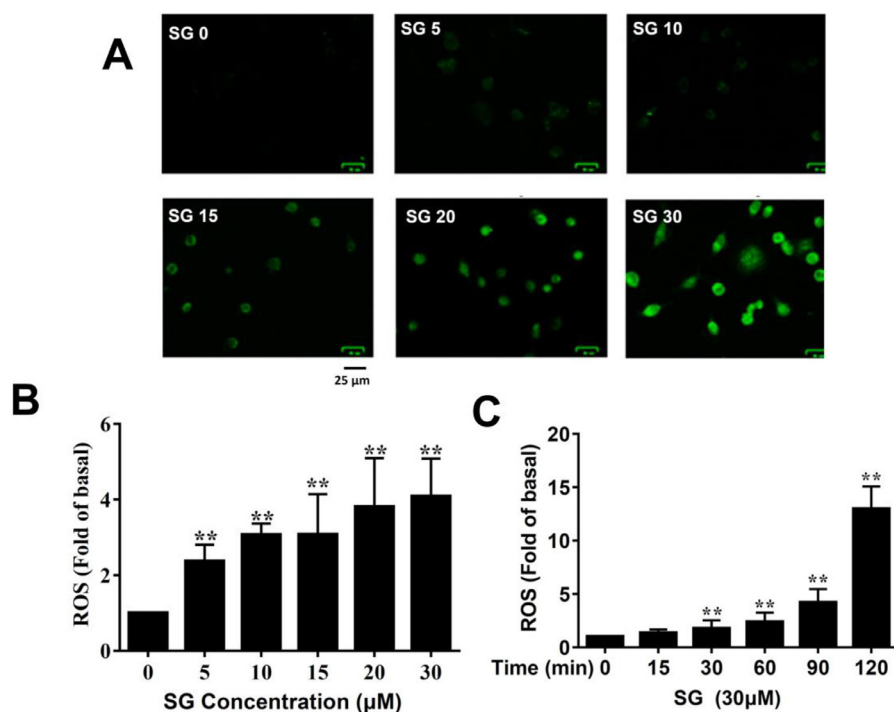


Fig. 3. Effects of sophoraflavanone G (SG) on reactive oxygen species (ROS) production in MDA-MB-231 cells. (A) Fluorescence microscope images of intracellular ROS. (B) Percentage of ROS detected in cells with the indicated SG concentrations compared to in untreated cells. Fluorescence intensity of intracellular ROS was detected using a Multi-Mode microplate reader. (C) ROS levels detected in MDA-MB-231 cells treated with 30 μM SG for the indicated periods of time. The data are presented as mean \pm SD of three independent experiments ($n = 6$). ** $p < 0.01$ compared to untreated cells (0 μM SG).

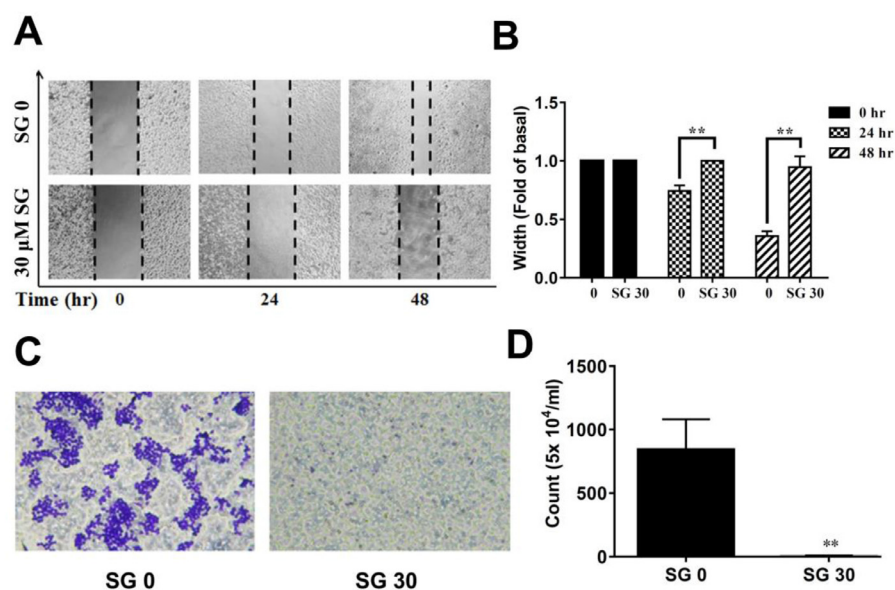


Fig. 4. Sophoraflavanone G (SG) treatment (30 μ M SG for 48 h) inhibited migration and invasion in wound healing assay (A, B) and transwell invasion assay (C, D). (A) Cell migration with and without SG treatment at different time-points. (B) Measured widths of the cell-free gap. Greater width indicates reduced cell migration. (C) Crystal violet-stained invasive cells, indicating that SG inhibited invasion. (D) Invasive cell numbers in the transwell assay. The data are presented as mean \pm SD of three independent experiments ($n = 6$). $**p < 0.01$ compared to untreated cells (0 μ M SG).

SG downregulated the phosphorylation of AKT, and MAPK pathway

The AKT and MAPK pathway is crucial for regulating cancer cell metastasis and invasion ability (Xu et al., 2014). Therefore, we assayed the phosphorylation of AKT and MAPKs. SG treatment significantly reduced the phosphorylation of AKT (Ser473), p38, ERK1/2, and JNK in MDA-MB-231 cells (Fig. 5A and B). Previous studies show that E-cadherin can increase cancer cell adhesion, preventing metastasis (Chen et al., 2018; Zhu et al., 2016b). We also assayed E-cadherin, and found that SG significantly increased E-cadherin expression compared to in the untreated group (Fig. 5C and D).

SG induced caspase activation in MDA-MB-231 cells

MDA-MB-231 cells were treated with SG for 24 h, and then caspase expressions were detected by western blot. We found that SG treatment

significantly and concentration-dependently increased the expressions of cleaved caspase-3, cleaved caspase-8, and cleaved caspase-9. SG treatment also increased cleaved PARP-1 expression compared to in the untreated group (Fig. 6A and B). We also used the caspase-3 substrate Ac-DEVD-pNA to measure caspase-3 activity, revealing that SG treatment enhanced caspase-3 activity in MDA-MB-231 cells (Fig. 6C).

Effects of SG on the intrinsic pathways in MDA-MB-231 cells

SG treatment significantly reduced Bcl-2 and Bcl-xL expressions, and significantly promoted Bax production in a concentration-dependent manner (Fig. 7A and B). SG also significantly decreased Bcl-2/Bax ratio compared to in the untreated group (Fig. 7C). We also found that NAC (as an antioxidant) could increase Bax expression, and SG combined with NAC more significantly promoted Bax signal expression compared to in the untreated group (Fig. 7D). Interestingly, SG also

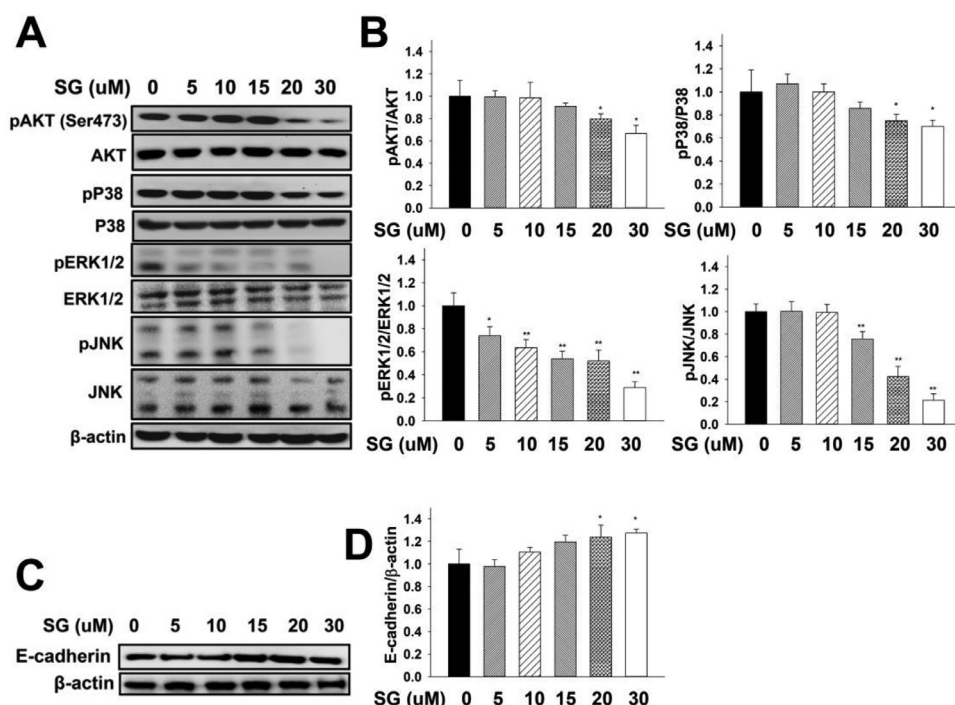


Fig. 5. Effect of varying concentrations (0–30 μ M) of sophoraflavanone G (SG) on phosphorylation of AKT and mitogen-activated protein kinases (MAPKs). (A, B) MDA-MB-231 cells were treated with SG for 24 h, and the indicated proteins were detected by western blot. Total AKT and MAPK levels were used as internal controls. (C, D) E-cadherin was also assessed by western blot, with β -actin was used as an internal control. The data are presented as mean \pm SD of three independent experiments ($n = 6$). $*p < 0.05$, $**p < 0.01$ compared to untreated cells (0 μ M SG).

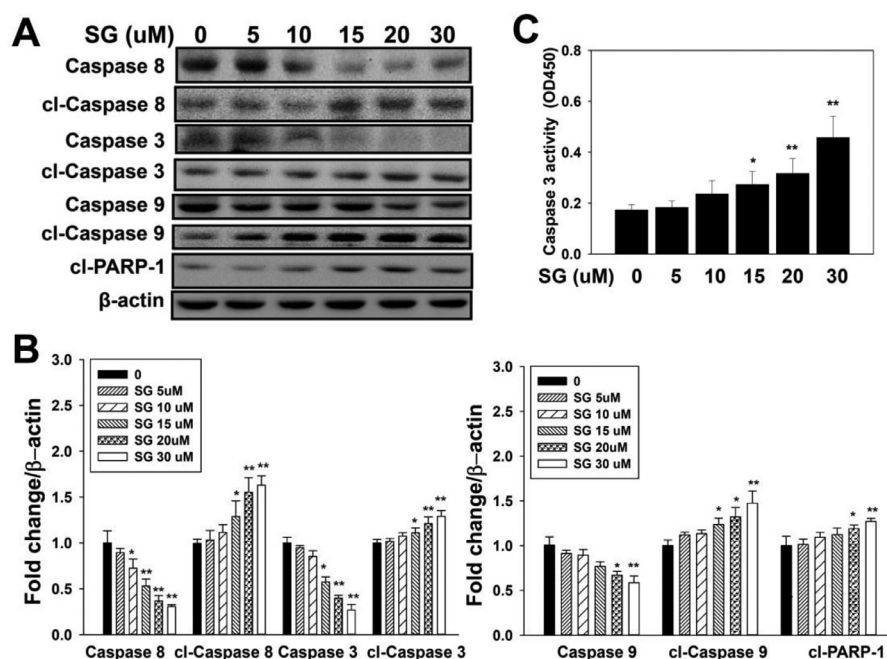


Fig. 6. Sophoraflavanone G (SG) cleaved apoptosis-related caspase proteins in MDA-MB-231 cells. (A, B) Cells were treated with SG for 24 h, and western blotting was performed to evaluate cleaved (cl) caspase-3, cleaved caspase-8, cleaved caspase-9, and cleaved PARP-1 expression. β-actin levels were used as internal controls. (C) SG concentration-dependently increased caspase-3 activity in MDA-MB-231 cells. Data are presented as mean ± SD. * $p < 0.05$, ** $p < 0.01$ compared to untreated cells (0 μM SG).

prompted the release of more cytochrome c from mitochondria into the cytoplasm (Fig. 8).

AKT and MAPK pathway regulated the intrinsic pathways and cell invasion

We used MAPK inhibitors (p38 inhibitor SB203580, JNK inhibitor SP600125, and ERK inhibitor PD98059) and Akt1/2 kinase inhibitor to detect invasion expression. The result demonstrated that SG, MAPK inhibitors and Akt1/2 kinase inhibitors could increase E-cadherin and invasion in MDA-MB-231 cells (Fig. 9A and B). Interestingly, SG combined with SP600125 could increase Bax expression compared to SP600125 group. However, SG combined with PD98059, SB203580 or Akt1/2 kinase inhibitors did not increase Bax expression compared to the treated inhibitor group, respectively (Fig. 9C). In addition, Z-WEHD-FMK (caspase 8 inhibitor) did not significantly caspase 3 activity. However, Z-DEVD-FMK (caspase 3 inhibitor) could decrease

caspase 3 activity compared to in the untreated group. Hence, we thought that caspase-8 was an upstream molecule of caspase-3 in this experimental mode (Fig. 9D).

SG regulated autophagy in MDA-MB-231 cells

SG significantly promoted LC3B (LC3I and LC3 II) protein levels compared to in the untreated group (Fig. 10). MDA-MB-231 cells treated with SG also could increase Atg5 and beclin 1 expressions, but reduce p62 protein expressions compared to untreated MDA-MB-231 cells. Furthermore, curcumin was widely used to study apoptosis of breast cancer cells (Banik et al., 2017; Sun et al., 2012; Zheng et al., 2012). We also found that MDA-MB-231 cells treated with curcumin and SG could increase the expressions of cleaved caspase-3 compared to in the untreated group. Both curcumin and SG reduced Bcl-2 expressions, and promoted Bax production (Fig. 11A). Moreover, SG was like

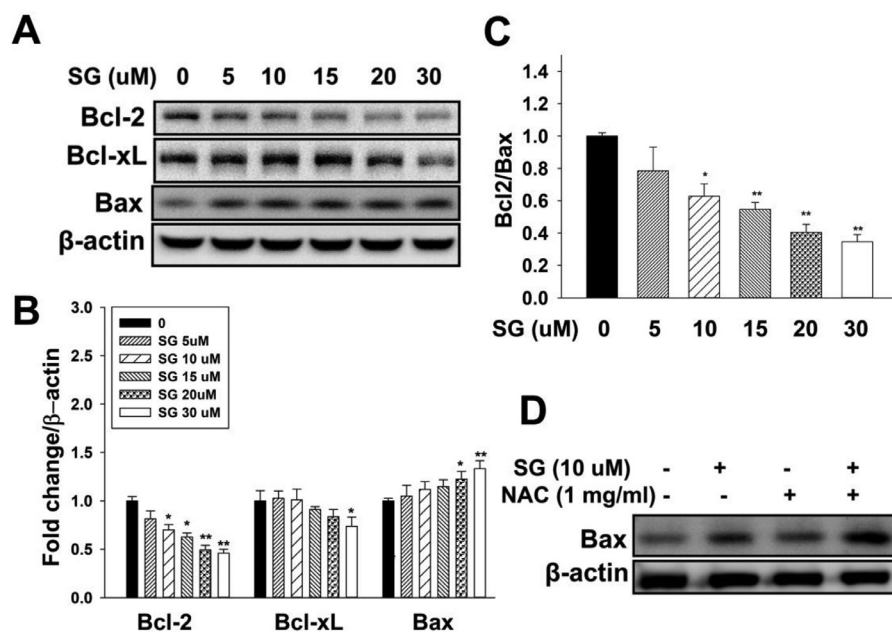


Fig. 7. (A, B) The apoptosis proteins Bcl-2, Bcl-xL, and Bax protein were measured in MDA-MB-231 cells with and without sophoraflavanone G (SG) treatment. β-actin was used as an internal control. (C) SG treatment affected the ratio of Bcl-2/Bax in MDA-MB-231 cells. (D) MDA-MB-231 cells treated with 1 mg/ml N-Acetylcysteine (NAC, as an antioxidant) for checked Bax expression. Data are presented as mean ± SD. * $p < 0.05$, ** $p < 0.01$ compared to untreated cells (0 μM SG).

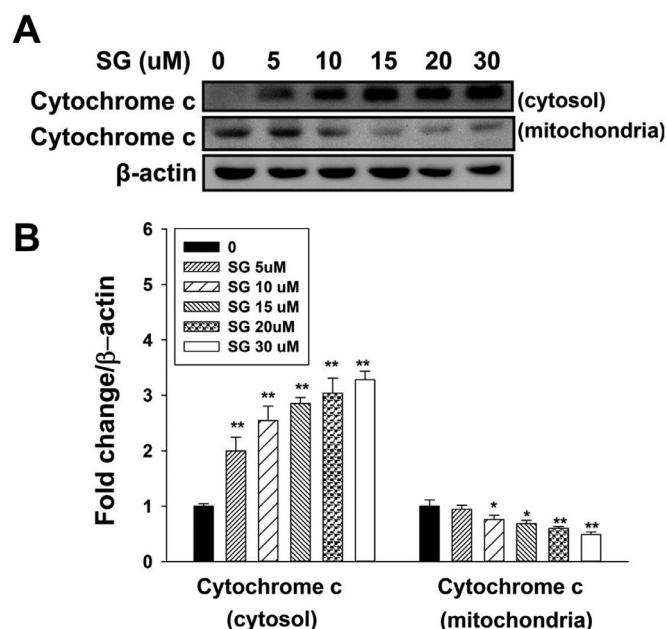


Fig. 8. (A, B) Sophoraflavanone G (SG) treatment affected the expression of apoptosis proteins in MDA-MB-231 cells. Cytochrome c was present in cytosol and mitochondria, and β-actin was used as an internal control. Data are presented as mean ± SD. * $p < 0.05$, ** $p < 0.01$ compared to untreated cells (0 μM SG).

curcumin could increase ROS levels and nuclear condensation for the induction of apoptosis in MDA-MB-231 cells (Fig. 11B and C).

Discussion

Breast cancer is a common tumor among women in both developed and developing countries (DeSantis et al., 2011). It is caused by the abnormal division and hyperplasia of breast ductal or mammary gland cells, which may form a malignant tumor (McGee et al., 2018). Breast cancer can progress as a non-invasive cancer that does not spread to nearby tissue, but breast cancer cells also have the potential to metastasize to other tissues (e.g., the lungs, bones, liver, brain, and other

organs), which is a common cause of death (Dieci et al., 2018). The main strategies for treating breast cancer include surgery, radiation therapy, chemotherapy, and hormone therapy. However, there remains a need for new drugs and treatments, particularly for the challenging triple-negative form of breast cancer (Valdora et al., 2018).

Multiple plant extracts and pure compounds can reportedly induce apoptosis in MDA-MB-231 triple-negative breast cancer cells (Kabala-Dzik et al., 2018; Lin et al., 2015). Pu-erh tea water extract and ziyuglycoside I can cause cell cycle arrest via regulation of p53, and induce apoptosis via intrinsic and extrinsic pathways (Xie et al., 2017; Zhu et al., 2016a). Cantharidin and astragaloside IV can inhibit MDA-MB-231 cell migration through suppression of the MAPK signaling pathway (Gu et al., 2017; Jiang et al., 2017; Li et al., 2017a). We previously found that SG induces apoptotic pathways in human leukemia HL-60 cells by attenuating the MAPK pathway (Li et al., 2016). In our present study, we explored whether SG could also induce apoptosis in MDA-MB-231 human breast cancer cells, and evaluated the underlying molecular mechanisms. Our results showed that SG significantly exerted anti-tumorigenic effects via apoptotic signaling pathway regulation. SG also reduced MDA-MB-231 cell migration and invasion, potentially blocking cancer cell metastasis, via regulation of the AKT and MAPK pathway.

MDA-MB-231 cells are a triple-negative breast cancer cell line that shows high migration and invasion capability (Gianfredi et al., 2017). Triple-negative breast cancers account for only about 15% of breast cancer cell types (DeSantis et al., 2011), but they exhibit the strongest metastatic ability and drug resistance, and are thus the most difficult breast cancer to treat (Shi et al., 2018). Blocking the metastasis of triple-negative breast cancer would substantially improve the success of breast cancer treatment. Our present results indicated that SG could reduce migration and invasion in MDA-MB-231 cells. Many studies show that MDA-MB-231 cells exhibit high levels of phosphorylation of AKT and MAPKs, which stimulate the snail pathway, resulting in reduced E-cadherin expression (Ito et al., 2016; Qiu et al., 2018). E-cadherin can reduce the transformation of epithelial cells into interstitial cells, and decrease cell migration and invasion, which promote cancer cell metastasis (Ashae and Chowdhury, 2016). Our results indicated that SG reduced phosphorylation of AKT and MAPKs, but we did not analyze the snail pathway. In addition to substantially inhibiting migration and invasion in MDA-MB-231 cells, SG also significantly enhanced E-cadherin expression.

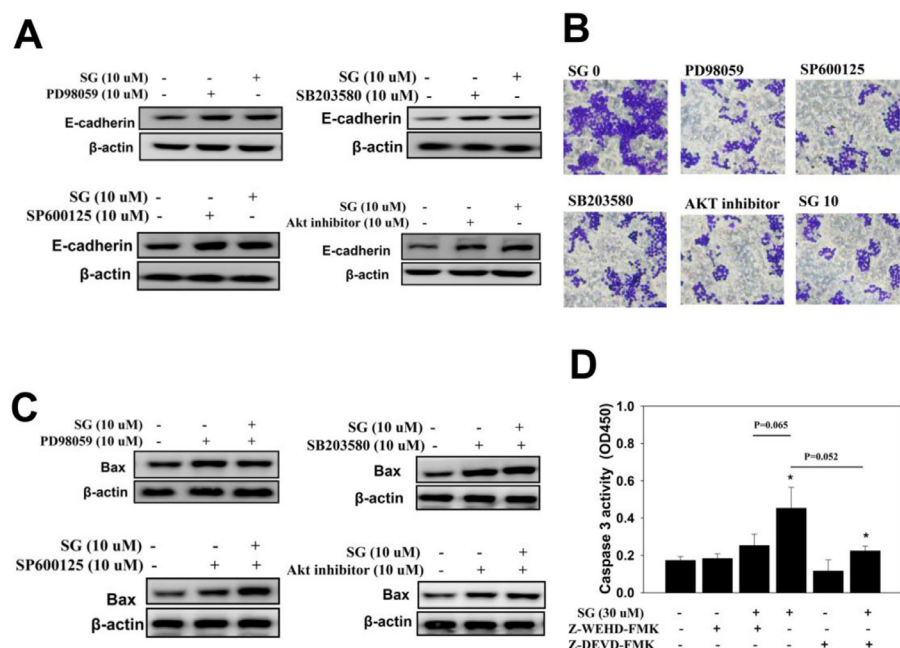


Fig. 9. AKT, and MAPK pathway regulated the intrinsic pathways and cell invasion (A) Sophoraflavanone G (SG), 10 μM MAPK inhibitors (p38 inhibitor SB203580, JNK inhibitor SP600125, and ERK inhibitor PD98059) and 10 μM Akt1/2 kinase inhibitor treated with cells to detect E-cadherin, (B) invasion, and (C) Bax expression. β-actin was used as an internal control. (D) Z-WEHD-FMK (caspase 8 inhibitor) and Z-DEVD-FMK (caspase 3 inhibitor) also treated with cells to detect caspase 3 activity. Data are presented as mean ± SD. * $p < 0.05$ compared to untreated cells (0 μM SG).

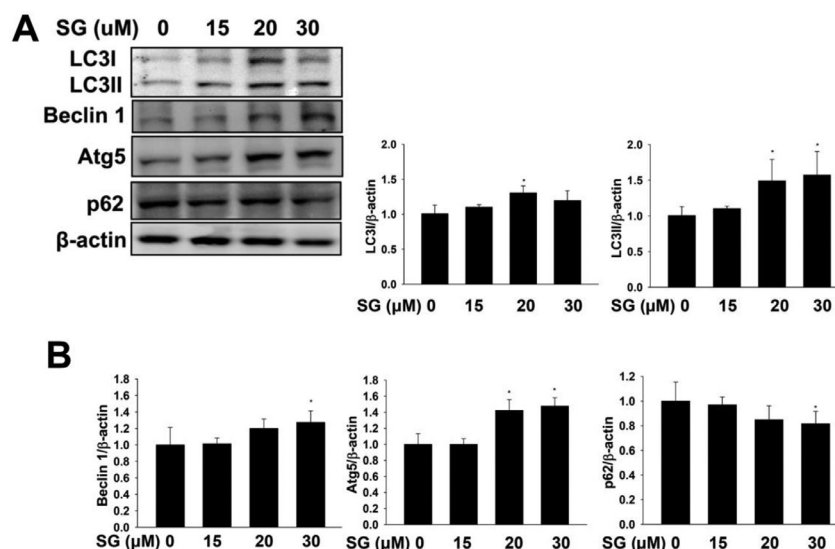


Fig. 10. Sophoraflavanone G (SG) regulated autophagy in MDA-MB-231 cells. (A) Western blot assay of the expression of beclin 1, Atg5, LC3B (LC3 I, LC3II), and p62 in MDA-MB-231 cells. (B) Quantification as the fold expression relative to the expression of untreated cells (0 μM SG). The data are presented as mean \pm SD of three independent experiments ($n = 3$). * $p < 0.05$ compared to untreated cells (0 μM SG).

Inducing cancer cell death is a promising strategy to block cancer progression

Apoptosis is a programmed cell death that is induced after receiving an apoptosis signal. Apoptosis pathways can be divided into intrinsic and extrinsic pathways (Burke, 2017). Some drugs and natural compounds can bind to the Fas receptor, and thereby induce extrinsic apoptotic pathways (Hassan et al., 2014). Kaempferol and curcumin can enhance expressions of cleaved caspase 8 and 3, thus inducing PARP-1 activation (Fan et al., 2016; Li et al., 2015, 2017b). Here we found that SG not only induced cleaved caspase-8 and 3 expressions, but also increased caspase-3 activity. This suggests that SG may partly support apoptosis in MDA-MB-231 cells through extrinsic pathways, by promoting PARP-1 cleaved DNA fragmentation.

Intrinsic apoptotic signaling pathways are induced by oxidative stress, radiation, and anticancer agents that change the mitochondrial membrane potential and activate Bcl family members (Martinou and Youle, 2011). ROS can activate numerous signaling pathways for regulating and enduring the environmental stress of cells. Excessive ROS production an important factor that can induce intrinsic apoptotic pathways (Malik et al., 2007). A previous study demonstrated that Bcl-2

family proteins in the mitochondrial outer membrane can regulate mitochondrial membrane potential and mitochondrial function (Martinou and Youle, 2011). Mitochondrial dysfunction causes the release of cytochrome c from mitochondria into the cytosol, and cytochrome c in the cytosol can bind with apoptotic protease activating factor-1, leading to caspase-9 activation (Malik et al., 2007). Alantolactone and curcumin induce apoptosis in MDA-MB-231 cells through ROS-mediated intrinsic mitochondria-dependent pathway (Cui et al., 2018; Dong et al., 2016). Another report shows that ω -hydroxyundec-9-enoic acid induces intracellular ROS generation, interfering with mitochondrial intrinsic pathways in breast cancer cells (Ahn et al., 2018). Moreover, Bcl-2 and Bcl-xL are anti-apoptotic proteins, and Bax can disrupt mitochondrial outer membranes, causing mitochondrial collapse in intrinsic mitochondria-dependent pathways (Martinou and Youle, 2011). Here we found that SG suppressed intracellular ROS levels, down-regulated Bcl-xL and Bcl-2 expression, and promoted Bax production. SG effectively released cytochrome c into the cytosol, and activated procaspase-9 to form cleaved caspase-9 in MDA-MB-231 cells.

Curcumin was reported that could increase ROS levels and apoptosis in MDA-MB-231 cells (Guan et al., 2016; Zheng et al., 2012). Our

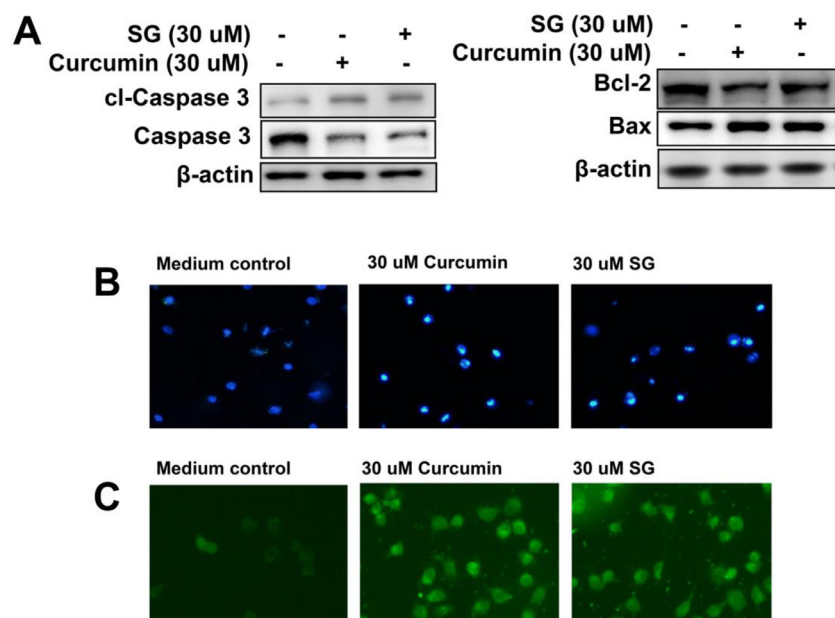


Fig. 11. (A) Sophoraflavanone G (SG) and curcumin treatment affected the expression of apoptosis proteins in MDA-MB-231 cells. (B) Morphological changes in MDA-MB-231 cells treated with SG and curcumin for 24 h and stained with DAPI. Effects of SG and curcumin on ROS production in MDA-MB-231 cells. (C) Fluorescence microscope images of intracellular ROS.

present results demonstrated that SG was similar to curcumin could promote ROS levels, nuclear condensation and apoptosis signal pathways in MDA-MB-231 cells. Furthermore, autophagy was thought that could regulate cellular stress to degrade and recycle the breakdown products (Sun et al., 2017). Previous studies show that curcumin could induce apoptosis and autophagy through blocked PI3K/Akt signal pathway (Guan et al., 2016). We also found that SG could enhance autophagy through modulation of beclin 1, LC3B, and Atg5 expression in MDA-MB-231 breast cancer cells.

Conclusion

Overall, our present findings provide evidence that SG may inhibit ROS production, and promote the mitochondria-induced intrinsic apoptosis pathway and the extrinsic apoptosis pathway—thus enhancing PARP-1 activation, causing DNA damage, and increasing apoptosis in MDA-MB-231 cells. SG also suppressed migration and invasion by inhibiting phosphorylation of ATK and MAPKs. 10–30 μ M SG at physiologically attainable concentration could effectively induce apoptosis and inhibit migration in breast cancer cells. Hence, these results support the possibility that SG may be a promising drug for treating triple-negative breast cancer.

Conflict of interest

The authors have no conflicts of interest to declare.

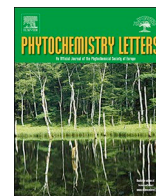
Acknowledgments

This study was supported in part by grants from Chang Gung Memorial Hospital (CMRPF1G0232, CMRPF1G0182, CMRPF1H0021, and CMRPF1F0051-3).

References

- Ahn, J., Chung, Y.W., Park, J.B., Yang, K.M., 2018. Omega-hydroxyundec-9-enoic acid induces apoptosis by ROS mediated JNK and p38 phosphorylation in breast cancer cell lines. *J. Cell Biochem.* 119, 998–1007.
- Ashaie, M.A., Chowdhury, E.H., 2016. Cadherins: the superfamily critically involved in breast cancer. *Curr. Pharm. Des.* 22, 616–638.
- Banik, U., Parasuraman, S., Adhikary, A.K., Othman, N.H., 2017. Curcumin: the spicy modulator of breast carcinogenesis. *J. Exp. Clin. Cancer Res.* 36, 98.
- Bielopolski, D., Evron, E., Moreh-Rahav, O., Landes, M., Stemmer, S.M., Salamon, F., 2017. Paclitaxel-induced pneumonitis in patients with breast cancer: case series and review of the literature. *J. Chemother.* 29, 113–117.
- Burke, P.J., 2017. Mitochondria, bioenergetics and apoptosis in cancer. *Trends Cancer* 3, 857–870.
- Celio, L., Fabbri, C., 2018. Pro-netupitant/palonosetron (IV) for the treatment of radio- and chemotherapy-induced nausea and vomiting. *Expert Opin. Pharmacother.* 19, 1267–1277.
- Chen, Z., Wu, J., Huang, W., Peng, J., Ye, J., Yang, L., Yuan, Y., Chen, C., Zhang, C., Cai, S., He, Y., Wu, S., Song, W., 2018. Long non-coding RNA RP11-789C1.1 suppresses epithelial to mesenchymal transition in gastric cancer through the RP11-789C1.1/MiR-5003/E-Cadherin axis. *Cell Physiol. Biochem.* 47, 2432–2444.
- Cui, L., Bu, W., Song, J., Feng, L., Xu, T., Liu, D., Ding, W., Wang, J., Li, C., Ma, B., Luo, Y., Jiang, Z., Wang, C., Chen, J., Hou, J., Yan, H., Yang, L., Jia, X., 2018. Apoptosis induction by alantolactone in breast cancer MDA-MB-231 cells through reactive oxygen species-mediated mitochondrion-dependent pathway. *Arch. Pharm. Res.* 41, 299–313.
- DeSantis, C., Siegel, R., Bandi, P., Jemal, A., 2011. Breast cancer statistics, 2011. *CA Cancer J. Clin.* 61, 409–418.
- DeSantis, C.E., Ma, J., Goding Sauer, A., Newman, L.A., Jemal, A., 2017. Breast cancer statistics, 2017, racial disparity in mortality by state. *CA Cancer J. Clin.* 67, 439–448.
- Dieci, M.V., Tsvetkova, V., Orvieto, E., Piacentini, F., Ficarra, G., Griguolo, G., Miglietta, F., Giarratano, T., Omarini, C., Bonaguro, S., Cappellesso, R., Aliberti, C., Vernaci, G., Giorgi, C.A., Faggioni, G., Tascia, G., Conte, P., Guarneri, V., 2018. Immune characterization of breast cancer metastases: prognostic implications. *Breast Cancer Res.* 20, 62.
- Dong, Y., Yin, S., Song, X., Huo, Y., Fan, L., Ye, M., Hu, H., 2016. Involvement of ROS-p38-H2AX axis in novel curcumin analogues-induced apoptosis in breast cancer cells. *Mol. Carcinog.* 55, 323–334.
- Fan, H., Liang, Y., Jiang, B., Li, X., Xun, H., Sun, J., He, W., Lau, H.T., Ma, X., 2016. Curcumin inhibits intracellular fatty acid synthase and induces apoptosis in human breast cancer MDA-MB-231 cells. *Oncol. Rep.* 35, 2651–2656.
- Gianfredi, V., Vannini, S., Moretti, M., Villarini, M., Bragazzi, N.L., Izzotti, A., Nucci, D., 2017. Sulforaphane and epigallocatechin gallate restore estrogen receptor expression by modulating epigenetic events in the breast cancer cell line MDA-MB-231: a systematic review and Meta-analysis. *J. Nutrigenet. Nutrigenomics* 10, 126–135.
- Gu, X.D., Xu, L.L., Zhao, H., Gu, J.Z., Xie, X.H., 2017. Cantharidin suppressed breast cancer MDA-MB-231 cell growth and migration by inhibiting MAPK signaling pathway. *Braz. J. Med. Biol. Res.* 50, e5920.
- Guan, F., Ding, Y., Zhang, Y., Zhou, Y., Li, M., Wang, C., 2016. Curcumin suppresses proliferation and migration of MDA-MB-231 breast cancer cells through autophagy-dependent Akt degradation. *PLoS One* 11, e0146553.
- Guo, C., Yang, L., Luo, J., Zhang, C., Xia, Y., Ma, T., Kong, L., 2016. Sophoraflavanone G from *Sophora alopecuroides* inhibits lipopolysaccharide-induced inflammation in RAW264.7 cells by targeting PI3K/Akt, JAK/STAT and Nrf2/HO-1 pathways. *Int. Immunopharmacol.* 38, 349–356.
- Hassan, M., Watari, H., AbuAlmaaty, A., Ohba, Y., Sakuragi, N., 2014. Apoptosis and molecular targeting therapy in cancer. *Biomed. Res. Int.* 2014, 150845.
- Huang, R., Liu, Y., Zhao, L.L., Chen, X.X., Wang, F., Cai, W., Chen, L., 2017. A new flavonoid from *Sophora flavescens* Ait. *Nat. Prod. Res.* 31, 2228–2232.
- Ito, K., Park, S.H., Nayak, A., Byerly, J.H., Irie, H.Y., 2016. PTK6 inhibition suppresses metastases of triple-negative breast cancer via SNAIL-dependent E-Cadherin regulation. *Cancer Res.* 76, 4406–4417.
- Jiang, K., Lu, Q., Li, Q., Ji, Y., Chen, W., Xue, X., 2017. Astragaloside IV inhibits breast cancer cell invasion by suppressing Vav3 mediated Rac1/MAPK signaling. *Int. Immunopharmacol.* 42, 195–202.
- Kabala-Dzik, A., Rzepecka-Stojko, A., Kubina, R., Iriti, M., Wojtyczka, R.D., Buszman, E., Stojko, J., 2018. Flavonoids, bioactive components of propolis, exhibit cytotoxic activity and induce cell cycle arrest and apoptosis in human breast cancer cells MDA-MB-231 and MCF-7 - a comparative study. *Cell Mol. Biol.* 64, 1–10.
- Kim, B.H., Won, C., Lee, Y.H., Choi, J.S., Noh, K.H., Han, S., Lee, H., Lee, C.S., Lee, D.S., Ye, S.K., Kim, M.H., 2013. Sophoraflavanone G induces apoptosis of human cancer cells by targeting upstream signals of STATs. *Biochem. Pharmacol.* 86, 950–959.
- Li, C., Zhao, Y., Yang, D., Yu, Y., Guo, H., Zhao, Z., Zhang, B., Yin, X., 2015. Inhibitory effects of kaempferol on the invasion of human breast carcinoma cells by down-regulating the expression and activity of matrix metalloproteinase-9. *Biochem. Cell Biol.* 93, 16–27.
- Li, H.C., Xia, Z.H., Chen, Y.F., Yang, F., Feng, W., Cai, H., Mei, Y., Jiang, Y.M., Xu, K., Feng, D.X., 2017a. Cantharidin inhibits the growth of triple-negative breast cancer cells by suppressing autophagy and inducing apoptosis in vitro and in vivo. *Cell Physiol. Biochem.* 43, 1829–1840.
- Li, S., Yan, T., Deng, R., Jiang, X., Xiong, H., Wang, Y., Yu, Q., Wang, X., Chen, C., Zhu, Y., 2017b. Low dose of kaempferol suppresses the migration and invasion of triple-negative breast cancer cells by downregulating the activities of RhoA and Rac1. *Oncotargets Ther.* 10, 4809–4819.
- Li, Z.Y., Huang, W.C., Tu, R.S., Gu, P.Y., Lin, C.F., Liou, C.J., 2016. Sophoraflavanone G induces apoptosis in human leukemia cells and blocks MAPK activation. *Am. J. Chin. Med.* 44, 165–176.
- Lin, C.H., Chang, C.Y., Lee, K.R., Lin, H.J., Chen, T.H., Wan, L., 2015. Flavones inhibit breast cancer proliferation through the Akt/FOXO3a signaling pathway. *BMC Cancer* 15, 958.
- Liou, C.J., Cheng, C.Y., Yeh, K.W., Wu, Y.H., Huang, W.C., 2018. Protective effects of casticin from *Vitex trifolia* alleviate eosinophilic airway inflammation and oxidative stress in a murine asthma model. *Front. Pharmacol.* 9, 635.
- Malik, F., Kumar, A., Bhushan, S., Khan, S., Bhatia, A., Suri, K.A., Qazi, G.N., Singh, J., 2007. Reactive oxygen species generation and mitochondrial dysfunction in the apoptotic cell death of human myeloid leukemia HL-60 cells by a dietary compound withaferin A with concomitant protection by N-acetyl cysteine. *Apoptosis* 12, 2115–2133.
- Martinou, J.C., Youle, R.J., 2011. Mitochondria in apoptosis: Bcl-2 family members and mitochondrial dynamics. *Dev. Cell* 21, 92–101.
- McGee, S.F., Mazzarello, S., Caudrelier, J.M., Lima, M.A.G., Hutton, B., Sienkiewicz, M., Stober, C., Fernandes, R., Ibrahim, M.F.K., Vandermeer, L., Hilton, J., Shorr, R., Fergusson, D., Clemons, M., 2018. Optimal sequence of adjuvant endocrine and radiation therapy in early-stage breast cancer - a systematic review. *Cancer Treat. Rev.* 69, 132–142.
- Mitra, S., Dash, R., 2018. Natural products for the management and prevention of breast cancer. *Evid. Based Complement Alternat. Med* 2018, 8324696.
- Peng, H.L., Huang, W.C., Cheng, S.C., Liou, C.J., 2018. Fisetin inhibits the generation of inflammatory mediators in interleukin-1 β -induced human lung epithelial cells by suppressing the NF- κ B and ERK1/2 pathways. *Int. Immunopharmacol.* 60, 202–210.
- Philchenkov, A.A., Balcer-Kubiczek, E.K., 2016. Molecular markers of apoptosis in cancer patients exposed to ionizing radiation: the post-Chornobyl view. *Exp. Oncol.* 38, 224–237.
- Qiu, Y., Liu, Y., Li, W.H., Zhang, H.Q., Tian, X.X., Fang, W.G., 2018. P2Y2 receptor promotes the migration and invasion of breast cancer cells via EMT-related genes snail and E-cadherin. *Oncol. Rep.* 39, 138–150.
- Shen, C.C., Lin, T.W., Huang, Y.L., Wan, S.T., Shien, B.J., Chen, C.C., 2006. Phenolic constituents of the roots of *Sophora flavescens*. *J. Nat. Prod.* 69, 1237–1240.
- Shi, Y., Jin, J., Ji, W., Guan, X., 2018. Therapeutic landscape in mutational triple negative breast cancer. *Mol. Cancer* 17, 99.
- Sun, S.H., Huang, H.C., Huang, C., Lin, J.K., 2012. Cycle arrest and apoptosis in MDA-MB-231/Her2 cells induced by curcumin. *Eur. J. Pharmacol.* 690, 22–30.
- Sun, T., Liu, H., Ming, L., 2017. Multiple roles of autophagy in the sorafenib resistance of hepatocellular carcinoma. *Cell Physiol. Biochem.* 44, 716–727.
- Valdora, F., Houssami, N., Rossi, F., Calabrese, M., Tagliafico, A.S., 2018. Rapid review: radiomics and breast cancer. *Breast Cancer Res. Treat.* 169, 217–229.
- Wong, R.S., 2011. Apoptosis in cancer: from pathogenesis to treatment. *J. Exp. Clin.*

- Cancer Res. 30, 87.
- Wun, Z.Y., Lin, C.F., Huang, W.C., Huang, Y.L., Xu, P.Y., Chang, W.T., Wu, S.J., Liou, C.J., 2013. Anti-inflammatory effect of sophoraflavanone G isolated from *Sophora flavescens* in lipopolysaccharide-stimulated mouse macrophages. *Food Chem. Toxicol.* 62, 255–261.
- Xie, J., Yu, H., Song, S., Fang, C., Wang, X., Bai, Z., Ma, X., Hao, S., Zhao, H.Y., Sheng, J., 2017. Pu-erh tea water extract mediates cell cycle arrest and apoptosis in MDA-MB-231 human breast cancer cells. *Front. Pharmacol.* 8, 190.
- Xu, Y., Li, N., Xiang, R., Sun, P., 2014. Emerging roles of the p38 MAPK and PI3K/AKT/mTOR pathways in oncogene-induced senescence. *Trends Biochem. Sci.* 39, 268–276.
- Zhang, A., Sheng, Y., Zou, M., 2017. Antiproliferative activity of Alisol B in MDA-MB-231 cells is mediated by apoptosis, dysregulation of mitochondrial functions, cell cycle arrest and generation of reactive oxygen species. *Biomed. Pharmacother.* 87, 110–117.
- Zheng, J., Payne, K., Taggart, J.E., Jiang, H., Lind, S.E., Ding, W.Q., 2012. Trolox enhances curcumin's cytotoxicity through induction of oxidative stress. *Cell Physiol. Biochem.* 29, 353–360.
- Zhu, X., Wang, K., Zhang, K., Zhang, T., Yin, Y., Xu, F., 2016a. Ziyuglycoside I inhibits the proliferation of MDA-MB-231 breast carcinoma cells through inducing p53-mediated G2/M cell cycle arrest and intrinsic/extrinsic apoptosis. *Int. J. Mol. Sci.* 17, 1903.
- Zhu, Y.W., Yan, J.K., Li, J.J., Ou, Y.M., Yang, Q., 2016b. Knockdown of radixin suppresses gastric cancer metastasis in vitro by up-regulation of E-Cadherin via NF-kappaB/Snail pathway. *Cell Physiol. Biochem.* 39, 2509–2521.

New bioactive $\Delta^{11(17)}$ -furano-eunicellins from an octocoral *Cladiella* sp.Ying-Fa Chen^{a,b}, Wu-Fu Chen^{c,d}, Zhi-Hong Wen^d, Tsong-Long Hwang^{e,f,g,h,***}, Zhi-Jun Zhang^{i,j,**}, Ping-Jyun Sung^{d,i,j,k,l,*}^a Department of Neurology, Chang Gung Memorial Hospital and Chang Gung University College of Medicine, Kaohsiung 83301, Taiwan^b Center for Parkinson's Disease, Kaohsiung Chang Gung Memorial Hospital and Chang Gung University College of Medicine, Kaohsiung 83301, Taiwan^c Department of Neurosurgery, Kaohsiung Chang Gung Memorial Hospital and Chang Gung University College of Medicine, Kaohsiung 83301, Taiwan^d Department of Marine Biotechnology and Resources, National Sun Yat-sen University, Kaohsiung 80424, Taiwan^e Research Center for Chinese Herbal Medicine, Research Center for Food and Cosmetic Safety, Graduate Institute of Healthy Industry Technology, College of Human Ecology, Chang Gung University of Science and Technology, Taoyuan 33303, Taiwan^f Graduate Institute of Natural Products, College of Medicine, Chang Gung University, Taoyuan 33302, Taiwan^g Chinese Herbal Medicine Research Team, Healthy Aging Research Center, Chang Gung University, Taoyuan 33302, Taiwan^h Department of Anaesthesiology, Chang Gung Memorial Hospital, Taoyuan 33305, Taiwanⁱ Graduate Institute of Marine Biology, National Dong Hwa University, Pingtung 94450, Taiwan^j National Museum of Marine Biology and Aquarium, Pingtung 94450, Taiwan^k Chinese Medicine Research and Development Center, China Medical University Hospital, Taichung 40447, Taiwan^l Graduate Institute of Natural Products, Kaohsiung Medical University, Kaohsiung 80708, Taiwan

ARTICLE INFO

Keywords:

Cladiella

Cladieunicellin

Sclerophytin

Elastase

Superoxide anion

Cytotoxicity

ABSTRACT

A new eunicellin diterpenoid, cladieunicellin U (1), along with a new natural eunicellin, cladieunicellin V (2), and two known analogues, sclerophytins A (3) and B (4), were obtained from an octocoral identified as *Cladiella* sp. The structures, including the absolute configurations, of eunicellins 1–4 were elucidated by using spectroscopic methods and compared with the spectroscopic and physical data reported in the literature. Eunicellins 1, 3 and 4 decreased the release of elastase, while eunicellins 2 and 4 showed inhibitory effects in terms of the generation of superoxide anions by human neutrophils. Eunicellins 1 and 4 were found to show moderate cytotoxicity toward the leukemia K562 cells (IC_{50} = 12.8, 11.4 μ g/mL, respectively) and 2 exhibited moderate cytotoxicity toward the leukemia MOLT-4 cells (IC_{50} = 18.8 μ g/mL).

1. Introduction

Since the first structure elucidation of an eunicellin-based diterpenoid (2,11-cyclized cembranoid), eunicellin, from the gorgonian coral *Eunicella stricta*, in 1968, by a single-crystal X-ray diffraction analysis of its brominated derivative (Kennard et al., 1968), a series of compounds of this group has been prepared from various octocorals belonging to the genus *Cladiella* (family Alcyoniidae) (Radhika, 2006), with complex structures and interesting bioactivities. During the course of our research on new natural metabolites from the marine invertebrates distributed in the waters of Taiwan, at the intersection of the Kuroshio current and the South China Sea surface current, a series of eunicellin-based diterpenoids, isolated from various octocorals belonging to the genus *Cladiella* were proven to possess various interesting bioactivities

(Chen et al., 2013, 2014a,b; Peng et al., 2016; Shih et al., 2013; Zhang et al., 2019). Recently, we have focused our studies on a species of octocoral identified as *Cladiella* sp. collected on the Penghu Archipelago, Taiwan. From the results of our studies on this species, we report the isolation, structural determination, and bioactivity of a new eunicellin, cladieunicellin U (1), a new natural eunicellin, cladieunicellin V (2), along with two known metabolites, sclerophytins A (3) and B (4) (Fig. 1) (Bernardelli et al., 2001; Friedrich et al., 2000; Friedrich and Paquette, 2002; Paquette et al., 2000; Sharma and Alam, 1988).

2. Results and discussion

Cladieunicellin U (1) was found to have the molecular formula $C_{36}H_{64}O_5$ and five degrees of unsaturation, as indicated from the

* Corresponding author at: National Museum of Marine Biology and Aquarium, Pingtung 94450, Taiwan.

** Corresponding author at: Graduate Institute of Marine Biology, National Dong Hwa University, Pingtung 94450, Taiwan.

*** Corresponding author at: Research Center for Chinese Herbal Medicine, Research Center for Food and Cosmetic Safety, Graduate Institute of Health Industry Technology, College of Human Ecology, Chang Gung University of Science and Technology, Taoyuan 33303, Taiwan.

E-mail addresses: htl@mail.cgu.edu.tw (T.-L. Hwang), goldchain116@gmail.com (Z.-J. Zhang), pjsung@nmba.gov.tw (P.-J. Sung).<https://doi.org/10.1016/j.phytol.2019.07.002>

Received 26 May 2019; Received in revised form 2 July 2019; Accepted 4 July 2019

1874-3900/ © 2019 Phytochemical Society of Europe. Published by Elsevier Ltd. All rights reserved.

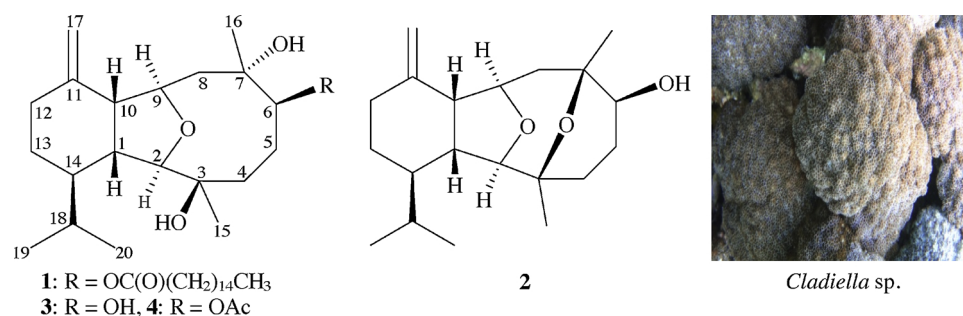


Fig. 1. Structures of cladieunicellins U (1), V (2) and sclerophytins A (3), B (4) and a picture of octocoral *Cladiella* sp.

Table 1

¹H (400 MHz, CDCl₃) and ¹³C (100 MHz, CDCl₃) NMR, COSY, HMBC data for 1.

Position	δ _H (J in Hz)	δ _C , type	COSY	HMBC
1	2.11 m	45.6, CH	H-10, H-14	C-3, C-9, C-14
2	3.68 s	90.6, CH	–	C-1, C-3, C-9, C-10, C-14, C-15
3		75.0, C		
4α/β	2.13 m; 1.70 m	39.9, CH ₂	H ₂ -5	C-2, C-3, C-5, C-6
5α/β	1.39 m; 2.09 m	28.2, CH ₂	H ₂ -4, H-6	C-3, C-4, C-6
6	5.62 d (4.4)	84.9, CH	H-5β	C-4, C-5, C-7, C-16
7		76.0, C		
8α	1.76 dd (14.8, 4.0)	45.4, CH ₂	H-8β, H-9	C-6, C-7, C-16
β	2.26 dd (14.8, 10.8)		H-8α, H-9	C-9, C-10
9	4.13 ddd (10.8, 7.2, 4.0)	78.1, CH	H ₂ -8, H-10	C-11
10	3.02 dd (7.6, 7.2)	53.3, CH	H-1, H-9	C-1, C-9, C-11, C-12, C-14, C-17
11		148.0, C		
12α/β	2.04 m; 2.23 m	31.7, CH ₂	H ₂ -13	C-10
13α/β	1.00 m; 1.73 m	24.9, CH ₂	H ₂ -12	C-14
14	1.30 m	43.6, CH	H-1, H ₂ -13, H-18	C-18
15	1.14 s	30.3, CH ₃		C-2, C-3, C-4
16	1.22 s	23.9, CH ₃		C-6, C-7, C-8
17a/b	4.65 br s; 4.62 br s	109.4, CH ₂		C-10, C-12
18	1.74 m	29.1, CH	H-14, H ₃ -19, H ₃ -20	C-19, C-20
19	0.96 d (6.8)	22.0, CH ₃	H-18	C-14, C-18, C-20
20	0.78 d (6.8)	15.6, CH ₃	H-18	C-14, C-18, C-19

HRESIMS at *m/z* 599.46479 (calcd for C₃₆H₆₄O₅ + Na, 599.46460). The diterpenoid structure of 1 was directly inferred from its ¹³C NMR spectra (Table 1), where it indicated that there were 20 carbon signals in total after subtraction of the 16 carbons ascribed to a palmitate group. Comparison of the ¹³C and DEPT data with the molecular formula indicated that there must be two exchangeable protons, requiring the presence of two hydroxy groups. This deduction was supported by a broad absorption in the IR spectrum at 3438 cm⁻¹. The ¹³C NMR data confirmed the presence of 36 signals, characterized by DEPT spectra as 5 methyls, 19 sp³–CH₂, 7 sp³–CH (including 3 oxymethines), 2 sp³ oxygenated quaternary carbons, 1 sp² methylene, 1 sp² quaternary carbon and 1 sp² carbonyl. Based on the ¹H and ¹³C NMR data (Table 1), 1 was determined to possess an exocyclic carbon-carbon double bond (δ_H 4.65, 1H, br s; 4.62, 1H, br s, H₂-17; δ_C 148.0, C-11; 109.4, CH₂-17). An ester carbonyl carbon (δ_C 174.7) was HMBC correlated by the methylene protons (δ_H 2.32, 2H, t, *J* = 7.6 Hz) of a long-chain ester unit, and the long-chain ester was found to be palmitate. In the ¹H NMR spectrum, two doublets at δ_H 0.96 and 0.78 (each 3H, d, *J* = 6.8 Hz, H₃-19 and H₃-20) were indicative of the two methyls of an isopropyl group. Two tertiary methyl groups bonded to oxygenated carbons were evident from the singlet signals at δ_H 1.22 (3H, s, H₃-16) and 1.14 (3H, s, H₃-15). Thus, in light of the ¹H and ¹³C NMR data

combined with the degrees of unsaturation, 1 was determined as a tricyclic eunicellin diterpene.

The ¹H NMR coupling information in the COSY spectrum of 1 enabled the determination of the proton sequences between H₂-4/H₂-5/H-6, H₂-8/H-9/H-10/H-1/H-14/H₂-13/H₂-12 and H-14/H₃-18/H₃-20 (Table 1). These data, together with the key HMBC from H-1, H-2, H-4α, H-5β, H₃-15 to C-3; H-6, H-8α, H₃-16 to C-7; and H-9, H-10 to C-11, permitted elucidation of the carbon skeleton (Table 1). An exocyclic carbon-carbon double bond at C-11 was confirmed by the HMBC from H₂-17 to C-10, C-12; and H-10 to C-17. In the HSQC spectrum, an oxymethine carbon (δ_C 84.9) correlated with a methine proton (δ_H 5.62), and this proton had a ³*J*-correlation with H-5β (δ_H 2.09) in COSY spectrum, ²*J*-correlations with C-5 and C-7, and ³*J*-correlations with C-4 and C-16, respectively, in HMBC spectrum. It thus confirmed the existence of a palmitate at C-6, although no HMBC was observed between H-6 and the palmitate carbonyl. Furthermore, an HMBC from H-2 (δ_H 3.68) to an oxygen-containing methine at δ_C 78.1 (CH-9) suggested the presence of a C-2/9 ether linkage in 1 for forming a tetrahydrofuran ring located between C-2 and C-9.

Based on NOESY correlations and further information provided by MM2 force field calculations (Allinger, 1977), the relative stereochemistry of 1 with a stable conformation is shown in Fig. 2. When H-1 is β-oriented, correlations from H-1 to H-10 and H₃-20 were observed, suggesting that H-1, H-10 and the isopropyl groups were on the β-face. A lack of constant coupling was detected between H-1 and H-2, indicating that H-2 should be α-oriented. H₃-15 showed a correlation with H-2, suggested the β-orientation of the hydroxy group at C-3. No correlation was found between H-9 and H-10, suggesting that H-9 was α-oriented. A correlation from H-10 to H-8 (δ_H 2.26) suggested that this

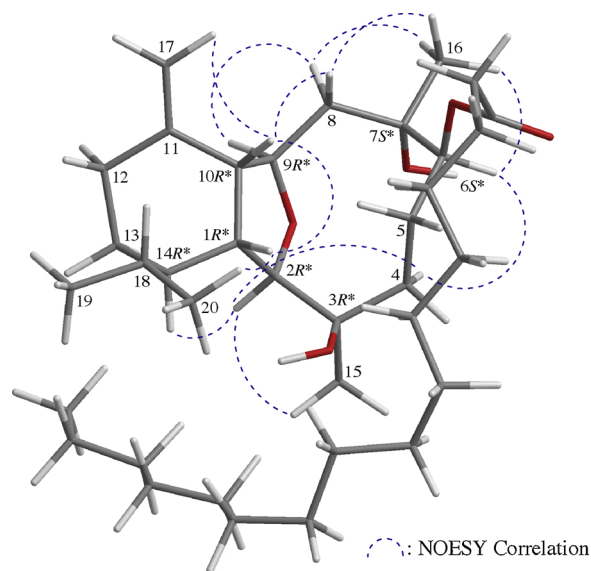


Fig. 2. Selected protons with key NOESY correlations of 1.

Table 2¹H (400 MHz, CDCl₃) and ¹³C (100 MHz, CDCl₃) NMR, COSY, HMBC data for **2**.

Position	δ_{H} (J in Hz)	δ_{C} , Mult.	COSY	HMBC
1	2.27 dd (11.2, 6.8)	44.9, CH	H-10, H-14	C-3, C-9, C-10, C-14, C-18
2	3.62 s	93.9, CH	–	C-3, C-4, C-9, C-10, C-14
3		76.0, C		
4 α	1.65 m	29.1, CH ₂	H ₂ -5	C-2, C-3, C-5, C-6
β	1.78 ddd (14.0, 13.2, 5.2)			C-2, C-3, C-5, C-6, C-15
5 α	2.71 dddd (14.4, 14.0, 6.4, 2.4) 1.69 m	24.6, CH ₂	H ₂ -4, H-6	C-4
β				C-7
6	3.29 br s	71.8, CH	H ₂ -5	–
7		76.8, C		
8 α	2.05 dd (14.4, 4.8)	44.4, CH ₂	H-9	C-6, C-7, C-9, C-10, C-16
β	1.93 dd (14.4, 1.6)			C-6, C-7, C-9, C-10, C-16
9	3.95 ddd (6.4, 4.8, 1.6)	82.2, CH	H ₂ -8, H-10	C-2, C-7, C-10, C-11
10	3.47 dd (6.8, 6.4)	49.6, CH	H-1, H-9	C-1, C-2, C-9, C-11, C-12, C-14, C-17
11		149.3, C		
12 α / β	1.96 m; 2.25 m	31.3, CH ₂	H ₂ -13	C-10, C-11, C-14
13 α / β	0.95 m; 1.69 m	24.5, CH ₂	H ₂ -12, H-14	C-1, C-11, C-12, C-14
14	1.23 m	43.8, CH	H-1, H ₂ -13, H-18	–
15	1.12 s	27.6, CH ₃		C-2, C-3, C-4
16	1.35 s	30.9, CH ₃		C-6, C-7, C-8
17a/b	4.67 s; 4.66 s	108.7, CH ₂		C-10, C-11, C-12
18	1.25 m	29.5, CH	H-14, H ₃ -19, H ₃ -20	–
19	0.95 d (6.8)	21.9, CH ₃	H-18	C-14, C-18, C-20
20	0.78 d (6.8)	15.8, CH ₃	H-18	C-14, C-18, C-19

proton is β , and the proton at δ_{H} 1.76 is 8α . Additionally, the proton signal of a methyl group displayed NOESY correlations with both H- 8α / β , which indicated that the Me-16 at C-7 was β -oriented. As one of the C-4 methylene (δ_{H} 2.13) exhibited a correlation to H-2, suggesting the α -orientation of this proton by modeling study and the other was assigned as H-4 β (δ_{H} 1.70). H-6 displayed correlations with H-4 α and H₃-16, but not with either H- 8α / β , demonstrating the β -orientation of the palmitate group at C-6. The aforementioned results enabled establishment of the relative configuration of **1**, and therefore its stereogenic carbons were assigned as 1*R**,2*R**,3*R**,6*S**,7*S**,9*R**,10*R**,14*R**.

Compound **2** was isolated as an amorphous powder that showed a pseudomolecular ion $[\text{M} + \text{Na}]^+$ at m/z 343.22435 in HRESIMS analysis. The results revealed that **2** had a molecular formula of C₂₀H₃₂O₃ (calcd for C₂₀H₃₂O₃ + Na, 343.22437), with five degrees of unsaturation. IR spectrum analysis showed that this compound had a broad absorption peak at 3356 cm^{−1}, suggesting that the structure of **2** included a hydroxy group. The ¹³C and DEPT spectra revealed that compound **2** had 20 carbons, including 4 methyls, 5 sp³ methylenes, 7 sp³ methines (including 3 oxymethines), 2 sp³ oxygenated quaternary carbons, 1 sp² methylene and 1 sp² quaternary carbon (Table 2). Therefore, according to the aforementioned data, one degree of unsaturation was accounted for, and **2** was identified as having four rings. From the COSY spectrum (Table 2), it was possible to differentiate the separate systems of H₂-4/H₂-5/H-6, H₂-8/H-9/H-10/H-14/H₂-13/H₂-12 and H-14/H-18/ H₃-19 (H₃-20). Together with results of key HMBC from protons to quaternary carbons, such as H-1, H-2, H₂-4, H₃-15 to C-3; H-5 β , H₂-8, H-9, H₃-16 to C-7; and H-9, H-10, H-12 β , H₂-13, H₂-17 to C-11 (Table 2), the data confirmed the main carbon skeleton of **2**.

In a previous study, eunicellin **2** was reported and named as sclerophytin A (Sharma and Alam, 1988). However, by comparison of the NMR data of **2** with those of sclerophytin A, we found that the NMR data for sclerophytin A reported by Sharma and Alam (1988) differed significantly from that of **2** reported in our studies. In fact, the structure of sclerophytin A reported by Sharma and Alam (Sharma and Alam, 1988) is the hydrolytic product of **2** as shown with the structure **3**, while compound **3** has also been obtained in this study (Fig. 1). The structure of **2** was confirmed by comparing the spectroscopic and physical data with those of the product **2** synthesized by Paquette's group. By comparison of the rotation value of **2** ($[\alpha]_{\text{D}}^{20}$ 5(20),

CHCl_3) with that of synthetic product **2** ($[\alpha]_{\text{D}}^{20}$ 5(20), CHCl_3) (Bernardelli et al., 2001; Paquette et al., 2002), the absolute configuration for the stereogenic carbons of **2** were determined as 1*R*,2*R*,3*R*,6*S*,7*R*,9*R*,10*R*,14*R*.

As **1** (cladieunicellin U) was isolated along with **2** from the same organism, it is reasonable on biogenetic grounds to assume that **1** has the same absolute configuration as **2**. Therefore, based on above findings, the configurations of the stereogenic centers of **1** were elucidated as 1*R*,2*R*,3*R*,6*S*,7*S*, 9*R*,10*R*,14*R*. On the other hand, to the best of our knowledge, there has been no report of eunicellin **2** being obtained from any natural sources, and this result proves that the setting of two oxygen bridges with the fused cyclodecanol B ring is a nature's way (Paquette et al., 2000). In order to avoid confusion, we suggested that eunicellin **2** be named as cladieunicellin V in future studies. Moreover, two known eunicellins were also isolated and identified as sclerophytin A (**3**) and sclerophytin B (**4**), by comparison with the spectroscopic and physical data reported in the literature (Bernardelli et al., 2001; Friedrich et al., 2000; Friedrich and Paquette, 2002; Paquette et al., 2000; Sharma and Alam, 1988).

In *in vitro* anti-inflammatory activity assay, it was found that eunicellins **1**, **3** and **4** showed inhibitory effects on the release of elastase, a marker of inflammation (inhibition rates = 12.01 ± 4.53, 11.35 ± 5.04 and 16.37 ± 8.14%, respectively), and eunicellins **2** and **4** showed 13.43 ± 1.57 and 28.12 ± 3.61% inhibitory effects on human neutrophils in terms of the generation of superoxide anions by human neutrophils, respectively, at a concentration of 10 μM . In addition, the cytotoxicity of eunicellins **1–4** against K-562 (human chronic myelogenous leukemia) and MOLT-4 (human acute lymphoblastic leukemia) tumor cells shown in Table 3. Eunicellins **1** and **4** were found

Table 3
Cytotoxic data of eunicellins **1–4**.

Cell lines IC ₅₀ ($\mu\text{g/mL}$)	Compounds				
	1	2	3	4	Doxorubicin ^a
K-562	12.76	> 20	> 20	11.39	0.23
MOLT-4	> 20	18.83	> 20	> 20	0.01

^a Doxorubicin was used as a positive control.

to show moderate cytotoxicity toward K562 cells and **2** exhibited moderate cytotoxicity toward MOLT-4 cells.

3. Experimental

3.1. General

The Jeol NMR spectrometer (model ECZ400S) was used to record the spectra with the solvent peak of CHCl_3 (δ_{H} 7.26 ppm) and CDCl_3 (δ_{C} 77.1 ppm) as internal references for ^1H NMR and ^{13}C NMR, respectively. ESIMS and HRESIMS were obtained from the Bruker mass spectrometer with 7 T magnets (model: Solarix FTMS system). Column chromatography, IR spectra and optical rotation were performed according to our earlier research (Zhang et al., 2019).

3.2. Animal material

Specimens of *Cladiella* sp. (Bayer, 1981) used for this study were collected in the Penghu Archipelago waters, Taiwan, in May 2017. A voucher specimen was deposited in the National Museum of Marine Biology and Aquarium (NMMBA) (voucher no.: NMMBA-TWSC-17032), Taiwan.

3.3. Extraction and isolation

The freeze-dried and sliced bodies (wet/dry weight = 570.3/202.8 g) of the coral specimen were prepared and extracted with a 1:1 mixture of MeOH and CH_2Cl_2 to give 25.8 g of crude extract which was partitioned between EtOAc and H_2O to obtain 16.8 g of the EtOAc extract. The EtOAc extract was eluted on silica gel column with gradients of n-hexane/EtOAc (100% n-hexane–100% EtOAc, stepwise), to furnish 16 fractions (fractions: A – P). Fractions E – I were combined and further chromatographed on silica gel column and eluted with gradients of n-hexane/EtOAc (50:1 – 100% EtOAc, stepwise) to afford 31 sub-fractions (fractions: E1 – E31). Afterward, fraction E11 was purified by normal-phase HPLC (NP-HPLC) using a mixture of n-hexane, Me_2CO and EtOAc (with volume:volume:volume = 16:1:2.5; at a flow rate = 2.0 mL/min) to afford **2** (3.9 mg). Fractions E18 and E19 were combined and separated by NP-HPLC using a mixture of n-hexane, Me_2CO and EtOAc (9:0.5:2.5) as solvent to obtain 8 subfractions (fractions: E18A – E18H). Then, fraction E18A was further separated by NP-HPLC using a mixture of n-hexane, Me_2CO and EtOAc (with volume:volume:volume = 21:0.5:2.5; at a flow rate = 2.0 mL/min) to afford **1** (1.5 mg). Fraction M was separated by NP-HPLC using a mixture of n-hexane and Me_2CO (with volume: volume = 3:1; at a flow rate = 4.0 mL/min) to afford **3** (16.6 mg). Fraction N was separated by NP-HPLC using a mixture of n-hexane and Me_2CO (with volume:volume = 2:1; at a flow rate = 4.0 mL/min) to afford **4** (1.2 mg).

3.4. Cladieunicellin U (**1**)

Amorphous powder; $[\alpha]_{\text{D}} -7$ (c 0.06, CHCl_3), IR (neat) ν_{max} 3438, 1720 cm^{-1} ; ^1H and ^{13}C NMR data, see Table 1. ESIMS: m/z 599 $[\text{M} + \text{Na}]^+$, HRESIMS: m/z 599.46479 (calcd for $\text{C}_{36}\text{H}_{64}\text{O}_5 + \text{Na}$, 599.46460).

3.5. Cladieunicellin V (**2**)

Amorphous powder; $[\alpha]_{\text{D}} -5$ (c 0.15, CHCl_3), IR (neat) ν_{max} 3356 cm^{-1} ; ^1H and ^{13}C NMR data, see Table 2. ESIMS: m/z 343 $[\text{M} + \text{Na}]^+$, HRESIMS: m/z 343.22435 (calcd for $\text{C}_{20}\text{H}_{32}\text{O}_3 + \text{Na}$, 343.22437).

3.6. Sclerophytin A (**3**)

Amorphous powder; $[\alpha]_{\text{D}} -3$ (c 0.83, CHCl_3), IR (neat) ν_{max}

3391 cm^{-1} ; ^1H and ^{13}C NMR data were found to be in absolute agreement with previous studies (Friedrich et al., 2000; Friedrich and Paquette, 2002; Paquette et al., 2000; Sharma and Alam, 1988). ESIMS: m/z 361 $[\text{M} + \text{Na}]^+$.

3.7. Sclerophytin B (**4**)

Colorless oil; $[\alpha]_{\text{D}} -10$ (c 0.06, CHCl_3), IR (neat) ν_{max} 3461 cm^{-1} ; ^1H and ^{13}C NMR data were found to be in absolute agreement with previous studies (Friedrich et al., 2000; Friedrich and Paquette, 2002; Paquette et al., 2000; Sharma and Alam, 1988). ESIMS: m/z 403 $[\text{M} + \text{Na}]^+$.

3.8. Molecular mechanics calculations

The molecular models were generated by implementing the MM2 force field (Allinger, 1977) in ChemBio 3D Ultra software (ver. 12.0) which was created by CambridgeSoft (PerkinElmer, Cambridge, MA, USA).

3.9. Superoxide anion generation and elastase release by human neutrophils

Human neutrophils were obtained by means of dextran sedimentation and Ficoll centrifugation. Measurements of elastase release and superoxide anion generation were carried out according to previously described procedures (Hwang et al., 2010; Yu et al., 2011). Briefly, superoxide anion production was assayed by monitoring the superoxide dismutase-inhibitable reduction of ferricytochrome c. Elastase release experiments were performed using MeO-Suc-Ala-Ala-Pro-Valp-nitroanilide as the elastase substrate.

3.10. MTT antiproliferation assay

K-562 and MOLT-4 cells were obtained from the American Type Culture Collection (ATCC; Manassas, VA, USA). Cells were maintained in RPMI 1640 medium supplemented with 10% fetal calf serum, 2 mM glutamine, and antibiotics (100 units/mL penicillin and 100 $\mu\text{g}/\text{mL}$ streptomycin) at 37 °C in a humidified atmosphere of 5% CO_2 . Cells were seeded at 4×10^4 per well in 96-well culture plates before treatment with different concentrations of the tested compounds. The compounds were dissolved in DMSO and further used with concentrations of 1.25, 2.5, 5, 10 and 20 $\mu\text{g}/\text{mL}$ in the *in vitro* experiment. After treatment for 72 h, the cytotoxicity of the tested compounds was determined using a MTT cell proliferation assay. The MTT is reduced by the mitochondrial dehydrogenases of viable cells to a purple formazan product. The MTT-formazan product was dissolved in DMSO. Light absorbance values ($\text{OD} = \text{OD}_{570} - \text{OD}_{620}$) were recorded at wavelengths of 570 and 620 nm using an ELISA reader to calculate the concentration that caused 50% inhibition (IC_{50}), i.e., the cell concentration at which the light absorbance value of the experiment group was half that of the control group. These results were expressed as a percentage of the control \pm SD established from $n = 4$ wells per one experiment from three separate experiments (Alley et al., 1988; Scudiero et al., 1988).

Acknowledgments

This research was supported by grants from the National Museum of Marine Biology and Aquarium; and the Ministry of Science and Technology, Taiwan (Grant Nos: MOST 104-2320-B-291-001-MY3 and 107-2320-B-291-001-MY3) awarded to Ping-Jyun Sung.

Appendix A. Supplementary data

Supplementary material related to this article can be found, in the online version, at doi:<https://doi.org/10.1016/j.phytol.2019.07.002>.

References

- Alley, M.C., Scudiero, D.A., Monks, A., Hursey, M.L., Czerwinski, M.J., Fine, D.L., Abbott, B.J., Mayo, J.G., Shoemaker, R.H., Boyd, M.R., 1988. Feasibility of drug screening with panels of human tumor cell lines using a microculture tetrazolium assay. *Cancer Res.* 48, 589–601.
- Allinger, N.L., 1977. Conformational analysis. 130. MM2. A hydrocarbon force field utilizing V_1 and V_2 torsional terms. *J. Am. Chem. Soc.* 99, 8127–8134.
- Bayer, F.M., 1981. Key to the genera of octocorallia exclusive of Pennatulacea (Coelenterata: Anthozoa), with diagnoses of new taxa. *Proc. Biol. Soc. Wash.* 94, 902–947.
- Bernardelli, P., Moradei, O.M., Friedrich, D., Yang, J., Gallou, F., Dyck, B.P., Doskotch, R.W., Lange, T., Paquette, L.A., 2001. Total asymmetric synthesis of the putative structure of the cytotoxic diterpenoid (–)-sclerophytin A and of the authentic natural sclerophytins A and B. *J. Am. Chem. Soc.* 123, 9021–9032.
- Chen, T.-H., Lu, M.-C., Chang, Y.-C., Su, Y.-D., Chen, Y.-H., Lin, N.-C., Fang, L.-S., Wu, Y.-C., Sung, P.-J., 2013. Discovery of new eunicellin-based diterpenoids from a Formosan soft coral *Cladiella* sp. *Mar. Drugs* 11, 4585–4593.
- Chen, T.-H., Chen, W.-F., Wen, Z.-H., Lu, M.-C., Wang, W.-H., Li, J.-J., Wu, Y.-C., Sung, P.-J., 2014a. Cladieunicellins M–Q, new eunicellins from *Cladiella* sp. *Mar. Drugs* 12, 2144–2155.
- Chen, T.-H., Cheng, C.-H., Chen, Y.-H., Lu, M.-C., Fang, L.-S., Chen, W.-F., Wen, Z.-H., Wang, W.-H., Wu, Y.-C., Sung, P.-J., 2014b. Cladieunicellin J, a new hydroperoxyeunicellin from *Cladiella* sp. *Nat. Prod. Commun.* 9, 613–614.
- Friedrich, D., Doskotch, R.W., Paquette, L.A., 2000. Revised constitution of sclerophytins A and B. *Org. Lett.* 2, 1879–1882.
- Friedrich, D., Paquette, L.A., 2002. Structural and stereochemical reassessment of sclerophytin-type diterpenes. *J. Nat. Prod.* 65, 126–130.
- Hwang, T.-L., Wang, C.-C., Kuo, Y.-H., Huang, H.-C., Wu, Y.-C., Kuo, L.-M., Wu, Y.-H., 2010. The hederagenin saponin SMG-1 is a natural FMLP receptor inhibitor that suppresses human neutrophil activation. *Biochem. Pharmacol.* 80, 1190–1200.
- Kennard, O., Watson, D.G., Riva di Sanseverino, L., Tursch, B., Bosmans, R., Djerassi, C., 1968. Chemical studies of marine invertebrates. IV. Terpenoids LXII. Eunicellin, a diterpenoid of the gorgonian *Eunicella stricta*. X-ray diffraction analysis of eunicellin dibromide. *Tetrahedron Lett.* 9, 2879–2884.
- Paquette, L.A., Moradei, O.M., Bernardelli, P., Lange, T., 2000. Synthesis of the alleged structure of sclerophytin A: the setting of two oxygen bridges within the fused cyclodecanol B ring is not nature's way. *Org. Lett.* 2, 1875–1878.
- Peng, K.-Y., Chen, N.-F., Chen, Z.-C., Tsui, K.-H., Wen, Z.-H., Su, Y.-D., Chang, Y.-C., Chen, Y.-H., Lu, M.-C., Fang, L.-S., Chen, J.-J., Wu, T.-Y., Wu, Y.-C., Sung, P.-J., 2016. Cladieunicellins R and S, new eunicellins from the Formosan octocoral *Cladiella tuberculosa*. *Tetrahedron Lett.* 57, 4239–4242.
- Radhika, P., 2006. Chemical constituents and biological activities of the soft corals of genus *Cladiella*: a review. *Biochem. Syst. Ecol.* 34, 781–789.
- Scudiero, D.A., Shoemaker, R.H., Paull, K.D., Monks, A., Tierney, S., Nofziger, T.H., Currens, M.J., Seniff, D., Boyd, M.R., 1988. Evaluation of a soluble tetrazolium/formazan assay for cell growth and drug sensitivity in culture using human and other tumor cell lines. *Cancer Res.* 48, 4827–4833.
- Sharma, P., Alam, M., 1988. Sclerophytins A and B. Isolation and structures of novel cytotoxic diterpenes from the marine coral *Sclerophyllum capitalis*. *J. Chem. Soc. Perkin Trans. I* 2537–2540.
- Shih, F.-Y., Chen, T.-H., Lu, M.-C., Chen, W.-F., Wen, Z.-H., Kuo, Y.-H., Sung, P.-J., 2013. Cladieunicellins K and L, new eunicellin-based diterpenoids from an octocoral *Cladiella* sp. *Int. J. Mol. Sci.* 14, 21781–21789.
- Yu, H.-P., Hsieh, P.-W., Chang, Y.-J., Chung, P.-J., Kuo, L.-M., Hwang, T.-L., 2011. 2-(2-Fluorobenzamido)-benzoate ethyl ester (EFB-1) inhibits superoxide production by human neutrophils and attenuates hemorrhagic shock-induced organ dysfunction in rats. *Free Radic. Biol. Med.* 50, 1737–1748.
- Zhang, Z.-J., Peng, B.-R., Hu, C.-C., Lin, N.-C., Yao, J.-W., Lu, M.-C., Wen, Z.-H., Wu, Y.-C., Sung, P.-J., 2019. Cladieunicellin T, a new eunicellin-based diterpenoid produced by the octocoral *Cladiella* sp. *Nat. Prod. Commun.* 14, 101–102.

Hydroperoxyditerpenoids from Octocorals

Jyh-Horng Sheu,^{*,[a]} Bo-Rong Peng,^[b, c, d] Lee-Shing Fang,^[e, f] Tsong-Long Hwang,^[g, h, i, j] Jui-Hsin Su,^[b, k] Yang-Chang Wu,^{*,[l, m, n, o]} and Ping-Jyun Sung^{*,[a, b, k, l, m, n]}

Abstract: The structures, names, bioactivities, and references of 75 marine diterpenoids from octocorals possessing a hydroperoxy group, including 46 cembranes, 8 eunicellins, 5 briaranes, 5 dolabellanes, 4 germacrane, 3 xenicins, 2 caryophyllanes, 1 decalin, and 1 pseudopterogenin, are summarized in this review article. All the hydroperoxyditerpenoids mentioned in this review were isolated from octocorals from Alcyonacea (*Briareum excavatum*, *Briareum polyanthes*, *Briareum violaceum*, *Briareum* sp., *Cespitularia* sp., *Cladiella tuberculosa*, *Cladiella* sp., *Clavularia inflata*, *Klyxum simplex*, *Lemnalia* sp., *Lobophytum crassum*, *Lobophytum* sp., *Neph-*

thea pacifica, *Sarcophyton cherbonnieri*, *Sarcophyton crassicaule*, *Sarcophyton glaucum*, *Sarcophyton mililatensis*, *Sarcophyton trocheliophorum*, *Sarcophyton* sp., *Sinularia arborea*, *Sinularia erecta*, *Sinularia flexibilis*, *Sinularia gibberosa*, *Sinularia manaarensis*, *Xenia umbellata*) and Gorgonacea (*Astrogorgia* sp., *Eunicea caliculata*, *Eunicea pinta*, *Eunicea succinea*, *Eunicea* sp., *Pseudopterogorgia* sp.). Among these isolates, 41 compounds exhibited potential biomedical activities, including cytotoxicity, antimalarial activity, anti-inflammatory activity, and antibacterial activity.

Keywords: Hydroperoxyditerpenoid · Alcyonacea · Gorgonacea · octocoral · biomedical activity

1. Introduction

Since the discovery of the first hydroperoxyditerpenoid **1** (Figure 1), a pseudopterogenin analogue obtained by Harvis *et al.* from the Caribbean gorgonian coral *Pseudopterogorgia* sp.,^[1] 75 diterpenoids featuring a hydroperoxy group have been

obtained from various octocorals. These marine-origin hydroperoxyditerpenoids continue to attract the attention of investigators owing to the structural complexity and interesting biological activities (e.g., cytotoxicity, anti-inflammatory activity, antibacterial activity, and antimalarial activity) asso-

[a] J.-H. Sheu, P.-J. Sung

Department of Marine Biotechnology and Resources, National Sun Yat-sen University, Kaohsiung 804, Taiwan
E-mail: sheu@mail.nsysu.edu.tw
pjsung@nmmmba.gov.tw

[b] B.-R. Peng, J.-H. Su, P.-J. Sung

National Museum of Marine Biology and Aquarium, Pingtung 94450, Taiwan

[c] B.-R. Peng

Doctoral Degree Program in Marine Biotechnology, National Sun Yat-sen University, Kaohsiung 80424, Taiwan

[d] B.-R. Peng

Doctoral Degree Program in Marine Biotechnology, Academia Sinica, Taipei 11529, Taiwan

[e] L.-S. Fang

Center for Environmental Toxin and Emerging-Contaminant Research, Cheng Shiu University, Kaohsiung 833, Taiwan

[f] L.-S. Fang

Super Micro Mass Research and Technology Center, Cheng Shiu University, Kaohsiung 833, Taiwan

[g] T.-L. Hwang

College of Human Ecology, Chang Gung University of Science and Technology, Taoyuan 333, Taiwan

[h] T.-L. Hwang

Graduate Institute of Natural Products, College of Medicine, Chang Gung University, Taoyuan 333, Taiwan

[i] T.-L. Hwang

Healthy Aging Research Center, Chang Gung University, Taoyuan 333, Taiwan

[j] T.-L. Hwang

Department of Anaesthesiology, Chang Gung Memorial Hospital, Taoyuan 333, Taiwan

[k] J.-H. Su, P.-J. Sung

Graduate Institute of Marine Biology, National Dong Hwa University, Pingtung 944, Taiwan

[l] Y.-C. Wu, P.-J. Sung

Chinese Medicine Research and Development Center, China Medical University Hospital, Taichung 404, Taiwan
E-mail: yachwu@kmu.edu.tw

[m] Y.-C. Wu, P.-J. Sung

Graduate Institute of Natural Products, Kaohsiung Medical University, Kaohsiung 807, Taiwan

[n] Y.-C. Wu, P.-J. Sung

Research Center for Natural Products and Drug Development, Kaohsiung Medical University, Kaohsiung 807, Taiwan

[o] Y.-C. Wu

Department of Medical Research, Kaohsiung Medical University Hospital, Kaohsiung 807, Taiwan

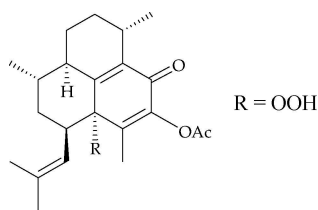


Figure 1. Structure of hydroperoxypseudopterosin **1**.

ciated with numerous compounds of this type. This survey is presented taxonomically according to genus and species.

2. Alcyonacea

2.1 *Briareum excavatum* (Family Briareidae)^[2]

The first hydroperoxybriarane, brianthin B (**2**) (Figure 2), was isolated from *B. excavatum*, collected from Sulawesi

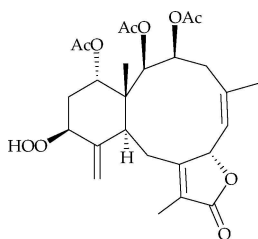
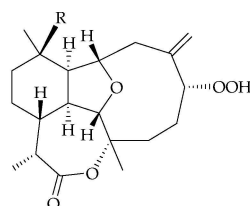


Figure 2. Structure of brianthin B (**2**).

Island, Indonesia.^[3] The structure of **2** was established by spectroscopic and chemical methods. At a concentration of 10 $\mu\text{g/mL}$, briarane **2** was found to exert cytotoxicity towards KB 3-1 and multidrug resistance cell line KB-C2 (inhibition rates = 26 and 37%, respectively).

2.2 *Briareum polyanthes*

Two 6-hydroperoxyeunicellin, briarellin K hydroperoxide (**3**) and briarellin D hydroperoxide (**4**) (Figure 3), was isolated



3: R = OAc, **4:** R = OC(O)(CH₂)₂CH₃

Figure 3. Structures of briarellin K hydroperoxide (**3**) and briarellin D hydroperoxide (**4**).

from *B. polyanthes*, collected by scuba divers near Cabo, Rojo, Puerto Rico.^[4] The structures of eunicellins **3** and **4** were established by spectroscopic methods and these two compounds showed toxic effects toward *Plasmodium falciparum*, the parasite responsible for the most severe forms of malaria, with IC₅₀ values of 9 $\mu\text{g/mL}$.^[4]

2.3 *Briareum violaceum*

A hydroperoxybriarane, briaviolide I (**5**) (Figure 4), was isolated from *B. violaceum*, collected from the waters off

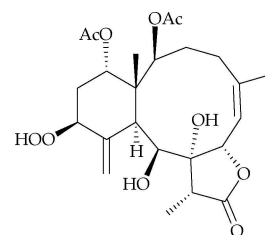


Figure 4. Structure of briaviolide I (**5**).

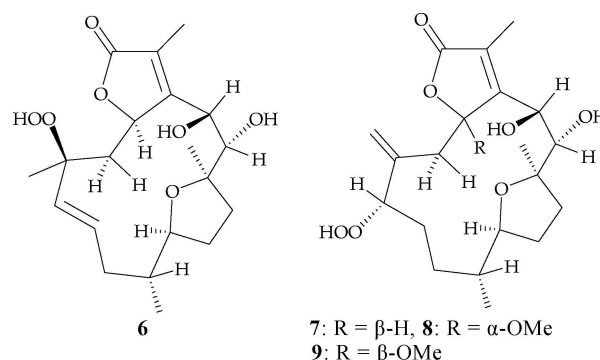


Figure 5. Structures of briaviodiols B–E (**6–9**).

Taiwan.^[5] The structure of **5** was established by spectroscopic methods. At a concentration of 10 $\mu\text{g/mL}$, **5** showed inhibitory activities on elastase release and superoxide anion production (inhibition rates = 29.0%, respectively) by human neutrophils in response to fMLP/CB.

Furthermore, four hydroperoxycembranoids, briaviodiols B–E (**6–9**) (Figure 5) were obtained from *B. violaceum*, collected off the waters of Taiwan. The structures of cembranoids **6–9** were determined by spectroscopic methods and cembranoids **6**, **8**, and **9** were found to reduce the level of iNOS to 43, 61, and 46%, respectively, at a concentration of 10 μM .^[6]

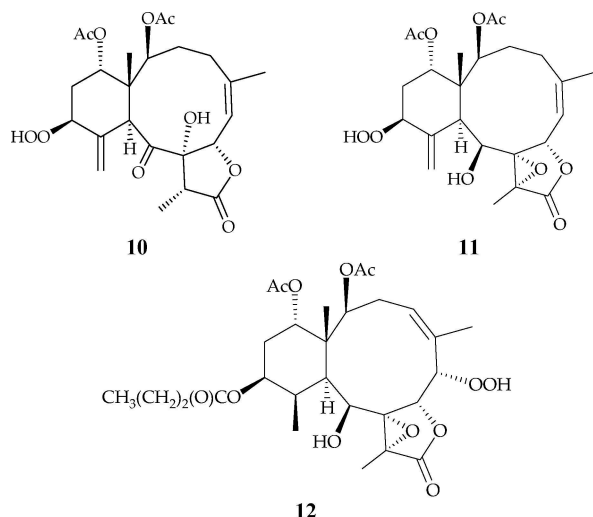


Figure 6. Structures of briarenolides B (10), D (11), and F (12).

2.4 *Briareum* sp.

In continuing studies of the constituents of octocorals identified as *Briareum* sp., collected from the waters off Southern Taiwan, three hydroperoxybriaranes, briarenolides B (10),^[7] D (11),^[8] and F (12),^[9] were obtained (Figure 6), and their structures were determined based on analysis of spectroscopic data; 12 was the first 6-hydroperoxybriarane analogue. In cytotoxicity testing, 11 showed cytotoxicity towards DLD-1 and CCRF-CEM tumor cells (ED_{50} = 2.0, 14.4 μ M, respectively).^[8] 12 was found to display an inhibitory effect on the generation of superoxide anions by human neutrophils (inhibition rate IC_{50} = 6.73 μ M).^[9]

2.5 *Cespitularia* sp. (Family Xeniidae)

In 2012, Roy *et al.* reported the isolation of two seco-type xenicin derivatives 13 and 14 (Figure 7), isolated from *Cespitularia* sp., collected off the coast of Zamami Island, Okinawa, Japan.^[10] Structural determination of 13 and 14 was conducted using spectroscopic methods. The IC_{50} values of isolates 13 and 14 against HCT 116 cancer cells were 39.2 and 71.4 μ M, respectively.^[10]

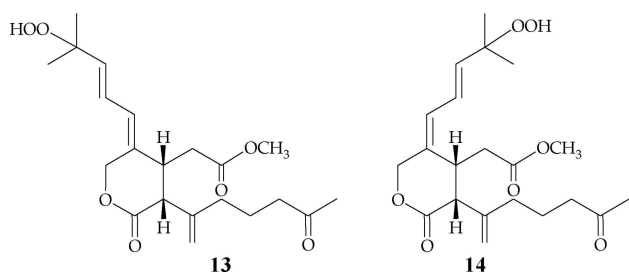


Figure 7. Structures of seco-type xenicins 13 and 14.

2.6 *Cladiella Tuberculosa* (Family Alcyoniidae)

An eunicellin-type diterpenoid possessing a hydroperoxy group, cladieunicellin S (15) (Figure 8), was isolated from *C.*

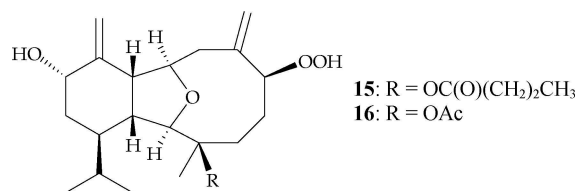


Figure 8. Structures of cladieunicellins S (15) and J (16).

tuberculosa, collected off the waters of Taiwan, and its structure was elucidated by spectroscopic methods.^[11] Eunicellin 15 was found to exhibit cytotoxic effects against MOLT-4, K-562, and SUP-T1 cells (IC_{50} = 14.3, 16.1, and 16.4 μ M, respectively).

2.7 *Cladiella* sp.

A hydroperoxyeunicellin, cladieunicellin J (16) (Figure 8), was isolated from *Cladiella* sp., collected off the coast of Penghu Archipelago, Taiwan, and its structure was elucidated by spectroscopic methods.^[12] Eunicellin 16 was found to exhibit cytotoxic effects on MOLT-4, K-562, CCRF-CEM, and DLD-1 cells (IC_{50} = 16.8, 27.7, 10.9, and 34.0 μ M, respectively).

2.8 *Clavularia Inflata* (Family Clavulariidae)

In 2001, a dolabellane diterpenoid, (1*R**,7*R**)-7-hydroperoxydolabella-4(16),8(17),11-triene-3,13-dione (17) (Figure 9),

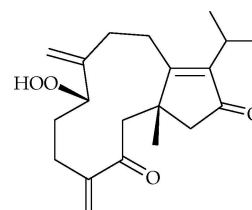
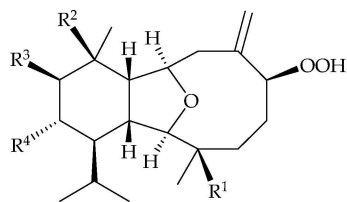


Figure 9. Structure of (1*R**,7*R**)-7-hydroperoxydolabella-4(16),8(17),11-triene-3,13-dione (17).

was isolated from *C. inflata*, collected from Orchid Island, off the coast of Taiwan.^[13] The structure of dolabellane 17 was established by spectral analysis, and this compound showed cytotoxicity towards P-388, A549, and HT-29 tumor cells, with IC_{50} values of 0.16, 1.72, and 0.93 μ M, respectively.^[13]



18: $R^1 = n\text{-OC(O)(CH}_2)_2\text{CH}_3$, $R^2 = \text{OAc}$, $R^3 = \text{H}$, $R^4 = \text{OH}$
19: $R^1 = R^3 = \text{OC(O)(CH}_2)_2\text{CH}_3$, $R^2 = \text{OH}$, $R^4 = \text{OAc}$
20: $R^1 = R^2 = \text{OAc}$, $R^3 = \text{H}$, $R^4 = \text{OH}$

Figure 10. Structures of klysimplexins D (**18**), M (**19**), and simplexin R (**20**).

2.9 Klyxum Simplex (Family Alcyoniidae)

In continuing studies of Formosan octocorals, the soft coral *K. simplex* (including cultured- and field-type) was a focus of study owing to its complex and interesting chemical constituents. Three hydroperoxyeunicellins, klysimplexins D (**18**) and M (**19**), along with simplexin R (**20**) (Figure 10), were isolated from *K. simplex*.^[14–16] The structures of eunicellins **18–20** were determined by spectroscopic methods. At a concentration of 10 μM , eunicellin **19** was found to significantly reduce the expression of inducible nitrogen oxide synthase (iNOS).^[15] Eunicellin **20** showed activity against the proliferation of K-562, CCRF-CEM, T-47D, and MOLT-4 tumor cells, with ED_{50} values of 15.9, 5.9, 29.7, and 8.4 μM , respectively.^[16]

2.10 Lemnalia sp. (Family Nephtheidae)

A decalin-type bicyclic diterpene glycoside, lemnalide C (**21**) (Figure 11), was isolated from *Lemnalia* sp., collected in

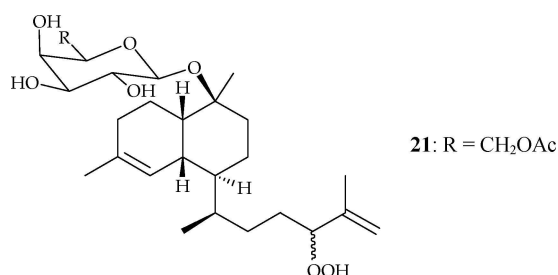


Figure 11. Structure of lemnalide C (**21**).

the South China Sea, Malaysia. The structure of decalin **21** was established by spectral data analysis.^[17]

2.11 Lobophytum Crassum (Family Alcyoniidae)

Two hydroperoxycembranoids, 2-hydroperoxysarcophine (**22**) and crassumolide E (**23**) (Figure 12), were isolated from *L.*

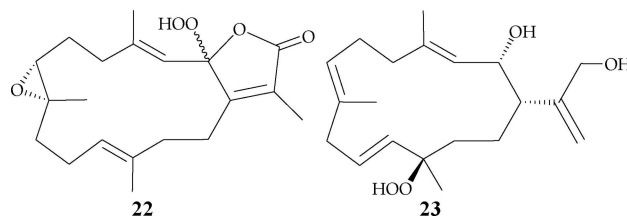


Figure 12. Structures of 2-hydroperoxysarcophine (**22**) and crassumolide E (**23**).

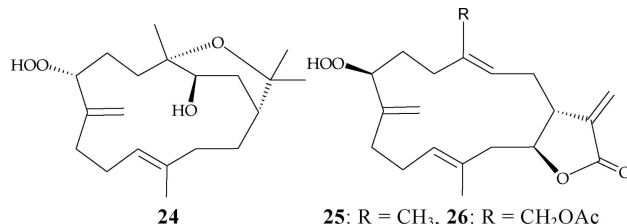


Figure 13. Structures of decaryiol D (**24**) and cembranoids **25** and **26**.

crassum collected from the waters off Hainan Island, China and off Taiwan, respectively.^[18,19] The structures of cembranoids **22** and **23** were established by spectroscopic analysis.

2.12 Lobophytum sp.

A hydroperoxycembranoid, decaryiol D (**24**) (Figure 13), was obtained from a soft coral identified as *Lobophytum* sp., collected along the coast of a small island located in the Bunaken Marine Park of Manado, North Sulawesi, Indonesia.^[20] The structure, including the absolute configuration, of **24** was established through spectroscopic analysis and chemical methods. Decaryiol D (**24**) was active against C6 rat glioma ($\text{IC}_{50} = 40 \mu\text{M}$) and H9c2 rat cardiac myoblast ($\text{IC}_{50} = 150 \mu\text{M}$) cells.^[20]

Two cembranoids, (1*R**,3*E*,7*S**,11*E*,14*S**)-7-hydroperoxy cembra-3,8(19),11,17(17)-tetraen-16,14-olide (**25**) and (1*R**,3*E*,7*S**,11*E*,14*S**)-18-acetoxy-7-hydroperoxycembra-3,8(19),11,15(17)-tetraen-16,14-olide (**26**) (Figure 13), were obtained from a South China Sea soft coral identified as *Lobophytum* sp.^[21] Structures of cembranoids **25** and **26** were elucidated by spectroscopic and these two compounds exhibited cytotoxicity against the SGC7901, A549, MCF7, HCT116, and B16 cells (IC_{50} values for **25** = 2.7, 3.2, 1.2, 4.5, 2.1 $\mu\text{g/mL}$; IC_{50} values for **26** = 2.3, 1.8, 2.9, 3.4, 5.6 $\mu\text{g/mL}$). The antibiotic assay revealed that compounds **25** and **26** exhibit inhibition against *Staphylococcus aureus* and *S. pneumoniae* with inhibition rates 90 % at 20 $\mu\text{g/mL}$.^[21]

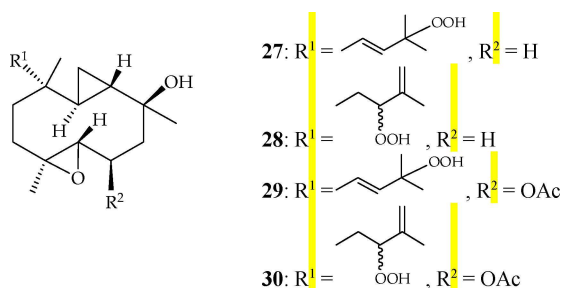


Figure 14. Structures of pacificins C (27), E (28), G (29), and H (30).

2.13 *Nephthea Pacifica* (Family Nephtheidae)

Following bioassay-guided fractionation of the cytotoxic organic extract of *N. pacifica*, four prenylcyclogermacrane diterpenoids, pacificins C (27), E (28), G (29), and H (30) were isolated (Figure 14).^[22] The structures of germacrane 27–30 were determined by spectral data analysis. Pacificins C (27) and H (30) exhibited cytotoxicity towards P-388 cells, with ED₅₀ values of 1.44 and 2.01 µg/mL, respectively.^[22]

2.14 *Sarcophyton Cherbonnieri* (Family Alcyoniidae)

Two hydroperoxycembranoids, cherbonolides B (31) and E (32) (Figure 15), were obtained from the Formosan soft coral

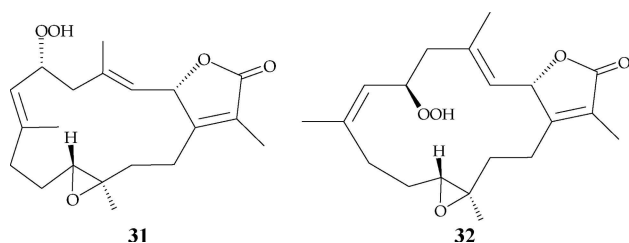


Figure 15. Structures of cherbonolides B (31) and E (32).

S. cherbonnieri, collected from Jihui Fish Port, Taiwan.^[23] The structures, including the absolute configurations, of cembranoids 31 and 32 were elucidated by spectroscopic analysis and chemical methods.^[23]

2.15 *Sarcophyton crassocaule*

A specimen of *S. crassocaule*, collected from the Xisha Islands of the South China Sea in 1998, yielded a hydroperoxycembranoid, scracophycrassolide A (33) (Figure 16). The structure of this compound was determined by spectroscopic methods and further confirmed by single-crystal X-ray diffraction analysis.^[24] In cytotoxicity testing, cembranoid 33

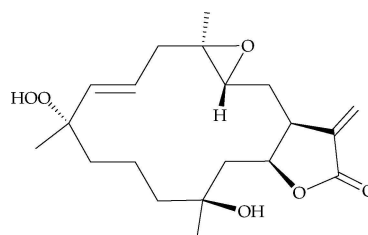


Figure 16. Structure of scracophycrassolide A (33).

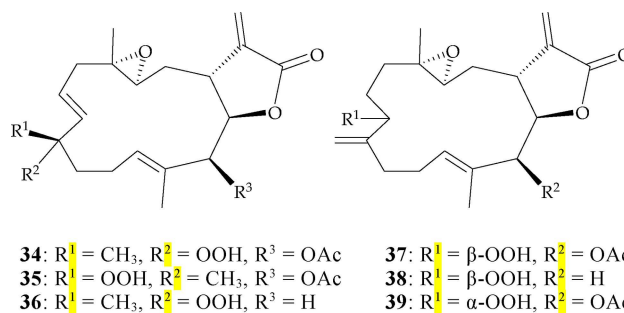


Figure 17. Structures of sarcocrassocolides F (34), G (35), J (36), and M–O (37–39).

exhibited significant cytotoxicity towards P-388 cells, with an IC₅₀ value of 0.1 µg/mL.^[24]

Six hydroperoxycembranoids, sarcocrassocolides F (34), G (35), J (36), and M–O (37–39) (Figure 17), were obtained from the soft coral *S. crassocaule*, collected off the Dongshan Atoll, South China Sea.^[25,26] The structures of cembranoids 34–39 were determined by spectroscopic methods. At a concentration of 10 µM Compounds 34–39 were found to significantly reduce the levels of iNOS protein.^[25,26] The cytotoxicity of compounds 34–39 against the proliferation of a limited panel of cancer cell lines, including Daoy, Hep-2, MCF7 and WiDr carcinoma cell lines was evaluated and the results showed that compounds 34 (ED₅₀ values of 7.3, 15.0, 19.4, 18.4 µM), 35 (ED₅₀ values of 8.3, 16.5, 9.6, 18.9 µM), 37 (ED₅₀ values of 6.6, 10.4, 10.6, >40 µM), 38 (ED₅₀ values of 5.2, 12.3, 10.1, 30.1 µM), and 39 (ED₅₀ values of 5.0, 12.4, 6.4, >40 µM) were found to exhibit cytotoxicity against most of the above carcinoma cell lines.^[25,26]

2.16 *Sarcophyton glaucum*

A specimen of *S. glaucum*, collected from the Egyptian Red Sea in 2009, yielded two hydroperoxycembranoids, 11(*S*)-hydroperoxylsarcoph-12(20)-ene (40) and 12(*S*)-hydroperoxylsarcoph-10-ene (41) (Figure 18). The structures, including the relative configurations, of these two compounds were established by spectroscopic methods and further confirmed by X-ray diffraction analysis.^[27] The absolute stereochemistries of cembranoids 40 and 41 were further determined via circular

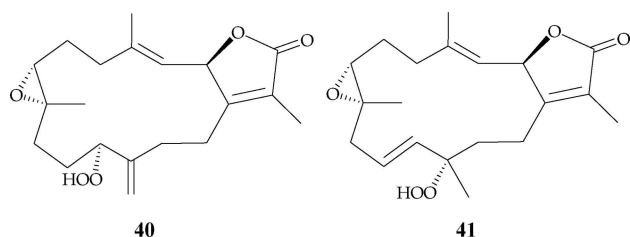


Figure 18. Structures of 11(S)-hydroperoxysarcoph-12(20)-ene (40) and 12(S)-hydroperoxysarcoph-10-ene (41).

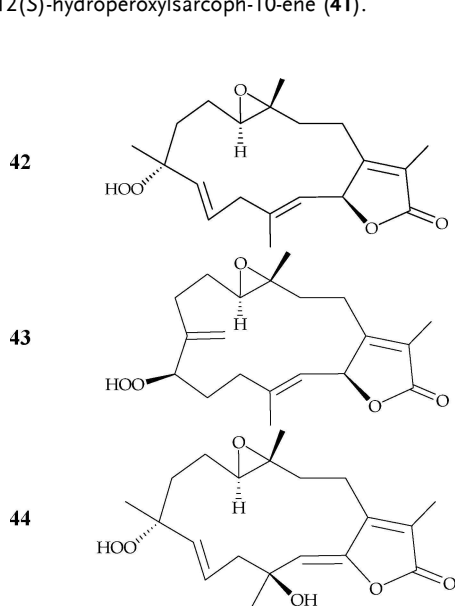


Figure 19. Structures of sarcomililatin A–C (42–44).

dichroism (CD) analysis.^[27] Cembranoid **41** was found to be promising as an inhibitor of cytochrome P₄₅₀ 1A activity (IC₅₀ = 2.7 nM), as well as an inducer of glutathione *S*-transferases (GST) and quinone reductase (QR) activities in *in vitro* assays.^[27]

2.17 *Sarcophyton mililatensis*

Three hydroperoxycembranoids, sarcomililatin A–C (42–44) (Figure 19), were isolated from *S. mililatensis*, collected from Weizhou Island, Guangxi Autonomous Region, China. The structures of metabolites 42–44 were elucidated by spectral analysis, and the absolute configurations of 42 and 43 were assigned using ECD spectroscopy.^[28] Sarcomililatin A (42) exerted an inhibitory effect on TNF α -induced nuclear factor kappa B (NF- κ B, a therapeutic target in cancer) activation, with an IC₅₀ value of 35.2 μ M.^[28]

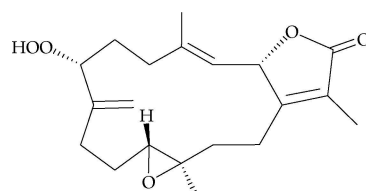


Figure 20. Structure of trocheliolide A (45).

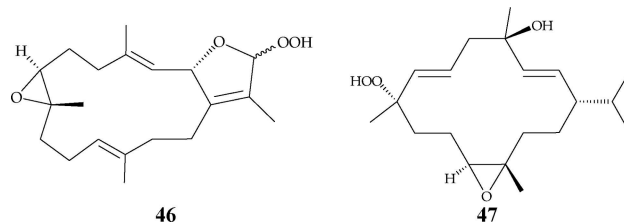


Figure 21. Structures of sarcophytonin F (46) and (1S*,2E,4R*,6E,8S*,11S*,12S*)-11,12-epoxy-8-hydroperoxy-4-hydroxy-2,6-cembradiene (47).

2.18 *Sarcophyton trocheliophorum*

A hydroperoxycembranoid, trocheliolide A (45) (Figure 20), was obtained from *S. trocheliophorum*, collected off the coast of Orchid Island (=Lanyu Island), Taiwan. The structure of cembranoid 45 was elucidated by spectral analysis.^[29]

2.19 *Sarcophyton* sp.

A 16-hydroperoxycembranoid, sarcophytonin F (46) (Figure 21), was obtained from a soft coral identified as *Sarcophyton* sp., collected off the coast of Dongsha Atoll, Taiwan. The structure of 46 was elucidated by spectral analysis, although the configuration of the stereogenic center at C-16 could not be elucidated at that stage.^[30]

In addition, a 8-hydroperoxycembranoid, (1S*,2E,4R*,6E,8S*,11S*,12S*)-11,12-epoxy-8-hydroperoxy-4-hydroxy-2,6-cembradiene (47) (Figure 21), was isolated from *Sarcophyton* sp., collected from Bohey Dulang, Semporna, Sabah, Malaysia. The structure of cembranoid 47 was elucidated by spectral analysis, and this compound was found to show strong inhibition of seaweed pathogens *Alteromonas* sp., *Cytophaga-Flavobacterium*, and *Vibrio* sp., at an antibiosis index of 0.5, 1.25, and 1.75, respectively.^[31]

2.20 *Sinularia arborea* (Alcyoniidae)

A non-cytotoxic 7-hydroperoxycembranoid, arbolide A (48) (Figure 22), was isolated from the soft coral *S. arborea*, collected from the coast of Southern Taiwan. The structure of cembranoid 48 was elucidated by spectroscopic methods.^[32]

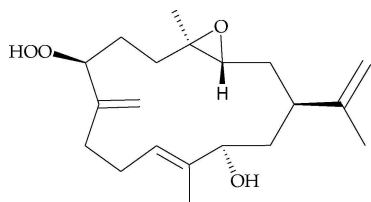


Figure 22. Structure of arbolide A (48).

2.21 *Sinularia erecta*

In 2016, Huang *et al.*, reported a 11-hydroperoxy-cembranoid, sinulirectol C (49) (Figure 23), obtained from *S. erecta*,

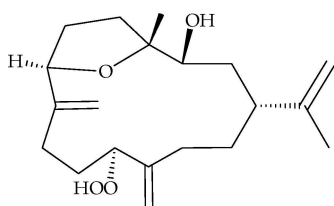


Figure 23. Structure of sinulirectol C (49).

collected off the coast of Dohgsha Atoll, Taiwan.^[33] The structure of cembranoid 49 was elucidated by spectroscopic methods, and this compound was found to exhibit cytotoxicity towards the K-562 tumor cells, with an IC₅₀ value of 9.2 μM.^[33]

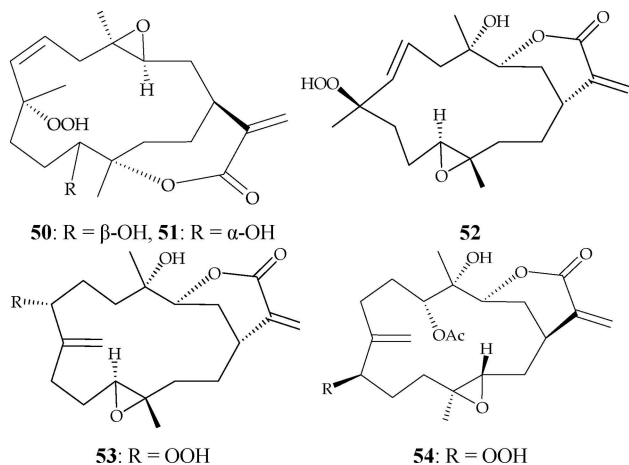


Figure 24. Structures of sinuladiterpenes A (50), B (51), 15,17-dedihydromanaarenolide E (52), 15,17-dedihydromanaarenolide A (53), and flexibilisolid H (54).

2.22 *Sinularia flexibilis*

Study of the soft coral *S. flexibilis*, collected from Green Island, Taiwan, afforded two 8-hydroperoxycebranoids, sinuladiterpenes A (50) and B (51) (Figure 24).^[34] The structures of cembranoids 50 and 51 were established by spectroscopic methods, and cembranoid 51 exhibited cytotoxicity against WiDR cells, with an ED₅₀ value of 22.9 μM. Moreover, two hydroperoxycebranoids, 15,17-dedihydromanaarenolide E (52) and 15,17-dedihydro-manaarenolide A (53) (Figure 24), were obtained from *S. flexibilis*, collected by scuba at Yalong Bay, Hainan Province, China.^[35] The structures of cembranoids 52 and 53 were elucidated by spectroscopic methods.^[35] Flexibilisolid H (54) (Figure 24), a hydroperoxyditerpenoid of the cembrane class, was isolated from *S. flexibilis*, collected by scuba off the coast of Liutiu, Taiwan, and the structure of this compound was elucidated by spectroscopic methods.^[36]

Chemical investigation of *S. flexibilis*, collected from the southern coast of Taiwan, has resulted two 8-hydroperoxycebranoids, flexilarins C (55) and D (56) (Figure 25).^[37] Structures of compounds 55 and 56 were established by spectroscopic methods and 56 exhibited potent cytotoxicity against Hela, Daoy, Hep2, and MCF7 cancer cells (ED₅₀ = 0.41, 1.24, 0.07, 1.24 μg/mL).^[37]

2.23 *Sinularia gibberosa*

Two hydroperoxy-bearing β-caryophyllene terpenoids, gibberosins A (57) and B (58), were isolated from Formosan *S. gibberosa*.^[38] Structures of 57 and 58 were determined by spectroscopic analyses. Compound 57 exhibited cytotoxicity

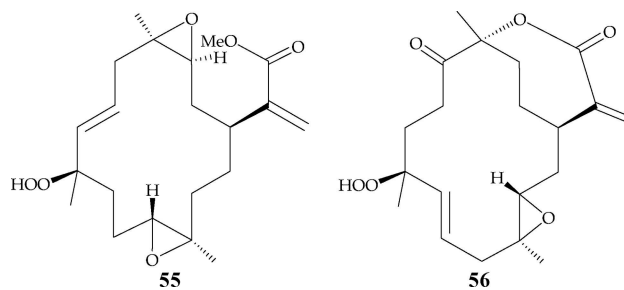


Figure 25. Structures of flexilarins C (55) and D (56).

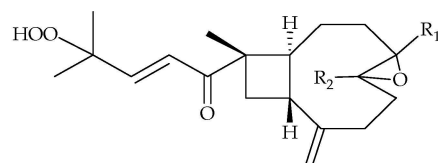
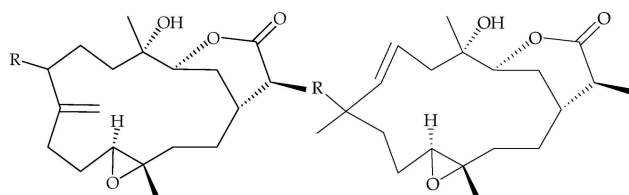


Figure 26. Structures of gibberosins A (57) and B (58).



59: R = α -OOH, 60: R = β -OOH 61: R = β -OOH, 62: R = α -OOH

Figure 27. Structures of manaarenolides A (59), B (60), E (61), and F (62).

towards Hep G2, A549, and MDA-MB-231 tumor cells with IC_{50} 's of 18.7, 18.5, and 15.2 μ g/mL.^[38]

2.24 *Sinularia manaarensis*

Chemical investigation of the Taiwanese soft coral *S. manaarensis*, collected off the coast of southern Taiwan, led to the isolation of four hydroperoxycembranoids, manaarenolides A (59), B (60), E (61), and F (62) (Figure 27). The structures, including the absolute configurations, of cembranoids 59–62 were determined on the basis of spectral data analysis and by comparison with spectral data from other known metabolites featuring a cembrane skeleton.^[39] These four compounds were the first hydroperoxy- cembranoids possessing a δ -lactone moiety to be isolated.

2.25 *Xenia umbellata* (Family Xeniidae)

A cytotoxic 9-hydroperoxyxenicane, xeniolide G (63) (Figure 28), was isolated from *X. umbellata*, collected at Green Island, Taiwan. The structure of 63 was elucidated by spectral analysis; however, the relative stereochemistry of the secondary hydroperoxy group at C-9 was not determined due to the flexibility of the nine-membered ring.^[31] This compound showed cytotoxicity against P-388, A549, and HT-29 cells, with ED_{50} values of 0.1, 13.7, and 23.9 μ M, respectively.^[40]

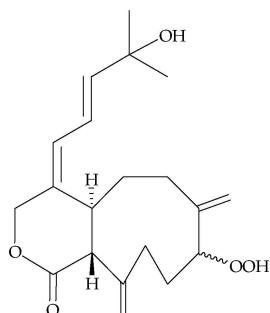


Figure 28. Structure of xeniolide G (63).

3. Gorgonacea

3.1 *Astrogorgia* sp. (Family Plexauridae)

A 6-hydroperoxyeunicellin, astrogorgin G (64) (Figure 29) was produced by a gorgonian *Astrogorgia* sp, collected from

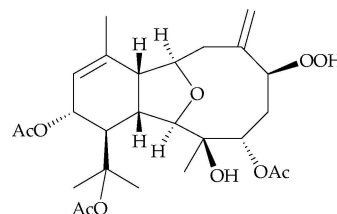


Figure 29. Structure of astrogorgin G (64).

the inner coral reef in Beibuwan Bay, GuangXi Province of China. The structure of eunicellin 64 was determined by spectroscopic analysis.^[41]

3.2 *Eunicea calyculata* (Family Plexauridae)

A dolabellane diterpenoid, calyculatine (65) (Figure 30), was obtained from *E. calyculata*, collected in deep waters adjacent

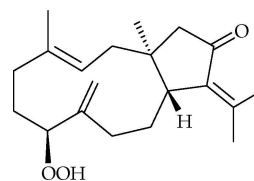


Figure 30. Structure of calyculatine (65).

to the Caribbean Sea of the Western Atlantic.^[42] The structure of 65 was elucidated by spectroscopic methods.^[42]

3.3 *Eunicea pinta*

Five 8-hydroperoxycembranoids, uprolides H (66), I (67), J (68), L (69), and M (70) (Figure 31), was obtained from *E. pinta*, collected along the southern coast of San Andrés Island in Colombia.^[43] The structures of cembranoids 66–70 were determined on the basis of the results of spectroscopic analysis and the structure of 66 was further confirmed by a single-crystal X-ray diffraction analysis.^[43] Uprolide H (66) showed cytotoxicity toward MOLT-4 tumor cells (IC_{50} = 0.01 μ g/mL).^[43]

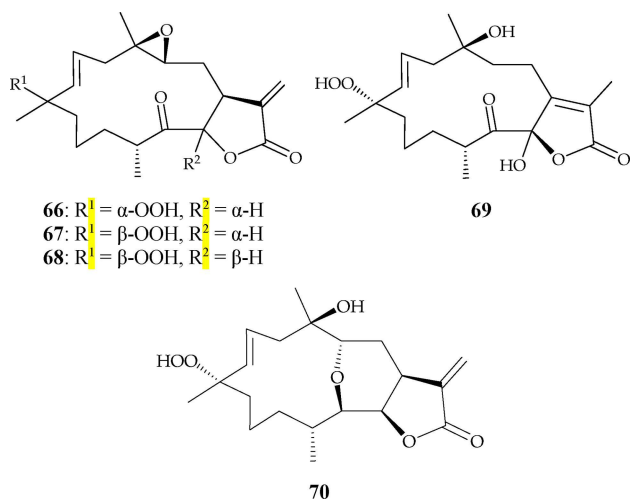


Figure 31. Structure of uprolides H (66), I (67), J (68), L (69), and M (70).

3.4 *Eunicea succinea*

Two hydroperoxycembranoids, uprolides O (71) and P (72) (Figure 32), were isolated from *E. succinea*, collected by hand

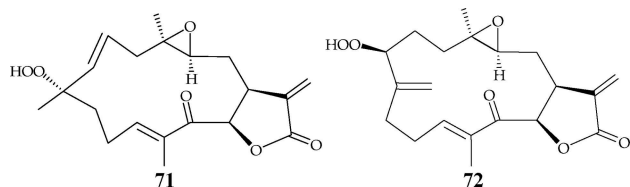


Figure 32. Structures of uprolides O (71) and P (72).

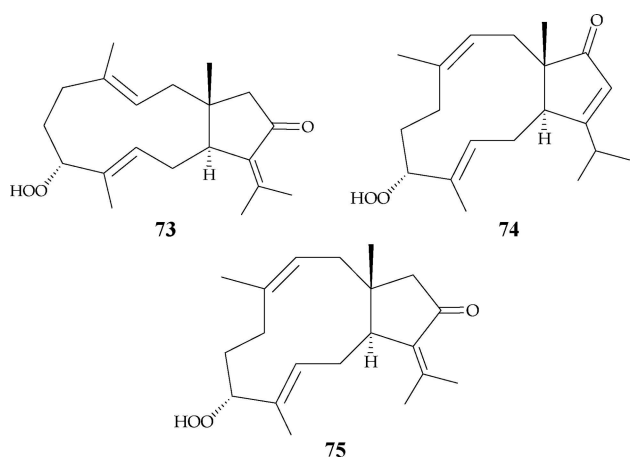


Figure 33. Structures of dolabellanes 73–75.

in Bastimentos National Park, Panama. The structures of cembranoids 71 and 72 were established by spectroscopic

methods and molecular modeling studies.^[44] Compounds 71 and 72 displayed anti-inflammatory activities by inhibiting the production of tumor necrosis factor (TNF) (IC_{50} = 2.73 and 2.27 μ M, respectively) and interleukin (IL)-6 (IC_{50} = 4.22 and 2.60 μ M, respectively) induced by lipopoly- saccharide (LPS) in murine macrophages.^[44]

3.5 *Eunicea* sp.

Wei *et al.* isolated three diterpenoids, 7*R**-hydroperoxy-13-keto-1*R**,11*S**-dolabell-3*E*,8*E*,12(18)-triene (73), 7*R**-hydroperoxy-14-keto-1*S**, 11*S**-dolabell-3*E*,8*E*,12*Z*-triene (74), and 7*R**-hydroperoxy-13-keto-1*R**, 11*S**-dolabell-3*Z*,8*E*,12(18)-triene (75) (Figure 33), each of which had a dolabellane skeleton, from *Eunicea* sp., collected from the coral reefs off Old Providence Island, Colombia.^[45] The structures of dolabellanes 73–75 were determined on the basis of spectroscopic analysis. Dolabellane 74 showed antimalarial activity against the chloroquine-resistant protozoan parasite *Plasmodium falciparum* W2, with an IC_{50} value of 9.4 μ M.^[45]

3.6 *Pseudopterogorgia* sp. (Family Gorgoniidae)

Harvis and coworkers isolated the first hydroperoxy-pseudopterogorgia analogue 1 from the Caribbean gorgonian coral *Pseudopterogorgia* sp. (Figure 1),^[1] and its structure was established by spectroscopic methods and chemical conversion.

4. Conclusion

Soft corals have proven to be rich sources of marine-origin diterpenoids. In the past 30 years, 75 hydroperoxy- diterpenoids, mainly formed by autoxidation of an alkene-an Ene reaction (Figure 34),^[46] have been isolated from various octocorals.

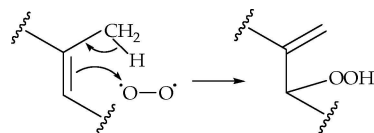


Figure 34. Autoxidation of an alkene-an Ene reaction

It is interesting to note that most of these compounds were isolated and reported after the year 2000 and 81% of these compounds (61/75) were produced by the octocorals distributed in the tropical Indo-Pacific Ocean, including Red Sea. These compounds included 46 cembranes, 8 eunicellins, 5 briaranes, 5 dolabellanes, 4 germacrane, 3 xenicins, 2 carophyllanes, 1 decalin, and 1 pseudopterogorgia analogue (Fig-

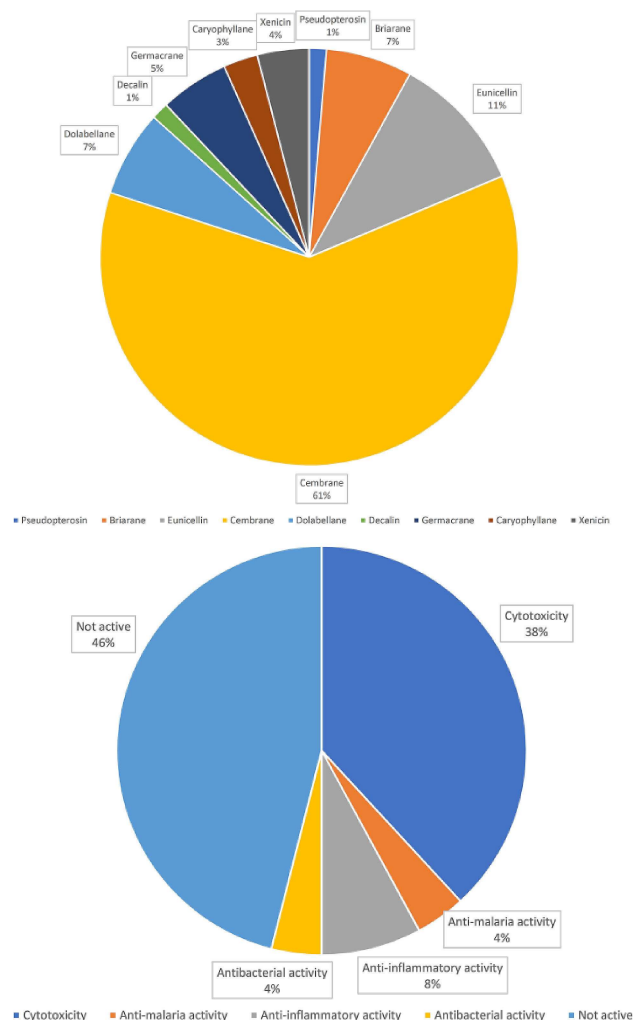


Figure 35. Carbon types of hydroperoxyditerpenoids and their biomedical activities.

ure 34), and approximately 54% of these hydroperoxyditerpenoids (41 compounds) have been found to exhibit interesting biomedical activities, particularly cytotoxicity (Figure 35). In light of potential medical use, studies of these interesting hydroperoxyditerpenoids isolated from octocorals will play an important role in biomedical natural product research.

Acknowledgements

This research was supported by grants from the National Museum of Marine Biology and Aquarium; the National Dong Hwa University; the National Sun Yat-sen University; and the Ministry of Science and Technology (Grant Nos. MOST 106-2320-B-291-001-MY3 and 107-2320-B-291-001-MY3), Taiwan, awarded to, Ping-Jyun Sung.

References

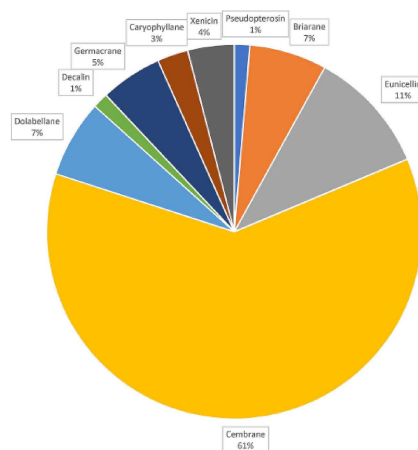
- [1] C. A. Harvis, M. T. Burch, W. Fenical, *Tetrahedron Lett.* **1988**, 29, 4361–4364.
- [2] K. Samimi-Namin, L. P. van Ofwegen, *Zookeys* **2016**, 557, 1–44.
- [3] S. Aoki, M. Okano, K. Matsui, T. Itoh, R. Satari, S. Akiyama, M. Kobayashi, *Tetrahedron* **2001**, 57, 8951–8957.
- [4] C. A. Ospina, A. D. Rodríguez, E. Ortega-Barria, T. L. Capson, *J. Nat. Prod.* **2003**, 66, 357–363.
- [5] C.-C. Liaw, Y.-B. Cheng, Y.-S. Lin, Y.-H. Kuo, T.-L. Hwang, Y.-C. Shen, *Mar. Drugs* **2014**, 12, 4677–4692.
- [6] P.-C. Huang, C.-C. Tseng, B.-R. Peng, C.-C. Hu, N.-C. Lin, N.-F. Chen, J.-J. Chen, Z.-H. Wen, Y.-C. Wu, P.-J. Sung, *Tetrahedron* **2019**, 75, 921–927.
- [7] J.-H. Su, P.-J. Sung, Y.-H. Kuo, C.-H. Hsu, J.-H. Sheu, *Tetrahedron* **2007**, 63, 8282–8285.
- [8] P.-J. Sung, M.-R. Lin, M. Y. Chiang, I.-C. Huang, S.-M. Syu, L.-S. Fang, W.-H. Wang, J.-H. Sheu, *Chem. Lett.* **2010**, 39, 1030–1032.
- [9] P.-H. Hong, Y.-D. Su, J.-H. Su, Y.-H. Chen, T.-L. Hwang, C.-F. Weng, C.-H. Lee, Z.-H. Wen, J.-H. Sheu, N.-C. Lin, Y.-H. Kuo, P.-J. Sung, *Mar. Drugs* **2012**, 10, 1156–1168.
- [10] P. K. Roy, W. Maarisit, M. C. Roy, J. Taira, K. Ueda, *Mar. Drugs* **2012**, 10, 2741–2748.
- [11] K.-Y. Peng, N.-F. Chen, Z.-C. Chen, K.-H. Tsui, Z.-H. Wen, Y.-D. Su, Y.-C. Chang, Y.-H. Chen, M.-C. Lu, L.-S. Fang, J.-J. Chen, T.-Y. Wu, Y.-C. Wu, P.-J. Sung, *Tetrahedron Lett.* **2016**, 57, 4239–4242.
- [12] T. H. Chen, C.-H. Cheng, Y.-H. Chen, M.-C. Lu, L.-S. Fang, W.-F. Chen, Z.-H. Wen, W.-H. Wang, Y.-C. Wu, P.-J. Sung, *Nat. Prod. Commun.* **2014**, 9, 613–614.
- [13] C.-Y. Duh, M.-C. Chia, S.-K. Wang, H.-J. Chen, A. A. H. El-Gamal, C.-F. Dai, *J. Nat. Prod.* **2001**, 64, 1028–1031.
- [14] B.-W. Chen, Y.-C. Wu, M. Y. Chiang, J.-H. Su, W.-H. Wang, T.-Y. Fan, J.-H. Sheu, *Tetrahedron* **2009**, 65, 7016–7022.
- [15] B.-W. Chen, C.-H. Chao, J.-H. Su, C.-W. Tsai, W.-H. Wang, Z.-H. Wen, C.-Y. Huang, P.-J. Sung, Y.-C. Wu, J.-H. Sheu, *Org. Biomol. Chem.* **2011**, 9, 834–844.
- [16] S.-L. Wu, J.-H. Su, C.-Y. Huang, C.-J. Tai, P.-J. Sung, C.-C. Liaw, J.-H. Sheu, *Mar. Drugs* **2012**, 10, 1203–1211.
- [17] G. Yao, N. B. Vidor, A. P. Foss, L. C. Chang, *J. Nat. Prod.* **2007**, 70, 901–905.
- [18] S.-W. Yin, Y.-P. Shi, X.-M. Li, B.-G. Wang, *Helv. Chim. Acta.* **2006**, 89, 567–572.
- [19] C.-H. Chao, Z.-H. Wen, Y.-C. Wu, H.-C. Yeh, J.-H. Sheu, *J. Nat. Prod.* **2008**, 71, 1819–1824.
- [20] E. Fattorusso, A. Romano, O. Tagliatalata-Scafati, C. Irace, C. Maffettone, G. Bavestrello, C. Cerrano, *Tetrahedron* **2009**, 65, 2898–2904.
- [21] M. Zhao, J. Yin, W. Jiang, M. Ma, X. Lei, Z. Xiang, J. Dong, K. Huang, P. Yan, *Mar. Drugs* **2013**, 11, 1162–1172.
- [22] A. A. H. El-Gamal, S.-K. Wang, C.-F. Dai, I.-G. Chen, C.-Y. Duh, *J. Nat. Prod.* **2005**, 68, 74–77.
- [23] C.-C. Peng, C.-Y. Huang, A. F. Ahmed, T.-L. Hwang, C.-F. Dai, J.-H. Sheu, *Mar. Drugs* **2018**, 16, 276.
- [24] X.-H. Xu, C.-H. Kong, C.-J. Lin, X. Wang, Y.-D. Zhu, H.-S. Yang, *Chin. J. Chem.* **2003**, 21, 1506–1509.
- [25] W.-Y. Lin, Y. Lu, J.-H. Su, Z.-H. Wen, C.-F. Dai, Y.-H. Kuo, J.-H. Sheu, *Mar. Drugs* **2011**, 9, 994–1006.
- [26] W.-Y. Lin, Y. Lu, B.-W. Chen, C.-Y. Huang, J.-H. Su, Z.-H. Wen, C.-F. Dai, Y.-H. Kuo, J.-H. Sheu, *Mar. Drugs* **2012**, 10, 617–626.

- [27] M. E. F. Hegazy, A. M. G. Eldeen, A. A. Shahat, F. F. Abdel-Latif, T. A. Mohamed, B. R. Whittlesey, P. W. Pare, *Mar. Drugs* **2012**, *10*, 209–222.
- [28] S. Li, F. Ye, Z. Zhu, H. Huang, S. Mao, Y. Guo, *Acta Pharm. Sin. B* **2018**, *8*, 944–955.
- [29] K.-M. Liu, C.-H. Cheng, W.-F. Chen, M.-C. Lu, L.-S. Fang, Z.-H. Wen, J.-H. Su, Y.-C. Wu, P.-J. Sung, *Nat. Prod. Commun.* **2015**, *10*, 1163–1165.
- [30] S.-P. Chen, B.-W. Chen, C.-F. Dai, P.-J. Sung, Y.-C. Wu, J.-H. Sheu, *Bull. Chem. Soc. Jpn.* **2012**, *85*, 920–922.
- [31] T. Kamada, I. I. Zamil, C.-S. Phan, C. S. Vairappan, *Nat. Prod. Commun.* **2018**, *13*, 123–124.
- [32] K.-H. Chen, C.-F. Dai, M.-C. Lu, J.-J. Li, J.-J. Chen, Y.-C. Chang, Y.-D. Su, W.-H. Wang, P.-J. Sung, *Mar. Drugs* **2013**, *11*, 3372–3380.
- [33] C.-Y. Huang, Y.-J. Tseng, U. Chokkalingam, T.-L. Hwang, C.-H. Hsu, C.-F. Dai, P.-J. Sung, J.-H. Sheu, *J. Nat. Prod.* **2016**, *79*, 1339–1346.
- [34] K.-L. Lo, A. T. Khalil, Y.-H. Kuo, Y.-C. Shen, *Chem. Biodiversity* **2009**, *6*, 2227–2235.
- [35] W.-T. Chen, J. Li, J.-R. Wang, X.-W. Li, Y.-W. Guo, *RSC Adv.* **2015**, *5*, 23973–23980.
- [36] C.-H. Wu, C.-H. Chao, T.-Z. Huang, C.-Y. Huang, T.-L. Hwang, C.-F. Dai, J.-H. Sheu, *Mar. Drugs* **2018**, *16*, 278.
- [37] Y.-S. Lin, C.-H. Chen, C.-C. Liaw, Y.-C. Chen, Y.-H. Kuo, Y.-C. Shen, *Tetrahedron* **2009**, *65*, 9157–9164.
- [38] S.-P. Chen, C.-H. Chao, H.-C. Huang, Y.-C. Wu, C.-K. Lu, C.-F. Dai, J.-H. Sheu, *Bull. Chem. Soc. Jpn.* **2006**, *79*, 1547–1551.
- [39] J.-H. Su, A. F. Ahmed, P.-J. Sung, C.-H. Chao, Y.-H. Kuo, J.-H. Sheu, *J. Nat. Prod.* **2006**, *69*, 1134–1139.
- [40] C.-Y. Duh, A. A. H. El-Gamal, C.-Y. Chiang, C.-J. Chu, S.-K. Wang, C.-F. Dai, *J. Nat. Prod.* **2002**, *65*, 1882–1885.
- [41] D. Lai, D. Liu, Z. Deng, L. van Ofwegen, P. Proksch, W. Lin, *J. Nat. Prod.* **2012**, *75*, 1595–1602.
- [42] W. Xiang, L. C. Chang, *Planta Med.* **2006**, *72*, 735–739.
- [43] Y.-P. Shi, A. D. Rodriguez, C. L. Barnes, J. A. Sánchez, R. G. Raptis, P. Baran, *J. Nat. Prod.* **2002**, *65*, 1232–1241.
- [44] D. Torres-Mendoza, Y. Gonzalez, J. F. Gomez-Reyes, H. M. Guzman, J. L. Lopez-Perez, W. H. Gerwick, P. L. Fernandez, M. Gutierrez, *Molecules* **2016**, *21*, 819.
- [45] X. M. Wei, A. D. Rodriguez, P. Baran, R. G. Raptis, *J. Nat. Prod.* **2010**, *73*, 925–934.
- [46] B. F. Bowden, B. J. Cusack, A. Dangel, *Mar. Drugs* **2003**, *1*, 18–26.

Manuscript received: January 30, 2019

Revised manuscript received: February 23, 2019

Version of record online: ■■■



*J.-H. Sheu**, *B.-R. Peng*, *L.-S. Fang*,
T.-L. Hwang, *J.-H. Su*, *Y.-C. Wu**, *P.-J. Sung**

1 – 12

**Hydroperoxyditerpenoids from
Octocorals**

複頻超音波對於臺灣金線連水草物化學組成之影響 Influence on Chemical Composition of *Anoectochilus formosanus* Hayata. Water Extract Treated with Multi-Frequency Ultrasound

林昱文¹ 李明怡² 魏莉雯¹ 鍾成沛^{3*}
Yu-Wen Lin¹ Ming-Yi Lee² Li-Wen Wei¹ Cheng-Pei Chung^{3*}

¹實踐大學食品營養與保健生技系（所）

²長庚科技大學保健營養系

³中華科技大學餐飲管理系

¹Department of Food Science, Nutrition, and Nutraceutical Biotechnology, Shih Chien University

²Department of Nutrition and Health Science, Chang Gung University of Science and Technology

³Department of Food & Beverage Management, China University of Science and Technology

摘要

臺灣金線連 (*Anoectochilus formosanus* Hayata.) 是珍貴的蘭科植物，全植株均可食用，含有豐富生理活性成分，於藥典中被記載具有輔助治療肺結核咳血、糖尿病、腎臟發炎、膀胱炎、重症肌無力、風濕性關節炎、熱痙攣或毒蛇咬傷，其中之生理活性成份主要為酚類 (phenolic compounds) 與醣苷類 (glycosides)，國內多開發為養生藥膳、茶飲或保健食品原料，為不致使原料浪費，增進利用效率成為業界重要發展目標。超音波 (ultrasound) 可輔助降低各種食材烹調或加工處理時間、增進萃取效能，廣泛被應用於萃取物製備或加工過程，尤其是價格昂貴、取得不易的保健機能性素材，而近年來複頻 (multi-frequency) 超音波技術發展快速，被認為具有較一般單頻超音波設備更優良之效能。本試驗使用具有 28 kHz 及 68 kHz 之複頻超音波設備，進行市售金線連茶包及金線連葉樣品熱水萃取物 (*A. formosanus* water extract, AWE) 之製備，發現複頻超音波處理可快速提升茶湯糖度 (degrees Brix, °Bx)，且透過該等處理程序所得之 AWE 中總多酚含量 (total polyphenol)、清除 1,1-二苯基-2-三硝基苯肼自由基 (1,1-diphenyl-2-picrylhydrazyl, DPPH) 能力均顯著高於未經處理之組別 ($p < 0.05$)，萃取率及總糖 (total sugar) 含量均有上升趨勢，顯示複頻超音波技術輔助處理效能優良，未來若可發展商業化設備將具有高度潛力。

關鍵詞：臺灣金線連、複頻超音波、水草萃取物、總多酚、清除 1,1-二苯基-2-三硝基苯肼自由基

Abstract

Anoectochilus formosanus Hayata. is a valuable orchid and the whole plant is edible. *A. formosanus* contains abundant physiological phytochemicals, mainly phenolic compounds and glycosides, and was recorded in the pharmacopoeia that helps tuberculosis hemoptysis, diabetes, nephritis, cystitis, myasthenia gravis, rheumatoid arthritis, febrile convulsion and snakebite. In catering industries, it is often developed as health medicinal diets, beverages, and functional food extracts. In order to avoid wasting, elevating application efficiency becomes an important goal. Ultrasound auxiliarily reduces cooking, processing time and elevates extracting efficiency, as well as that is applied for extract preparation or process, especially for expensive and difficult to obtained functional materials. Nowadays, multi-frequency ultrasound technology is developed rapidly, and is regarded that possesses better efficacy than regular single-frequency equipments. In the present report, a multi-frequency ultrasound equipment with 28 kHz and 68 kHz generators was composed, and was used in tea and water extract of *A. formosanus* (AWE) preparation. The degrees Brix ($^{\circ}\text{Bx}$) rose faster when treated with multi-frequency ultrasound, and also the total polyphenol content and 1,1-diphenyl-2-picrylhydrazyl (DPPH) radical-scavenging ability of AWE were significantly increased as compared with extract without ultrasound treatment ($p < 0.05$). Additionally, the yield (%) and total sugar content were elevated. The results suggested that multi-frequency ultrasound treatment enhanced extracting efficiency, and is highly potential if developing as commercial equipments.

Keywords: *Anoectochilus formosanus* Hayata., multi-frequency ultrasound, water extract, total polyphenol content, 1,1-diphenyl-2-picrylhydrazyl radical-scavenging ability

I.前言

臺灣金線連 (*Anoectochilus formosanus* Hayata.) 是臺灣特有蘭科植物 (圖 1)^[1], 具有調節血糖、抗發炎、預防肝損傷、促進免疫等效用^[2], 市面上有許多金線連葉入菜的養生料理, 如雞湯、排骨盅或涼拌小菜等, 除了常見的維生素、礦物質、類黃酮 (flavonoids) 或其他酚類物質 (phenolic compounds) 等生理活性物質外, 金線連醣苷 (kinsenocide) 是其特有的成分。曾有學者針對金線連相關文獻進行回顧, 於藥典中被記載具有輔助治療結核咳血、糖尿病、膀胱炎、重肌無力、風濕性關節炎、熱痙攣或毒蛇咬傷, 其中之生理活性成份主要為酚類 (phenolic compounds) 與醣苷類 (glycosides) (圖 2)^[3], 亦有學者進行分離純化工作, 並針

對其中成份加以探討其相關生理活性^[4]。過去金線連均採自野外，常遭遇植株成份受到產地、氣候、土壤、品種、生長時間、水質等多項因素影響之窘境，進而造成於產品規格與品質管控上不易，近年來已可透過發光二極體（light-emitting diode, LED）光源照射、組織培養^[5]等植物工廠經營模式取得^[6]，但技術門檻高且成本昂貴，仍使金線連價格居高不下，為了不致使原料浪費，提升萃取率、增進機能性成分相對含量或改良風味等需求，進一步提升其經濟價值，加強金線連的利用性、完整度，成為國內產業界重要的發展目標，若可結合複頻超音波技術，使金線連中的酚類物質萃取率、萃取物活性上升，且得到相對較高量的金線連醣苷，對於金線連發展為保健食品原料上將具優良潛力；另若延伸至料理、飲品等設計，當前餐飲業普遍均已導入標準作業程序概念，選擇食材處理時間、湯液糖度（degrees Brix, °Bx）、湯液黏度、色澤等可快速測量、控制的因子，其中糖度量測是茶飲與湯品相當普遍、方便且基本的項目，藉此估算當中固形物比例，進而初步評估湯液濃度、風味或色澤等官能項目，更者或可視快速之總活性物質（如酚類、還原醣、醣苷等標的化合物）測定結果，綜合評比藉以取得標準作業程序相關控制因子，以求產品品質均一。

隨著國人健康飲食概念提升，物理性輔助處理程序具有無毒、無殘留、環保的特性，且可減少部分食品添加物的使用，其中超音波（ultrasound）是被應用於食品相關產業的重要技術之一^[7]。超音波是超過人類聽覺數倍甚至百倍的周波振動，目前使用最為廣泛的介質為液體（如水、酒精等），當超音波在液體中被發射時，液體分子經超音頻推擠拉扯後將產生許多極為細小的氣泡，稱為空穴現象（cavitations），有時會形成真空狀態，當其破裂時會產生瞬間極大音壓（sound pressure）而具有相當衝擊力，利用空穴化泡沫、機械與熱效應，具高剪切的壓力波會增加萃取物的質傳，類似活塞作用於介質表面，可以透過增大介質分子的運動速度來增強介質的穿透力，並增加固液相接觸面積及有效成分之溶解度，達到萃取植物細胞中成分的目的^[8]。研究證實，超音波可幫助殺除致病菌或降低其活力^[9]、提升萃取效率^[10]且增加萃取物質的效能^[11]、增強酵素活性^[12]，同時可改變植物或動物組織的質地、加快澱粉糊化或蛋白質變性速度、幫助熱傳遞等功用^[7]，均證實超音波之處理確實可為食品餐飲領域所應用。

然而，超音波使用過程中，震盪子將會有頻率飄移與能量衰退的現象產生，當輸出頻率不穩定與能量隨時間衰退，或因能量駐波現象（standing waves）導致超音波音壓被不當增強或削減，因而造成超音波效能降低，故目前介質中超音波強度穩定均勻化是極為重要的課題。近年來複頻（multi-frequency）超音波技術被認為可改善介質中各區域震盪強度不均之狀況，曾有學者發表若將單一頻率 20

kHz 與 25 kHz 以及複頻 20 kHz 加上 25 kHz 於 MathWorks MATrix LABoratory (Matlab) 數學軟體進行模擬，20 kHz、25 kHz 與複頻 20 kHz 加上 25 kHz 空化泡的最大半徑分別為 56.27 μm 、56.53 μm 與 56.62 μm ，空化泡崩潰時間為 1.42×10^{-5} 秒、 1.31×10^{-5} 秒與 1.19×10^{-5} 秒，證實複頻超音波的空化泡半徑大於單頻超音波，且空化泡崩潰時間小於單頻超音波，因此在相同的單位時間，複頻超音波具有更為顯著的空穴效應發生^[13]；爰此，若以上述結果為基礎，倘利用適當裝備、配置或設計將複頻超音波之聲場 (sound field) 均勻度提升，複頻超音波將可顯著提升超音波輔助處理之效能。

綜上，本試驗擬利用複頻超音波輔助處理介入金線連原料之熱浸泡程序模擬茶湯製備過程，於各時間點觀察其糖度變化，並於萃取終點測定總糖、總多酚及總固形物含量，藉此以生理活性物質總量觀察萃取物中酚類及其糖苷衍生物、含醣物質之變化量，評估並證實複頻超音波設備輔助萃取之效能，做為未來研究之基礎。

II. 材料及方法

一、金線連茶飲試驗樣品與茶湯糖度測定

經調查市售金線連茶包商品，均為混合其他草本植物或茶葉調合，為符合餐飲食品業界現況，隨機選擇市售華建中藥行（址設桃園市楊梅區萬大路 37 號）販售之金線連茶茶包，內容物為各草本植物破片，參考商品包裝上印製之建議沖泡條件，選擇 85°C 之 20 倍重量體積熱水 (w/v) 萃取 20 分鐘做為對照，分別於 0.5、1.0、2.5、5.0 及 10.0 分鐘做為糖度計觀測之時間點，最終時間為 20.0 分鐘，進一步以複頻超音波輔助處理，設定未經超音波處理者 (placebo)、單頻 28 kHz、68 kHz 處理及兩頻率共同處理（設定功率均為 110W）等組別，於同樣上述時間點藉由手持光學式糖度計進行糖度觀察；另取茶包內容物破片以磨粉機破碎，取得粉末樣品，兩者以同樣條件處理取得茶湯，相互比較複頻超音波處理對於茶湯糖度變化之影響，詳細步驟如圖 3 所示。

二、複頻超音波輔助處理介入金線連萃取物製備

為避免野生植物各植株、產地或品種難以確定進而造成天然物含量或成份不一之情況，本試驗使用三愛農業科技股份有限公司植物工廠生產之臺灣金線連葉樣品，取得後以 70°C 烘箱乾燥 3 日後，以磨粉機破碎後得到金線連葉破片，再經研磨成粉末，以 20 倍重量體積水 (w/v) 於 85°C 萃取 20 分鐘，取得未經超音波處理者 (placebo)、單頻 28 kHz、68 kHz 處理者及兩頻率共同處理者（設定功率

均為 110W)，均分別以上開萃取方法進行試驗，接著以離心機於 3000 rpm 離心 10 分鐘去除殘渣，取上清液藉由手持光學式糖度計觀察最終糖度，部分以冷凍乾燥機乾燥取得金線連熱水萃取物 (*A. formosanus* water extract, AWE) 並秤重，以利後續分析，詳細步驟如圖 3 所示。

三、金線連萃取物相關特性測定

(一) 總糖測定方法

參考文獻對於不同方式測定總糖之結果比較，採用具代表性之苯酚硫酸法 (phenol-sulfuric acid assay) 測定總糖^[14]，原理與步驟簡述如下。糖類遇到硫酸時，將迅速脫水生成糖醛衍生物，將與苯酚生成橙黃色化合物，因此藉由已知濃度 D-葡萄糖 (glucose, Glc) 標準品製作標準曲線，並配製藉由單頻 28 kHz、68 kHz 處理及兩頻率共同處理 (設定功率均為 110W) 之各不同濃度 AWE 水溶液與硫酸反應，利用比色法 (490nm 波長吸光值) 計算其糖類的濃度，接著與未經超音波處理 (placebo) 之組別進行組間統計分析比較差異性。

(二) 總多酚測定方法

利用酚類指示劑 (Folin & Ciocalteus phenol reagent) 與試驗樣品反應，如樣品裡含有酚類化合物將與該試劑反應呈藍紫色，乃取沒食子酸 (gallic acid) 為標準品，配製各不同濃度之沒食子酸溶液與酚類指示劑反應，經測量其於 750 nm 波長之吸收值製作標準曲線^[15]，與藉由單頻 28 kHz、68 kHz 處理及兩頻率共同處理 (設定功率均為 110W)、與未經超音波處理 (placebo) 等組別之已知濃度 AWE 酒精溶液樣品，和酚類指示劑反應後測定 750 nm 下吸光值，利用標準曲線以求得總多酚含量，單位以沒食子酸當量 (gallic acid equivalent, GAE) 表示，並進行組間統計分析比較差異性。

(三) 1,1-二苯基-2-三硝基苯肼 (1,1-diphenyl-2-picrylhydrazyl, DPPH) 自由基清除能力測定方法

DPPH 是一種穩定的自由基，當其溶於乙醇中會呈現藍紫色，當加入的成分樣品可以和 DPPH 自由基直接反應，則會阻斷 DPPH 自由基的連鎖反應，使藍紫色的 DPPH 溶液轉為澄清黃色。乃取藉由單頻 28 kHz、68 kHz 處理及兩頻率共同處理 (設定功率均為 110W)、與未經超音波處理 (placebo) 等組別之已知濃度 AWE 酒精溶液樣品，與 DPPH 反應後測定 512 nm 下之吸光值變化，利用標準曲

線計算樣品對於 DPPH 自由基的清除率^[15]。因 AWE 本身帶有顏色，故於測定吸光值時先行測定各萃取物本身於 512 nm 下之吸光值，後續將之做為背景值扣除，避免產生誤差。

(四) 統計分析方法

各組樣品至少進行三重複試驗，使用 IBM SPSS 商業套裝統計分析軟體進行單向變異數分析 (one way analysis of variance, ANOVA) 及鄧肯多重差距檢定 (Duncan's new multiple range test, DMRT)，取 95% 信賴區間，以 p 小於 0.05 視為具有統計分析上之顯著意義。

III. 結果與討論

一、複頻超音波輔助處理對於金線連茶湯糖度之影響

利用複頻超音波設備輔助進行金線連茶湯製備方面，草本破片之糖度變化情形如圖 4 (A) 所示。placebo 為未經超音波處理者之空白組，28 kHz、68 kHz (功率均設定為 110 W) 或兩頻率共同處理之複頻超音波處理調整其強度以符合功率設定；經處理後所得茶湯置於離心管，以 3,000 rpm 離心 10 分鐘以區分殘渣，取上清液備用。量測結果顯示，若不以超音波處理，以熱水浸泡青草破片所得茶湯最終糖度約為 0.2 至 0.3 之間，而若以超音波處理，不管使用何種頻率，最終糖度幾可達 1.0，糖度上升之速度以 28 kHz 組別較快；然若使用相同強度之複頻超音波處理，最終糖度可高於 1.0，且糖度上升速度更快，顯示複頻超音波處理具有較單頻者更好的效能，在較短的時間內即可達其他處理之最高糖度，且觀察各處理組別間的色澤、透光度或濁度沒有明顯不同，氣味亦未出現差異。

經過破碎磨粉的金線連茶樣品之糖度變化量測結果如圖 4 (B) 所示，若不以超音波處理，以熱水浸泡青草粉末所得茶湯最終糖度約為 1.9，較以破片浸泡所得茶湯高出許多；而若以單頻超音波處理 (28 kHz 或 68 kHz)，最終糖度較空白組略高，但亦為 1.9 左右，但糖度上升之速度較快，而使用相同強度之複頻超音波處理，最終糖度可高於 2.0，且糖度上升速度更快，顯示複頻超音波處理粉末樣品亦具有較單頻者更好的效能，同樣在較短的時間內即可達其他處理之最高糖度，觀察各處理組別間的色澤、透光度或濁度亦沒有明顯不同，氣味亦未出現差異。文獻指出利用空穴泡沫原理應用於植物萃取程序，依序是空穴泡沫於植物材料表面生成、活塞作用造成空穴泡沫的爆裂，該爆裂產生之微射流作用於植物基質，進而破壞細胞壁，使細胞內容質進入萃取溶劑中^[16]，表示若將茶包內容物經過適當破碎，可能並非必須經磨粉程序，即可利用超音波技術加以處理提升其萃取效能，更快速得到符合最終需求標準之茶湯。

結果顯示，以超音波輔助處理介入金線連茶湯萃取，不論破片或粉末型態之樣品進行，以超音波處理均可在較短時間內達到單純以熱水浸泡者之糖度（圖 4），且在破片條件下之輔助提升現象特別明顯，且以相同強度之複頻超音波處理均可得到更高的糖度，且茶湯外觀同樣屬清澈、透光，氣味則未有明顯的差異，證實複頻超音波處理對於青草茶大量製備具有相當之優勢，除了可節省時間、樣品，更可得到品質優良的產品，具有實質經濟效益。

二、複頻超音波輔助處理對於金線連水草物特性之影響

Placebo 為未經超音波處理之空白組，而 28 kHz、68 kHz（功率均設定為 110 W）或兩頻率 28 kHz 與 68 kHz 共同處理之複頻超音波處理調整其強度以符合功率設定，各組之萃取物重、萃取率、總糖、總多酚含量如表 1 所示。0.5 克乾燥金線連葉粉末以熱水草取（placebo）、28 kHz、68 kHz 或 28 kHz 與 68 kHz 共同處理者分別可得到 0.143 ± 0.011 克、 0.153 ± 0.028 克、 0.147 ± 0.023 克及 0.167 ± 0.005 克 AWE，萃取率則分別為 28.7%、30.7%、29.3% 及 33.3%，雖經統計分析後未發現各組間具有顯著差異，但就複頻超音波處理者之萃取物重量有上升之趨勢；綜合糖度變化之數據，結果顯示複頻超音波可幫助萃取，得到較多的萃取物，萃取液亦具有較高之糖度，但差異均不顯著，推測原因為該樣品已研磨成為粉末，萃取效能已較片狀樣品提升，進而造成超音波輔助處理效用影響萃取過程之程度不大；另可能因為設定之超音波強度較低（110W），而使各處理組間的差異不明顯，但實驗結果顯示複頻超音波的確具有較單頻者較好的輔助萃取功效，且各組別得到之萃取物外觀即不盡相同（圖 5），除了複頻超音波萃取者外觀呈現類似砂糖受潮結晶狀外，其餘三者均呈現較為蓬鬆之型態，顏色亦較複頻超音波萃取者淺，顯示各萃取物之組成應有所不同，故進而針對該萃取物中之總糖及總多酚物質進行測定。

金線連熱水草取未經超音波處理者（placebo）、以 28 kHz、68 kHz 及 28 kHz 與 68 kHz 共同處理者之總糖含量分別為 178 ± 4 、 164 ± 8 、 181 ± 3 及 182 ± 10 mg Glc/g sample，複頻超音波處理者顯著高於 28 kHz 處理者（ $p < 0.05$ ），但與其餘二者沒有顯著差異；總多酚含量則分別為 53.2 ± 5.4 、 93.9 ± 6.4 、 71.7 ± 16.6 、 75.4 ± 6.4 mg GAE/g sample，複頻超音波處理者顯著高於未經超音波處理者（ $p < 0.05$ ），其中以 28 kHz 處理者最高。根據上述得到之實驗結果，發現超音波處理對於萃取過程產生複雜的影響，雖各處理組別對於萃取率沒有影響，但萃取物中的總糖以複頻超音波組及 68 kHz 組較高，總多酚則以 28 kHz 組最高，但複頻組及 68 kHz 組亦均顯著高於未經超音波處理者，顯示複頻超音波可兼具兩種不同頻率對於特

定活性成分的萃取效能提升，進而達到在總醣及總多酚含量方面均顯著高於空白組，且萃取率有高於其他各組的趨勢，代表在固定時間、溫度下確實可應用於萃取程序，未來若提高功率、或對應餐食製備模式直接使用葉片整體，應可觀察到更為明確的結果。

在 DPPH 自由基清除率之結果方面，因金線連萃取物本身帶有顏色，故於測定吸光值時先行測定各萃取物酒精溶液本身之吸光值，後續將之做為背景值扣除。量測未經超音波處理者、28 kHz、68 kHz 及複頻處理者於 512 nm 下之吸光值分別略為 1.839、1.034、1.877 及 1.939，證實各萃取物中的成分組成的確具有差異，可能進而導致各組 AWE 外觀不一（圖 5）。各組萃取物對於清除 DPPH 自由基之能力如表 1 所示，在 50 mg/mL 之各組 AWE 共同反應下，未經超音波處理者、28 kHz、68 kHz 及複頻處理者的 DPPH 清除率分別為 21.1 ± 2.3 、 16.6 ± 2.3 、 28.1 ± 3.1 及 $26.6 \pm 2.7\%$ ，複頻組顯著高於空白組及 28 kHz 組，而與 68 kHz 組沒有差異（ $p < 0.05$ ），結果證實複頻超音波處理除了提升萃取率外，對於成分組成亦產生影響，且具有相對高的 DPPH 自由基清除率，然其中確切的天然物組成、比例與多寡，尚需進一步分析。

IV. 結論

本試驗以複頻超音波輔助處理介入金線連茶湯萃取，發現不論破片或粉末型態之樣品藉由複頻超音波處理均可在較短時間內達到單純以熱水浸泡者之糖度，破片條件下之輔助提升現象特別明顯，且以相同強度之複頻超音波處理則可得到更高的糖度；另於輔助萃取之固形物、生理活性物質含量及抗氧化活性均較單頻超音波處理者更加良好。結果顯示複頻超音波技術確實可為餐飲食品領域所應用，對於茶湯大量製備、萃取利用率等方面均可節省時間、提升效能，於現今國人注重健康餐飲、養生風潮高漲之環境下，未來對於珍貴食材或藥膳製備上具有高度發展潛力。

致謝

本研究感謝科技部「專題研究計畫（產學合作研究計畫-應用型）」（106-2622-E-157-002-CC3）支持。

V. 參考文獻

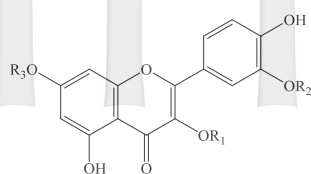
1. 台灣金線連 (<http://tai2.ntu.edu.tw/Specimen/specimen.php?taiid=221691>), 台灣植物資訊整合查詢系統網站。
2. 林文川。臺灣金線連的研究近況。2004 國際藥用植物發展研討會專刊 2004 : 231-238。
3. Ye S, Shao Q, Zhang A. *Anoectochilus roxburghii*: A review of its phytochemistry, pharmacology, and clinical applications. *J Ethnopharmacol* 2017; 209: 184-202.
4. 林宗輝。臺灣蘭科植物—石斛、連珠石斛與臺灣金線連之化學成分及藥理活性研究。2001。中國醫藥學院中國藥學研究所博士論文。臺中。
5. Shiao YJ, Sagare AP, Chen UC, Yang SR, Tsay HS. Conservation of *Anoectochilus formosanus* Hayata by artificial cross-pollination and in vitro culture of seeds. *Bot Bull Acad Sin* 2002; 423: 123-130.
6. 李國基。台灣金線連及蘭菌之鑑定與生產技術改進。2001。國立臺灣大學園藝學研究所博士論文。臺北。
7. Zhou C, Ma H, Yu X, Liu B, Yagoub Ael-G, Pan Z. Pretreatment of defatted wheat germ proteins (by-products of flour mill industry) using ultrasonic horn and bath reactors: Effect on structure and preparation of ACE-inhibitory peptides. *Ultrason Sonochem* 2013; 20(6): 1390-1400.
8. 陳仲仁。超音波在植物功能成分萃取之應用。食品工業 2012 ; 44 : 56-69。
9. 王文亮、蔡慧君、林小玲、薛月娥。臭氧與超音波振盪殺菌效果之研究—I 對霍亂弧菌的模擬試驗。臺灣省水產試驗所試驗報告 1991 ; 50 : 291-299。
10. Villkhu K, Mawson R, Simons L, Bates D. Application and opportunities for ultrasound assisted extraction in the food industry - A review. *Inn Food Sci Emerg Technol* 2008; 9(2): 161-169.
11. 曾永仁、洪昆源。超音波及微波萃取綠茶抗氧化活性之比較。林業研究專訊 2006 ; 13 : 39。
12. Jin J, Ma H, Wang K, Yagoub AA, Owusu J, Qu W, He R, Zhou C, Ye X. Effects of multi-frequency power ultrasound on the enzymolysis and structural characteristics of corn gluten meal. *Ultrason Sonochem* 2015; 24: 55-64.
13. 丘泰球、曾榮華、張曉燕。雙頻超聲波強化提取的機理。華南理工大學學報 2006 ; 34 : 89-92。
14. Liu XH, Chen YG, Lin L, Zhuang MX, Fang XJ. Comparison of methods in determination of polysaccharide in *Lycium Barbarum* L. *Food Sci Technol* 2009; 34(9): 270-272.

15. Lin CW, Yu CW, Wu SC, Yih KH. DPPH Free-radical scavenging activity, total phenolic contents and chemical composition analysis of forty-two kinds of essential oils. J Food Drug Anal 2009; 17(5): 386-395.
16. Patist A, Bates D. Ultrasonic innovations in the food industry: from the laboratory to commercial production. Inn Food Sci Emerg Technol 2008; 9(2): 147-154.



圖 1. 臺灣金線連

Figure 1. *Anoectochilus formosanus* Hayata.



isorhamnetin: $R_1=R_3=H$, $R_2=CH_3$

isorhamnetin-3-*O*- β -*D*-glucopyranoside: $R_1=glucopyranose$, $R_2=CH_3$, $R_3=H$

isorhamnetin-7-*O*- β -*D*-glucopyranoside: $R_3=glucopyranose$, $R_2=CH_3$, $R_1=H$

isorhamnetin-3-*O*- β -*D*-rutinoside: $R_1=rutinose$, $R_2=CH_3$, $R_3=H$

isorhamnetin-3-*O*-neohesperidoside: $R_1=neohesperidose$, $R_2=CH_3$, $R_3=H$

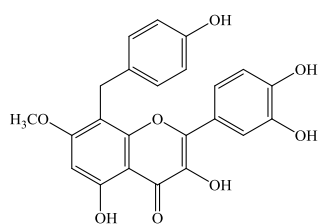
isorhamnetin-3,4'-*O*- β -*D*-diglucoside: $R_1=R_2=glucose$, $R_3=H$

isorhamnetin-3,7-*O*- β -*D*-diglucoside: $R_1=R_3=glucose$, $R_2=CH_3$

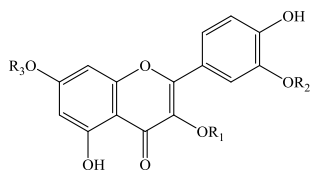
isorhamnetin-7-*O*- β -*D*-diglucoside: $R_3=diglucose$, $R_2=CH_3$, $R_1=H$

rhamnazin: $R_1=H$, $R_2=R_3=CH_3$

rhamnazin-3-*O*- β -*D*-glucoside: $R_1=glucose$, $R_2=R_3=CH_3$



8-*C*-*p*-hydroxybenzylquercetin



quercetin: $R_1=R_2=R_3=H$

quercetin-3-*O*-glucoside: $R_1=glucose$, $R_2=R_3=H$

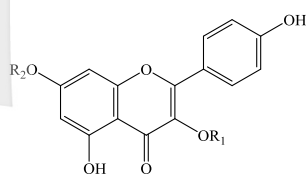
quercetin-3'-*O*-glucoside: $R_2=glucose$, $R_1=R_3=H$

quercetin-3-*O*-glucoside: $R_1=glucose$, $R_2=R_3=H$

quercetin-7-*O*- β -*D*-glucoside: $R_3=glucose$, $R_1=R_2=H$

quercetin-3-*O*- β -*D*-rutinoside: $R_1=rutinose$, $R_2=R_3=H$

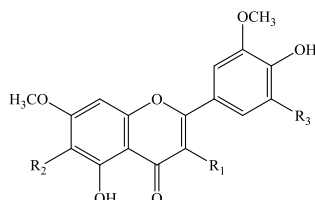
quercetin-7-*O*- β -[6"-*O*-(*trans*-feruloyl)]-glucopyranoside: $R_3=[6"-O-(trans-feruloyl)]-glucopyranose$, $R_1=R_3=H$



kaempferol-3-*O*- β -*D*-glucopyranoside: $R_1=glucopyranose$, $R_2=H$

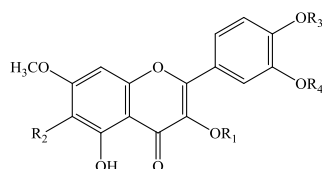
kaempferol-7-*O*- β -*D*-glucopyranoside: $R_3=glucopyranose$, $R_1=H$

kaempferol-3-*O*-(6"-*p*-coumaroyl)-glucopyranoside: $R_1=(6"-p-coumaroyl)-glucopyranose$, $R_2=H$



roxburosides: $R_2=R_3=H$, $R_1=O-(6"-p-coumaroyl)-glucopyranose$

5,6,3,4'-tetrahydroxy-7,5'-dimethoxyflavonol-3-*O*-glucoside: $R_1=H$, $R_2=OH$, $R_1=O-glucose$



3',4',7-trimethoxy-3,5-dihydroxyflavone: $R_1=R_2=H$, $R_3=R_4=CH_3$

5-hydroxy-3',4',7-trimethoxyflavonol-3-*O*- β -*D*-rutinoside: $R_2=H$, $R_3=R_4=CH_3$, $R_1=rutinose$

7-methoxy-3',4',5-trihydroxyflavonol-3-*O*- β -*D*-glucoside: $R_2=R_3=R_4=H$, $R_1=glucose$

5,4'-dihydroxy-6,7,3'-trimethoxyflavone: $R_1=R_2=R_3=R_4=H$

圖 2. 曾於金線連中發現的類黃酮化合物及其糖苷衍生物

Figure 2. Flavonoids and the derivatives that have been found in *Anoectochilus roxburghii*

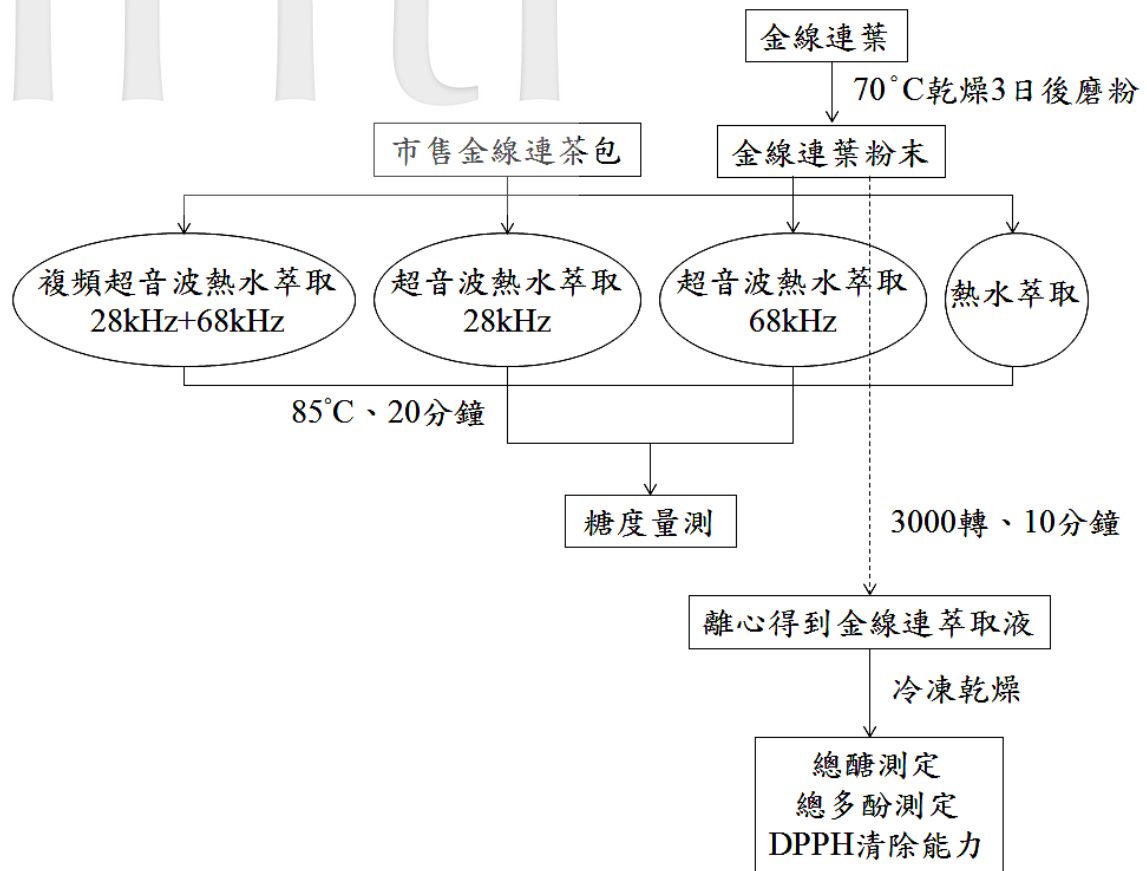


圖 3. 實驗流程圖

Figure 3. Experimental flowchart

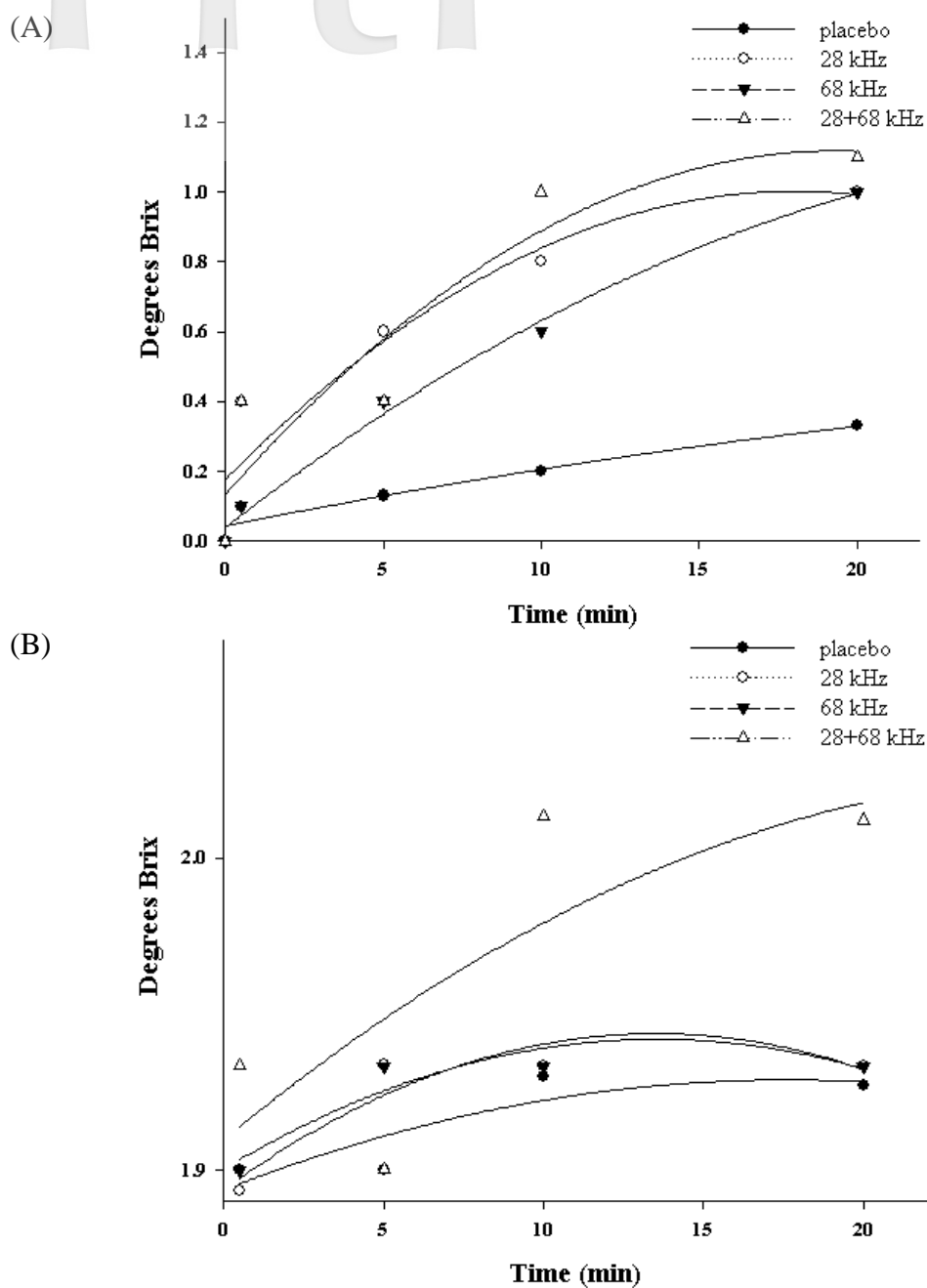


圖 4. 市售金線連茶包 (A) 草本破片型態及 (B) 粉末型態於熱水浸泡或經不同超音波輔助處理過程之糖度變化

Figure 4. Influences on degrees Brix ($^{\circ}\text{Bx}$) of commercial *Anoectochilus formosanus* Hayata. tea bags in (A) herbal fragments or (B) powder form treated with or without different ultra-sound conditions

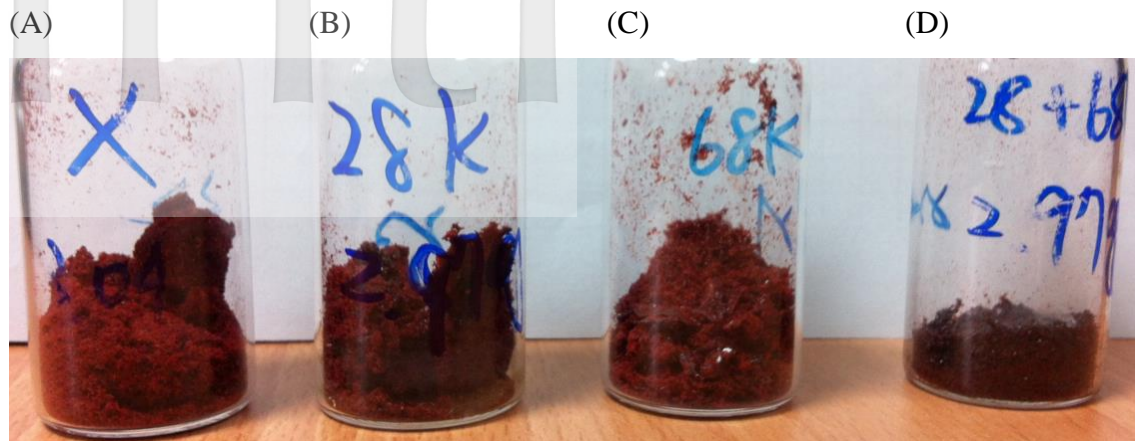


圖 5. (A) 未經超音波處理之金線連粉末水草物、(B) 28 kHz、(C) 68 kHz 及 (D) 28 kHz 與 68 kHz 複頻處理之金線連粉末水草物外觀

Figure 5. Appearance of (A) *Anoectochilus formosanus* Hayata. water extraxt and treated with (B) 28 kHz, (C) 68kHz, and (D) 28kHz + 68kHz multi-frequency ultrasound

表 1. 超音波條件對金線連萃取物重、萃取率、總糖、總多酚含量及 DPPH 自由基清除率之影響

Table 1. Influence on extract weight, yield, total sugar content, total polyphenol, and DPPH scavenging activities treated with different ultra-sound condition

Groups	Extract weight (g)	Yield (%)	Total sugar content (mg Glc/g sample)	Total polyphenol (mg GAE/g sample)	DPPH scavenging activity (%) at 50 mg/mL
placebo	0.143±0.011	28.7	178± 4 ^{ab}	53.2± 5.4 ^a	21.1±2.3 ^a
28kHz	0.153±0.028	30.7	164± 8 ^a	93.9± 6.4 ^c	16.6±2.3 ^a
68kHz	0.147±0.023	29.3	181± 3 ^b	71.7± 6.6 ^b	28.1±3.1 ^b
28+68kHz	0.167±0.005	33.3	182± 10 ^b	75.4± 6.4 ^b	26.6±2.7 ^b

數值表示為平均值正負標準偏差（三重複試驗）。各組間數值間統計分析比較結果以 p 小於 0.05 視為具有統計上的顯著差異，組間是否具有顯著差異如標註所示。

All data are expressed as means ± standard deviations (SD) (n = 3). Data in the same row with different letters are significantly different at $p < 0.05$.

含雙苯乙炔基之側鏈液晶聚環氧丙烷之合成與鑑定

吳麗娟¹ 陳振智² 林志鴻^{3*}Synthesis and Characterization of Liquid Crystalline Polyoxanes
Containing Tolane Mesogenic Side GroupsLi-Chuan Wu¹, Cheng-Chih Chen², Chih-Hung Lin^{3*}

摘要

合成一系列含有雙苯乙炔基並有不同長度的間隔基之環氧丙烷液晶單體，並以陽離子開環聚合的方式進行聚合，得到四個含雙苯乙炔基聚環氧丙烷之側鏈液晶聚合物。所有的液晶單體及聚合物均使用核磁共振光譜儀、微差掃描卡計及偏光顯微鏡偏光測得其化學結構、熱性質及液晶相之研究。

關鍵詞：側鏈液晶、聚環氧丙烷、雙苯乙炔

ABSTRACT

A series of oxetane liquid crystal monomers containing tolane mesogenic groups having spacers of different lengths were synthesized and polymerized by cationic ring-opening polymerization to obtain four side-chain liquid crystals polyoxanes containing tolane mesogenic side groups. The chemical structure, thermal properties and liquid crystalline phase of the liquid crystal monomers and polymers were measured by NMR spectroscopy, differential scanning calorimeter and polarized light microscopy.

Keywords: side chain liquid crystal, polyoxetanes, tolane

壹、前言

自從 1987 年德國的 Finkelmann 和 Ringsdorf 等人 [1-4] 首先合成出側鏈液晶高分子後，側鏈液晶高分子已被廣泛的開發與應用，然而，

被研究的高分子聚合物骨架並不多，大部份的高分子主幹乃以 polysiloxane、polymethacrylate 和 polyacrylate 為主，而液晶聚合物之高分子主幹對其所顯現之液晶相有很大影響。為了尋求感應較快的側鏈型液晶高分子，高分子骨架應

¹ 輔英科技大學應用化學及材料科學系講師

² 長庚科技大學化妝品應用系助理教授

³ 長庚科技大學通識教育中心教授、民生學院中草藥研究中心成員

使用較柔軟者，以往均以 polysiloxane 為主。polysiloxane 液晶聚合物之聚合方法大多以矽氧化 (hydrosilation) 和自由基聚合反應為主，所合成的液晶聚合物分子量不確定，分子量分佈都很廣，因此所呈現的液晶性質也較不確定，這對液晶聚合物之真正應用有很大的影響 [5-6]。

1991 年，Yusuke Kawakami, Koji Takahashi 和 Hiroshi Hibino 等人提出以 3-(hydroxymethyl)-3-methyloxetane 為骨幹的單體 [7-9]，單體具有 biphenyl 的液晶團基以及包含三種不同的末端取代基、烷氧基、氰基、氟基，這些液晶團基所形成的環氧丙烷衍生物進行陽離子開環聚合後，共有氰基及氟基的高分子聚合物，在間距為 4 個碳時可形成層列型 (smectic) 液晶相，但是烷氧基的液晶相都不確定，而此結果與側鏈具相同液晶基的聚丙烯酸酯或聚丁烯酸酯其間距為 6 個碳的結果相同，可表示骨架的柔軟性優於 polyacrylate 和 polymethacrylate。

由於環氧丙烷聚合所形成之高分子主鏈具有不錯的柔軟性 [10~12]，本研究將以環氧丙烷為其高分子主幹，以 tolane 液晶團，試圖合成出含有不同長度的間距及末端烷基之一系列聚環氧丙烷液晶。

貳、儀器及材料

一、試藥

實驗中所使用之藥品均分別採購自 Aldrich、Merck、Acros、Lancaster、TCI、昭和及聯工公司等，不經純化直接使用。所有溶劑係購自六和或景明公司。無水四氫呋喃 (tetrahydrofuran, THF) 以鈉金屬乾燥，並加入 benzophenone 為指示劑，在氮氣條件下迴流一日後蒸餾出使用。無水二氯甲烷 (dichloromethane) 則以氫化鈣進行乾燥，在氮氣條件下迴流一日後蒸餾出使用。

二、儀器

為了鑑定及測試所合成化合物之化學結構及物理特性，採用下列測試儀器：

(一) 核磁共振光譜儀 (Nuclear Magnetic Resonance, NMR)

使用 Varian-300 MHz 核磁共振儀。其中以 d-chloroform 為溶劑，氫譜以 tetramethylsilane 作為 $\delta = 0.00$ ppm 為內部基準，化學位移單位為 ppm。光譜資料中：符號 s 表示單峰 (singlet)，d 表示二重峰 (doublet)，t 表示三重峰 (triplet)，q 表示四重峰 (quartet)，m 表示多重峰 (multiplet)。

(二) 偏光顯微鏡 (Polarizing Optical Microscope, POM)

使用 Zeiss Axiophot 型光學顯微鏡。放大倍率為 200 倍，配備照相系統，並使用 Mettler FP82 型控溫器及 FP90 型控溫系統。在使用上必須配合熱工作臺使用，其原理為將樣品置於上下垂直的偏光板中，當樣品具有雙折射性 (如固相及液晶相) 性質，其能將入射光之光軸偏折，而顯示出特殊紋理圖。再加上在此溫度的樣品如果具有流動性，則此樣品可能就具有液晶性質；可利用 POM 中所得的紋理圖來判別何種形式的液晶。

(三) 色層分析 (Chromatography)

薄膜色層分析 (thin layer chromatography, TLC) 係使用 Merck 5735 DC Silica gel 60 F-254 型塑膠薄片。管柱色層分析 (column chromatography) 係使用 Merck 7734 Kiesel gel 60 (70~230 mesh) 型矽膠，溶劑以重力方式沖提，分瓶收集，再用 TLC 片，以紫外光 (UVGL-25 型) 顯色。

(四) 微差掃描卡計 (Differential Scanning Calorimeter, DSC)

使用 SEIKO SSC 6000 DSC 及 Computer/

Thermal Analyzer，溫度以鉬與錫作校正。另外使用 liquid nitrogen cooling accessory 冷卻系統提供低溫環境。實驗時秤取樣品 2~5 mg，加熱及冷卻掃描速率視化合物性質而有所不同分別，其原理乃紀錄樣品發生相變化時所產生之吸熱或放熱的溫度及熱焓之變化。熱向性液晶其液晶相是介於固、液相間，所以不論是吸熱或放熱過程中，在 DSC 圖譜中會有至少兩根訊號出現，這表示固相 - 液相間的轉換；可以由 DSC 圖譜中得知液晶相的範圍及其熱焓的變化。

(五) 凝膠滲透層析儀 (Gel Permeation Chromatography, GPC)

使用 Applied Biosystems 的 400 Solvent Delivery System；偵測器為 UV 和 Differential Refractometer；管柱係 American Polymer Standards Corporation 所生產 ultrastylene gel；試樣濃度取 5.0 mg/mL，以聚苯乙烯 (polystyrene) 當基準，沖提溶劑為四氫呋喃 (THF)，流速為 1.0 mL/min。

參、討論

一、化合方法及鑑定

合成含雙苯乙炔基的單體及聚合物之合成步驟如合成流程圖 (圖一、圖二) 所示，所有化合物的純度及結構鑑定均以色層分析、核磁共振光譜儀及微差掃描卡計等儀器測定。聚合物則以再沉澱方法純化 [13]。

1. 3-[(3-Bromopropoxy)methyl]-3-methyloxetane

(1a)

3-[(4-Bromobutoxy)methyl]-3-methyloxetane

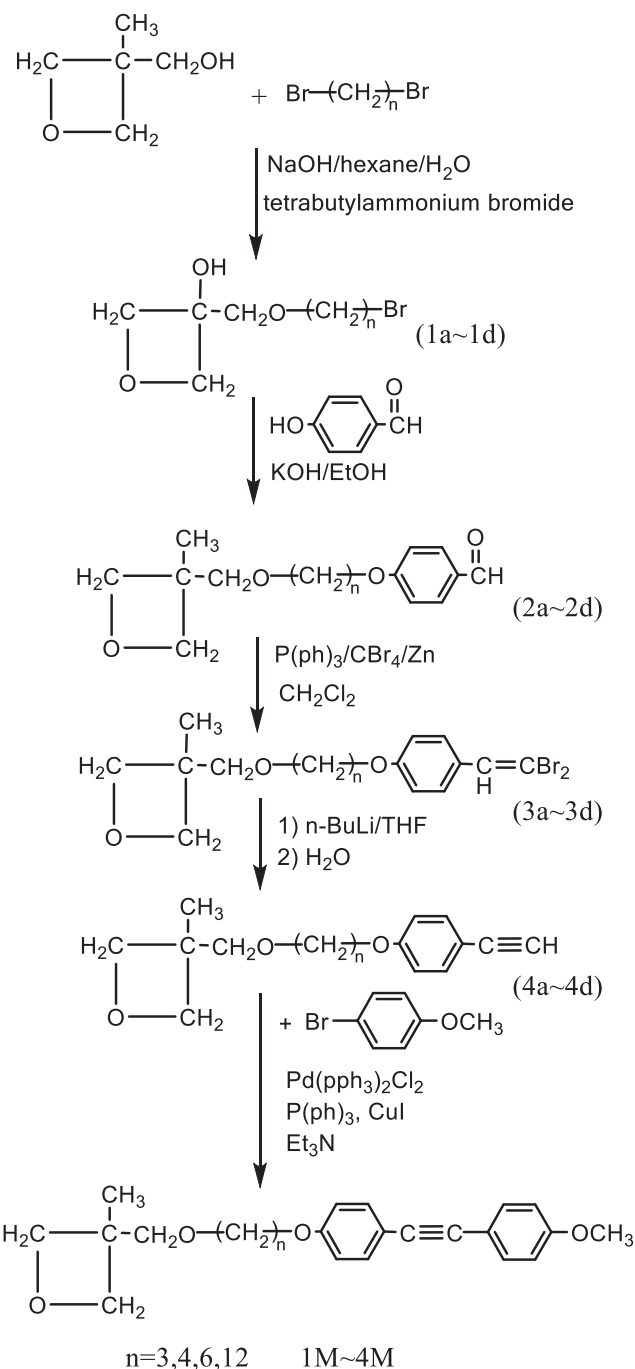
(1b)

3-[(6-Bromohexoxy)methyl]-3-methyloxetane

(1c)

3-[(12-Bromododecoxy)methyl]-3-methyloxetane (1d)

以化合物 (1c) 的合成為例；此步驟為兩相催化反應，先將氫氧化鈉 64.7 克 (1.618 莫耳) 和水 150 毫升，加入 500 毫升圓底瓶後攪拌，待其溶液放熱後，冷卻到室溫，繼續加入正己烷 120 毫升及各 3-(hydroxymethyl)-3-methyl



圖一：單體 1M~4M 合成流程圖

oxetane 10 克 (0.098 莫耳), dibromohexane 73.2 克 (0.299 莫耳), 最後加入介界活性劑 TBAB (tetrabutylammonium bromide) 1 克 (取反應物 oxetane 十分之一量), 在室溫下快速攪拌 12 小時, 然後加熱迴流半小時, 等溶液溫度回到室溫後, 以 300 毫升的正己烷, 分三次萃取, 有機層再用水洗一次, 然後用無水硫酸鎂乾燥、過濾、濃縮, 所得產物以減壓蒸餾純化, 得透明無色液體。

化合物 (1a~1d) 的產率及 $^1\text{H-NMR}$ 結果如下:

(1a): 產率 62.5%; $^1\text{H-NMR}$ (CDCl_3 , TMS, δ , ppm):

1.25(s, 3H, $-\text{CH}_3$ on the oxetane ring), 2.06(t, 2H, $-\text{OCH}_2\text{CH}_2\text{CH}_2-$), 3.44-3.57(m, 6H, $-\text{CH}_2\text{OCH}_2\text{CH}_2\text{CH}_2\text{Br}$), 4.29, 4.45(AB quartet, each 2H, $-\text{CH}_2-\text{O}$ on the oxetane ring).

(1b): 產率 81.7%; $^1\text{H-NMR}$ (CDCl_3 , TMS, δ , ppm):

1.26(s, 3H, $-\text{CH}_3$ on the oxetane ring), 1.69, 1.89(d, each 2H, $-\text{OCH}_2(\text{CH}_2)_2\text{CH}_2\text{Br}$), 3.37-3.47(m, 6H, $-\text{CH}_2\text{OCH}_2(\text{CH}_2)_2\text{CH}_2\text{Br}$), 4.29, 4.44(AB quartet, each 2H, $-\text{CH}_2-\text{O}$ on the oxetane ring).

(1c): 產率 80.3%; $^1\text{H-NMR}$ (CDCl_3 , TMS, δ , ppm):

1.30(s, 3H, $-\text{CH}_3$ on the oxetane ring), 1.46-1.90(m, 8H, $-\text{OCH}_2(\text{CH}_2)_4\text{CH}_2-$), 3.39-3.48(m, 6H, $-\text{CH}_2\text{OCH}_2(\text{CH}_2)_4\text{CH}_2\text{Br}$), 4.34, 4.51(AB quartet, each 2H, $-\text{CH}_2-\text{O}$ on the oxetane ring).

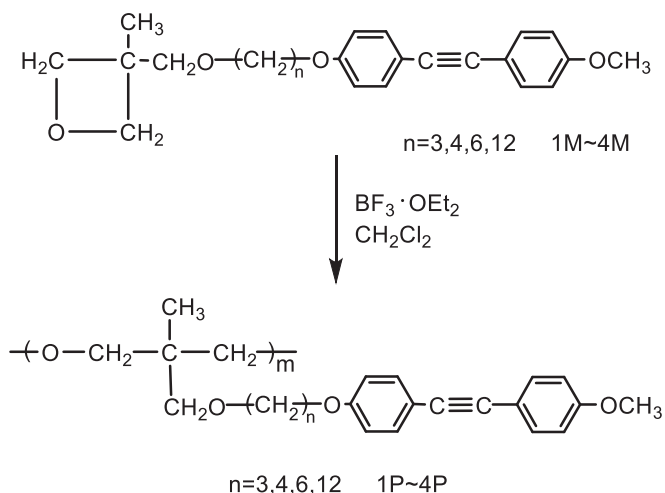
(1d): 產率 77.2%; $^1\text{H-NMR}$ (CDCl_3 , TMS, δ , ppm):

1.27(s, 3H, $-\text{CH}_3$ on the oxetane ring), 1.28-1.46(m, 16H, $-\text{OCH}_2(\text{CH}_2)_8\text{CH}_2-$), 1.51, 1.81(t, each 2H, $-\text{OCH}_2\text{CH}_2(\text{CH}_2)_8\text{CH}_2\text{CH}_2\text{Br}$), 3.40-3.47(m, 6H, $-\text{CH}_2\text{OCH}_2(\text{CH}_2)_{10}\text{CH}_2\text{Br}$), 4.34, 4.49(AB quartet, each 2H, $-\text{CH}_2-\text{O}$ on the oxetane ring).

2. 3-[[3-(4-Hydroxybenzaldehyde)propoxy]methyl]-3-methyl oxetane (2a)
- 3-[[4-(4-Hydroxybenzaldehyde)butoxy]methyl]-3-methyl oxetane (2b)
- 3-[[6-(4-Hydroxybenzaldehyde)hexoxy]methyl]-3-methyl oxetane (2c)
- 3-[[12-(4-Hydroxybenzaldehyde)dodecoxy]methyl]-3-methyl oxetane (2d)

以化合物 (2c) 的合成為例: 將 4-羥基苯甲醛 (4-hydroxy-benzaldehyde) 4.45 克 (0.036 莫耳), 氫氧化鉀 2.04 克 (0.036 莫耳) 和碘化鉀 0.2 克, 溶於 100 毫升之乙醇 (95%) 中, 加熱迴流 1 小時後, 再慢慢滴入化合物 (1d) 8 克 (0.030 莫耳), 加熱迴流 12 小時, 冷卻、過濾、濃縮後, 再以醋酸乙酯及水做萃取, 萃取液以 10% 的氫氧化鉀水溶液 50 毫升洗三次, 然後以無水硫酸鎂乾燥、濃縮後, 以矽膠作快速色層分析 (醋酸乙酯 / 正己烷) 純化, 得淡黃色液體。

化合物 (2a~2d) 的產率及 $^1\text{H-NMR}$ 結果如下:



圖二: 聚合物 1P~4P 合成流程圖

(2a): 產率 77.8% ; $^1\text{H-NMR}$ (CDCl_3 , TMS, δ , ppm):

1.27(s, 3H, $-\text{CH}_3$ on the oxetane ring), 2.06(t, 2H, $-\text{OCH}_2\text{CH}_2\text{CH}_2-$), 3.48(m, 4H, $-\text{CH}_2\text{O}-$), 4.01(t, 2H, $-\text{CH}_2-\text{OPh}$), 4.31, 4.48(AB quartet, each 2H, $-\text{CH}_2-\text{O}$ on the oxetane ring), 6.97, 7.81(d, each 2H, aromatic protons), 9.88(s, 1H, aldehyde protons).

(2b): 產率 80.1% ; $^1\text{H-NMR}$ (CDCl_3 , TMS, δ , ppm):

1.31(s, 3H, $-\text{CH}_3$ on the oxetane ring), 1.76-2.04(m, 4H, $-\text{OCH}_2(\text{CH}_2)_2\text{CH}_2-$), 3.49-3.57(m, 4H, $-\text{CH}_2\text{OCH}_2(\text{CH}_2)_2-$), 4.06(t, 2H, $-\text{CH}_2\text{CH}_2-\text{Oph}$), 4.35, 4.51 (AB quartet, each 2H, CH_2 of the oxetane ring), 6.99, 7.92 (d, each 2H, aromatic protons), 9.89(s, 1H, aldehyde protons).

(2c): 產率 82.5% ; $^1\text{H-NMR}$ (CDCl_3 , TMS, δ , ppm):

1.30(s, 3H, $-\text{CH}_3$ on the oxetane ring), 1.40-1.82(m, 8H, $-\text{OCH}_2(\text{CH}_2)_4\text{CH}_2-$), 3.46(m, 4H, $-\text{CH}_2\text{O}-$), 4.04(t, 2H, $-\text{CH}_2-\text{Oph}$), 4.33, 4.49(AB quartet, each 2H, $-\text{CH}_2-\text{O}$ on the oxetane ring), 6.96, 7.81(d, each 2H, aromatic protons), 9.87(s, 1H, aldehyde protons).

(2d): 產率 79.6% ; $^1\text{H-NMR}$ (CDCl_3 , TMS, δ , ppm):

1.30(s, 3H, $-\text{CH}_3$ on the oxetane ring), 1.29-1.80(m, 20H, $-\text{OCH}_2(\text{CH}_2)_{10}\text{CH}_2-$), 3.42(m, 4H, $-\text{CH}_2\text{O}-$), 4.01(t, 2H, $-\text{CH}_2-\text{Oph}$), 4.34, 4.98(AB quartet, each 2H, $-\text{CH}_2-\text{O}$ on the oxetane ring), 6.96, 7.80(d, each 2H, aromatic protons), 9.87(s, 1H, aldehyde protons).

3. 3-[[3-(4-2,2-Dibromovinyl)phenoxy]propoxy]methyl-3-methyl oxetane (3a)

3-[[4-(4-2,2-Dibromovinyl)phenoxy]butoxy]methyl-3-methyl oxetane (3b)

3-[[6-(4-2,2-Dibromovinyl)phenoxy]hexoxy]methyl-3-methyl oxetane (3c)

3-[[12-(4-2,2-Dibromovinyl)phenoxy]dodecoxy]methyl-3-methyl oxetane (3d)

以化合物 (3c) 的合成爲例；在室溫下，將四溴化碳 14.3 克 (0.043 莫耳)，鋅粉 2.8 克 (0.043 莫耳) 及無水二氯甲烷 150 毫升，加入 250 毫升圓底瓶中，在氮氣下，逐次加入 Triphenyl phosphine 11.3 克 (0.043 莫耳)，在室溫下攪拌 48 小時，再加入化合物 (2c) 6 克 (0.019 莫耳)，繼續反應 12 小時，形成深棕色之溶液，過濾，以醋酸乙酯和正己烷萃取產物，將殘餘物以二氯甲烷溶解，再以醋酸乙酯和正己烷萃取，過濾，重覆三~四次，將所得濾液濃縮後，以矽膠做快速色層分析 (醋酸乙酯 / 正己烷) 來純化產物。

化合物 (3a~3d) 的產率及 $^1\text{H-NMR}$ 結果如下：

(3a): 產率 34.1% ; $^1\text{H-NMR}$ (CDCl_3 , TMS, δ , ppm):

1.27 (s, 3H, CH_3 on the oxetane ring), 2.06 (t, 2H, $-\text{CH}_2\text{CH}_2-\text{Oph}$), 3.47 (s, 2H, $-\text{CH}_2\text{OCH}_2\text{CH}_2-$), 3.62 (t, 2H, $-\text{CH}_2\text{OCH}_2\text{CH}_2-$), 4.12 (t, 2H, $-\text{CH}_2\text{CH}_2-\text{Oph}$), 4.13, 4.47 (AB quartet, each 2H, CH_2 of the oxetane ring), 6.96, 7.79 (d, each 2H, aromatic protons), 7.38 (s, 1H, ph-CH=CHBr_2).

(3b): 產率 40.8% ; $^1\text{H-NMR}$ (CDCl_3 , TMS, δ , ppm):

1.34 (s, 3H, CH_3 on the oxetane ring), 1.77~1.93 (m, 4H, $-\text{OCH}_2(\text{CH}_2)_2\text{CH}_2-\text{Oph}$), 3.51 (m, 4H, $-\text{CH}_2\text{OCH}_2\text{CH}_2-$), 4.00(t, 2H,

-CH₂CH₂-Oph), 4.37, 4.53 (AB quartet, each 2H, CH² of the oxetane ring), 6.84, 7.43 (d, each 2H, aromatic protons), 7.38 (s, 1H, ph-CH=CB₂).

(3c): 產率 44.7% ; ¹H-NMR (CDCl₃, TMS, δ, ppm):

1.29 (s, 3H, CH₃ on the oxetane ring), 1.43~1.80(m, 8H, -OCH₂(CH₂)₄CH₂-Oph), 3.43 (m, 4H, -CH₂OCH₂CH₂-), 3.93(t, 2H, -CH₂CH₂-Oph), 4.33, 4.49 (AB quartet, each 2H, CH₂ of the oxetane ring), 6.84, 7.39 (d, each 2H, aromatic protons), 7.39 (s, 1H, ph-CH=CB₂).

(3d): 產率 37.6% ; ¹H-NMR (CDCl₃, TMS, δ, ppm):

1.16~1.77 (m, 23H, CH₃ on the oxetane ring, -OCH₂(CH₂)₁₀CH₂-Oph), 3.37 (m, 4H, -CH₂OCH₂CH₂-), 3.93(t, 2H, -CH₂CH₂-Oph), 4.33, 4.49 (AB quartet, each 2H, CH₂ of the oxetane ring), 6.85, 7.47 (d, each 2H, aromatic protons), 7.39 (s, 1H, ph-CH=CB₂).

4. 3-[[3-(4-ethynylphenoxy)propoxy]methyl]-3-methyl oxetane (4a)

3-[[4-(4-ethynylphenoxy)butoxy]methyl]-3-methyl oxetane (4b)

3-[[6-(4-ethynylphenoxy)hexoxy]methyl]-3-methyl oxetane (4c)

3-[[12-(4-ethynylphenoxy)dodecoxy]methyl]-3-methyl oxetane (4d)

以化合物 (4c) 的合成為例：將化合物 (3c) 4 克 (0.008 莫耳) 溶於無水四氫呋喃 (THF) 中，在氮氣下，冷卻到 -78°C，於此溫度下慢慢 11.14 毫升 (16M in 15% hexane) 的 n-BuLi 滴入，反應 1 小時後，將溫度回到室溫，繼續反應 1

小時後，加入過量的水，以二氯甲烷萃取產物，所得萃取液經濃縮後，以矽膠作快速色層分析 (醋酸乙酯 / 正己烷)，得白色固體。

化合物 (4a~4d) 的產率及 ¹H-NMR 結果如下：

(4a): 產率 80.6% ; ¹H-NMR (CDCl₃, TMS, δ, ppm):

1.27 (s, 3H, CH₃ on the oxetane ring), 2.06 (t, 2H, -CH₂CH₂-Oph), 2.98 (s, 1H, -ph-C ≡ CH), 3.47 (s, 2H, -CH₂OCH₂CH₂-), 3.62 (t, 2H, -CH₂OCH₂CH₂-), 4.12 (t, 2H, -CH₂CH₂-Oph), 4.13, 4.47 (AB quartet, each 2H, CH₂ of the oxetane ring), 6.96, 7.79 (d, each 2H, aromatic protons).

(4b): 產率 72.6% ; ¹H-NMR (CDCl₃, TMS, δ, ppm):

1.34 (s, 3H, CH₃ on the oxetane ring), 1.77~1.93 (m, 4H, -OCH₂(CH₂)₂CH₂-Oph), 3.02 (s, 1H, -ph-C ≡ CH), 3.51 (m, 4H, -CH₂OCH₂CH₂-), 4.02(t, 2H, -CH₂CH₂-Oph), 4.37, 4.53 (AB quartet, each 2H, CH₂ of the oxetane ring), 6.84, 7.43 (d, each 2H, aromatic protons).

(4c): 產率 77.6% ; ¹H-NMR (CDCl₃, TMS, δ, ppm):

1.29 (s, 3H, CH₃ on the oxetane ring), 1.43~1.80(m, 8H, -OCH₂(CH₂)₄CH₂-Oph), 2.98 (s, 1H, -ph-C ≡ CH), 3.39 (m, 4H, -CH₂OCH₂CH₂-), 3.92(t, 2H, -CH₂CH₂-Oph), 4.33, 4.48 (AB quartet, each 2H, CH₂ of the oxetane ring), 6.79, 7.39 (d, each 2H, aromatic protons).

(4d): 產率 37.6% ; ¹H-NMR (CDCl₃, TMS, δ, ppm):

1.16~1.77 (m, 23H, CH₃ on the oxetane ring, -OCH₂(CH₂)₁₀CH₂-Oph), 2.97 (s, 1H, -ph-C ≡ CH), 3.36 (m, 4H,

-CH₂OCH₂CH₂-), 3.91(t, 2H, -CH₂CH₂-Oph), 4.33, 4.48 (AB quartet, each 2H, CH₂ of the oxetane ring), 6.80, 7.38 (d, each 2H, aromatic protons).

5. 3-[3-(4'-methoxytolan-4-yloxy)propoxy methyl]-3-methyl oxetane (1M)

3-[4-(4'-methoxytolan-4-yloxy)butoxy methyl]-3-methyl oxetane (2M)

3-[6-(4'-methoxytolan-4-yloxy)hexoxy methyl]-3-methyl oxetane (3M)

3-[12-(4'-methoxytolan-4-yloxy)dodecoxy methyl]-3-methyl oxetane (4M)

以化合物 3M 的合成爲例：在氮氣下，將 60 毫克的 copper (I) iodide、60 毫克的 bis (triphenylphosphine) palladium (II)、120 毫克的 triphenyl phosphine 及 50 毫升的 triethyl amine 放入 100 毫升的圓底瓶中，繼續加入 4-bromoanisole 1.93 克 (0.010 莫耳)，反應加熱 1 小時後，最後加入化合物 (4c) 2 克 (0.006 莫耳)，加熱迴流 12 小時後，回復室溫，加入少許飽和氯化銨溶液攪拌半小時，此時水層呈寶藍色，再用二氯甲烷萃取，有機層用稀鹽酸溶液洗二次，最後以無水硫酸鎂乾燥、過濾、濃縮，產物以矽膠作快速色層分析 (醋酸乙酯 / 正己烷)，得淺黃色固體。

單體 (1M~4M) 的產率及 ¹H-NMR 結果如下：

1M: 產率 11.7% ; ¹H-NMR (CDCl₃, TMS, δ, ppm):

1.27 (s, 3H, CH₃ on the oxetane ring), 2.05 (t, 2H, -CH₂CH₂-Oph), 3.47 (s, 2H, -CH₂OCH₂CH₂-), 3.63 (t, 2H, -CH₂OCH₂CH₂-), 3.79(s, 3H, -phOCH₃), 4.06 (t, 2H, -CH₂CH₂-Oph), 4.31, 4.47 (AB quartet, each 2H, CH₂ of the oxetane ring), 6.82, 7.39 (each m, each 4H, aromatic

protons).

2M: 產率 13.6% ; ¹H-NMR (CDCl₃, TMS, δ, ppm):

1.22 (s, 3H, CH₃ on the oxetane ring), 1.65~1.78 (m, 4H, -OCH₂(CH₂)₂CH₂-Oph), 3.38 (m, 4H, -CH₂OCH₂CH₂-), 3.73(s, 3H, -phOCH₃), 4.02(t, 2H, -CH₂CH₂-Oph), 4.25, 4.41 (AB quartet, each 2H, CH₂ of the oxetane ring), 6.73, 7.31 (each m, each 4H, aromatic protons).

3M: 產率 14.2% ; ¹H-NMR (CDCl₃, TMS, δ, ppm):

1.30 (s, 3H, CH₃ on the oxetane ring), 1.43~1.80(m, 8H, -OCH₂(CH₂)₄CH₂-Oph), 3.46 (m, 4H, -CH₂OCH₂CH₂-), 3.81(s, 3H, -phOCH₃), 3.95(t, 2H, -CH₂CH₂-Oph), 4.34, 4.50 (AB quartet, each 2H, CH₂ of the oxetane ring), 6.84, 7.42 (each m, each 4H, aromatic protons).

4M: 產率 16.8% ; ¹H-NMR (CDCl₃, TMS, δ, ppm):

0.91~1.80(m, 23H, CH₃ on the oxetane ring, -OCH₂(CH₂)₁₀CH₂-Oph), 3.37 (m, 4H, -CH₂OCH₂CH₂-), 3.82(s, 3H, -phOCH₃), 3.96(t, 2H, -CH₂CH₂-Oph), 4.34, 4.49 (AB quartet, each 2H, CH₂ of the oxetane ring), 6.83, 7.41 (each m, each 4H, aromatic protons).

6. 開環聚合反應

側鏈液晶聚環氧丙烷合成步驟如合成流程圖 (圖二) 所示，所有開環聚合反應均以 BF₃•OEt₂ 爲起始劑，取 0.5 毫莫耳的單體，在冰浴下，以無水二氯甲烷 5~10 毫升溶解，再取稀釋 10 倍量的起始劑 12.6 微升，以細長針頭打入，冰浴及氮氣下反應 24 小時；所得的

聚合物以乙醇及水做再沉澱純化。

成功合成含雙苯乙炔的四個單體及四個聚合物，在單體的合成過程中，產率都偏低，尤其在合成單體的最後一個步驟所得產率最低，而所得副產物雙苯雙乙炔的產率特別高 [14]。所得單體經核磁共振，質譜分析光譜而證實其結構及純度。聚合物則以再沉澱方法純化，使用凝膠滲透層析儀 (GPC) 測其分子量，所有聚合物之聚合度並不高，分子量在 1100 左右，可見本系列開環聚合反應較不合適使用 $\text{BF}_3 \cdot \text{OEt}_2$ 作為起始劑。

二、液晶相與熱性質的探討

所合成的單體及聚合物皆使用微差掃描卡計 (DSC) 及偏光顯微鏡 (POM) 測量其熱力學性質及判斷其液晶相種類。所合成的四個單體 1M~4M 由微差掃描卡計測得的相轉移溫度與熱焓值，詳列於表 1。由表 1 可發現此系列單體都有 supercooling 現象，從偏光顯微鏡下觀察證實都只出現一般的結晶相。

將所合成的環氧丙烷單體以 $\text{BF}_3 \cdot \text{OEt}_2$ 為起

始劑進行陽離子開環聚合反應而合成出四個側鏈液晶聚合物 1P~4P，由微差掃描卡計測得的相轉移溫度與熱焓值，詳列於表 2。1P 及 2P 具有較短間距 ($n = 3, 4$) 的側鏈液晶聚合物，都呈現很明顯的玻璃轉移溫度，以聚合物 1P 的 DSC 圖來看，除了非常明顯的玻璃移溫度外，在 74.3°C 只有一微小的轉移溫度波峰，在偏光顯微鏡下觀察，此溫度並無明顯的相變化，而在 DSC 冷卻掃描圖中發現其轉移溫度出現於 43.2°C ，聚合物 2P 的 DSC 圖與聚合物 1P 類似，都只出現一 T_g 點和一相轉移波峰，此二聚合物在偏光顯微鏡下都未呈現可以辨識的液晶紋理；至於具有較長間距 ($n = 6, 12$) 的側鏈液晶聚合物 3P 及 4P，均未發現玻璃轉移溫度，主要由於間距太長而較易形成規則性結晶相，致使其玻璃轉移溫度不明顯，在偏光顯微鏡下聚合物 3P 則呈現類似層列 A 相 (S_A) 之液晶紋理，如圖三所示，聚合物 4P 呈現很明顯的結晶相。由上述結果推測，此系列聚合物，其含雙苯基乙炔液晶基構造太剛硬，因此大部份聚合物只呈現結晶相。所有聚合物經 GPC 測其分子量，其聚合度並不高，這可能也是其未能呈現液晶相

表 1：單體 1M~4M 之熱轉移溫度和熱焓值

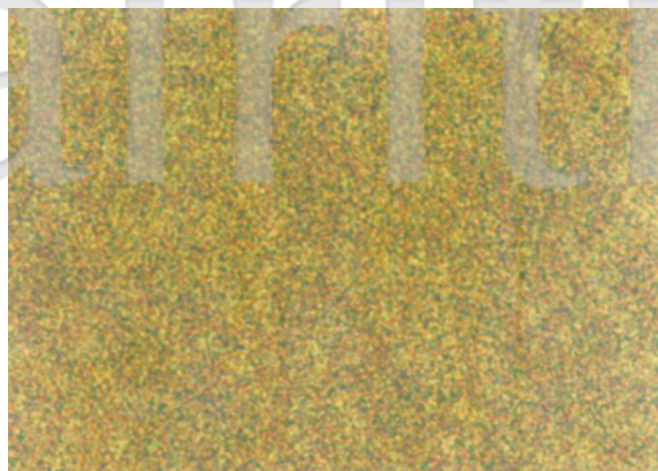
Compound	Phase transitions, $^\circ\text{C}$ (corresponding enthalpy changes, Kcal/mol)	
	$\frac{\text{heating}}{\text{cooling}}$	
1M	$K_1 -17.7(1.21) K_2 1.7(0.77) K_3 64.4(2.80) I$ $I 45.8(0.18) K$	
2M	$K 14.9(0.51) I$ $I - 30.1(1.49) K$	
3M	$K_1 23.0(3.05) K_2 69.5(8.27) I$ $I 20.9(2.07) K$	
4M	$K 55.2(6.07) I$ $I 33(5.34) K_2 19.1(0.09) K_1$	

I = isotropic, K = crystal
determined by optical polarizing microscopic observation.

表 2：聚合物 1P~4P 之熱轉移溫度和熱焓值

Compound	Phase transitions, $^\circ\text{C}$ (corresponding enthalpy changes, Kcal/mol)	
	$\frac{\text{heating}}{\text{cooling}}$	
1P	$K 74.3(0.026) I$ $I 43.2(-0.288) K$	
2P	$K 92.3(0.036) I$ $I 25.0(-0.427) K$	
3P	$K 66.4(-)^a S_A 72.9(2.41) I$ $I 58.9(-1.34) S_A 52.6(-)^a K$	
4P	$K 65.0(12.5) I$ $I 45.8(-12.1) K$	

S_A = smectic A, I = isotropic, K = crystal
determined by optical polarizing microscopic observation.

圖三：聚合物 3P 之 S_A 液晶紋理圖

之原因，可見本系列開環聚合反應較不合適使用 $\text{BF}_3 \cdot \text{OEt}_2$ 作為起始劑；未來將選擇其它起始劑，以期能有效的進行此系列化合物之開環聚合反應，仔細的控制其分子量，才能對聚合物結構與性質間做更詳細的探討。

肆、結語

本研究成功地合成出四個含雙苯乙炔液晶基之單體及四個側鏈液晶聚環氧丙烷聚合物，研究中發現柔軟間距的長短會影響其液晶的行為。間距較短者有明顯的玻璃轉移溫度，均向性溫度均較低，可能是液晶團基雙苯乙炔本身具低黏度特性的關係，本系列聚合物採以 $\text{BF}_3 \cdot \text{OEt}_2$ 作為開環聚合反應之起始劑，得到的聚合物之聚合度不高，而影響聚合物液晶性質，只有 3P 出現 S_A 的液晶相，其餘均出現結晶。

伍、致謝

本研究報告是由長庚科學大學在經費資助，計畫案號為 EZRPF3I0051。

參考文獻

- [1] H. Finkelmann, H. Ringsdorf, H. Windorf, (1987). *Makromol. Chem.*, 179, 273.
- [2] H. Finkelmann, M. Happ, M. Portugal, H. Ringsdorf, (1987). *Makromol. Chem.*, 179, 2541.
- [3] H. Finkelmann, G. Rehage, (1984). *Adv. Polym. Sci.*, 60/61, 99.
- [4] L. L. Chapoy, "Recent Advances in Liquid Crystal Polymers", (1985). Elsevier Applied Sci. London and N. Y.
- [5] H. J. Coles, R. Simon, (1986). *Polymer*, 27, 811.
- [6] G. Kaempf, (1987). *Polym. J.*, 19, 257.
- [7] Y. Kawakami, K. Takahashi, (1991). *Polymer Bulletin*, 25, 439.
- [8] Y. Kawakami, K. Takahashi, H. Hibino, (1991). *Macromol.*, 24, 4531.
- [9] Y. Kawakami, K. Takahashi, S. Nishiguchi, K. Toida, (1993). *Polym. Int*, 31, 35.
- [10] Y. H. Lu, C. S. Hsu, (1995). *Macromol.*, 28, 1673.
- [11] H. Boucekif, M. Philbin, E. Colclough, A. J. Amass. (2010). *Macromol.*, 43, 845.
- [12] J. Lee, D. K. Oh, C. V. Yelamaggad, S. A. Nagamani, J. Jin, (2002). *J. Mater. Chem.*, 12, 2225.
- [13] C. H. Lin, (2015), *Asian J. Chem.*, 27, 1495.
- [14] D. R. Robello, (1990). *J. Polym. Sci., Part A: Polym. Chem.*, 28, 1101.

功能性靜電紡絲纖維薄膜應用於羅漢果皂苷甜味劑之轉化

王如邦¹ 邱群惠^{2*}

Development of Functionalized Electrospun Nanofiber Mat for Sweetener Production from Mogrosides

Reuben Wang¹, Chun-Hui Chiu^{2*}

摘要

零卡甜味劑為目前全球最大使用量之食品添加物。然而隨健康意識抬頭與對人工甜味劑負面的研究結果，使得近年市場成長速度最快的零卡天然甜味劑需求大增，其中來自植物萃取的羅漢果皂苷成長最為顯著。羅漢果皂苷除了為目前天然甜味劑中甜度最高的甜味劑之外，部分具甜味的皂苷單體也具顯著抗糖尿病活性，展現高度市場潛力；然其皂苷萃取物內風味最接近蔗糖且甜度最高之羅漢果皂苷 Saimenoside I (S I) 單體在羅漢果中含量稀少，是目前全球專利與生物科技研究努力增加含量的目標。另外，皂苷萃取物之醣基修飾有助於苦味及風味之改善，也是目前保健食品與相關飲品開發中符合消費者嗜好性需求所努力研發的方向。本文提出透過目前能發揮高度酵素穩定性及活性的靜電紡絲酵素奈米纖維膜製程技術，用以進行特定形式的酵素固定化，配合專一性酵素與連續式薄膜填充管柱酵素反應裝置，一方面對羅漢果萃取物中的主要皂苷形式進行轉換，用以產生 S I 單體為主並改善羅漢果甜味劑風味；另一方面提高羅漢果皂苷萃取物於甜味劑與保健食品的應用性，提昇酵素於實際生產時的經濟效應。

關鍵詞：天然甜味劑、皂苷、電紡、酵素固定化

ABSTRACT

Non-caloric artificial sweeteners (NAS) are currently the world's most widely used food additives. But recent research shows that there are still controversies. As a result, natural sweeteners had gained much attention than NAS. Recently, the fastest growing market of natural sweetener is the sweeteners made from monk fruit, not only because its extracts are highest in sweetness among various natural sweeteners but also parts of the sweetness compounds have significant anti-diabetic activity. However, one of the components in monk fruit extracts called Saimenoside I (S I), which found to be the most

¹ 東海大學食品科學系助理教授

² 長庚科技大學健康產業科技研究所助理教授、民生學院中草藥研究中心成員、民生學院食品暨化妝品安全研究中心成員

sweetness compound and taste most closely to sucrose, are relatively low in contents. As the results, the development of methods to enrich the contents of S I in monk fruit extracts and related products are the goals for the current natural sweetener manufacturers. The bitter tastes and flavors of saponins-containing functional foods and related beverages are still the issues to be addressed. Here, we proposed to take the advantage of the electrospun nanofiber membrane's high enzyme immobilizing efficiency and stabilizing properties, together with the continuous packed-bed column, to obtain S I from MG V. These not only improve the taste of monk fruit extracts as natural sweeteners but also help to gain access of pure S I compound. Accordingly, we proposed a method to improve the saponins usages as a natural sweetener and as a health food ingredient through enzymes immobilized on electrospun nanofiber mat.

Keywords: natural sweeteners, saponins, electrospinning, enzyme immobilization

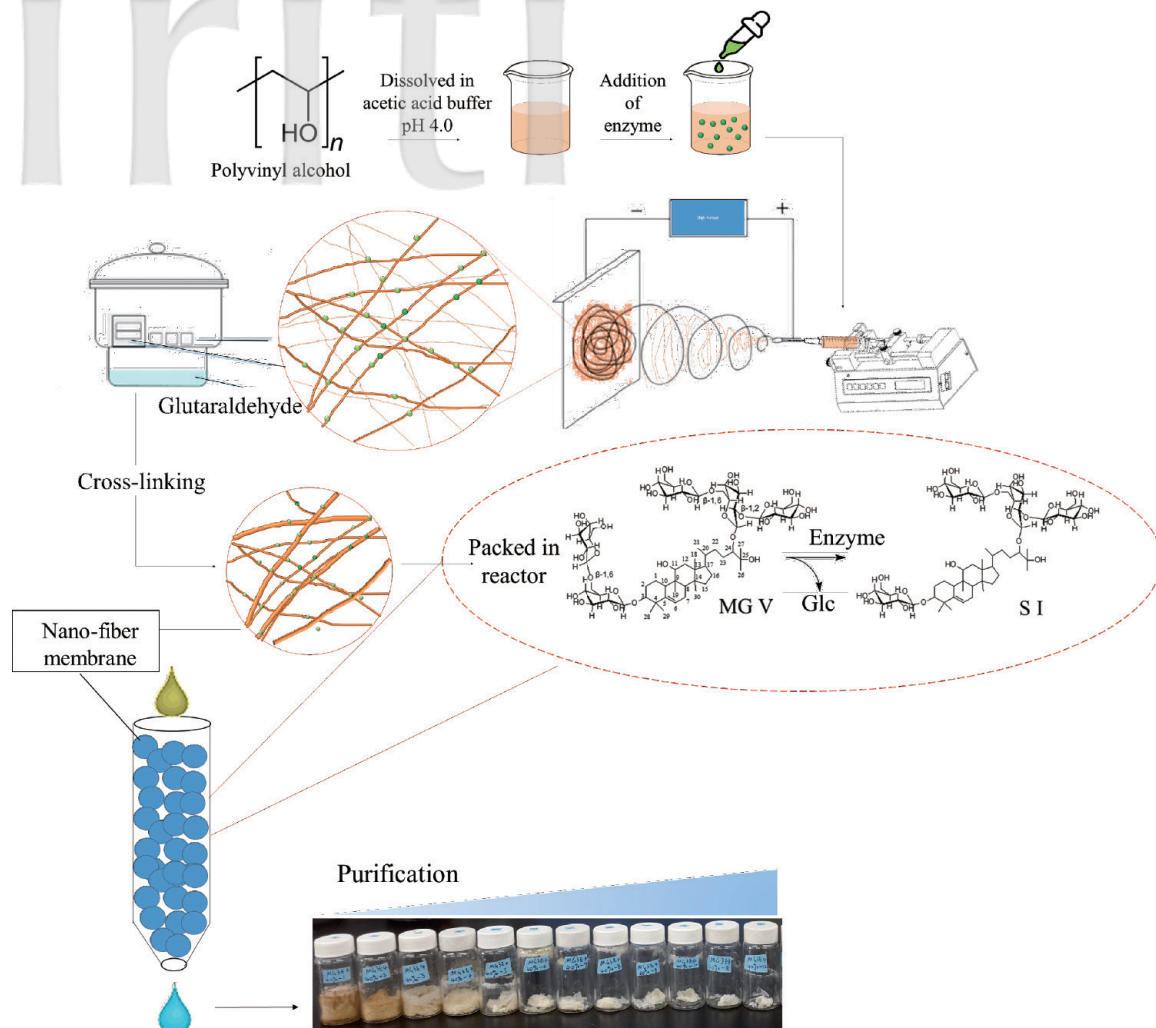
壹、前言

根據全球甜味劑產業市場分析資料，天然甜味劑是目前甜味劑發展重點趨勢，常為健康人士與肥胖者使用。過去曾有全球專利（專利字號 WO 2014/150127 A1）以酵素水解羅漢果皂苷糖基方法，用以改良羅漢果皂苷的甜味，此專利目標是找出產生高量的 Siamenoside I (S I) 羅漢果皂苷之酵素與反應條件。然而，此專利嘗試 62 種商業酵素後皆無法專一性產出 S I (Zhou et al., 2014)。以 2018 各大藥廠之標準品價格計算，純度 98% 以上的 S I 平均落在 70 美元 /mg。因此若能取得高度專一性生產 S I 的酵素，將可順利改善甜味劑風味，並具有實質產業與經濟效益。過去研究已有將環狀糊精葡聚糖轉移酶 (cyclodextrin glucanotransferase, CGTase) 固定於奈米多孔矽膠材質與奈米顆粒的研究，並有效改善酵素乘載含量與活性，用於製造食品添加劑或藥物輸送載體；但由於多孔性奈米材質及酵素奈米顆粒複合體易導致質傳及酵素回收率低 (J. Kim, 2006; J. Kim, Grate, & Wang, 2006)。而目前酵素固定化技術逐漸走向以奈米結構材料作為酵素支持素材，包括多孔奈米物質、奈米顆粒及奈米纖維，與過去傳統酵素支持材料相比，奈米結構材質含有極高比

表面積，可大幅改善固定化酵素的效率。因此將酵素結合於奈米纖維材料中，特別是以電紡絲方式所產生之奈米纖維酵素複合體，是未來酵素固定化與有效利用酵素的趨勢，也是解決過去因質量傳輸問題而無法提高酵素基質濃度的方法 (H. F. Jia et al., 2002; Saallah et al., 2016)。綜合以上研究背景，若能夠固定專一性轉換 S I 酵素於靜電紡絲纖維膜上，並安裝於連續發酵裝置有效生產 S I，可將食品工業應用奈米加工技術推向全新紀元，促進人類生活福祉（圖一）。

貳、羅漢果皂苷之酵素轉化

羅漢果皂苷具有很強甜味的特性，再加上具有抗糖尿病症狀的特性，可以當成代糖，作為糖尿病患者的食用添加物。目前市面上已經出現多種羅漢果為原料的代糖產品，如：LakantoTM 與 Sweet SensationTM，其健康訴求包括低熱量、低升糖指數 (glycemic index, GI)、不含其他人工添加物、不影響血糖與胰島素釋放、是糖尿病患者適用的代糖產品等。Newayceutical Inc. 公司的產品 Sweet SensationTM 更提到它可以用於各種形式的食用方式，適用於烘焙與烹調。羅漢果皂苷萃取物甜味劑已廣布於歐美市場，但其甜味



圖一：酵素化奈米纖維薄膜之酵素固定化技術與微型填充床式連續酵素反應器於羅漢果皂苷 S I 之轉化。

感覺仍與蔗糖有所差異。例如甜味與蔗糖比較時，某些人會有甜味遲遲不散的感覺，也會有無法產生立即甜味的感覺，雖羅漢果皂苷有其優點，但開發出改變羅漢果皂苷甜味缺點的方法是必要的。於 2014 年的全球專利 (專利字號 WO 2014/150127 A1) (Zhou et al., 2014)，是用酵素水解羅漢果皂苷上糖基的方法，達成修飾羅漢果皂苷的甜味。專利也提及其他糖基型式的羅漢果皂苷如 S I、mogroside IV (MG IV) 及 mogroside III E (MG III E) 之甜味餘後感較 mogroside V (MG V) 好；S I、MG IV 甜度比 MG III E 高；S I 又比 MG IV 味道更好。因此，此專利嘗試 62 種市面

販售的 cellulases、dextranases、galactosidases、glucanases、glucosidases 或 pustulanases 等酵素，試著找出能夠產生最多 S I 及 MG IV 的酵素與反應條件，其目的就是以產生最多比例的 S I 為目標 (Zhou et al., 2014)。

目前對於改變皂苷糖基技術主要有化學法、酵素法及微生物法。化學法主要指利用酸來水解皂苷上的糖基 (X. B. Chen et al., 2011; Takemoto, Arihara, Nakajima, & Okuhira, 1983)，但此法易生氧化型苷元，不僅專一性差，且嚴重環境污染。傳統上是以酸水解 MG V 上的糖基並配合後續純化步驟 (MG V 的含量佔成熟羅漢果乾果的 1.5%

以上)；雖然操作方法簡單，但專一性差，也導致後端純化步驟效率極低，在無法取得足夠之純化物質情況下，限制後續生物活性研究之進行與應用性。為解決專一性問題，酵素法及微生物法為產生特定糖基形式皂苷之新趨勢。以酵素水解為例，MG V 可利用麥芽糖酶 (maltase) 在 37°C 下反應一星期或以纖維酵素 (cellulase) 於 40°C 下反應 20 小時後 (Li, Chen, Liu, Wang, & Zhao, 2007) 可得到 mogroside IV E (MG IV E)、mogroside II E (MG II E)、mogroside I E (MG I E)、mogroside I E 1 (MG I E 1) 與 mogroside I E 2 (MG I E 2)。

研究發現 MG V 經由酵母菌發酵後，產生了帶有不同葡萄糖鍵結的 S I、MG IV 和 MG III E，並且最終產物 MG III E 具有對抗糖尿病之潛力 (Tao, Cao, et al., 2017; Tao, Yang, et al., 2017)。後續研究為確認轉換羅漢果皂苷之酵素，因此透過酵母菌資料庫尋找葡萄糖水解酵素 (β -glucosidase) 之相關酵素，選出可能參與葡萄糖水解之基因，結果發現 *exg1 Δ* 及 *kre6 Δ* 可影響羅漢果皂苷降解途徑，其中 *kre6 Δ* 酵母菌突變菌株可專一性快速產生羅漢果皂苷 MG III E，而 Exg1 則具有選擇性水解羅漢果皂苷之 β -1, 6- 葡萄糖鍵結的能力，透過補償性實驗將 *EXG1* 和 *KRE6* 補償回個別 *exg1 Δ* 和 *kre6 Δ* 突變株後，羅漢果皂苷轉換的結果與 wild-type 酵母菌所相似 (Chiu, Wang, Lee, Lo, & Lu, 2013)。由此可知 *EXG1* 是負責酵母菌羅漢果皂苷轉化之基因，但 *kre6 Δ* 突變株較快速產生 MG III E 之機制推測可能與 *kre6 Δ* 突變株之細胞壁結構的完整性有關 (Roemer, Paravicini, Payton, & Bussey, 1994)，後續研究證實 Exg1 仍是 *kre6 Δ* 細胞中負責轉化皂苷的酵素，且基於 ScExg1 基因表現量不變下，*kre6 Δ* 細胞有更多 Exg1 溢散於細胞外，是造成較快轉化皂苷糖基的主因，而分配更多 Exg1 到細胞外之特性，推測可能與 *kre6 Δ* 細胞之細胞壁異常有關。進一步透過選擇其他細胞壁突變株進行各別菌株之多種細胞壁結構分析

實驗與皂苷發酵分析實驗，文獻歸納出只有無法將細胞壁表面之甘露糖蛋白固定在細胞壁上之特定突變株，會造成甘露糖蛋白溢散在培養基中，並伴隨較快羅漢果皂苷轉化特性，促進 MG III E 產生 (R. B. Wang et al., 2015)。2019 年，王等人於食品化學期刊發表酵母菌轉化羅漢果皂苷研究，測試 18 種酵母菌轉化羅漢果皂苷之結果，顯示來自於 *Dekkera bruxellensis* 酵母菌的外泌酵素 DbExg1 可專一性將 MG V 轉化為 S I (R. Wang et al., 2019)。然而此酵素於 *D. bruxellensis* 的產出效率極低，因此透過基因重組實驗將 DbExg1 轉入其他高度表現的宿主或微生物，將有助於酵素生產與後續固定化酵素的需求。

參、電紡奈米纖維技術

目前先進之酵素固定化技術逐漸走向以奈米結構材料作為酵素支持素材，包括多孔奈米物質、奈米顆粒及奈米纖維；特別是以電紡絲方式所產生之奈米纖維將是未來酵素固定化的趨勢 (H. F. Jia et al., 2002; Saallah et al., 2016)。靜電紡絲是一種製造奈米級纖維薄膜的高分子加工方法。其材料來源廣泛且製程簡單，是近年來高分子工程上一個非常重要的研究主題。除了材料本身的性質外，在加工過程中的各種因子也會影響到高分子微細結構的改變。高分子的微細結構決定了成品的應用範圍。靜電紡絲製程中的溶液濃度、工作電壓與紡絲距離等因子，對其靜電紡絲與成形膜形態有重大影響。

一、靜電紡絲薄膜製程

傳統紡絲技術利用熔融紡絲、乾式紡絲、濕式紡絲或凝膠紡絲所製備出的微米纖維直徑約在 2 μm ~100 μm 之間。因受限於纖維加工成形及設備之限制，傳統紡絲法並無法製備直徑小於 1 μm 的奈米纖維，對此也限制了纖維領域的未來

發展性。因此學術及商業上發展出多種製備高分子奈米纖維之技術，其中以靜電紡絲製程最具有發展潛力。靜電紡絲 (Electrospinning) 製程成為奈米纖維薄膜最具發展潛力之原因有下列兩項：

(1) 纖維種類的多樣性，幾乎任何種類的高分子材料都可以製成奈米纖維，只要能找到適當的溶劑將高分子溶解成溶液，並經電紡製程即可得到；
(2) 製程簡易性，若能求得適當之加工條件，藉由高壓電場的電力效應即可得到電紡纖維。製程可分為 base、jet、spraying 及 collection 四個部分。高分子溶液倒入針筒後經 Micropump 輸送至毛細管 (Capillary) 或針 (Syringe) 流出，將針接上高壓直流電源，待溶液由針頭前端流出 (C. H. Chen, Huang, & Fuh, 2017; Ren, Xia, Shao, Zhang, & Li, 2017)。初始之半圓形液滴會受到高壓電場之作用，形狀變成 Taylor Cone 之外觀，同時在 Cone 之底端噴射出微米級之液柱 (Jet)，形成 Cone-Jet 的型態。液柱直徑會隨著遠離 Cone 之距離而逐漸變細，此為牽伸過程。在液柱的最底端由於溶液表面之單位電荷量過大，液體表面強烈電斥力作用下，Jet 被進一步分散 (Spraying) 開，形成許多更細的次微米級之 Tiny Jet。次微米級之 Tiny Jet 揮動噴灑於所施加之電場中，經電力進一步強力拉伸，可形成更細之 Tiny Jet，而溶劑則因液柱變細而更易揮發。最後纖維收集在接地之收集板 (Collection) 上，如此即完成微奈米級纖維膜的製作。

二、酵素固定化奈米載體

近幾十年來，一維奈米結構材料由於其獨特的特性和有趣的應用而受到關注。一維奈米材料通常是纖維狀、電線狀、棒狀、帶狀、管狀、螺旋態或環狀的形式呈現，並分別以不同方法製成。然於不同製程中電紡絲法為目前對奈米纖維材料製作最直接且新穎之方法，可製成長度極長、直徑一致且材質多變的纖維絲。此特性使

電紡絲製成的奈米纖維能適用於多種領域，如射出成形模板之製作 (Liu, 2004; Sun, Xu, Zhou, & Tan, 2003)、硬體結構之強化 (J. S. Kim & Reneker, 1999a, 1999b)、過濾用途 (Yoon et al., 2006)、催化劑 (Stasiak, Studer, Greiner, & Wendorff, 2007)、生物醫藥和藥物應用 (Welle et al., 2007) 及電子和光學元件 (C. Kim & Yang, 2003)，尤其是在生物催化領域，電紡絲奈米纖維所展現的特性，有其特殊貢獻。

國內外研究成果回顧，酵素是具有高度特異性的綠色催化劑，其專一性主要透過基質特異性、分子辨認特異性和光學異構特異性達成 (Ju & Parales, 2006)，且酵素的溫和性和特異性也賦予它們應用於藥物合成、食品加工、生物感測、生物復育、蛋白質水解及蛋白體學之研究 (Hasan, Shah, & Hameed, 2006a, 2006b)。然而，酵素的應用受其不穩定性和不可消耗性的限制，因此，固定化酵素可克服某些程度的限制。傳統酵素之多點連接固定於載體上的方式，可能導致蛋白質結構變化並限制酵素活性；又酵素於固定化後之活性與效能常與固定化過程所用之酵素乘載物質特性有關，如承載物之材質種類、組成成分與結構型態。因此截至目前為止，已有許多不同奈米結構之酵素固定化載體因應而生，如奈米孔洞形的矽氧化樹脂、奈米管、奈米顆粒和奈米纖維。以奈米結構作為酵素載體時與其他載體較之下，擁有極高比表面積，讓高量酵素穩定乘載於奈米材料中 (J. Kim et al., 2006)。然而，奈米結構材質之載體也有缺點需克服，例如多孔洞的矽氧化樹脂易發生部分酵素深陷孔洞深處所導致的基值擴散與酵素反應限制問題，使酵素轉化率降低。而奈米顆粒及奈米管之結構載體雖可克服因質量傳輸限制所導致的轉化率降低問題，但此類固定化酵素的材質因不易固定且會散布於反應槽中，大幅影響後續酵素回收與再利用。相反的，電紡絲奈米纖維之酵素載體可克服這些問題：(1) 電紡絲可以

各種材質呈現、(2) 具有高度孔洞化及孔洞間之交聯特性能，克服質傳問題、(3) 奈米纖維絲表面特性可進行改質來促進酵素活性。近期試驗則是利用聚乙烯醇材料和所需固定化之酵素混和並進行電紡絲，最後再透過交聯反應將酵素固定於奈米纖維薄膜 (Saallah et al., 2016; Sirisha, Jain, & Jain, 2016) 來克服此些問題。

三、酵素於奈米纖維絲中的固定

酵素在奈米纖維中的包覆可以透過酵素和其他組成份 (有機或無機材料) 的直接共電紡製作而成 (Saallah et al., 2016)。基於絕大多數酵素溶於水的特性，與酵素共同電紡的材質需有一定程度水溶性或能與酵素混和成均質狀態。均質態混和液能確保降低液體表面張力並防止纖維絲製成時之不連續斷點 (Doshi & Reneker, 1995)。常用的酵素共紡絲材質有聚乙烯醇 (poly vinyl-alcohol, PVA) (Wu, Yuan, & Sheng, 2005) (Xie & Hsieh, 2003)、聚環氧乙烷 (poly ethylene-oxide, PEO) 及聚 (N- 乙基 -2- 吡咯烷酮) (poly(N-vinyl-2-pyrrolidone), PVP) (Sawicka, Gouma, & Simon, 2005)。這些材料除價格低廉外也與酵素有良好親和特性。PVA 及 PEO 與天然生物大分子具有不同的結構且能與蛋白質形成二次鍵能力，並可以解離蛋白質間的氫鍵作用力等特性，使其成為良好之共電紡絲材質 (Frenot, Henriksson, & Walkenstrom, 2007; Y. T. Jia et al., 2007)。共電紡絲方法提供了將酵素固定在奈米纖維中的簡單方法，並且大幅提升酵素負載量 (酵素比例可占紡絲成品高達 50% 比例) (Y. Wang & Hsieh, 2008)，此特性可將富含酵素奈米纖維絲直接用於生物感測電極的製備 (Sawicka et al., 2005)。

四、聚乙烯醇共紡絲材料於酵素固定相關研究

聚乙烯醇由於其良好的成膜能力、高親水性、高生物相容性及良好的化學耐受力和機械抗

力，被廣泛應用於工業生物技術和生物醫學領域。其中以聚乙烯醇合成的奈米纖維絲更常用於過濾材質製作、藥物傳遞、細胞皮膚組織重建、奈米感測及生物催化酵素的載體製作。雖有以上優點，但聚乙烯醇用於固定酵素進行酵素轉化的研究仍占少數：僅纖維素 (Hung et al., 2011; Wu et al., 2005)、乙酰膽鹼酯酵素、脂解酶 (Y. Wang & Hsieh, 2008)、漆酶 (Xu, Chi, Li, & Zhang, 2013) 及葡萄糖氧化酶之固定化 (Ge, Zhao, Mo, Li, & Li, 2012)。然而由聚乙烯醇所製成的奈米纖維薄膜易吸水，使其抗機械力降低，並導致酵素損失，因此纖維絲需再經過硼酸或戊二醛蒸氣之交聯處理增加酵素於纖維絲中之穩定性 (Nunes et al., 2015)。

肆、實際應用於羅漢果甜味劑 SI 及 MG III E 轉化程序

微型填充床式連續酵素反應器可以參考 Mário Nunes 於 2013 年所發表的微型生物反應器為設計雛型 (Nunes et al., 2016)。以降低空隙容積 (void volume) 為設計重點，用 2.2~5.0 mL 之 QSP 離心管為反應器本體，上下打孔接上直徑為 3 mm 之塑膠軟管作為進樣與出樣端，進樣端會另與蠕動幫浦連結連續性的控制進樣速率。試驗會將此微型填充床式連續酵素反應槽裝置預計填入酵素含量約 30~50 mg L⁻¹ 的 PVA- 酵素奈米纖維薄膜，約莫會佔有 1.7 mL 的體積量，並以 10~50 mL h⁻¹ 的流速供給羅漢果基質液進入微型反應槽中，進行羅漢果皂苷上糖基的水解反應。依照不同流速、薄膜填充量、反應體積、溫度等條件計反應器各條件下之體積產率 (volumetric productivity)、專一性產率 (specific productivity) 及滯留時間 (residence time, 小時)；同時也將針對反應器耐用程度以數學公式進行模擬換算，提供未來放大製程之參考依據。計算公式如下所示：體積產率 [γ_P (mMh⁻¹)

$= C \times F/V$, C 還原糖產量 (mM)、 F 流速 ($L h^{-1}$)、 V 反應槽空隙容積 (L) (預計為 $2.5 \sim 3 \times 10^{-4} L$) ; 專一性產率 [q_p ($mM h^{-1} mg^{-1}_{enz}$) = 體積產率 ($mM h^{-1}$) / 酵素濃度 ($mg L^{-1}$)] ; 滯留時間 (h) [$\tau(h) = VF$, F 流速 ($L h^{-1}$)、 V 反應槽空隙容積 (L) (預計為 $2.5 \sim 3 \times 10^{-4} L$)]。預計使用線性倒數模型, 預測反應器催化活性削弱程度與時間關係 [$Act(t) = Act_{t=0} / (1 + K_{deact}t)$, $Act(t)$ 及 $Act_{t=0}$ 分別表示酵素於 t 時間點的活性與一開始零點時的活性、 K_{deact} 是活性削弱速率常數、 t 是系統操作時間]。

伍、結論

本文所收集與彙整國內外食品科學領域中奈米科技之最新相關文獻與重點。由微型填充床式連續酵素反應器透過評估流速、酵素薄膜乘載量、與欲轉化基質之傳輸特性生產 SI, 將可提昇酵素以奈米紡絲處理之研發能力, 有助於天然羅漢果皂苷甜味劑工程與植物皂苷萃取物風味轉化之準確性, 進而增進經濟發展與人類健康, 同時促進酵素固定化技術之應用與升級, 使國內固定化酵素於天然物轉換之範疇進入奈米等級, 增加國內食品科學於奈米尺度之研發動能與研究方向之廣度。

參考文獻

Chen, C. H., Huang, C. T., & Fuh, Y. K. (2017). Optical method for in situ monitoring of electrospinning process and porosity characterization of microporous membrane. *Journal of Micro-Nanolithography Mems and Moems*, 16(2).

Chen, X. B., Zhuang, J. J., Liu, J. H., Lei, M., Ma, L., Chen, J., ... Hu, L. H. (2011). Potential AMPK activators of cucurbitane triterpenoids from

Siraitia grosvenorii Swingle. *Bioorganic & Medicinal Chemistry*, 19(19), 5776-5781.

Chiu, C. H., Wang, R. B., Lee, C. C., Lo, Y. C., & Lu, T. J. (2013). Biotransformation of Mogrosides from Siraitia grosvenorii Swingle by *Saccharomyces cerevisiae*. *Journal of Agricultural and Food Chemistry*, 61(29), 7127-7134. doi: Doi 10.1021/Jf402058p

Doshi, J., & Reneker, D. H. (1995). Electrospinning Process and Applications of Electrospun Fibers. *Journal of Electrostatics*, 35(2-3), 151-160.

Frenot, A., Henriksson, M. W., & Walkenstrom, P. (2007). Electrospinning of cellulose-based nanofibers. *Journal of Applied Polymer Science*, 103(3), 1473-1482.

Ge, L., Zhao, Y. S., Mo, T., Li, J. R., & Li, P. (2012). Immobilization of glucose oxidase in electrospun nanofibrous membranes for food preservation. *Food Control*, 26(1), 188-193. doi: 10.1016/j.foodcont.2012.01.022

Hasan, F., Shah, A. A., & Hameed, A. (2006a). Industrial applications of microbial lipases. *Enzyme and Microbial Technology*, 39(2), 235-251.

Hasan, F., Shah, A. A., & Hameed, A. (2006b). Influence of culture conditions on lipase production by *Bacillus* sp FH5. *Annals of Microbiology*, 56(3), 247-252.

Hung, T. C., Fu, C. C., Su, C. H., Chen, J. Y., Wu, W. T., & Lin, Y. S. (2011). Immobilization of cellulase onto electrospun polyacrylonitrile (PAN) nanofibrous membranes and its application to the reducing sugar production from microalgae. *Enzyme and Microbial Technology*, 49(1), 30-37. doi: 10.1016/j.enzmict.2011.04.012

- Jia, H. F., Zhu, G. Y., Vugrinovich, B., Kataphinan, W., Reneker, D. H., & Wang, P. (2002). Enzyme-carrying polymeric nanofibers prepared via electrospinning for use as unique biocatalysts. *Biotechnology Progress*, 18(5), 1027-1032.
- Jia, Y. T., Gong, J., Gu, X. H., Kim, H. Y., Dong, J., & Shen, X. Y. (2007). Fabrication and characterization of poly (vinyl alcohol)/chitosan blend nanofibers produced by electrospinning method. *Carbohydrate Polymers*, 67(3), 403-409.
- Ju, K. S., & Parales, R. E. (2006). Control of substrate specificity by active-site residues in nitrobenzene dioxygenase. *Applied and Environmental Microbiology*, 72(3), 1817-1824.
- Kim, C., & Yang, K. S. (2003). Electrochemical properties of carbon nanofiber web as an electrode for supercapacitor prepared by electrospinning. *Applied Physics Letters*, 83(6), 1216-1218.
- Kim, J. (2006). COLL 577-Nanostructures for enzyme stabilization. *Abstracts of Papers of the American Chemical Society*, 232.
- Kim, J., Grate, J. W., & Wang, P. (2006). Nanostructures for enzyme stabilization. *Chemical Engineering Science*, 61(3), 1017-1026.
- Kim, J. S., & Reneker, D. H. (1999a). Mechanical properties of composites using ultrafine electrospun fibers. *Polymer Composites*, 20(1), 124-131.
- Kim, J. S., & Reneker, D. H. (1999b). Polybenzimidazole nanofiber produced by electrospinning. *Polymer Engineering and Science*, 39(5), 849-854.
- Li, Q. Y., Chen, H. B., Liu, Z. M., Wang, B., & Zhao, Y. Y. (2007). Cucurbitane triterpenoids from *Momordica charantia*. *Magnetic Resonance in Chemistry*, 45(6), 451-456.
- Liu, T. Q. (2004). Preparation of a novel micro/nano tubes via electrospun fiber as a template. *Journal of Materials Science & Technology*, 20(5), 613-616.
- Nunes, M. A. P., Martins, S., Rosa, M. E., Gois, P. M. P., Fernandes, P. C. B., & Ribeiro, M. H. L. (2015). Improved thermostable polyvinyl alcohol electrospun nanofibers with entangled naringinase used in a novel mini-packed bed reactor. *Bioresource Technology*, 213, 208-215. doi: 10.1016/j.biortech.2016.03.058
- Nunes, M. A. P., Martins, S., Rosa, M. E., Gois, P. M. P., Fernandes, P. C. B., & Ribeiro, M. H. L. (2016). Improved thermostable polyvinyl alcohol electrospun nanofibers with entangled naringinase used in a novel mini-packed bed reactor. *Bioresource Technology*, 213, 208-215.
- Ren, L. F., Xia, F., Shao, J. H., Zhang, X. F., & Li, J. (2017). Experimental investigation of the effect of electrospinning parameters on properties of superhydrophobic PDMS/PMMA membrane and its application in membrane distillation. *Desalination*, 404, 155-166.
- Roemer, T., Paravicini, G., Payton, M. A., & Bussey, H. (1994). Characterization of the Yeast (1-6)-Beta-Glucan Biosynthetic Components, Kre6p and Skn1p, and Genetic Interactions between the Pkc1 Pathway and Extracellular-Matrix Assembly. *Journal of Cell Biology*, 127(2), 567-579. doi: DOI 10.1083/jcb.127.2.567

- Saallah, S., Naim, M. N., Lenggoro, I. W., Mokhtar, M. N., Abu Bakar, N. F., & Gen, M. (2016). Immobilisation of cyclodextrin glucanotransferase into polyvinyl alcohol (PVA) nanofibres via electrospinning. *Biotechnology Reports*, 10, 44-48. doi: 10.1016/j.btre.2016.03.003
- Sawicka, K., Gouma, P., & Simon, S. (2005). Electrospun biocomposite nanofibers for urea biosensing. *Sensors and Actuators B-Chemical*, 108(1-2), 585-588.
- Sirisha, V. L., Jain, A., & Jain, A. (2016) Enzyme Immobilization: An Overview on Methods, Support Material, and Applications of Immobilized Enzymes. In: Vol. 79. *Advances in Food and Nutrition Research* (pp. 179-211).
- Stasiak, M., Studer, A., Greiner, A., & Wendorff, J. H. (2007). Polymer fibers as carriers for homogeneous catalysts. *Chemistry-a European Journal*, 13(21), 6150-6156.
- Sun, Z. C., Xu, J. X., Zhou, T., & Tan, N. (2003). Study on influence of bending-torsion coupling in an impacting-rub rotor system. *Applied Mathematics and Mechanics-English Edition*, 24(11), 1316-1323.
- Takemoto, T., Arihara, S., Nakajima, T., & Okuhira, M. (1983). Studies on the Constituents of Fructus Momordicae. 2. Structure of Sapogenin. *Yakugaku Zasshi-Journal of the Pharmaceutical Society of Japan*, 103(11), 1155-1166.
- Tao, L. J., Cao, F. Y., Xu, G. H., Xie, H. F., Zhang, M. A., & Zhang, C. F. (2017). Mogroside IIIIE Attenuates LPS-Induced Acute Lung Injury in Mice Partly Through Regulation of the TLR4/MAPK/NF-kappa B Axis via AMPK Activation. *Phytotherapy Research*, 31(7), 1097-1106.
- Tao, L. J., Yang, J. Y., Cao, F. Y., Xie, H. F., Zhang, M. A., Gong, Y. Q., & Zhang, C. F. (2017). Mogroside IIIIE, a Novel Anti-Fibrotic Compound, Reduces Pulmonary Fibrosis through Toll-Like Receptor 4 Pathways. *Journal of Pharmacology and Experimental Therapeutics*, 361(2), 268-279.
- Wang, R., Chen, Y.-C., Lai, Y.-J., Lu, T.-J., Huang, S.-T., & Lo, Y.-C. (2019). *Dekkera bruxellensis*, a beer yeast that specifically bioconverts mogroside extracts into the intense natural sweetener siamenoside I. *Food Chemistry*, 276, 43-49. doi: <https://doi.org/10.1016/j.foodchem.2018.09.163>
- Wang, R. B., Lin, P. Y., Huang, S. T., Chiu, C. H., Lu, T. J., & Lo, Y. C. (2015). Hyperproduction of beta-Glucanase Exg1 Promotes the Bioconversion of Mogrosides in *Saccharomyces cerevisiae* Mutants Defective in Mannoprotein Deposition. *Journal of Agricultural and Food Chemistry*, 63(47), 10271-10279.
- Wang, Y., & Hsieh, Y. L. (2008). Immobilization of lipase enzyme in polyvinyl alcohol (PVA) nanofibrous membranes. *Journal of Membrane Science*, 309(1-2), 73-81.
- Welle, A., Kroger, M., Doring, M., Niederer, K., Pindel, E., & Chronakis, I. S. (2007). Electrospun aliphatic polycarbonates as tailored tissue scaffold materials. *Biomaterials*, 28(13), 2211-2219.
- Wu, L. L., Yuan, X. Y., & Sheng, J. (2005). Immobilization of cellulase in nanofibrous PVA membranes by electrospinning. *Journal of Membrane Science*, 250(1-2), 167-173.
- Xie, J. B., & Hsieh, Y. L. (2003). Thermosensitive poly(N-isopropylacrylamide) hydrogels bonded

- on cellulose supports. *Journal of Applied Polymer Science*, 89(4), 999-1006.
- Xu, R., Chi, C., Li, F., & Zhang, B. (2013). Laccase-polyacrylonitrile nanofibrous membrane: Highly immobilized, stable, reusable, and efficacious for 2,4,6-trichlorophenol removal. *ACS Applied Materials and Interfaces*, 5(23), 12554-12560. doi: 10.1021/am403849q
- Yoon, K., Kim, K., Wang, X. F., Fang, D. F., Hsiao, B. S., & Chu, B. (2006). High flux ultrafiltration membranes based on electrospun nanofibrous PAN scaffolds and chitosan coating. *Polymer*, 47(7), 2434-2441.
- Zhou, Y., Armentrout, R. W., Woodrhyer, R. D., Bridges, J. R., Schunk, T. C., & Fletcher, J. N. (2014).

葛根素微脂體製備並評估其對紫外線照射皮膚損傷的影響

林琬蓉^{1†} 李依潔^{2†} 謝明發^{3*} 鄭靜宜^{4*}

Preparation and Evaluation of Liposomal Puerarin for Skin Damage Caused by Ultraviolet Radiation

Wan-Jung Lin^{1†}, Yi-Chieh Lee^{2†}, Ming-Fa Hsieh^{3*}, Ching-Yi Cheng^{4*}

摘要

人體隨著年齡增長，老化現象也隨之產生，尤其皮膚的老化更為人們最重視的顏面，因此抗老化的產品及方法開發從古至今持續著備受關注。引起皮膚老化成因有許多，其中紫外線所導致之皮膚光老化，為日常中最普遍的原因。過去文獻指出葛根素屬於天然的異黃酮類化合物，在不同疾病上分別具有對抗發炎、抗氧化及抑制 DNA 損傷的功能，因此本篇將利用體外試驗探討葛根素是否可以抑制皮膚因紫外光導致光老化的情形，然而葛根素雖具有良好的藥理作用，單純的葛根素卻於人體中的生物利用率低，因此，在本文中我們將比較純葛根素與脂質體葛根素的抗炎或抗凋亡作用，希望可以藉由將葛根素包覆於藥物載體提升其生物利用率。由初步結果顯示，經由 ANOVA 統計分析找到製備微脂體最佳比例為 E6C2T2P2，載藥量：16.23%，粒徑約在 140 nm。在細胞實驗，葛根素本身具有改善 HaCaT 細胞因 UVB 導致的細胞凋亡及發炎反應的趨勢，然而將葛根素包覆於微脂體後，卻不具有相同的改善效果，因此未來可再針對包載葛根素的藥物載體進行研究及改善。

關鍵詞：皮膚老化、發炎、細胞凋亡、葛根素、微脂體

ABSTRACT

With the increase of age, the aging phenomenon also occurs, especially the aging of the skin is the most important face of people. Therefore, the development of anti-aging products and methods has been receiving much attention since ancient times. There are many causes of skin aging, and the photoaging of the skin caused by ultraviolet rays is the most common cause in daily life. In the past, it was pointed out that puerarin belongs to natural isoflavones and has anti-inflammatory, anti-oxidative and DNA-inhibiting

¹ 長庚科技大學健康產業科技研究所碩士研究生² 中原大學生物醫學工程學系碩士研究生³ 中原大學生物醫學工程學系教授兼工學院副院長⁴ 長庚科技大學健康產業科技研究所助理教授、民生學院食品暨化妝品安全研究中心成員、民生學院中草藥研究中心成員

functions in different diseases. Therefore, this article will investigate whether puerarin can inhibit skin light caused by ultraviolet light in cell model. However, puerarin has a good pharmacological effect, but it has low bioavailability in human body. Therefore, we will compare the anti-inflammatory or anti-apoptosis effects of pure puerarin to that of liposomal puerarin. It is hoped that the bioavailability can be enhanced by coating puerarin in a drug carrier. Preliminary results showed that the optimal ratio of preparation of liposome was E6C2T2P2 by ANOVA statistical analysis, the drug loading was 16.23%, and the particle size was about 140 nm. In the UVB-stimulated keratinocyte experiment, puerarin tends to improve the apoptosis and inflammatory responses in HaCaT cells. However, liposomal puerarin does not have the same improvement effect, so it can be further research and improvement of drug carriers containing puerarin.

Keywords: skin aging, inflammation, apoptosis, puerarin, liposome

壹、前言

隨著年齡的增長，老化也隨之到來，老化是發生於生物體中所有器官的複雜生物現象，其機制主要分為兩種 [1]。其一為內在衰老，內臟器官出現的不可逆組織變性是因為年齡增長所致，而皮膚則開始會產生變薄、細紋、乾燥等現象。其二則是外在衰老，由於外在因素，如睡眠習慣、重力、紫外線等原因造成衰老的發生，其中皮膚位人體的最外層，且最易與紫外線接觸而導致衰老，因此紫外線是導致皮膚老化最關鍵的主因，也就是所謂的光老化 (photoaging) [2]。

太陽輻射為紫外線的來源，其分為長波紫外線 UVA (320-400 nm)，中波紫外線 UVB (290-320 nm) 及短波紫外線 UVC (200-290 nm) [3]。三種不同波長的紫外線分別會促使皮膚產生不同的生理情形，當中可穿透至皮膚表皮層的 UVB 紫外線，因能量較高，所以可短時間致皮膚曬傷及角質增厚等情況發生，因此市上防曬乳大多設計用於抵抗 UVB 以防止皮膚損傷 [4, 5]。因此本篇將利用 UVB 刺激細胞以建立皮膚光老化模型。另外，過去文獻指出，紫外線在導致皮膚老化的過程是

透過誘發皮膚產生發炎情形及 DNA 損傷等 [6]。當皮膚長時間暴露在紫外線的環境下，便會促使體內環氧合酶-2 (Cyclooxygenase-2, COX-2) 的表現，接著 COX-2 會將花生四烯酸 (Arachidonic acid, AA) 轉化為前列腺素 (prostaglandin E₂, PGE₂) [7]。PGE₂ 則會導致皮膚產生紅斑的發炎反應 [8, 9]。而當皮膚長時間的接觸紫外線也會引發皮膚細胞凋亡的發生，過程透過前期的凋亡蛋白構型改變，如 Bak、Bax。進而打開細胞粒線體的陽離子通道並減少其細胞膜電位，而導致 Cytochrome C 被釋放至細胞質中與 Caspase 9、Apaf-1 等蛋白質結合，進一步誘導 Caspase 3 蛋白活化，促使染色質濃縮，且 Caspase 3 也會裁切下游蛋白，如 DNA 修補酵素 (nuclear poly (ADP-ribose) polymerase, 簡稱 PARP) [10]。因此本篇將利用葛根素的抗發炎、抗 DNA 損傷之特性應用在觀察抗紫外線誘導之皮膚老化情形。

葛根素屬於天然異黃酮類，C- 苷 (C-glycoside) 化合物。其主來源為葛根屬植物，當中被廣泛使用的有野葛 (*Pueraria lobata* (Willd.) Ohwi) 及甘葛藤 (*Pueraria thomsonii*)，而野葛是其中富含最多葛根素的植物 [11]。過去文獻發現，葛根素於 50

μM 的劑量可有效透過 NF- κB 訊息途徑，進一步抑制發炎相關蛋白 C-react protein (CRP) 的表現，進而達到改善脂多糖所誘發的外周血單核細胞之發炎反應 [12]。另外也有研究指出，葛根素在 $100 \mu\text{M}$ 的劑量可透過 Nrf-2 途徑促使 HO-1 蛋白表現，進而抑制羧甲基離氨基酸 (CML) 所誘發之小鼠腎絲球細胞發炎因子 COX-2 的表現 [13]。而在 DNA 損傷的部分過去文獻也提出，葛根素因具雌激素特性透過活化雌激素受體依賴性 G β 1/PI3K/Akt 路徑，而促使血鐵質氧化酶 -1 (heme oxygenase-1, HO-1) 表現，進而抑制由 T-BHP 活化之凋亡蛋白 caspase-3 表現 [14]。另外也有研究發現葛根素可透過調控 PI3K/Akt/eNOS 訊息路徑，進而抑制細胞凋亡蛋白 caspase-3 表現而達到治療腎損傷的大鼠功效 [15-17]。然而過去有研究發現，將葛根素使用固態脂質奈米微粒進行載體包覆後在人體內的生物利用率較單純葛根素口服給藥大為提升 [18, 19]。

而現今社會藥物奈米載體已日益興盛，其功能可助於提升藥物動力學，目前於經皮給藥的方法具微小顆粒 (minute particles)、皮膚微針 (cutaneous microneedles) 等方法，但由於皮膚微針給藥法具侵入性，因此本篇選用顆粒載體做為研究方向，而顆粒載體目前已知的有微胞 (Micelles)、微乳液 (Microemulsions)、樹枝高分子 (Dendrimers)、微脂體 (Liposomes)、奈米顆粒 (Nanoparticles)、奈米乳液 (Nanoemulsions) 等 [20]。當中生物相容性較高的為微脂體，源自於微脂體之成分與細胞膜很相似，因此藥物運送過程較易克服皮膚表皮屏障 (Epidermal barrier)，加上微脂體可令生物分解且不具有毒性，因此本篇藥物載體將選擇使用微脂體。

綜合上述，本篇研究將分別探討葛根素是否可改善紫外線所導致的皮膚發炎及細胞凋亡反應。另外，將葛根素包覆於微脂體中，比較純葛根素與微脂體葛根素的抗炎或抗凋亡效果，希望

可以藉由將葛根素包覆於藥物載體提升其生物利用率。

貳、材料與方法

一、微脂體

本篇利用傳統薄膜法 (film hydration) 及離子梯度法 (remote loading) 執行微脂體製備，從中選出製備葛根素微脂體之最佳方法，其主成分包含：(1) 膽固醇 (Cholesterol) (2) 維生素 E (3) 大豆卵磷脂 (L- α -phosphatidylcholine, EGG PC) (4) 聚乙二醇琥珀酸酯 (D- α -Tocopherol polyethylene, TPGS)。接著分別將不同重量比的蔗糖及 EGG PC 之蔗糖水溶液執行薄膜水合。最後使用 Design Expert 軟體以 Two Level Factorial 將全部四種成分設計成不同的成分組合比例，並找出最佳微脂體組合比例。

二、薄膜水合法

以乙醇將 Cholesterol、EGG PC、Puerarin、TPGS 進行溶解後，以減壓濃縮法將乙醇移除，並執行一小時抽真空以確認完全移除溶劑，即可得取脂質薄膜。接著以蔗糖水或 PBS 磷酸鹽緩衝液進行水合，並於 60°C 水浴槽中執行一小時超音波震盪，隨後以凍融法 (-196°C 提升至 60°C) 以提升微脂體包覆率。接著以擠壓器加上 200 nm 之過濾膜處 60°C 中進行二十次擠壓便可得粒徑均勻之微脂體。最後將微脂體以蔗糖水溶液 (同水合過程之濃度) 利用透析法移除未被包覆到的藥物並利用液態氮高速冷凍微脂體並進行冷凍乾燥，完成後放入乾燥箱中保存。

三、離子梯度法

以氯仿將 Cholesterol、Egg PC、TPGS 進行溶解 (莫爾比 6:1:1) 以減壓濃縮法將氯仿移除，並執行一小時抽真空以確認完全移除溶劑。以 0.5

M 醋酸鈉溶液進行水和並於 60°C 水浴槽中執行一小時超音波震盪，隨後以擠壓器加上 200 nm 之過濾膜處 60°C 中進行二十次擠壓便可得粒徑均勻之空白微脂體。接著以 HBSS-MES 緩衝液進行透析，促使微脂體之內外部形成離子的梯度。首先，把葛根素以 HBSS-MES 緩衝液進行溶解，接著把空白的微脂體及葛根素溶液分別加熱至 60°C，待 10 分鐘後，把兩溶液混勻並於 60°C 環境中反應一小時，此時葛根素會藉由離子梯度被包覆入空白微脂體中，最後以 HBSS-MES 緩衝液移除未被包覆之葛根素。經測量微脂體之包覆率及載藥量後，執行冷凍乾燥。

四、載藥量計算

本篇根據 Bartlett 之論點作為計算，1 莫爾的磷表示一莫爾之微脂體，以此算出微脂體濃度，並算出含葛根素之微脂體中藥物的載藥量。其中磷的濃度計算法，為以比色法進行檢測磷之含量。首先將磷酸根分子進行水解為無機磷並加入鉬酸銨使其轉換為磷酸鉬銨，接著注入 Fiske-SubbaRow reagent 使其還原為深藍色產物後，以紫外光可見光分光光譜儀進行磷含量之測定。

其實驗方法：將各玻璃試管分別注入 1 mL 去離子水及 0.5 mL 硫酸 (10 N)，接著分別注入磷酸根之標準品 (3.2 $\mu\text{mole}/\mu\text{L}$)：0、5、10、20、40 μL 或 20 μL 微脂體溶液，進行高速震盪數秒並置於 210°C 中油浴反應執行 75 分鐘後冷卻至室溫，接著加入過氧化氫 100 μL 並高速震盪數秒，再置於 210°C 中油浴反應執行 30 分鐘後冷卻至室溫，接著加入 0.22% 鉬酸銨溶液 4.6 mL 及 Fiske-SubbaRow reagent (3 g NaHSO_3 , 0.05 g 4-Amino-3-hydroxyl-1-naphthalene sulfonic acid, 0.1 g Na_2SO_3 , 20 mL d.d. H_2O , 抽氣過濾) 200 μL 並高速震盪後，利用鋁箔紙進行封口，並置 100°C 水浴槽中反應 7 分鐘並冰浴至室溫。最後利用紫外光可見光分光光譜儀檢測，以 825 nm 之吸光值條件，首先以

標準品建立檢量線。接著將微脂體置入乙醇中，置於 4°C 反應 20 分鐘以打破微脂體，並 250 nm 吸光值量測微脂體內葛根素含量。其載藥量之計算方法如下為：

$$\text{Percentage of drug loading} = \frac{\text{Mole}_{\text{puerarin}}}{\text{Mole}_{\text{PC}}} \times 100\%$$

五、粒徑分析

當微小粒子處於液體中時會產生布朗運動，其速度 (小粒子速度快，大粒子反之) 將影響其散射之光波動速度，即為光消逝之速度。由於大粒子移動速度較慢，因此散射光之消逝的程度相較小，所以散射光之強度 (intensity) 則將維持於較高的位置，小粒子則反之。本實驗之儀器為動態光散射粒徑分析儀進行微脂體之粒徑分布及分布率 (PDI) 的偵測，首先置 1 mL 微脂體之溶液入樣品槽中，儀器溫度設定為 25°C、光散射角：90°C、折射率 1.33，本儀器會以 90°C 角之雷射偵測器，將散射光消逝之訊號進行收集，接著把訊號以相關函數 $C(t)$ (Correlation function) 呈現以計算粒徑大小。

六、細胞培養

本篇研究細胞使用人類角質細胞 (Human keratinocyte cell line, HaCaT)，細胞來自 Cell lines service, number: 300493。HaCaT 細胞培育於 Dulbecco's modified medium (DMEM) 培養基 (含 10% 胎牛血清及 1% Penicilin 抗生素)，環境條件為 37°C、5% CO_2 。

七、單純葛根素與葛根素微脂體對細胞多樣性之影響分析

將細胞種於 24 孔盤內，培養兩天後，將培養基更換為含 10% FBS 之 DMEM 培養基 500 μL /well，並分別加入單純微脂體或葛根素微脂體或單純葛根素溶液，置入培養箱一小時，接著加入

MTT 溶液 (5 mg/mL) 50 μ L/well 並放入培養箱作用 30 分鐘，最後移除培養基且加入異丙醇使紫色結晶溶出。以分光光譜儀 OD 570 nm 條件偵測吸光值。控制組為未加藥物組別。公式：細胞生物多樣性百分率 = 待測物吸光值 / 控制組吸光值 $\times 100\%$

八、定量蛋白質分析 (BCA)

本篇研究之蛋白質濃度定量分析，按照 Thermo Scientific Pierce BCA Protein Assay Kit 建議之步驟進行，首先梯度配製不同濃度之白蛋白標準品並分別取 10 μ L 待測物注入 96 孔盤中，將 Kit 中 A、B 溶液依比例 (A : B = 50 : 1) 配製成混和液並分別於每格孔洞注入 200 μ L 並置於 37°C 反應 30 分鐘，最後以分光光譜儀 OD 562 nm 條件偵測吸光值。以梯度配製的白蛋白標準品的吸光值建立標準曲線，並依曲線公式換算出待測物之蛋白質濃度。

九、萃取蛋白質

將細胞種入 3.5 cm 培養皿，等細胞八至九成滿時，更換新鮮含 10% FBS 之 DMEM 培養基 1 mL/well，依實驗將細胞做不同處置後，分別在培養皿中注入 300 μ L Lysis buffer 並將細胞刮取下，置入離心機離心，條件如下 10,000 rpm、4°C、10 分鐘，接著進行 BCA 蛋白質定量，並利用 Lysis Buffer 調整待測物至濃度呈一致性，最後加入五倍 sample buffer 並以 95°C 條件加熱五分鐘。

十、西方點墨法

將待測物分別注入架好之 10% polyacrylamide gel 孔槽，並進行 SDS-PAGE 電泳，接著將膠上的蛋白質轉漬於 PVDF 膜上，完成後浸入適量 Blocking buffer 置室溫搖晃反應 30 分鐘，將 PVDF 膜空白處填上蛋白質，接著以 TTBS 洗滌 PVDF 膜 10 分鐘 3 次後，注入適量一級抗體

(以 Blocking buffer 1:1000 稀釋) 置 4°C 冰箱作用一天，接著以 TTBS 洗滌 PVDF 膜 10 分鐘 3 次，接著注入適量第二級抗體 (以 Blocking buffer 1:10000 稀釋) 於室溫作用 1 小時並以 TTBS 洗滌 PVDF 膜 10 分鐘 3 次，最後將 PVDF 膜以 ECL reagents 處理並利用 Image Lab™ Software (Bio-Rad Laboratories, Inc., Hercules, CA, USA) 進行檢測並定量特定蛋白質之含量。

十一、酵素免疫分析法

利用抗原及抗體間專一的鍵結特性，以進行待測物的檢測；因原先結合於 96 孔盤上的抗體或抗原具免疫活性，因此利用其鍵結特性，並結合酵素的呈色作用，便可得知特定抗體或抗原存在與否，同時可藉由呈色的深淺執行分析定量。本篇利用酵素免疫分析法 (ELISA) kit 提供之建議步驟進行檢測培養基中 PGE₂ 含量濃度。

參、結果與討論

一、微脂體製備

本篇運用離子梯度法以及傳統薄膜法篩選出最合適之製備方法並完成微脂體製備。其主成分包含：(1) 膽固醇 (Cholesterol) (2) 維生素 E (3) 大豆卵磷脂 (L- α -phosphatidylcholine, EGG PC) (4) 聚乙二醇琥珀酸酯 (D- α -Tocopherol polyethylene, TPGS)。接著分別將不同重量比的蔗糖及 EGG PC 之蔗糖水溶液執行薄膜水合。最後使用 Design Expert 軟體進行各成分之餘微脂體參數是否具影響的探討，其以 Two Level Factorial 將全部四種成分設計成不同的成分組合比例，各成分皆有一個高、低質，經計算後得知不同的組合比例共有 16 種，且以 ANOVA 之統計方法進行各組成分之微脂體分布粒徑及載藥量的影響分析，參數之設計結果如表一。

表一：以 Two Level Factorial 設計不同組合成分比例 [21]

Name	Units	Type	Low	High
EGG PC	mole	Factor	6	10
Cholesterol	mole	Factor	1	2
TPGS	mole	Factor	1	2
Puerarin	mole	Factor	1	2
Diameter	nm	Response	N/A	N/A
Percentage of drug loading	%	Response	N/A	N/A

(一) 最佳微脂體製備之方式篩選

為備製具較高載藥量的微脂體，因而篩選較佳微脂體製備之方法，本篇將兩種製備方法分別為傳統薄膜法及離子梯度法進行比較。如表二得知離子梯度法之製備法無法適當提高微脂體對葛根素之載藥量，可能原因為藥物特性與離子梯度法之間具很大的影響，因離子梯度法是透過藥物以分子的方式進入微脂體並解離，所以必須注重環境酸鹼值以及藥物的 pKa 值的調控。根據過去文獻得知葛根素分別具解離常數 (1) pKa1: 6.91 (2) pKa2: 9.93 [22-24]，本篇進行微脂體製備的過程中，其內、外部之酸鹼值分別為 PH 8.40 及 5.99，並以醋酸鈉離子以梯度法進行微脂體製備，以上條件理應可包覆更高劑量之藥物，然而不如預期。可能為葛根素本身不易解離，導致以離子梯度法進行製備過程會較不易將藥物送入微脂體中。由此得知相較離子梯度法，傳統薄膜法較適合做為葛根素微脂體製備的方法。

表二：各製備法之載藥量比較 [21]

Liposome	Puerarin Concentration	Loading content
Film-2	54.21 µg/mL	9.2%
Remote	27.33 µg/mL	4.6%

(二) 選定最佳微脂體之成分比例

經凍融法、薄膜水合法及濾膜擠壓法進行微脂體製備後，以動態光散射粒徑分析儀分析粒徑分布，其載藥量之計算方式如下：

$$\text{Percentage of drug loading} = \frac{\text{Mole}_{\text{puerarin}}}{\text{Mole}_{\text{PC}}} \times 100\%$$

並使用紫外光可見光分光光譜儀分析藥物濃度，而 EGG PC 濃度則以磷濃度法進行計算。下表三為不同組合之微脂體與其粒徑分布及載藥量。

表三：微脂體不同組合比例、粒徑分布及載藥量 [21]

Factor 1 EGG PC (mole)	Factor 2 Cholesterol (mole)	Factor 3 TPGS (mole)	Factor 4 Puerarin (mole)	Response 1 Diameter (nm)	Response 2 Percentage of drug loading (%)
10	2	1	2	137.5	2.41
10	1	1	2	121	3.08
10	2	2	1	138.9	3.23
10	1	1	1	127	3.24
10	1	2	2	125.3	3.5
10	1	2	1	122.4	4.69
10	2	1	1	133.5	4.75
10	2	2	2	140.2	4.94
6	1	1	2	123.3	4.29
6	2	2	1	122.8	4.43
6	2	1	1	133.3	4.48
6	1	1	1	116.9	5.1
6	1	2	1	109.4	5.42
6	1	2	2	108	6.25
6	2	1	2	135.8	8.04
6	2	2	2	130.8	9.87

表四為各組合對微脂體粒徑的影響，其以 ANOVA 分析結果得知，膽固醇為影響微脂體分布粒徑最多的參數 ($P < 0.0001$)。

表四：不同組合比例與微脂體粒徑的 ANOVA 分析結果 [21]

Diameter	p-value
A-EGG PC	0.0039
B-Cholesterol	< 0.0001
C-TPGS	0.1188
D-Puerarin	0.3474

最後進行不同組合與載藥量之間的影響探討，於 ANOVA 分析中得知主要之影響成分為 EGG PC ($p = 0.0127$)，下表五。經比較本篇選定最佳微脂體組合比例為 E6C2T2P2 (EGG PC :

Cholesterol : TPGS : Puerarin = 6 : 2 : 2 : 2)。

表五：不同微脂體組合比例及載藥量之 ANOVA 分析 [21]

Loading content	p-value
A-EGG PC	0.0127
B-Cholesterol	0.3019
C-TPGS	0.2775
D-Puerarin	0.2710

二、細胞實驗

本篇將人類角質細胞 (HaCaT cell line) 使用紫外線 UVB 照射刺激，誘導細胞老化以模擬人類皮膚光老化情形，接著進行不同的分析實驗進行研究，分別為：細胞多樣性分析 (MTT assay)、西方墨點法 (Western blotting)、ELISA。

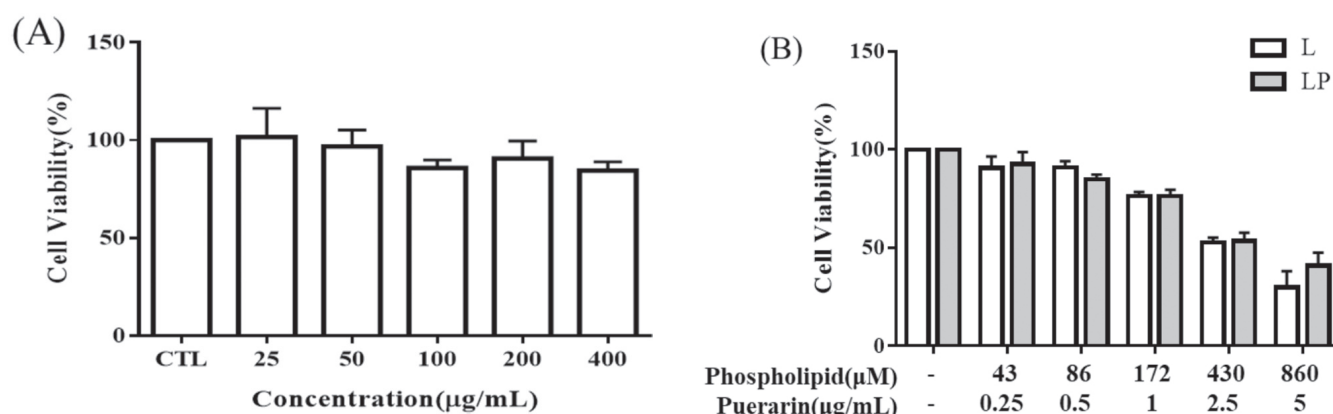
(一) 單純微脂體、葛根素微脂體與單純葛根素之細胞毒性測試

將 HaCaT 細胞分別進行不同濃度的單純微脂體、葛根素微脂體與單純葛根素處理並培養 1 小時，接著利用 MTT assay 進行細胞毒性分析，結果顯示，單純葛根素 25~400 $\mu\text{g/mL}$ 的濃度皆未有造成細胞的死亡，如圖一 (A)，因此最後選用

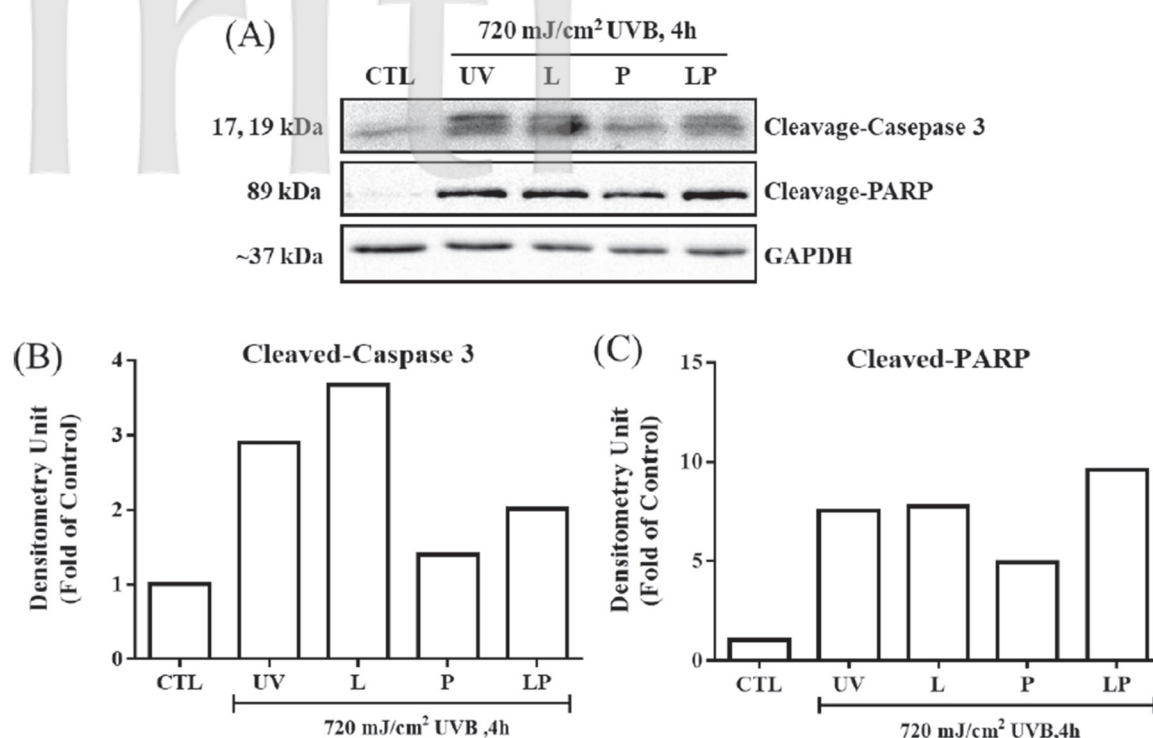
200 $\mu\text{g/mL}$ 作為後續實驗藥物濃度條件，而單純微脂體及葛根素微脂體之 MTT 結果發現，葛根素微脂體在葛根素 1 $\mu\text{g/mL}$ 以上的濃度開始會導致細胞存活率下降至 80% 以下，如圖一 (B)，由此得知微脂體在高濃度情況之下會造成細胞毒性反應，因此後續實驗將選用 0.5 $\mu\text{g/mL}$ 作為後續實驗藥物濃度條件。

(二) 葛根素微脂體及單純葛根素對抗紫外光致細胞凋亡之作用

HaCaT 細胞分別經單純葛根素 (P)、單純微脂體 (L)、葛根素微脂體 (LP) 等藥物處理 1 小時後，以 720 mJ/cm^2 UVB 紫外線照射後培養 4 小時，經 Western blotting 分析結果顯示，單純葛根素皆可抑制細胞凋亡蛋白 Cleaved-Caspase 3 與 Cleaved-PARP 表現，然而葛根素微脂體雖會有改善 UVB 照射細胞所導致的 Cleaved-Caspase 3 增加，但抑制效果卻不如單純葛根素的組別佳，另外在 Cleaved-PARP 凋亡蛋白結果中，卻也發現反而更提升了細胞凋亡的蛋白表現，如圖二，由此可知葛根素微脂體相較單純葛根素在抑制紫外線致細胞凋亡的效果並不佳。



圖一：藥物細胞毒性測試。將 HaCaT 細胞利用不同濃度單純葛根素、單純微脂體 (L)、葛根素微脂體 (LP) 進行處置後，進行 MTT 試驗以評估藥物對於細胞的毒性影響。本實驗各組別數據皆至少三次以上結果，並以平均值之 \pm 標準差作為計算。(A) 單純葛根素 MTT 結果 (B) 單純微脂體及葛根素微脂體 MTT 結果 [21]。



圖二：藥物作用於 HaCaT 細胞凋亡相關蛋白表現。HaCaT 細胞經葛根素不同處理的藥物處理 1 小時後，以 720 mJ/cm² UVB 紫外線照射 4 小時，接著萃取蛋白質並進行 Western blotting 分析。(A) 細胞凋亡相關蛋白 Western blotting 結果 (B-C) Western blotting 定量結果。藥物濃度：P-200 µg/mL、LP-500 ng/mL [21]。

(三) 葛根素微脂體及單純葛根素對抗紫外光致細胞發炎之作用

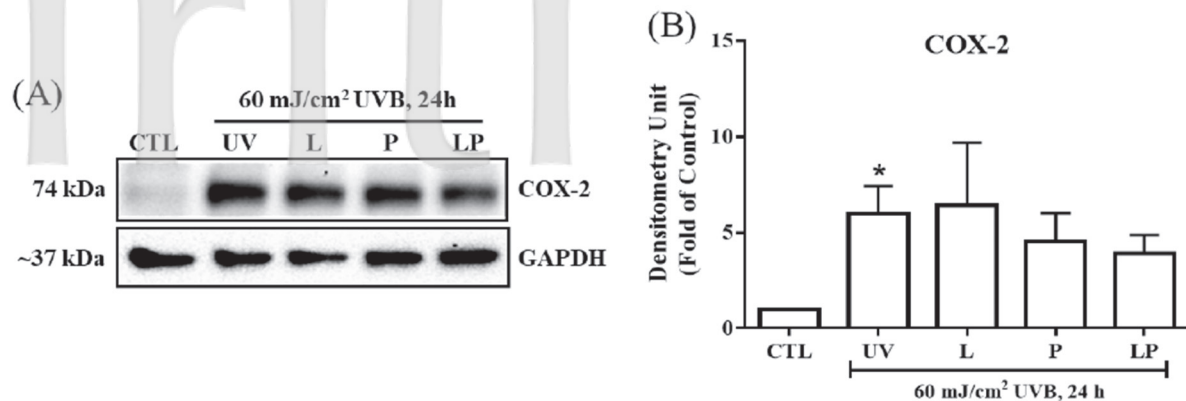
HaCaT 細胞分別經單純葛根素 (P)、單純微脂體 (L)、葛根素微脂體 (LP) 等藥物處理 1 小時後，以 UVB 60 mJ/cm² 紫外線照射後培養 24 小時，經 Western blotting 分析結果顯示，單純葛根素及葛根素微脂體皆有抑制 UVB 致細胞發炎蛋白 COX-2 提升的表現，然而現象不具顯著差異，如圖三。另外在 ELISA 的結果顯示，單純葛根素皆可抑制細胞發炎相關激素 PGE₂ 的表現，然而葛根素微脂體雖會有改善 UVB 照射細胞所導致的 PGE₂ 表現增加，但抑制效果卻不如單純葛根素的組別佳，如圖四。由此可知，葛根素微脂體相較單純葛根素在抑制紫外線導致細胞發炎的效果不佳，但仍有待評估。

HaCaT 細胞經葛根素不同處理的藥物處理 1

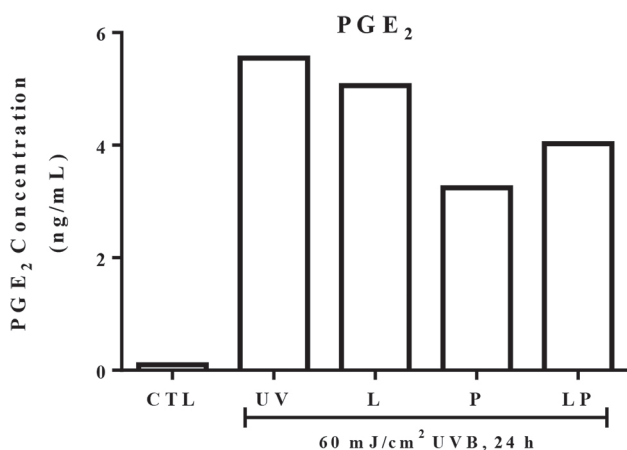
小時後，以 UVB (60 mJ/cm²) 紫外線照射後培養 24 小時，接著收集細胞培養液並進行 ELISA 分析。藥物濃度：P-200 µg/mL、LP-500 ng/mL。

肆、結論

皮膚老化最主要的外在原因為紫外線照射導致的光老化 [2]。當皮膚受紫外線照射導致皮膚老化的過程是透過誘發皮膚產生發炎情形及 DNA 損傷等 [6]。過去文獻指出紫外線長時間照射皮膚後會促使體內 COX-2 的表現，COX-2 則會將 AA 轉化為 PGE₂ [7]，進而導致皮膚產生發炎反應 [8, 9]，另外也有研究發現紫外線長期照射皮膚，會導致一連串生理反應而促使細胞凋亡相關蛋白如 Caspase 3 活化進而裁切 DNA 修補酵素 (PARP) 導致細胞產生凋亡現象 [10]。而過去文獻提出葛根



圖三：藥物作用於 HaCaT 細胞發炎相關蛋白表現 HaCaT 細胞經葛根素不同處理的藥物處理 1 小時後，以 UVB (60 mJ/cm²) 紫外線照射 24 小時，接著萃取蛋白質並進行 Western blotting 分析。本實驗各組別數據皆至少三次以上結果，並以平均值之 \pm 標準差作為計算，統計分析結果與控制組相比具統計意義，* $p < 0.05$ 。(A) 細胞發炎相關蛋白 Western blotting 結果 (B) Western blotting 定量結果。藥物濃度：P-200 μ g/mL、LP- 500 ng/mL[21]。



圖四：藥物作用於 HaCaT 細胞發炎相關細胞激素表現 [21]。

相關因子 COX-2 及 PGE₂ 的表現，然而葛根素微脂體在不造成細胞毒性的 500 ng/mL 劑量下卻不具有相同的效果，甚至還會促使 Cleaved-PARP 的表現。另從，結果發現單純微脂體處理的細胞組別，不管在細胞凋亡蛋白及發炎相關因子，幾乎都有促使凋亡及發炎反應的趨勢，因此推測葛根素微脂體的效果不如單純葛根素組別的原因為微脂體可能對細胞尚具有毒性的疑慮。

總結上述，本研究確立了葛根素本身可透過

抑制細胞凋亡蛋白 Cleaved-Caspase 3、Cleaved-PARP 與發炎相關因子 COX-2 及 PGE₂ 的表現進而達到改善 UVB 誘導 HaCaT 細胞的發炎及細胞凋亡反應，然而葛根素微脂體的效果卻不佳，推測原因為微脂體本身對細胞尚有毒性的疑慮，因此未來將針對微脂體備製進行探討及改善。

參考文獻

1. El-Domyati, M., et al., *Intrinsic aging vs. photoaging: a comparative histopathological, immunohistochemical, and ultrastructural study of skin*. Exp Dermatol, 2002. 11(5): p. 398-405.
2. Raut, S., et al., *Lecithin organogel: A unique micellar system for the delivery of bioactive agents in the treatment of skin aging*. Vol. 2. 2012. 8-15.
3. Widel, M., et al., *Induction of bystander effects by UVA, UVB, and UVC radiation in human fibroblasts and the implication of reactive oxygen species*. Free Radic Biol Med, 2014. 68: p. 278-

- 87.
4. Batista, L. F. Z., et al., *How DNA lesions are turned into powerful killing structures: Insights from UV-induced apoptosis*. Mutation Research-Reviews in Mutation Research, 2009. 681(2-3): p. 197-208.
5. Tulah, A. S. and M. A. Birch-Machin, *Stressed out mitochondria: The role of mitochondria in ageing and cancer focussing on strategies and opportunities in human skin*. Mitochondrion, 2013. 13(5): p. 444-453.
6. Harshit Shah, S. R. M., *Photoaging: New insights into its stimulators, complications, biochemical changes and therapeutic interventions*. Biomedicine & Aging Pathology, 2013. 3(3): p. 161-169.
7. Kim, S. R., et al., *Anti-wrinkle and anti-inflammatory effects of active garlic components and the inhibition of MMPs via NF-kappaB signaling*. PLoS One, 2013. 8(9): p. e73877.
8. Wolfle, U., et al., *UVB-induced DNA damage, generation of reactive oxygen species, and inflammation are effectively attenuated by the flavonoid luteolin in vitro and in vivo*. Free Radical Biology and Medicine, 2011. 50(9): p. 1081-1093.
9. Marwaha, V., et al., *T-oligo treatment decreases constitutive and UVB-induced COX-2 levels through p53- and NF kappa B-dependent repression of the COX-2 promoter*. Journal of Biological Chemistry, 2005. 280(37): p. 32379-32388.
10. Zeng, J. P., et al., *Repeated exposure of mouse dermal fibroblasts at a sub-cytotoxic dose of UVB leads to premature senescence: A robust model of cellular photoaging*. Journal of Dermatological Science, 2014. 73(1): p. 49-56.
11. Jiang, R. W., et al., *A comparative study on aqueous root extracts of Pueraria thomsonii and Pueraria lobata by antioxidant assay and HPLC fingerprint analysis*. J Ethnopharmacol, 2005. 96(1-2): p. 133-8.
12. Yang, X., et al., *Puerarin inhibits C-reactive protein expression via suppression of nuclear factor kappaB activation in lipopolysaccharide-induced peripheral blood mononuclear cells of patients with stable angina pectoris*. Basic Clin Pharmacol Toxicol, 2010. 107(2): p. 637-42.
13. Kim, K. M., et al., *Puerarin suppresses AGEs-induced inflammation in mouse mesangial cells: A possible pathway through the induction of heme oxygenase-1 expression*. Toxicology and Applied Pharmacology, 2010. 244(2): p. 106-113.
14. Hwang, Y. P. and H. G. Jeong, *Mechanism of phytoestrogen puerarin-mediated cytoprotection following oxidative injury: Estrogen receptor-dependent up-regulation of PI3K/Akt and HO-1*. Toxicology and Applied Pharmacology, 2008. 233(3): p. 371-381.
15. Liu, C. M., J. Q. Ma, and Y. Z. Sun, *Puerarin protects rat kidney from lead-induced apoptosis by modulating the PI3K/Akt/eNOS pathway*. Toxicology and Applied Pharmacology, 2012. 258(3): p. 330-342.
16. Kim, J., et al., *Puerarin inhibits the retinal pericyte apoptosis induced by advanced glycation end products in vitro and in vivo by inhibiting NADPH oxidase-related oxidative stress*. Free Radic Biol Med, 2012. 53(2): p. 357-65.
17. Sook Kim, Y., I. Soo Lee, and J. Sook Kim,

- Protective effects of puerariae radix extract and its single compounds on methylglyoxal-induced apoptosis in human retinal pigment epithelial cells.* J Ethnopharmacol, 2014. 152(3): p. 594-8.
18. Luo, C. F., et al., *Pharmacokinetics, tissue distribution and relative bioavailability of puerarin solid lipid nanoparticles following oral administration.* International Journal of Pharmaceutics, 2011. 410(1-2): p. 138-144.
19. Luo, C. F., et al., *Metabolic profile of puerarin in rats after intragastric administration of puerarin solid lipid nanoparticles.* Int J Nanomedicine, 2013. 8: p. 933-40.
20. Cevc, G. and U. Vierl, *Nanotechnology and the transdermal route: A state of the art review and critical appraisal.* J Control Release, 2010. 141(3): p. 277-99.
21. 葛根素微脂體製備與其對皮膚光老化的抑制作用。2015：李依潔。
22. Xi, J. Q. and R. Guo, *Acid-base equilibrium of puerarin in CTAB micelles.* Journal of Pharmaceutical and Biomedical Analysis, 2007. 43(1): p. 111-118.
23. Guo, J. X. R., *Interactions of Puerarin with Micelles: pKa Shifts and Thermodynamics.* Journal of Solution Chemistry, 2008. 37(1): p. 107-118.
24. Xi, J. and R. Guo, *Interactions of Puerarin with Micelles: pKa Shifts and Thermodynamics.* Vol. 37. 2007. 107-118.

慢性腎臟病合併糖尿病患者之血磷狀況與 營養衛教成效

黃雋¹ 林可欣¹ 劉珍芳^{1,2}

The Serum Phosphate Status and Improvement of Nutrition Education in Chronic Kidney Disease Patients with Diabetes

Jyun Huang¹, Ke-Shin Lin¹, Jen-Fang Liu^{1,2}

¹Department of Nutrition, Chang Gung Memorial Hospital, ²Department of Nutrition and Health Sciences, Research Center for Food and Cosmetic Safety, and Research Center for Chinese Herbal Medicine, College of Human Ecology, Chang Gung University of Science and Technology

(Received: October 8, 2018. Accepted: November 28, 2018.)

Diabetes is one of major causes of chronic kidney disease (CKD), higher dietary phosphorus intake and improper use of phosphate binder may result in hyperphosphatemia. Medical chart review was adopted with the source of Care and Health Education Plan for Patients with Pre-End-stage Renal Disease (Pre-ESRD) from July of 2016 to May of 2018. We assessed the prevalence of hyperphosphatemia in Chronic Kidney Disease-Diabetes (CKD-D) and Chronic Kidney Disease-Non Diabetes (CKD-ND). Furthermore, the effectiveness of nutrition education on phosphate levels and the causes of hyperphosphatemia were evaluated in CKD-D group combined with hyperphosphatemia. There are 153 and 169 patents respectively in CKD-D and CKD-ND. Results showed that the prevalence of hyperphosphatemia was significantly higher in CKD-D group than in CKD-ND group. After nutrition education, the serum phosphate levels and the multiplication of calcium (Ca) and phosphate (P) levels were decreased significantly in CKD combined with hyperphosphatemia without using phosphate binder. The main causes of hyperphosphatemia in CKD-D were processed food product intake and impaired renal function. Besides, there was 56% CKD-D patients using phosphate binder inappropriately. In conclusion, CKD patients with diabetes were prone to combine hyperphosphatemia. Moreover, nutrition education may help decrease phosphate levels.

Key words: Diabetes, Chronic kidney disease, Hyperphosphatemia, Nutrition education, Phosphate binders

前 言

根據衛生福利部 2007 年統計顯示，國人慢性腎臟病（Chronic kidney disease, CKD）的盛行率為

* Corresponding author: Jen-Fang Liu
E-mail: liujenfa@mail.cgu.edu.tw

11.3%⁽¹⁾。國家衛生研究院針對 20 歲以上進行健康檢查者的前瞻性研究結果也指出，台灣 CKD 的盛行率為 11.9%，其中第 3 期至第 5 期的盛行率為 7.1%⁽²⁾。糖尿病是造成末期腎臟病的主要原因之一，糖尿病控制不佳時，會加速腎功能惡化，研究發現，糖化血色素（Hemoglobin A1c, HbA1c）增加 1%，將來發生微量白蛋白尿及巨量白蛋白尿的風險分別增加 1.08 倍及 1.10 倍⁽³⁾。糖尿病合併 CKD 時，不但會增加罹患心血管疾病的風險，同時也會增加全死因死亡率（all-cause mortality）⁽⁴⁾。

腎絲球過濾率（estimated glomerular filtration rate, eGFR） $< 30 \text{ mL/min/1.73 m}^2$ 時，腎臟無法維持血磷的清除與平衡⁽⁵⁾，因此可能導致高血磷的發生，而長期高血磷則可能造成副甲狀腺功能亢進、骨病變、血管鈣化、心血管疾病等併發症⁽⁶⁾。過去文獻也指出，當血磷濃度增加 1 mg/dL ，eGFR 會降低 $0.154 \text{ mL/min/1.73 m}^2/\text{month}$ ，同時也會提高死亡風險^(7,8)。此外，血磷值增加，使鈣磷乘積隨之增加，而鈣磷乘積增加與心肌組織鈣化成正相關⁽⁹⁾。因此，維持適當的鈣磷平衡對 CKD 患者十分重要，根據美國國家腎臟基金會（National Kidney Foundation's Kidney Disease Outcomes Quality Initiative, K/DOQI）臨床指引，成年 CKD 第 3 期及第 4 期者血清磷應維持在 $2.7\text{--}4.6 \text{ mg/dL}$ ，鈣磷乘積應 $< 55 \text{ mg}^2/\text{dL}^2$ ；CKD 第 5 期者血清磷應維持在 $3.5\text{--}5.5 \text{ mg/dL}$ ，鈣磷乘積應 $< 55 \text{ mg}^2/\text{dL}^2$ ⁽¹⁰⁾。

CKD 患者可以經由適當的飲食控制及正確的使用磷結合劑控制血磷值。eGFR 介於 $25\text{--}55 \text{ mL/min/1.73 m}^2$ 時，由飲食中攝取的磷總量若能控制在 $5\text{--}10 \text{ mg/kg/day}$ ，大部分患者的血磷值都能維持在正常範圍內⁽¹⁰⁾。許多食物都富含磷，除了內臟、碳酸飲料、加工品等，未精製之全穀雜糧類、乳製品、堅果類等也為高磷食物來源。糖尿病患者常有應多選擇未精製之全穀雜糧類與堅果類等會有助於血糖控制的飲食觀念，但合併 CKD 的患者在接受慢性腎臟病中的低磷飲食衛教後，常表示糖尿病與慢性腎臟病的飲食控制原則互相矛盾，認為不知道該如何遵從。因此，如何讓 CKD 合併糖尿病患者可以維持血磷正常且飲食更多樣化對於醫護人員及營養師都是個重要的課題。

當飲食控制已無法維持腎衰竭病患正常血磷值時，需合併使用磷結合劑以改善高血磷⁽¹¹⁾，目前常用的磷結合劑分為三大類，分別為含鈣或鋁及不

含鈣或鋁的磷結合劑。本院常開立的為含鈣磷結合劑，包含碳酸鈣（calcium carbonate）及醋酸鈣（calcium acetate）。磷結合劑的作用機制主要是透過與食物中的磷結合以減少磷的吸收，進而降低血磷，因此磷結合劑需在餐中與食物一同食用，且若與食物混合的越均勻，降磷的效果越好^(11,12)。臨床上由於病患可能因為不了解磷結合劑的使用目的，或其正確的使用方式，易造成磷結合劑用藥不當的情形發生，但是目前少有研究探討 CKD 患者使用磷結合劑的現況及用藥不當之原因。

衛生福利部中央健康保險署於民國 96 年推動 Health Education Plan for Patients with Pre-End-stage Renal Disease（Pre-ESRD）預防性計畫及病人衛教計畫，本研究擬藉由收集 Pre-ESRD 計畫轉介至 CKD 衛教室初診病患的血液生化值及飲食攝取情形，探討 CKD 患者合併糖尿病與否之初診患者，其高血磷人數之差異；另外分析 CKD 合併糖尿病患者造成高血磷之可能原因及經營養師衛教後血磷改善成效。

研究對象與方法

一、收案對象

本研究經財團法人長庚紀念醫院人體試驗審議委員會核准後開始執行（計畫編號：1807240032）。收案對象為經 Pre-ESRD 計畫轉介至 CKD 衛教室之初診病患，納入條件為 CKD 第 3b 期（eGFR 介於 $30\text{--}44 \text{ mL/min/1.73 m}^2$ ）、第 4 期（eGFR 介於 $15\text{--}29 \text{ mL/min/1.73 m}^2$ ）及第 5 期（eGFR $< 15 \text{ mL/min/1.73 m}^2$ ）者。經腎臟專科醫師評估，若符合收案條件，則將病患轉介至慢性腎臟病衛教室予以收案。資料分析時，排除年齡 < 18 歲、懷孕期或哺乳期、資料不完整（如不願提供飲食記錄、磷結合劑使用方式、無血清血磷值等）、衛教後三個月內已開始透析或死亡者。

二、收案與衛教流程

CKD 患者轉介至慢性腎臟病衛教室後，CKD 衛教師將會紀錄個案疾病史、藥物使用情形、生活型態、體位及血液生化值等，並進行護理衛教；接著由營養師以 24 小時飲食回憶法為依據，評估個案平日飲食攝取情形，同時詢問個案磷結合劑使用現

況，最後由營養師根據個案狀況給予個人化營養衛教與飲食計畫。若個案有使用磷結合劑，也會衛教磷結合劑之使用目的及正確使用方式。所有衛教結束後，提醒個案，衛教後三個月需回慢性腎臟病衛教室追蹤。參與本研究之所有營養師及 CKD 衛教師皆受過慢性腎臟病課程，並取得專業證照。

三、資料收集及分組

本研究回溯 105 年 7 月至 107 年 5 月底之病歷，收集病患下列資料：（1）基本資料：年齡、性別、有無糖尿病或高血壓；（2）體位資料：身高、體重，並計算身體質量指數（body mass index, BMI）；（3）收縮壓及舒張壓；（4）血液生化值：尿素氮、肌酸酐、HbA1c、血色素、血清鈣（calcium, Ca）及磷（phosphate, P）濃度；（5）飲食評估：每日熱量、蛋白質攝取量及食物種類；（6）磷結合劑：磷結合劑種類、劑量及使用方式。另外，根據 2012 年 K/DOQI 臨床指引建議，採 Modification of Diet in Renal Disease (MDRD) Study equation 公式計算 eGFR，作為 CKD 分期標準⁽¹⁰⁾。並計算鈣磷乘積。

MDRD 公式：

$$\begin{aligned} \text{eGFR (mL/min/1.73 m}^2\text{)} \\ = 175 (\text{Serum Creatinine})^{-1.154} \times (\text{Age})^{-0.203} \\ \times 0.742 (\text{if female}) \times 1.21 (\text{if African American}) \end{aligned}$$

四、資料分析與統計方法

資料分析部分，將 CKD 患者依有無糖尿病分為兩組，分別為慢性腎臟病合併糖尿病組（Chronic Kidney Disease-Diabetes, CKD-D）及慢性腎臟病無合併糖尿病組（Chronic Kidney Disease-Non Diabetes, CKD-ND），並依據本院生化數值檢驗建議，將血清磷 < 2.4 mg/dL 定義為低血磷，數值介於 2.4-4.6 mg/dL 為正常，數值 > 4.6 mg/dL 為高血磷。

資料以 SPSS 16.0 版統計軟體進行資料分析，數值均以平均值 ± 標準差、人數（n）或百分比（%）呈現，以 independent t-test 及 Chi-Square test 分析 CKD-D 組與 CKD-ND 組之基本資料、體位資料、血壓、血液生化值及飲食攝取量之差異，並以 Fisher exact test 分析兩組血清磷分佈狀況。以線性迴歸分析進一步瞭解 CKD-D 組中患者血磷控制不佳之原因。CKD-D 組中高血磷者衛教前後之體位資料、血液生化值、熱量及蛋白質攝取量則以 paired t

-test 及 Wilcoxon 進行分析。當 $p < 0.05$ 定義為具統計上之差異。

結 果

一、基本資料

本研究符合條件者共 322 位，CKD-D 組為 169 位，CKD-ND 組為 153 位，兩組患者之基本資料如表一所示。平均年齡 CKD-D 組為 65.8 ± 12.2 歲，CKD-ND 組為 64.3 ± 16.0 歲。CKD 分期部分，CKD-D 組第 3b 期、第 4 期及第 5 期比例則分別為 28.4%、36.7% 及 34.9%，而 CKD-ND 組分別為 25.5%、35.9% 及 38.5%，兩組的分期分佈無顯著差異。CKD-D 組之平均體重及 BMI 顯著高於 CKD-ND 組（ 69.2 ± 13.7 kg 及 63.1 ± 14.0 kg, $p < 0.001$ ； 26.7 ± 4.3 kg/m² 及 24.8 ± 4.8 kg/m², $p < 0.001$ ）。兩組病患舒張壓無顯著差異，但 CKD-D 組之平均收縮壓顯著高於 CKD-ND 組（ 145.5 ± 23.7 mmHg 及 138.6 ± 19.3 mmHg, $p = 0.001$ ）。

二、血液生化值及飲食攝取情形

兩組血液生化值如表二所示，平均 HbA1c CKD-D 組為 7.5 ± 1.6 %，CKD-ND 組為 5.7 ± 0.5 %（ $p < 0.001$ ）。平均肌酸酐、尿素氮、eGFR、血色素兩組間皆無顯著差異。

兩組飲食攝取量如表二所示，CKD-D 組及 CKD-ND 組平均熱量攝取分別為 21.5 ± 6.1 kcal/kg body weight/day 及 24.8 ± 6.6 kcal/kg body weight/day（ $p < 0.001$ ）；平均蛋白質攝取量分別為 0.7 ± 0.3 g/kg body weight/day 及 0.8 ± 0.3 g/kg body weight/day（ $p < 0.001$ ）。

三、血清磷

CKD-D 組平均血清磷濃度為 4.4 ± 1.0 mg/dL，CKD-ND 組則為 4.2 ± 1.0 mg/dL，兩組間未達顯著差異（ $p = 0.079$ ）（表二）。進一步了解兩組血清磷分佈情形，結果顯示，CKD-D 組無低血磷者，血磷正常及高血磷者之比例分別為 63.3% 及 36.7%；而 CKD-ND 組低血磷者之比例為 1.9%，血磷正常者之比例為 70.6%，高血磷者之比例為 27.5%，CKD-D 組及 CKD-ND 組之血清磷分佈達顯著差異（ $p = 0.035$ ）（表三）。

表一 慢性腎臟病無合併糖尿病組及慢性腎臟病合併糖尿病組患者之基本資料¹⁻³Table 1. Characteristics of chronic kidney disease with or without diabetes¹⁻³

	CKD-ND 組 (n = 153)	CKD-D 組 (n = 169)
性別 (男/女)	82/71	98/71
年齡 (year)	64.3 ± 16.0	65.8 ± 12.2
慢性腎臟病分期		
第 3b 期	39 (25.5%)	48 (28.4%)
第 4 期	55 (35.9%)	62 (36.7%)
第 5 期	59 (38.6%)	59 (34.9%)
身高 (cm)	159.3 ± 8.9	160.6 ± 8.6
體重 (kg)	63.1 ± 14.0	69.2 ± 13.7*
身體質量指數 (kg/m ²)	24.8 ± 4.8	26.7 ± 4.3*
舒張壓 (mmHg)	76.4 ± 12.4	74.6 ± 11.4
收縮壓 (mmHg)	138.6 ± 19.3	145.5 ± 23.7*

¹ 數值以人數 (n)、平均值 ± 標準差或百分比 (%) 表示。² CKD-ND: Chronic Kidney Disease-Non Diabetes; CKD-D: Chronic Kidney Disease-Diabetes。³ 以 independent *t*-test 及 Chi-Square test 進行統計分析, **p* < 0.05 表示具統計上之顯著差異。表二 慢性腎臟病無合併糖尿病組及慢性腎臟病合併糖尿病組患者之飲食攝取及血液生化值¹⁻³Table 2. Dietary intake and blood biochemical values of chronic kidney disease with or without diabetes¹⁻³

	CKD-ND 組 (n = 153)	CKD-D 組 (n = 169)
熱量攝取 (kcal/kg body weight/day)	24.8 ± 6.6	21.5 ± 6.1*
蛋白質攝取 (g/kg body weight/day)	0.8 ± 0.3	0.7 ± 0.3*
肌酸酐 (mg/dL)	3.7 ± 2.0	3.6 ± 2.0
尿素氮 (mg/dL)	50.1 ± 23.9	52.1 ± 25.1
eGFR (mL/min/1.73 m ²)	21.2 ± 11.6	22.4 ± 11.6
HbA1c (%)	5.7 ± 0.5	7.5 ± 1.6*
血清鈣 (mg/dL)	8.9 ± 0.7	8.9 ± 0.6
血清磷 (mg/dL)	4.2 ± 1.0	4.4 ± 1.0
鈣磷乘積 (mg ² /dL ²)	37.0 ± 9.0	38.6 ± 8.1
血色素 (g/dL)	10.6 ± 2.0	10.8 ± 2.0

¹ 數值以人數 (n) 或平均值 ± 標準差表示。² CKD-ND: Chronic Kidney Disease-Non Diabetes ; CKD-D: Chronic Kidney Disease-Diabetes ; eGFR: estimated glomerular filtration rate ; HbA1c: Hemoglobin A1c。³ 以 independent *t*-test 進行統計分析, **p* < 0.05 表示具統計上之顯著差異。

四、CKD-D 組中高血磷者，衛教前後血液生化值及飲食攝取變化

CKD-D 組中合併高血磷且複診時有完整血液生化值及飲食記錄者共 62 位，結果如表四所示。衛教前後患者之體重、BMI、尿素氮、eGFR、血清鈣及血色素皆未達顯著差異，但平均血清磷濃度由 5.5 ±

0.8 mg/dL 降低至 5.1 ± 1.0 mg/dL (*p* = 0.009)，且鈣磷乘積也由 47.3 ± 6.4 mg²/dL² 降低至 44.6 ± 7.8 mg²/dL² (*p* = 0.006)，然而肌酸酐卻由 5.1 ± 2.2 mg/dL 增加至 5.6 ± 2.8 mg/dL (*p* < 0.05)。

衛教前後飲食攝取變化如表四所示。結果顯示，衛教前後患者之熱量攝取未達顯著差異，但平均蛋白質攝取量由 0.8 ± 0.3 g/kg body weight/day 顯

表三 慢性腎臟病無合併糖尿病組及慢性腎臟病合併糖尿病組患者之血清磷分佈狀況¹⁻²**Table 3.** Distribution of phosphorus in chronic kidney disease-non diabetes group and chronic kidney disease-diabetes group patients¹⁻²

	CKD-ND 組	CKD-D 組
P < 2.4 mg/dL	3 (1.9%)	0
2.4 ≤ P ≤ 4.6 mg/dL	108 (70.6%)	107 (63.3%)
P > 4.6 mg/dL	42 (27.5%)	62 (36.7%)
總人數 (人)	153	169

¹ 數值以人數 (n) 或百分比 (%) 表示。² CKD-ND: Chronic Kidney Disease-Non Diabetes ; CKD-D: Chronic Kidney Disease-Diabetes ; P: phosphorus 。表四 慢性腎臟病合併糖尿病的高血磷患者，衛教前後體重、飲食攝取及血液生化值變化¹⁻³**Table 4.** Changes in body weight, dietary intake and blood biochemical values before and after nutrition education in chronic kidney disease patients with diabetes and hyperphosphatemia¹⁻³

	衛教前 (n = 62)	衛教後 (n = 62)
體重 (kg)	67.4 ± 12.3	66.3 ± 15.3
身體質量指數 (kg/m ²)	26.5 ± 3.3	26.1 ± 4.8
熱量攝取 (kcal/kg body weight/day)	21.3 ± 5.7	21.3 ± 4.4
蛋白質攝取 (g/kg body weight/day)	0.8 ± 0.3	0.7 ± 0.2*
肌酸酐 (mg/dL)	5.1 ± 2.2	5.6 ± 2.8*
尿素氮 (mg/dL)	71.9 ± 24.6	72.8 ± 28.8
eGFR (mL/min/1.73 m ²)	14.0 ± 8.6	13.4 ± 9.3
血清鈣 (mg/dL)	8.8 ± 0.7	8.7 ± 0.8
血清磷 (mg/dL)	5.5 ± 0.8	5.1 ± 1.0*
鈣磷乘積 (mg ² /dL ²)	47.3 ± 6.4	44.6 ± 7.8*
血色素 (g/dL)	9.7 ± 1.6	9.8 ± 1.7

¹ 數值以人數 (n) 或平均值 ± 標準差表示。² eGFR: estimated glomerular filtration rate 。³ 以 paired t-test 進行統計分析，**p* < 0.05 表示具統計上之顯著差異。

著減少為 0.7 ± 0.2 g/kg body weight/day (*p* < 0.001)。

五、高血磷 CKD-D 病患未使用磷結合劑者，衛教前後血液生化值及飲食攝取變化

為了瞭解上述結果中血清磷濃度改善是否是因為磷結合劑使用，故進一步排除 18 位使用磷結合劑者，最後共 44 位高血磷 CKD-D 患者納入分析，結果如表五所示。衛教前後患者之體重、BMI、肌酸酐、尿素氮、eGFR、血清鈣及血色素皆未達顯著差異，而平均血清磷濃度由 5.2 ± 0.5 mg/dL 降低至 5.0 ± 0.9 mg/dL (*p* < 0.05)，且鈣磷乘積由 45.7 ± 4.3 mg²/dL² 降低至 43.1 ± 6.8 mg²/dL² (*p* < 0.05)，表示未使用磷結合劑的狀況下，高血磷 CKD-D 患者

仍可透過控制飲食改善高血磷。

未使用磷結合劑的高血磷 CKD-D 患者，飲食攝取變化發現，衛教前後患者之熱量攝取量 (kcal/kg body weight/day) 及蛋白質攝取量 (g/kg body weight/day) 皆未達顯著差異 (表五)。

六、CKD-D 組中高血磷且合併使用磷結合劑者，衛教前後血清磷、鈣及鈣磷乘積變化

此部分共有 18 位患者納入分析，結果顯示，CKD-D 組高血磷且合併使用磷結合劑者，衛教前後平均血清磷濃度分別為 6.0 ± 1.0 mg/dL 及 5.6 ± 0.9 mg/dL，衛教前後之血清磷濃度未達顯著差異 (*p* = 0.23)；衛教前後平均血清鈣濃度分別為 8.5 ± 0.5

表五 慢性腎臟病合併糖尿病、高血磷且無使用磷結合劑者，衛教前後體重、飲食攝取及血液生化值變化¹⁻³
Table 5. Changes in body weight, dietary intake and blood biochemical values before and after nutrition education in without taking phosphate binder patients with hyperphosphatemia and chronic kidney disease with diabetes¹⁻³

	衛教前 (n = 44)	衛教後 (n = 44)
體重 (kg)	68.7 ± 12.4	67.3 ± 16.3
身體質量指數 (kg/m ²)	27.2 ± 3.3	26.7 ± 5.3
熱量攝取 (kcal/kg body weight/day)	20.6 ± 5.6	21.4 ± 4.6
蛋白質攝取 (g/kg body weight/day)	0.7 ± 0.3	0.7 ± 0.2
肌酸酐 (mg/dL)	4.6 ± 2.1	4.9 ± 2.5
尿素氮 (mg/dL)	66.6 ± 22.6	64.3 ± 23.7
eGFR (mL/min/1.73 m ²)	15.6 ± 9.3	15.4 ± 10.0
血清鈣 (mg/dL)	8.7 ± 0.7	8.7 ± 0.8
血清磷 (mg/dL)	5.2 ± 0.5	5.0 ± 0.9*
鈣磷乘積 (mg ² dL ²)	45.7 ± 4.3	43.1 ± 6.8*
血色素 (g/dL)	9.6 ± 1.6	9.7 ± 1.8

¹ 數值以人數 (n) 或平均值 ± 標準差表示。

² eGFR: estimated glomerular filtration rate。

³ 以 paired t-test 進行統計分析，* $p < 0.05$ 表示具統計上之顯著差異。

表六 慢性腎臟病合併糖尿病者，血磷控制不佳之原因分析¹⁻²

Table 6. Factors related to hyperphosphatemia in chronic kidney disease with diabetes patients¹⁻²

	血清磷濃度	
	Mean ± SD	β^3
攝取加工品 (罐頭類、醃製品、烘焙類食品等)	4.7 ± 1.0	0.17*
攝取碳酸飲料、湯品、茶飲者等	4.5 ± 1.2	0.04
攝取乳製品等	4.4 ± 1.0	-0.09
攝取未精製全穀雜糧類、豆類、堅果類等	4.4 ± 1.0	0.06
腎功能不全 (eGFR < 10 mL/min/1.73 m ²)	5.8 ± 1.1	0.55**
蛋白質攝取過多	4.5 ± 1.1	-0.09

¹ eGFR: estimated glomerular filtration rate。

² n=169；以 Linear regression 進行統計分析，* $p < 0.01$ 、** $p < 0.001$ 表示具統計上之顯著差異。

³ β ：標準化迴歸係數。

mg/dL 及 8.7 ± 0.9 mg/dL，衛教前後之血清鈣濃度未達顯著差異 ($p = 0.23$)。衛教前鈣磷乘積為 50.5 ± 8.9 mg/dL，衛教後則為 48.5 ± 7.2 mg/dL，衛教前後亦未達顯著差異 ($p = 0.199$)。

七、CKD-D 組中，血磷控制不佳之原因分析

本研究分析 CKD-D 組患者 eGFR 值及所攝取之食物種類，並進一步分析造成其高血磷的可能原

因，結果如表六所示。與無攝取加工品相比，攝取加工品者之平均血清磷濃度會增加 0.17 mg/dL ($p < 0.01$)；與 eGFR ≥ 10 mL/min/1.73 m² 相比，腎功能不全者 (eGFR < 10 mL/min/1.73 m²) 之平均血清磷濃度會增加 0.55 mg/dL ($p < 0.001$)。而攝取碳酸飲料、湯品、茶飲者等或攝取乳製品或攝取未精製全穀雜糧類、豆類、堅果類等或蛋白質攝取過多與血磷控制不佳皆無顯著相關。

討 論

幾乎所有食物中都含有磷，除了磷含量外，也需考量食物中磷的吸收率，磷的吸收率會因其存在的型式而不同，若以磷-蛋白質比（phosphorus-to-protein ratio）作為衛教依據，選擇攝取磷-蛋白質比 $< 15 \text{ mg/g}$ 之食物有助於 CKD 患者血磷值調控^(13,14)。動物性來源的食物多以有機磷的型式存在，經腸胃道消化後吸收率約 40-60%，而植物性來源的食物雖也為有機磷，但多以植酸的型式儲存，故吸收率僅約 10-30%^(14,15,16)。此外，過去研究也指出，飲食中蛋白質-纖維比（protein-fiber ratio）和血中 *p-cresyl sulfate*（PCS）及 *indoxyl sulfate*（IS）濃度有關⁽¹⁷⁾，Patel 等人也發現，相較於未限制蛋白質來源者，食用植物性蛋白質的素食者，其 PCS 及 IS 產生量顯著較少⁽¹⁸⁾。全穀雜糧、豆類及堅果種子類雖為高磷食物來源，但本研究結果顯示，此類食物並非造成血磷控制不佳之主因。此類食物雖然磷吸收率較低，可能不是導致高血磷的主要原因，但因其低生物價蛋白質含量較多，故建議 CKD 患者仍需避免攝取。而針對蛋白質來源，研究證實與動物性蛋白質相比，攝取植物性蛋白質能改善尿素氮、血清磷濃度及蛋白尿情形⁽¹⁹⁾。

本研究結果，高血磷患者中攝取乳製品者約 8%，表示仍有不少 CKD 患者不知需限制乳製品之攝取。乳製品之磷-蛋白質比大部分皆介於 15-30 mg/g⁽¹⁴⁾，且乳製品中的磷多與酪蛋白結合，以 *casein phosphate* 的型式儲存⁽²⁰⁾，因此難以再被磷結合劑結合，故建議有攝取乳製品習慣之 CKD 患者，應避免攝取一般乳類與乳製品，可以市售低磷鉀之慢性腎臟病配方取代一般乳製品。

文獻指出，加工品除了食物本身所含的磷以外，其所含之食品添加物，如磷酸氫鈣、偏磷酸鈉、焦磷酸鉀等通常都以無機磷的型式存在，吸收率高達 80-100%^(14,16)，而避免攝取含磷添加物之食品可改善高血磷症⁽²¹⁾。本研究結果顯示，高血磷患者中攝取加工品及碳酸飲料之比例超過 50%，因此建議應加強病患食品標示閱讀能力，並加強衛教以天然、新鮮食物取代加工品之觀念，以有效控制血磷值。

碳酸鈣及醋酸鈣為含鈣的磷結合劑，因副作用少、價格相對便宜且與磷結合力佳，故临床上廣泛

被使用，而磷結合劑服用的時機及方式會影響其效果，如碳酸鈣磨粉拌於食物中降磷效果最佳，醋酸鈣則可於餐間整顆吞食⁽²²⁾。

臨床常見病患因不清楚磷結合劑之使用目的，而導致磷結合劑使用不當。本研究 CKD 合併糖尿病且高血磷者中，共 18 位使用磷結合劑，其中磷結合劑使用不當之比例達 56%。常見磷結合劑使用不當的原因包含（1）服用多種藥物，因而忘記服用部分藥物；（2）不清楚磷結合劑之使用目的，故未隨餐服用（空腹或飯後服用）；（3）認為將磷結合劑磨粉或分散於餐中服用太麻煩或味道不佳，因此一口吞下磷結合劑；（4）服用磷結合劑後造成便秘，因此自行停藥；（5）認為磷結合劑用於補鈣，自行購買鈣片補充。

除了磷結合劑的使用方式外，磷結合劑的使用劑量也應隨食物的磷含量而調整，當蛋白質攝取量增加時，磷結合劑劑量也應隨之增加。然而，針對晚期 CKD 患者，每日由飲食或磷結合劑中所攝取的總鈣量不宜超過 2000 mg，其中磷結合劑中所含的鈣應控制在 1500 mg 內，以減少 CKD 患者血管硬化的風險⁽²³⁾。CKD 照護團隊如何讓 CKD 患者能以最小劑量的磷結合劑發揮最大的磷結合效果是個重要的課題。

適當的營養教育可改善患者知識及行為之遵從度，且與血磷濃度降低有關⁽²⁴⁾。Thomas 等人研究也指出，當透析的腎衰竭患者對於高血磷併發症及飲食有足夠知識，加上正向遵從醫療人員指導的態度和良好的支持下，其血磷控制較佳⁽²⁵⁾。本研究經 Pre-ESRD 計畫收案，藉由跨領域醫療團隊合作，探討 CKD 合併糖尿病患者血磷控制不佳之原因，並針對原因給予正確的飲食觀念及提高磷結合劑服用遵從度，進而改善高血磷。期望本研究能提供醫護人員及營養師臨床照護 CKD 或 CKD 合併糖尿病患者之參考，以減少骨病變、心血管疾病等併發症，進而提升患者的生活品質，同時減少醫療資源支出。

本研究限制為研究期間僅三個月，且個案數較少。未來計畫經 Pre-ESRD 計畫收案的患者，將每三個月持續接受衛教直到進入透析治療，故本研究也將追蹤長期衛教對於患者飲食遵從度、血磷值及磷結合劑使用情形等之影響，作為臨床衛教之參考。

結 論

CKD 患者合併糖尿病時可能較易有高血磷之問題，建議營養師於病患初診時，需衛教高磷食物種類及食物選擇技巧，尤其應減少其加工品攝取頻率及攝取量。CKD 患者合併糖尿病，若有使用磷結合劑時，亦需詳細說明磷結合劑之使用目的及正確服用方式，以有效維持鈣磷平衡。

致 謝

感謝慢性腎臟病照護團隊（營養治療科、腎臟科及慢性腎臟病衛教師）共同努力，使本研究順利完成，特此一併感謝。

參考文獻

1. 白其卉、王玉皎、湯藻薰、孫建安。2007 年台灣地區高血壓、高血糖、高血脂之追蹤調查研究專輯，2007。
2. Wen CP, Cheng TY, Tsai MK, Chang YC, Chan HT, Tsai SP, Chiang PH, Hsu CC, Sung PK, Hsu YH, Wen SF. All-cause mortality attributable to chronic kidney disease: a prospective cohort study based on 462 293 adults in Taiwan. *Lancet*. 2008;371:2173-82.
3. Retnakaran R, Cull CA, Thorne KI, Adler AI, Holman RR; UKPDS Study Group. Risk factors for renal dysfunction in type 2 diabetes: U.K. Prospective Diabetes Study 74. *Diabetes*. 2006;55:1832-9.
4. Collins AJ, Foley RN, Herzog C, Chavers B, Gilbertson D, Ishani A, Kasiske B, Liu J, Mau LW, McBean M, Murray A, St Peter W, Guo H, Gustafson S, Li Q, Li S, Li S, Peng Y, Qiu Y, Roberts T, Skeans M, Snyder J, Solid C, Wang C, Weinhandl E, Zaun D, Arko C, Chen SC, Dalleska F, Daniels F, Dunning S, Ebben J, Frazier E, Hanzlik C, Johnson R, Sheets D, Wang X, Forrest B, Constantini E, Everson S, Eggers P, Agodoa L. US Renal Data System 2010 Annual Data Report. *Am J Kidney Dis*. 2011;57 (1 Suppl 1):A8, e1-526.
5. Slatopolsky E, Gradowska L, Kashemsant C, Keltner R, Manley C, Bricker NS. The control of phosphate excretion in uremia. *J Clin Invest*. 1966;45:672-7.
6. Llach F, Velasquez Forero F. Secondary hyperparathyroidism in chronic renal failure: pathogenic and clinical aspects. *Am J Kidney Dis*. 2001;38(Suppl 5):S20-33.
7. Voormolen N, Noordzij M, Grootendorst DC, Beetz I, Sijpkens YW, van Manen JG, Boeschoten EW, Huisman RM, Krediet RT, Dekker FW; PREPARE study group. High plasma phosphate as a risk factor for decline in renal function and mortality in pre-dialysis patients. *Nephrol Dial Transplant*. 2007;22:2909-16.
8. Palmer SC, Hayen A, Macaskill P, Pellegrini F, Craig JC, Elder GJ, Strippoli GF. Serum levels of phosphorus, parathyroid hormones, and calcium and risk of death and cardiovascular disease in individuals with chronic kidney disease: a systematic review and meta-analysis. *JAMA*. 2011;305:1119-27.
9. Rostand SG, Sanders C, Kirk KA, Rutsky EA, Fraser RG. Myocardial calcification and cardiac dysfunction in chronic renal failure. *Am J Med*. 1988;85:651-7.
10. Inker LA, Astor BC, Fox CH, Isakova T, Lash JP, Peralta CA, Kurella Tamura M, Feldman HI. KDOQI US commentary on the 2012 KDIGO clinical practice guideline for the evaluation and management of CKD. *Am J Kidney Dis*. 2014;63:713-35.
11. Schucker JJ, Ward KE. Hyperphosphatemia and phosphate binders. *Am J Health Syst Pharm*. 2005;62:2355-61.
12. Emmett M, Sirmon MD, Kirkpatrick WG, Nolan CR, Schmitt GW, Cleveland MB. Calcium acetate control of serum phosphorus in hemodialysis patients. *Am J Kidney Dis*. 1991;17:544-50.
13. Kalantar-Zadeh K, Fouque D. Nutritional Management of Chronic Kidney Disease. *N Engl J Med*. 2017;377:1765-76.
14. Kalantar-Zadeh K, Gutekunst L, Mehrotra R, Kovesdy CP, Bross R, Shinaberger CS, Noori N, Hirschberg R, Benner D, Nissenson AR, Kopple JD. Understanding sources of dietary phosphorus in the treatment of patients with chronic kidney disease. *Clin J Am Soc Nephrol*. 2010;5: 519-30.
15. Uribarri J. Phosphorus homeostasis in normal health and in chronic kidney disease patients with special emphasis on dietary phosphorus intake. *Semin Dial*. 2007;20:295-301.
16. Noori N, Sims JJ, Kopple JD, Shah A, Colman S, Shinaberger CS, Bross R, Mehrotra R, Kovesdy CP, Kalantar-Zadeh K. Organic and inorganic dietary phosphorus and its management in chronic kidney disease. *Iran J Kidney Dis*. 2010;4:89-100.
17. Rossi M, Johnson DW, Xu H, Carrero JJ, Pascoe E, French C, Campbell KL. Dietary protein-fiber ratio associates with circulating levels of indoxyl sulfate and p-cresyl sulfate in chronic kidney disease patients. *Nutr Metab Cardiovasc Dis*. 2015;25:860-5.
18. Patel KP, Luo FJ, Plummer NS, Hostetter TH, Meyer TW. The production of p-cresol sulfate and indoxyl sulfate in vegetarians versus omnivores. *Clin J Am Soc Nephrol*. 2012;7:982-8.
19. Azadbakht L, Esmailzadeh A. Soy-protein consumption and kidney-related biomarkers among type 2 diabetics: a crossover, randomized clinical trial. *J Ren Nutr*. 2009; 19:479-86.
20. Srinivasan Damodaran KLP, Owen R. Fennema. Fennema's Food Chemistry, Fourth Edition. (Food Science and Technology). 2007.
21. Sullivan C, Sayre SS, Leon JB, Machekano R, Love TE, Porter D, Marbury M, Sehgal AR. Effect of food additives on hyperphosphatemia among patients with end-stage

- renal disease: a randomized controlled trial. JAMA. 2009; 301:629-35.
22. Coladonate JA: Control of hyperphosphatemia among patients with ESRD. J Am Soc Nephrol. 2005;16 Suppl 2:S107-14.
23. Guérin AP, London GM, Marchais SJ, Metivier F. Arterial stiffening and vascular calcifications in end-stage renal disease. Nephrol Dial Transplant. 2000;15:1014-21.
24. Schlatter S and Ferrans CE. Teaching program effects on high phosphorus levels in patients receiving hemodialysis. ANNA J. 1998;25:31-6.
25. Thomas LK, Sargent RG, Michels PC, Richter DL, Valois RF, Moore CG. Identification of the factors associated with compliance to therapeutic diets in older adults with end stage renal disease. J Ren Nutr. 2001;11:80-9.

慢性腎臟病合併糖尿病患者之血磷狀況與 營養衛教成效

黃雋¹ 林可欣¹ 劉珍芳^{1,2}

¹林口長庚紀念醫院 營養治療科

²長庚學校財團法人長庚科技大學民生學院保健營養系暨食品暨化妝品安全研究中心
和中草藥研究中心

(收稿日期：107 年 10 月 8 日。接受日期：107 年 11 月 28 日)

摘要 糖尿病為造成慢性腎臟病 (Chronic kidney disease, CKD) 主要原因之一，當飲食控制不佳及磷結合劑使用不當時可能導致高血磷。本研究回溯 105 年 7 月至 107 年 5 月之病歷，對象為 Health Education Plan for Patients with Pre-End-stage Renal Disease (Pre-ESRD) 計畫轉介至營養師進行衛教之患者，探討 CKD 合併糖尿病與否之初診患者，其高血磷人數之差異；另分析慢性腎臟病合併糖尿病患，造成高血磷之可能原因及經營養師衛教後血磷改善成效。本研究慢性腎臟病合併糖尿病 (Chronic Kidney Disease-Diabetes, CKD-D) 及慢性腎臟病無合併糖尿病 (Chronic Kidney Disease-Non Diabetes, CKD-ND) 病患分別為 153 及 169 位。結果顯示 CKD-D 組高血磷之比例顯著高於 CKD-ND 組，其中高血磷且未使用磷結合劑者，經衛教後其血磷值及鈣磷乘積皆顯著降低。造成 CKD-D 組血磷控制不佳的主因為加工品攝取過多及腎功能不全。CKD-D 組使用磷結合劑的病患中，使用不當者之比例達 56%。綜合以上，CKD 合併糖尿病時較易有高血磷，而營養教育有助於改善患者之血磷值。

關鍵詞：糖尿病、慢性腎臟病、高血磷、營養衛教、磷結合劑

* 通訊作者：劉珍芳

通訊地址：333 桃園市龜山區文化一路 261 號長庚科技大學保健
營養系

TEL: 03-2118999 ext 5487, FAX: 03-2118666

E-mail: liujenfa@mail.cgust.edu.tw

健身指導教練對於提供運動營養資訊 之學習需求

錢桂玉¹、張凱馨¹、劉珍芳²、簡麗瑜³

¹ 臺灣 桃園市 國立體育大學運動科學研究所

² 臺灣 桃園市 長庚學校財團法人長庚科技大學民生學院保健營養系
暨食品暨化妝品安全研究中心和中草藥研究中心

³ 臺灣 桃園市 長庚學校財團法人長庚科技大學護理學系

摘 要

目的：探討健身指導教練在運動營養指導上的經驗與學習需求。**方法：**本研究採質性研究法及半結構式深度訪談，依立意取樣原則邀請 7 位臺灣北部具備一年以上經驗，及在教學過程中具有運動營養指導經驗之專業健身指導教練。健身指導教練沒有從事運動指導教學五年以上為排除條件。訪談期間為 2017 年 9 月到 2018 年 3 月，每位受訪者依訪談指引進行一至二次訪談，以錄音方式進行資料搜集，並在訪談結束後將受訪者所陳述的感受與經驗轉換成文字敘述並進行厚實描述 (thick description)，並以內容分析方法進行資料分析。本研究遵循確實性、可轉化性、可靠性以及可確認性原則，採用內容分析法進行資料分析。**結果：**研究結果發現健身指導教練在運動營養指導上，面對學員基本疑問能夠應對無礙，而在學習需求上，則希望能學習到能幫助特殊群體的運動營養知識、生活化的食物選擇及代換的知識、當前流行議題的運動營養知識、有說服力的溝通與表達技巧、以及能活用的學習方式。**結論：**接受訪談的健身指導教練表示於日常指導時大多能夠應對學員提出的運動營養問題，但仍有針對特定議題之運動營養知識以及溝通與表達技巧的學習需求，也期望以活用的學習方式來獲取知識。建議未來在設計健身指導訓練課程時，能依據健身指導教練的需求，及成人的學習特質來安排訓練課程，使運動指導教練能夠達到自我期望，獲得專業成就感。

關鍵詞：運動指導員、身體活動、飲食、進修

壹、緒 論

近年來運動風氣逐漸盛行，無論是路跑、健身、自行車、鐵人三項等運動都有越來越多

民眾投入。民眾除了關切如何運動之外，像是飲食上該如何搭配等等的相關營養知識，也越來越受到關注，運動營養成了近年新興的議題。運動營養除了探討營養在專業運動員身上如何應用之外 (陳文毅, 2008; 陳宴瑄、邵于玲、

田鈴玉，2009；黃艾君、游鳳芸，2007），其在亞健康或是慢性疾病健康促進的需求也是日與俱增（World Health Organization, 2014）。

健身指導教練普遍被認為是提供運動及運動營養指導適合的人選（Barnes, Ball, & Desbrow, 2016a），主要因為健身指導教練是可以協助建立健康生活方式的專業人員（姜慧嵐，2005），健身教練會試圖幫助學員改善與健康相關的問題，包括飲食行為（Fleig, Kerschreiter, Schwarzer, Pomp, & Lippke, 2014）。由於健身指導教練與學員常以一對一的教學方式進行健身指導，所以與學員的關係密切（Keyzer et al., 2014），學員也習慣遇到運動營養的問題就直接詢問健身指導教練（Barnes et al., 2016b）。然而相關研究指出，健身指導教練往往不能提供正確且足夠的營養建議給民眾（Barnes et al., 2016b）。如果健身指導教練本身的運動營養觀念具有偏差而誤導民眾錯誤之運動營養觀念，可能導致學員身體產生負面影響（McKean, Slater, Oprescu, & Burkett, 2015; Weissman, Magnus, Niyonsenga, & Sattleshight, 2013）。

國外學者已針對健身指導教練對於提供營養照護（nutrition care）的看法（Barnes et al., 2016b），以及健身指導教練的營養訊息來源是否可信（Bennie, Wiesner, van Uffelen, Harvey, & Biddle, 2017）進行相關研究。Bennie 等（2017）將健身指導教練的知識來源分為高質量（相關學術課本、研討會、專業課程及科學期刊）及低質量（其他健身指導教練的見解、健身雜誌及網路上的資訊）的知識來源，而結果指出，健身指導教練的知識來源為高質量知識來源的不及一半，這樣可能會使健身指導教練獲得錯誤的運動營養知識的機率變高，甚至傳遞錯誤訊息給學員。對於運動訓練之運動營養部分目前還沒有成熟的知識系統（武桂新等，2015），即便教練資訊來源來自由專家學者所編撰的參考書籍，其內容大多依照學者們的思維及角度去撰寫及編輯，內容較多以學術理論為主。學術的理論知識到實務上的運用，必須經由多次練習及實務上的操作

演練才能運用得當，使得健身指導教練在實際提供建議上較難立即應用與發揮（Barnes et al., 2016b; Barnes, Desbrow, & Ball, 2016a）。此外，上述學習資源並非依照健身指導教練所面對到之民眾的問題或健身指導教練們的需求所設計，因此可能造成學習與問題解決之間的鴻溝。

截至目前為止沒有以健身指導教練為角度對於運動營養的看法及需求的研究，若能了解健身指導教練的學習需求為何，就能進一步設計出更有效解決健身指導教練工作時所遇到的運動營養疑難，為其專業增能。因此本研究目的為，探討健身指導教練對於提供運動營養資訊的學習需求，從健身指導教練提供運動營養建議的現況去探討目前的困境及需求為何，可提供日後對於健身指導教練培訓課程之安排及改善的依據，及其他有興趣執行相關研究及辦理相關課程者之參考。

貳、方 法

本研究採用質性研究法，從半結構訪談過程中瞭解受訪者的感受及生活經驗之陳述，透過深度訪談進入受訪者的真實生活中，藉此瞭解健身指導教練對於運動營養的經驗與學習需求。從每一位健身指導教練不同的經驗來分析出共同的學習需求，展現受訪者對學習需求的本質。本研究所稱學習需求是指個人為了達到期望或是成就感，而希望藉由學習來提升自己的價值（莊國銘，2000）。

一、研究對象

本研究採立意取樣，邀請具備運動營養指導經驗之健身指導教練作為訪談對象，受訪者納入條件：1. 具有專業健身指導教練資格國際執照之教練；2. 具備健身指導教學經驗至少一年以上；3. 在健身指導過程中具有提供運動營養建議之經驗。排除條件為：離開運動指導職場五年以上。本研究通過輔仁大學人體試驗委員會審核通過，通過證號：C1050140。

二、研究設計與流程

本研究以質性研究方法之程序進行研究設計、資料搜集方式、研究資料整理與分析等步驟。本研究採立意取樣進行收案，於 2017.09.01 至 2018.3.31 期間邀請具備運動營養指導經驗之健身指導教練作為訪談對象，若符合收案條件者，研究者將會以電話或是通訊軟體及網站聯繫，主動詢問並向受訪者說明研究目的及方式，受訪者瞭解研究目的與內容之後，再與受訪者約定對受訪者方便的訪談時間及安靜且不受干擾的地點，簽署受試者同意書後依訪談指引進行訪談。本研究之半結構式訪談指引如表 1 所示。本研究共招募 7 位符合收案條件的受訪者，每位受訪者進行一至二次不等的訪談，為了避免遺漏重要訊息及資料完整而影響研究的確實性，除於訪談過程簡單記錄在筆記本上，並於訪談過程中採全程錄音。在訪談之後，研究者會反覆聆聽錄音內容與閱讀訪談記錄，將錄音的訪談內容繕打為逐字稿，確實地呈現訪談者的口語內容，以供進一步的分析與解讀。此外，為了完整並真實反映受訪者在訪談中傳達之訊息，對其非語言訊息將加以註明及標示，之後再進行資料整理與分析。本研究基於受訪者個資的保護，在受訪者基本資料表及訪談逐字稿中編號以英文字母順序作為代號，以方便本研究之撰述，分別為 A、B、C、D、E、F、G。

表 1

半結構式訪談指引

1. 請談談在運動指導過程中遇過給予運動營養建議的經驗。
需要營養諮詢的學員中，比較常見的是哪一種？
請談談比較印象深刻的經驗？
您所擁有的運動營養知識，夠不夠回答學員的問題？（有沒有遇到學員問題，您沒辦法回答出來的？）
針對您提到的（受訪者提到學員問問題的經驗），請說明一下那個情境（例如您當時怎麼回答？結果是甚麼？）
2. 對自己在運動營養指導上的期望為何。
如果想達到您運動營養指導上的期望，那個期望是什麼？（對自己的期望？對學員的期望？）
3. 有沒有想學習什麼，是對您在運動營養指導上達到自我期望是有價值的。
假如您想達到您自己的期望，有沒有想要多加強或多學習的東西？
您覺得需要哪些改變（知識、技能或心態上），才能把工作做好，達到自身的期望？

三、資料整理與分析

本研究採用 Tesch (1990) 的內容分析法 (content analysis) 進行分析，研究者在訪談結束後，儘速將錄音檔繕打為逐字稿，以獲得個案原始資料，並詳讀資料內容所隱含的意義，找出逐字稿中浮現的主要內容類別並且歸類，將有關學習需求的句子，在逐字稿中強調出來以及將訪談主題相似的句子歸類在一起，將歸類後的字句轉為編碼 (code)，並且檢視是否再有新的編碼出現，將性質相似的編碼組成類別 (categories)，最終將類別概念化轉為主題 (theme)。在過程中，研究者不斷地回頭檢視分析步驟，並且進行同儕討論，將相同類別資料聚集而成並賦予一個概念，每一個概念會有一個明確的意義，並且檢視分析結果是否能反應出受訪者的經驗，再統合研究的主題，整理出更詳盡的整體性描述。

四、研究嚴謹度

質性研究的嚴謹度以信賴度 (trustworthiness) 稱之 (Denzin & Lincoln, 2011; Ryan, Bernard, Denzin, & Lincoln, 2000)。為確保研究品質，本研究的信賴度採 Lincoln 與 Guba (1985) 所提出的確實性 (credibility)、可轉化性 (transferability)、可靠性 (dependability)，及可確認性 (confirmability) 來說明。本研究透過研究同儕相互討論，及反覆聆聽錄音檔與閱讀逐字稿，來提高確實性；將受訪者所陳述的感受與經驗轉換成文字敘述並進行厚實描述 (thick description)，以達到可轉化性；在每次訪談結束後將訪談過程中情境變化及受訪者之非語言反應等記錄於訪談日誌當中，並進行資料編碼分析，再將研究分析結果有疑慮的地方向受訪者進行確認，以免語意不清或表達不全而影響資料分析，來達到可靠性；最後，將所有與受訪者接觸的原始資料包括訪談的錄音檔案、訪談過程中之簡單記錄和資料分析記錄皆完整的妥善保存，作為日後查證時之參考依據，以達到可確認性。

參、結 果

本研究訪談的 7 位健身指導教練中，有 3 位男性、4 位女性，平均年齡為 24.4 歲 (介於 21~33 歲)，平均教學經驗時間為 3.5 年 (介於 1~9 年)，其他基本資料如表 1 所示。本研究結果歸納出以下六個主題：面對學員基本疑問能夠應對無礙、能幫助特殊群體的運動營養知識、生活化的食物代換的知識、當前流行議題的運動營養知識、有說服力的溝通與表達技巧以及能活用的學習方式，以下針對研究結果做進一步的闡述。

表 2

受訪者資料

代號	年資	工作場域	工作性質	主要服務對象	與本研究相關 受訓主題
A	1	健身房	私人教練 巡場教練	25-56 歲 女性上班族	三大營養素計算 食物分配
B	3	健身房	私人教練 團課教練	30-50 歲 女性居多	營養素的功能 三大營養素計算
C	2	健身房	私人教練 巡場教練	25-45 歲 上班族、婦女	三大營養素計算 三餐如何配熱量
D	5	社區大學 健身房	私人教練	15-96 歲 銀髮族較多	從食物判斷熱量 三大營養素分配
E	9	俱樂部	私人教練	40-60 歲 婦女	三大營養素計算 食物分配
F	3	健身房	私人教練 團課教練	30-45 歲 婦女	高齡運動營養 運動員運動營養 三大營養素計算
G	1.5	工作室	私人教練	25-40 歲 上班族	三大營養素及熱 量計算 食物份數概念

一、面對學員基本疑問能夠應對無礙

7 位受訪者裡有 6 位認為，在面對學員在運動營養相關知識上的疑惑，普遍都還能直接為學員做解答，受訪者表示於工作時服務對象大多為一般民眾，學員的問題方向大多為基本的飲食常識，受訪者認為此類型的問題不會太艱深，能夠直接用本身所擁有的運動營養相關知識為學員解答。

「現在都還能應對，目前都還能應付得了，…，其實很簡單耶，就是減肥是一定要飲食控制嗎？然後一定要吃肉才會長肌肉嗎，他們其實都問其實都跟飲食方面會比較相關的，他們其實常問的都環繞在要怎麼減，要怎麼減脂啊，怎麼樣什麼之類的」(A)

「因為他們都問得很基本，像是減肥我應該要怎麼吃，他們就會問說「那教練我吃水煮餐可以嗎？就是什麼都不要，鹽啊那些什麼都不要」(C)

「如果是以運動營養學來看的話，目前來說都還夠，我還沒有遇到會問到非常深入的問題，對啊，因為大部分一般人不會問到太深入的飲食，…，頂多就是可能喝高蛋白，就是增肌的學生他要喝高蛋白，對，他會問說高蛋白到底好不好啊之類的」(E)

「我覺得夠，因為他們（即學員）也問不出什麼太艱深的問題，因為他們問的大部分都是常識，大部分在健身房運動的人都問的是常識，…，「運動完到底該不該吃啊？」、「啊可以吃什麼啊？」，對啊，然後，「因為我要減重要快，我是不是什麼東西比較不能吃啊？」，對啊，「如果我要增肌的話我最好要吃什麼，那個量要吃多少啊？」(F)

「營養方面好像，因為好像也不會問到很…很艱澀的問題，它 [營養] 確實很重要可是我覺得，就是我覺得他對一般人的重要性，知道大方向沒有什麼差錯，…，然後那個飲食方式又是健康的這樣就夠了」(G)

進一步分析受訪之健身指導教練對於運動營養相關知識來源，除了受訓時曾接受運動營養相關訓練之主題 (表 1) 外，本研究並未確認健身指導教練給予學員的運動營養資訊正確性。然而在提供運動營養資訊過程中若遇到問題，健身指導教練表示他們會進行資訊搜尋或尋求專業，其中 7 位受訪者中有 4 位表示會從網路上搜尋資料，3 位表示會從專業書籍找尋所需資訊，有 2 位會尋求營養專業人員協助，有 3 位則會尋求資深運動指導員協助。

二、能幫助特殊群體的運動營養知識

透過訪談內容可知，7 位健身指導教練裡有 5 位會遇到 65 歲以上的學員、患有慢性疾病的學員或專業或業餘的運動競技選手。在面對到上述群體時，健身指導教練所具備的運動營養知識，不足以回答、解決特殊群體的疑問，訪談中可以發現，部分受訪者期待得到這方面的知識，來提升自己在職場上的價值。

「年長者的運動營養的部分，我會想要學是因為銀髮族是很大的市場，應該說是超大，然後老人家你要他喝蛋白，其實一方面老人家可能會擔心這東西到底是可不可以喝，…，而且有些人可能是腎不好、什麼不好，可能就是不適合喝這個東西，…，那至少讓老人家會比較安心，因為有些老人家有可能會有三高、有的有糖尿病，那他到底要怎樣吃、要怎麼攝取，那哪個量其實對老人家是會比較好的。」(F)

「也會有糖尿病的學生啦、高血壓的學生，或是吃不胖的學生這一塊去做。這一塊路線，就是他們身上很多疾病的這些人的路線，飲食控制跟指導上，那比如說我在指導上可能需要怎麼樣不容易受傷？然後不容易累？或著他們怎麼吃來運動會比較好？我比較想要注重比較有病患的身上，還是都會很容易遇到這種」(C)

「遇到比較難的 case 會是特殊族群，比如說肩關節開過刀，然後另外一種，就是身體會有狀況的這種會是比較難的。…，以一般人來說，我們被需要的需求度是最低的，但是你特殊族群他就是不一樣，他需要你來幫助他，因為他們狀況很特殊，一般人可以做的他們不一定有辦法做」(E)

「吃很多藥的老人，也不一定是老人，就是吃很多藥的人，那可能包含他們本身疾病的控制，那那些藥對身體造成對副作用會不會影響到營養素的攝取和吸收？那跟運動之間又要怎麼去搭配？可能運動前一個小時吃藥啊或是吃飽飯吃藥，那可能多久後才能去運動這些相關的知識」(B)

「當然是依個人規劃為主，因為每個人攝取的蛋白質還有碳水量等等都不一樣，還有他 [學員] 的需求是什麼，他很有可能要減脂，他可能要備賽等等這些，然後來去客製化他的課表」(A)

三、生活化的食物代換的知識

受訪的 7 位健身指導教練裡有 6 位雖然對於回答學員的基本飲食常識認為都還因應，但 3 位受訪者仍表達想要學習食物代換相關知識，以及協助以外食方式的學員面對五花八門外食的篩選，以解決在回答學員運動營養問題過程中學員對於飲食問題的疑問。

「因為我覺得這部分應該算是，教練們最缺少的東西啦，這應該也是只有營養師會比較清楚，算份量這個東西，啊還有食物代換之類的這個東西，份量的算法啊、食物代換啊、要吃什麼啊」(B)

「因為其實現在人都是問你一些很貼切的問題，就是真的很生活化的東西，就是我每天早上都吃麥片，所以吃麥片真的會瘦嗎，那要吃什麼麥片，我要配什麼吃，高脂的牛奶？低脂的牛奶？我們現在生活化太多種類可以選，所以我就覺得說可能要再專攻這個可能要很努力」(A)

「很多人是外食主義比較多，那如果是外食的話要怎麼吃會更好，因為不可能每個人三餐都可以自己煮，很難，住外面很難，對啊，所以我想要注重外食這塊」(C)

四、當前流行議題的運動營養知識

7位健身指導教練裡有3位在回答學員有關運動營養問題的過程中遇到許多生酮飲食的提問，受訪者在訪談中也提及，由於新聞媒體大肆報導生酮飲食法，自己必須了解當前流行議題、更新運動營養相關知識。

「我什麼會有效？」或是「我用某某的派別的方式去吃會瘦比較快？」，應該其實大部分學生[學員]會問營養應該都是問這種東西，對，或是「不吃碳水是不是就會也很快變瘦？」之類的，我覺得他們大部分會問的問題都是一些比較像是可能現在是流行的，然後可能新聞最近一直狂報有效的方式，然後他們當然就會好奇，然後就會想問這到底是不是這麼有效」(G)

「生酮飲食，生酮飲食要怎麼吃？那個好嗎？」，然後前一陣子不是還有什麼，只吃肉，然後其他東西都不吃，然後是只吃醣，然後不吃其他東西，只吃蛋白質之類的東西，…，然後希

望可以的話[機會學習]，會有針對就是針對現在市面上就是比較熱門的幾種飲食法」(B)

「比如說像，他們要問生酮[飲食]的內容，或者是一些像是間歇性斷食的東西，就是比較不夠，比較回答不出來」(E)

五、具有說服力的溝通與表達技巧

7位受訪者裡有4位表示，在回答學員運動營養問題過程中，自己的溝通技巧有所欠缺，需要透過學習來加強，以提升專業指導的有效性及說服能力。

「因為有時候自己說的跟自己腦袋想講，腦袋想的跟說出來的還是會有出入，所以表達方式還有跟客戶溝通的技巧，怎麼樣能夠把你想表達的、清楚的、簡單的轉述給你的客戶知道，這東西可能會隨著經驗越來越多，就會有越來越多的心得感想，那我覺得以我這個菜鳥來講，我還是要慢慢去加強這個部分」(B)

「我怕我跟他[學員]講的太深奧，他可能會一頭的霧水，…，所以我會想要多瞭解的是，可不可以簡單化的方法跟他們講說有什麼方法可以讓他們補充什麼東西」(A)

「我有教過一對比較，50歲以上的，年紀比較大的夫妻這樣子，比如說他們也會拍照給我看，我就會跟他們說，這樣蛋白質吃太少了，他們可能就會問說「為什麼呢？蛋白質要吃這麼多？蛋白質真的可以吃這麼多嗎？」，…，那我覺得最難的應該是他們有沒有把這件事真的內化到自己的

心，就說「喔，好，那所以我應該要吃更多的蛋白質」，就我覺得最難的是要怎麼讓他們去接受觀念，而不是去回答，因為我覺得回答，沒有到非常困難，可是我覺得比較困難的事，要怎麼去讓他們接受這件事情，對這我覺得應該是最，應該是最困難的一點吧」(G)

「在健身房工作，我要不斷提昇我的口條，我給人的感覺，是不是夠誠懇，對，是不是這個我給他[學員]的感覺，跟我回答他的東西，跟我可以幫他解決的事，…，可能講每個都會講，你用一台錄音機放在那邊給他聽，可是，他感覺不到那台錄音機的價值阿，因為他是一個死的東西，人的價值，我把我的價值散發給你，你會覺得不單單只是來入會而已，還得到更多附加價值」(F)

六、能活用的學習方式

當健身指導教練被詢問到想學習什麼時，受訪者表達了他們希望能夠結合實際案例，增加上課時的靈活度，希望能夠以實例分享的方式獲得專業知識，透過課堂中實際操作的方式，更能夠靈活運用學習到的內容。

「我的話我現在這個部分[學習運動營養]會想要了解怎麼幫學生，就是如果那個講師是很有經驗的話，會比較想要了解他是怎麼用他的經驗去幫他的學生做個體差異的調配」(D)

「我比較喜歡聽案例啦，因為案例感覺比較真實，…，然後大家一起討論做一個分享，那真的感覺有學到一個東西之類的」(C)

「就是更實務面的東西，生活化一點，貼切一點，因為其實現在人都是問你一些很貼切的問題，就是真的很生活化的東西」(A)

「就是可以有訓練[實際操作]，不用到一定要整個課表做到滿，就是你可以去做完這個東西之後、這組運動，然後，再去[進行]在吃的部分，可能在第二天的部分，你可以稍微去做現場做烹煮，…，就是說每一種方法啦，生酮飲食、間歇性斷食阿什麼的，自己都可以先用自己的身體去試一試，設定一個週期、設定一段時間去試，到底是不是這麼的通，啊效果到底是不是這麼的好」(F)

「我想用一種方式，這種方式可能，時間拉長，但是上課的堂數很少，中間的時間可以進行實際操作的，因為每個東西[飲食方式]他都要需要適應期[時間]，所以中間操作時間的長短，就會影響到我們等下進行的實驗[飲食及運動的實驗]，那所以這堂課[的時間]可能就會拉很長[才能看到實驗的成果]，…，還有經驗分享，然後有點互動的會比較喜歡這種方式」- 受訪者 B

「就更實務化，像有些人說，我們吃了一個東西，可是我如果不加肉呢，可以換成什麼是不是熱量會不一樣，就是攝取的東西又更不一樣，就好比我們今天明明同吃一碗麵，你也吃一碗麵，我也吃一碗麵，我把我的裡面的肉全部換成青菜，是不是就會不一樣，…，是不是我只要把全部的肉換成蔬菜就可以改善？」(A)

肆、討 論

本研究結果發現受訪的健身指導教練爲了達到個人期望或是成就感，希望藉由學習來提升自己價值的內容，包含能幫助特殊群體的運動營養知識、生活化的食物選擇及代換的知識、當前流行議題的運動營養知識、以及有說服力的溝通與表達技巧。

一、能幫助特殊群體的運動營養知識

本研究結果發現，健身指導教練會面對到高齡者、患有慢性疾病的學員、專項運動員及選手等。認爲自己所具備的運動營養知識，不足以回答和解決此群體的疑問。健身指導教練也展現出想要服務上述群體的興趣，進而想要學習相關運動營養知識。此結果呼應了 Bennie 等 (2018) 的研究結果，亦即健身指導教練對於服務患有慢性疾病的學員及專項運動員及選手展現出興趣，McKean 等 (2015) 也指出學員與健身指導教練討論運動營養的議題多與疾病相關，高達 51.4% 的學員會找健身指導教練討論心臟疾病的運動營養，其次，討論糖尿病及血糖相關運動營養問題的比率也高達 48.3%。此結果也呼應了 World Health Organization (2014) 所稱，運動營養在亞健康或是慢性疾病健康促進的需求有日與俱增的趨勢。臺灣目前在健身指導教練訓練課程中，雖有與中高齡運動營養相關課程 (美國有氣體適能協會，2018)，但此類課程尚不普及。在需求相對與日俱增的趨勢下，健身指導教練訓練課程應該廣設中高齡、亞健康、慢性疾病相關的運動營養課程，以使健身指導教練具備相關的專業知識及能力來幫助這些族群，進而提升健身指導教練的專業價值。

二、生活化的食物的知識

本研究結果顯示，健身指導教練希望學習生活化的飲食代換知識。McKean 等 (2015) 及 Barnes 等 (2017) 的研究結果同時指出，健身指導教練需能針對學員的現有飲食狀況給予修正及建議食物選擇的方式。然而，從受訪者基本

資料表可知並非所有健身指導教練皆接受過食物代換的相關運動營養知識 (表 2)。由於國人生活型態改變，選擇外食的人口比例高達 79% (國家衛生研究院，2016)，健身指導教練也會指導到越來越多以外食爲主的學員，因此除了「三大營養素計算」、「熱量判斷」以及「食物分配」等相關知識，健身指導教練也需要具備更完整的食物代換的相關知能，才能協助學員解決在面對多元的食物該怎麼選擇的問題。

三、當前流行議題

根據本研究結果，由於新聞媒體大肆報導生酮飲食法、間歇性斷食以及其他熱門的飲食方法等等，以致健身指導教練認爲自己必須了解當前流行議題以及更新運動營養相關知識，才能向學員提出更好的建議以及方法。除了本研究之外，McKean 等 (2015) 的研究也指出學員會與健身指導教練討論特殊飲食方法，健身指導教練爲了不讓學員懷疑自己的專業知識與能力，會想要時常更新自身的知識，來維持在學員心目中的專業印象 (De Lyon & Cushion, 2013)。此結果反映了健身指導教練需要具備不斷更新自身知識的能力與動力，才能應付資訊發達的當代飲食流行趨勢所衍伸出的運動營養問題。

四、具有說服力的溝通與表達技巧

本研究結果顯示，健身指導教練覺得自己在溝通與表達能力的技巧上有所欠缺，需要透過學習來加強。其原因爲健身指導教練無法用淺顯易懂的傳達方式傳達知識及技巧給學員、無法用簡單化的方式讓學員釐清知識，以及難以說服並導正學員的錯誤觀念而感到困擾。本研究結果呼應了 Barnes 等 (2016a, 2016b) 指出健身指導教練對於運動營養建議過程給予建議時是沒有自信的，其原因可能爲健身指導教練對於要自身所擁有的運動營養知識與實際在職場上給予學員回答學員運動營養問題時覺得有所差距而感到困擾。然而，健身指導教練已被認爲在健身產業裡面是提供運動營養建議適當

的人選 (Barnes et al., 2016b; Keyzer et al., 2014; McKean et al., 2015)，要能將正確運動及運動營養觀念傳達給學員，也要以量身打造的運動計劃來指導學員 (李城忠、林孟潔，2005；George et al., 2008)，而在回答學員運動營養問題過程中，將健身指導教練所想要傳達及指導之觀念給學員，最重要關鍵就是溝通能力 (林志勳、蘇俊賢，2006)。健身指導教練若要將專業知識、觀念及技巧傳達給學員，必須轉換為淺顯易懂的語言使學員了解，因此要善盡溝通的能力 (Barnes et al., 2016b)。因此，依據本研究結果可知，健身指導教練所應具備能力，不僅止於的專業知識本身，還需要具備有效傳達訊息的溝通與表達能力，才能提升健身指導教練的專業價值。

五、能活用的學習方式

參與本研究的受訪者也提出了學習方式上的意見與看法，希望運動營養培訓課程內容，能夠結合實際案例，增加培訓內容的活用特質，也希望講員能夠以經驗分享方式帶入培訓內容，能夠從講員的思維及方法學習到實際的作法。在傳統的培訓過程中，大多的講員都以傳授學理知識為主，研究指出健身指導教練對於傳統的培訓課程並不是很滿意，受訪者認為傳統培訓課程的知識傳授方式都是固定一套模式，也覺得這種傳統的培訓課程所傳授的知識跟健身指導教練實際在職場運用覺得有所差距 (Barnes et al., 2016a; De Lyon & Cushion, 2013)，健身指導教練需要實際演練的機會，將學理知識轉換為實際操作，進而使這些學理知識更容易運用在職場中。

健身指導教練屬於成人學習者，依據 Knowles, Holton, 與 Swanson (2011) 所提出的成人學習理論，成年人對任何主題的學習都有其內在學習的動機與自我導向；有效的成人學習方式，是將其所累積的生活經驗帶入學習；成人重視可以和學習需求進行整合的學習經驗；也重視所學知識的即時應用，傾向以問題為中心的學習，而非學科中心。因此健身指導

訓練課程的設計者，應該依據成人的學習特質來安排訓練課程，並且可運用各種創新教學模式於健身指導教練的運動營養培訓課程中，例如案例討論或問題導向學習法 (problem based learning, PBL)，也可以運用磨課師 (massive open on-line course, MOOCs) 提供流行議題的運用營養知識，以改善健身指導教練培訓課程的學習效益。

給予消費者正確運動營養補充劑的正確訊息是相當重要的。過去研究指出健身指導教練認為補充劑消費的好處超過了風險，而且風險被認為是不確定的。因此，健身指導教練不會提出運動營養補充劑可能的副作用的疑慮，也不會向健身俱樂部會員傳達可能風險。反觀，營養師認為必須告知會員營養增補使用的可能風險，並且部分營養師認為雖然一般推薦攝取劑量並不危險，但並不一定有益，因此也不須推薦健身會員使用 (Druker & Gesser-Edelsburg, 2017)。健身指導教練是第一線服務民眾的專業人員，許多的健康議題，如：減肥、增加肌肉量...等都與運動以及營養關係密切，因此健身指導教練如果具備一般民眾都應具備的均衡健康飲食以及食物份數概念，則有助於其專業的發展。例如：高蛋白產品是目前訪問常見的健身營養補充品，健身指導教練需具備足夠健康飲食或食物代換的知識，確認學員飲食蛋白質攝取結合運動營養補充劑的蛋白質總量是否超過一日建議攝取量，並將正確一日建議攝取總量的觀念傳遞給民眾是相當重要的。除此之外，健身指導教練應重視運動禁藥以及國內食品安全相關法規知識 (例如：食品添加物使用範圍之營養添加劑、健康食品管理法、特殊營養食品與錠狀膠囊食品查驗與登記等)。健身運動指導教練應接受相關教育訓練，以確保健身指導教練不會誤用運動禁藥及其所使用產品安全性，也唯有具備相關知識才能將正確資訊提供給服務的民眾。必須強調的是，健身指導教練在傳遞相關運動營養訊息時並不能以提供“營養評估或營養諮詢”自居，給予民眾飲食設計

服務，尤其是針對慢性疾病的病人，否則會觸犯營養師法之規範。因此，建議健身指導教練若遇到民眾有飲食設計、營養評估的需求時應請營養師協助，共同合作，提供給予民眾最佳之專業服務。

本研究結果指出運動營養教練希望學習能幫助特殊群體的運動營養知識、生活化的食物選擇及代換的知識、當前流行議題的運動營養知識以及有說服力的溝通與表達技巧來提升自己的專業價值。建議未來在設計健身指導訓練課程時，能依據健身指導教練的需求，及成人的學習特質來安排訓練課程，運用各種創新教學模式，廣設中高齡、亞健康、慢性疾病相關的運動營養課程，增加食物選擇及代換的相關內容，隨時更新飲食流行趨勢知識，並培訓健身指導教練具備有效傳達訊息與溝通表達能力以及合法的業務執行範疇，使運動指導教練能夠達到自我期望，獲得專業成就感。

引用文獻

- 李城忠、林孟潔 (2005)。運動健身俱樂部個人教練之專業知能、顧客滿意度與顧客忠誠度之研究。《人文暨社會科學期刊》，1(2)，55-64。
- [Lee, C. J., & Lin, M. C. (2005). A study on relationships between professional knowledge of fitness clubs' personal trainers and customer satisfaction and loyalty. *Journal of Humanities and Social Sciences*, 1(2), 55-64.]
- 林志勳、蘇俊賢 (2006)。從個人教練證照檢定精神與內容談應試技巧。《大專體育》，87，163-169。
- [Lin, C. H., & Su, C. H. (2006). The interview skills of personal fitness trainer certification-principles and content. *Sports Research Review*, 87, 163-169.]
- 武桂新、吳嚴冰、計慧、馬愛英、伊木清、方子龍、...王啓榮 (2015)。“運動營養學”教學知識結構體系研究。《中州體育：少林與太極》，5，43-48。
- [Wu, G. X., Wu, Y. B., Ji, H., Ma, A. Y., Yi, M. C., Fang, Z. L., ... Wang, C. R. (2015). The structure system of teaching knowledge in sport nutrition [Electronic version]. *Academic Journal of Shaolin and Taiji (Zhongzhou Sports)*, 5, 43-48.]
- 姜慧嵐 (2005)。健身產業人力運用現況與管理趨勢。《國民體育季刊》，34(2)，76-81。
- [Chang, C. (2005). Human resource employment and management trends in the fitness industry [Electronic version]. *National Sports Quarterly*, 34(2), 76-81.]
- 美國有氧體適能協會 (2018)。研習課程。取自 http://www.t-wi.com.tw/workshop_index.html
- [National Academy of Sports Medicine. (2018). *Workshop*. Retrieved from: http://www.t-wi.com.tw/workshop_index.html]
- 美國運動委員會 (2018)。研習課程。取自 https://www.fittaiwan.com/index.php?option=com_content&view=article&id=17&Itemid=202#
- [American Council on Exercise. (2018). *Workshop*. Retrieved from: https://www.fittaiwan.com/index.php?option=com_content&view=article&id=17&Itemid=202#]
- 陳文毅 (2008)。中長跑選手的營養攝取。《大專體育》，99，179-184。doi: 10.6162/SRR.2008.99.28
- [Chen, W. Y. (2008). Nutrients intake in middle and long distance runners. *Sports and Exercise Research*, 99, 179-184.]
- 陳宴瑄、邵于玲、田羚玉 (2009)。女子壘球運動員營養知識與飲食行為之研究。《臺灣營養學會雜誌》，34(4)，133-141。

- [Chen, Y. H., Shao, Y. L., & Tien, Y. L. (2009). Nutritional knowledge and dietary practices of female softball players. *Nutritional Sciences Journal*, 34(4), 133-141.]
- 國家衛生研究院。(2016)。外食人口調查。臺北：國家衛生研究院。
- [National Health Research Institutes. (2016). *The survey of out eating population*. Taipei: National Health Research Institutes]
- 莊國鎔 (2000)。臺北市國小教師生涯發展與學習需求之研究 (未出版之碩士論文)。國立臺灣師範大學，臺北市。
- [Jhuang, G. G. (2000). *Elementary school teacher career development and learning needs in Taipei*. National Taiwan Normal University. Taipei.]
- 黃艾君、游鳳芸 (2007)。桌球運動與營養調節策略之探討。《大專體育》，92，188-195。doi: 10.6162/SRR.2007.92.28
- [Huang, A. A., & You, F. Y. (2007). The investigation of nutrition strategy in table tennis players. *Sports and Exercise Research*, 92, 188-195.]
- Barnes, K., Ball, L., & Desbrow, B. (2016a). Promotion of nutrition care by Australian fitness businesses: A website analysis. *Public Health*, 140, 45-49. doi: 10.1016/j.puhe.2016.08.026
- Barnes, K., Ball, L., & Desbrow, B. (2017). Personal trainer perceptions of providing nutrition care to clients: A qualitative exploration. *International Journal of Sport Nutrition and Exercise Metabolism*, 27(2), 186-193. doi: 10.1123/ijsnem.2016-0141
- Barnes, K., Desbrow, B., & Ball, L. (2016b). Personal trainers are confident in their ability to provide nutrition care: A cross-sectional investigation. *Public Health*, 140, 39-44. doi: 10.1016/j.puhe.2016.08.020
- Bennie, J. A., Thomas, G., Wiesner, G. H., van Uffelen, J. G. Z., Khan, A., Kolbe-Alexander, T., ... & Biddle, S. J. H. (2018). Australian fitness professionals' level of interest in engaging with high health-risk population subgroups: Findings from a national survey. *Public Health*, 160, 108-115. doi: 10.1016/j.puhe.2018.03.035
- Bennie, J. A., Wiesner, G. H., van Uffelen, J. G., Harvey, J. T., & Biddle, S. J. (2017). Sources of practice knowledge among Australian fitness trainers. *Translational Behavioral Medicine*. doi: 10.1007/s13142-017-0482-4
- De Lyon, A. T., & Cushion, C. J. (2013). The acquisition and development of fitness trainers' professional knowledge. *Journal of Strength and Conditioning Research*, 27(5), 1407-1422. doi: 10.1519/JSC.0b013e3182653cc1
- Denzin, N. K., & Lincoln, Y. S. (2011). *The sage handbook of qualitative research: Sage*. Thousand Oaks, CA: Sage Publication.
- Druker, I., & Gesser-Edelsburg, A. (2017). Identifying and assessing views among physically-active adult gym members in Israel on dietary supplements. *Journal of the International Society of Sports Nutrition*, 14(1), 37. doi: 10.1186/s12970-017-0194-7
- Fleig, L., Kerschreiter, R., Schwarzer, R., Pomp, S., & Lippke, S. (2014). 'Sticking to a healthy diet is easier for me when I exercise regularly': Cognitive transfer between physical exercise and healthy nutrition. *Psychology and Health*, 29(12), 1361-1372. doi: 10.1080/08870446.2014.930146
- Keyzer, P., Coyle, I. R., Dietrich, J., Norton, K., Sekendiz, B., Jones, V., & Finch, C. F. (2014). Legal risk management and injury in the fitness industry: The outcomes of focus group research and a national survey of fitness professionals. *Journal of Law and Medicine*, 21(4), 826-844.
- Knowles, M. S., Holton, E. F., & Swanson, R. A. (2011). *The adult learner: The definitive classic in adult education and human resource development* (7th ed.). Houston, Tex.: Gulf Pub. Co.

- Lincoln, Y. S., & Guba, E. A. (1985). *Naturalistic inquiry*. Beverly Hills, CA: Sage Publication.
- McKean, M. R., Slater, G., Oprescu, F., & Burkett, B. J. (2015). Do the nutrition qualifications and professional practices of registered exercise professionals align? *International Journal of Sport Nutrition and Exercise Metabolism*, 25(2), 154-162. doi: 10.1123/ijsnem.2014-0051
- Ryan, G. W., & Bernard, H. R. (2000). Data management and analysis methods. In N. K. Denzin, & Y. S. Lincoln (Eds.). *Handbook of qualitative research* (pp.769-802.). Thousand Oaks, CA: Sage Publication.
- Tesch, R. (1990). *Qualitative research: Analysis types and software tool*. New York, NY: Falmer.
- Weissman, J., Magnus, M., Niyonsenga, T., & Sattleshight, A. (2013). Sports nutrition knowledge and practices of personal trainers. *Journal of Community Medicine and Health Education*, 3(254), 2161-2171.
- World Health Organization. (2014). *Management of substance abuse unit. Global status report on alcohol and health*. Retrieved from http://www.who.int/substance_abuse/publications/global_alcohol_report/msb_gsr_2014_1.pdf

投稿日期：107 年 10 月

通過日期：108 年 03 月

The learning needs of sport nutrition for fitness instructor to provide sport nutrition services

Kuei-Yu Chien¹, Kai-Hsin Chang¹, Jen-Fang Liu² and Li-Yu Chien³

¹Graduate Institute of Sports Science, National Taiwan Sport University, Taoyuan City, Taiwan

²Department of Nutrition and Health Sciences, Research Center for Food and Cosmetic Safety, and Research Center for Chinese Herbal Medicine, College of Human Ecology, Chang Gung University of Science and Technology, Taoyuan City, Taiwan

³Department of Nursing, Chang Gung University of Science and Technology, Taoyuan City, Taiwan

Abstract

Introduction: This study explored the experiences and learning needs of sport nutrition for fitness instructors when providing sports nutrition advices. **Methods:** Qualitative design was adopted with semi-structured in-depth interviews in present study. With purposive sampling, seven fitness instructors who possessed at least one-year experience and had given sport nutrition advices were invited to participate in this study. Fitness instructors who had not engaged in fitness instruction for more than five years were excluded from this study. The interviews were conducted during September 2017 and March 2018, and each participant received 1 to 2 interviews with an interview guide. The interview data were recorded, and the feelings and experiences stated by the participants were transcribed verbatim after interview. With thick description, the data were analyzed by content analysis method. Principles of credibility, transferability, dependability and confirmability were adhered for ensuring rigor in this study. **Results:** The participating fitness instructors perceived they were capable of responding to the clients' basic sport/exercise nutrition questions with ease. In terms of learning needs, the instructors expressed they would like to possess sport nutrition knowledge that could help clients with special needs, with daily dietary exchange, and with the updated popular nutritional issues relates to sports. The fitness instructors also expressed that they would like to obtain persuasive communication skills, and to learn all the sport nutrition knowledge with approaches that could make the knowledge with flexible use. **Conclusion:** Although most fitness instructors stated they were able to provide answers to clients' questions regarding sports nutrition, there are learning needs required regarding persuasive communication skills and specific sports nutrition knowledge. The fitness instructors also expected to possess knowledge in ways that are more practical and flexibility. It is recommended that fitness instructors' learning needs and adult learning attributes should take into account when designing fitness instructor training course.

Key words: exercise instructors, physical activity, diet, training course

分析供膳場所人員工作聲音環境之感受與 相關因素探討

張家臻¹ 邱麗玲² 薛如婷²

¹聖約翰科技大學老人服務事業系

²長庚學校財團法人長庚科技大學民生學院保健營養系暨
食品暨化妝品安全研究中心和中草藥研究中心

收到日期：106.10.25 修訂日期：107.6.10 接受日期：107.8.29

摘要

國內擁有近百萬人口從事餐飲服務業，當中供膳場所人員在高分貝的供膳環境，可能會造成身心壓力。本研究主要探討供膳場所人員對職場聲音環境、情緒疲勞、幸福感受及工作效能之現況。參考國內外文獻發展「聲音環境影響供膳場所人員相關因素調查問卷」，立意選取332位員工進行問卷調查。結果顯示供膳人員對工作環境當中的抽油煙機所發出的噪音感到焦慮，工作後經常覺得精疲力盡及緊張不安是影響成情緒疲勞的主要原因；但供膳人員普遍擁有中等以上的幸福感受及自覺工作效佳；進一步分析年齡逾50歲及供膳場所人數在31人之從業人員的幸福感受較高，亦為供膳從業人員之保護因子。根據上述均可作為供膳場所未來推廣健康促進及環境營造參酌。

關鍵詞：聲音環境、供膳場所人員、情緒疲勞、工作效能、滿意度

*通訊作者：邱麗玲

33303 桃園市龜山區文化一路261號

電話：03-2118999 #5479 E-mail：llchiu@mail.cgust.edu.tw

DOI:10.6615/HAR.201809_(82).0008

壹、背景

一、供膳人員工作環境現況

行政院主計處在「中華民國行業標準分類第八次修訂草案」之行業名稱及定義中，將餐飲業細分為餐館業、飲料店業、餐飲攤販業及其他餐飲業，其中「其他餐飲業」之定義為凡從事上述三種以外餐飲服務之行業均屬之，如餐飲承包服務（含喜宴承辦、團膳供應等）及基於合約僅對特定對象供應餐食之學生餐廳或員工餐廳等（行政院主計總處（編），2006），本研究稱「供膳場所人員」，泛指提供上述食品或飲料製備之從業人員。長期以來，餐飲供膳等相關產業投入，對於推動經濟增長，刺激人民消費需求發揮重要作用，在就業、市場以及人民生活水平質量等方面，都做出了貢獻。

生活環境當中隨時充滿了各式各樣的噪音干擾人們的作息，而在廚房工作環境當中也不例外。廚房裡為了減少油煙，因此裝置抽油煙機，依此因為吸力效能佳、不滴油等防備功能完善，但其運轉時產生的聲音，卻是廚房內主要的噪音來源（魏名汎，2005）。引據學者提及供膳環境又可分為物理及心理兩方面，物理環境是指外在看得見的設備、物質及公司組織型態等；隨著都市多元化的發展，民眾對飲食精緻與多樣化的要求提升，造就油炸、燒烤、烘焙等熱食從業人員蓬勃發展，但熱食從業人員由於長期暴露於烹調過程器具碰撞敲擊所發出的噪音之中，集中力需要較高，加上供膳場所中的噪音導致噪音性聽力損失（Noise induced hearing loss--NIHL）等問題。加上個體需要承受心理造成的工作壓力，這些都有可能導致勞工的健康造成影響，引起情緒不適的情形，於本研究中指稱「情緒疲勞」為供膳從業人員出現情緒不安、感覺憂鬱或心情低落等反應。若

長期處於高壓狀態，將會造成職業倦怠而影響離職（柯宏君，2011）。故研究者應對場域環境音源暴露進行評估，維護從事人員的健康和安全（陳志郎、徐佩鈴，2009）。

供膳場域中的心理環境指團隊中容忍度、溝通性、組織文化等內在因素（桃樂斯·雷諾、華特·史瓦普，2000），其影響個體對於整體生活的「幸福感受」（個人由心理及社會等面向，主觀評估生活品質的感受），甚至影響日常的「工作效能」（含工作成效及工作感受兩個構面）。為提升工作效能，除了考慮個人的因素外，工作場所的環境與設備也是很大的影響，若業者不重視廚房環境的規劃，還想減少廚房的坪數來擴大外場的坪數來增加業績，這絕對行不通的，試想一個狹隘、擁擠、潮濕、吵雜的廚房，廚師的工作情緒又會高昂嗎？於此過往研究指出在工作上環境的滿足，可以刺激員工在工作上的效能，來達到公司的績效（Tsai, 2003）。廚房環境本身就非常的悶熱及吵雜，唯有改善工作環境才能改善廚師及供膳人員對工作上的滿意程度，進而改善產品的品質及出餐的效率。

因此供膳相關從業人員之對產業的認同、使命感及工作態度與食品安全管制系統之落實運作相關密切（藍群傑，2007）。其工作效能的提升即是餐廳經營水準的指標之一，業者應注重人力資源的開發與工作效能的提升，以人性化及科學化的管理制度來運作。對於例行化且重複性高的團膳工作，應在瞭解員工對於工作特性的了解後，該如何適當安排組織工作，讓員工更加投入工作內容，取得工作最大的效果（黃郁文，2011）。

二、供膳人員健康狀況

餐飲或供膳場所屬於製造性的服務產業，由於目前的工作操作愈來愈快速，重覆性的動

作也越加頻繁，以致累積性的職業傷害與日俱增，無形的過勞也常損害員工的健康（全中好、邱雅琴、陳志勇、李中一，2009）。然而，國內從事餐飲相關產業的勞工，肌肉骨骼不適均有增加的趨勢，其潛在的危險因子包括長時間工作、不正確的姿勢與上肢重複性動作。而工作中須頻繁接觸大量的水、清潔劑、食物原料和極冷的溫度，因此報告有皮膚不適之文獻也相當普遍（吳桂琳，2003）。

社會上從事高溫或密閉空間職業的工作者比如廚房從業人員、勞工或農人，常在高溫環境下工作，對健康之危害更加不能忽視。一般作業場域中，包括廚房空間較為密閉，且包含有油炸、燒烤、熱炒等作業區，因此從業人員長時間暴露於高熱環境中，可能影響勞工健康（黃種克、陳志郎，2009）。加上供膳場所具有多種潛在性的危害，比如吸入過多油煙造成慢性呼吸器官疾病、烹飪或燒燙傷、噪音問題所引起之聽力損傷、地板濕滑等所引起之跌倒摔傷、處理食材所造成之切割傷、固定動作或搬運等造成肌肉骨骼傷病包含肌腱炎、關節炎、下背痛、腕隧道症候群等，這些危害都可能在供膳從業人員身上發生（黃建平、劉立文、黃奕孝、李聯雄、張振平，2010）。

烹調業所排放之油煙嚴重影響從業勞工健康與空氣品質之重要因素，現場工作油煙與未經處理排放的油煙會使勞工健康風險增加。採取適當的方法來降低油煙之排放與防止污染為必要的工作（陳琮翰，2012）。烹飪油煙中的危害物包括多環芳香族碳氫化合物、多環胺、硝基多環芳香族碳氫化合物，烹飪油煙暴露除了對人體呼吸道疾病、細胞毒性、肺癌等之健康危害，並可能有心血管疾病之危害（潘致弘、陳秋蓉、胡瓊文，2014）。在台灣，肺癌不論男女一直是國人十大死因之首，過去認為抽菸和肺癌有關，在台灣女性抽菸的比例卻不高，除

了抽菸之外，廚房油煙是家庭污染物主要的來源，華人傳統的烹飪方式以快炒、煎、油炸為主，這些烹調方式往往會產生許多的油煙，這些油煙中有許多常見對人體有害的污染物像是醛類、懸浮微粒和多環芳香烴及VOC，這些污染物經過許多研究證實對人類的肺部會造成危害（林子翔，2016）。

自古以來，音樂在生活中一直扮演著極為重要的角色，透過音樂可以達到生理及心理層面的治療。生理層次的部份，音樂能刺激自主神經系統，進而調節心跳、呼吸速率、血壓、以及內分泌，研究發現慢板、平靜、以及輕柔的音樂有助於降低因壓力而導致的生理性反應；相對地，節奏快的音樂則有助於提高生理反應（Standley, 1986）。在心理層次方面，音樂能有效地降低住院患者的焦慮及改善情緒（Evans, 2002）。亦即聲音能夠喚起強烈的情緒經驗（emotional experiences），構成每個人獨特的音樂經驗，影響其腦部、身體與情感的發展（Reimer, 2004）。研究顯示，節奏舒緩柔和或是熟悉的音樂或聲音，會讓顧客認為時間過得較慢，以至於自然地放慢腳步，進而增加顧客在店裡消費的時間；而速度較快、節奏較強的音樂則會讓顧客認為時間過得較快，無形中加快腳步，使得顧客的消費時間縮短。綜合以上的論述，操弄不同場域的聲音種類、音量及速度等，均可能影響或改變消費行為（Jacob, Guéguen, & Boulbry, 2010; Magnini & Thelen, 2008）。

回顧上述提及國內從事餐飲或供膳等相關服務業，其中供膳場所人員在高分貝的供膳環境極易影響其身心狀況。因此本研究目的主要分析供膳場所人員其職場聲音環境、幸福感受、情緒疲勞及工作效能之現況，並以性別、年齡、工作年資及工作場所人數等變項進行檢定；研究假設供膳從業人員對上述變項結果均

· 分析供膳場所人員工作聲音環境之感受與相關因素探討 ·

屬負面，且不同背景變項具有顯著差異，其結果可作為未來改善或調整供膳場域之參考。

貳、研究方法

本研究採方便取樣，立意選取供膳場所員工為研究對象，以研究者彙整「供膳場所人員工作聲音環境之相關因素調查表」為研究工具，探討供膳人員對於供膳場所聲音環境感受、情緒疲勞、幸福感受及工作效能等情形（圖一）。

一、研究對象

本問卷主要針對國內供膳場所員工進行調查，根據中華民國勞動部2016年勞動統計月報指出，目前國內從事服務及餐飲等相關行業受雇人數為833000人，進行Sample Size Calculator軟體選擇信賴水準95%，抽樣誤差為正負6百分點，得選取267位研究對象進行施測。本研究據此以透過線上問卷系統進行施測，並運用各大社群平台張貼施測訊息，知會各地餐館、飲料店、餐飲攤販業及其他餐飲業者進行填寫；或運用電子郵件聯繫告知，統計問卷最後發放339人，並回收332份，回收率為97.93%。

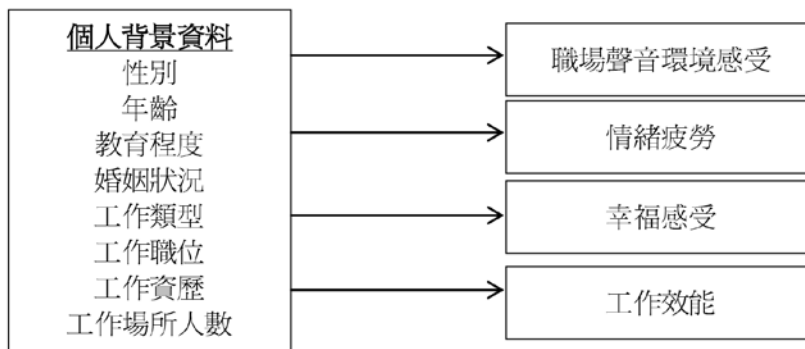
二、研究工具

本研究工具「供膳場所人員工作聲音環境之相關因素調查表」係參考「財團法人健康

精神基金會幸福感」、「台北市衛生局職場疲勞量表」及「員工績效考核表」等問卷，並綜合參考文獻與專家意見編製而成；共計個人背景變項、供膳場所聲音環境感受、情緒疲勞、幸福感受及工作效能等五大項目計36題，根據李克特五分量表，除工作效能第三及四題，所述「我認為自己勉強勝任工作，少有工作表現」及「我認為自己工作效率低，偶爾會出錯」屬於反向題目，因此須轉向成為非常不同意為5分，以此類推。各題多數以五分法（1至5分）核計，包括「非常不同意」、「不同意」、「沒意見」、「同意」及「非常同意」，分數越高表示越該項目認同程度越高。問卷另進行信效度檢定，其內部一致性檢定指出各向度介於.70~.87，內容效度居於.77~.87，顯示各題項均有較高的內容一致性，及其內容符合研究目的，具有良好效度。

三、統計方法

針對研究目的以SPSS 22.0 for windows套裝軟體進行資料分析，計算各題項之次數、百分、平均數之描述性統計數值；並以獨立樣本t檢定及單因子變異數分析探討背景變項對於各項變項之影響結果。



圖一 研究架構圖

參、結果與討論

一、研究對象基本資料

本研究受試者以女性居多計236人（佔71.1%），男性為96人（佔28.9%）；年齡在35~49歲者124人（佔37.3%），50歲以上159人（佔47.9%）等居多；教育程度以高中職以下最多共226人（佔68.1%）、大學則有67人（佔20.2%）；婚姻狀況已婚居多（258人，佔77.7%）、未婚為72人（佔21.7%）；工作類型以團膳公司最多為188人（佔56.6%）、次之為餐廳88人（佔26.5%）；工作職位最多為內外場人員145人（佔43.7%）；工作經歷10年以上居多計130人（佔39.2%）；工作場所人數最多為5人以下計118人（佔35.5%）；工作地點最多為北部有306人（佔92.2%）。（表一）

二、供膳場所聲音環境感受現況

根據供膳場所聲音環境感受結果，整體平均分數為3.35（SD=.72）（滿分為5分；參考表2），分數最高為「抽油煙機的聲音對我造成困擾」為3.54（SD=.95），分數最低為「工作時的聲音會降低工作效率」為3.13（SD=.93）。當中顯示供膳人員認為工作環境中主要影響工作效率及感受，首以抽油煙機的聲音首當其衝，這與研究調查主動式抽油煙機噪音抑制系統之研究結果相同，其所指稱工作場所的條件（如工作場所感覺到的安全和健康狀況，壓力和焦慮）與工人的生活質量顯著相關，而隨著現在人們對於工作環境中的要求，業者如果想要把離職率降低，公司就要改善工作人員的生活質量及提升工作環境品質（魏名汎，2005）。盡量減少對工作人員造成的風險從而減輕工人的壓力和焦慮（Liang & Kuo, 2002）。

三、情緒疲勞及幸福感受統計

依據情緒疲勞統計表3結果顯示平均分數為2.27（SD=.74），分數最高的為「工作一天後

會覺得筋疲力盡」（ $M=2.76$ ； $SD=1.06$ ）及「緊張不安」（ $M=2.70$ ； $SD=2.70$ ）；分數最低則為「我有自殺的想法」（ $M=1.34$ ， $SD=.77$ ）。參考前述提及供膳人員因為吵雜及繁複的作業環境，加上較高的工作壓力會容易導致工作緊張，影響情緒變化，久而久之就會形成職業倦怠，會使從業人員會有想換工作的意識（柯宏君，2011）。因此供膳場所的音源是直接影響從業人員的主觀感受，且會造成負面的情緒感受，甚至嚴重影響日常生活（陳志郎、徐佩鈴，2009）。

分析幸福感受結果平均分數為3.72（SD=.55），包括「我覺得自己的生命過得有意義」（ $M=3.84$ ， $SD=.72$ ）及「我和別人相處起來覺得滿意」的選項中（ $M=3.83$ ， $SD=.67$ ）得分最高；最低為和一般人比較，「我對自己的身份和地位感到滿意」（ $M=3.61$ ， $SD=.67$ ）。依據結果說明多數供膳人員認為其自己生命有意義並自覺滿意。這與學者的研究發現類似，推測良好的同事關係可視為壓力傷害的緩衝因子（黃寶園、林世華，2007）。彼此互相支持時，有助於提升員工的工作效能與健康。有研究指出工作場合當中員工的人際關係會影響其工作滿足（Danish & Usman, 2010; Zainudin, 2010）。所以當員工處於正向的情緒狀態當中，較能以自身的熱情表現出良好的人際關係，而能在工作上達到較高的滿足感（陳欽雨、呂博裕、莊可欣，2015）。

四、供膳人員工作效能

根據工作效能結果顯示其平均分數為3.24（SD=.49）（參考表4），正向題項得分最高為「我認為自己能勝任工作」（ $M=3.74$ ； $SD=.69$ ）；反向題中得分則以「我認為自己工作效率低，偶爾會出錯」得分最低（ $M=.76$ （ $SD=.92$ ）。結果指出供膳人員普

遍認為自己能勝任工作，而且工作滿意度高於他人。這可能與學者在內部行銷一書提到落實員工滿意之方式，包括其工作設計需以企業體深入了解員工工作需求，以便安排人力時，能夠了解到員工的想法，給予適切的工作內容，讓從業人員能夠因為喜歡工作而真正樂於工作（蕭富峰, 1997）。

五、供膳環境不同背景身心與工作效能

分析供膳場所員工不同社會人口學背景變項對身心與工作效能的影響，性別與工作資歷變項均無顯著差異；但年齡變項結果在「情緒疲勞」及「幸福感受」等變項多有差異；前者20至49歲之從業人員之情緒疲勞程度皆顯著高於50歲以上者（ $F=4.08$ ； $p=.01$ ）；後者則指出50歲以上者其幸福感受顯著高於20至35歲者（ $F=3.68$ ； $p=.01$ ）。工作場所人數分布31人以上者，其幸福感受也顯著高於6至10人之場域（ $F=3.10$ ； $p=.02$ ）。

參考國內分析其他職業類別其年齡影響身心感受之研究，指出40歲以上之護理人員主觀幸福感最高（陳盈穎, 李維綸, 蔡享翰, & 蔡照文, 2013）；或以高中職餐旅群教師為母群體發現，51歲以上的教師相較於其他年齡擁有更多的幸福感受（洪怡靜 & 陳紫玲, 2015）；與本研究同樣顯示高於50歲以上者其幸福感受較高結果相同。因此較年長者之供膳從業人員，面對繁複的工作環境，推論其能以更為正向的態度因應壓力，提升其在幸福感受的程度。

在工作場所人數31人以上的供膳人員，覺得自己在工作環境當中比較幸福且工作效率也比較高。這可能與大公司福利制度有相關性，因為大公司比小公司支付較高的福利比率（張秋蘭、林淑真, 2007），其中可能包含公司給予員工特休、員工旅遊、入股分紅等福利，使得員工在於工作中感到幸福及工作效率提高（劉

燕霖, 2009）。公司如想要留住人才可藉由貼近員工需求的福利政策，而好的福利政策不僅是滿足員工實質上的需求，更可以提高員工對工作上的滿意度。

肆、結論

本研究結果顯示，供膳人員對工作環境中的抽油煙機所發出的噪音感到困擾或焦慮，進而影響其身心狀況，其場域中因為運轉馬達而產生之干擾音源，包括俱足吸力的抽油煙機雖有不同電機質量、運轉速度，但對多數從業人員仍有相同負面的感受。情緒疲勞則顯示供膳人員經常覺得筋疲力盡或緊張不安；幸福感部分多數從業人員對於生活品質普遍覺得滿意，或者認為與其他人員相處甚洽。在工作效能的展現上，多數員工認為「我認為自己能勝任工作，效率高於標準」，即便因為供膳環境影響情緒，但整體而言仍多傾向於與他人相處得宜，或者亦能勝任工作狀態。

進一步，針對性別與工作年資檢定與上述變項並無相關差異；但年齡逾50歲以上者則形成保護因子，其對於供膳環境中的情緒疲勞感較低，及幸福感受較高，其與本研究回顧比較幸福感受之其它文獻結果相同，同樣指出因為年齡增長或過往生活經驗的累積，均提升研究對象在情緒或是心理感受的正向影響。相對其工作場所人數亦與幸福感受具有顯著相關，本研究指出員工人數在31人以上的企業其幸福感受較高，其推論為較為大型的供膳機構，因為擁有較為齊全的公司制度，或是品牌形象，因此對於員工福利，或是提供健康促進資源等，因此較大規模的員工場域其員工幸福感受較為正面，與其它文獻結果相同。

伍、建議

現今餐飲業蓬勃發展，欲提升工作效能，供膳環境極具影響，研究指出抽油煙機，其產生之噪音對於從業人員產生負面影響，因此需針對改項設備具體提出具體改善機制，針對供膳場所首當減少環境干擾，並將該場所主要噪音源改善列為建議事項，大幅降低因為不當機具音響造成身心影響。參考文獻建議亦可建議職場可增加正面聲音環境激勵員工，推動在廚房播放音樂的風潮，使員工在任何情況下與人相處和樂，對自身感到滿意也提升工作時的效率；音樂類型選擇多數人所偏好的語言及節奏，或可改善供膳人員在工作時出現之負面情緒；藉由減少工作場合的噪音，減輕工作時的煩躁感，並增加廚師對工作的滿意度，進而提高產品品質及出餐的效率，達到最佳的供膳場所績效。

此外，年齡較長之供膳從業人員對於情緒疲勞及幸福感受等變項，可形成正向的保護因子，減少因為負面環境的過度危害造成身心干擾，未來亦可針對上述資深員工進行訪談，了解其身心狀態及心理防衛機轉，作為降低因為供膳環境導致員工負面反應之程度，促進員工健康促進狀態，提升工作效益。

參考文獻

Danish, R. Q., & Usman, A. (2010). Impact of reward and recognition on job satisfaction and motivation: An empirical study from Pakistan. *International journal of business and management*, 5(2), 159.

Evans, D. (2002). The effectiveness of music as an intervention for hospital patients: a systematic review. *Journal of advanced nursing*, 37(1), 8-18.

Jacob, C., Guéguen, N., & Boulbry, G. (2010).

Effects of songs with prosocial lyrics on tipping behavior in a restaurant. *International Journal of Hospitality Management*, 29(4), 761-763.

Liang, W.-M., & Kuo, H.-W. (2002). Effects of Workplace Conditions on Taiwanese Workers. *Mid-Taiwan Journal of Medicine*, 7(4), 206-214.

Magnini, V. P., & Thelen, S. T. (2008). The influence of music on perceptions of brand personality, décor, and service quality: The case of classical music in a fine-dining restaurant. *Journal of Hospitality & Leisure Marketing*, 16(3), 286-300.

Reimer, B. (2004). New brain research on emotion and feeling: Dramatic implications for music education. *Arts Education Policy Review*, 106, 21-30.

Standley, J. M. (1986). Music research in medical/dental treatment: meta-analysis and clinical applications. *Journal of music therapy*, 23(2), 56-122.

Tsai, G. (2003). Documented Human Resource Policies Raise Worker Productivity. Pricewaterhouse Coopers International Limited.

Zainudin, A. (2010). Research methodology for business and social science. Shah Alam: Universiti Teknologi Mara Publication Centre (UPENA).

全中好、邱雅琴、陳志勇、李中一（2009）。大專餐飲學生肌肉骨骼傷病預防與健康促進之研究。餐旅暨家政學刊，6（3），221-238。

行政院主計總處（編）（2006）。中華民國行業標準分類（第8次修訂）。台北市：行

- 政院主計處。
- 吳桂林（2003）。學校廚務人員肌肉骨骼傷害與皮膚疾患調查。成功大學環境醫學研究所學位論文，1-94。
- 林子翔（2016）。裝設導煙機於廚房空氣汙染物之影響探討。高雄醫學大學公共衛生學系職業安全衛生碩士班學位論文。
- 柯宏君（2011）。國際觀光旅館從業人員工作壓力、職業倦怠與離職傾向關係之研究，國立高雄應用科技大學觀光與餐旅管理系碩士論文。
- 洪怡靜、陳紫玲（2015）。高中職餐旅群教師教學效能與幸福感之研究。師資培育與教師專業發展期刊，8（2），99-132。
- 桃樂斯·雷諾、華特·史瓦普（2000）。施貞夙譯，「激發團隊創意—運用管理引導團隊發揮創意」，新北縣：中國生產力中心。
- 張秋蘭、林淑真（2007）。1600大企業之福利實施與員工福利需求差異探討，人力資源管理學報，7（1），19-40。
- 陳志郎、徐佩鈴（2009）。熱食作業噪音暴露調查。環境汙染控制評估研討會。新竹市：元培科技大學，2009年6月26日，17。
- 陳盈穎、李維綸、蔡享翰、蔡照文（2013）。護理人員工作壓力、因應策略與幸福感相關性之探討。美和學報，32（2），83-97。
- 陳欽雨、呂博裕、莊可欣（2015）。人際關係及正向情緒對工作滿足及晉陞機會之影響。數據分析，10（6），191-215。
- 陳琮翰（2012）。烹飪油煙處理劑效能及運作條件實驗。崑山科技大學環境工程研究所學位論文。
- 黃建平、劉立文、黃奕孝、李聯雄、張振平（2010）。中式餐飲業職業衛生問題與現場輔導之研究。海峽兩岸與香港、澳門地區職業安全健康學術研究會論文集，198-207。
- 黃郁文（2011）。團膳員工工作特性、工作投入與工作績效關係之研究—以高雄市為例。高雄餐旅學院餐飲管理研究所在職專班學位論文。
- 黃種克、陳志郎（2009）。餐飲作業熱暴露評估。環境汙染控制評估研討會，新竹市：元培科技大學，2009年6月26日。
- 黃寶園、林世華（2007）。人格特質與社會支持對壓力反應歷程影響之研究：結合統合分析與結構方程模式二計量方法。教育心理學報，39（2），263-294。
- 劉燕霖（2009）。勞工特質、勞工福利滿意度與工作績效相關之研究，中國文化大學社會福利學系碩士班碩士論文。
- 潘致弘、陳秋蓉、胡瓊文（2014）。暴露烹飪油煙對餐館業勞工之氧化傷害效應。勞工安全衛生研究季刊，22（1），50-59。
- 蕭富峰（1997）。內部行銷，台北：天下文化出版社。
- 藍群傑（2007）。即食餐食工廠從業人員之教育訓練。大仁科技大學教師研究計畫成果報告。
- 魏名汎（2005）。主動式抽油煙機噪音抑制系統之研究。南台科技大學資訊工程研究所碩士論文。

表1 基本資料表 (n=332)

變項	項目	次數	百分比
性別	男	96	28.9
	女	236	71.1
年齡	≤19歲	7	2.1
	20-34歲	42	12.7
	35-49歲	124	37.3
	≥50歲	159	47.9
教育程度	高中職以下	226	68.1
	大學	67	20.2
	研究所以上	6	1.8
婚姻狀況	已婚	258	77.7
	未婚	72	21.7
工作類型	餐廳	88	26.5
	團膳公司	188	56.6
	飯店	7	2.1
	小吃店	27	8.1
	咖啡廳	4	1.2
	老闆	28	8.4
工作職位	外場人員	43	13.0
	內場人員	145	43.7
	內外場人員	102	30.7
工作資歷	<1年	49	14.8
	1~3年	60	18.1
	4~6年	45	13.6
	7~9年	42	12.7
	>10年	130	39.2
工作場所人數	≤5人	118	35.5
	6~10人	117	35.2
	11~20人	41	12.3
	21~30人	18	5.4
	>31人	24	7.2
工作地點	北部	306	92.2
	中部	12	3.6
	南部	5	1.5
	離島	1	.3

表2 供膳場所聲音環境感受分佈表 (n=332)

題目	平均數	標準差
1.工作時的聲音讓我厭煩、吵雜	3.46	1.03
2.工作時的聲音讓我疲勞	3.29	.96
3.工作時的聲音會降低工作效率	3.09	.93
4.爐灶、快速爐的聲音對我造成干擾	3.39	.93
5.抽油煙機的聲音對我造成干擾	3.54	.95
6.整體而言，工作時發出的聲音讓我困擾	3.34	.87
平均	3.35	.72

表3 情緒疲勞及幸福感受統計表 (n=332)

題目	平均數	標準差
情緒疲勞		
1.緊張不安	2.70	1.96
2.容易苦惱或動怒	2.51	.92
3.憂鬱、心情低落	2.34	.88
4.比不上別人	2.16	.92
5.難以入睡，易醒或早睡	2.60	1.09
6.有自殺的想法	1.34	.77
7.心力交瘁	2.17	.99
8.對工作感到挫折	2.15	.94
9.工作一天後會覺得筋疲力盡	2.76	1.06
10.想到隔天又要上班就覺得無精打采	2.43	1.03
11.上班時覺得每一分鐘都很難熬	1.95	.96
平均值	2.27	.74
幸福感受		
1.我認為將來會更好	3.65	.86
2.我和別人相處起來覺得滿意	3.83	.67
3.我對自己的成就等各方面感到滿意	3.71	.69
4.我對自己的身份和地位感到滿意	3.61	.67
5.我覺得自己的生命過得有意義	3.84	.72
6.我認為自己所付出的一切很值得	3.78	.75
平均值	3.72	.55

表4 工作效能統計表 (n=332)

題目	平均數	標準差
1. 我認為自己工作效率高，具有創意	3.68	.71
2. 我認為自己能勝任工作，效率高於標準	3.74	.69
3. 我認為自己勉強勝任工作，少有工作表現	2.79	.93
4. 我認為自己工作效率低，偶爾會出錯	2.76	.92
平均值	3.24	.49

表5 不同背景影響職場聲音環境感受、情緒疲勞、幸福感受與工作效能情形統計表

項目	職場聲音環境感受				情緒疲勞				幸福感受				工作效能			
	平均值	t/F	p		平均值	t/F	p		平均值	t/F	p		平均值	t/F	p	
性別																
男	21.05	2.46	.02		25.73	1.03	.30		21.97	-1.29	.19		12.87	-.59	.56	
女	19.72				24.66				22.50				13.01			
年齡																
≤19歲	20.29	.13	.94		24.43	4.08**	.01		23.00	3.68**	.01		13.00	.56	.64	
20~34歲	19.95				27.95	2>4			21.03	4>2			12.68			
35~49歲	20.31				25.82	3>4			22.10				12.91			
≥50歲	20.01				23.37				22.88				13.10			
工作資歷																
<1年	19.36	.52	.72		25.30	.15	.96		21.27	1.92	.11		12.87	.19	.94	
1~3年	20.49				25.51				21.93				13.03			
4~6年	20.00				24.33				22.66				13.19			
7~9年	20.08				24.95				22.71				12.95			
>10年	20.31				24.79				22.66				12.93			
工作場所人數																
≤5人	20.25	.62	.65		24.42	.55	.70		22.65	3.10*	.02		12.87	1.96	.10	
6~10人	20.05				25.59				21.74	5>2			12.75			
11~20人	19.63				24.77				22.05				12.98			
21~30人	21.67				26.63				22.07				12.80			
>31人	20.30				23.83				24.17				13.92			

備註：*(p<.05)、**(p<.01)

Investigation of Noise Levels and Correlation Factors for the Foodservice Staff in a Work Environment

Chia-Chen Chang¹ Li-Ling Chiu² Ju-Ting Hsueh²

¹ Department of senior citizen service business, St. John's University

²Department of Nutrition and Health Sciences, Research Center for Food and Cosmetic Safety, and Research Center for Chinese Herbal Medicine, College of Human Ecology, Chang Gung University of Science and Technology

Received 25 October 2017 ; accepted 29 August 2018

Abstract

Approximately one million people are employed in the restaurant service industry in Taiwan. Foodservice employees in this industry work in an environment with high noise levels, possibly causing physical and mental stress. This study addressed the noise levels, emotional fatigue, happiness, and work efficiency of foodservice employees during the preparation of meals. We developed a questionnaire to investigate factors related to the ambient noise levels experienced by foodservice employees, and we selected 332 employees to complete the questionnaire. The results demonstrated that foodservice employees are concerned by the noise produced by range hoods and that younger employees are more adaptable to high noise levels in the workplace. Foodservice employees feeling nervous is the main contributing factor for emotional fatigue, and employees who work with more than 31 colleagues have higher feelings of happiness. Finally, foodservice employees generally think that they are competent in their work, and their job satisfaction is higher than publics. These findings can serve as a guide to enhance health promotion and environmental construction.

Key words: noise, foodservice employees, emotional fatigue, efficiency, satisfaction

*Corresponding author : Li-Ling Chiu

國際吞嚥困難飲食標準中文繁體版本

張家臻¹ 陳惠櫻² 李蕙蓉² 林宗豪³ 謝佩君⁴ 張雁雲⁴ 邱麗玲^{5,*}

摘 要

因應全球人口老化趨勢，吞嚥困難現象更為普遍，根據推估台灣約有一百萬以上潛在的吞嚥障礙人口數。許多國家致力發展各種適應標準，但術語和級別複雜無法順利轉換。有鑑於此，2013 年國際吞嚥困難飲食標準委員會著手制定國際吞嚥困難飲食標準（The International Dysphagia Diet Standardisation Initiative, IDDSI），滿足不同個體在食物質地與液體稠度需求，現已轉譯為各國語文流通使用。為使國內吞嚥困難者理解不同階段標準，並能透過居家叉子、筷子或針筒等常見物品習得檢測食物質地及稠度流程，本文係以延續授權翻譯為中文繁體版本，及邀請國內營養學、復健科、語言治療、質地及食物製備專家等進行內容效度檢驗，以供國內高齡或吞嚥困難者後續參考使用。

關鍵詞：吞嚥困難、液體、固體、高齡者

誌謝

感謝衛生福利部國民健康署提供「針對不同營養狀態、飲食型態，研發適合老年人之飲食指引，以供選材、備餐之參據（106-107 年）」委託計畫（編號：MOHW106-HPA-M-114-112403），讓研究團隊可以針對國際飲食質地分級制度進行探討與研究，為臺灣高齡社會及牙口功能減退民眾的膳食製備工作可以更精準、完善。

此研究工作除了營養團隊本身的專業能力外，還需仰賴其他醫療專業人員的協助，在此特別感謝長庚醫療財團法人醫師群的協助，包含桃園長庚紀念醫院復健科張韋瀚醫師、林口長庚紀念醫院復健科陳美慧語言治療師、林口長庚紀念醫院義齒補綴科黃意方醫師的協助，方能將原先的國際吞嚥困難飲食標準如實呈現該有的樣貌與語意。

最後，感謝研究團隊的成員日以繼夜地蒐集文獻、與國際吞嚥困難飲食標準制定團隊商討譯本內容，才能有這次甜美的碩果。

¹ 聖約翰科技大學民生學院老人服務事業系

² 惠璿諮詢中心

³ 長庚醫療財團法人林口長庚紀念醫院一般內科暨高齡醫學科

⁴ 衛生福利部國民健康署社區健康組

⁵ 長庚學校財團法人長庚科技大學民生學院保健營養系暨食品暨化妝品安全研究中心和中草藥研究中心；長庚醫療財團法人林口長庚紀念醫院

* 通訊作者：邱麗玲

E-mail：llchiu@mail.cgust.edu.tw

壹、前言

本文轉譯自「國際吞嚥困難飲食標準版」(2007)作為國內吞嚥困難者選用食物質地與稠度之參考，並運用常見的叉子、筷子或針筒等物品作為檢測，共同邀請國內營養學、復健科、語言治療、質地及食物製備專家等進行內容效度檢驗，作為國內高齡或吞嚥困難者參考運用。參考轉譯流程，本版本參考國際吞嚥困難飲食標準委員會原 2017 年 5 月 4 日版本翻譯而成。初始於 106 年 5 月邀請兩位譯者將英文 IDDSI 翻譯成中文，召開第一次團隊討論會議，後協調為兩份中文版「國際吞嚥困難飲食標準中文版 I」與「國際吞嚥困難飲食標準中文版 II」（圖 1）。同年 7 月邀請兩位高齡者進行討論，針對字義進行確認，後經會議決議定稿為一份，於 8 到 9 月期間邀請國內營養學、復健科、語言治療、質地及食物製備專家等進行內容效度審議，換算 CVI (content validity index) 值為 .64 至 .83（表 1），顯示此版本各層級具有較佳的重要性及適當性，惟明確性受限於部分用字流暢性為 .64，而後經研究團隊確稿如下表所示。

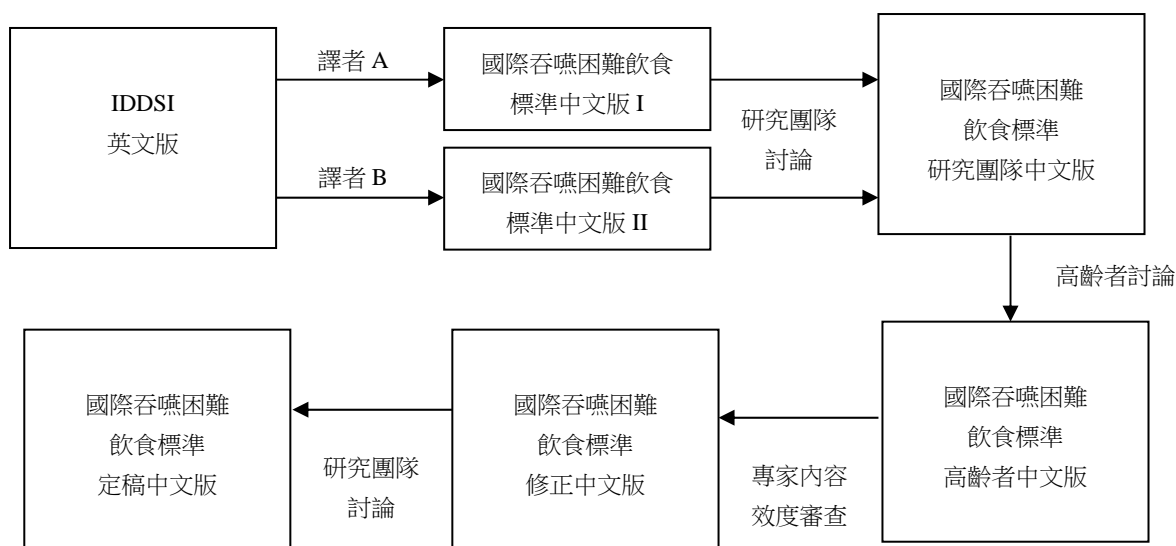


圖 1 轉譯流程圖

表 1 轉譯流程表

期程	轉譯項目	參與人員
106 年 5 月	兩位譯者進行翻譯	兩位譯者
106 年 6 月	團體討論及修正	兩位譯者、研究人員
106 年 7 月	團體討論及修正	高齡者、研究人員
106 年 8~9 月	專家效度審定	營養學、復健科、語言治療、質地及食物製備等專家
106 年 10 月	修定文稿	研究人員

貳、IDDSI 架構與詳細定義

第 0 級 THIN 稀薄	
描述／特徵	<ul style="list-style-type: none"> • 流速如水 • 流速快 • 適合任何年齡或方法，可用任何類型的奶嘴、杯子、吸管飲用

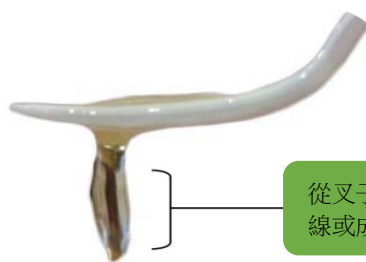
此稠度適用的生理條件	<ul style="list-style-type: none"> 能有效安全地飲用各類型的液體
測試方法 IDDSI 流量測試	<ul style="list-style-type: none"> 測試液體在 10 秒內完全流過 10 c.c.針筒，且無殘留液（參考 IDDSI 測試方法）。

第 1 級 SLIGHTLY THICK 輕微稠	
描述／特徵	<ul style="list-style-type: none"> 比水稍微濃稠 比稀薄的液體需要多一點力氣飲用 可流過吸管、針筒、和奶嘴 濃稠度類似於市售防吐奶（新諾兒 AR）的嬰兒配方奶粉稠度
此稠度適用的生理條件	<ul style="list-style-type: none"> 主要用於嬰幼兒，做為降低流速的增稠飲品，但其稠度仍能通過奶嘴。應依個別狀況決定是否適用奶嘴的流速
測試方法 IDDSI 流量測試	<ul style="list-style-type: none"> 測試液體流過 10c.c.針筒，10 秒後還剩餘 1-4c.c 殘留液（參考 IDDSI 測試方法）。

第 2 級 MILDLY THICK 稍微稠	
描述／特徵	<ul style="list-style-type: none"> 可從湯匙流下 可啜飲，可以從湯匙迅速倒出，但比稀薄液體速度慢 使用標準口徑的吸管（標準吸管口徑= 直徑 0.209 英寸或 0.53 公分），需稍微費力才能吸取
此稠度適用的生理條件	<ul style="list-style-type: none"> 如果無法安全地控制流速太快的稀薄液體，此稍微稠的液體稠度流速則較慢 此級別適合舌頭控制能力稍輕微不佳者
測試方法 IDDSI 流量測試	<ul style="list-style-type: none"> 測試液體流過 10c.c.針筒，10 秒後還剩餘 4-8c.c 殘留液（參考 IDDSI 測試方法）。

第 3 級 MODERATELY THICK／LIQUIDISED 中稠度/液狀	
描述／特徵	<ul style="list-style-type: none"> 可以使用杯子飲用 需要稍微用力才能從標準或寬口徑的吸管吸取（寬口徑吸管= 0.275 英寸或 0.69 公分） 無法在餐盤上成型 無法用叉子進食，因為它會從叉齒縫隙間滴下 可以透過湯匙進食 可啜飲，可從湯匙上慢慢滑下來 不需要透過口腔加工或是咀嚼，可以直接吞嚥 質地滑順，沒有塊狀（團塊、纖維、帶皮或帶殼、外殼、碎骨）
此稠度適用的生理條件	<ul style="list-style-type: none"> 此層級適用於舌頭無法控制稍微稠的液體者，則可採用此中稠度液體 能進行更長時間的口部控制 需要一些舌頭推進的力量 吞嚥疼痛者
測試方法 IDDSI 流量測試	<ul style="list-style-type: none"> 測試液體流過 10c.c.針筒，10 秒後還剩餘超過 8c.c.殘留液（參考 IDDSI 測試方法）
叉子滴落測試	<ul style="list-style-type: none"> 在叉齒縫隙間會以成團方式緩慢滴下 以叉子戳壓，表面不會留下清楚的印痕 溢出時會擴散開來

第 3 級 MODERATELY THICK/LIQUIDISED 中稠度/液狀	
湯匙傾斜測試	• 當湯匙傾斜時會緩滿滴下，不會黏附在湯匙上
筷子測試	• 筷子不適合運用在此種質地的食物
手指測試	• 這種食物的質地無法用手指拿取，同時這種質地的食物會輕易的從指間滑落，並留下食物的痕跡
食物種類舉例	<ul style="list-style-type: none"> • 以下的食物均屬於中稠度 • 嬰幼兒的初級食品（米糊或是果泥） • 醬料或是調味醬 • 果漿

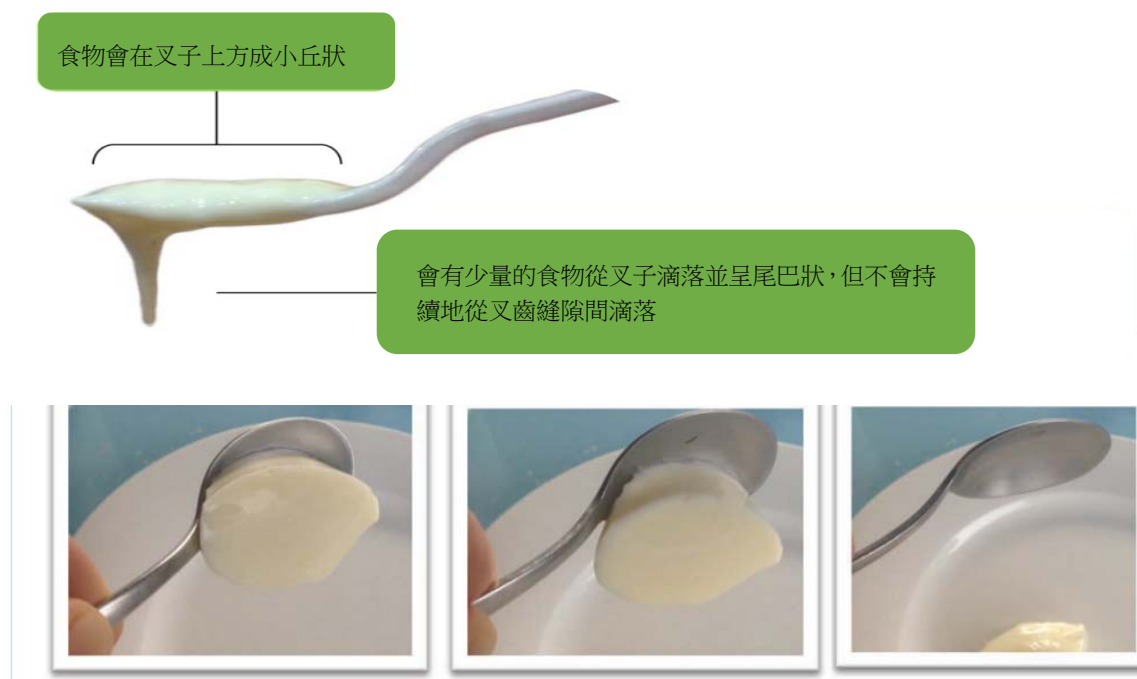


從叉子的縫隙中緩慢滴下或成線或成團狀的滴下

IDDSI 叉子滴落測試

第 4 級 EXTREMELY THICK/PUREED 高稠度/泥狀	
描述／特徵	<ul style="list-style-type: none"> • 通常可用湯匙進食（也可以用叉子） • 不能以杯子飲用 • 不能以吸管吸取 • 不需要咀嚼 • 可分層堆積或成型於餐盤 • 在重力作用下會緩慢移動，但不會溢出 • 當湯匙傾斜時會整塊掉落，但能在盤子上成型 • 不含塊狀 • 不黏稠 • 液體不會從固體分離出來（離水現象）
此稠度適用的生理條件	<ul style="list-style-type: none"> • 如果舌頭控制力明顯不足，此級別也許最適合飲用 • 比 5 級、6 級、7 級需要較少的推動力，但比 3 級需要更多力道 • 不需要撕咬或咀嚼 • 如果食物稠度過高，會有增加食物殘留的風險 • 任何需要口腔咀嚼，控制或成團的食物都不屬於該級 • 適用於咀嚼或吞嚥會感到疼痛者 • 適用於缺牙或配戴不合假牙者
測試方法 IDDSI 流量測試	• 測試液體倒入 10 c.c. 針筒，10 秒後不會流出或滴落（參考 IDDSI 測試方法）。
叉子壓力試驗	<ul style="list-style-type: none"> • 利用叉子叉壓食物，在食物表面留下清晰的印痕 • 無塊狀
叉子滴落試驗	• 食物會在叉子上方形形成小丘狀，會有少量的食物從叉子間滴下並呈尾巴狀，但不會持續地滴落

第 4 級 EXTREMELY THICK / PUREED 高稠度/泥狀	
湯匙試驗	<ul style="list-style-type: none"> • 有足夠的凝聚力，在湯匙上可維持原狀 • 如果湯匙傾斜，整勺食物會直接從湯匙中掉落；或只需輕敲就可從湯匙中滑落，只殘留少許在湯匙上。此類食物不會結塊或黏稠 • 在平坦的表面上可能會稍微擴散開或緩慢散落
筷子測試	<ul style="list-style-type: none"> • 筷子不適合運用在此種質地的食物
手指測試	<ul style="list-style-type: none"> • 可以用手指拿取，可在指間輕易滑動，且留下明顯地殘留物
食物過於濃稠指標	<ul style="list-style-type: none"> • 傾斜時不會從湯匙上滑落 • 會黏在湯匙上
具體食物範例	<ul style="list-style-type: none"> • 以下品項可能適用於此類別： • 適合嬰幼兒的泥狀輔食品（肉泥、濃稠的麥精糊）



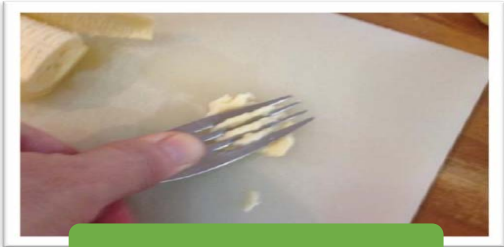

湯匙傾斜測試：可以在湯匙上保持形狀，有黏性，但不堅固，在湯匙上留下極少殘留物

第 5 級 MINCED & MOIST 細碎型	
描述／特徵	<ul style="list-style-type: none"> • 可以用叉子或湯匙進食 • 如果較好的手部控制能力，有些情況下可以使用筷子進食 • 可以成形於盤子上（例如：球形） • 柔軟潮濕且無液體分離流出 • 食物中有小塊物 <ul style="list-style-type: none"> ➢ 兒童 0.2~0.4 公分 ➢ 成人 0.4 公分 • 塊狀物可輕易被舌頭壓扁
此稠度適用的生理條件	<ul style="list-style-type: none"> • 不需要咬斷 • 幾乎不需咀嚼 • 只要用舌頭力量，就可以將此級別的食物小塊壓碎

第 5 級 MINCED & MOIST 細碎型	
	<ul style="list-style-type: none"> • 需要靠舌頭力量移動食糰 • 咀嚼時會感到疼痛或疲累者 • 適用於缺牙或配戴不合假牙者
測試方法	<ul style="list-style-type: none"> • 用叉子按壓時，食物會輕易地分開並穿過叉齒縫隙
叉子壓力試驗	<ul style="list-style-type: none"> • 可以輕易地用叉子壓碎食物（所使用的壓力不應使拇指指甲變白）
叉子滴落試驗	<ul style="list-style-type: none"> • 若用叉子挖取食物，可在叉子上呈現小丘狀，食物不會輕易從叉齒縫隙中掉落
湯匙傾斜測試	<ul style="list-style-type: none"> • 具有足夠的凝聚力，在湯匙上可維持一定的形狀 • 如果湯匙傾斜、翻面或輕輕搖動，則整杓食物會從湯匙上滑落，食物會輕易地從湯匙上滑落，或很少殘留，即食物不應太黏糊 • 舀食物在盤子上，食物會稍微擴散或塌陷
筷子測試	<ul style="list-style-type: none"> • 如食物濕潤凝著時，且手部控制能力良好，則可使用筷子夾取
手指測試	<ul style="list-style-type: none"> • 可以用手指輕易地拿取該質地的食物，手指能輕易壓扁小、柔軟、滑順的圓形顆粒。潮濕的食物則會讓手上留下濕潤感
具體食物範例	<p>肉類</p> <ul style="list-style-type: none"> • 適當剁碎、細碎或細嫩 ➢ 兒童 0.2~0.4 公分 ➢ 成人 0.4 公分 • 搭配濃厚的醬汁或肉汁 • 如果食材不能被充分剁碎，則製作成肉泥 <p>魚類</p> <ul style="list-style-type: none"> • 充分搗成糊狀，可搭配濃厚的醬汁或肉汁 ➢ 兒童 0.2~0.4 公分 ➢ 成人 0.4 公分 <p>水果</p> <ul style="list-style-type: none"> • 充分搗碎 • 瀝掉多餘的果汁 ➢ 兒童 0.2~0.4 公分 ➢ 成人 0.4 公分 <p>蔬菜類</p> <ul style="list-style-type: none"> • 適當剁碎、細碎或糊狀 • 瀝掉多餘的液體 ➢ 兒童 0.2~0.4 公分 ➢ 成人 0.4 公分 <p>穀類</p> <ul style="list-style-type: none"> • 非常濃厚滑順，含有 0.2~0.4 公分柔軟小團塊 • 食材需要完全軟化 • 不會有任何牛奶或液體，進食前瀝掉多餘的液體 <p>麵包</p> <ul style="list-style-type: none"> • 膠凝狀的麵包，麵包食材潮濕或呈現膠狀 • 避免食用較乾的麵包 <p>米飯</p> <ul style="list-style-type: none"> • 不應為黏稠糯米狀（特別是短粒米），在烹調或進食時也不應為一粒粒分開的顆粒狀（特別是長粒米）

第 5 級 MINCED & MOIST 細碎型	
 <p>用叉齒的縫隙（0.4cm）來確定碎塊的大小是否合適</p>	

第 6 級 SOFT 軟質型	
描述／特徵 質地限制統整於總結表格	<ul style="list-style-type: none"> • 可用叉子、湯匙或筷子進食 • 可以用叉子、湯匙或筷子將其壓碎 • 不需刀子切割，但需要用刀子輔助叉子或湯匙盛取食物 • 吞嚥前需要咀嚼 • 食材柔軟、細嫩及濕潤，但不會分離出液體 • “一口大小”的食物應為口腔能處理的合適大小 <ul style="list-style-type: none"> ➢ 兒童 0.8 公分 ➢ 成人 1.5 公分
此稠度適用的生理條件	<ul style="list-style-type: none"> • 不需要咬斷 • 需要咀嚼 • 在咀嚼時需要透過舌頭的力量和移動以咀嚼，並讓食物穩定的停留在口中 • 吞嚥時，需要舌頭的力量來後送食團 • 咀嚼時會感到疼痛或疲累者 • 適用於缺牙或配戴不合假牙者
測試方法	
叉子壓力試驗	<ul style="list-style-type: none"> • 以叉子側面即可以將食物切成較小塊 • 用拇指以叉子底部按壓食物（1.5×1.5 公分）至拇指指甲變白時，食物會被擠壓及改變形狀，但將叉子移開後，食物不會恢復原狀
湯匙壓力測試	<ul style="list-style-type: none"> • 以湯匙側面可以將食物切斷或切成小塊 • 用拇指以湯匙底部按壓食物（1.5×1.5 公分），食物會被擠壓及改變形狀，將湯匙移開後，食物不會恢復成原樣
筷子測試	<ul style="list-style-type: none"> • 用筷子可將食物分成較小塊狀
手指測試	<ul style="list-style-type: none"> • 取一塊拇指大小的食物（1.5 公分 x 1.5 公分），可用手指壓扁，而拇指、食指指甲會發白，食物也無法恢復原狀
具體食物範例	肉類 <ul style="list-style-type: none"> • 煮熟、鬆軟 <ul style="list-style-type: none"> ➢ 小孩 0.8 公分 x 0.8 公分 ➢ 大人小於 1.5 公分 x 1.5 公分 • 如果尺寸在 1.5 公分 x 1.5 公分時，質地不夠鬆軟，則應濕潤且切碎

第 6 級 SOFT 軟質型	
	<p>魚類</p> <ul style="list-style-type: none"> • 煮熟鬆軟的魚肉，可用叉子、湯匙、筷子分成小塊 <ul style="list-style-type: none"> ➢ 孩為 8 釐米小塊 ➢ 大人為 15 釐米=1.5 公分小塊 • 沒有魚骨 <p>熱菜／燉菜／咖哩</p> <ul style="list-style-type: none"> • 醬汁部分必須濃稠（根據臨床標準，或參考 IDDSI 0 到 4 級） • 食材內容可為肉類，魚類或蔬菜食物，煮完後柔軟細嫩 • 沒有硬塊 <p>水果</p> <ul style="list-style-type: none"> • 為搗碎狀 <ul style="list-style-type: none"> ➢ 小孩為 8 釐米小塊 ➢ 大人為 15 釐米=1.5 公分小塊 • 不包括水果的纖維部分 • 濾掉多餘的果汁 • 應評估個人是否有能力進食含水量高的水果（例如西瓜），因為在口中咀嚼時，水果的水分和固體會分離 <p>蔬菜</p> <ul style="list-style-type: none"> • 蒸熟或燙熟後的蔬菜 <ul style="list-style-type: none"> ➢ 小小孩為 8 釐米小塊 ➢ 小大人為 15 釐米=1.5 公分小塊 • 拌炒後的蔬菜通常太硬，不夠細嫩 <p>穀類</p> <ul style="list-style-type: none"> • 滑順且鬆軟的小塊 <ul style="list-style-type: none"> ➢ 小小孩為 8 釐米小塊 ➢ 小大人為 15 釐米=1.5 公分小塊 • 食材需充分軟化 • 瀝除多餘的牛奶或液體 <p>麵包</p> <ul style="list-style-type: none"> • 除非經過吞嚥困難專家評估為合適，否則不可食用（可接受的尺寸大小幼兒為 8 釐米小塊；大人為 1.5cm*1.5cm） <p>白飯</p> <ul style="list-style-type: none"> • 不能為顆粒分明，也不能太粘
 <p>拇指指甲會變白</p>	 <p>食物被擠壓並無法恢復成原樣</p>
IDDSI 叉子測試	

第 7 級 REGULAR 常規食物	
描述／特徵 質地限制統整於總結表格	<ul style="list-style-type: none"> • 常規食物，適合各年齡層的各種日常食物皆為此級別 • 任何方法都能被用來進食這些食物 • 食物可能很硬、很脆或本來就柔軟的 • 食物的尺寸在第七級較不受限，但仍有尺寸範圍 <ul style="list-style-type: none"> ➢ 小孩小於 8 mm 小塊 ➢ 大人為 15 mm=1.5 cm 小塊 • 包含堅硬、難嚼、多纖維狀、有筋的、有黏性、乾燥、酥脆的、脆的、易碎的塊狀 • 含有小核籽、種子、果皮、外殼或骨頭的食物 • 包括雙重質地或是混合質地的食物或液體
此稠度適用的生理條件	<ul style="list-style-type: none"> • 可以咀嚼任何堅硬或柔軟的食物，並使其成為柔軟可吞嚥的食團 • 可輕易的咀嚼所有質地的食材而不會覺得疲累 • 可安全的吐掉食物中不能吞嚥的骨頭或軟骨
測試方法	無

過渡性食物

描述／特徵	<ul style="list-style-type: none"> • 當被潤濕（例如加水或唾液）或有溫度變化時（例如：加熱），食物從一種質地（例如堅硬的固體）轉變到另一種質地
此稠度適用的生理條件	<ul style="list-style-type: none"> • 不需要咬斷 • 需要稍微咀嚼 • 食物一旦改變溫度或加入水分/唾液，便可以用舌頭弄碎這些食物 <ul style="list-style-type: none"> ➢ 可用於咀嚼技巧的發展、訓練或復健（例如：兒童或有發育障礙族群的咀嚼訓練；中風後咀嚼功能的復健）
測試方法 叉子壓力測試	<ul style="list-style-type: none"> • 食物一旦被溫度或濕潤改變，便會輕易地變形且不會再恢復成原樣 • 取一拇指指甲大小（1.5 公分×1.5 公分）的食物加入 1cc 的水後等待一分鐘，用拇指持叉子底面按壓直到指甲變白，當移除叉子壓力後，食物呈現以下狀態即稱為過渡性食物： <ul style="list-style-type: none"> ➢ 食物已被擠壓並碎裂，不再回覆原狀 ➢ 食物已明顯溶化，不再保持原狀（例如：碎冰）
湯匙壓力測試	<ul style="list-style-type: none"> • 使用湯匙的底面代替叉子，重複上述的步驟
筷子測試	<ul style="list-style-type: none"> • 取一拇指指甲大小（1.5 公分×1.5 公分）的食物加入 1cc 的水後等待一分鐘後，食物可輕易地用筷子分開
手指測試	<ul style="list-style-type: none"> • 取一拇指指甲大小（1.5 公分×1.5 公分）的食物加入 1cc 的水後等待一分鐘後，再用拇指和食指揉搓，食物會完全捏碎且不會恢復原樣
具體食物或其他範例	<p>此質地可能包括下列食物但不僅限於此：</p> <ul style="list-style-type: none"> • 碎冰 • 冰淇淋／冰沙（如果吞嚥困難專家評估為合適） • 日式吞嚥困難訓練果凍，採用 0.1mm×1.5mm 大小薄片 • 威化餅（包含教會所食用的餐餅） • 甜筒餅乾 • 甜餅乾／鹹餅乾／薄脆餅乾 • 洋芋片－只允許碎片的型態（例如：品客） • 奶油酥餅 • 蝦餅

<p>具體實例用於兒童或成人吞嚥困難障礙</p>	<p>市售的過渡性食物例子：</p> <ul style="list-style-type: none"> • 蔬果脆片 Veggie Stix™ • 芝多起士求 Cheeto Puffs™ • 米餅 Rice Puffs™ • 寶貝媽媽脆餅 Baby Mum Mums™ • 嘉寶穀物水果星星泡芙 Gerber Graduate Puffs™ <p>以上列出的品牌並非推薦，可根據個人喜好選擇相似質地的食材</p>
--------------------------	---

- 在食物中加入 1cc 的水
- 等候 1 分鐘



過渡性食物

參、IDDSI 測試方法

依循 IDDSI 系統性回顧建議，液體和固體食物依照口腔作用、口腔運輸和食物流動的各種生理過程進行分類。為此，需使用不同的工具才能最恰當地描述食團的性狀和動作(Steele et al., 2015)

一、飲品和其他液體

精確測量液體的流動性是一項複雜的任務。迄今為止，現有的研究或國際術語都推薦以飲品的黏稠度為基準進行分類。然而，大多數的臨床醫生或護理人員並無法進行黏稠度測量。此外，黏稠度並不是唯一的相關參數：在飲用時，飲品的流動性還會受許多其他因素的影響，包括密度、抗拉強度、溫度、推進壓力和脂肪量(O'Leary et al., 2010; Sopade et al., 2007, Sopade et al., 2008a, b; Hadde et al., 2015a, b)。系統性回顧指出，許多廣泛備使用的測量技術，包括剪切速率、樣品溫度、密度和抗拉強度很少被提及(Steele et al., 2015; Cichero et al., 2013)。添加不同增稠劑的增稠飲飲品也許在黏性測量中具有一致的剪切速率，卻在應用中表現出截然不同的流動性(Steele et al. 2015; O'Leary et al., 2010; Funami et al., 2012; Ashida et al., 2007; Garcia et al., 2005)。除了不同的流速與飲品的種類有關，吞嚥時的預期流速也會根據年齡和吞嚥功能的損害程度而不同(O'Leary et al., 2010)。

基於這些因素，在 IDDSI 的描述中並未包含測量黏稠度。反之，建議使用 10 ml 針筒進行液體重重力流動的測試(10 秒流動後，針筒中剩餘的樣品量)。並透過常見的吸管或量杯進行控制。IDDSI 流量測試在設計和測量原理方面也與乳品業用於測量液體濃稠度的 Posthumus Funnel 相似(Van Vliet, 2002; Kutter et al., 2011)。事實上

Posthumus Funnel 看起來像一個大型針筒（Van Vliet, 2002; Kutter et al., 2011），其測試包含對定量樣品流動時間的測量，及對經過一段固定時間後剩餘液體量的測量。Van Vliet（2002）認為 Posthumus Funnel 的幾何形狀包含一個剪切和伸長的部份，這與口腔內的流動條件更為接近。

以針筒作為 IDDSI 流量測試的工具雖然簡單，但目前已經證明針筒能可靠地分類不同的液體，並且符合現有的專家判斷和實驗室的試驗結果。對於不同的飲用溫度而產生濃稠度間的細微變化也及具敏感度。

（一）IDDSI 流量測試

IDDSI 的流量測試使用的是 10 ml 的滑鎖皮下針筒，如下圖所示



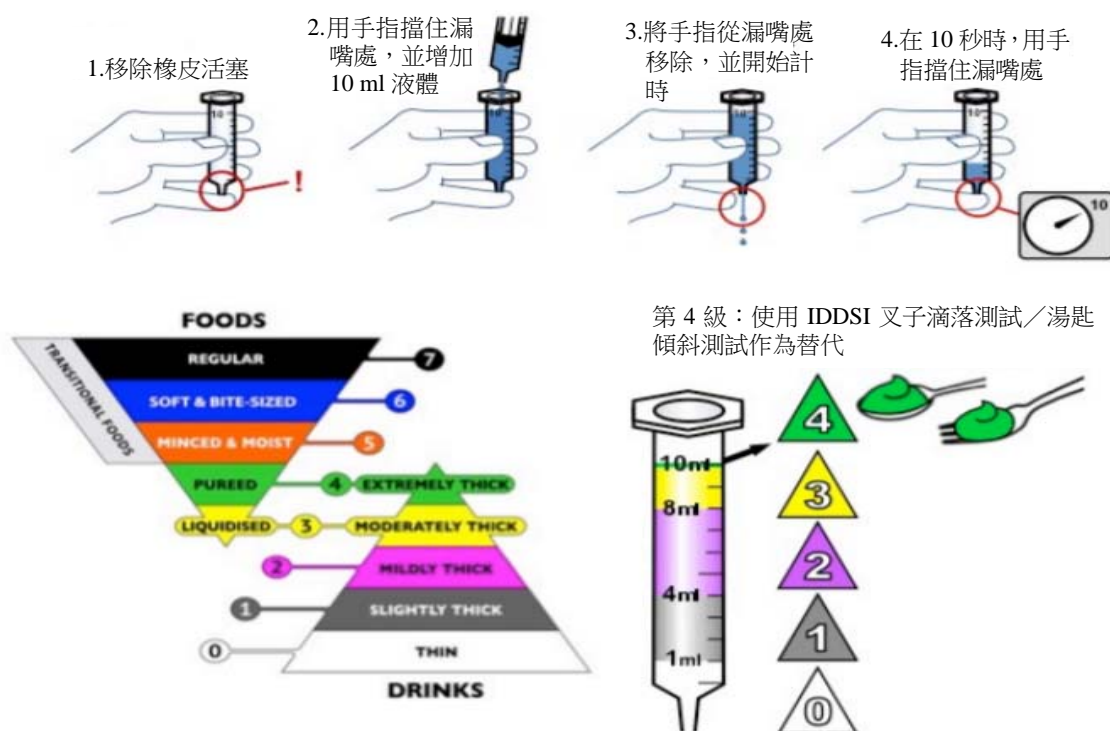
根據國際 ISO 標準（ISO 7886-1），最初認為 10 ml 針筒在世界各地是相同的，但隨後確定 ISO 文件所指的僅限針筒的針頭，在不同品牌針筒中橡皮活塞的長度和大小仍存在差異。準確的說，IDDSI 流量測試所使用的針筒為從 0 ml 刻度到 10 ml 刻度的測量長度為 61.5 mm（以 BD™ 針筒製造商代碼 301604 作為基準）。IDDSI 發現有一些針筒雖標記為 10 ml，但實際上卻是 12 ml 的容量。若使用 12 ml 針筒所測試出的結果與真正為 10 ml 針筒的測試的結果並不相同。因此，事先檢查針管的長度(如下圖所示)十分重要，詳細的測量流程如下圖所示。IDDSI 流量測試的視頻可在以下網址觀看：[Http://iddsi.org/framework/drink-testingmethods/](http://iddsi.org/framework/drink-testingmethods/)

IDDSI 流量測試（0-3 級）可以測量飲品和液體，包括肉汁、醬汁和營養補充品；第 4 級的飲品已經非常濃稠，10 秒內無法流過 10 ml 針筒，最好以湯匙食用，建議使用 IDDSI 叉子測試和/或湯匙傾斜測試作為確定質地的方法。

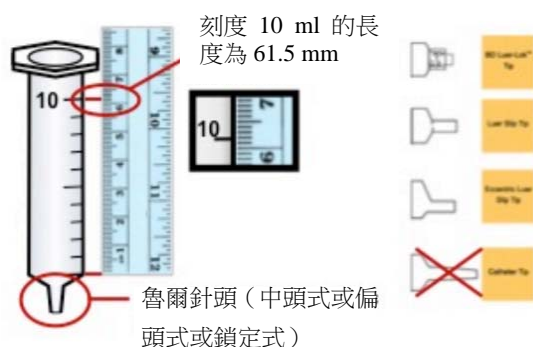
（二）IDDSI 流量測試作為液體濃稠度分級

根據國際吞嚥困難飲食標準化倡議（IDDSI）架構項目和定義，說明液體稠度測量工具。針筒的流量測試依照不同流速分類為 IDDSI 的 0-3 級。第 4 級則使用 IDDSI 叉子滴落測試／湯匙傾斜測試作為替代。

1. 移除橡皮活塞
2. 用手指擋住漏嘴處，並增加 10 ml 液體
3. 將手指從漏嘴處移除，並開始計時
4. 在 10 秒時，用手指擋住漏嘴處



針筒規格：測試時須使用以下針筒尺寸才能獲得正確的測驗結果



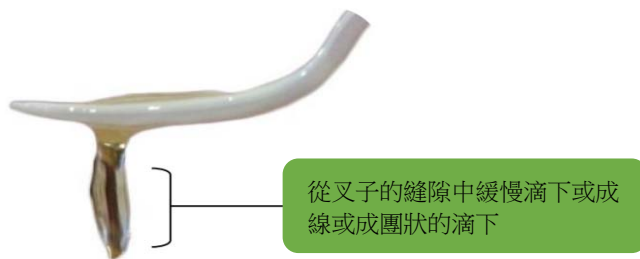
二、食物

迄今在食物質地測量領域的研究皆需要複雜且昂貴的機器，如物性分析儀儀。有鑑於難以取得這種設備且測試和解釋測驗結果皆需仰賴專業知識，許多國家的專業術語皆使用更詳盡的方式來描述食物的質地。系統性回顧文獻指出，硬度、黏稠度和潤滑度皆為需考慮的重要因素 (Steele et al, 2015)，此外，食品樣本的大小和形狀已被確認為噎咳風險的相關因素 (Kennedy et al., 2014; Chapin et al 2013; Japanese Food Safety Commission, 2010; Morley et al., 2004; Mu et al., 1991; Berzlanovich et al 1999; Wolach et al., 1994; Centre for Disease Control and Prevention, 2002, Rimmell et al., 1995; Seidel et al., 2002)。

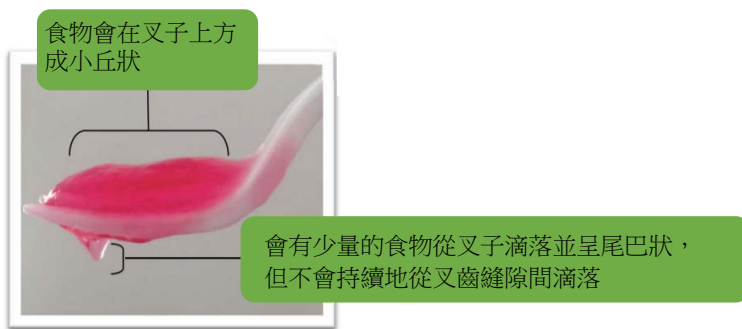
基於這些資料，食物的測量需要取得食物的物理特性（例如：硬度、內聚性、黏稠度等）和幾何形狀特性。IDDSI 對於食物質地和特徵的描述，均源自於國際專業術語和探討增加噎咳風險等研究文獻。為了確認食物質地所屬的級別，需以一系列的方法測試。測試細泥型、軟質型、堅硬和固態食物的方法包括：叉子滴落測試、湯匙傾斜測試、叉子或湯匙壓力測試、筷子測試和手指測試，關於這些測試方法的示範影片可在下列網址觀看：
<http://iddsi.org/framework/food-testing-methods/>

（一）叉子滴落測試

濃稠的飲品和流質食物（3 級和 4 級）可以透過它們是否流經叉齒縫，及比較每個級別的詳細描述作為測試。目前在澳大利亞、愛爾蘭、紐西蘭和英國等國家專業術語中皆有提及叉子滴落測試（Atherton et al., 2007; IASLT and Irish Nutrition & Dietetic Institute 2009, National Patient Safety Agency, Royal College speech & Language Therapists, British Dietetic Association, National Nurses Nutrition Group, Hospital Caterers Association 2011）。第 3 級流態型／中稠度的圖像如下圖所示。



第 4 級細泥型／高稠度的圖像如下圖所示。



（二）湯匙傾斜測試

湯匙傾斜測試作為確認食物的黏稠度（黏著性）及食物凝聚在一起的能力（內聚性）。目前在澳大利亞、愛爾蘭、紐西蘭和英國的國家專業術語中皆有提及湯匙傾斜測試（Atherton et al., 2007; IASLT and Irish Nutrition & Dietetic Institute 2009; National Patient Safety Agency, Royal College Speech & Language Therapists, British Dietetic Association, National Nurses Nutrition Group, Hospital Caterers Association 2011）。

湯匙傾斜測試主要用於測量 4 級和 5 級的食物，食物應為：

- 具有足夠的內聚性，使其能在湯匙上保持形狀
- 如果湯匙傾斜或翻面或輕微晃動，則食物會整杓掉落，但若食物僅少許殘留在湯匙上，則會很容易滑落，因此，食物不應為黏稠狀

- 盤子上的食物可能會擴散或輕微滑落



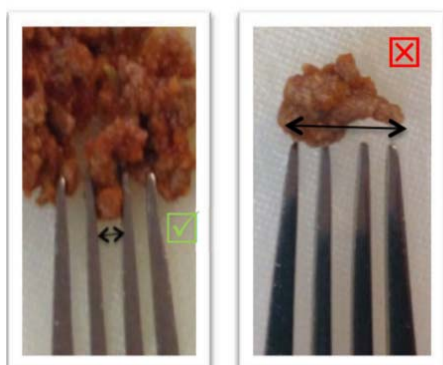
(三) 軟質、堅硬和固態食物質地評估

叉子可作為評估軟質、堅硬和固態食物質地的工具，因為叉子除了可以評估食物的硬度，也能評估顆粒尺寸的大小。

(四) 評估 4mm 顆粒尺寸的標準

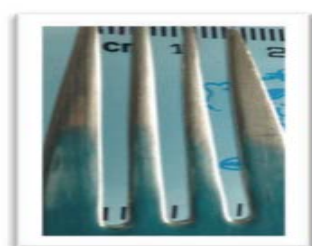
對於成年人而言，吞食前咀嚼完的固體食物的平均尺寸為 2-4mm (Peyron et al., 2004; Woda et al., 2010)。標準鐵製叉子的尖齒／尖頭之間的槽／間隙通常測量為 4mm，可有效測量第 5 級細碎型食物的顆粒尺寸。為了確保定嬰兒可安全食用，食物尺寸應小於兒童第五隻指頭（小指）的最大寬度，此測量同時也預測為新生兒氣管內管的內側直徑，可以避免窒息的風險 (Turkistani et al., 2009)。

可用叉子的縫隙確認食物是否符合 4 mm 的大小



(五) 評估 15mm (1.5cm) 顆粒尺寸的標準

對於軟質、堅硬和固態食物，建議食物的最大尺寸為 1.5 x 1.5 cm，尺寸大致和成年人拇指指甲相同 (Murdan, 2011)。標準叉子的整個測量寬度也大約為 1.5cm，如下圖所示。第 6 級軟質型的顆粒尺寸也建議為 1.5 x 1.5 cm，以降低因為食物噎咳所引起窒息的風險 (Berzlanovich et al., 2005)。



（六）叉子壓力測試和湯匙壓力測試

將叉子作為測量工具時，可透過叉子施加壓力於食物並觀察食物的變化，施加於食物上的壓力須為可使拇指指甲變白所需的壓力，如圖中的箭頭所示。

使拇指指甲變白所需的壓力經測量為 17 kPa，此壓力與吞嚥期間使用的舌肌力是相同的（Steele et al., 2014）。在右圖中，使用愛荷華口腔能力測試儀（Iowa Oral Performance Instrument）測得壓力。此測試儀器也可作為測量舌壓的工具。

進行叉子壓力測試時，將叉子壓在食物上，並將拇指放在叉子的凹槽上（位於叉齒底部）直到看到指甲變白，如左圖所示。但叉子在世界某些地方並不容易取得，因此可以用湯匙底部施加壓力作為替代工具。

（七）筷子測試和手指測試

IDDSI 的測試方法中包含筷子測試和手指測試，在某些國家手指測試已被認可是最方便的測試方法。

三、過渡性食物質地分析

過渡性食物為食物一開始為一種質地（例如：堅固的固體），添加水分後（例如：水、唾液）或者溫度發生變化（例如：加熱），便會轉變為另一種質地。可用於咀嚼技巧的發展、訓練或復健，例如目前已經用於兒童或有發育障礙/發展遲緩族群的咀嚼訓練（Gisel 1991, Dovey et al., 2013）。評估樣品是否符合過渡性食物的定義，需進行以下的步驟確認：

取一個拇指大小的食物（1.5 x 1.5 cm），加入 1 ml 的水放入食物上並等待 1 分鐘，透過叉子施加壓力於食物上，直到拇指指甲變白。移除叉子壓力後，樣品若為過渡性食物則符合下列：

- 移除叉子後，食物被壓扁並分解，不再為原本的狀態
- 以筷子施加最小壓力便可輕鬆分解食物
- 用食指和拇指揉捏可徹底將食物捏碎，且不會恢復原狀
- 食物已經明顯溶化，不能再恢復原狀（例如：碎冰）

- 在食物中加入 1cc 的水
- 等候 1 分鐘



參考文獻

1. Ashida I, Iwamori H, Kawakami SY, Miyaoka Y, Murayama A. Analysis of physiological parameters of masseter muscle activity during chewing of agars in healthy young males. *J Texture Stud.* 2007;38:87–99.
2. Atherton M, Bellis-Smith N, Cichero JAY, Suter M. Texture modified foods and thickened fluids as used for individuals with dysphagia: Australian standardised labels and definitions. *Nutr Diet.* 2007;64:53–76.
3. Berzlanovich AM, Muhm M, Sim E, Bauer G. Foreign body asphyxiation—an autopsy study. *Am J Med* 1999;107: 351–5.
4. Centre for Disease Control and Prevention. Non-fatal choking related episodes among children, United States 2001. *Morb Mortal Wkly Rep.* 2002; 51: 945–8.
5. Chapin MM, Rochette LM, Abnneest JL, Haileyesus, Connor KA, Smith GA. Nonfatal choking on food among children 14 years or younger in the United States, 2001–2009, *Pediatrics.* 2013; 132:275–281.
6. Cichero JAY, Steele CM, Duivesteyn J, Clave P, Chen J, Kayashita J, Dantas R, Lecko C, Speyer R, Lam P. The need for international terminology and definitions for texture modified foods and thickened liquids used in dysphagia management: foundations of a global initiative. *Curr Phys Med Rehabil Rep.* 2013;1:280–91.
7. Dovey TM, Aldridge VK, Martin CL. Measuring oral sensitivity in clinical practice : A quick and reliable behavioural method. *Dysphagia.* 2013; 28:501–510.
8. Funami T, Ishihara S, Nakauma M, Kohyama K, Nishinari K. Texture design for products using food hydrocolloids. *Food Hydrocolloids.* 2012;26:412–20.
9. Garcia JM, Chambers ET, Matta Z, Clark M. Viscosity measurements of nectar- and honey-thick liquids: product, liquid, and time comparisons. *Dysphagia.* 2005;20:325–35.
10. Gisell EG. Effect of food texture on the development of chewing of children between six months and two years of age. *Dev Med Child Neurol.* 1991;33:69–79.
11. Hadde EK, Nicholson TM, Cichero JAY. Rheological characterisation of thickened fluids under different temperature, pH and fat contents. *Nutrition & Food Science,* 2015a; 45 (2): 270 – 285.
12. Hadde EK, Nicholson TM, Cichero JAY. Rheological characterization of thickened milk components (protein, lactose and minerals). *J of Food Eng.* 2015b; 166:263–267.
13. IASLT & Irish Nutrition and Dietetic Institute. Irish consistency descriptors for modified fluids and food. 2009. <http://www.iaslt.ie/info/policy.php> Accessed 29 April 2011.
14. ISO-7886-1: 1993 (E) Sterile hypodermic syringes for single use: Part 1: syringes for manual use. *International Standards Organisation* www.iso.org
15. Japanese Food Safety Commission, Risk Assessment Report: choking accidents caused by foods, 2010.
16. Kennedy B, Ibrahim JD, Bugeja L, Ranson D. Causes of death determined in medicolegal investigations in residents of nursing homes: A systematic review. *J Am Geriatr Soc.* 2014; 62:1513–1526.
17. Kutter A, Singh JP, Rauh C & Delgado A. Improvement of the prediction of mouthfeel attributes of liquid foods by a posthumus funnel. *Journal of Texture Studies,* 2011, 41: 217–227.
18. Morley RE, Ludemann JP, Moxham JP, Kozak FK, Riding KH. Foreign body aspiration in infants and toddlers: recent trends in British Columbia. *J Otolaryngol* 2004; 33: 37–41.
19. Mu L, Ping H, Sun D. Inhalation of foreign bodies in Chinese children: a review of 400 cases. *Laryngoscope* 1991; 101: 657–660.
20. Murdan S. Transverse fingernail curvature in adults: a quantitative evaluation and the influence of gender, age and hand size and dominance. *Int J Cosmet Sci,* 2011, 33:509–513.
21. National Patient Safety Agency, Royal College Speech and Language Therapists, British Dietetic Association, National Nurses Nutrition Group, Hospital Caterers Association. *Dysphagia diet food texture descriptions.* 2011. <http://www.ndruk.org/Generalnews/dysphagia-diet-food-texture-descriptors.html>, Accessed 29 April 2011.
22. O’Leary M, Hanson B, Smith C. Viscosity and non-Newtonian features of thickened fluids used for dysphagia therapy. *J of Food Sci,* 2010: 75(6): E330–E338.

23. Peyron MA, Mishellany A, Woda A. Particle size distribution of food boluses after mastication of six natural foods. *J Dent Res*, 2004; 83:578–582.
24. Rimell FL, Thome A Jr, Stool S, Reilly JS, Rider G, Stool D, Wilson CL. Characteristics of objects that cause choking in children. *JAMA* 1995; 274: 1763–6.
25. Seidel JS, Gausche-Hill M. Lychee-flavoured gel candies. A potentially lethal snack for infants and children. *Arch Pediatr Adolesc Med* 2002; 156: 1120–22.
26. Sopade PA, Halley PJ, Cichero JAY, Ward LC. 2007. Rheological characterization of food thickeners marketed in Australia in various media for the management of dysphagia. I: water and cordial. *J Food Eng* 79:69–82.
27. Sopade PA, Halley PJ, Cichero JAY, Ward LC, Liu J, Teo KH. 2008a. Rheological characterization of food thickeners marketed in Australia in various media for the management of dysphagia. II. Milk as a dispersing medium. *J Food Eng* 84(4):553–62.
28. Sopade PA, Halley PJ, Cichero JAY, Ward LC, Liu J, Varlivi S. 2008b. Rheological characterization of food thickeners marketed in Australia in various media for the management of dysphagia. III. Fruit juice as a dispersing medium. *J Food Eng* 86(4):604–15.
29. Steele CM, Alsanei WA, Ayanikalath S, Barbon CE, Chen J, Cichero JA, et al. The influence of food texture and liquid consistency modification on swallowing physiology and function: A systematic review. *Dysphagia*. 2015; 30: 2-26.
30. Steele, C., Molfenter, S., Péladeau-Pigeon, M., Polacco, R. and Yee, C. Variations in tongue-palate swallowing pressures when swallowing xanthan gum-thickened liquid. *Dysphagia*. 2014;29:1-7.
31. Turkistani A, Abdullah KM, Delvi B, Al-Mazroua KA. The 'best fit' endotracheal tube in children. *MEJ Anesth* 2009, 20:383-387.
32. Van Vliet T. On the relation between texture perception and fundamental mechanical parameters of liquids and time dependent solids. *Food Quality and Preference*, 2002: 227-236.
33. Woda, A, Nicholas E, Mishellany-Dutour A, Hennequin M, Mazille MN, Veyrune JL, Peyron MA. The masticatory normative indicator. *Journal of Dental Research*, 2010; 89(3): 281-285.
34. Wolach B, Raz A, Weinberg J, Mikulski Y, Ben Ari J, Sadan N. Aspirated bodies in the respiratory tract of children: eleven years experience with 127 patients. *Int J Pediatr Otorhinolaryngol* 1994; 30: 1–10.

The International Dysphagia Diet Standardisation Initiative in Chinese Traditional version

Chia-Chen Chang¹ Huei-Ying Chen² Huei-Rong Lee² Tsung-Hao Lin³
Pei-Chun Hsieh⁴ Yen-Yun Chang⁴ Li-Ling Chiu^{5,*}

Abstract

As the global population continues to age, dysphagia is becoming increasingly prevalent. According to research, an estimated total of approximately 1 million people potentially have swallowing disorders in Taiwan. Many countries are committed to developing various food texture standards; however, because of the terminology and level of complexity involved, a standard approach could not be successfully established. As a result, in 2013, the International Dysphagia Diet Standardisation Initiative Committee was established to develop the The International Dysphagia Diet Standardisation Initiative, a framework to satisfy different requirements of texture-modified foods and thickened liquids for individuals that has been translated and circulated in several languages. The initiative aims to help those experiencing dysphagia domestically understand the different levels of the framework and instructs them in the use of forks, chopsticks, syringes, and other common tools at home for the detection of food texture and consistency. This article is a continuation of the authorised version, translated into traditional Chinese, and includes information on domestic nutrition, rehabilitation, language therapy, texture, and food preparation, and experts have performed a content validity test. We hope to provide elderly people who experience difficulties due to dysphagia with a valuable point of reference.

Keywords: dysphagia, liquid, food, elderly people

¹ Department of senior citizen service business, college of human ecology and design, St. John's University

² Wise & Shine Nutrition Consultant Center

³ Division of General Medicine and Geriatric Medicine, Chang Gung Memorial Hospital at Linkou, Chang Gung University College of Medicine

⁴ Health Promotion Administration community Health Division

⁵ Department of Nutrition and Health Sciences, Research Center for Food and Cosmetic Safety, and Research Center for Chinese Herbal Medicine, College of Human Ecology, Chang Gung University of Science and Technology; Chang Gung Memorial Hospital at Linkou, Chang Gung University College of Medicine

* Correspondence author: Li-Ling Chiu

E-mail : llchiu@mail.cgu.edu.tw